Walt Lounsbery

ACC 3007

AIRCRAFT CONFIGURATION SYNTHESIS

PART II: AERODYNAMICS

PREPARED BY

W.B. GILLETTE

WM. McINTOSH

THE BOEING COMPANY

SEATTLE, WA.

EDITION 1

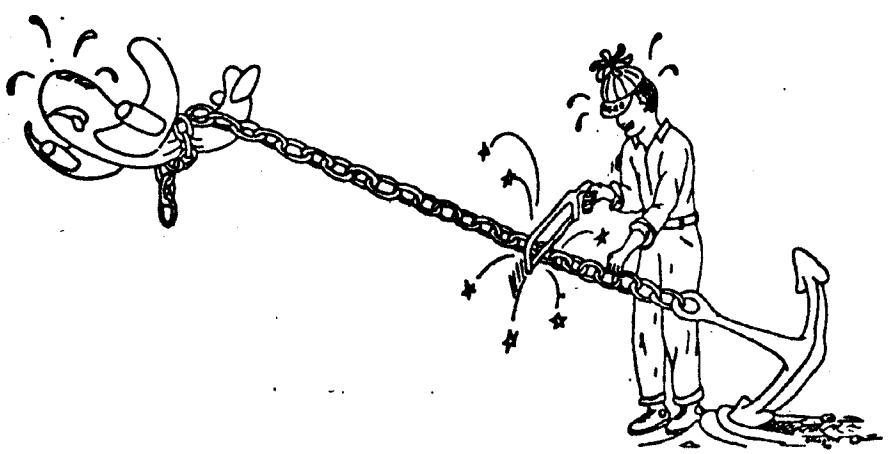

AIRCRAFT CONFIGURATION SYNTHESIS, PART II
COURSE OUTLINE

CHAPTER	CONTENTS	BY
1	INTRODUCTION: design overview, terms, equations, fluid mechanics review	G
2	2-D CRUISE AIRFOILS: theory, design, analysis; transonic airfoils; test procedures	G
3	2-D LOW-SPEED AIRFOILS: single & multiple element; design & test procedures	McI
4	SUBSONIC WINGS: wing theory, sweep theory, design choices, design procedures	G
5	SUBSONIC WING TESTING: test environment, procedures; performance testing	G
6	LOW SPEED WING DESIGN & TESTING: design procedures for multi-element wings; test techniques	McI
7	TRANSONIC & SUPERSONIC WINGS: design & test procedures; area rule	G
8	STABILITY & CONTROL CONSIDERATIONS: empennage design, control devices; test procedures	McI
9	ENGINE INSTALLATION DESIGN: types of installations, inlet design, afterbody design	G
10	ENGINE INSTALLATION TESTING: thrust-drag bookkeeping, powered models, calibration	G
11	OTHER CONFIGURATION DETAILS: cabs, winglets, fairings, local area rule, etc.	G
12	FLIGHT TESTING: predicting & measuring flight performance, inflight diagnosis techniques	McI

COURSE GOALS:
1. DESCRIBE AERODYNAMIC PRINCIPLES THAT AFFECT CONFIGURATION CHOICES.
2. OUTLINE DESIGN PROCEDURES FOR CONTOUR DESIGN.
3. REFER TO SELECTED ANALYSIS & DESIGN COMPUTER PROGRAMS.

AFTER-HOURS AERO COURSES

COURSE	CONTENT	INTENDED FOR
AERODYNAMICS FOR ENGINEERS (J. Lee/E. Tinoco)	Explanation of basic concepts in Aerodynamics; develops a general theoretical background. Prepares non-aerodynamicists for further Aero courses.	All Staffs
AIRPLANE PERFORMANCE (A. Ginter)	Describes how the performance of an aircraft is computed in all flight regimes. Gives general background in aircraft performance.	All Staffs
AIRCRAFT CONFIGURATION SYNTHESIS-PART II (W. Gillette, W. McIntosh)	Discusses aerodynamic principles that affect configuration choices; tells how aerodynamic contours are designed.	All Staffs
AERODYNAMICS OF WINGS AND BODIES II (Dr. W. Chin)	Graduate level course, in three parts, intended to provide a comprehensive physical and mathematical understanding of modern aerodynamic theory.	Aerodynamicists only

CHAPTER 1. INTRODUCTORY CONCEPTS

CHAPTER 1. INTRODUCTORY CONCEPTS

1.1 INTRODUCTION

The purpose of this course is to give a general background into analysis, design and testing techniques for aircraft configuration types of interest to Boeing engineers. The perspective of that background will be from the configuration aerodynamicist's point of view. Table 1.1 defines the field of aerodynamic interest at Boeing for the configuration aerodynamicist. The job divisions shown in the Table are not traditional; the Table applies only to The Boeing Company, although other large aerospace firms may have similar job breakdowns.

The Boeing configuration aerodynamicist does not directly determine airloads, stability and control characteristics, aircraft performance or design complete engine installations. The principal responsibilities of the configuration aerodynamicist are detailed in Table 1.2; however, in the process of performing the principal assignments, the other areas of airloads, stability and control and airplane performance are touched on and a general knowledge of these areas is of value. Referring to Table 1.2, the configuration aerodynamist has four main duties. First, and throughout an assignment, it is his responsibility to provide lift and drag data to the performance engineer for airplane performance calculations, for which the configuration aerodynamicist prepares preliminary lift and drag curves. The second duty is to design the specific aerodynamic contours for the configuration. This step requires extensive use of analytical design procedures and numerical lofting programs. The third duty is to measure the actual performance of the aerodynamic contours by means of wind tunnel testing. Throughout the second and third duties, he may be required to update the lift and drag data given to the performance aerodynamicist. The final duty is to measure the aerodynamic results of the full scale aircraft.

Naturally, the first three duties are done much more often than is the last. And during these activities, the configuration aerodynamicist's primary preoccupation is drag. Figure 1.1 highlights the problem. Aerodynamic lift is usually achieved fairly easily, with the exception of low speed maximum performance, and little time is spent worrying about the lift of the configuration. Drag is entirely another matter. The design objective is nearly always to achieve the desired lift at the minimum drag. Most design decisions will be based on the question, will it reduce the drag? Then, extremely careful experimental techniques must be employed to get a true measure of the drag. Nearly all the agonies of wind tunnel testing will be associated with drag; very little will be devoted to the lift measurement. Figure 1.1 also shows that the configuration aerodynamicst must also remain aware of stability and control considerations, since his aerodynamic contours will in large part determine those characteristics.

In summary, the role of the configuration aerodynamicist is to predict the aerodynamic characteristics, design the contours, then test to verify the characteristics of the external aerodynamic contour of the aircraft. This course will outline the procedures whereby that role is fulfilled.

1.2 CONFIGURATION SELECTION PROCESS

The time when one individual would choose the shape and size of the wing or the tail has long past from the large aircraft design environment. Today, those selections and other key geometric characteristics of an aircraft are either slowly realized after seemingly endless performance trade studies or by management (Vice President or higher) decree. The configuration aerodynamicist's role in this process is limited to producing drag polars, pitching moment curves and maximum l'ft predictions for candidate designs.

The procedure whereby the aerodynamic, weights, flight controls and propulsion characteristics are combined and matched against customer desires and constraints is complex and will not be described herein. Several attempts have been made to characterize the general process; one of the most thorough attempts is described in the IPAD feasibility documents (Ref. 1.1).

In general, the result of the Staff inputs will be displayed as "thumbprint" charts, an example of which is shown on Figure 1.2. This type of graph provides a visualization of the design space for the wing, for example. For a given wing sweep, etc., an optimum wing area and its performance can be selected. Other thumbprints allow a trade of best performance versus wing sweep to be drawn. Thus, the best wing sweep for the design mission can be selected. All principal aircraft dimensions will be chosen in this manner. When the configuration aerodynamicist is told to design the wing, the sweep, aspect ratio, area, thickness and type of wing section will have already been chosen. The remaining task will be to find a three-dimensional wing section description which will attain the desired lift objective at minimum drag.

In recognition of the current method of design selection, this course will not attempt to describe further how the configuration design parameters are achieved. The course will concentrate on how the aerodynamic contours which produce the needed performance will be designed and tested.

1.3 FUNDAMENTALS

A consistent definition of terms, equations and physical units is necessary before the main content of this course can begin. This will also provide a review of certain fundamentals which may not have been used for some time.

1.3.1 Equation of State

The relationship between pressure, temperature and density of a non-reacting gas is given by:

$$P = g R \rho T \tag{1.1}$$

where

P= pressure , lbf/ft^2
g= gravitational constant = 32.174 $lbm \cdot ft / lbf \cdot sec^2$
R= gas constant = 53.35 $lbf\text{-}ft / lbm\,^\circ R$ (air)
ρ= density in $lbf\,sec^2/ft^2$ (= lbm/ft^3)
T= absolute temperature in $^\circ R$

1.3.1 Equation of State (continued)

Example: If $\rho = 2.377 \times 10^{-3}$ lbm $/ft^3$ and
$T = 518.67\ ^\circ R$

then $P = (32.174)(53.35)(2.377 \times 10^{-3})(518.67)$

$= 2116.22$ lbf $/ft^2$

1.3.2 Reference Conditions; Standard Atmosphere

Rearranging equation (1.1) shows that different states of a gas are related by:

$$\frac{\rho_1 T_1}{P_1} = \frac{\rho_2 T_2}{P_2} \tag{1.2}$$

In aerodynamics, reference conditions are necessary as a basis to perform comparable calculations. By definition, conditions representing average sea level conditions have been agreed as follows:

SEA LEVEL REFERENCE CONDITIONS

$$P = 2116.22 \text{ lbf}/ft^2$$
$$\rho = 2.377 \times 10^{-3} \text{ lbf sec}^2/ft^4 \quad (\text{lbm}/ft^3)$$
$$T = 518.67\ ^\circ R \tag{1.3}$$

With the condition that the velocity is zero

However, these conditions apply only at sea level on this "standard day." A model atmosphere is used to state how these quantities change with altitude. Table 1.3 gives values of P, ρ and T for the 1956 ARDC atmosphere. Also contained are several ratios which will appear in subsequent equations:

TEMPERATURE: $\theta = T / T_{SL}$

PRESSURE: $\delta = P / P_{SL}$ (1.4)

DENSITY: $\sigma = \rho / \rho_{SL} = \delta / \theta$

1.3.3 Velocity Effects on Fluid Properties

The atmospheric conditions detailed in Table 1.3 are for the atmosphere at rest. As the fluid gains velocity, the fluid properties change from those at rest. The way the properties change are best characterized by the Mach number of the flowing fluid:

$$M = V/a \tag{1.5}$$

1.3.3 Velocity Effects on Fluid Properties (continued)

where V = fluid velocity in ft/sec

a = local speed of sound in ft/sec

The local speed of sound in turn depends only on local temperature:

$$a = \sqrt{g R \gamma T} \quad \text{ft/sec}$$

$$= 49.02\sqrt{T} \quad \text{ft/sec} \quad \text{for air} \tag{1.6}$$

where g = gravitational constant = 32.174

R = gas constant = 53.35 lbt - ft/lbm^{o}R

γ = specific heat ratio = 1.400

T = local fluid temperature ^{o}R

The relationships between fluid properties at rest and when the fluid is in motion at some Mach number, M, are given by:

$$\text{TEMPERATURE:} \quad T_s/T_o = \left(1 + \frac{\gamma-1}{2} M^2\right)^{-1}$$

$$\text{PRESSURE:} \quad P_s/P_o = \left(1 + \frac{\gamma-1}{2} M^2\right)^{\frac{-\gamma}{\gamma-1}} \tag{1.7}$$

$$\text{DENSITY:} \quad \rho_s/\rho_o = \left(1 + \frac{\gamma-1}{2} M^2\right)^{\frac{-1}{\gamma-1}}$$

where the subscript ( )s denotes the property of the fluid in motion and the subscript ( )$_o$ denotes the fluid property at rest. These relationships apply to adiabatic and isentropic flow, and are collectively referred to as the isentropic flow equations.

The fluid condition at rest is often called stagnation condition, while those in motion are called static conditions. It is important to realize the relationship of these to ambient. For the real airplane, ambient conditions, such as those of Table 1.3, become static conditions. The airplane motion at speed V through the fluid, which is at rest, causes the airplane to sense total conditions as follows:

$$a = 49.02\sqrt{T_{ambient}} \sim \text{ft/sec}$$

$$M = V/a$$

$$T_o = \left(1 + \frac{\gamma-1}{2} M^2\right) \cdot T_{ambient} \sim {}^{o}R \tag{1.8}$$

$$P_o = \left(1 + \frac{\gamma-1}{2} M^2\right)^{\frac{\gamma}{\gamma-1}} \cdot P_{ambient} \sim \text{lbf/ft}^2$$

$$\rho_o = \left(1 + \frac{\gamma-1}{2} M^2\right)^{\frac{1}{\gamma-1}} \cdot \rho_{ambient} \sim \text{lbm/ft}^3$$

1.3.3 Velocity Effects on Fluid Properties (continued)

Most wind tunnels used by Boeing aerodynamicists are closed-circuit, continuous-run designs that utilize air exchange for cooling. Thus, some point in the circuit, usually just ahead of the stilling chamber upstream of the test section, is exposed to atmospheric conditions. Since the velocity there is very low, the tunnel circuit pressure there is essentially total pressure and is equal to ambient pressure. The tunnel total temperature is not equal to ambient, however, due to work done on the fluid by the tunnel fan. The ambient density will be determined by the perfect gas equation. So for the typical wind tunnel model, conditions sensed by the model follow the reverse equations from the real airplane:

$$T_s = \left(1 + \frac{\gamma-1}{2} M^2\right) \cdot T_o \sim {}^\circ R$$

$$P_s = \left(1 + \frac{\gamma-1}{2} M^2\right)^{\frac{-\gamma}{\gamma-1}} \cdot P_{AMBIENT} \sim lbf/ft^2 \qquad (1.9)$$

$$\rho_s = \frac{P_s}{g R T_s} \sim lbm/ft^3$$

where T_o must be measured in the tunnel stilling chamber and the test section Mach number is determined through tunnel calibrations. The distinction between ambient conditions for the airplane versus the wind tunnel model is important to understand, so Figure 1.3 has been included to further highlight the differences.

1.3.4 Area Effects on Fluid Properties

For flow through a confined region, such as in a nozzle, continuity of mass establishes a relationship between density, velocity and area. This can be blended with the isentropic flow equations above to produce a complete description of flow properties anywhere in the nozzle, under the condition that the flow remain isentropic. The effect of area change in the nozzle can be incorporated by reference to the area change that produces local sonic velocity. These formulae are contained in NACA 1135 (Ref. 1.2); further discussion of nozzle flow will be delayed until the session on engine installations (Session 9). However, the table of flow relationships from NACA 1135 through low subsonic speeds it reproduced herein as Table 1.4.

1.3.5 Shock Wave Effects on Fluid Properties

When fluid increases in velocity from subsonic flow to supersonic conditions, it does so without losses. But when supersonic flow decelerates, it does so through a shock wave. This discontinuous change of state is adiabatic, thus total temperature is conserved, but it is an irreversible process and is accompanied by an increase in entropy. For one dimensional flow (i.e., a planar shock, normal to the flow direction) the downstream flow will be subsonic. The change in fluid properties will be determined by the Mach number M_1 just upstream of the shock wave:

$$P_{o_2} = \left[\frac{(\gamma+1)M_1^2}{(\gamma-1)M_1^2+2}\right]^{\frac{\gamma}{\gamma-1}} \left[\frac{\gamma+1}{2\gamma M_1^2 - (\gamma-1)}\right]^{\frac{1}{\gamma-1}} P_{o_1}$$

$$T_{o_2} = T_{o_1} \qquad (1.10)$$

1.3.5 Shock Wave Effects on Fluid Properties

$$M_2 = \sqrt{\frac{(\gamma-1)M_1^2+2}{2\gamma M_1^2-(\gamma-1)}} \qquad (1.10)$$

(CONT.)

The subscript 2 denotes properties downstream of the shock wave. The above equations when used with the equation of state (eq. 1.1) and the isentropic flow relationships (eqns 1.7) yield a complete description of flow properties downstream of the normal shockwave.

In flows having more than one dimension, it is possible to have shocks that are other than normal. However, at the swept shock wave, conditions through the shock wave that are normal to the wave front will change, whereas those tangential to the wave fron will remain unchanged:

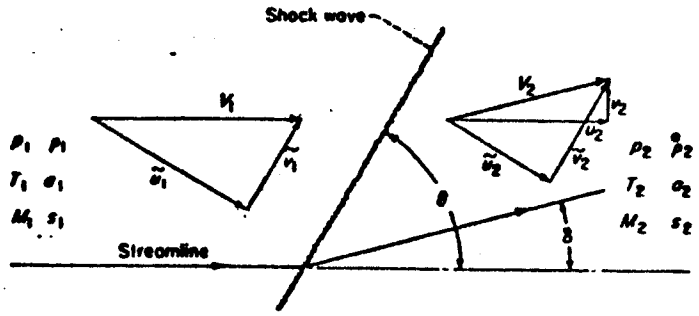

That is, u_2 will change from u_1 according to normal shock relationships, but u_2 will be the same as u_1. It is important to note that flow downstream of an oblique hock wave may still be supersonic. The relationships for flow across an oblique shock are quite complex; they are dealt with in detail in NACA 1135 (Ref. 1.2).

1.3.6 Energy (Bernoulli) Equation

The energy equation is usually stated for basic aerodynamics in a simplified form known as the Bernoulli equation. It is written in an incompressible form and a compressible form:

$$P_o = P_s + \tfrac{1}{2}\rho_s V^2 \quad \text{(incompressible Bernoulli)} \qquad (1.11)$$

where P_o = total pressure in lbf/ft^2

P_s = static pressure in lbf/ft^2

ρ_s = static density in $lbf\ sec^2/ft^4$ $(=slug/ft^3)$

V = velocity in ft/sec

EXAMPLE: IF $P_s = 2104.34$ lbf/ft²

$\rho = 2.377 \times 10^{-3}$ lbm/ft³

$V = 100$ ft/sec

then

$$P_o = 2104.34 + (0.5)(2.377 \times 10^{-3})(100)^2$$

$$= 2116.22 \text{ lbf/ft}^2$$

$$\frac{\gamma}{\gamma-1} P_o \frac{\rho_s}{\rho_o} = \frac{\gamma}{\gamma-1} P_s + \frac{1}{2} \rho_s V^2 \quad \text{(compressible Bernoulli)} \qquad (1.12)$$

where γ = ratio of specific heats = 1.4 for air

P_o = total pressure in lbf/ft²

ρ_s = static density in lbf sec²/ft⁴

ρ_o = total density in lbf sec²/ft⁴

P_s = static pressure in lbf/ft²

V = velocity in ft/sec.

Equations 1.2 and 1.3 have three parts to them. Using the concept of pressure, the left handside is denoted as the total pressure, the first term on the right-hand side is denoted as the static pressure, and the term containing velocity is denoted as the dynamic pressure. Strictly speaking, this nomenclature applies only to the incompressible Bernoulli, where the pressure concept expresses the total mechanical energy. It is customary, however, to denote the term $\frac{1}{2}\rho_s V^2$ as dynamic pressure in both compressible and incompressible flow.

It is often advantageous to define a static pressure coefficient, for use in regions of the fluid where the local velocity is other than free stream. The definition of this is:

$$C_p = \frac{p - p_s}{q_s} \tag{1.13}$$

where p = local static pressure, lbf/ft^2

P_s = reference static pressure, lbf/ft^2

q_s = reference dynamic pressure

$= \frac{1}{2}\rho_s V_s^2$

Pressure coefficient can be related to local Mach number through the isentropic equations, so that

$$C_p = \frac{2}{\gamma M_\infty^2}\left\{\left[\frac{2 + (\gamma-1)M_\infty^2}{2 + (\gamma-1)M_1^2}\right]^{\frac{\gamma}{\gamma-1}} - 1\right\} \tag{1.14}$$

where M_∞ = freestream Mach number

M_1 = local Mach number

or to local velocity,

$$C_p = \frac{2}{\gamma M_\infty^2}\left[\left\{1 - \frac{\gamma-1}{2}M_\infty^2\left[\left(\frac{U}{U_\infty}\right)^2 - 1\right]\right\}^{\frac{\gamma}{\gamma-1}} - 1\right] \tag{1.15}$$

where U = local velocity

U_∞ = freestream velocity

1.3.7 Scaling Laws

Since building prototypes of every candidate configuration is prohibitively expensive both in cost and time, the configuration aerodynamicist must rely on scale models tested in wind tunnels to provide the aerodynamic characteristics of aircraft configurations. Of the many scaling laws allowed by the Buckingham PI theorem, only three are essential to aerodynamic scaling. These are:

GEOMETRIC: $\frac{L_{model}}{L_{aircraft}}$ = SCALE FACTOR

COMPRESSIBLE: $\sqrt{\frac{\text{inertia force}}{\text{compressibility force}}} = \sqrt{\frac{\rho V^2/L}{\rho a^2/L}} = \frac{V}{a} \equiv$ MACH NUMBER

VISCOUS: $\frac{\text{inertia force}}{\text{friction force}} = \frac{\rho V L}{\mu} \equiv$ REYNOLDS NUMBER

where L = length

ρ = density

V = velocity

a = speed of sound

μ = absolute viscosity

If, for a model of a certain scale, the Mach number and Reynolds number are identical, then the forces on the model will be identically scaled from those on the fullscale geometry. In that regard, Mach number offers no problem, since it is independent of model dimensions. Unfortunately, Reynolds number has length as one of determining properties. In practice, the velocity V will have been chosen to match Mach number. For a model 1/20 of full size, the ratio of ρ/μ would have to change by a factor of 20 to preserve Reynolds number. This is not practical, with the exception of cryogenic concepts which are still under development. As a consequence, Reynolds number causes the greatest difficulty in model testing. Because of this, it will be discussed separately.

1.3.8 Reynolds Number Effects

A change in Reynolds number from full scale to model scale causes many changes in the flow on and about the configuration. Before discussing these, however, the calculation of Reynolds number and order of magnitude comparisons from model to full scale will be demonstrated. The definition of Reynolds number:

$$R_e = \frac{\rho V L}{\mu} \tag{1.16}$$

$$R_e = \frac{VL}{\nu} \tag{1.17}$$

1.3.8 Reynolds Number Effects (continued)

where ρ = static density, lbf sec^2/ft^4

V = static velocity, ft/sec

L = total length of object in flow direction, ft

μ = absolute static viscosity, lbfsec/ft^2

$\nu = \mu/\rho$ = kinematic static viscosity, ft^2/sec

The absolute viscosity is a function of temperature:

$$\mu = 2.270 \frac{T_s^{3/2}}{T_s + 198.6} \times 10^{-8} \quad \text{lbf} \cdot \text{sec}/\text{ft}^2 \tag{1.18}$$

where T_s = static temperature in $^\circ R$

Reynolds number is often quoted in a dimensional way, to allow rapid calculation of Reynolds numbers over different parts of the configuration. That is,

$$Re/_{ft} = \frac{\rho V}{\mu} \quad 1/ft \tag{1.19}$$

Tables of Reynolds number per foot can be made, and then only the reference length is needed for the particular aircraft or component. Two examples:

(1) at $M = 0.80$, $h = 30{,}000$ ft

$a = 995.1$ ft/sec
$\rho = 8.89 \times 10^{-4}$ lbf sec^2/ft^4
$T = 411.7\ ^\circ R$
} from Table 1.3

$$\mu = \frac{(2.270)(411.7)^{3/2}}{411.7 + 198.6} \times 10^{-8}$$

$$= 3.11 \times 10^{-7} \text{ lbf sec}/\text{ft}^2 \text{ (from EQ. 1.15)}$$

$$V = M \cdot a = (.80)(995.1)$$

$$= 796.1 \text{ ft/sec}$$

then, $$Re/_{ft} = \frac{(8.89 \times 10^{-4})(796.1)}{3.11 \times 10^{-7}}$$

$$= 2.28 \times 10^6/ft \tag{1.20}$$

1.3.8 Reynolds Number Effects (continued)

(2) in the Boeing Transonic Wind Tunnel at M=0.80

$T_o = 621.7^\circ R$

$P_o = 2150 \ lbf/ft^2$

$T_s = .8865 \ T_o = 551.1^\circ R$

$P_s = 0.656 \ P_o = 1410 \ lbf/ft^2$

} from Table 1.4

$\rho_s = \frac{P_s}{gRT_s} = 1.491 \times 10^{-3} \ lbf\,sec^2/ft^4$ (eq. 1.1)

$\mu_s = 3.917 \times 10^{-7} \ lbf\,sec/ft^2$ (eq. 1.15)

$a = 49.02\sqrt{T_s}$

$= 1151 \ ft/sec$

$V = (0.80)(1151) = 921 \ ft/sec$

then, $Re/ft = \frac{(1.491 \times 10^{-3})(921)}{3.917 \times 10^{-7}}$

$= 3.51 \times 10^6 /ft$ (1.21)

For a section of the 747 wing having a chord of 40 feet, the Reynolds number in flight would be, from (1.20),

$$Re_{\text{full scale}} = (2.28 \times 10^6)(40) = 91.2 \times 10^6 \quad (1.22)$$

In contrast, for an 0.06 scale model in BTWT, the Reynolds number would be, from (1.21)

$$Re_{\text{model scale}} = (3.51 \times 10^6)(40)(.06) = 8.40 \times 10^6 \quad (1.23)$$

P. 1.11

1.3.8 Reynolds Number Effects (continued)

These examples show that the model Reynolds number is less than 10% of the full scale value.

For ease of calculation, values of Reynolds number per foot versus altitude and Mach number are given on Figure 1.4. Values of Reynolds number per foot versus speed are shown on Figure 1.5 for BTWT, UWAL and BLSRT.

The first way in which lack of full scale Reynolds number affects model data is in the value of skin friction drag felt by the surface of the configuration. Figure 1.5 gives curves of flat plate turbulent skin friction versus chord Reynolds number for various Mach numbers. Note that for the examples of (1.22) and (1.23), the skin friction is 0.00198 for the full scale aircraft, but 0.00286 for the wind tunnel model. On a normalized basis, the drag of the model would be almost fifty percent larger than the full-scale aircraft. This difference must be allowed for; Chapter 5 will describe ways in which corrections are attempted.

The above difference would be the result for the case where both model and full scale geometries had fully turbulent boundary layers. But most boundary layers begin life as laminar, whose drag is about half that of a turbulent boundary layer. But laminar boundary layers exist only at low Reynolds numbers. This means that the wind tunnel model may have much of its surface covered by laminar boundary layers, in contrast to the full scale airplane, whose surface will be almost entirely covered by turbulent boundary layers. Procedures for correcting this situation will also be considered in Chapter 5.

The third way in which Reynolds number differences interfere with proper aerodynamic scaling is in the growth rate of the boundary layer. The presence of the boundary layer alters slightly the pressure distribution on the surface; a thick boundary layer has a large effect, a thin boundary layer has little effect. For the pressures on a model wing to be the same as on a full scale wing, the ratio of boundary layer thickenss to wing chord must be the same. But boundary layer growth is approximated by these formulae:

$$\text{(1) Laminar: } \delta = \frac{5.2\,x}{Re^{1/2}} \quad ft$$

$$\text{(2) turbulent: } \delta = \frac{0.37\,x}{Re^{1/5}} \quad ft \qquad (1.24)$$

where x = distance from leading edge, ft

Re = Reynolds number based on total length

For the previous example, the trailing edge condition for full scale would be:

$$\delta_{\text{full scale}} = \frac{(0.37)(40)}{(91.2 \times 10^6)^{1/5}} = 0.38 \text{ ft}$$

$$\delta/L = \frac{0.38}{40} = 0.95\%$$

P 1.12

1.3.8. Reynolds Number Effects (continued)

FOR MODEL SCALE:

$$\delta_{\text{model scale}} = \frac{(0.37)(40)(.06)}{(8.4 \times 10^6)^{1/5}}$$

$$= 0.037 \text{ ft}$$

$$\delta/L = \frac{0.037}{(40)(.06)} = 1.53\%$$

The boundary layer on the model is seen to be almost twice too thick. This will be dealt with further in Chapter 5.

The fourth way in which lack of Reynolds number scaling affects model data is because the point where a boundary layer separates in an adverse situation is dependent on Reynolds number. For the same pressure gradient, a thick boundary layer will separate before a thinner one. This means that wind tunnel models will experience separations that the full scale geometry may not. This is an effect which cannot be corrected for.

To summarize, the Reynolds number difference from model to full scale is the most serious difficulty of model testing. An extensive art has arisen to work around the problem; that art will be described in detail throughout this course.

1.3.9 Aircraft Forces and Moments

The configuration aerodynamicist at Boeing is principally concerned with configurations that are in steady, unaccelerated flight. For this course, definitions of the three principal forces and three moments will be sufficient; the equations of motion will not be needed. Throughout the course, coefficients will be used for each:

LIFT: $C_L = \frac{L}{qS}$

DRAG: $C_D = \frac{D}{qS}$

SIDE FORCE: $C_Y = \frac{Y}{qS}$

PITCHING MOMENT: $C_M = \frac{M}{qS\bar{c}}$

YAWING MOMENT: $C_n = \frac{N}{qSb}$

ROLLING MOMENT: $C_\ell = \frac{L'}{qSb}$

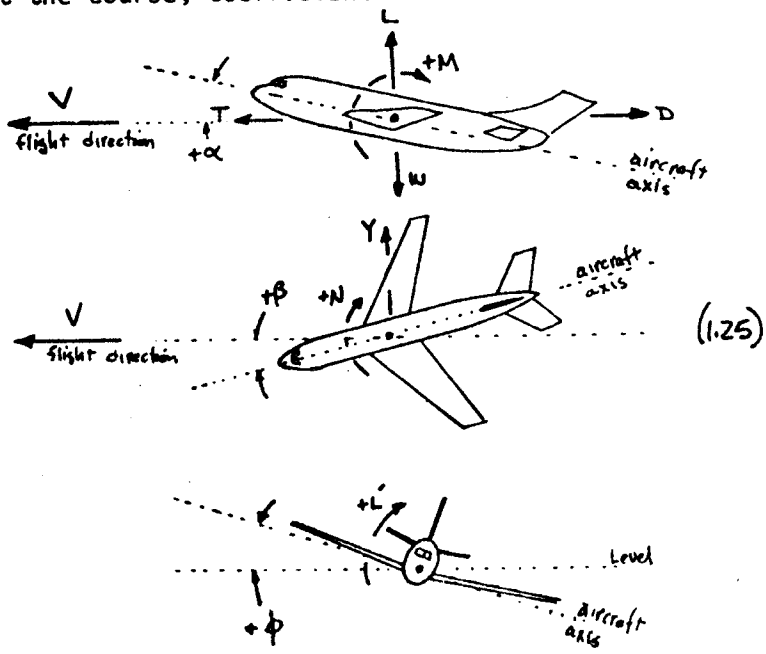

(1.25)

P 1.13

1.3.9 Aircraft Forces and Moments (continued)

where:
- L = lift, lbs
- D = drag, lbs
- Y = side force, lbs
- M = pitching moment, ft-lbs
- N = yawing moment, ft-lbs
- L' = rolling moment, ft-lbs
- W = weight
- q = dynamic pressure
  - = $\frac{1}{2} \rho V^2$ lbf/ft^2
- S = wing reference area, ft^2
- $\bar{c}$ = aerodynamic reference chord, ft
- b = wing span, ft
- T = thrust

1.3.10 Performance Equations

The configuration aerodynamicist works with the knowledge that more lift and less drag are the correct directions for design efforts. The performance calculation procedure is quite involved and will not be dealt with in this course. However, the basic range and endurance equations will be summarized in order to demonstrate their implications on configuration design:

$$\text{RANGE} = \left(\frac{V}{TSFC}\right)\left(\frac{L}{D}\right) \ln \frac{W_1}{W_2}$$

$$= \underbrace{W \ \frac{NAM}{LB}}_{\text{"RANGE FACTOR"}} \ln\left(\frac{W_1}{W_2}\right) \qquad (1.26)$$

$$\text{ENDURANCE} = \frac{1}{TSFC}\left(\frac{L}{D}\right) \ln\left(\frac{W_1}{W_2}\right)$$

$$= \frac{W}{W_f} \ln\left(\frac{W_1}{W_2}\right) \qquad (1.27)$$

where:
- V = velocity in knots
- TSFC = Thrust specific fuel consumption, lbm fuel/hr/lbf thrust
- (L/D) = ratio of lift to drag at cruise, lbm/lbf
- W_1 = weight at start of cruise
- W_2 = weight at end of cruise
- W = aircraft gross weight, lbm
- W_f = fuel flow, lbm/hr

1.3.10 Performance Equations (continued)

Note the unusual mixture of dimensions, whereby L has been equated to weight in lbm, D has been equated to thrust in lbf. That is, the gravitational constant, g, is by custom buried in (L/D) and (TSFC), allowing use of this mixture of English units.

Range is often expressed in an alternate form where

$$\text{RANGE} = \left(\frac{a}{TSFC}\right)\left(M\,\frac{L}{D}\right) \ln \frac{w_1}{w_2} \qquad (1.28$$

where a = speed of sound, knots

M = mach number

The important difference between designing for range (the usual goal) or for endurance is that range depends on (L/D) and speed, whereas endurance depends only on (L/D). The objective is to maximize the aerodynamic efficiency (L/D) at the highest possible speed. For this reason, equation 1.28 is often used, whereby (ML/D) is optimized. Endurance, for example, wants to maximize (L/D), regardless of the speed involved.

Since the lift of the aircraft equals its weight, the task of optimizing L/D becomes one of reducing drag. Again, the point is that the configuration aerodynamicist is far more concerned with drag than lift.

1.4 METHODS OF ANALYSIS

Computer analysis, and increasingly, design by computer is an integral part of the configuration aerodynamicist's daily life. Specific techniques and particular computer programs will be described in detail in subsequent chapters. This section will briefly summarize the primary types of analysis programs that will be encountered.

1.4.1 Potential Flow

This encompasses a large range of flow situations which have constant total pressure, that is, equations which by and large, satisfy the Bernoulli equation (eqn's 1.11 and 1.12). Flow fields which obey this requirement will be ones which have no losses nor have any work done on them. Excluded from potential flow solutions are boundary layers, shock waves, and propulsive devices which add work to the flow field. Other than these limitations, there is no limitation on Mach number.

For subsonic flows where viscous effects are small and for supersonic flows over slender bodies, the equations for potential flow can be linearized. The aerodynamic nature of the flow field will be characterized by discrete sources and sinks, line vortices and doublets. The effect of each of these elements sums together to satisfy an equal number of boundary conditions, and the whole flow field to infinity can be determined. Because of the linearized form of the equations, a direct solution by matrix algebra, is performed. This means that for a given modelling of a stated problem, the answer is unique.

Potential flow programs are the mainstay of current analysis. There are a number of mature computer programs available at Boeing to cover geometries from airfoil sections to complete aircraft, from zero speed up to supersonic cruise Mach numbers. And since aircraft currently being designed by Boeing have very little separation on them and little transonic flow, the potential flow solution provides a result very close to experiements.

1.4.2 Transonic and Viscous Flow

There are areas, however, where potential flow is not fully satisfactory. The three primary areas are for wing sections and nacelle cowl shapes that have an imbedded supersonic region on them which terminates in a shock wave, and for boundary layers on the aft regions of the aircraft components which may be very near separation. For these kinds of flow fields, a "finite element" or discrete particle approach is taken. The component of interest is surrounded by a mesh of points, the equations of the fluid are formulated, and the flow properties at each point are solved iteratively. In essence, the solution is "relaxed" from an initial, arbitrary state to one in which the fluid properties at each mesh point are in equilibruim with these around it.

Relaxation and finite difference techniques can do very well at predicting non-linear effects which cannot be calculated by potential flow means. But they have several disadvantages. First, they are considerably more costly than equivalent potential flow solutions. Secondly, and more importantly, since these methods must converge to a result after a large number of iterations, there is no

exact answer, and a change in convergence procedures, initial conditions and solution constraints means that the final set of printout will not be unique. Another user may achieve a considerably different result for the same problem.

Despite these drawbacks, there are certain areas where relaxation solutions are an important analysis tool. These special uses will be described in subsequent chapters.

CHAPTER I REFERENCES

1.1 "Feasibility Study of an Integrated Program for Aerospace Vehicle Resign (IPAD)," Vol. II, The Design Process, W. B. Gillette, et al, D6-60181-2.

1.2 Report 1135, "Equations, Tables, and Charts for Compressible Flow," NACA - Ames Research Staff, 1953.

TABLE 1.1 AERODYNAMIC FIELDS OF INTEREST AT BOEING

FUNCTION	ASSIGNED TO	STAFF	
AIRPLANE PERFORMANCE	PERFORMANCE AERODYNAMICIST	AERODYNAMICS	
AIRPLANE CONFIGURATION CONTOUR DESIGN	CONFIGURATION AERODYNAMICIST	AERODYNAMICS	THIS COURSE
AIRPLANE PERFORMANCE CHARACTERISTICS	CONFIGURATION AERODYNAMICIST	AERODYNAMICS	
AIRPLANE FLIGHT CHARACTERISTICS	STABILITY & CONTROL AERODYNAMICIST	FLIGHT CONTROLS	
COMPONENT AND SURFACE AIRLOADS	AIRLOADS AERODYNAMICIST	STRUCTURES	
FLUTTER	FLUTTER SPECIALIST	STRUCTURES	
PROPULSION SYSTEM INTERNAL AIRFLOW	PROPULSION SPECIALIST	PROPULSION	

TABLE 1.2 PRINCIPAL DUTIES OF THE CONFIGURATION AERODYNAMICIST

DUTY	TIME	
1. PROVIDE LIFT & DRAG CHARACTERISTICS FOR PERFORMANCE	20%	
2. DESIGN AND LOFT THE DETAILED AERODYNAMIC CONTOUR.	30%	THIS COURSE
3. DIRECT THE DESIGN, FABRICATION AND TESTING OF WIND TUNNEL MODELS.	40%	
4. PARTICIPATE IN FLIGHT TESTS TO DETERMINE THE AIRPLANE LIFT AND DRAG CHARACTERISTICS.	10%	

TABLE 1.3 1956 STANDARD ATMOSPHERE

Alt ft	Temp t °F	°R	°C	Press. P in. Hg	lb/ft²	$\frac{\rho}{\rho_o}=\sigma$	$\sqrt{\frac{\rho}{\rho_o}}$	$\frac{P}{P_o}=\delta$	$\frac{T}{T_o}=\theta$	$\sqrt{\frac{T}{T_o}}$	q/M^2	c ft/sec	c knots
0	+59.0	518.7	+15.0	29.92	2116.	1.000	1.000	1.000	1.000	1.000	1481.	1117	661.7
1000	+55.4	515.1	+13.0	28.86	2041.	.9711	.9854	.9644	.9931	.9965	1430.	1113	659.5
2000	+51.9	511.6	+11.0	27.82	1968.	.9428	.9710	.9298	.9862	.9931	1378.	1109	657.2
3000	+48.3	508.0	+9.1	26.82	1897.	.9151	.9566	.8962	.9794	.9896	1329.	1105	654.9
4000	+44.7	504.4	+7.1	25.84	1828.	.8881	.9424	.8637	.9725	.9862	1280.	1101	652.6
5000	+41.2	500.9	+5.1	24.90	1761.	.8617	.9283	.8320	.9656	.9826	1234.	1098	650.3
6000	+37.6	497.3	+3.1	23.98	1696.	.8359	.9143	.8014	.9587	.9791	1188.	1094	647.9
7000	+34.0	493.7	+1.1	23.09	1633.	.8106	.9003	.7716	.9519	.9757	1144.	1090	645.6
8000	+30.5	490.2	-0.8	22.22	1572.	.7860	.8864	.7428	.9450	.9721	1101.	1086	643.3
9000	+26.9	486.6	-2.8	21.39	1513.	.7620	.8729	.7148	.9381	.9686	1060.	1082	640.9
10000	+23.3	483.0	-4.8	20.58	1455.	.7385	.8594	.6877	.9312	.9650	1020.	1078	638.6
11000	+19.8	479.5	-6.8	19.79	1400.	.7156	.8459	.6614	.9244	.9615	980.6	1074	636.2
12000	+16.2	475.9	-8.8	19.03	1346.	.6932	.8326	.6360	.9175	.9579	942.9	1070	633.8
13000	+12.6	472.3	-10.8	18.29	1294.	.6713	.8193	.6113	.9106	.9543	906.3	1066	631.5
14000	+9.1	468.8	-12.7	17.58	1243.	.6500	.8062	.5875	.9037	.9506	870.9	1062	629.1
15000	+5.5	465.2	-14.7	16.89	1194.	.6292	.7932	.5643	.8969	.9470	836.6	1058	626.7
16000	+1.9	461.6	-16.7	16.22	1147.	.6090	.7804	.5420	.8900	.9434	803.5	1054	624.3
17000	-1.6	458.1	-18.7	15.57	1101.	.5892	.7676	.5203	.8831	.9397	771.4	1050	621.9
18000	-5.2	454.5	-20.7	14.94	1057.	.5699	.7549	.4994	.8762	.9361	740.3	1045	619.4
19000	-8.8	450.9	-22.6	14.34	1014.	.5511	.7424	.4791	.8694	.9324	710.3	1041	617.0
20000	-12.3	447.4	-24.6	13.75	972.5	.5328	.7299	.4595	.8625	.9287	681.3	1037	614.6
21000	-15.9	443.8	-26.6	13.18	932.4	.5150	.7176	.4406	.8556	.9250	653.2	1033	612.1
22000	-19.5	440.2	-28.6	12.64	893.7	.4976	.7054	.4223	.8487	.9212	626.1	1029	609.6
23000	-23.0	436.7	-30.6	12.11	856.3	.4806	.6933	.4045	.8419	.9176	599.9	1025	607.2
24000	-26.6	433.1	-32.5	11.60	820.2	.4642	.6813	.3876	.8350	.9138	574.6	1021	604.7
25000	-30.2	429.5	-34.5	11.10	785.3	.4481	.6694	.3711	.8281	.9100	550.2	1016	602.2
26000	-33.7	426.0	-36.5	10.63	751.6	.4325	.6576	.3552	.8212	.9062	526.6	1012	599.7
27000	-37.3	422.4	-38.5	10.17	719.1	.4173	.6460	.3398	.8144	.9024	503.8	1008	597.2
28000	-40.9	418.8	-40.5	9.725	687.8	.4025	.6344	.3250	.8075	.8986	481.8	1004	594.6
29000	-44.4	415.3	-42.5	9.297	657.6	.3881	.6230	.3107	.8006	.8948	460.7	999.4	592.1
30000	-48.0	411.7	-44.4	8.885	628.4	.3741	.6116	.2970	.7937	.8909	440.3	995.1	589.5
31000	-51.6	408.1	-46.4	8.488	600.3	.3605	.6004	.2837	.7869	.8871	420.6	990.7	587.0
32000	-55.1	404.6	-48.4	8.106	573.3	.3473	.5893	.2709	.7800	.8832	401.6	986.4	584.4
33000	-58.7	401.0	-50.4	7.737	547.2	.3345	.5784	.2586	.7731	.8793	383.4	982.0	581.8
34000	-62.2	397.4	-52.4	7.382	522.1	.3220	.5675	.2467	.7662	.8753	365.8	977.7	579.2
35000	-65.8	393.9	-54.3	7.041	498.0	.3099	.5568	.2353	.7594	.8714	348.8	973.3	576.6
36089	-69.7	390.0	-56.5	6.683	472.7	.2971	.5450	.2234	.7519	.8671	331.1	968.5	573.8
37000	-69.7	390.0	-56.5	6.397	452.4	.2844	.5333	.2138	.7519	.8671	317.0	968.5	573.8
38000	-69.7	390.0	-56.5	6.097	431.2	.2710	.5206	.2038	.7519	.8671	302.1	968.5	573.8
39000	-69.7	390.0	-56.5	5.811	411.0	.2583	.5082	.1942	.7519	.8671	287.9	968.5	573.8
40000	-69.7	390.0	-56.5	5.538	391.7	.2462	.4962	.1851	.7519	.8671	274.4	968.5	573.8
41000	-69.7	390.0	-56.5	5.278	373.3	.2346	.4844	.1764	.7519	.8671	261.5	968.5	573.8
42000	-69.7	390.0	-56.5	5.030	355.8	.2236	.4729	.1681	.7519	.8671	249.2	968.5	573.8
43000	-69.7	390.0	-56.5	4.794	339.1	.2131	.4616	.1602	.7519	.8671	237.6	968.5	573.8
44000	-69.7	390.0	-56.5	4.569	323.2	.2031	.4507	.1527	.7519	.8671	226.4	968.5	573.8
45000	-69.7	390.0	-56.5	4.355	308.0	.1936	.4400	.1455	.7519	.8671	215.8	968.5	573.8
46000	-69.7	390.0	-56.5	4.151	293.6	.1845	.4295	.1387	.7519	.8671	205.7	968.5	573.8
47000	-69.7	390.0	-56.5	3.956	279.8	.1758	.4193	.1322	.7519	.8671	196.0	968.5	573.8
48000	-69.7	390.0	-56.5	3.770	266.7	.1676	.4094	.1260	.7519	.8671	186.8	968.5	573.8
49000	-69.7	390.0	-56.5	3.593	254.1	.1597	.3996	.1201	.7519	.8671	178.0	968.5	573.8
50000	-69.7	390.0	-56.5	3.425	242.2	.1522	.3901	.1145	.7519	.8671	169.7	968.5	573.8
51000	-69.7	390.0	-56.5	3.264	230.8	.1451	.3809	.1091	.7519	.8671	161.7	968.5	573.8
52000	-69.7	390.0	-56.5	3.111	220.0	.1383	.3719	.1040	.7519	.8671	154.1	968.5	573.8
53000	-69.7	390.0	-56.5	2.965	209.7	.1318	.3630	.09909	.7519	.8671	146.9	968.5	573.8
54000	-69.7	390.0	-56.5	2.826	199.8	.1256	.3544	.09444	.7519	.8671	140.0	968.5	573.8
55000	-69.7	390.0	-56.5	2.693	190.5	.1197	.3460	.09001	.7519	.8671	133.4	968.5	573.8
56000	-69.7	390.0	-56.5	2.567	181.5	.1141	.3378	.08578	.7519	.8671	127.2	968.5	573.8
57000	-69.7	390.0	-56.5	2.446	173.0	.1087	.3297	.08176	.7519	.8671	121.2	968.5	573.8
58000	-69.7	390.0	-56.5	2.331	164.9	.1036	.3219	.07792	.7519	.8671	115.5	968.5	573.8
59000	-69.7	390.0	-56.5	2.222	157.2	.09877	.3143	.07426	.7519	.8671	110.1	968.5	573.8
60000	-69.7	390.0	-56.5	2.118	149.8	.09414	.3068	.07078	.7519	.8671	104.9	968.5	573.8
61000	-69.7	390.0	-56.5	2.018	142.8	.08972	.2995	.06746	.7519	.8671	100.0	968.5	573.8
62000	-69.7	390.0	-56.5	1.924	136.1	.08551	.2924	.06429	.7519	.8671	95.31	968.5	573.8
63000	-69.7	390.0	-56.5	1.833	129.7	.08150	.2855	.06127	.7519	.8671	90.84	968.5	573.8
64000	-69.7	390.0	-56.5	1.747	123.6	.07767	.2787	.05840	.7519	.8671	86.58	968.5	573.8
65000	-69.7	390.0	-56.5	1.665	117.8	.07403	.2721	.05566	.7519	.8671	82.52	968.5	573.8
66000	-69.7	390.0	-56.5	1.587	112.3	.07055	.2656	.05305	.7519	.8671	78.64	968.5	573.8
67000	-69.7	390.0	-56.5	1.513	107.0	.06724	.2593	.05056	.7519	.8671	74.95	968.5	573.8
68000	-69.7	390.0	-56.5	1.442	102.0	.06409	.2532	.04819	.7519	.8671	71.44	968.5	573.8
69000	-69.7	390.0	-56.5	1.374	97.19	.06108	.2471	.04592	.7519	.8671	68.08	968.5	573.8
70000	-69.7	390.0	-56.5	1.310	92.63	.05821	.2413	.04377	.7519	.8671	64.89	968.5	573.8
71000	-69.7	390.0	-56.5	1.248	88.28	.05548	.2355	.04172	.7519	.8671	61.84	968.5	573.8
72000	-69.7	390.0	-56.5	1.190	84.14	.05288	.2300	.03976	.7519	.8671	58.94	968.5	573.8
73000	-69.7	390.0	-56.5	1.134	80.19	.05040	.2245	.03789	.7519	.8671	56.18	968.5	573.8
74000	-69.7	390.0	-56.5	1.081	76.43	.04803	.2192	.03611	.7519	.8671	53.54	968.5	573.8
75000	-69.7	390.0	-56.5	1.030	72.84	.04578	.2140	.03442	.7519	.8671	51.03	968.5	573.8
76000	-69.7	390.0	-56.5	.9815	69.42	.04363	.2089	.03280	.7519	.8671	48.63	968.5	573.8
77000	-69.7	390.0	-56.5	.9355	66.16	.04158	.2039	.03127	.7519	.8671	46.35	968.5	573.8
78000	-69.7	390.0	-56.5	.8916	63.06	.03963	.1991	.02980	.7519	.8671	44.18	968.5	573.8
79000	-69.7	390.0	-56.5	.8497	60.10	.03777	.1943	.02840	.7519	.8671	42.10	968.5	573.8
80000	-69.7	390.0	-56.5	.8099	57.28	.03600	.1897	.02707	.7519	.8671	40.13	968.5	573.8
81000	-69.7	390.0	-56.5	.7718	54.59	.03431	.1852	.02580	.7519	.8671	38.24	968.5	573.8
82021	-69.7	390.0	-56.5	.7349	51.98	.03267	.1807	.02456	.7519	.8671	36.41	968.5	573.8
83000	-68.1	391.6	-55.6	.7012	49.59	.03104	.1762	.02343	.7550	.8689	34.74	970.5	575.0
84000	-66.4	393.3	-54.7	.6685	47.28	.02947	.1717	.02234	.7582	.8707	33.12	972.5	576.2
85000	-64.8	394.9	-53.8	.6374	45.08	.02798	.1673	.02130	.7613	.8725	31.58	974.5	577.4
86000	-63.2	396.5	-52.9	.6079	43.00	.02658	.1630	.02032	.7645	.8744	30.12	976.6	578.6
87000	-61.5	398.2	-51.9	.5799	41.02	.02525	.1589	.01938	.7677	.8762	28.73	978.6	579.8
88000	-59.9	399.8	-51.1	.5533	39.13	.02399	.1549	.01849	.7708	.8780	27.42	980.6	581.0
89000	-58.2	401.5	-50.1	.5280	37.35	.02280	.1510	.01765	.7740	.8798	26.16	982.6	582.2
90000	-56.6	403.1	-49.2	.5040	35.65	.02167	.1472	.01684	.7772	.8816	24.97	984.6	583.4
91000	-54.9	404.8	-48.3	.4811	34.03	.02061	.1436	.01606	.7804	.8834	23.84	986.6	584.6
92000	-53.3	406.4	-47.4	.4594	32.49	.01960	.1400	.01545	.7835	.8852	22.76	988.6	585.7
93000	-51.6	408.1	-46.4	.4387	31.03	.01864	.1365	.01466	.7867	.8870	21.74	990.6	586.9
94000	-50.0	409.7	-45.6	.4191	29.64	.01773	.1332	.01401	.7899	.8888	20.76	992.6	588.1
95000	-48.3	411.4	-44.6	.4004	28.32	.01687	.1299	.01338	.7931	.8906	19.84	994.6	589.3
100000	-40.1	419.6	-40.1	.3195	22.60	.01320	.1149	.01068	.8089	.8994	15.83	1005	595.2
110000	-23.7	436.0	-30.9	.2062	14.58	.008196	.09053	.006890	.8407	.9170	10.21	1024	606.7
120000	-7.19	452.5	-21.8	.1352	9.561	.005179	.07197	.004518	.8724	.9340	6.698	1043	618.1
130000	+9.27	469.0	-12.6	.09000	6.365	.003327	.05768	.003008	.9041	.9508	4.459	1062	629.2
140000	+25.7	485.4	-3.50	.06076	4.297	.002170	.04658	.002031	.9359	.9674	3.011	1081	640.2
150000	+42.2	501.9	+5.67	.04156	2.940	.001436	.03789	.001389	.9676	.9837	2.059	1099	650.9
160000	+49.1	508.8	+9.5	.02872	2.032	.000979	.03128	.000960	.9809	.9904	1.423	1106	655.4
170000	+49.1	508.8	+9.5	.01987	1.406	.000677	.02602	.000664	.9809	.9904	.9846	1106	655.4
180000	+36.0	495.7	+2.2	.01371	0.9695	.000479	.02190	.000458	.9557	.9776	.6792	1092	646.9
190000	+14.8	474.3	-9.7	.00932	0.6587	.000340	.01845	.000311	.9144	.9562	.4615	1068	632.8
200000	-6.78	452.9	-21.5	.00621	0.440	.000238	.01542	.000208	.8732	.9345	2.059	1044	650.9

24

TABLE 1.4 COMPRESSIBLE FLOW

$\gamma = 7/5$

M	$\frac{p}{p_t}$	$\frac{\rho}{\rho_t}$	$\frac{T}{T_t}$	θ	$\frac{q}{p_t}$	$\frac{A}{A^*}$	$\frac{V}{a_t}$
0	1.0000	1.0000	1.0000	0	0	∞	0
.01	.9999	1.0000	1.0000	.0068	.0100	57.8738	.0101
.02	.9997	.9998	.9998	.0137	.0200	28.9421	.0201
.03	.9991	.9993	.9995	.0205	.0300	19.3004	.0302
.04	.9980	.9987	.9992	.0273	.0399	14.4816	.0402
.05	.9970	.9980	.9990	.0341	.0499	11.5914	.0503
.06	.9955	.9970	.9985	.0409	.0598	9.6630	.0603
.07	.9944	.9960	.9984	.0477	.0697	8.2915	.0703
.08	.9930	.9948	.9982	.0545	.0796	7.2616	.0803
.09	.9916	.9940	.9976	.0613	.0895	6.4613	.0904
.10	.9903	.9928	.9975	.0681	.0994	5.8218	.1004
.11	.9888	.9916	.9972	.0749	.1093	5.2992	.1104
.12	.9864	.9903	.9961	.0817	.1192	4.8643	.1205
.13	.9844	.9888	.9956	.0885	.1290	4.4999	.1305
.14	.9823	.9873	.9949	.0953	.1388	4.1924	.1406
.15	.9798	.9857	.9941	.1021	.1486	3.9103	.1506
.16	.9777	.9840	.9934	.1089	.1584	3.6727	.1607
.17	.9753	.9822	.9926	.1157	.1681	3.4615	.1708
.18	.9728	.9803	.9918	.1225	.1778	3.2779	.1809
.19	.9702	.9783	.9910	.1293	.1875	3.1193	.1910
.20	.9675	.9764	.9901	.1361	.1972	2.9813	.2011
.21	.9647	.9743	.9892	.1429	.2068	2.8593	.2113
.22	.9619	.9722	.9883	.1497	.2164	2.7508	.2214
.23	.9589	.9700	.9874	.1565	.2260	2.6539	.2315
.24	.9559	.9678	.9864	.1633	.2355	2.5670	.2417
.25	.9528	.9655	.9854	.1701	.2450	2.4885	.2518
.26	.9496	.9632	.9844	.1769	.2544	2.4174	.2620
.27	.9464	.9608	.9833	.1837	.2638	2.3528	.2721
.28	.9430	.9584	.9822	.1905	.2731	2.2936	.2823
.29	.9397	.9559	.9811	.1973	.2824	2.2393	.2925
.30	.9362	.9534	.9800	.2041	.2917	2.1894	.3026
.31	.9326	.9508	.9788	.2109	.3009	2.1433	.3128
.32	.9290	.9482	.9777	.2177	.3100	2.1007	.3230
.33	.9253	.9455	.9765	.2245	.3191	2.0612	.3332
.34	.9216	.9428	.9753	.2313	.3282	2.0245	.3434
.35	.9177	.9400	.9741	.2381	.3372	1.9904	.3536
.36	.9138	.9371	.9729	.2449	.3462	1.9586	.3638
.37	.9098	.9342	.9717	.2517	.3551	1.9289	.3740
.38	.9057	.9312	.9704	.2585	.3640	1.9012	.3842
.39	.9016	.9282	.9692	.2653	.3728	1.8753	.3944
.40	.8974	.9251	.9679	.2721	.3816	1.8512	.4046
.41	.8932	.9220	.9666	.2789	.3904	1.8285	.4148
.42	.8889	.9188	.9653	.2857	.3991	1.8073	.4250
.43	.8845	.9155	.9640	.2925	.4078	1.7873	.4352
.44	.8801	.9122	.9627	.2993	.4164	1.7685	.4454
.45	.8756	.9089	.9613	.3061	.4250	1.7508	.4556
.46	.8711	.9055	.9600	.3129	.4336	1.7341	.4658
.47	.8665	.9021	.9586	.3197	.4421	1.7184	.4760
.48	.8619	.8986	.9572	.3265	.4506	1.7035	.4862
.49	.8572	.8951	.9558	.3333	.4590	1.6895	.4964
.50	.8525	.8916	.9543	.3401	.4674	1.6762	.5066
.51	.8477	.8880	.9529	.3469	.4757	1.6637	.5168
.52	.8430	.8844	.9514	.3537	.4840	1.6518	.5270
.53	.8382	.8807	.9499	.3605	.4923	1.6405	.5372
.54	.8333	.8770	.9484	.3673	.5005	1.6298	.5474
.55	.8284	.8732	.9469	.3741	.5087	1.6197	.5576
.56	.8235	.8694	.9454	.3809	.5168	1.6102	.5678
.57	.8185	.8656	.9438	.3877	.5249	1.6011	.5780
.58	.8135	.8617	.9423	.3945	.5329	1.5926	.5882
.59	.8085	.8578	.9407	.4013	.5409	1.5845	.5984
.60	.8035	.8538	.9392	.4081	.5488	1.5768	.6086
.61	.7984	.8498	.9376	.4149	.5567	1.5696	.6188
.62	.7933	.8458	.9360	.4217	.5645	1.5628	.6290
.63	.7881	.8417	.9344	.4285	.5723	1.5564	.6392
.64	.7829	.8376	.9328	.4353	.5800	1.5504	.6494
.65	.7777	.8334	.9312	.4421	.5877	1.5447	.6596
.66	.7725	.8292	.9296	.4489	.5953	1.5395	.6698
.67	.7672	.8250	.9280	.4557	.6029	1.5346	.6800
.68	.7619	.8207	.9263	.4625	.6104	1.5301	.6902
.69	.7566	.8164	.9247	.4693	.6179	1.5259	.7004
.70	.7513	.8121	.9230	.4761	.6253	1.5221	.7106
.71	.7459	.8077	.9213	.4829	.6327	1.5185	.7208
.72	.7405	.8033	.9197	.4897	.6401	1.5153	.7310
.73	.7350	.7989	.9180	.4965	.6474	1.5123	.7412
.74	.7296	.7944	.9163	.5033	.6546	1.5096	.7514
.75	.7241	.7899	.9146	.5101	.6618	1.5072	.7616
.76	.7186	.7853	.9129	.5169	.6689	1.5050	.7718
.77	.7131	.7808	.9112	.5237	.6760	1.5031	.7820
.78	.7075	.7761	.9095	.5305	.6830	1.5014	.7922
.79	.7020	.7715	.9078	.5373	.6899	1.5000	.8024
.80	.6964	.7668	.9060	.5441	.6968	1.4989	.8126
.81	.6907	.7621	.9043	.5509	.7036	1.4980	.8228
.82	.6851	.7574	.9026	.5577	.7104	1.4973	.8330
.83	.6794	.7527	.9008	.5645	.7171	1.4969	.8432
.84	.6737	.7479	.8991	.5713	.7237	1.4967	.8534
.85	.6681	.7431	.8973	.5781	.7303	1.4968	.8636
.86	.6624	.7383	.8955	.5849	.7368	1.4971	.8738
.87	.6567	.7335	.8938	.5917	.7433	1.4976	.8840
.88	.6509	.7286	.8920	.5985	.7497	1.4984	.8942
.89	.6452	.7237	.8902	.6053	.7561	1.4994	.9044
.90	.6395	.7188	.8884	.6121	.7624	1.5007	.9146
.91	.6337	.7138	.8866	.6189	.7687	1.5022	.9248
.92	.6279	.7088	.8848	.6257	.7749	1.5040	.9350
.93	.6221	.7037	.8830	.6325	.7810	1.5060	.9452
.94	.6163	.6986	.8812	.6393	.7871	1.5083	.9554
.95	.6105	.6935	.8793	.6461	.7931	1.5109	.9656
.96	.6046	.6883	.8775	.6529	.7990	1.5138	.9758
.97	.5988	.6831	.8756	.6597	.8049	1.5170	.9860
.98	.5929	.6778	.8737	.6665	.8107	1.5205	.9962
.99	.5870	.6725	.8718	.6733	.8164	1.5242	1.0064
1.00	.5811	.6672	.8699	.6801	.8221	1.5283	1.0166
1.01	.5752	.6618	.8680	.6869	.8277	1.5327	1.0268
1.02	.5693	.6565	.8661	.6937	.8333	1.5374	1.0370
1.03	.5634	.6510	.8642	.7005	.8388	1.5424	1.0472
1.04	.5574	.6456	.8623	.7073	.8443	1.5477	1.0574
1.05	.5515	.6401	.8603	.7141	.8497	1.5533	1.0676
1.06	.5455	.6346	.8584	.7209	.8551	1.5592	1.0778
1.07	.5396	.6290	.8564	.7277	.8604	1.5654	1.0880
1.08	.5336	.6234	.8545	.7345	.8657	1.5719	1.0982
1.09	.5276	.6178	.8525	.7413	.8709	1.5787	1.1084
1.10	.5216	.6122	.8505	.7481	.8761	1.5858	1.1186
1.11	.5156	.6065	.8485	.7549	.8812	1.5932	1.1288
1.12	.5096	.6008	.8465	.7617	.8863	1.6009	1.1390
1.13	.5035	.5951	.8445	.7685	.8913	1.6090	1.1492
1.14	.4975	.5894	.8425	.7753	.8963	1.6174	1.1594
1.15	.4914	.5836	.8405	.7821	.9013	1.6261	1.1696
1.16	.4854	.5778	.8384	.7889	.9062	1.6352	1.1798
1.17	.4793	.5720	.8364	.7957	.9110	1.6446	1.1900
1.18	.4732	.5661	.8343	.8025	.9158	1.6544	1.2002
1.19	.4671	.5602	.8323	.8093	.9205	1.6645	1.2104
1.20	.4611	.5543	.8302	.8161	.9252	1.6750	1.2206
1.21	.4550	.5483	.8281	.8229	.9298	1.6858	1.2308
1.22	.4489	.5424	.8260	.8297	.9344	1.6970	1.2410
1.23	.4428	.5364	.8239	.8365	.9389	1.7085	1.2512
1.24	.4367	.5303	.8218	.8433	.9434	1.7204	1.2614
1.25	.4307	.5243	.8197	.8501	.9478	1.7327	1.2716
1.26	.4246	.5182	.8176	.8569	.9521	1.7453	1.2818
1.27	.4185	.5121	.8155	.8637	.9564	1.7583	1.2920
1.28	.4124	.5060	.8134	.8705	.9606	1.7717	1.3022
1.29	.4063	.4999	.8113	.8773	.9648	1.7855	1.3124
1.30	.4002	.4938	.8092	.8841	.9689	1.7997	1.3226
1.31	.3942	.4877	.8071	.8909	.9729	1.8143	1.3328
1.32	.3881	.4816	.8050	.8977	.9769	1.8293	1.3430
1.33	.3821	.4755	.8029	.9045	.9808	1.8447	1.3532
1.34	.3760	.4694	.8008	.9113	.9847	1.8606	1.3634
1.35	.3700	.4633	.7987	.9181	.9885	1.8769	1.3736
1.36	.3640	.4572	.7966	.9249	.9923	1.8937	1.3838
1.37	.3580	.4511	.7945	.9317	.9960	1.9109	1.3940
1.38	.3520	.4450	.7924	.9385	.9997	1.9286	1.4042
1.39	.3461	.4390	.7903	.9453	1.0033	1.9468	1.4144
1.40	.3401	.4329	.7882	.9521	1.0069	1.9655	1.4246
1.41	.3342	.4268	.7861	.9589	1.0105	1.9847	1.4348
1.42	.3282	.4208	.7840	.9657	1.0140	2.0044	1.4450
1.43	.3223	.4147	.7819	.9725	1.0175	2.0246	1.4552
1.44	.3164	.4087	.7798	.9793	1.0209	2.0453	1.4654
1.45	.3105	.4026	.7777	.9861	1.0243	2.0665	1.4756
1.46	.3046	.3966	.7756	.9929	1.0277	2.0882	1.4858
1.47	.2988	.3906	.7735	.9997	1.0310	2.1105	1.4960
1.48	.2929	.3845	.7714	1.0065	1.0343	2.1333	1.5062
1.49	.2871	.3785	.7693	1.0133	1.0375	2.1567	1.5164
1.50	.2813	.3725	.7672	1.0201	1.0407	2.1806	1.5266

$\gamma = 7/5$

M or M_1	$\frac{p}{p_t}$	$\frac{\rho}{\rho_t}$	$\frac{T}{T_t}$	θ	$\frac{q}{p_t}$	$\frac{A}{A^*}$	$\frac{V}{a_t}$	ν	μ	M_2	$\frac{p_2}{p_1}$	$\frac{\rho_2}{\rho_1}$	$\frac{T_2}{T_1}$	$\frac{p_{t_2}}{p_{t_1}}$	$\frac{p_2}{p_{t_1}}$
1.00	0.5283	0.6339	0.8333	0	0.3898	1.000	1.00000	0	90.00	1.000	1.000	1.000	1.000	1.000	0.5283
1.01	.5221	.6287	.8305	.1418	.3738	1.000	1.00031	.0473	81.93	.9901	1.022	1.017	1.007	1.000	.5221
1.02	.5160	.6234	.8278	.2836	.3578	1.000	1.00126	.1227	78.64	.9805	1.047	1.033	1.013	1.000	.5160
1.03	.5099	.6181	.8250	.2408	.3787	1.001	1.00284	.2294	76.14	.9713	1.071	1.050	1.020	1.000	.5100
1.04	.5039	.6129	.8222	.3827	.3818	1.001	1.00506	.3510	74.08	.9620	1.095	1.067	1.026	.9999	.5039
1.05	.4979	.6077	.8193	.3202	.3842	1.002	1.00114	.4874	72.35	.9531	1.120	1.084	1.033	.9999	.4980
1.06	.4919	.6024	.8166	.3516	.3868	1.003	1.00723	.6387	70.83	.9444	1.144	1.101	1.039	.9997	.4920
1.07	.4860	.5972	.8137	.3657	.3896	1.004	1.00731	.7972	69.16	.9360	1.168	1.118	1.046	.9996	.4861
1.08	.4800	.5920	.8108	.4078	.3919	1.006	1.00833	.9680	67.81	.9277	1.194	1.135	1.052	.9994	.4803
1.09	.4742	.5868	.8080	.4337	.3944	1.008	1.07321	1.148	66.56	.9196	1.219	1.152	1.058	.9992	.4746
1.10	.4684	.5817	.8052	.4483	.3967	1.008	1.08134	-1.336	66.38	.9118	1.245	1.170	1.065	.9989	.4689
1.11	.4626	.5766	.8023	.4618	.3990	1.010	1.09013	1.532	64.28	.9041	1.271	1.186	1.071	.9986	.4633
1.12	.4568	.5716	.7994	.3944	.4011	1.011	1.09909	1.735	63.23	.8966	1.297	1.203	1.078	.9982	.4577
1.13	.4511	.5665	.7966	.3282	.4033	1.013	1.10820	1.944	62.25	.8892	1.323	1.221	1.084	.9978	.4521
1.14	.4455	.5615	.7937	.5474	.4052	1.015	1.11746	2.160	61.31	.8820	1.350	1.238	1.090	.9973	.4467
1.15	.4398	.5565	.7908	.3879	.4072	1.017	1.12689	2.381	60.41	.8750	1.378	1.255	1.097	.9967	.4413
1.16	.4343	.5515	.7879	.3879	.4090	1.020	1.13797	2.607	59.55	.8682	1.403	1.273	1.103	.9961	.4360
1.17	.4287	.5465	.7851	.6074	.4108	1.022	1.13661	2.839	58.73	.8616	1.430	1.290	1.109	.9953	.4307
1.18	.4232	.5415	.7822	.6284	.4125	1.024	1.14721	3.074	57.94	.8549	1.458	1.307	1.115	.9946	.4255
1.19	.4178	.5365	.7793	.6491	.4141	1.028	1.15877	3.314	57.18	.8488	1.486	1.324	1.122	.9937	.4204
1.20	.4124	.5315	.7764	.6833	.4157	1.030	1.15935	3.559	56.44	.8422	1.513	1.342	1.128	.9928	.4184
1.21	.4070	.5265	.7736	.6812	.4171	1.033	1.16475	3.808	55.74	.8360	1.541	1.359	1.134	.9918	.4104
1.22	.4017	.5215	.7708	.6979	.4185	1.037	1.17319	4.062	55.05	.8300	1.570	1.376	1.141	.9907	.4055
1.23	.3964	.5165	.7679	.7102	.4198	1.040	1.18067	4.321	54.39	.8241	1.598	1.394	1.147	.9895	.4006
1.24	.3912	.5116	.7648	.7323	.4211	1.043	1.18792	4.585	53.75	.8183	1.627	1.411	1.153	.9884	.3958

AND GOD SAID . . . .

$$C_L = \int_x \int_y (C_{P_L} - C_{P_U})\, dx\, dy$$

AND THERE WAS LIFT.

BUT THE DEVIL SAID . . . .

$$C_D = C_{D_{P_{MIN}}} + \frac{C_L^2}{\pi AR e} + \Delta C_{D_P} + \Delta C_{D_M} +$$

$$+ \left(\Delta C_{D_{FPR=MCRT}} - \Delta C_{D_{FPR=RAM}}\right) + \left(C_{D_{PROD.NOZ}} - C_{D_{FLOW\ NOZ}}\right)_{RAM} +$$

$$+ \left(\Delta C_{D_{BOUYANCY}}\right)_{BTWT\ FILLET\ FLAP} + C_L \sin \alpha_{upflow}$$

$$- \Delta C_{D_{P_{MIN}}}\Big|_{FLT\ Re\ -\ BTWT\ Re} + \Delta C_{D_{WAVE}} - C_L \cdot g(C_L)_{WALL} +$$

$$+ \Delta C_{D_{SPILL}} + \Delta C_{D_{EXCRESENCE}} - \Delta C_{D_{SUPPORT}} +$$

$$+ Q_3 \int (\text{ert})^{mrf}\, dz - 2/3(\text{MANAGEMENT REQM'T}) + \Delta C_{D_{TRIM}} -$$

$$- \Delta C_{D_{BLOCKAGE}} - \Delta C_{D_{TRIP}} - C_{D_{INTERNAL}} + C_{D_{BASE,\ STING}}$$

$$- f(\text{actor})^{(BTWT - \text{z/3 UNVAL})} \pm 2\sigma + \text{H.O.T.} + C$$

AND THERE WAS DRAG.

THEN A VOICE FROM THE WILDERNESS SAID . . . .

"DON'T FORGET STABILITY AND CONTROL"

GILLETTE 12-26-77

FIGURE 1.1 THE AERODYNAMICIST'S RELIGION

FIXED: RANGE = 2820 NMI
PAYLOAD = 175 PAX
CRUISE MACH = 0.98

EXAMPLE DESIGN: TOFL = 7000 FT
V_{APP} = 132 KTS
TOGW = 312,500 LB
ICA = 37,700 FT
THRUST, SLS = 100,000 LB
S_{WING} = 2703 SQ. FT.

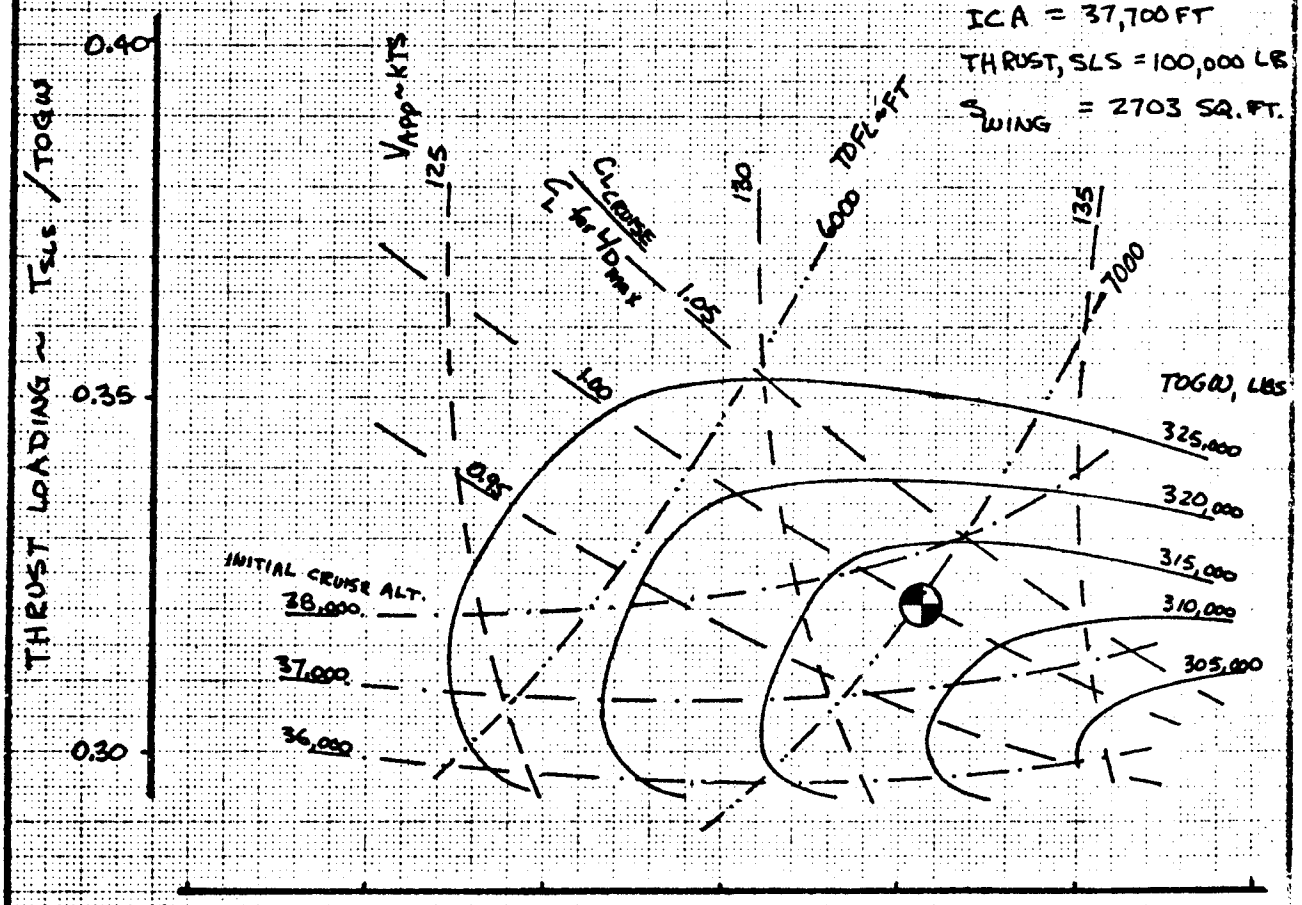

CALC	GILLETTE	12-26-77	REVISED	DATE
CHECK				
APP				
APP				

AIRCRAFT DESIGN SELECTION FIG 1.2
"THUMBPRINT"

BOEING

PAGE 1.23

THE AIRPLANE

ATMOSPHERIC CONDITIONS

- $T_{AMBIENT}$
- $P_{AMBIENT}$
- $\rho_{AMBIENT}$

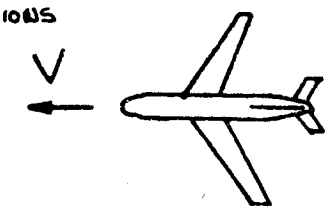

AIRPLANE MOVES WITH VELOCITY V

$$a = 49.02\sqrt{T_{AMBIENT}}$$

$$M = V/a$$

$$\left.\begin{aligned} T &= T_{AMBIENT} \\ P &= P_{AMBIENT} \\ \rho &= \rho_{AMBIENT} \end{aligned}\right\} \text{"STATIC" CONDITIONS}$$

THE AIRPLANE SENSES "TOTAL" CONDITIONS GIVEN BY THE ISENTROPIC EQUATIONS

$$\frac{T}{T_o} = \left(1 + \frac{\gamma-1}{2}M^2\right)^{-1} \qquad \frac{P}{P_o} = \left(1 + \frac{\gamma-1}{2}M^2\right)^{\frac{-\gamma}{\gamma-1}} \qquad \frac{\rho}{\rho_o} = \left(1 + \frac{\gamma-1}{2}M^2\right)^{\frac{-1}{\gamma-1}}$$

WHERE $(-)$ ← "STATIC"; ← "TOTAL" OR "STAGNATION"

THE WIND TUNNEL MODEL

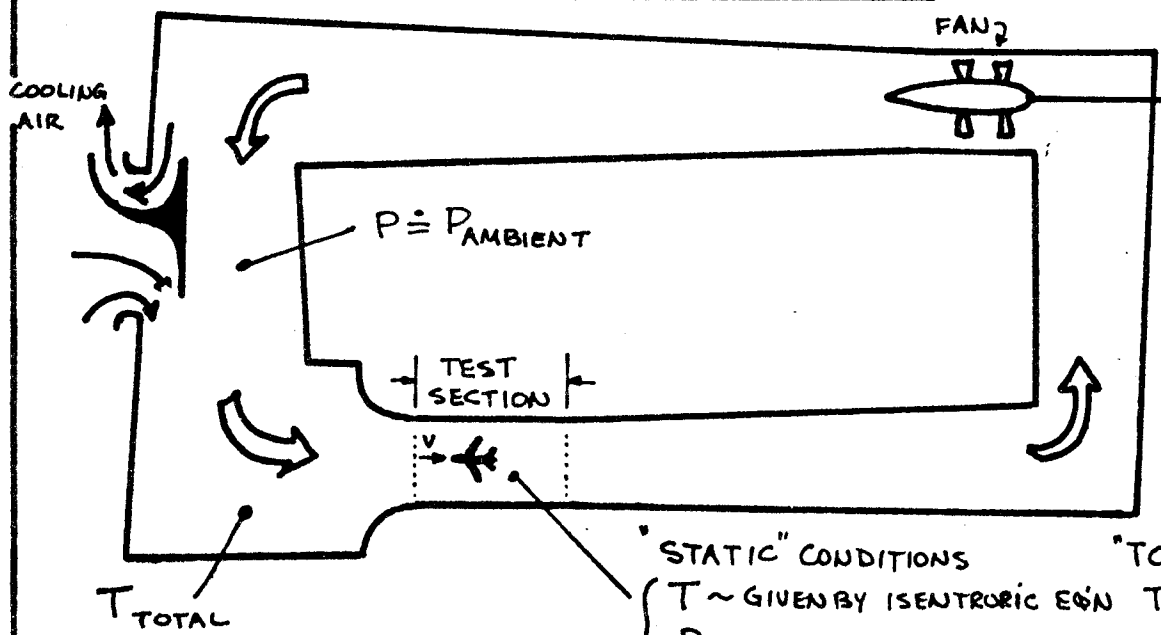

$a = 49.02\sqrt{T}$

$M = V/a$

T_{TOTAL}

~MEASURED IN STILLING CHAMBER

"STATIC" CONDITIONS

- T ~ GIVEN BY ISENTROPIC EQN
- P ~ SAME
- ρ ~ SAME

"TOTAL" COND'NS

- T_o ~ MEASURED
- $P_o \doteq P_{AMBIENT}$
- $\rho_o = \frac{P_o}{gRT_o}$

FIGURE 1.3 AIRPLANE VS. WIND TUNNEL FLOW CONDITIONS

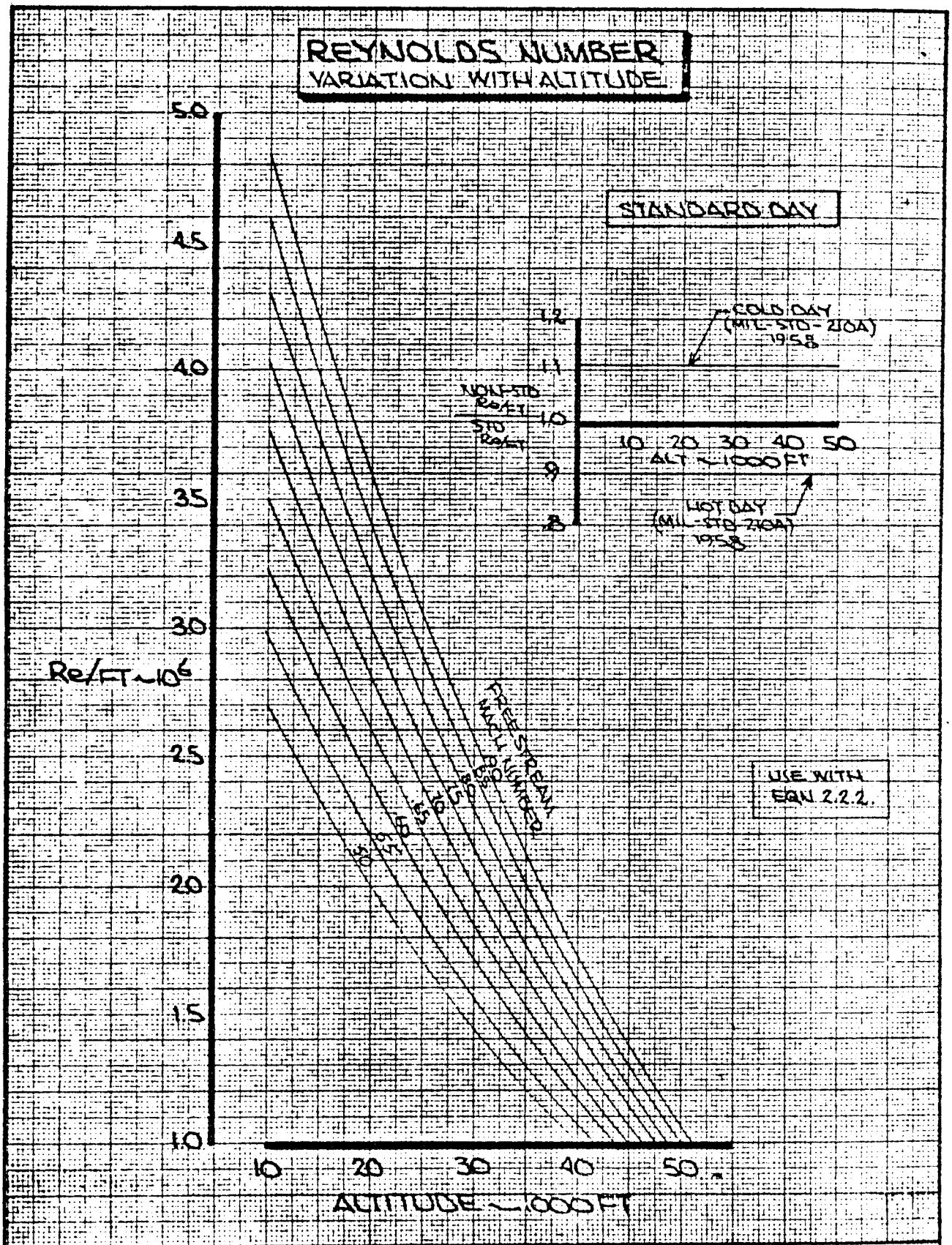

CALC			REVISED	DATE	REYNOLDS NUMBER VARIATION WITH ALTITUDE	FIG 1.4
CHECK	FINCH	3.27.69	FINCH	11-17-69		D6-24229
APR						
APR					THE BOEING COMPANY	P. 1.25
	[illegible]	1.30.70				

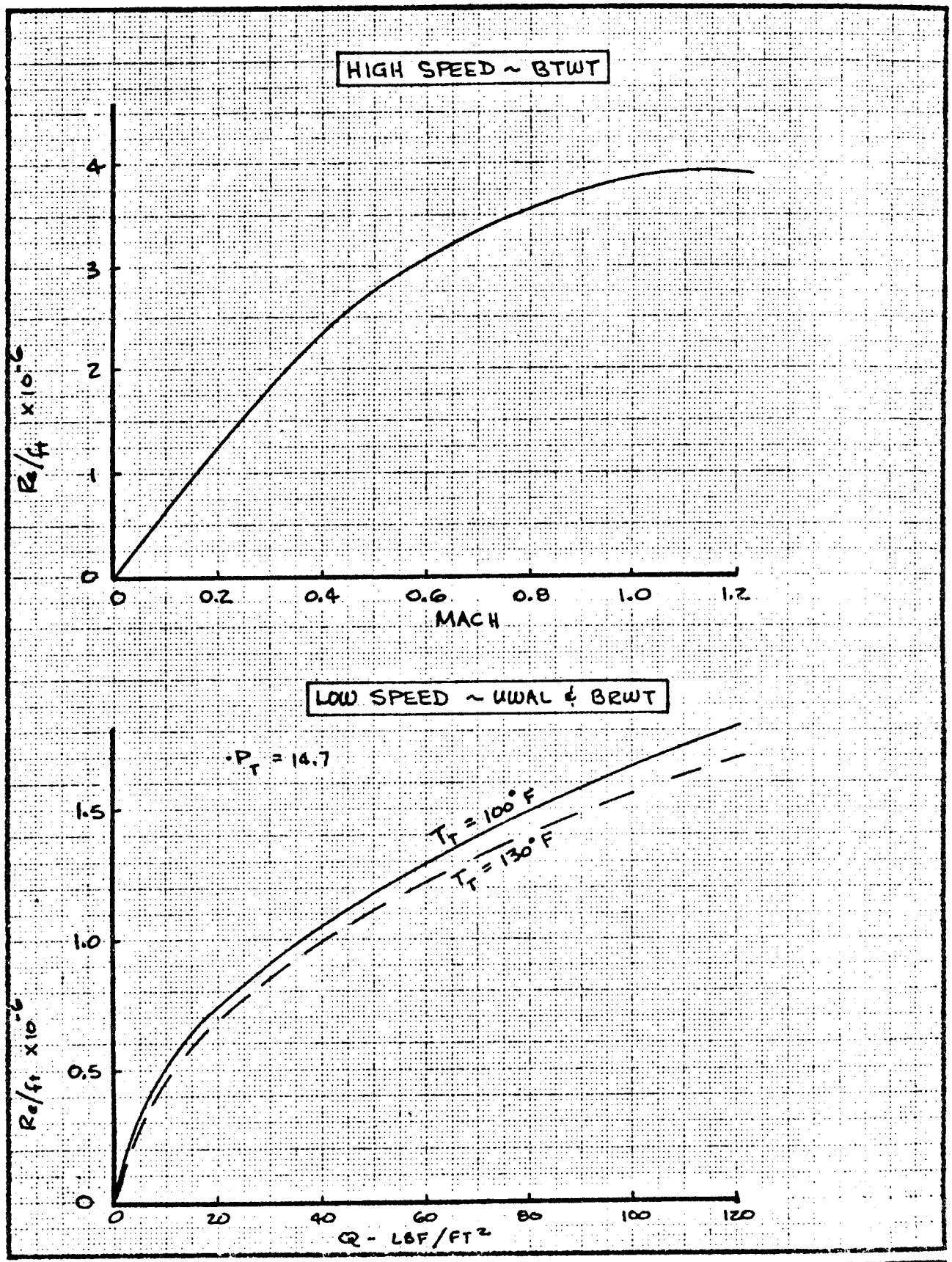

CALC	GILLETTE	12-2677	REVISED	DATE	WIND TUNNEL REYNOLDS NO.	FIG. 1.5
CHECK						
APR						
APR					BOEING	PAGE 1.26

DT 4100 3260 ORIG. 3/71

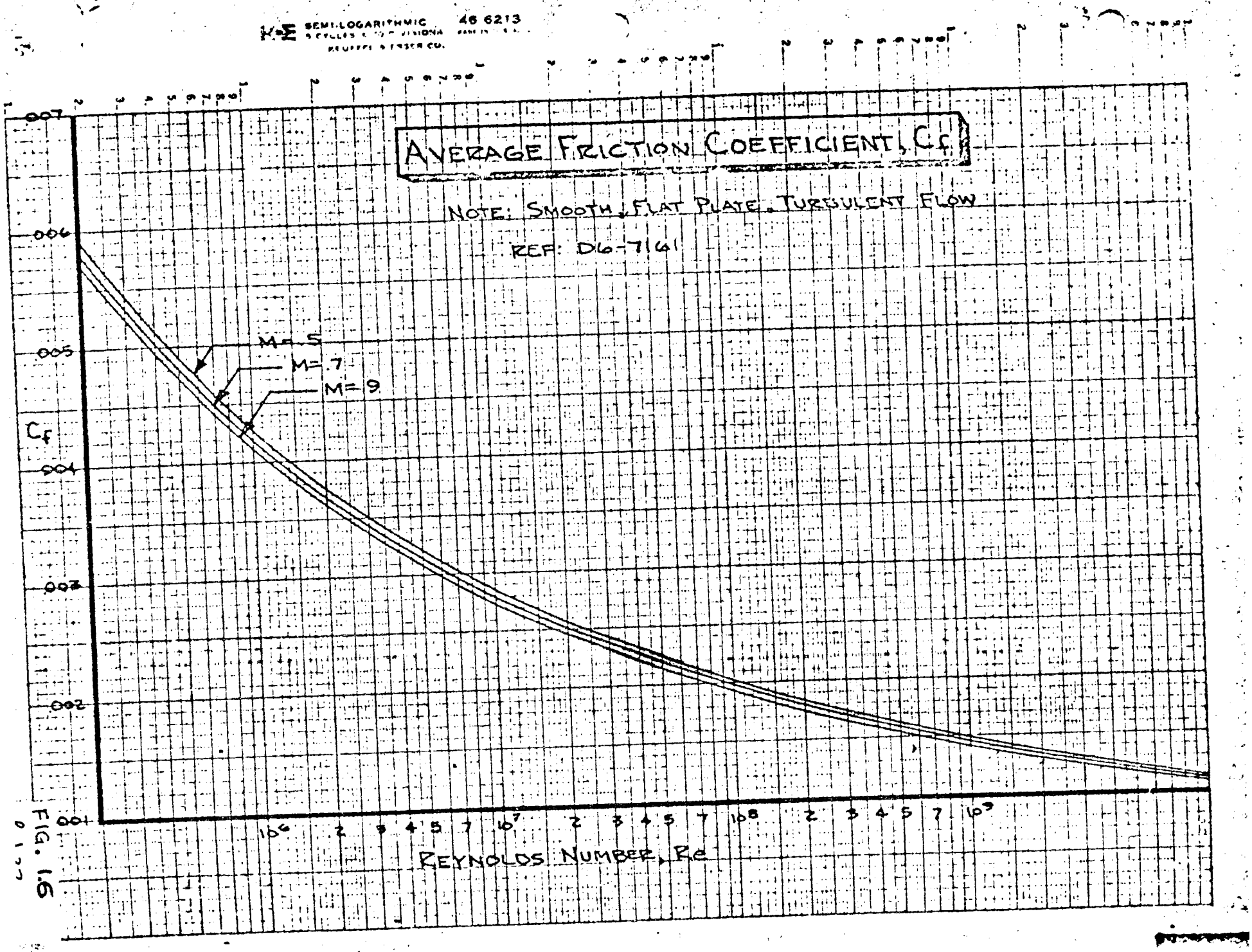
SEMI-LOGARITHMIC
46 6213
KEUFFEL & ESSER CO.
AVERAGE FRICTION COEFFICIENT, Cf
NOTE: SMOOTH, FLAT PLATE, TURBULENT FLOW
REF: D6-7141
M=5
M=7
M=9
Cf
.007
.006
.005
.004
.003
.002
.001
REYNOLDS NUMBER, Re

FIG. 16

CHAPTER 1 ADDENDUM: BOUNDARY LAYER TERMINOLOGY

LAMINAR

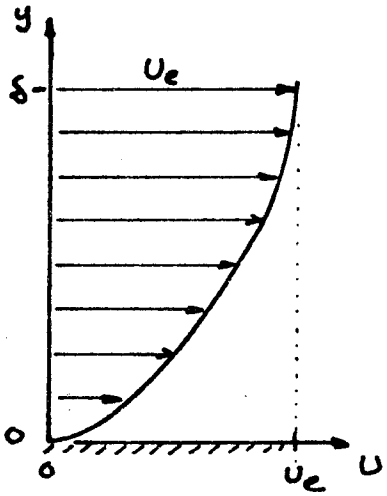

TURBULENT

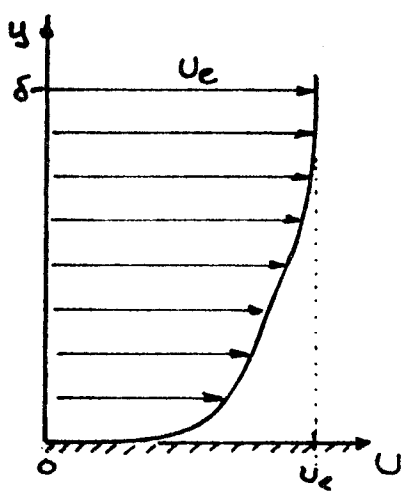

DISPLACEMENT THICKNESS

deficit in mass flux is the same as $U_e \delta^*$, where

$$\delta^* = \int_{y=0}^{\delta} \left(1 - \frac{U}{U_e}\right) dy$$

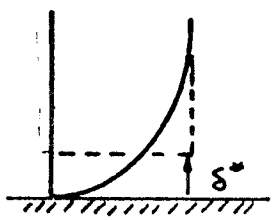

MOMENTUM THICKNESS

momentum deficit is given by

$$\theta = \int_{y=0}^{\delta} \frac{U}{U_e}\left(1 - \frac{U}{U_e}\right) dy$$

ENERGY THICKNESS

energy deficit is given by

$$\delta^{**} = \int_{y=0}^{\delta} \frac{U}{U_e}\left(1 - \left(\frac{U}{U_e}\right)^2\right) dy$$

SHAPE FACTORS

$$H = \frac{\delta^*}{\theta} \qquad K = \frac{\delta^{**}}{\theta}$$

SKIN FRICTION

$$c_f = \frac{\tau_0}{q}$$

where τ_0 = wall shear stress
q = local freestream dynamic pressure

and

$$\tau_0 = \mu \frac{\partial u}{\partial y}$$

where μ = absolute viscosity

1.8.78
GILLETTE

CHAPTER 2. TWO-DIMENSIONAL CRUISE AIRFOIL DESIGN

CHAPTER 2. TWO-DIMENSIONAL CRUISE AIRFOIL DESIGN

2.1 AIRFOILS FOR SUBCRITICAL SPEEDS

The equations to describe the characteristics of devices which produce lift have been known for more than a century. Indeed, the lift of simple shapes has been calculable since the beginning of manned flight. An understanding of these simple formulations is essential to understanding how airfoils work. The following discussion in this chapter will pertain only to airfoils of infinitely long span.

2.1.1 Classical Considerations

The most simple lifting device is a flat plate. Anyone who has carried plywood or panelling on top of their car can testify to that fact. As the flat plate is given an angle with respect to the oncoming stream, velocity differences occur, with the upper surface having a higher velocity. This is due to circculation, the discussion of which will not be dealt with here. A concise discussion is available in Reference 2.1. From the incompressible Bernoulli equation (1.11), the velocity on the upper surface gives rise to a pressure:

$$\tfrac{1}{2}\rho u^2_{UPPER} + P_{UPPER} = \tfrac{1}{2}\rho U_s^2 + P_s \qquad (2.1)$$

Likewise on the lower surface:

$$\tfrac{1}{2}\rho u^2_{LOWER} + P_{LOWER} = \tfrac{1}{2}\rho U_s^2 + P_s \qquad (2.2)$$

The velocity in both cases varies with position along the plate. The difference in pressures gives rise to a force normal to the plane of the plate:

$$n = \int_0^c \left[(P_s - P_u) - (P_s - P_l) \right] dx \qquad (2.3)$$

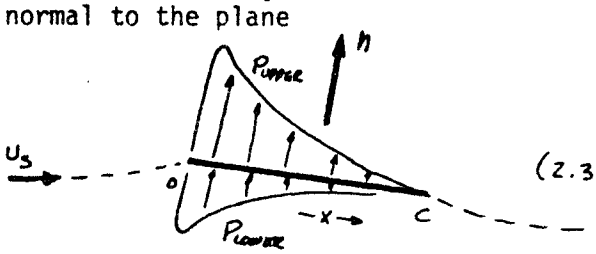

Using equations (2.1) and (2.2), this becomes

$$n = q \int_0^c (C_{p_l} - C_{p_u})\, dx \qquad (2.4)$$

where C_p is local pressure coefficient:

$$C_p = 1 - \left(\frac{u}{U_s}\right)^2 = \frac{P - P_s}{q} \qquad (2.5)$$

The velocity on the upper surface will be higher than static, so that C_{p_u} is negative; on the lower surface the velocity will be less than static so that C_p is positive:

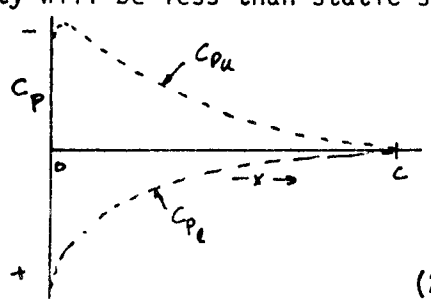

It is usual to define a force coefficient, rather than force, So,

$$C_n = \frac{n}{qS} \qquad (2.6)$$

2.1.1 (cont.)

where S is the reference area. Taking the span as one unit of length, then (2.6) becomes

$$C_n = \frac{n}{qc}$$

$$= \frac{q}{qc}\int_0^c (C_{p_l} - C_{p_u})\, dx$$

or

$$C_n = \int_0^1 (C_{p_l} - C_{p_u})\, d(x/c) \qquad (2.7)$$

As angle of attack, α, is changed, C_M will also change. Classical hydrodynamic theory shows that

$$C_n = 2\pi\alpha, \quad \alpha \text{ in radians}$$

$$= \frac{\pi^2}{90}\alpha, \quad \alpha \text{ in degrees} \qquad (2.8)$$

This force is in a direction normal to the flat plate, but it is more desirable to express the force in components orthogonal to the wind axis:

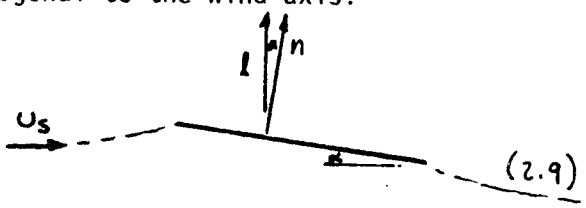

The lift: $l = n\cos\alpha$ or $C_l = C_n\cos\alpha$ (2.9)

For small angles, it is usually assumed that $C_l \doteq C_n$, so that

$$C_l = 2\pi\alpha, \quad \alpha \text{ in radians} \qquad (2.10)$$

2.1.1 (cont.)

For inviscid flow, Kutta (1902) and later Joukowsky (1906) proved through momentum considerations that the drag force, C_d, disappears.

Another characteristic of the flat plate is that a moment is developed as lift is developed:

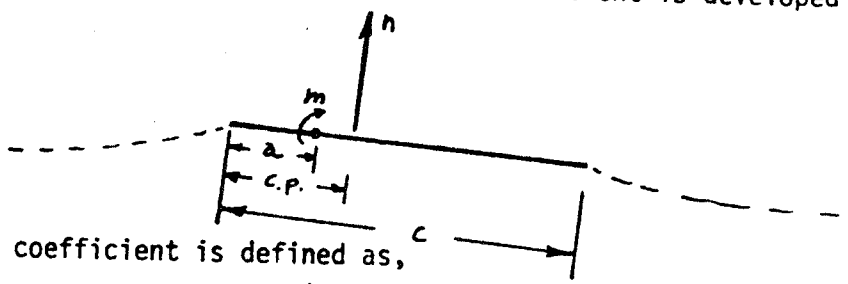

Pitching moment coefficient is defined as,

$$C_{m_a} = \frac{m}{qc} - \frac{n(c.p.-a)}{qc} \qquad (2.11)$$

where a leading-edge up direction is positive. If the point "a" is made to be the center of pressure, "c.p.", then pitching moment will be independent of angle of attack. Hydrodynamic theory demonstrates that the center of pressure is at 0.25c. For this point,

$$C_{m_{.25c}} = \frac{m}{qc} \qquad (2.12)$$

The .25c point is referred to as the aerodynamic center. Furthermore, the theory shows that for the flat plate, not only is pitching moment independent of lift coefficient, it is also zero.

In summary, the two-dimensional flat plate appears to be an excellent lifting device in inviscid flow:

$$C_l = 2\pi\alpha, \quad \alpha \text{ in radians}$$

$$C_d = C_{m_{.25c}} = 0 \qquad (2.13)$$

Airfoil characteristics are usually plotted in three standard formats. These are (1) the lift versus angle of attack, (2) the lift versus drag (a plot first suggested by Otto Lilienthal because of the difficulties in measuring in testing) and (3) lift versus pitching moment. For the flat plate in inviscid flow:

2.1.1 (cont.)

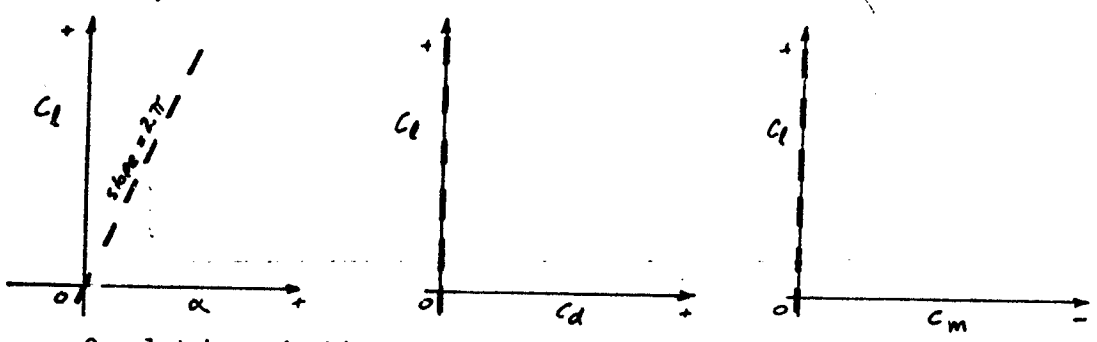

The c_l versus C_m plot has pitching moment plotted on the reverse because an "increasing" curve in this quadrant would denote a stable change of pitching moment with lift. That is, as the pitch increases, lift increases but the airfoil has more nose-down moment. The flat plate, however, has neutral stability in inviscid flow.

Unfortunately, the flat plate airfoil must be expected to perform in the real world, where viscous effects significantly alter its performance. First the drag of the flat plate at zero angle of attack is not zero but is that given by skin friction drag on the two sides. As the angle of attack is increased, the boundary layer drag increases due to the appearance of form drag (discussed in further detail below), which is the combination of skin friction and pressure drag. But at about four degrees angle of attack, a most serious defect appears. The flow separates from the flat plate's upper surface at the leading edge:

These effects give rise to a true drag polar:

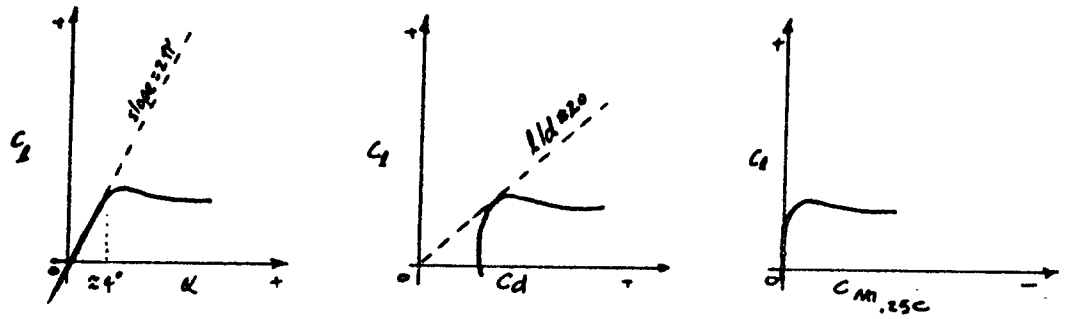

The obvious improvement to the flat plate would be to bend the leading edge down so that it would be perfectly aligned with the incoming flow. This change in shape, called "camber" in airfoil terminology, reduces the pressure peaks and the chordwise loading at the leading edge

2.1.1 (cont.)

relative to the flat plate:

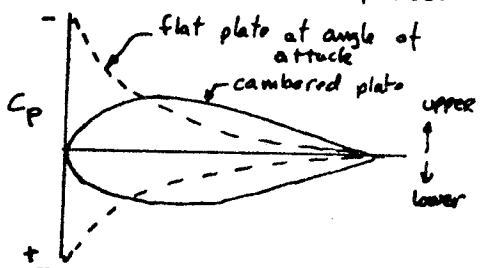

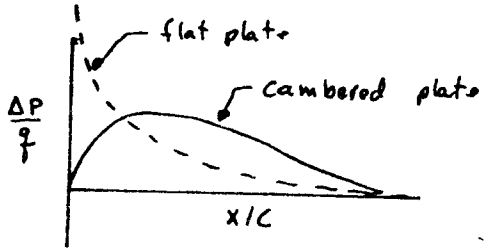

The streamlines approaching the cambered plate:

Cambering alters the aerodynamics of the flat plate by introducing an offset to lift and moment:

$$C_l = \alpha_o + 2\pi\alpha \quad , \alpha \text{ in radians}$$

$$C_m = C_{m_{\alpha=0}} \equiv C_{m_o} \tag{2.13}$$

The cambered plate thus produces a good ratio of lift to drag at higher lift coefficients, but it will suffer the same kind of separation at the leading edge at about four degrees above it's design condition:

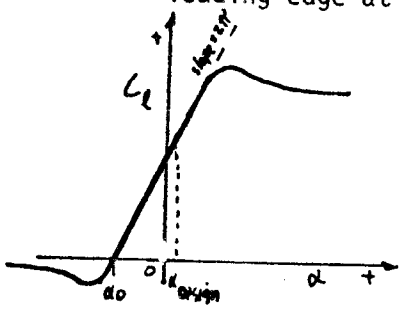

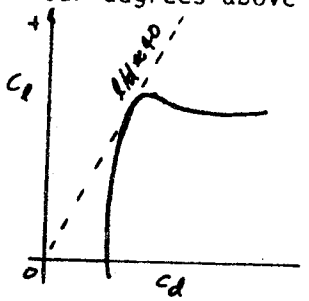

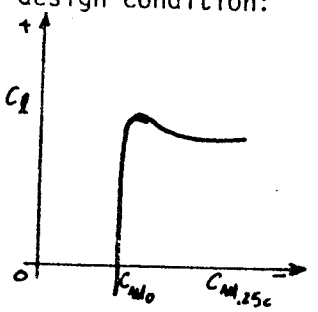

The performance of the cambered airfoil is still limited by leading edge separation. The next step in product improvement is to add thickness to the cambered plate. This thickness allows a round leading edge which will be less sensitive to angle of attack:

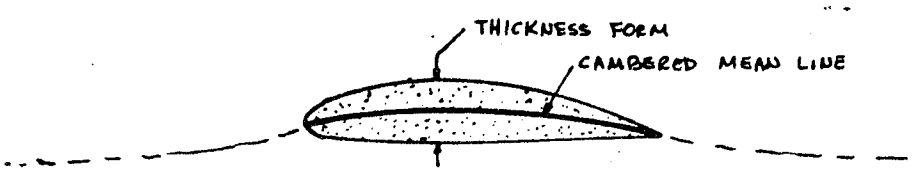

Hydrodynamic theory shows that the addition of thickness does not alter the lifting characteristics of the cambered plate (denoted now as the mean line); consequently, equation (2.13) remains as the descriptor of the two-dimensional airfoil.

2.1.1 (cont.)

The performance characteristics become:

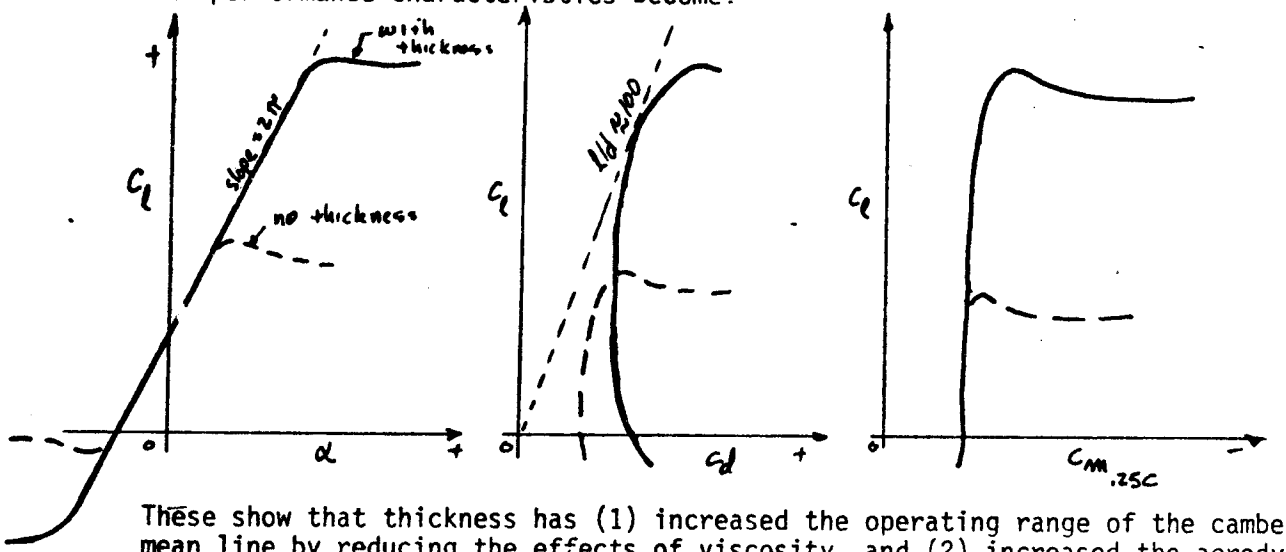

These show that thickness has (1) increased the operating range of the cambered mean line by reducing the effects of viscosity, and (2) increased the aerodynamic efficiency by allowing much higher lifts at only slightly higher drag. The increased drag is due to the increased wetted area of the airfoil with thickness and to the closure of the thickness form. These effects will be dealt with later.

The effects of thickness, camber and angle of attack can be combined very simply by superposition. This theory states that the pressure coefficient on an airfoil is obtained by a linear combination of effects due to the three parameters:

$$C_p = 1 - \left(\frac{V}{V_o} \pm \frac{\Delta V}{V_o} \pm \frac{\Delta V_a}{V_o} \right)^2 \qquad (2.14$$

Where

(1) V/V_o is the velocity ratio over the basic thickness form at zero angle of attack. This ratio versus chord position has been tabulated for a large number of airfoil sections by NACA and summarized in Reference 2.1. For a thickness ratio different from the one shown in the Reference table, the valued of U/V_o can be obtained approximately by scaling linearly with thickness ratio:

$$\left(V/V_o\right)_{t_2} = \left[\left(V/V_o\right)_{t_1} - 1 \right] \frac{t_2}{t_1} + 1 \qquad (2.15$$

(2) $\frac{\Delta V}{V_o}$ is the difference between upper and lower surface velocities due to the shape of the camber line. Families of camber, or mean lines are also contained in Reference 2.1. The ratio $\Delta V/V_o$ is tabulated at some design lift, c_{l_i}, versus chordwise location. For some other design lift coefficient, the proper $\Delta V/V_o$ ratio is obtained by direct scaling of the $\Delta V/V_o$ ratio:

$$\left(\Delta V/V_o\right)_{c_l} = \frac{c_l}{c_{l_i}} \left(\Delta V/V_o \right)_{c_{l_i}} \qquad (2.16$$

Note that this term is always used at the design angle of attack.

(3) $\Delta V_a/V_o$ corresponds to the additional flat plate load distribution due to angle of attack being different from the design angle of the camberline, and is included with the thickness form data. The tabulated values shown will produce

2.1.1 (cont.)

an incremental lift coefficient of one above that produced by the mean line. For a design coefficient other than unity, the $\Delta V_a/V_\infty$ is obtained by:

$$\left(\Delta V_a/V_\infty\right)_{c_\ell} = \left(c_\ell - c_{\ell_i}\right)\left(\Delta V_a/V_\infty\right)_{c_{\ell_i}} \quad . \tag{2.17}$$

An example is given on Figure 2.1, and the resulting pressure distribution is shown on Figure 2.2a. The Figure shows the pressure distribution due to the basic thickness form, the effect of camber and incremental effect due to angle of attack. A convention has arisen in airfoil design and evaluation, called linear superposition, which states that the pressure distribution on an airfoil can be decomposed into two parts, one due to thickness and one due to camber (which contains the angle of attack effect also):

$$C_{p_{thickness}} = \frac{(C_{p\ upper} + C_{p_{lower}})}{2}$$

$$C_{p_{camber}} = \frac{(C_{p\ upper} + C_{p_{lower}})}{2} \tag{2.17}$$

This decomposition is correct in demonstrating that the basic thickness form produces no lift at zero angle of attack. All lifting effects are attributed to the camber line and to angle of attack. The pressure distribution of Figure 2.2a is decomposed according to equation (2.17) on Figure 2.2b. Note that linear decomposition does not depict the thickness and camber effects completely correctly as compared to the NACA buildup. The differences are small, however, and linear decomposition is a useful way of quickly separating the approximate effects of lift and thickness.

2.1.2 NACA AIRFOILS

From the mid-1920's until the early 1950's, the NACA tested a large number of thickness forms and airfoils employing camber. These geometres have provided the mainstay of wing and propellor sections for most of the history of our industry. Not until recently have the aircraft manufacturers begun to develop their own airfoils; even those find parallels in contemporary NASA work. The standard reference for this mass of airfoil data is "Theory of Wing Sections" by Abbott and Von Doenhoff (Reference 2.1). The configuration aerodynamicist even today will find this to be a useful reference to provide shapes for fairings, pylons and perhaps vertical fins, and to understand camber and thickness effects.

The NACA data are given as thickness forms and mean lines. Any thickness form is added to any mean line as follows:

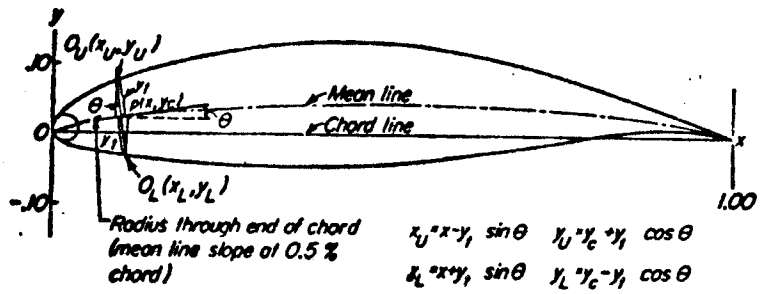

Sample calculations for derivation of the NACA 65,3-818 airfoil (a = 1.0)

x	y_t*	y_c†	tan θ	sin θ	cos θ	$y_t \sin\theta$	$y_t \cos\theta$	x_U	y_U	x_L	y_L
0	0	0	.....	.....	.....	0	0	0	0	0	0
0.005	0.01324	0.00300	0.336961	0.31932	0.94768	0.00423	0.01255	0.00077	0.01455	0.00923	−0.01055
0.05	0.03831	0.01264	0.18744	0.18422	0.98288	0.00706	0.03765	0.04294	0.05029	0.05706	−0.02501
0.25	0.08093	0.03580	0.06996	0.06979	0.99756	0.00565	0.08073	0.24435	0.11653	0.25565	−0.04493
0.50	0.06593	0.04412	0	0	1.00000	0	0.06593	0.50000	0.13005	0.50000	−0.04181
0.75	0.04456	0.03580	−0.06996	−0.06979	0.99756	−0.00311	0.04445	0.75311	0.08025	0.74689	−0.00865
1.00	0	0	.....	.....	.....	0	0	1.00000	0	1.00000	0

* Thickness distribution obtained from ordinates of the NACA 65,3-018 airfoil.
† Ordinates of the mean line, 0.8 of the ordinate for a_i = 1.0.
‡ Slope of radius through end of chord.

Note that the thickness form is added normally to the mean line. This is straightforward in construction of the airfoil, but means that decomposition of an airfoil into thickness and camber is an iterative situation.

The NACA airfoils have been cataloged into several groups. The earliest group are the four-digit sections. These trace their origins to the WWI era, to the Göttinger 398 and Clark-Y airfoils. They are characterized by a thickness form given by an analytical equation and a mean line composed of two parabolic arcs. An example, NACA 2412, is shown on Figure 2.3. This class of airfoils dominated aircraft design in the late 1920's and early 1930's, and are collectively known as the four-digit series.

The results of tests of four-digit airfoils showed that maximum lift increased as the position of maximum camber was shifted either forward or aft of the mid-chord position. The rearward positions of maximum camber were not of much interest because of increased pitching moment, but the forward positions were not desirable

2.1.2 (cont.)

either. So a new class of mean line was developed, denoted the five digit series. These are based on the same thickness forms as the four-digit series, but have a camberline which has decreasing curvature from the leading edge to slightly aft of the maximum camber position, where the curvature becomes zero. These airfoils appeared in the early 1930's, and most WW II airfoils are of these series. NACA 23012, a widely used member of this family is shown on Figure 2.3.

Following development of the five-digit series, the NACA investigated a large variety of sections of a number of different classes. The only one of these classes to find wide use are the 6-series wing sections. This is a very large class of airfoils, and turned out to have successful use for two different reasons. In the late 1930's, testing began to show the possibility of extensive laminar flow, even at flight conditions. An example of this class is 63_1-412, shown in Figure 2.3, and is representative of the kind of airfoil used on the P-51.

However, none of the previous types of airfoils showed good high speed capability, that is, the ability to operate at Mach numbers much above 0.65. It was found through testing that the 65-XXX and 66-XXX series of the NACA 6-series airfoils did demonstrate improved drag characteristics at higher Mach numbers. An example is NACA 65-412 shown on Figure 2.3. These found use in the first swept wing aircraft, and the 707 airfoil uses a 65-series thickness form in combination with a NACA mean line.

Airfoil development has continued at NASA in the areas of supercritical flow and for general aviation. The supercritical airfoils will be discussed in the next section.

The mass of NACA airfoil data allow an examination of the effects of thickness and camber on airfoil properties. Figure 2.4 compares the NACA 0012 section with 0%, 2% and 4% camber. The benefit of camber is to raise the drag polar so that $(l/d)_{max}$ is higher and occurs at a lower c_l and to reduce the drag at typical operational c_l values. The drag at c_l =0.4 is ten percent less for NACA 4412 than that of NACA 0012. Maximum lift also increases with camber for a bit, but then begins to decrease. The 2% cambered airfoil has a higher $c_{l_{max}}$ than does the 4% cambered airfoil. The penalty for camber is that pitching moment becomes increasingly negative. This represents a performance penalty to the aircraft since a downward-directed tail load is required to offset the pitching moment.

Figure 2.5 reveals the effect of increasing thickness at constant camber. Increasing thickness causes asteady deterioration in $(l/d)_{max}$ and an increase in drag at c_l =.0.4. Maximum lift increases to about 15% thickness ratio, then begins to decrease. Pitching moment, which depends only on camber, remains unchanged. Clearly, the best airfoil will be the thinnest one which still allows a useful $c_{l\ max}$. Airfoil thickness will invariably be thicker on an aircraft because of structural, fuel volume or other reasons than would be best for optimum aerodynamic performance.

2.1.3 ANALYTICAL METHODS

Airfoils such as those developed by the NACA can be dealt with very easily by analytical techniques. The most direct process is to represent the outer shape of the airfoil with discrete vortices, on the order of 100 or so. Each of these vortices also contains a boundary condition whereby the flow will be perpendicular to a surface normal at that point on the airfoil. Solution of the linearized equation for potential flow simultaneously for these 100 vortices will yield the strength of each vortex necessary to satisfy the boundary conditions. Then, the pressure coefficient on the airfol, off the airfoil at any point in space, and the velocity vector off the airfoil at any point in space can be calculated. The standard program for doing this calculation is A-280 (Reference 2.2). For a typical airfoil, the cost of a solution is very cheap, being only about 0.05 CU. And the results compare very favorably with experimental information, as seen on Figure 2.6 for A-280 pressures versus experiment for the NACA 23012 airfoil.

Whereas A-280 calculatesthe pressure distribution about the airfoil and its lift, it does not compute the drag. This must be done by a boundary layer program. The st ındard program for this computation is A-200 (Reference 2.3). This program uses integral boundary layer theory, so-called because the shape of the boundary layer has been related to its characteristics δ/C, δ^*/C, θ/C, H and C_f by integration of a parametrically expressed profile shape. This kind of method is extremely rapid and is quite valid for cases where there is no boundary layer separation. Required inputs to A200 are the shape of the airfoil, it's pressure distribution and the chord Reynolds number. The upper and lower surface boundary layer characteristics as calculated by A-200 for the NACA 23012 airfoil are shown on Figure 2.7. The drag of the airfoil can then be calculated by the Squire-Young formula (Reference 2.4):

$$C_{D_{one\ surface}} = 2\frac{\theta_{TE}}{C}\left(\frac{U_{TE}}{U_\infty}\right)^{\left(\frac{H_{TE}+5}{2}\right)} \qquad (2.18)$$

where θ_{TE} = trailing edge momentum thickness

U_{TE} = velocity at trailing edge

U_∞ = freestream velocity

C = air foil chord

H_{TE} = boundary layer shape factor, δ^*/θ, AT trailing edge; δ^* = displacement thickness

This equation produces a drag coefficient of 0.0074 for the NACA 23012 at $C_\ell = 0.62$, as compared to the experimental value of 0.0066.

When used together, the programs A-280 and A-200 can be used to calculate the performance of any arbitrary airfoil shape, subject to the limitations discussed next.

2.1.4 VISCOUS EFFECTS

It has already been stated that, except for viscosity, the perfect airfoil would be a flat plate. Thus all aspects of airfoil design are dominated by visious considerations. It is important to understand these effects.

The most notable feature of viscosity is that it results in drag. For the subsonic airfoil, the drag arises from two sources, friction and pressure. Indeed the only forces which can be felt by the airfoil are tangential (frictional) and normal (pressure). The frictional are the result of scrubbing by the boundary layer, and the sum of these forces are:

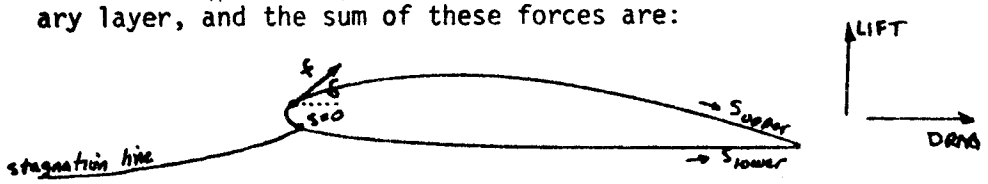

(2.19)

$$F_{DRAG} = \int_0^{s_{upper}} f_{upper} \cos\delta \, ds + \int_0^{s_{lower}} f_{lower} \cos\delta \, ds$$

$$F_{LIFT} = \int_0^{s} f_{upper} \sin\delta \, ds - \int_0^{s} f_{lower} \sin\delta \, ds$$

Note that the surface skin friction produces both a drag and a lift force. However the F_{lift} is usually very small, and is ignored, and since $F = C_F q S$, we have,

$$C_F = \int_0^{s_{upper}} c_{f_{upper}}(s) \cos\delta(s) \, ds + \int_0^{s_{lower}} c_{f_{lower}}(s) \cos\delta(s) \, ds \qquad (2.20)$$

where C_F is the total integral of skin friction drag, and $c_f(s)$ is the local value. A typical history of the local value of C_f is shown on Figure 2.7. Note the change in C_f at the point of transition. Note also how C_f is reduced near the airfoil's trailing edge.

This is due to the increasing boundary layer thickness caused by the adverse pressure gradient encountered by the boundary layer as it approaches the airfoil's trailing edge. In fact, if the pressure gradient were so severe as to cause separation, then the skin friction drag would go to zero.

The reason this is not a good idea is because of the other part of drag, the

2.1.4 pressure drag. The pressure integral around an airfoil is given by:

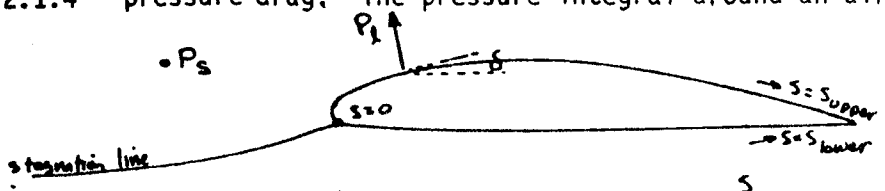

$$P_{DRAG} = \int_0^{s_{upper}} \left[P_s - P_l(s)\right] \sin\delta(s)\, ds + \int_0^{s_{lower}} \left[P_l(s) - P_s\right] \sin\delta(s)\, ds \qquad (2.21)$$

$$P_{LIFT} = \int_0^{s_{upper}} \left[P_s - P_l(s)\right] \cos\delta(s)\, ds + \int_0^{s_{lower}} \left[P_l(s) - P_s\right] \cos\delta(s)\, ds \qquad (2.22)$$

Potential flow theory states that for a closed two-dimensional body, the drag integral will be zero. That is, equation (2.21) sums to zero in potential flow. In viscous flow, however, the thickness of the boundary layer alters the surface pressure distribution:

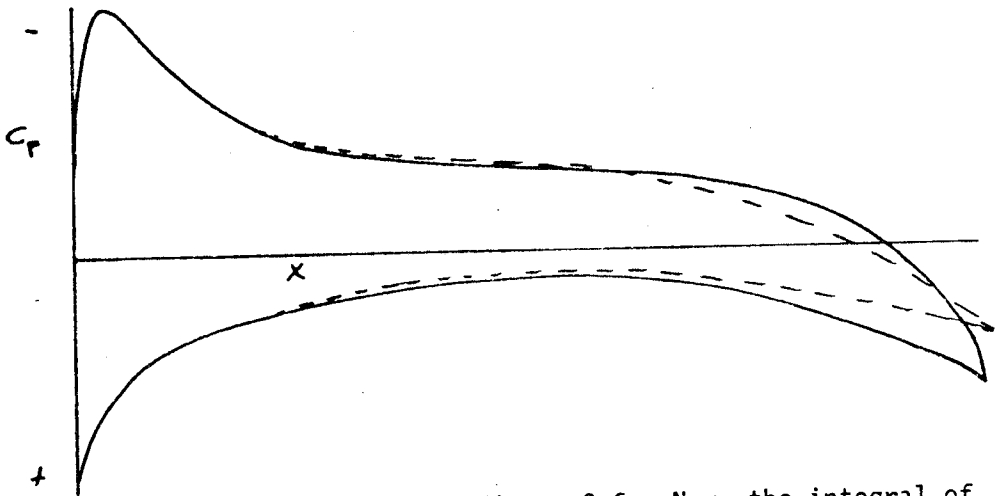

This difference can be observed on Figure 2.6. Now, the integral of equation (2.21) will not be zero. The amount it is not zero will be the pressure drag:

$$P_{DRAG} = \int_0^{s_{upper}} \left(P_{l_{Re=0}} - P_{l_{viscous}}\right) \sin\delta\, ds + \int_0^{s_{lower}} \left(P_{l_{viscous}} - P_{l_{Re=0}}\right) \sin\delta\, ds \qquad (2.23)$$

$$= \int_{surface} (\text{real pressure}) - \int_{surface} (\text{inviscid pressure})$$

P 2.13

2.1.4 (cont.)

This equation results because the integral of the inviscid pressures are zero in the drag direction.

The total drag of the airfoil, called <u>form drag</u> or <u>profile drag</u>, is the sum of the two components:

$$C_{d_{form}} = C_{d_{friction}} + C_{d_{pressure}} \tag{2.24}$$

For the well-designed thin airfoil at it's intended angle of attack, skin friction drag will comprise perhaps 80% of the total drag. But as the airfoil becomes thicker or is operated at higher lift coefficients, the pressure gradients become more severe on the upper surface of the airfoil. Skin friction drag will decrease but pressure drag will increase more rapidly, so that the total drag increases. When the airfoil's upper surface finally separates, the pressure drag will become very large. This behavior causes the characteristic airfoil polar shape.

Thus, the second important feature of viscosity is that it limits the lift of the airfoil. Once the boundary layer has separated, the airfoil cannot in general produce much more lift. The behavior after separation, however, is dependent on the kind of separation, or stall, caused by the airfoil's shape. Sharp leading edged airfoils will usually suffer a catastrophic failure in lift when the flow abrubtly separates from the leading edge. Large leading-edge radius airfoil will show signs of approaching separation as the trailing edge boundary layer becomes thicker and finally separates:

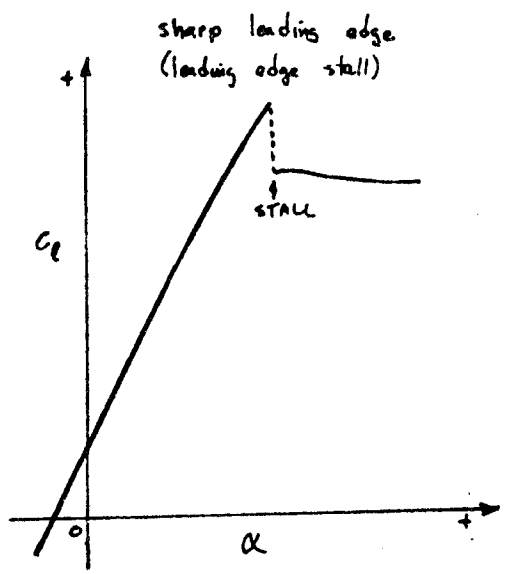

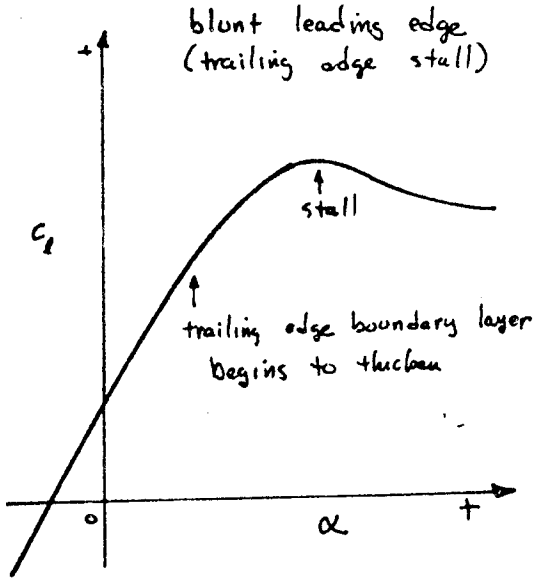

2.1.4 (cont.)

Incipient trailing edge and then slight trailing edge separation can be seen in the pressure distribution:

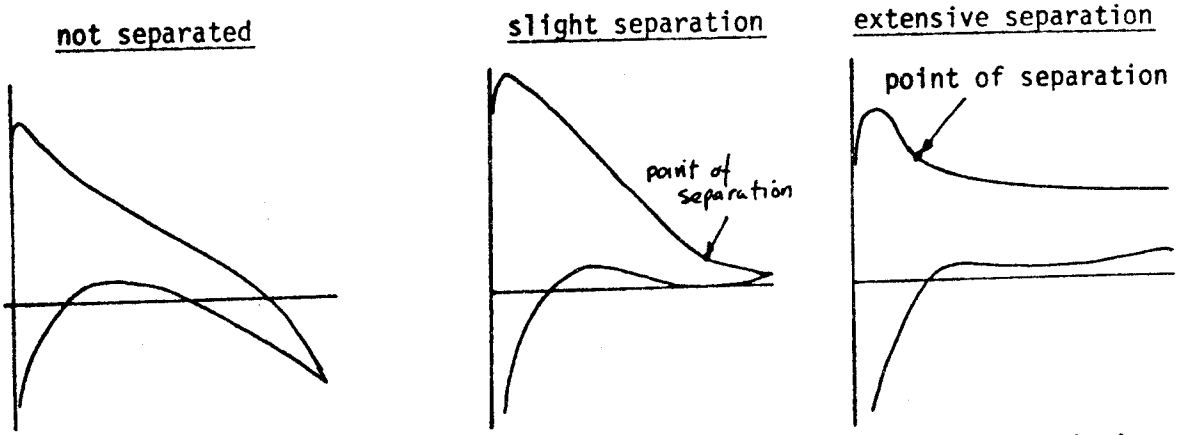

Good success has been achieved recently in modelling separated wakes on 2-D airfoils and thus calculating the pressure distribution on the separated airfoil. The Boeing program is A- (Reference 2.5)

2.2 AIRFOILS FOR TRANSONIC SPEEDS

The NACA 65- and 66-series airfoils were used on virtually all early sweptwing transonic aircraft. Like the early NACA airfoils, however, these have been replaced by new concepts for transonic airfoils. This section will trace the development of transonic airfoils over the past 15 years.

2.2.1 MACH EFFECTS ON NACA AIRFOILS

The effect of Mach number on an airfoil is principally to alter it's pressure distribution. This in turn alters the performance of the airfoil. In principle, the effects begin at zero velocity. However, for practical purposes, the effects do not become significant until about M = 0.3. The pressure on the surface changes in proportion to the Mach number is a linear fashion. A number of correction formula have been derived. One of the most widely used is the Prandtl-Glauert:

$$C_{P_M} = C_{P_{M=0}} \left[\frac{1}{\sqrt{1-M^2}} \right] \qquad (2.25)$$

This causes a scaling to appear as:

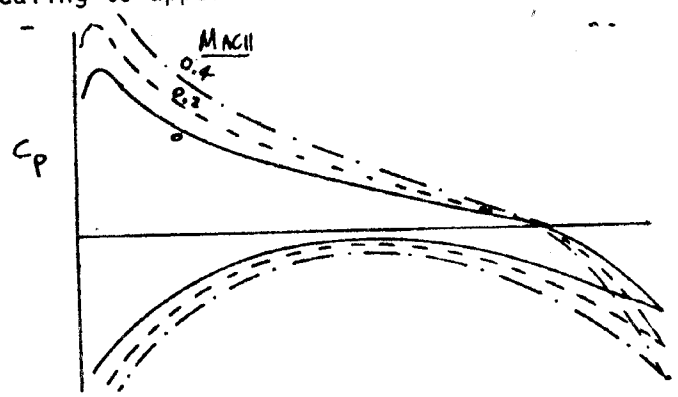

P2.15

2.2.1 (cont.)

This causes a similar change in lift at a constant angle of attack:

$$c_{l_M} = c_{l_{M=0}} \left[\frac{1}{\sqrt{1-M^2}} \right] \qquad (2.26)$$

Thus, the lift curve slope increases with increasing Mach number. The drag and the pitching moment are relatively unaffected by the compressible effects.

As Mach number is increased, however, local regions of supersonic flow begin to appear on the airfoil. The flow in these regions no longer obeys a simple compressibility correction, and the shape of the pressure distribution begins to alter. Soon a shock wave appears, and the lift, drag and pitching moment all show deviations. As the non-linear transonic region begins to appear, the "lift will increase even more rapidly than predicted by equation (2.26). The drag at this point is relatively unchanged. The pitching moment will begin to become more negative due to the development of supersonic flow aft of the quarter-chord point. As Mach number is increased, the transonic region will enlarge and begin to terminate in a shock wave. The appearance of the shock wave marks the onset of drastic changes in the behavior of the airfoil. Separation will occur at the shock wave, causing a break in $dc_l/d\alpha$ due to a loss in lift, the drag will rise drastically due to separation-caused pressure drag and wave drag, and the pitching moment will become increasingly negative. Figure 2.8 relates these effects for NACA 2309 (from Ref. 2.6).

The performance characteristics of an airfoil are usually summarized in a plot of drag divergence Mach number versus lift coefficient and c_l for (l/d) max. where the two cross is usually denoted the design point. This is shown on Figure 2.9 for NACA 2309. The "drag divergence" Mach number is defined as being the condition where:

$$\frac{d(c_l)}{d(c_d)} = 0.1 \quad \text{at} \quad c_l = \text{constant} \qquad (2.27)$$

This is illustrated on Figure 2.8.

The performance of the NACA 2309 airfoil and similar airfoils were found to be inadequate for swept-wing aircraft. For example, if the 707 had used the NACA 2309 airfoil it would have a 40° swept wing only 7% thick. This kind of wing would have severly reduced the 707 performance. Extensive wind tunnel research by the NACA lead to the NACA 65-series airfoils, which were the first to have useful transonic capabilities. Experimental work had shown that an important criterion for better transonic performance could be seen in the incompressible pressure distribution. Figure 2.10 shows a typical NACA 65-series airfoil upper surface pressure distribution. The upper surface pressures scale according to linear compressibility concepts up to the point where locally supersonic flow first appears (Fig. 2.10a). This Mach number is devoted M* Above this point, the nature of the pressure distribu ion begins to change, with a very rapid development of the shock wave (Fig. 2.10b). The drag divergence Mach number is soon reached (Fig. 2.10c), however, there is a useful margin between the first appearance of M* and M_{DD}.

2.2.1 (cont.)

These NACA-type airfoils employed a good amount of camber and this gave good low speed drag characteristics. The 707, 727, and 737 wings utilize airfoils of this class. Boeing airfoil TR-7 ("TR" means TRansonic) is representative of the 707 outboard wing; its pressure distribution, drag rise and performance characteristics are shown on Figure 2.11.

2.2.2 ADVANCED TRANSONIC AIRFOILS

Despite having a good balance between low speed, off design characteristics and those near M_{DD}, the NACA 65-type airfoils left much to be desired at higher Mach numbers. If TR 7 could be increased in M_{DD} from 0.717 to 0.80, for example, then the sweep of the 707 wing could be reduced almost to zero. So many investigators began to search for more advanced transonic airfoils.

This search was dominated by the work of Pearcy, who first published significant findings in 1962 (Reference 2.7). His understanding of the transonic nature of airfoils and a classification of types have become widely accepted. First, he recognized that the reason that airfoils like TR 7 begin their drag rise was because of the basically circular upper surface shape. This kind of continually high curvature causes expansions to leave the surface relatively far aft on the airfoil. These expansion waves reflect off the sonic line as compression waves, which coalesce at the airfoil surface as a shock wave:

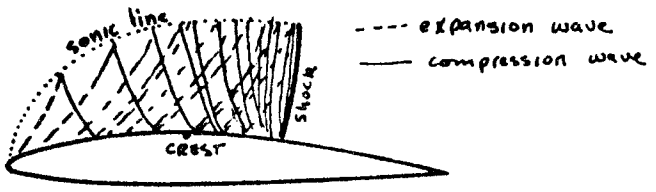

This shock wave will be quite strong and aft of the crest of the airfoil as well, leading to a rapid rise in wave drag and pressure drag.

Upon examining large numbers of these kinds of airfoils, Pearcey found they were all somewhat similar, having a "roof-top" shaped incompressible pressure distribution:

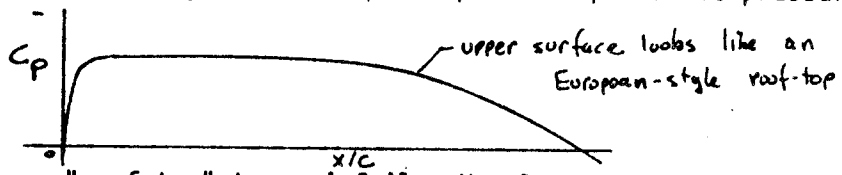

Hence the name "roof-top" type airfoil. He also examined another way of examining airfoils, by replotting their pressure distribution versus the vertical ordinate, to produce a "suction loop" diagram. Figure 2.12 displays the suction loop and how it is defined. This pressure diagram is constructed from the incompressible pressures. The part of interest is the suction part of the diagram, for it shows what happends to a roof-top airfoil as the drag divergence Mach number is increased. Figure 2.13 gives an experimental example; note how the M=.40 shape changes and a drag loop resulting from the shock wave crossing the crest appears. This marks the point where drag begins to increase rapidly.

2.2.2 (cont.)

The reason for the appearance of the shock wave so far aft could be modified by altering the nature of the airfoil to produce more expansions forward on the airfoil. This would allow the supersonic region to recompress over a longer distance:

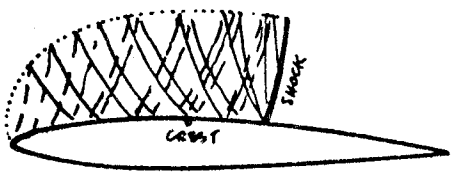

This would be achieved by altering the airfoil leading edge to produce a slight peak in the incompressible pressures. The resulting airfoil, denoted "roof-top with suction peak," is depicted in Figure 2.14.

Pearcey went further in altering the airfoil shape. By blunting the airfoil leading edge, and causing a very rapid expansion near the leading edge, then flattening the airfoil upper surface from about .2 x/c until past the shock wave, the expansion waves would have a good chance to be almost completely cancelled by the compression waves, resulting in a very low shock strength and a delayed drag rise:

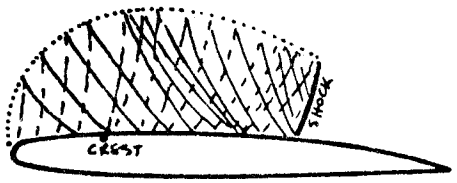

An example of this class of airfoil behavior is displayed on Figure 2.15. These kinds of airfoils are referred to as peaky airfoils.

A final type of airfoil was recognized by Pearcey; the triangular pressure distribution. Figure 2.16 illustrates this kind of airfoil behavior; it is characterized by excessive drag creep and will give the poorest transonic performance of any of the classes of airfoils.

Figure 2.17 summarizes the comparative features of the four kinds of transonic pressure characteristics. Note that TR 38 and TR 38-1 have a concavity on the lower surface near the trailing edge. This feature is denoted as "rear loading." Recall from the previous discussion how the airfoil critical Mach number is related to the upper surface Mach number. For a given airfoil thickness, the upper surface Mach number is related to the airfoil lift coefficient. For a required lift, the upper surface Mach number can be reduced if more lift can be carried by the lower surface, or if more lift could be carried aft on the airfoil

2.2.2 (cont.)

behind the upper surface shock position. Both of these can be achieved by introducing camber to the rear portion of the airfoil:

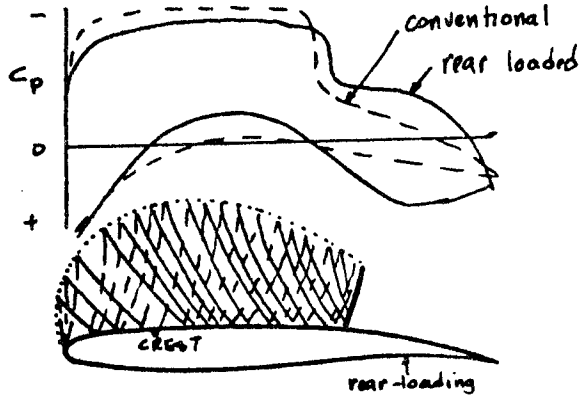

In both cases, the airfoils produce the same lift. The limit to rear loading is reached when the boundary layer separates at either point "A" or point "B. Figure 2.18 shows the effect of increasing the aft loading. The rear loading airfoil concept was also introduced by Pearcy.
Rear-loading increases drag divergence Mach number by reducing upper surface velocites for a stated lift. Another way to increase MDD is by reducing the trailing edge angle by simply leaving the trailing edge blunt; Whitcomb airoils have some degree of trailing edge bluntness. Figure 2.19 compares two transonic airfoils, TR 34 with a conventional sharp trailing edge and TR 48 with a 1.1% chord blunt trailing edge. Note that the blunt trailing edge does increase M_{DD}, but $(\ell/d)_{max}$ is decreased by almost 20%. In most applications, this loss in aerodynamic efficiency will be more important than the slight gain in M_{DD}.

Most of the airfoils shown so far have been about 10% thick. Substantially thicker airfoils are difficult to achieve without upper surface trailing edge separation. One way to overcome this is with upper surface blowing. Figure 2.20 compares an 18% thick airfoil, TR 47, with blowing to TR 38-1. The thick airfoil achieves very creditable performance with blowing,but in most cases the complications of BLC will not offset aerodynamic benefits.

In many respects, the preferred transonic airfoil would be like TR 38 or TR 38-1, with either a peaky or almost peaky suction loop, and with rear loading. Airfoils in this class owe their origins to Pearcey of Britain, not withstanding the attention (and US patent) received by Richard Whitcomb of NASA for his "supercritical airfoils." Indeed, the European A-300B Airbus employs a section very much like TR 38-1; that wing was designed at Hawker-Siddeley in about 1963.

There are several other aspects of advanced sections that preclude their automatic adoption for new airplanes. First, the rear loading doubles or perhaps even triples the load carried by the airfoil structure aft of the rear span. This will incur a weight penalty of some degree. Second the rear loading makes the wing pitching moment more negative, which must be trimmed out by a larger tail down-load. Third, the peaky leading edge may cause earlier stall. All these factors must be considered in the wing design (Chapter 4).

The definitive source on transonic airfoil design within Boeing is "The Design of

2.2.2 (cont.)

Efficient Transonic Airfoils" (Ref. 2.8). Most of the preceeding discussion is from that source. The details of how transonic airfoils are designed can be reviewed in that reference.

2.2.3 ANALYTICAL METHODS

The discussion above and Reference 2.8 as well emphasizes the incompressible pressure distribution and suction loop. This was done for several reasons. First, an understanding of these concepts is important in realizing how the transonic flow field develops. Second, the ability to calculate incompressible pressure distributions has existed since the mid-1960's. The program to do this is currently A-280. This program used the vortex polygon approach to model the surface of the airfoil; the linearized potential flow equation is solved exactly. No iterations are required and the solution will be consistant for a given geometry regardless of the user's skill in using the program.

In the early 1970's, the ability appeared to calculate the mixed transonic flow field with shock waves. These methods were iterative, relaxation techniques. The quality of the solution was limited by the user's skill and by the fact that viscous efferts had been ignored. By the mid-1970's, solutions began to appear with viscosity included. This kind of solution is available in program A-423 (Reference 2.9) Whereas this program has not supplanted the necessity for testing, it does provide the ability to do very realistic airfoil design studies. In general, this program will predict the shock wave position within about 5% chord, but will pessimistic in M_{DD} by about 0.02.

2.1.4 AIRFOIL TEST APPARATUS

Having designed a transonic airfoil, the aerodynamicist will of course desire to get test data on its performance. Ideally, the data would reflect the 2-D characteristics of the airfoil. This is no easy task to achieve experimentally, for two reasons. First, it is almost impossible to test the airfoils at conditions equivalent to full-scale Reynolds number. Second, it is also extremely difficult to design a strictly two-dimensional test arrangement.

Airfoils can in principle be tested at full scale conditions in a cryogenic tunnel. Only one exists to date, and that is at NASA-Langley Research Center. Full scale conditions could also be achieved with airfoils of three to four foot chord in a pressure tunnel such as CALSPAN, but aerodynamic loads on the model make that structurally impractical. Boeing testing has centered on airfoils of 20 inch chord in the Boeing Transonic Wind Tunnel, yielding a chord Reynolds number of 6×10^6. This, of course, is more than an order of magnitude below typical full scale values, but is an order of magnitude larger than the chord Reynold number of the average wing section of a typical BTWT model.

The test apparatus used by Boeing in BTWT is depicted on Figure 2.20. This rig takes a constant-chord airfoil and places it vertically on a turntable. The free end of the airfoil is capped by a large end-plate. Obviously, this kind of test rig will have substantial corner flow at each end of the airfoil, and the forces on the endplate would also be on the balance. But it is felt that the flow will essentially two-dimensional in the center of the airfoil span. So the forces on the two-dimensional airfoil are measured as follows. The normal force, C_n, is determined by integrating the chordwise pressure difference between upper and lower surface.

2.1.4 (cont.)

Although the model is pitched on the turntable, whose angular setting is measured, the tunnel crossflow is not known, so the angle of attack is not known. Because of this, the airfoil lift, c_l, normal to the flow direction cannot be determined. However, for small angles c_l and c_n will be practically identical. The drag force is measured by a wake rake which traverses through the wake. Drag of the airfoil is determined by integrating the momentum deficit in the wake.

2.3 AIRFOILS FOR SUPERSONIC SPEEDS

Airfoils intended for fully supersonic flow are rarely needed; even for an SST, performance will be substantially enhanced by choosing a planform with a subsonic leading edge (Chapter 7). In a way this is unfortunate, because the characteristics of an airfoil in full supersonic flow are easily calculated. Consider first a flat plate at angle of attack in supersonic flow:

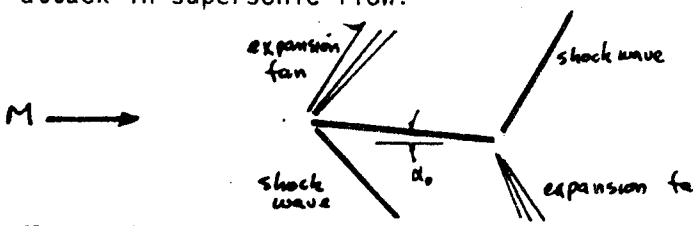

(2.28)

The upper surface flow undergoes an expansion to a pressure level P_{upper} as determined by M and α_o. This pressure, which is less than free stream, is constant along the entire upper surface to the trailing edge. There, the flow is recompressed and turned to the free stream direction through a shock wave. On the lower surface, the flow is pressurized through a shock wave, then expanded at the trailing edge back to free stream conditions. The C_p of the upper surface and lower surface have the same magnitude, but are of opposite sign:

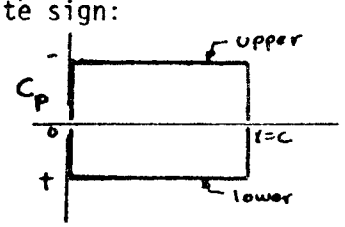

The lift and drag will be:

$$l = (c_{p_l} - c_{p_u})\, q\, c \cos\alpha_o$$
$$d = (c_{p_l} - c_{p_u})\, q\, c \sin\alpha_o \qquad (2.28)$$

Note that, unlike subsonic potential flow, where the airfoil has no drag in the absence of viscosity, there will be drag in supersonic flow. The shape of the pressure distribution above also shows that pitching moment will be independent of angle of attack if the aerodynamic reference is taken at mid-chord. Recall that for subsonic flow, the corresponding point will be at the quarter-chord.

For small angles, the pressure coefficient can be approximated by

$$\ldots \quad C_p = \mp \frac{2\alpha_o}{\sqrt{M^2-1}} = \mp \frac{2\alpha_o}{\beta} \qquad (2.29)$$

where $\beta = \sqrt{M^2-1}$

P 2.21

2.3 (cont.)

Putting this into equation (2.28) we have

$$c_l = \frac{4\alpha_0}{\beta}$$

$$c_d = \frac{4\alpha_0^2}{\beta} \qquad (2.30)$$

In short, the lift and drag of a supersonic flat plate are uniquely determined by its inclination to the flow and the Mach number of the flow. This is a vast simplification over the difficulties of calculating the lift of a subsonic airfoil. Furthermore, the slope of the lift curve of the supersonic flat plate is

$$\frac{dc_l}{d\alpha} = \frac{4}{\beta} \qquad (2.31)$$

As in the two-dimensional case, camber may be added to the flat plate. The theory for supersonic flow demonstrates that the lift and drag will be dependent upon the local angle of attack:

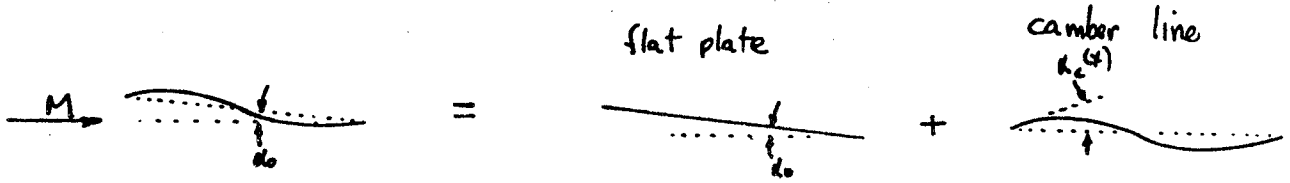

$$c_l = \frac{4\bar{\alpha}(x)}{\beta} \qquad (2.32)$$

$$c_d = \frac{4}{\beta}\,\bar{\alpha}^2(x)$$

where $\bar{\alpha}(x) = \frac{1}{c}\int_0^c \alpha(x)\,dx$

$= \overline{(\alpha_0 + \alpha_c)}$

$= \bar{\alpha}_0 + \bar{\alpha}_c = \alpha_0$, since $\int_0^c \bar{\alpha}_c\,dx = 0$.

and

$$\bar{\alpha}^2(x) = \overline{(\alpha_0+\alpha_c)^2} = \bar{\alpha}_0^2 + 2\overline{\alpha_0\alpha_c} + \bar{\alpha}_c^2$$

$$= \alpha_0^2 + \bar{\alpha}_c^2$$

2.3 (cont.)

These relationships lead to:

$$c_l = \frac{4\alpha_0}{\beta} \tag{2.32}$$

$$c_d = \frac{4}{\beta}\left[\alpha_0^2 + \overline{\alpha_c^2(x)}\right]$$

This somewhat surprising result says that for the supersonic thin airfoil, camber adds nothing to lift, but increases drag. The most efficient supersonic airfoil in inviscid flow is thus the flat plate without camber.

Likewise, thickness can be examined at zero lift. For a simple diamond airfoil;

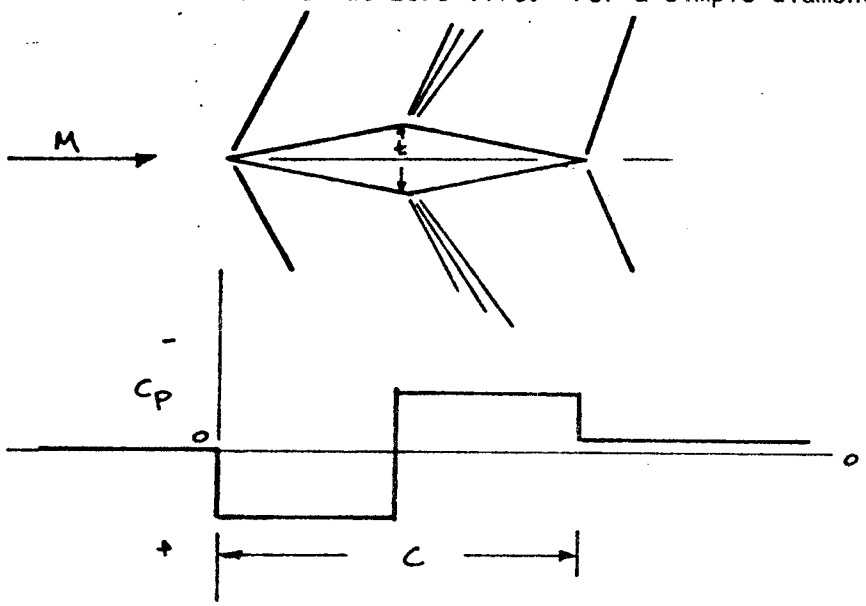

There is no lift produced, since the upper surface and lower surface pressures are equal and opposite. However, note that the pressure downstream of the airfoil has not returned to the free stream value. This is due to the fact that the shock at the rear of the airfoil is in a different Mach field than the shock at the leading edge. This drag term is given by:

$$c_d = \frac{4}{\beta}\left(\frac{t}{c}\right)^2 \tag{2.33}$$

In a more general form,

$$c_d = \frac{4}{\beta}\left[\left(\frac{\overline{dh}}{dx}\right)^2\right] \tag{2.34}$$

P2.23

2.3 (cont.)

where $h(x)$ is the local value of airfoil thickness and $\overline{h(x)}$ represents an average value:

$$\left(\frac{\overline{dh}}{dx}\right)^2 = \frac{1}{c}\int_0^c \frac{dh(x)}{dx}\,dx \tag{2.35}$$

Figure 2.21 summarizes the characteristics of the supersonic airfoil. The lift depends only on the mean angle and on free-stream Mach number. The drag is made of three components, drag due to lift, due to camber, and drag due to thickness. In contrast to the subsonic airfoil whose inviscid drag is zero, the supersonic airfoil has these three components, all due to shock waves and thus denoted as wave drag.

Of course, the force characteristics of the supersonic airfoil are altered by viscosity. Form drag will be added to the wave drag. And boundary layer separation is always a possibility should pressure gradients become too adverse. But in general, the operational range of the supersonic airfoil is so slight that separation is not too likely. Reference 2.10 contains a further discussion of the supersonic airfoil.

CHAPTER 2. REFERENCES

2.1 "Theory of Wing Sections," I. H. Abbott and A. E. Von Doenhoff, Dover Publications.

2.2 C/S 6-8320-679, A-280 User's Guide.

2.3 C/S AMEP-M-644,A-200 User's Guide.

2.4 Schlichting, J. and Ulrich,A., "For Berechnung Des Umschlages Laminar Turbulenten," Jahrbuch 1942 Der Deutschen Luftfahrt-Forschung.

2.5 For information on PAN2D, contact M. Henderson or J. L. Lundry.

2.6 "Complete Tabulation in the United States of Tests of 24 Airfoils at High Mach Numbers," Antonio Ferri, NACA Wartime Report L-143 (ACRL5E21), June, 1945.

2.7 "The Aerodynamic Design of Section Shapes for Swept Wings," H. H. Pearcey, Advances in Aeronautical Sciences, Vol. 3, p. 277, Pergamon Press, 1962.

2.8 "The Design of Efficient Transonic Airfoils," I. J. Gilchrist, D6-41783TN, 1975.

2.9 C/S AMEP-M-796, A 423 User's Guide.

2.10 "Elements of Gasdynamics," H. W. Liepmann and A. Roshko, John Wiley & Sons, 1958.

EXAMPLE: CALCULATE THE PRESSURE COEFFICIENT AT X/C=.25 ON NACA 23012 AT $C_\ell = 0.5$

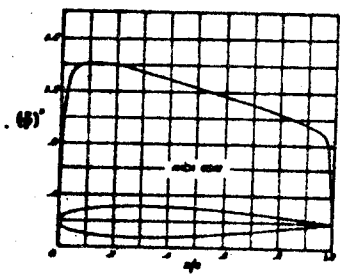

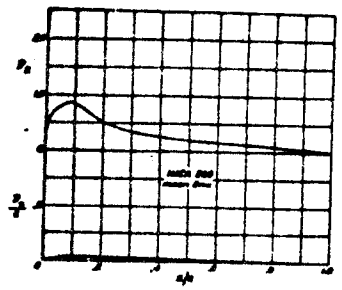

0	0	0	0	1.000
0.5	.....	0.640	0.800	1.475
1.25	1.884	1.060	1.006	1.180
2.5	2.615	1.361	1.114	0.984
5.0	2.885	1.378	1.174	0.955
7.5	4.200	1.608	1.184	0.860
10	4.883	1.611	1.188	0.475
15	5.346	1.611	1.188	0.288
20	5.787	1.500	1.183	0.210
25	5.941	1.378	1.174	0.273
30	6.008	1.300	1.160	0.200
40	6.200	1.300	1.135	0.157
50	6.304	1.220	1.105	0.140
60	4.888	1.105	1.050	0.115
70	3.004	1.100	1.063	0.088
80	2.000	1.044	1.022	0.056
90	1.440	0.988	0.978	0.044
95	0.207	0.956	0.963	0.039
100	0.126	0	0	0

L.E. radius: 1.58 per cent c

NACA 0012 Basic Thickness Form

0	0	0.30800	0	0
1.25	0.267	0.36504	0.032	0.122
2.5	0.000	0.22929	0.073	0.105
5.0	1.136	0.16347	0.781	0.196
7.5	1.488	0.10702	0.863	0.213
10	1.701	0.06174	0.889	0.215
15	1.888	− 0.00009	0.875	0.170
20	1.787	− 0.02208	0.819	0.120
25	1.688		0.419	0.105
30	1.548		0.891	0.080
40	1.288		0.276	0.089
50	1.104		0.217	0.054
60	0.000		0.177	0.044
70	0.002	− 0.02308	0.144	0.038
80	0.440		0.106	0.026
90	0.221		0.000	0.017
95	0.110		0.062	0.011
100	0		0	0

Data for NACA Mean Line 230

(1) V/V_0: $(V/V_0)_{tk=.12} = 1.174$

(2) $\Delta V/V_0$: $(\Delta V/V_0) = 0.105$ AT $C_{\ell_i} = 0.30$

(3) $\Delta V_a/V_0$: $(\Delta V_a/V_0) = 0.273$ for $C_\ell = 1$

$$(\Delta V_a/V_0)_{C_\ell=.5} = (.5-.3)(.273) = 0.546$$

(4) $C_{P_{UPPER}} = 1 - (1.174 + .105 + .0546)^2 = -.78$

$C_{P_{LOWER}} = 1 - (1.174 - .105 - .0546)^2 = -.02$

FIGURE 2.1 CALCULATION of AIRFOIL PRESSURE COEFFICIENT BY SUPERPOSITION

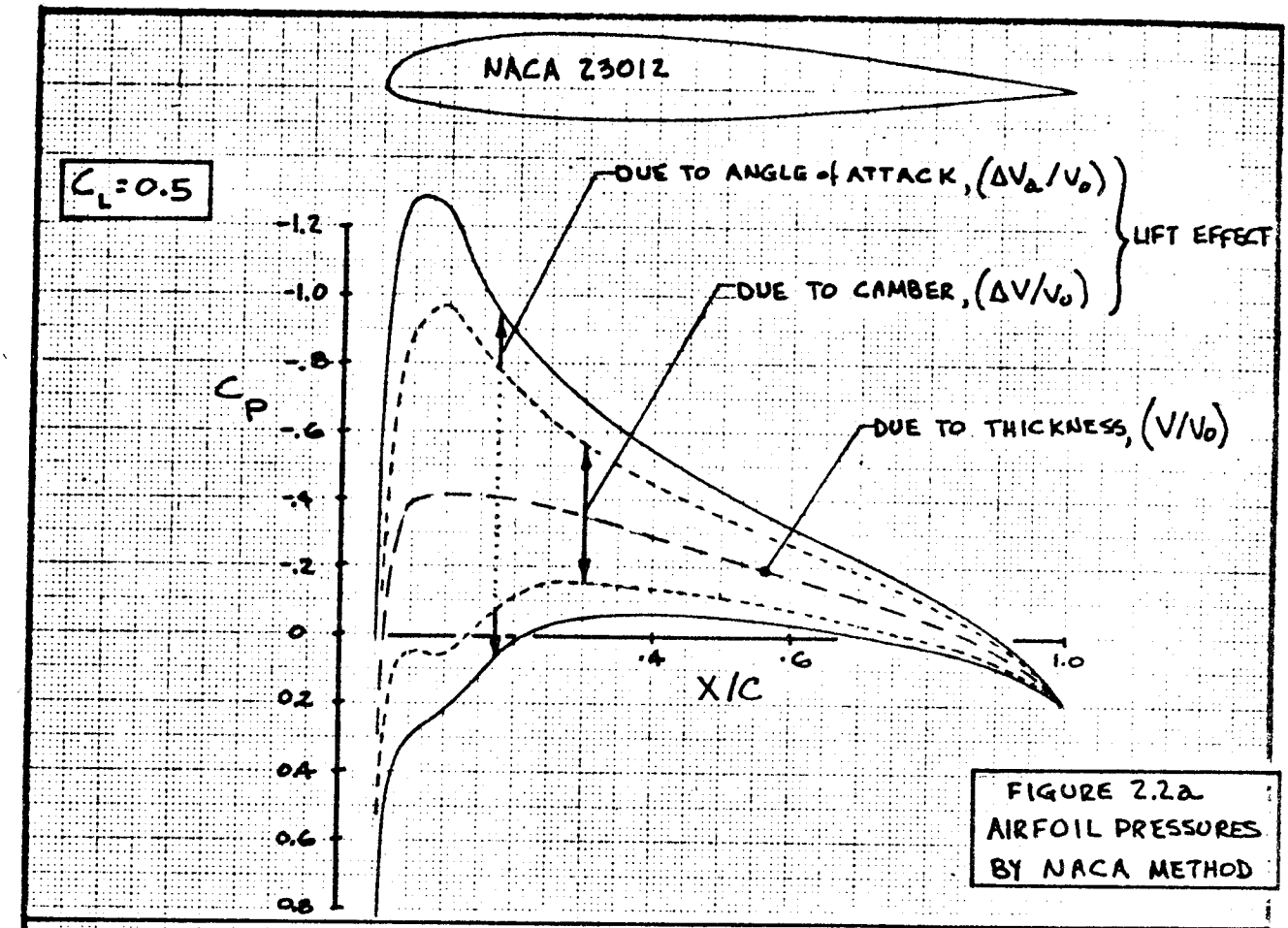

FIGURE 2.2a
AIRFOIL PRESSURES
BY NACA METHOD

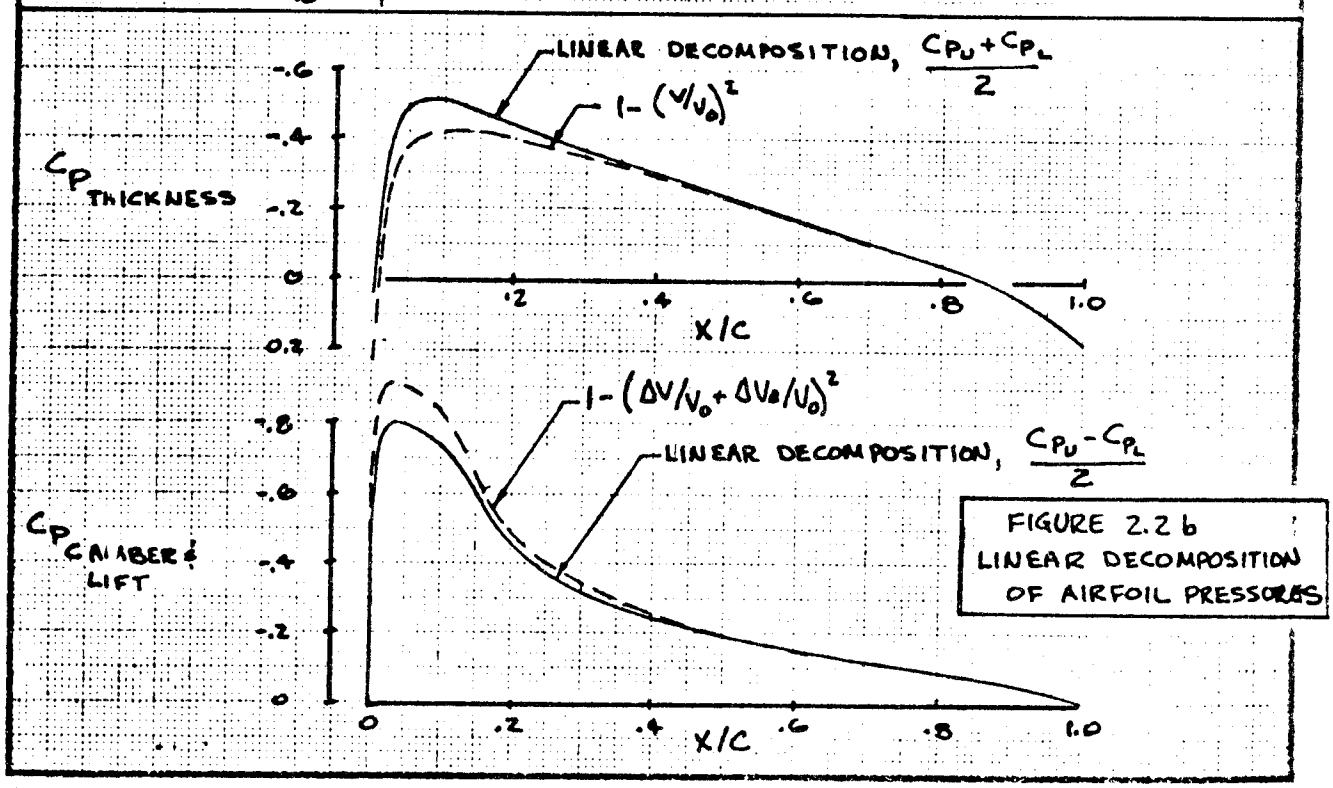

FIGURE 2.2b
LINEAR DECOMPOSITION
OF AIRFOIL PRESSURES

CALC	GILLETTE	11-29-77	REVISED	DATE
CHECK				
APR				
APR				

CONSTRUCTION of AIRFOIL PRESSURES FROM THICKNESS AND CAMBER EFFECTS — FIG. 2.2

BOEING

PAGE 2.27

D1 4100 3260 ORIG. 3/71

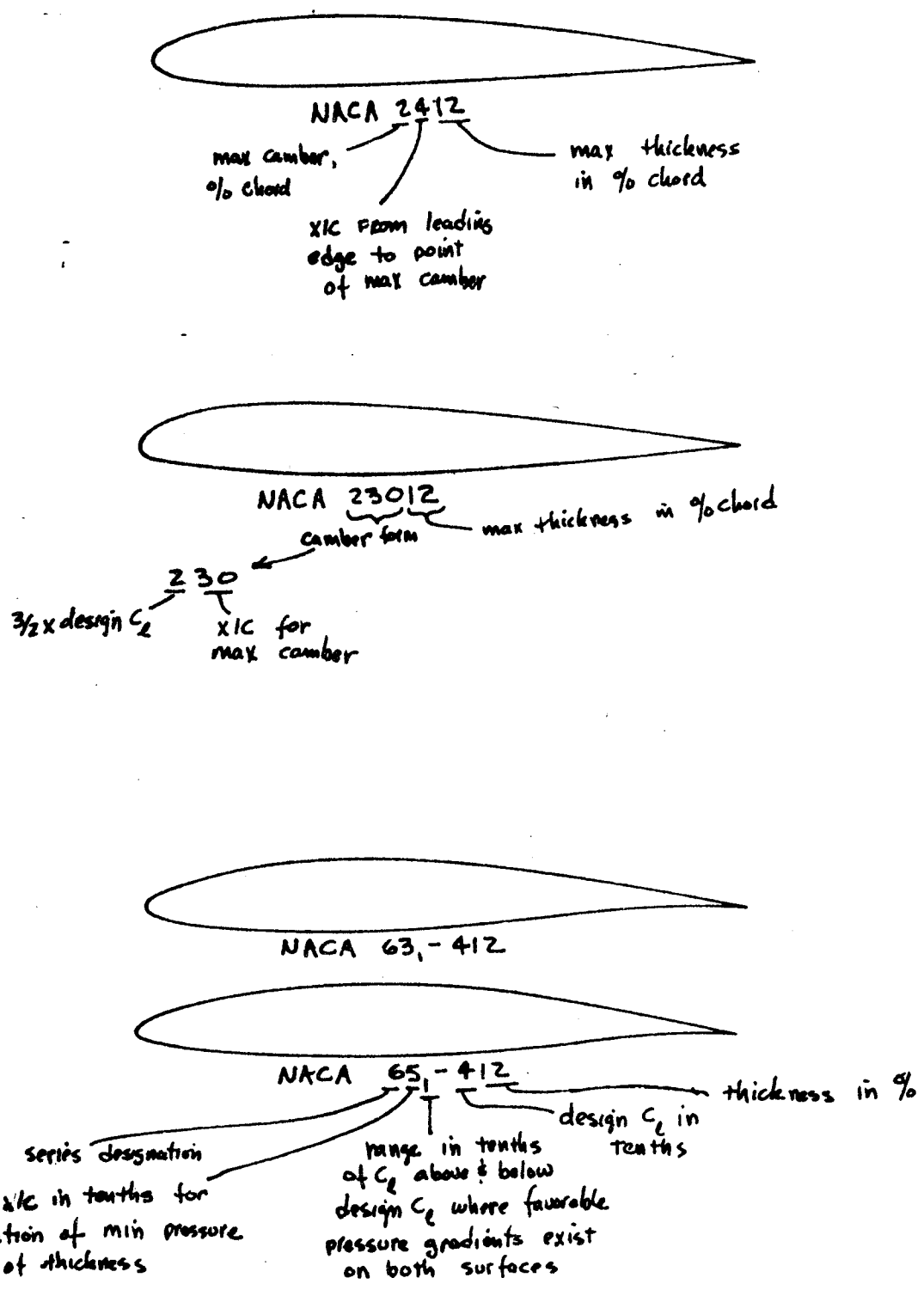

FIGURE 2.3 NACA AIRFOILS

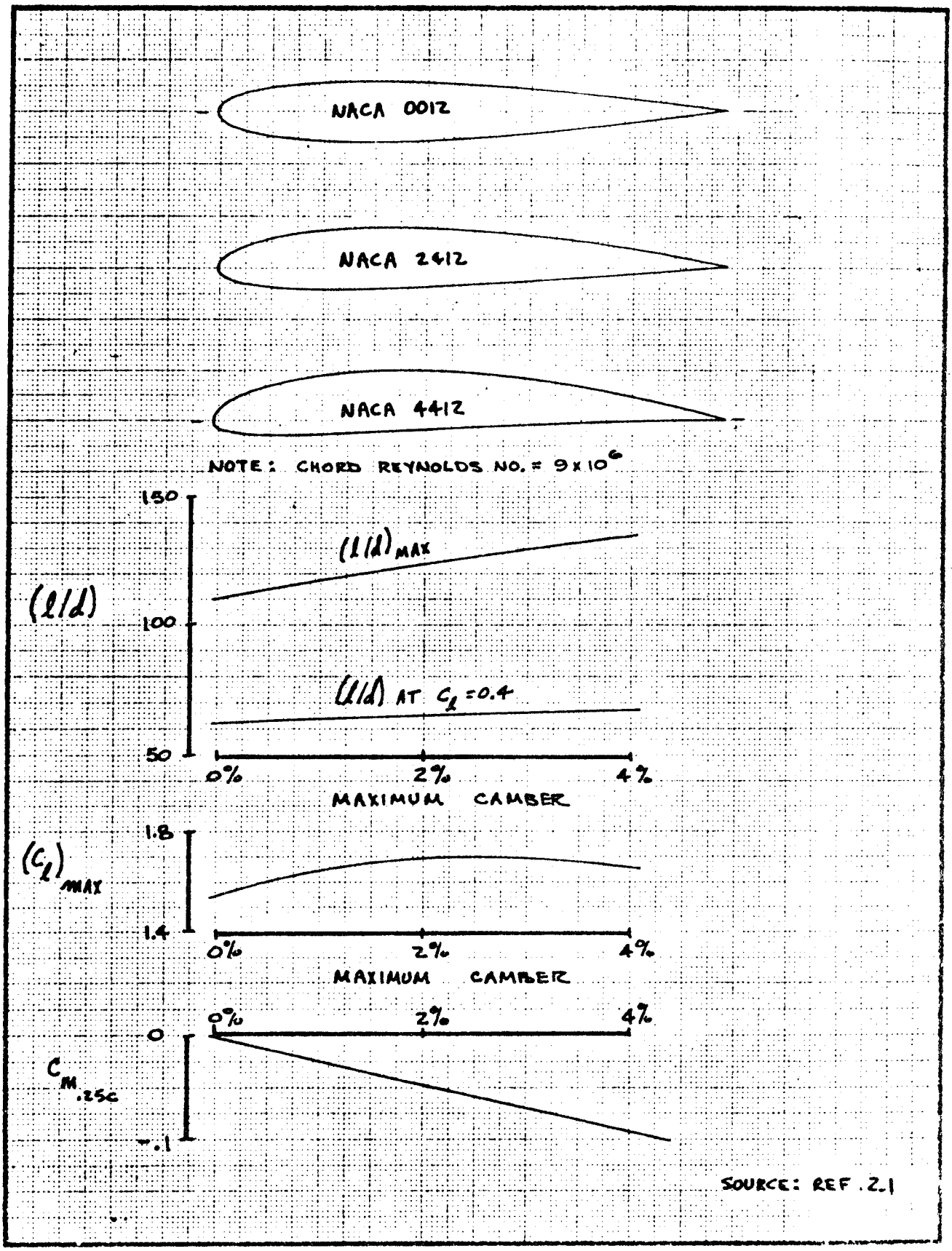

CALC	GILLETTE	1-29-77	REVISED	DATE	EFFECT OF CAMBER ON AIRFOIL PERFORMANCE
CHECK					
APR					
APR					
					BOEING

FIG 2.4

PAGE 2.29

D1 4100 3260 ORIG. 3/71

61

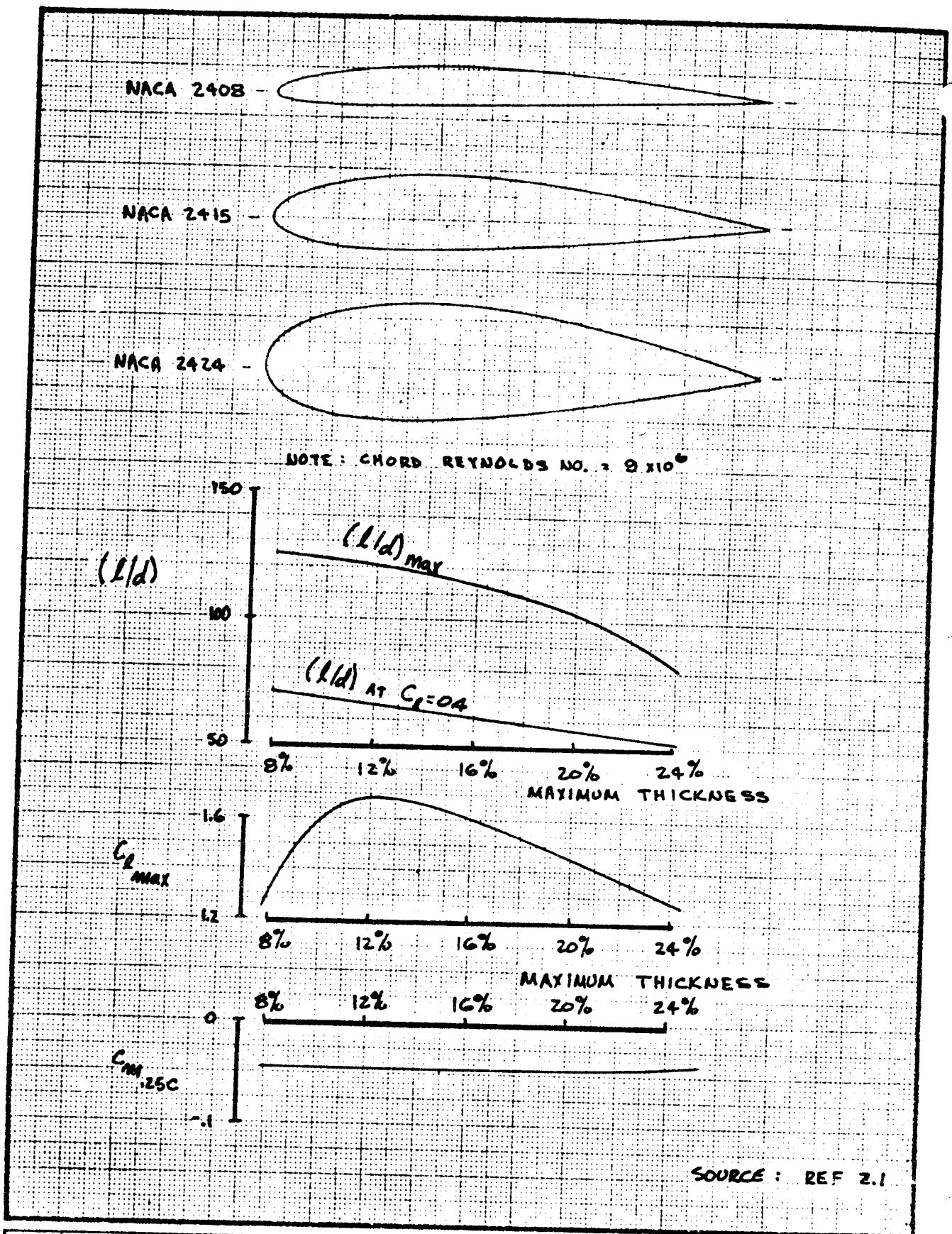

CALC	GILLETTE	11-21-77	REVISED	DATE	EFFECT OF THICKNESS ON AIRFOIL PERFORMANCE
CHECK					FIG. 2.5
APP					
APP					BOEING
					PAGE 2.30

D1 4100 3260 ORIG 3/71

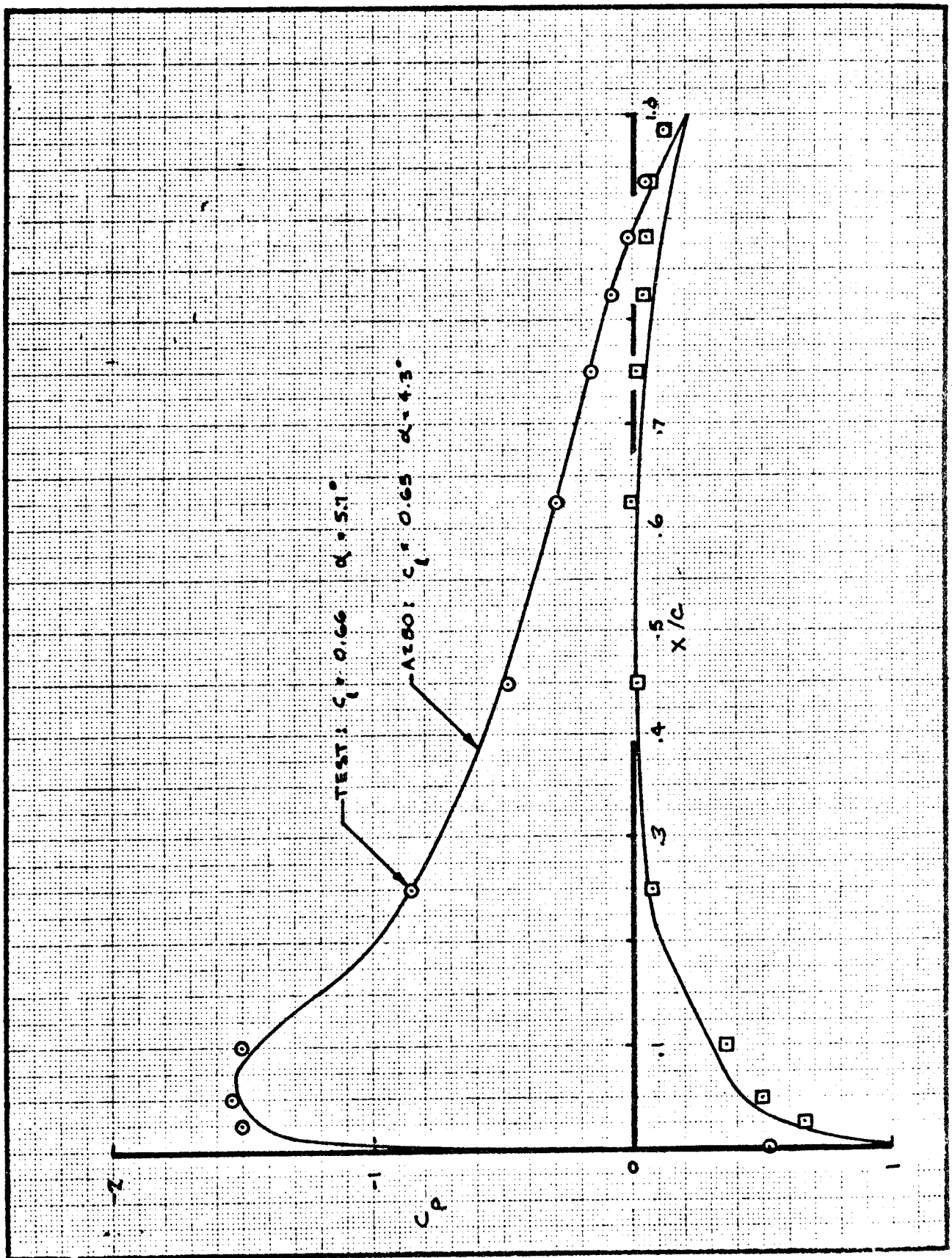

CALC	GILLETTE	12-19-77	REVISED	DATE	COMPARISON OF TEST & ANALYSIS FOR NACA 23012
CHECK					FIG. 2.6
APR					
APR					BOEING
					PAGE 2.31

D1 6100 3260 ORIG. 3/71

115.047

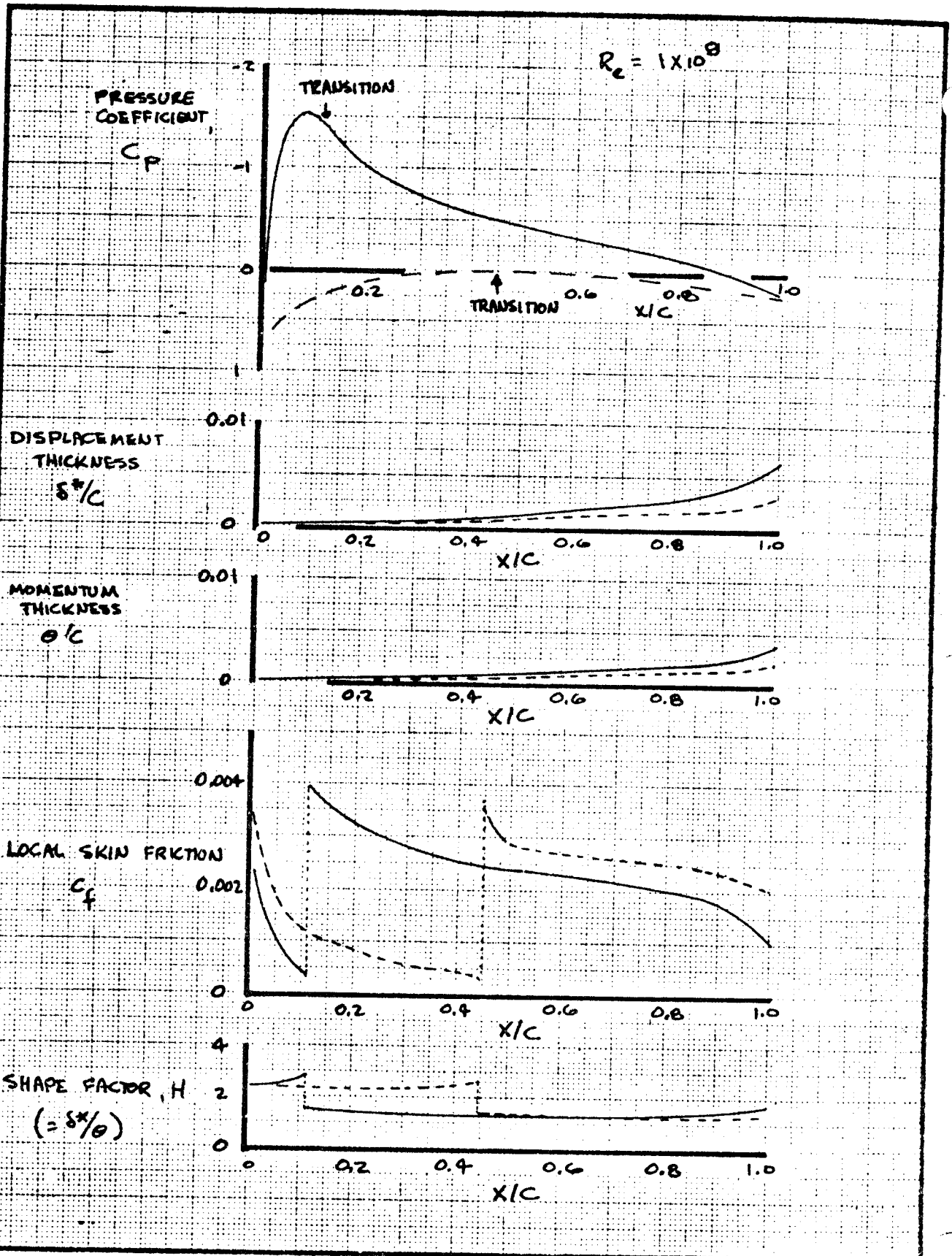

CALC	GILLETTE 1.2.78	REVISED	DATE	COMPUTED BOUNDARY LAYER CHARACTERISTICS FOR NACA 23012 FIG 2.7
CHECK				
APR				
APR				BOEING PAGE 2.32

D1 4100 3260 ORIG. 3/71

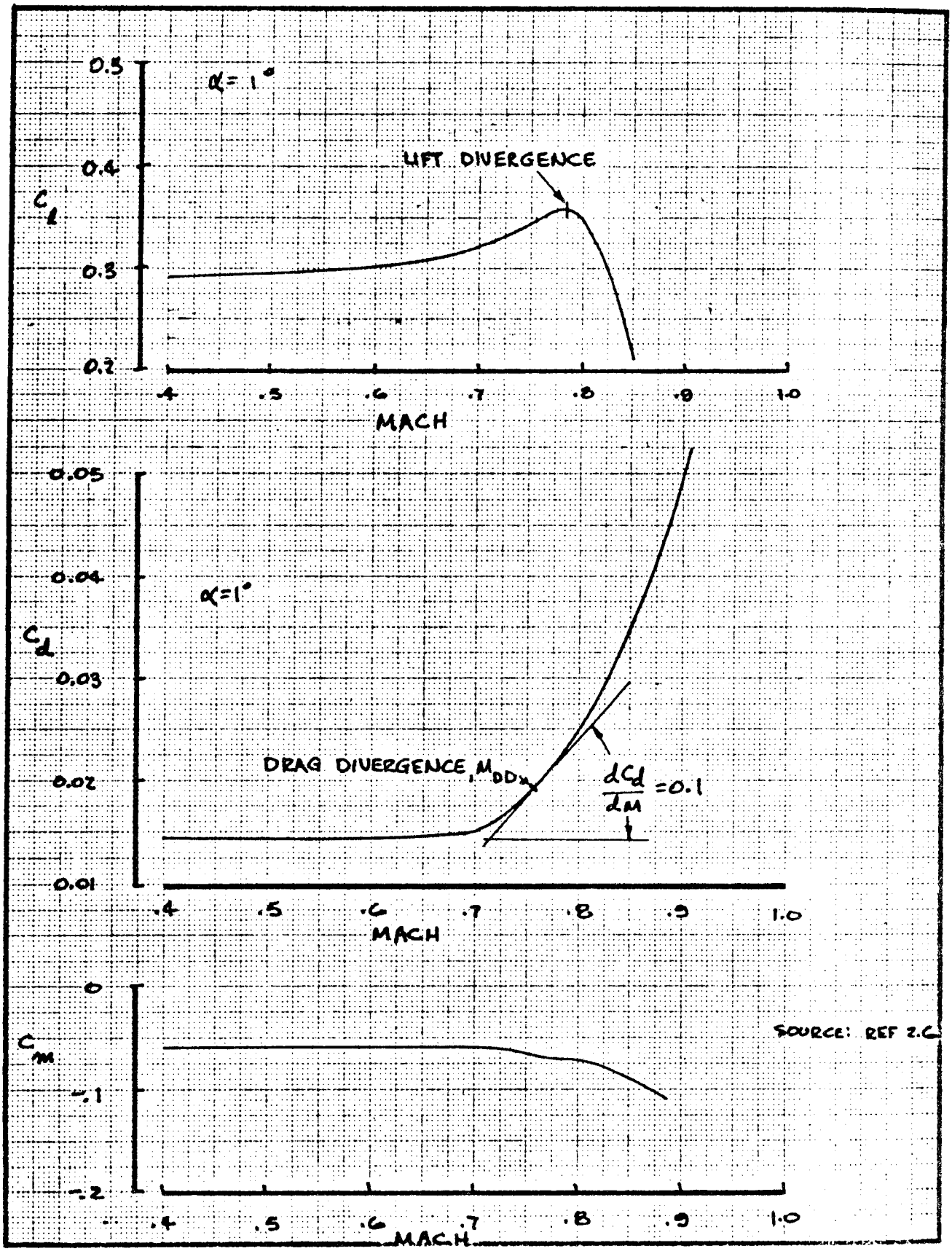

SOURCE: REF 2.C

CALC	GILLETTE	11/24/77	REVISED	DATE	NACA 2309 TRANSONIC FORCE & MOMENT EFFECTS
CHECK					
APR					
APR					BOEING

FIG 2.B

PAGE 2.33

D1 4100 3260 ORIG. 3/71

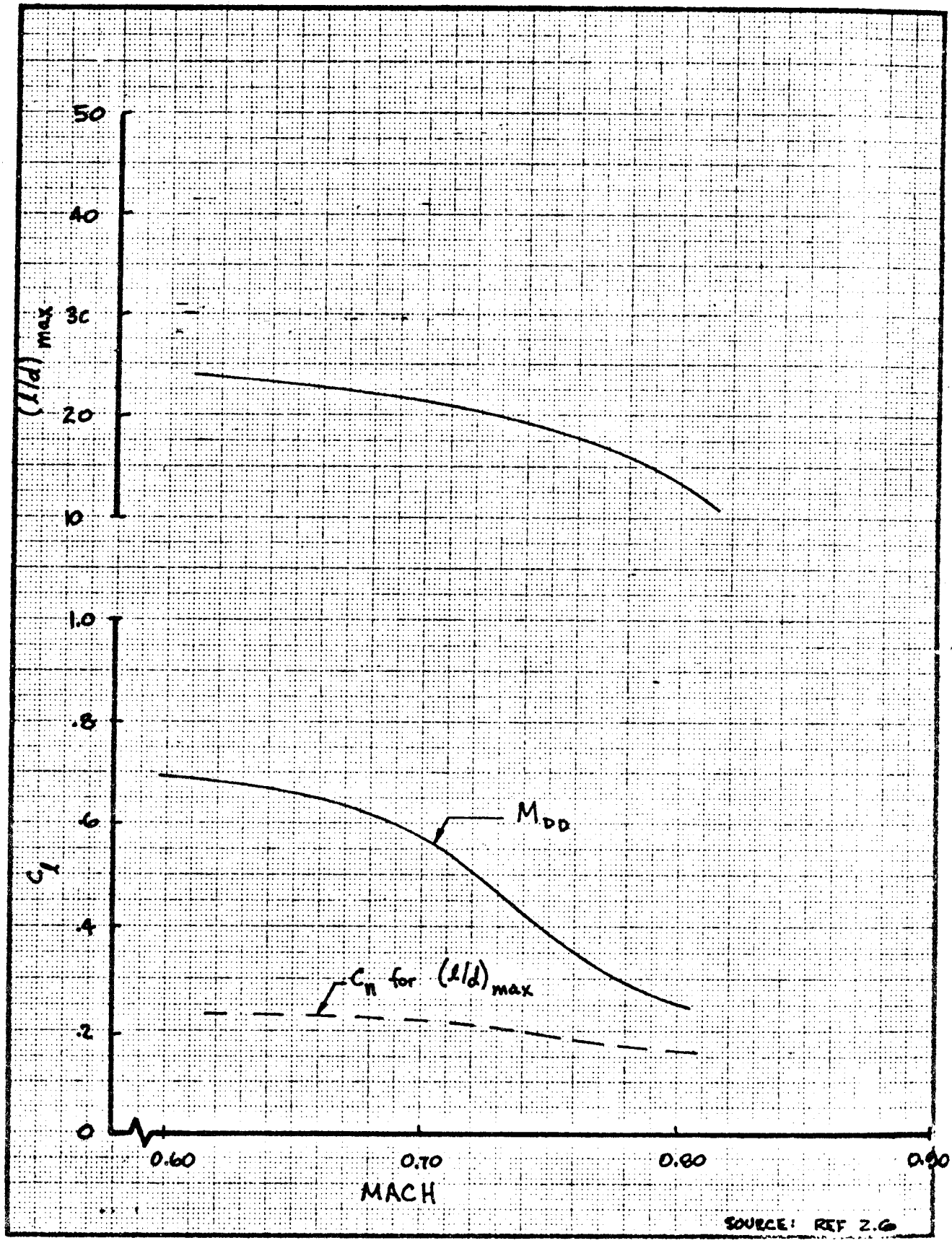

CALC	GILLETTE	11-24-77	REVISED	DATE	NACA 2309 TRANSONIC DRAG CHARACTERISTICS	FIG 2.9
CHECK						
APR						
APR					BOEING	PAGE 2.34

D1 4100 3260 ORIG. 3/71 115-047

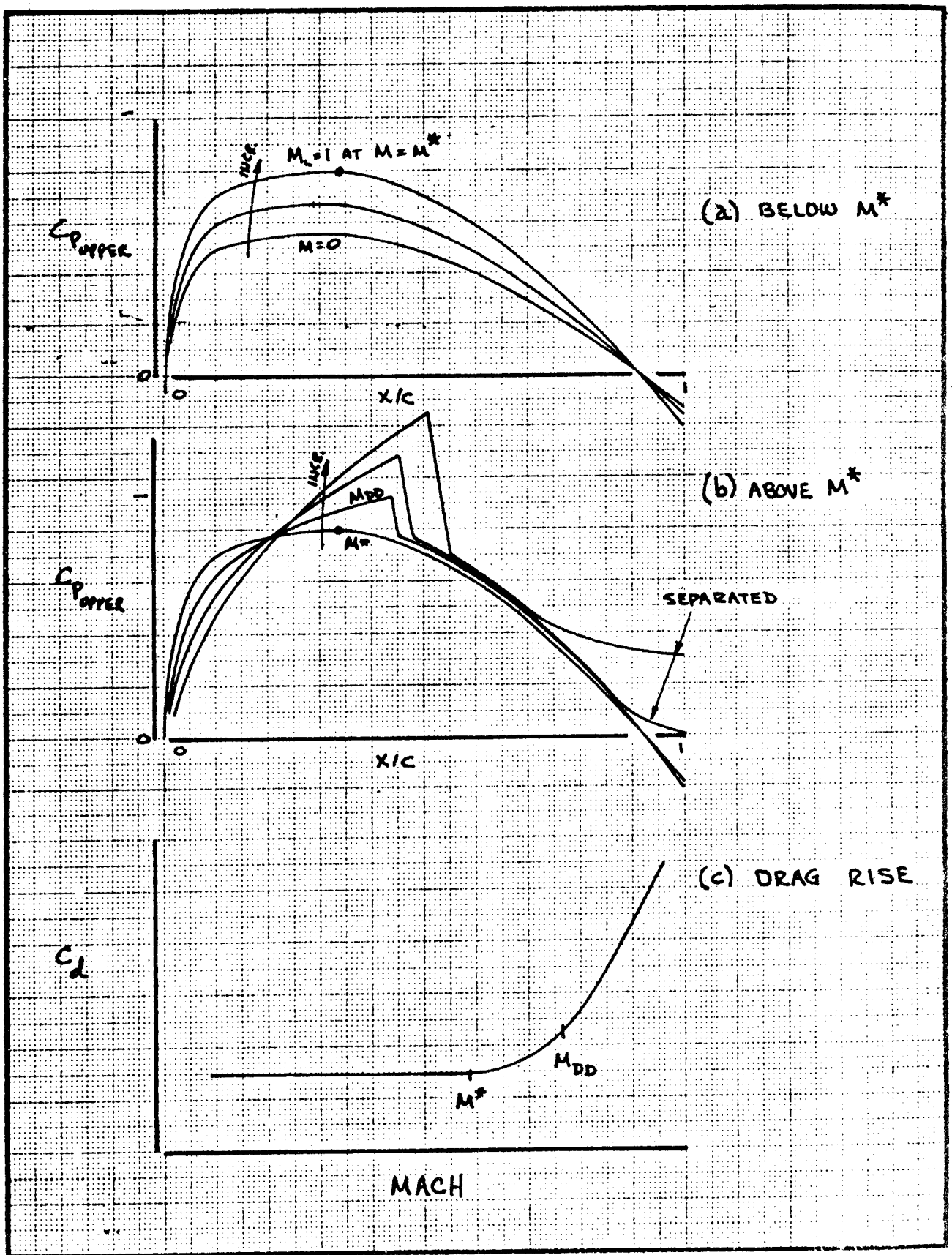

CALC	GILLETTE	11-24-77	REVISED	DATE	DRAG RISE AND AIRFOIL UPPER SURFACE PRESSURES — FIG 2.10
CHECK					
APR					
APR					BOEING — PAGE 2.35

D1 4100 3-60 ORIG. 3/71

J15.047.

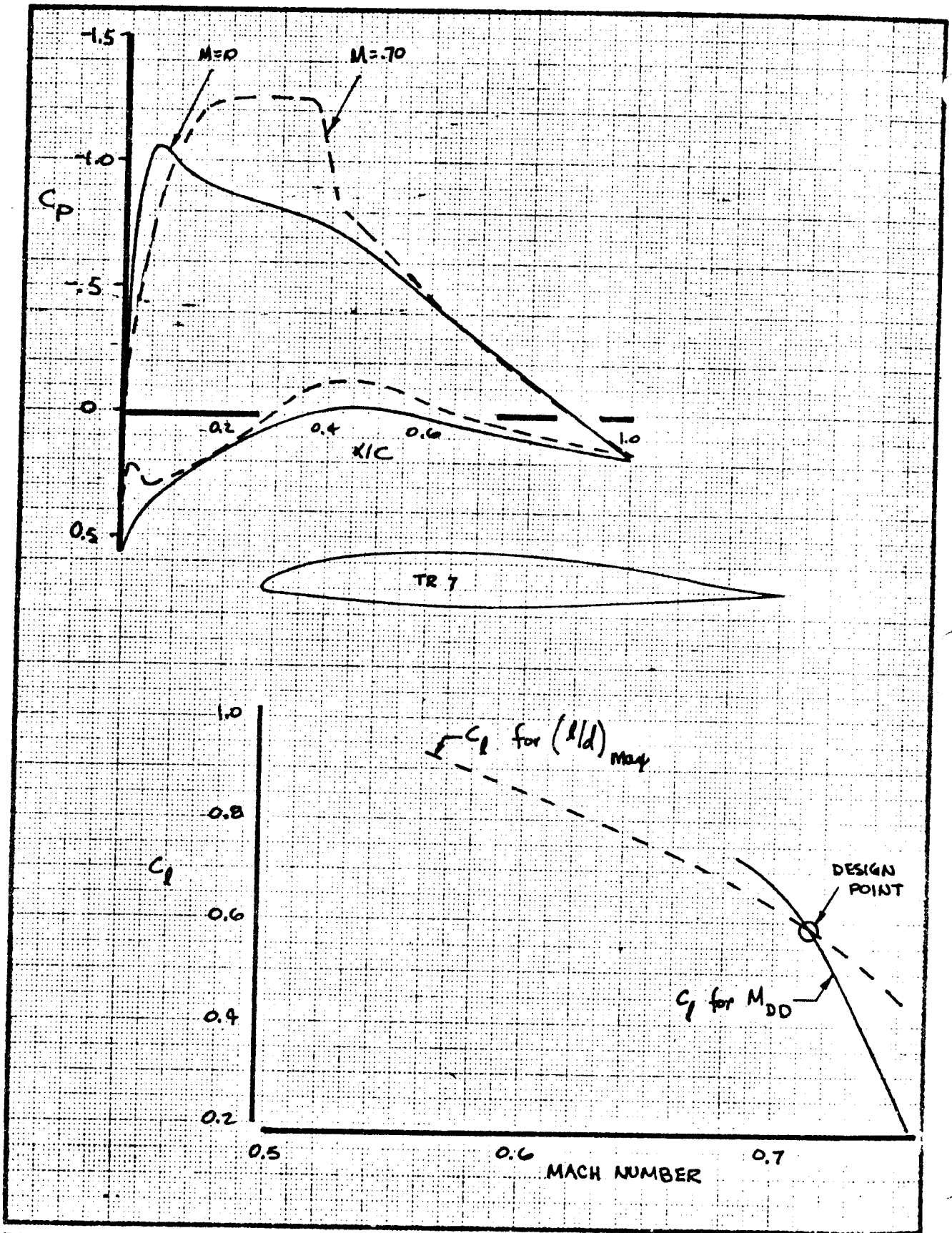

CALC	GILLETTE	1-2-78	REVISED	DATE
CHECK				
APR				
APR				

TR 7 (707) CHARACTERISTICS

FIG 2.11

BOEING

PAGE 2.36

D1 4100 3260 ORIG. 3/71

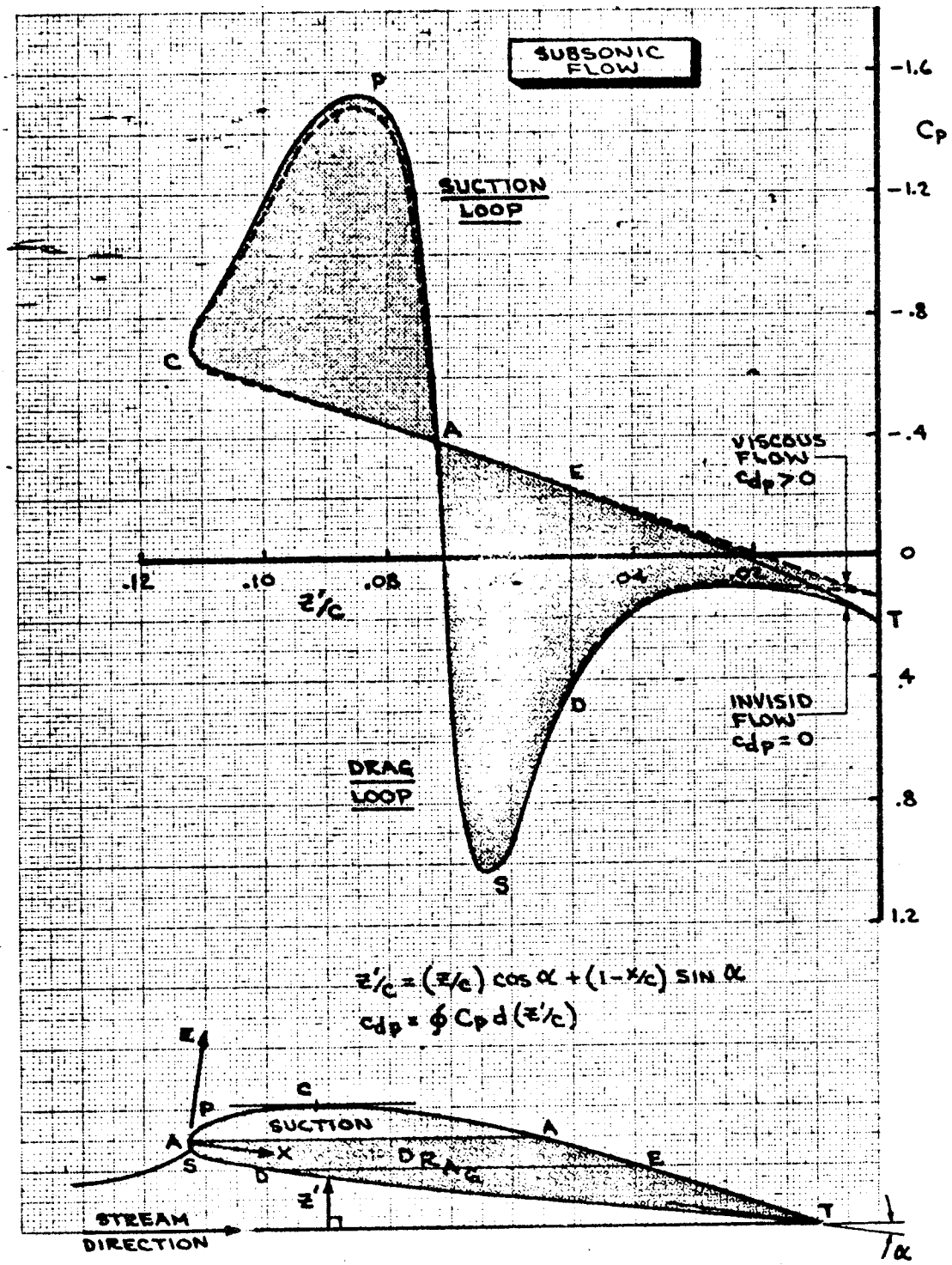

CALC	E.GEORGE	8-75	REVISED	DATE	DRAG ANALYSIS OF SURFACE PRESSURES	FIG 2.12
CHECK						DC-41783 TN
APPD						
APPD					THE BOEING COMPANY	PAGE 2.37

AD 4068 C

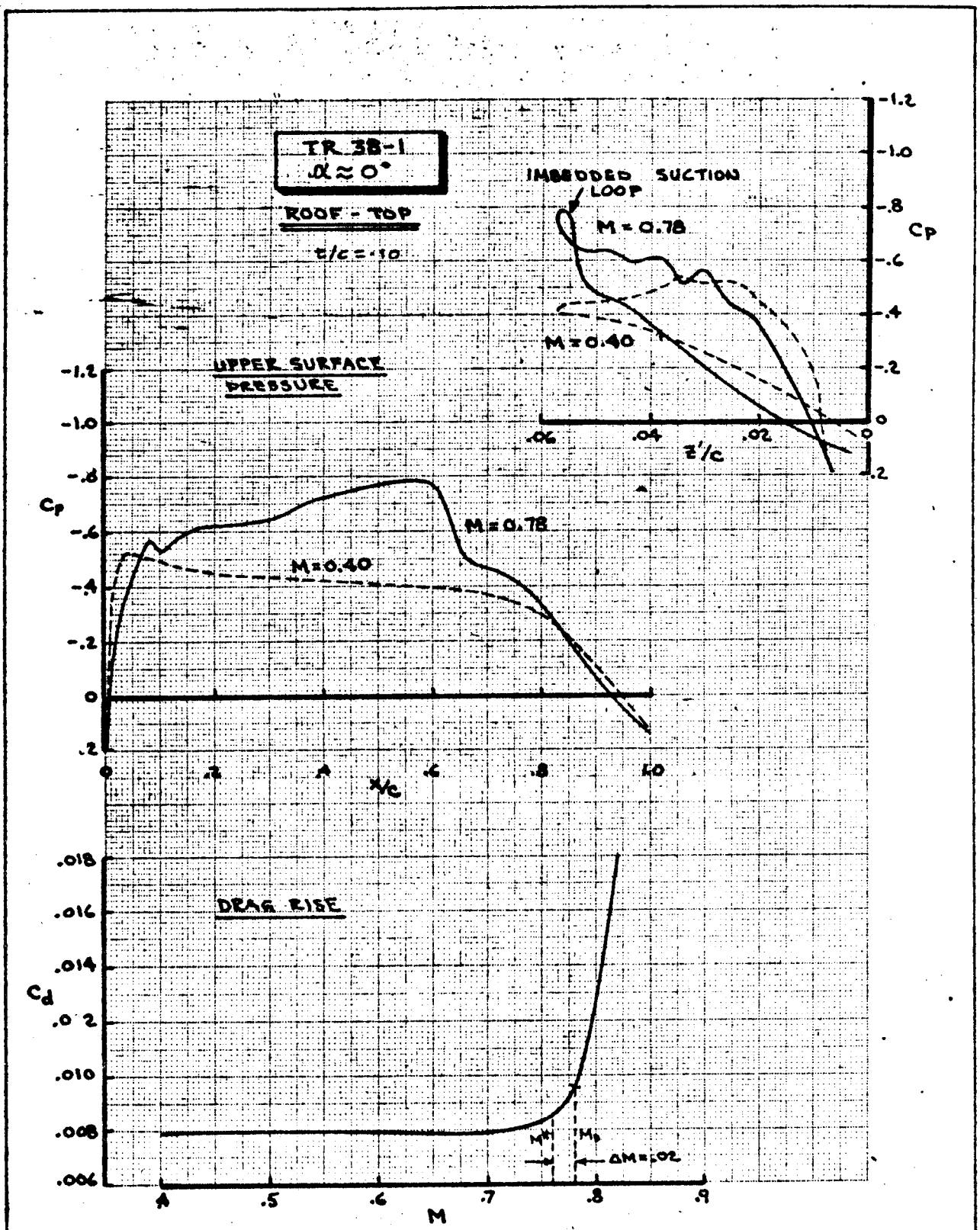

CALC	E. GEORGE	3-75	REVISED	DATE	EFFECT OF SUCTION LOOP SHAPE ON DRAG DIVERGENCE MACH NO.~ ROOF TOP AIRFOIL	FIG. 2.13
CHECK						D6-41783 TN
APPD					THE BOEING COMPANY	PAGE 2.38
APPD						

AD 4992 C

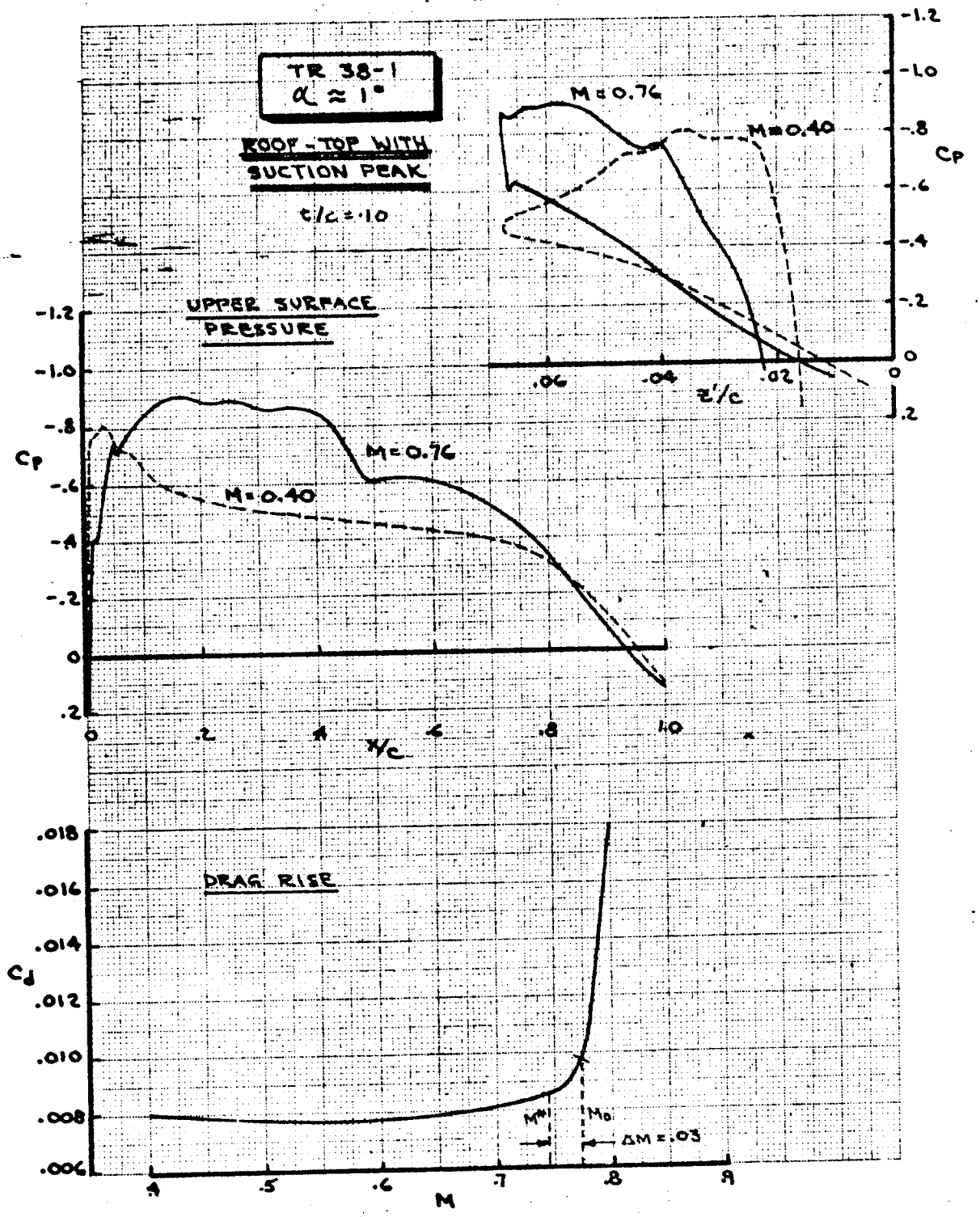

CALC	E. GEORGE	3-75	REVISED	DATE	EFFECT OF SUCTION LOOP SHAPE ON DRAG DIVERGENCE MACH NO. ~ ROOF TOP WITH SUCTION PEAK AIRFOIL
CHECK					
APPD					
APPD					

FIG. 2.14

D6-41783 TN

PAGE 2.39

THE BOEING COMPANY

8-5000

AD 4992 C

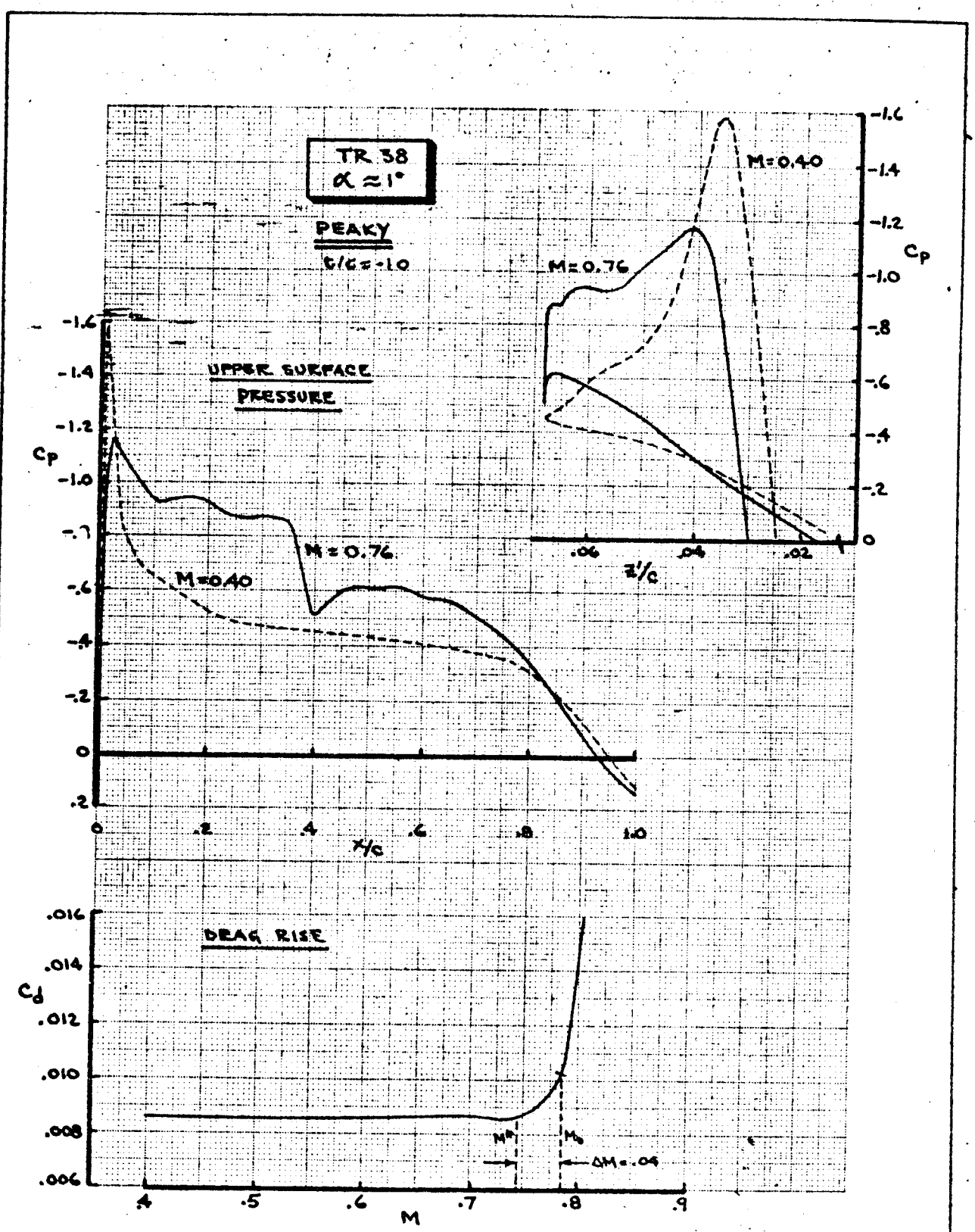

CALC	E. GEORGE	3-75	REVISED	DATE	EFFECT OF SUCTION LOOP SHAPE ON DRAG DIVERGENCE MACH NO. ~ PEAKY AIRFOIL	FIG. 2.15
CHECK						D6-41783 TN
APPD					THE BOEING COMPANY	PAGE 2.90
APPD						

AD 4092 C

6-5000

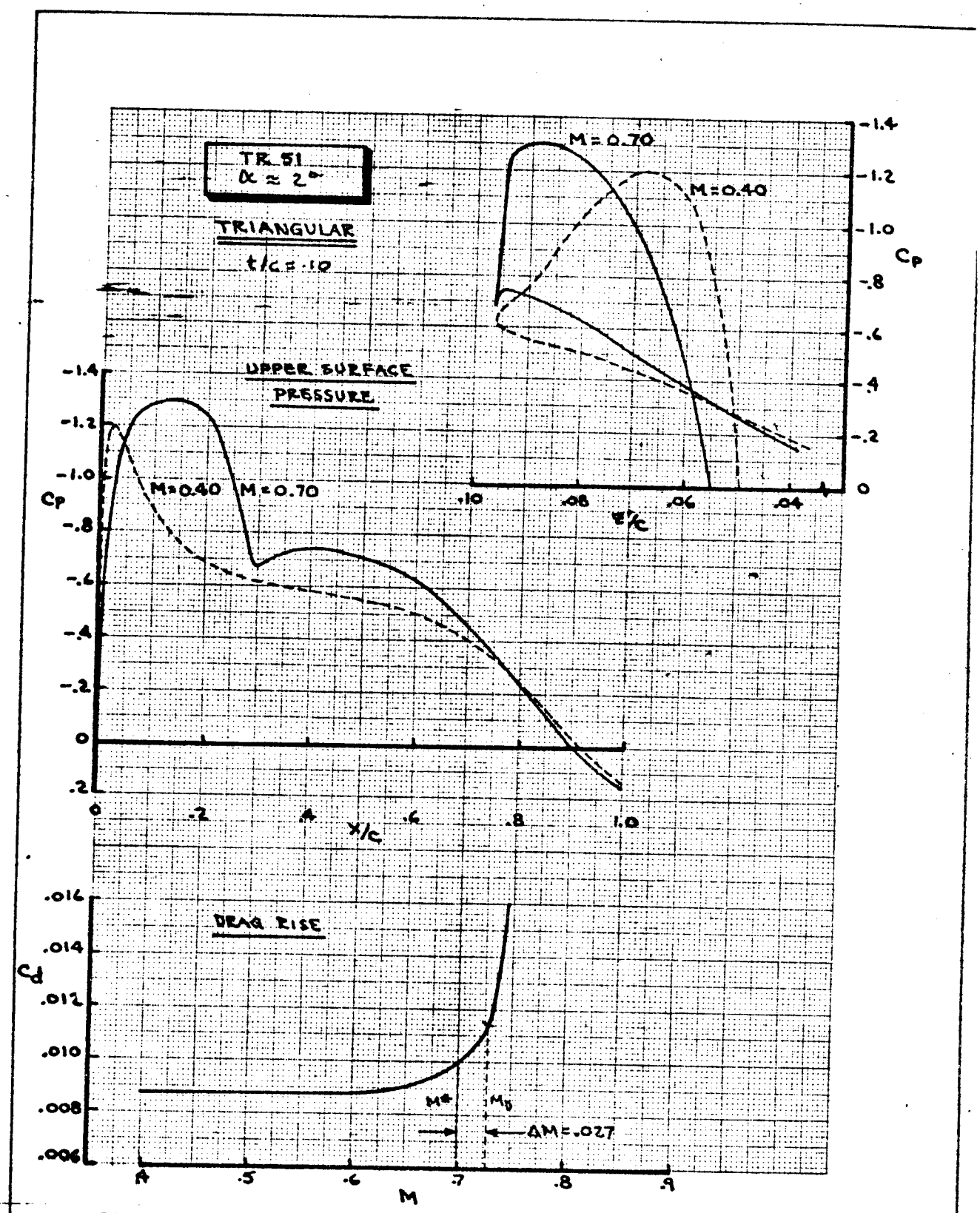

CALC	E. GEORGE	3-75	REVISED	DATE	EFFECT OF SUCTION LOOP SHAPE ON DRAG DIVERGENCE MACH NO.~ TRIANGULAR PRESSURE DISTRIBUTION	FIG 2.16
CHECK						D6-41783 TN
APPD						
APPD					THE BOEING COMPANY	PAGE 2.190

TYPE	SUCTION LOOP	CHORDWISE PRESSURE	AIRFOIL
ROOF-TOP	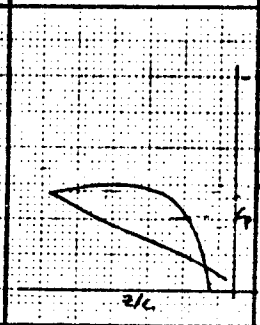	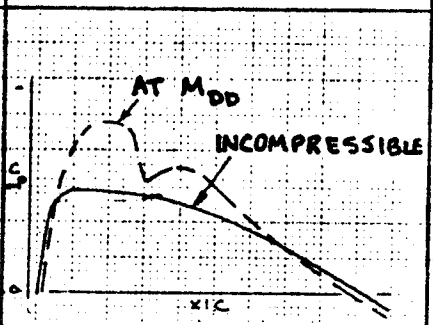	TR 7 (707) 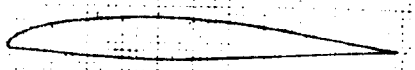
ROOF-TOP WITH SUCTION PEAK	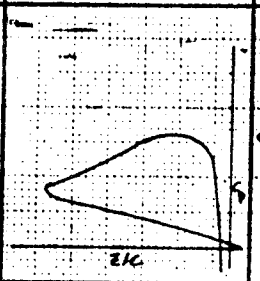	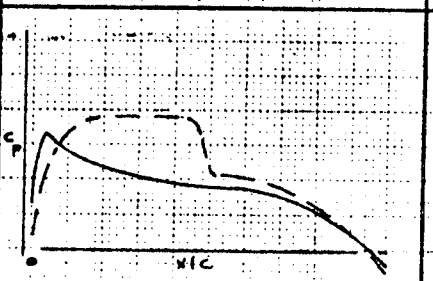	TR 38-1 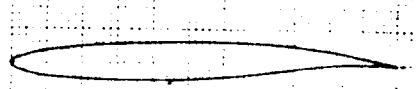
PEAKY	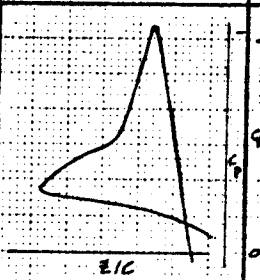	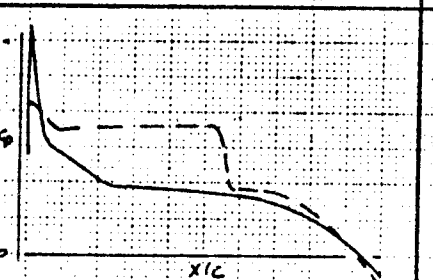	TR 38 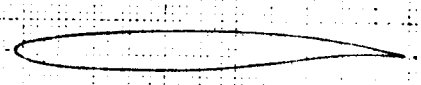
TRI-ANGULAR	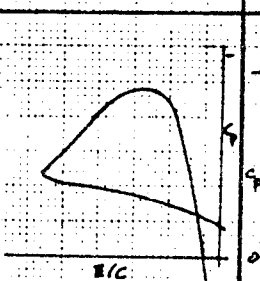	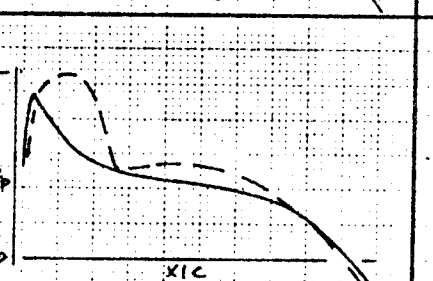	TR 51 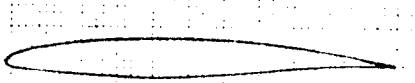

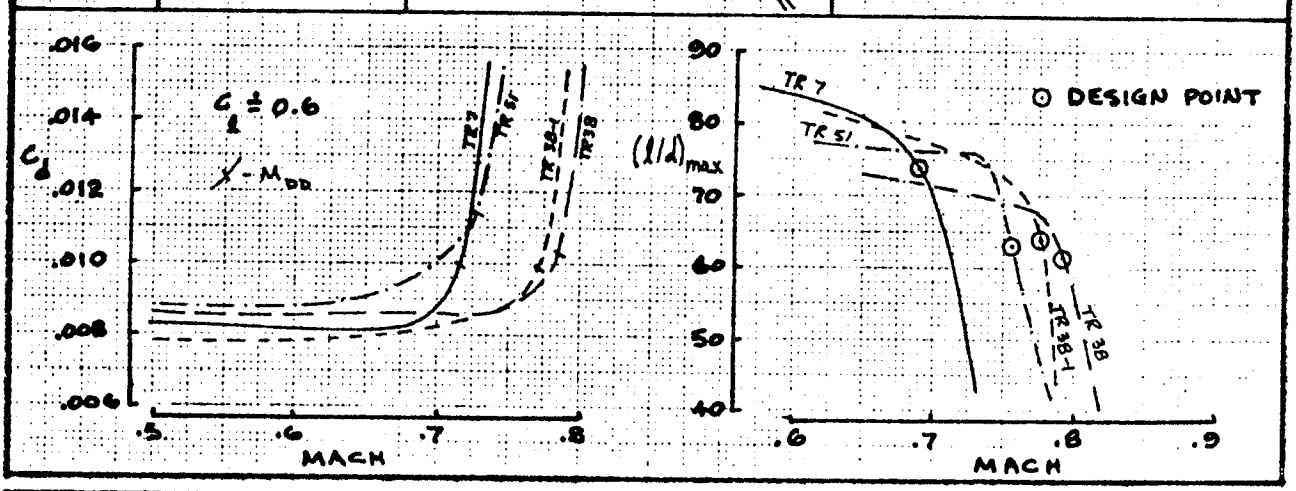

CALC	GILLETTE	12-9-77	REVISED	DATE
CHECK				
APR				
APR				

TRANSONIC AIRFOIL CLASSES FIG 2.17

BOEING

PAGE 2-42

D1 4100 3290 ORIG. 3/71

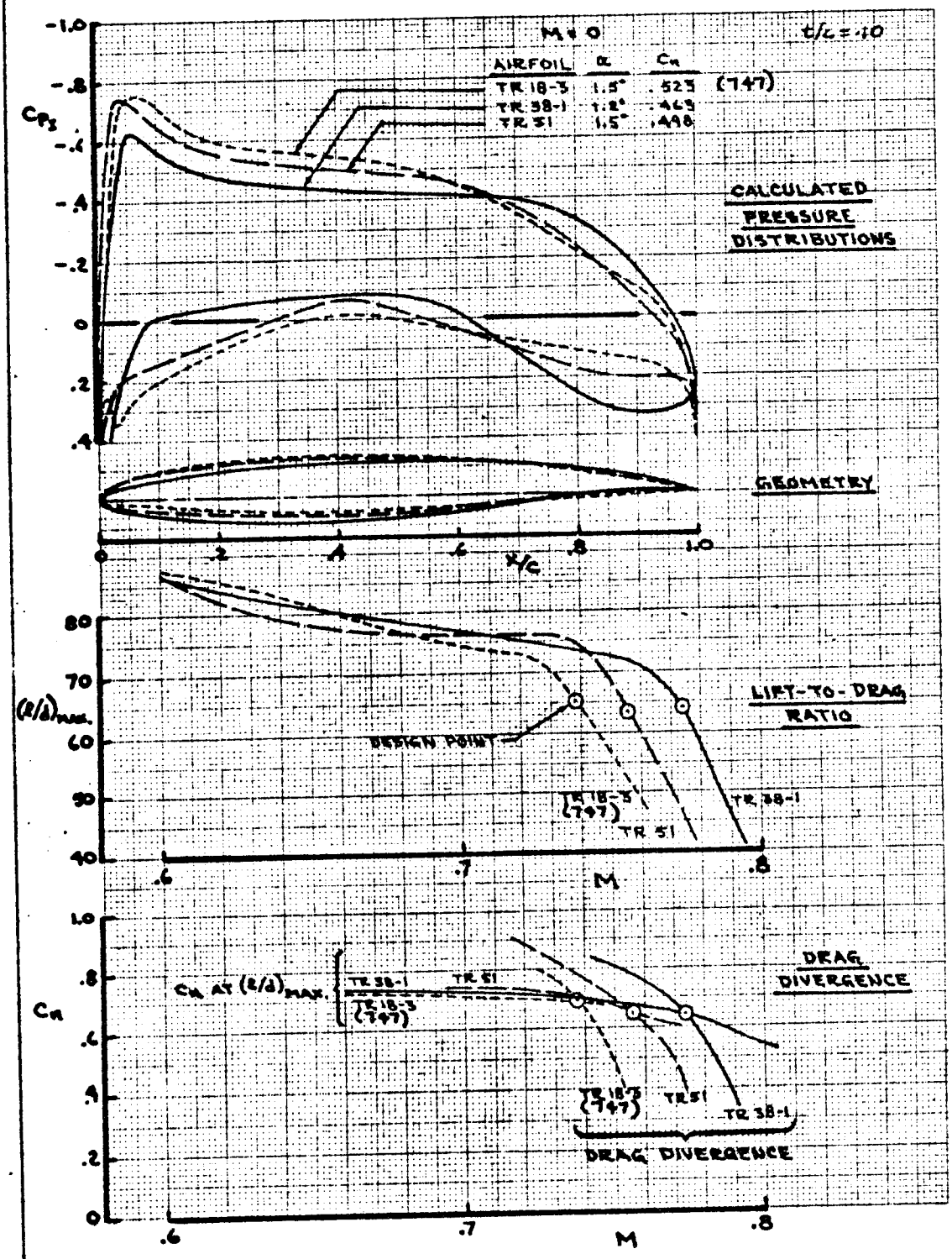

CALC	E. GEORGE	4-75	REVISED	DATE	EFFECTS OF INCREASING AFT LOADING	FIG 2.18
CHECK						D6-41783 TN
APPD						
APPD					THE BOEING COMPANY	PAGE 2.428

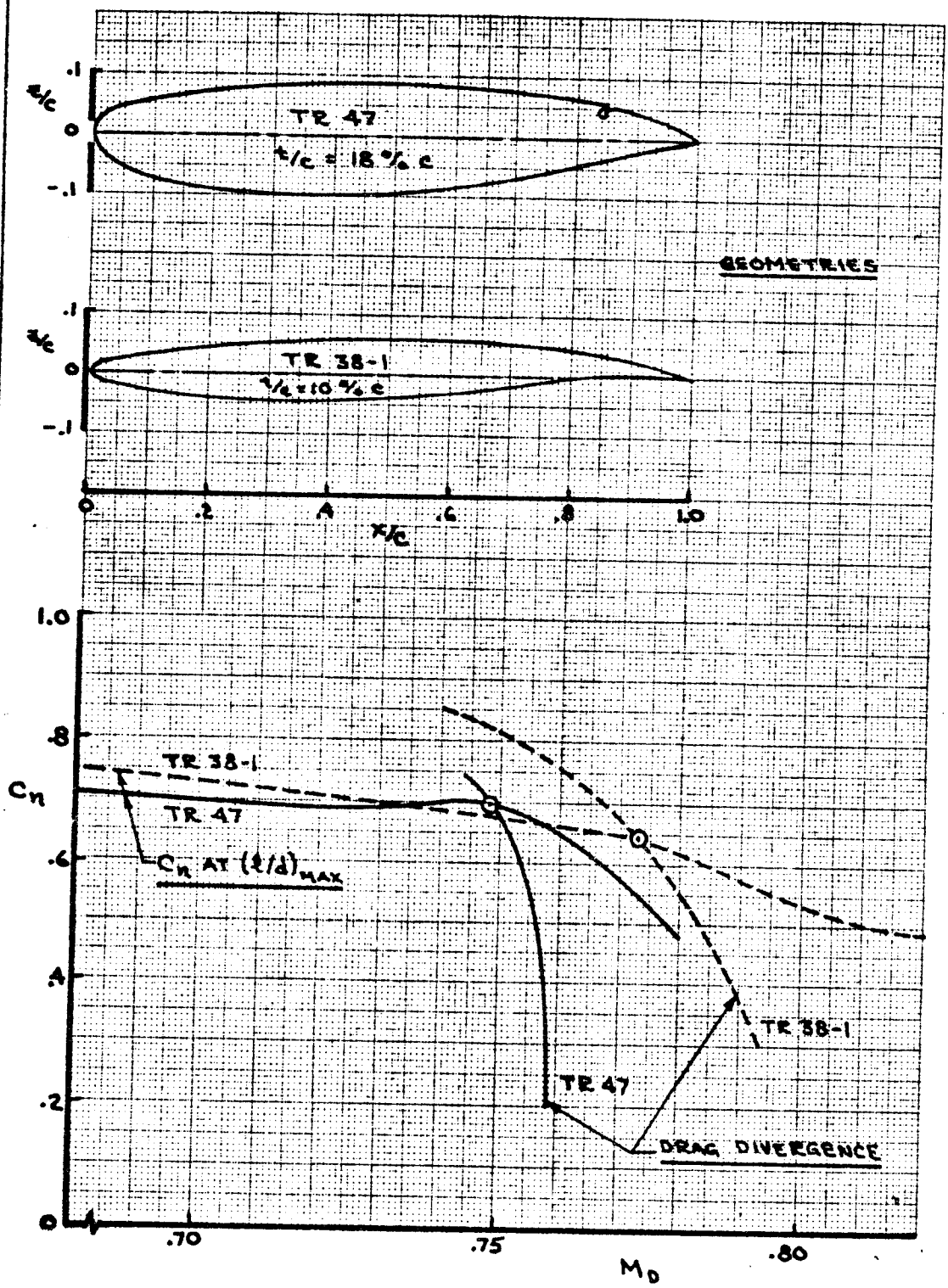

CALC	E. GEORGE	4-75	REVISED	DATE	BOUNDARY LAYER CONTROL APPLIED TO THICK AIRFOIL -
CHECK					
APPD					
APPD					
					THE BOEING COMPANY

FIG. 2.19

D6-41783 TN

6-8000

AIRFOIL = FLAT PLATE AT MEAN ANGLE + CAMBER LINE + THICKNESS FORM

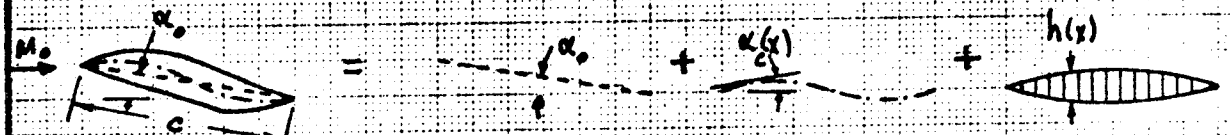

$\beta = \sqrt{M_\infty^2 - 1}$

$$C_l = \frac{4}{\beta}\alpha_0 + 0 + 0$$

$$C_d = \frac{4}{\beta}\alpha_0^2 + \frac{4}{\beta}\frac{1}{c}\int_0^c \alpha_c^2(x)\,dx + \frac{4}{\beta}\frac{1}{c}\int_0^c \left[\frac{dh(x)}{dx}\right]^2 dx$$

$$= \frac{4}{\beta}\left[\alpha_0^2 + \overline{\alpha_c}^2 + \left(\overline{\frac{dh(x)}{dx}}\right)^2\right]$$

= DRAG DUE TO LIFT + DRAG DUE TO CAMBER + DRAG DUE TO THICKNESS

$$C_{m_{.5c}} = 0 + \frac{4}{\beta}\frac{1}{c^2}\int_0^c \alpha_c(x)[1-x]\,dx + 0$$

CALC	GILLETTE	11-21-77	REVISED	DATE	SUPERSONIC AIRFOIL CHARACTERISTICS — FIG. 2.21
CHECK					
APR					
APR					BOEING — PAGE 2.46

CHAPTER 3 LOW SPEED AIRFOIL DESIGN

CHAPTER 3. LOW SPEED AIRFOIL DESIGN

3.1 INTRODUCTION

Low speed airfoil design for high lift applications is an extremely complex subject. The performance of a two-dimensional high lift system is limited by the viscous effects, which on a multi-element airfoil include:

1) Laminar Boundary Layers
2) Turbulent Boundary Layers
3) Separations
4) Bubbles
5) Wakes
6) Confluent boundary layers (merging B.L.'s

Figure 1 illustrates most of these phenomena on a typical multi-element airfoil. It becomes obvious that to start out looking at such a complex system will make it difficult. Let us start out then by looking at single element airfoils as a primer from which we can carry the insights gained to the more difficult multi-element case.

3.2 SINGLE ELEMENT AIRFOILS

Perhaps the logical place to start out is by examining the different types of stall that can occur on a single element airfoil and the limitations they impose.

3.2.1 Types of Stall

There are three classical types of stall that can occur on an airfoil. The three types are illustrated on Figures 2 and 3 and are:

1) Trailing edge stall
2) Leading edge stall
3) Thin airfoil stall

An excellent illustration of these three types of stall is found in Reference 1 and is shown on Figure 4. The 63_1-018 shows a classical trailing edge stall, while the 63_1-012 and 63-009 show the characteristic sharp lift break of the leading edge stall. The NACA 64A006 has a kink

3.2.1 Types of Stall (Continued)

in the C_L vs α curve just above 4^o. The corresponding drag polars are shown on Figure 5 and illustrate very clearly the effects of the separations. Figures 6a thru 6d are the pressure distributions corresponding to the lift curves of Figure 4 and some study of the pressures will reveal the stall characteristics shown in Figures 2 and 3 illustrated very clearly. A blow up of the pressure distributions near the leading edge region of two of the airfoils is shown in Figure 7 and indicate the characteristic bump in the pressure distribution which is characteristic of a bubble on the surface. The data of Figures 4 thru 7 were obtained at a constant Reynolds number of 5,800,000, and since the flow is viscous dominated,one would expect the results to be Reynolds number dependent. Indeed they are Reynolds number sensitive and the sensitivity has been generalized versus Reynolds number in Figure 8 from Reference 2. Another limiting factor on the high lift capabilities of airfoils is imposed by Mach number effects. The results shown on Figure 9 which was obtained from Reference 3 indicates that the maximum lift is limited by the local flow reaching sonic (critical) conditions.

3.2.2 Airfoil Designs past and Present

Perhaps the best source of past design practice and performance is the work done at the NACA which is beautifully summarized in Reference 3. To get some idea of the sensitivity of airfoils to their primary variables, thickness, camber (or C_{ℓ_i}) and Reynolds number, the data of Figures 10 and 11 have to be extracted from Reference 3 for the NACA 65 series airfoils which are the basis of the early Boeing wings including the 707, 727 and 737. Also shown on Figure 11 for comparison is some Boeing data on the 707 airfoil. These airfoils were not designed with maximum lift in mind, and it is only recently that the computational tools have become available to consider designing to high lift requirement and at the desired operating Reynolds number. Figures 12 and 13 show a series of airfoils designed (Reference 4) to 2,000,000 and 30,000,000 Reynolds number respectively. The approach taken was to move the point of the pressure recovery to the trailing edge, from near the leading edge to about 60-65% chord and design airfoils on the resultant pressure distributions. The typical pressure distributions are shown on Figure 14. The results in terms of C_ℓ and E* (C_{ℓ}/C_d) shown on the right of Figure 12 and 13 indicate that the low Reynolds number design should have the recovery

3.2.2 Airfoil Designs Past and Present (Continued)

point at about mid-chord, whereas the high Reynolds number design appears optimum with a quarter chord recovery. The difference in shape of the optimum airfoils is quite dramatic and illustrates the problem of designing and testing at low Reynolds numbers and scaling to full scale. Another interesting parameter was explored in Reference 4 and the results are shown on Figure 15. This illustrates the effect of the choice of H distribution on the performance and shape of the airfoil. These data suggest that an exponential H distribution will yield higher performance airfoils and more reasonable shapes than the traditional constant H factor distribution. A comparison of some of the airfoils derived using this approach with the classical airfoils from the literature designed by Liebeck and Wortman for gliders is shown on Figure 16. The McMasters airfoils look quite reasonable.

3.2.3 Why Go Beyond Single Element?

The answer may be obvious, but Figure 17 illustrates very clearly that the lift levels available with single element airfoils results in very high approach speeds. The range of desired approach speeds requires C_{L_S} values between 2.5 to 3.2. The technology levels actually demonstrated at Boeing are shown on Figure 18 and indicate that the required C_{L_S} levels are indeed achievable. Perhaps the next question then should be, why not powered lift? This question can be answered in terms of economics. Figure 19 shows the relationship for todays technology levels between DOC and $C_{L_{MAX}}$. The figure indicates that for reasonable field length goals (FL$\geq$6000 Ft) the application of powered lift concepts will result in a severe economic penalty. Only as the field length goals approach the order of 2000 ft. does it appear that powered lift will pay. The historical progress in $C_{L_{MAX}}$ shown on Figure 20 indicates that the AMST (YC-14) has $C_{L_{MAX}}$ levels of 5 to 6, which corresponds to the minimum DOC for a 2000 ft. (STOL) field length on Figure 19. Another interesting factor on Figure 20 is that apparently we have peaked out in our ability to improve $C_{L_{MAX}}$ with mechanical (CTOL) flaps. More on that subject later.

3.3 MULTI-ELEMENTS AIRFOILS

Now that we have come to the conclusion that the single element airfoil can't do the job we must look for ways to get the required performance levels. The multi-element (flapped) airfoil is the traditional answer, but before we look at how it is done we should ask, why do multi-element airfoils work?

81

3.3.1 Why do Multi-Element Airfoils work?

Perhaps the best discussion on this subject can be found in AMO Smith's Wright Brothers lecture (Reference 5). The following discussion is drawn from his paper. The multi element airfoil relies on the following for their improved performance.

1) Slat effect
2) Circulation effect
3) Dumping effect
4) Off-the-surface pressure recovery
5) Fresh boundary layer effect

Let's look at these factors one by one starting with the slat effect. Figure 21 illustrates the slat effect very clearly by positioning a lifting vortex ahead of a wing and examining the effects on the wing. The vortex or slats main effect on the wing is to reduce the peak velocities on the leading edge. This effect reduces the pressure peak on the wing without significantly effecting the lift of the total system. Figure 22 shows three identical airfoils flying in formation with their pressure distributions. Also shown for reference is the simple airfoil pressure distribution. The slat effect is quite clear in that the pressure peaks on each subsequent are reduced except for the first element where additional loading is evident.

This leads us to the second factor, the circulation effect. Figure 23 shows the effect of a lifting vortex placed behind an airfoil. The effect of the vortex is to raise the velocities over the complete upper surface resulting in a considerable increase in lift. Figure 24, 25 and 26 indicate that almost anything placed behind the airfoil that modifies the circulation can exhibit a circulation effect with a 50^{o}-60^{o} orientation showing the highest lift levels. The velocities due to the vortex on Figure 23 also increase the velocities at the trailing edge. This leads us to the next factor, the dumping effect. Any airfoil with a trailing element which modifies its circulation can benefit from the dumping effect. The velocities at the trailing edge are dumped on the leading element at velocities higher than free stream. This eases the boundary layer's problem since boundary layer hate to slow down, consequently higher lift can be carried on the element without risk of separation. This then leads to the next factor that benefits multi-element airfoils, the off-the-surface pressure recovery factor. Since the boundary layer at the trailing edge of the forward elements is dumped at veclocities above free stream the

3.3.1 Why do Multi-Element Airfoils Work? (Continued)

boundary layer recovery to free stream occurs off-the-surface where it can't cause trouble. The last factor is perhaps the most obvious, the fresh boundary layer effect. Each airfoil of a multi-element airfoil system has its own stagnation point at which the boundary layer starts fresh, thin and laminar. Understanding these five factors will be a great aid in interpreting high lift data. Some typical two dimensional pressure distributions from the Boeing Research Wind Tunnel (BRWT) are shown on Figures 27 thru 31, the slat, circulation and dumping effect can be found quite clearly in this data. The other two effects require us to look at the boundary layer. Figure 32 shows some force data from the same test and the lift effects in particular that we saw in the simple examples show up in this data.

3.3.2 Boeing High Lift Designs

Figures 33 thru 36 show the high lift design of the current Boeing family of airplanes. The 707-320B geometry shown on Figure 33 is the end of a long evolutionary period that started with the 367-80/ KC-135. The initial design had no leading edge devices and the circular arc fixed geometry vane/main trailing edge flap shown in Figure 33. The leading edge devices on the -320B are simply the lower surface of the wing folded out with a rounded "bullnose" leading edge added (referred to as the flat Kruger flap). The next Boeing product, the 727 is shown on Figure 34 and features two position slotted slats (up/down) outboard with the flat kruger inboard. This airplane also introduced a triple slotted flap that was actuated on a track and roller system that allowed a varying geometry with flap angle and a large fowler motion (extended chord). The 737 geometry shown on Figure 35 is similar to the 727 with the exception that it incorporated a three position slat (up, takeoff, and landing positions).

The 747 basic high lift system shown on Figure 36 introduced the variable camber leading edge device. This device uses a flexible fiberglass panel on the wing lower surface. As the flap extends a linkage warps the fiberglass panel and extends a folding bullnose resulting in a highly cambered slotted krueger flap. Inboard the familiar flat krueger is employed. The trailing edge triple slotted

3.3.2 Boeing High Lift Designs (Continued)

flaps are similar to the 727, 737 family. The 747SP, because of the reduced takeoff and landing weights has moved to a single slotted linkage actuated flap. This type of flap also saved weight in the design.

3.3.3 Trailing Edge Work at Boeing

The High Lift Research group at Boeing did a great deal of testing and design work in a search for improved technology. A matrix of the configurations tested is shown on Figure 37 with the geometries displayed on Figure 38. Some of the detail flap shape changes are shown on Figure 39 and indicate the range of geometries attempted. Figures 40 and 41 summarize the results of the trailing edge flap research testing. The results are presented in terms of the parameters $\eta_{\alpha=0}$, $C_{\ell_{MAX}}$ AND δf_{e_q} which are defined as follows:

$$\eta_{\alpha=0^\circ} = \frac{C_\ell \text{ at } \alpha = 0^\circ \text{ in the experiment}}{C_\ell \text{ at } \alpha = 0^\circ \text{ in potential flow}}$$

$C_{\ell_{MAX}}$ = Section maximum lift coefficient achieved in the wind tunnel.

δf_{e_q} = The equivalent plain flap angle that gives the same lift as the multi-slotted device in potential flow

The last parameter is an attempt to non-dimensionalize the performance of the slotted device for the number of slots involved. Figure 40 and 41 reveal that the double slotted flap has a significant performance benefit over the single slotted flap and has almost the performance levels of the triple slotted flap except at the very high flap angles. Some interesting data is shown on Figure 42 that indicates the range of the evaluation parameters for double slotted flaps. Figure 43 shows an interesting conclusion that can be drawn from this data, namely that if the flap is double slotted, the performance is relatively insensitive to the flap split between the elements. Figure 44 shows some data on the effect of flap position on the minimum pressure coefficient of the first flap element. The significant point is that the Boeing data indicates smaller flap overlaps are desirable. The NASA data had been the source of design data for years and was quite misleading.

3.3.4 Leading Edge Work at Boeing

A leading edge experimental program similar to the trailing edge study was also performed. The range of shapes and device chord is shown on Figures 45 and 46 with Figure 45 showing the sealed devices tested and Figure 46 the slotted devices. The range in philosophies is apparent in Figure 46 which shows two types of curved devices with differing pressure recovery points, versus the simple flat krueger flap. A typical set of data for the sealed curved devices is shown on Figure 47 with the potential flow predicted lift curve slopes, note again that the slat has a small effect on lift at constant angle of attack, but a large effect on $C_{\ell_{MAX}}$ and the angle for $C_{\ell_{MAX}}$. Figure 48 shows a summary of the results of the leading edge device testing and it is at this point that other performance evaluation criteria are introduced, $(L/D)_{MAX}$ and $(L/D)_{\alpha = 8^o}$. The value of $(L/D)_{MAX}$ should be self evident, but the $(L/D)_{\alpha = 8^o}$ is an attempt to evaluate the lift to drag ratio of the devices at a typical climbout attitude where (L/D) is important. The main feature of the data on Figure 48 is that curved devices are superior to the flat devices regardless of the aerodynamic figure of merit, $C_{\ell_{MAX}}$ or L/D. Figure 49 shows an interesting piece of data on the effect of bullnose radius on C_ℓ and C_d. The bullnose effect is particularly important from a $C_{\ell_{MAX}}$ standpoint.

3.3.5 Leading Edge Optimization

The data from the previous section was obtained using some nominal values for position, which was probably not optimum for each configuration. An optimization of each device would be a very time consuming process. An attempt was made to see if the two dimensional potential flow computer program could be of some help in the optimization process. A matrix of gaps, heights and angles was run in the potential program and evaluated in terms of two parameters, the wing minimum C_p and a wake parameter defined as follows:

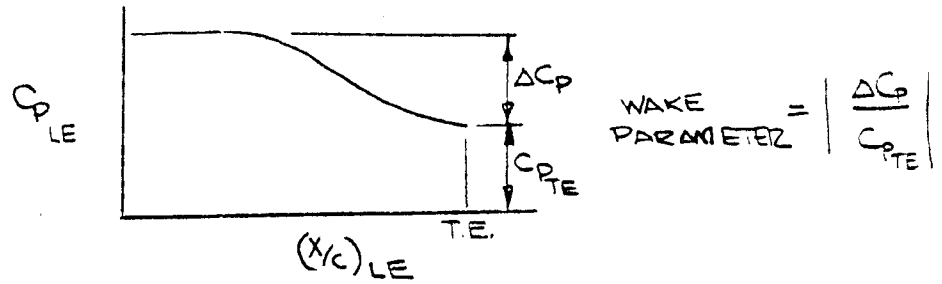

3.3.5 Leading Edge Optimization (Continued)

A typical output for one particular gap is shown on Figure 50. The wing $C_{P_{MIN}}$ appears to have an optimum position indicated by $(\Delta Y/_C)$ OPT which was used to develop a similar line on the wake parameter plot. A summary plot of the results of all of the potential flow calculations is shown on Figure 51. Since the calculations are inviscid (no boundary layers included) the method could not really be expected to properly predict the gap, but the data does indicate a good trade between angle and height that could be a good starting point for a tunnel test. A summary of the test results of the optimization on Figure 52 indicated an optimum configuration with 47^o deflection $\Delta Y/_C$=.028 and G/C = .18. It is interesting to spot this point on Figure 51, perhaps potential flow has some value after all.

An interesting piece of data that came out of the testing is shown on Figure 53. The figure shows the effect of fairing in the lower surface of the leading edge device and indicates that the fairing has little effect above $\alpha = 8^o$. It is only at the low α's where the lower surface is separated that the fairing helps and the truncated fairing is almost as good as the full fairing. As a conclusion, Figure 54 shows the technology levels of the various leading edge flaps with the L-39 shape showing the highest $C_{\ell_{MAX}}$, however the chords required are large and the L38 device appears to be about on the "elbow" of the curve.

3.3.6 High Reynolds Number Effects

A high Reynolds number test was performed using a 707 airfoil section and trailing edge flaps, but with various leading edge devices. The leading edge and main wing potential flow pressure distributions are shown on Figures 55 and 56 for the landing and takeoff flaps near the maximum lift condition. The slat devices (L_{43}) show significant pressure peaks while the variable camber type devices (L_{44}, L_{22} and L_{31}) show reduced peaks. The basic airfoil and flapped airfoil without leading edge devices were tested first and a comparison of the results with other data in the literature is shown on Figure 57. The Reynolds number sensitivities are very similar for the section data available and correlates quite well with the BRWT data which includes a Mach number variation. The flaps down no leading edge case shows a fairly dramatic effect of Reynolds number, but this configuration also has the highest pressure gradients at the leading edge. Figures 58 and 59 show the takeoff and landing

3.3.6 High Reynolds Number Effects (Continued)

configuration Reynolds number sensitivity with the leading edge devices tested. The Reynolds number sensitivity with leading edges is reduced, and the 747 device in particular (L_{44}) shows a very small Reynolds number effect. A particularly interesting effect is shown on Figure 59. At wind tunnel Reynolds numbers (RN$\approx$1.5 x 10^6) the 747 device is clearly superior to the 737 slotted slat, but at RN = 10 x 10^6 they are about even. This data indicates that predicting scale effects for high lift systems is a risky business. The three dimensional data shown on Figure 60 indicates that the 737 is indeed more sensitive to Reynolds number effects than the 747.

3.4 B.L.C. AND POWERED LIFT

While we have shown that powered lift and BLC concepts are probably not required for a conventional transport a good deal of work has been done onthese concepts that is of interest. The various blowing BLC concepts investigated are shown on Figure 61 and a summary of the performance is shown on Figure 62. Leading edge BLC appears to be quite linear, and even small amounts of blowing can help, but the trailing edge effects can be quite non-linear. The suction BLC concepts investigated are shown on Figure 63 with a summary of the performance on Figure 64. Again the leading edge appears to be very linear, while the trailing edge concepts show distinct plateau with various suction levels. Some of the powered lift concepts considered are shown on Figure 65. Data for most of these concepts is shown on Figure 66. The USB flap has performance almost as good as the much more complicated IBF and it is perhaps no surprise that it was chosen for the YC-14.

3.5 ANALYSIS AND DESIGN COMPUTATIONAL TOOLS

Before 1974, basically the only computational tool available to the high lift designer was a two dimensional multi-element potential flow program and a single element boundary layer program.

Figure 67 shows a comparison for a single element airfoil of potential flow and experiment. Figure 68 shows the effect of adding the boundary layer, a marked improvement in correlation except at the higher α's. Figure 69 shows where we are today with the ability to model separated flows. The single element correlation is excellent. Figure 70 shows the correlation in pressure coefficient at $C_{\ell_{MAX}}$, again it is excellent. Figures 71, 72 and 73 show the pressure distributions at several angles and are a classical example of a trailing edge stalling airfoil. Figure

74 shows how the same capability was used to model an airfoil with a spoiler deflected, the experimental pressures are well predicted. Okay, so the single element case is in hand, what about multi-element airfoils? Figure 75 shows the correlation for the most simple multi-element case, separation on the aft element only. This capability has been reported in the literature many times, but the correlation uses the Boeing program. The Boeing program uses an iterative two-dimensional potential flow design and analysis program coupled to a simple boundary layer program. This capability exists now in a prototype form, but a production version will be available to the high lift designer within a year. The capability discussed to date basically is where the majority of the world is, so now let's see how far we can use this tool. Figure 76 shows the results for an airfoil system that has separation on two surfaces, the correlation is excellent, and as far as the literature is concerned this capability is unique. The data shown in this section so far was obtained by the NASA on their General Aviation Wing No. 1 (GAW-1) airfoil. The next step in the evaluation of the capability is to compare the calculation capability with Boeing data obtained on a practical transport high lift flap system. Figure 77 shows a comparison of potential flow, potential flow plus the boundary layer and potential flow plus boundary layer plus the separated wake modeling. The addition of the boundary layer improves the correlation with experiment, but the separated wake modeling is required for good correlation even at the operating angles of attack. Figures 78, 79 and 80 show the results of the separated wake modeling method with experimental data with separations on one, two and all four elements. The comparisons are quite impressive and represent a capability unequaled in the industry. This capability (Reference 7) gives us the equivalent of a two-dimensional multi-element analytical wind tunnel. If a good boundary layer capability existed that could handle the confluent boundary layer problem we would indeed have a two-dimensional analytical capability. The capability that was used to design the separated wake can also be used to design flap and airfoil shapes. Figure 81 shows how the program was used to modify a trailing edge flap shape. The number of iterations required for convenience is quite small and a smooth modified geometry was produced. Figure 82 shows an example of a leading edge design done on the NASA/Boeing QSRA program. The problem in this case was between the nacelles, a

high pressure peak was causing premature separation. The design was performed in less than a week using the program and proved successful. Incidentally an experienced designer had been working for two months to try to solve this problem by cut and try iteration. He never solved the problem. Figure 83 shows the results of a much more difficult design task, the design of a slotted leading edge device to a specified input pressure distribution, a truly remarkable accomplishment that we could only dream of five years ago. A plea was heard earlier for a multi-element viscous flow program capable of analyzing configurations with confluent boundary layers. Boeing has just completed a contract with the NASA in which they took a NASA multi-element viscous flow program and modified it heavily. Beforehand the program would not run about 40% of the time and the answers were poor the rest of the time. Boeing obtained some high quality data on a flap system to be used as one standard of comparison for program evaluation. Figure 84 shows the number of stations surveyed on the airfoil and the total pressure profiles at these stations. Figure 85 shows how the program (Reference) compares with experiment before and after modification. A marked improvement is obvious, plus how the program is more reliable and runs most of the cases input.

3.6 TWO-DIMENSIONAL WIND TUNNEL TESTING

Boeing has performed many hours of two-dimensional wind tunnel testing in both our own and outside facilities. Until recently this was our only way to evaluate ideas. But two dimensional flow and Reynolds number simulation are not easy to achieve. Let us now discuss some of the facilities used and the test techniques for the tests.

3.6.1 Facilities

The primary facility for two-dimensional testing at Boeing is the Boeing Research Wind Tunnel (BRWT). The tunnel was originally configured as a 3' by 8' section, but has been recently revised to 5' by 8'. In addition honeycomb and screens were added to the bell-mouth to give a very smooth low turbulence testing environment. A

3.6.1 Facilities (Continued)

cross-section of the test section is shown on Figure 86. The figure shows the main features of the tunnel, 1) front wall blowing slots ahead of the model used to get an even velocity distribution across the tunnel despite the wall boundary layer, 2) end plate blowing slots on the rotating end plates to take care of the local boundary layer problems at the leading edge of each flap segment, and 3) the traversing integrating wake rake that is used for drag measurement. The tunnel supports the model on both ends which are attached to a balance, however integrated pressure data is the main source of lift and pitching moment, and the wake rake is used for drag. Figures 87 through 91 show several views of a model in the tunnel and the salient features of the tunnel can be seen. Figure 92 shows the slightly different approach to testing taken at the National Aeronautical Establishments (NAE) 5' by 5' high Reynolds number facility in Ottawa, Canada. The NAE relies on side wall suction ahead of the model (see figure 93) to take care of the basic wall boundary layer, but the other features of the test setup are similar to the BRWT. The NAE tunnel was used to obtain all of the two-dimensional high Reynolds number data shown previously.

3.6.2 Testing Techniques

Figures 94, 95 and 96 are examples of the primary flow visualization technique used at Boeing known as china clay. The material consists of a sublimating rare earth that is mixed with kerosene and painted on the model. Pictures like Figures 94 and 95 which was obtained at an α close to $C_{\ell_{max}}$ are used to set the turntable blowing and establish the two-dimensionality of the test setup. Figure 96 shows an excellent example of the use of chaina clay to understand the boundary layer state on the model. It is a close-up of the leading edge device and a laminar bubble is apparent at about 40% chord. The flow on the surface is laminar to this point and turbulent after the bubble. Similar laminar runs can be seen on the main airfoil, but without the laminar bubble. Figures 97, 98 and 99 show some example photographs of a method known as the helium bubble method. Neutrally bouyant helium filled soap bubbles are introduced upstream of the model in a darkened tunnel. A light shining up the tunnel

illuminates the bubbles and reveals the flow pattern. The patterns are very difficult to photograph except where they are drawn into a vortex core which is readily visible in all three pictures. The method does give excellent visibility of the details of the flow even though they may not photograph well. Figures 100 and 101 show views of the split film anemometer setup that was used to obtain the boundary layer data of Figures 84 and 85. The basic anemometer itself is a small quartz rod with a coating of metal on its surface as shown below:

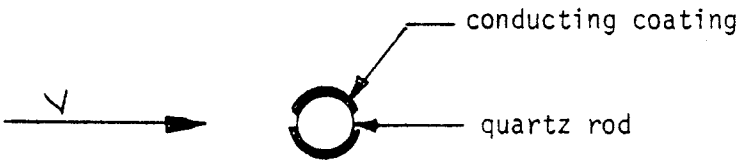

The metal surfaces are maintained at a constant temperature, and the velocity is determined from the current required. Differential heating from upper to lower can be used to determine flow angularity. The rod itself is quite small and can be obtained in a cruciform configuration so that the full three-dimensional flow velocity can be deduced.

CHAPTER 3 REFERENCES

1. NACA TN2502 "Examples of Three Representative Types of Airfoil - Section Stall at Low Speed," G. B. McCullough and D. E. Gault. 1952.

2. Thain, J. A.: "Reynolds Number Effects at Low Speeds on the Maximum Lift of Two-Dimensional Aerofoil Sections Equipped with Mechanical High Lift Devices." Rept. No. DME/NAE 1973(3), in Quarterly Bulletin of the Div. of Mech. Eng. and the Nat. Aero. Est., Ottawa.

3. "Theory of Wing Sections," I. H. Abbott and A. E. Von Doenhoff, Dover Publications.

4. B-8320-1868, "Initial Progress Report on a Moderate-to-High Lift Airfoil Parametric Study," J. H. McMasters, Dec. 1977.

5. "High Lift Aerodynamics," Wright Brothers Lecture, A.M.O. Smith, AIAA Paper 74-939, August 1974.

6. D6-41068TN, "Wind Tunnel Investigation of Single, Double, and Triple-Slotted Trailing-Edge Flaps," M. Emmett Omar, March 1973.

7. "A Solution to the 2-D Separated Wake Modeling Problem and Its Use to Predict $C_{L_{MAX}}$ of Arbitrary Airfoil Sections," M. L. Henderson, AIAA Paper 78-156, January 1978.

8. D6-45100, "A Critical Evaluation of the Predictions of the NASA/Lockheed Multi-Element Airfoil Computer Program," G. W. Brune and J. W. Manke, Oct. 1977.

9. D6-25114TN, "Theoretical and Experimental Investigation of the Optimum Setting of a Slotted Leading Edge Flap on a 20 Degrees Flapped Wing Section," Timothy Wang, April 1975.

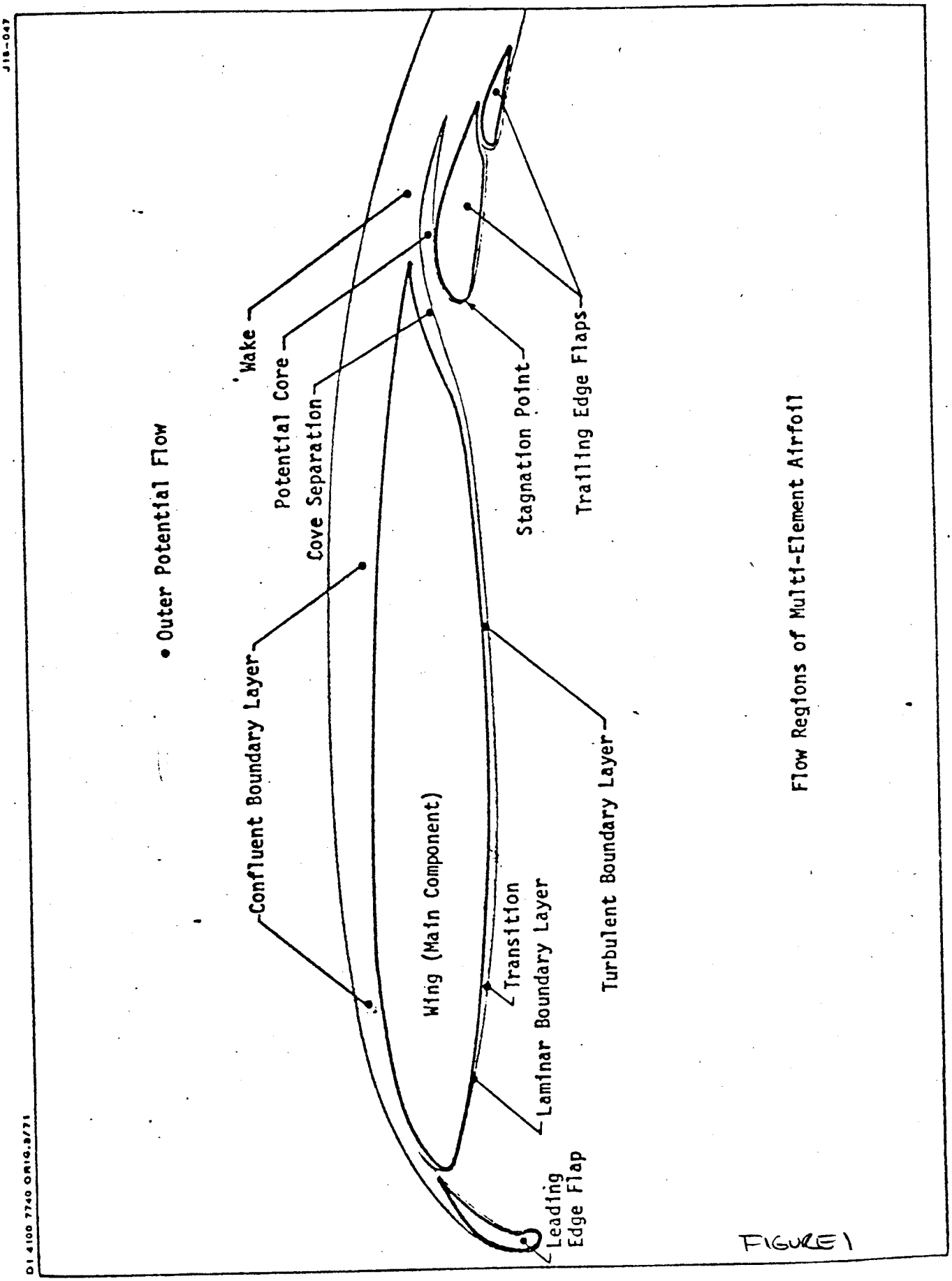

FIGURE 1

REV SYM

BOEING

PAGE P3.15

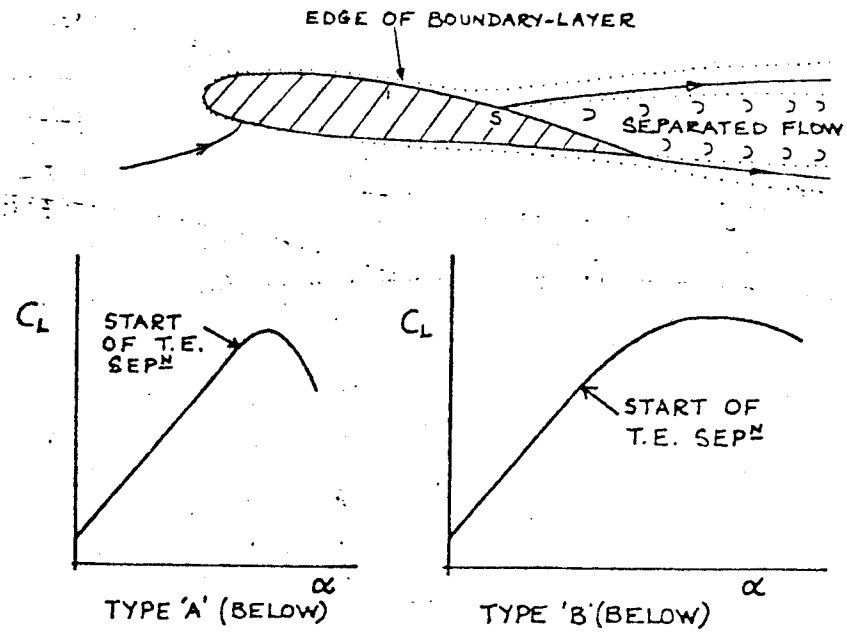

Trailing-edge stall

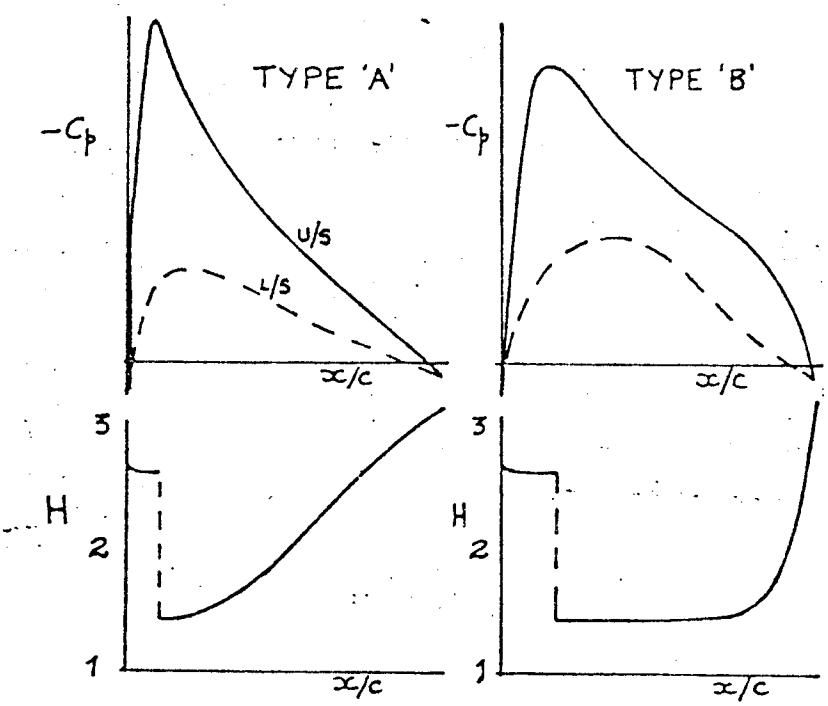

Pressure distributions and shape parameters for 2 types of trailing-edge stall

Figure 2
P3.16

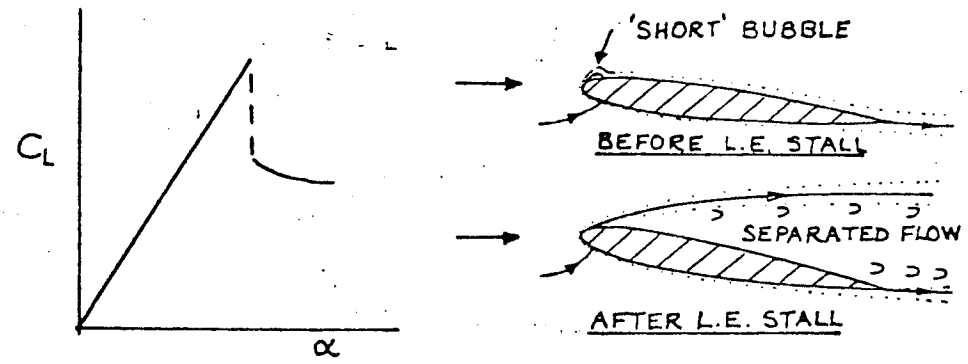

Leading-edge stall

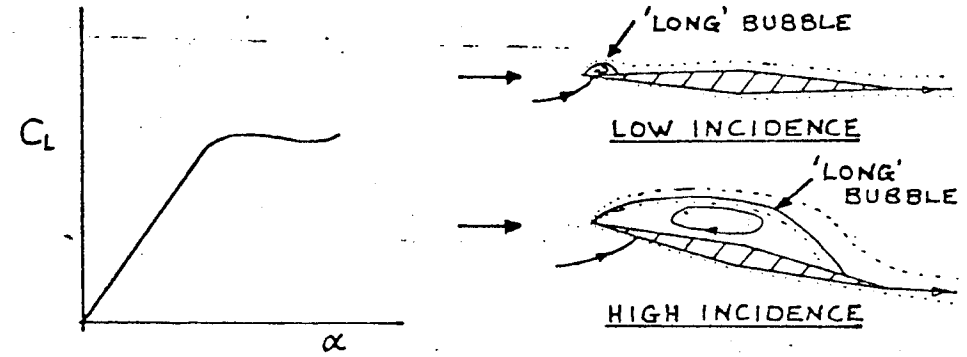

Thin aerofoil stall – sharp leading-edge

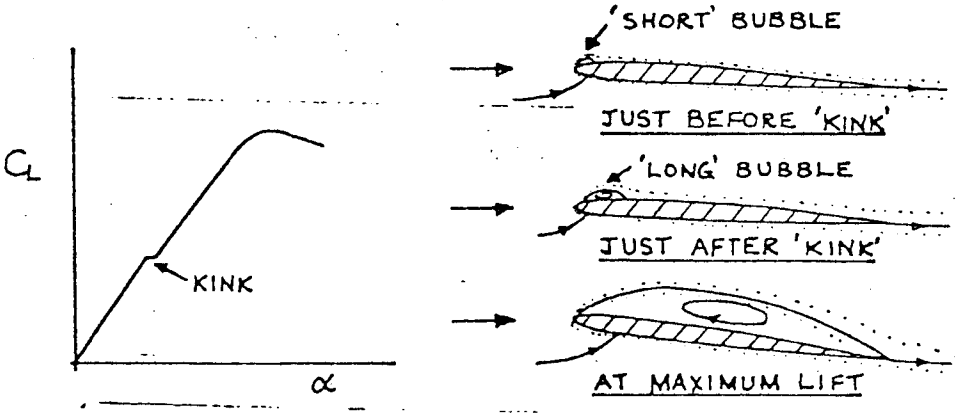

Thin aerofoil stall – rounded leading-edge

Figure 3
P3.17

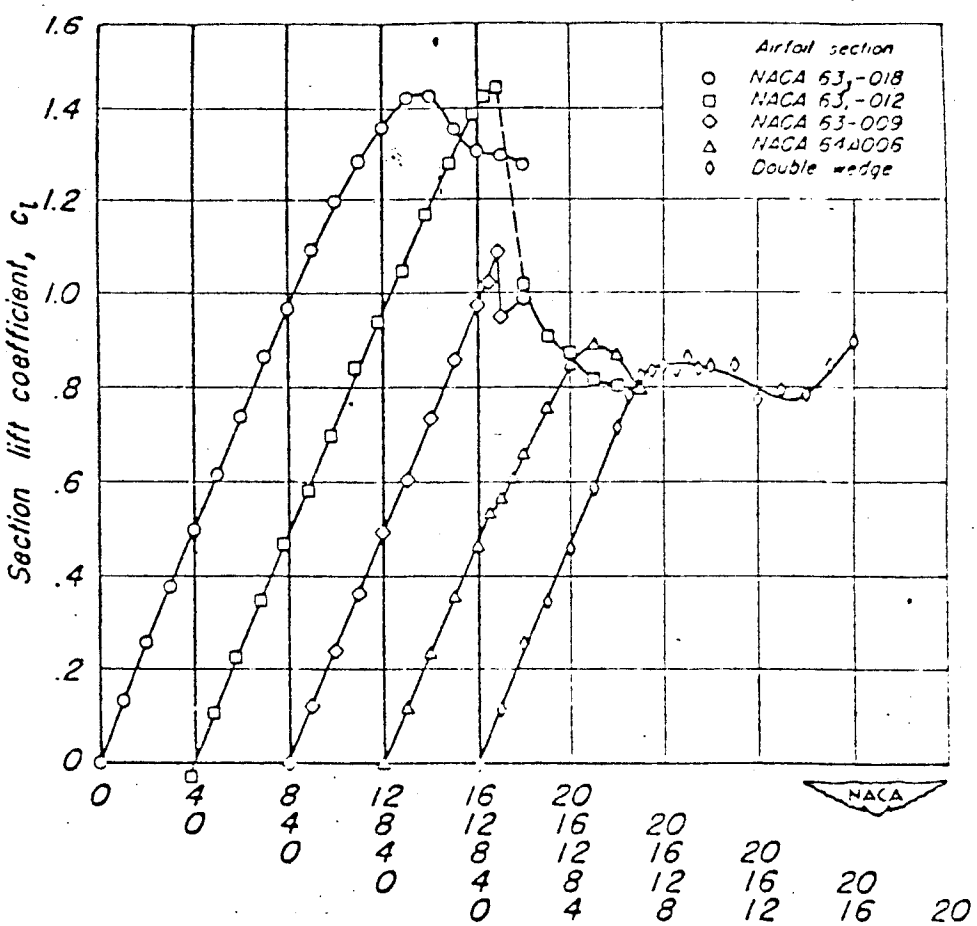

(a) Lift.

Aerodynamic characteristics of the five airfoil sections. Reynolds number, 5,800,000.

Figure 4

P3.18

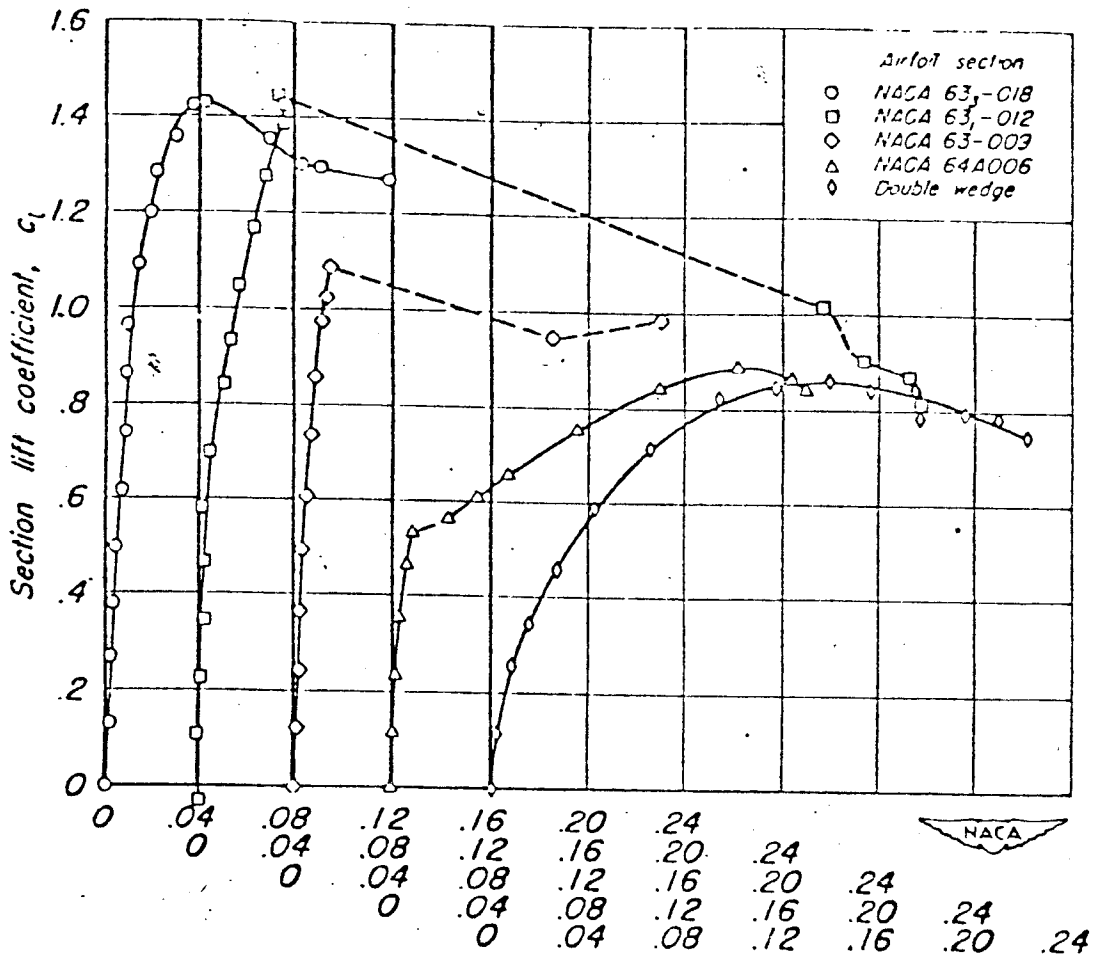

(b) Pressure drag.

Figure 5
P3.19

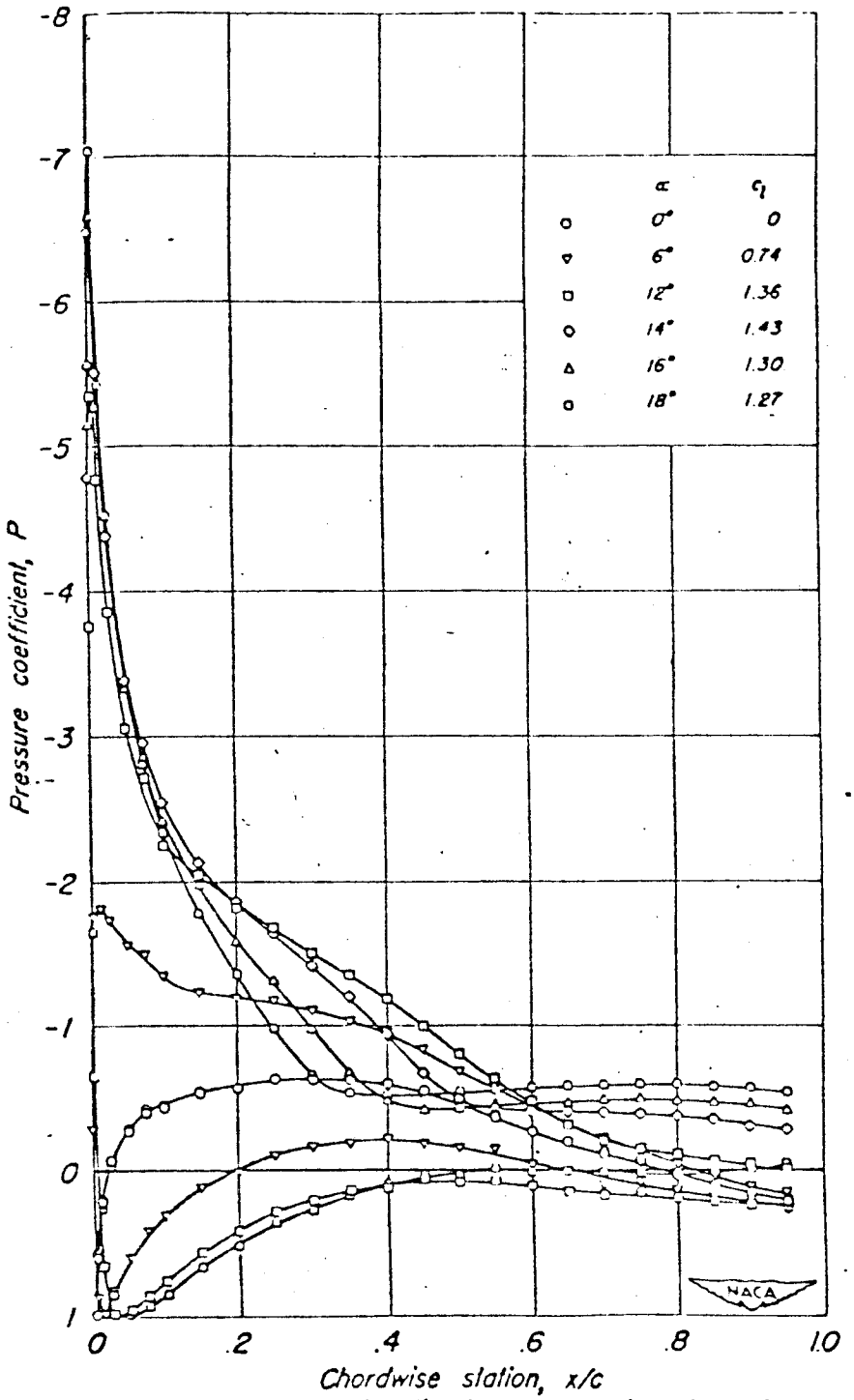

Pressure distribution over the NACA 63_3-018 airfoil section.

Figure 6a

P3.20

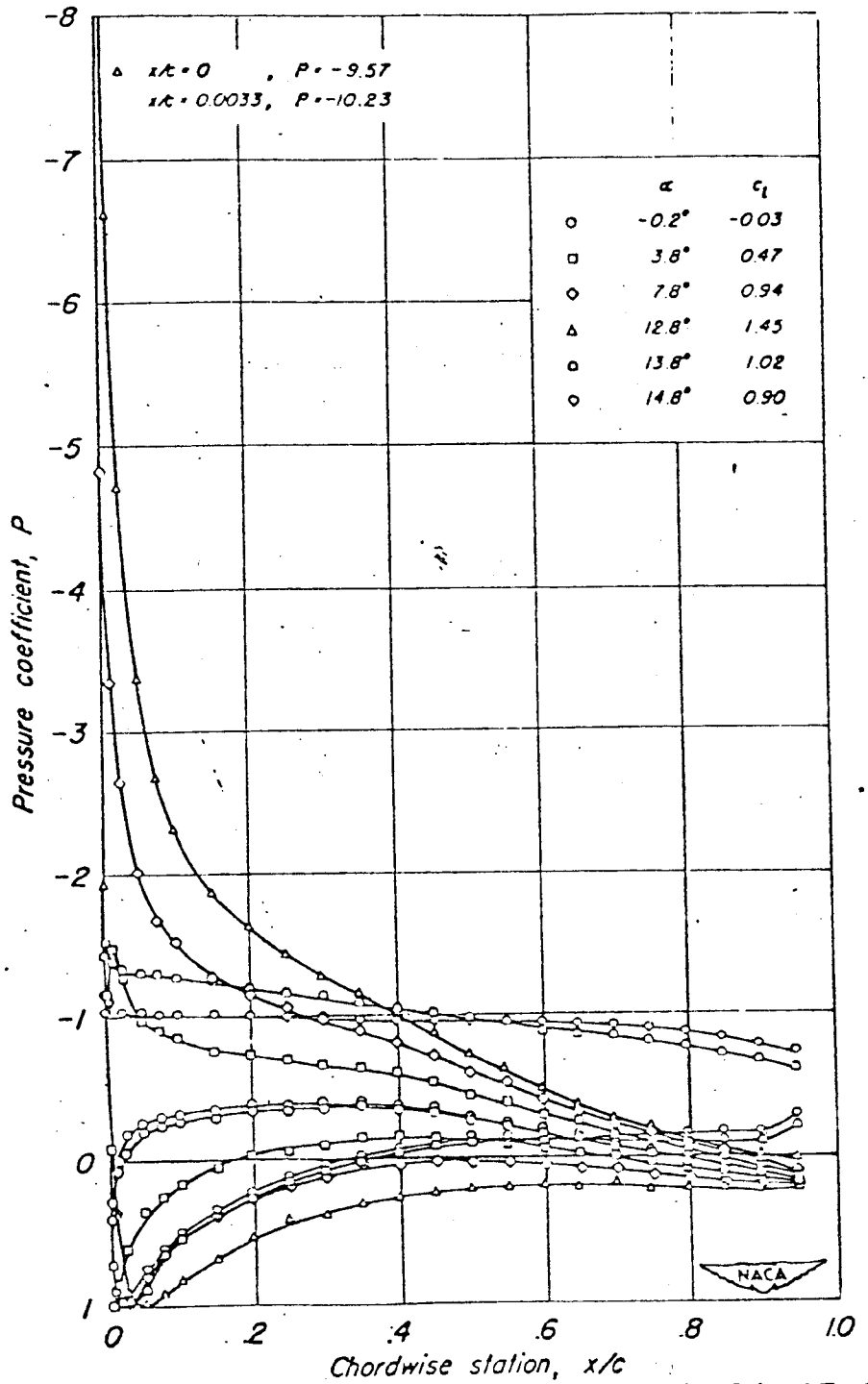

Pressure distribution over the NACA 63,-012 airfoil section.

Figure 6b

P3.21

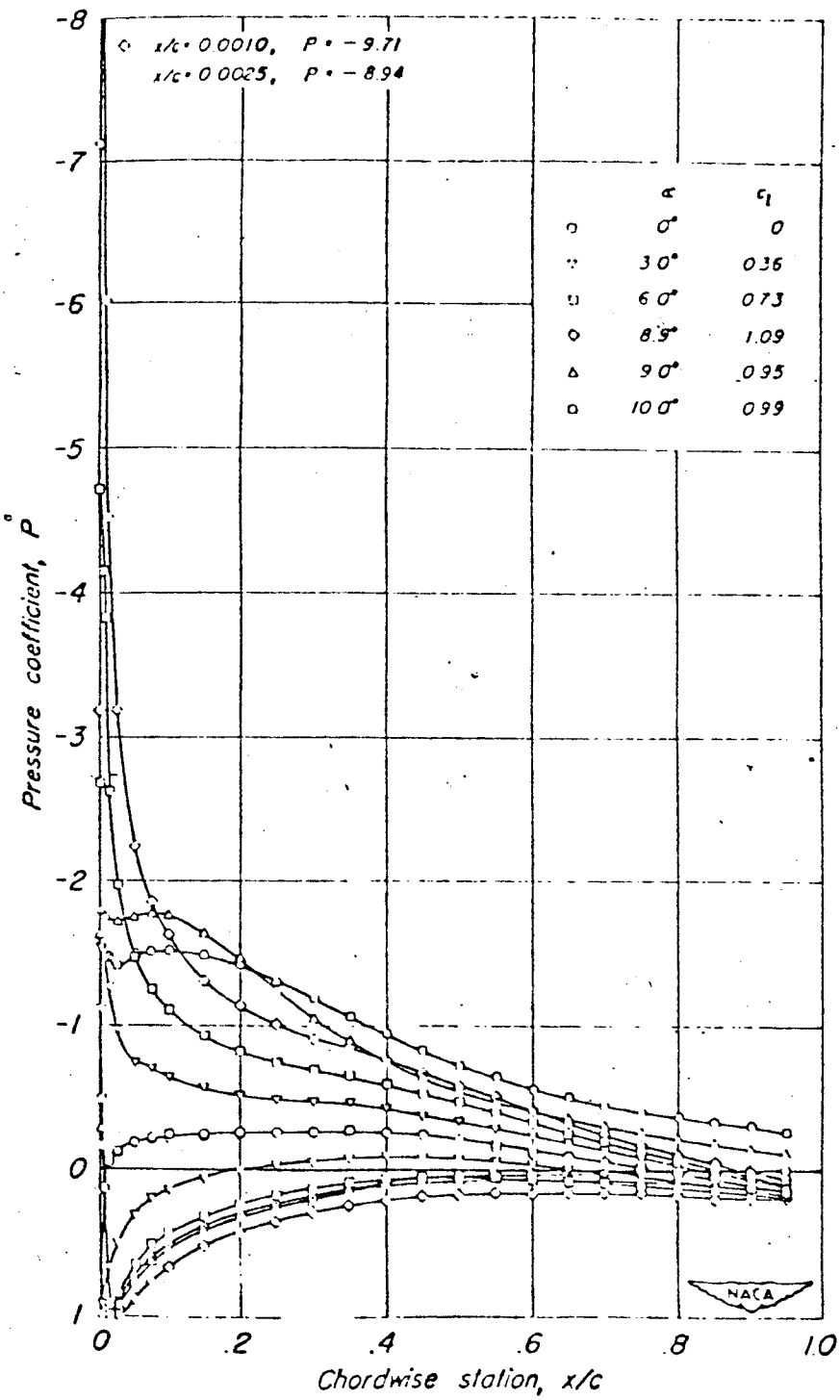

Pressure distribution over the NACA 63-009 airfoil section.

Figure 6C

P3.22

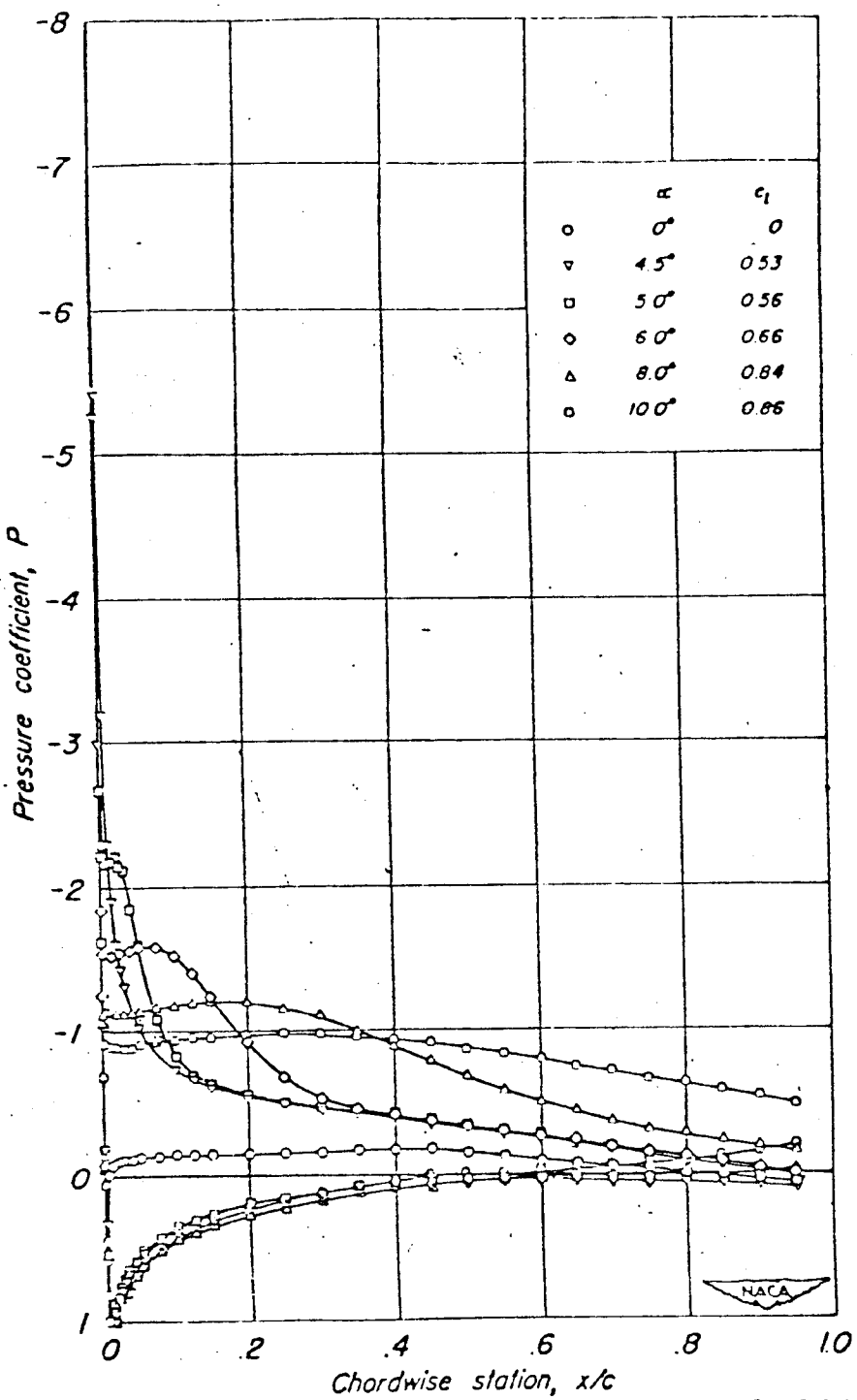

Pressure distribution over the NACA 64A006 airfoil section.

Figure 6 d

P3.23

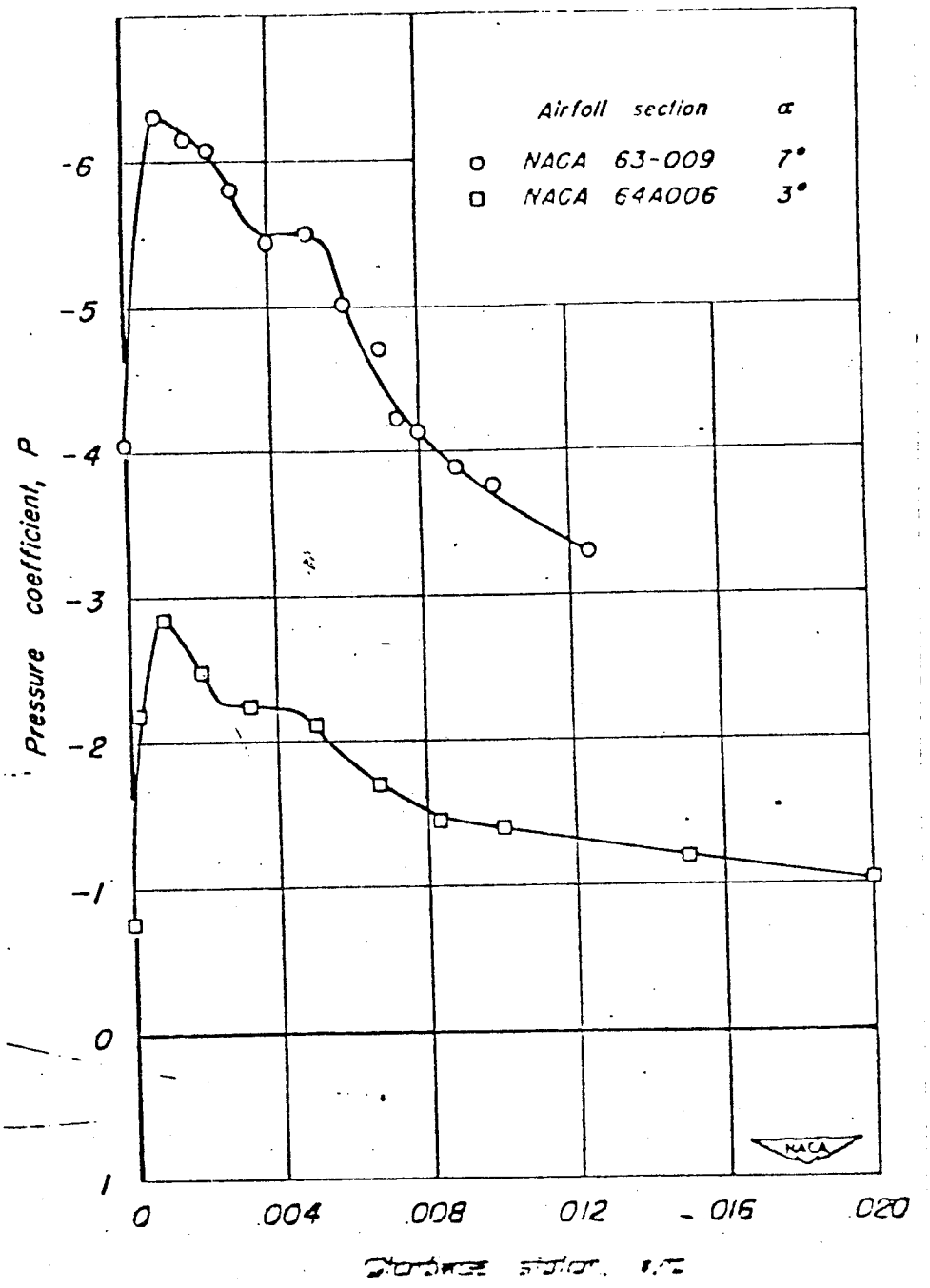

Detailed pressure distribution in the vicinity of the bubble of laminar separation

Figure 7

P3.24

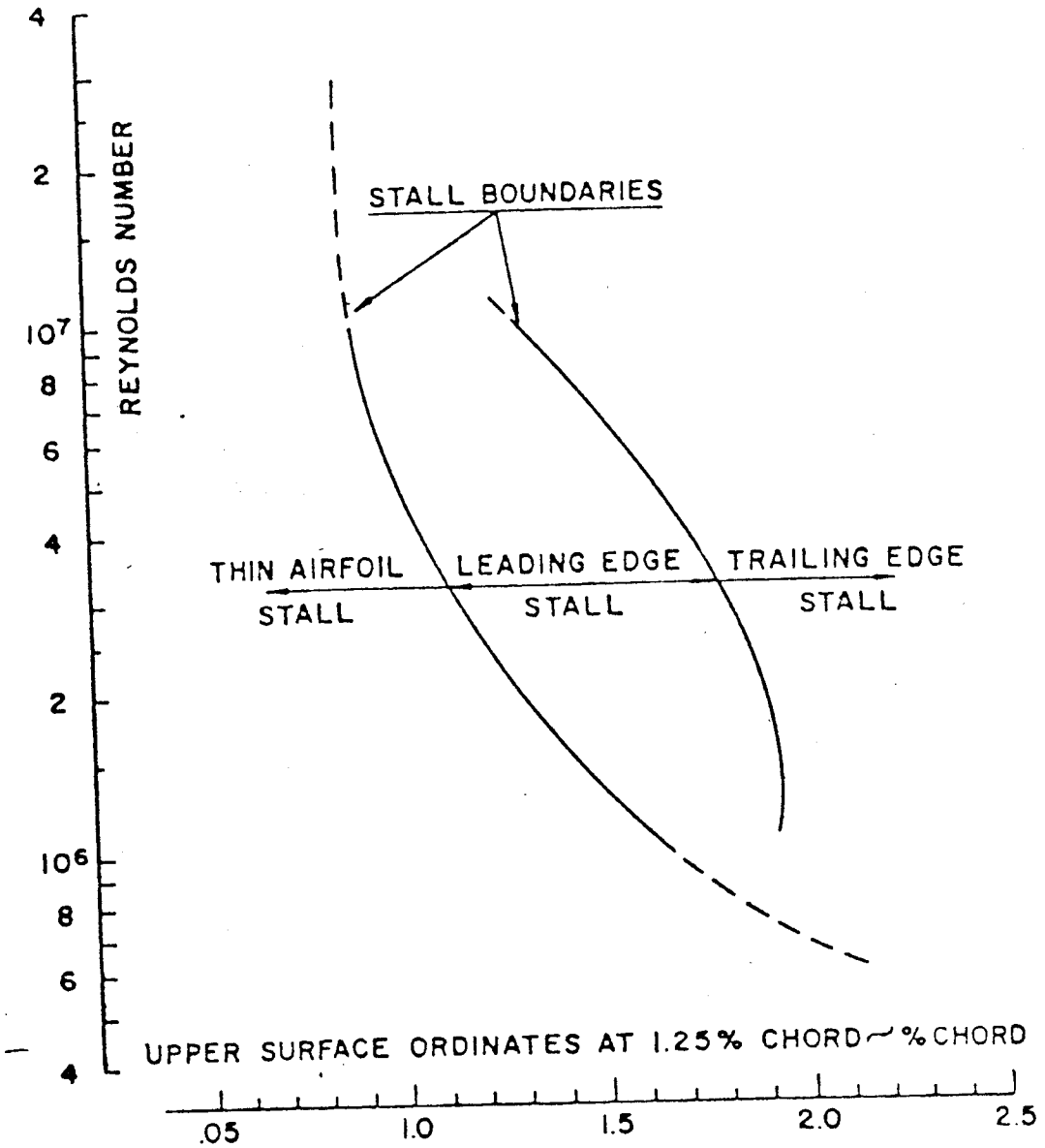

Effect of Reynolds number on the stalling characteristics of clean aerofoil sections as a function of aerofoil geometry, according to Thain and Gault

Figure 8

P3.25

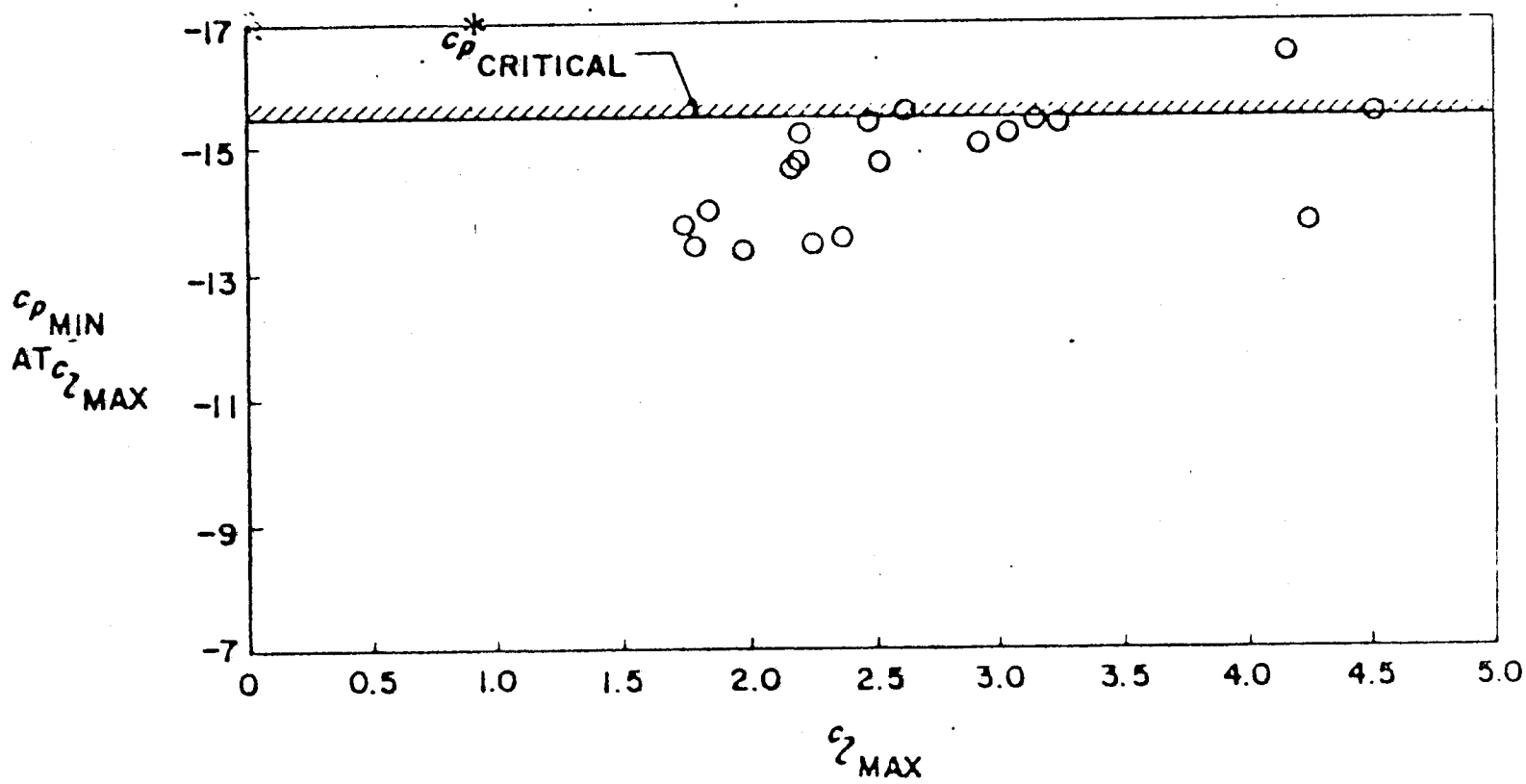

Experimentally measured leading-edge minimum pressure coefficient at $c_{\ell max}$ for a variety of two-dimensional high-lift configurations. Test Mach number = 0.20.

Figure 9

P3.26

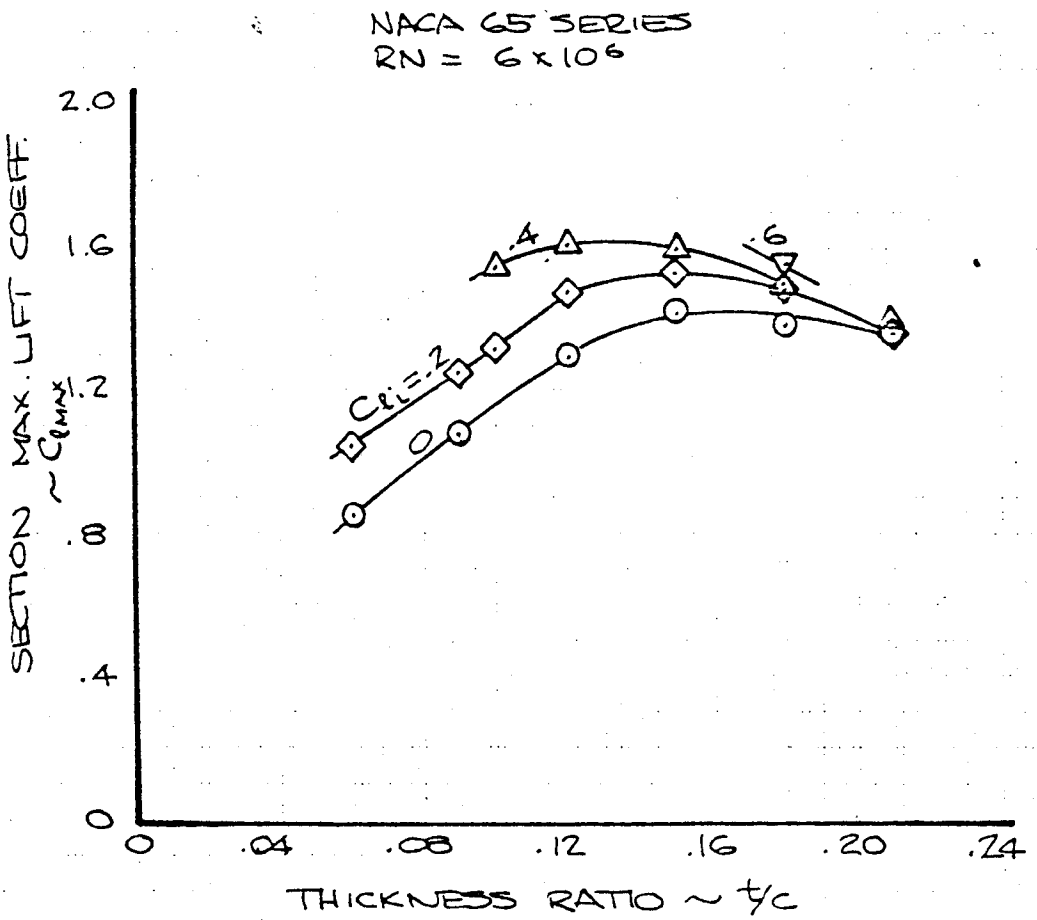

Figure 10

EFFECT OF t/c ON SECTION
$C_{l_{max}}$ ~ NACA 65 SERIES

P3.27

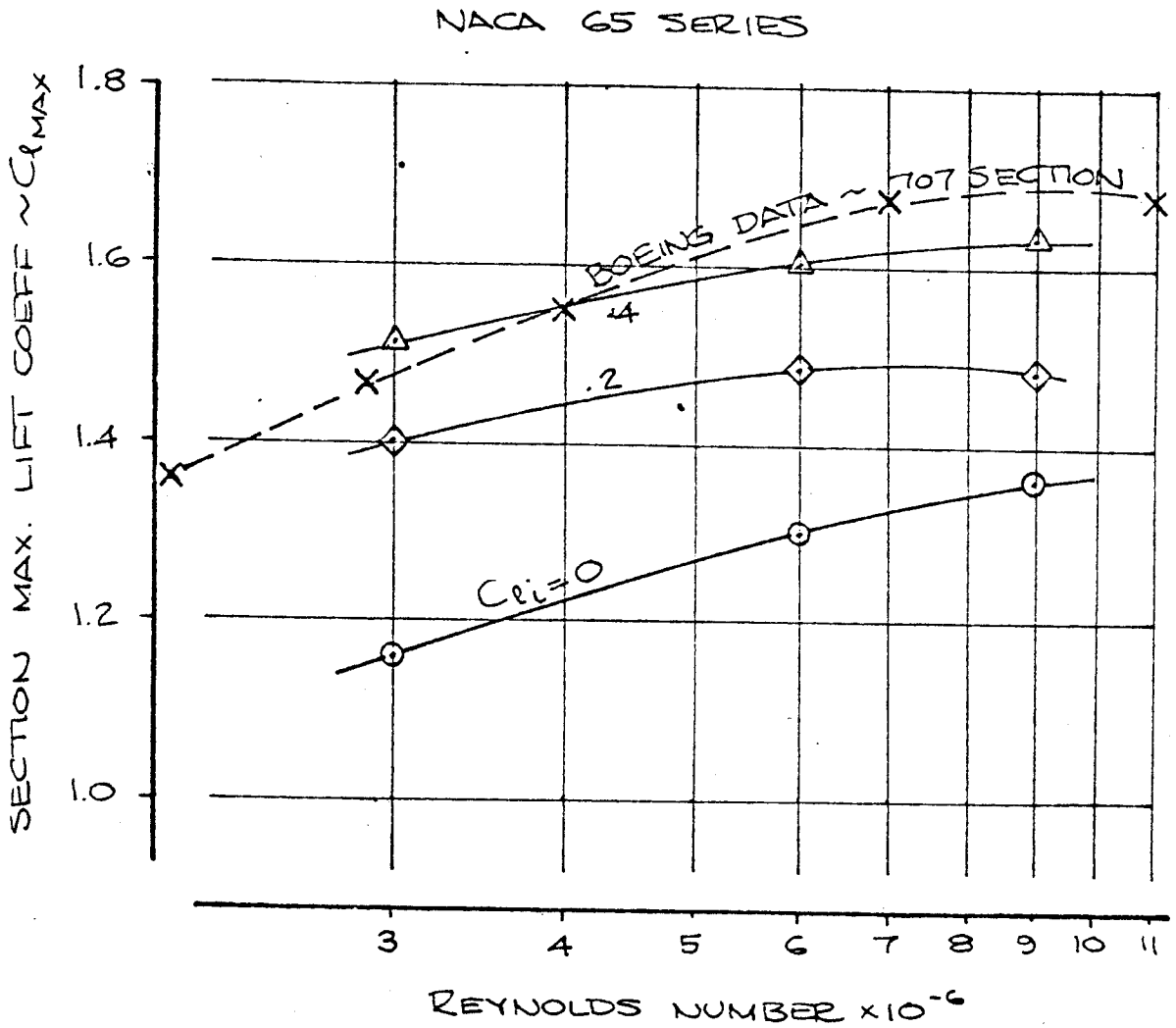

Figure 11

ENGR.			REVISED	DATE	EFFECT OF REYNOLDS NUMBER ON $C_{\ell MAX}$
CHECK					
APR					
APR					THE BOEING COMPANY RENTON, WASHINGTON
					P3.28

AD 1017-R6

6-7000

BHL 120-300-xr/xtr - E1.45.2.4

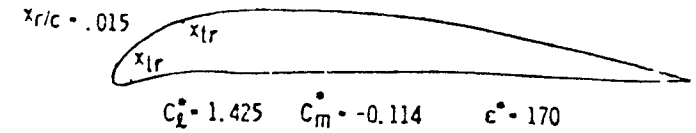

$C_\ell^* = 1.425$ $C_m^* = -0.114$ $\epsilon^* = 170$

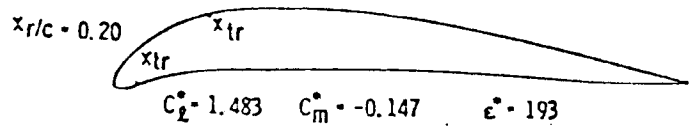

$C_\ell^* = 1.483$ $C_m^* = -0.147$ $\epsilon^* = 193$

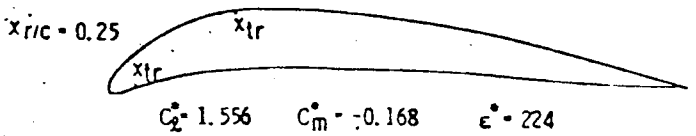

$C_\ell^* = 1.556$ $C_m^* = -0.168$ $\epsilon^* = 224$

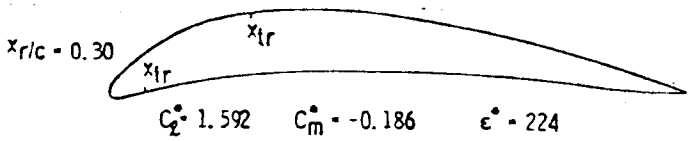

$C_\ell^* = 1.592$ $C_m^* = -0.186$ $\epsilon^* = 224$

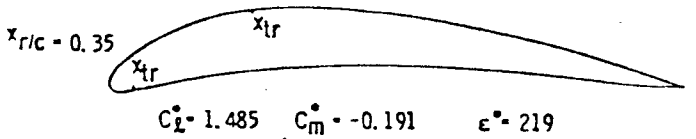

$C_\ell^* = 1.485$ $C_m^* = -0.191$ $\epsilon^* = 219$

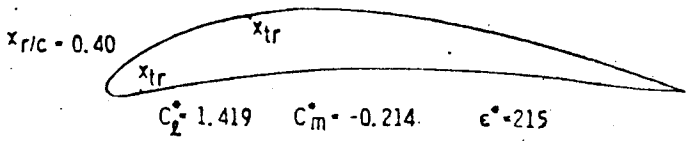

$C_\ell^* = 1.419$ $C_m^* = -0.214$ $\epsilon^* = 215$

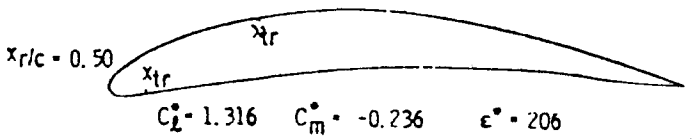

$C_\ell^* = 1.316$ $C_m^* = -0.236$ $\epsilon^* = 206$

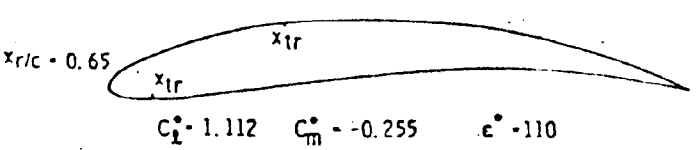

$C_\ell^* = 1.112$ $C_m^* = -0.255$ $\epsilon^* = 110$

Rn = 30 X 10^6
M = 0.20
t/c = 0.12
Natural Transition
$\epsilon = C_\ell/Cd$

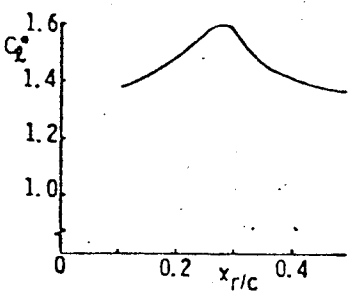

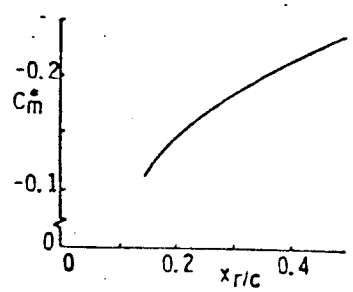

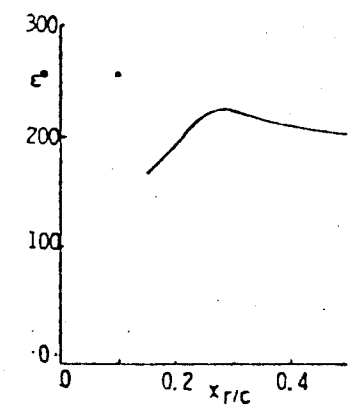

$Rn^* = 30 \times 10^6$
Natural Transition

A Family Of Airfoils With Exponential Form Parameter Designed at Rn = 30 X 10^6

Figure 13

P3.29

BHL 120-20- x_r/x_{tr} - E1.46/2.4

$Rn = 2 \times 10^6$
$M = 0.1$
t/c = 0.12
Natural Transition
$\epsilon = C_\ell/Cd$

$x_r/c = 0.20$

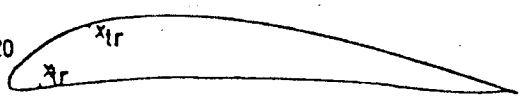

$C_\ell^* = 1.251$ $C_m^* = -0.136$ $\epsilon^* = 99$

$x_r/c = 0.30$

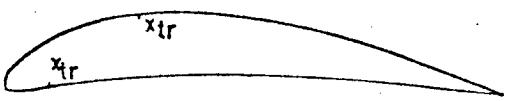

$C_\ell^* = 1.336$ $C_m^* = -0.174$ $\epsilon^* = 118$

$x_r/c = 0.40$

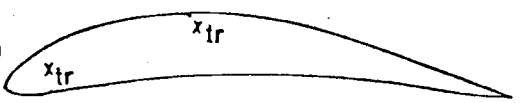

$C_\ell = 1.374$ $C_m = -0.210$ $\epsilon^* = 129$
$\epsilon_{max} = 145$
@ $C_\ell = 1.66$

$x_r/c = 0.5$

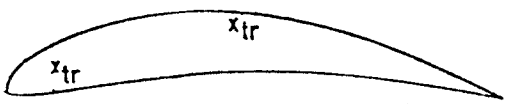

$C_\ell^* = 1.398$ $C_m^* = -0.250$ $\epsilon^* = 146$
$\epsilon_{max} = 170$
@ $C_\ell = 1.72$

$x_r/c = 0.60$

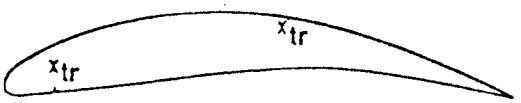

$C_\ell^* = 1.392$ $C_m^* = -0.287$ $\epsilon^* = 163$

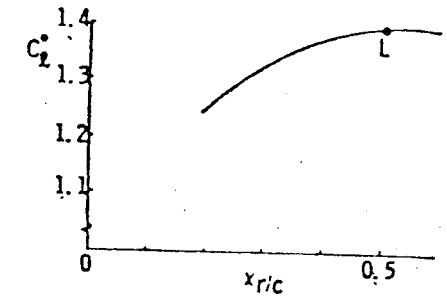

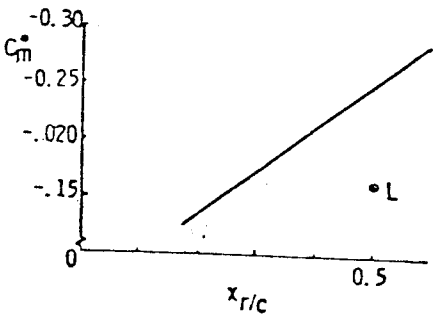

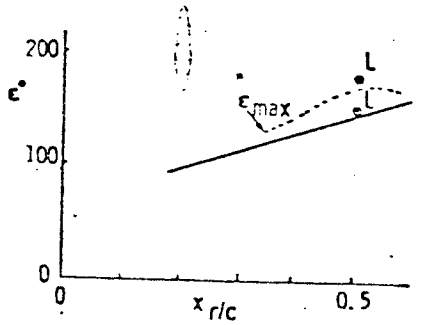

$Rn = 2 \times 10^6$
Natural Transition

x_r
BHL 120-20-50/46-L1.46/1.97

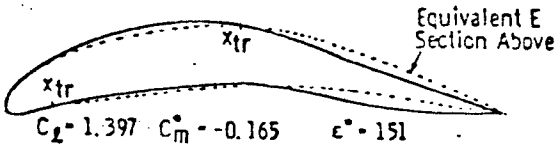

$C_\ell = 1.397$ $C_m = -0.165$ $\epsilon^* = 151$
$\epsilon_{max} = 182$
@ $C_\ell = 1.82$

A Family Of Airfoils
With Exponential Form Parameter
Designed At $Rn = 2 \times 10^6$

Figure 12

P3.30

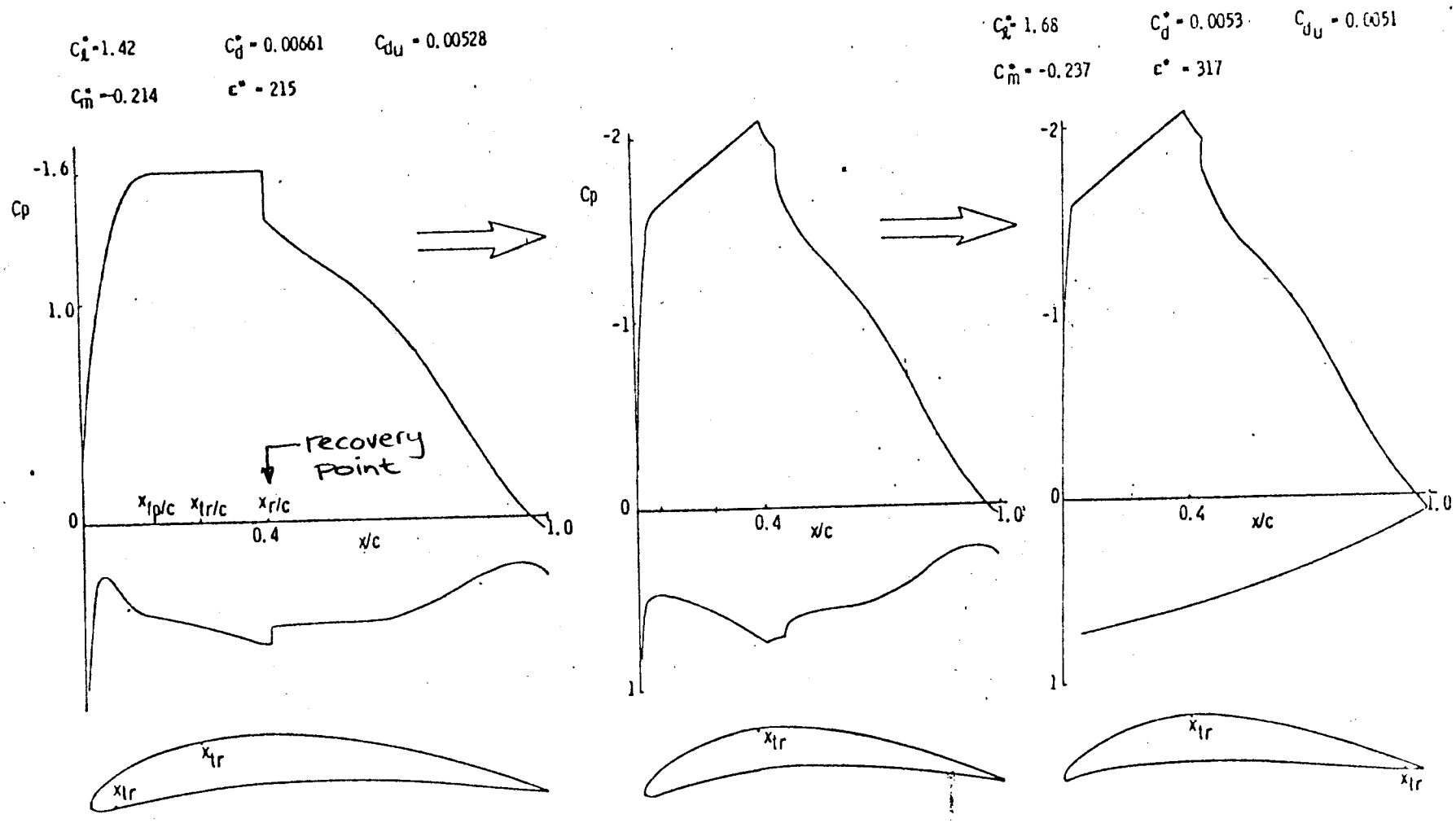

BHL 120-300-40/25-El.45/2.4

BHL 120-300-40/38-El.45/2.4 mod.

Examples Of Basic Pressure Distribution Architecture

Figure 14

D3.31

Comparison Of Pressure Distributions And Corresponding Airfoil Geometries Resulting From Different Specifications Of Recovery Region Boundary Layer Form Parameter (H).

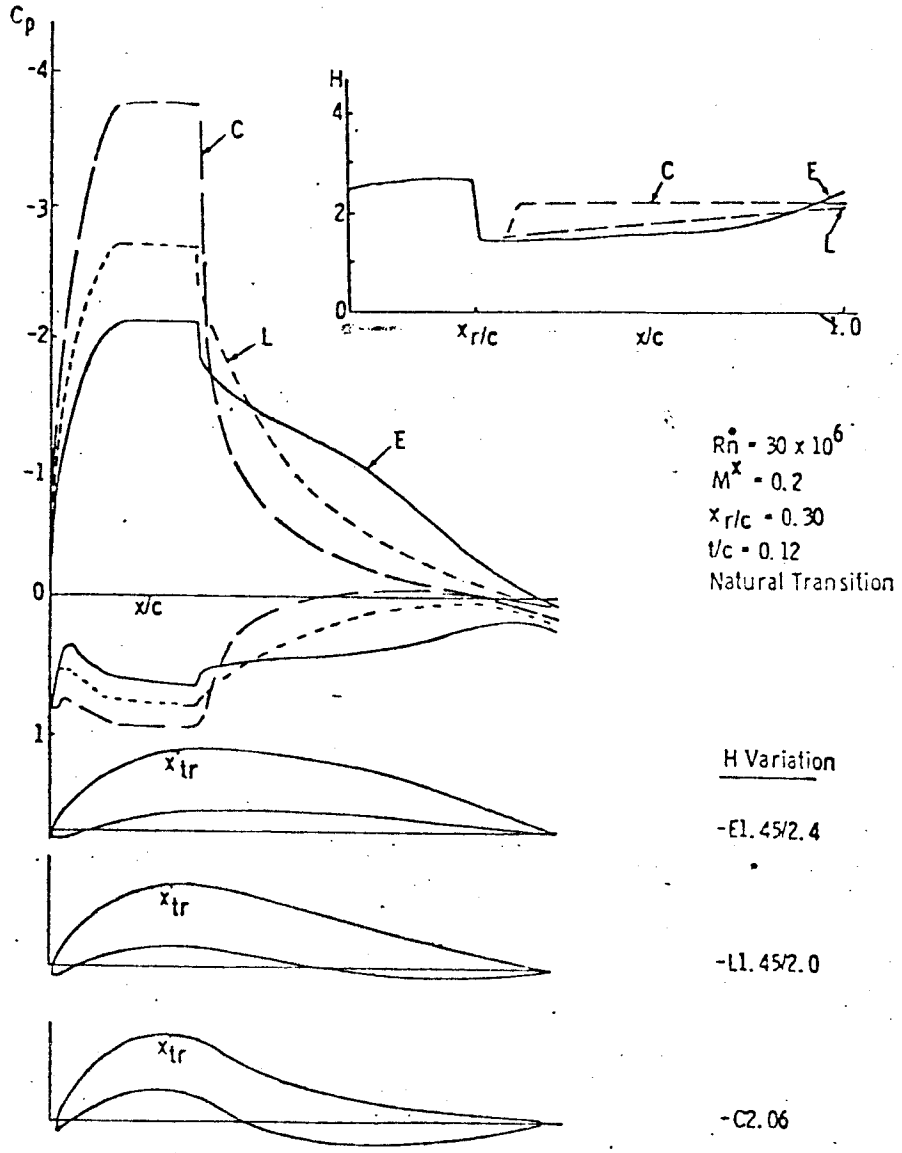

BHL 120-300-30/28- (H-Variation)

H Variation	$C_{\ell}^{\bullet}$	$C_m^{\bullet}$	$\varepsilon^{\bullet}$	ε_{max}	$C_{\ell\,max}$
E1.45/2.4	1.592	-0.186	226	-240	-2.3
L1.45/2.0	1.563	-0.058	216	216	-2.05
C2.06	1.603	+0.057	172	172	-1.97

Figure 15

P3.32

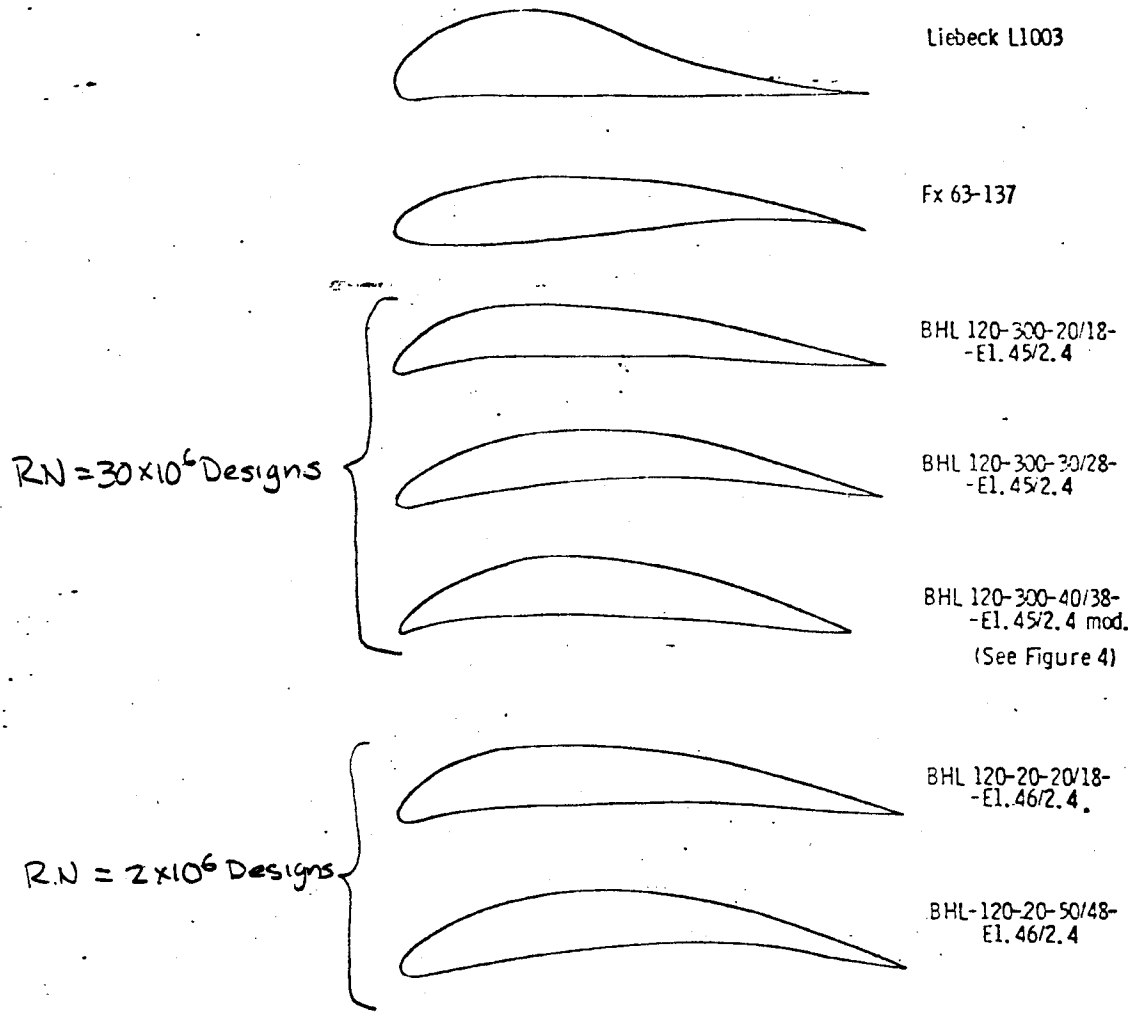

Figure 16

P 3.33

///

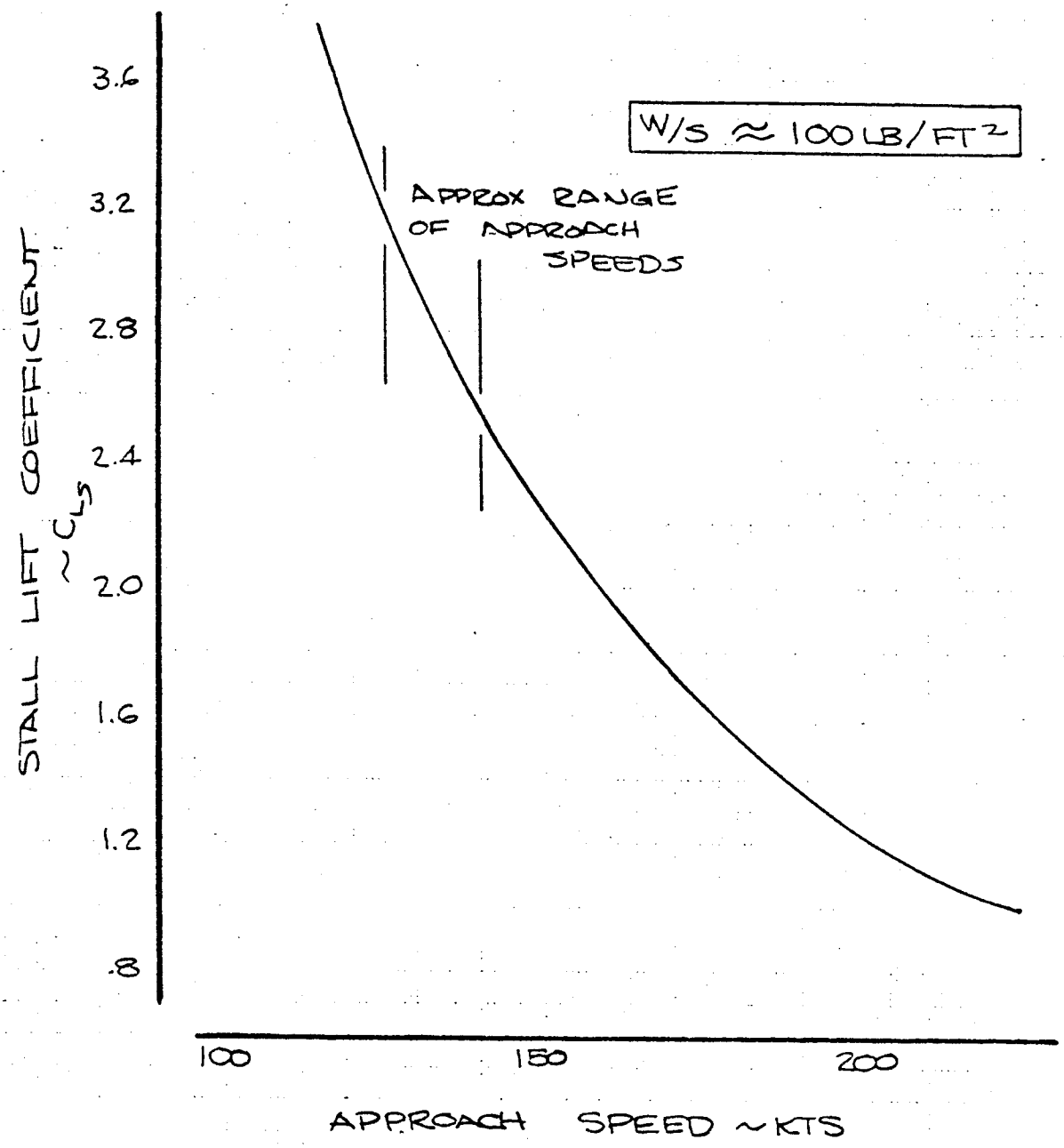

FIGURE 17

EFFECT OF C_{LS} ON APPROACH SPEED

P3.34

DEMONSTRATED $C_{L_{MAX}}$ LEVELS

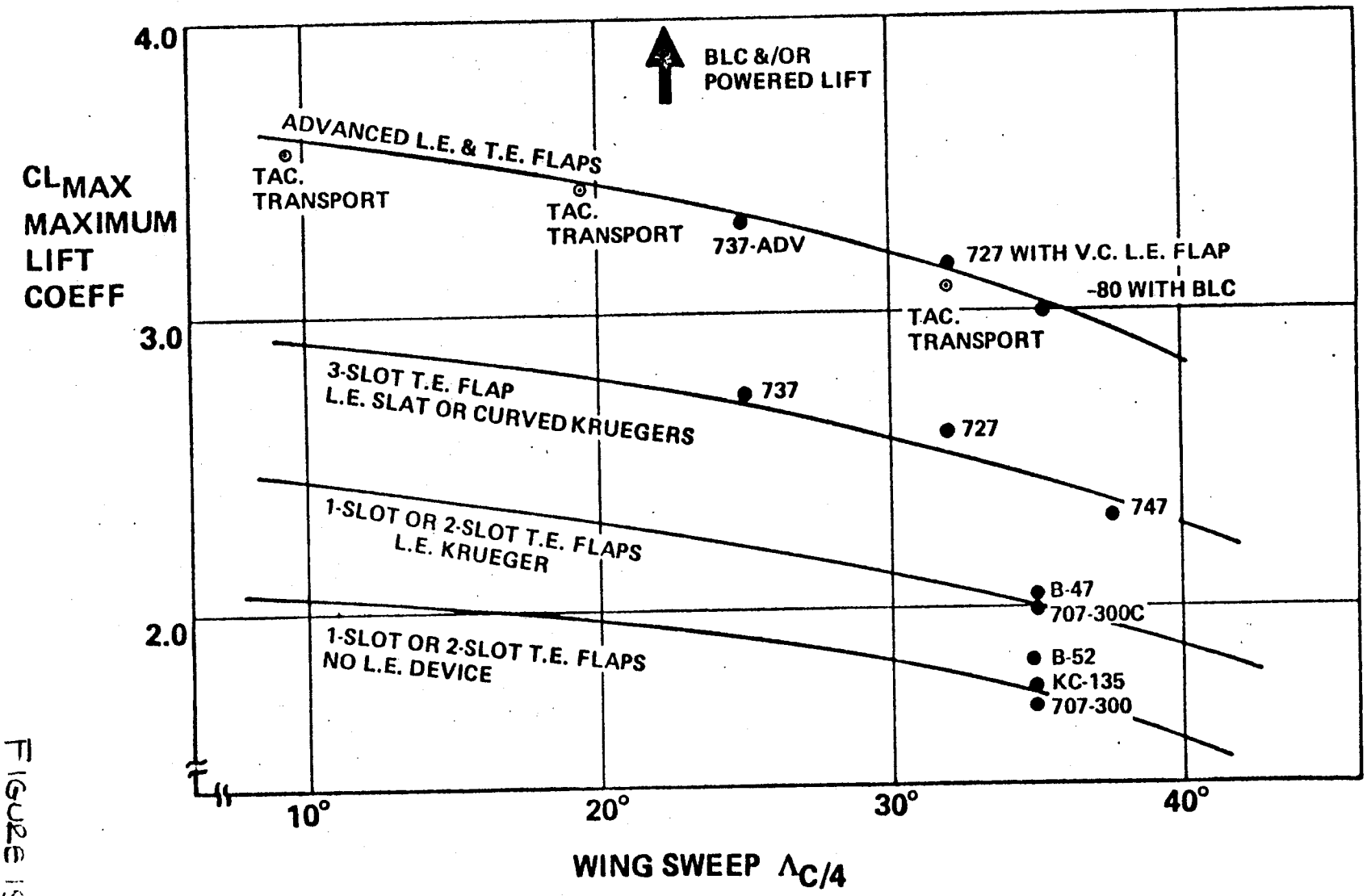

FIGURE 15

P3.35

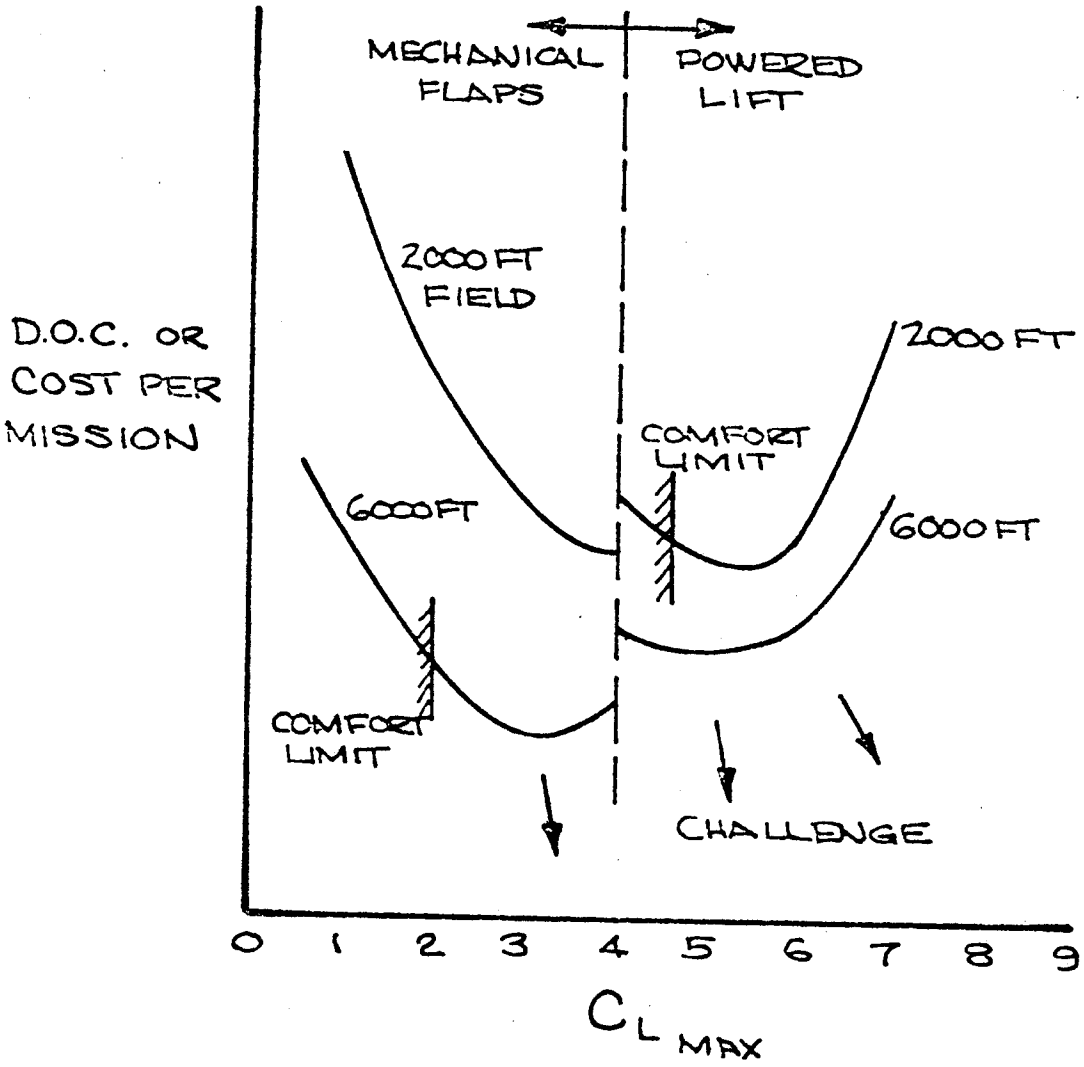

FIGURE 4

ENGR.			REVISED	DATE	EFFECT OF $C_{L_{MAX}}$ ON ECONOMICS	
CHECK						
APR						
APR						
					THE BOEING COMPANY RENTON, WASHINGTON	P3.36

AD 1017-R6

6-7000

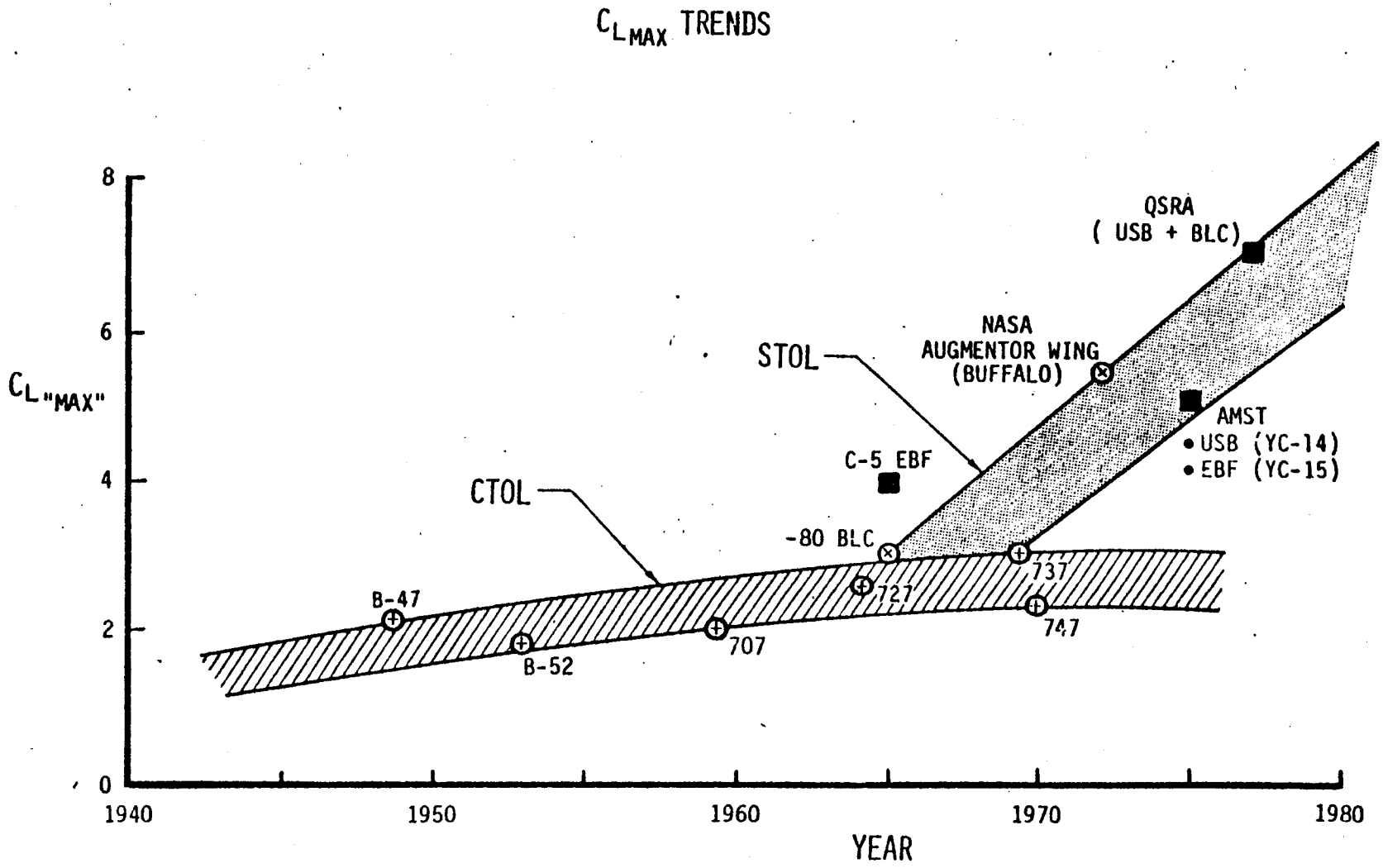

FIGURE 20
P3.37

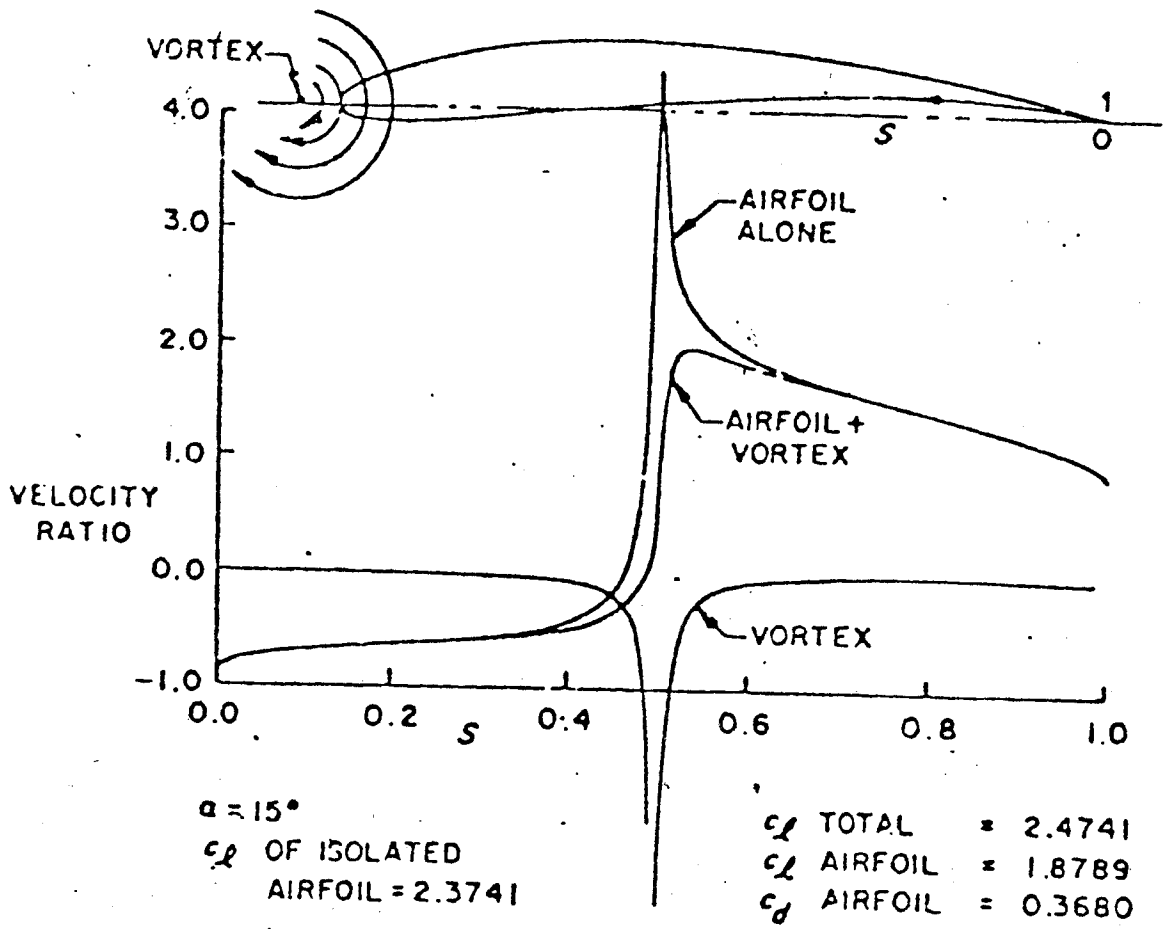

Velocity distributions on an airfoil with and without a vortex located as shown. S is the arc length around the airfoil surface beginning at the trailing edge, measured in a clockwise direction. Total perimeter is unity. Curve labeled vortex shows velocities induced on the airfoil by the vortex in the absence of stream flow.

FIGURE 21

P3.38

116

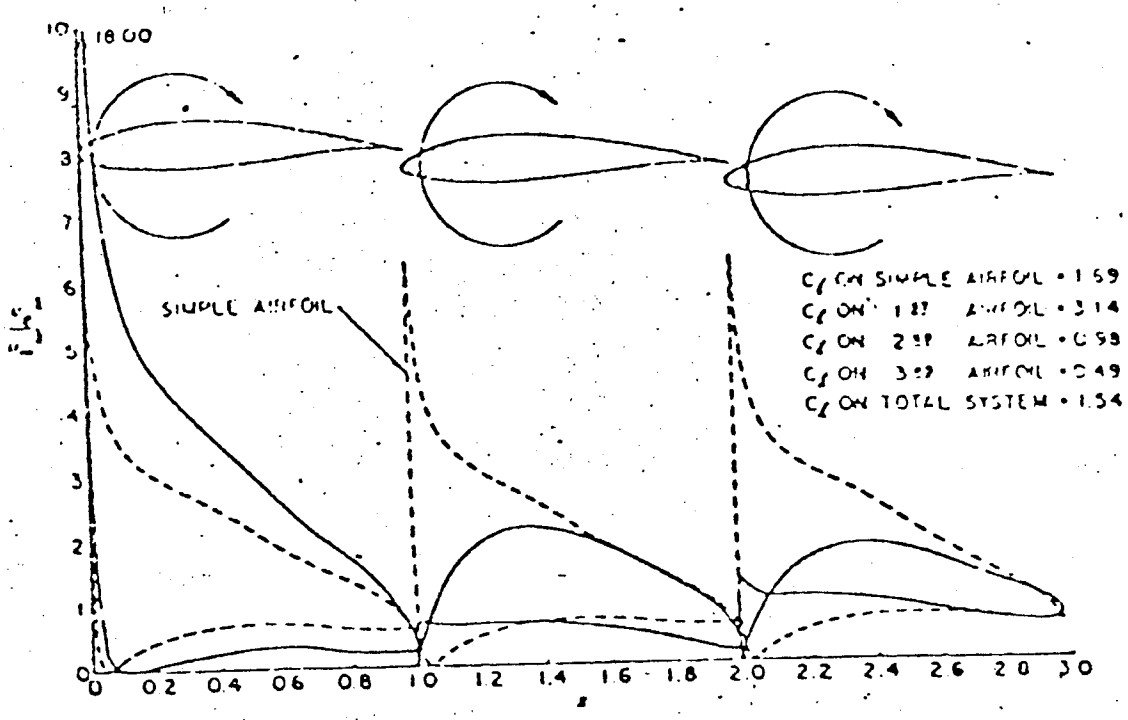

Pressure distribution on three-element airfoil formed from three NACA 632-615 sections, arranged as shown. All are at the same angle of attack, 10°. Shown also is the pressure distribution on the basic simple airfoil at 10° of attack. Slot gaps are 1% of each chord.

FIGURE 22

P3,39

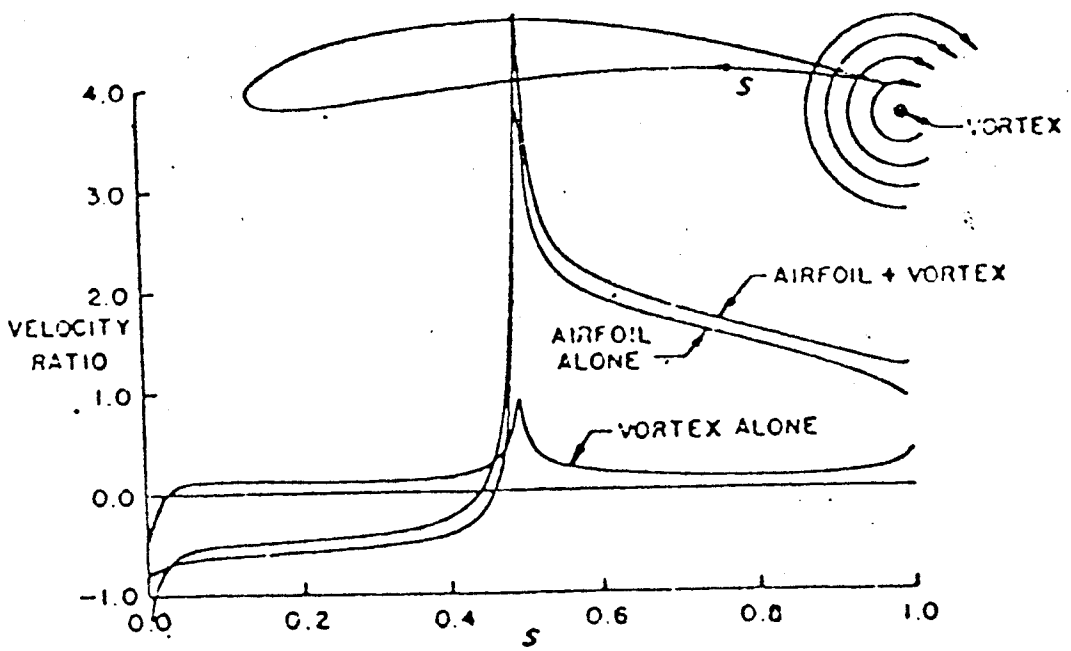

$\alpha = 15°$
c_l OF ISOLATED AIRFOIL = 2.5937

c_l TOTAL = 3.4937
c_l AIRFOIL = 3.3631
c_d AIRFOIL = −0.0763

A point vortex used to simulate a slotted flap. Vortex increases c_ℓ of airfoil at $\alpha = 15°$ from 2.59 to 3.36. Leading-edge pressures are greatly increased by action of the vortex.

FIGURE 23

P3.40

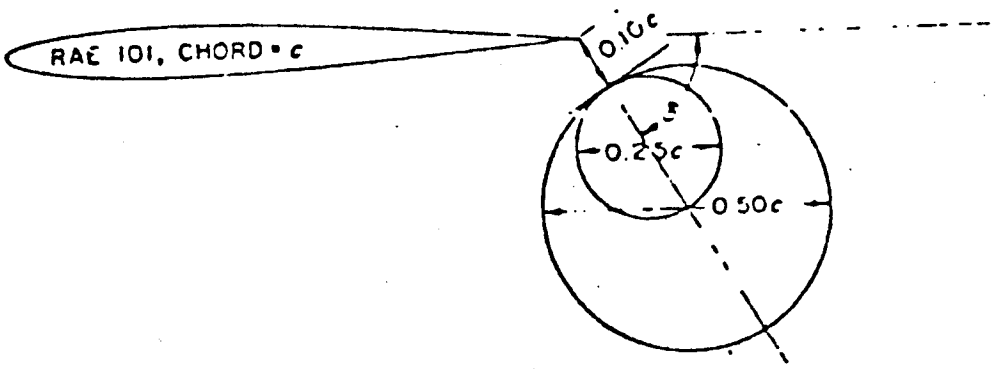

Airfoil-circular-cylinder combinations studied to learn effect of an obstruction on circulation.

FIGURE 24

P3.41

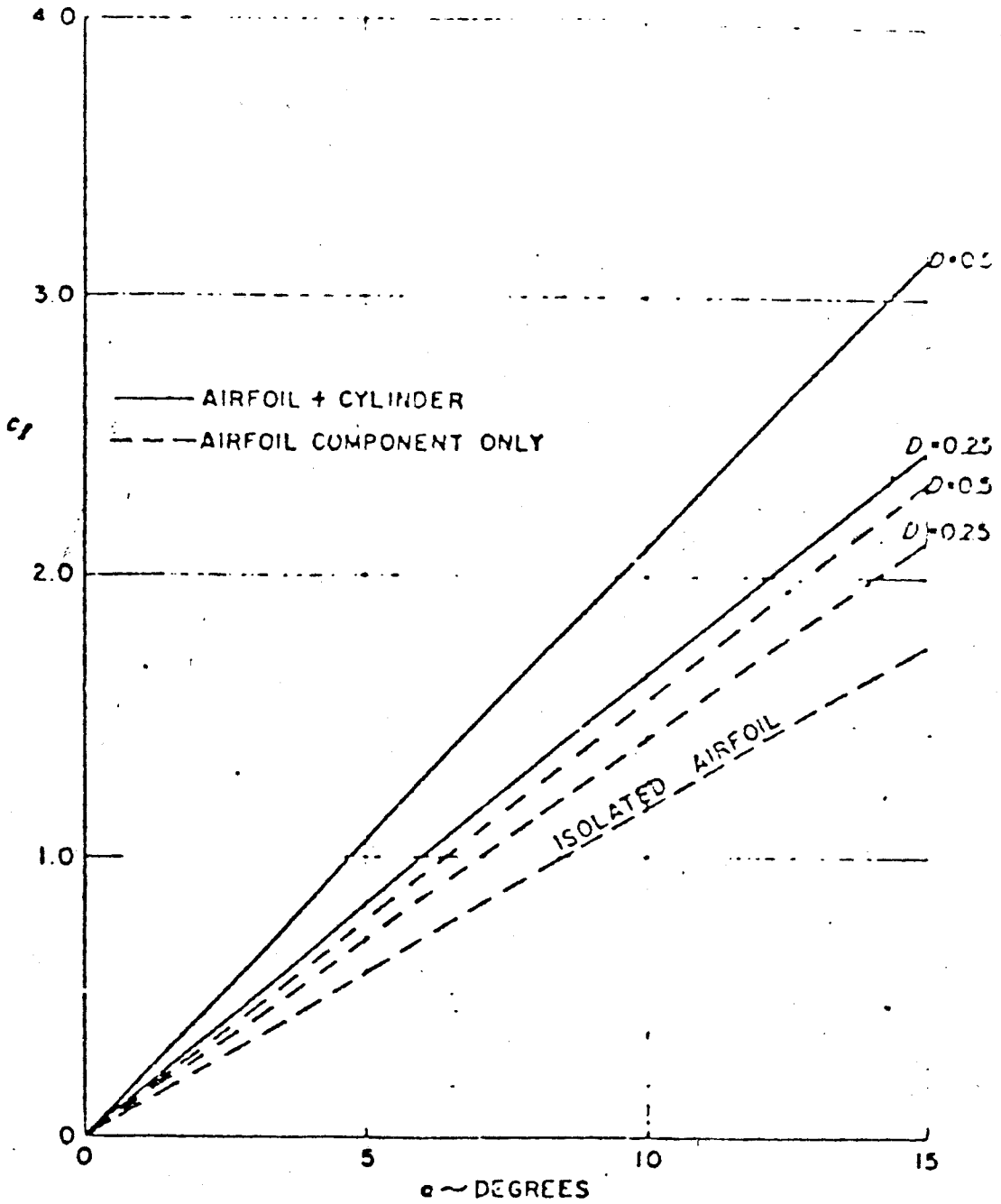

C_ℓ vs α curves for airfoil-cylinder combinations, showing strong effects on circulation. Deflection δ of cylinder = 0°.

FIGURE 35

20

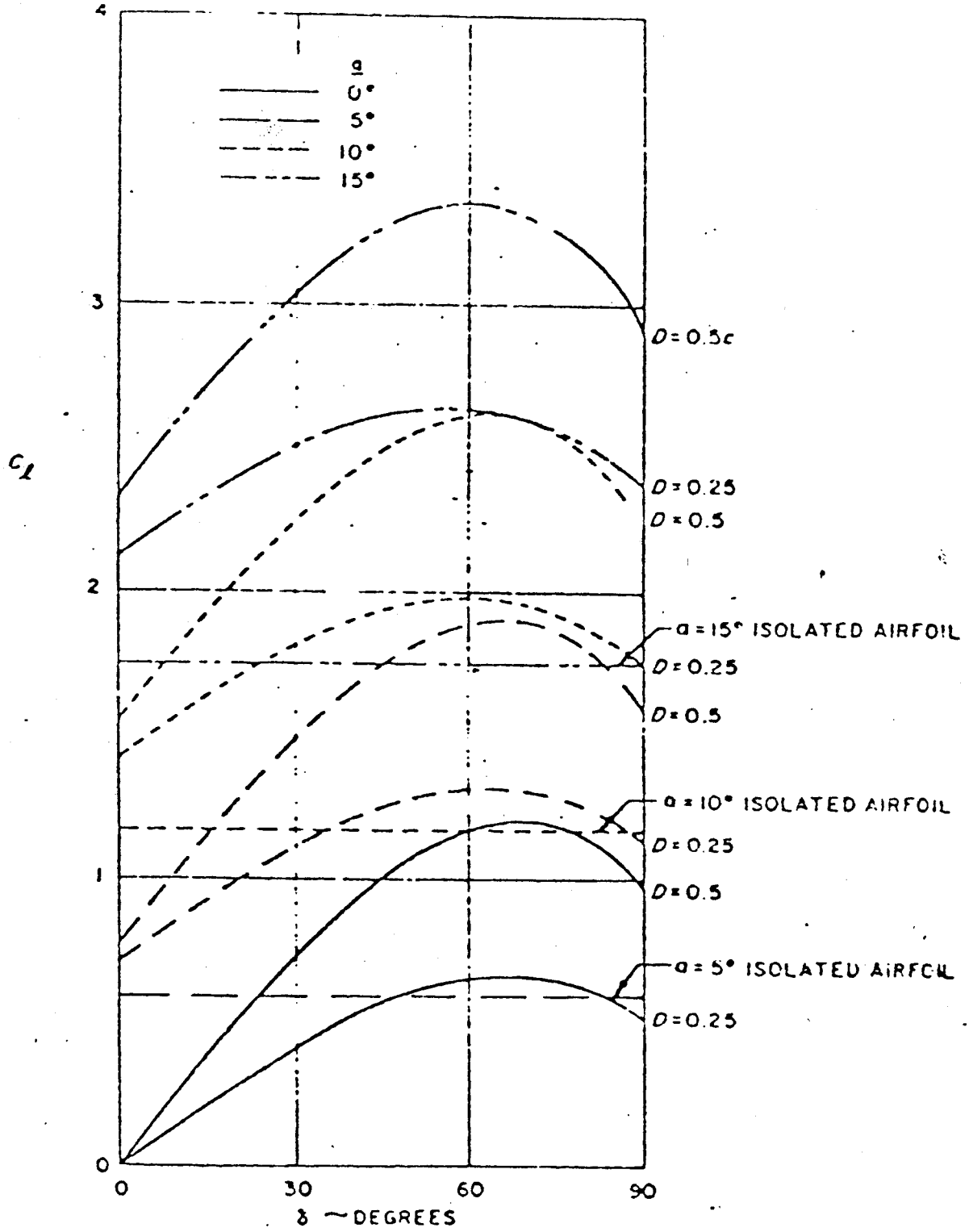

Airfoil-circular-cylinder combinations. Effect of α, δ, and diameter on lift coefficient.

FIGURE 26

P343

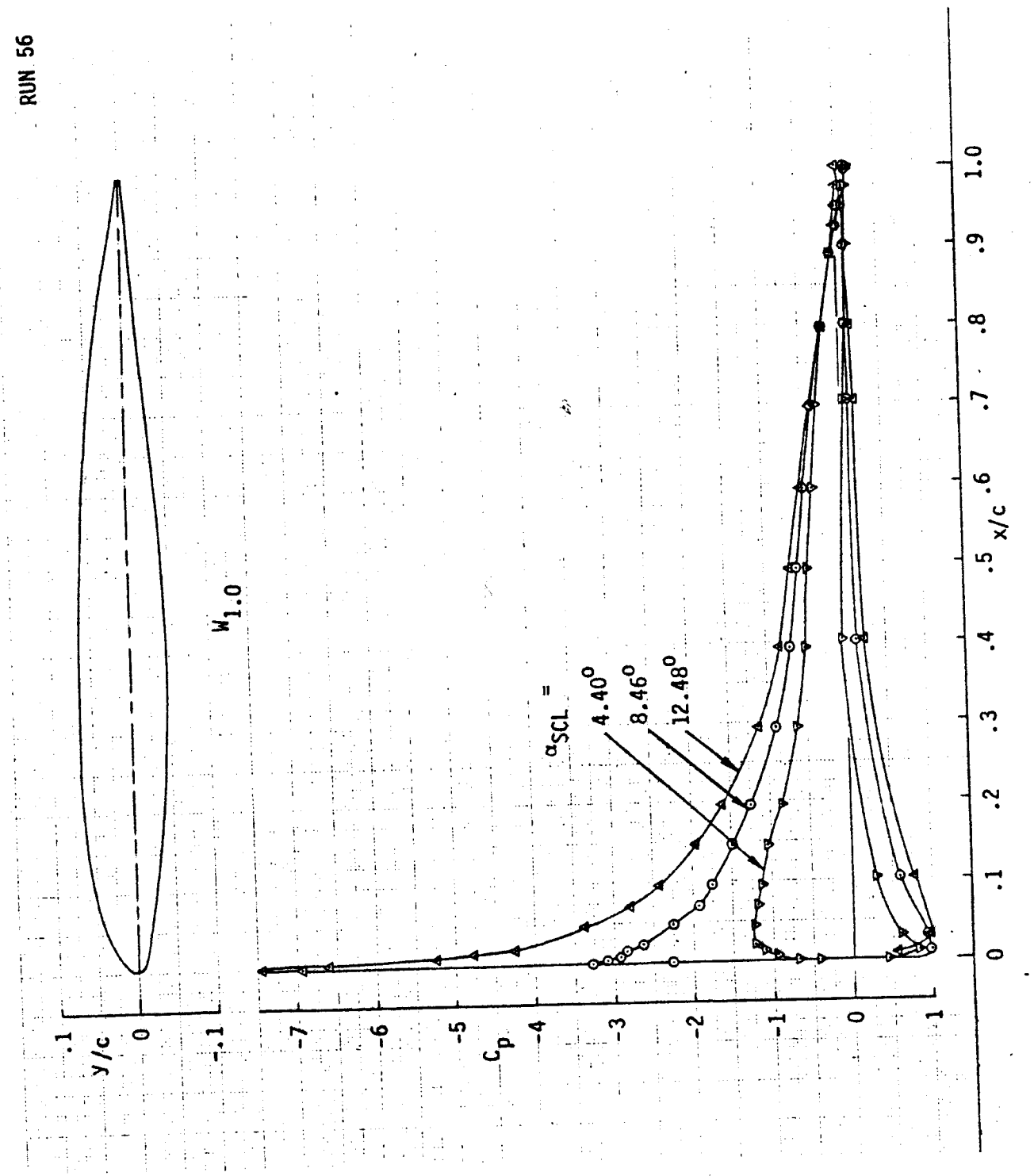

SURFACE PRESSURE DISTRIBUTION --- FLAPS UP

FIGURE 17

P 344

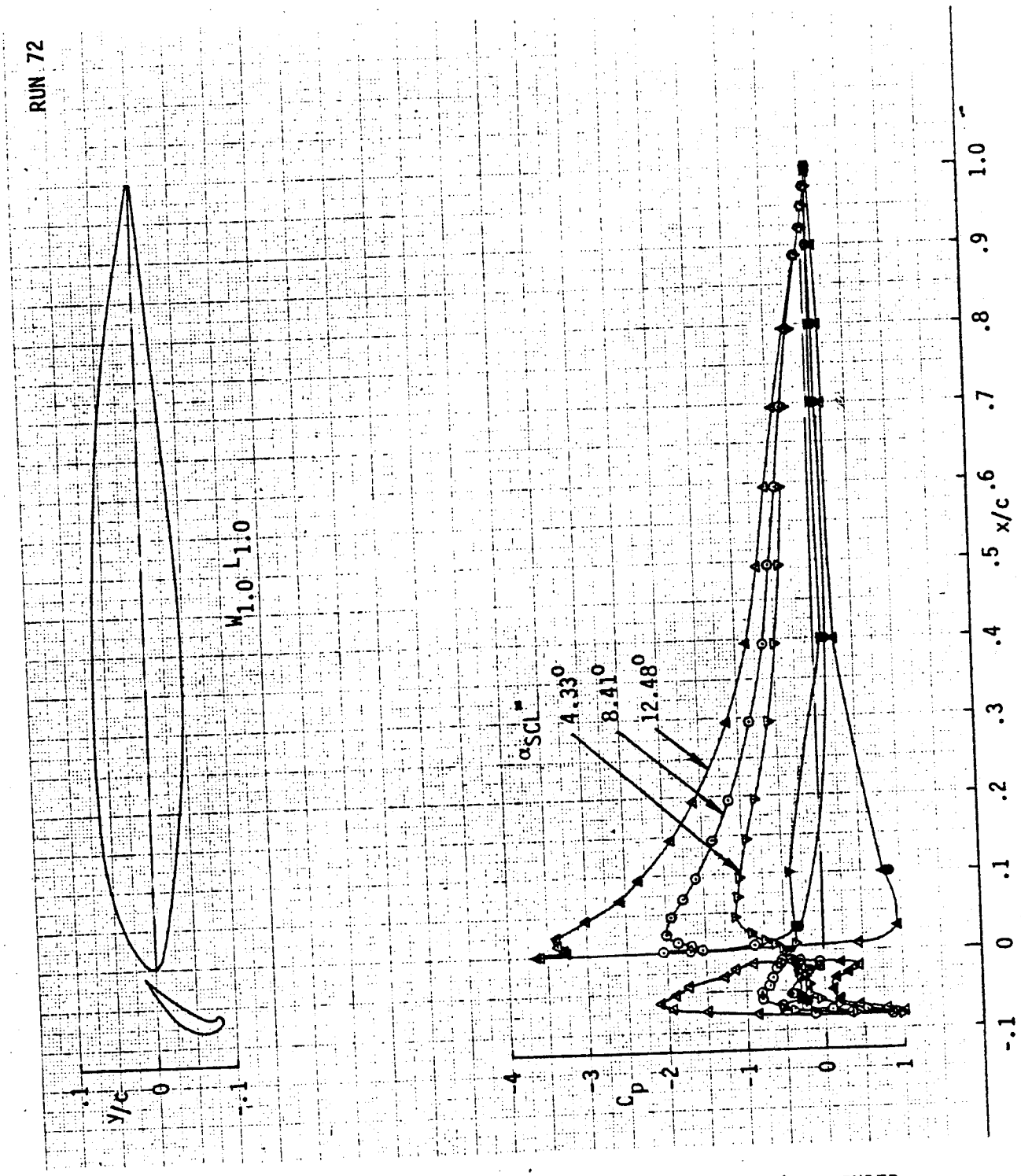

SURFACE PRESSURE DISTRIBUTION — L.E. ($L_{1.0}$) EXTENDED

FIGURE 23

P 3.45

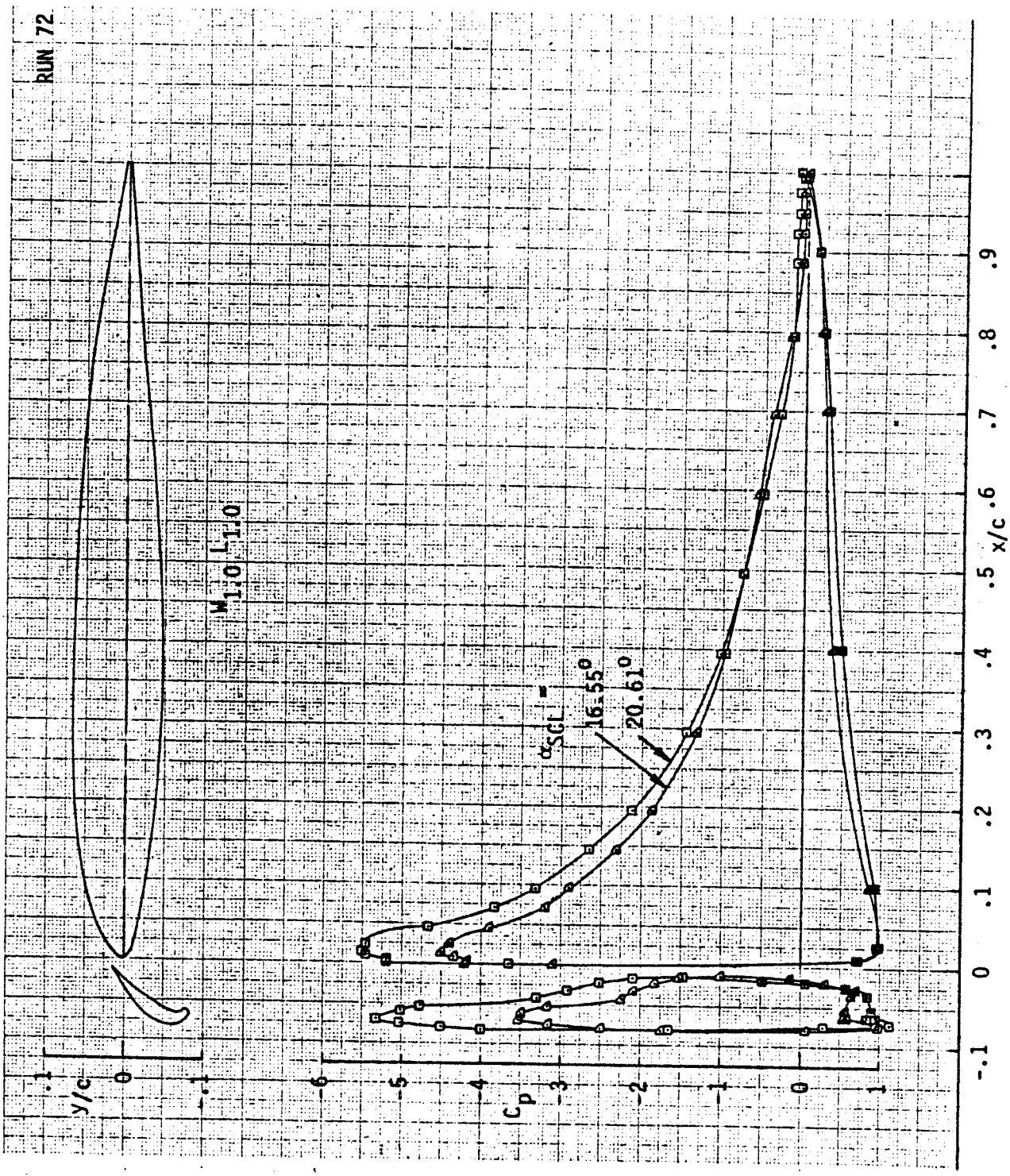

SURFACE PRESSURE DISTRIBUTION --- L.E. ($L_{1.0}$) EXTENDED

FIGURE 29

P3.46

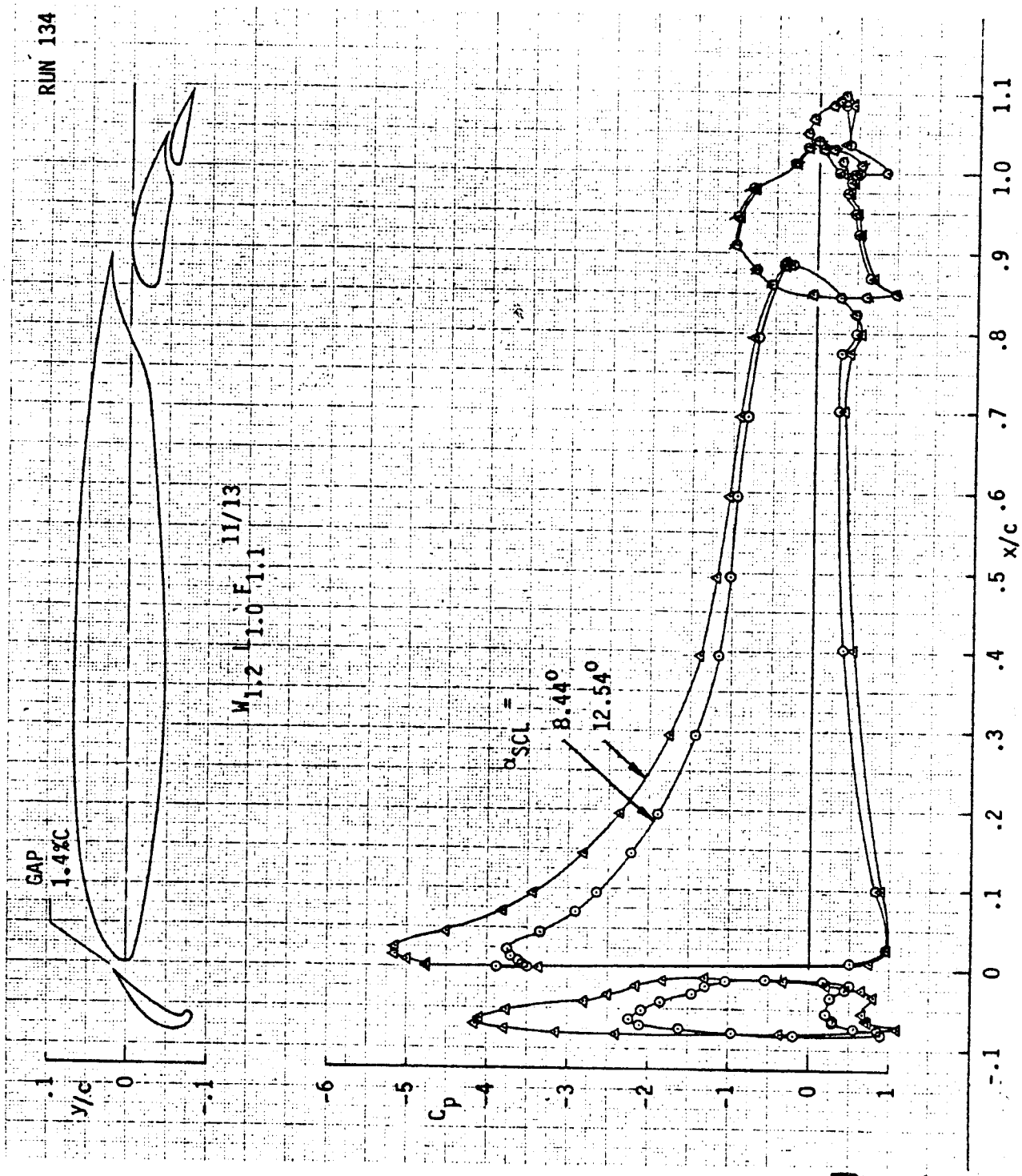

SURFACE PRESSURE DISTRIBUTION — TAKEOFF FLAPS BASELINE GAP

P3.47

125

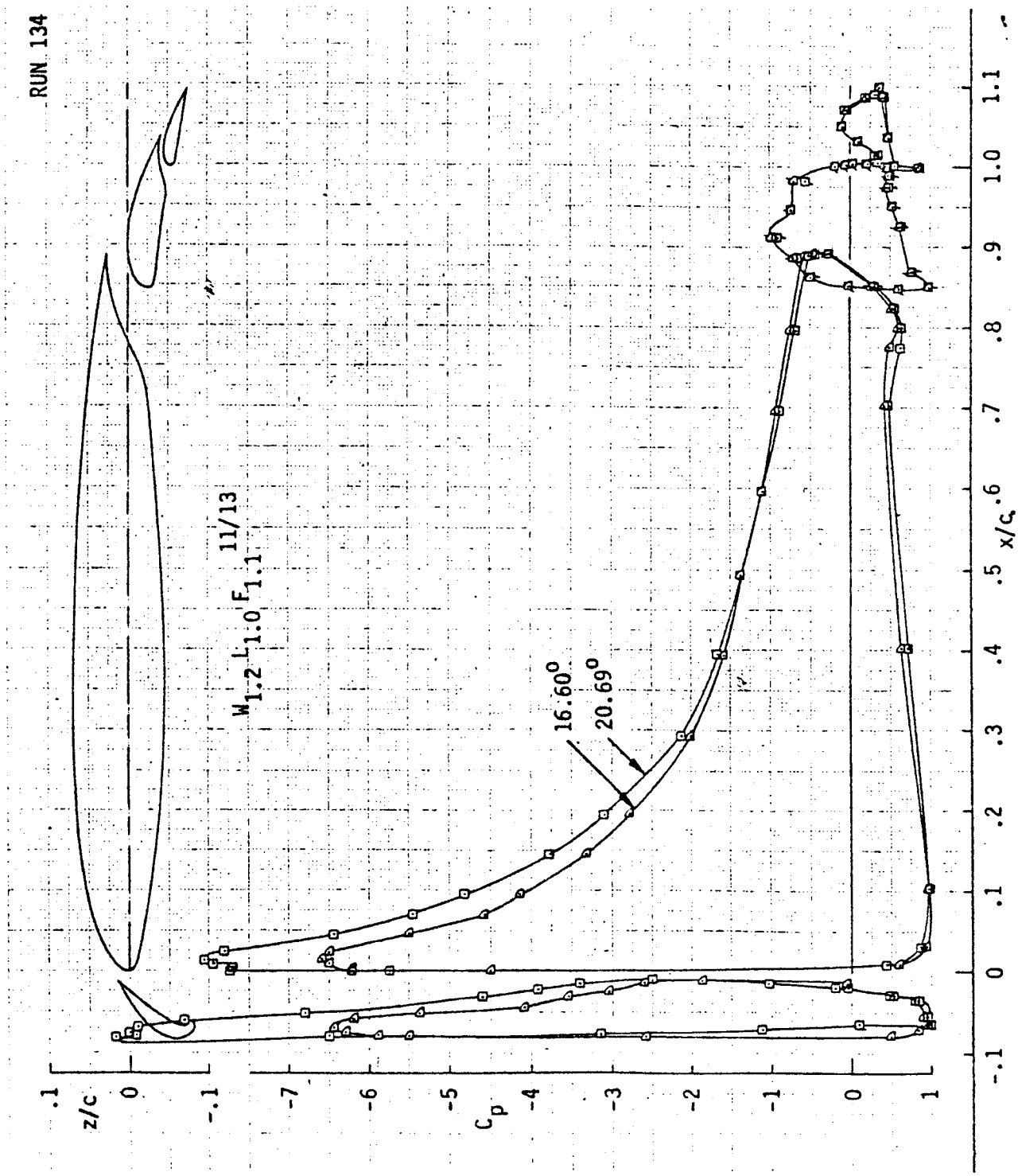

FIGURE 31

SURFACE STATIC PRESSURE DISTRIBUTION --- FLAPS DOWN

P3.49

126

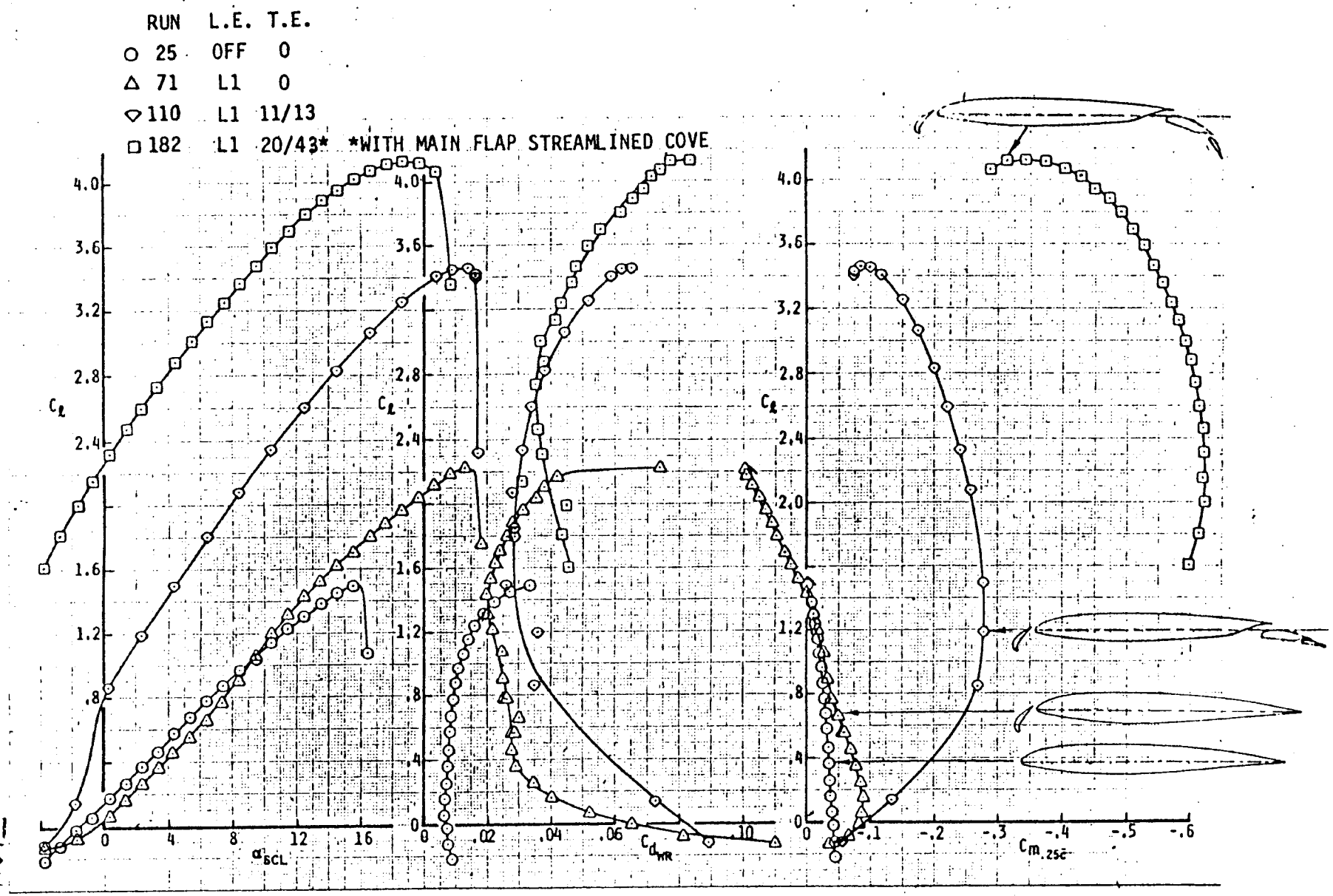

HIGH LIFT DEVICE BUILDUP/BASELINE SETTINGS FIGURE 32

P3.49

198

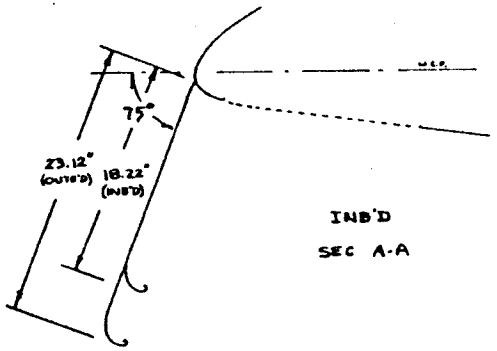

INB'D
SEC A-A

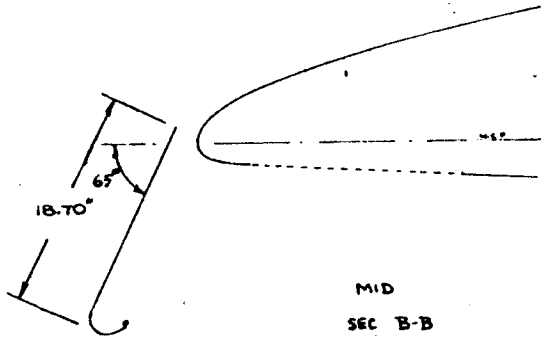

MID
SEC B-B

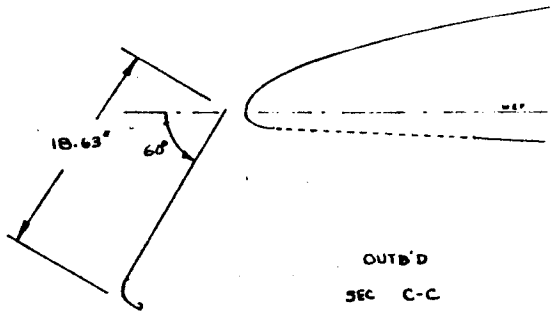

OUTB'D
SEC C-C

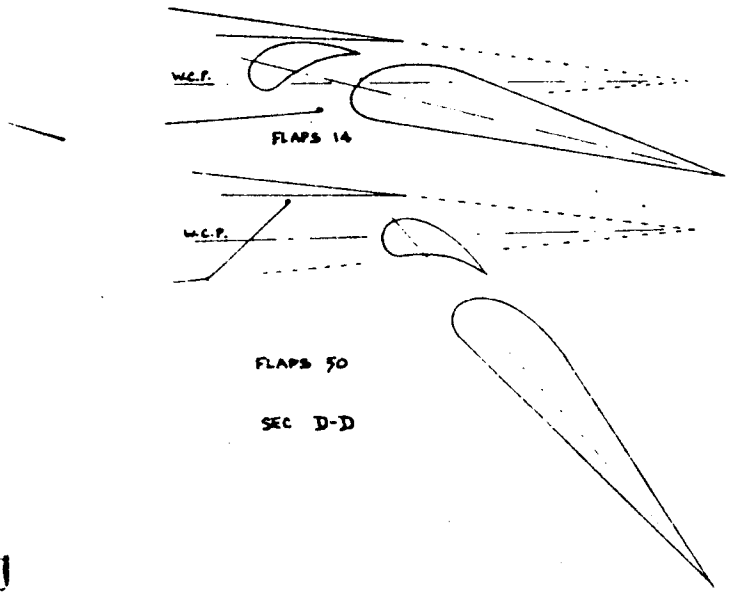

SEC D-D

WING SUMMARY	
SEMI-SPAN	875 IN.
AREA	2892 ft^2
ASPECT RATIO	7.35
TAPER RATIO	.727
MAC	272.3 IN.
SWEEPBACK $\Lambda_{c/4}$	35°

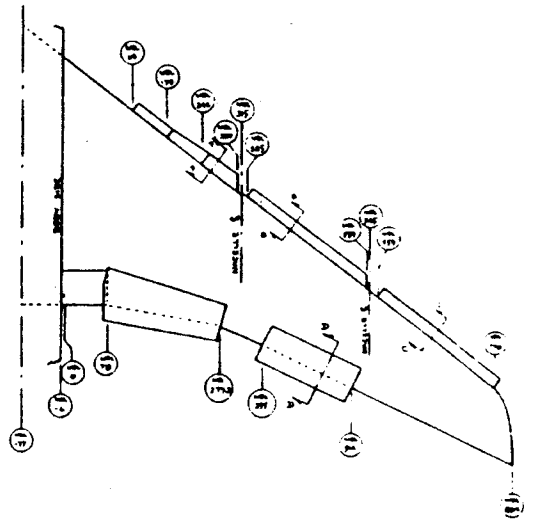

NOTE : DRAWING NOT TO SCALE

CALC		REVISED	DATE	HIGH LIFT SYSTEM	707-320B
CHECK					
APR					
APR				THE BOEING COMPANY	PAGE
J.L. LEE	9-17-70				

AD 1017 B

6-7500

Figure 31

P 250

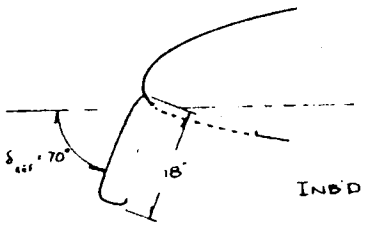

INB'D

SEC A-A

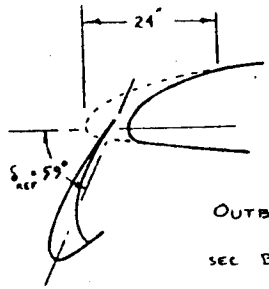

OUTB'D

SEC B-B

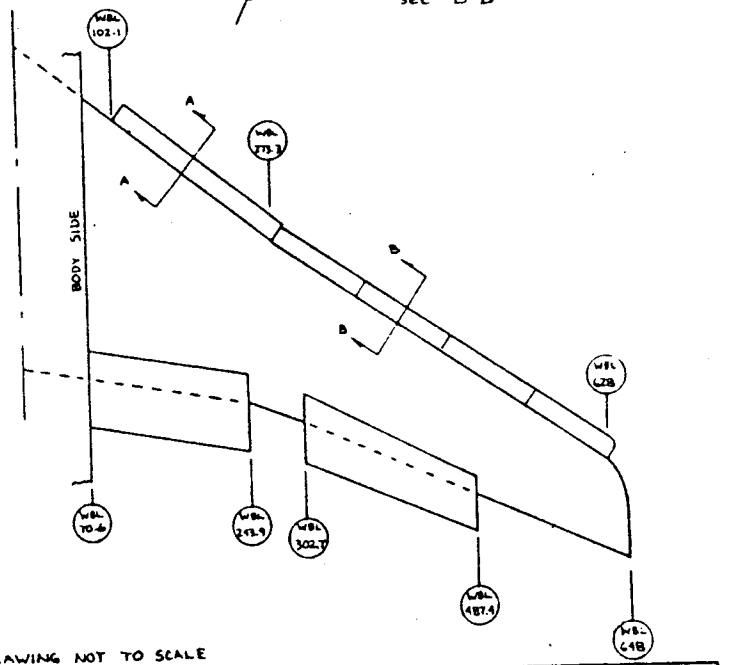

WING SUMMARY	
SEMI-SPAN	648 IN.
AREA	1560 FT^2
ASPECT RATIO	7.48
TAPER RATIO	.372
MAC	180 IN.
SWEEPBACK $\Lambda_{c/4}$	32°

FLAPS 10

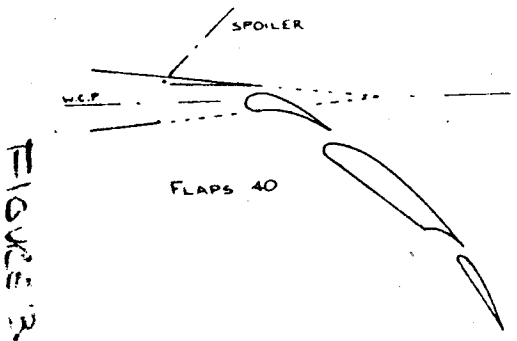

FLAPS 40

NOTE: DRAWING NOT TO SCALE

		REVISED	DATE		
CALC				HIGH LIFT SYSTEM	727
CHECK					
APR					
APR				THE BOEING COMPANY	PAGE
J.L. LEE	9-16-70				

D6-7900

D351

AD 1017 B

130

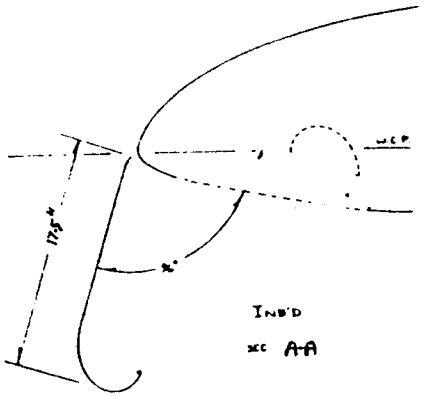

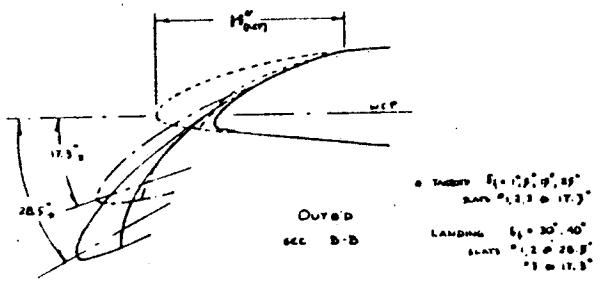

WING SUMMARY	
SEMI-SPAN	557.5 INCHES
AREA	980 ft^2
ASPECT RATIO	8.83
TAPER RATIO	.341
MAC	134.5 IN.
SWEEPBACK $\Lambda_{c/4}$	25°

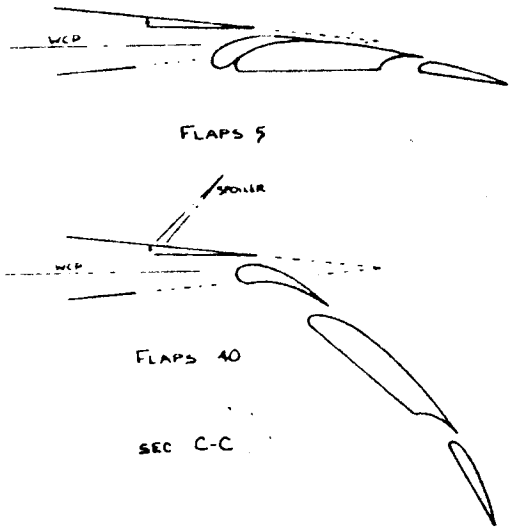

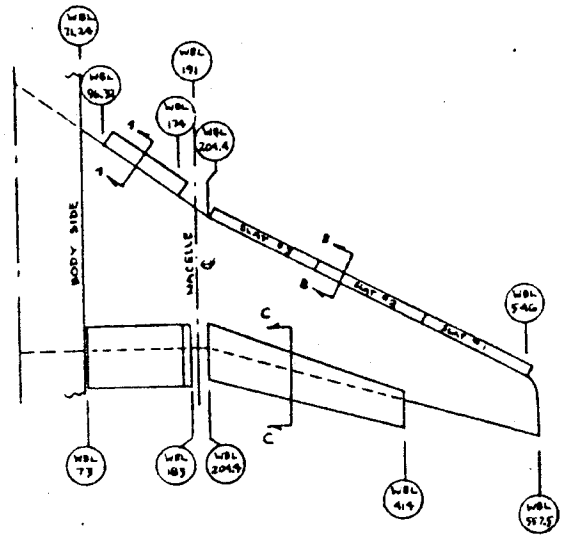

NOTE : DRAWING NOT TO SCALE

		REVISED	DATE		
CALC				HIGH LIFT SYSTEM	737-100
CHECK					
APP					
APP				THE BOEING COMPANY	PAGE
J.L. LEE	9-16-70				

6-7800

FIGURE 3.5
P 3.52

131

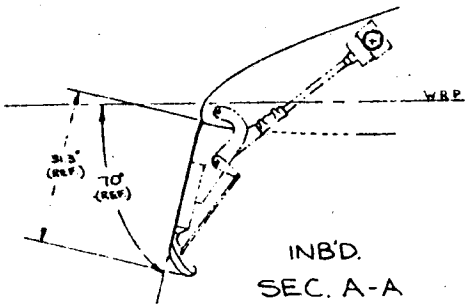

INB'D.
SEC. A-A

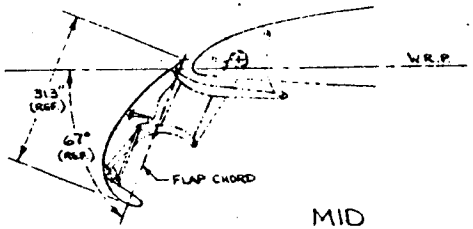

MID
SEC. B-B

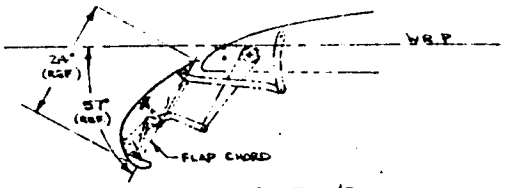

OUTB'D.
SEC. C-C

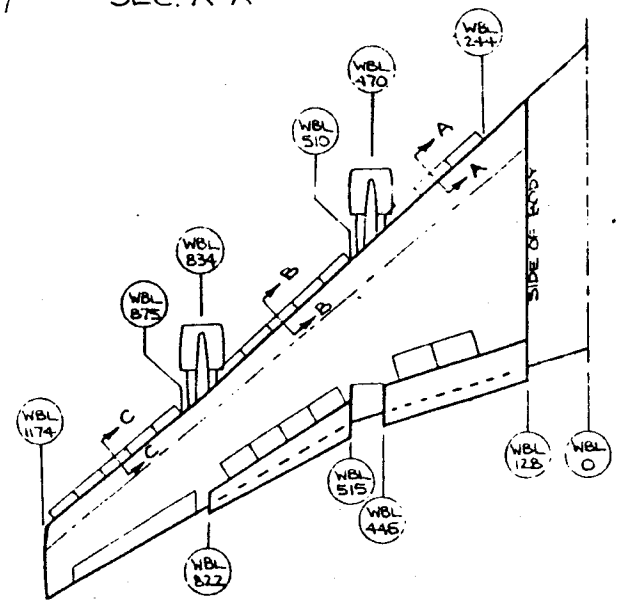

WING SUMMARY	
SEMI-SPAN	91 FEET - 0 INCHES
AREA	5500 SQ. FEET
ASPECT RATIO	6.96
TAPER RATIO TIP CHORD / BASIC CHORD TIP CHORD / ROOT CHORD	.356 .245
MAC (BASIC ONLY)	321.7795 INCHES
SWEEPBACK, C/4	37½°
DIHEDRAL	7°
INCIDENCE	2°

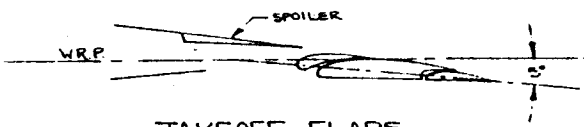

TAKEOFF FLAPS

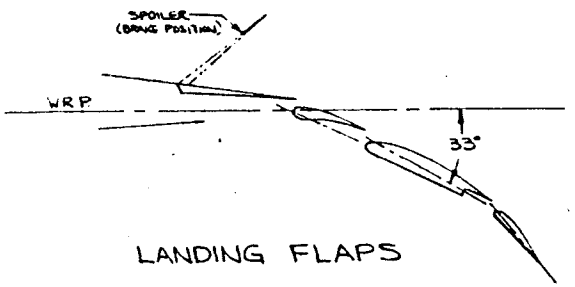

LANDING FLAPS

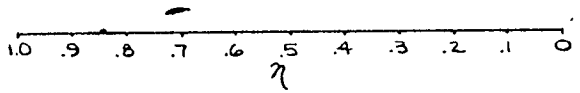

CALC	M. LANG	7/30/68	REVISED	DATE	HIGH LIFT SYSTEM	747
CHECK	J.W.B. MARTIN	8/13/68				
APP						
APP						
					THE BOEING COMPANY RENTON WASHINGTON	PAGE

NOTE: DRAWING NOT TO SCALE.

FIGURE 35
D253

GEOMETRIC CHARACTERISTICS OF THE TRAILING-EDGE FLAPS

FLAP	CHARACTERISTIC	c_f/c	c'/c	c_f'/c'	c_{f_1}/c, c_{f_2}/c, c_{f_3}/c
F2	727 type triple-slotted flap	.246	1.222	.285	.093, .173, .092
F46	707 type double-slotted flap	.266	1.222	.285	.118, .236
F47	Boeing C-5A type double-slotted flap	.295	1.222	.285	.237, .118
F48	Double-slotted flap with segments of equal length	.266	1.222	.285	.179, .177
F50	Single-slotted flap	.314	1.19	.266	.314
F56	Mod. of F46: Vane trailing-edge camber was reduced to eliminate trailing-edge separation on the vane	.266	1.222	.285	.117, .236
F57	Mod. of F46: Aft segment trailing-edge camber was increased to simulate aft loaded sections	.266	1.222	.285	.118, .237
F58	Triple-slotted flap consisting of the F46 vane and the F71 fore and aft segments	.316	1.352	.354	.118, .237, .118
F71	Mod. of F47: Leading-edge camber was added to the fore segment to reduce the severity of its stall characteristics	.295	1.222	.285	.237, .118
F72	Slotted spoiler was simulated to reap the benefits of larger flap chord without resorting to excessive Fowler motion. Employs the F71 fore and aft segments.	.295	1.222	.38	.119, .237, .118

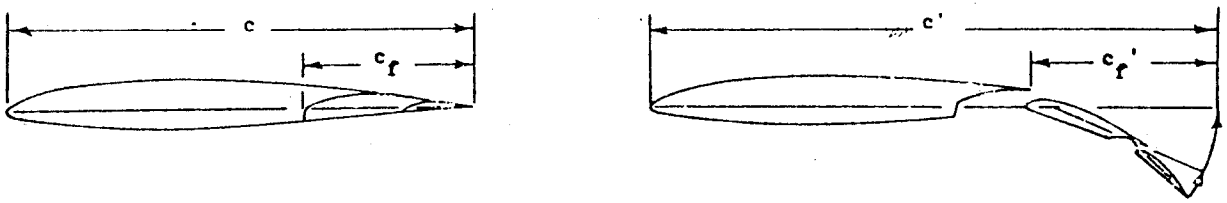

Figure 37

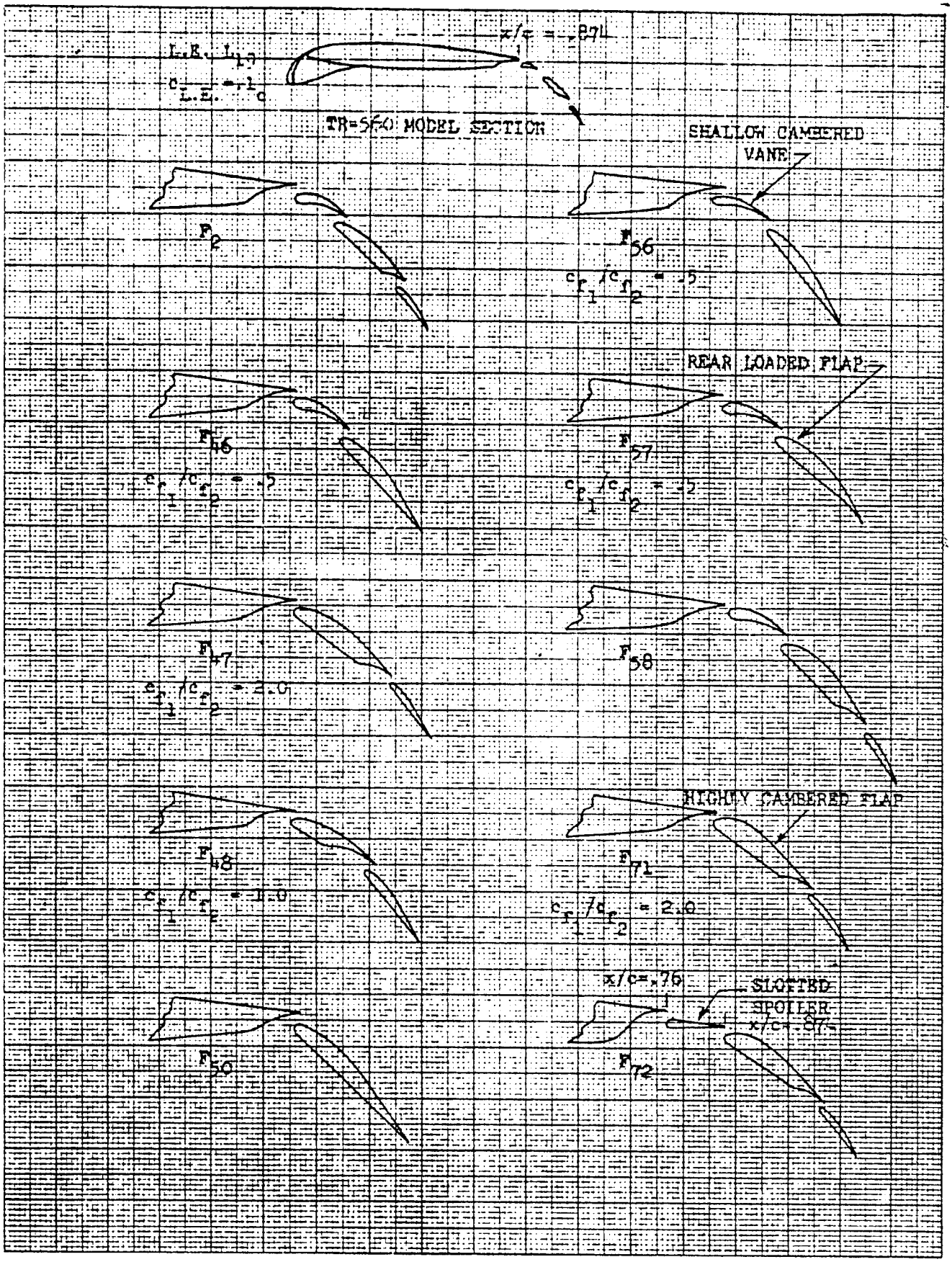

CALC	E. OMAR	9/72	REVISED	DATE	TR-560 TRAILING-EDGE FLAPS
CHECK					
APR					FIGURE 23
APR					THE BOEING COMPANY
	M^2				PAGE P3.55

133

MODEL SCALE

——— F_{46} & F_{57} VANE

- - - - F_{56} VANE

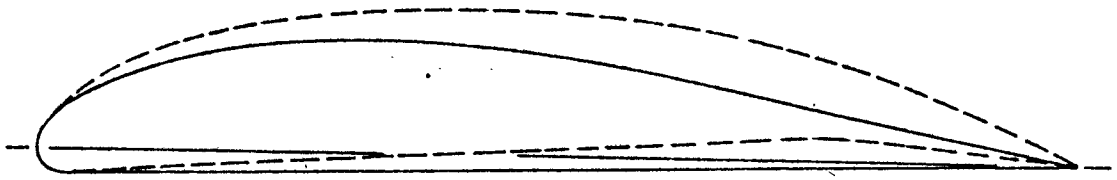

——— F_{46} & F_{56} FLAP

- - - - F_{57} FLAP

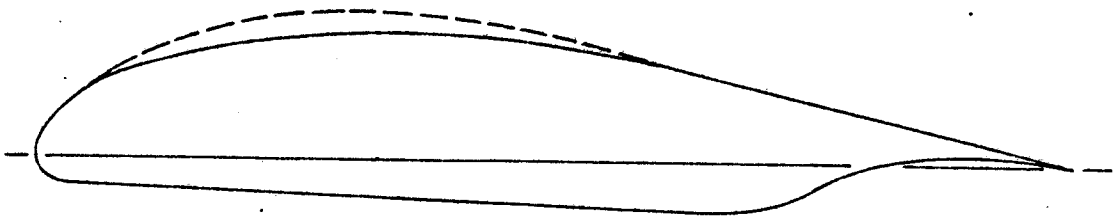

——— F_{47} FORE SEGMENT

- - - - F_{71} FORE SEGMENT

FIGURE 39

CALC	E. OMAR	9/72	REVISED	DATE	COMPARISON OF DOUBLE-SLOTTED FLAP SEGMENT GEOMETRY
CHECK					
APPD					
APPD					
	M2				THE BOEING COMPANY RENTON, WASHINGTON

PAGE P3.56

TD 973 D-83

6 7000

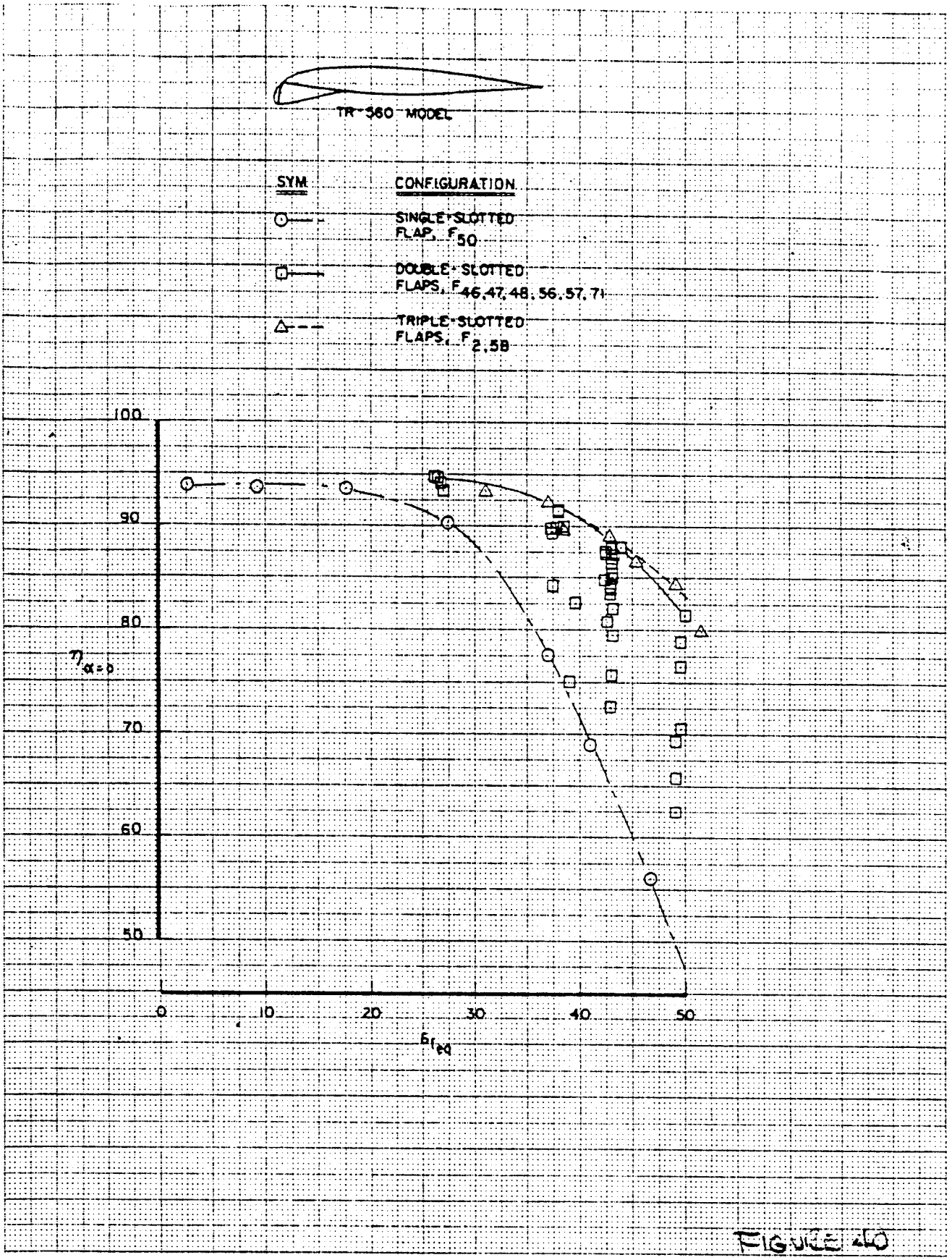

FIGURE 40

CALC	E OMAR	10/72	REVISED	DATE	ENVELOPES OF LIFT EFFICIENCY VERSUS EQUIVALENT FLAP DEFLECTION FOR SINGLE, DOUBLE, AND TRIPLE-SLOTTED FLAPS
CHECK					
APR					
APR					THE BOEING COMPANY
	M^2				PAGE P3.57

D1 4100 3260 ORIG 3/71

K-Σ ALBANENE 1951 TRACING PAPER

135

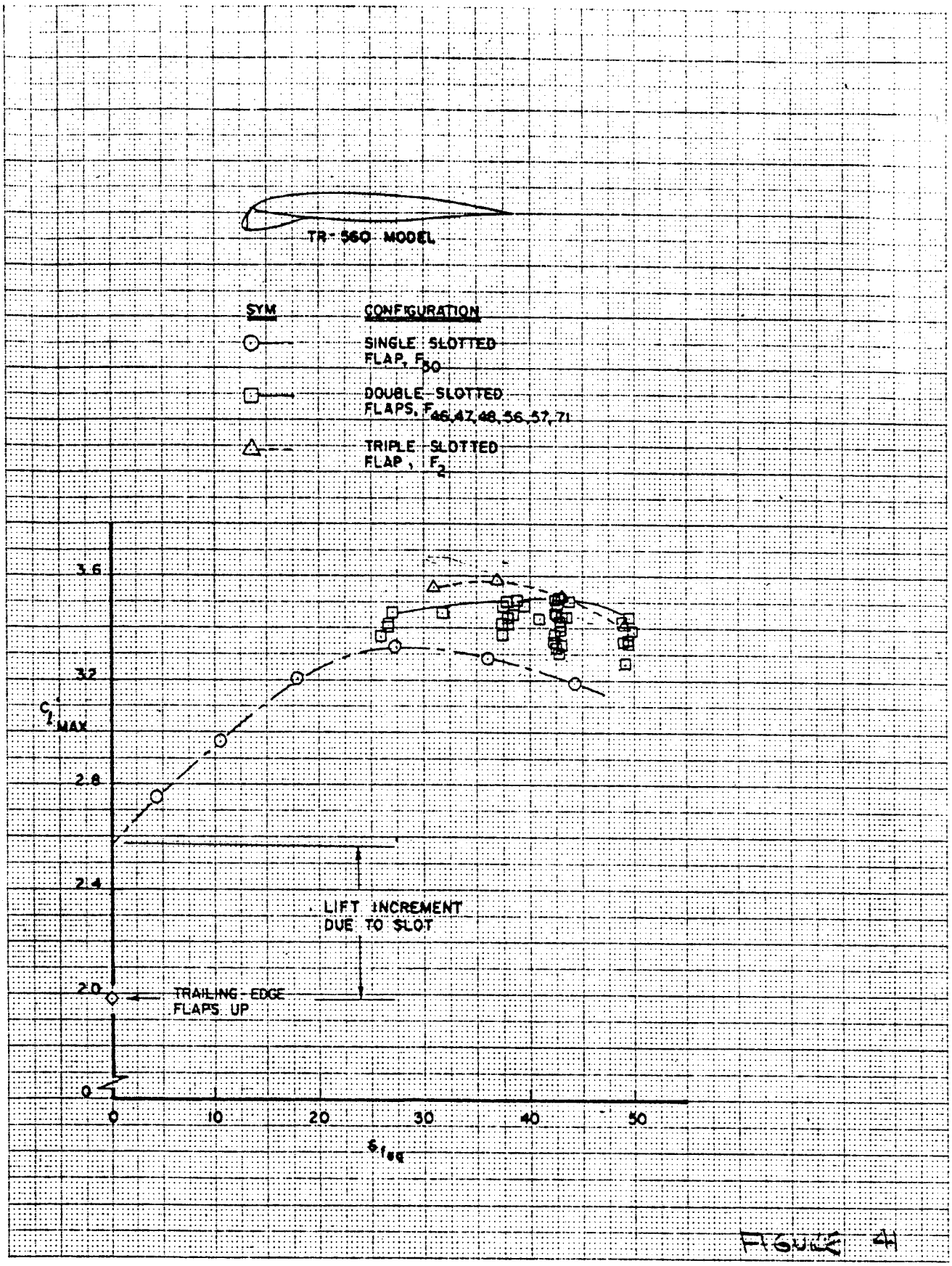

FIGURE 4

CALC	E OMAR	10/72	REVISED	DATE	VARIATION OF $C_{l_{MAX}}$ WITH EQUIVALENT FLAP DEFLECTION FOR SINGLE, DOUBLE, AND TRIPLE-SLOTTED FLAPS
CHECK					
APR					
APR					THE BOEING COMPANY
	M^2				PAGE P3.58

136

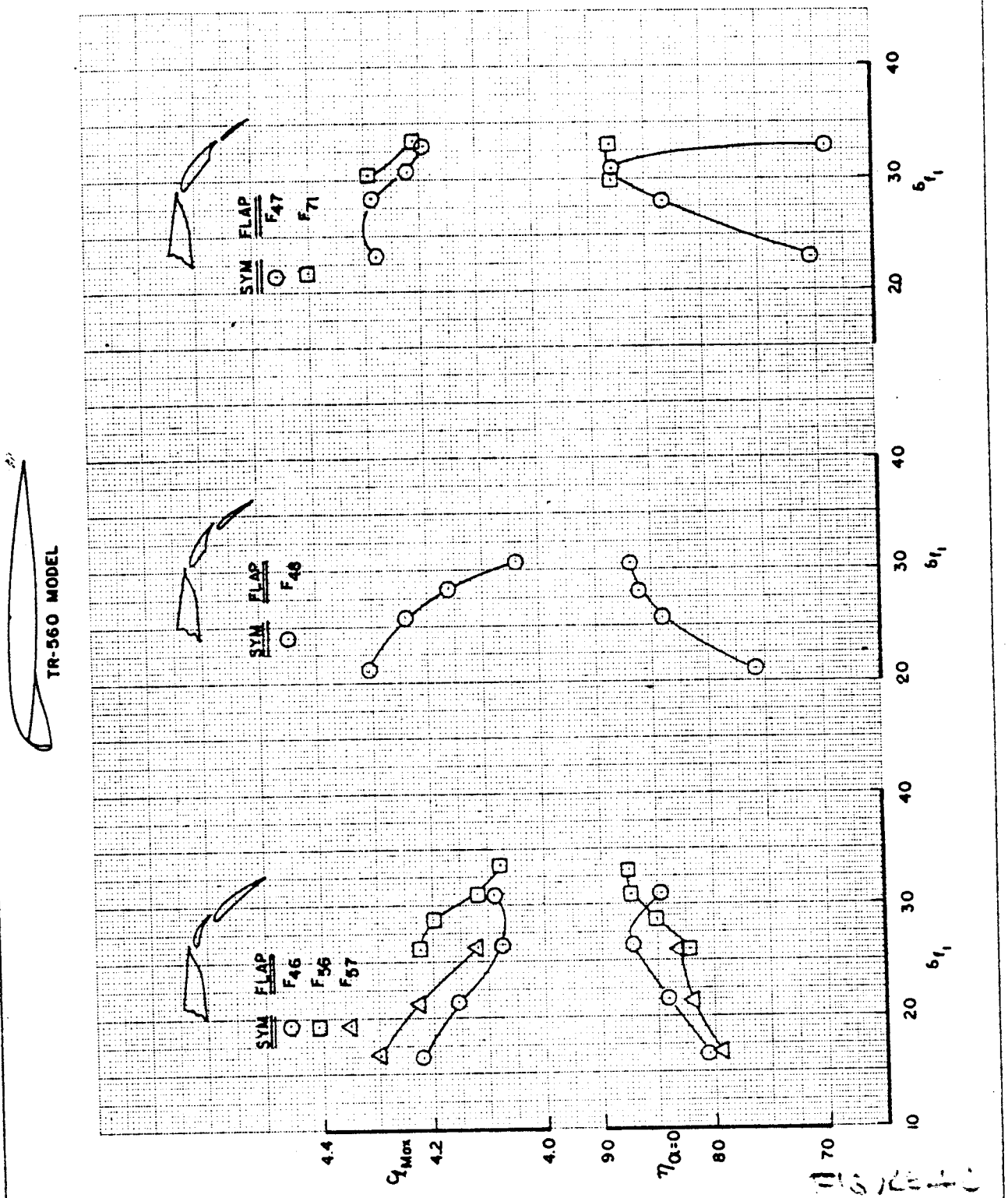

CALC	OMAR	10/72	REVISED	DATE
CHECK				
APPD				
APPD				
	M^2			

VARIATION OF $C_{l_{MAX}}$ AND $\eta_{\alpha=0}$ WITH DOUBLE-SLOTTED FLAP SEGMENT DEFLECTION COMBINATION AT $\delta_{f_{eq}} = 43°$

THE BOEING COMPANY

PAGE D2-11159

AD 4992 C

6-5000

137

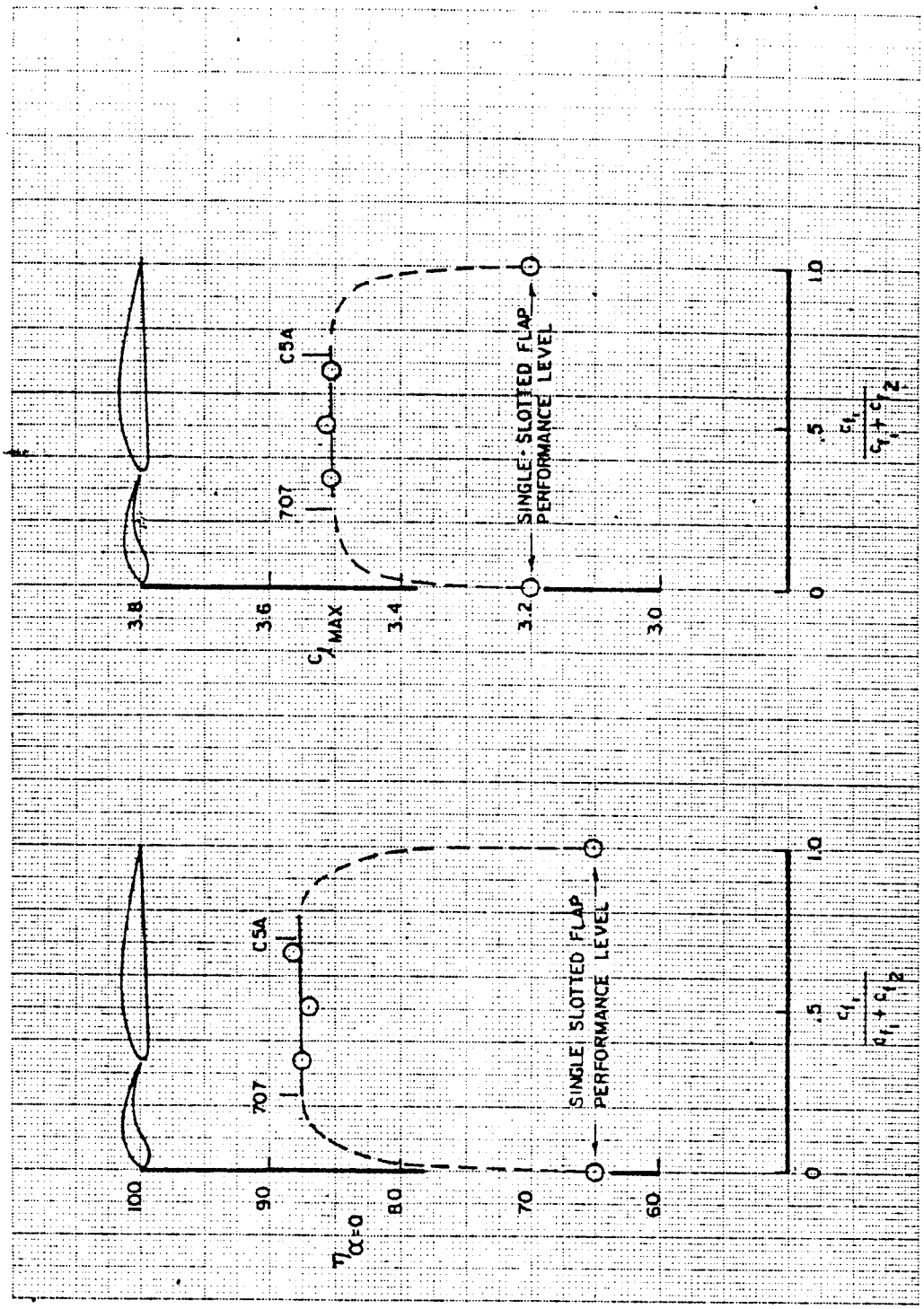

FIGURE 43

CALC	OMAR	10/72	REVISED	DATE	VARIATION OF $C_{\ell_{MAX}}$ AND $\eta_{\alpha=0}$ WITH LOCATION OF THE SECOND SLOT OF DOUBLE-SLOTTED FLAPS
CHECK					
APPD					
APPD					
	M^2				THE BOEING COMPANY

PAGE P3.60

AD 4992 C

6-5000

138

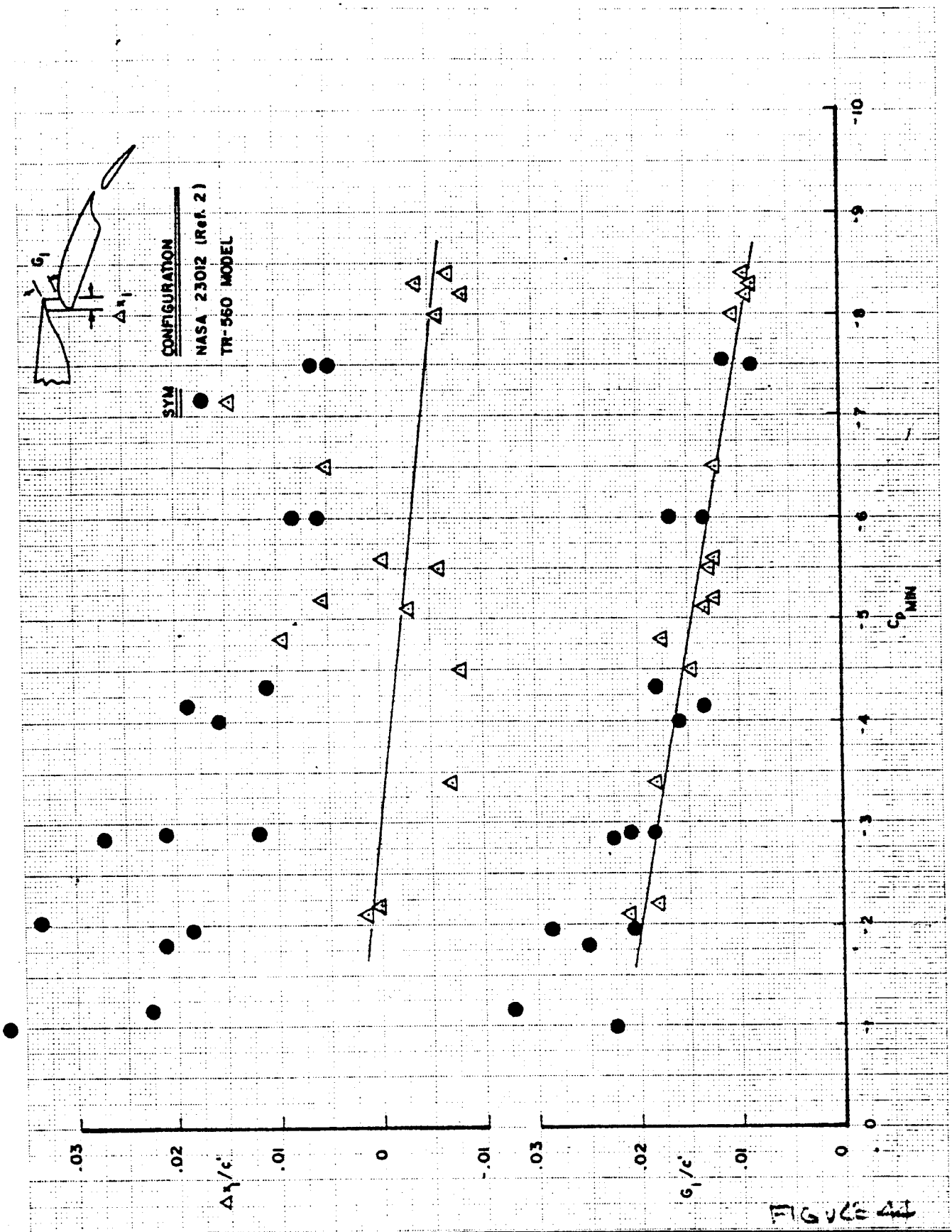

FIGURE 44

CALC	OMAR	10/72	REVISED	DATE	VARIATION OF FIRST TRAILING-EDGE SLOT GAP AND SEGMENT OVERLAP WITH FIRST FLAP SEGMENT SUCTION PEAK PRESSURE
CHECK					
APR					
APR					THE BOEING COMPANY
	M2				PAGE P3.61

TD 461 D

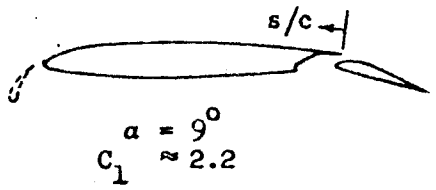

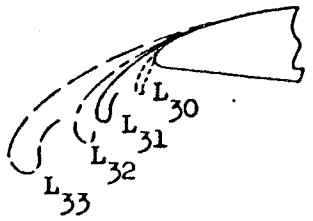

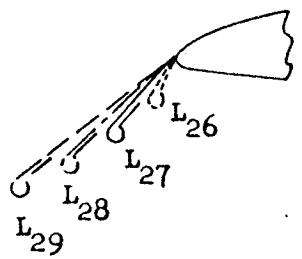

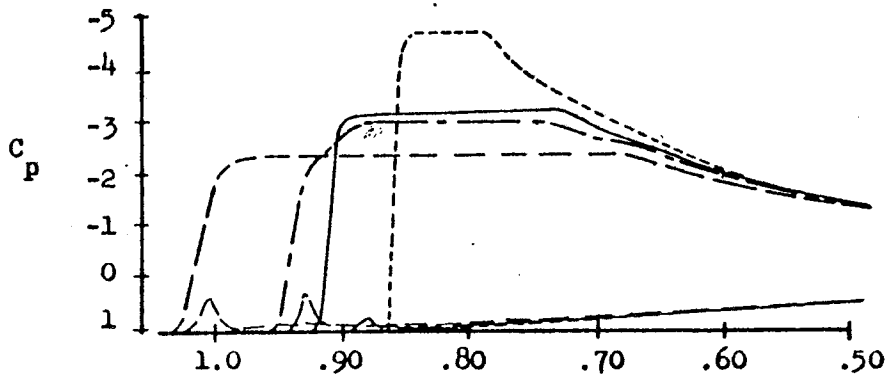

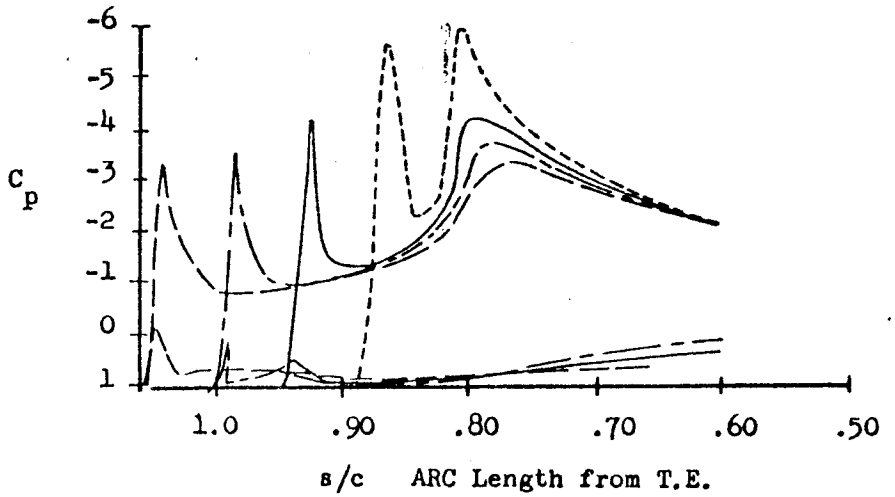

Design Pressure Distribution for Two Families of Sealed LEF's

FIGURE 45

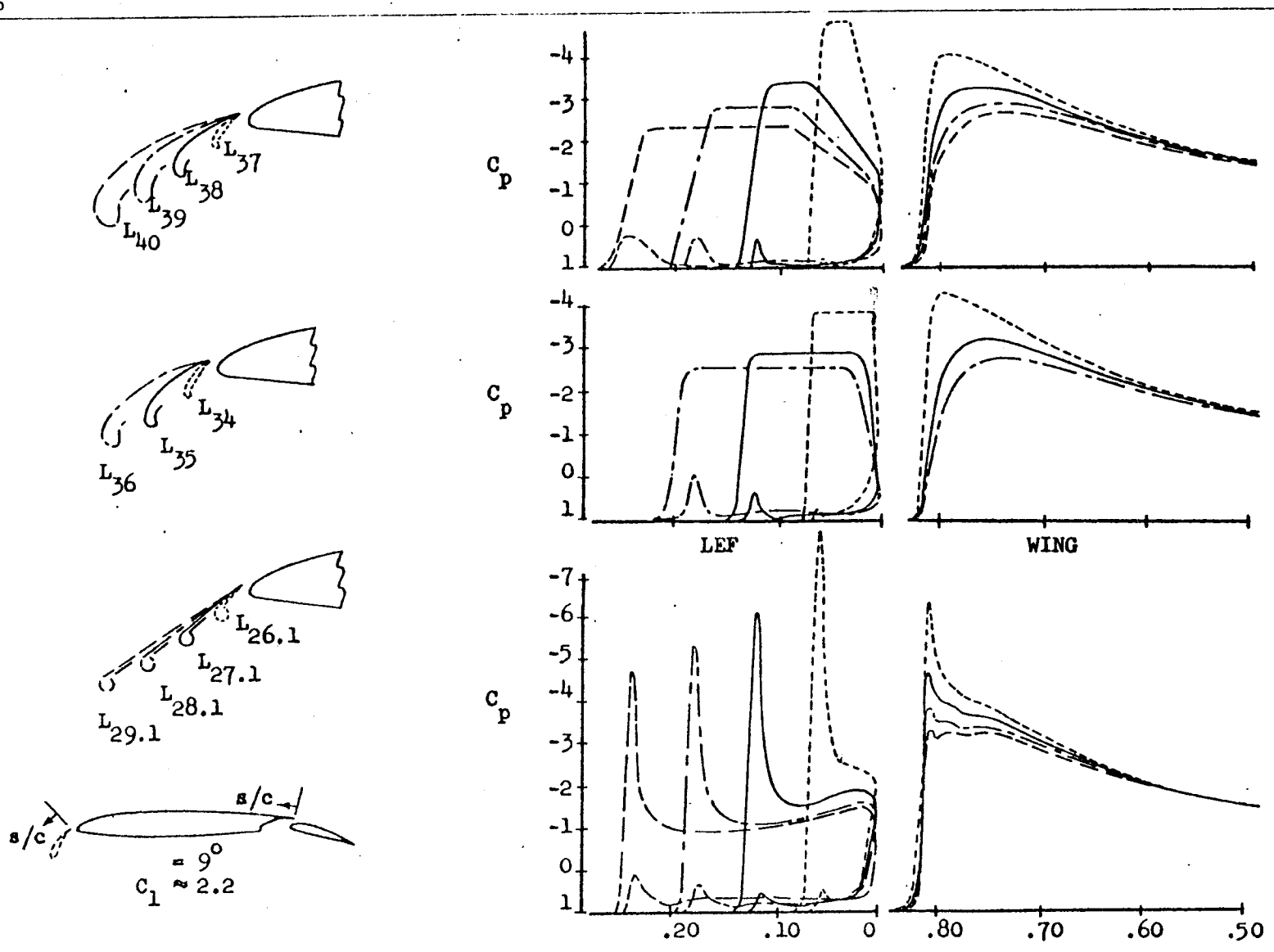

Design Pressure Distribution for Three Families of Slotted LEF's

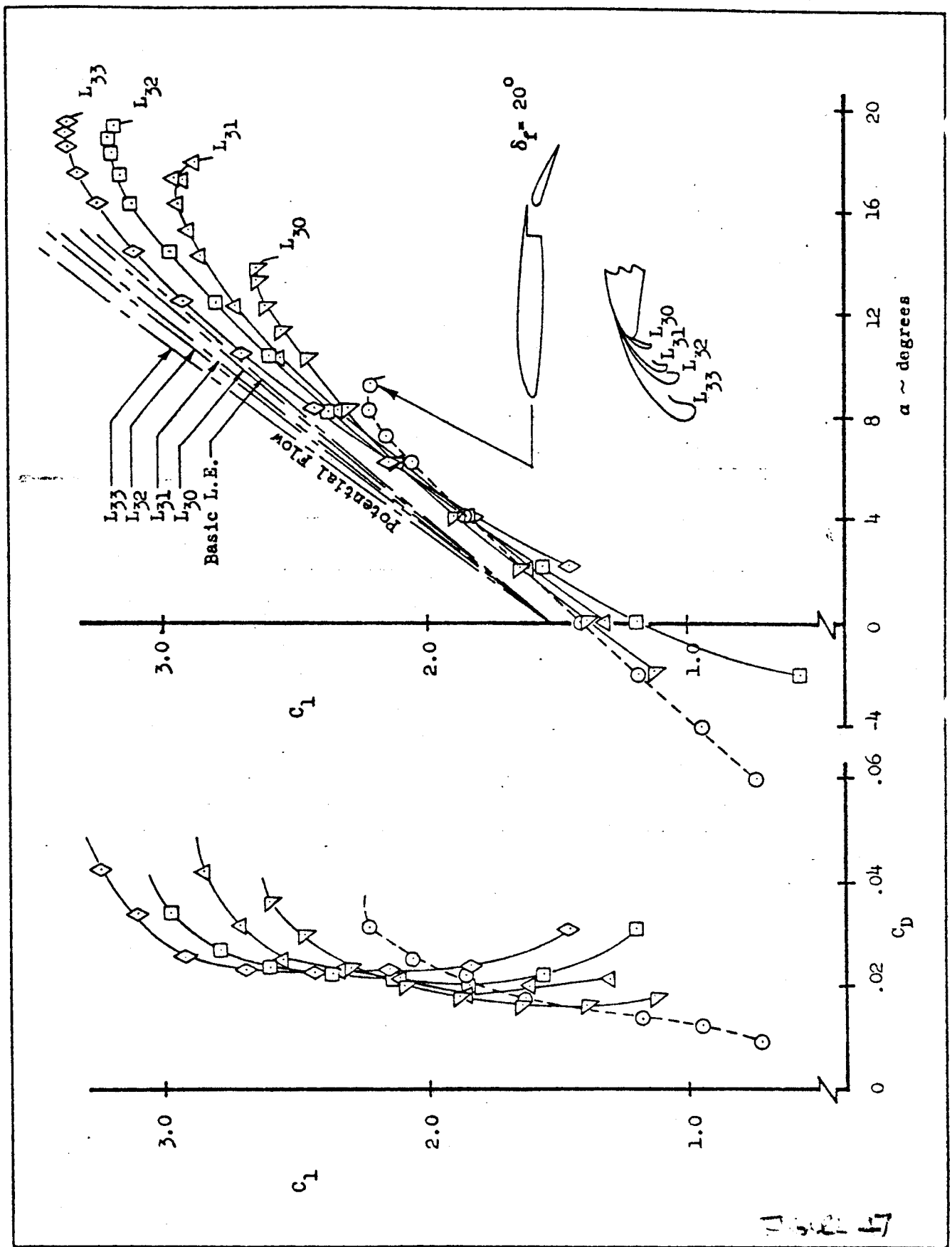

CALC			REVISED	DATE	
CHECK					
APR					
APR					

THE BOEING COMPANY

PAGE D3.64

AD 461 C-R4

K-E ALBANENE 1951

142

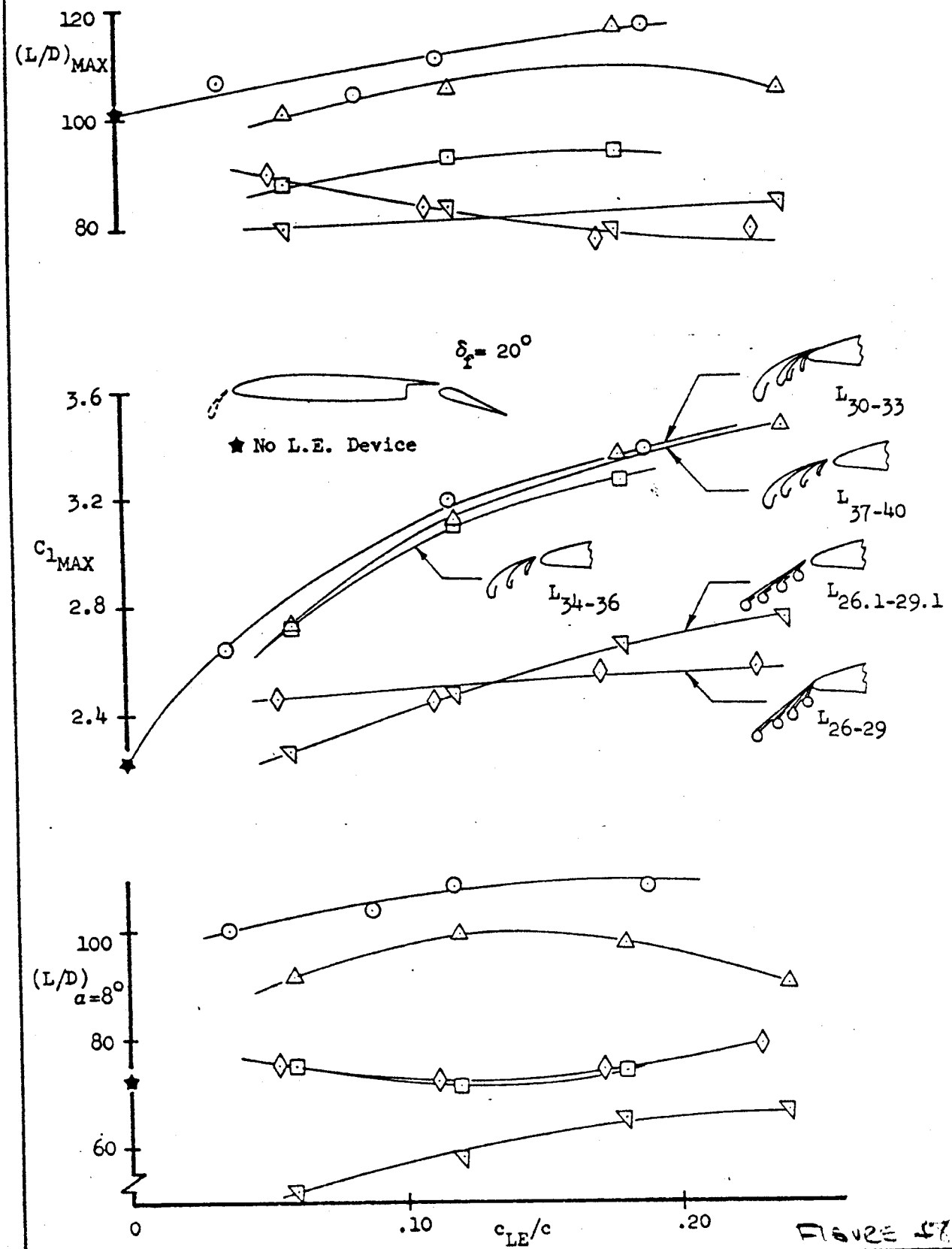

FIGURE 57

CALC			REVISED	DATE	EFFECT OF LEADING EDGE FLAP CHORD	
CHECK						
APR						
APR					THE BOEING COMPANY	PAGE D3.65

TD 441 C-R4

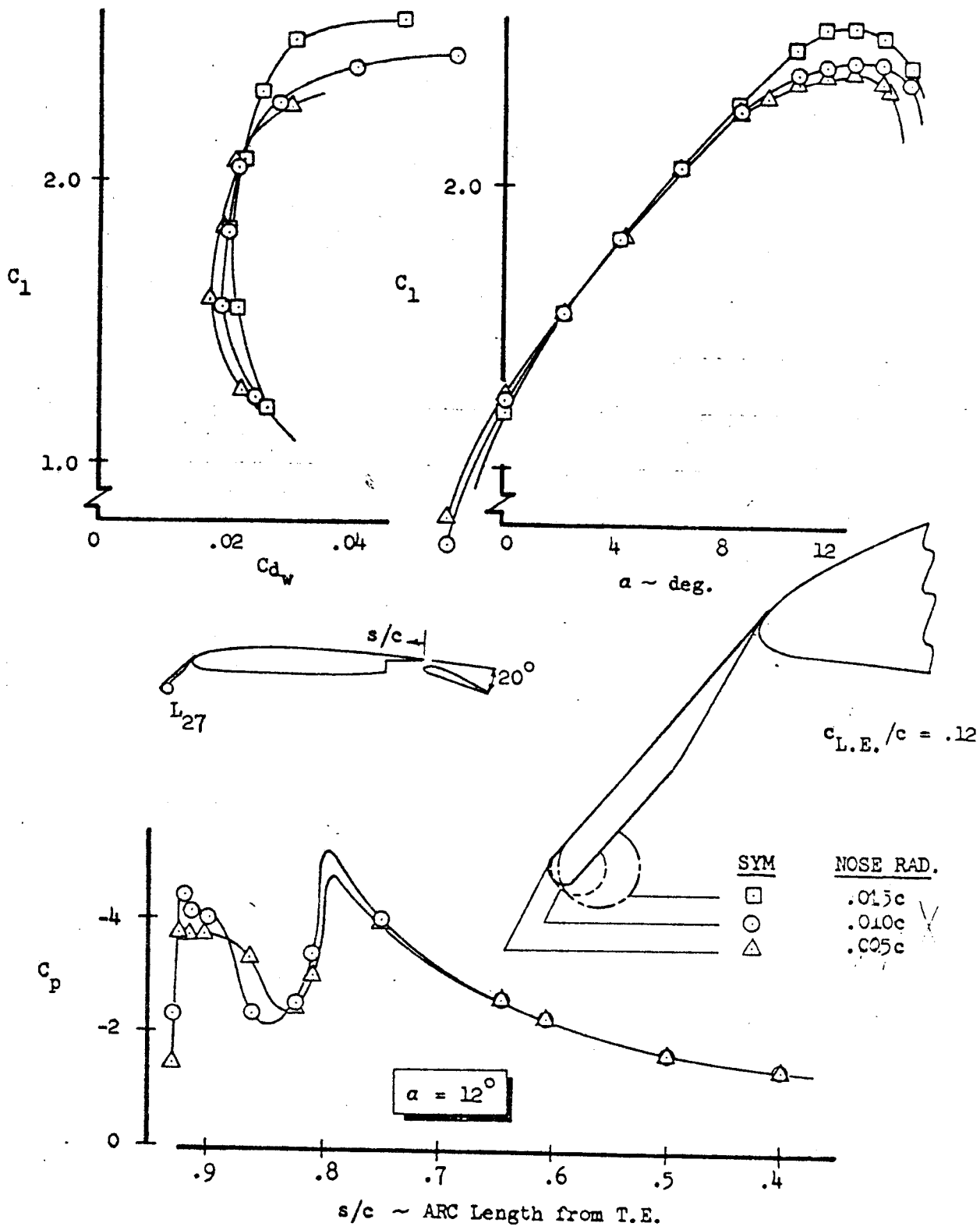

Figure 49

CALC			REVISED	DATE	EFFECT OF L_{27} NOSE RADIUS
CHECK					
APR					
APR					
					THE BOEING COMPANY

PAGE D3.66

AD 461 C-R4

K·E ALBANENE 1961 TRACING PAPER

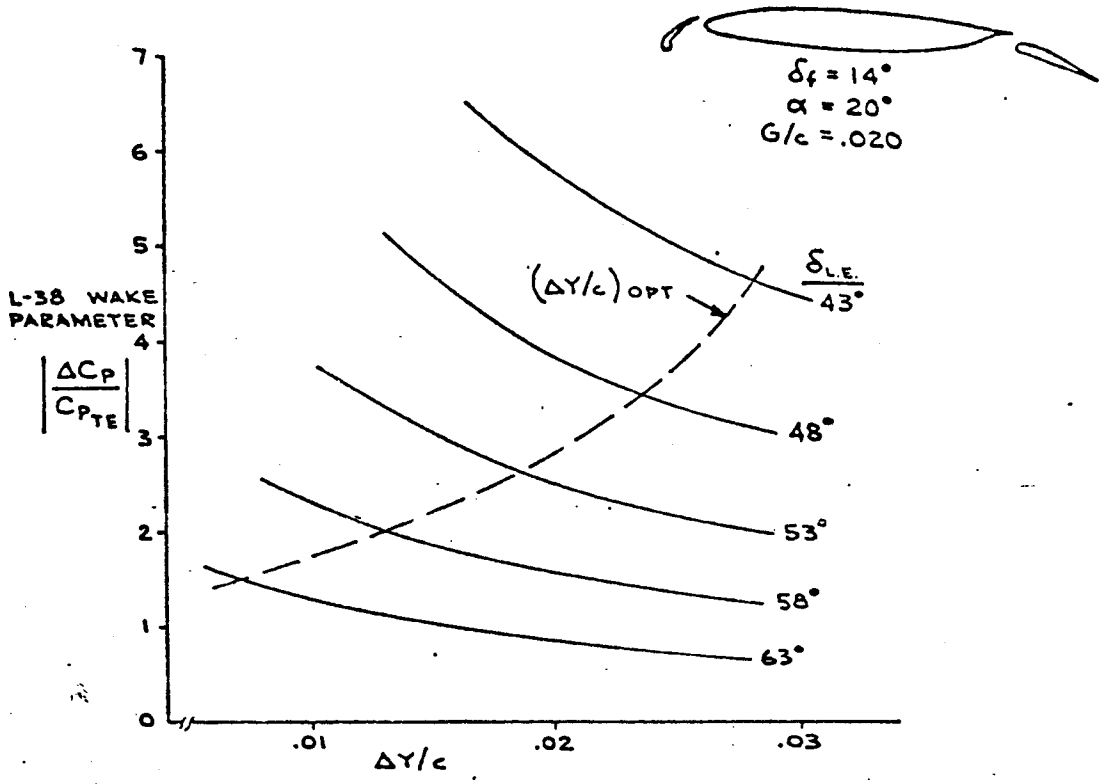

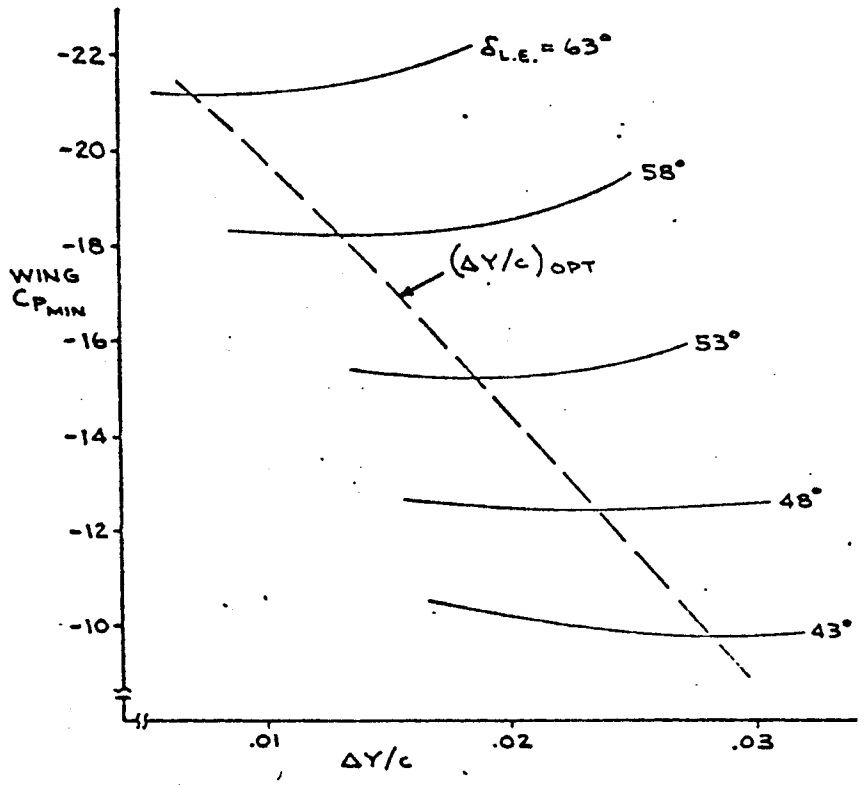

FIGURE 50

ENGR.	WANG		REVISED	DATE	VARIATION OF L-38 WAKE PARAMETER AND WING $C_{P_{MIN}}$ WITH $\Delta Y/c$ IN POTENTIAL FLOW	
CHECK						
APR						
APR					BOEING	P3. 67

D1 4100 5320 REV. 8/71

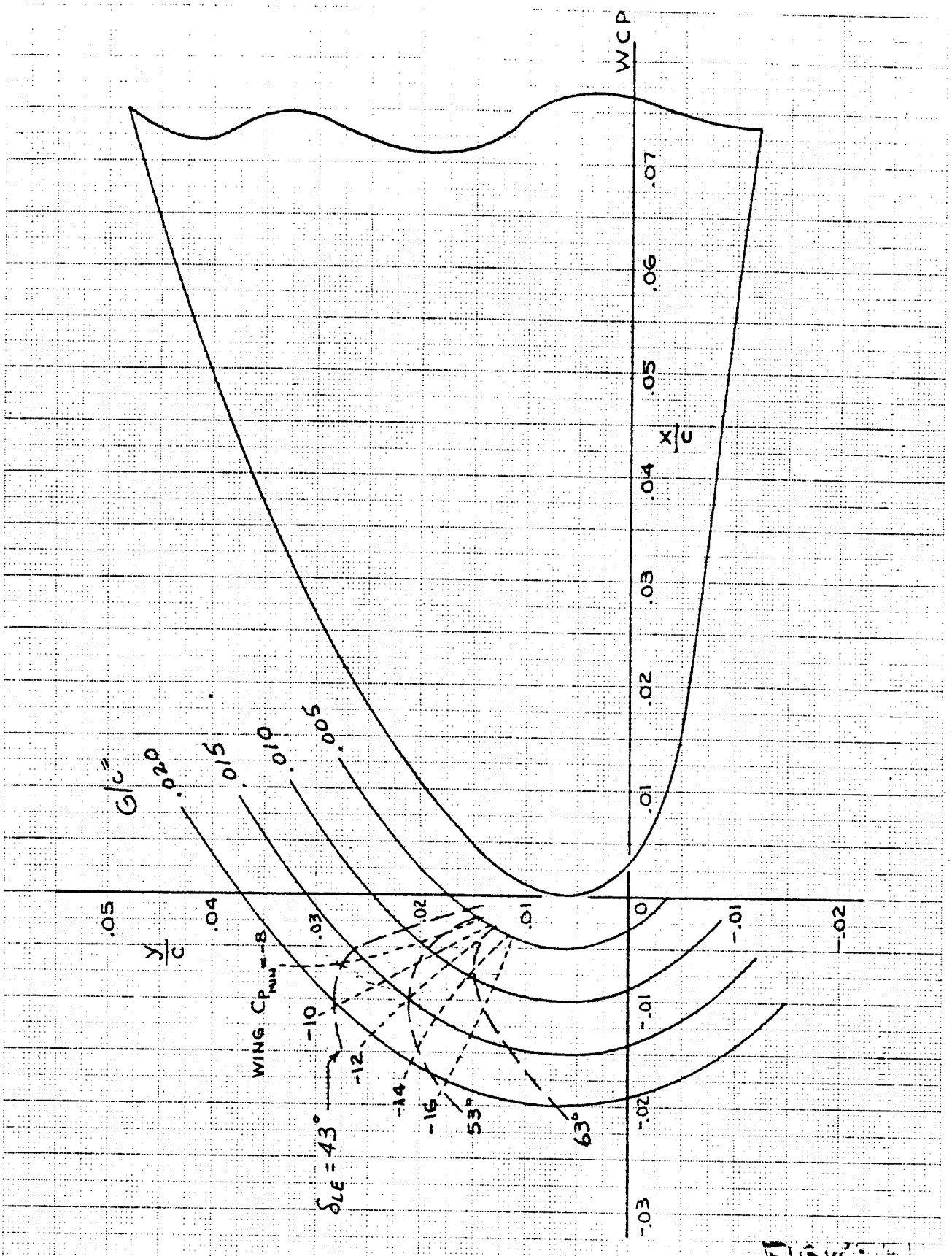

CALC			REVISED	DATE	L-38 T. E. LOCATIONS AT $(\Delta y/c)_{OPT.}$
CHECK					
APR					
APR					THE BOEING COMPANY
					PAGE D3.68

TD 461 D

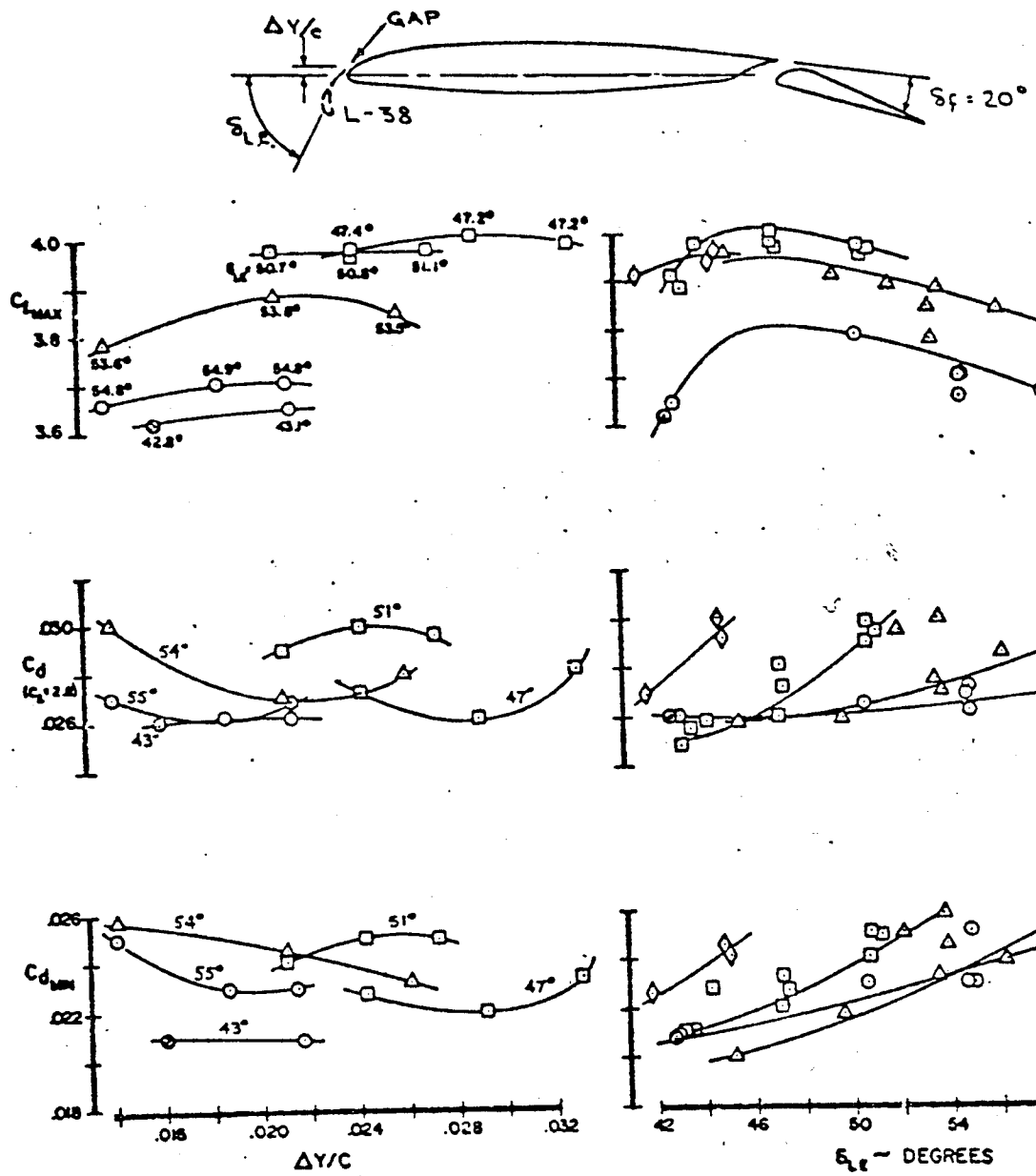

FIGURE 52

SUMMARY OF RESULTS FROM SLOTTED L.E. FLAP OPTIMIZATI

P3.69

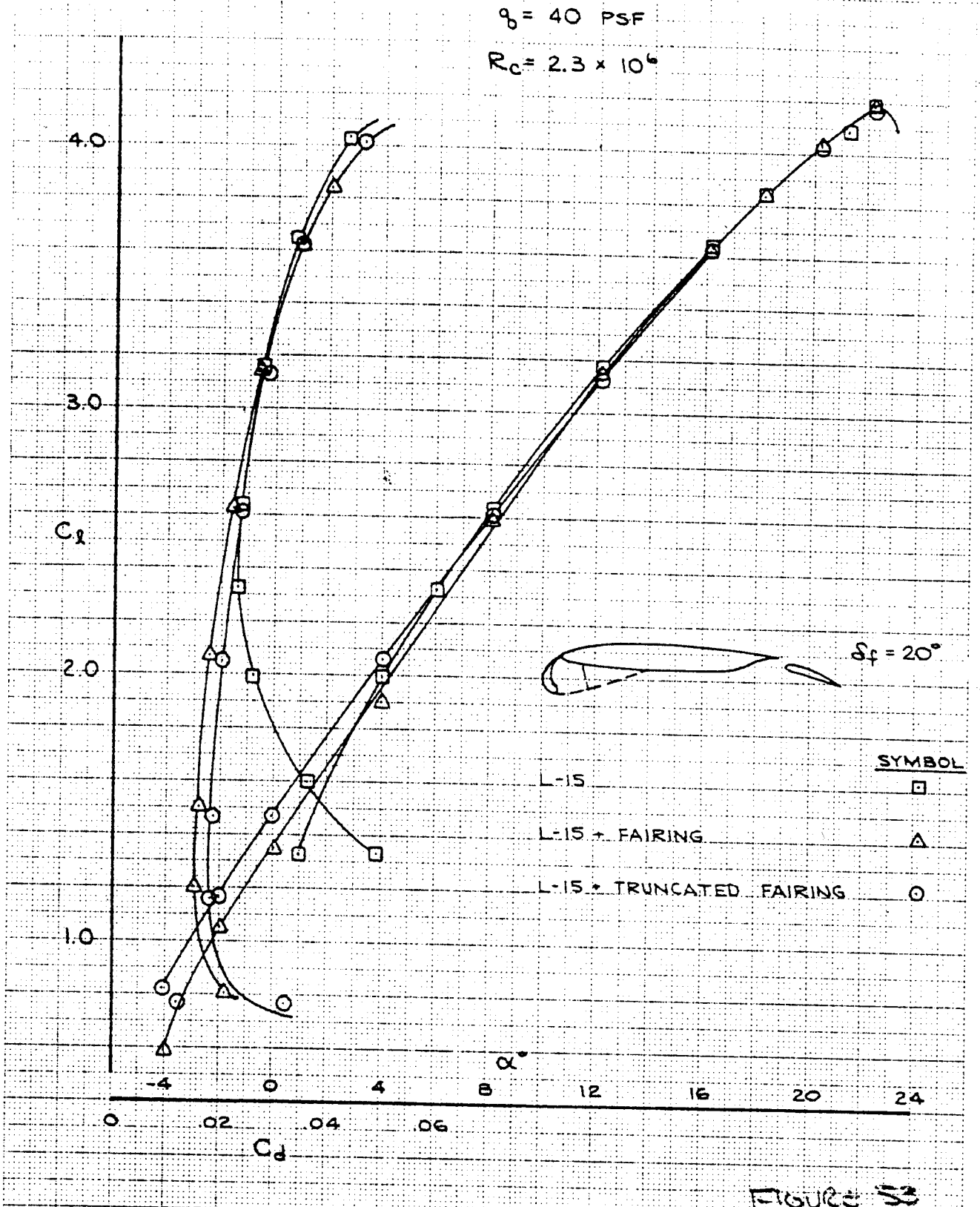

FIGURE 52

CALC	WANG		REVISED	DATE	EFFECTS OF L-15 LOWER SURFACE FAIRING
CHECK					
APR					
APR					
					THE BOEING COMPANY

PAGE P3.70

DI 4ICO 3260 ORIG 3/71

K-E ALBANENE 105L TRACING PAPER

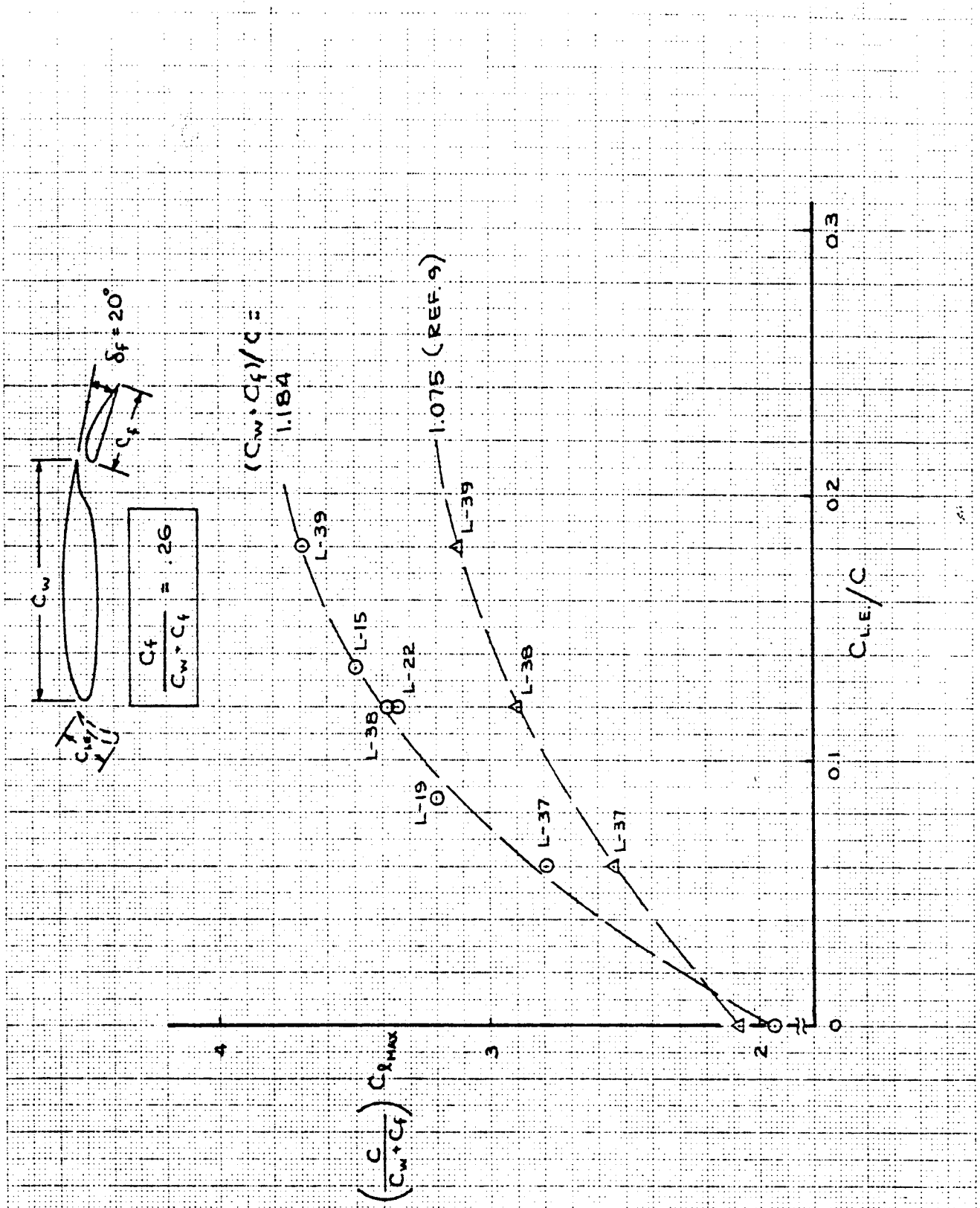

FIGURE 54

CALC	Wang	7/70	REVISED	DATE	MAXIMUM LIFT COMPARISON
CHECK			Wang	7/72	
APR					
APR					THE BOEING COMPANY
					PAGE D3.71

D1 4100 3200 ORIG 3.71

K·E ALBANENE 1981 TRACING PAPER

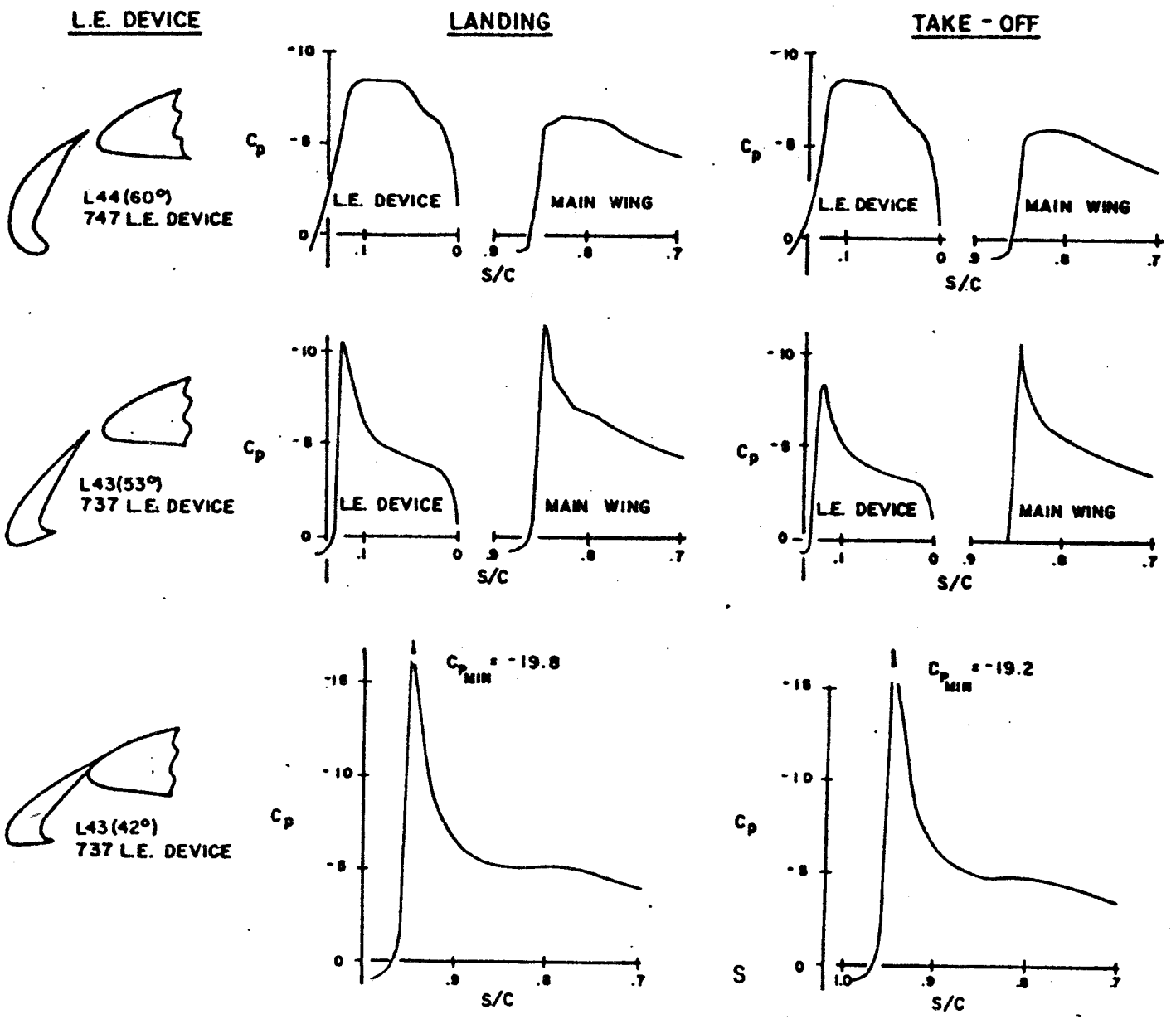

LEADING EDGE THEORETICAL PRESSURE DISTRIBUTIONS NEAR MAXIMUM LIFT CONDITIONS
~ 737/747 DEVICES

Figure 55

P3.72

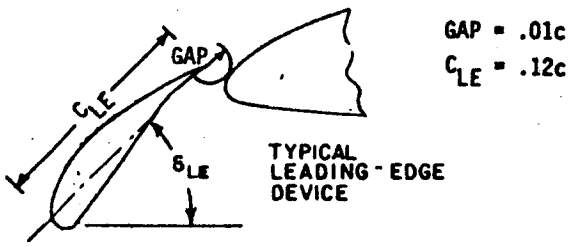

GAP = .01c
C_{LE} = .12c

LANDING CONFIGURATION

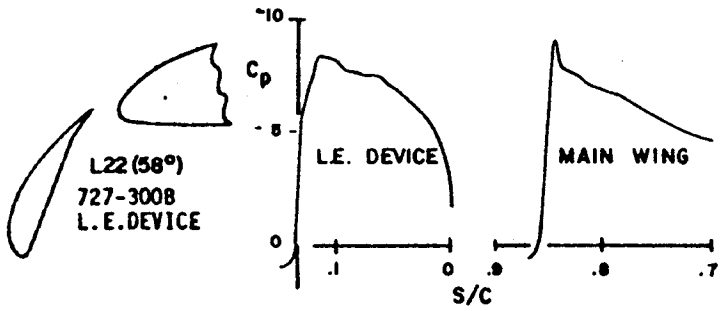

TAKE-OFF CONFIGURATION

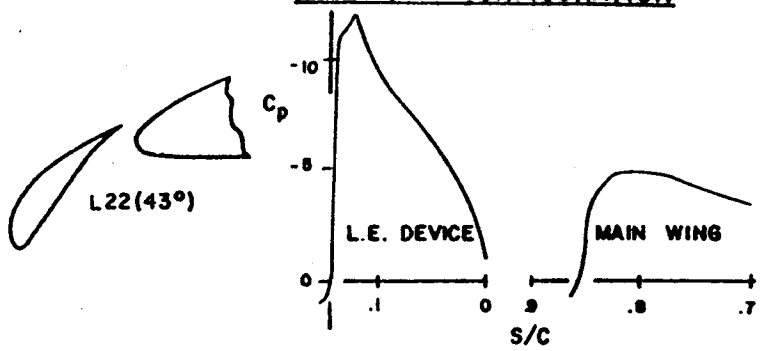

TAKE-OFF CONFIGURATION

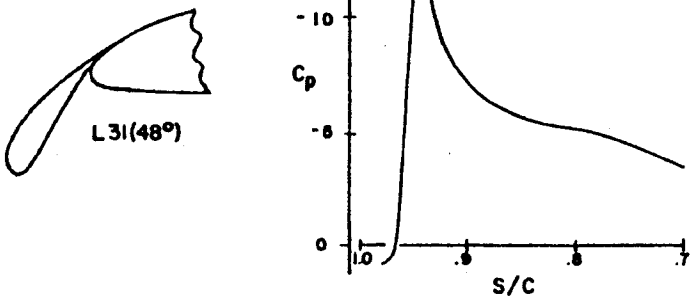

TAKE-OFF CONFIGURATION

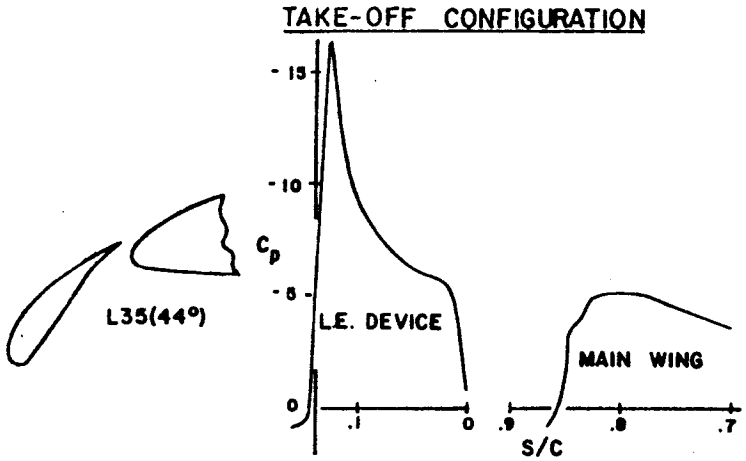

FIGURE 23

LEADING EDGE THEORETICAL PRESSURE DISTRIBUTIONS NEAR MAXIMUM LIFT CONDITIONS
~ RESEARCH DEVICES

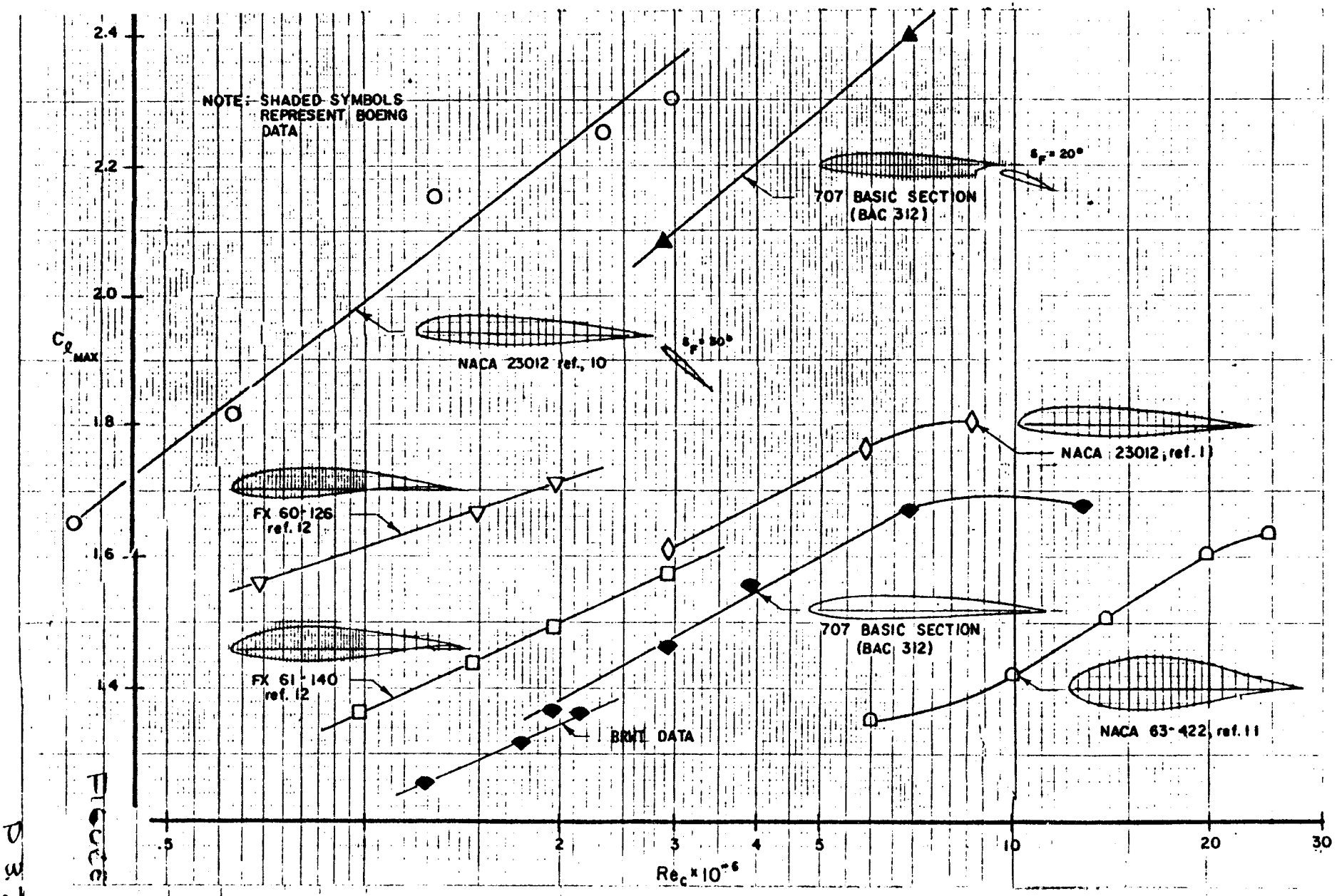

COMPARISON OF BOEING DATA WITH PUBLISHED DATA (NO L.E. DEVICE)

Page 74

153

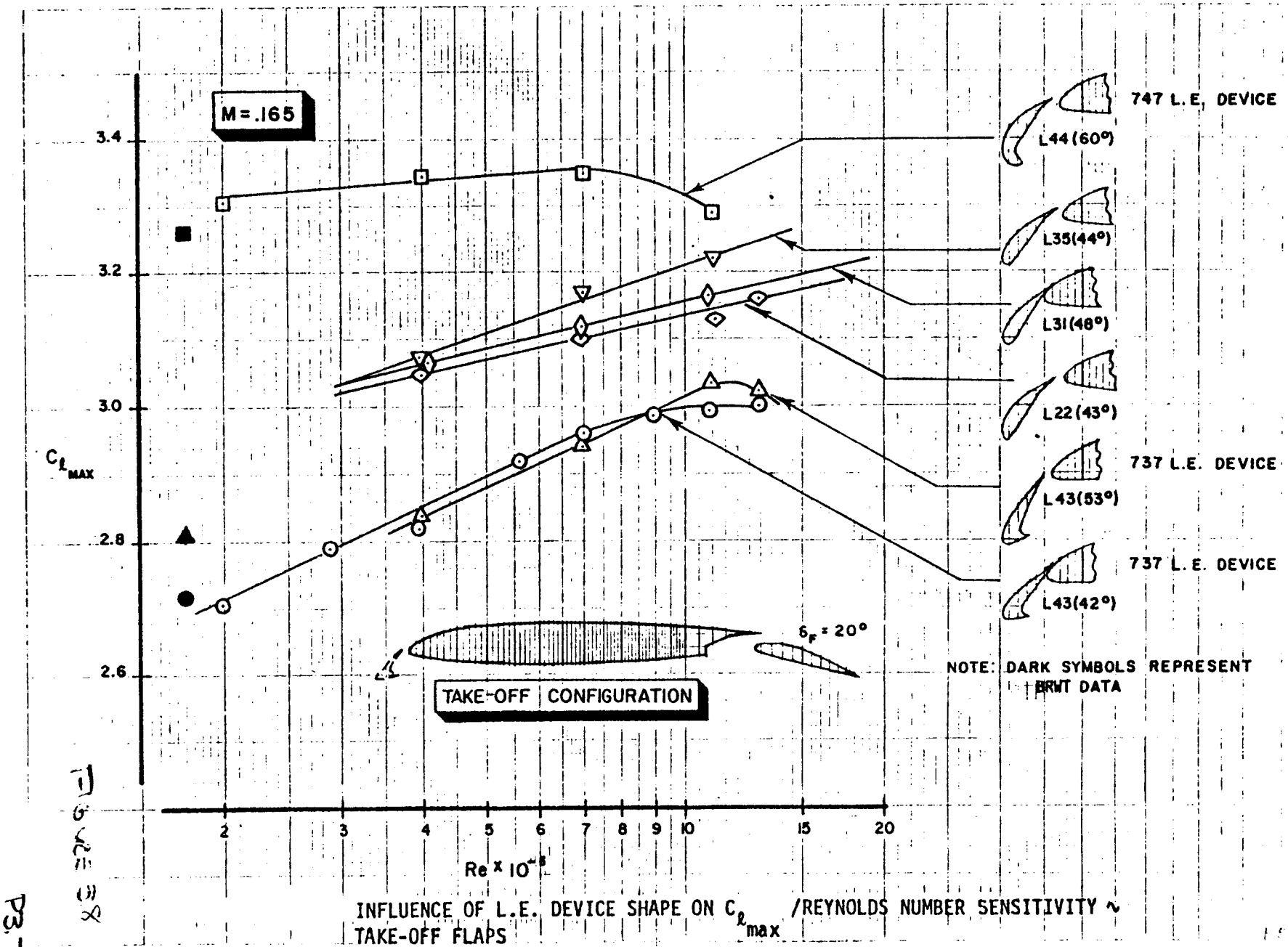

INFLUENCE OF L.E. DEVICE SHAPE ON $C_{\ell_{max}}$ /REYNOLDS NUMBER SENSITIVITY ~
TAKE-OFF FLAPS

ST 34

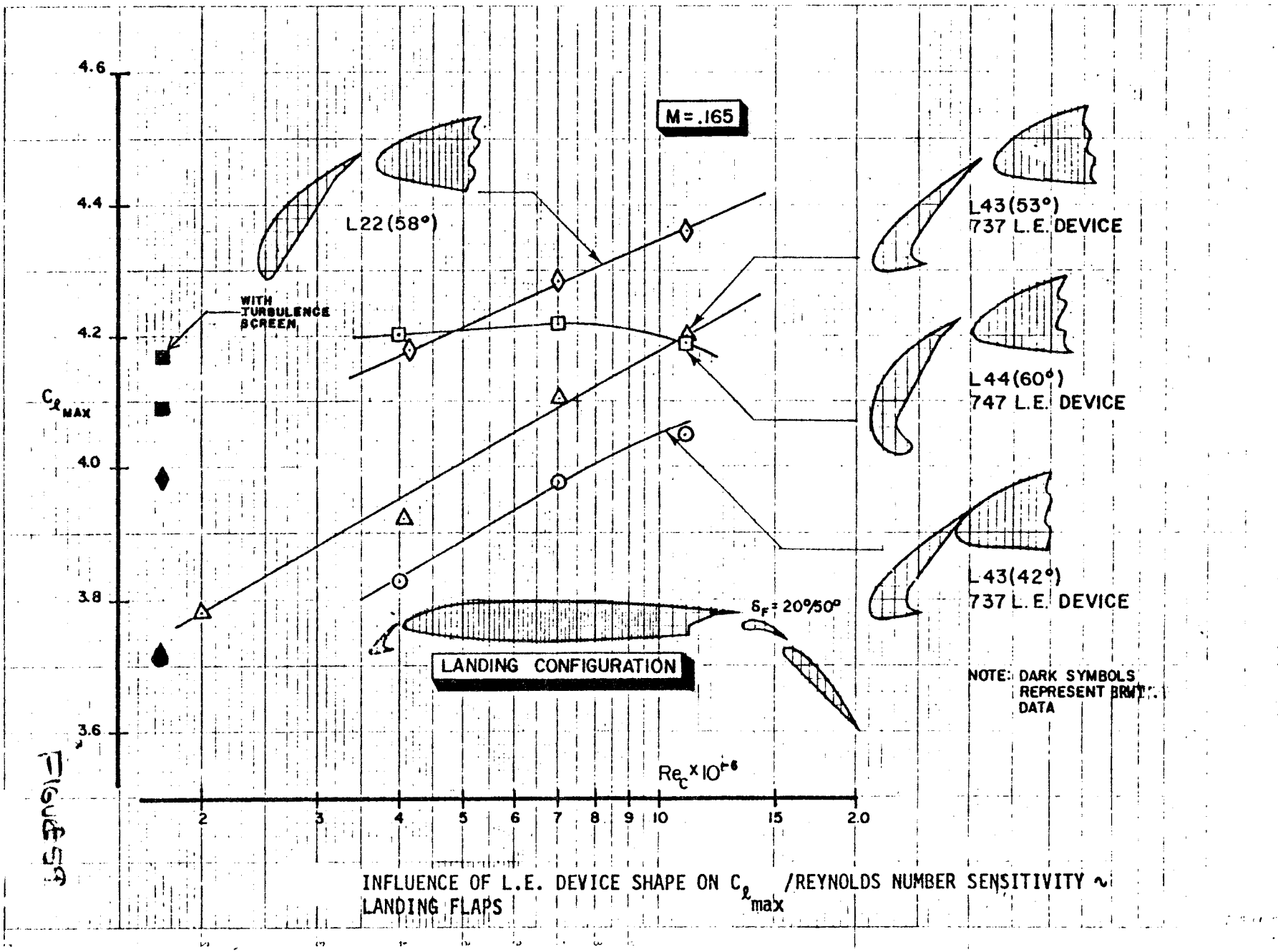

Figure 59

INFLUENCE OF L.E. DEVICE SHAPE ON $C_{\ell_{max}}$ /REYNOLDS NUMBER SENSITIVITY ~ LANDING FLAPS

p. 3.76

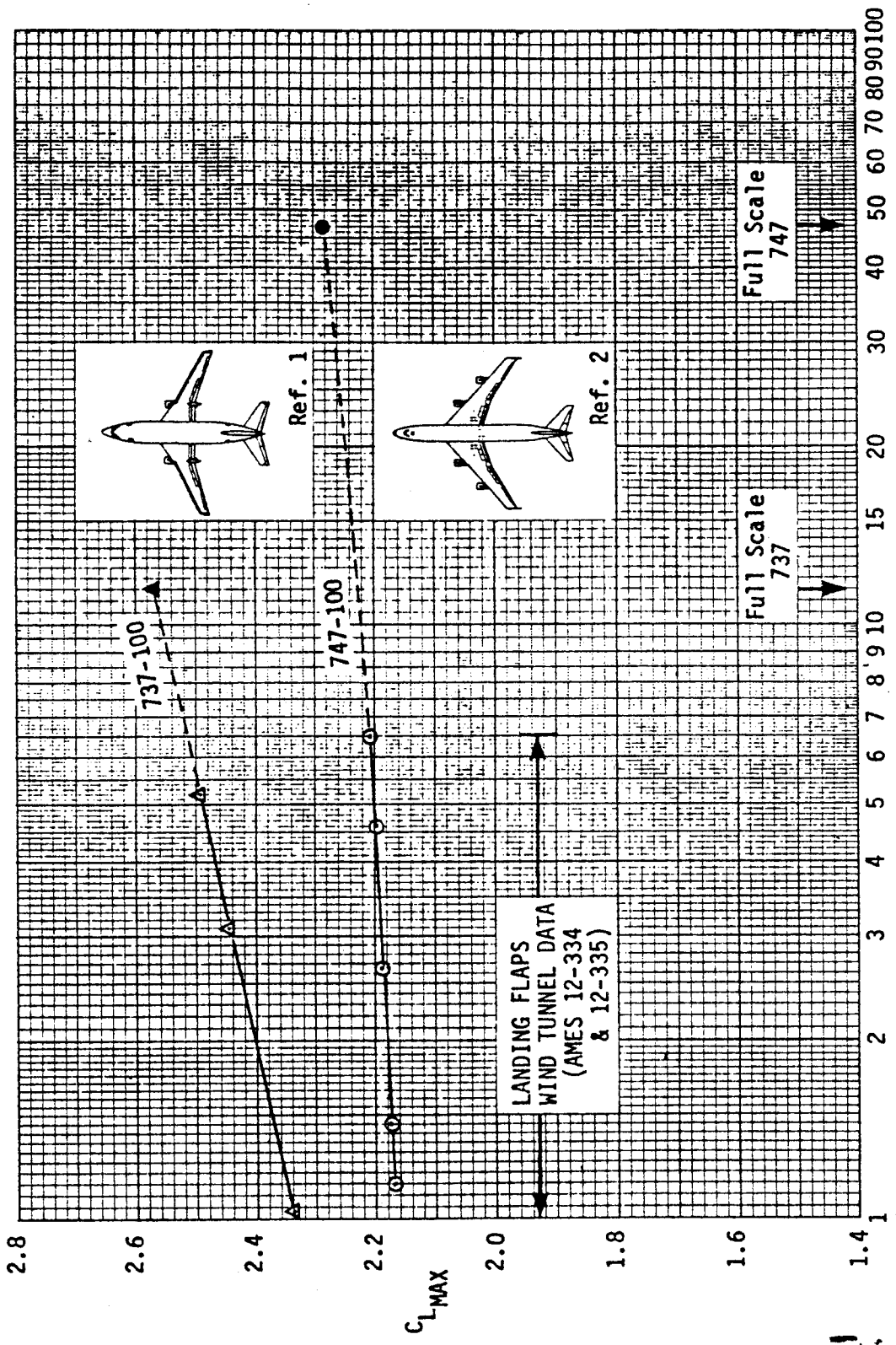

FIGURE 30

ENGR.			REVISED	DATE	REYNOLDS NUMBER EFFECT ON 737 & 747 MAXIMUM LIFT
CHECK					
APR					
APR					BOEING
					P 3.77

D1 4100 5300 REV. A/71

J15-047

155

BLOWING BLC CONCEPTS

LEADING-EDGE

MULTI-SLOT BLOWING

BLOWING-KRUEGER FLAP

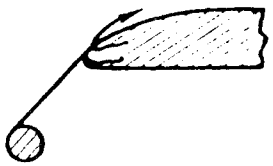

BLOWING-SLOTTED FLAP

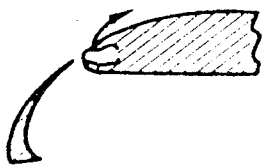

TRAILING-EDGE

SHROUD BLOWING

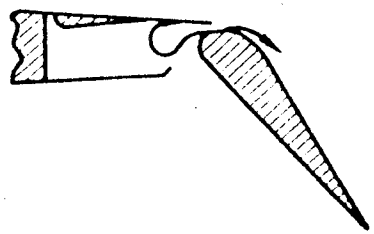

FLAP BLOWING

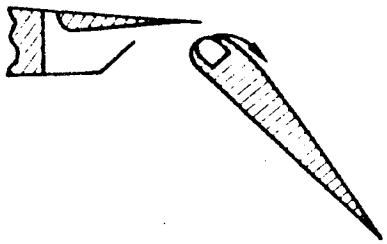

EJECTOR NOZZLE

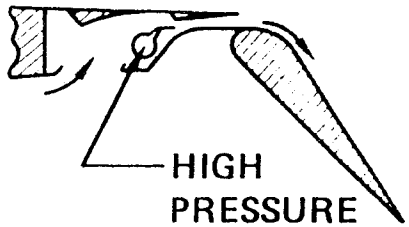

BLOWING BLC PERFORMANCE

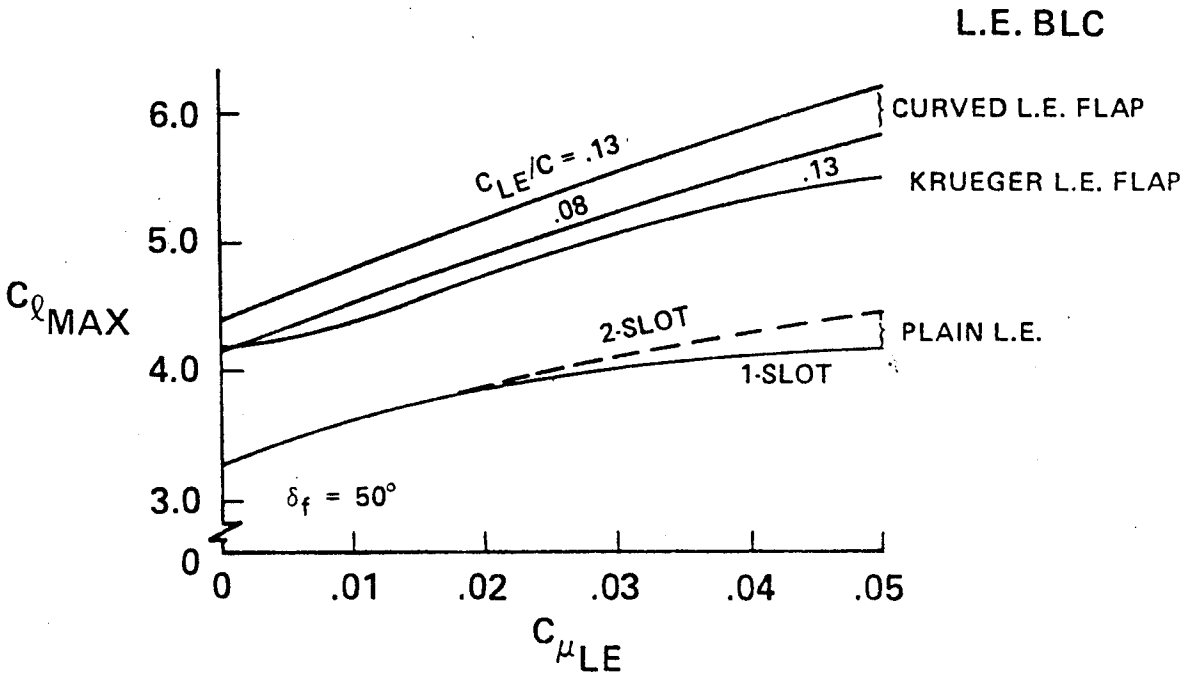

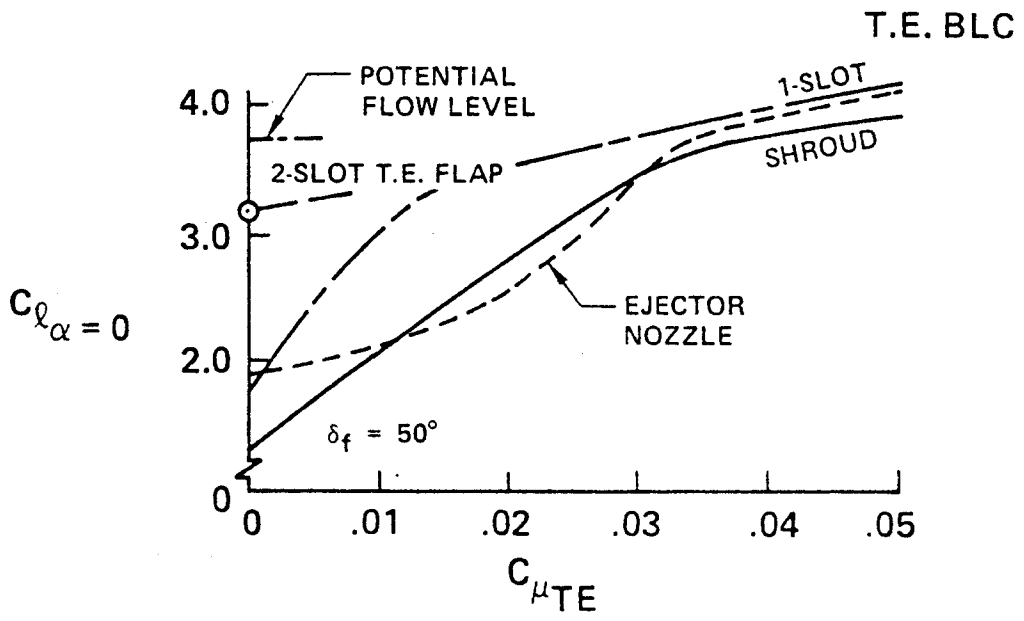

2-D W.T. DATA M = .165

157

FIGURE 62
P3.79

SUCTION BLC CONCEPTS

LEADING-EDGE

AREA SUCTION

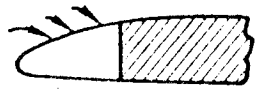

SLOT SUCTION-CURVED FLAP

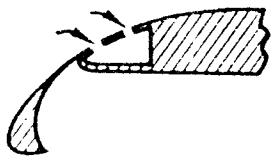

SLOT SUCTION-SLOTTED FLAP

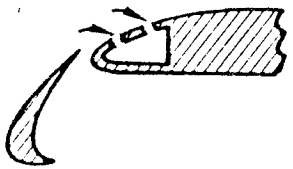

TRAILING-EDGE

AREA SUCTION

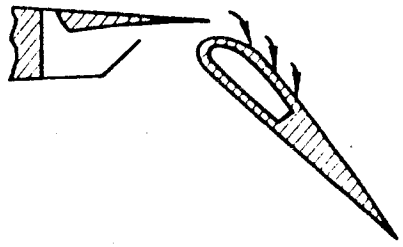

SLOT SUCTION

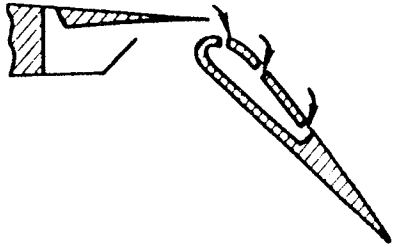

COMBINED SUCTION AND BLOWING

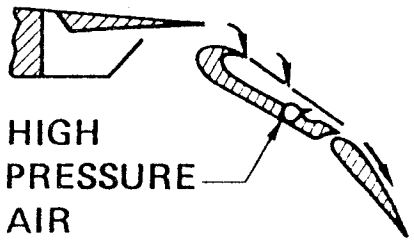

SUCTION BLC PERFORMANCE

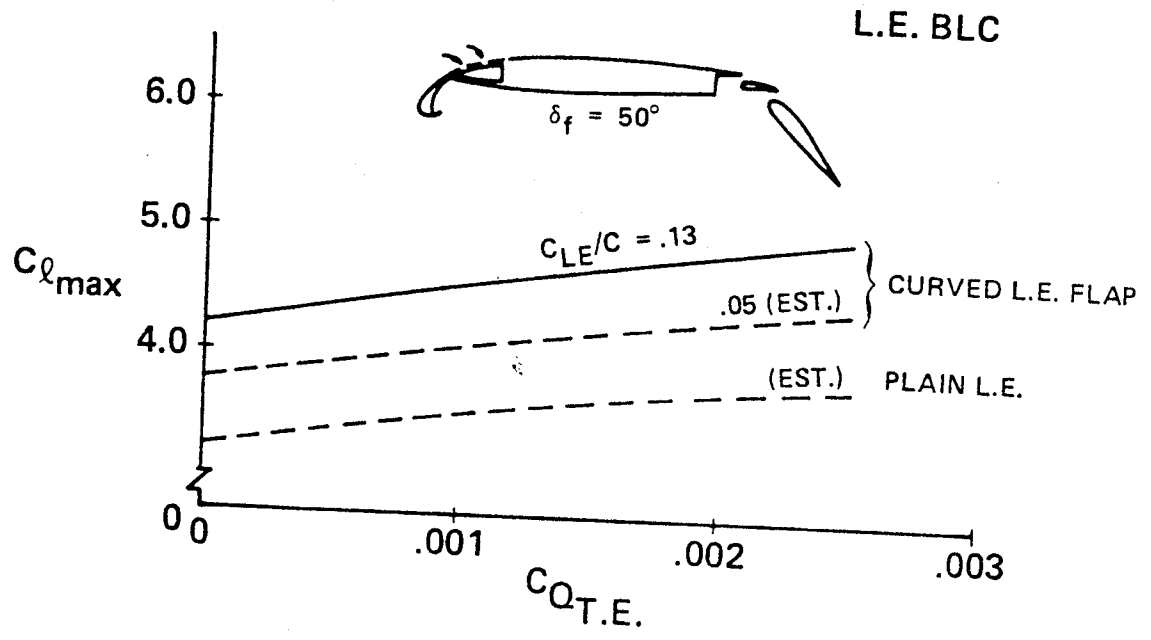

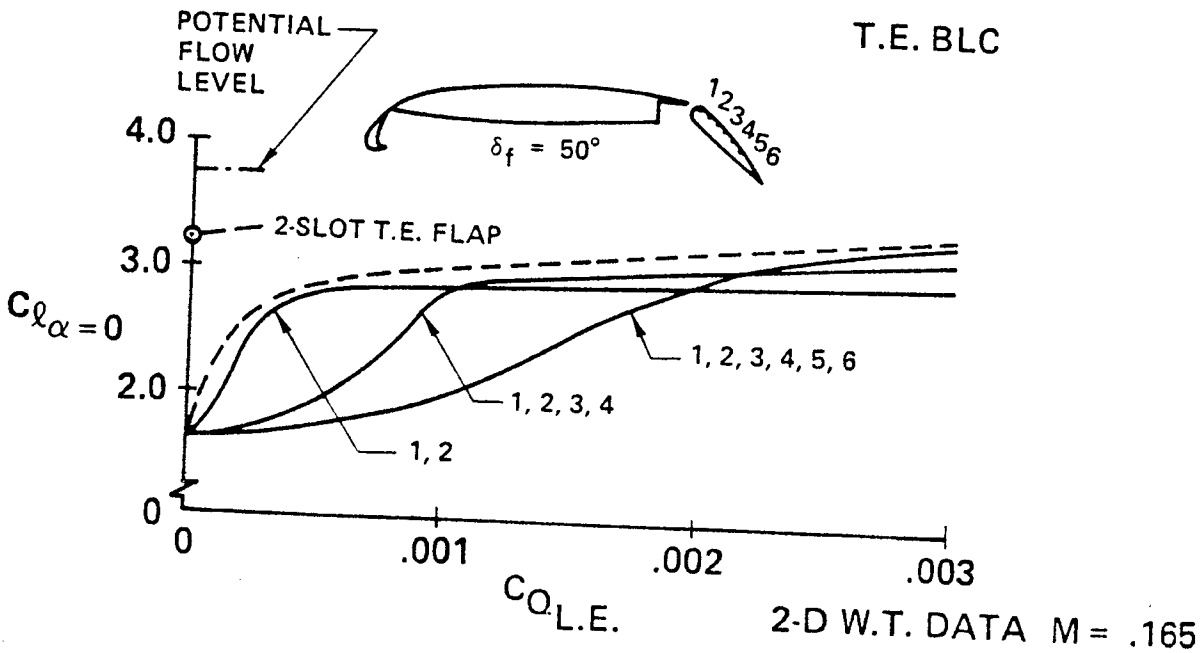

2-D W.T. DATA M = .165

FIGURE 44

P3.81

160

POWERED LIFT CONCEPTS

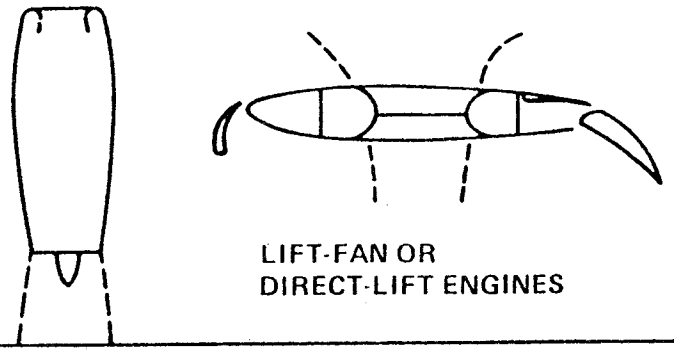

LIFT-FAN OR
DIRECT-LIFT ENGINES

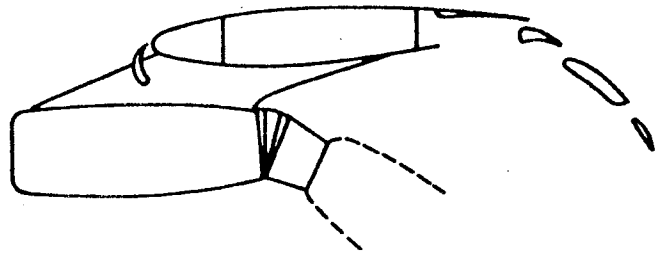

VECTORED THRUST

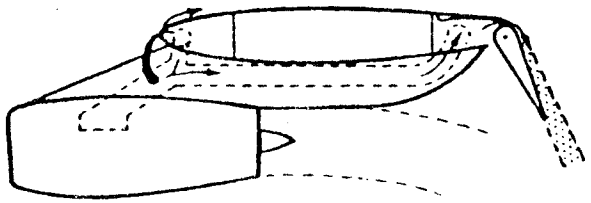

INTERNALLY
BLOWN JET FLAP

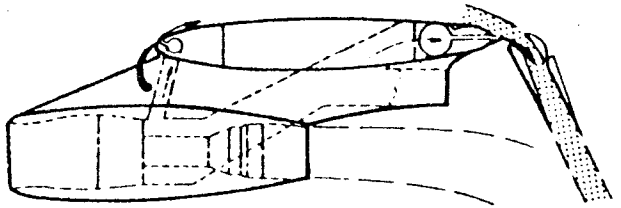

AUGMENTOR WING

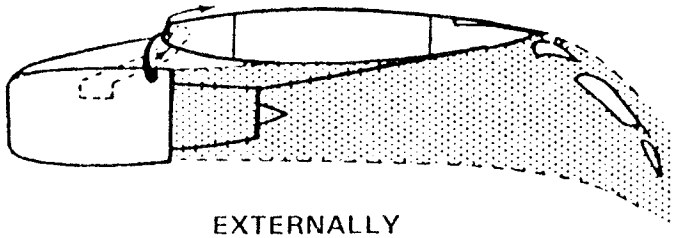

EXTERNALLY
BLOWN JET FLAP

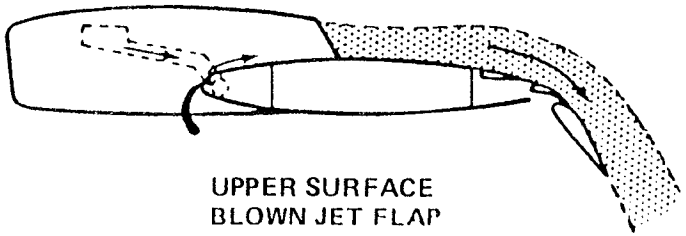

UPPER SURFACE
BLOWN JET FLAP

FIGURE 3.

P3.82

POWERED LIFT POLAR COMPARISON

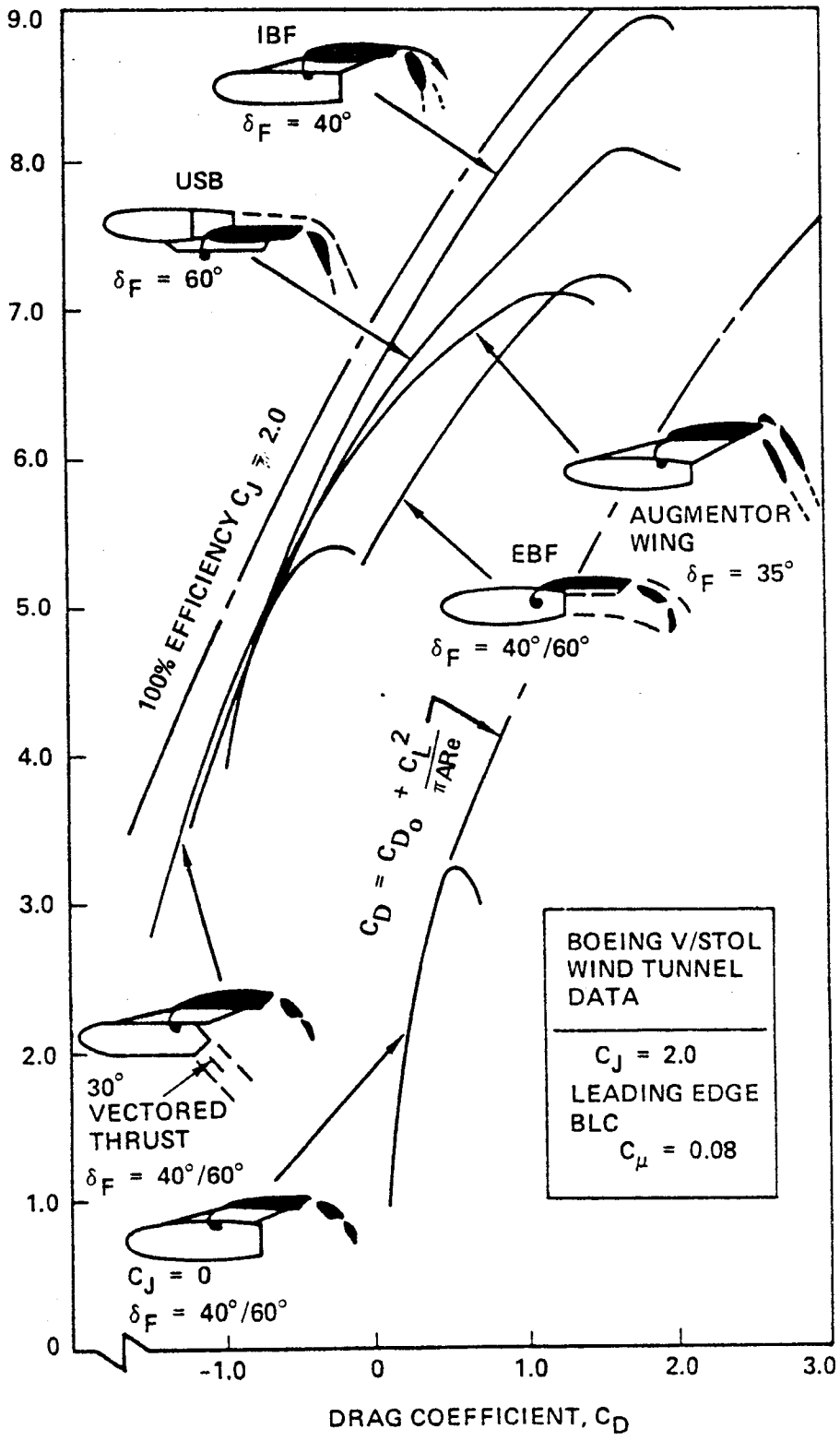

FIGURE 6-1
D3.83

RELATIVE IMPORTANCE OF SEPARATION EFFECTS

ANALYSIS OF GEOMETRY ALONE

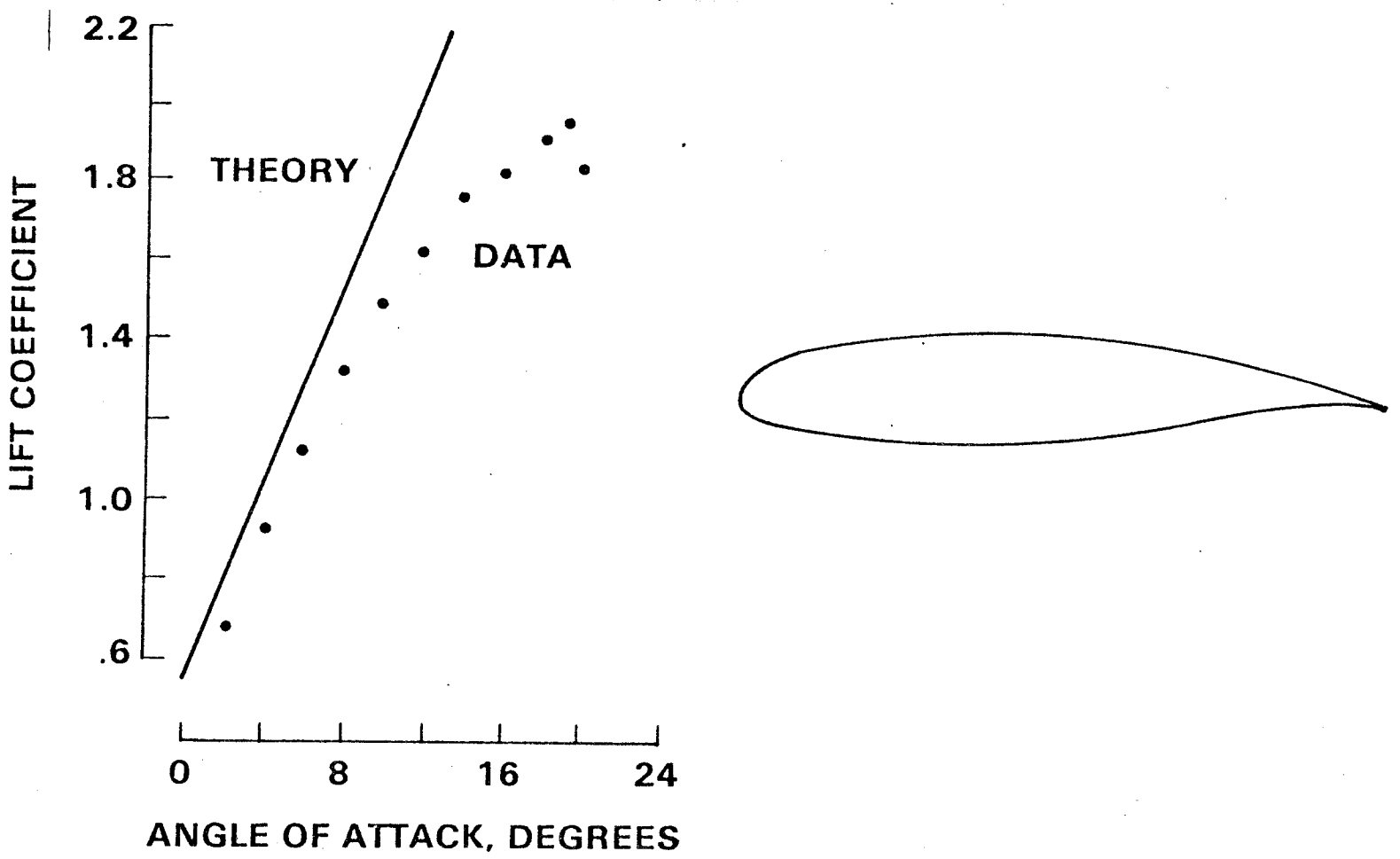

RELATIVE IMPORTANCE OF SEPARATION EFFECTS

ANALYSIS WITH BOUNDARY LAYER MODELED

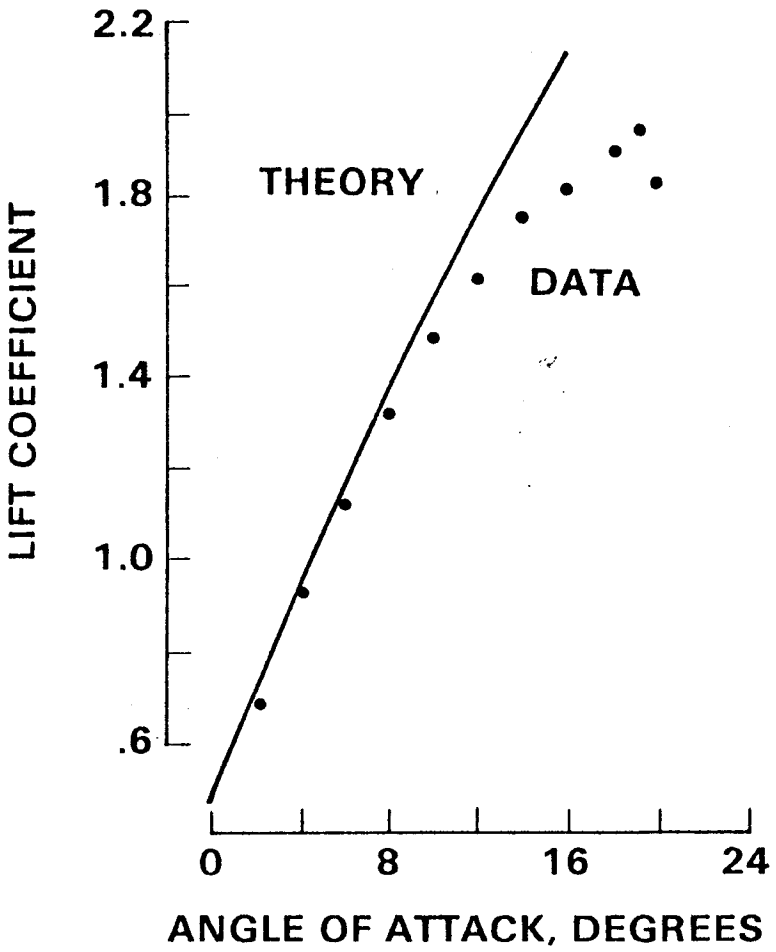

RELATIVE IMPORTANCE OF SEPARATION EFFECTS

ANALYSIS WITH BOUNDARY LAYER AND SEPARATED WAKE MODELED

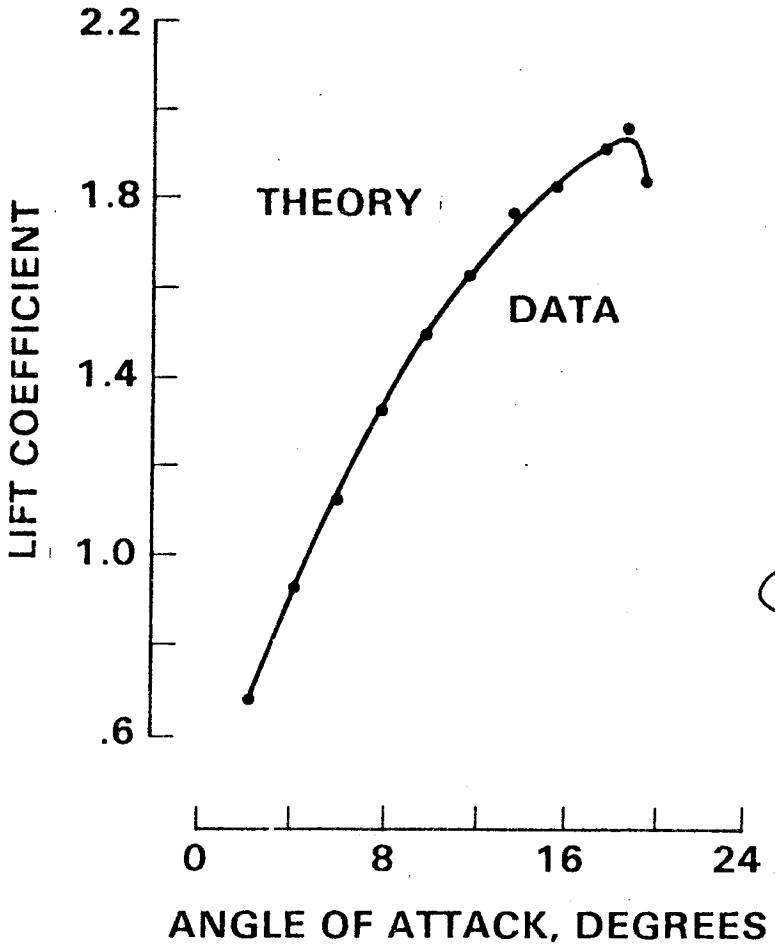

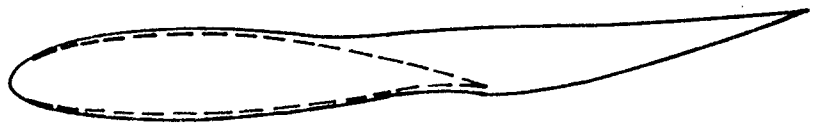

COMPARISON OF EXPERIMENTAL AND THEORETICAL PRESSURE DISTRIBUTIONS

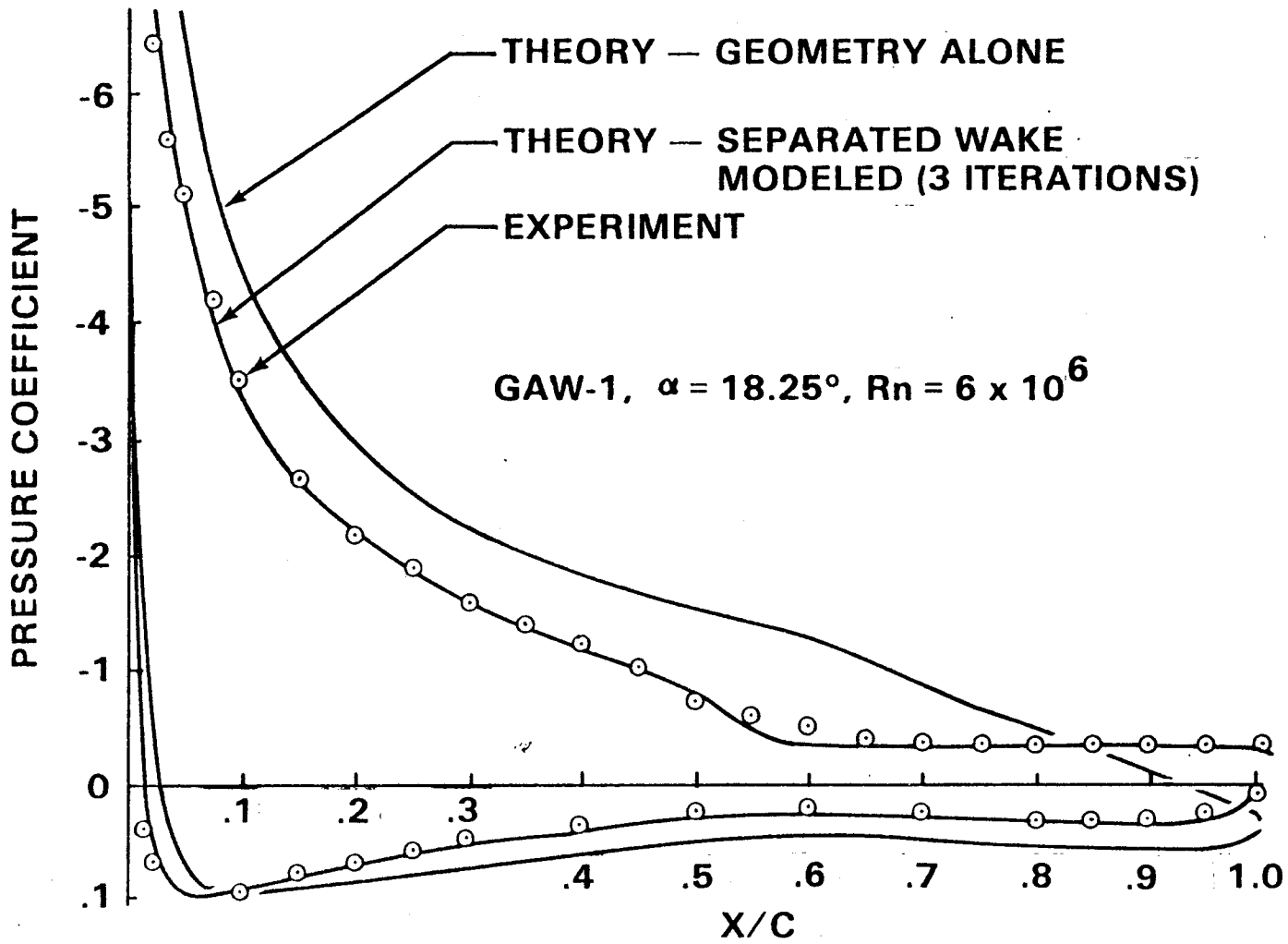

FIGURE 70

D3.87

COMPARISON OF EXPERIMENTAL AND CALCULATED PRESSURE DISTRIBUTIONS ON A PARTIALLY SEPARATED SINGLE ELEMENT AIRFOIL

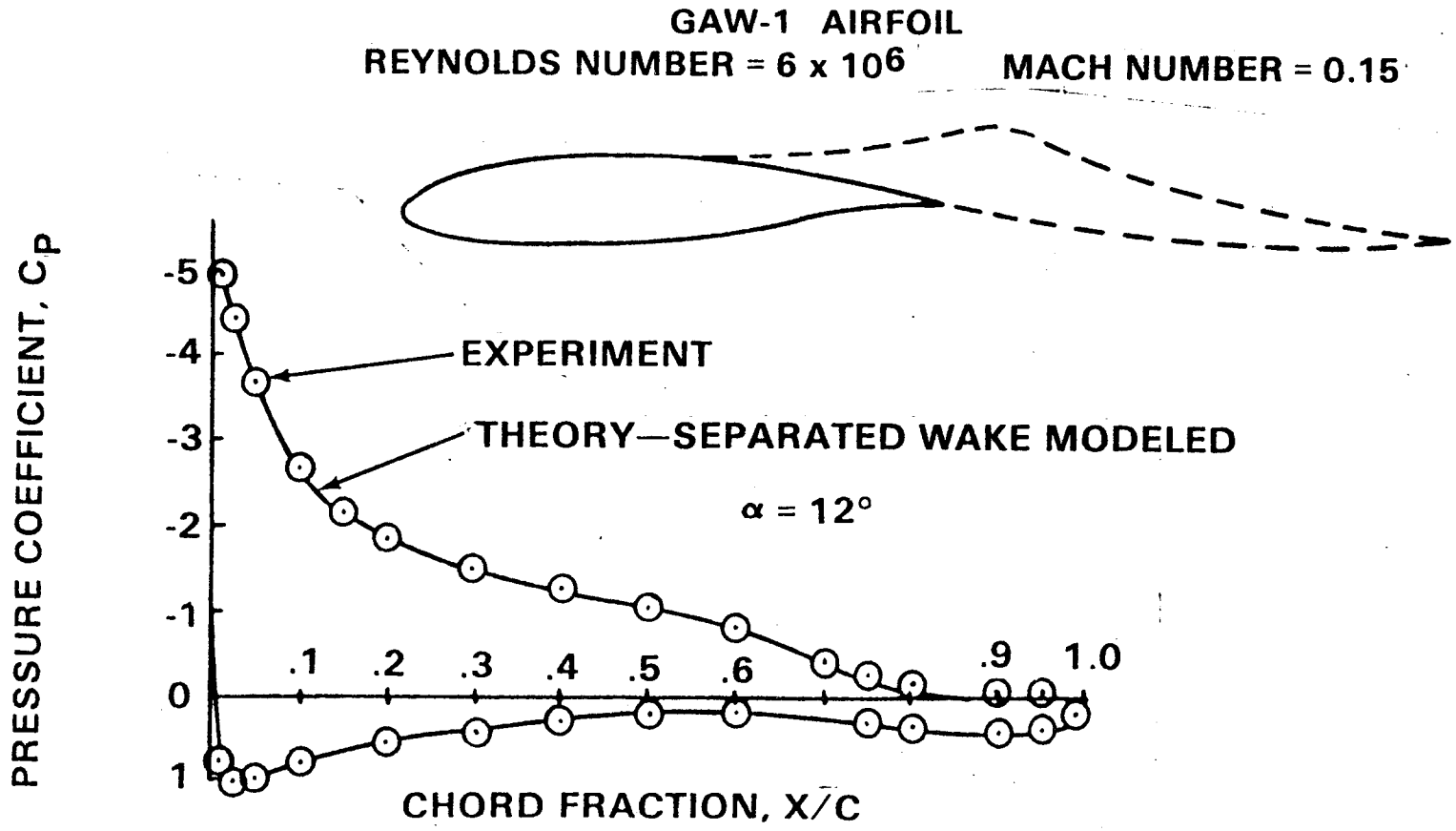

Fig. 28
P3.88

COMPARISON OF EXPERIMENTAL AND CALCULATED PRESSURE DISTRIBUTIONS ON A PARTIALLY SEPARATED SINGLE ELEMENT AIRFOIL

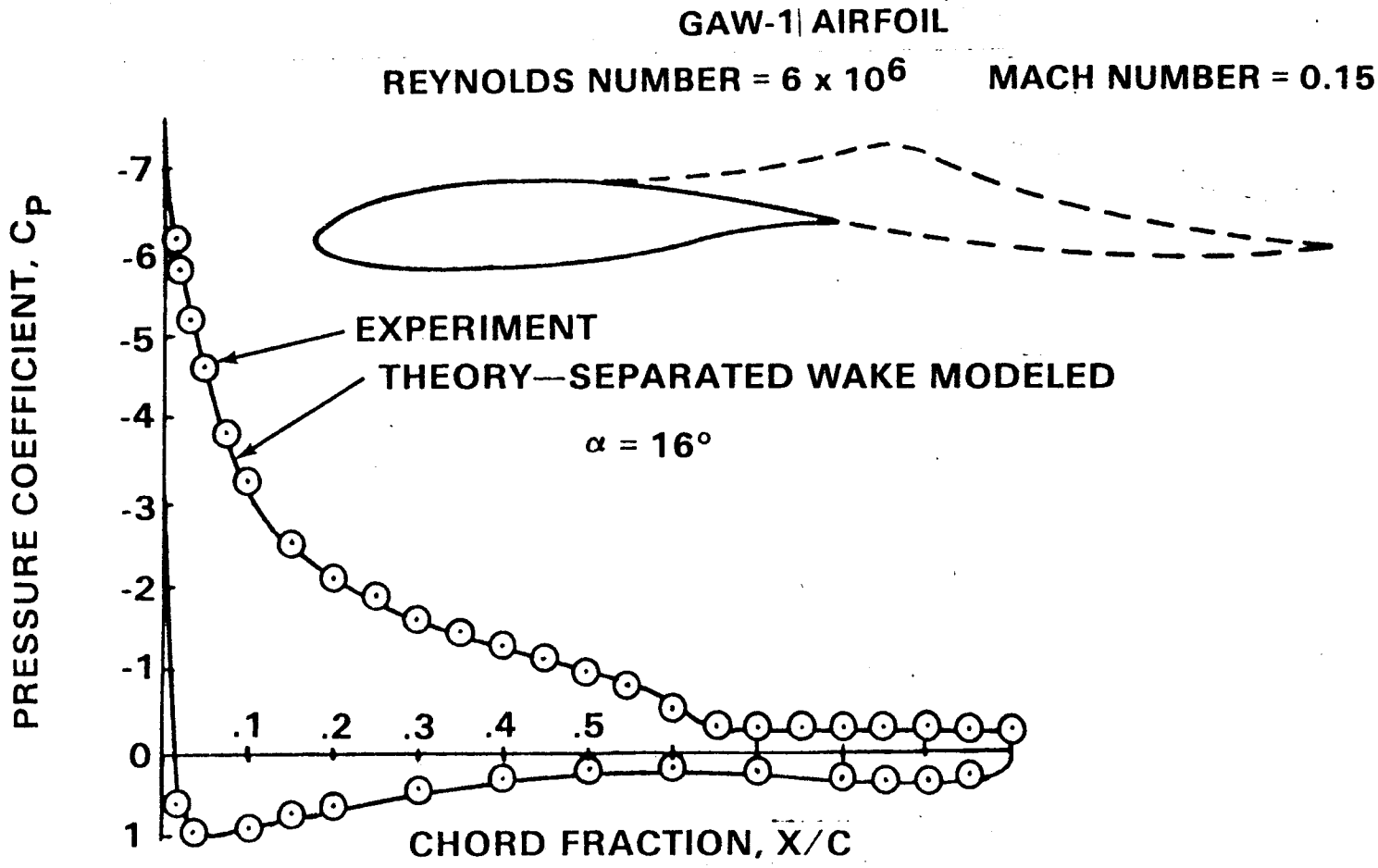

COMPARISON OF EXPERIMENTAL AND CALCULATED PRESSURE DISTRIBUTIONS ON A PARTIALLY SEPARATED SINGLE ELEMENT AIRFOIL

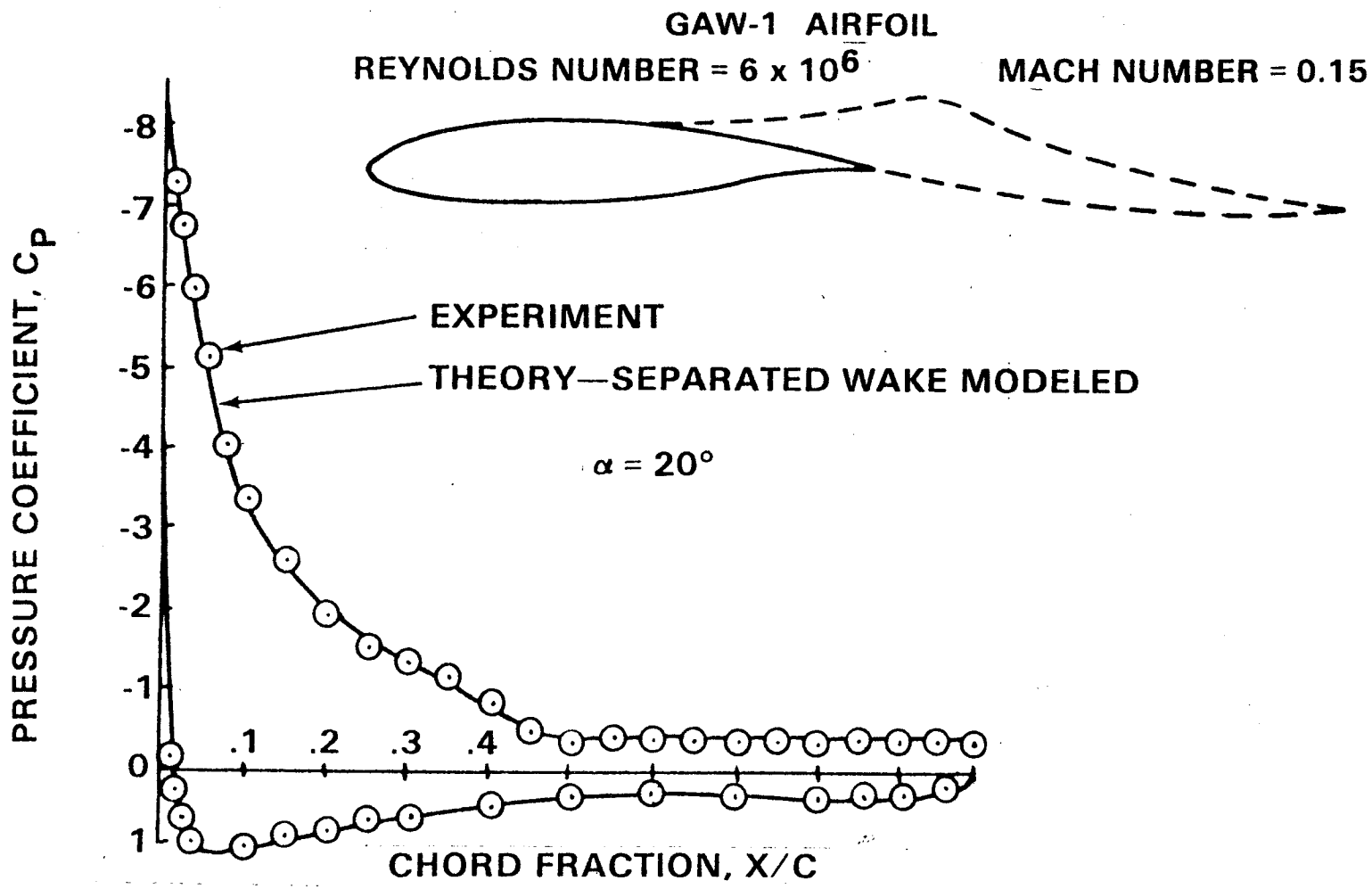

COMPARISON OF EXPERIMENTAL AND CALCULATED PRESSURE DISTRIBUTIONS ON AN AIRFOIL WITH DEFLECTED SPOILER

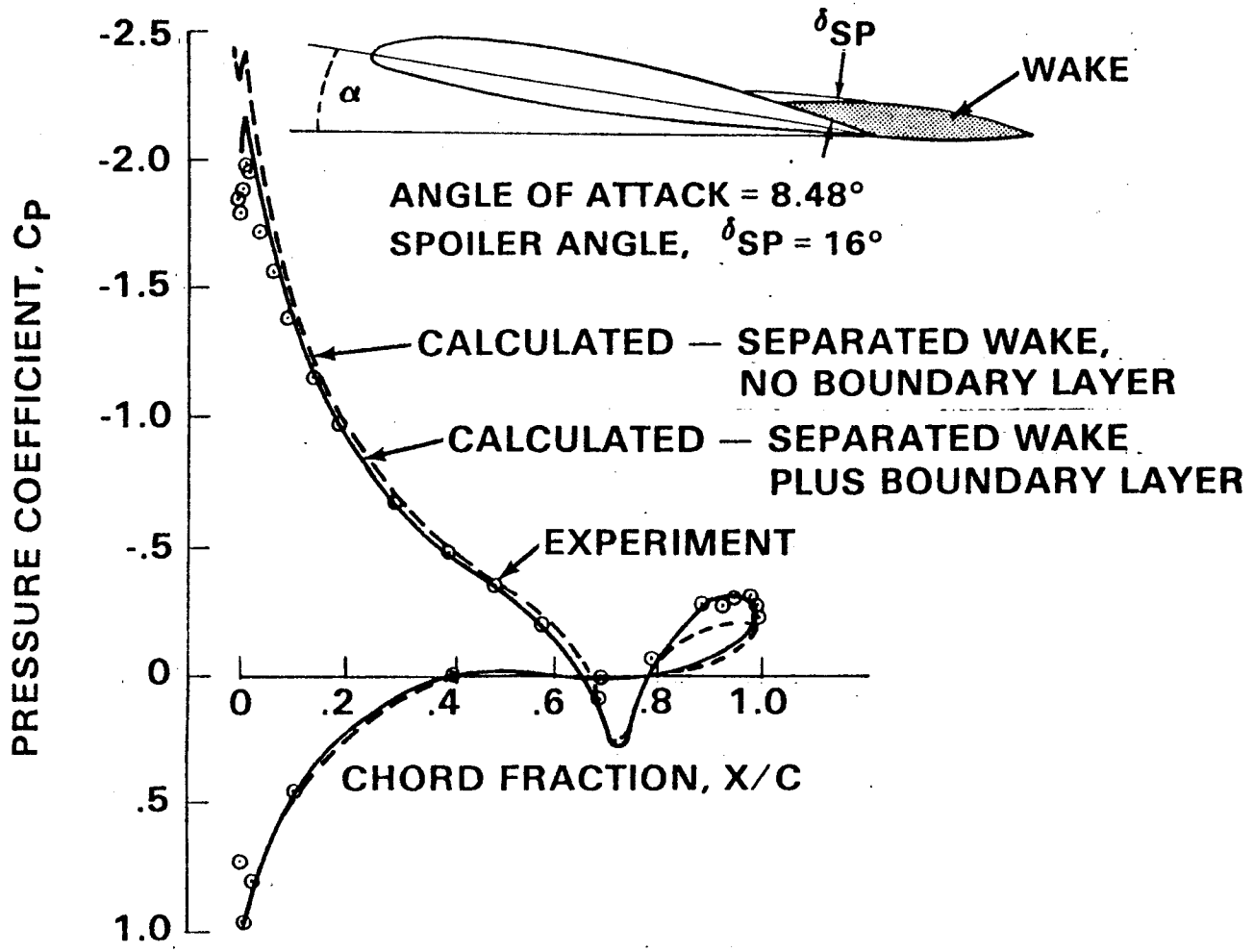

Figure 74
D3-91

COMPARISON OF EXPERIMENTAL AND CALCULATED PRESSURE DISTRIBUTIONS ON A TWO-ELEMENT AIRFOIL WITH SEPARATION ON ONE SURFACE

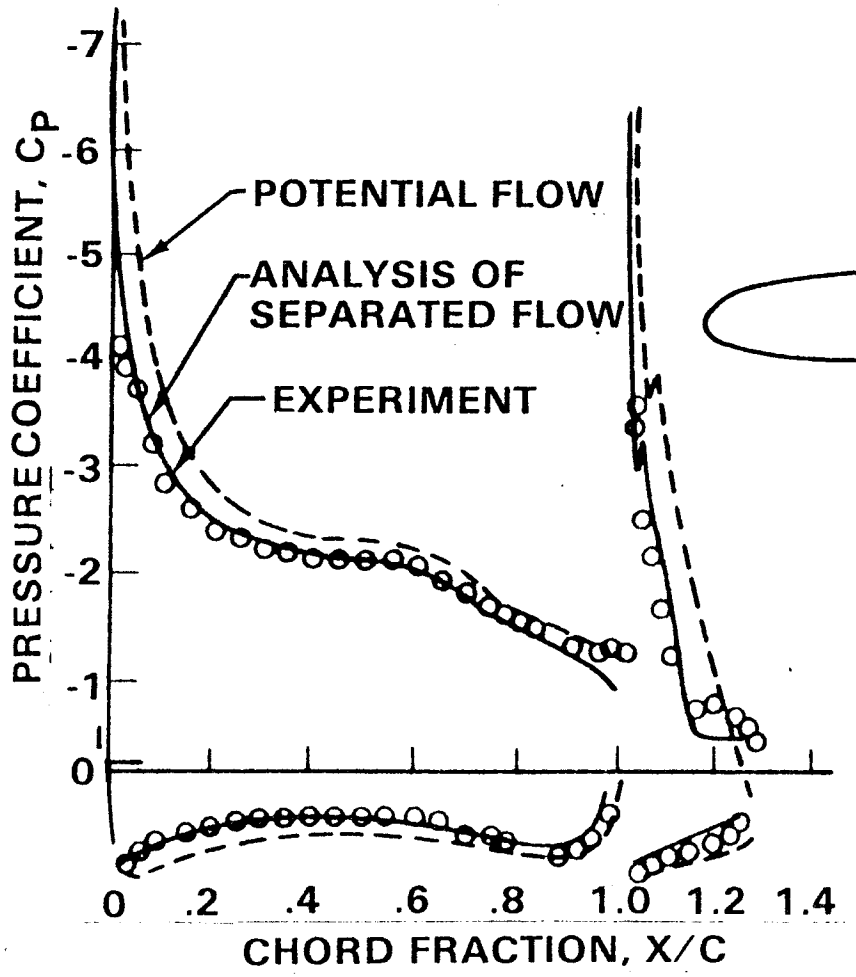

NASA GAW-1 AIRFOIL
30% FOWLER FLAP

ANGLE OF ATTACK = 0°

FLAP ANGLE = 40°

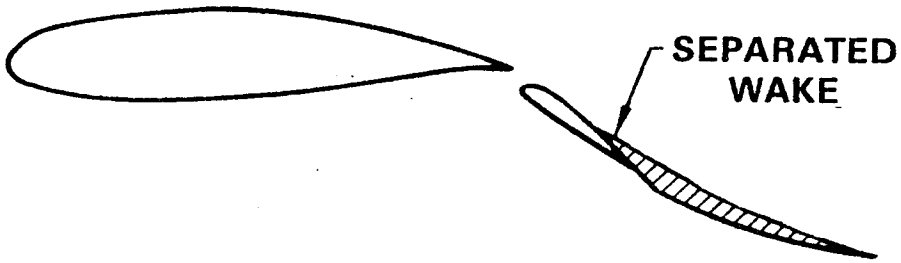

FIGURE 15

D3.92

COMPARISON OF EXPERIMENTAL AND CALCULATED PRESSURE DISTRIBUTIONS ON A TWO-ELEMENT AIRFOIL WITH SEPARATION ON BOTH SURFACES

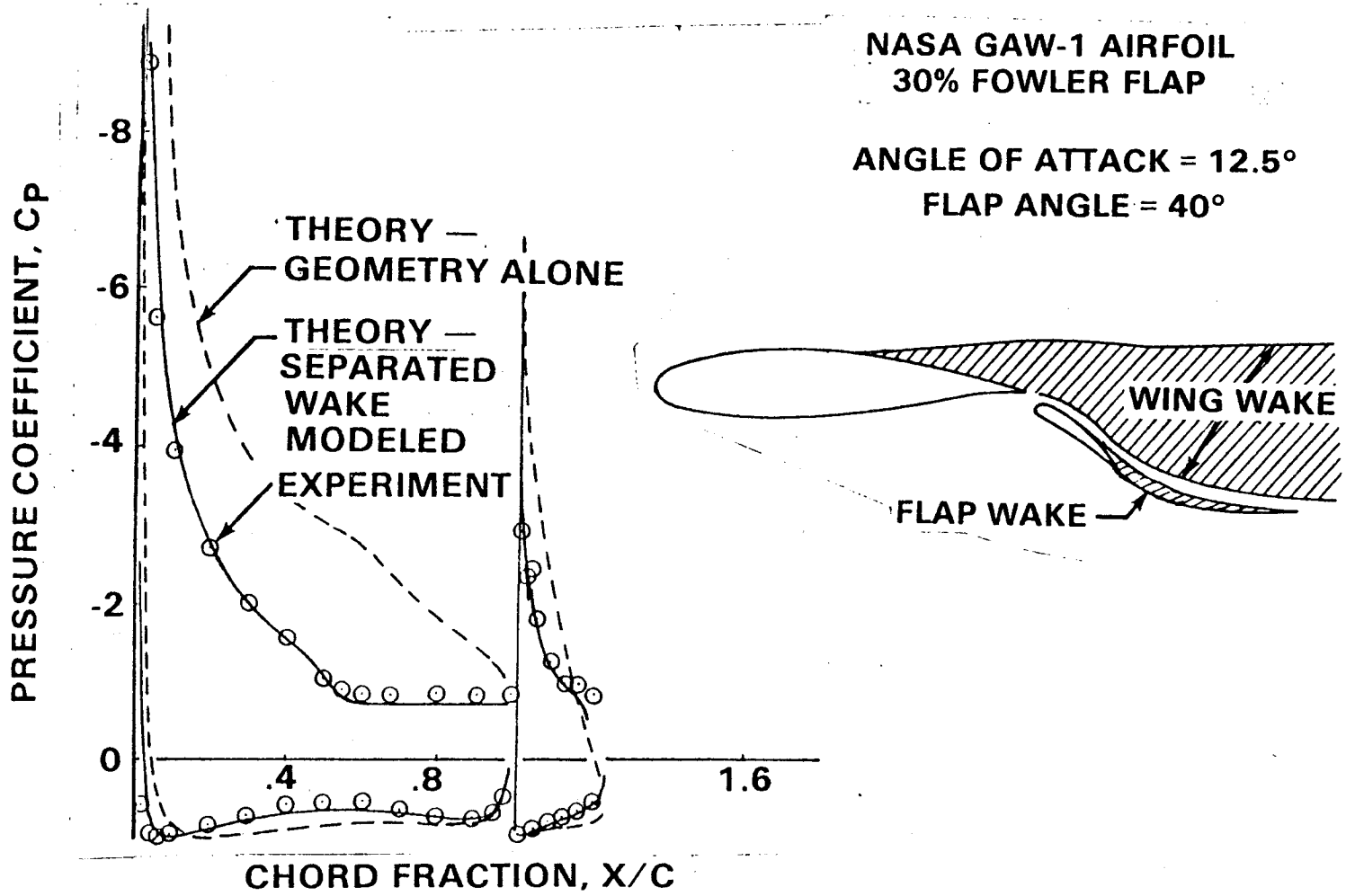

Figure 7.5
P3.93

COMPARISON OF THEORETICAL AND EXPERIMENTAL LIFT AND PITCHING MOMENT CURVES

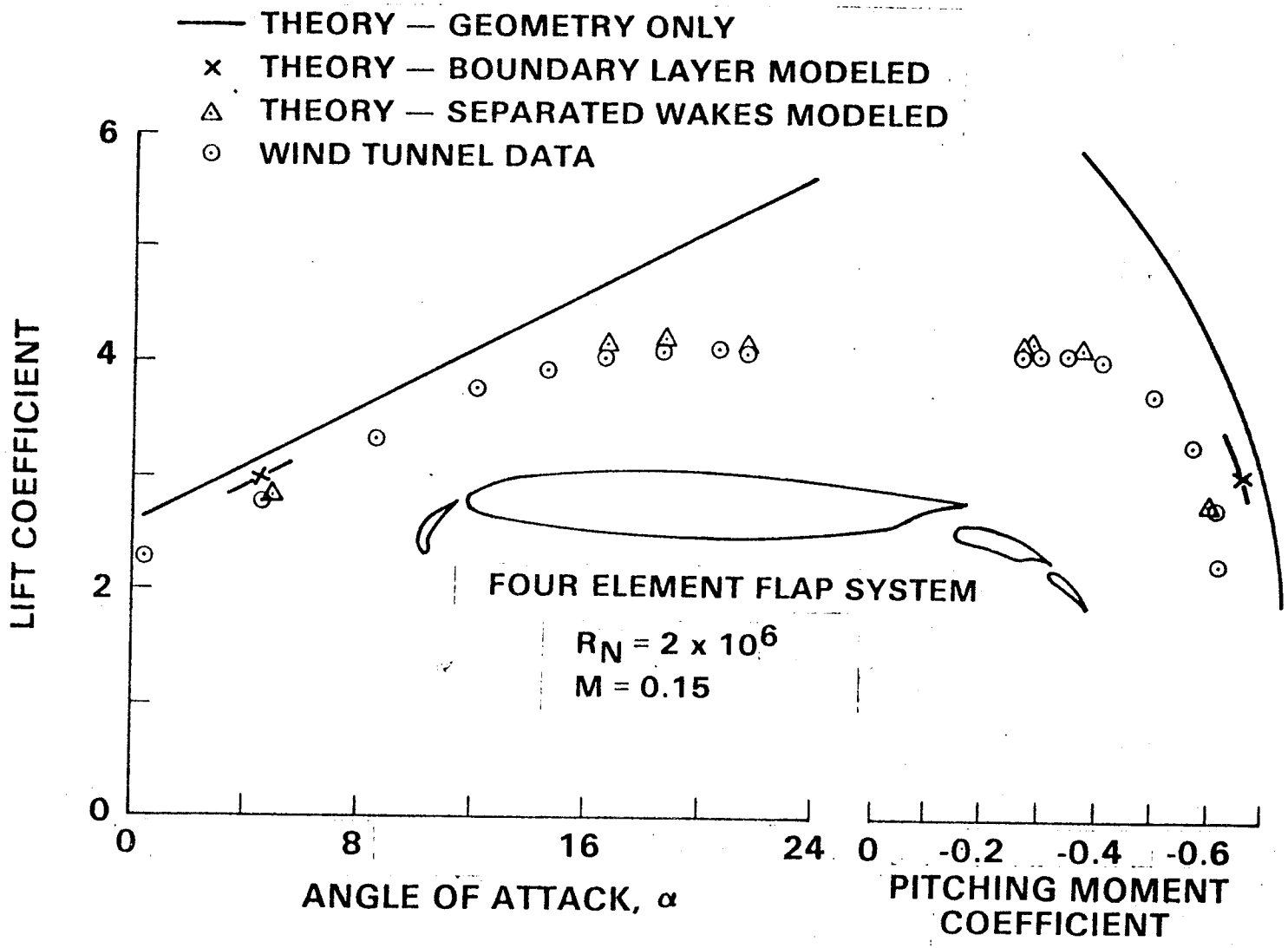

Figure 11
P3,94

COMPARISON OF THEORETICAL AND EXPERIMENTAL PRESSURE DISTRIBUTION ON FOUR-ELEMENT AIRFOIL, $\alpha = 4.4^0$

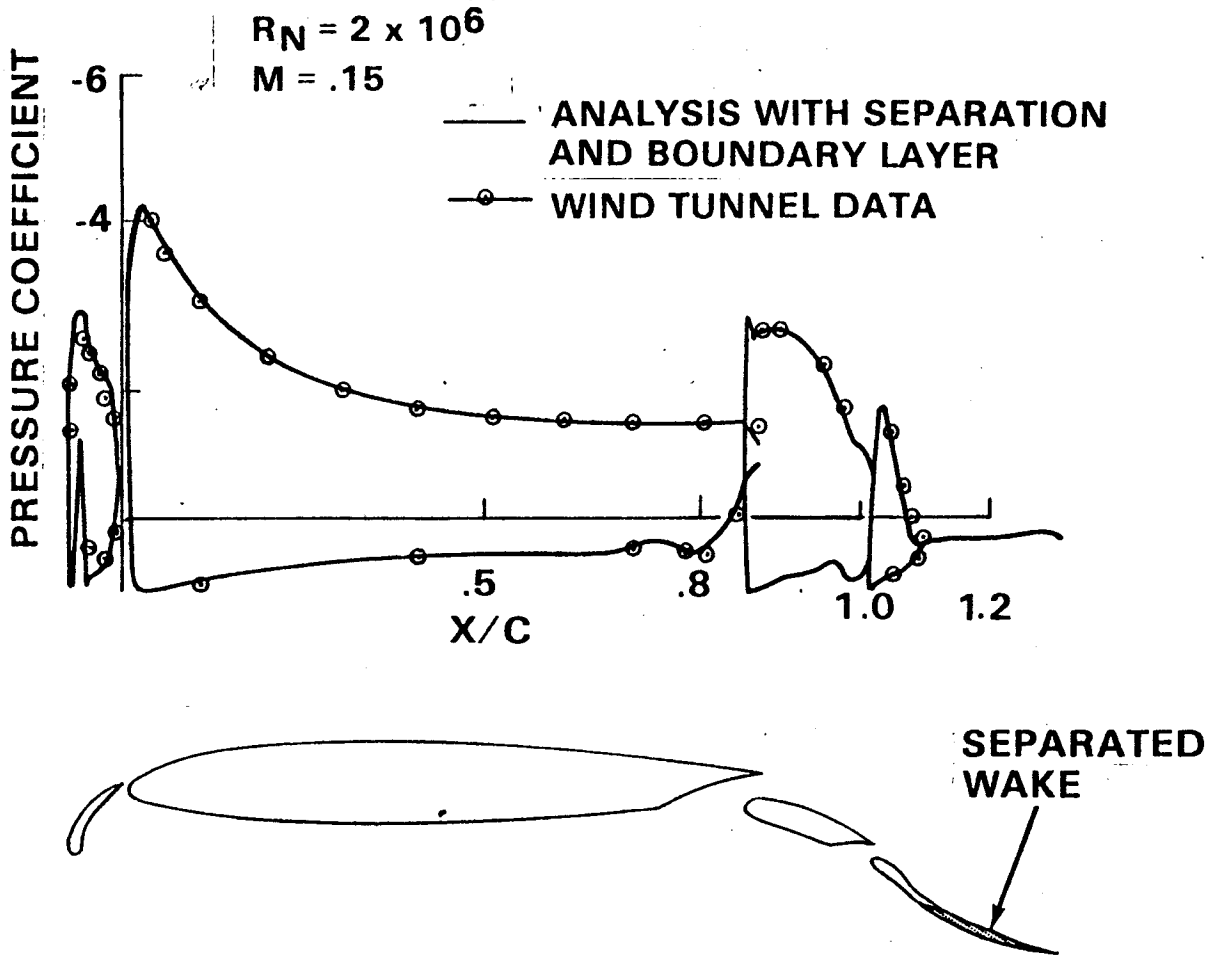

COMPARISON OF THEORETICAL AND EXPERIMENTAL PRESSURE DISTRIBUTION ON FOUR-ELEMENT AIRFOIL, $\alpha = 16.6^0$

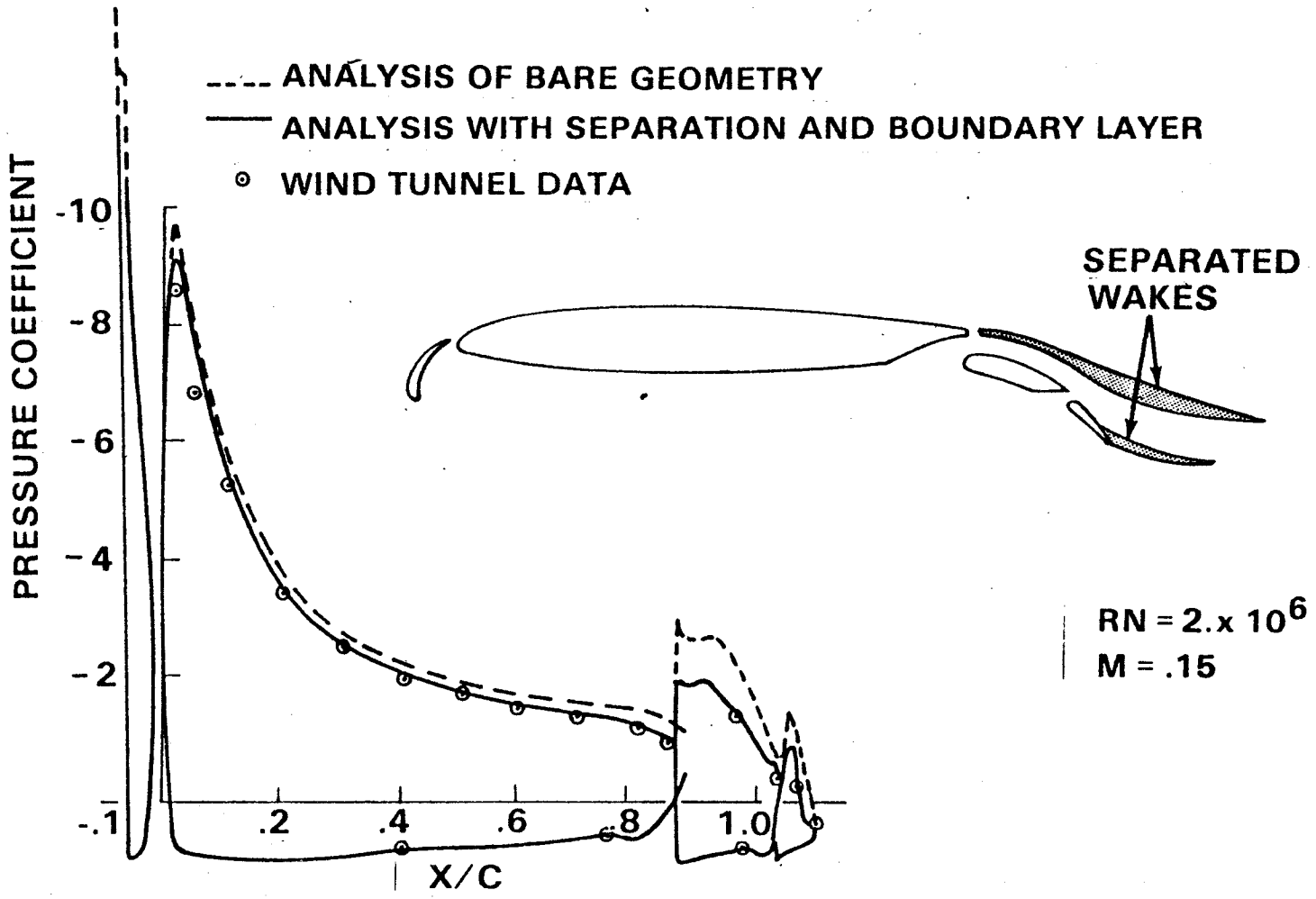

FIGURE 79

D3.96

COMPARISON OF THEORETICAL AND EXPERIMENTAL PRESSURE DISTRIBUTIONS, $\alpha = 21.7^0$

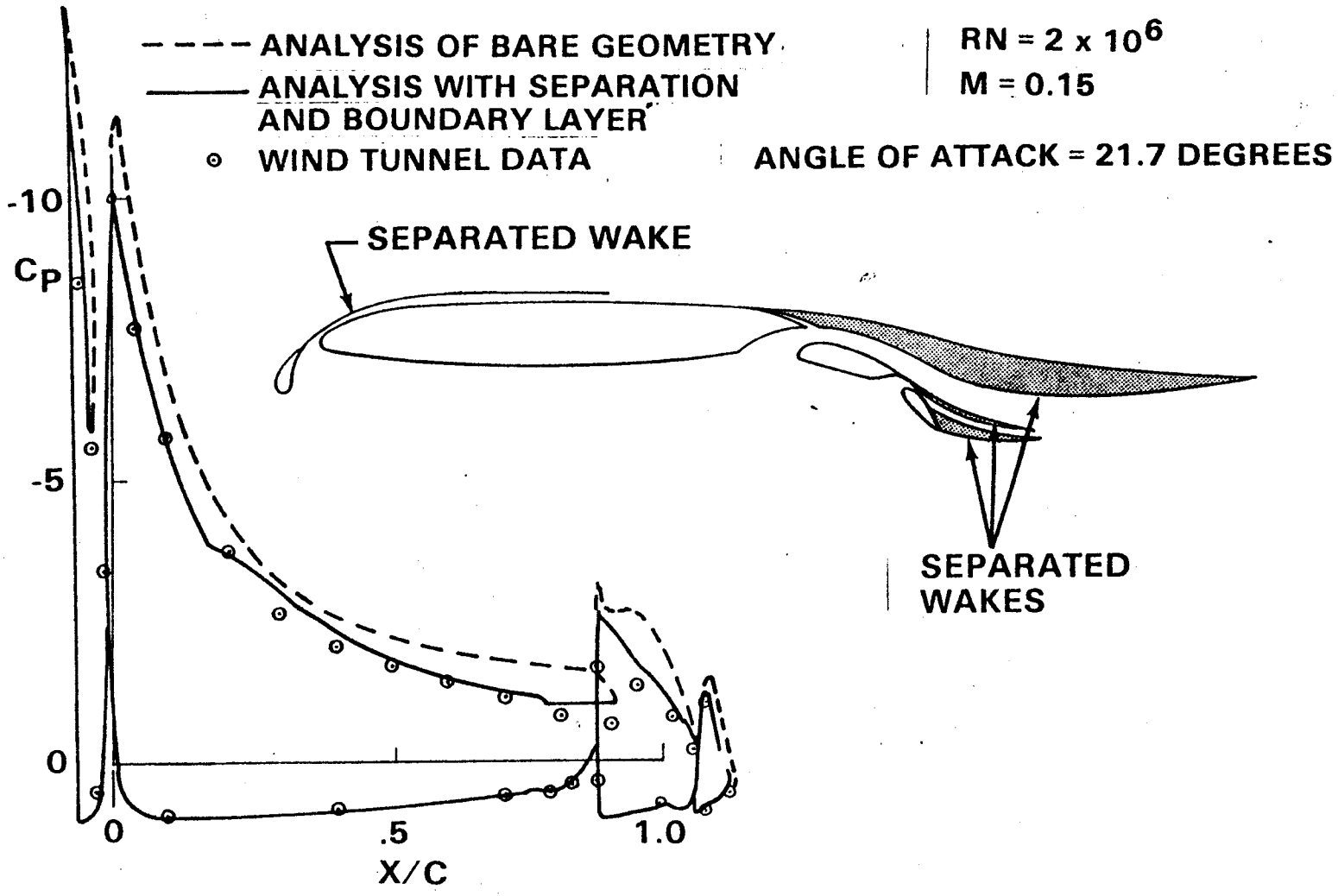

Figure 30
P3976

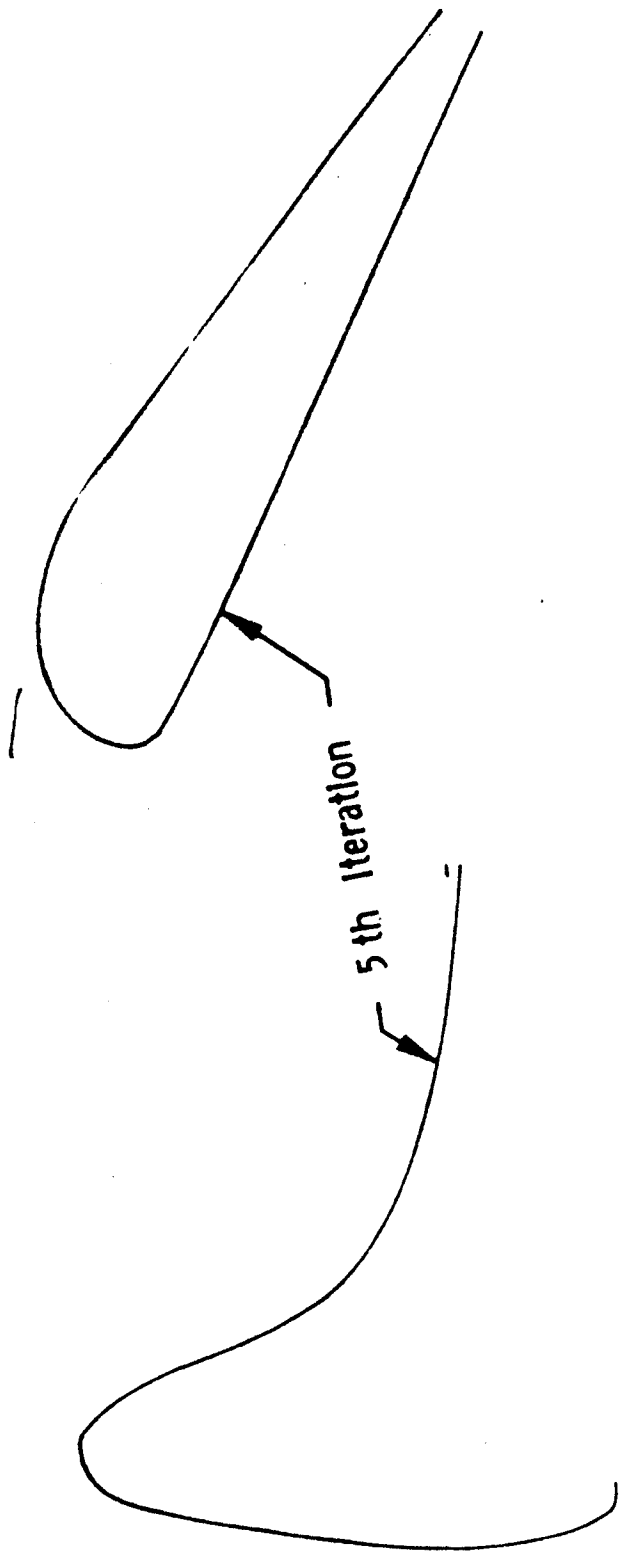

FIG 31 O/L
RED

P3.976

Aerodynamic Technology	MULTI - ELEMENT DESIGN PROGRAM	BOEING

7X7 TRAILING EDGE DESIGN

PRESSURE DISTRIBUTION

GEOMETRY

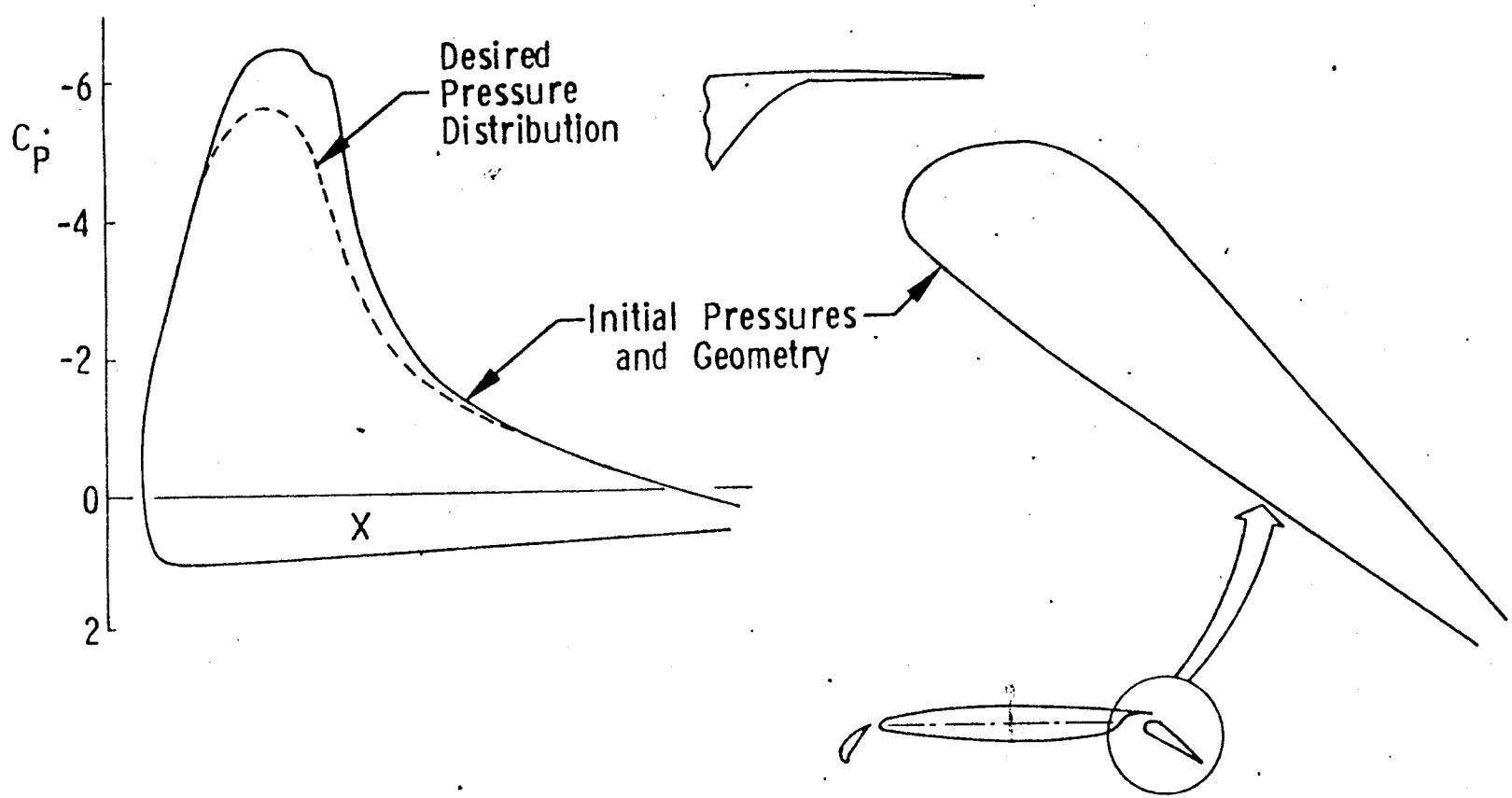

FIGURE 21

D3-9889

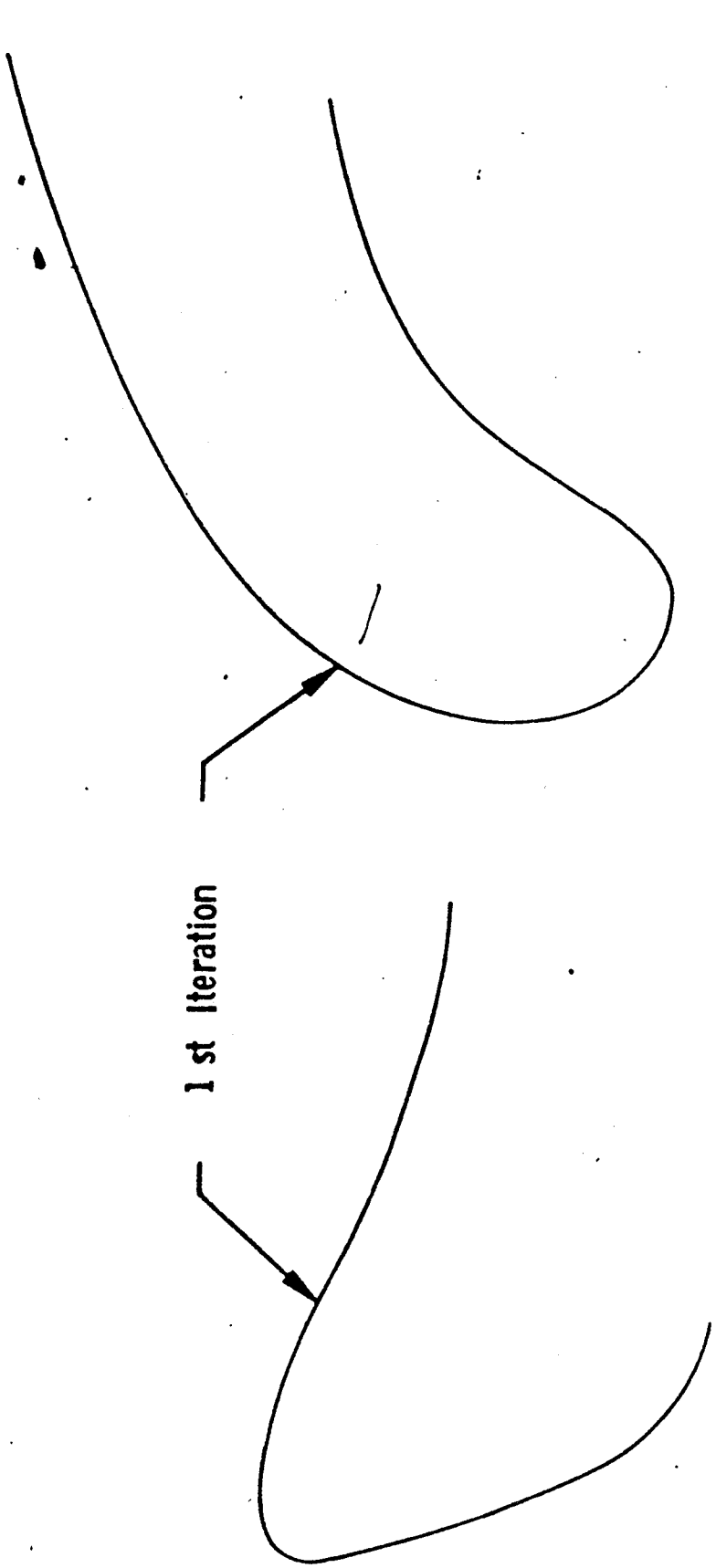

178

P3.98 b

FIG 82 O/L
GREEN

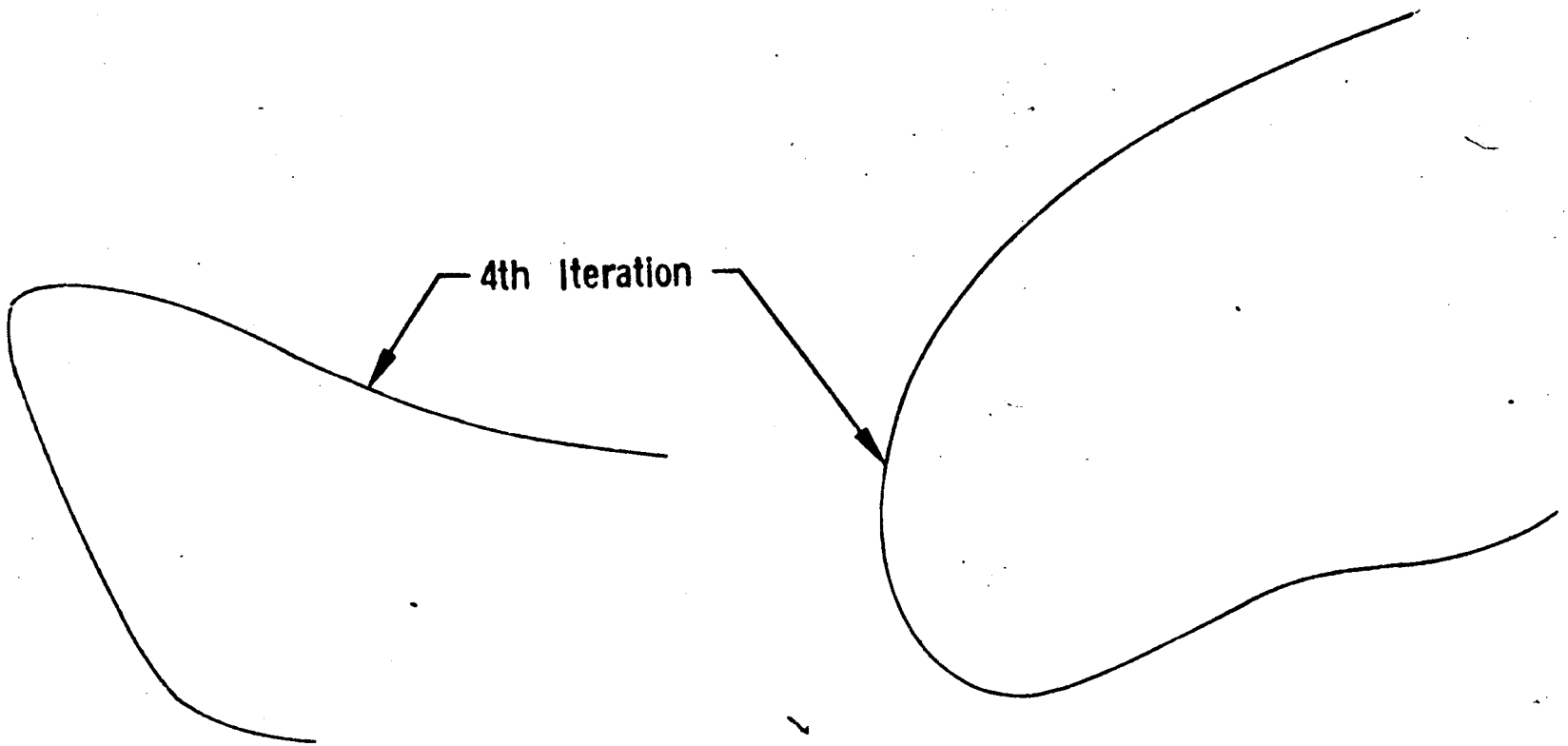

P 3.98C

Fig 8.20/1
RED

Aerodynamic Technology	MULTI - ELEMENT DESIGN PROGRAM	BOEING

QSRA LEADING EDGE DESIGN

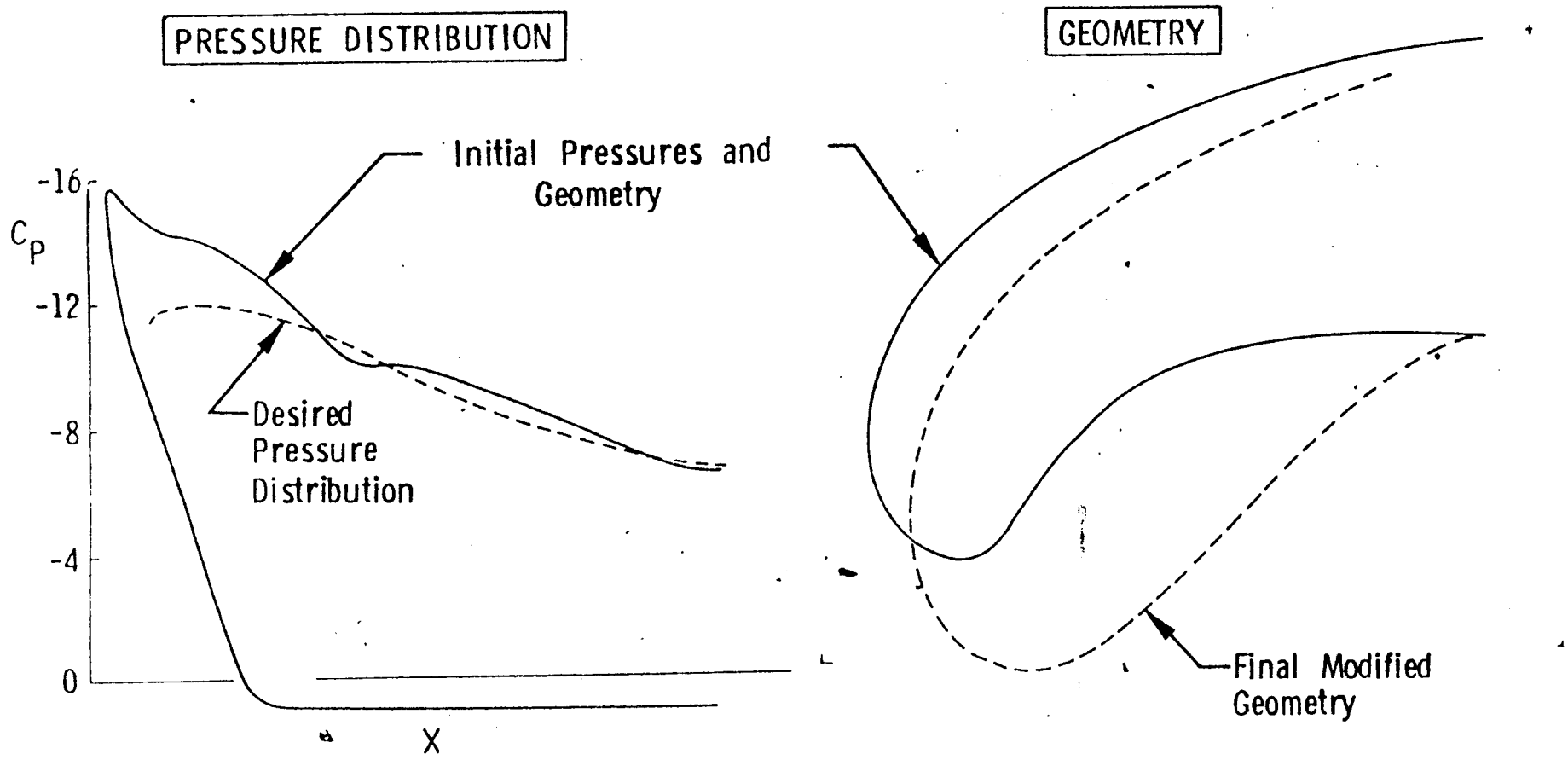

FIGURE 3.2-
P 3.99

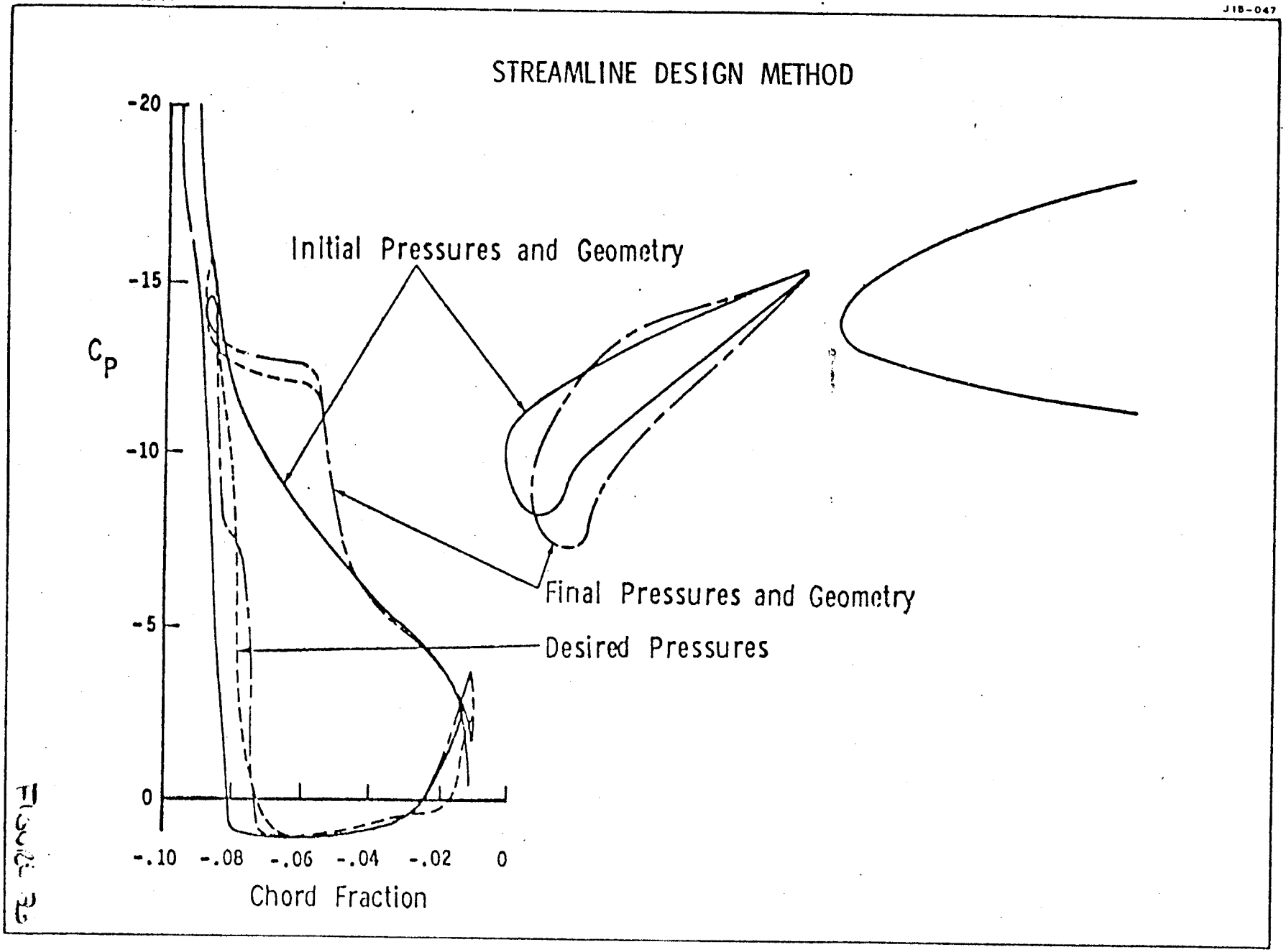

Figure 3b

BOEING FOUR-ELEMENT AIRFOIL

BOUNDARY-LAYER PROFILES

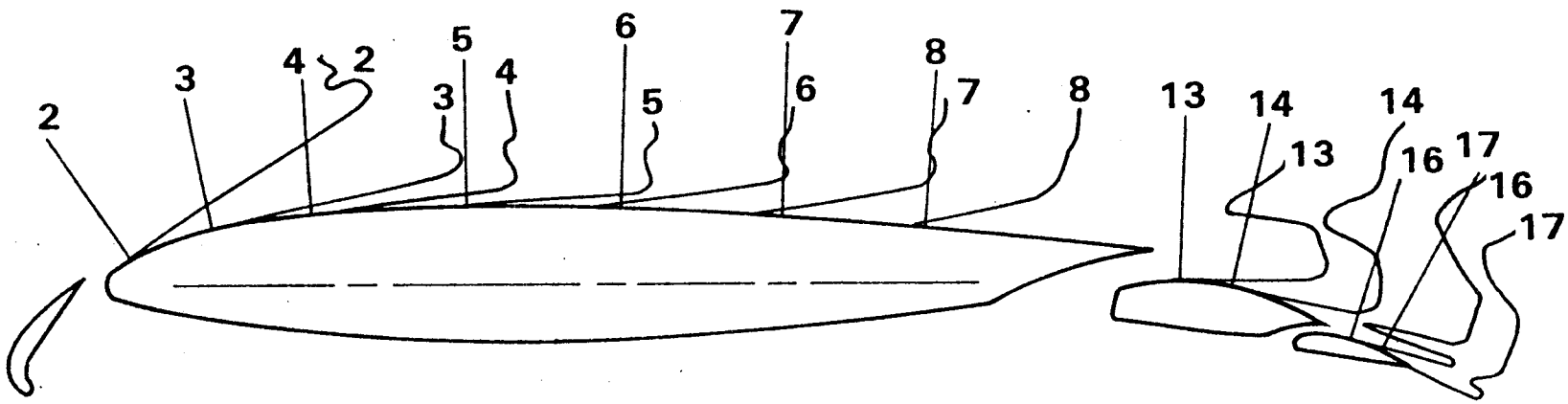

BOUNDARY LAYER PROFILES

BOUNDARY LAYER PROFILES ON UPPER WING SURFACE OF BOEING FOUR-ELEMENT AIRFOIL

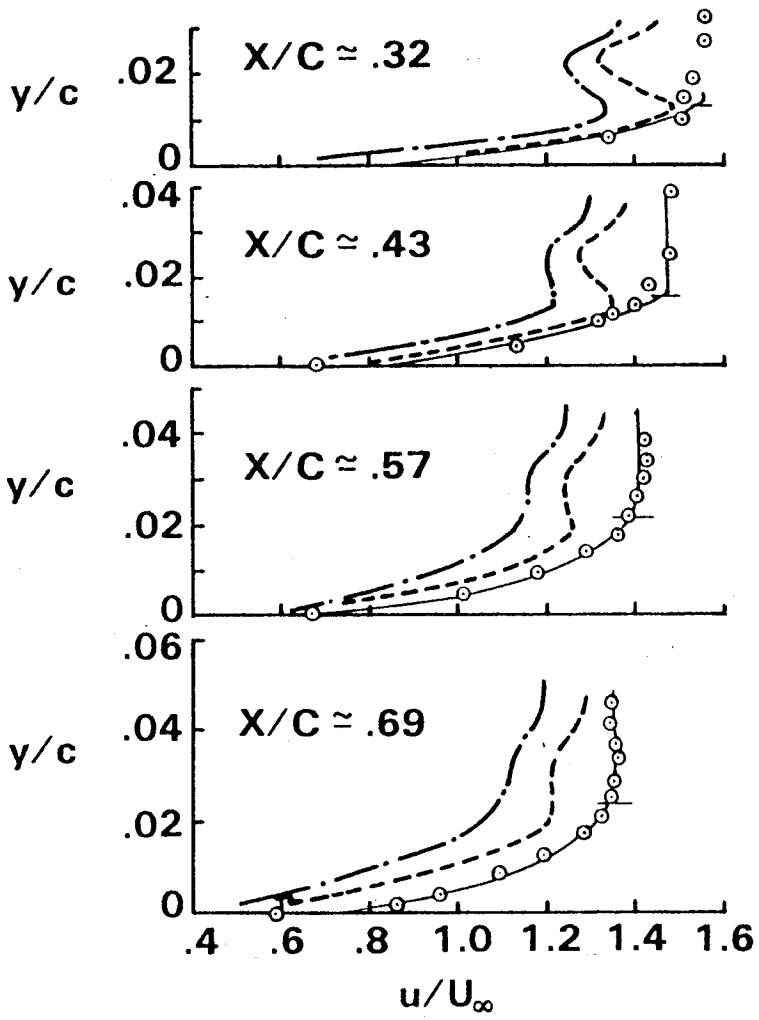

$\alpha = 8.4°$
$M = 0.16$
$R_N = 2 \times 10^6$

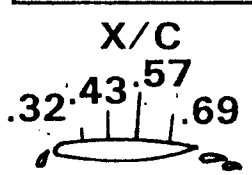

EXPERIMENT
VERSION A
VERSION B
VERSION C

FIGURE 37
P3.102

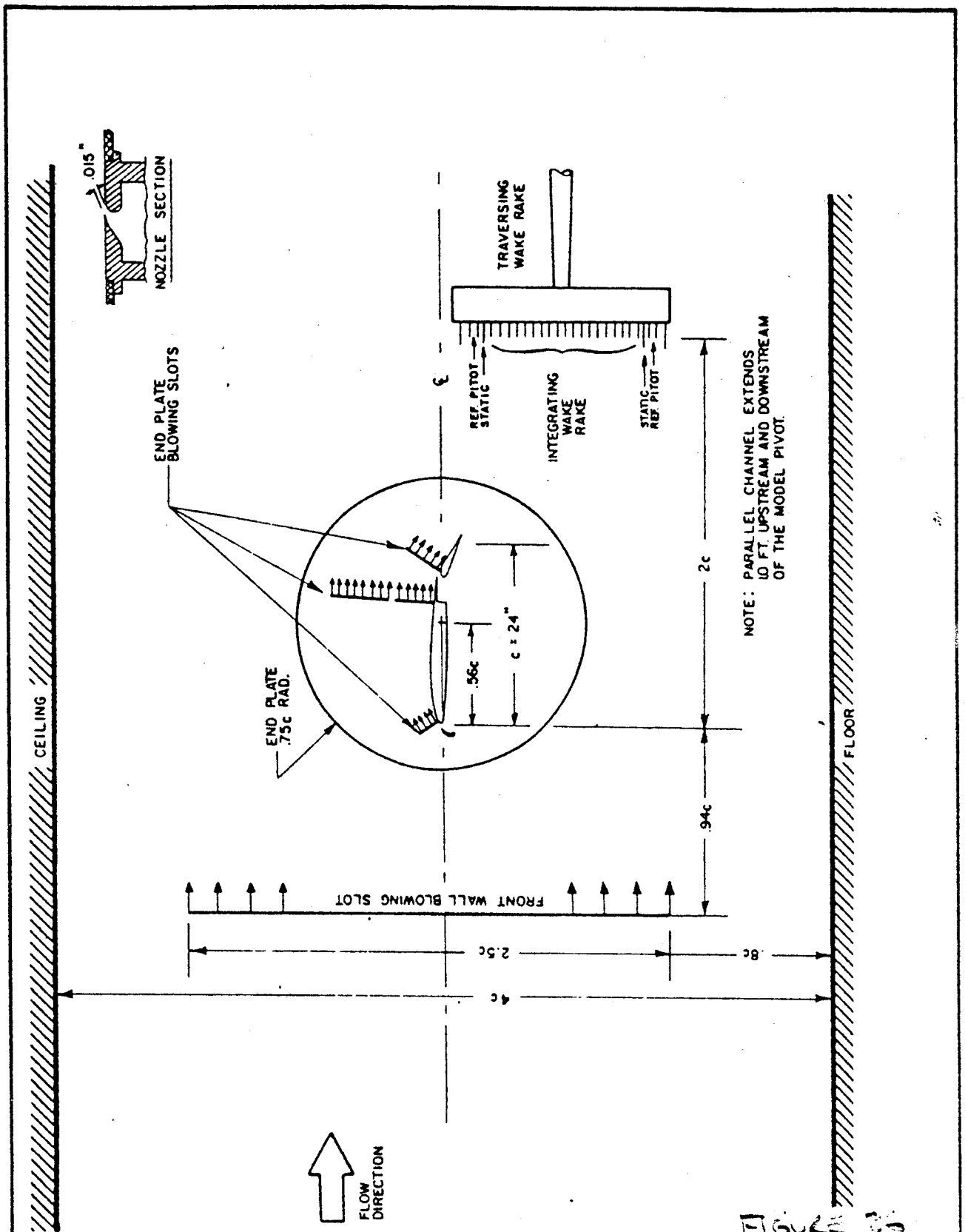

FIGURE 3.5

CALC	E. OMAR	9/72	REVISED	DATE	BRWT TEST SECTION
CHECK					
APPD					
APPD					
	M2				THE BOEING COMPANY RENTON, WASHINGTON — PAGE

AD 973 D-R3

6 7000

184

P3.103

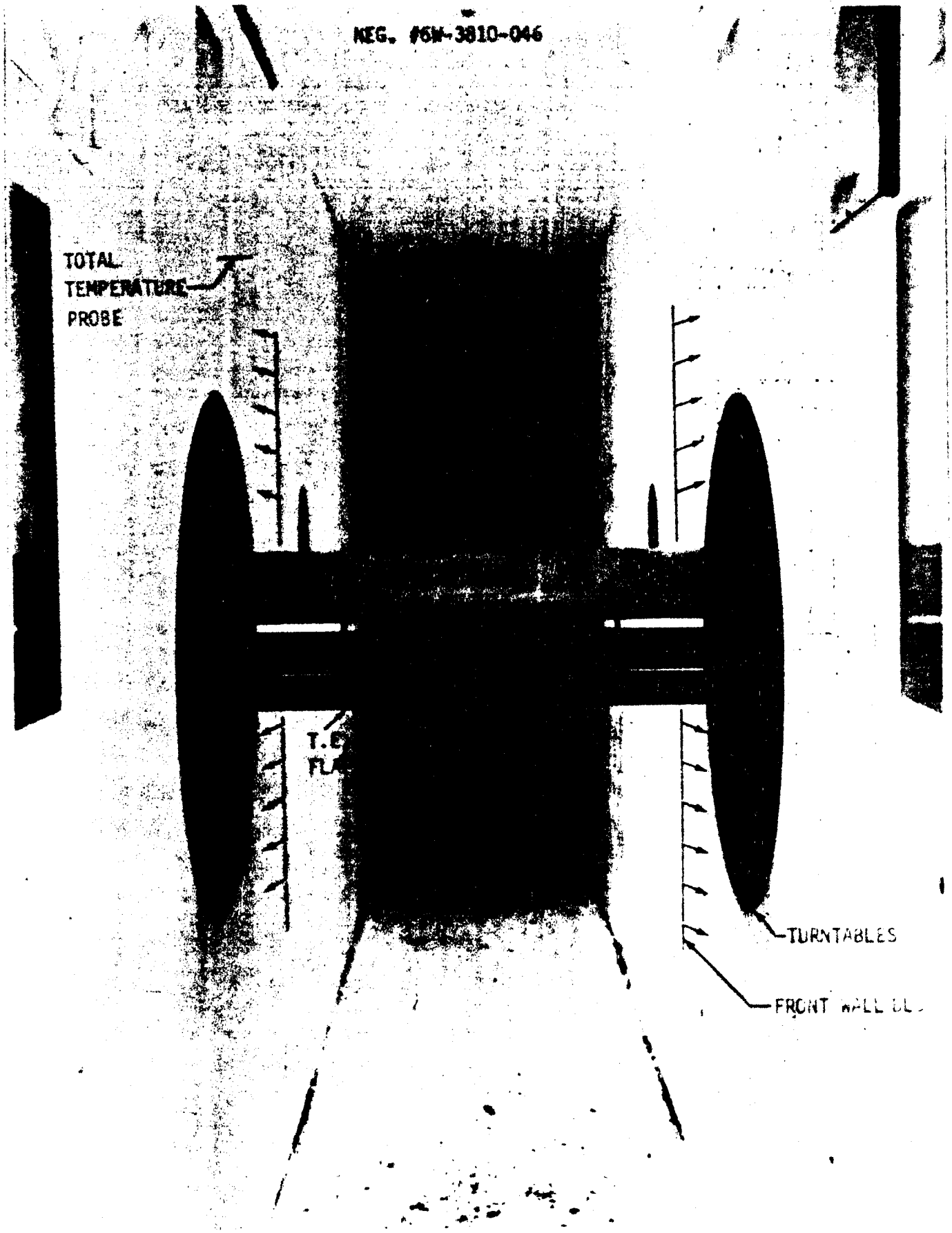

FIGURE MODEL INSTALLATION

BOEING FIG 87
P3.104

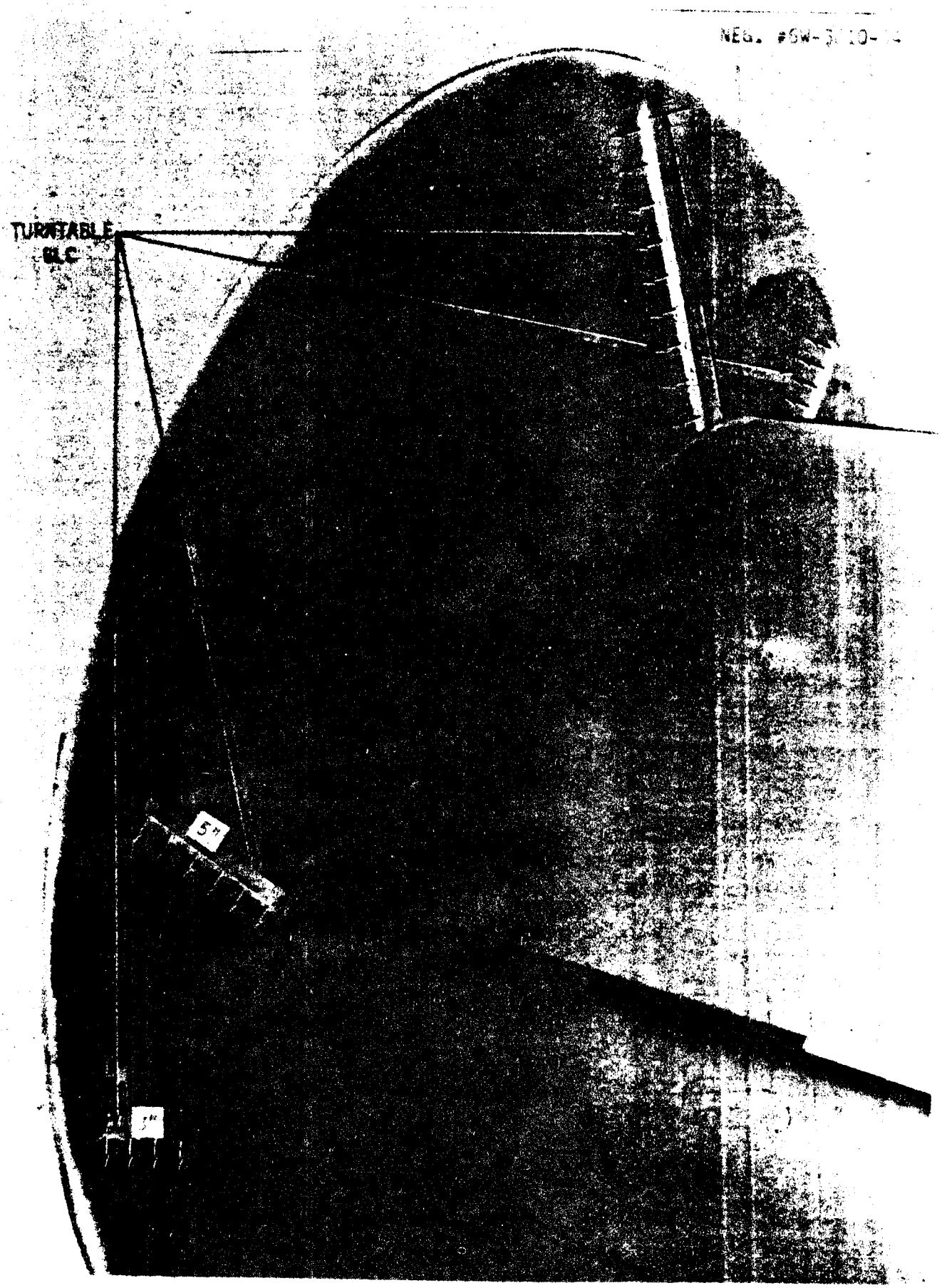

TURNTABLE PI

FIG 8c

P 3.105

BOEING

186

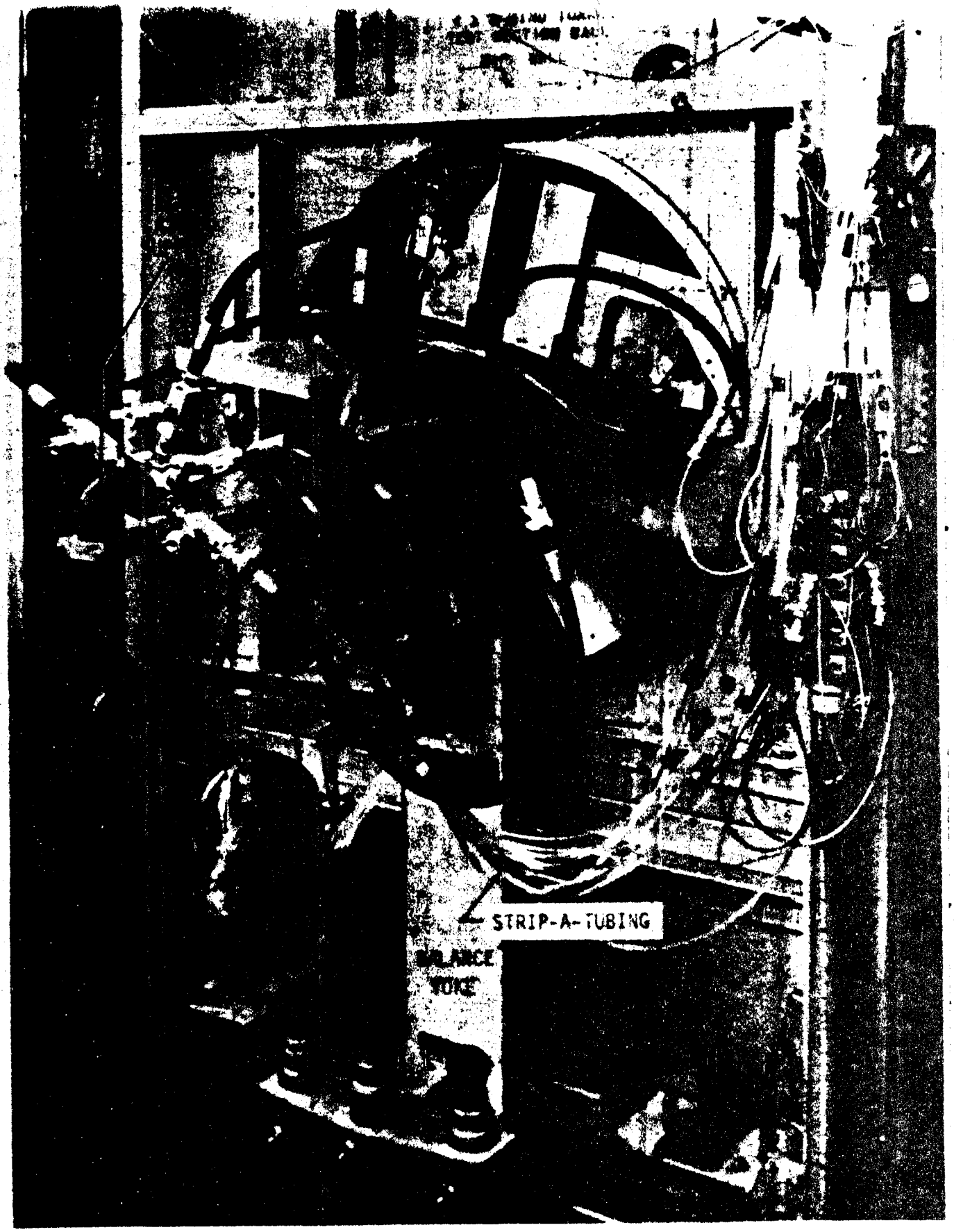

FIGURE 26 EXTERNAL TEST [illegible] FIG 83

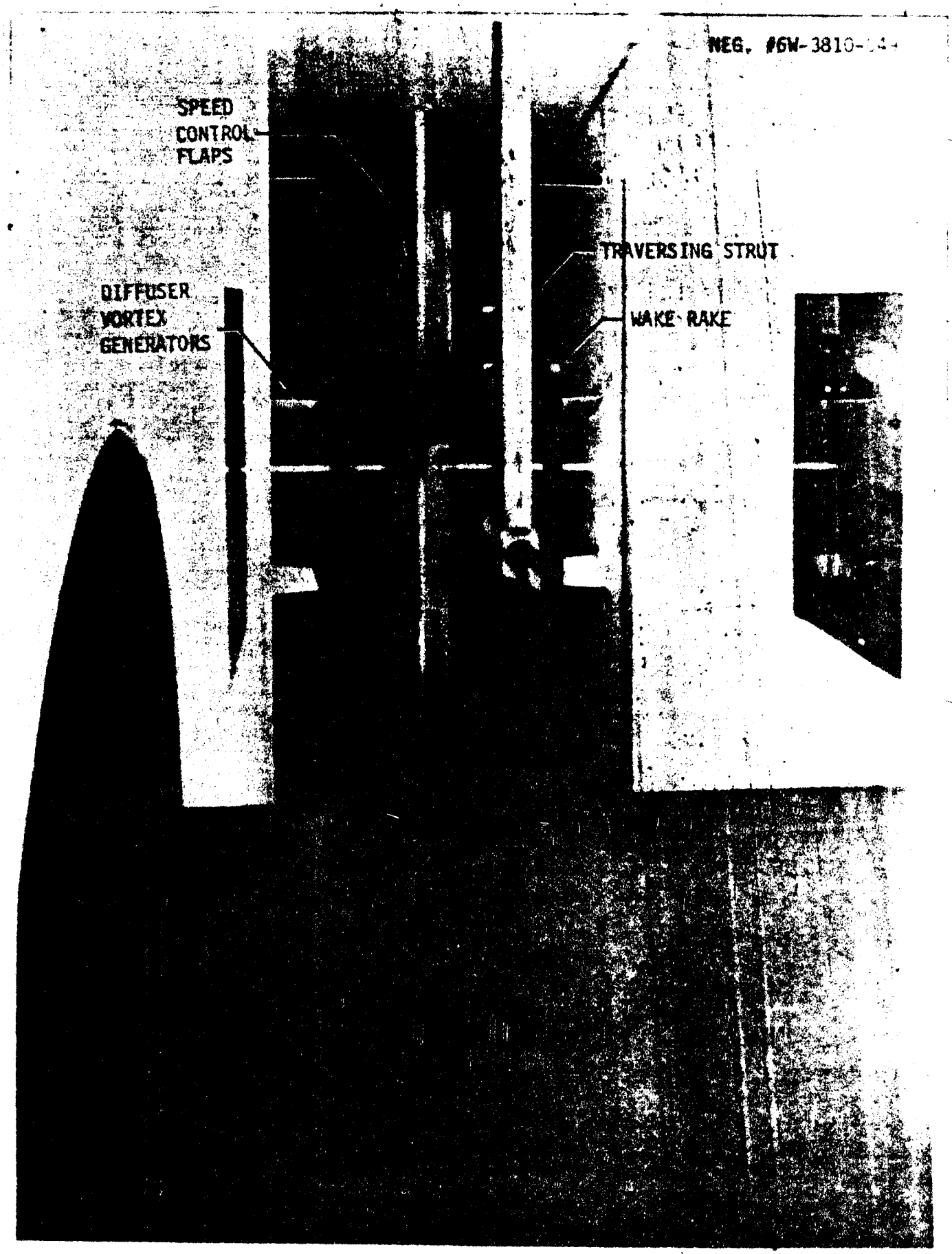

FIGURE 24 AFT TEST SECTION

FIGURE 9c

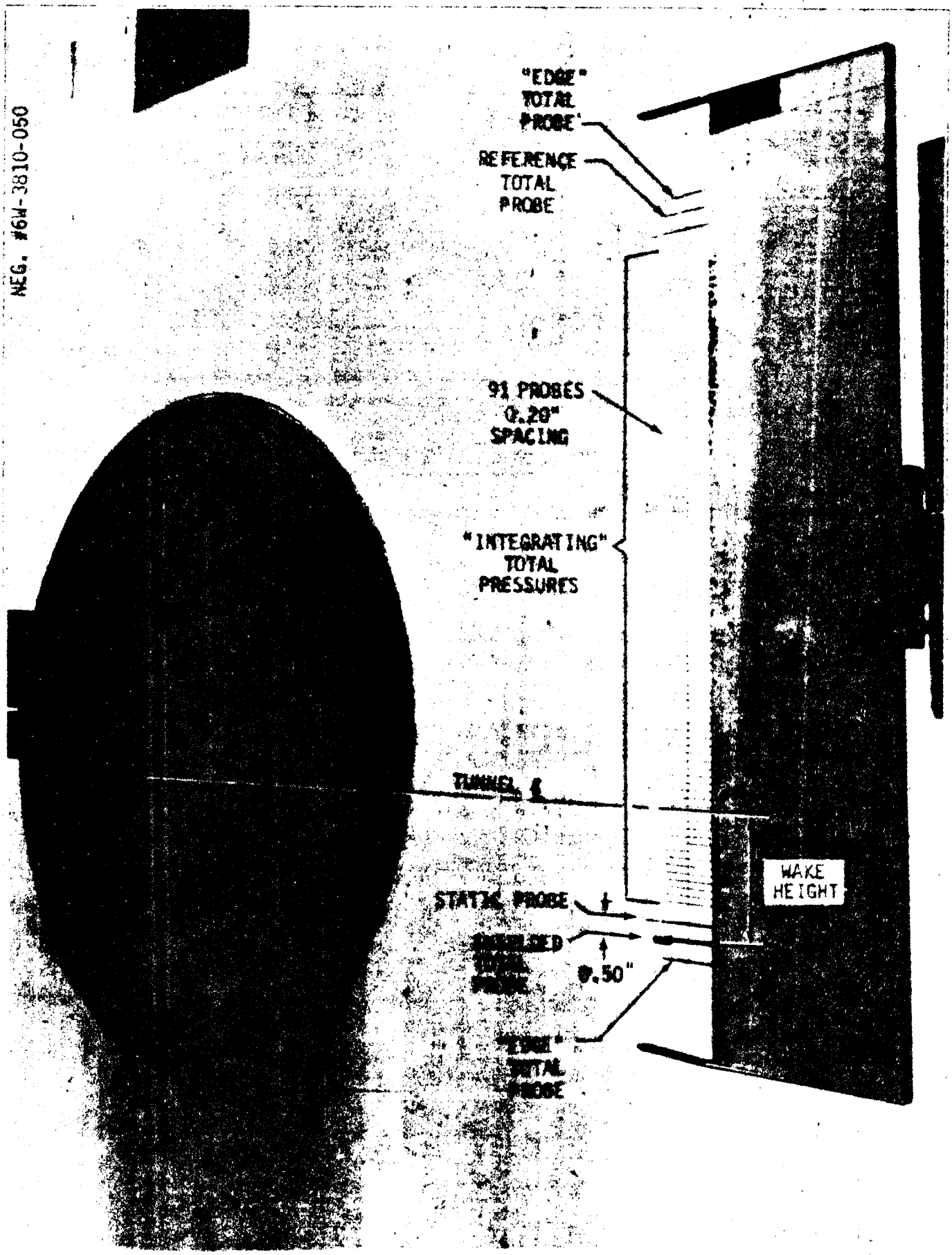

FIGURE 91

P3.108

189

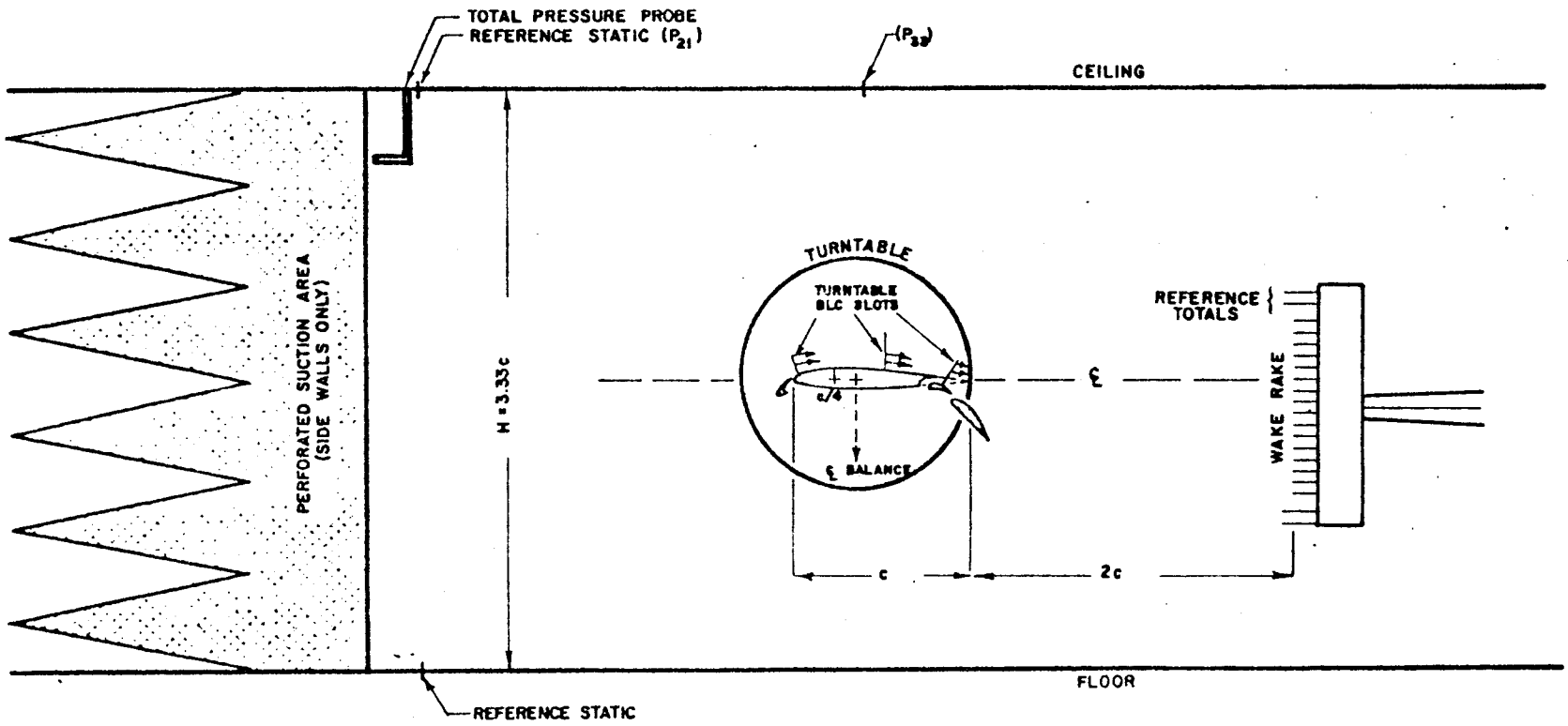

TEST SET-UP IN THE NAE WIND TUNNEL (5'x 5')

FIGURE 33

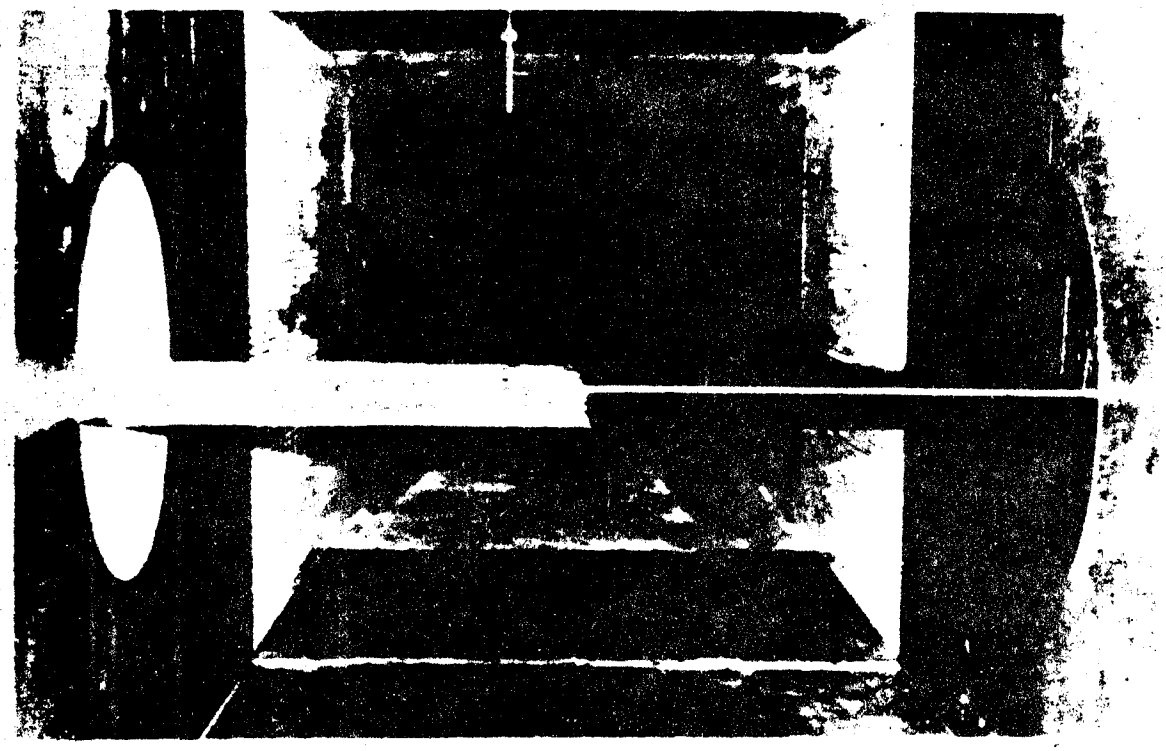

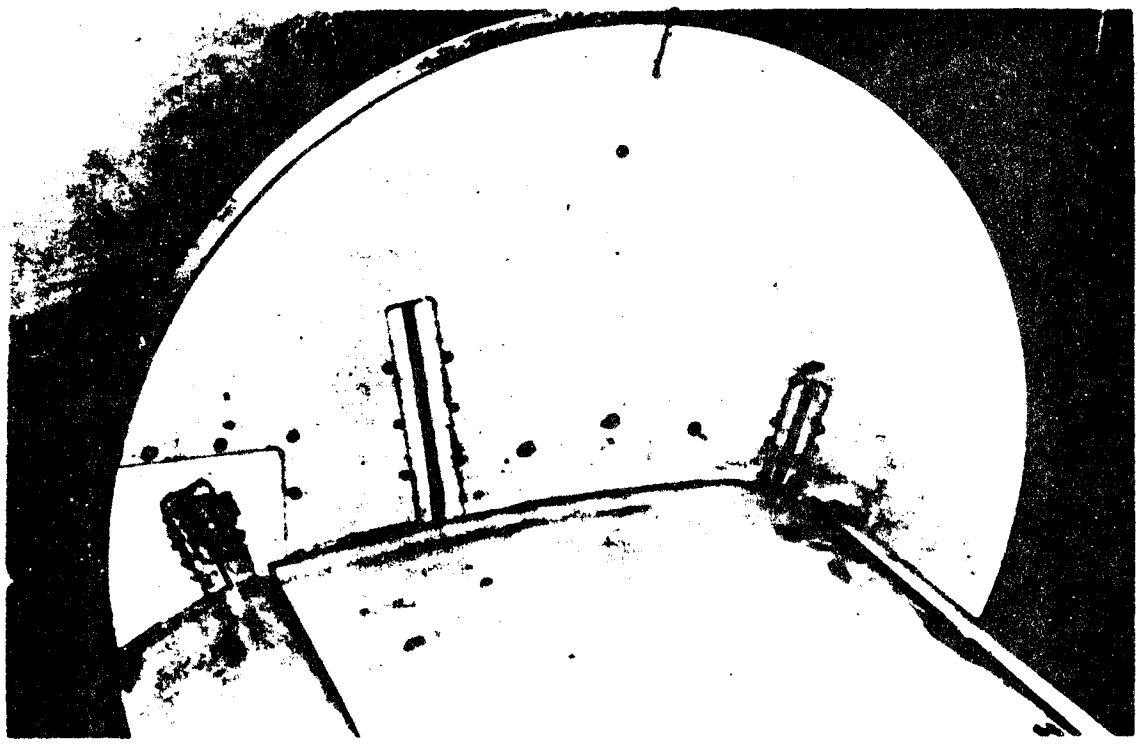

FIG 93
P3.110

AD 1546 D

REV SYM

BOEING

6-7000

191

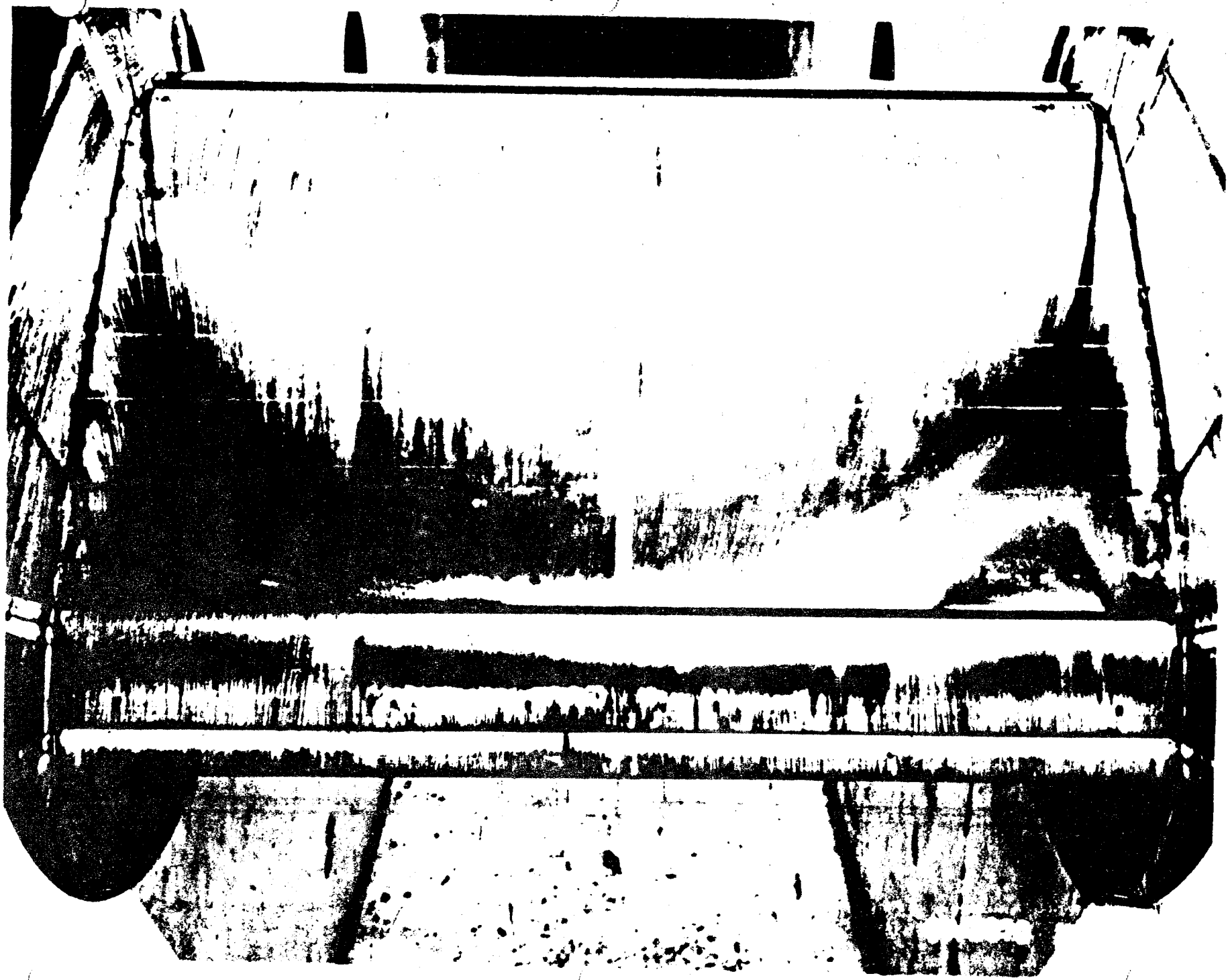

FIG 94
U 3 111

FIG. 95
P.3.112

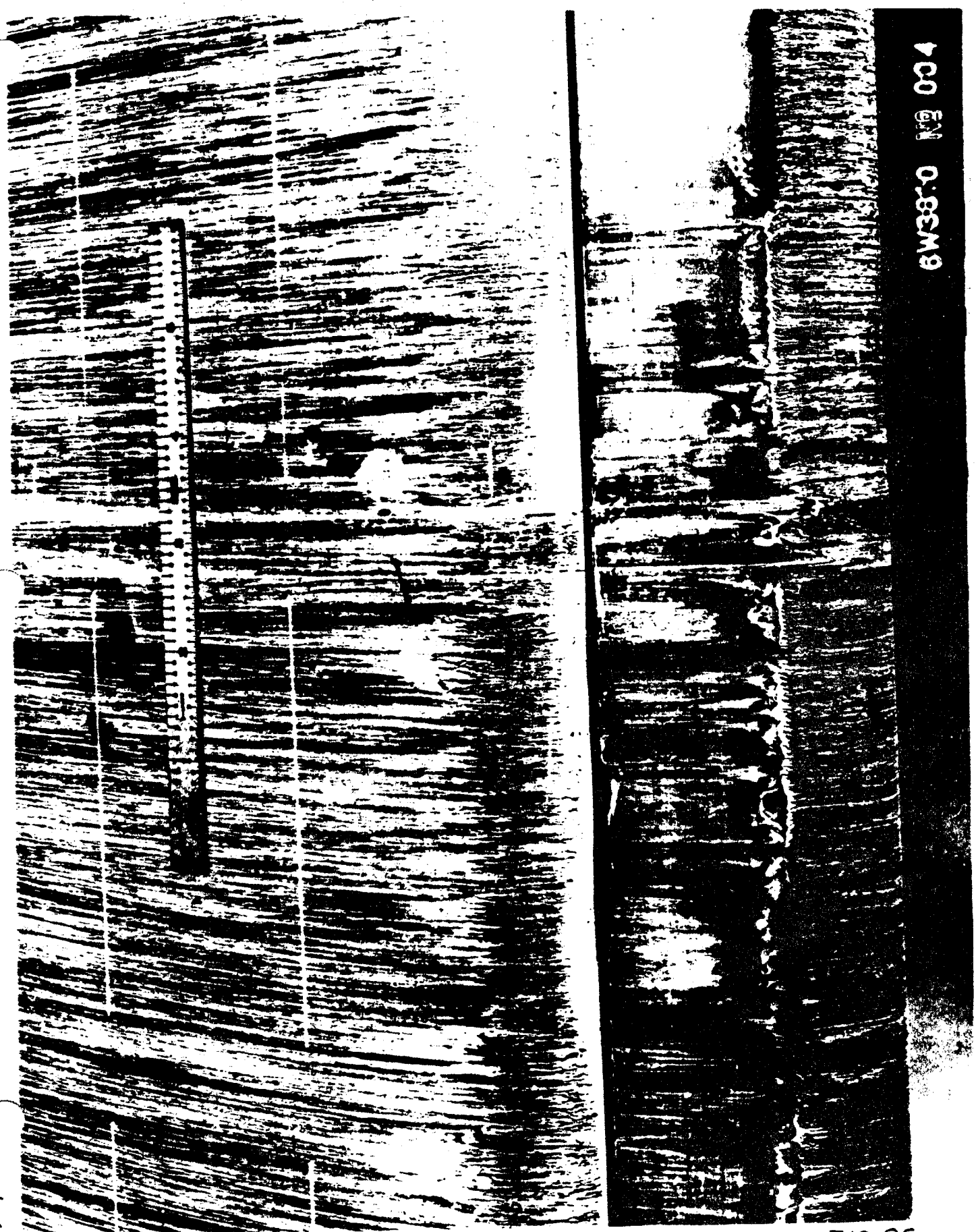

FIG 96
P3.113

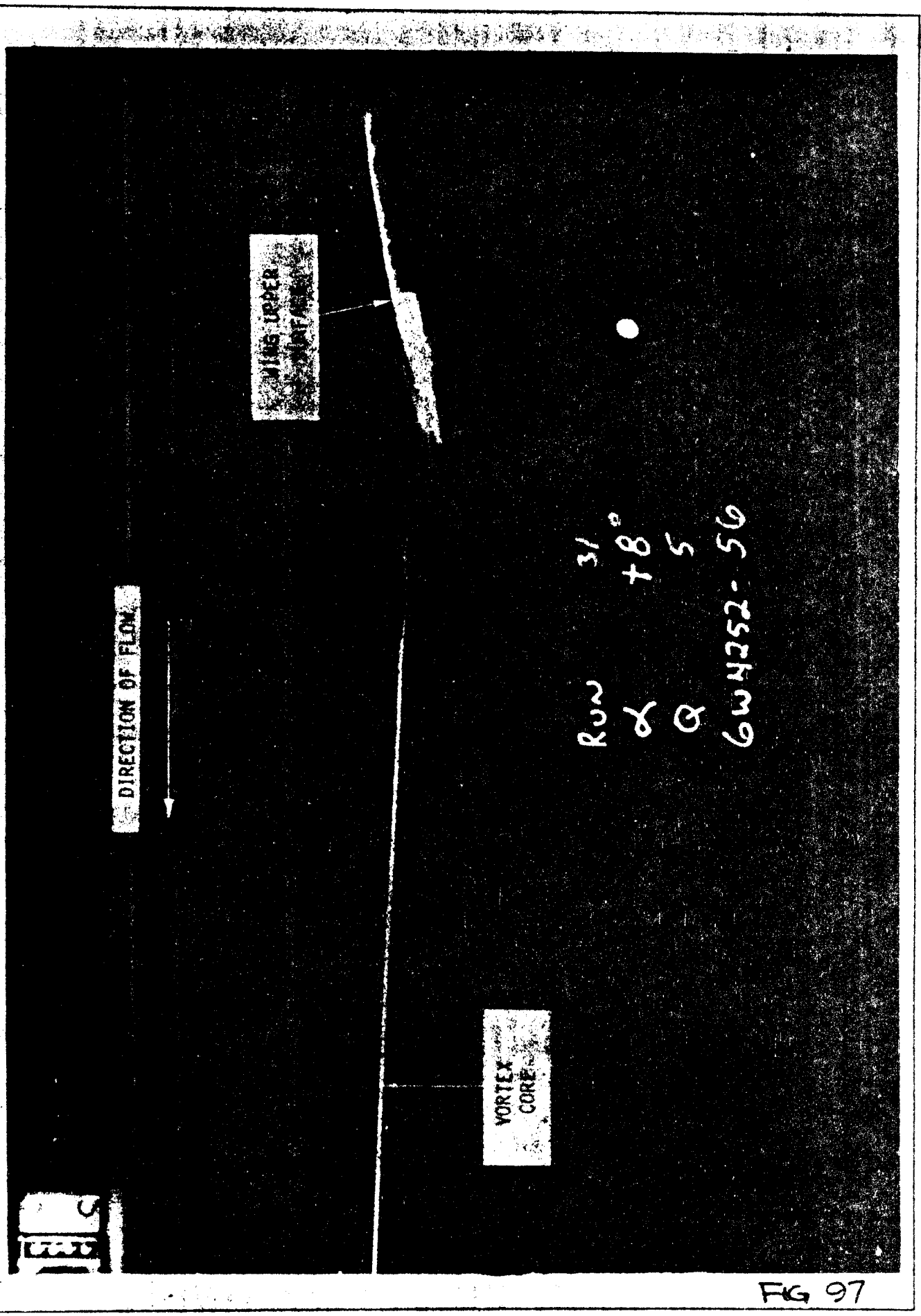

FIG 97

REV SYM FIG. 4.8a BASIC WING TIP VORTEX (SIDE VIEW)

BOEING NO. D6-45114TN PAGE 31 P3.114

7.a

195

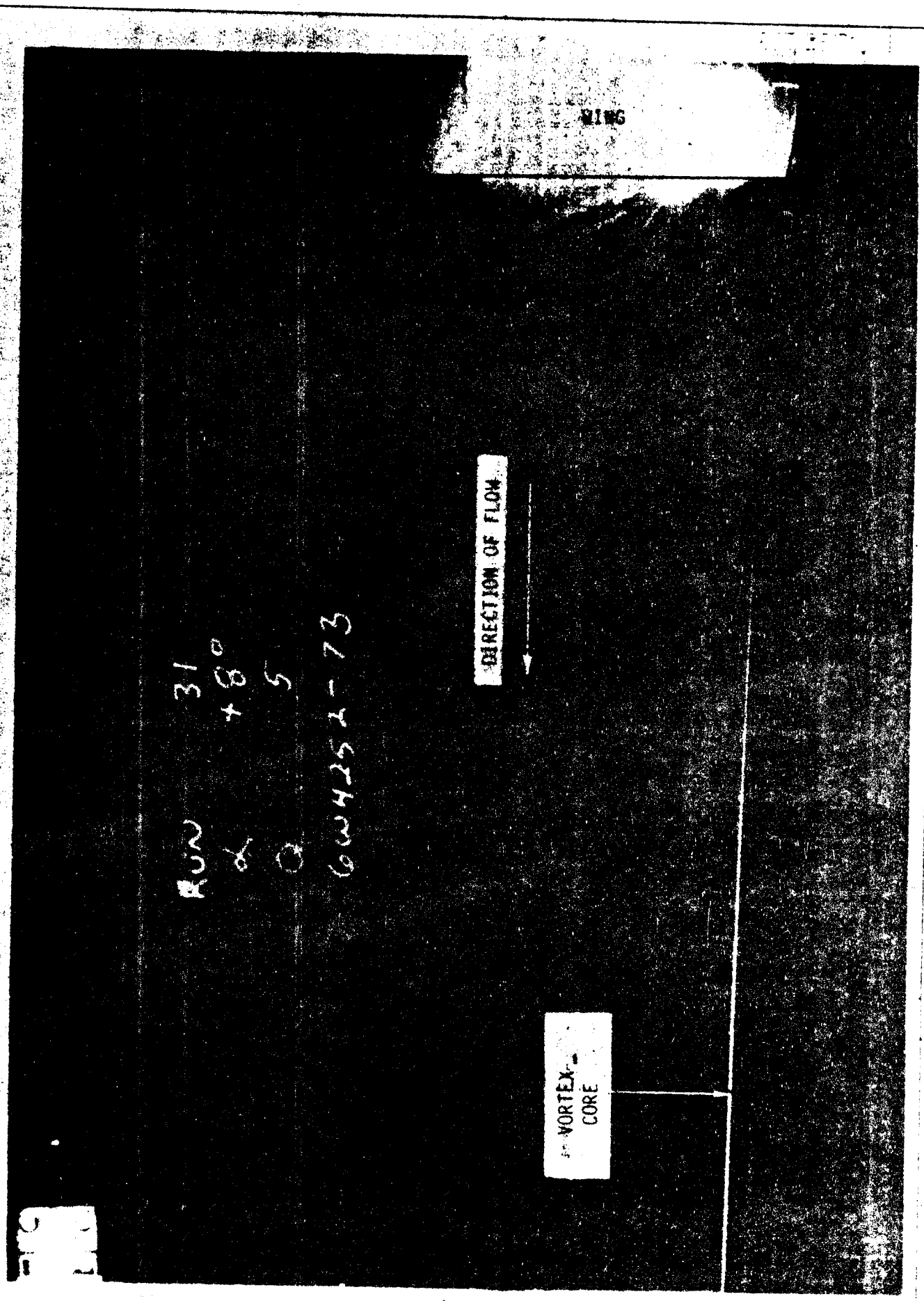

FIGURE 9e

REV SYM FIG. 4.8b BASIC WING TIP VORTEX (TOP VIEW)

BOEING NO. [illegible]

PAGE [illegible] P3.115

AD 1546 D

AD 1546 D

FIGURE 3

REV SYM 4.9 PART-SPAN FLAP-IN VORTEX (SIDE VIEW)

BOEING NO

PAGE P3.16

197

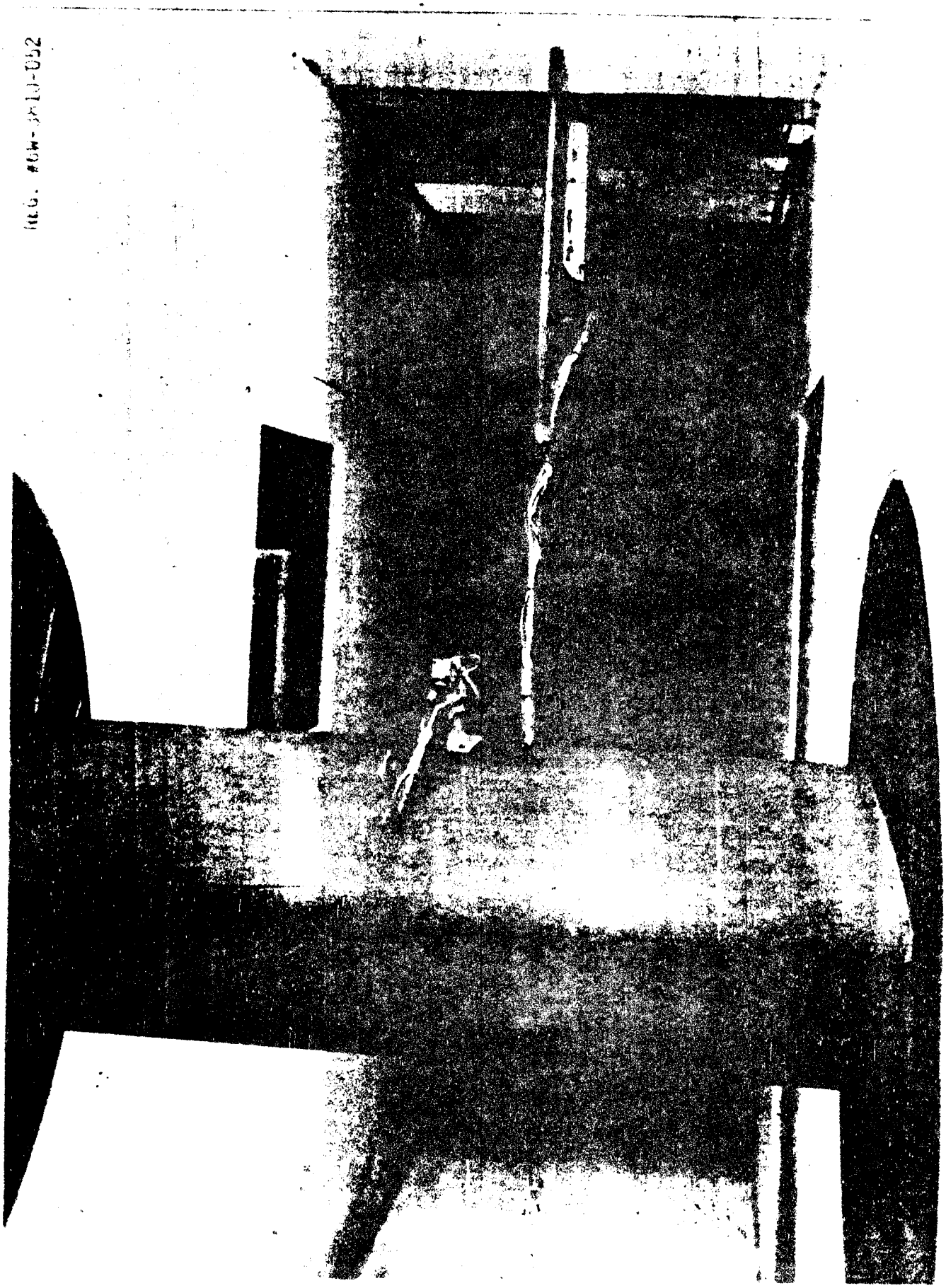

FIGURE 100

BOEING P3.117

FIGURE 101

BOEING P3.118

CHAPTER 4. SUBSONIC WING DESIGN

CHAPTER 4. SUBSONIC WING DESIGN

4.1 STRAIGHT WING CONCEPTS

The pioneers of manned flight began their investigations with wings having essentially constant sections. Not until the early 1900's did experimentalists begin to systematically study airfoil sections as a separate subject. But an understanding of the essential characteristics was not achieved until after 1910. Since that time, the fundamentals of straight wing design have remained essentially unchanged.

4.1.1 Definitions and Terminology

Representative straight wing planforms are shown on Figure 4.1. The simplest is the rectangular wing of constant section (Fig. 4.1a). Also often used is a wing having taper (Fig. 4.1b). For these two planforms, essential aerodynamic parameters are defined as follows:

Reference Area

$$S = b \cdot c_{AVG} \quad , ft^2$$

Aspect Ratio

$$AR = b / c_{AVG}$$

Taper Ratio

$$\lambda = \frac{c_{TIP}}{c_{ROOT}} \qquad (4.1)$$

Mean Aerodynamic Chord

$$\bar{c} = \frac{2}{3}\left(\frac{1 - c_{ROOT} \cdot c_{TIP}}{c_{ROOT} + c_{TIP}} \right) \quad , ft$$

Average Chord

$$c_{AVG} = \frac{c_{ROOT} + c_{TIP}}{2} \quad , ft$$

TRAPEZOIDAL PLANFORM CHARACTERISTICS

The mean aerodynamic chord is that part of the wing which gives pitching moment characteristics representative of the entire wing. The principal geometric ratios are aspect ratio, AR, representing the span to chord ratio, and the taper ratio. Note on taper ratio that a smaller number indicates more taper. The performance of the wing depends on the airfoil sections used for the wing and on the parameters denoted in equation 4.1.

The planform may also be curved. This is seldom done because of manufacturing costs. The most benefit in having curved leading edges is achieved when the chord distribution varies elliptically with span, as shown on Figure 4.1c. A notable example of this kind of planform is the British Spitfire fighter of World War II. The advantage of this kind of planform will be discussed later.

The lift of the wing can be related to the lift arising along each section of the wing (see Figure 4.2). For the section A-A shown, the local lift will be :

$$l_{AA} = qc \int_0^1 (c_{p_l} - c_{p_u})\, d(x/c) \qquad \text{(eqn 2.7)}$$

$$= qc\, \overline{\Delta C_p} \qquad (4.2)$$

where $\overline{\Delta C_p} = \int_0^1 (c_{p_l} - c_{p_u})\, d(x/c)$

Defining the local lift coefficient,

$$c_{l_{AA}} = \frac{l}{qc} = \int_0^1 (c_{p_l} - c_{p_u})\, d(x/c) = \overline{\Delta C_p} \qquad (4.3)$$

For the entire wing, the lift is the spanwise integral of local lifts:

$$L = \int_{-b/2}^{b/2} l(y)\, dy$$

$$= b/2 \int_{-1}^{1} l(y)\, d\left(y/b/2\right)$$

Defining $\eta = y/b/2$, and using equation 4.3,

$$L = b/2 \int_{-1}^{1} q\,(c\,c_\ell)_\eta \, d\eta$$

$$L = q\,b \int_{0}^{1} (c_\ell c)_\eta \, d\eta \qquad (4.4)$$

Since $C_L = L/qS = \frac{L}{qb\,c_{avg}}$

$$C_L = \frac{1}{c_{avg}} \int_{0}^{1} (c_\ell c)_\eta \, d\eta \qquad (4.5)$$

Figure 4.2 shows how this "span loading" curve representing equation 4.5 can be expressed in three different ways, either to give (C_L C_{avg}), to give C_L, or such that the integral is unity. Any of these three forms will show the spanwise distribution of local lift, which will be of important later.

In a similar fashion, the local airfoil profile drag can be integrated to yield the profile drag of the wing:

$$D_p = q\,b \int_{0}^{1} (c_{d_p} c)_\eta \, d\eta$$

$$C_{D_p} = \frac{1}{c_{avg}} \int_{0}^{1} (c_{d_p} c)_\eta \, d\eta$$

where the subscript "p" denotes profile drag.

Unfortunately, the profile drag is not the only drag component created by the wing. A second term exists, which may be as large or larger than the profile drag. This term, induced drag, must be fully understood for successful wing design.

4.1.2 Induced Drag

When a wing has less than infinite span, an additional drag term occurs. This term was named "induced drag" by Max Munk in 1921, because the equations by which it is described are analagous to those for electromagnetic induction. There are two widely held beliefs about induced drag:

(1) Induced drag is inversely dependent on aspect ratio; the higher the aspect ratio, the lower the induced drag, and,

(2) Induced drag is a minimum when the spanwise lift distribution (see Figure 4.2) is elliptic.

Both statements are incorrect, and the aerodynamicist who realizes that fact will have a better understanding of wing aerodynamic optimization. Before revealing the error of the statements above, it is necessary to provide an explanation of induced drag.

Figure 4.3a shows a rectangular wing with each section having the same lift. In that case, potential flow theory states that the lift is the result of a U-shaped vortex which is imbedded in the wing and trails downstream at the tips. The strength of that vortex is denoted as its circulation, Γ:

$$\Gamma = \frac{L}{\rho V b} \qquad (ft^2/sec) \tag{4.7}$$

where L = lift in lbf
ρ = density in lbm/ft^3
V = velocity in ft/sec
b = wing span in ft

and, since $C_L = L/qS$, the circulation can also be expressed as

$$\Gamma = \frac{C_L V C_{avg}}{2} \tag{4.8}$$

where C_L = wing lift coefficient
V = velocity, ft/sec
C_{AVG} = average chord, ft

Note that the effect of the "horseshoe" shaped vortex will be to displace a mass of air downward behind the wing. The momentum of this displaced air will equal the lift being generated.

Instead of constant circulation arising from one vortex, suppose there were several vortex elements adding up as shown in Figure 4.3b. Then the circulation would be additive on the wing, and the lift would be the result of the sum of all the circulations. The pattern in Figure 4.3b would cause the most lift at the centerline (Γ_R), with the lift the least at the tip. This situation is representative of what occurs on a wing of finite span; at the tip, the higher pressure air from the lower surface comes around to the lower pressure region on the upper surface. The result is a fall off in lift towards the tip and formation of a strong vortex core at the tip of the wing. This results in a loss in lift per unit span, relative to the infinite wing. But the loss in lift is not the most serious consequence of this shed vorticity.

For any part of the wing, the presence of the vortex lying in the wing plane generates an upflow ahead of the wing and a downwash behind the wing, as shown on Figure 4.4. This velocity is denoted w, and is termed the downwash velocity, because at the airfoil's aerodynamic center it is downward directed, and becomes twice as large in the downward direction aft of the wing. At the airfoil quarter chord, the apparent wind direction is the vector result of free stream velocity V and w. The section lift, l_R is generated by the circulation normal to the apparent wind V_R. However, the forces relative to the direction of motion as denoted by the true wind axis now have both a lift and a drag component:

Induced angle

$$\phi = \tan \frac{w}{V}$$

Induced lift

$$l = l_R \cos\phi \qquad (4.9)$$

Induced drag

$$d_i = l_R \sin\phi$$

Thus, there is a drag term induced by circulation from the lift term.

Usually the ratio w/V is small enough that small-angle approximations can be used. Also, the induced drag for the complete wing is

dependent on the velocities induced all along the span and by the nature of the change in local circulation. This derivation is complex (see Ref. 4.1), but finally leads to:

$$D_i = \frac{1}{V} \int_{-b/2}^{b/2} L(y)\, w(y)\, dy \qquad (4.10)$$

Where D_i = induced drag, lbf
V = true velocity, ft/sec
$L(y)$ = local lift, lbf
$w(y)$ = local downwash velocity, ft/sec
y = spanwise dimension

Since $L(y) = dL/dy = \rho \Gamma(y) V_\infty$

The result is finally

$$D_i = \frac{\rho}{4\pi} \int_{-b/2}^{y=b/2} \int_{-b/2}^{y'=b/2} \Gamma(y') \frac{\partial \Gamma(y')}{\partial y}\, dy\, \frac{dy'}{y'-y} \qquad (4.11)$$

where ρ = density in lbm/ft^3

$\Gamma(y)$ = local circulation in ft^2/sec

This is the complete equation for induced drag, with the double integral representing the fact that a change in vorticity at point y affects the circulation and downwash at point y'.

This equation was achieved in the early 1900's, and considerable effort was done to understand its practical applications. One of the principal investigators was Trefftz (Ref. 4.2). Recalling that the early 1900's were pre-digital computer, many complex integrals were approached from an analytical point of view. Trefftz first realized that if the circulation were elliptical in variation with span, namely,

$$\Gamma(y) = \Gamma_R \sqrt{1-(y/b/2)^2} \qquad ft^2/sec \qquad (4.12)$$

where Γ_R = circulation at the wing root,

Then the downwash would be the constant along the span:

$$w(y) = \frac{\Gamma_R}{2b} \qquad ft/sec \qquad (4.13)$$

Since $L = \rho V \int_{-b/2}^{b/2} \Gamma(y)\, dy = \rho V \Gamma_R\, b\, \pi/4$

then $$w = \frac{2L}{\pi \rho V b^2} \qquad (ft/sec) \qquad (4.14)$$

and finally

$$\boxed{D_i = \frac{1}{\pi q}\left(\frac{L}{b}\right)^2 \qquad lbf} \qquad (4.15)$$

where L = total lift ~ lbf

b = span ~ ft

q = dynamic pressure ~ lbf/ft^2

Equation (4.15) is the classical expression for induced drag. It applies for a wing whose distribution of circulation with span is elliptic. Note that the induced drag depends only on lift, span, and dynamic pressure. Aspect ratio is not a factor in induced drag. At a given aircraft weight, speed and altitude, an increase in span will reduce induced drag. Of course, equation 4.15 can be rearranged to include aspect ratio, but the point remains that only span among the wing parameters affects induced drag. This has ramifications on "aspect ratio" studies which are often conducted on airplane programs; this will be discussed later.

After many other analytical descriptions of the relationship between local circulation and span, Trefftz came to the conclusion that the elliptic variation of circulation stated by equation 4.12 not only results in constant downwash, but also results in the least value of induced drag.

Subsequent investigation has modified that conclusion. Equation 4.11 reveals that induced drag arises when the local circulation changes with span, that is, when vorticity is shed along the span. Indeed, if the circulation were constant, then there would be no induced drag. Trefftz' conclusion is correct for wings having continuously changing span loading, but for span loadings which change discontinously, or other than elliptically, the induced drag can be more or less than for the elliptically loaded wing.

To account for these variations, it is customary to define a more general form of equation (4.15),

$$D_i = \frac{1}{\pi q e}\left(\frac{L}{b}\right)^2 \qquad (4.16)$$

where e = efficiency factor relative to elliptic loading.

For the elliptic loaded case, e = 1. For all other cases of smoothly changing circulation on a single surface airfoil, e is less than 1. Typical values are in the range of 0.93 to 0.96 for wing alone, but drop to 0.80 to 0.85 for the complete jet aircraft at cruise conditions.

However, for certain kinds of discontinous loadings, e can become larger than one, and consequently the induced drag will be less than the elliptic case. Figure 4.5 shows the kind of discontinuity required. A vertical fence which alters the wing loading discontinuously can reduce the $\partial\Gamma/\partial y$ term in equation (4.11). The discontinuity does not cause a corresponding gain, because in reality it is matched by the same increase in the vertical plane on the fence. Note that the discontinuity will have the most benefit where $\partial\Gamma/\partial y$ is large, which occurs near the tip. Note also that an underwing fence will carry a net load outboard when it is below the wing, but inboard when it is above the wing. This characteristic is further described in Ref. 4.3. Use will be made of this concept in subsequent discussions of nacelle installations and of winglets.

Most airplane drag accounting is done using drag coefficients, for which equation 4.16 becomes;

$$C_{D_i} = \frac{D_i}{qS} = \frac{D_i}{q \cdot b \cdot C_{avg}} \quad -$$

$$= \frac{L^2}{\pi q^2 b^2 C_{avg} e}$$

but $L = C_L q S = C_L q b \cdot C_{avg}$

Thus $C_{D_i} = \frac{C_L^2 C_{avg}}{\pi b e}$

and since $AR = b/C_{avg}$

$$\boxed{C_{D_i} = \frac{C_L^2}{\pi AR e}} \qquad (4.17)$$

That is the equation most used to define "induced drag", and it does depend on aspect ratio. The misconception arises because induced drag coefficient is dependent on aspect ratio, but induced drag, which must be overcome by thrust, is dependent on span only and not aspect ratio.

4.1.3 Planform and Wing Section Aerodynamic Effects

The lift curve slope of a wing with finite aspect ratio is dependent on aspect ratio:

$$\frac{dC_L}{d\alpha} = 2\pi\left[\frac{AR}{AR+2}\right] \tag{4.18}$$

Thus, increasing aspect ratio makes the lift curve steeper, reaching the two-dimensional airfoil value at very large aspect ratios. Likewise the angle of attack where the two-dimensional lift is realized will be given by

$$\alpha_{wing} = \alpha_{airfoil} + \alpha_{induced}$$

$$= \alpha_{airfoil} + \frac{C_L}{\pi AR} \tag{4.19}$$

The drag coefficient will be given by

$$C_{D_{wing}} = C_{D_{airfoil}} + C_{D_{INDUCED}}$$

$$= C_{D_{P_{airfoil}}} + \frac{C_L^2}{\pi AR} \tag{4.20}$$

All these apply for the case of an elliptically loaded wing. They show that the principal effect of finite span is to require the wing section to operate at a higher angle of attack relative to freestream and to carry an additional drag penalty.

Taper ratio has a small effect on the wing's performance. If the wing is kept flat, and the section is held constant, then the least induced drag is realized at a taper ratio of about 0.4, where the penalty is only about one percent. An alternative would be to have the airfoil be of constant nondimensional section, and vary the airfoil chord elliptically (see Figure 4.1c). In this case, the section load, $C_l C$, will vary elliptically and the induced drag will be that for the elliptically loaded wing. This causes considerable manufacturing cost, however, and has rarely been done because of the small offsetting gain in performance.

So far in the discussion of the straight wing, the airfoil sections have all been considered to be in a flat plane, that is, to have no twist. For the wing with infinite span, all sections would be operating at the same angle of attack. When the wing is limited in span, a change in upwash occurs that affects the local angle of attack. Figure 4.6 shows that the flat wing will overload in the outboard region. The wing sections must be given washout (nose down twist) in order to return to a constant section lift. For aspect ratios of eight or so, typical washout for an untapered wing would vary almost linearly from zero at the wing root to about one degree of nosedown twist at the tip.

A combination of taper and twist can also be used to achieve the desired elliptical curve to $C_l C$. Taper will reduce the local chord outboard, and twist can be used to make the final adjustment in section lift to achieve the desired elliptic shape. However, the twisted, tapered wing is quite expensive to build. Since most light aircraft operate at quite low lift coefficients (0.2 or so) and the induced drag is low, they typically employ a flat wing of constant chord or an outboard taper, but do not bother with twist.

The third means to produce an elliptic loading curve would be to use "aerodynamic" twist, that is, reduce the airfoil section camber outboard. This is frequently done, and reduces C_l at the same local upwash. Typically, a NACA section will be called out from root to the point where taper begins, resulting in a wing of constant section, then another NACA of reduced camber at the tip:

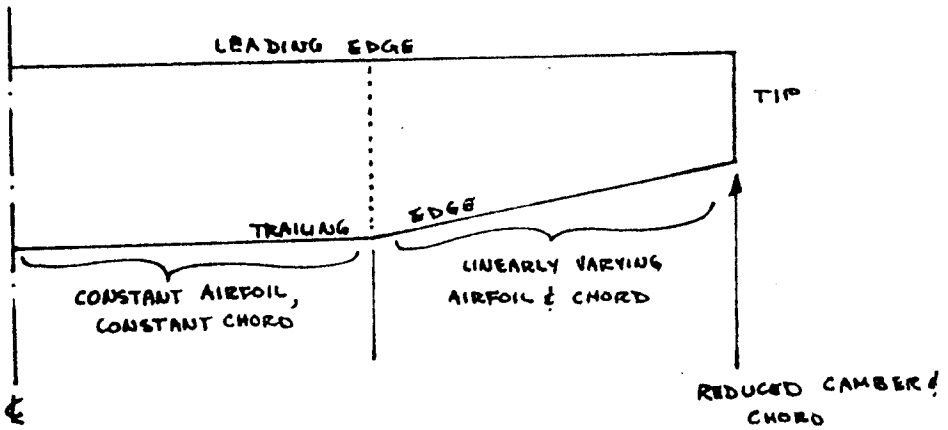

So far, only the isolated wing has been examined. Mounting the wing on the body should introduce major changes in the wing's aerodynamics. The answer is mixed, and the effects of the body on the wing are not very well understood. Consider the progression of increasing body sizes shown on Figure 4.7. A body of a small size will only slightly reduce the total lift. In particular, according to reference 4.4, the total lift can be approximated from the lift occurring on the outboard wing and from the body diameter to total span ratio:

$$
\left.
\begin{aligned}
C_{L_W}{}^* &= \text{lift on exposed wing} \\
\sigma &= D_{body}/b_{wing} \\
\text{Then} \quad C_{L_W} &= L_W{}^*(1+\sigma)^2 \\
&= \text{lift on exposed wing + "wing carryover" lift inside body} \\
C_{L_B} &= L_W{}^* \sigma (1+\sigma)^2 \\
&= \text{lift on body induced by wing} \\
C_{L_{W_B}} &= L_W{}^* (1+\sigma)^3 \\
\text{and} \quad \frac{L_B}{L_{W_B}} &= \frac{\sigma}{1+\sigma}
\end{aligned}
\right\} \quad (4.21)
$$

As an example, for the 707 at $C_{L_{W_B}} = 0.45$,

$$
\begin{aligned}
\sigma_{707} &= 0.085 \\
L_W{}^* &= 0.352 \\
L_W &= 0.414 \text{ (wing carryover is 0.062)} \\
L_B &= 0.035
\end{aligned}
$$

and the body is generating almost 8% of the total lift. In case (c) of Figure 4.7, the lift on the exposed wing will be much less, but the formulas of 4.21 show that more lift will be carried by the body. There will be a net loss in total lift, however, since it is obvious that when the body diameter equals the wing span, there will be no lift at all.

The body also has an effect on induced drag, according to theoretical considerations. Reference 4.5 concludes that downstream of the wing and body, the trailing vortices and resulting downwash will have come to equilibrium in a plane perpendicular to the flow direction called

the "Trefftz plane", and the effective span will have been reduced by

$$b^2_{effective} = 1 - D^2/b^2$$

Since induced drag is dependent on $1/b^2$, the net result will be an increase in induced drag. This effect has not been demonstrated experimentally, and is typically ignored in comparing experimental results to elliptic induced drag. More will be said of this in Chapter 5.

Another effect of the body is related to the vertical placement of the wing and body. Consider the case of Figure 4.8a, where the wing is in the middle of the body. Typically, the wing lower surface will have a net downward loading, giving a net reduction in total span loading. The wing net lift will blend smoothly with the body lift as shown. However, suppose the wing were placed on top of the body such that its upper surface was exposed, as shown in Figure 4.8b. In this case, the wing upper surface lift carries over onto the body, but the lower surface download terminates at the body side. The result is a discontinuity in span loading at the body side.

Three-dimensional analysis computer programs will yield exactly the result of Figure 4.8b, and experimentally, there is always a strong vortex shed by the wing-body intersection indicative of a span loading discontinuity. On the other hand, potential flow theory suggests that the lower wing surface lift of Figure 4.8b will carryover onto the body and the discontinuity in lift will disappear. Whether or not the jump in span load exists for the partially exposed wing has neither been proven nor disproven experimentally. Fortunately, this has little bearing on the low wing mounted configuration typically used by commercial transports because they are more like the mid-wing case. Tailoring techniques for the wing body intersection will be dealt with in Chapter 11.

4.1.4 Wing Sweep Aerodynamic Effects

The two-dimensional airfoil data of Figure 2.17 suggest that a wing with a 10% thick TR 7 (707 section) would achieve a critical Mach number of around 0.72 at a C_L of 0.6. How then can a higher speed be achieved? The well-known answer is to apply sweep to the wing. Consider the rectangular wing of aspect ratio = 5 shown on Figure 4.9. If the wing were pivoted to an angle Λ, keeping the same airfoil and structural aspect ratio, ℓ/s, a change in flow conditions would arise. The primary effect is denoted by the vectors V, V_N, and V_S. The velocity V_S will have no effect on the aerodynamic pressures developed by the airfoil section S; the pressures will be determined by V_N. Since

$$V_N = V \cos \Lambda$$

and

$$\frac{V_N}{a} = \frac{V}{a} \cos \Lambda$$

Then $M_N = M \cos \Lambda$

or $M_{swept} = M_{unswept}/\cos \Lambda$

That is, the effect of sweep is to increase the Mach number the swept wing operates at for the same airfoil section. At 30^0 of sweep, the TR 7 airfoil would provide a critical Mach number of 0.83, which is in the area where current subsonic transports operate. For the simple rectangular planform of Figure 4.9, it can also be shown that:

Simple Sweep Formulae

$$C_{L_{SWEPT}} = C_{L_{UNSWEPT}} \cos^2 \Lambda$$

$$D_{INDUCED,\,SWEPT} = D_{INDUCED,\,UNSWEPT} / \cos^2 \Lambda$$

$$C_{p_{SECTION\ "C"}} = C_{p_{SECTION\ "S"}} \cos^2 \Lambda$$

$$\left(\frac{dC_L}{d\alpha}\right)_{SWEPT} = 2\pi \left[\frac{AR}{AR+2}\right] \cos \Lambda \qquad (4.23)$$

$$(AR)_{SWEPT} = (AR_{UNSWEPT}) \cos^2 \Lambda$$

$$t/c_{SECTION\ "C"} = t/c_{SECTION\ "S"} \cos \Lambda$$

NOTE: FOR CONSTANT STRUCTURAL PLANFORM

The trend of each of these aerodynamic characteristics with sweep is illustrated on Figure 4.10, for a structural aspect ratio of 5 and for a 10% TR 7 section. Note that the swept wing is achieved by

rotating the wing so that the airfoil section normal to the leading remains unchanged; achieving the swept wing by simply shearing the planform will not work. Sweep brings a mixture of good and bad aerodynamic effects, as follows:

(a) Critical Mach Number - The principal motive for sweep is to increase the Mach number at which drag rise occurs. This applies for wings of moderate thickness (8% or more), moderate aspect ratio (6 or more) and moderate lift coefficient (0.3 or more). High critical Mach number can also be achieved by low lift coefficients and thin wing sections; that will be discussed in Chapter 7. Figure 4.10 shows that 30^0 of sweep results in a cruise Mach number capability in excess of 0.80.

(b) Lift curve slope - Another advantageous result of sweep is that the wing lift curve slope is reduced. At 30^0 sweep, the lift curve slope is less than 85% of the unswept value. This has two advantages. The first is in passenger ride comfort. The response of an airplane to a gust of a given magnitude is directly proportional to its lift curve slope. Straight wing aircraft respond noticeably harder to turbulence than do swept wing aircraft. In fact, a serious obstacle to STOL commercial flight is passenger reaction to the ride, based on an Eastern Airlines trial of the Dassault-Brueget 914.

The second benefit is also related to gusts. The airplane's structural design envelope is defined by a "V-n" diagram, where V is velocity and n is the load factor, or "g's", given by n = L/W. Of course, for normal flight, n = 1. The FAA regulates the V-n design envelope:

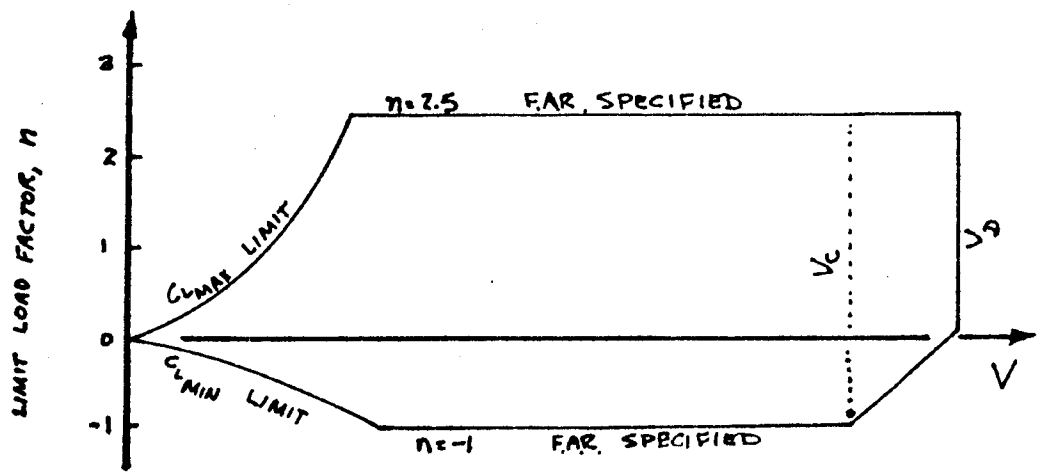

The structural design must be such that the airplane can be operated anywhere within this envelope without structural failure.

Superimposed on this diagram is one caused by gusts. The FAA regulations specifically state the size of the gust in feet per second at various points in the V-n envelope:

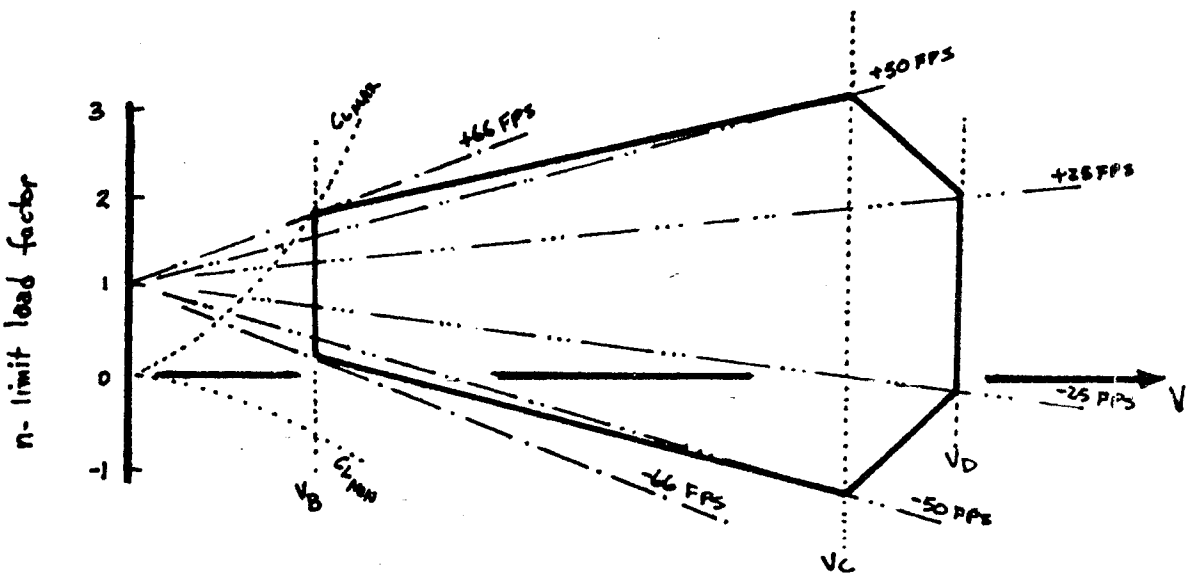

The value of n at any of the defining CORNERS is given by:

$$n = 1 + K U_{gust} \left(\frac{dC_L}{d\alpha}\right)_{WING} \qquad (4.23)$$

where K represents a series of terms based on aircraft weight, wing area, gust characteristics and aircraft speed. The point is that the wing lift curve slope determines directly the corners of the gust design envelope.

The wing design must be such to satisfy the greater of the maneuver and gust envelopes. Figure 4.11 shows two cases. A wing with no sweep on Figure 4.11a is seen to have parts of the maneuver envelop exceeded by the gust envelope. This wing will be said to be "gust designed", and will bear a structural weight greater than that for the normal envelope. Figure 4.11b shows the same wing with 30° sweep;

the reduction in $(dC_l/d\alpha)$ due to sweep has brought the gust envelope entirely within the maneuver envelope. The wing is now said to be "strength designed" and will have a smaller structural weight.

Airfoil technology today would now allow new airplanes to have a wing of only 10^o to 15^o sweep, and still cruise at M = 0.80. However, gust design weight penalties and passenger ride comfort arising from decreased lift curve slope are two important reasons why new airplane designs still employ about 30^o of wing sweep.

(c) Flutter Speed - Flutter speed increases with sweep at a rate slightly greater than $1/\cos \Lambda$, up to sweep angles of 50^o to 60^o. Above that, flutter speed begins to decline rapidly with sweep. The trend of increasing flutter speed with sweep applies only when structural aspect ratio is held constant, of course.

Those are the beneficial effects of sweep. Returning to Figure 4.10, the adverse effects of sweep are:

(a) Induced Drag - At constant structural aspect ratio, increasing sweep reduces the aerodynamic span. According to equation 4.16, this results in an increase in induced drag (not necessarily in induced drag coefficient). For 30^o sweep, the induced drag will be increased by about 30%.

(b) Aspect Ratio - Because of the reduction in span and simultaneous increase in streamwise chord, the aerodynamic aspect ratio will be reduced by sweep at constant structural aspect ratio.

(c) Lift Coefficient - Sweep reduces the lift coefficient from the unswept wing value. For the same weight, the wing will have to be made larger, introducing performance penalties because of increased weight and increased friction drag.

(d) Streamwise Airfoil Thickness - Sweep reduces the airfoil thickness as measured in the streamwise direction. This is really not a penalty when viewed in the context that the structural aspect ratio has not changed. But in sizing studies, the streamwise airfoil thickness is quoted, making sweep appear to penalize airfoil thickness.

Sweep introduces other effects such as reduced $C_{l_{max}}$ and nonlinear stability and control effects. These will be dealt with in later sections.

The discussion above relates to the effects of so called "simple sweep theory". The discussion below concerning real wings will show that in the real case, things are not "simple". In fact, the real wing will be found to be very complex.

4.2 WING DESIGN CHOICES

The following discussion will emphasize the swept wing, because in general it represents a more challenging design case than the straight wing. The techniques developed for the swept wing will be applicable to the straight wing, however. This section will deal with planform design choices, wing section tailoring, the design sequence, and analytical procedures.

4.2.1 Wing Planform Choices

The general planform of the swept wing is detailed in Figure 4.12. Note that there is a basic trapzoid , a leading edge modification called a glove, a trailing edge extension called a yehudi and a raked tip modification. There may be no leading or trailing edge modifications, or there may be more than one. The 727, 737 and 747 all have a glove, named because early applications "gloved" the modification over the original wing; the glove on the 747 extends all the way to 70% semispan. All Boeing airplanes have a yehudi, named (according to Boeing lore via George Schairer) after Yehudi Menuhin, because no one could understand how the trailing edge extension improved the B-47 aerodynamics, just as no one could understand how Menuhin played the violin as well as he did. The 707-300 Advanced has two yehudis, that is, two trailing edge planform breaks before the basic trapezoid is reached.

For planforms with gloves or yehudis, a controversy invariably arises as to what the reference area should be. Various formulas attempt to include the planform breaks in some manner. However, the calculation of induced drag in the Trefftz plane downstream of the wing is completely insensitive to planform. Also, reference area does not ultimately matter in the calculation of airplane performance, since it disappears when lift and drag are calculated. For these reasons, the basic trapezoid has been used most often in recent years to define the wing geometrical properties.

Formulas for aspect ratio (AR), taper ratio (λ), average chord (C_{ave}), mean aerodynamic chord ($\bar{c}$) and spanwise position of $\bar{c}$ ($\bar{y}$), all based on the basic trapezoid, are given on Figure 4.12.

Span Load Shape - A key decision which impacts the planform selection process is the spanwise distribution of load. The aerodynamic ideal would be to have an elliptical load distribution at cruise, which is a load factor, n, of one. There are two important reasons why production wings never have an elliptic load distribution. The first is displayed on Figure 4.13 and involves the structural design of the wing.

Suppose the wing were designed to have an elliptical load distribution at the cruise condition where $n = 1$ (i.e., $L = W$). Recalling Figure 6, the section lift change with α, $dC_L/d\alpha$, is higher for the outboard sections than for the

inboard sections. Consequently, as the wing angle of attack is increased and n goes to the 2.5 "g" design condition, the outboard wing will load up much more than the inboard wing, as shown on Figure 4.13a. The aerodynamic result is a wing at n = 2.5 with a spanwise center of lift located relatively far outboard.

If the initial n = 1 load were triangular, as shown on Figure 4.13b, then at n = 2.5, the spanwise load would have its centroid located nearer to the wing root. Obviously, the triangularly loaded wing would be considerably lighter than the elliptically loaded wing.

The triangularly loaded wing does not necessarily carry an induced drag penalty, either. The formula,

$$D_{INDUCED} = \frac{1}{\pi q e}\left(\frac{L}{b}\right)^2 \qquad (4.16)$$

recognizes that the induced drag is altered by an efficiency factor, e. For the triangularly loaded wing by itself, e would be less than one; typically in the range of 0.92 to 0.97.

However, the wing does not act alone. The horizontal tail will have shed vorticity which will mix with that of the wing. The total induced drag will be that as measured in the Trefftz plane downstream of the aircraft where all vorticity has mixed together. Since the tail is typically downloaded, the tail span load reduces the wing span load over the extent of the tail span. If the wing load is triangular, then the effect of the tail will be to produce a combined span load which is more elliptic, as shown on Figure 4.14.

Trade studies will always show the slightly triangular load for the wing to be most optimum when the weight versus drag trade is considered. Figure 4.15 shows the cruise span loading of various current production aircraft; the curves may be used for initial design considerations.

Sweep and Airfoil Selection - Selection of the planform sweep requires first that an airfoil section or section technology level be chosen for the outboard wing. The choice of an airfoil for the wing is itself a major decision, and typically, exhaustive trade studies will be required to select the most appropriate airfoil type. For example, the 707-type airfoil has a low drag level and good subcritical lift capability, giving high values of $(L/D)_{max}$. But because of its relatively low drag divergence Mach number, a wing of only 8% t/c and having 35° of sweep will be necessary to insure 0.8 Mach cruise. Selection of the most recent supercritical airfoil would allow the wing to be 10-11% thick outboard with less than 30° sweep, resulting in a lighter wing. But the drag level of the wing could be higher,

and the $(L/d)_{max}$ may be less, except at the single Mach and C_l where the airfoil operates best. In other words, the most advanced section may produce too much of a point-designed wing. For reasons such as these, new airplane programs will in general emphasize airfoils which are more advanced than the 707/747 class, but not as advanced as the most recent TR-series airfoils.

Wing lift and drag characteristics as a function of outboard airfoil selection and wing sweep can be predicted by several methods from an estimate of the two-dimensional airfoil's performance. The essential steps are detailed in Reference 4.6. Easier to use is the RADEM computer program, Reference 4.7. The most important item these methods provide is an estimate of the sweep required to achieve a required speed capability and cruise lift coefficient for a stated airfoil technology and wing thickness. Figure 4.16 is an example of the "design space" of sweep versus wing thickness for TR38-1 at a wing lift of $C_L = 0.4$. The principal difference between the equations of Ref. 4.6 and 4.7 and the simple equations (4.22 and 4.23) is that the swept wing critical Mach number will not achieve the simple sweep value in the real case:

$$M_{CRIT_{SWEPT}} = \left(\frac{M_{CRIT_{2-D}}}{\cos \Lambda} \right) \xi \qquad (4.24)$$

Where ξ = sweep efficiency factor.

Experimental values of ξ are in the range of 0.93 to 0.96 for well-designed wings. There are several reasons why the real wing cannot achieve the Mach capability of the infinitely yawed wing of constant airfoil section (i.e., $\xi = 1$). First, the presence of the body generates a supervelocity, causing the wing to fly in a flow field which has a local Mach number greater than the freestream value. Second, the wing root will be thicker than the outboard sections and will cause supervelocities to be spread from the root to the outboard sections along Mach characteristic lines, thus increasing the supersonic flow outboard. (This will be described in further detail below). Third, the wing root airfoils may be so thick as to cause early drag rise. Fourth, the shock wave may sweep forward off the wing tip, thus causing an earlier drag rise. Fifth, for the tapered wing, the sweep of the shock along the 50 to 60% chord line will be less than the sweep of the quarter-chord line, and the sweep of the shock line tends to dominate drag rise. Thus the effective transonic sweep is less than the sweep of the quarter chord.

Even with the use of data such as that on Figure 4.16, the configuration aerodynamicist is not allowed to choose the wing sweep and outboard

thickness. At best, he can point out the sweep, thickness and Mach which would make the best use of the airfoil selected, as indicated by the "optimum use" point on Figure 4.16; this is where TR38-1 when swept 31.1° would convert its best airfoil C_l (=0.60) to a wing C_L of 0.40, under the assumption that the average outboard lift was 1.1 times the average lift over the entire span. Any other combination of sweep, thickness and wing lift coefficient selected from Figure 4.16 would not actually use TR 38-1, but a derivative of it scaled up or down.

The calculations above were performed as follows:

(1) $C_{l_{2D}} = 0.60$ for $M_{2D\ \text{DRAG DIVERGENCE}} = 0.776$ } TR38-1

$t/c_{2D} = 0.101$

(2) desired $C_{L_{WING}} = 0.40$

assume $\frac{C_{l_{OUTB'D}}}{C_{L_{WING}}} = 1.1$, since $C_{L_\omega} = C_{l_{AVG}}$

since $C_{L_{OUTB'D}} = C_{l_{2D}} \cos^2\Lambda$

then $\Lambda = \cos^{-1}\sqrt{\frac{(0.40)(1.1)}{0.60}}$

$= 31.1°$

(3) $t/c_{WING} = t/c_{2D} \cdot \cos\Lambda$

$= (.101)(\cos 31.1°) = 0.086$

(4) Assume $\varepsilon = 0.95$

$M_{CRIT} = (M_{DD}/\cos\Lambda)\,\varepsilon$

$= \frac{(0.776)(.95)}{\cos 31.1°} = 0.861$

For lack of more definitive information, a safe starting point would be the required wing C_L and the intended cruise Mach number. Available TR-series airfoils could then be surveyed to see which one best fit the requirements with a moderate sweep and thickness. For reasons described above, sweeps of 25^o to 30^o and outboard wing thickness of 8% to 10% seem to be desirable.

Another consideration affecting airfoil choice is the margin between cruise and buffet. Figure 4.17 shows a typical cruise Mach critical boundary versus C_L. Along this boundary the wing must be free of buffet due to shock-induced separation. Furthermore, the wing must be capable of providing some maneuver margin before buffet occurs. Although not specifically called out in the FAR, most airlines require a 1.3g margin to buffet, which corresponds to a 40^o bank. The 707/747 class of airfoils easily provide this capability, because of the nature of C_L versus Mach given by their gradual separation. The most advanced TR airfoils may give little warning from C_L for M_{CRIT} to $C_{L_{buffet}}$ (Figure 4.17b) because of their tendency to be point designs.

The 1.3g requirement is not a hard one; some airlines currently require only 1.2 g's to buffet, which corresponds to a 34^o bank. However, the design of a new wing should not allow the buffet margin to drop below 1.3 g's. To do so would reduce future growth capability. The airfoil section choice is the most direct way to influence the margin between cruise and buffet.

The remaining major considerations regarding sweep selections are stability and control, high lift and passenger ride quality. As metnioned above, ride quality improves with increased sweep, although no hard rule exists on $dC_L/d\alpha$ for acceptable ride. High lift gets poorer with increased sweep, this will be discussed further in Chapter 6. Increasing sweep aids some aspects of stability and penalizes others; these will be discussed in Chapter 8.

After trade studies have been run and the sweep has been selected, one choice would appear to remain. That is, should the wing be swept forward or aft? Almost unanimously, wings have been swept aft. But aft-swept wings cause the boundary layer from the inboard wing to sweep outboard and cause earlier separation of the outboard sections. The forward-swept wing would run the boundary layer flow toward the root, allowing the wing tip to operate at higher lifts. However, the forward-swept wing requires increased angle of attack relative to the root, in contrast to the aft-swept wing which washes out the outboard wing. The forward-swept wing will develop a much further outboard center of lift, resulting in a higher wing structural weight. Finally, the forward-swept wing just doesn't look right, and that is a powerful design constraint for commercial aircraft.

Wing area, span and aspect ratio - Once the sweep has been selected, then the span can be chosen. Wing area will have already been specified, since it helped determine the cruise C_L of the wing, which in turn had a bearing on the airfoil selection and thus the sweep. Span will be determined by two limiting factors, first, an airline "gate" requirement based on ground handling considerations, and second, wing weight. The first constraint is quite arbitrary and will usually change several times during the life of the project. The second is based entirely on the trade between reduced induced drag as span increases versus the increase in wing structural weight. This choice can be made reliably from trade studies. Once the span has been chosen, then the aspect ratio can be calculated. But remember that induced drag is totally unrelated to aspect ratio; that is why the preceding discussion dealt with span.

Upper surface isobars - The wing upper surface isobars must be considered before the selection of wing taper can be discussed. Suppose the wing upper surface isobars were as shown on Figure 4.18a, where all isobars, including the shock wave, lay exactly along wing span lines of constant % chord. At first, this would seem to be a very desirable isobar pattern, because all sections of the wing would be working in harmony. However, for reasons which will be discussed in Section 4.2.2, the crest dividing forward versus aft facing wing surfaces will move forward in the wing root. This causes a large degree of suction pressure from the wing supersonic flow ahead of the shock to occur near the side of the body, and the drag would be large. A desirable feature of the isobar pattern would be that separation would likely occur all along the span, causing primarily a drag increase with little change in pitching moment.

A much better isobar pattern would be to sweep the isobars forward in the root, so that the shock wave followed the crest. This kind of pattern and resulting section lift versus span is shown on Figure 4.18b. The design shown there further alleviates the shock wave in the root so that it is gone at the body side. Probable onset of separation would occur near midspan, causing slight pitchup in addition to a drag rise.

Suppose the section lift were spread even further outboard, as shown on Figure 4.18c. This kind of span loading will be very undesirable, because the outboard wing is working far too hard, and premature drag rise and severe pitchup will occur. Clearly that kind of isobar pattern is to be avoided.

The opposite extreme is shown in Figure 4.18d, where the wing root is highly loaded. Characteristically, the shock wave will unsweep as it approaches the body side, becoming less swept. The result will be premature drag rise and a very poor critical Mach number.

An alternative to Figure 4.18b is an isobar pattern whereby the shock wave system bifurcates near the body, as shown on Figure 4.18e. This can have the identical section lift distribution as 4.18b. In addition, the double shock system can actually have less wave drag than a single shock. Most Boeing production aircraft have a shock pattern like 4.18e.

Taper ratio - Isobar patterns will be described in further detail below, but Figure 4.19 repeats the most desirable shape of C_l versus span from Fig. 4.18. From that curve, and from the span loading curve chosen previously, the wing chord versus span can be selected. Figure 4.19 illustrates the process:

at a given spanwise station,

(a) obtain $\frac{c_\ell c}{c_{avg}}$ from span loading curve

(b) obtain C_ℓ from C_l versus span curve

(c) obtain C_{ave}:

$$C_{ave} = \frac{S_{ref}}{b}$$

where S_{ref} = wing reference area

b = wing span

(d) the local chord value will be

$$c(\eta) = \left(\frac{c_\ell c}{c_{avg}}\right)_\eta \frac{c_{avg}}{c_\ell(\eta)}$$

(e) compare the desired section chord versus chord values for various taper ratios to select the best fit.

Note that, with the triangular span load shown on Figure 4.19, taper ratios around 0.2 to 0.25 will be preferred over higher taper ratios. Note also that the chords shown are for a trapezoidal wing.

Obviously, planform taper is indicative of where the spanwise centroid of lift will occur at the n = 2.5g design case. A wing with little taper ($\lambda \approx .5$ or higher) will load up badly on the outboard wing because of large chord. A wing with maximum taper ($\lambda = 0$) will load up the least. So taper ratio becomes an important parameter in wing weight trade studies.

glove - Figures 4.18 and 4.19 indicate two potential design difficulties for the trapezoidal wing. First, it is very desirable to have forward isobar sweep in the wing root (Fig. 4.18b and 4.18e). This translates into a requirement to have less section lift near the side of body. The section lift curve of Figure 4.19b shows the trend for the lift coefficient at the body side to be a reduction of about 40% from that of the outboard sections.

Figure 4.19c shows that this means a longer chord is desired in the wing root. The chord extension over the basic trapezoid is best applied in this case as an extension of the leading edge. Figure 4.20 describes the principal effects of the leading edge glove. All current Boeing production commercial aircraft have leading edge gloves. Gloves were added to the existing 707-120 wing to produce the 720B wing and later the 707-300 Advanced wing. The 720B was Boeing's answer to the competitive threat of the higher cruise speed of the Convair 880. Adding the glove to the 707-120 wing increased the critical Mach number by 0.02. This gloved 720B wing with 3° less sweep then became the baseline from which the 727 wing was derived.

The 707-320B wing had a root insert as well as a glove added to the 707-120 wing. The net effect of both was a gain of 0.02 in Mach for $(L/D)_{max}$ and 2% in $(L/D)_{max}$. The gain in Mach number can be attributed to the glove. The 747 wing glove extends to the outboard nacelle at 70% semispan. It too was added to increase the wing critical Mach number.

Since a properly designed glove pulls the shock wave forward in the root and thus increases the speed capability of the root, the glove may be used to increase the wing root thickness. Whether t/c increases or not is dependent on the actual changes in thickness and chord.

The main detriment of the glove is to increase pitchup at stall. The glove moves the center of pressure for the inboard airfoils forward. When the outboard airfoils separate, the wing pitchup will be more severe. And when the glove leading edge angle exceeds around 42° to 45°, the situation is made much worse by appearance of a leading edge vortex. The inboard wing will now operate much like a delta wing and pitchup is made much more severe.

Since most new wings under design at Boeing have less sweep than the 727, a moderately sized glove should be considered as an option for any wing design problem. The glove may be able to provide increased wing root thickness for no penalty in cruise speed.

Gear stowage - The wing planform aerodynamically is considered completely satisfactory as either a trapezoid or with a glove as described above. There is no aerodynamic performance advantage to be gained by a trailing edge extension. The need for such an extension, termed the yehudi, arises primarily because of gear stowage requirements and secondarily because of structural reasons involving the location of the wing's elastic axis relative to the rear spar. The process begins by finding where the main gear must be, as detailed on Figure 4.21. Then two possibilities exist for stowing the gear. The usual method, that of a trailing edge extension, allows the gear to swing sideways to the body and be stowed in side the body. Since the gear post swings aft of the rear spar, an auxiliary spar or gear beam is required. The yehudi is simply the minimum aerodynamic fairing required to cover the gear beam. The other stowage concept shown on Figure 4.21 has the gear swing aft and be contained in a gear pod. Only Tupolev-designed Soviet aircraft have used this design. The landing gear tires must be quite small, usually a six-wheel truck, in order to keep the size of the gear pod down. The stowed position of the gear also penalizes wing flutter speed because the gear c.g. is aft. There is an offsetting reduction in OEW since the body pressure vessel is not interrupted for the gear well.

Aerodynamic considerations of yehudi versus gear pod are shown on Figure 4.22. The natural tendency of the yehudi is to unsweep the root isobars. This will have an adverse effect on speed performance. This tendency is offset by designing the yehudi such that little or no lift is generated by the yehudi (Figure 4.22b). In fact, the yehudi itself may be downloaded. In contrast to the glove, the yehudi cannot in general increase the root thickness, although a slight gain in rear spar depth arises because of its position on the airfoil chord. Since the yehudi is in essence merely an aerodynamic fairing, its effect on high speed performance is to add from one to three drag counts to the aircraft drag.

The aerodynamic effect of the gear pod, shown on Figure 4.22c, can be favorable to the wing drag rise, since the gear pod can act as an transonic "speed pod". However, gear pod studies show that the best designed gear pods add from three to nine counts of aircraft drag.

Because of design complexity, increased number of tires (which reduces dispatch reliability severely), flutter problems and drag level penalties, Boeing design has always chosen the yehudi over the gear pod. And for low winged transports, yehudis have usually been added because of landing gear constraints.

High aspect ratio wings - Most production wings have aspect ratios ranging from 7 to 9. Wings having higher aspect ratios, in the range of 11 or higher, may offer performance advantages due to a reduction in induced drag because of increased span. However, they may lose some or all of the increased performance to higher wing weight. In this case, special considerations are in order for the wing section choice.

Current production wings have outboard t/c values of 8% to 9% and trailing edge closure angles of 11^0 (707,727,747), 13^0 (737), 14^0 (DC-9) and 10^0 (DC-10). These kinds of airfoils produce relatively good drag levels due to their thinness and sharp trailing edges. A drag polar for these wings with AR = 8 would appear as shown on Figure 4.23.

For the high aspect ratio wing, an increase in rear spar depth would help offset the weight gain due to increased span. For example, wings of AR up to 12 are being reviewed by the new airplane groups; these wings have sections up to 10% thick with closure angles as high as 18^0. Figure 4.23 shows that the trade being made is to allow an increase in profile drag, which is more than offset by the reduction in induced drag. This trade must be done very carefully, in order to optimize the weight-drag trade.

4.2.2 Wing Section Choices

With the outboard airfoil chosen above, along with the geometric description of the planform, the task now becomes one of tailoring the wing contours to produce the intended performance. But first, the sources of drag of the wing must be understood.

Wing Section Drag - Figure 4.24 reveals the general nature of wing drag, by giving section drag versus span, $\frac{C_d C}{C_{ave}}$ versus η. First shown is the distribution of induced drag. Due to the nature of the shed vorticity and the resulting wing twist, most of the rearward rotation of the section lift vectors occurs inboard. In fact, the outboard 15% to 20% of a properly designed wing will actually be producing thrust, based on integration of its surface pressures. The integral of the area under the curve of Figure 4.24 will be the wing induced drag coefficient.

Figure 4.24b adds the viscous part of the drag, usually called the form drag. Note that there are two components; skin friction and pressure drag due to displacement effects. With the addition of form drag, the tip is no longer producing a net thrust.

Figure 4.24c completes the wing drag by adding the effects of the wing shock waves. There will be a major part due to wave drag and a smaller part due to viscous effects. Of course, at higher Mach numbers the separation effects will become increasingly larger. The configuration aerodynamicist's job is to see that none of the three drag sources on Figure 4.24 become excessive.

Upper Isobar Pattern - Having chosen the outboard wing section, the upper surface pressures are corrected by the local spanline sweep angle using equation 4.23. These become the isobar pattern for the wing, from about 40% semispan outward (the tip will be dealt with later). Figure 4.25 illustrates the process. Then, in the root region, the isobar pattern should be altered in one of several ways. First,

the isobars can sweep forward, merely bunching the outboard pressure levels forward so that the high negative pressures are well ahead of the crest of the wing. Second, the local pressure peaks can be allowed to increase. Both measures are intended to prevent the formation of a shock wave aft on the root airfoils. The second method, that of increasing local pressure peaks near the side of the body, is more effective since it further reduces the chance of subsequent re-expansion aft on the root airfoils. The third option (not shown) is to reduce the overall level of pressures in the root from those of the outboard airfoil sufficiently to eliminate the shock wave near the body. Usually this would result in too low lifts inboard, forcing the outboard wing to work too hard.

The specific trailoring done to the upper surface isobars in the root region is dependent on the planform, design mission and thickness properties required of the wing. Previous wings similar to the wing under design should be reviewed to gain an idea of the proper tailoring.

Once the desired isobar pattern has been drawn for the wing's upper surface, it becomes a principal guideline for the wing contour design.

Kuchemann Theory - In the early 1950's D. Kuchemann of the RAE published a description of the basic nature of the effects of sweep on isobars (Reference 4.8). It begins with a recognition of the effect of the vorticity lying in the plane of the wing as it crosses the centerline of the aircraft. Figure 4.26 shows how some of the vortex filaments leave the trailing edge, and how those who remain inside the wing bend to cross the vertical plane of symmetry. The nature of these vortices cause a distortion in both chordwise and spanwise directions to the distribution of lift.

As an example, consider the wing shown on Figure 4.27. The wing has a constant 9% thickness form, but local section camber and twist will be altered to satisfy the C_l and $\frac{C_l C}{C_{avg}}$ versus span shown on the figure. The most immediate item of note is the large increase in twist required near the centerline.

But the chordwise loading has also been altered by the nature of the velocity. Figure 4.28 shows how the camber must be varied along the span to preserve a constant upper surface isobar pattern. Of particular interest is the large negative camber required near the centerline. Figure 4.29 shows selected wing sections, where the unusual nature of the root airfoil is displayed. That airfoil is essentially upside down, with an upper surface that actually has a concavity. The unusual root airfoil design results from the way the wing vorticity behaves in the root region.

Figure 4.30 shows the calculated isobar pattern for the wing. Note how the upper surface isobar pattern is essentially along lines of constant percent chord. The super VC-10 wing was designed according to these principals; Figure 4.31 portrays its subcritical isobar pattern and the resulting cruise isobar pattern. Note the favorable position of the shock wave; it has more sweep than the wing outboard, sweeps forward in the wing root and disappears.

Outboard Wing - The Kuchemann technique chose to achieve the desired outboard isobars and span loading by having constant twist but continually changing the airfoil camber line. A much easier technique is to retain a constant airfoil section and use twist to achieve the desired span loading. If the taper ratio has been chosen properly, then the section C_l will be relatively constant over the outboard wing, and the twist necessary to achieve the desired loading will at the same time produce an acceptable upper isobar pattern. The proper twist can be found by analysis, as will be described in section 4.2.4 below.

Wing root airfoil design - The root design begins at the wing spanwise station where merely twisting the wing no longer produces acceptable upper surface isobars. From there inboard to the side of the body, both the thickness and camber of the wing will be altered.

The first general step in creating a successful wing root design is to move the position of maximum thickness forward, as shown on Figure 4.32a. Typically, the maximum thickness of the outboard section will be at about 40% chord. At the side of the body, the maximum thickness will have moved forward to about the 15% to 20% chord position. The previous Kuchemann wing example did not alter the location of maximum thickness, but at the same time, neither did it increase the maximum thickness.

For structural and fuel volume reasons, the wing must get thicker as it approaches the body. Figure 4.32b shows the relation of root t/c to outboard section t/c for current production wings. The ratio is typically 1.4 to 1.6, with maximum side-of-body less than 16% t/c. There are two reasons for this limit. First, as t/c increases, profile drag begins to go up, with a "knee" in the curve somewhere around 18%. Second, a trade study for a new wing on the 707-300 Advanced showed that wing weight was least at 18% t/c, and began to increase above that. The cause was that above around 18% t/c, the rear spar became so deep that stiffeners were necessary for the spar web.

The actual shape of the root sections will arise from the specified upper surface isobars and span loading, as described below in section 4.2.2. However, some historical trends should be noted. First, the Kuchemann root section of Figure 4.29 shows a large degree of negative camber, resulting in an airfoil with almost no upper surface curvature aft of x/c = 0.35. This root airfoil is repeated on Figure 4.33. Next shown is the 720B wing root. It also is straight from about 35%

chord. This wing root modification added about 0.02 to the critical Mach number of the 707-120 wing. Next is the 727 wing root airfoil. It too is similar in nature. Overlaid on the 727 root airfoil is the DC-10 side of body airfoil; the similarity to the 727 airfoil is striking. Finally, Figure 4.33 shows the 737 and 747 root airfoils. All the airfoils shown are similar in upper surface design philosophy aft of about 35% to 40% wing chord.

Why would the flat upper surface appear to be a good design practice? Figure 4.34 shows the tendency of secondary expansions to occur due to aft curvature on the root airfoil. This tendency is due to (1) the curvature sensed by the flow as it flows downward across the body, and (2) the way the wing circulation is concentrated in the wing root.

The point to be made is not that the only possible successful root airfoil will be devoid of curvature on its upper aft surface. Figure 4.35 shows the root airfoils of the 707-120, 707-300 Advanced, DC-8 and DC-9. The point is that the flat root airfoils of Figure 4.33 offer a greater chance of success, and a wing design problem constrained in time would probably be more safely done with a root airfoil like those of Figure 4.33.

So far the root airfoil lower surface shape has not been addressed. The lower surface will be constrained by considerations described in 4.2.4 below, but a general tendency is displayed on Figure 4.36. Part a shows an airfoil with a fairly blunt leading edge. The lower surface pressures will show an initial expansion, but fairly low levels across the crest. Part b shows an airfoil with a sharper leading edge. The difference in pressures will be that much more lift will be carried forward on the wing. This has a favorable effect on trim drag, because the wing with the type b root airfoil will have a less negative pitching moment, thus requiring less tail down load and less trim drag. The limit to the type b design is the point where the crest pressures begin to become sonic.

Wing tip design - Should the outboard wing section be carried completely to the tip, and the twist continued linearly, then the tip would have an unswept shock. This is because the vorticity sweeps forward at the tip, according to Kuchemann. The forward sweep of the shock is not desirable because early drag creep will result, and the tip thrust shown on Figure 4.24 will be lost. There are several ways to work the tip design to prevent this from happening, as illustrated on Figure 4.37.

The easiest way is to have a raked tip. This is known in Europe as a Kuchemann tip and was used on the 707-300 Advanced. The idea is simply to move the isobars (and vorticity) aft to keep the tip from unloading too quickly.

The second way is to alter the tip airfoil by moving the thickness aft and adding camber. The aft thickness position moves the crest aft, trapping the shock wave, and the camber means that the lift will be retained.

The third method is to give the tip added washout. This also moves the crest aft, trapping the shock, and rotates the section lift vector forward, although the section lift is reduced.

Of the three methods, the raked tip is easiest to implement. The application of increased washout is least effective, but has a bonus of delaying tip stall.

Application of Twist - Most twist distributions will have a general appearance like that on Figure 4.38. The fabrication of the trailing edge flaps would be vastly simplified if, in the jig, the twist linear in the span where the flaps are. Figure 4.38b shows that the 1-g twist would be compromised only slightly to achieve this. Of course, the performance penalty would have to be found during wind tunnel testing.

The other consideration involving twist is the line about which the twist would be done. On the DC-10, the leading edge was kept straight, and twist was applied about the leading edge. This increases the effective dihedral and improves the flap ground clearance. Applying the twist about the trailing edge will reduce the effective camber and ground clearance of wing mounted nacelles. There is no strong performance effect either way, so the choice of the twist axis will be determined from other, usually manufacturing, considerations.

Use of Mach Characteristic Lines - Lines of downstream influence (characteristic lines) have already been discussed for two-dimensional airfoils. For the supersonic zone on a wing's upper surface, a three-dimensional counterpart exists. At any point inside the supersonic zone, two such lines will be created (Figure 4.39). The angle of the two lines will be determined by the local Mach number, such that the rays will move downstream at $\pm \sin^{-1}(1/M_L)$, measured relative to the local streamline. For a swept wing, the inboard-directed line moves off the trailing edge. But the outboard-directed line moves more or less along the entire span. In fact, at the drag divergence condition the outward bound characteristic lines lie almost entirely along spanlines, and where they coalesce, is where the shock wave will be located. An example is given on Figure 4.40. This kind of data can be constructed from an experimentally measured isobar pattern, thus giving M_L, and from a knowledge of the local streamline directions.

Figure 4.39 shows how a "disturbance" arising at point A, well inboard, will affect the wing pressures along the entire span. An example of how powerful this effect can be is given on Figure 4.41. In this case,

a "hole" was created in the fuselage near the wing root leading edge. The critical Mach pressures are shown at 80% semispan with and without the concavity in the body. Note that, with the hole, the wing upper surface supersonic pressures have been suppressed all the way out the wing. The characteristic lines have conveyed the aerodynamic effect of the body concavity along the entire wing.

The point of discussing wing characteristic lines is to alert the wing designer to the reason why the wing root design can show up as an outboard wing problem. The strongest shock wave may indeed occur at 40% semispan. But the cure may be to alter the wing sections at 15% semispan, not at 40%. In fact, Whitcomb of NASA has stated that if he has an outboard wing shock problem, and he feels that the outboard twist is proper, then he begins to tailor the upper surface of the wing near the body.

Two design rules arise from consideration of characteristic lines:

(1) A poorly designed or over-designed wing root may actually appear as an outboard wing problem

(2) In-tunnel tailoring may produce the best results when the wing root is altered.

The preceeding discussion has covered the principal design concepts for subsonic, swept wings. The design of any new wing should be done with a knowledge of the characteristics of previous successful wings. A thorough discussion of Boeing and McDonnell-Douglas wing design is contained in Reference 4.9.

4.3 SUBSONIC DESIGN PROCEDURE

The design of the specific contours is done with the support of analysis programs which predict the wing pressures. Until recently, these analyses had to be done at a Mach number low enough that no regions of supersonic flow would exist on the wing. Typically, subcritical Mach numbers of 0.6 to 0.7 would be sufficiently low to allow reliable calculations. Now, new transonic wing-body programs allow calculation of the wing flow field at the intended cruise Mach number. This chapter will describe the earlier design sequence, however, for several reasons:

(1) The designer remains continually aware of all aspects of the design, such as rear spar depth,

(2) More attention can be paid to the overall wing design,

(3) The designer has a better understanding of how the design is evolving, so that good trades can be made.

The complete design sequence contains three separate stages, first, an initial design using A-236, second, a-refinement using A-230 (both ~~at~~ subcritical speeds) and third, a final proof in a transonic program.

A-236 design sequence. The following is taken primarily from Reference 4.10, which should be consulted for further details. Before describing the design sequence in detail, several characteristics of A-236 must be noted (The A-236 user's guide is Ref. 4.11).

The A-236 program uses a linearized analysis and design procedure for the wing, and an exact solution for the body. The linear theory concept allows for the separation of a subcritical pressure distribution into a term due only to thickness and a term due only to camber, which includes angle of attack in A-236. The thickness pressure is the average of the upper and lower surface pressures, and the camber pressure is the pressure increment from the average, or thickness pressure, to the upper surface pressure. Consequently, the thickness and the resulting thickness pressure contribute nothing to the section lift, and the section lift is twice the integral of the pressure increment due to camber. The upper isobar pattern will be the result of the camber pressures subtracted from the thickness pressures.

A-236 currently has three modes of analysis. The direct analysis mode finds the wing thickness and camber pressures and the body pressures, given the complete wing section geometry and twist and the body geometry. The twist design mode finds the wing twist, the wing thickness and camber pressures and the body pressures, given the wing sections, body geometry, and span loading. The same method of solution for the thickness pressure is used in both modes. The section design mode finds the wing thickness form, camber shape, twist distribution and body pressures, given the wing upper and lower isobar patterns. Specifying the isobar patterns gives at one time the thickness pressure, the camber pressure, the section lift coefficient and thus the span loading. The method of solution for the thicknes pressure in this mode is different than that used in the other two modes. The result is that the design sequence does not exactly repeat itself, that is, going from geometry to pressure calculation back to geometry by design does not exactly duplicate the original geometry. However, only the section thickness is affected, and usually the differences are small.

4.3 (Cont.)

Several other characteristics of A-236 are important to note. The lifting surface (camber surface) representation is not correct matematically at the tip station, and the lift of the most outboard station is overpredicted. Also the vortex lattice method of A-236 will overpredict the loading of the rear part of the airfoil slightly unless the points defining the wing section are evenly spaced chordwise. These characteristics will be noted where they affect the design sequence.

The specific design sequence is summarized below and on Figure 4.42:

(1) Choose the specific upper isobar pattern desired and select several initial thickness forms. Run the candidate thickness forms in the twist design mode and pick the thickness form that most nearly satisfies all constraints. This usually requires two runs.

(2) Manually iterate to the desired sectional thickness form, excluding the tip design. These runs are done by manual modification of the thickness forms along the span, and the analysis is done in the twist design mode. Three runs are usually required.

(3) Design the camber and twist at the design Mach number, by inputting the desired upper isobar pattern and the lower isobar pattern resulting from the final thickness pressure of step (2) into the section design mode. The trapezoidal tip is still used. One run is required for this step.

(4) The final geometry is assembled by using the thickness forms from step (2) and the camber form and twist distribution from step (3), and checking the result by analyzing the wing in the direct analysis mode. One run is required.

(5) A twist change will be required to achieve the design span loading at the cruise Mach number. This is calculated by running the geometry of step (4) in the twist design mode at the cruise Mach number by specifying the spanload calculated for step (4). This will produce the twist to be used with sections of step (4). One run is required for this step.

(6) The tip design is done by evaluation of the information from step (3) and from empirical information. No runs are required for this step. The wing design is now completed for the cruise Mach number.

4.3 (Cont.)

Before beginning the actual design sequence, the subcritical Mach number and design C_L are chosen. Usually,

$$M_{Design} = \frac{0.60}{\cos \Lambda_{effective}} \tag{4.25}$$

where 0.60 suggests that the 2-D airfoil will have no supercritical flow at M = .60

Λ effective is the sweep of the expected outboard shock

M_{Design} = A236 design Mach number

Then, using the ratio of M_{Design}/M_{Cruise}, Figure 4.43 is used to find the subcritical design lift coefficient. This procedure allows for the growth in C_L with Mach at constant angle of attack.

The span load and upper isobar target must now be drawn. The span load at cruise will be determined as described previously. But it must be adjusted for the effect of the design Mach number being less than the cruise Mach number. The adjustment is required because the lift curve slopes of the outboard airfoils, $dC_l/d\alpha$ increase more than at the inboard stations. Figure 4.44 demonstrates how the adjustment should be made.

The upper surface isobar target must be generated next, as shown on Figure 4.45. The process begins by taking the 2-D airfoils pressure distribution at at the design C_l:

$$C_p^* = C_{p_{2D}} \cos^2 \Lambda_{SHOCK\ ANGLE} \tag{4.26}$$

where C_p^* = pressure vs x/c on an infinite yawed wing

$C_{p_{2D}}$ = pressure vs x/c on 2-D airfoil

$\Lambda_{shock\ angle}$ = sweep angle of the x/c spanline where the shock is expected.

Then, the infinite yawed wing pressures are corrected for taper according to a procedure suggested by Lock (Ref. 4.14).

$$C_{p_{3D}} = \frac{f-1}{0.7\, M^2_{DESIGN}} + f C_p^* \tag{4.27}$$

235

4.3 (Cont.)

where $C_{P_{3D}}$ = pressure vs X/C to be drawn on the tapered wing

M_{Design} = the subcritical design Mach number from equation 4.25

f = Lock's correction factor

$$= \left\{ \frac{1 + .2M^2_{Design} \cos^2 \Lambda_{effective}}{1 + .2M^2_{Design} \cos^2 \Lambda^*} \right\}^{3.5}$$

Λ^* = sweep of an individual X/C spanline on the tapered planform

Using the $C_{P_{3-D}}$ versus X/C, the outboard upper isobars are constructed. Then the root upper isobars are drawn following guidelines previously discussed.

An initial evaluation of possible thickness forms to begin the design sequence. This is accomplished by choosing two or more desirable lines for the chordwise location of the maximum thickness versus span. Outboard, the line should be at the percent chord of the two-dimensional section. As the root is approached one likely choice is to move the line of maximum thickness forward relative to the trapezoid. This aids in sweeping the isobars forward. Another likely choice is to continue the line straight in along a chordline relative to the trapezoid. This location, having the thickness more aft, would benefit the rear spar depth. In general, sweeping the line of maximum thickness aft as the body is approached will not be a usable solution.

Once a line of maximum thickness is chosen, this information is used along with the prior constraint of the spanwise variation of maximum t/c to produce scaled versions of the two-dimensional section. The two-dimensional section is oriented steamwise on the wing according to simple sweep, the thickness is scaled to match the desired t/c at that span station, and the thickness form is transformed linearly in the chordwise direction to match the desired location of maximum thickness. The manipulation program SECMOD described in Appendix C of Reference 4.10 can be used in the "SWEEP" option to do these modifications automatically. This process is to be done at fifteen to twenty evenly-spaced stations along the span, in order to produce "defining sections" at those locations. These defining stations will be used and modified throughout the design sequence, and will constitute the wing definition for the GCS loft at the end of the design. A section at the centerline should always be included, so that the loft in the spanwise direction will be smooth.

An A-236 run is now to be made for each of the wings resulting from different choices for the line of maximum thickness. This run is to be made in the twist design mode (CASE = -6. on card 2), as this will compute both the upper and lower pressures for each station, while satisfying the span load requirement. The wing must be evenly panelled spanwise (A 236 card 6), and it is very desirable to have the chordwise panel spacing as evenly as possible (A 236 card 7).

4.3 (Cont.)

Typical output from thse various preliminary wings is shown on Figure 4.46. As indicated for the example station, the thickness pressures (the camber pressures are not used in this step) are first matched against the upper isobar goal (step 2 on Figure 4.46), and then the complete pressure distribution for each candidate line of maximum thickness is completed by:

$$C_{P_{LOWER}} = 2C_{P_{THICKNESS}} - C_{P_{UPPER\ ISOBAR\ GOAL}} \quad (4.28)$$

The completed pressures are shown as Step 3 on Figure 4.46. Several criteria aid in the selection of the initial thickness form. Firstly, the recovery point on the lower surface must be at a reasonable pressure, a general rule being that

$$C_{P_{LOWER}} \geq 2/3\ C_{P_{UPPER}}, \quad (4.29)$$

where $C_{P_{UPPER}}$ is taken at the same chordwise location. Secondly, the most severe gradient of the pressure recovery on the lower surface should be no greater than one and a half times that of the outboard design stations. Thirdly, the section lift coefficient should be within ten percent of that required by the span loading constraint.

Experience has shown that an initial thickness form whose thickness pressures when combined with the desired upper isobar meet these constraints can usually be successfully modified to the desired result. In general, the more aft location of the line of maximum thickness has less of a chance of meeting these constraints, and the designer will most likely choose the most aft line that satisfies these three constraints.

The objective of the thickness form design is to find the thickness form at each spanwise defining station that will produce the desired upper surface isobars, the desired span loading distribution, and satisfactory lower surface isobars. The first two requirements are specified by the design constraints. The last requirement is not clearly specified, but the final lower surface pressures should be reasonably smooth, with a maximum negative pressure level that produces Mach numbers less than sonic. The pressure recovery gradients on the rear should not be too severe; a good rule is that they should not be much worse than that on the upper surface.

The thickness form design is done by inputting the complete defining stations (both camber and thickness forms) and the required span loading into the twist design mode of A 236 (CASE = .6. on card 2). The calculation will produce both the camber and thickness pressures.

The thickness form design requires only the thickness pressure and this part of the design could be done in the direct analysis mode. However, doing the design in the twist mode allows the designer to continually appraise all of the wing isobars as the design progresses, since they match the span load constraint, to see how well the upper isobar constraint is being matched.

4.3 (Cont.)

The thickness form development for a design station is illustrated on Figure 4.47. The sequence consists of obtaining the thickness pressure for the design station, and finding the derived lower surface pressure (not the pressure actually calculated) by use of Equation 4.28. This allows the derived lift coefficient, dependent on the upper isobar goal and the calculated thickness pressure, to be found. The section lift coefficient produced by the upper isobar design goal and the derived lower surface pressures is compared to that required by the span loading constraint, and the derived lower surface pressure is examined. When both are satisfactory, the thickness form for that station has been found.

Three typical steps are shown on Figure 4.47. Step 1 is an analysis of the original thickness form. Step 2 is an attempt to achieve the proper pressure distribution without disturbing the rear spar. Step 3 is a more drastic thinning of the section, and produces a usable section pressure. With experience, the designer can usually produce the final thickness form by the second modification to the original form. The manipulation program SECMOD described in Appendix C, in the "INCREMENT" option, can be used as an automated aide in modifying the section thickness forms.

The design of the camber surface requires one run in the complete design mode of A 236 (CASE = 5. on card 2). The inputs for this mode are the upper surface isobar goal pressures and the derived lower surface pressures, which are found by Equation 4.28 from the upper isobar pressures and the thickness pressures for the final thickness forms. These inputs will satisfy both the upper isobar design goal and the span loading, as these were two constraints on the design of the final thickness forms. It is very important to use equal chordwise spacing of the panel edges for the A 236 solution if an accurate answer is desired.

The results of the A 236 design will be the camber and twist are to be separated, and the thickness form is to be combined with the camber line at each defining station to produce the final sections.

Special considerations arise as to the best way of combining the camber and thickness. The camber surface from the A 236 will be defined at only a small number of points, usually less than twenty, whereas the original two-dimensional section camber line will be specified typically at fifty chordwise locations, with very tight spacing near the leading edge. In order to preserve the precise camber shape at the nose, it is recommended to increment the section camber that has been carried throughout the design to the desired camber, rather than replacing the original camber. In this way, for the parts of the wing out of the influence of the root or the tip, leaving the camber increment zero for the first ten percent chord or so will preserve the original leading edge definition. The manipulation program SECMOD described in Appendix C, in the "INCREMENT" option, can be used as an automated aide in incrementing the section camber shapes. If complete camber replacement is desired, the program can be run in the "REPLACEMENT" option.

It is advisable to run a straight analysis of the assembled geometry (CASE = -5 on card 2), using the final sections at the computed twist. This serves two purposes, first to check the section geometries for any errors that may have occurred during asssembly of the thickness and camber forms, and secondly to obtain the actual span loading at the design condition. This should be very close to the span loading constraint established prior to doing the wing design.

238

4.3 (Cont.)

A revised twist will be required to produce the desired span loading at the cruise condition. That twist is computed by running the final sections and the span loading found in the geometry check above in the twist design mode (CASE = -6. on card 2) at the cruise Mach number. The cruise Mach number should be limited to .95, however. The twist found is essentially dependent only on the camber portion of the solution, and will not be adversely affected by the increased Mach number. A typical comparison of design twist and cruise twist is shown on Figure 4.48.

It would be possible to delete this step if the original camber design were done at the cruise Mach number, rather than at the design Mach number. The A-236 design sequence does not do the initial camber design at the cruise Mach number for the following reason: one of the more valuable uses of the analytical methods is to prevent the design of a geometry that is rough, in terms of its pressure distribution. In order to assure a smooth pressure distribution, the A-236 process considers it very desirable to do the complete section and twist design at a common Mach number.

The tip design has been kept until last. As was described above, three options are available for the tip, as illustrated on Figure 4.49. Experience has shown that for wings designed to M .96 or above, all of these techniques, namely tip rake, section changes, and a slight tip washout should be used. For lower Mach numbers, section changes, tip washout, or a combination of the two will probably be sufficient. Section changes can be evaluated in A-236, as can an estimate of the tip washout. It should be remembered that the camber pressures and thus the section lift will be overpredicted by A-236 for the most outboard pressure station.

Initial GCS Loft From the A-236 design sequence above, about 15 to 20 evenly-spaced streamwise wing airfoils and their appropriate twist have been found. The next step in the design sequence is to loft these into a continuously defined wing. The program for this within the Aero Staff is GCS (Reference 4.12). Two choices will have to be made before the loft can be done. First, the line about which the airfoils will be twisted must be chosen. This did not matter to A-236 since twist is achieved there by linear theory and not by actually twisting the sections. The line for twisting will be chosen under the considerations discussed previously. The second choice involves wing shearing. This may be done to increase nacelle ground clearance, as on the 747 program. Dihedral is another matter, and is usually done by rotating the wing about the side of body once the loft has been made. Again, A 236 does not recognize dihedral or shear, so they have not been important up to this point.

A 230 Design refinement The next major step is to take the twisted, sheared wing with dihedral and model it along with the body in A 230 (Reference 4.13). This program is better than A 236 in that the geometry is modelled exactly, so that effects such as shear and dihedral can be calculated. A 230 in general gives a result closer to experiment than A 236. Program A 230 cannot be used efficiently for the complete design process, however, because it is costly to use and has no design options. Like A 236, program A 230 is limited to subsonic flow conditions.

4.3 (Cont.)

The first step in the A230 sequence is to input the lofted wing and body and get a flow solution at the same Mach and α as was used in A236. The A230 isobar pattern and span loading are then constructed and compared to the target values. Assuming that the final A236 solution was of good quality and quite close to the target values, there will be only slight differences between the A230 results and the target.

At the position of each defining airfoil, the ΔC_p between target and actual A230 pressures are found for both the upper and lower surfaces:

$$\Delta C_p = C_{p_{A230}} - C_{p_{target}} \tag{4.30}$$

This ΔC_p is then applied to the isobar values form the final A236 run:

$$C_{p_{next}} = C_{p_{A236}} - \Delta C_p$$

A design run is made in A236 using the corrected isobars. This run will produce a slightly different geometry. By comparing this new design run geometry against that used for the first loft in GCS, a geometry correction is obtained:

$$Z_{new\ loft} = Z_{old\ loft} + \left(Z_{new\ A-236} - Z_{PRELOFT\ A-236}\right) \tag{4.32'}$$

where $Z_{new\ loft}$ = new surface ordinate, either upper or lower, at a particular station on the wing

$Z_{old\ loft}$ = corresponding point on original GCS loft used for A230 analysis

$Z_{new\ A236}$ = corresponding point on latest A236 run

$Z_{\substack{preloft \\ A236}}$ = corresponding point on A236 run prior to original loft.

This process is illustrated on Figure 4.50, and utilizes A236 to achieve a geometry increment which corresponds to the pressure increment needed to cause A230 to yield the desired isobars. The new geometry is relofted in GCS and analyzed in A230. This has proven to be a very efficient process, with only one cycle usually required. The second A230 solution will usually produce pressures identical to the target valves.

Transonic Analysis_ The final step amounts to a proof of the design in one of the most recent transonic wing-body programs. Since this is an area of rapidly developing technology, the Aerodynamics Reaearch Unit should be consulted to see which program is currently considered to be best.

4.3 (Cont.)

It would be possible, of course, to conduct the entire design sequence in the transonic wing-body program. This is not recommended, however, for several reasons:

(1) The transonic programs are very expensive to use,

(2) The transonic programs have not been as extensively calibrated against experiment,

(3) The transonic programs do not have the flexibility of design options available in A236,

(4) The final A230 solution is required as the baseline to guide the nacelle installation design (chapter 9).

CHAPTER 4. REFERENCES

4.1 Applied Hydro- and Aeromechanics," L. Prandtl and O.G. Tietjens, Dover Publications, 1934.

4.2 "The Airfoil and Propellor Theory of Prandtl," E. Trefftz, F. Angew, Math, Mech. (German), Vol. 1, p. 206, 1921.

4.3 NASA CR 1218, "A Numerical Solution for the Minimum Induced Drag and Corresponding Loading of Non-planar Wings", J. L. Lundry, Nov. 1968.

4.4 "Comment on Simplification of the Wing-Body Problem/" A.H. Flax, J. Aircraft, Vol. 10, N. 10.

4.5 Res. Note 20, "Fuselage Effects on Induced Drag," P.E.Rubbert, June,1970.

4.6 "A Method for Estimation of Polar Shape and Drag Rise of a Family of Wings," Wm. McIntosh, C/S AE-NTP-200, Feb. 16, 1972.

4.7 "Rapid Airplane Drag Estimation Method," D. George-Falvy, unreleased document, 1976.

4.8 "A Simple Method for Calculating the spanwise and Chordwise Loading on Straight and Swept Wings of any Given Aspect Ratio at Subsonic Speeds," D. Kucheman, R&M No. 2935, August, 1952.

4.9 "Selected Subsonic Wing Design Methods -A Survey and Evaluation," R. J. Marhefka, D6-43836TN, February, 1977.

4.10 "The Advanced Transport Program Method for Subsonic and Transonic Wing-Body Design," W. B. Gillette, D6-40103 (unreleased).

4.11 C/S AMEP-M-174D, A-236 User's Guide.

4.12 D6-24200TN, "Wing/Empennage Geometry Control System User's Document," P. L. LeRoy, April, 1972.

4.13 D6-15047-1, "A General Method for Determing the Aerodynamic Characteristics of Fan-in-Wing Configurations," P. E. Rubbert, et al, November, 1967.

4.14 "An Equivalence Law Relating Three - and Two-Dimensional Pressure Distributions," R. C. Lock, R&M No. 3346, May 1962.

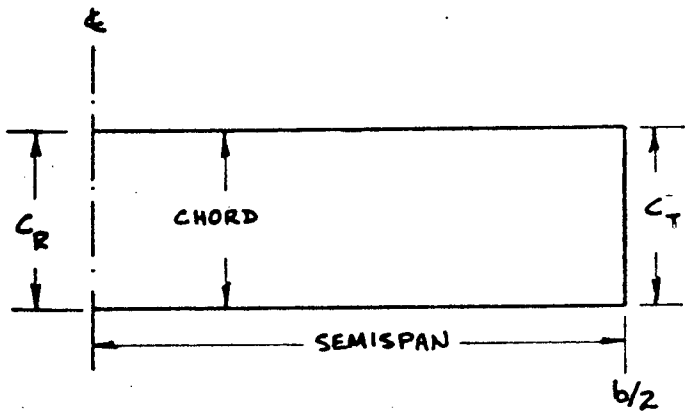

(a) RECTANGULAR WING ~ CONSTANT CHORD

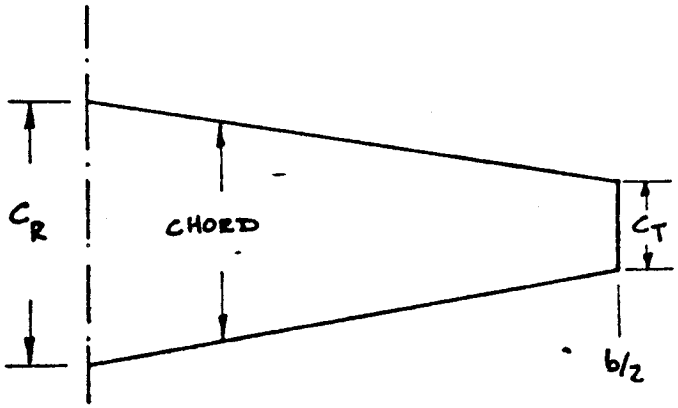

(b) TAPERED WING ~ CHANGES LINEARLY FROM ROOT TO TIP

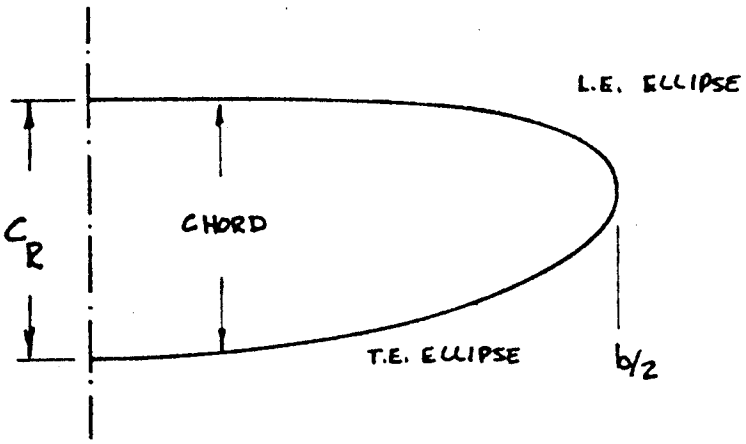

(c) ELLIPTIC WING ~ CHANGES ELLIPTICALLY FROM ROOT TO TIP

FIGURE 4.1 PLANFORMS FOR UNSWEPT WINGS

AIRFOIL

$$c_\ell(\eta) = \int_0^1 \left(c_{p_{lower}} - c_{p_{upper}} \right) d(x/c)$$

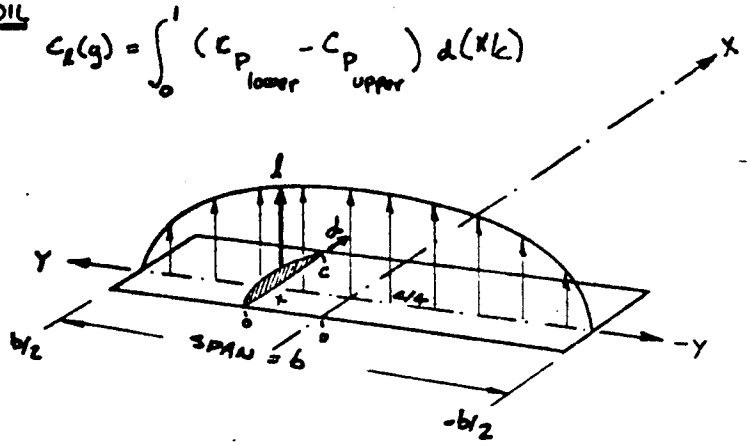

SPAN LOADING CURVE

(a) $c_\ell c$

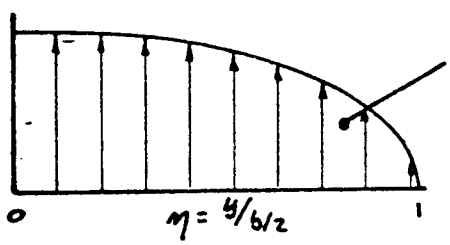

$$\int_0^1 c_\ell c \, d\eta = C_L c_{AVG.}$$

(b) $\frac{c_\ell c}{c_{AVG}}$

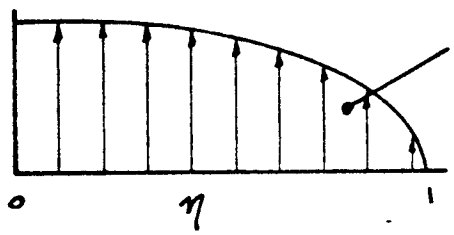

$$\int_0^1 \frac{c_\ell c}{c_{AVG}} d\eta = C_L$$

(c) $\frac{c_\ell c}{c_{AVG} C_L}$

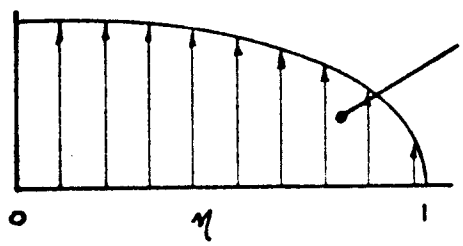

$$\int_0^1 \frac{c_\ell c}{c_{AVG} C_L} d\eta = 1$$

FIGURE 4.2 INTEGRATION OF SECTION LIFT TO GET WING LIFT

(a) WING WITH CONSTANT CIRCULATION

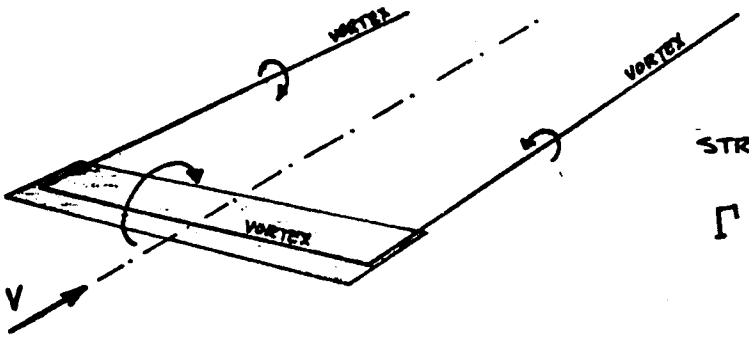

STRENGTH OF VORTEX:

$$\Gamma = \frac{C_L V C_{AVG}}{2}$$

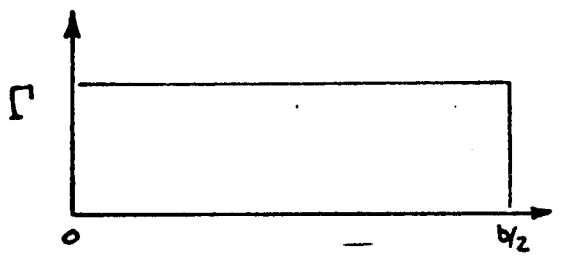

(b) WING WITH VARYING CIRCULATION

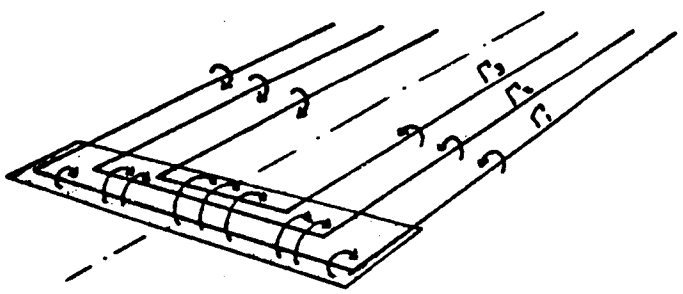

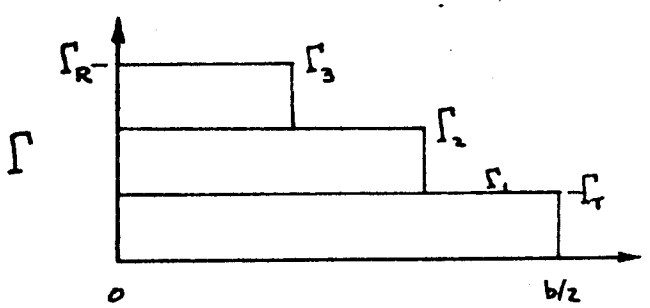

FIGURE 4.3 CIRCULATION

(a) DOWNWASH VELOCITY

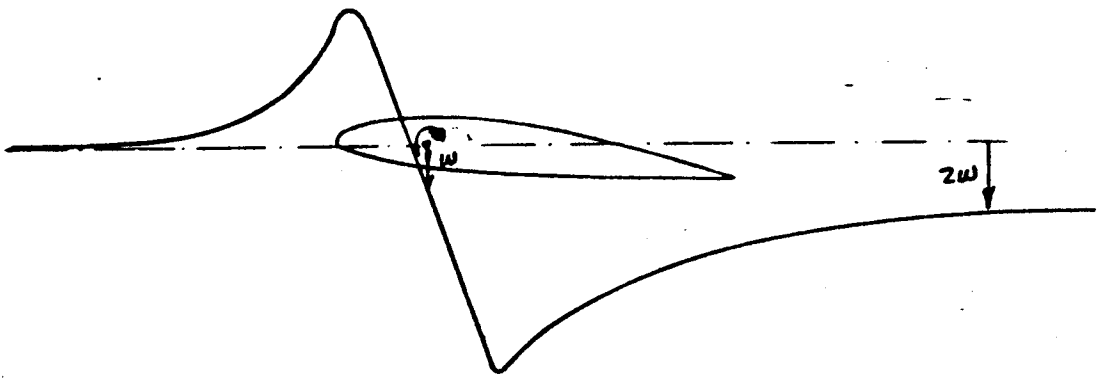

(b) EFFECT ON AERODYNAMIC FORCES

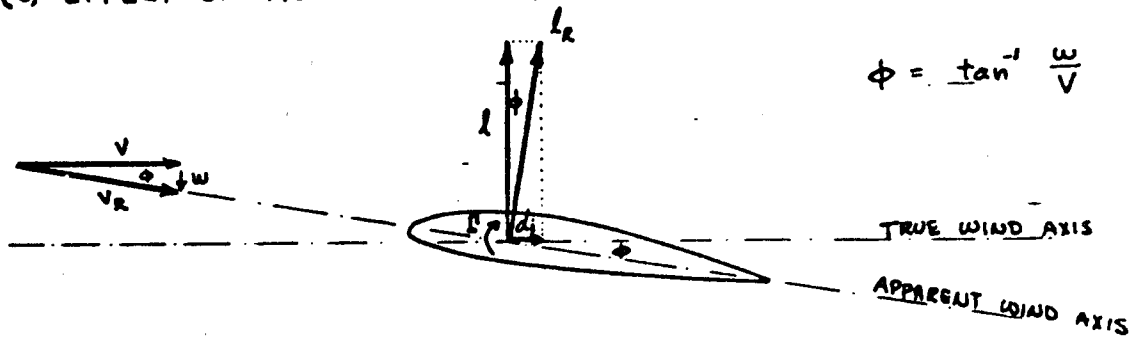

$$\phi = \tan^{-1} \frac{w}{V}$$

l_R = TRUE LIFT GENERATED BY APPARENT WIND = $f(\Gamma)$

l = LIFT RELATIVE TO WIND AXIS = $l_R \cos\phi$

d_i = INDUCED DRAG RELATIVE TO WIND AXIS = $l_R \sin\phi$

FIGURE 4.4 EFFECT OF CIRCULATION ON FORCES

(a) CONTINUOUS LOADING

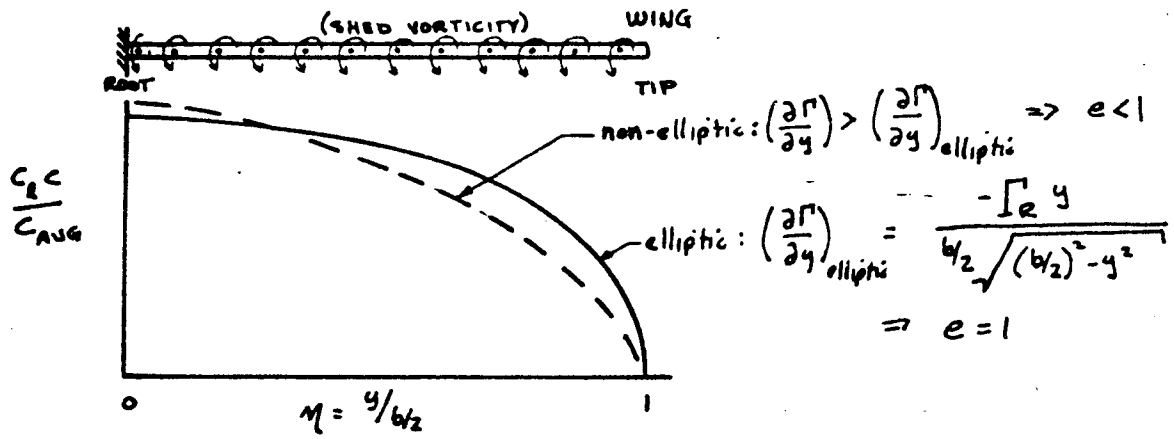

(b) DISCONTINUOUS LOADING

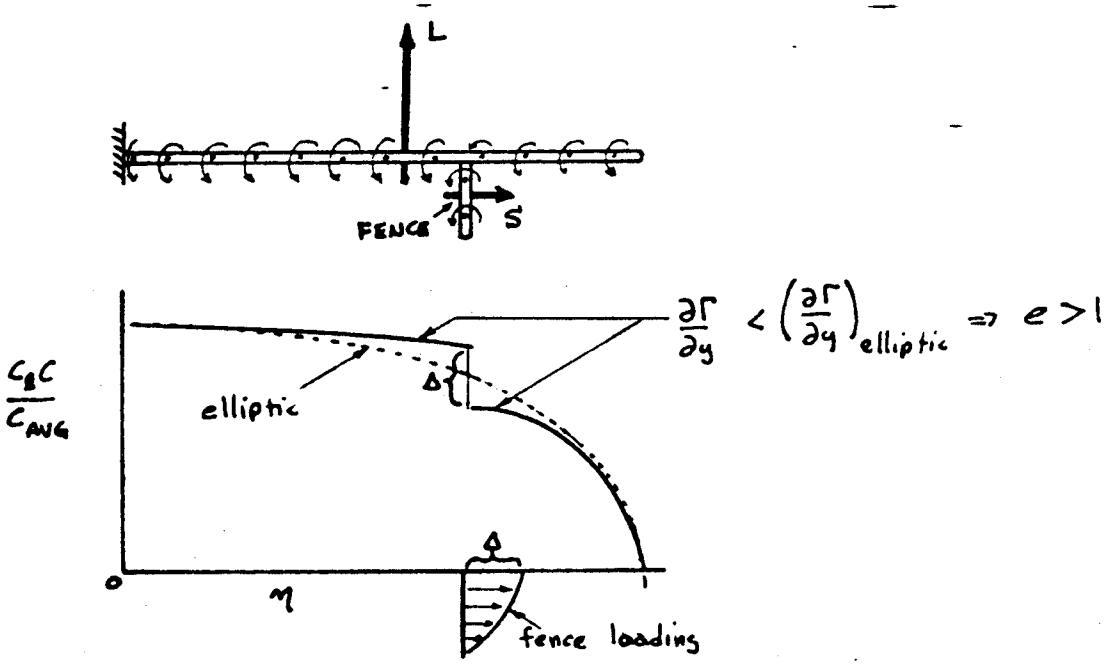

$$D_i = \frac{1}{\pi q_f e}\left(\frac{L}{b}\right)^2$$

FIGURE 4.5 EFFECT OF SPAN LOADING ON INDUCED DRAG

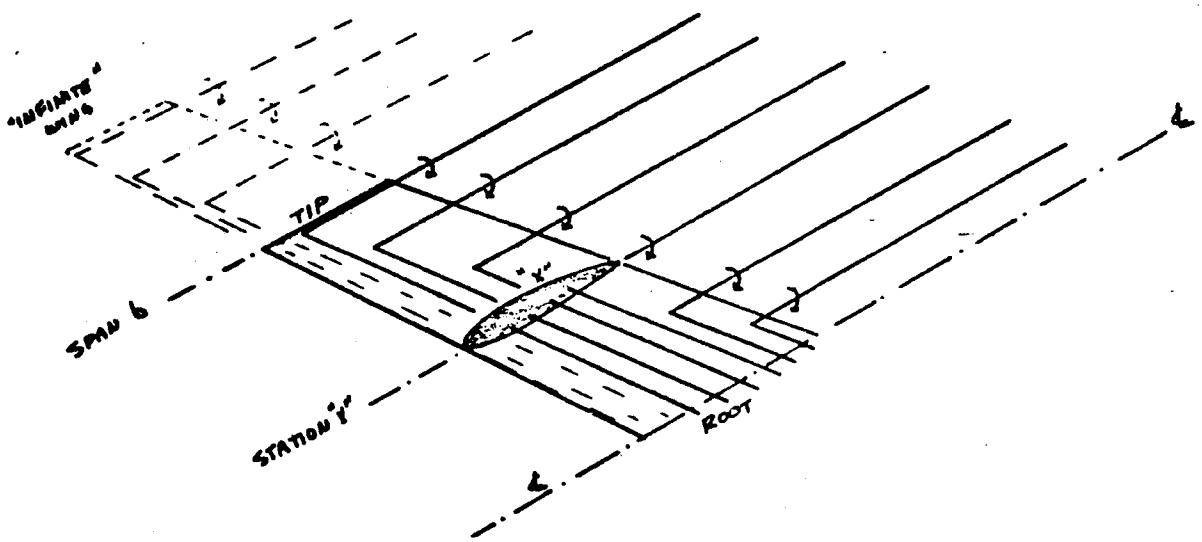

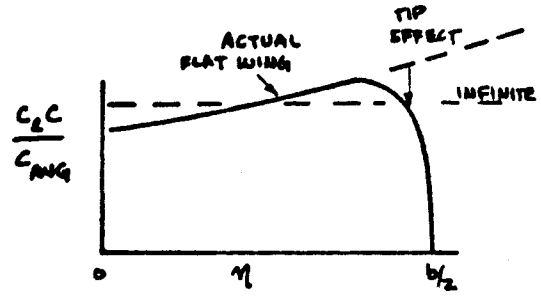

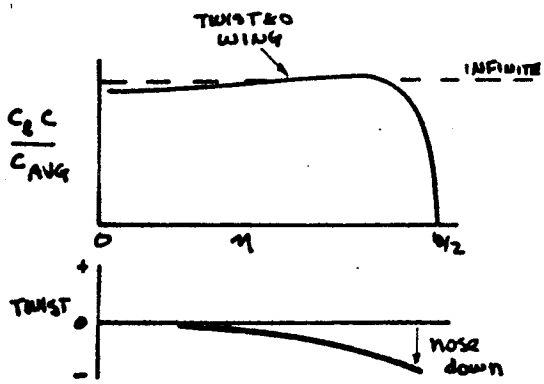

① SHED VORTICITY INBOARD OF STATION "x" IS INCREASING LOCAL ANGLE OF ATTACK

② SHED VORTICITY OUTBOARD OF STATION "x" IS DECREASING LOCAL ANGLE OF ATTACK

③ FOR "INFINITE" WING, THESE EFFECTS CANCEL AT STATION "x"

④ FOR WING WITH SPAN "b", OUTBOARD VORTICITY IS REMOVED, RESULTING IN NET INCREASE IN ANGLE OF ATTACK AT STATION "x"

⑤ EFFECT INCREASES AS "x" MOVES TOWARDS "b"

⑥ SPAN LOAD OF FLAT WING WILL BE OVER LOADED NEAR THE TIP

⑦ WING TWIST (WASHOUT) WILL RESTORE SECTION LIFTS TO CONSTANT VALUE

FIGURE 4.6 WING TWIST

(a) WING ALONE

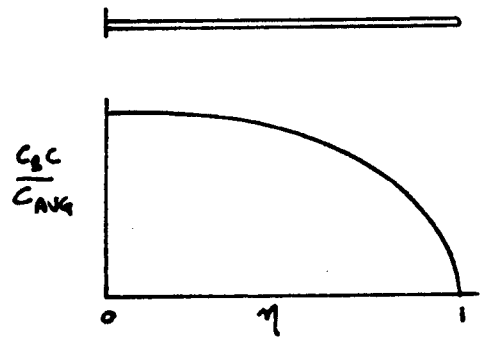

$\sigma \equiv D_{body} / b_{wing}$

$\sigma = 0$

(b) WING WITH SMALL BODY

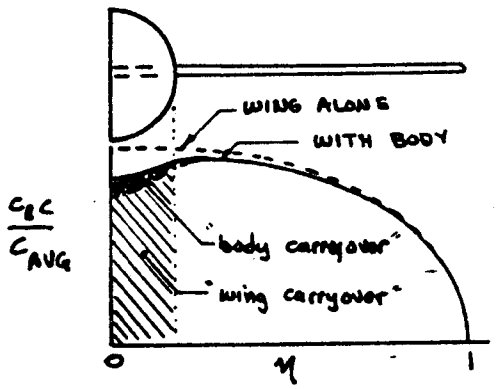

$\sigma \approx 0.20$ OR LESS; VERY LITTLE LOSS IN WING-ALONE LIFT

(c) WING WITH LARGE BODY

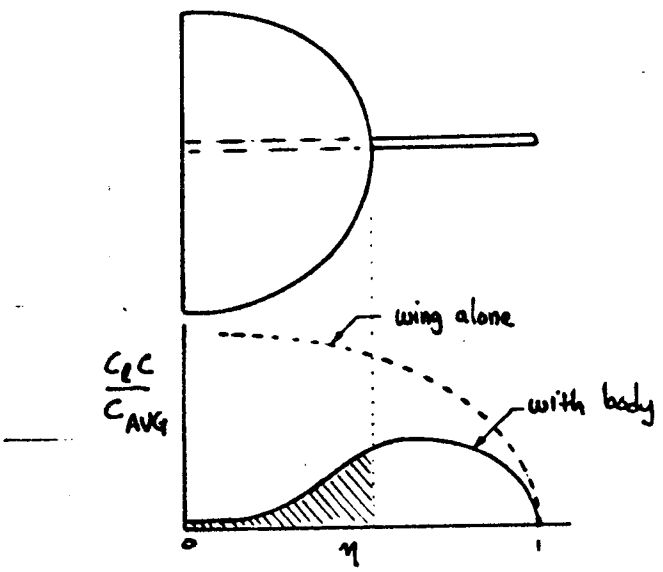

$\sigma \approx 0.4$ OR MORE; SUBSTANTIAL LOSS IN WING-ALONE LIFT

FIGURE 4.7 EFFECT OF BODY TO SPAN RATIO

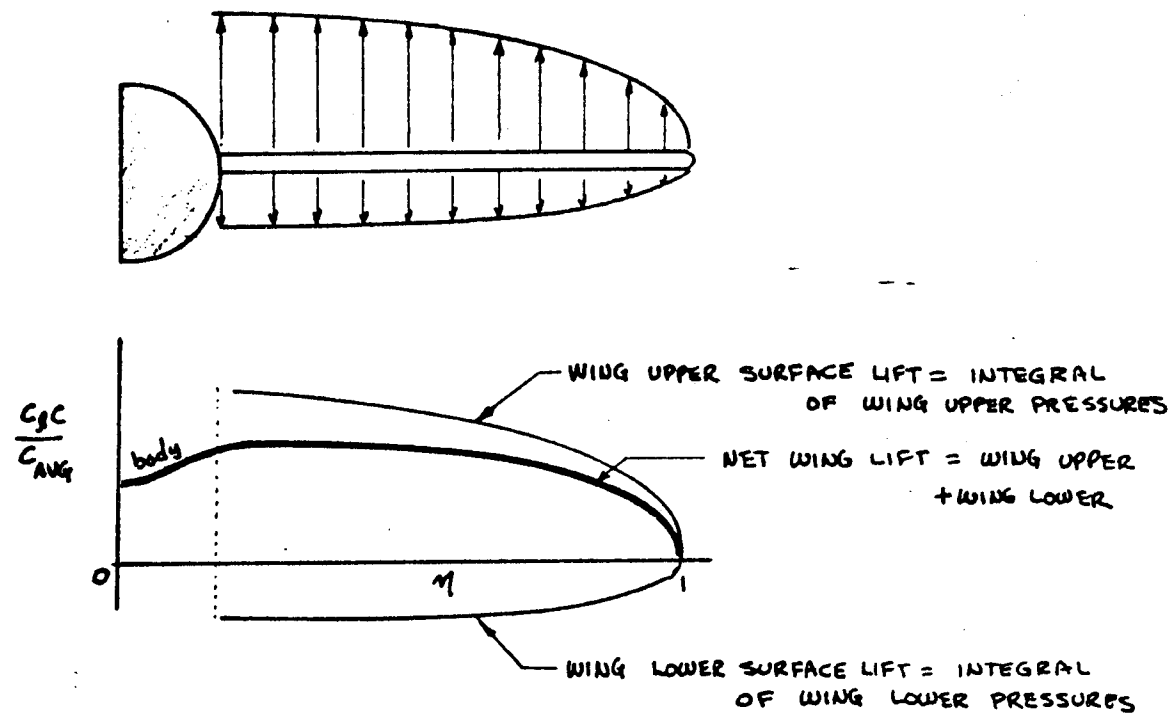

(a) LIFT FOR WING POSITIONED AT MID-BODY

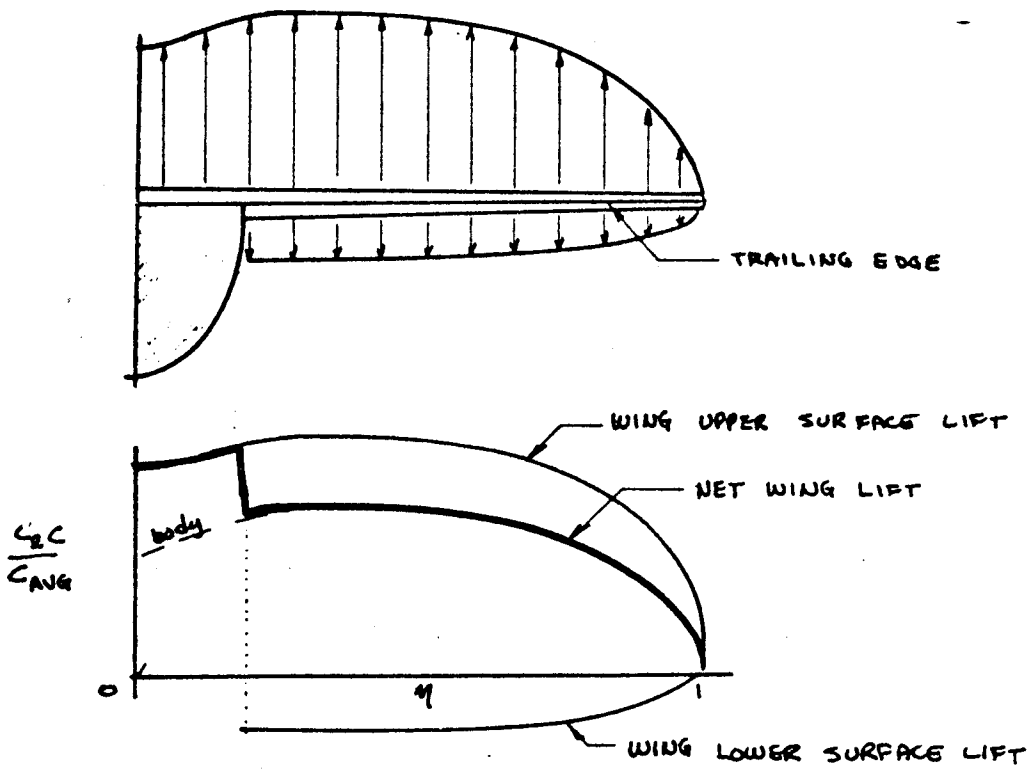

(b) LIFT FOR WING PARTIALLY EXPOSED ABOVE BODY

FIGURE 4.8 EFFECT OF WING VERTICAL POSITION

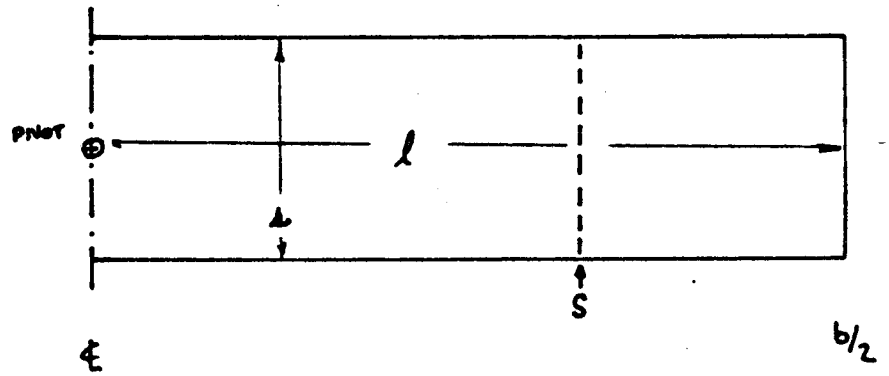

UNSWEPT

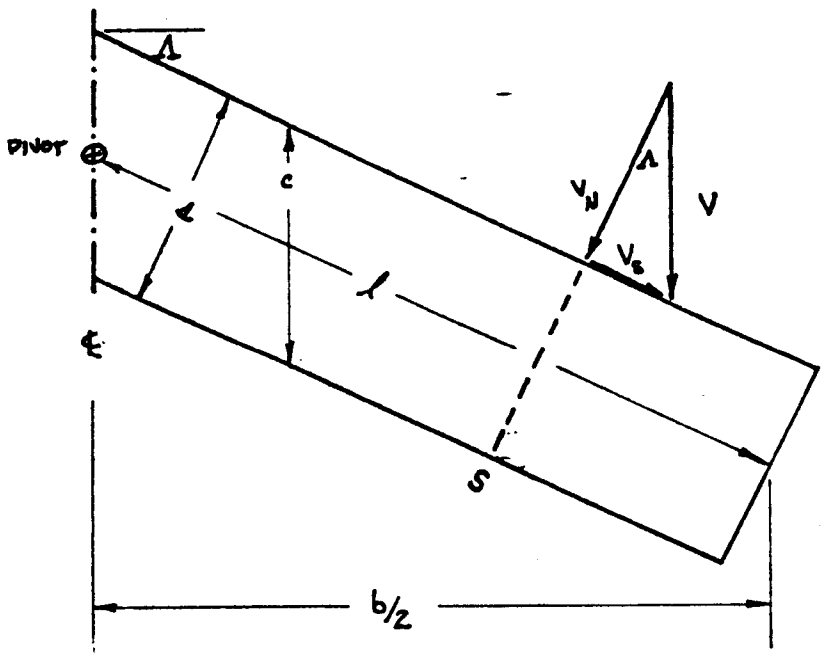

SWEPT

$V_N = V \cos \Lambda$

V_N CONTROLS AERODYNAMICS OF SECTION S

$$M_{DD_{SWEPT}} = M_{DD_{UNSWEPT}} / \cos \Lambda$$

FIGURE 4.9 SIMPLE SWEEP EFFECT

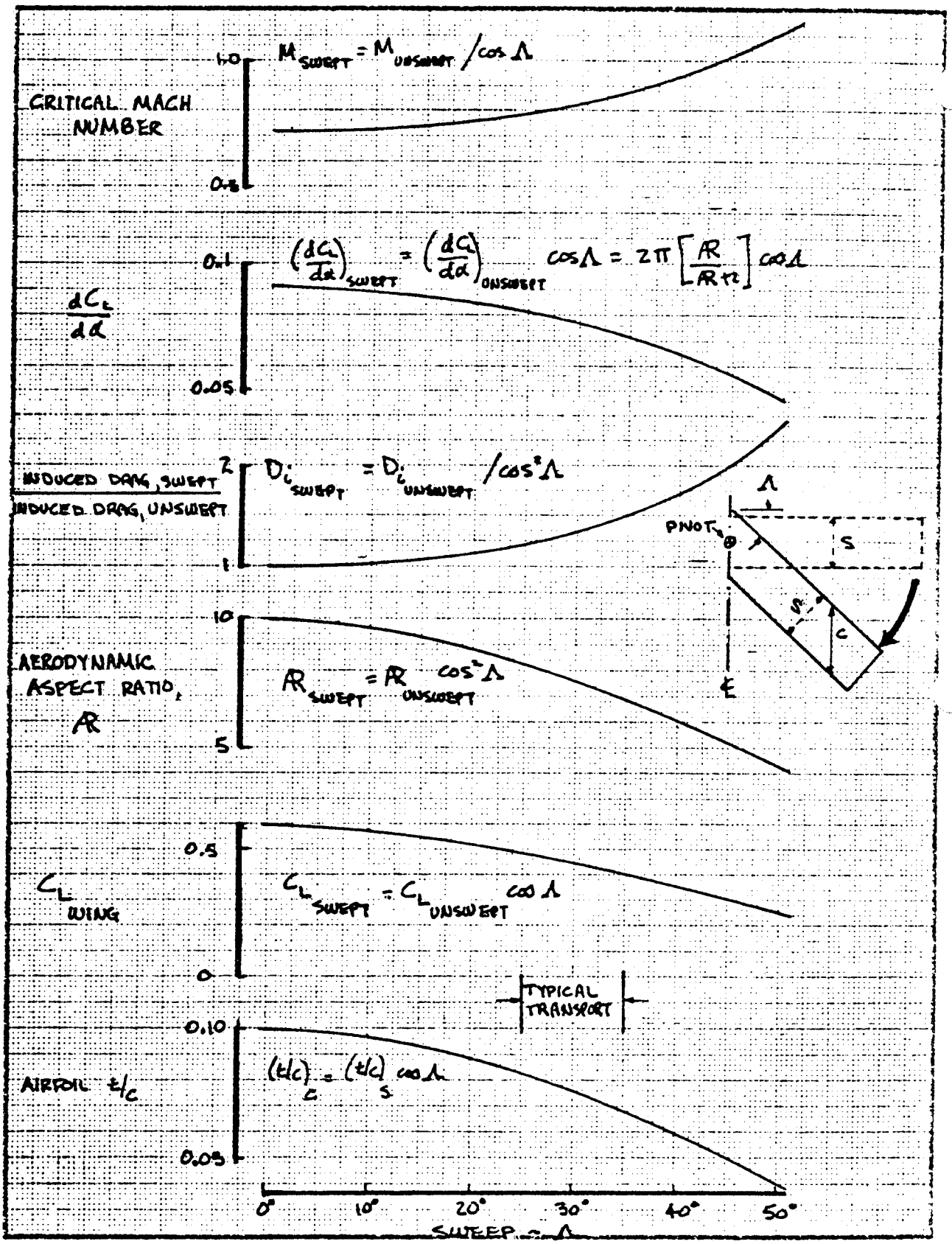

CALC	GILLETTE	1.7.78	REVISED	DATE
CHECK				
APP				
APR				

SIMPLE SWEEP EFFECTS FOR CONSTANT STRUCTURAL ASPECT RATIO

FIG 4.10

BOEING

PAGE 4.53

252

(a) UNSWEPT WING, HIGH $dC_L/d\alpha$

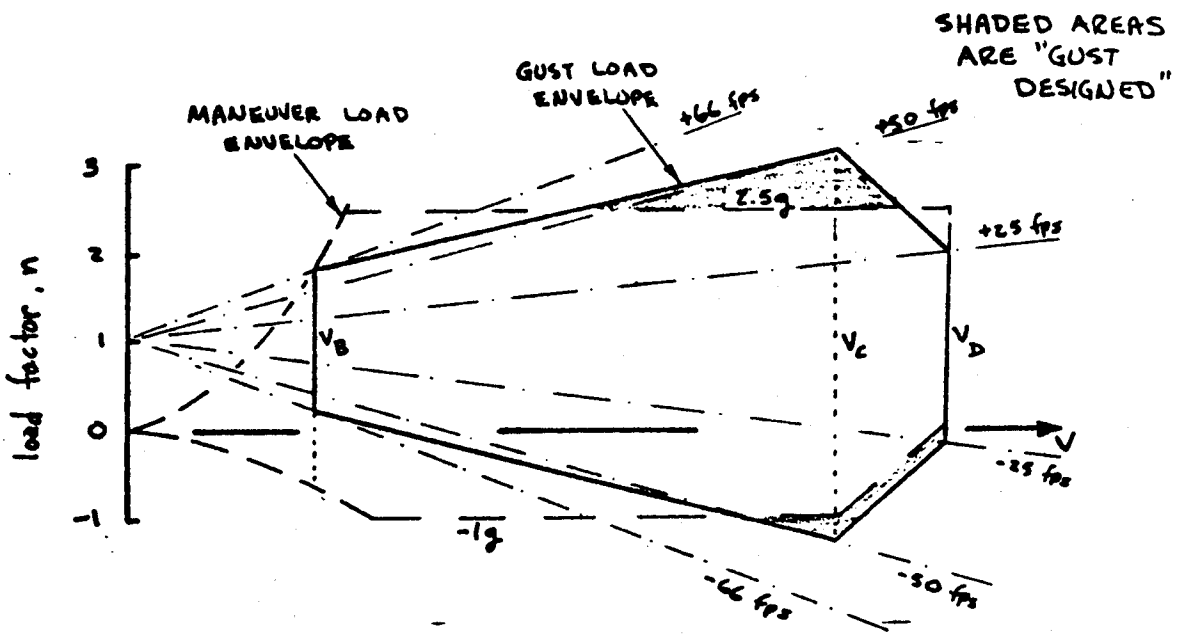

(b) SWEPT WING, REDUCED $dC_L/d\alpha$

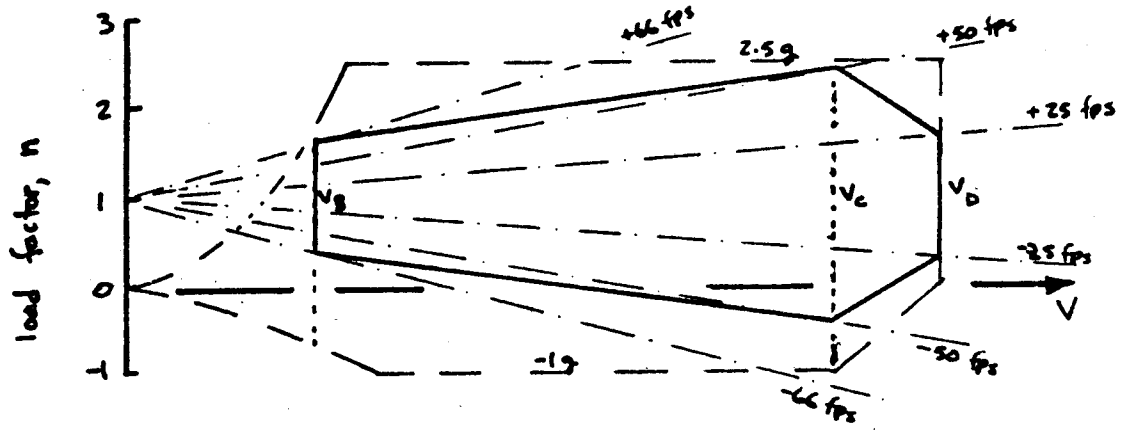

FIGURE 4.11 EFFECT OF SWEEP ON V-n DESIGN ENVELOPE

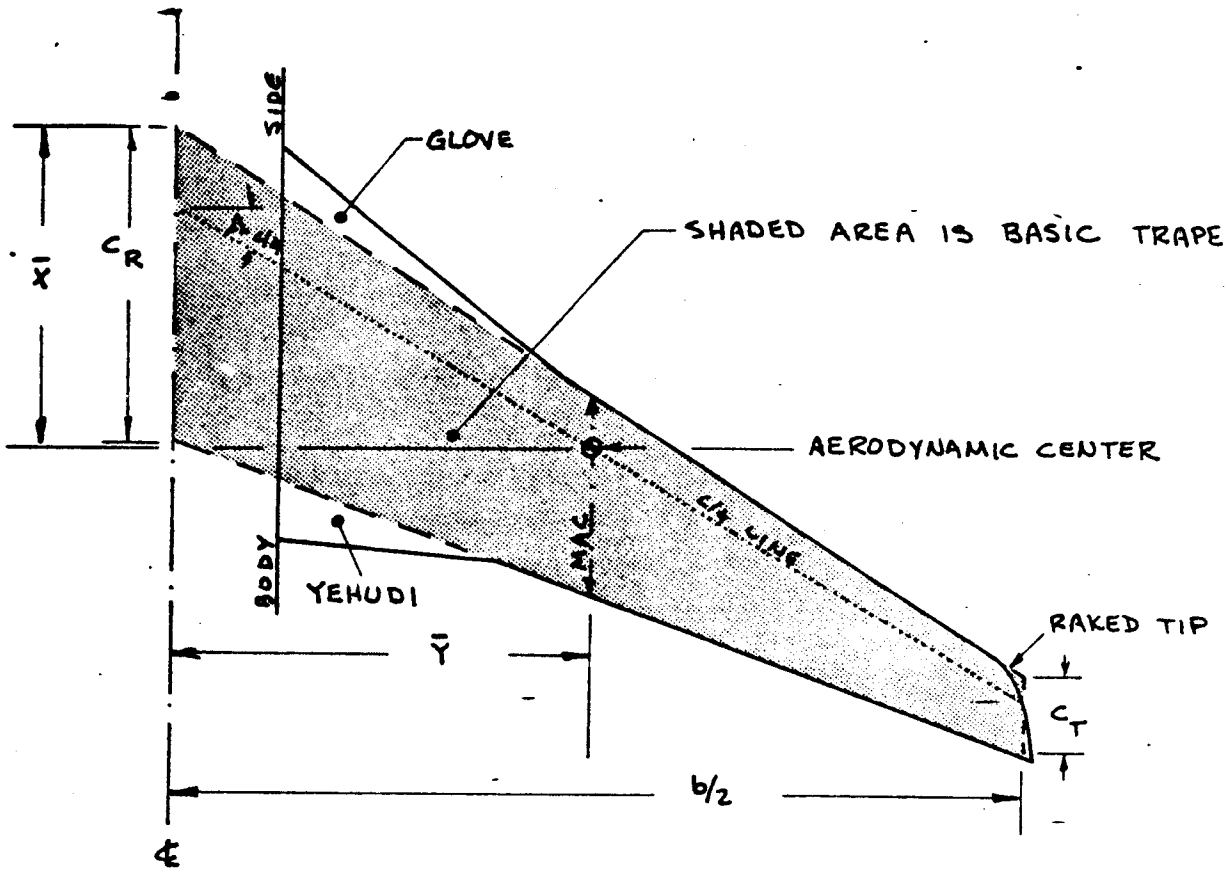

$$C_{AVG} = \frac{C_R + C_T}{2} \sim \text{AVERAGE CHORD}$$

b = TRAPEZOIDAL SPAN

$$S_{TRAPEZOID} = C_{AVG} \cdot b = \frac{b}{2}(C_R + C_T)$$

$$\lambda = C_T / C_R \sim \text{TAPER RATIO}$$

$$\bar{c} = MAC = \tfrac{2}{3} C_R \left(\frac{\lambda^2 + \lambda + 1}{\lambda + 1}\right) \sim \text{MEAN AERODYNAMIC CHORD}$$

$$\bar{Y} = \frac{b}{6}\left(\frac{1 + 2\lambda}{1 + \lambda}\right) \sim \text{SPANWISE POSITION OF } \bar{c}$$

$$\bar{X} = \bar{Y} \tan \Lambda_{c/4} + C_R/4 \sim \text{distance to } \bar{c}/4 \text{ FROM WING APEX}$$

$$AR = \frac{b^2}{S} = \frac{b}{C_{AVG}} \sim \text{ASPECT RATIO}$$

FIGURE 4.12 PLANFORM GEOMETRIC DEFINITIONS

(a) SPAN LOAD CHARACTERISTICS ~ ELLIPTIC CRUISE LOADING

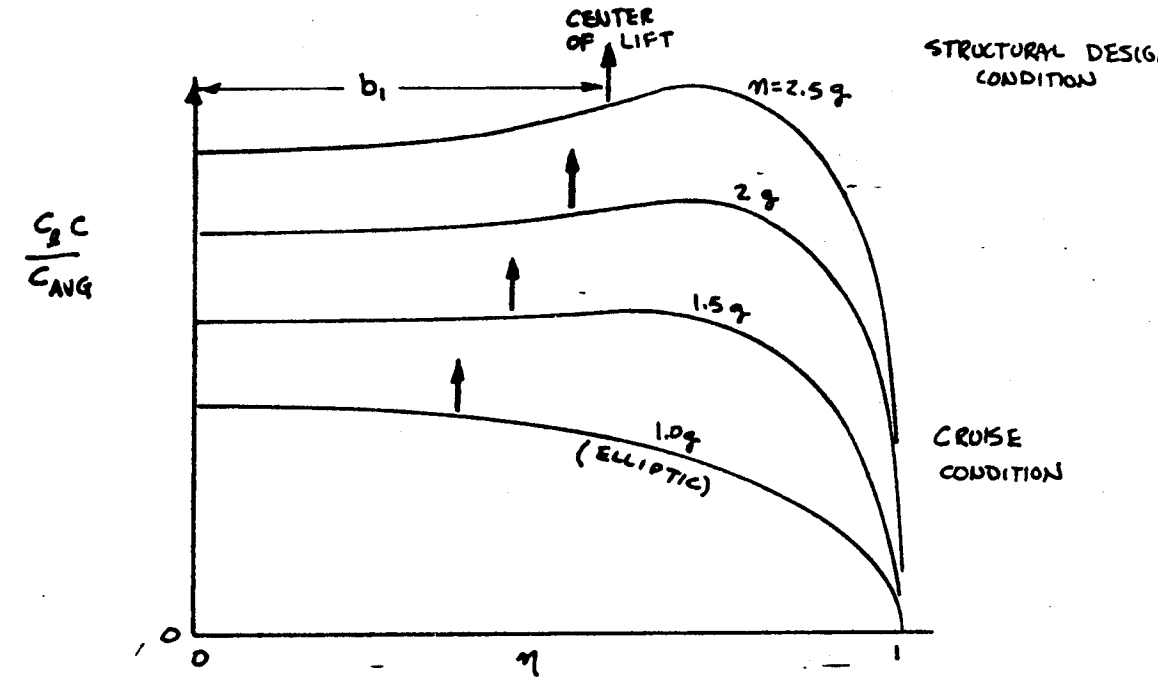

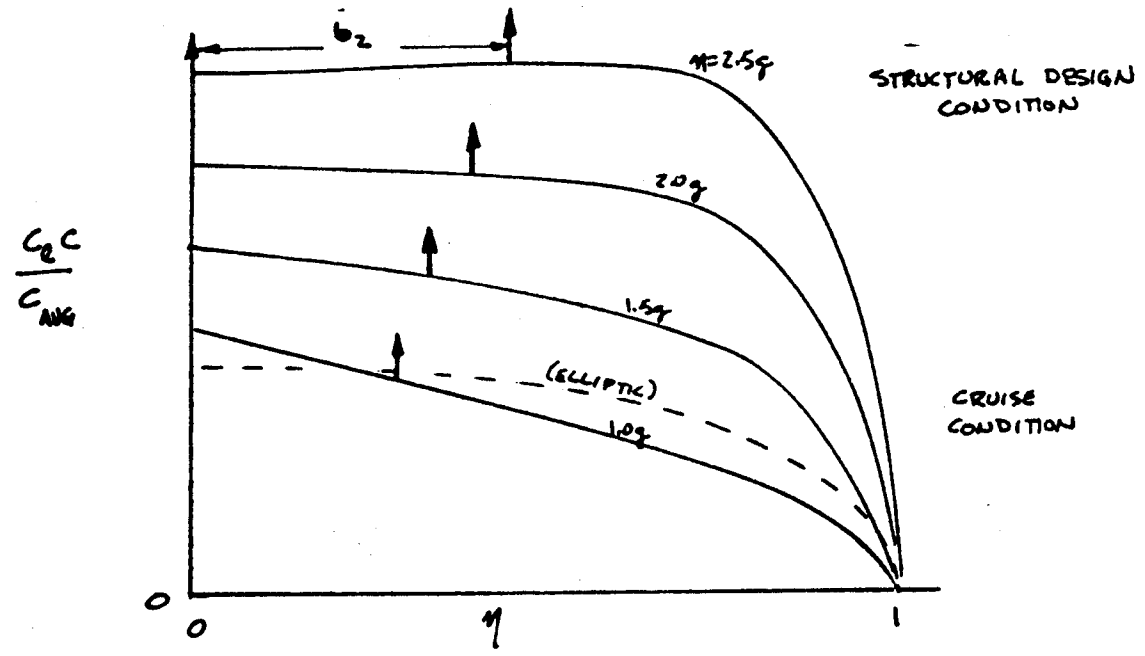

(b) SPAN LOAD CHARACTERISTICS ~ TRIANGULAR CRUISE LOADING

FIGURE 4.13 TRIANGULAR vs ELLIPTIC CRUISE LOADING

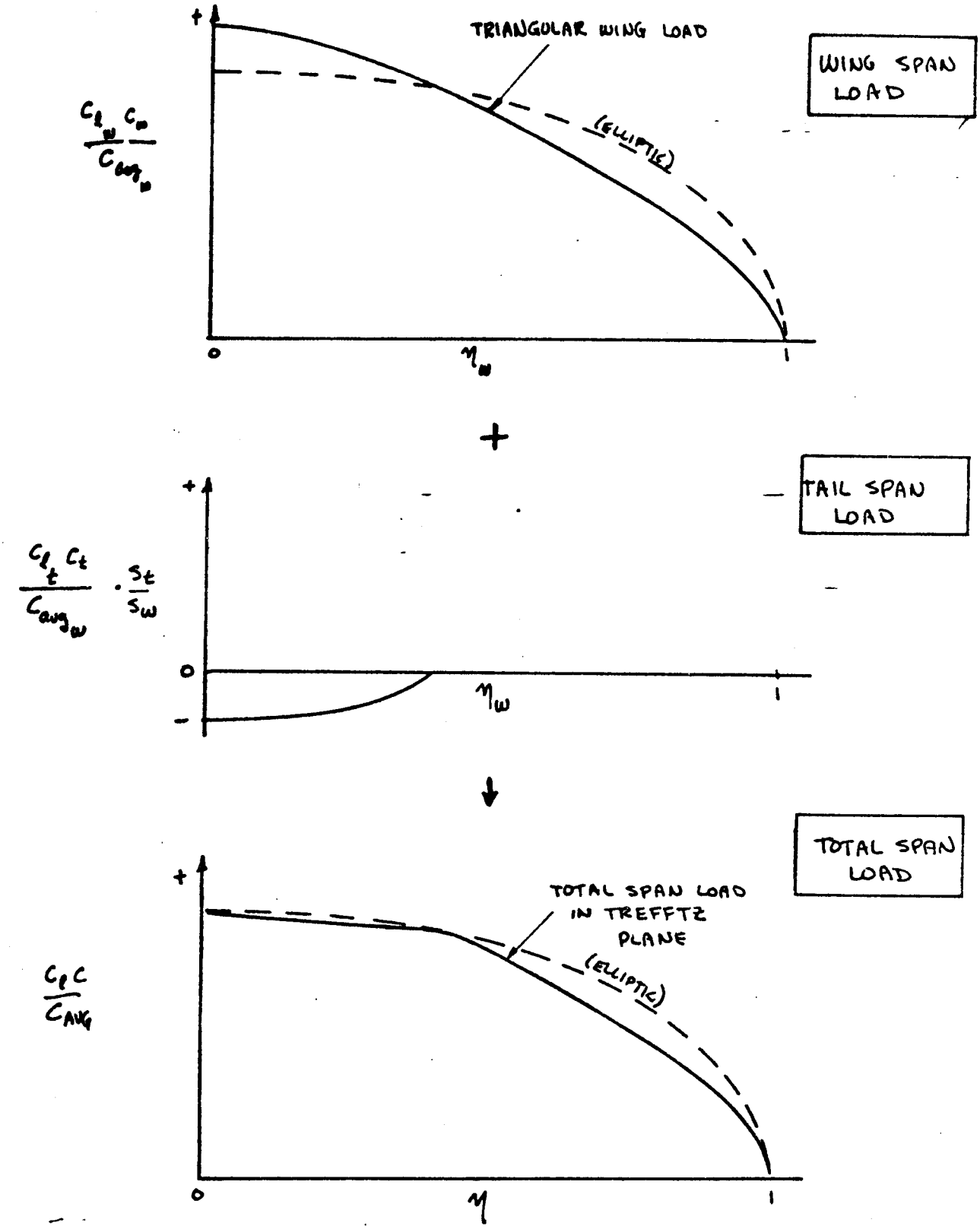

FIGURE 4.14 TAIL & WING COMBINED SPAN LOAD

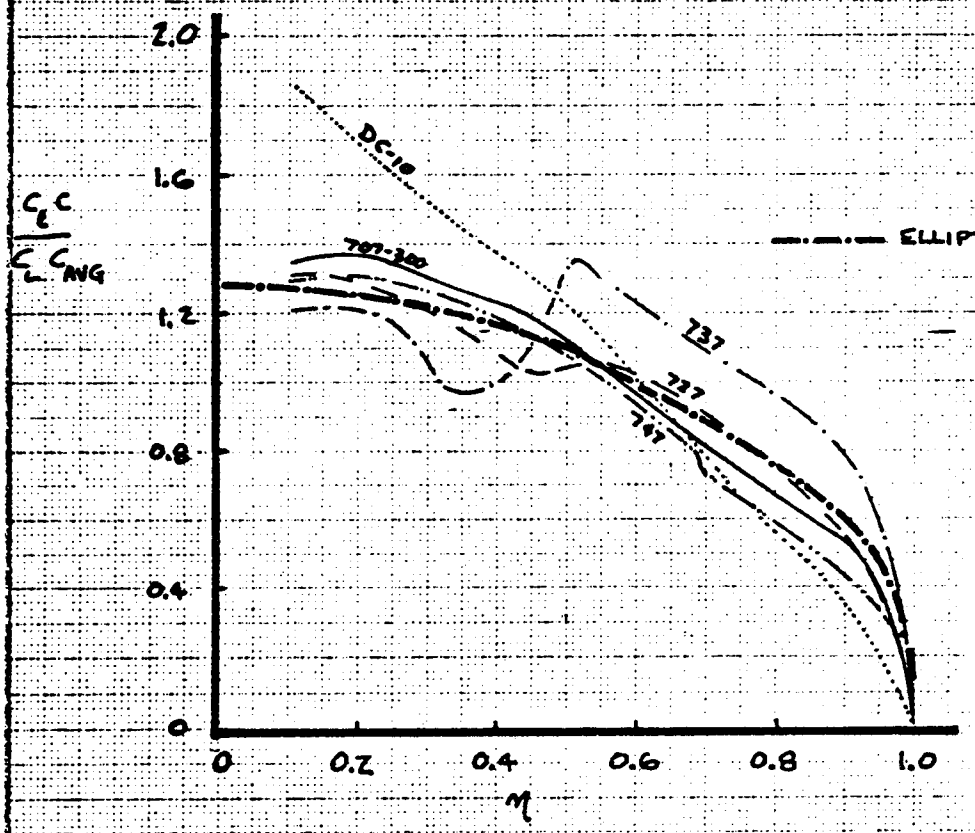

SOURCE: DG-43836 TN
R.J. MARHEFKA

CALC	GILLETTE	1.7.78	REVISED	DATE
CHECK				
APP				
APP				

WING SPAN LOADINGS OF SELECTED PRODUCTION AIRCRAFT FIG 4.15

BOEING

Page 4.58

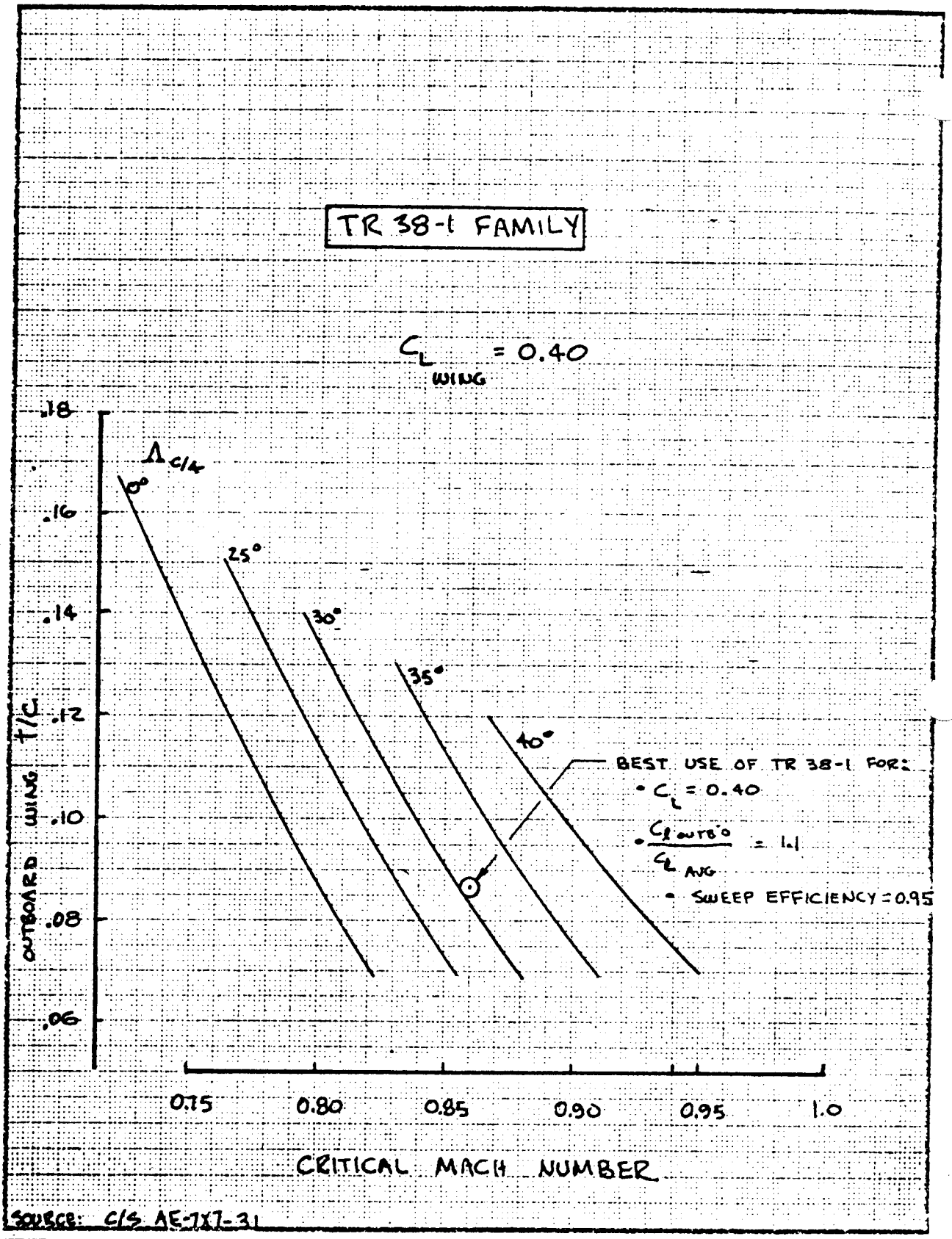

SOURCE: C/S AE-7X7-31

CALC D. Geary-Falvy 3-16-73	REVISED	DATE	EXAMPLE SWEEP-THICKNESS & AIRFOIL BEST USE
CHECK			FIG 4.16
APP			
APP			
TRACE Gillette 1-7-78			BOEING PAGE 4.59

D1 6130 3260 CRIG 3/71

15-347

852

(a) DESIRABLE MARGIN BETWEEN CRUISE & BUFFET

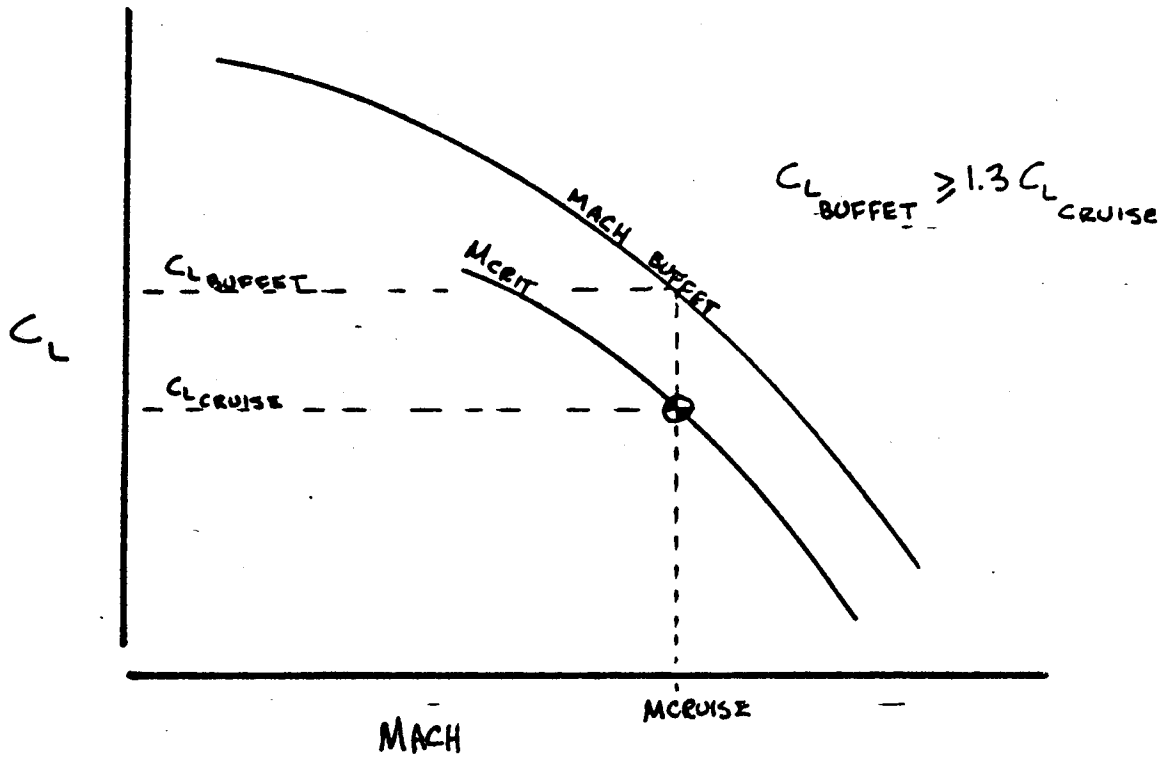

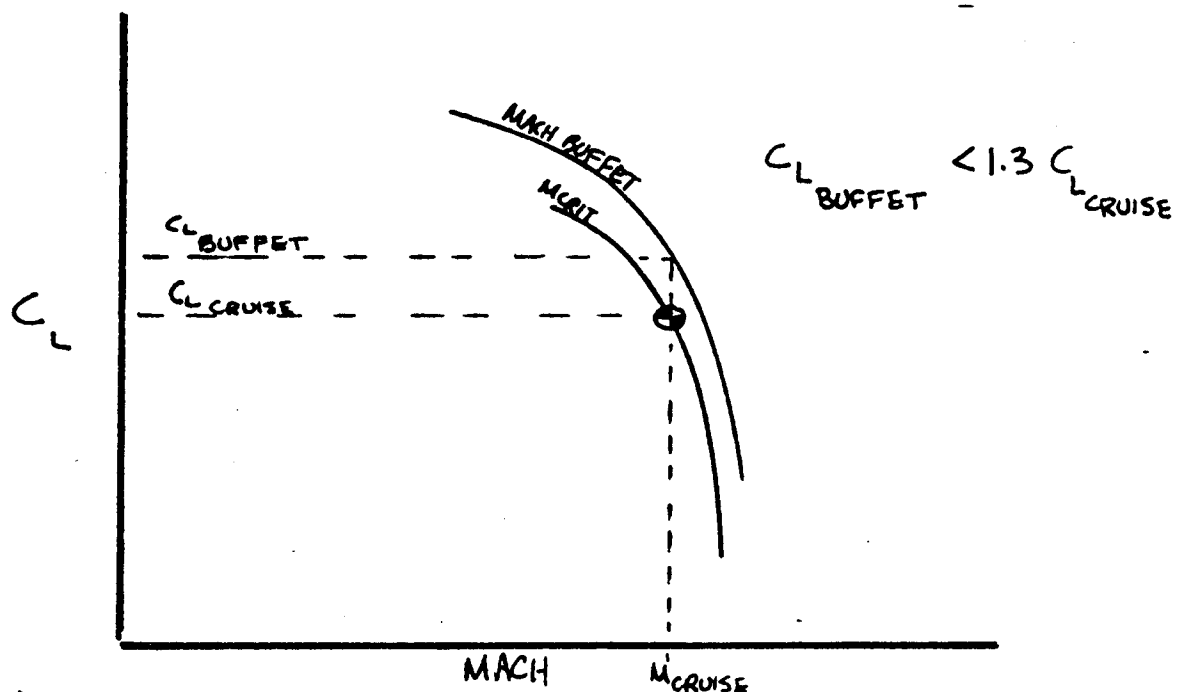

(b) INSUFFICIENT MARGIN BETWEEN CRUISE & BUFFET

FIGURE 4.17 CRUISE-TO-BUFFET MARGIN

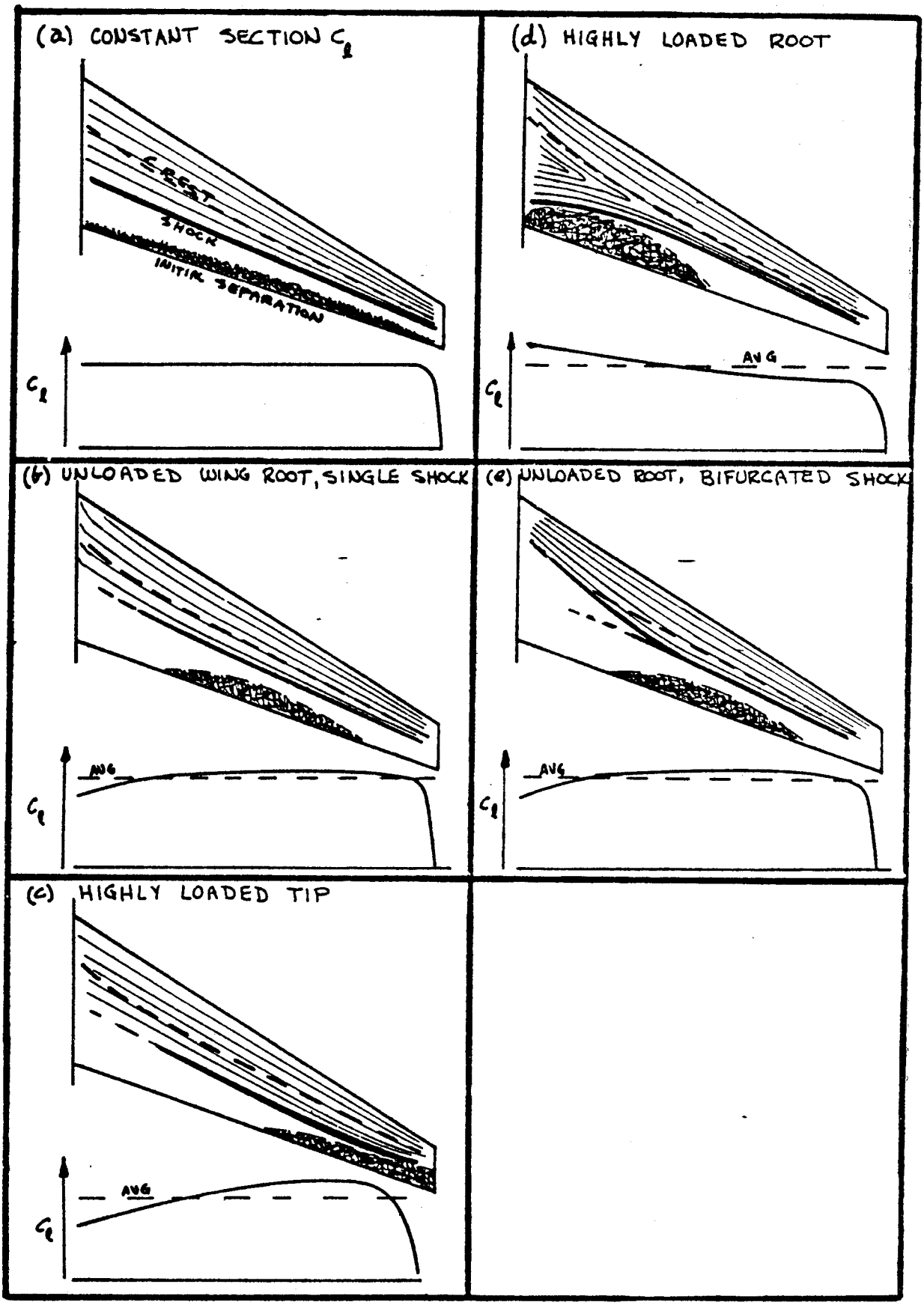

FIGURE 4.18 WING SHOCK & INITIAL SEPARATION CHARACTERISTICS

1-7-78
GILLETTE

(a) DRAW DESIRED SPAN LOAD

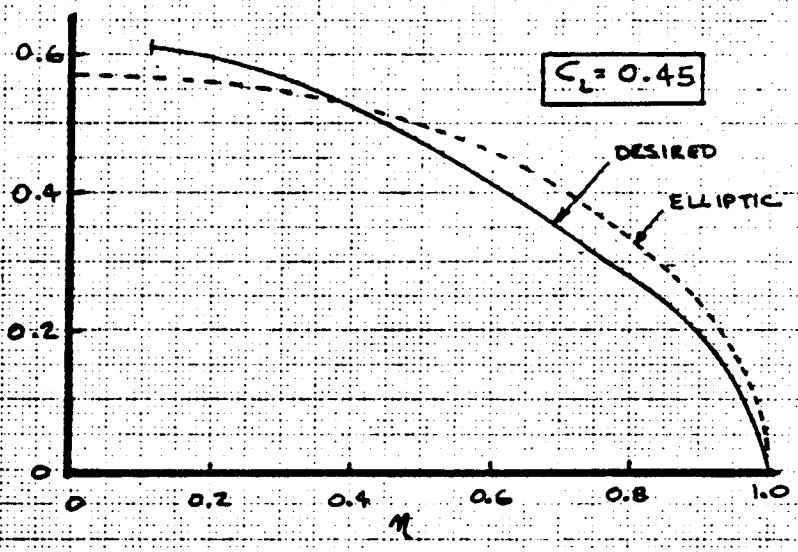

(b) DRAW DESIRED SECTION LIFT

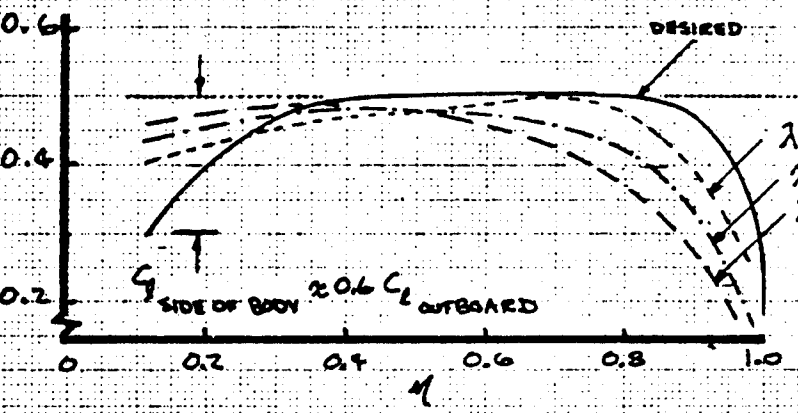

(c) COMPUTE $C_{AVE} = \frac{S_{REF}}{b} = \frac{3000 \text{ SQ. FT.}}{150 \text{ FT}} = 20 \text{ FT}$ (EXAMPLE)

(d)

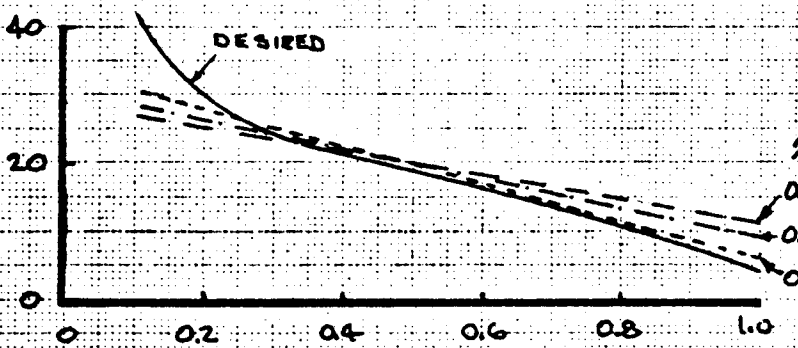

CALC	GILLETTE	1-7-78	REVISED	DATE	SELECTION OF PLANFORM TAPER RATIO
CHECK					
APP					
APP					
					BOEING

FIG 4.19

PAGE 4.62

D1 4100 3260 ORIG. 3/71

191

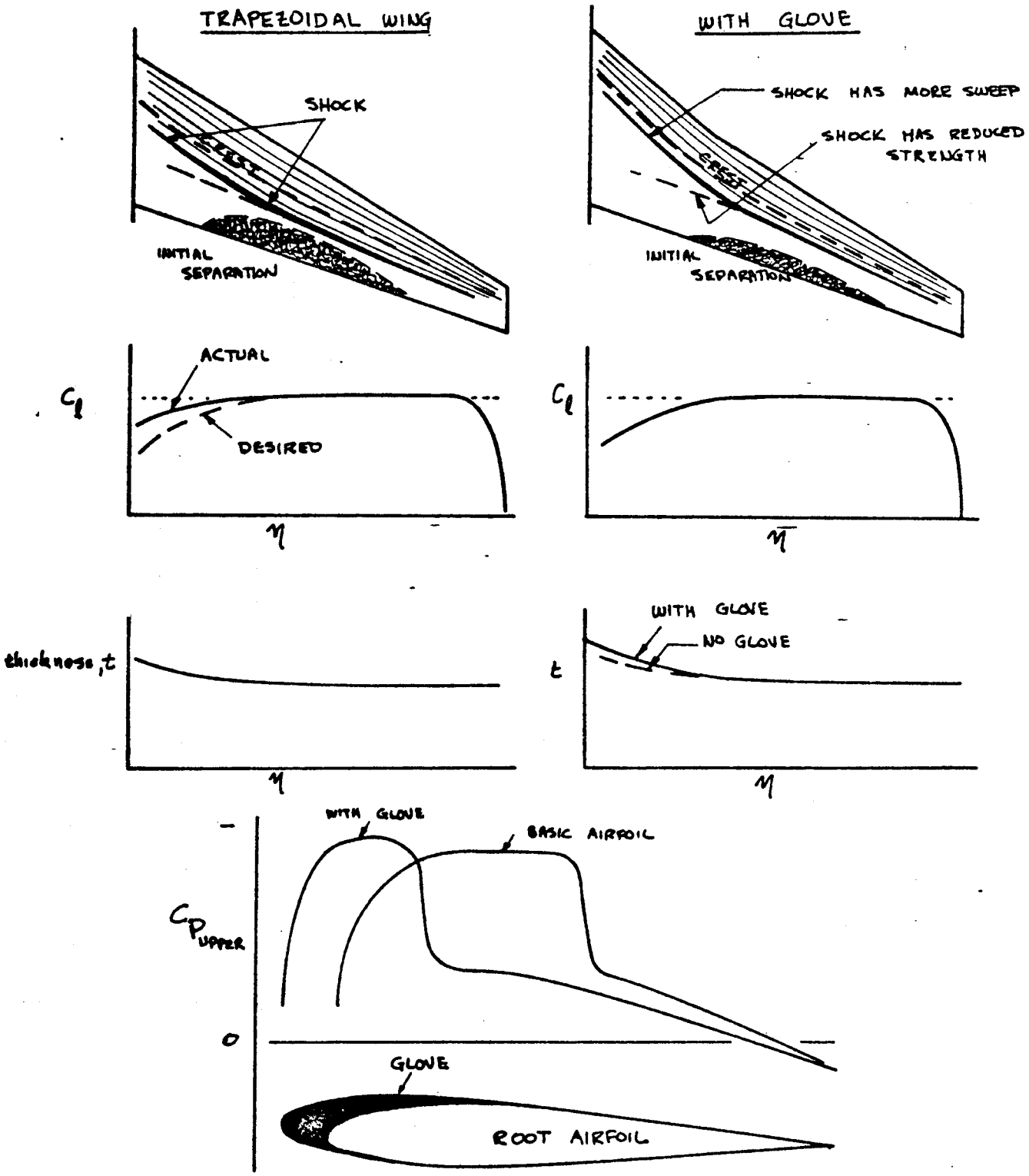

FIGURE 4.20 LEADING EDGE GLOVE

(a) WITH YEHUDI ~ GEAR FOLDS SIDEWAYS INTO BODY

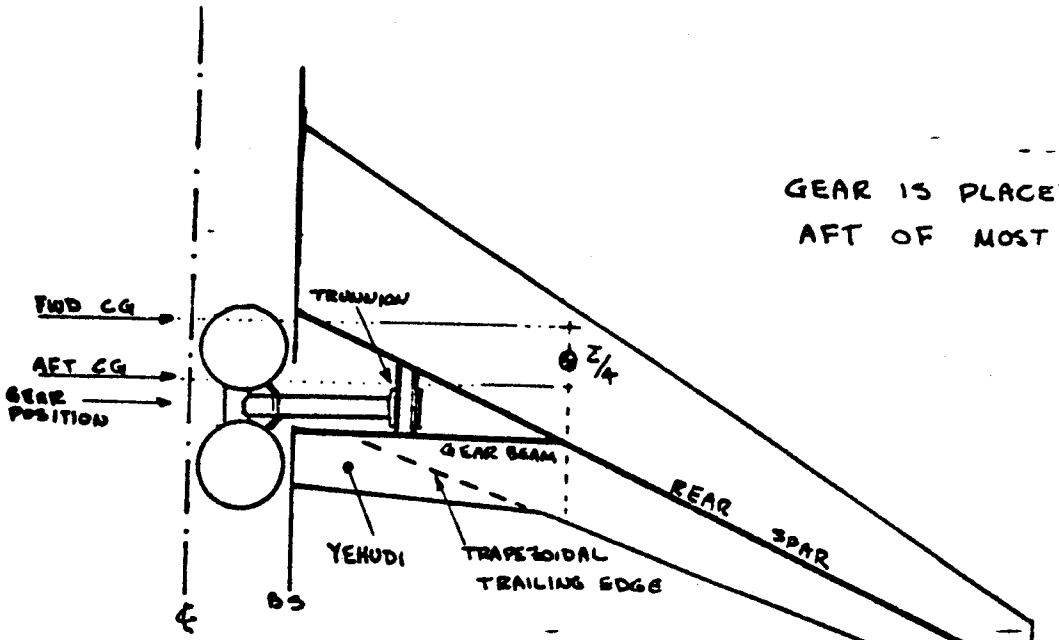

GEAR IS PLACED 3% TO 5% MAC AFT OF MOST AFT CG.

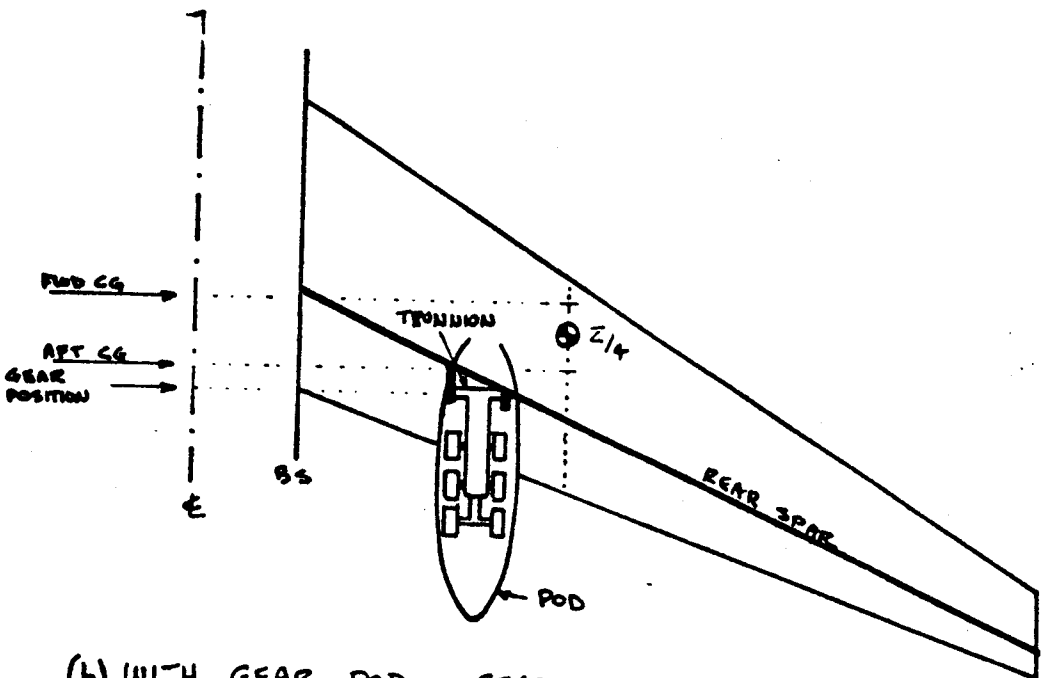

(b) WITH GEAR POD ~ GEAR FOLDS REARWARD INTO POD

FIGURE 4.21 GEOMETRIC CONSIDERATIONS OF YEHUDI VS. GEAR POD

(a) TENDENCY OF YEHUDI IS TO UNSWEEP ISOBARS

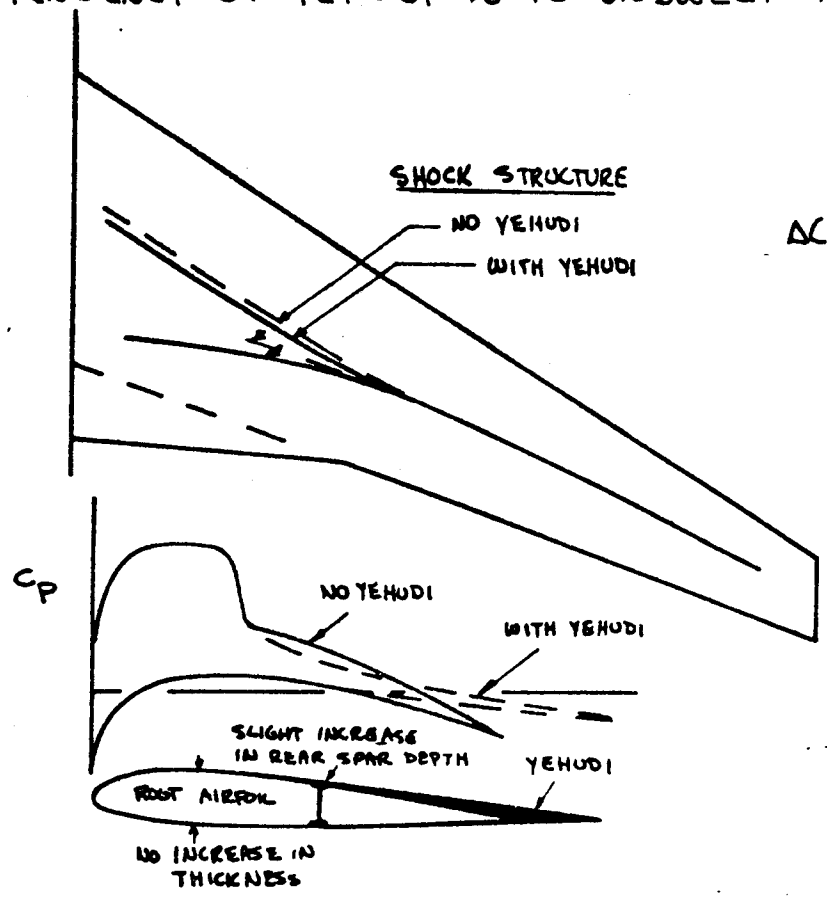

(b) GEAR POD CAN ACT AS "SPEED POD"

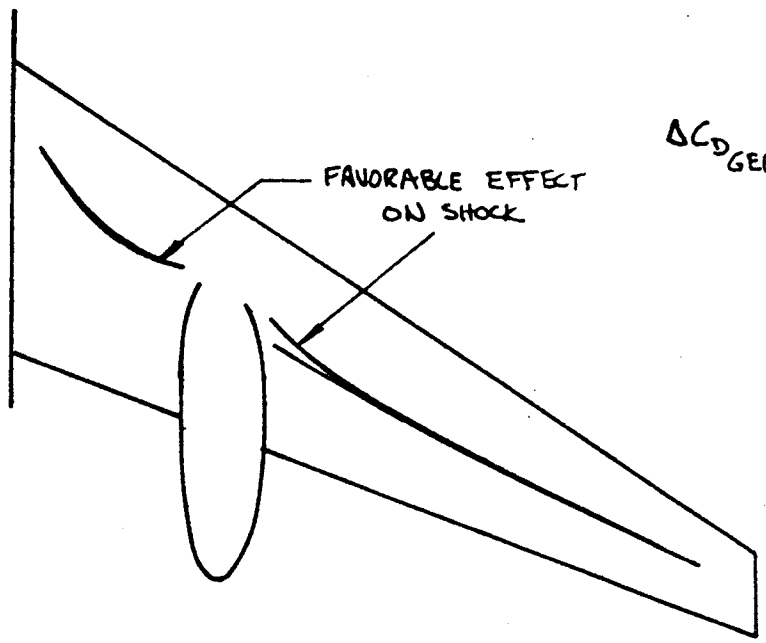

FIGURE 4.22 AERODYNAMIC CONSIDERATIONS OF YEHUDI VS GEAR POD

1.7.78
GILLETTE

① THE HIGH AR WING GIVES UP PROFILE DRAG (C_{D_p}) TO GAIN A THICKER REAR SPAR

② THE WING WEIGHT IS LESS, DUE TO THE THICKER SPAR

③ THE CRUISE (L/D) OF THE HIGH AR WING WILL BE HIGHER BECAUSE OF REDUCED INDUCED DRAG

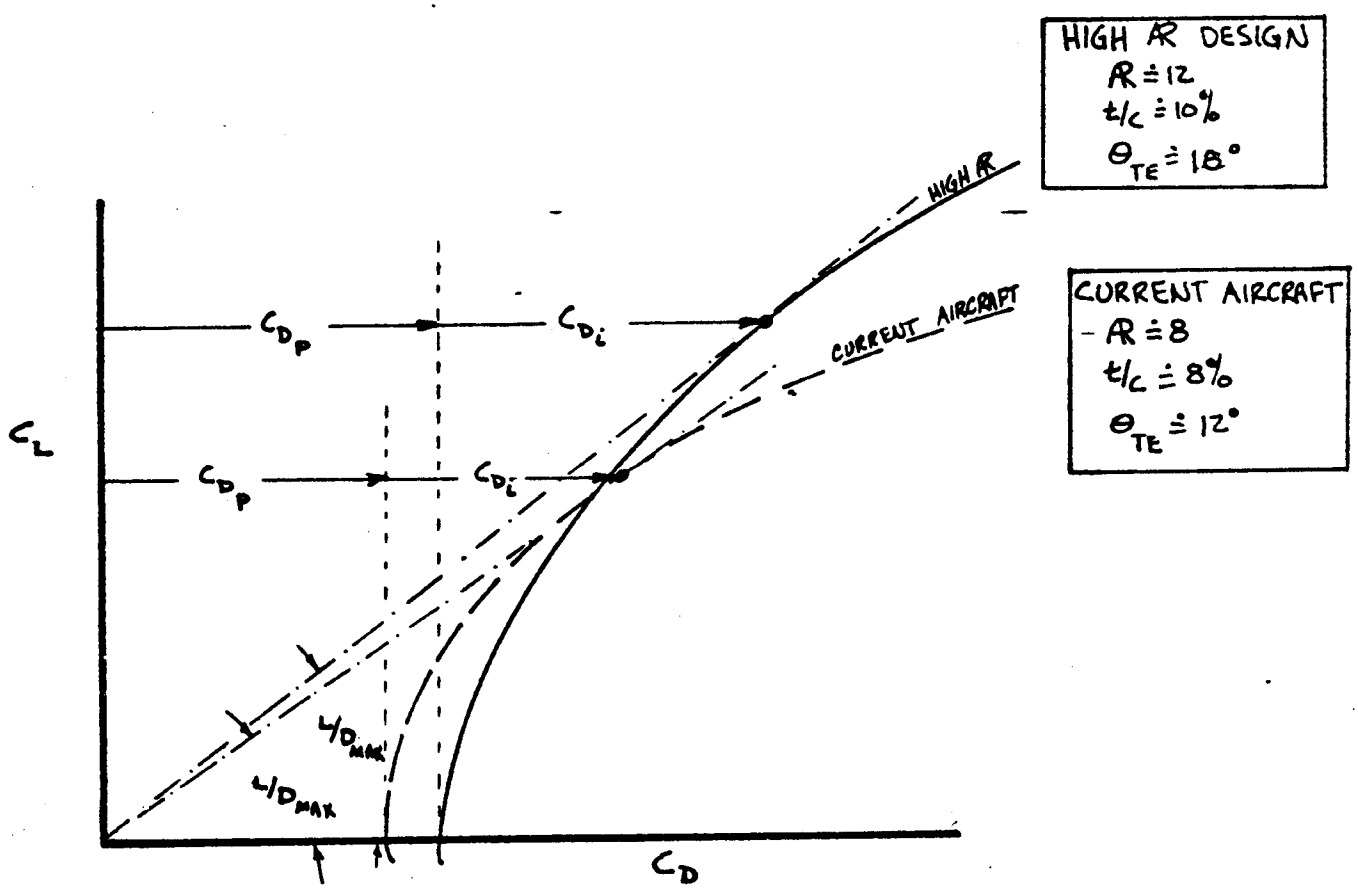

FIGURE 4.23 SECTION DESIGN CONSIDERATIONS FOR HIGH AR WINGS

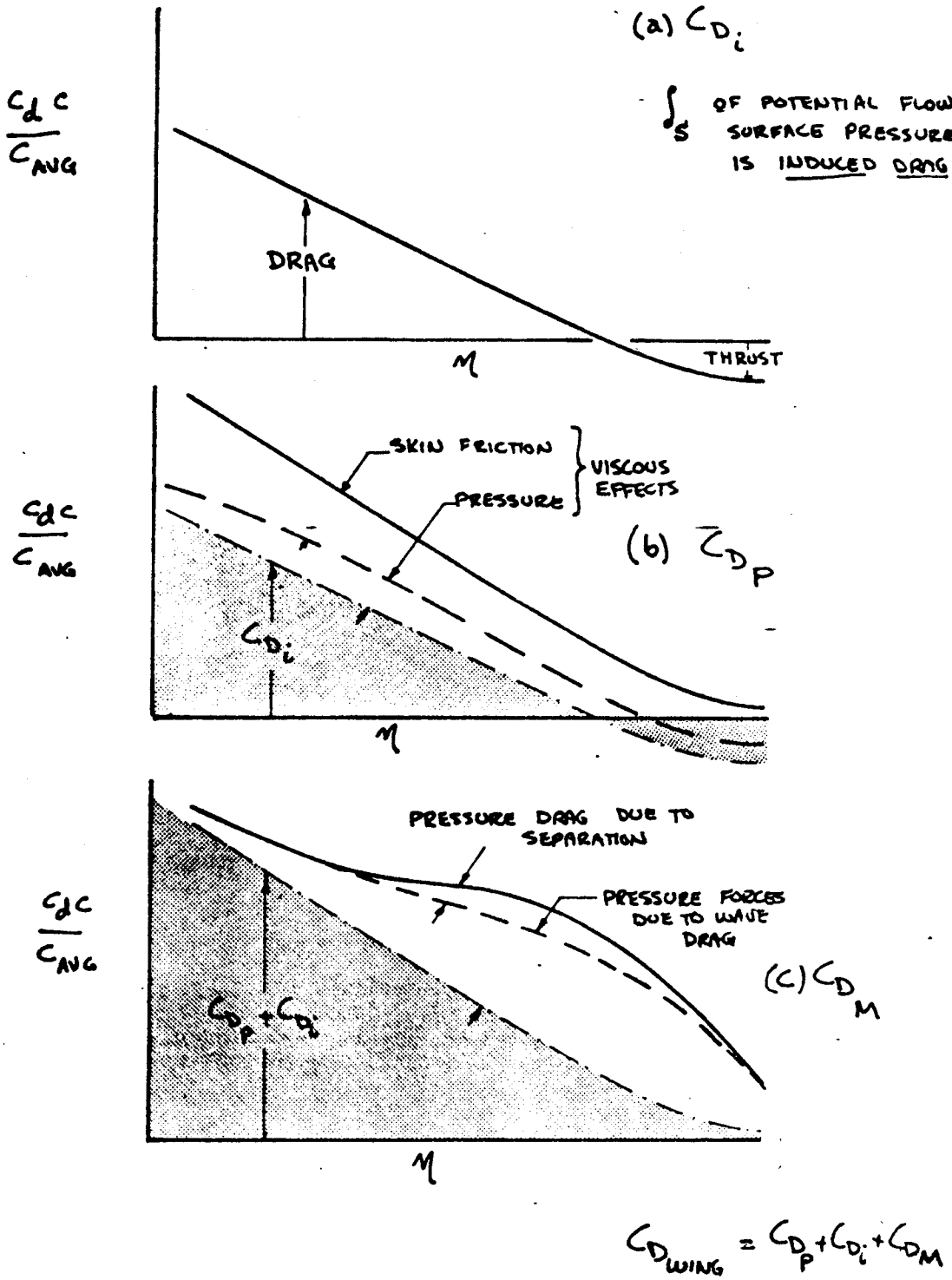

$$C_{D_{WING}} = C_{D_P} + C_{D_i} + C_{D_M}$$

FIGURE 4.24 WING SECTION DRAG

(a) UPPER SURFACE OUTBOARD DESIGN ISOBAR PATTERN

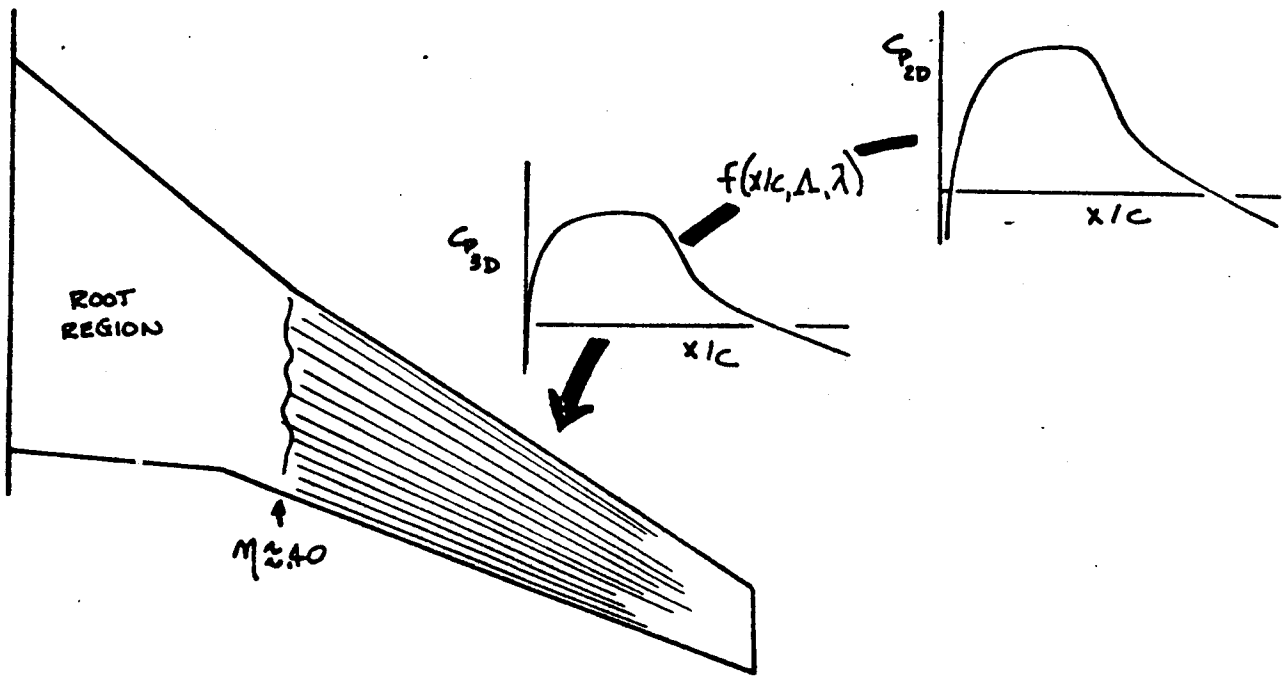

(b) UPPER SURFACE ROOT REGION DESIGN ISOBAR PATTERNS

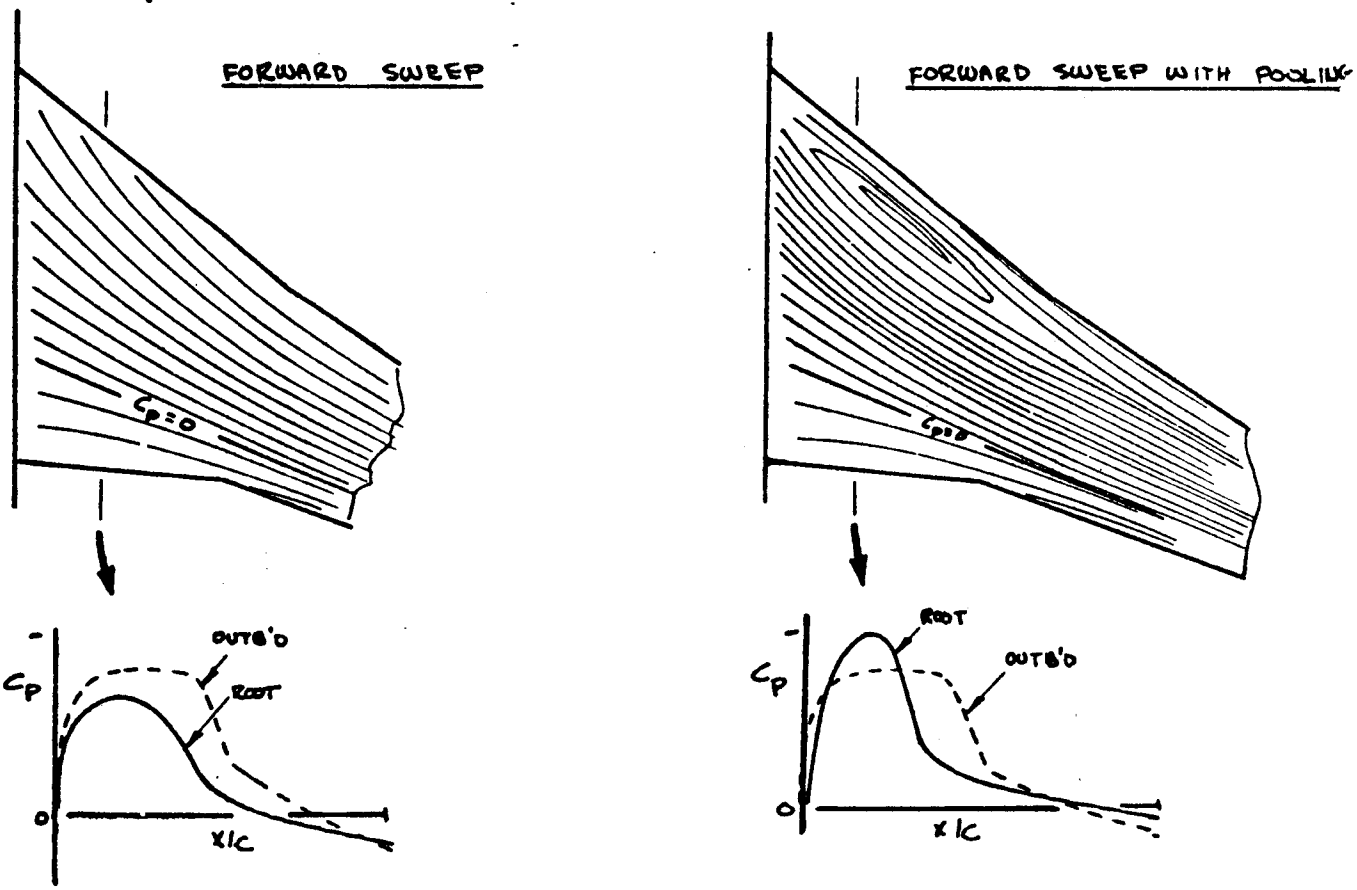

FIGURE 4.25 UPPER SURFACE DESIGN ISOBAR PATTERN

REV SYM

REF: BRITISH R&M 2882

$\alpha = 0°$
$C_L = 0.$

C_p = -0.2 MIN -0.2 -0.1 0

$\alpha = 8.2°$
$C_L = .41$

C_p = -0.8 -0.7 -0.6 -0.5 -0.4 -0.3 -0.2 -0.1 0

MIN. = -1.4

C_p = 0.8 0.7 -0.6

ISOBARS ON WING UPPER SURFACE (WIND TUNNEL RESULTS)

REF: BRITISH R&M 2935

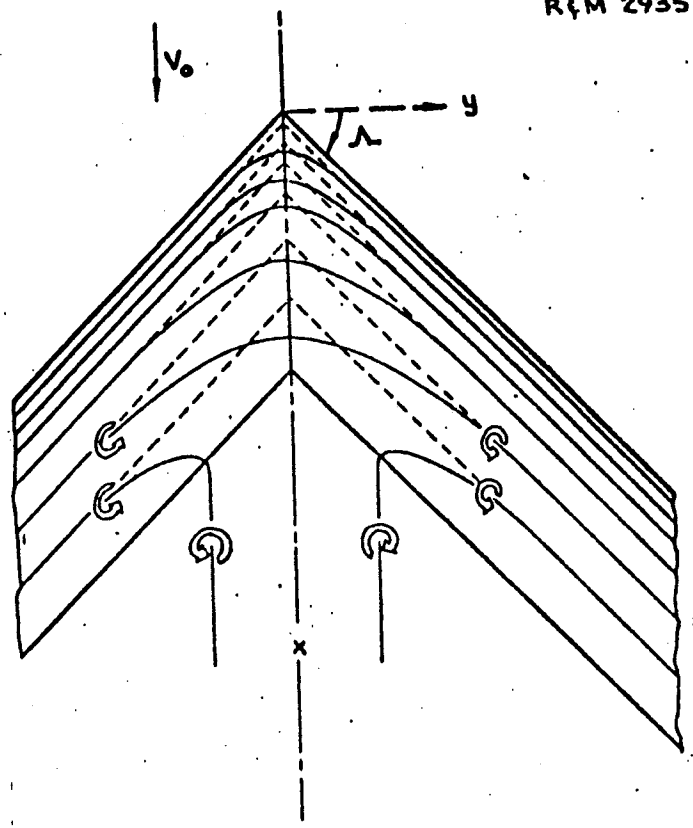

VORTEX SYSTEM FOR KÜCHEMANN METHOD

J.M. KLANSNIK 4-8-76

BOEING

FIG. 4.26
NO. 16-43836 TN
PAGE 4.69

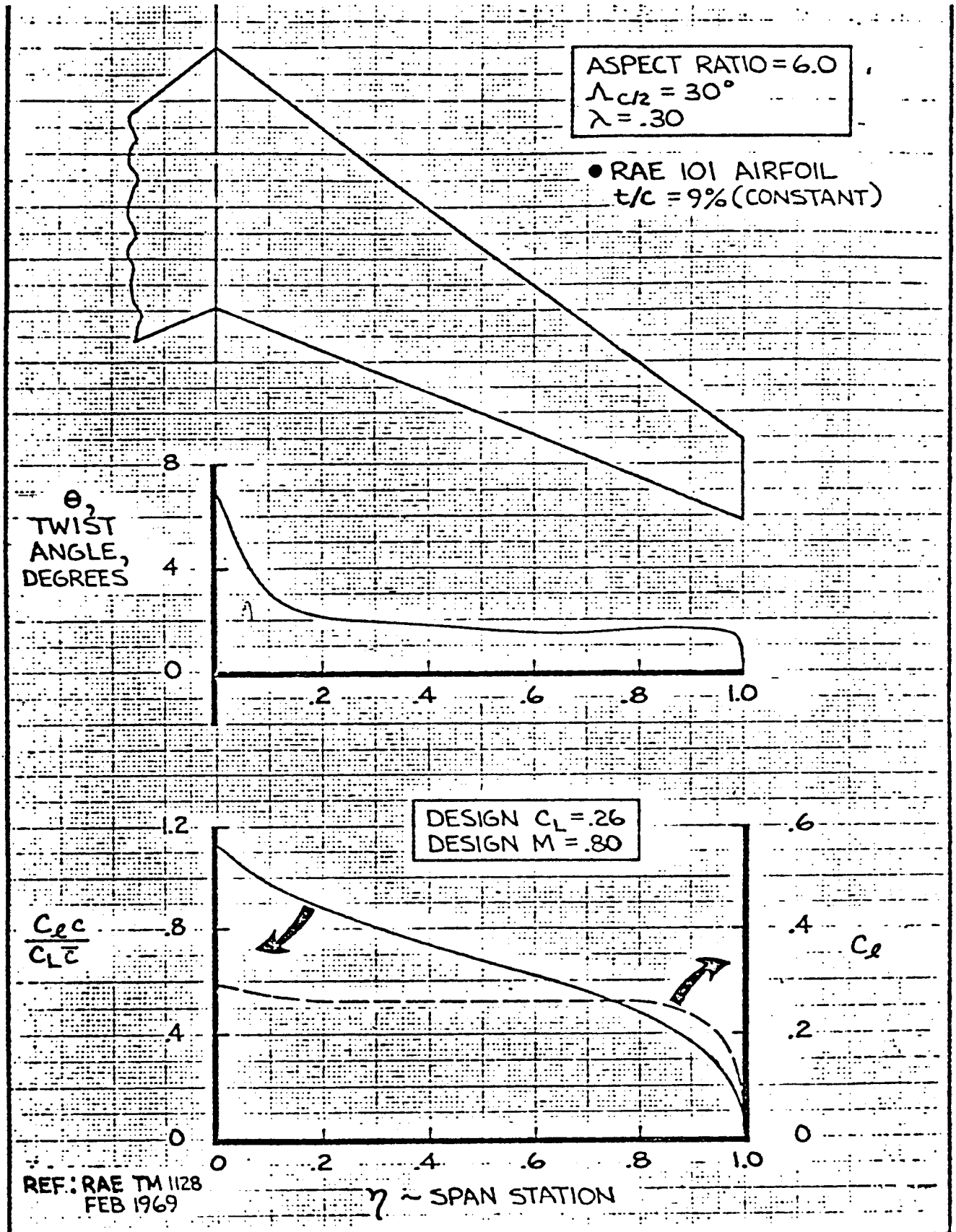

CALC			REVISED	DATE	WING B PLANFORM, SPAN LOADING AND CALCULATED TWIST
CHECK					
APR					
APR					
DWN	J.M.KLANSNIC	3-15-76			THE BOEING COMPANY

FIG. 4.27
D6-43836TN
PAGE 4.70

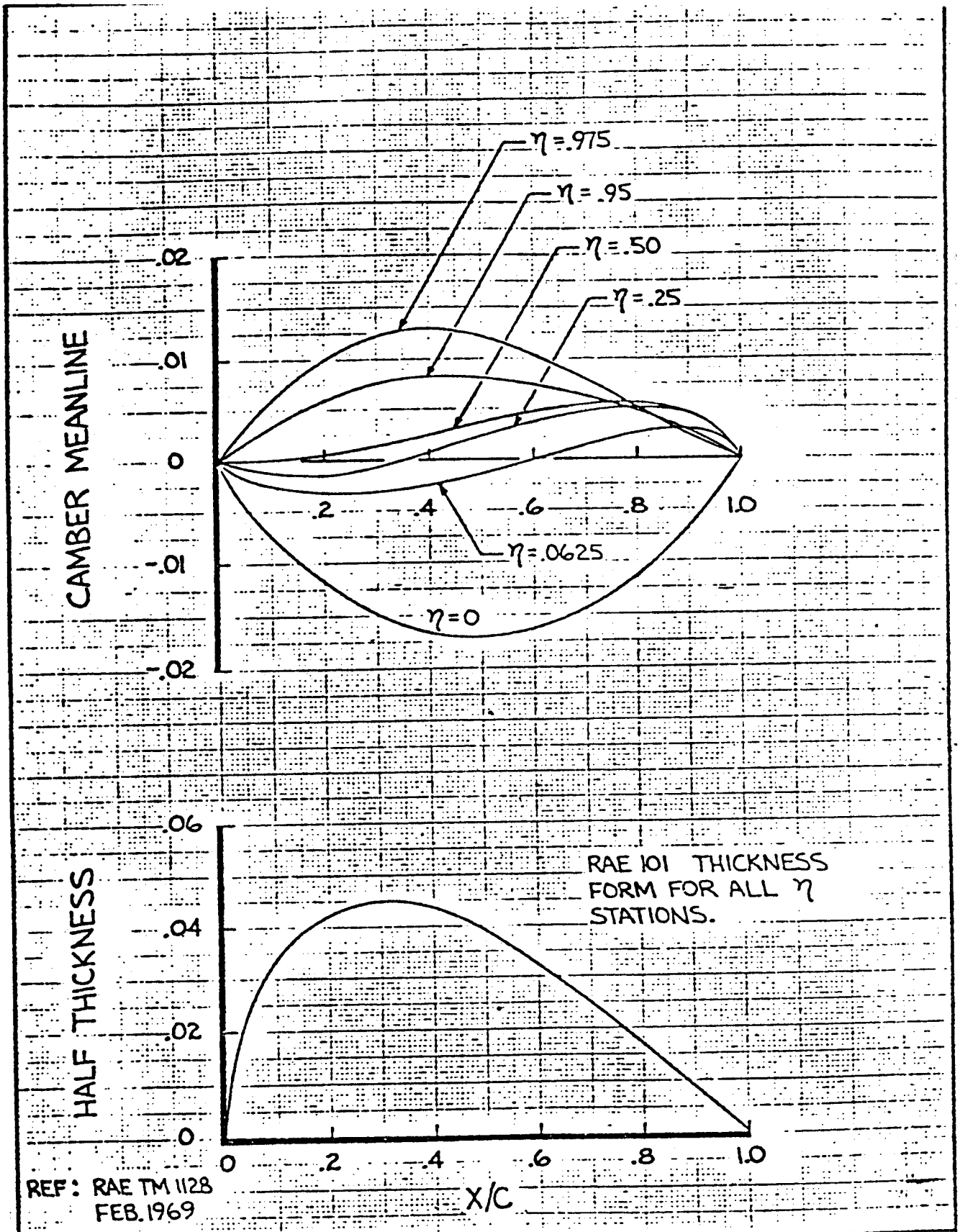

CALC			REVISED	DATE	WING B CAMBER AND THICKNESS FORM
CHECK					
APR					
APR					
DWN	J.M. KLANSNIC	3-17-76			THE BOEING COMPANY

FIG. 4.2B

D6-43836TN

PAGE 4.71

D1 4100 3240

K-E ALBANENE TOOL

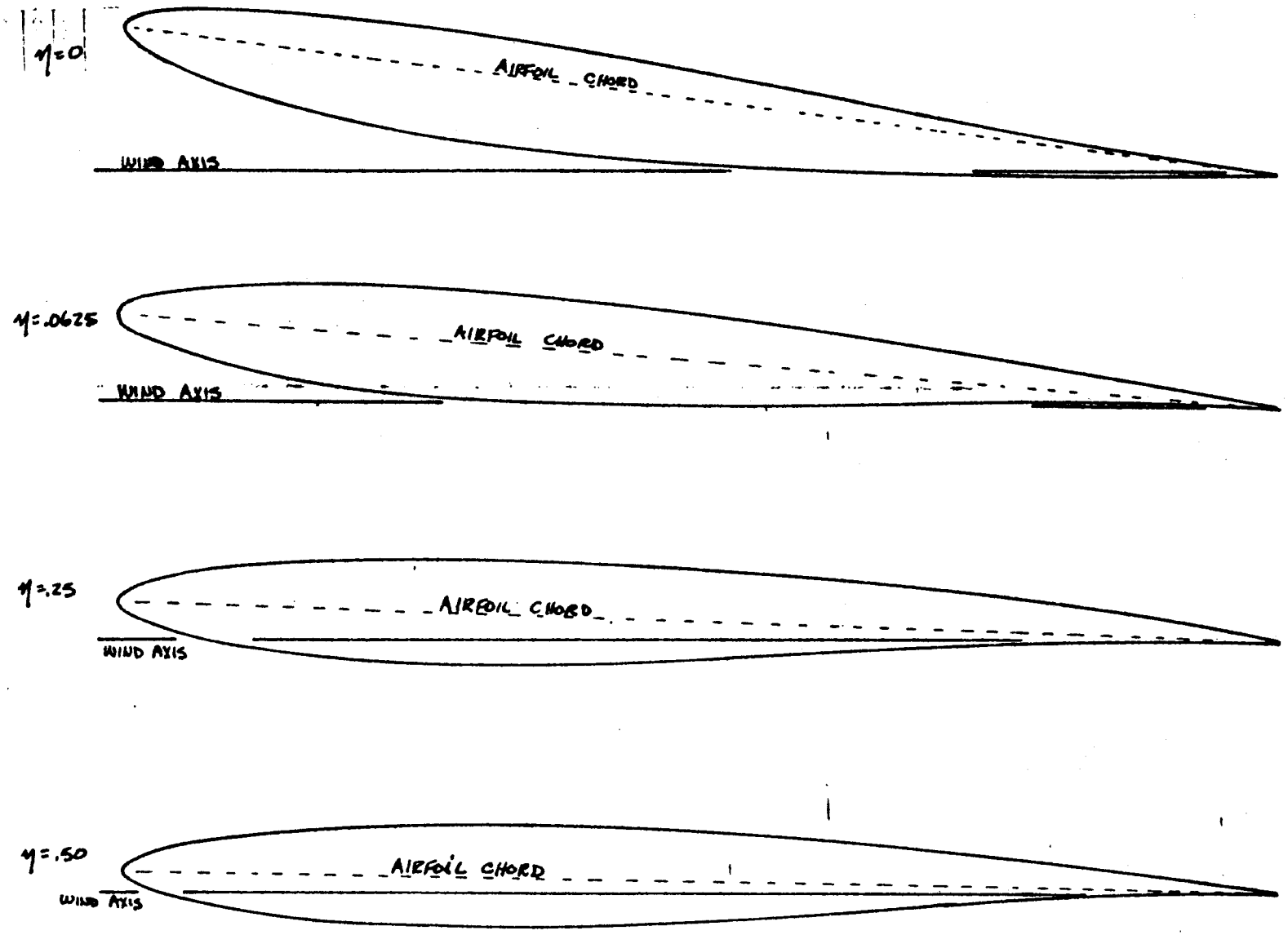

FIGURE 4.29 WING B WING SECTIONS SHOWN RELATIVE TO WIND AXIS

DESIGN $C_L = .26$
DESIGN $M = .80$

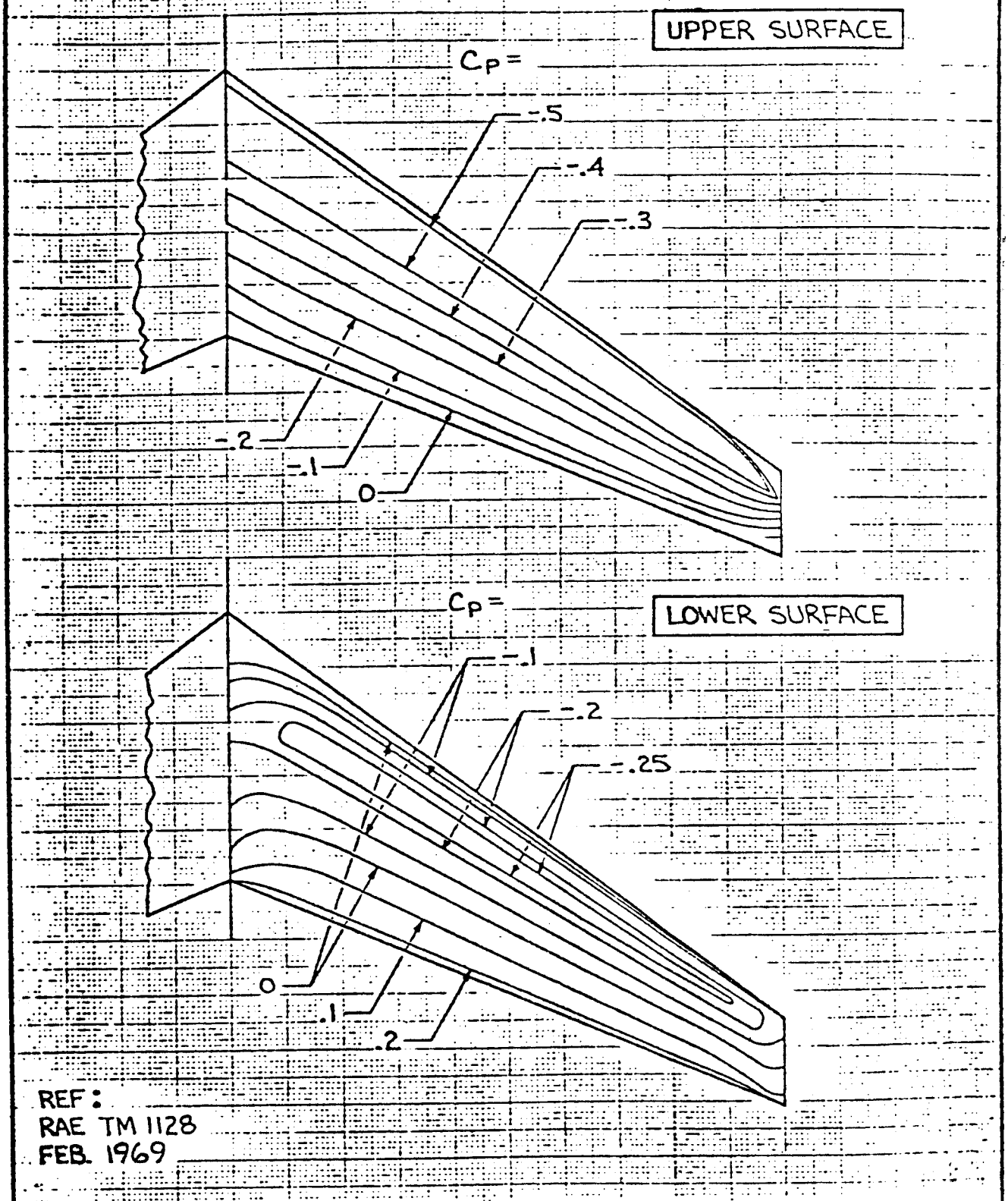

REF:
RAE TM 1128
FEB. 1969

CALC			REVISED	DATE	WING B CALCULATED ISOBAR PATTERNS
CHECK					
APR					
APR					
DWN	J.M. KLANSNIC	3-16-76			THE BOEING COMPANY

FIG. 4.30
D6-43836TN
PAGE 4.73

278

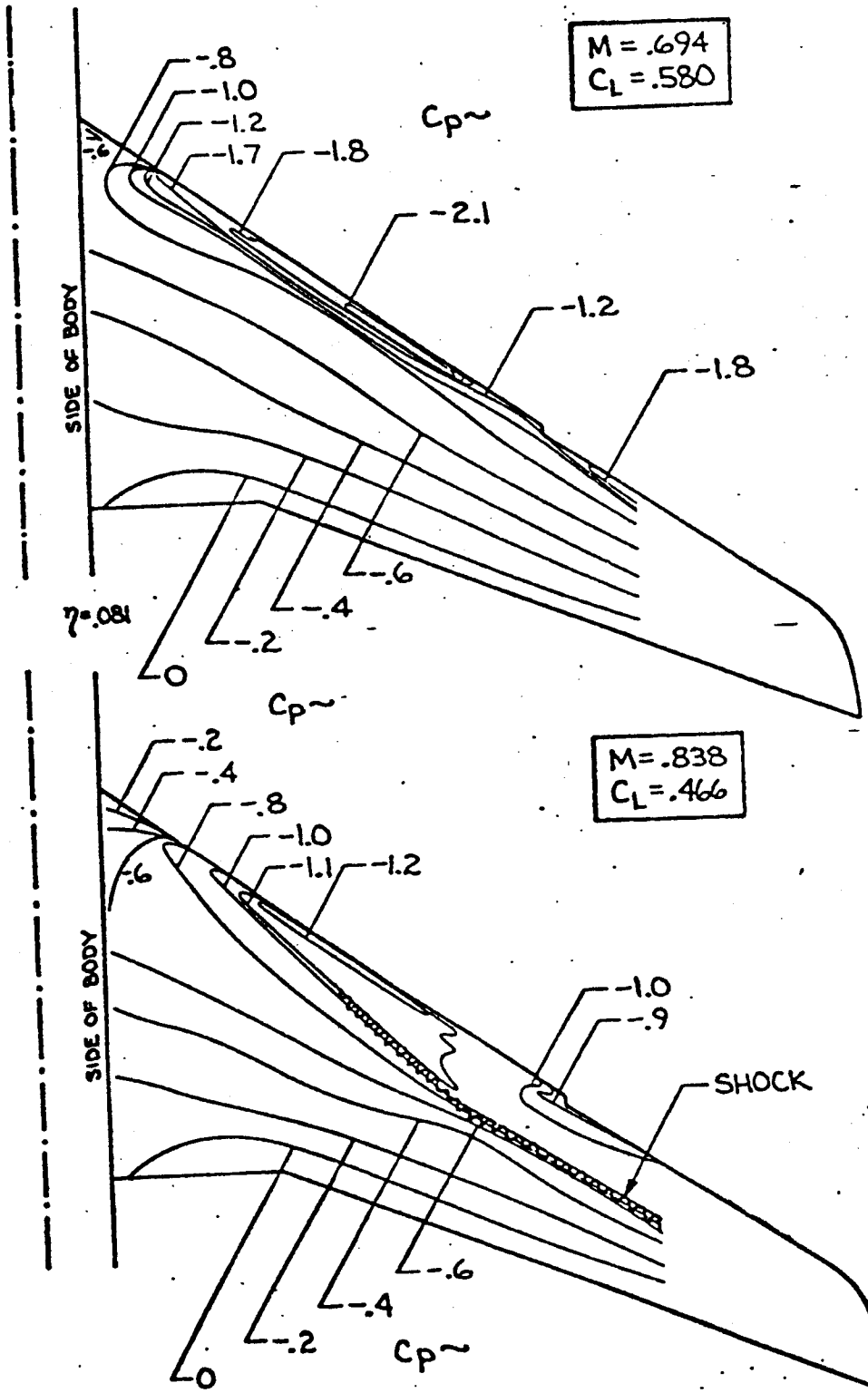

SUPER VC-10
WIND TUNNEL ISOBARS

REF. R+M 3707

J.M. KLANSNIC 4-5-76

FIG 4.3

BOEING | NO. D6-43836TN | PAGE 4.74

REV SYM

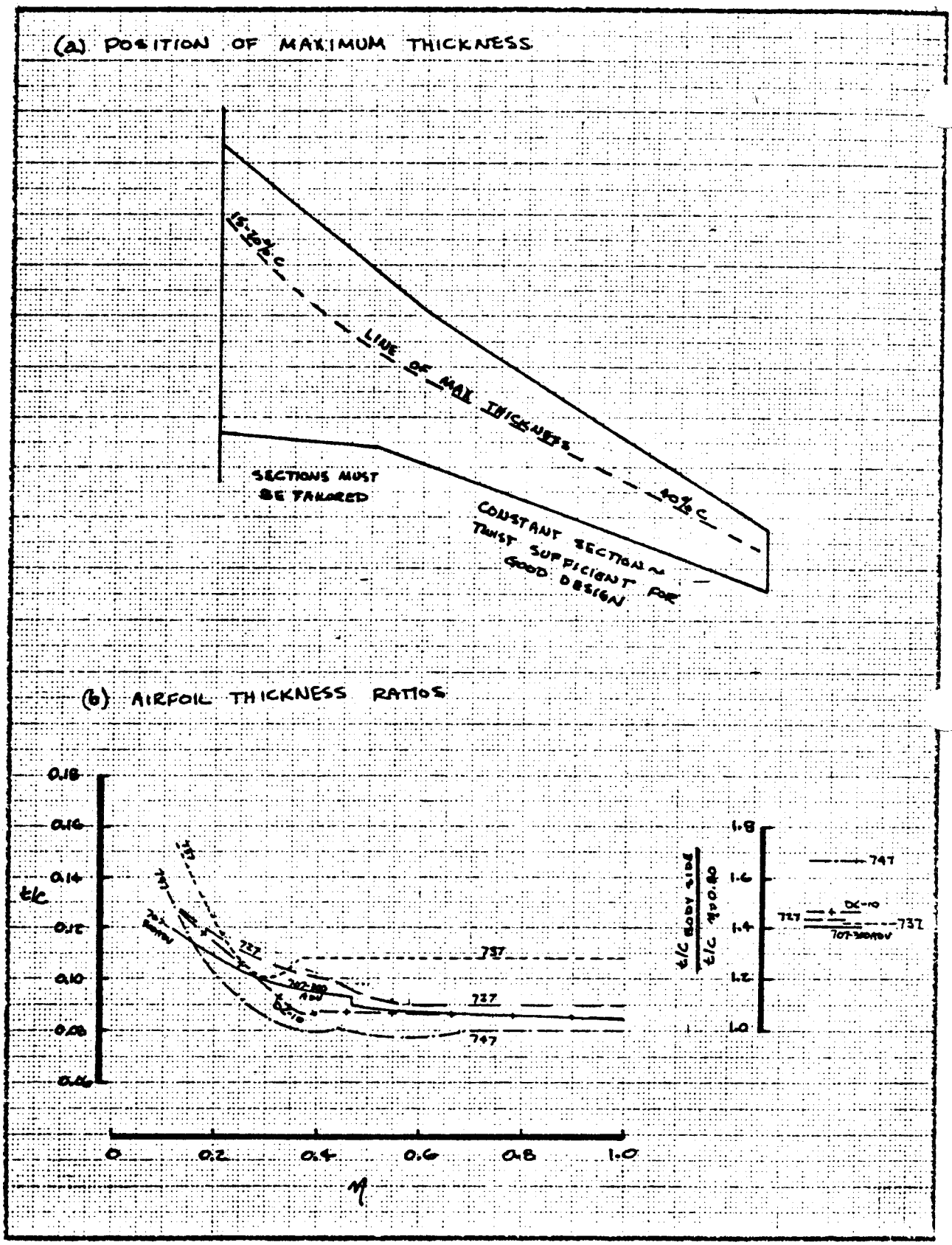

CALC	GILLETTE	1.13.78	REVISED	DATE	WING SECTION THICKNESS RATIO TRENDS
CHECK					
APP					FIG. 4.32
APP					
					BOEING

D1 4100 3760 ORIG 3/71

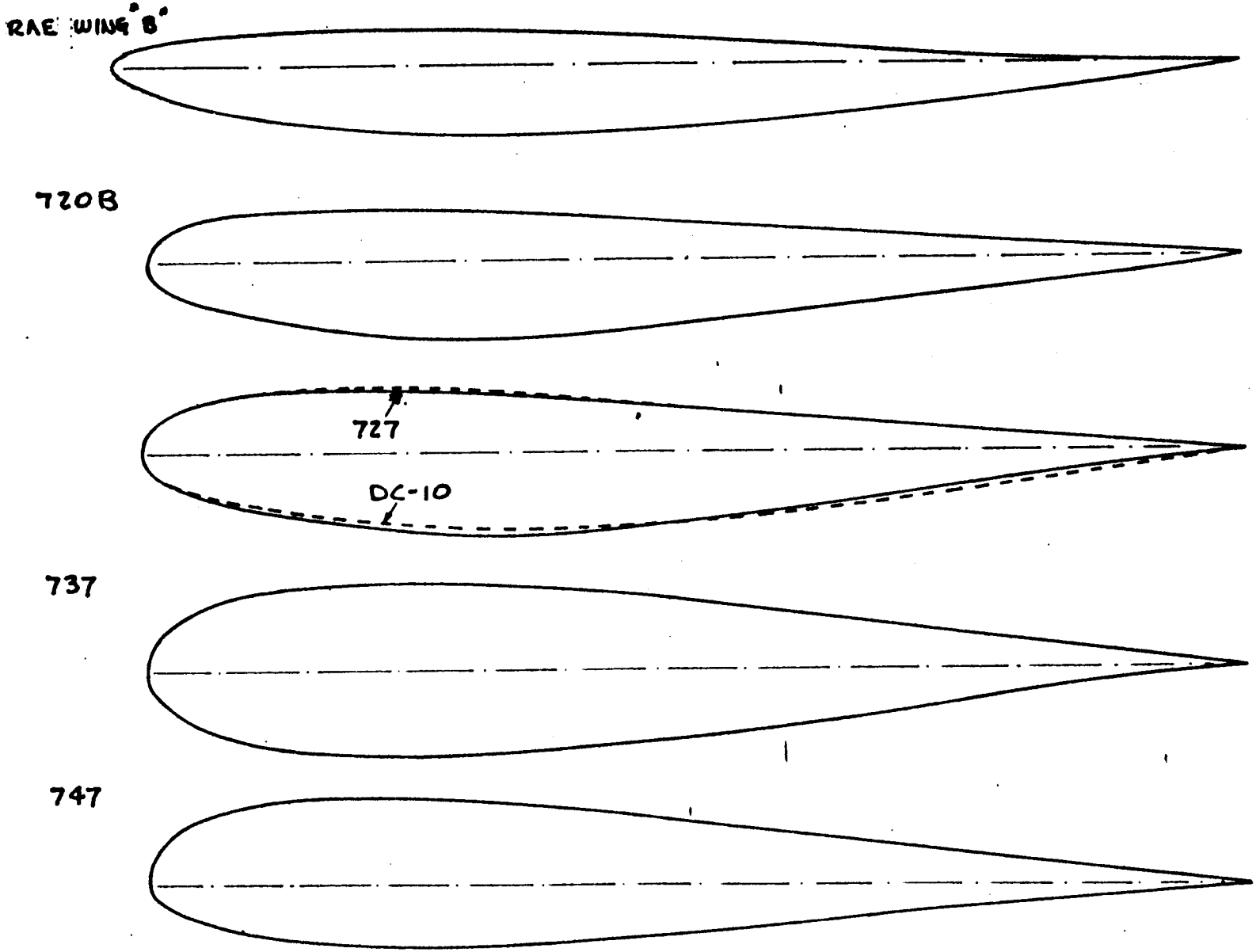

FIGURE 4.33 SELECTED ROOT AIRFOILS

1.14.78
GILLETTE

(a) ROOT AIRFOIL WITH REDUCED UPPER CURVATURE

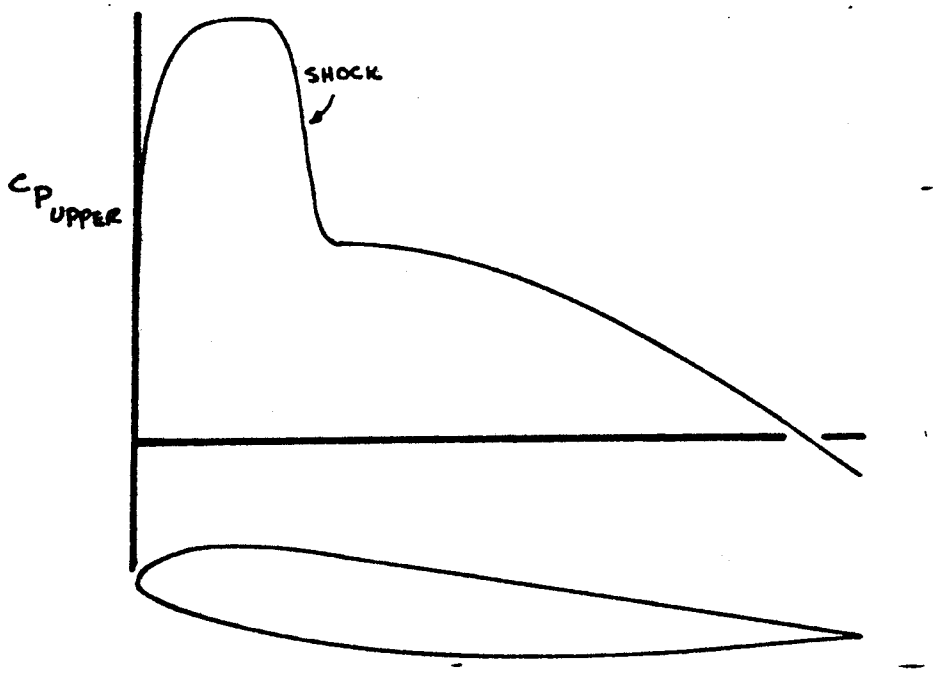

(b) ROOT AIRFOIL WITH CONTINUED UPPER CURVATURE

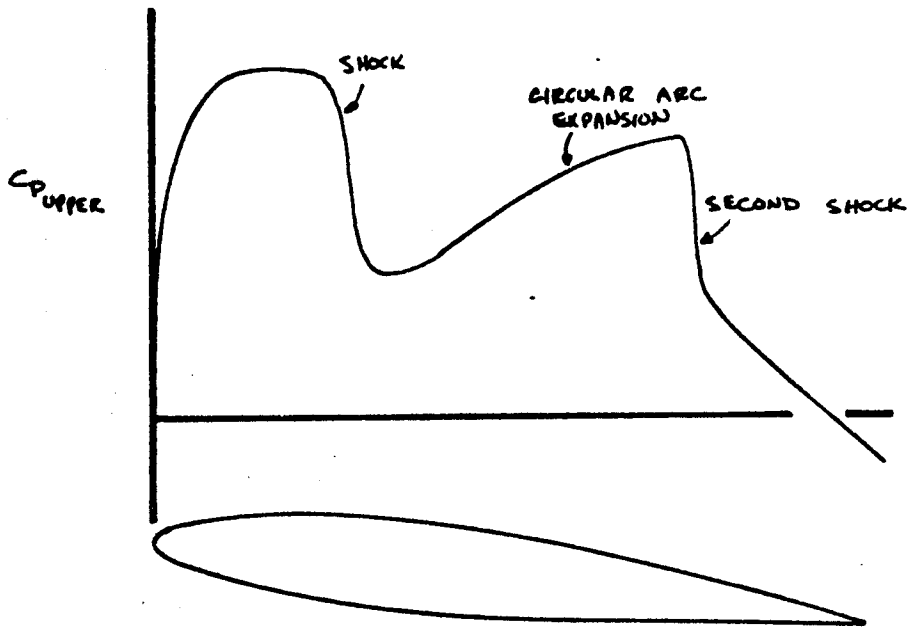

FIGURE 4.34 ROOT AIRFOIL UPPER SURFACE PRESSURE TRENDS

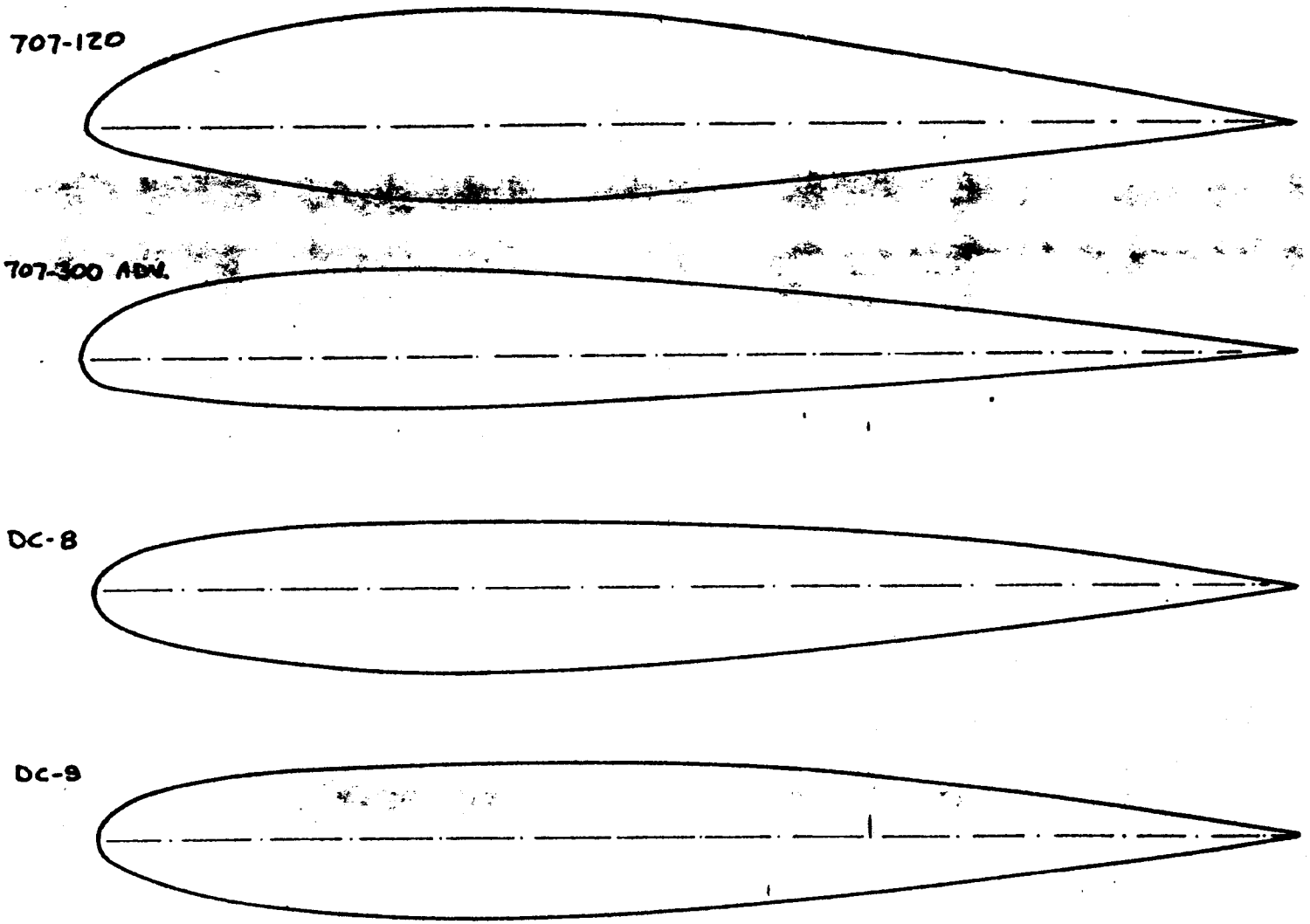

FIGURE 4.35 ROOT AIRFOILS WITH CONTINUOUS UPPER SURFACE CURVATURE

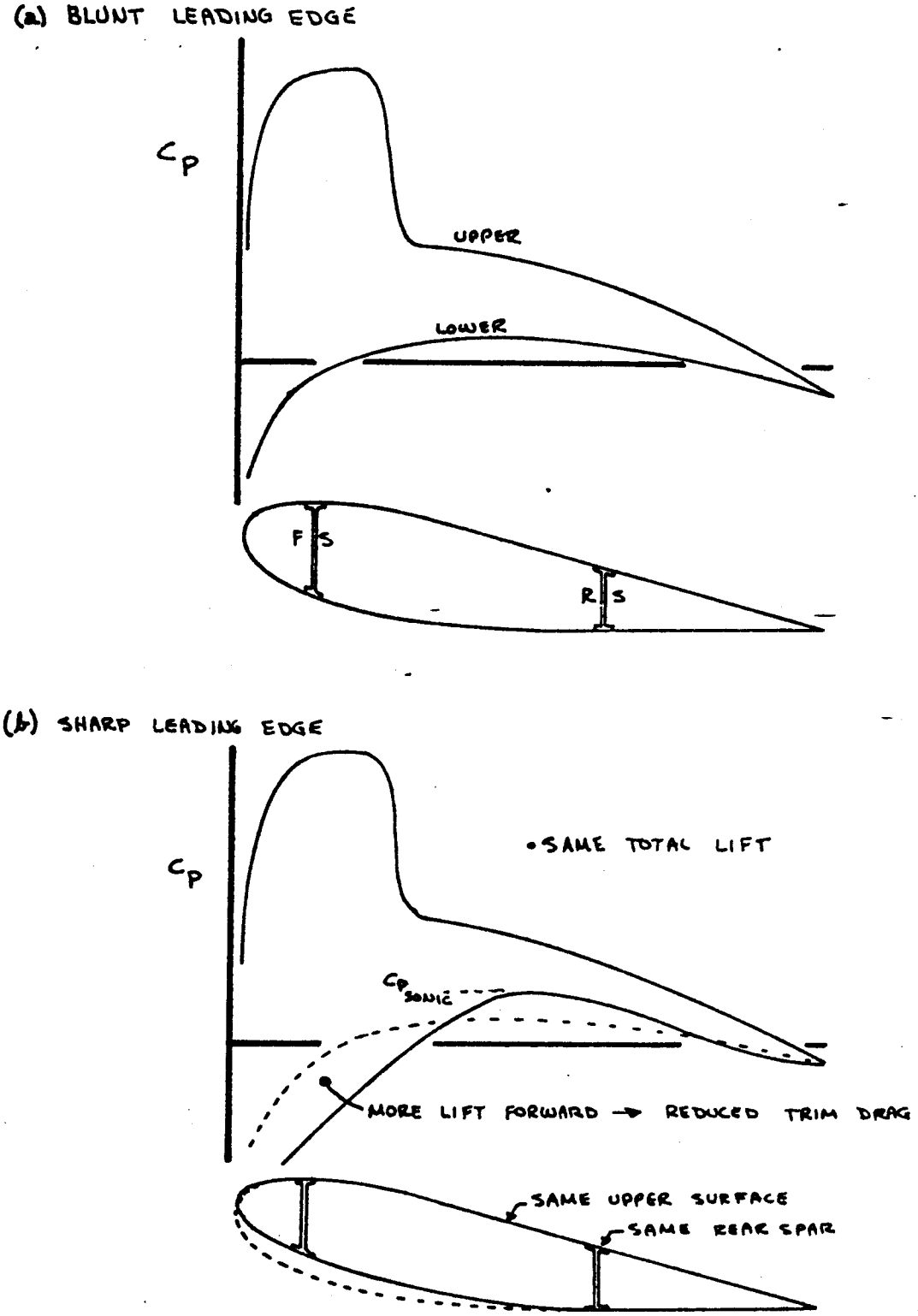

FIGURE 4.3C ROOT AIRFOIL LOWER SURFACE OPTIONS

(a) UNTAILORED TIP

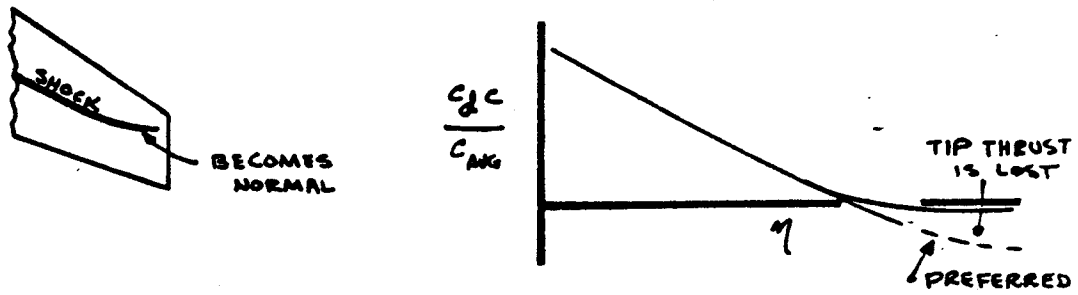

(b) RAKED TIP

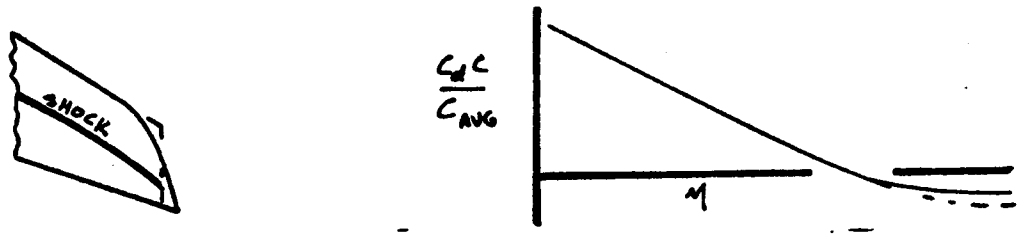

(c) TAILORED TIP SECTION

(d) TWISTED TIP

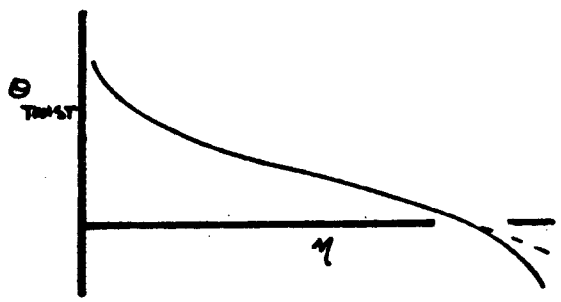

FIGURE 4.37 WING TIP DESIGN CONSIDERATIONS

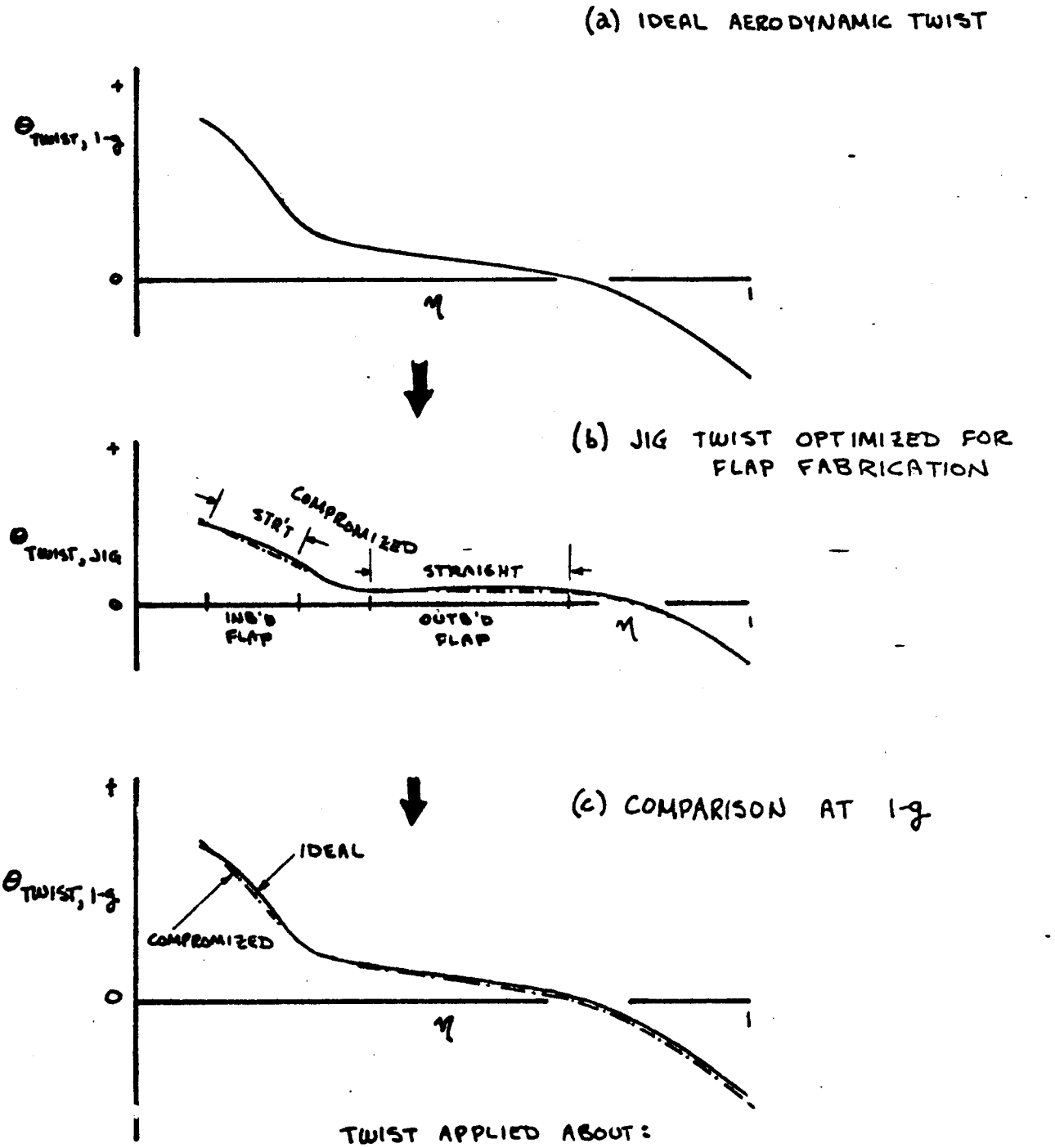

TWIST APPLIED ABOUT:

LEADING EDGE ~ INCREASES EFFECTNE DIHEDRAL, INCREASES FLAP GROUND CLEARANCE

TRAILING EDGE ~ REDUCES EFFECTNE DIHEDRAL, REDUCES ENGINE GROUND CLEARANCE

FIGURE 4.38 SECTION TWIST CONSIDERATIONS

(a) MACH CHARACTERISTIC LINE

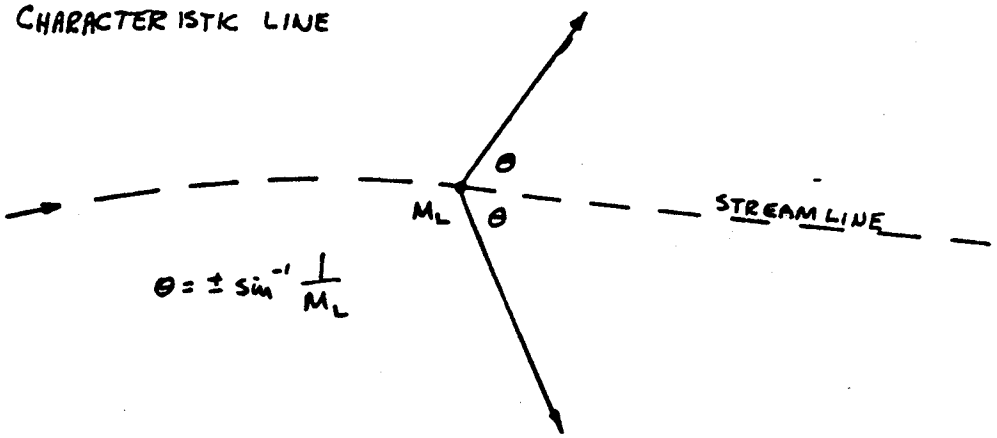

(b) PATH OF CHARACTERISTIC LINE INSIDE WING SUPERSONIC FLOW

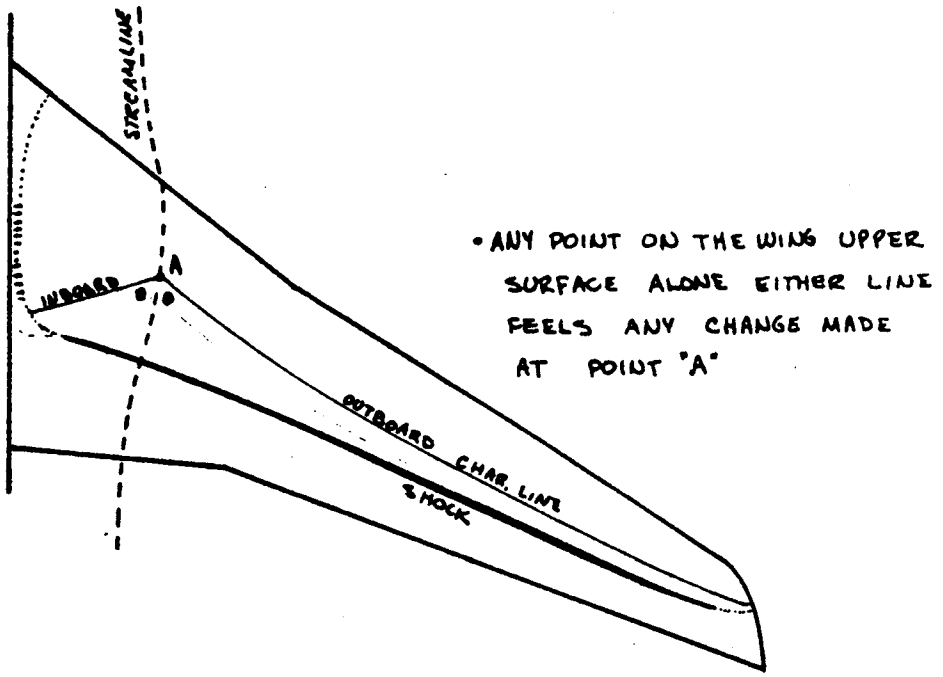

FIGURE 4.39 DESCRIPTION OF MACH CHARACTERISTIC LINES

1.14.78
GILLETTE

281

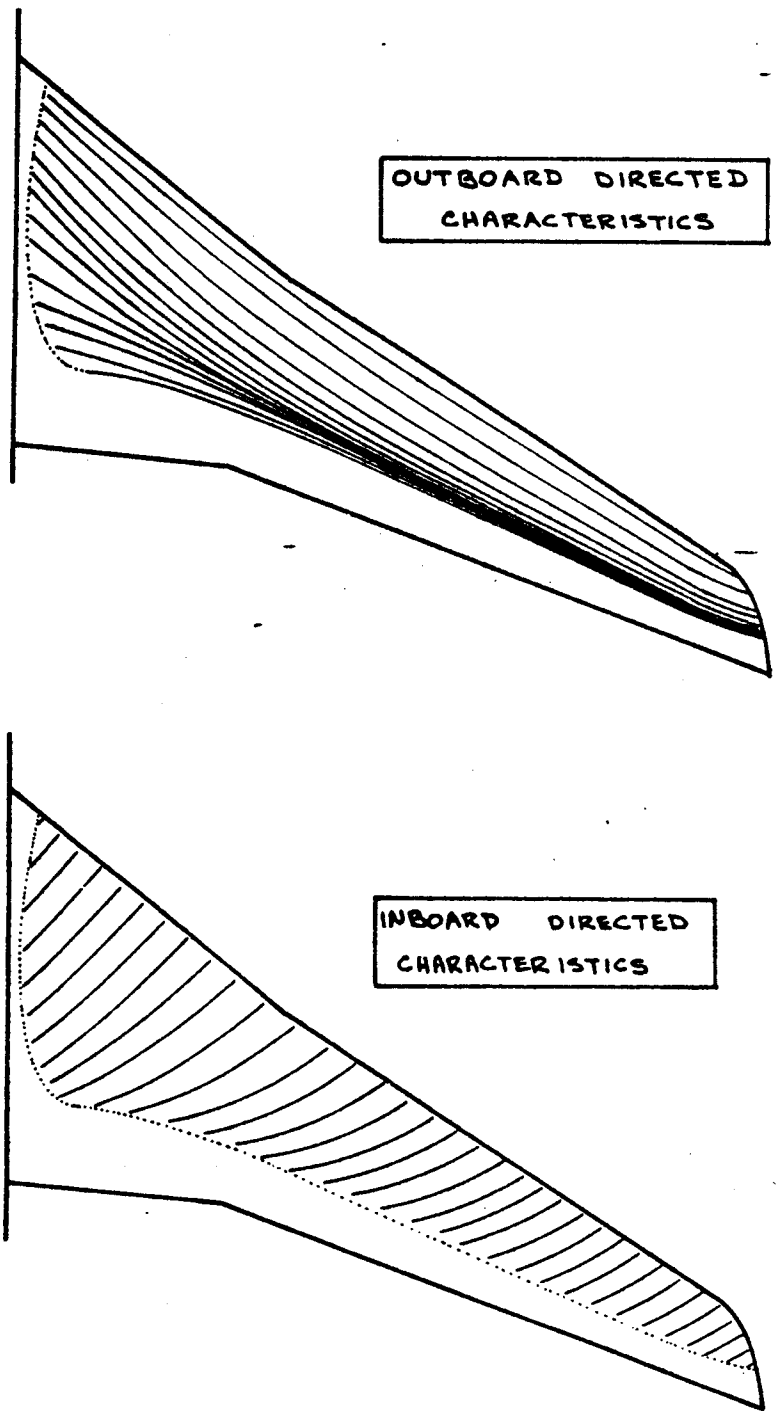

= FIGURE 4.40 EXAMPLE OF SURFACE CHARACTERISTICS

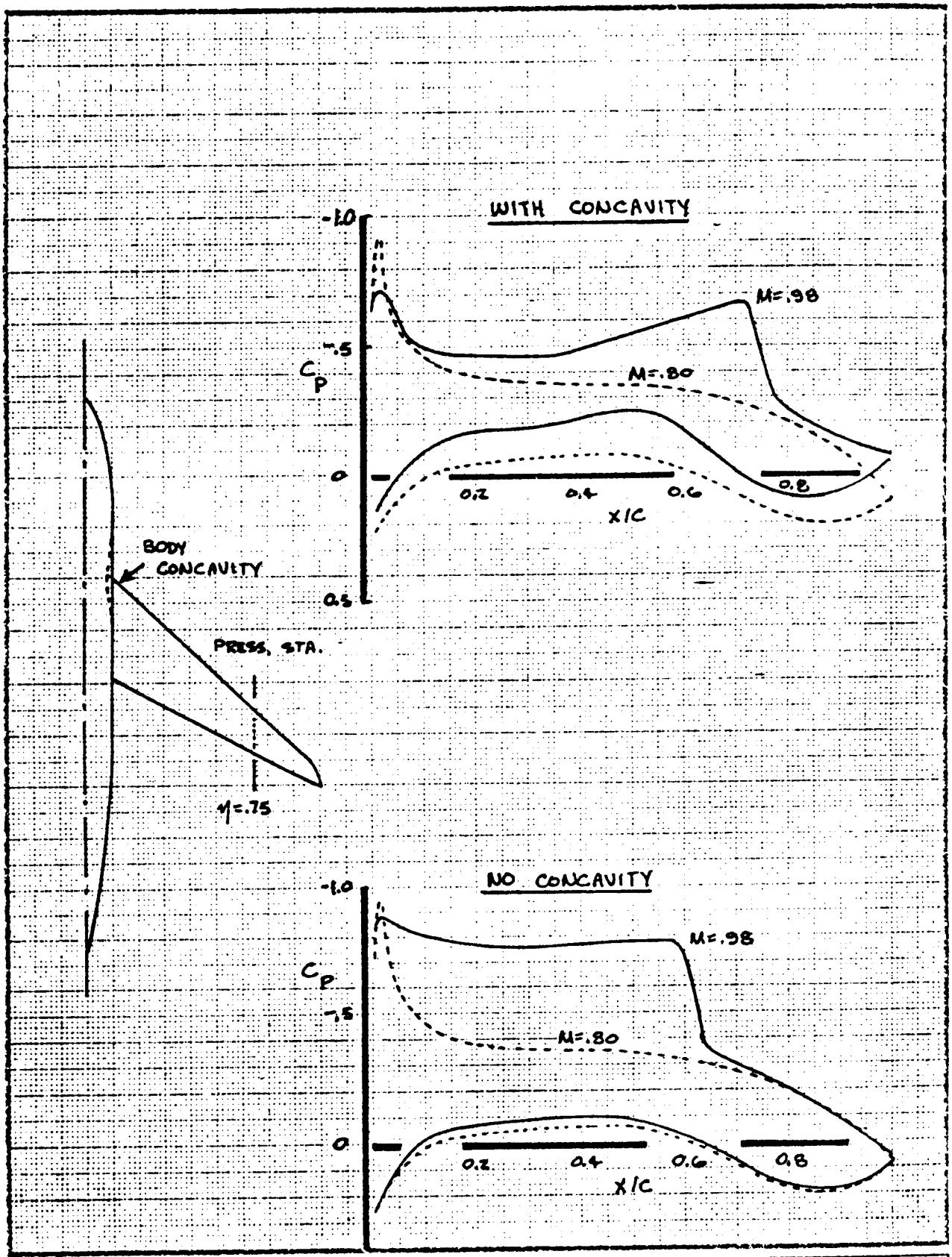

CALC	GILLETTE	1-14-78	REVISED	DATE
CHECK				
APR				
APR				

DEMONSTRATION OF CHARACTERISTIC LINE PROPAGATION EFFECT

FIG 4.41

DRAWING

PAGE 4.84

AD 18460

REV SYM

A-236 WING DESIGN SEQUENCE

STEP/FUNCTION	TEA 236 MODE *	INPUTS	RESULT
Selection of design constraints	--	Range/Payload Cruise Mach number	Design C_L, Planform, 2-D Section, Sweep, Taper
1. Upper isobar selection and initial thickness evaluation	Twist	Various x/c locations for maximum t/c; span load	Selection of best thickness form to continue design
2. Thickness design	Twist	Manually tailored thickness forms; span load	Final thickness forms
3. Camber design	Design	Upper and lower isobar pattern	Camber shape for each defining station
4. Check final sections	Analysis	Final sections; span load	Check final sections for errors and smoothness
5. Twist design	Twist	Final sections; span load, run at cruise Mach number.	Twist to produce design span load at cruise
6. Tip design	--	Empirical rules	Tip planform, sections and twist

*MODE	Case	Inputs	Outputs
Analysis	-5.	Sections, twist	UPPER and lower pressures
Design	5.	Upper and lower isobars	Sections, twist
Twist	-6.	Sections, span load	Upper and lower pressures, twist

BOEING NO. FIG. 4.42 PAGE 4.85

$(C_L)_{\alpha = CONST.}$ VS. $\frac{M\ DESIGN}{M\ CRUISE}$

• TAKEN FROM NAP & ATP WIND TUNNEL DATA

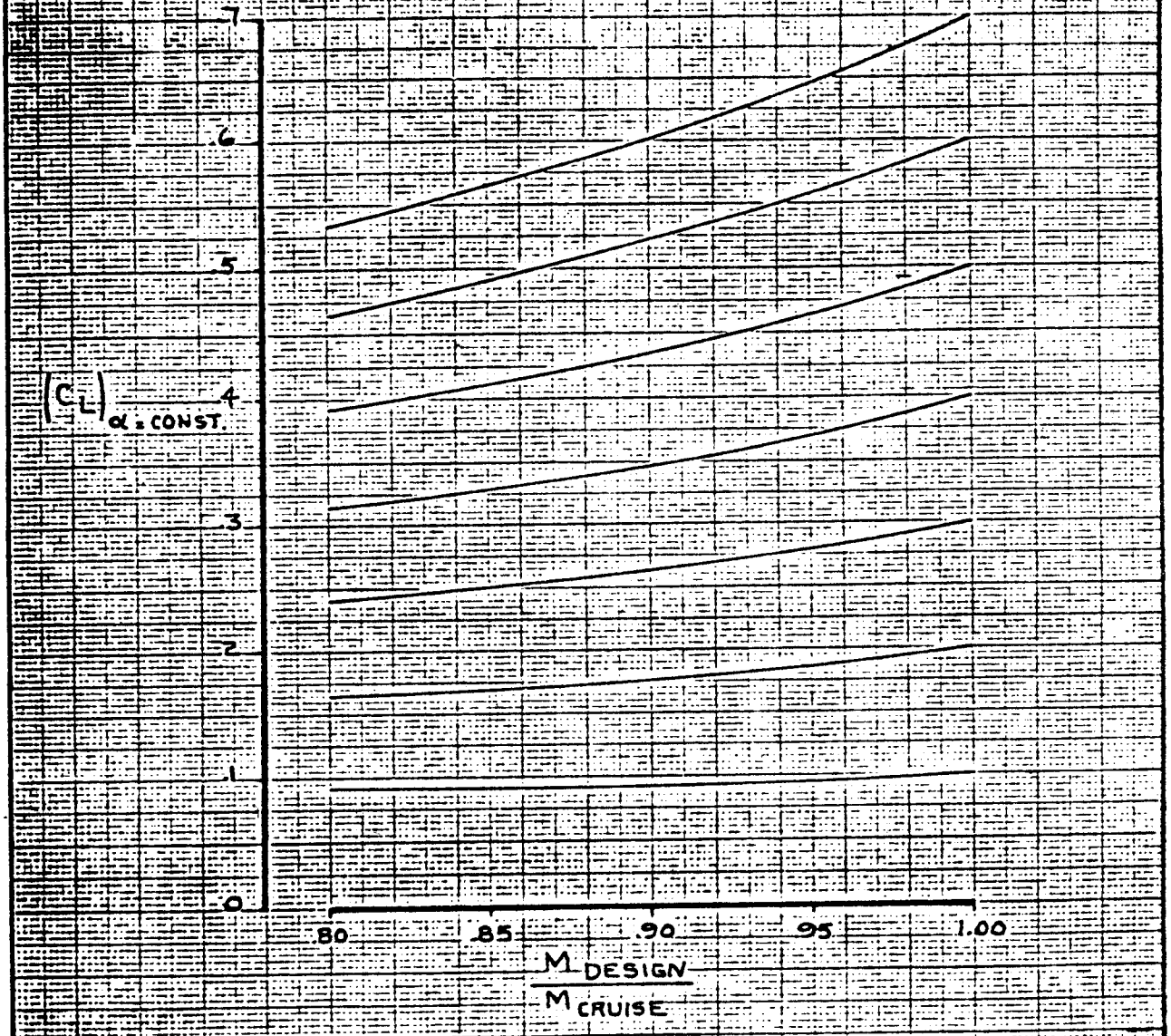

CALC	GILLETTE	1971	REVISED	DATE	INCREASE IN LIFT WITH MACH NUMBER	
CHECK						FIG. 4.43
APR					THE BOEING COMPANY	PAGE 4.86
APR						

DI 4100 3240

K-E ALBANENE 1001

285

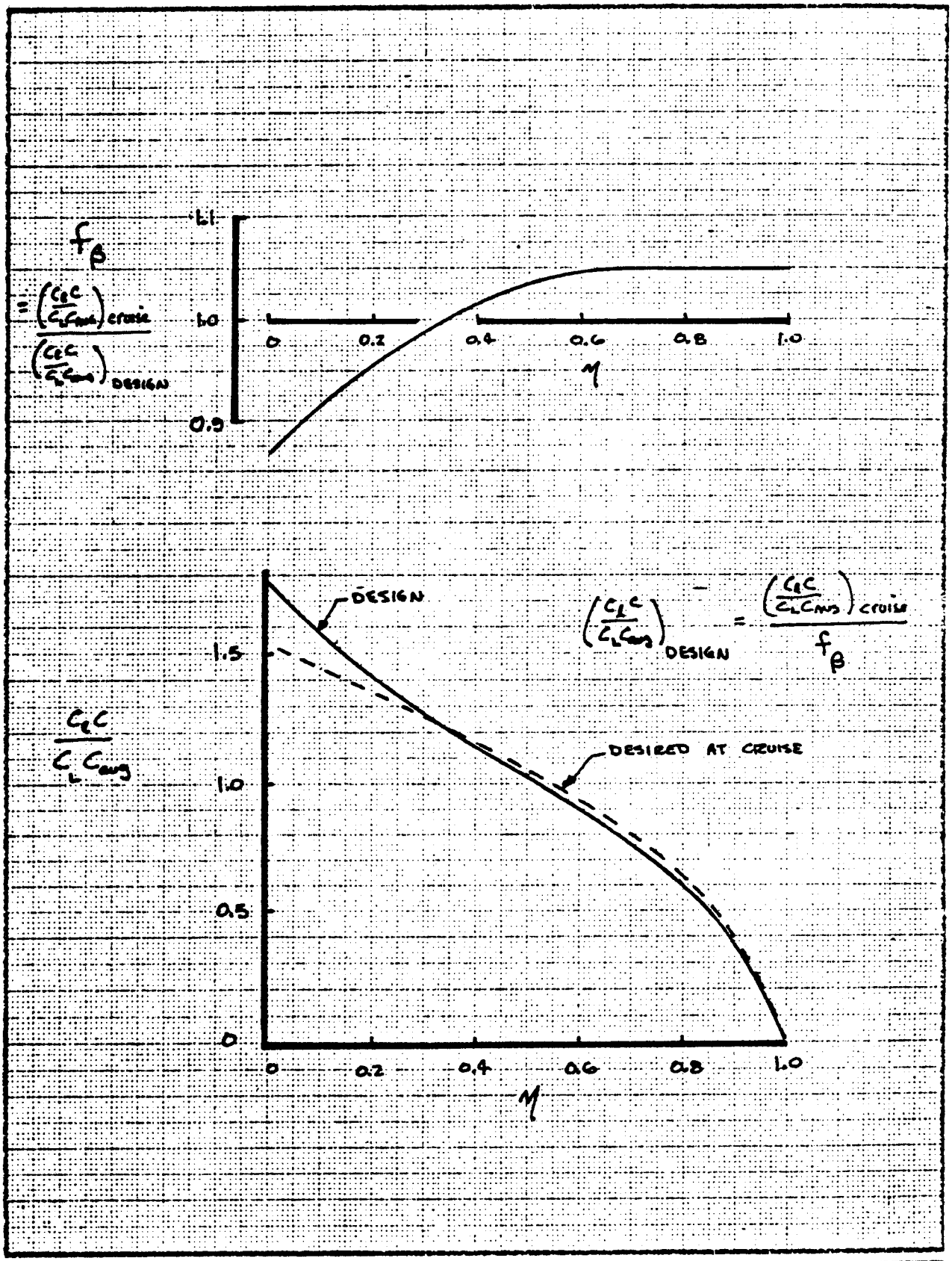

CALC	GILLETTE	1.14.78	REVISED	DATE
CHECK				
APR				
APR				

MACH CORRECTION TO DESIGN LIFT CURVE

FIG 4.44

BOEING

PAGE 4.87

D1 4100 3260 ORIG 3/71

UPPER ISOBAR CONSTRAINT — DESIGN PROCESS

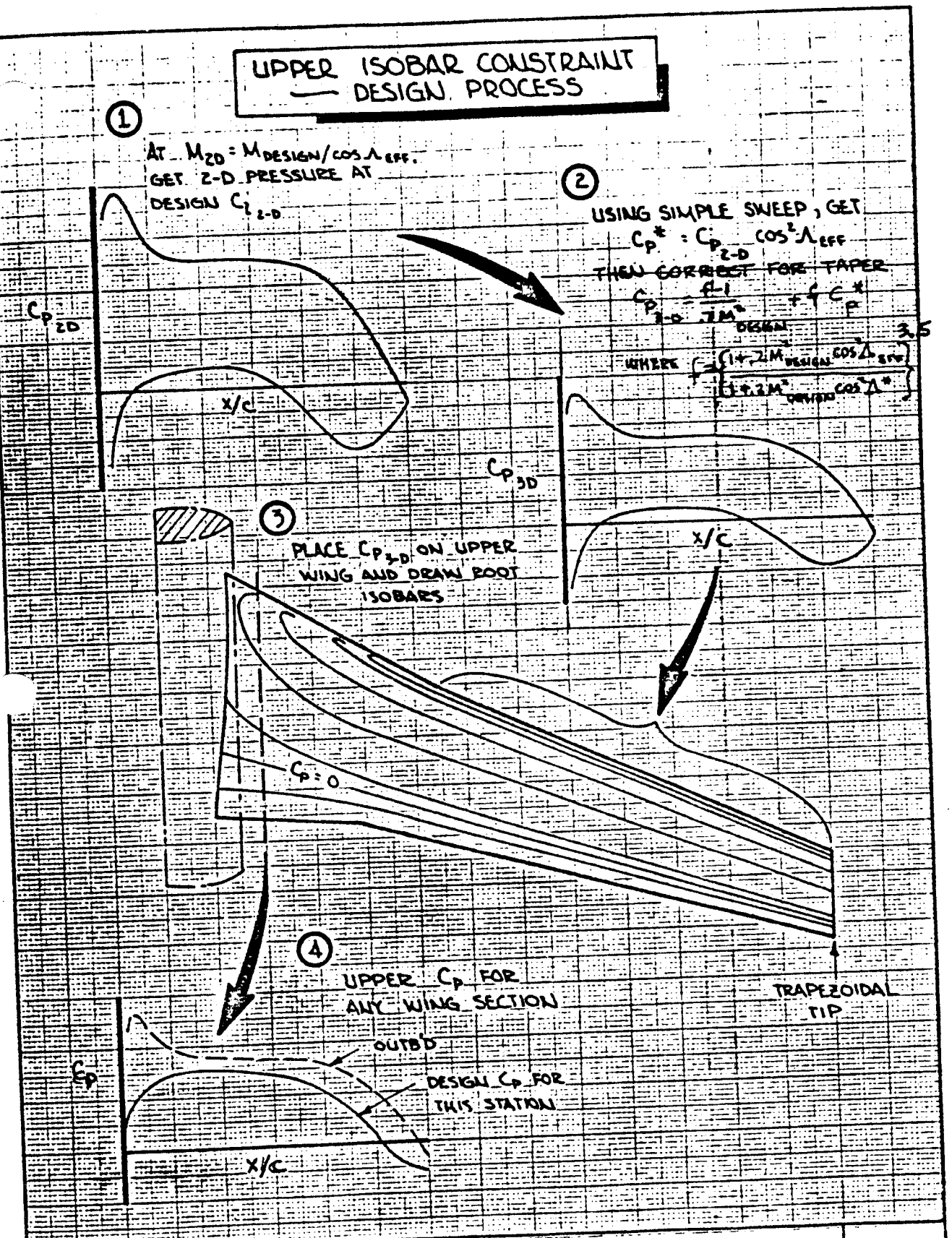

CALC	GILLETTE	1971	REVISED	DATE
CHECK				
APR				
APR				

DESIGN PROCESS FOR UPPER ISOBAR CONSTRAINT

FIG. 4.45

THE BOEING COMPANY

PAGE 4.88

D1 4100 3840

K-E ALBANENE 1901

287

INITIAL EVALUATION FOR LOCATION OF $t/c_{MAX.}$

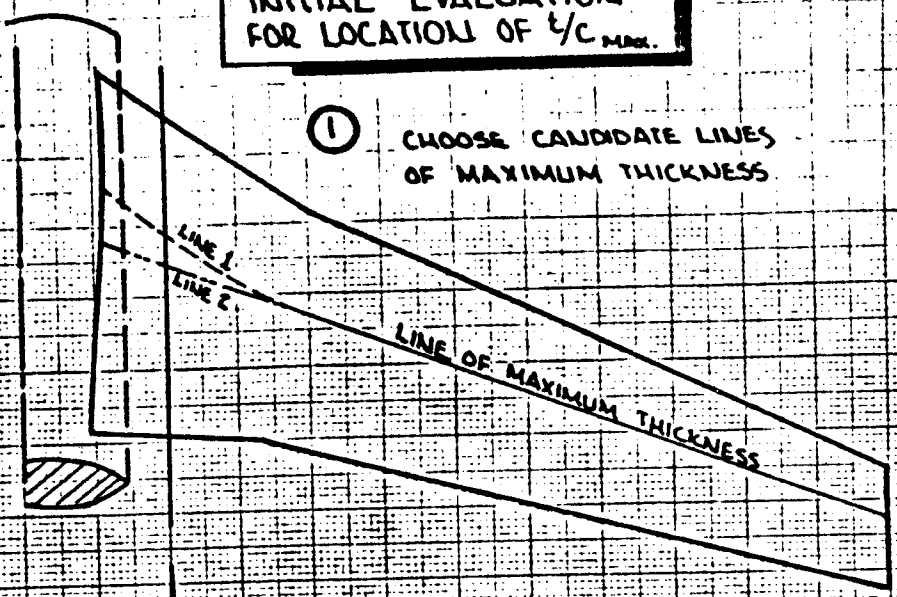

① CHOOSE CANDIDATE LINES OF MAXIMUM THICKNESS

② FIND $C_{P_{THICKNESS}}$

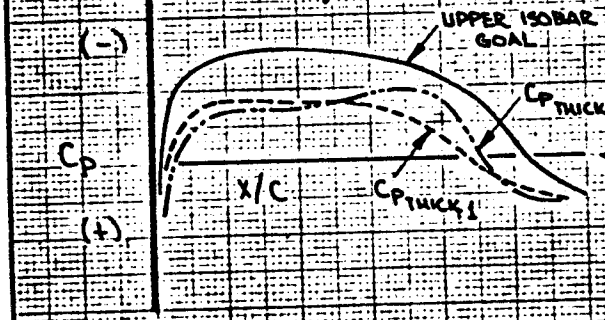

③ COMPLETE SECTION PRESSURE SHAPE ($C_{P_L} = 2C_{P_t} - C_{P_U}$)

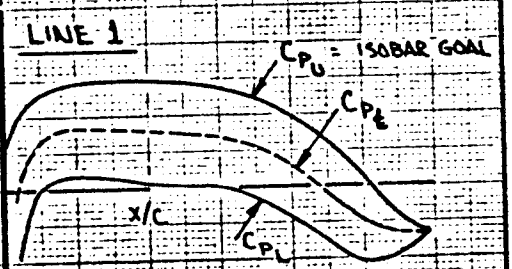

CRITERIA FOR SATISFACTORY DESIGN:

1.) RECOVERY POINT —
$C_{P_L} \geq 2/3\ C_{P_U}$

2) $\left(\frac{dC_{P_L}}{d\,x/c}\right)_{MAX.} \leq 1.5 \left(\frac{dC_{P_L}}{d\,x/c}\right)_{MAX.,\ OUTB'D}$

3) $C_{l_{SECTION}} \approx C_{l_{REQ'D\ BY\ SPAN\ LOAD}}$

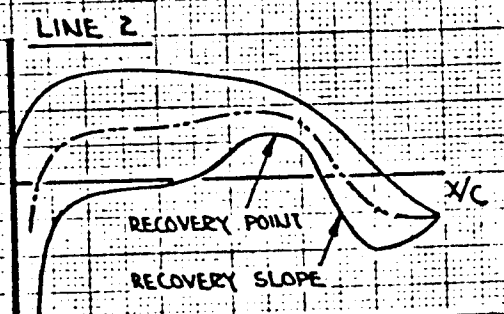

CALC				REVISED	DATE	INITIAL EVALUATION FOR LOCATION OF t/c_{MAX}
CHECK						FIG. 4.46
APR						THE BOEING COMPANY
APR						PAGE 4.89

THICKNESS FORM DESIGN

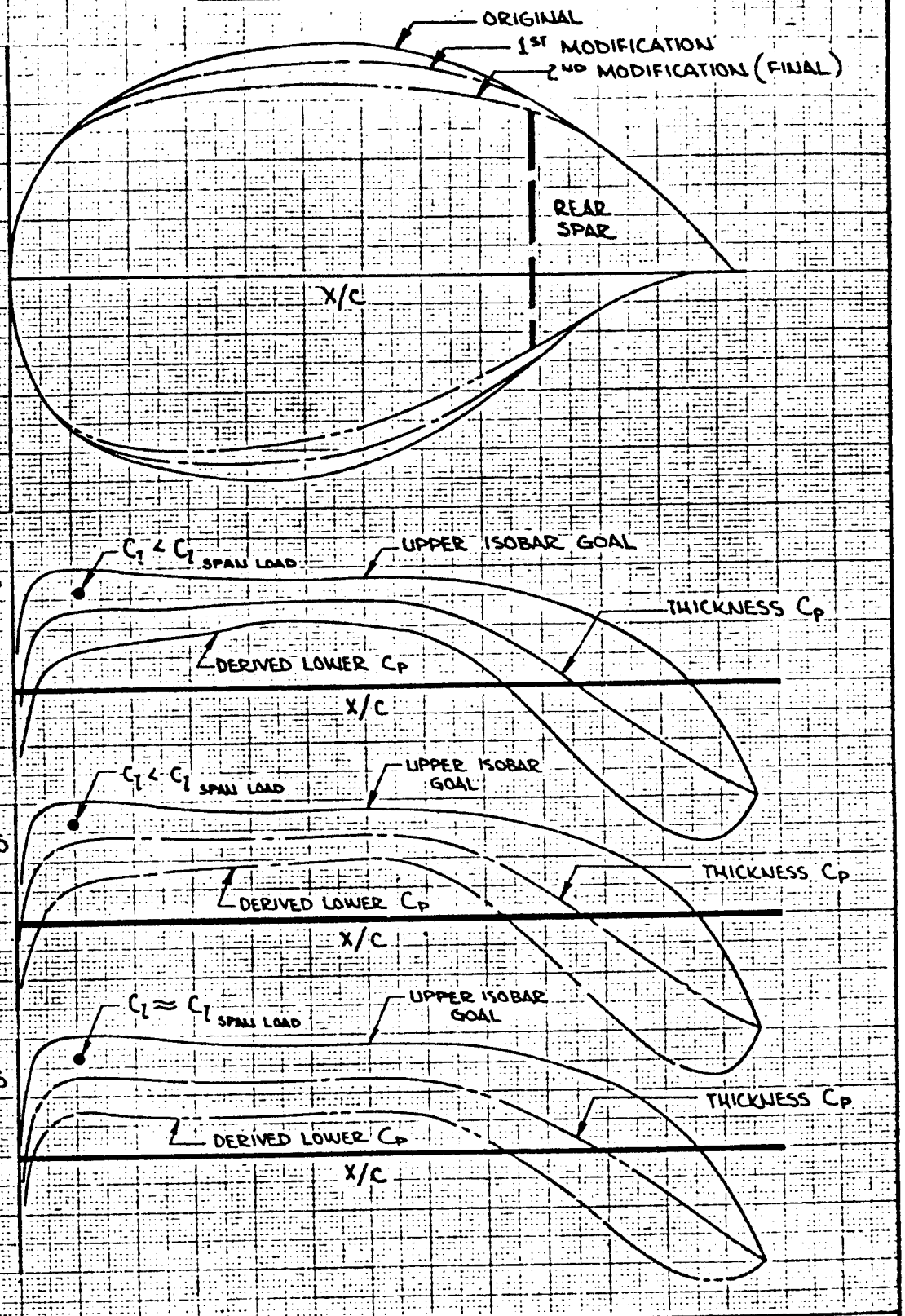

			REVISED	DATE	TYPICAL SECTION THICKNESS FORM DESIGN	
CALC						FIG 4.47
CHECK						
APR					THE BOEING COMPANY	PAGE 4.90
APR						

WING TWIST

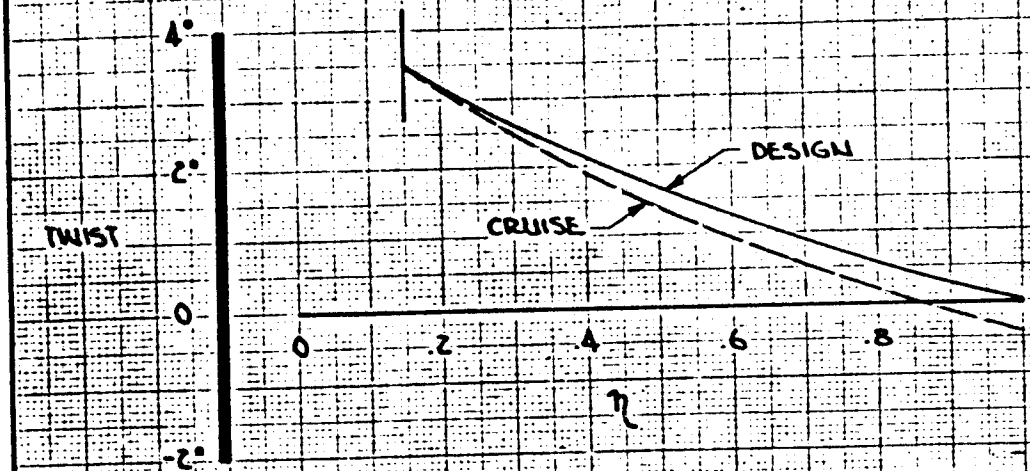

FIGURE 17a. TYPICAL TWIST DISTRIBUTION

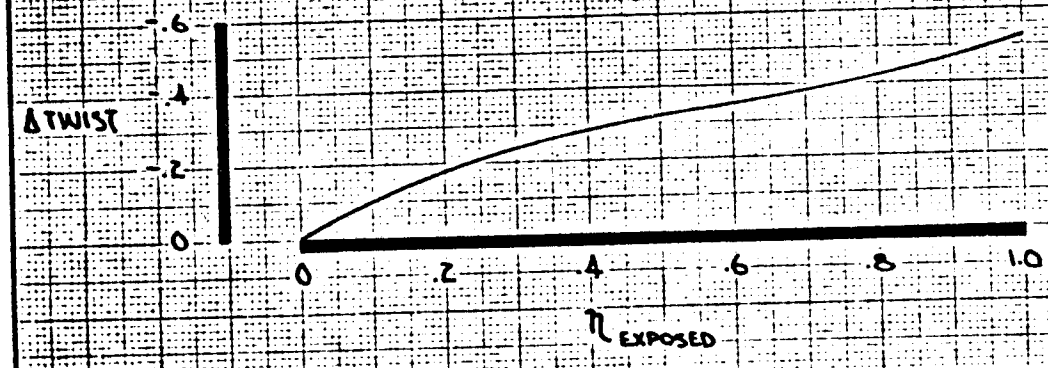

FIGURE 17b. TWIST CORRECTION — DESIGN TO CRUISE MACH

CALC	GILLETTE	4-3-71	REVISED	DATE	TYPICAL TWIST AND TWIST CORRECTION	
CHECK						FIG. 4.48
APR						
APR					THE BOEING COMPANY	PAGE 4.91

290

TIP DESIGN

① TIP RAKE

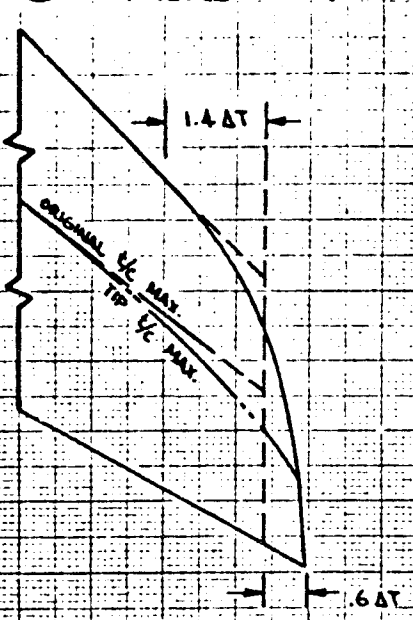

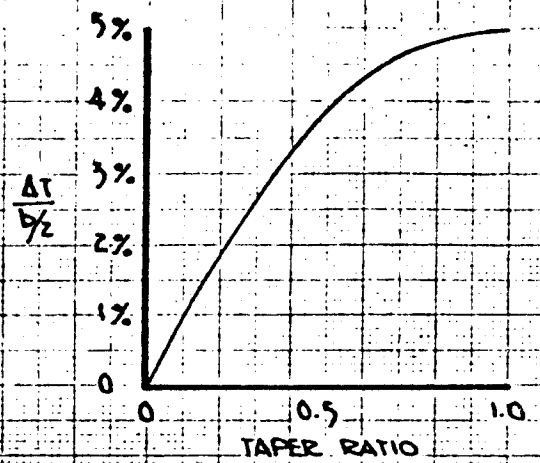

② SECTION CHANGE

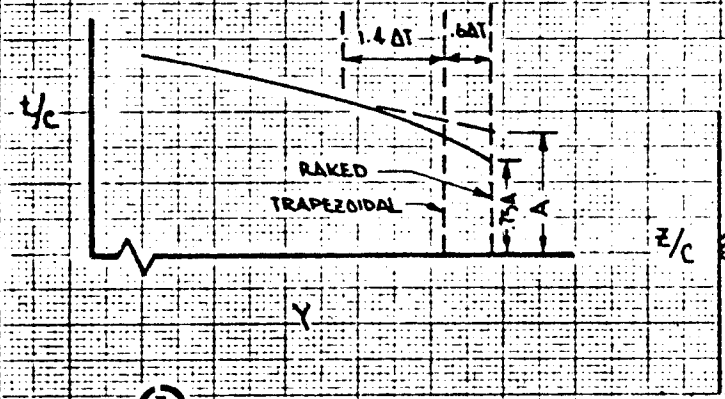

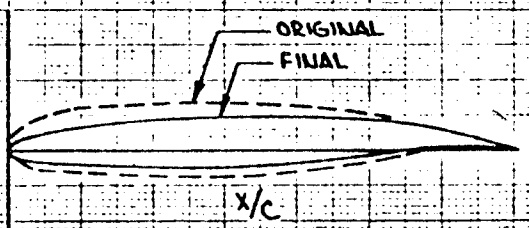

③ TWIST CHANGE

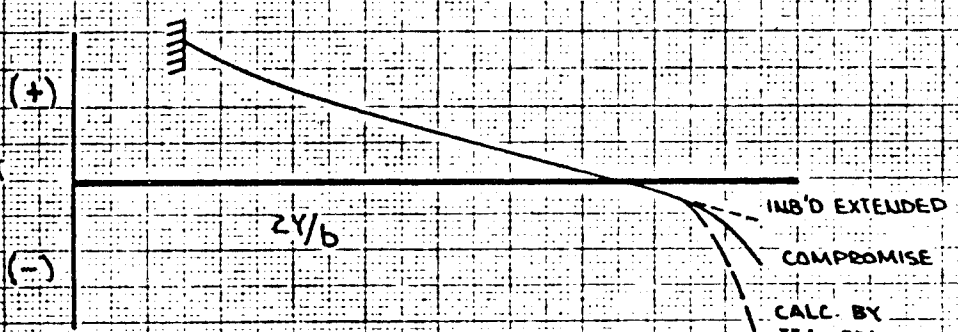

CALC			REVISED	DATE	TIP DESIGN TECHNIQUES	
CHECK						FIG. 4.4.9
APR						
APR					THE BOEING COMPANY	PAGE 4.92

(a) DETERMINE CORRECTION PRESSURES WHICH WOULD MAKE A230 ISOBARS AGREE WITH TARGET ISOBARS

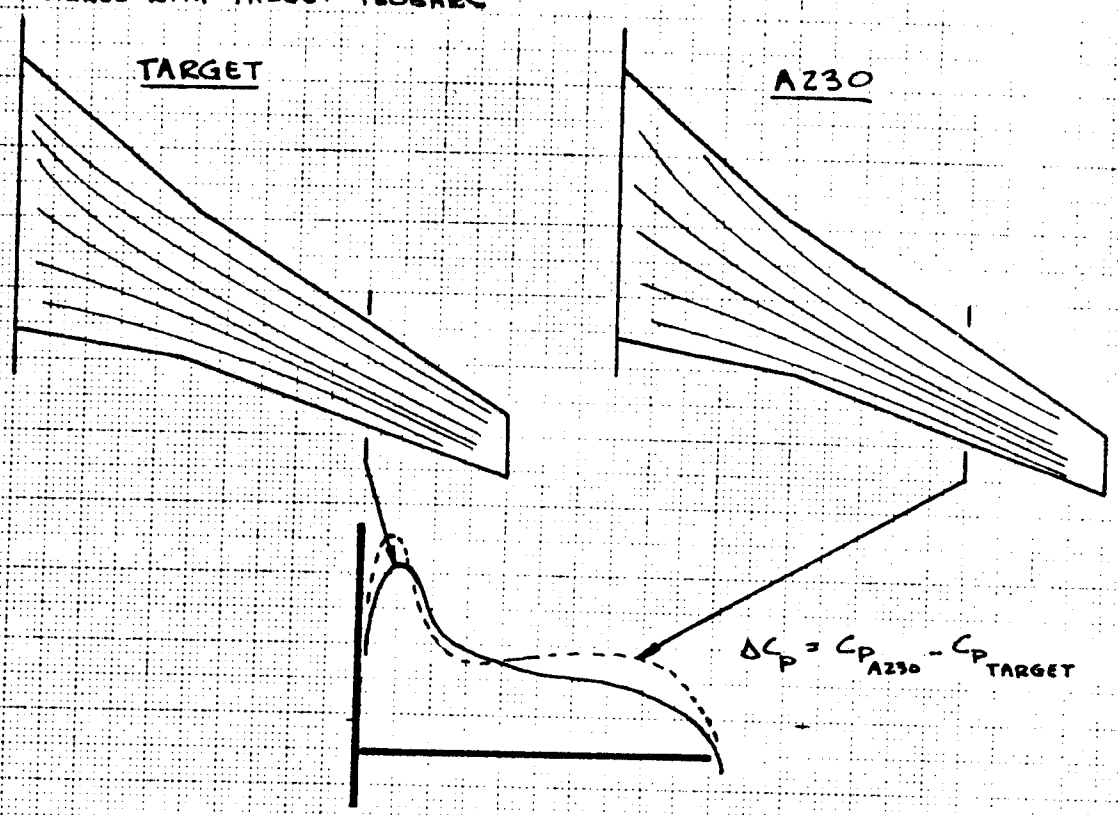

(b) USE A236 TO OBTAIN A GEOMETRY CORRECTION INCREMENT

(1) APPLY ΔC_p TO PRELOFT A236 ISOBARS

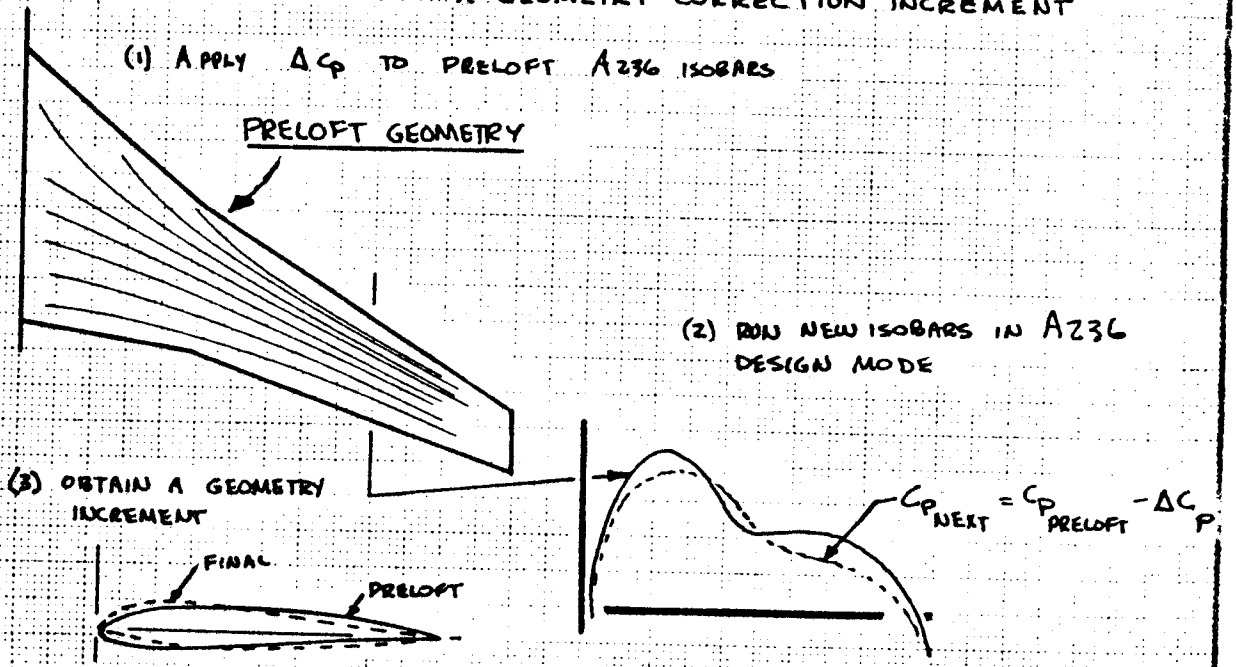

$$Z_{NEW\ LOFT} = Z_{OLD\ LOFT} + (Z_{NEW\ A236} - Z_{PRELOFT\ A236})$$

CALC	GILLETTE	1.14.78	REVISED	DATE
CHECK				
APR				
APR				

WING CONTOUR REFINEMENT AFTER A230 SOLUTION

FIG 4.50

BOEING

PAGE 4.93

D1 4100 3260 ORIG 3/71

J.S.G.47

CHAPTER 5. SUBSONIC WING TESTING

CHAPTER 5. SUBSONIC WING TESTING

5.1 TEST GOALS

Subsonic wing-body testing is devoted towards several categories. The bulk of test time will be devoted to performance tests, with lesser amounts to Flight Controls evaluations and airload data.

The main emphasis of performance testing is to acquire data which can be used to reliably predict the performance of the full-scale geometry. In addition to measuring the drag polars of the wing, the pitching moment characteristics, drag rise and buffet characteristics are all of interest. Since the wind tunnel environment does not perfectly reproduce that of the full scale aircraft, an elaborate art of "trip strips" has arisen to attempt to simulate full scale conditions. The primary skills to be learned by the configuration aerodynamicist are how to use trip strips properly and correct for the influences of the mounting systems necessary to hold the model.

Flight controls testing is another area where trip strip technology and elimination of mounting system effects are the principal preoccupation. The Flight Controls engineer works in an environment having additional variables, those due to yaw as well as pitch, and due to control surface deflections. A further handicap is the necessity of acquiring meaningful force data at the corners of the flight envelope where extensive separations occur on the configuration.

The Loads engineer is concerned with wing surface pressures, in the corners of the flight envelope There are not difficult to acquire, the principal obstacle being one of cost.

The following parts of this chapter will deal primarily with the tasks of the configuration aerodynamicist.

5.2 TEST ENVIRONMENT

5.2.1 Tunnel Environment

Most wind tunnels are continuous-run facilities, with a fan providing the power to overcome losses. The air is continually in motion, and the net effect of turning vanes in the corners, the fan blades and stators, and air exchanges for cooling purposes results in the flow in the test section being of less then ideal quality.

Flow angularity. Even with carefully designed screens and honeycomb flow straighteners, some flow angularity remains in the test section flow. That going sideways is termed crossflow; that in a vertical plane is termed upflow. Values of upflow and crossflow in BTWT are less than 1^{0}, and it would seem that these would be acceptably small errors. Unfortunately, this is not so.

Lift and drag forces must be known relative to the true direction of the airstream. Figure 5.1 shows a case where the upflow is positive. The model is installed relative to the tunnel centerline and the instantaneous angle of attack, α, is measured relative to the tunnel axis. The model balance will measure C_L and C_D

5.2 (Cont.)

relative to α. However, the wind direction is given by $\alpha + \alpha_u$ The true C_L and C_D must be resolved from the C_L and C_D measured by the balance.

$$C_{L_{\text{wind axis}}} = C_L \cos\alpha_u - C_D \sin\alpha_u \qquad (5.1)$$

$$C_{D_{\text{wind axis}}} = C_L \sin\alpha_u + C_D \cos\alpha_u$$

where C_L = lift measured normal tunnel axis

C_D = drag measured along tunnel axis

$C_{L_{\text{wind axis}}}$ = lift measured normal to wind axis

α_u = upflow relative to tunnel axis

Example: If $C_L = 0.40$, $C_D = 0.025$, $\alpha_u = 1^o$

Then $C_{L_{\text{wind axis}}} = 0.3995$ (a loss of 0.13%)

$C_{D_{\text{wind axis}}} = 0.0319$ (a gain of 28%)

The problem of upflow is exposed by the example; only one degree of upflow increase the true drag by almost 30%. The reason is that C_L is from 15 to 20 times larger then C_D, and the main effect is given by

$$\Delta C_{D_{\text{upflow}}} \doteq C_L \sin\alpha_u \qquad (5.2)$$

Suppose the upflow was knownincorrectly by 0.1^o. The error in drag due to this error in upflow measurement would by 0.00070, or almost 3% in drag. The danger ir upflow, then, is not in its presence but in the very high accuracy to which upflow must be known. In fact, to produce less than a ± ½% error in drag for the example quoted above, the upflow must be known to within ±0.028 degree.

The preferred technique for measuring upflow is to run a wing-body model upright and then inverted. Figure 5.2 compares the lift curve for the upright versus inverted cases. At a constant C_L, the two will be different in angle of attack of twice the upflow:

$$\alpha_u = \left[\frac{(\alpha_{\text{upright}} - \alpha_{\text{inverted}})}{2}\right] \quad \begin{matrix} C_L = \text{Const} \\ M = \text{Const} \end{matrix} \qquad (5.3)$$

5.2 (Cont.)

A plot can then be drawn of α_u for various Mach at constant C_L. Usually, upflow is fairly independent of C_L, so over a small range of lift coefficients, the upflow angle will change only with Mach number.

Ideally, the upflow correction, when applied via equation 5.1, will collapse both C_L versus α and C_L versus C_D. Unforunately, real data rarely experience this degree of agreement. An entirely different α_u could be calculated from equation 5.3, but from the C_D versus α curve. The usual custom is to use upflow calculated from the lift curve because of the dominance of the term $(C_L \sin\alpha_u)$.

The operators of the wind tunnel will usually have a standard reference model (at BTWT, this is the TR 1142 model), with which they will have measured upflow. When other information is not available, this measurement of upflow can be used. But a more correct value will be obtained by testing the model of interest both inverted and upright. An individual model will likely have a wing planform considerably different from that of the reference model; consequently the wing will be in a different upflow field. Remembering the extreme accuracy required in the measurement of upflow, any serious testing program must make provisions to test its model upright and inverted.

The same problem exists with crossflow, whereby

$$C_{Y_{\text{wind axis}}} = C_Y \cos\beta_c - C_D \sin\beta_c \qquad (5.4)$$

$$C_{D_{\text{wind axis}}} = C_Y \sin\beta_c + C_D \cos\beta_c$$

Where β_c is the crossflow angle. The effect of crossflow on drag is far less, however, since C_Y never becomes as large as C_L. The amount of crossflow is determined by yawing the model at constant C_L, or, if this is not possible, by using the upright and inverted pitch series. Typically, however, no correction is made to performance data for crossflow.

Mach gradient Unless the wind tunnel walls have just the right amount of divergence or use a carefully controlled wall suction, there will likely be a Mach gradient from the front to the rear of the wind tunnel test section. In BTWT, the characteristic effect was a drop in Mach number, as shown on Figure 5.3. As the Mach number decreases, the static pressure rises. When combined with the rearward facing areas on the back of the model, the net effect will be a push, or bouyancy, effect on the model. For the case like BTWT, the drag of the model will be reduced. This bouyancy effect in BTWT was part of the reason why the drag of the 737 was underpredicted.

There are two ways to remove the bouyancy effect from the measured drag. The most desirable way is to modify the wind tunnel so that the Mach gradient is zero over the length of the model. To achieve this in BTWT, flaps were installed at the rear of the tunnel test section in the corner fillets. A schedule for these

5.2 (Cont.)

fillet flaps was then determined such that the clean tunnel would have no Mach gradient. The second way to remove the bouyancy effect is to measure the surface pressures on the rear of the model and make a correction based on pressure times fronted area.

Both methods have limitations. The BTWT fillet flap-schedule is established without a model being in the tunnel. The presence of the model will alter slightly the proper setting . Also, should the fillet flaps not be set, the drag of a half-model may change as much as 0.003 in C_D. This is an indication of the precision needed in the setting of the fillet flaps.

Measurement of the surface pressures on the model faces a more serious limitation. It is not possible from these measurements to deduce an absolute bouyancy correction, because the pressures on the model are not known for the case where no bouyancy exists. The bouyancy correction would be ΔC_p times projected area, where the ΔC_p would be the difference in surface pressures with and without a Mach gradient. Measurement of surface pressures is useful only when a bouyancy correction from one tunnel to another is desired.

Flow turbulence The early NACA Variable Density Tunnel had such a high free stream turbulence that the apparent Reynolds number as measured by transition on a sphere was 40% to 60% higher than that based on free stream conditions. Any test results which may be sensitive to the degree of laminar versus turbulent flow would be questionable in this kind of tunnel. Whenever tunnel turbulence is more than 0.2% to 0.3%, the possibility exists that the boundary layer on the model may be artifically disturbed. Besides quieting the tunnel flow, the next step is to accurately determine where on the model transition occurs from laminar to turbulent flow. With this information, a correction can be made for skin friction drag effects.

Wall effects The presence of walls around the test section presents a blockage to circulation and thus interferes with lift, and at higher Mach numbers (near 1.0), can cause alterations in the flow awound the model due to transonic blockage. Lift blockage has been studied experimentally for years, and analytically in recent years. The operators of the wind tunnel will routinely apply a correction based on model to tunnel size, lift coefficient, and tunnel wall porosity. It is possible to have wall porosity such that the lift blockage is negligible for typical models. For example, in the late 1960's, NASA tested a C-5A model in a number of wind tunnels. In the CALSPAN tunnel at Buffalo, N.Y., which has distributed suction through angled holes, no wall effect was observed.

Mach blockage is very difficult to predict, and can change dramatically with tunnel porosity. The best way to establish the right porosity is to use a body of revolution, having about the same length and cross sectional areas as the model being tested. This body of revolution must have measured on its surface pressures taken in free flight, that is, from a drop test. Comparison of wind tunnel versus free flight pressures will indicate when the porosity is properly adjusted. Usually, Mach blockage is not a problem below M=0.95 or so.

5.2.2 MODEL MOUNTING TECHNIQUES

Until NASA perfects their superconducting magnetic suspension scheme, all models require some kind of physical restraint. This provides both control over the model's position and a means of measuring the forces on the model, that is the end of the good news about mounting systems. The bad news is that all mounting systems produce interference effects which cannot be completely removed from the data.

There are three principal types of mounting systems for full models: plate mount, strut mount and sting mount. The strut mount is used only for low speed testing. In addition, half models will mount against the floor or wall.

The strut mount for low speed models is shown on Figure 5.4, which is a photo of a full model mounted in the UWAL low speed wind tunnel. The mount strut allows both pitch and yaw to be changed easily, but roll is more difficult, requiring a special adapter in the model. The forces and moments are measured by a large balance below the test section. The size of the mount strut is such that high pressure air can be conveyed to the model to simulate blowing effects.

The interference due to the mount strut can be deduced by inverting the model, then testing with and without a copy of the mount strut sticking out of the model. The dummy mount must not be on balance, that is, its load must not be measured, only the effect it has on the model's forces. These mount tares can then be removed from the data acquired when the model is upright.

Low speed testing often involves the use of a ground plane to simulate the ground effect when the aircraft is close to the ground. The most simple ground plane is a large board. This will develop a boundary layer and thus the velocity profile between the aircraft and the ground will not be properly modelled. The easiest fix is to provide a blowing slot on the ground plane just ahead of the model, the intent being to remove the characteristic boundary layer deficit. This is only partially successful since a boundary layer buildup begins again immediately downstream of the blowing slot. The most desirable solution from the point of view of data quality is the moving belt ground plane. This procedure actually uses a flexible belt as wide as the ground plan which is motor-driven to have the same speed as the free stream air. Thus no boundary layer forms on the plate and the full scale situation is properly simulated. The moving ground plane has two disadvantages, first, it is quite unreliable because of mechanical complexity, and second, it requires a sting mount, rather than a strut mount.

The sting mount system is the most often used mount, and has many variations. Figure 5.5 shows the most simple kind of sting mount, being used for a wing-body test in BTWT. The straight sting is mounted onto a mechanism that pitches the model, with the model pitch center being at the model's quarter-MAC, so that the model stays in the same place in the tunnel (recall the discussion about test section environment and upflow). Forces and moments are

5.2.2 (Cont.)

measured by a six-component strain-gage balance mounted inside the model. The straight sting mount has one main advantage-- it leaves the wing in a relatively isolated environment. For this gain, it introduces a number of disadvantages:

1. The internal strain gage balance is inherently less accurate than a tunnel main balance which is out of the airstream.

2. The sting deflects due to model load, making the angular position of the model less certain, which affects the accuracy of the drag correction due to upflow.

3. The sting alters substantially the flow over the aft body in a way that cannot be adjusted, making it impossible to measure the drag level of the geometry without mount effects.

4. For transonic testing, the sting alters the area distribution over the model.

5. The model cannot be yawed.

The first refinement to the sting is the bent sting, known locally as a "dogleg" sting. This is done to allow high angle of attack testing and testing near a moving ground plane. A photo of a model mounted in the Vertol tunnel near the ground plane on a bent string is given on Figure 5.6.

Another refinement to the straight sting is the swept strut sting, shown on Figure 5.7. This is used for stability and control tests, because of two reasons. First, it moves the sting out of the aft body, thus allowing the empennage to be mounted properly, and, second, it allows the model to be yawed. An internal balance is used as before. Unlike the straight or bent sting which come out a large hole in the aft body, it is possible to determine the aerodynamic tare of the swept strut sting. This is done by inverting the model so that the swept strut comes out the top, then mounting a dummy strut out the lower body to simulate the normal swept strut sting.

A variant of the swept strut sting is to replace the vertical fin with the swept strut. In principal, the flow around the aft body is quite natural, except that the drag of the fin is no longer being measured, and for T-tails, no tail-on testing can be done.

The final principal variation to the sting mount is the fork mount, where the sting splits and holds the model by the wing tips, as drawn on Figure 5.8. This mount is rarely used, since it is prone to dynamic instability and since the balance is outside the model. It is used when details of the flow on the body are to be observed.

The remaining principal type of mounting system for full model testing is the

5.2.2 (Cont.)

plate mount, shown on Figure 5.9. This system utilizes a thin plate which is attached to the tunnel main balance. A mechanism termed the rocking horse provides for pitch of the model, with the point of rotation being at the wing quarter-MAC. An island fairing covers the rocking horse mechanism. Prior to 1969, plates had typically been of the same length as the model, but tests in that year showed that the front and rear of the plate imposed pressure peaks on the model. Consequently the plate was lengthened into a "super-plate" to remove pressure perturbations. The plate mount has the following advantages:

1. It is a very steady mount, and model angle of attack is known very accurately.
2. It utilizes the tunnel main balance.
3. It does not change the longitudinal area distribution over the model.
4. Tail-on tests for longitudinal stability can be done.

Unfortunately, it suffers from the following disadvantages:

1. The model cannot be yawed.
2. The plate and island fairing alter the local flow field slightly, although this can be alleviated somewhat by a tunnel recalibration.
3. The aft body drag is not reliable because of the wake from the plate.
4. The plate mount tares are difficult to remove.
5. The drag of the plate, which is almost as large as that of the model, is also measured by the balance.

This last problem is alleviated by mounting the model on a stub sticking up from the plate and attached to an internal strain gage balance. However, some accuracy is lost due to the internal balance. The plate mount is used at BTWT for almost half of the testing done. This is a much higher percentage than at most other facilities, primarily because most transonic wind tunnels lack a tunnel main balance and must rely on sting mounted models.

Another frequent installation into BTWT is a half model, as drawn on Figure 5.10. This is an excellent installation for incremental tesing of wing-mounted nacelle installations because:

1. The model scale is large (typically 0.06 to 0.075) allowing high precision in modelling the aircraft contours.

5.2.2 (Cont.)

2. Data quality is high because of the large size of the model and the use of the tunnel main balance.

3. Data repeatability is good because of the splitter plate installation.

The halfmodel can be tested in pitch only, and empennage or cab details cannot be investigated. But it is the preferred installation for nacelle or winglet performance testing.

The mount techniques described above all measure the forces on the entire model. Many times, however, the forces on a selected part of the model are needed to higher accuracy, or are needed to be measured separately. In these instances, special balances are used. The most often are small strain gage balances to measure aileron, rudder and elevator hinge moments. Also, separate balances are used to measure the loads on the nacelle and pylon or on the empennage components. Often, those will measure all six components.

Special balances are also used for drag measurement. One-way to measure aft body drag would be to mount the model on a yoke sting from the wing tips, then separate the aft body and mount it on a separate balance, as shown on Figure 5.11. The balance would be sized to measure just the loads on the aft body. Details such as aft body closure, APU exhaust and inlet contours, aft nacelle integration could be examined with greater precision. This would be the ideal case. In practice, however, difficulties with special balances often arise which make the special balance less accurate than using a larger balance and measuring the load on the entire model:

(1) The metric break in the model must be sealed to prevent air leakage. This may introduce hysteresis in the data.

(2) The metric break also produces a surface discontinuity, which may alter the forces.

(3) It may be difficult to calibrate the balance in the model.

(4) There may be insufficient room for instrumentation leads, thus requiring contour alterations.

(5) The small special balance may be less accurate than a larger one.

In the typical case, the sum of all the effects describe means that the data with the special balance will be of less quality than if more data were acquired using a complete model and statistics were applied to the large balance data. For the reasons described above, special balances are used only where absolutely necessary, such as for control surface hinge moments.

5.3 TEST TECHNIQUES

Having designed a wing and body, the aerodynamicist must then measure its performance in the wind tunnel. Even if the design is perfect, the test faces a major obstacle-- Reynolds number. And, if the design has gone awry, the aerodynamicist must use certain techniques to enable him to understand the source of the difficulty.

5.3.1 Performance Data

The intent of the performance test is to measure the lift and drag of the model in a way that the full scale performance can be predicted. The drag of the full scale airplane is made up of only two types of forces, frictional and pressure, as shown on Figure 5.12a. The frictional drag is the integral of the surface frictional forces in the wind axis direction, and the pressure drag is the integral of the pressure forces projected normal to the wind axis direction; these two divisions of forces are all that exist on the aircraft. This simplicity may be sufficient for Mother Nature, but it is not sufficient for the Boeing aerodynamicist. The drag components have been reassigned as shown on Figure 5.12b:

(1) The minimum, lift-independent drag of the wing-body configuration at a subcritical Mach number, where no separations or Mach effects exist, is denoted as minumum profile drag, $C_{D_{Pmin}}$. This is also referred to as form drag, and is scalable with Reynolds number.

(2) An additional drag, ΔC_{D_P}, exists which at Boeing is used as the catchall for whatever drag is left. It is stated as:

$$\Delta C_{D_P} = C_{D_{M=subcritical}} - C_{D_{i\,elliptic}} - C_{D_{Pmin}} \qquad (5.2)$$

As such, it contains (a) that part of induced drag which is not elliptic, (b) that part of profile drag which is lift-dependent (c) any separations, and (d) any errors in calculation of $C_{D_{Pmin}}$ for the wind tunnel model, as will be shown later. The C_{D_P} term is considered not to be Reynolds number scalable, although part (b) of it obviously is.

(3) The drag of the elliptically loaded wing, given by $C_{D_i} = C_L{}^2/\pi AR$. No one has yet built an aircraft with only ideal induced drag. In fact, the induced drag efficiency factor for commercial jet aircraft at their cruise condition is quite low. Where e is the efficiency factor

$$C_{D_i} = \frac{C_L{}^2}{\pi AR e}$$

5.3.1 (Cont.)

valves of e are typically:

AIRPLANE	M	C_L	e
707-300 ADV	.80	.45	0.71
727	.80	.35	0.73
737	.76	.35	0.61
747	.84	.45	0.76
DC-10	.82	.45	0.77

Source: Reference 5.1

The part, $\Delta C_{D_i} = \frac{C_L^2}{\pi AR}\left[\frac{1}{e} - 1\right]$ (5.4)

is included in ΔC_{D_P} in Boeing drag methodology. Since induced drag is a pressure term, it is not Reynolds number scalable.

(4) The drag increase between the subcritical Mach number, (where the drag is completely independent of Mach number) and the drag at some higher Mach number is denoted as ΔC_{D_M}. This is considered to be due only to pressure effects and is not scaled by Reynolds number, although in realty the early part of drag rise until shock-induced separation occurs is dependent on Reynolds number to a small degree.

The manner in which the full scale drag of the wing-body geometry is predicted is shown on Figure 5.13. The drag in the wind tunnel is measured at two different conditions; at a subcritical Mach number, usually in the range of 0.6 to 0.7, below which it is assumed that the drag is independent of Mach number, then at some higher Mach number. The difference between the polars for these two conditions is carried to full scale without change. The subcritical polar is then divided into four separate parts. First, the mount tares are removed from the measured polar. Then, elliptic induced drag is removed. The remaining drag is defined as being made of profile drag, separation drag, and vortex drag due to non-elliptic loading. The complication is that this remaining drag is separated into two parts, a minimum profile drag, $C_{D_{Pmin}}$, and the C_{D_P} term.

This division is done by calculating, via the current Boeing aerodynamics drag book (Ref. 5.2), the $C_{D_{Pmin}}$ value for the wing and body at wind tunnel and at flight Reynolds number. The ΔC_{D_P} term is simply the difference between the remaining wind tunnel drag and the calculated value, as stated in equation 5.2.

Note that the largest separate component of drag form the wind tunnel model is the combined $C_{D_{Pmin}} + \Delta C_{D_P}$ term. Most of this term gets scaled by Reynolds

5.3.1 (Cont.)

number. It is often stated that it is not necessary to measure absolute drag in the wind tunnel, since only ΔC_{D_P} and ΔC_{D_M} are used from the wind tunnel model. This is a fallacy; the absolute drag of the wind tunnel model must be measured correctly. For example, suppose on Figure 5.13a that the subcritical polar had been measured incorrectly and included an extra amount of drag, $\Delta C_{D_{error}}$. This term would remain in the accounting of the wind tunnel data since only $\Delta_{C_{DM}}$, C_D and $C_{D_{mount}}$ are subtracted:

$$\left(C_{D_{P_{MIN}}} + \Delta C_{D_P} + \Delta C_{D_{ERROR}}\right) = C_{D_{MEASURED}} - \Delta C_{D_M} - C_{D_i} - C_{D_{MOUNT}} \tag{5.5}$$

Then, the C_{Dpmin} is estimated via the handbook and a single term is left

$$\left(\Delta C_{D_P} + \Delta C_{D_{ERROR}}\right) = \left(C_{D_{P_{MIN}}} + \Delta C_{D_P} + \Delta C_{D_{ERROR}}\right) - C_{D_{P\,MIN,EST}} \tag{5.6}$$

$C_{DPmin,est}$ is corrected for Reynolds number, then all the terms are added again:

$$C_{D_{AIRPLANE}} = C_{D_{P_{MIN,EST,FLIGHT\ RE}}} + \left(\Delta C_{D_P} + \Delta C_{D_{ERROR}}\right) + C_{D_i} + \Delta C_{D_M} \tag{5.7}$$

It is easily seen from this that the absolute drag of the wind tunnel model must be measured correctly; failure to do so results in ΔC_{Derror} being non-zero, and that term will find its way to the full scale polar.

Of course, the full scale polar of the wing-body geometry is never known, so the accuracy to which the above procedure successfully conveys wind tunnel to flight data is not known. Figure 5.14 does show the predicted full scale wing-body polars for all Boeing aircraft and the DC-10, as determined in Reference 5.1.

The other performance parameter determined in the wind tunnel for the wing-body configuration is the expected airplane buffet boundary. During the design stages of a new airplane, it is very important to know where buffet will occur, since buffet at too low lift or Mach can severly limit the airplane's operational envelope. Early knowledge of a buffet problem will allow selection of an alternate wing section or change in wing design. Buffet occurs because separations due to stall (lift buffet or shock waves (Mach buffet)) cause pressure fluctuations which either shake the wing structure or a control surface sufficiently hard for the pilot to feel the vibration. Usually the pilot will feel structural vibration rather than control surface vibration. And the vibration does not occur simultaneously with the onset of separation; the wing and body structure provide some degree of damping.

Traditional techniques for predicting buffet from wind tunnel data have relied on a break in the lift at constant Mach to predict Mach buffet, as depicted in Figure 5.15. However, these methods have failed to accurately predict the true buffet boundary of the airplane as seen on Figure 5.16. A new technique is in use by the Aero Staff which gives much better correlation to measured airplane buffet boundaries. That procedure is also detailed on Figure 5.15, and Figure 5.16 shows how the current process predicts flight buffet.

5.3.1 (Cont.)

The new method uses an increase in wing root bending moment as measured by a strain gage to predict lift buffet. An empirical factor of 13.5% is added to represent Reynolds number scaling and structural damping. Mach buffet is predicted by a break in the axial force on the model (not the drag force); again, an empirical factor of 1^{o} in angle of attack is included to allow for Reynolds number and structural damping. Details of the current procedure are contained in Reference 5.3.

5.3.2 Dealing With Reynolds Number

The test information described above seems relatively simple to acquire, with the only difficult parts lying in the path of predicting full scale drag being the mount tares and the estimate of C_{DPmin} which is scaled for Reynolds number. But that old devil, Reynolds number, does not allow such a simple way out. Reynolds number effects are the worst trap awaiting the configuration aerodynacimist and an elaborate art has arisen for dealing with these effects.

Drag level trip strips - Figure 5.13 showed how an estimate of C_{DPmin} is made for the wind tunnel model. It is extremely important that this estimate be accurate. The typical wind tunnel model will have sizable areas of laminar flow; the wing upper surfact to 20% to 30% chord, the lower surface to 50% to 60% chord, the empennage to 50% chord. Since the drag in laminar regions is about one-half that of turbulent regions, a knowledge of the extent of laminar flow must be know. And, since the transition point from laminar to turbulent flow will change with lift coefficient, this would introduce into ΔC_{Dp} a polar effect due to transition. These undesirable effects are avoided by the use of trip strips.

The purpose of the trip strip is to trip, that is, cause to transist to turbulent flow, the boundary layer at a known position. Trip strips applied at 10% chord, for example, to all surfaces will allow a constant correction to be applied to C_{DPmin} for the small extent of laminar flow. Also, the effect of transition on ΔC_{Dp} will be prevented. So, use of a trip, typically at 10% chord, is standard Boeing practice for drag level testing.

There are a variety of ways to provoke artificial transition; cavities, protrusions and sound waves. The use of sound waves to cause transition can be discarded as it is not practical; the sonic energy required to cause early transition also has a tendency to destroy the model. The method of cavities works by placing a series of shallow grooves perpendicular to the flow. These cavities, when properly spaced, amplify the naturally occurring instability in the laminary boundary layer (called Tollman-Schlichting waves) to the point where transition occurs. When properly designed, this concept produces no extra "trip drag," but once applied to a model, it is difficult to move the position. Also, a laminar boundary layer stability analysis must be conducted to guide the placement of the cavities. Perhaps the only application of cavity trip strips would be to the inside of nacelles and ASME nozzles, since the flow is relatively uniform and since the cavities would not reduce throat area.

5.3.2 (Cont.)

By far the most widely used trip strip type is to put protuberances on the surface. Typical examples are small spheres, called ballatine balls, flat disks, craters made by a centerpunch, carborundum grit and bug bits. The latter is not considered good practice, although in a atmospheric exchange tunnel like BTWT, it is a frequent occurrence. The idea of protuberance trip strips is to generate instability and hence transition by shedding a wake within the laminar boundary layer. The standard Boeing practice for model trip strips is the use of carborundum grit, hereafter referred to as "grit".

The proper application of grit trip strips was extensively studied by NASA (Reference 5.4). They showed that the size of the grit was quite critical. Too small a size would not trip the boundary layer; too large a size would add drag above that just due to changing the boundary layer from laminar to turbulent. Figure 5.17 shows the trend of drag with trip size. Note that there is a narrow range of proper grit size. This is not a universal range; it depends on the details of the pressure distribution of the particular model. During the "performance testing" of an airplane model, an exhaustive trip grit size study is necessary to establish that the plateau value is being measured.

Procedures have been established at Boeing for determing a grit size which will cause transition in the typical case(Reference 5.5). The process begins by determining, at a representative spanwise position, the apparent roughness Reynolds number from Figure 5.18. Then, the position of the trip strip is chosen, and Figure 5.19 is used to select the height of the roughness particle required. Finally, Figure 5.20 selects the grit size to be used. An example:

Apply a trip at 10% chord. For selected positions on the wing, to be used at M=0.80,

η	0.20	0.50	0.90	
CHORD, INCHES	14	8	2	
R_k	610	690	1300	← FIG 5.18
DISTANCE FROM STAGNATION POINT, INCHES	1.4	0.8	0.2	
PARTICLE HEIGHT, INCHES	.0045	.0042	.0049	← FIG 5.19
GRIT SIZE	~150	~150	~130	← FIG.5.20

So the trip strip in this example would begin at the root with #150 grit, changing to #130 grit somewhere near the tip.

5.3.2 (Cont.)

Having made an estimate of the proper size, Reference 5.4 states that the ideal grit trip strip would cover only about 3% of the area where it is applied. The idea is to have widely separated "peaks" of grit sticking up into the boundary layer. The wakes from all these peaks will merge within 10% chord or less, resulting in a fully turbulent boundary layer. The proper application, then, is to put the grit in a strip, typically 0.1 inch wide, at about 100 to 150 grains per inch. Recalling the shape on Figure 5.17 for a performance test intended to show guarantee compliance, actually counting grains at representative positions is not too much to ask.

An additional caution is advised. The method of application is to mask the boundary of the trip strip, apply a quick spray of Krylon, then spray the grit in place. The masking tape is removed and an overspray of Krylon is applied. When done properly, the Krylon overspray holds the grit in place and preserves the shape of the grit. All too often, however, the initial spray is too thick, and a solid ridge is left. These are illustrated on Figure 5.21. The aerodynamicist must inspect the trip strips with a flashlight whose beam is almost parallel with the surface to see that there is no ridge. The consequence of a ridge will be to move the drag level up from the turbulent plateau. Once applied, the effectiveness of the trip strip in promoting transition should be checked by methods of flow visualization. These will be described later.

Drag rise trip strips The nature of the effects of Reynolds number on drag rise are caused by two primary interactions; (1) that between the normal shock wave and the boundary layer, and (2) the relationship between the trailing edge boundary layer thickness and its control on total circulation around the airfoil. The trailing edge effect has been shown experimentally to be by far the dominant one.

Figure 5.22 shows the calculated transonic flow about the TR 38 airfoil at M=0.79 with three different boundary layer conditions; first, with no boundary layer; second, with a thin boundary layer representative of flight Reynolds numbers, and third, with a thick boundary layer more typical of wind tunnel test conditions. The significant change in total lift and hence in shock position is due to the progressively decreasing δ^*(displacement thickness) as Reynolds number is increased, the limit being the inviscid case, where δ^* is zero. The displacement thickness effect near the trailing edge is especially powerful in controlling the circulation; the pressure distribution on airfoil at two different Reynolds numbers will be identical if δ^*/c is identical over the entire airfoil, and nearly identical if δ^*/c at the trailing edge is matched.

The nature of the interaction between a normal shock wave and the boundary layer is depicted on Figure 5.23. The process is shown in a timewise progression from a time t_1 where the shock instantaneously appears. The flow through the shock becomes subsonic downstream of the shock and there is a large rise in the static pressure. This pressure rise is propagated forward through the subsonic layer of the boundary layer. At time t_2 the boundary

5.3.2 (Cont.)

layer has thickened forward of the shock because of the adverse pressure gradient. The sonic line in the boundary layer is now curved, and the outer flow begins to develop compression waves. As a consequence, the shock moves forward. After sufficient time, the flow has reached equilibrium; the boundary layer begins to thicken well in advance of the shock, a separation bubble has appeared beneath the shock wave, and the shock position has moved forward substantially.

The forward movement of the shock wave can be correlated to the thickness of the subsonic layer within the boundary layer. On Figure 5.24, it is seen that δ_s/c must be similar between wind tunnel and flight in order to get the shock positioned correctly. Simulation of the flow downstream of the shock wave then depends on boundary layer mixing; the best simulation will be achieved if the upstream boundary layer is turbulent in the wind tunnel.

The consequences of improperly modelling the flight shock wave-boundary layer interaction is given by the C-141 wing pressures, on Figure 5.24b. During the development of the airplane, model data were acquired with a forward trip located at 7.5% chord. This positioned the shock at about mid chord. However, flight data showed that the shock was much further aft, at about 70% chord. This change in shock position caused two limitations to the C-141 performance; first, pitching moment was more negative than predicted, so there was a limit to forward c.g. position due to insufficient tail power to trim, and second, the airplane's Mach number was limited to less than guaranteed because of a wing torsional limit. Subsequent investigations showed that the shock position would move aft on the model as the point of transition was moved aft, with the best simulation being achieved with no trip.

The reason for this behavior is shown on Figure 5.25. The growth rate with X/C of the full scale turbulent boundary layer is shown on 5.25b. The growth rate at BTWT Reynolds number for a typical full model is also shown for a laminar boundary layer and then for turbulent boundary layers having various trip positions. Suppose the fullscale shock wave was at 0.6 X/C. Then a drag level trip at 0.1 X/C would result in a boundary layer at the shock that would be 50% thicker than at full scale. Moving the trip rearward and delaying transition will obviously reduce the wind tunnel model's boundary layer. For the example shown on Figure 5.25 positioning the high speed trip at 0.3 X/C would result in perfect simulation of the full scale boundary layer at the shock. However, the trailing edge δ^*/c may not be simulated, and the circulation will be wrong.

The use of a high speed trip is altered by testing the model at higher chord Reynolds numbers. It is generally felt that testing at increasing chord Reynolds number will invariably improve the simulation. This is not the case.

5.3.2 (Cont.)

For certain airfoils, Reynolds number ranges halfway between the typical BTWT value and flight valves may in fact produce the poorest simulation. Figure 5.26 illustrates how this might occur. At BTWT conditions, the trip strip position is chosen as previously described. At a "high Reynolds number" test condition, however, the natural transition point has moved to the leading edge. Since the turbulent boundary layer growth rate is still greater than at full scale conditions, proper simulation cannot be achieved; in fact, the "high Reynolds number" test may yield the poorest result.

Lockheed, in fact, conducted high Reynolds number airfoil tests after the C-141 flight difficulties were discovered. Figure 5.27 compares the airfoil characteristics at various Reynolds numbers to the flight values in the case of the C-141 airfoil, testing at BTWT-type conditions without a trip strip produced as good a result as the highest Reynolds number tested. Of course, it is easy to make this judgement once flight results are known. In general, the only way to be safe would be to measure the airfoil performance at the exact flight Reynolds number.

The ability to simulate high Reynolds number shock interations with trip strips is dependent to some degree on the specific nature of the airfoil's pressure distribution. Consider the pressure distribution shown on Figure 5.28; this is taken from a wing having TR 38-1 as an outboard section. The boundary layer thickness, displacement thickness and shape factor are shown for the upper surface for the range of full scale Reynolds number normally encountered in flight. The previous discussion suggested that the trailing edge δ^*/C would be the critical dimension, with the thickness of the subsonic layer just ahead of the shock also being quite important. This latter value is not provided by A200; it will be assumed that two boundary layers with identical $\delta/C, \delta^*/C$ and H, all at the same time, will have identical values of δ_s/C. For the example on Figure 5.28, at the trailing edge the values are:

$$\delta/C \approx .021$$
$$\delta^*/C \approx .0056$$
$$H \approx 1.9$$

Wind tunnel boundary layer conditions are shown on Figure 5.29 for the same geometry being tested in BTWT as a full model. Boundary layer conditions are shown for the wind tunnel model for natural transition and for trip strips placed at various X/C positions. The best simulation of the full scale boundary layer condition would exist with a trip at around 45% chord, where at the trailing edge:

$$\delta/C \approx .0215$$
$$\delta^*/C \approx .0058$$
$$H \approx 1.95$$

While not in exact agreement with the full scale values, the overall boundary layer shape will be quite similar. Note that for this airfoil, natural transition would produce a boundary layer quite different from the full scale condition.

5.3.2 (Cont.)

Figure 5.30 shows the same curves for the wing tested as a typically sized BTWT half model, where the chord Reynolds number has almost doubled. In this case, placing the trip strip at 40% chord would result in very good duplication of the full scale parameters.

$\delta/c \approx .0205$

$\delta^*/c \approx .00565$

$H \approx 1.90$

Finally, Figure 5.31 shows the boundary layer growth for test conditions representative of the highest Reynolds number currently achievable in model testing. The trip off case would result in:

$\delta/c \approx .0215$

$\delta^*/c \approx .0062$

$H \approx 1.95$

These are not in any better agreement with the full scale values than when an aft trip is applied to the BTWT full model. And, suppose the model finish of the high Reynolds number model was slightly rough, such that transition occurred at around 10% chord. In fact, a very high quality finish would be required to prevent this from occurring. In this case, Figure 5.31 shows that there would be a large discrepancy between test boundary layer conditions and flight boundary layer conditions.

The preceding discussion showed how the full model tested at BTWT could give results comparable to full scale by proper selection of the trip location, for a TR38-1 airfoil. Proper results could also be achieved in a "high Reynolds number" test; that is, no damage would be done by testing at Reynolds numbers between BTWT and full scale. This is a very tenuous situation, in that a slight change in airfoil pressure distribution will alter that conclusion.

Consider the pressure distribution of Figure 5.32. This identical to TR 38-1, except that at the leading edge a slight pressure peak has been added. The full scale boundary layer conditions are shown on the Figure for this pressure distribution. Figure 5.33 shows the boundary layer condition on a BTWT full model with this pressure distribution. Use of an aft trip at 40% chord would produce perfect agreement in δ^*/c with the full scale value, but the shock-boundary layer interaction, which is dependent on δ_s/c, would not be well modelled. Figure 5.34 shows the same situation for the BTWT half model, and for this case, a 30% trip location would produce reasonably good values of δ_s/c and δ^*/c at the trailing edge. So either the full model or the half model in BTWT with a properly selected trip strip would do a reasonably good job of modelling the full scale condition.

Consider, however, the effect at a "high Reynolds number" condition of 10 million as shown on Figure 5.35. Relative to the TR 38-1 pressure distribution, the slight peak on the upper surface causes transition at this Reynolds number near the leading edge. The resulting boundary layer growth is much too rapid compared to that at full scale conditions, and a serious difference is incurred in δ^*/c at the trailing edge. In this case, a "high Reynolds number" test would likely produce results substantially different from full scale. Recall that for the C-141A, the worst disagreement between flight and wind tunnel testing, trip off, occurred around this Reynolds number.

So far, the discussion has been concerned with the upper wing surface. This is the most critical, because of shock-boundary layer interactions. Aft trips are also used on the

5.3.2 (Cont.)

lower surface for high speed drag measurements. The lower surface will have a 10% X/C trip applied for drag level determination at the same time as the 10% X/C trip is applied to the upper surface. When the aft trip is applied to the upper surface, the trip is also moved rearward on the lower surface. The purpose is to place the trip just ahead of where natural transition would occur, so that transition is occurring at a known position, and so that the boundary layer would be as thin as possible. The thickness of the boundary layer alters the airfoil's lift at a given angle of attack, especially for rear-loaded airfoils, thus the best simulation of full-scale lift occurs when the boundary layer is thin. The lower surface trip strip is placed just ahead of where the lower surface pressure recovery occurs; Figure 5.36 gives two examples.

The elegant way to determine the proper location of the high speed trip strips would be to first run the wing in a transonic wing-body program, then compute the upper and lower surface boundary layers to determine where the trip should be placed to achieve proper simulation at the shock wave and at the trailing edge on the upper and lower surface. There are two problems with this approach. First, it is time-consuming, and second, transition prediction on swept wings is a still-developing technology. Consequently, the method most often used is strictly experimental. The model in the wind tunnel is tested trip off at the condition of interest. Flow visualization (discussed below) is applied and the natural transition positions are noted. The high speed trip is applied at about 10% chord ahead of transition on the upper surface and about 5% chord ahead on the lower surface.

The trip off transition position on the upper surface will usually be the shock location. Obviously, this will change with lift coefficient. So, the aft trip will ideally be applied for several different conditions. Except for key performance tests, however, it is usual practice to place the high speed trip for a single high speed cruise condition and assume the trip is proper for conditions in the neighborhood of that point, that is, $\pm$.02 Mach or so and $\pm$.2 in lift coefficient.

Drag data from the two trip positions must then be put together to synthesize a full scale drag rise curve. The procedure is shown on Figure 5.37, where the drag level of the aft trip data is adjusted downward to match the drag level of the forward trip data to make a composite drag level curve. Then, ΔC_{D_M} for the drag polar buildup is the increment in drag of this composite curve from the drag level at the Mach number for the subcritical polar buildup.

There is a final cautionary note, however. It has not yet been proven that aft trip strip technology will work for all classes of airfoils. Consider the 707-type airfoil pressure distribution shown on Figure 5.38a. In the wind tunnel, natural transition with trip off will occur at the shock. This means that the trip can be placed aft on the upper surface for simulation of the full-scale shock-boundary layer interaction and trailing edge δ^*/c. Now consider the pressure distribution of Figure 5.38b. In this case, the adverse pressure gradient begins near the leading edge. Natural transition in the wind tunnel will occur near the leading edge, thus preventing use of the aft trip technique. Proper prediction of scale effects for this type of airfoil must be determined by 2-D high Reynolds number testing at full scale conditions.

5.3.3 Flow Visualization

The previous section discussed how trip strip technology might be used to represent full scale Reynolds number. The process requires that the position of the shock wave and natural transition be determined. The manner in which this is done is with surface visualization, which is also used to see that the trip strips are performing as intended. Surface visualization is also used to detect local flow directions, vortices and separation. There are also certain kinds of off-the-surface visualization. The first category is most often used and will be discussed first.

There are three categories of surface visualization techniques; those which employ a fluid which is photographed while still wet, those which utilize a fluid that leaves particles behind as it dries, and those which cause a change in condition in a surface film:

TYPE	EXAMPLES	USE		
		Shows boundary layer state	Shows surface flow direction	Can be examined after run
Photograph while wet	Oil with fluorescent particles	Yes	Yes	No
Fluid leaves particles	China clay Lampblack	No	Yes	Yes
Surface particles change condition	Sublimation	Yes	No	Yes

The chart shows that no single type of flow visualization works for all three uses. Before describing how each kind works, however, it is necessary to describe the relationship between surface flows and the flow in the free stream off the surface.

Surface flow characteristics The flow on the surface will always be at the bottom of the boundary layer, and thus will often be altered from the flow condition at the outer edge of the boundary layer. Figure 5.39a shows the simplest case, that of flow on a flat plate. In this case the boundary layer profile lies entirely in a plane, and the flow on the surface is going in a direction identical with that of the external flow. Figure 5.39b shows the flow over a swept wing. In this case, crossflow has developed within the boundary layer and the particle path on the surface is considerably different from that of a particle in the free stream at the edge of the boundary layer.

This occurs because of the reason shown on Figure 5.40. The flow in the boundary layer has less velocity than does the flow at the edge of the boundary layer, and so has less momentum. This causes the boundary layer to react more to pressure gradients than does the external flow as seen on Fig. 5.40a. As an example, the upper surface pressure distributios for two adjacent sections of a swept wing are shown on Figure 5.40b. At point C on line A, the boundary layer sees less pressure at point C on line B, so the boundary layer is pushed towards B. This gives rise to crossflow within the boundary layer as described in Figure 5.40c. The obvious implication is that the direction on the surface

3/2

5.3.3 (Cont.)

can never be trusted as being identical to the external flow direction at the edge of the boundary layer.

If the pressure gradients are sufficiently severe, then three-dimensional boundary layer separation appears, as demonstrated on Figure 5.41a, which shows a typically observed separation pattern on a swept wing. Inboard, at Section A-A, the pattern is indicating a situation with only a slight bit of crossflow. At section B-B, however, the crossflow is so severe that the surface particles leave the surface at point C. Beneath this dividing streamline is another layer of particles which are being swept spanwise, as shown in Figure 5.41c. Note that all these motions below path e-e are in the boundary layer.

The relationships above prevail when the boundary layer is relatively thick so there is room for crossflows to develop. When there is vortex motion above the surface, however, the mixing due to the vortex thins the boundary layer and there is a strong correlation between the direction outside the boundary layer and on the surface. If there is a vortex lying just above the surface, a very distinctive pattern will be made on the surface, as shown on Figure 5.42. The vortex is revealed by the divergence and convergence of the surface streamlines towards and from limiting lines; an example will be given later.

Shock waves also have distinctive flow patterns. A swept shock wave will produce a kink in the surface flow that will be quite distinct (Fig. 5.43a) when the steamlines are viewed from a shallow angle. The surface pattern beneath a normal shock depends on the nature of the shock. A weak shock wave of limited extent will be noticed by a divergence in the flow across the shock (Fig. 5.43b). However, if the shock wave is strong enough, a vortex can be produced at the edge of the shock wave as demonstrated on Figure 5.43c.

A frequently encountered flow pattern which is quite complex is that where two surfaces meet at a relatively large angle. This is depicted on Figure 5.44 for the case of a circular cylinder at right angles to a flat plate. The flow approaches the cylinder from the left, and the fluid in streamline A sees the presence of the cylinder as an adverse pressure gradient and separation occurs at point B. The fluid in that streamline then leaves the surface nad reattaches on the cylinder at C. It then divides into two streams and flows around each side of the cylinder. The two surface streamlines approaching the cylinder on either side of A turn sharply at B and go on either side of the cylinder. This part of the flow is relatively simple. What happens inside the separated region is quite complex. The flow from B to C along the streamline A generates a vortex inside the separated part, denoted V_1.

5.3.3 (Cont.)

The vortex flow goes from B to C then drives downward toward the plate. But it too cannot negotiate the corner and separates at point D, reattaching at point E. The vortex thus formed peals aft on either side of the cylinder, leaving the characteristic vortex feathering lines. The remaining flow down in the corner between the cylinder and the plate is occupied by a second vortex, V_2, which is opposite in sign to V_1. Typically, V_1 will be much larger than V_2. These two vortices are shed on either side of the cylinder and trail downstream. This complex pattern occurs because the fluid along streamline A cannot make it to the cylinder without separating.

The reason for describing the case of the circular cylinder is because it demonstrates the pattern often seen at geometry junctures on aircraft. An obvious case is the wing-body junction shown on Figure 5.45. The features of the separation are exactly similar to those of the cylinder. If the flow cannot make it along the body to the wing and separation occurs, then vortex V_1 will appear, and usually V_2 as well. The two vortices add to drag because they increase the suction velocities on the wing's rearward facing areas above the value normally generated in potential flow.

A final case of vortex flows is shown in Figure 5.46, for the flow over the top of a delta wing at an angle high enough to promote leading edge vortex formation. Usually three vortices are present as shown. The exact way in which the dividing streamlines appear above the surface has been drawn in various ways; one commonly drawn curve is shown.

The various kinds of flow visualization commonly used at Boeing will now be described. The most frequently used is fluorescent oil flow followed by lampblack and china clay, then sublimation. The way to mix the various solutions is described in Reference 5.6.

Oil flow This process utilizes fluorescent particles suspended in heavy oil. The model is painted with the oil and the tunnel is started. The oil is blown along surface lines, thus revealing surface streamline directions, and is blown away from an area at a rate dependent on the local shearing stress. Thus the oil thins more rapidly beneath a turbulent boundary layer than under a laminar one. The flow pattern is recorded on film using untraviolet light. Where the oil is thick, the surface will appear bright and where it is thin, the surface will be darker. Figure 5.47 is such a photograph of the TR 1142 calibration model at M=.050. Note the light area on the forward part of the wing. This denotes a laminar boundary layer. This region is pierced by several wedges of turbulent boundary layer that is sweeping the oil to the trailing edge. The aft 40% of the airfoil has transisted to fully turbulent flow. As soon as oil leaves the laminar region it is conveyed off the trailing edge, hence the turbulent region is darker since the oil is thinner.

Figure 5.48 shows the same wing at M=0.90. There are more turbulent wedges since the Reynolds number is higher, and since the speed is higher the shear stress in the laminar boundary layer is also higher, so the laminar region is less bright than in Figure 5.42. Where the shock wave lies, a laminar bubble is formed as evidence by a bright line separating the laminar and turbulent regions.

5.3.3 (Cont.)

Oil flow has the advantage of simultaneously showing the surface streamline direction and the boundary layer condition. It has liabilities in that it must be photographed to be seen, thus only regions that are visible to a camera can be examined. It has a further liability that oil flow substantially alters the separation position and consequently the interaction between the shock wave and the boundary layer.

Lampblack and china clay These are equivalent techniques in which a very fine particle is suspended in heavy oil or kerosene. Lampblack requires that the model be painted white or some other light color; china clay requires that it be painted black. Recently, other colors have been used in BTWT as well.

The procedure is to paint the model with the mixture and run the tunnel until the surface is dry. While the tunnel is running, the flow moves the liquid on the surface along streamlines. The fluid leaves behind it a trail of particles. These have the advantage of being permanent records which can be minutely examined when the tunnel is stopped, thus surfaces not visible to a tunnel camera can be inspected. They suffer the disadvantage of not being able to reveal whether the boundary layer is turbulent or laminar. An example of a lampblack is given on Figure 5.49.

Rather than painting the entire surface, sometimes the surface is dotted with oil. The result is a pattern like the photograph on Figure 5.50. This gives a clear indication of where vortices are merging. Note for example the limiting streamlines on the aft body near the body downward break. This use of lampblack procedure highlights the presence of vortices, but reveals less than would a conventional lampblack under the gaze of an experienced aerodynamicist.

The proceding methods have failed to provide two invaluable requirements: (1) positive proof that all trip strips are working, and (2) readily observable indication of shockwave position for application of aft trip strips. Both needs are filled by fluorene sublimation. This procedure dissolves fluorene, a white crystalline substance, in a solvent. The mixture is then sprayed on the surface with a spray gun. The solvent evaporates, leaving behind a continuous coating of fluorene. The tunnel flow is turned on and the crystals begin to sublimate (turn directly from solid to gas) at a rate dependent on local surface velocity. Figure 5.51 is the use of sublimation equivalent to Figure 5.47 at M=0.50. The process has been stopped at the point where the fluorene has all disappeared from the turbulent region, but not from the laminar regions. Since the sublimation ceases when the tunnel flow stops (unless the model is too hot), the pattern can be examined minutely, even with a magnifying glass, on interior surfaces as well as exterior surfaces. Each individual grit of the trip strip can be examined to see if it is producing transition.

5.3.3 (Cont.)

Sublimation has an even more important application, in that it can clearly demark where the shock wave is causing transition, without altering the position of the shock, as oil flow will do. Figure 5.52 shows a sublimation photo of the wing flow field on the TR 1142 model at M=0.90. Comparison of this photo to Figure 5.48 reveals that the oil flow has altered the position of the shock wave. This interference with the flow field by oil has been known for some time (see Reference 5.7, done in 1961), yet most BTWT customers continue to use oil flow for aft trip position determination.

Tufts Low speed testing will often employ tufts attached to the surface to indicate fluid direction. An example is given in Figure 5.53. These are handy when a number of conditions are to be observed, but suffer from two serious shortcomings: (1) the tufts interfere with downstream rows, thus altering the flow situation, and, (2) they do not indicate flow details nearly so well as does china clay oil flow.

The flow off the surface can be determined by several ways. It is very common to use a stream of smoke from a manually positioned smoke wand during low speed testing. This can be especially educational for revealing the nature of off-the-surface streamlines. Helium bubble streams are another type of flow visualization. This is especially useful for highlighting vortices, since the helium, being lighter than air, will penetrate to the core of a vortex.

A method recently developed for BTWT offers a powerful, but expensive, tool for determining vortex paths at high speeds. The device is a split-film anemometer mounted on a survey probe. Successive surveys at varying streamwise stations allow the shed vortices to be mapped. Figure 5.54 shows how the technique has been used to reconstruct the paths of vortices shed by the YC-14 body and gear pod.

5.3.4 Pressure measurements

The final type of observation usually made in wind tunnel tests are pressure measurements. This is a well-established art, involving measurement of the pressure on the surface (static pressure) or of the total head (total pressure). The only precautions required concern hole geometry for static pressures and probe geometry for total probes. These are adequately described in Reference 5.8.

5. REFERENCES

5.1 "7X7 Airplane Drag Comparison," L.L. Herrick & D. George -Falvy, D6-42130TN, March ,1973.

5.2 "Drag Prediction Methods for Subsonic Airplanes," B.O.G. Montgomerie-Jensen and E.C. Finch, D6-24229, June, 1970.

5.3 "Results of Wind Tunnel to Flight Buffet Boundary Correlations," R. H. Wickemeyer, C/S AE-PD-282, 8/12/77.

5.4 "Use of Grit-Type Boundary-Layer-Transition Trips on Wind Tunnel Models," Braslow, A.L., Hicks, R.M., and Harris, R.J., NASA TN D-3579 (1966).

5.5 "An Important Trip Size Selection Criteria for a Certain Class of Wings, G. A Blom, C/S AE-7X7-71, Oct. 18, 1973.

5.6 "Trip Strip Technology and Application at BTWT," B.O. Bohn, January, 1976, D6-43354.

5.7 "The Motion of a Thin Oil Sheet Under the Steady Boundary Layer on a Body," Squire, L.C., RAE, 1961.

5.8 "Pressure Probes for Velocity Measurement," R. J. Moffat, Short Course given at Boeing in 1974 (Notes).

3/7

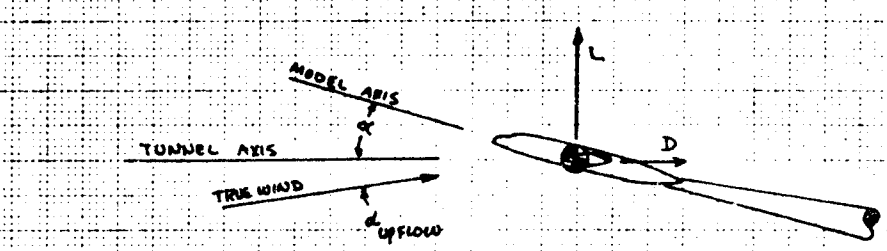

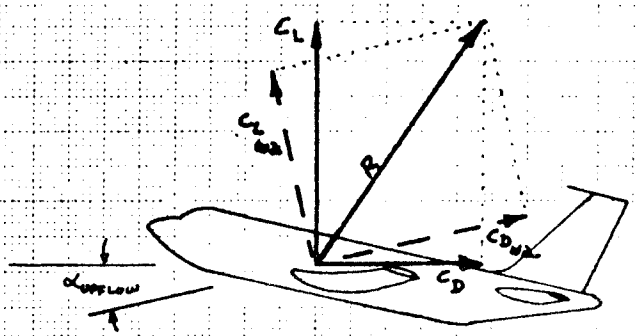

C_L, C_D RELATIVE TO TUNNEL AXIS, MEASURED BY BALANCE

$C_{L_{WA}}$, $C_{D_{WA}}$ RELATIVE TO WIND AXIS; ARE AIRPLANE FORCES FOR FLIGHT ACCOUNTING

CORRECTION DUE TO UPFLOW

$$C_{L_{WA}} = C_L \cos \alpha_u - C_D \sin \alpha_u$$

$$C_{D_{WA}} = C_L \sin \alpha_u + C_D \cos \alpha_u$$

WHEN α_u IS SMALL, THEN

$$C_{L_{WA}} \doteq C_L$$

$$C_{D_{WA}} \doteq C_D + C_L \sin \alpha_u$$

$$= C_D + \Delta C_{D_{UPFLOW}}$$

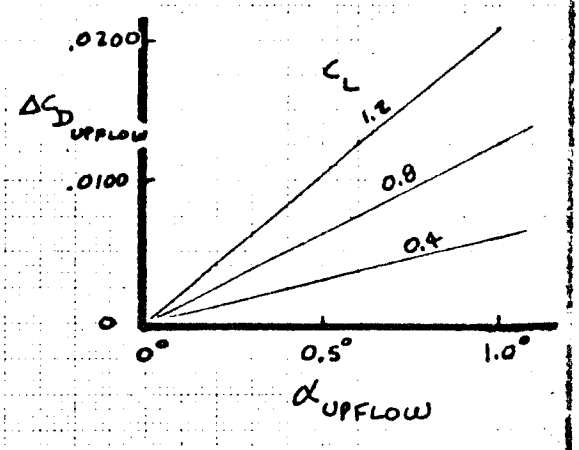

CALC	GILLETTE	1-27-78	REVISED	DATE
CHECK				
APR				
APR				

EFFECT OF UPFLOW ON LIFT & DRAG

FIG. 5.1

BOEING

5.26

(a) TEST MODEL UPRIGHT AND INVERTED

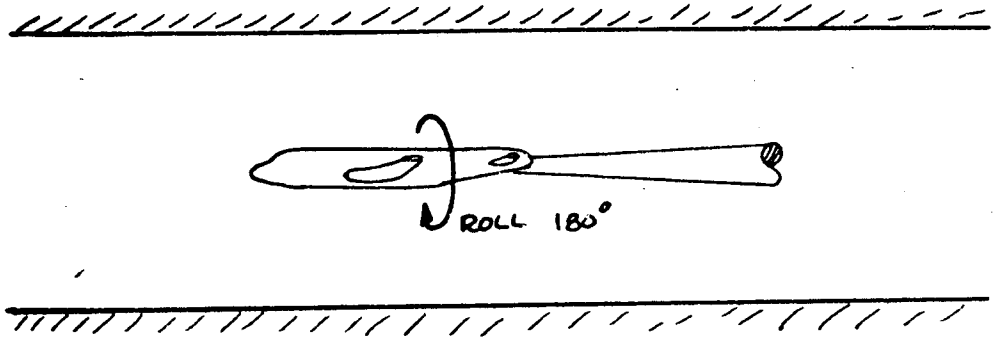

(b) COMPARE UPRIGHT & INVERTED LIFT CURVES

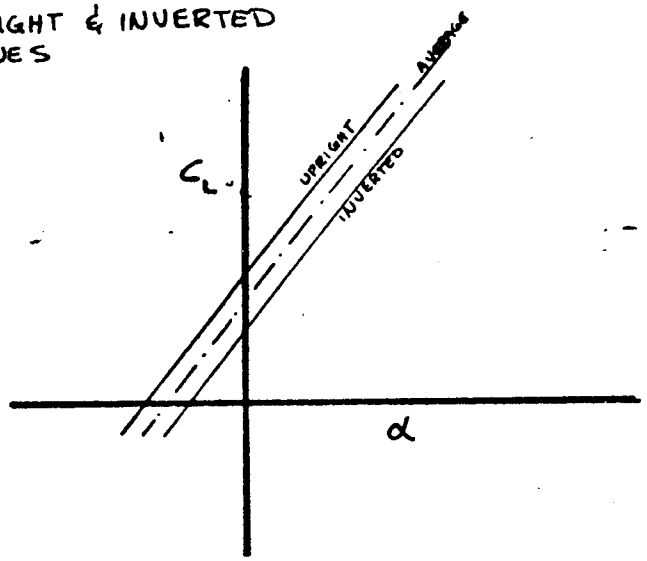

(c) COMPUTE $\alpha_{UPFLOW} = \left(\frac{\alpha_{UPRIGHT} - \alpha_{INVERTED}}{2}\right)_{C_L = CONSTANT}$

(d) PLOT VERSUS C_L & MACH

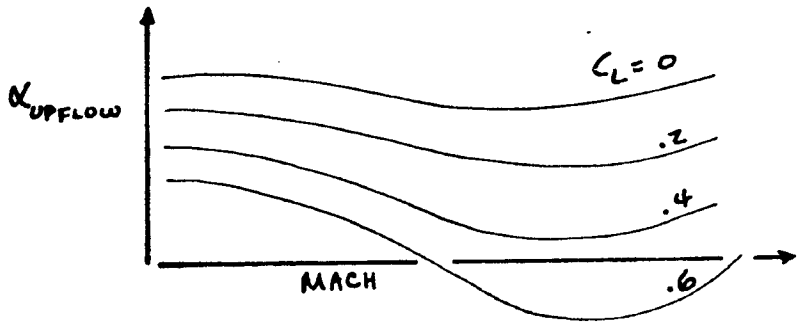

FIGURE 5.2 MEASUREMENT OF UPFLOW

1-27-78
CULETTE

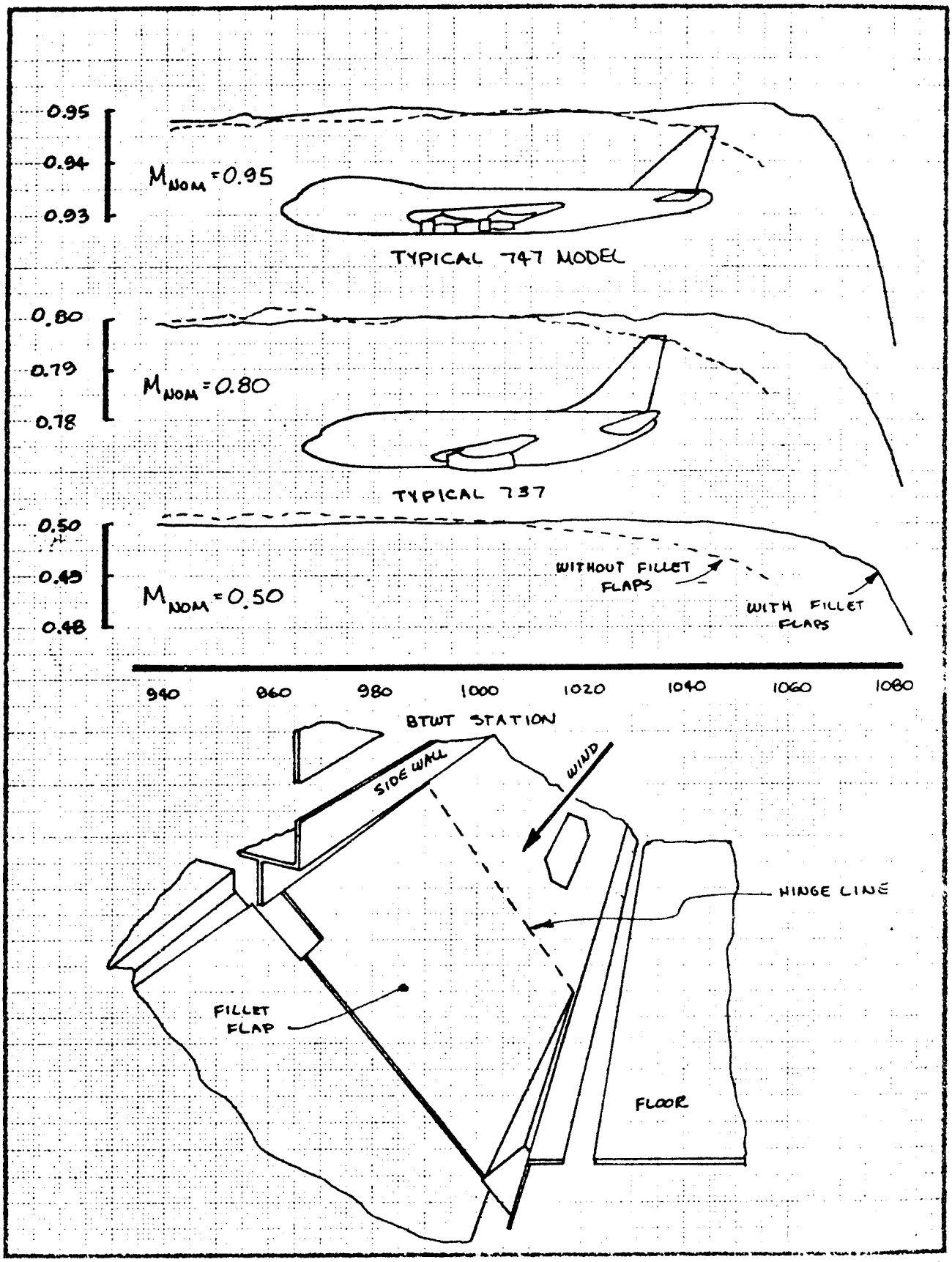

CALC	1-28-78		REVISED	DATE
CHECK	GILLETTE			
APP				
APP				

EFFECT OF FILLET FLAPS ON BTWT BOUYANCY

FIG. 5.3

BOEING

PAGE 5.28

320

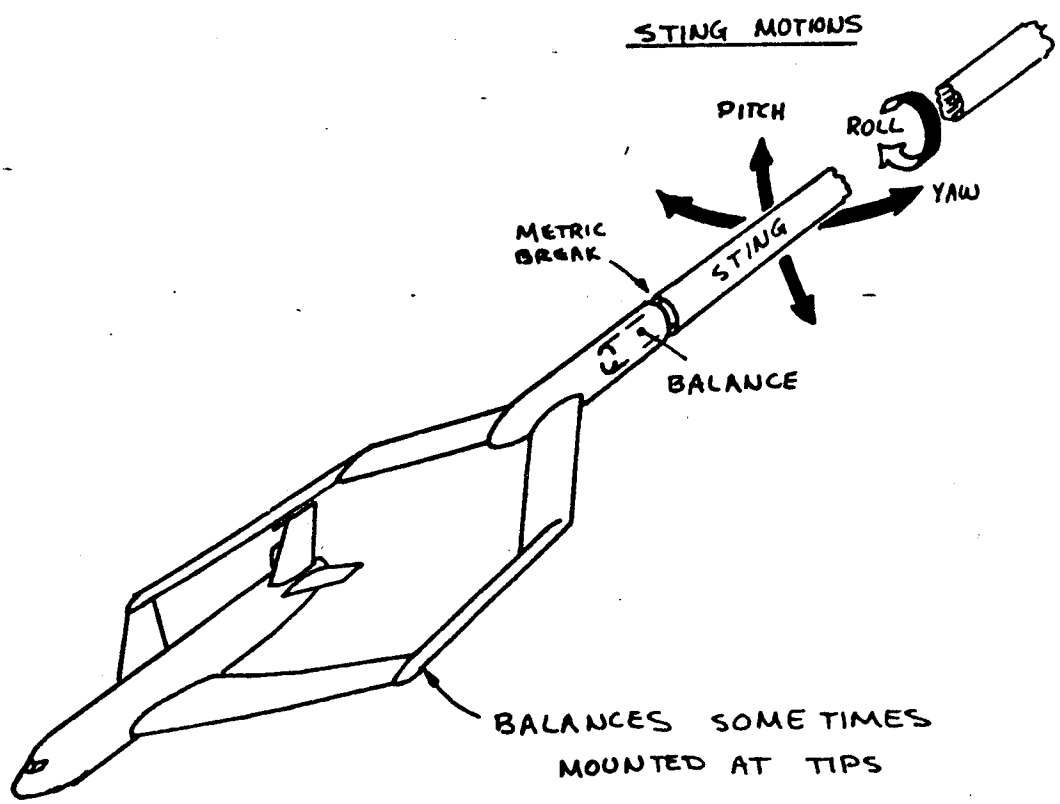

FIGURE 5.8 FORK STING MOUNT

1.27.78
GILLETTE

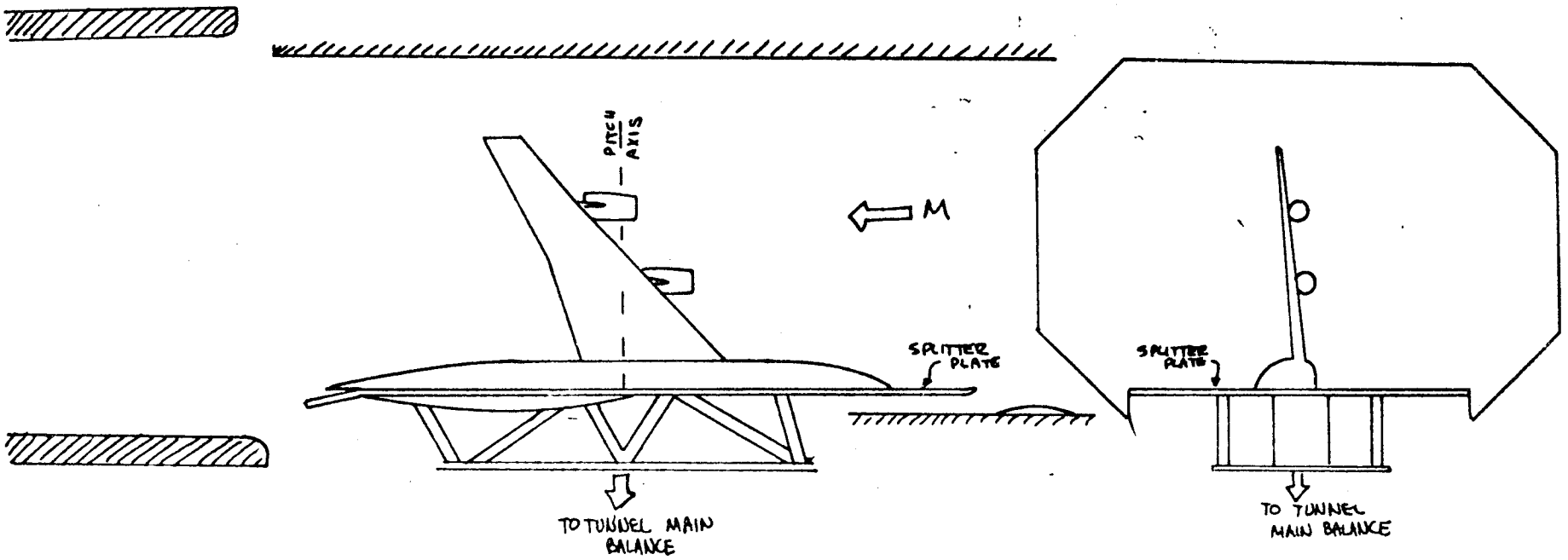

FIGURE 5.10 BTWT HALF-MODEL INSTALLATION

0.5.35

2.4.78
GILLETTE

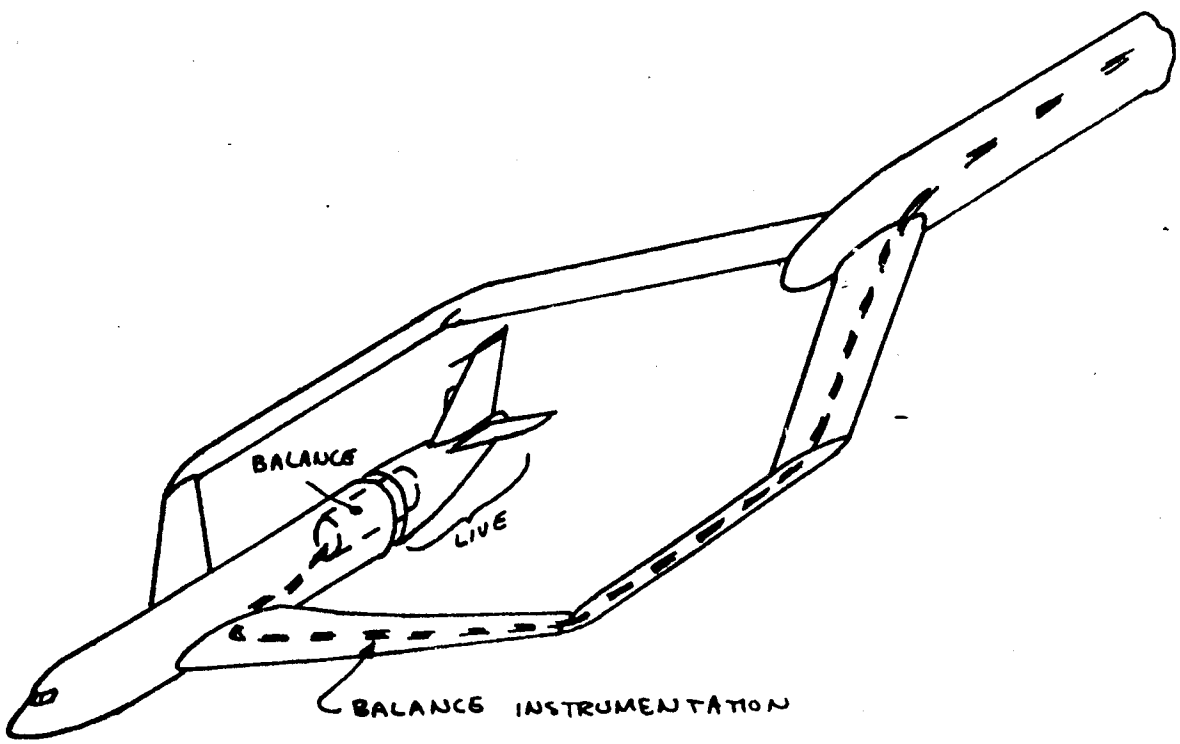

FIGURE 5.11 SPECIAL BALANCE

(a) SUMMATION OF THE TWO FORCES OF DRAG ON FULL-SCALE AIRPLANE

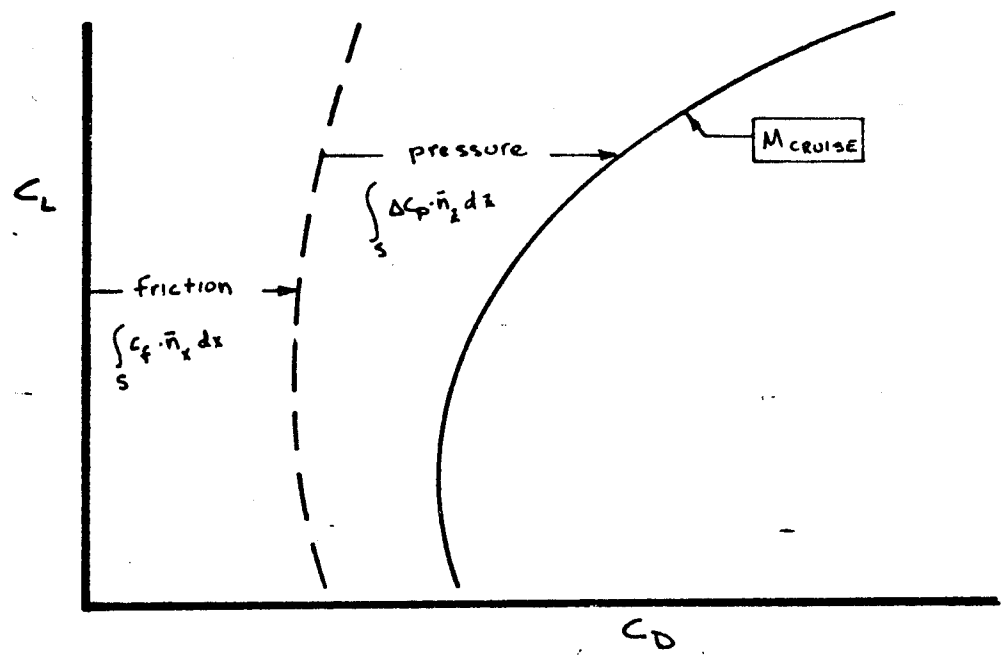

(b) BOEING DEFINITION OF COMPONENTS

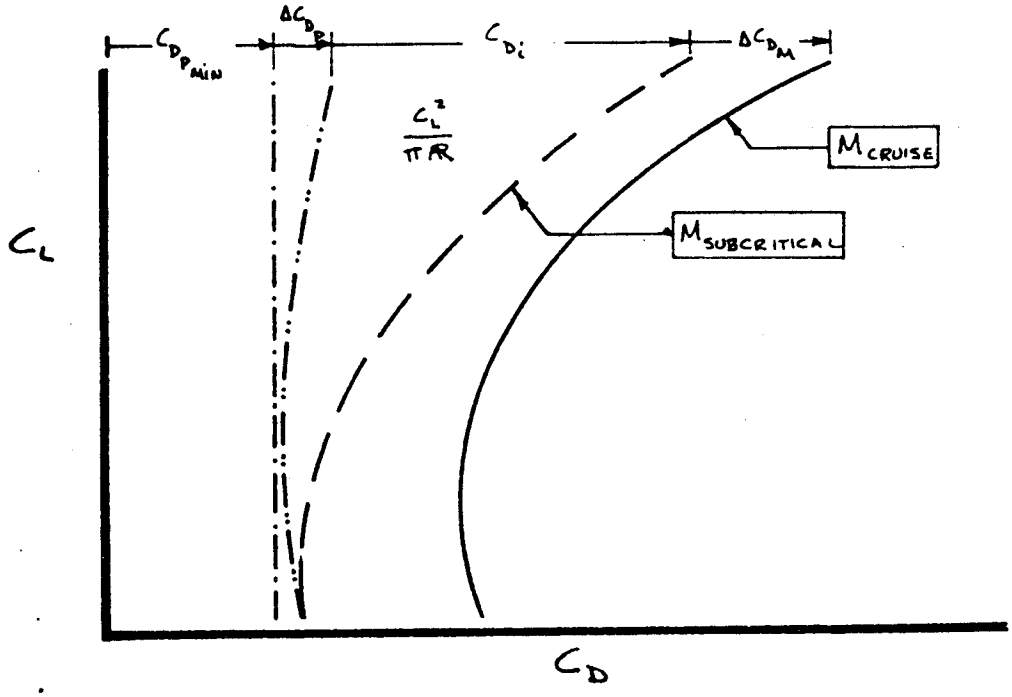

FIGURE 5.12 DRAG BREAKDOWN ~ FULL SCALE AIRPLANE

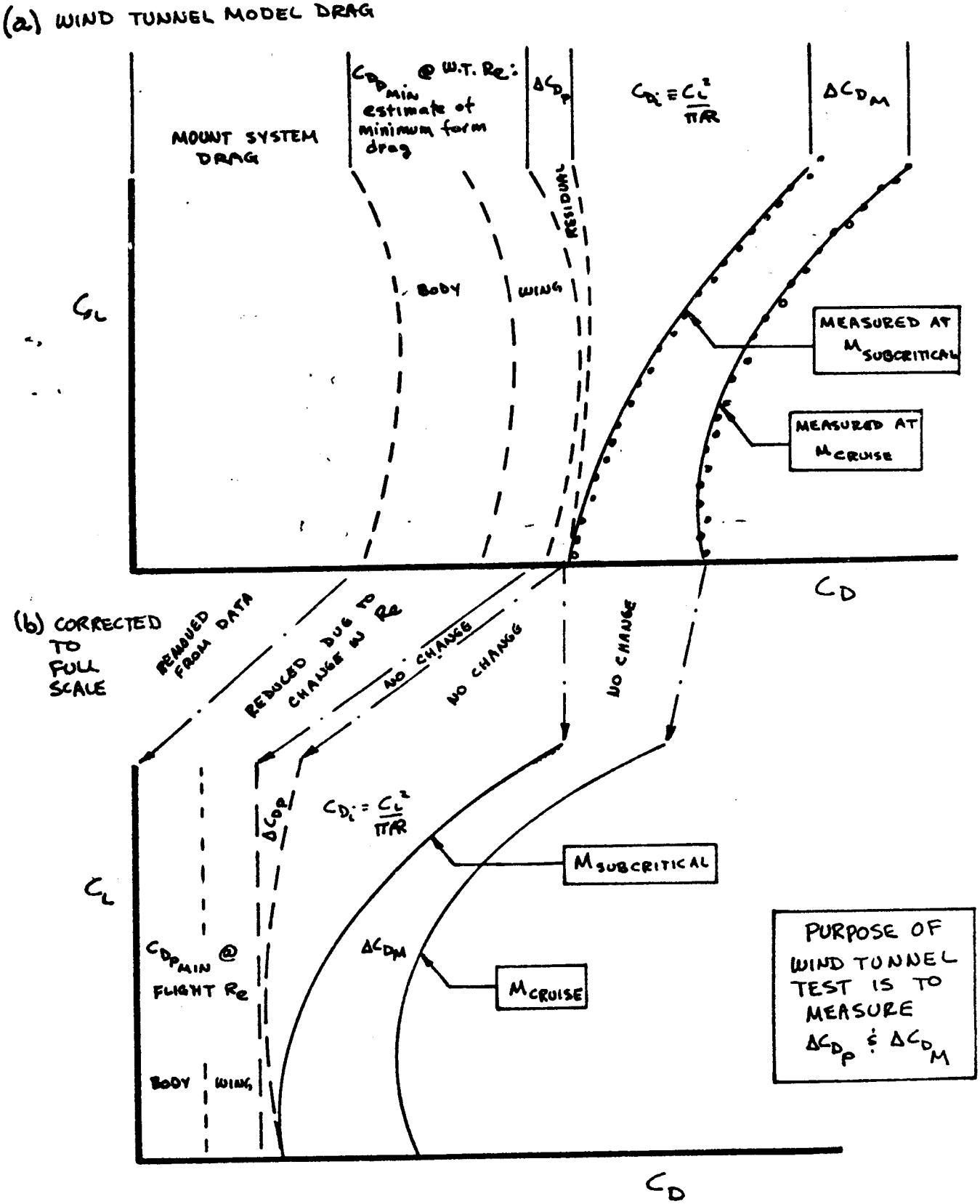

FIGURE 5.13 USE OF WIND TUNNEL DATA TO PREDICT FULL SCALE DRAG (WING - BODY EXAMPLE)

1.28.78
GILLETTE

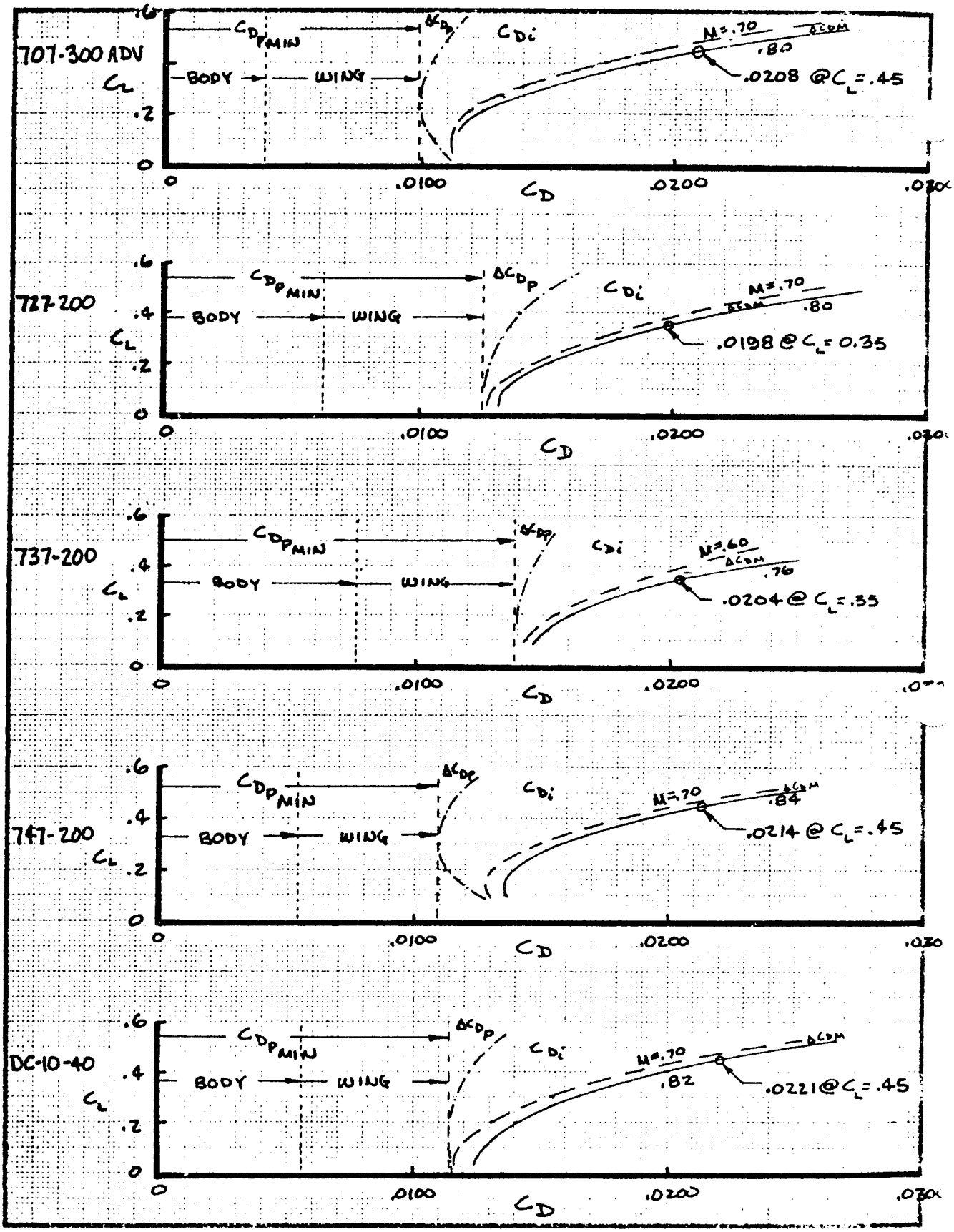

CALC	GILLETTE	1.28.78		DATE	
CHECK					
APR					
APR					

ESTIMATED FLIGHT DRAG OF SELECTED WING-BODY GEOMETRIES

SOURCE: D6-42130TN FIG 5.14

BOEING

5,39

D1 4100 3260 ORIG 3/71

326

(a) TRADITIONAL TECHNIQUE TO PREDICT BUFFET BOUNDARY

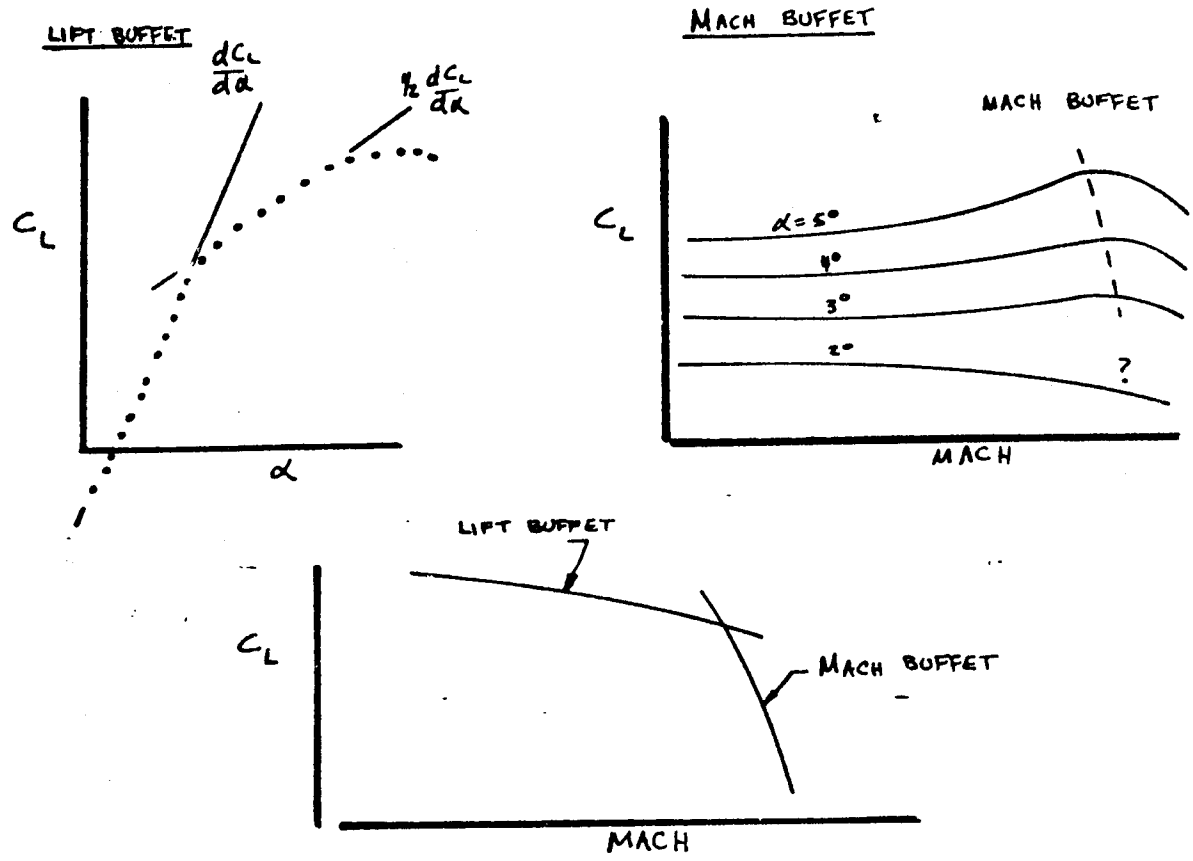

(b) CURRENT TECHNIQUE TO PREDICT BUFFET BOUNDARY
SOURCE: C/S AE-PD-282

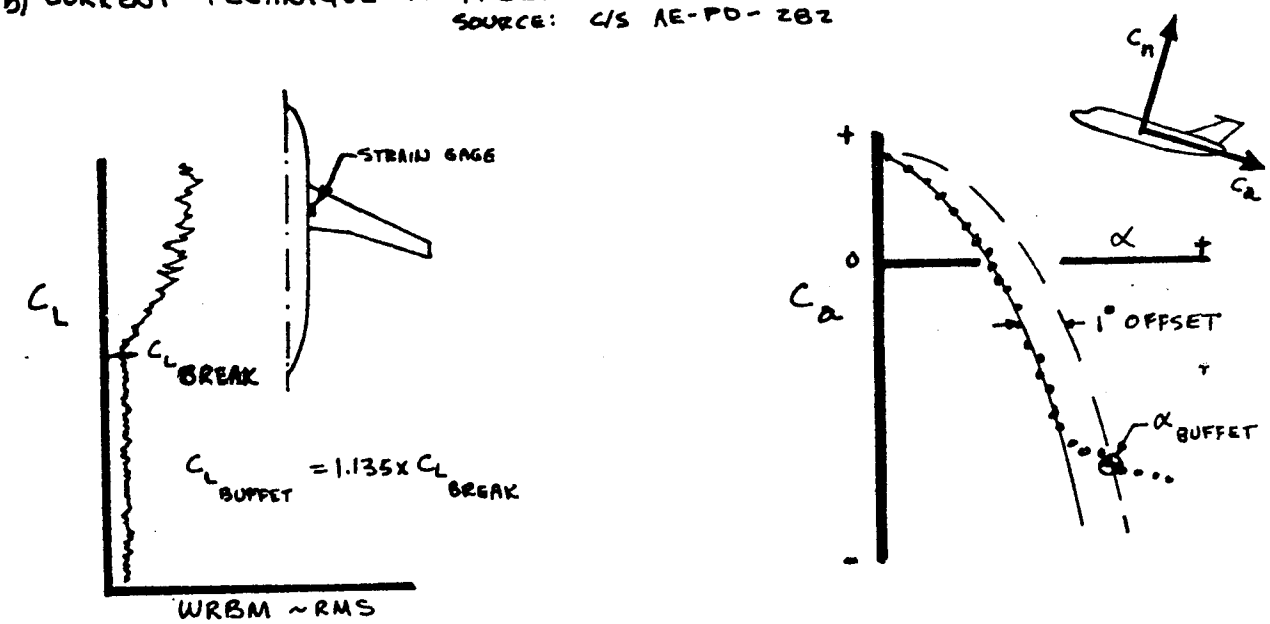

FIGURE 5.15 PREDICTION OF AIRCRAFT BUFFET BOUNDARY

1.28.78
GILLETTE

P. 5.40

307

Attachment to C/S AE-PD-282

FIGURE 5.16 BUFFET PREDICTION

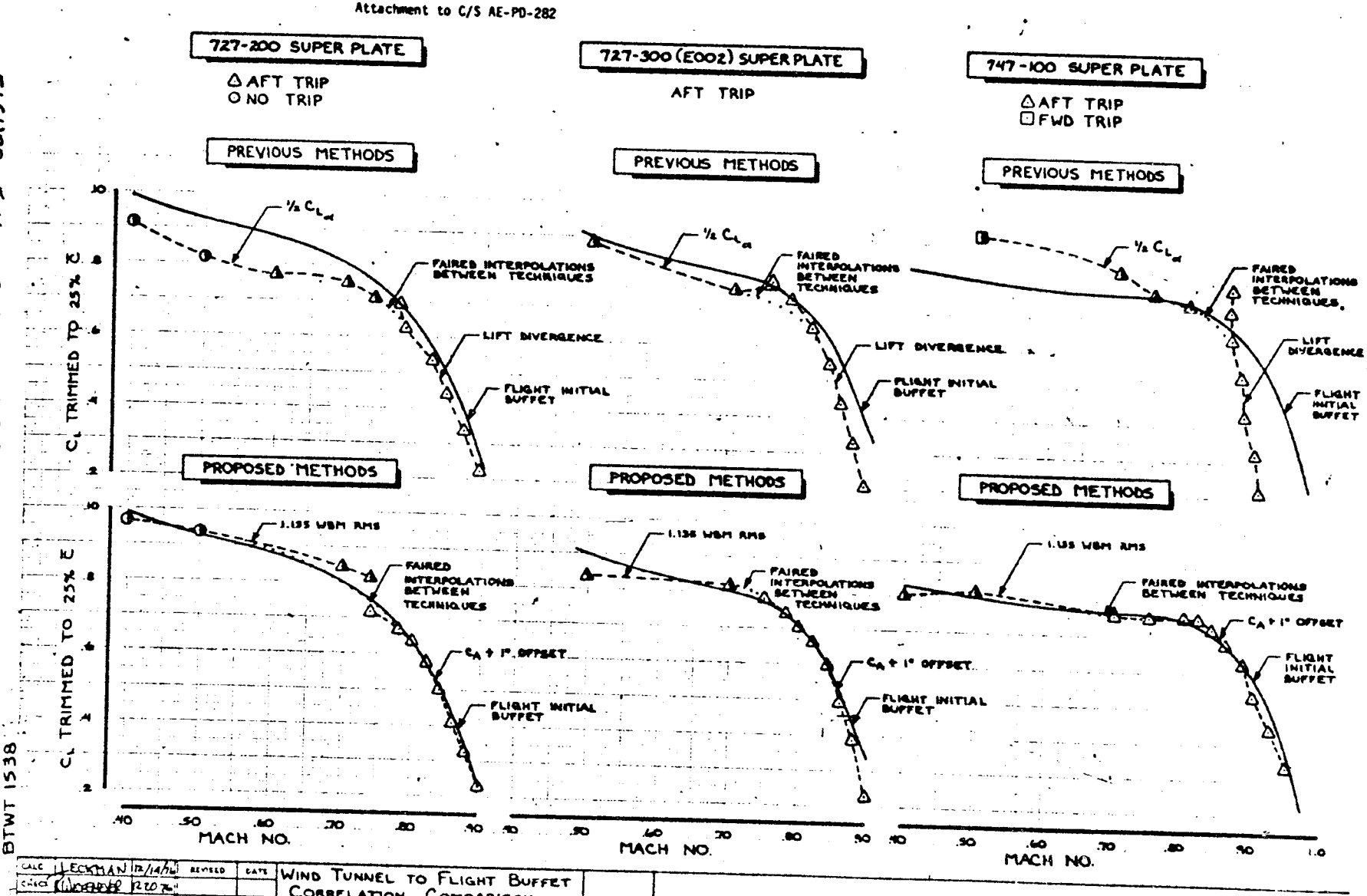

CALC	ECKMAN	12/14/76	REVISED	DATE	WIND TUNNEL TO FLIGHT BUFFET CORRELATION COMPARISON
CHKD	[illegible]	12/20/76			
ENG					Fig. 1
APP					
	VAN HISE	12/15/76			THE BOEING COMPANY
					PAGE 6

BTWT 1538

D 1 A 1

(a) SUBSONIC & TRANSONIC FLOW

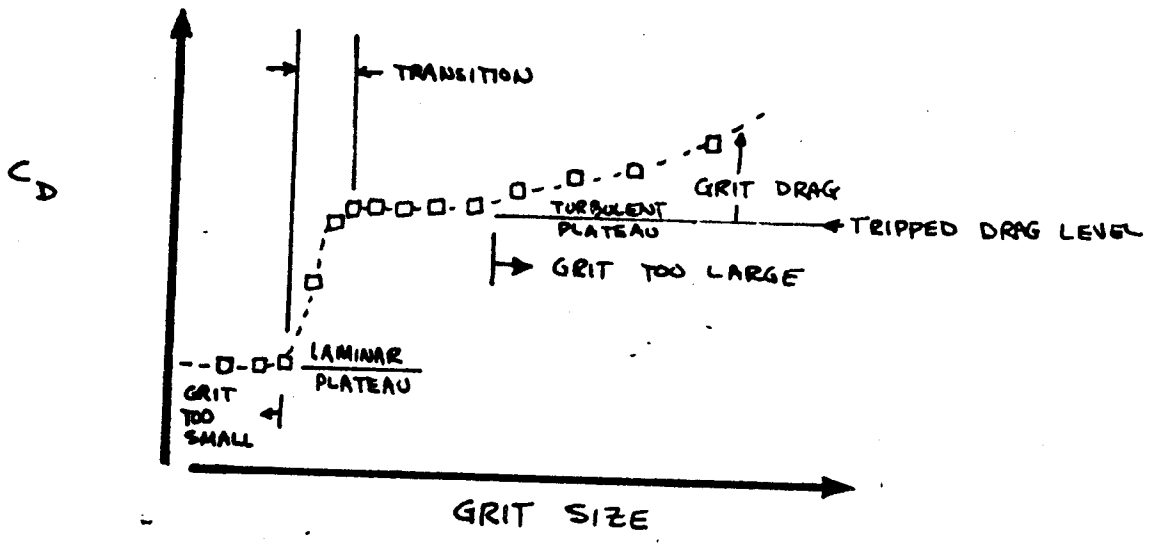

(b) SUPERSONIC FLOW

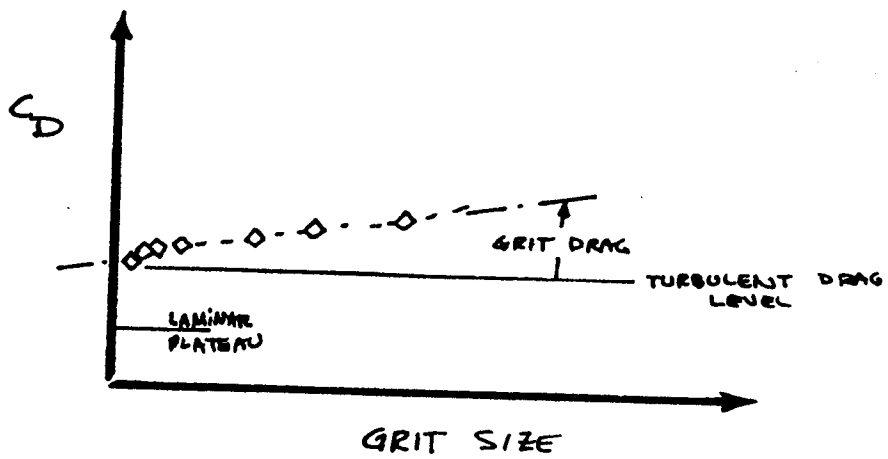

FIGURE 5.17 EFFECT OF GRIT SIZE ON DRAG LEVEL

1-28-78
GILLETTE

Attachment C/8 AE-7X7-71 (2)

REF NACA TN4363

PT	TEST	RUN	M	C_L	MODEL	WING	AIRFOIL
1	1335	51	.82	.35	TR1265	W_1	TR38
3	1335	47	.84	.35			
5	1335	49	.84	.35			
6	1335	50	.86	.45			
7	1335	51	.82	.35			
9	1335	47	.84	.35			
10	1335	48	.84	.45			
11	1335	49	.86	.35			
14	1336	55	.82	.42	TR1258	$W_{8.1}$	TR38-1
15	1336	56	.82	.55			
16	1342	2	.86	.35	TR1265	$W_{1.3}$	TR38

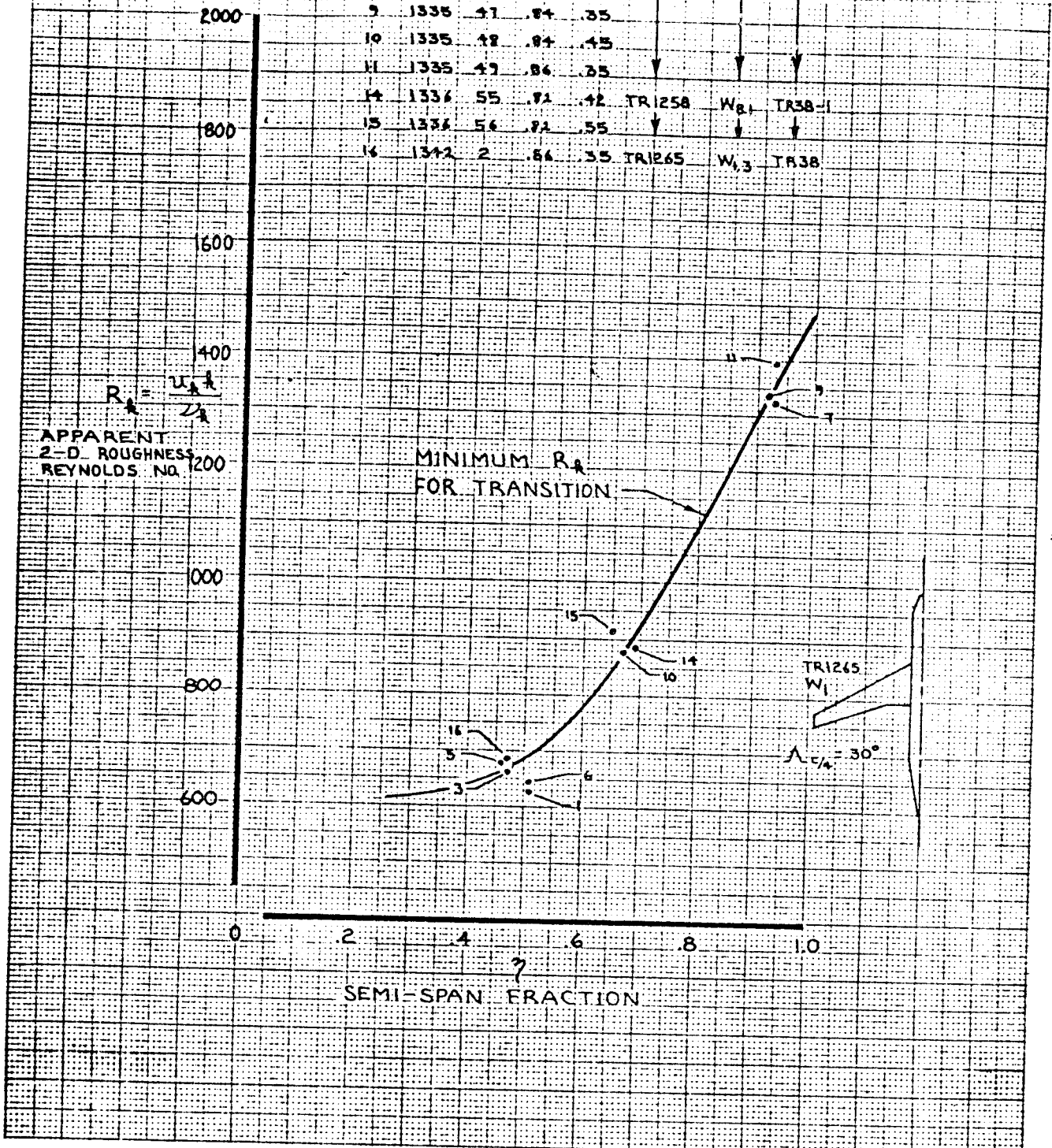

CALC	BLOM	6/14/73	REVISED	DATE	MINIMUM ROUGHNESS REYNOLDS' NUMBER FOR TRANSITION — FIG 5.18
CHECK					
APR					
APR					THE BOEING COMPANY — PAGE 5.43

D1 4100 3260 ORIG 3/71

K-E ALBANENE 1001

330

REF NACA TN4363

FOR P_T = ATMOSPHERIC
$T_T \cong 600°$ R

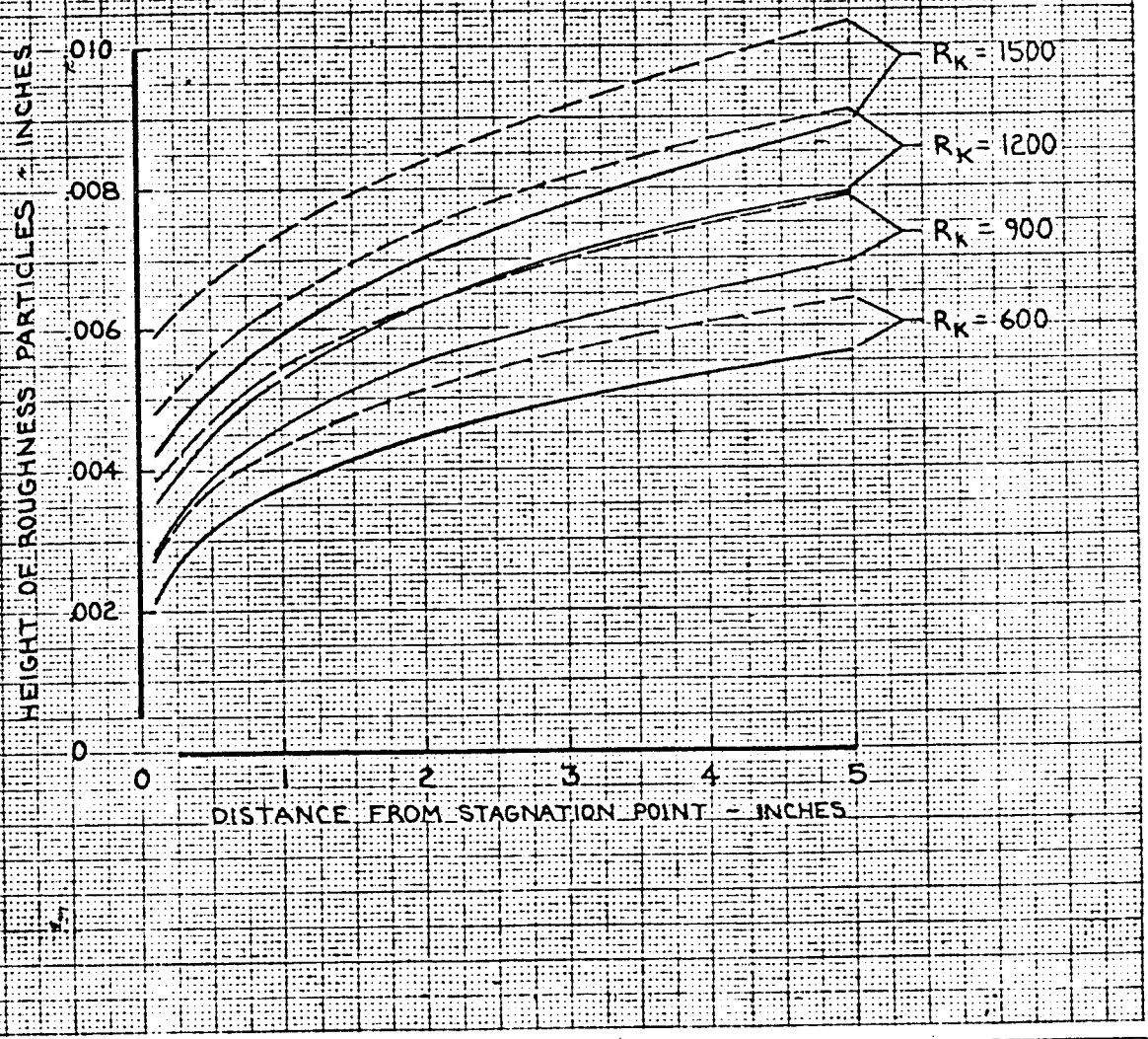

CALC	BLOM	6/26/73	REVISED	DATE	PARTICLE HEIGHT REQUIRED P_T = ATMOSPHERIC	FIG 5.19
CHECK						
APR						
APR					THE BOEING COMPANY	PAGE 5.44

Attachment C/8 AE-7X7-71 (5)

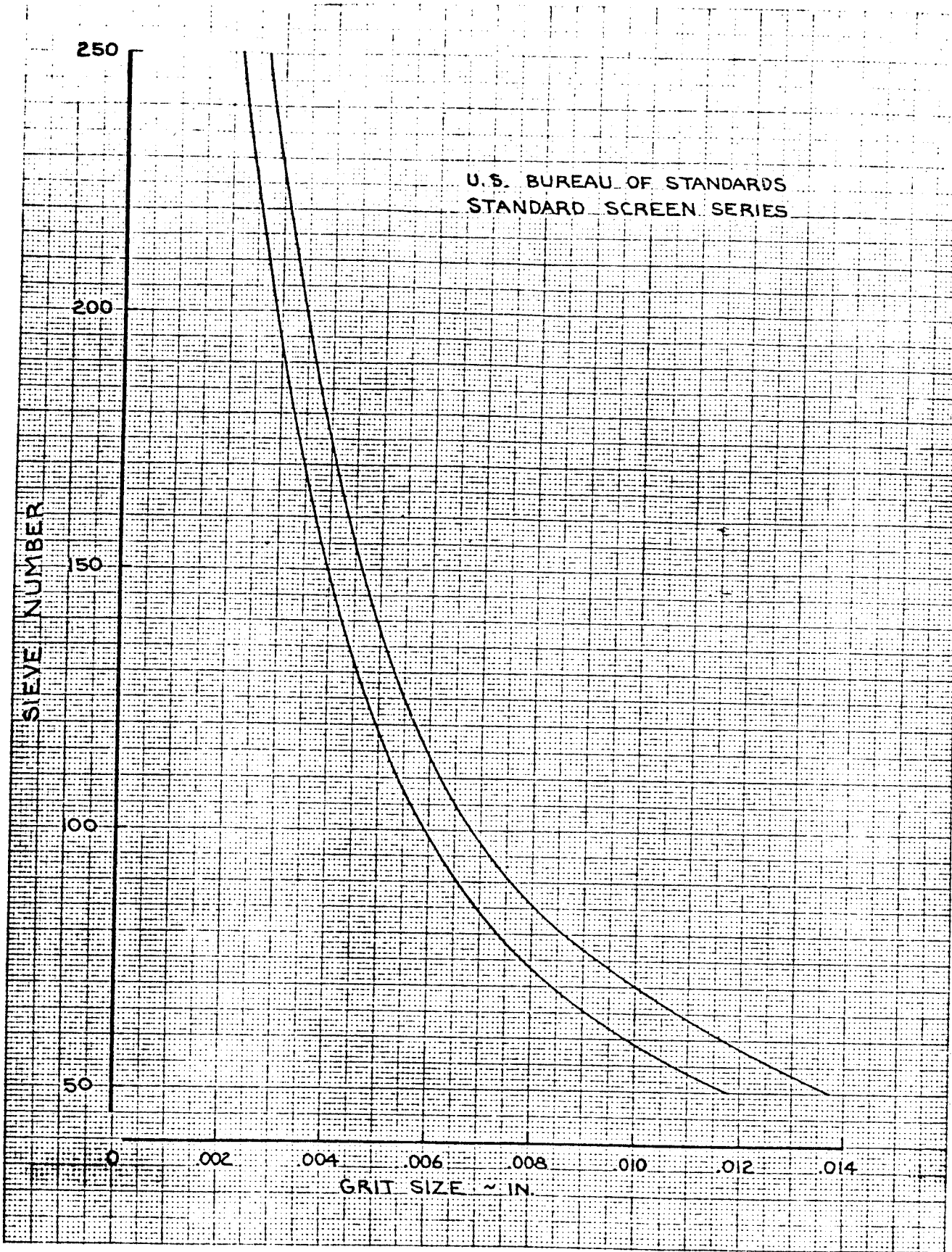

CALC	BLOM	7/1-/73	REVISED	DATE	SIEVE NO. vs GRIT SIZE	FIG 5.20
CHECK						
APR						
APR					THE BOEING COMPANY	PAGE 5.4-5

D6 4100 3260 ORIG 3/71

K-E ALBANENE 1961

332

(a) PROPERLY APPLIED GRIT

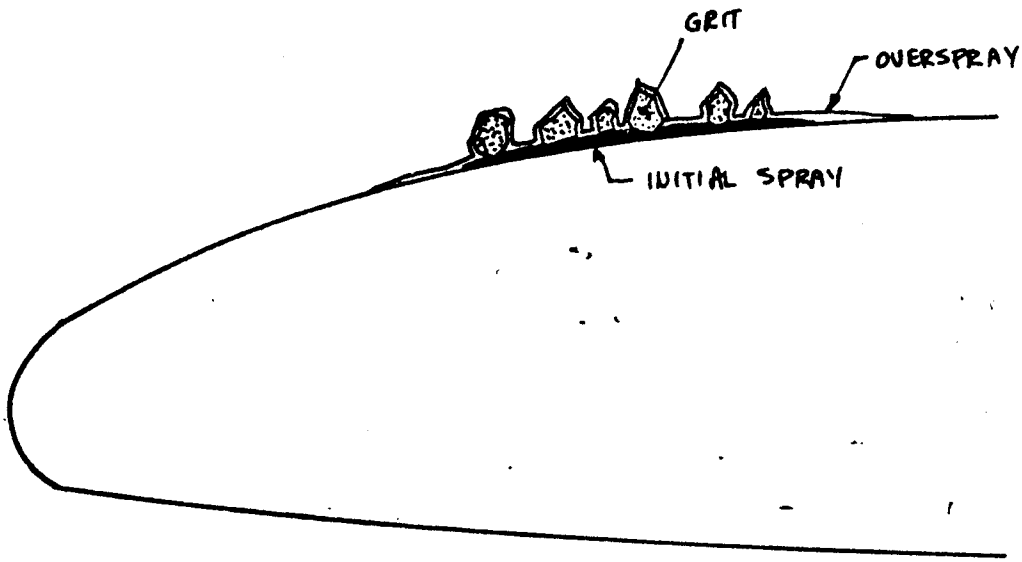

(b) IMPROPERLY APPLIED GRIT

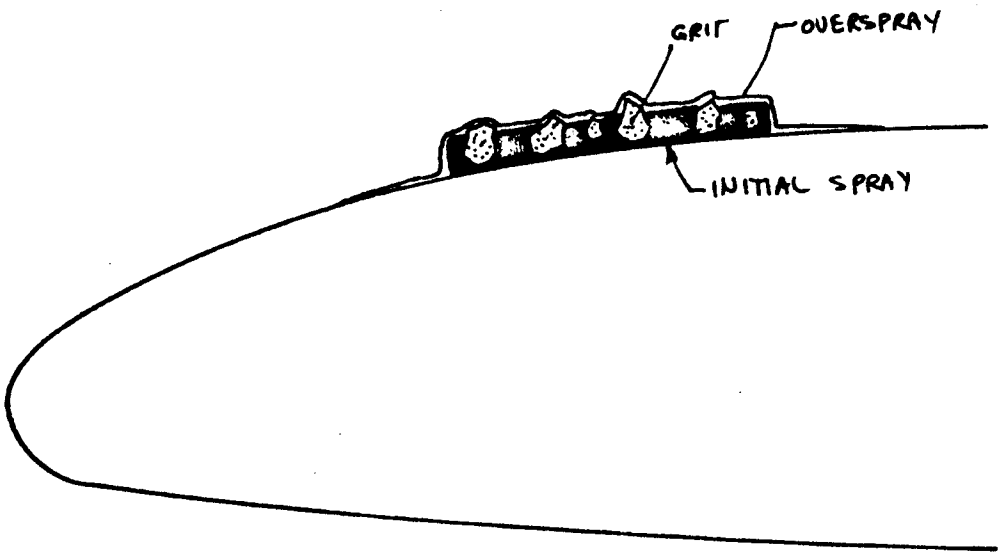

FIGURE 5.21 APPLICATION OF GRIT

1.28.78
GILLETTE

P. 5.46

• CONSTANT ANGLE OF ATTACK

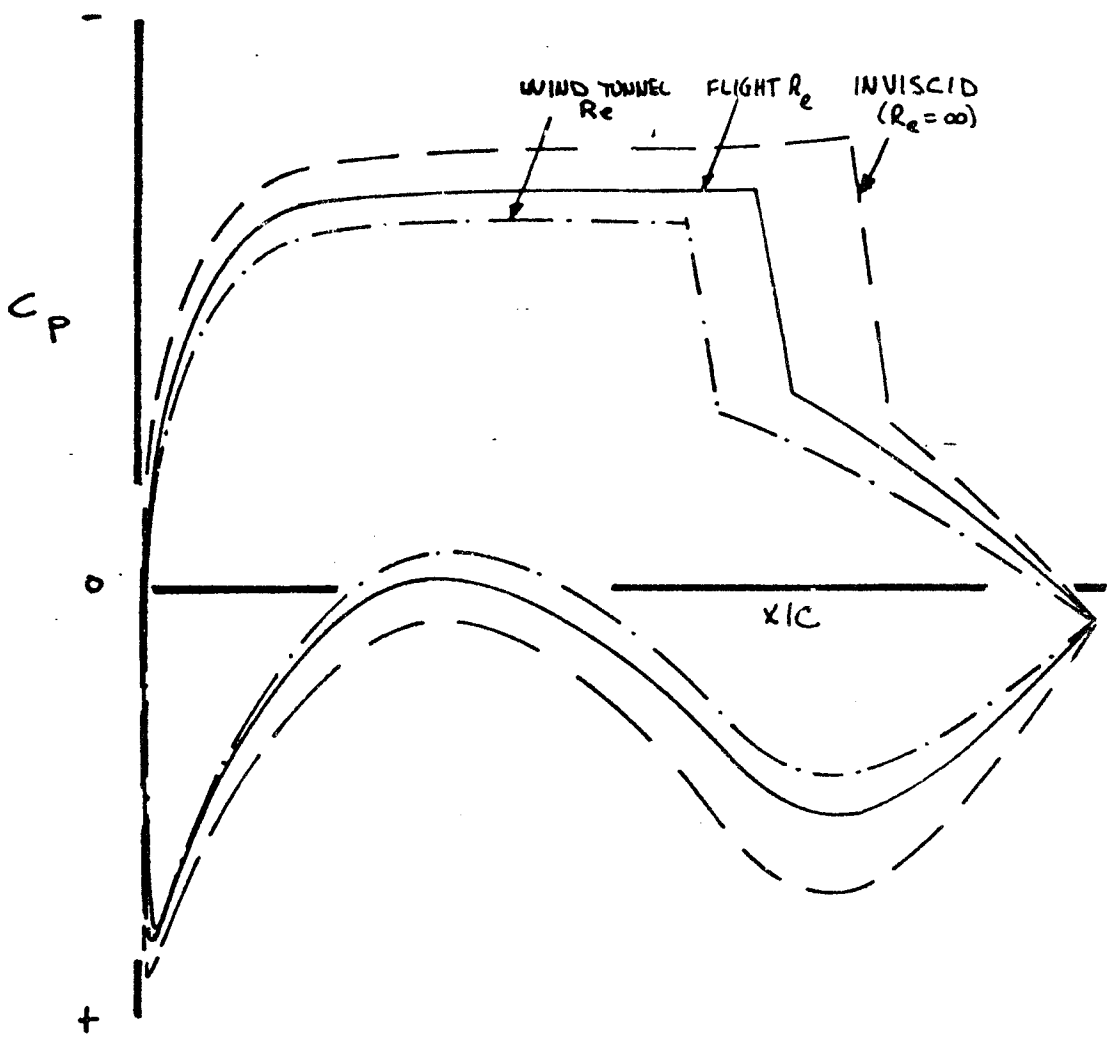

FIGURE 5.22 RELATION BETWEEN REYNOLDS NO. & C_p

1.28.78
GILLETTE

9.5.47

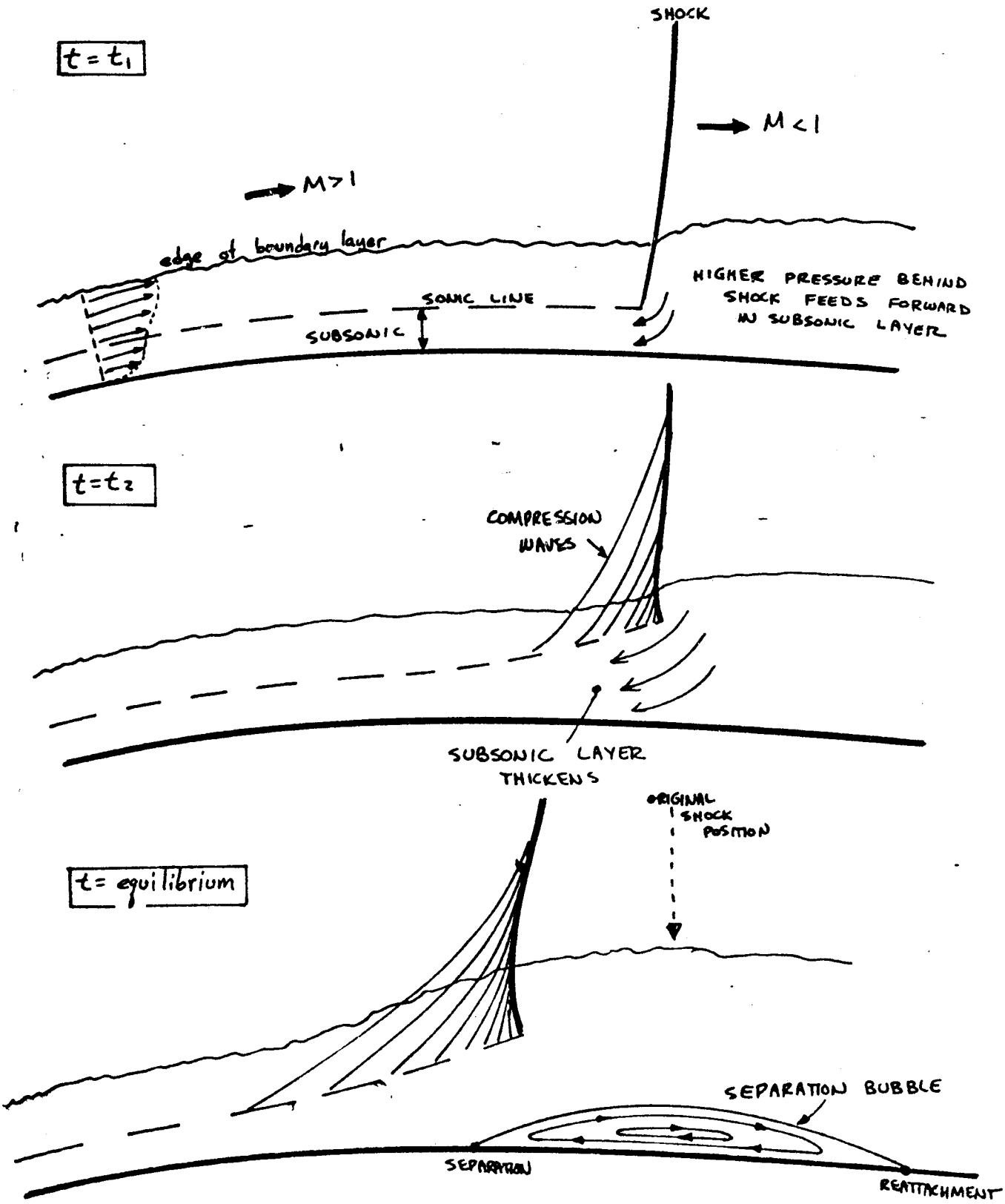

FIGURE 5.23 NORMAL SHOCK ~ BOUNDARY LAYER INTERACTION

1.28.78
GILLETTE

P.5.48

335

(a) IMPORTANCE OF BOUNDARY LAYER THICKNESS

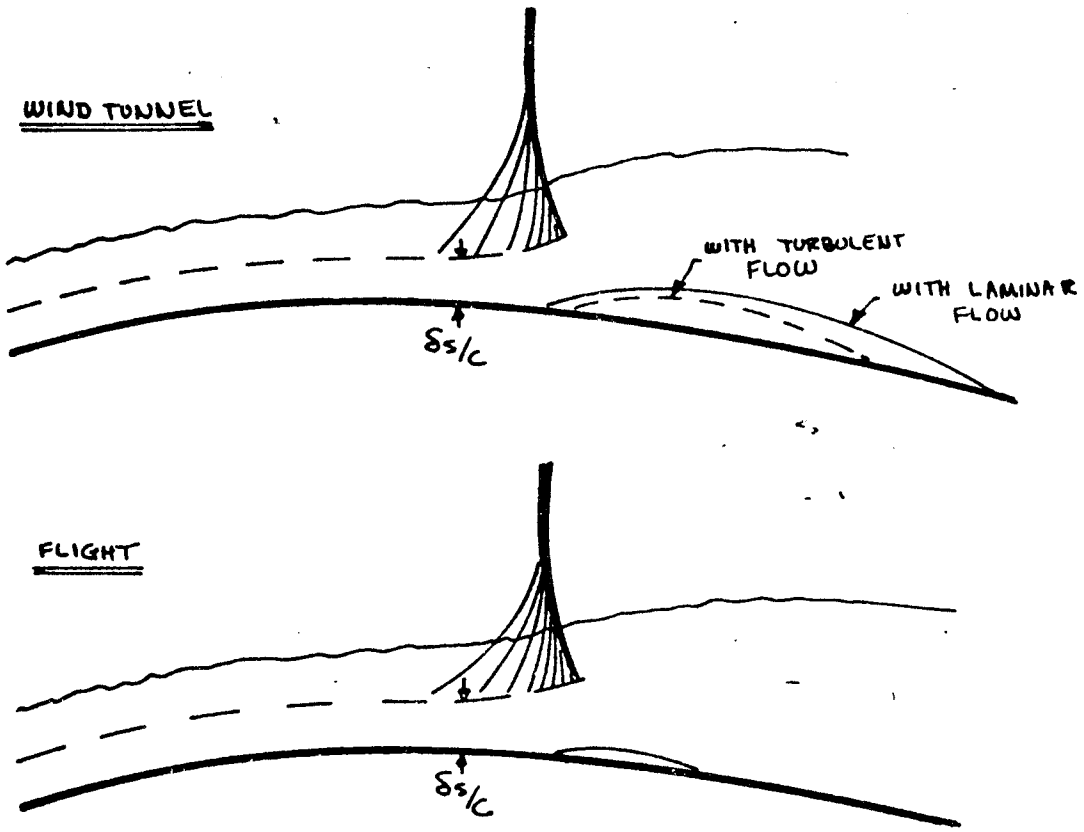

INTERACTION IS SIMULATED WHEN δ_s/c IS IDENTICAL TO FLIGHT & BOUNDARY LAYER IS TURBULENT

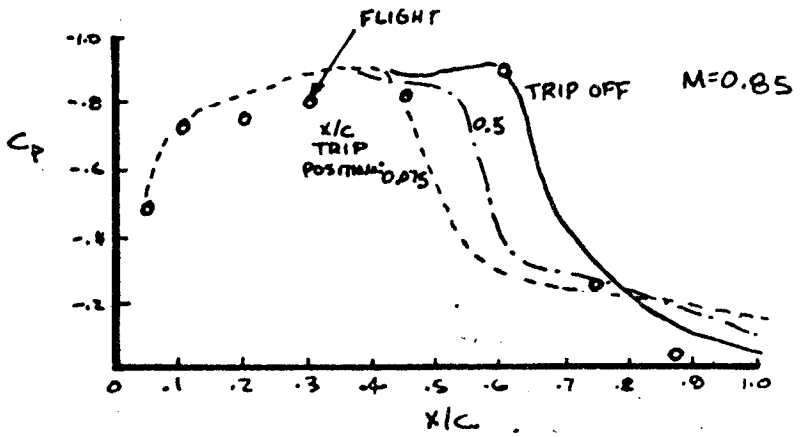

(b) THE C-141 EXAMPLE

FIGURE 5.24 SIMULATION OF SHOCK-BOUNDARY LAYER INTERACTION

1.28.78
GILLETTE

(a) PROPER SHOCK-BOUNDARY LAYER INTERACTION IS ACHIEVED WHEN
(1) δ_s/c IS SAME FROM W.T. AND FLIGHT
(2) W.T. BOUNDARY LAYER TURBULENT AT THE SHOCK WAVE

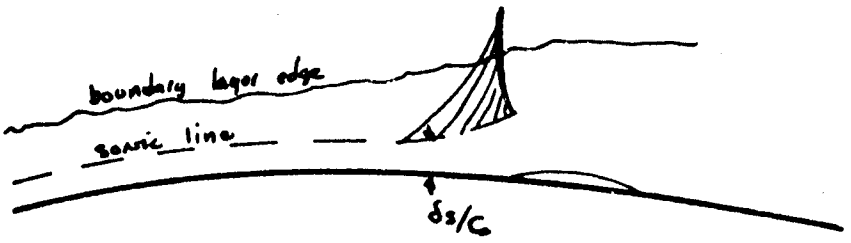

(b) THE BOUNDARY LAYER GROWTH RATE DEPENDS ON REYNOLDS NUMBER

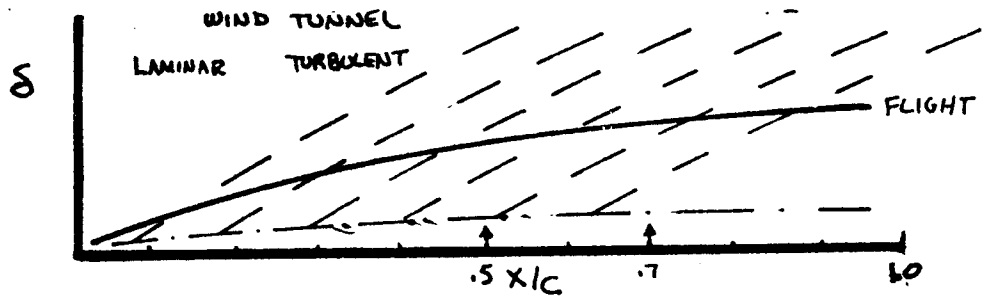

(c) THE TRIP STRIP POSITION IS CHOSEN BASED ON EXPECTED SHOCK POSITION:
(1) IF THE FULL-SCALE SHOCK WAVE IS EXPECTED TO BE AT 0.7 X/C, THEN
(2) THE WIND TUNNEL MODEL TRIP WOULD BE AT 0.5 X/C FOR THE CASE SHOWN IN (b)

BUT
THE δ^*/c AT THE TRAILING EDGE CONTROLS TOTAL CIRCULATION (AND THEREBY THE SHOCK POSITION) AND MAY NOT BE PROPERLY SIMULATED.

FIGURE 5.25 SELECTION OF HIGH SPEED TRIP POSITION

1.28.78
GILLETTE

(a) AT BTWT CONDITIONS ($R_e \approx 3 \times 10^6$)

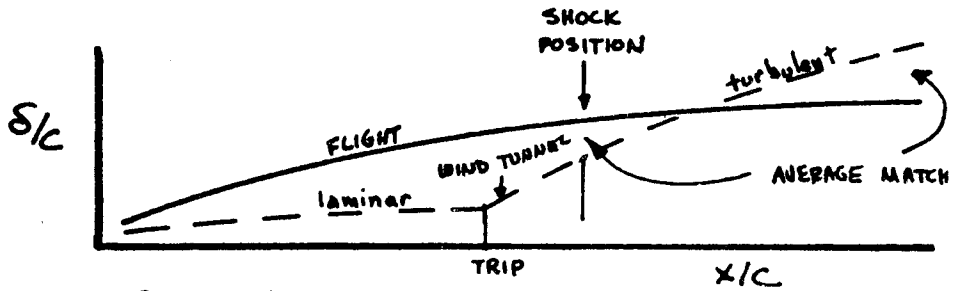

• PROPER SIMULATION MAY BE ACHIEVED WITH TRIP STRIP

(b) AT INTERMEDIATE CONDITIONS ($R_e \approx 10 \times 10^6$); USUALLY DENOTED "HIGH REYNOLDS NUMBER CONDITIONS"

- NATURAL TRANSITION HAS MOVED TO LEADING EDGE, PREVENTING SELECTION OF HIGH SPEED TRIP LOCATION
- GROWTH RATE IS STILL LARGER THAN FLIGHT
- BOUNDARY LAYER δ^*/c AT SHOCK & TRAILING EDGE IS TOO THICK

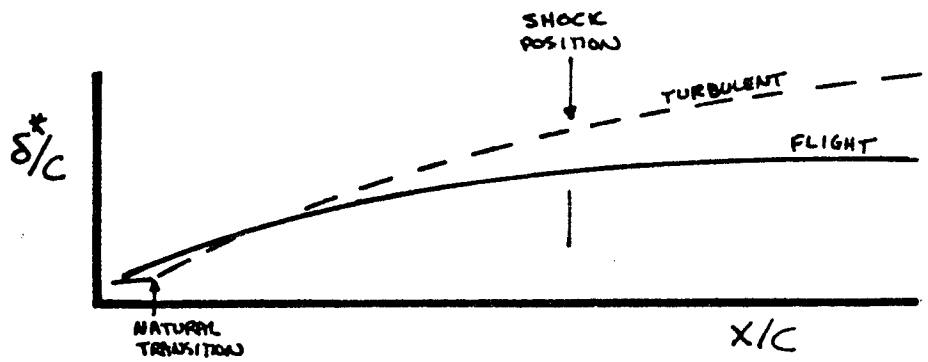

FIGURE 5.2C HIGH REYNOLDS NUMBER TESTING CONSIDERATIONS

1.28.78
Gillette

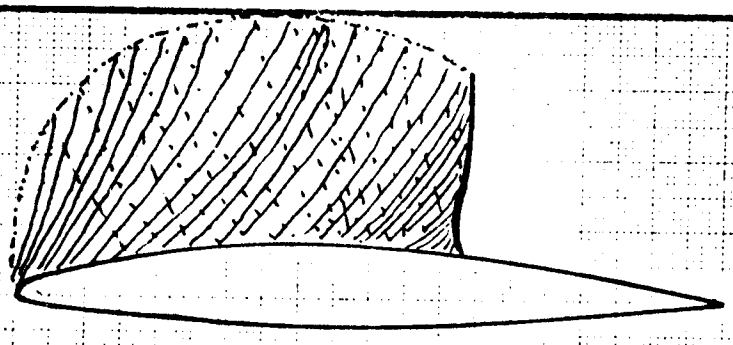

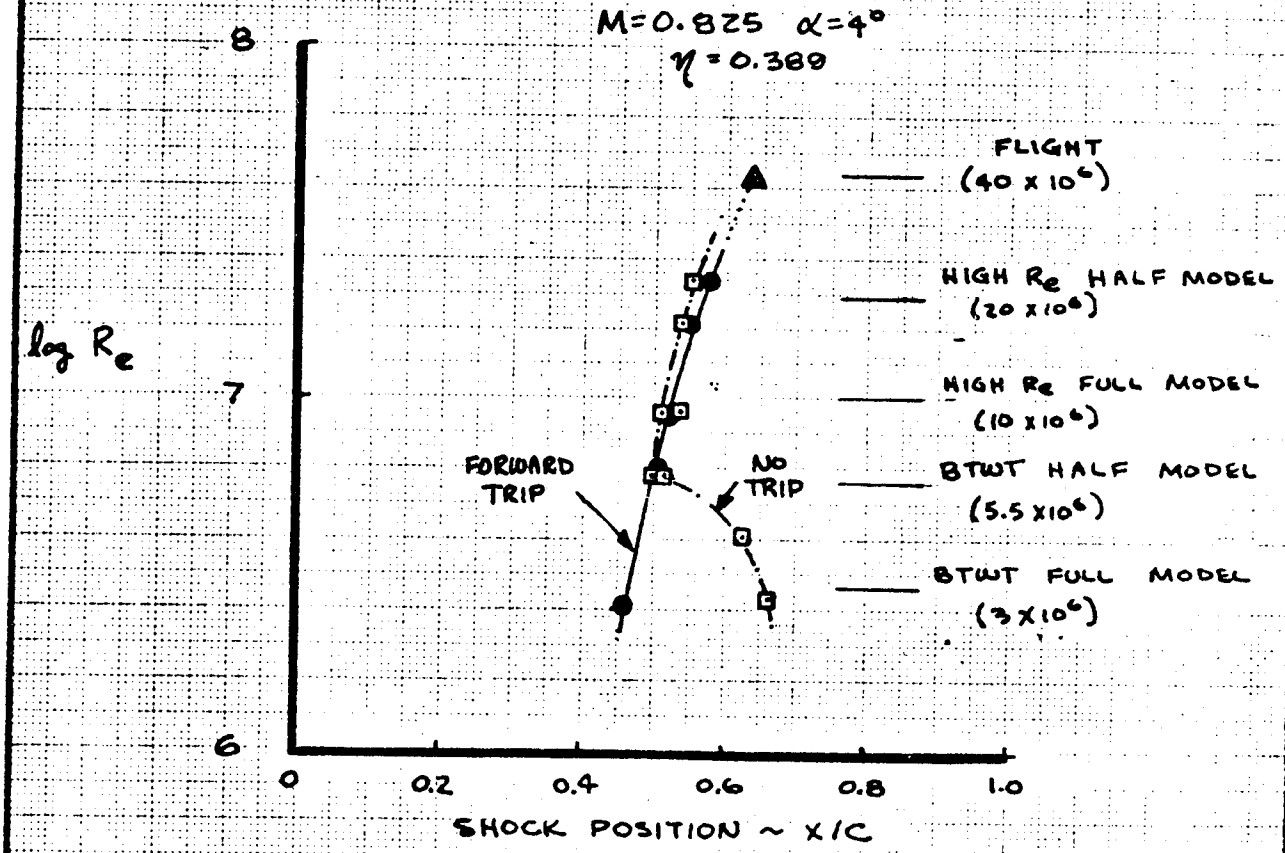

REF: NASA CR-2604
FEB. 1975

CALC	GILLETTE 1-28-78	REVISED	DATE	C-141A EXPERIENCE OF SHOCK POSITION VS. REYNOLDS NUMBER
CHECK				
APR				
APR				
				BOEING

FIG 5.27
PAGE 5.5-2

D1 4100 J260 ORIG 3/71

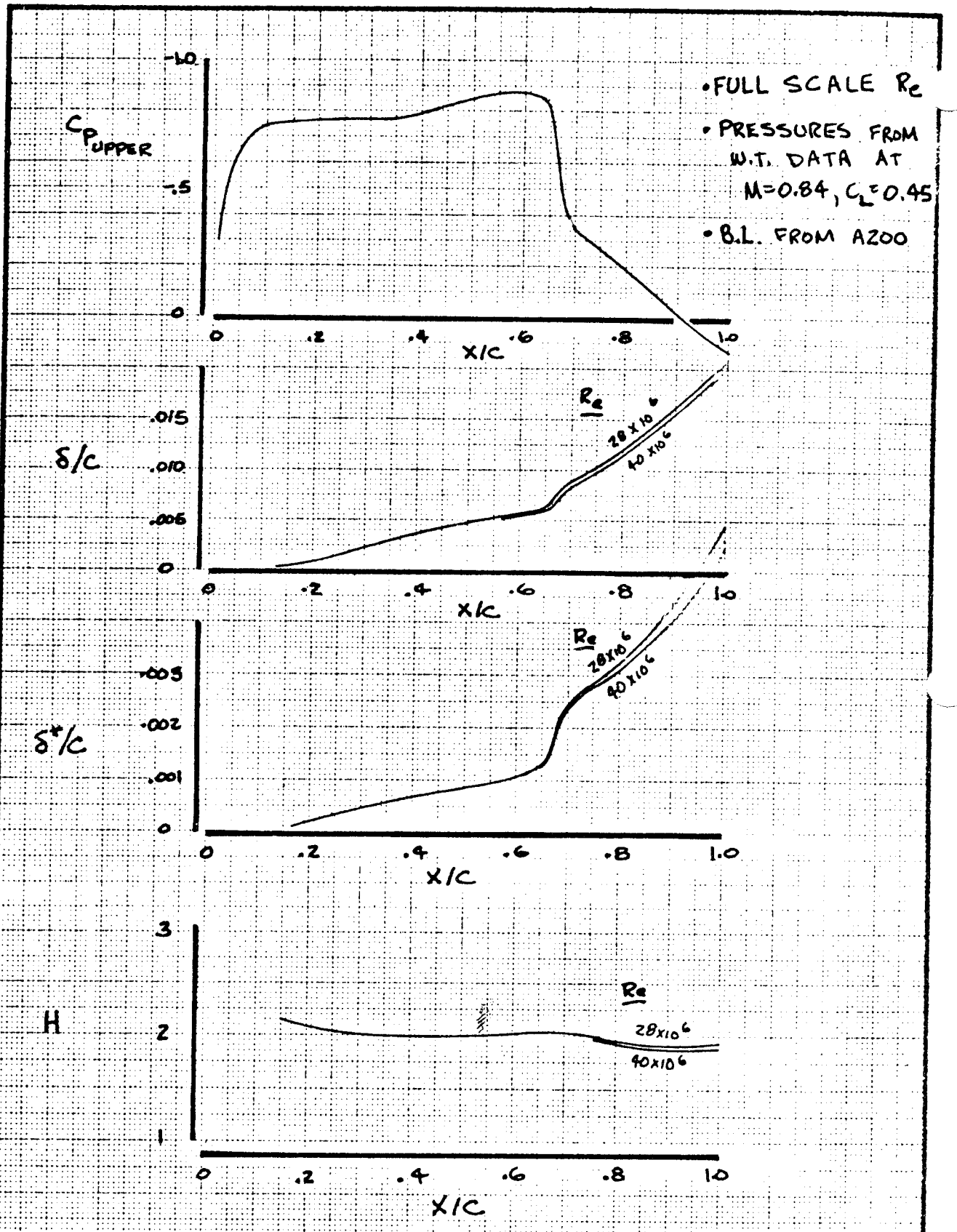

CALC	GILLETTE 8-29-77	REVISED	DATE	UPPER WING SECTION BOUNDARY LAYER CHARACTERISTICS ~ FULL SCALE
CHECK				
APR				FIG 5.28
APR				DATE 5.53

BOEING

D1 4100 3260 ORIG. 3/71

340

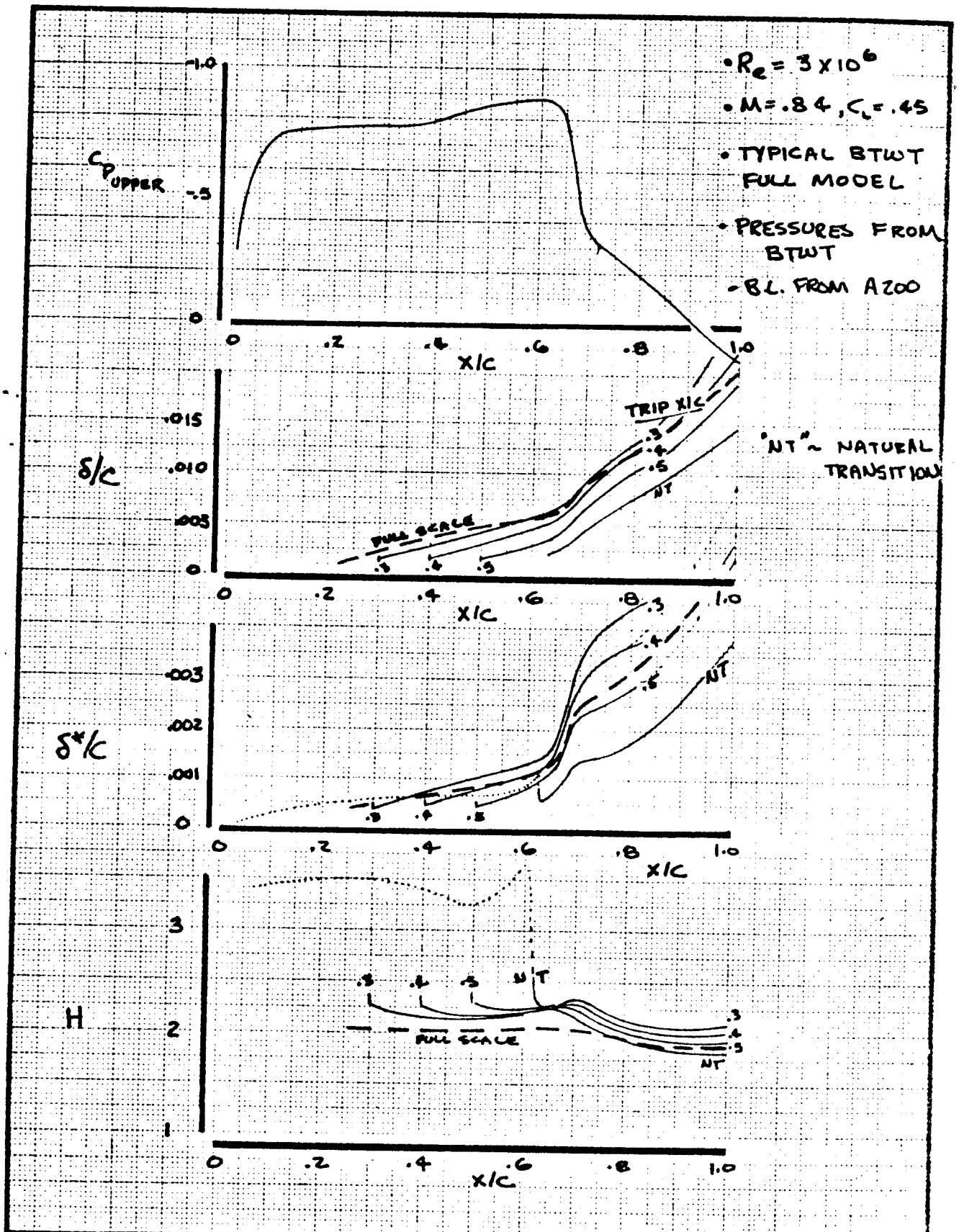

CALC	GILLETTE 12-29-77	REVISED	DATE	UPPER WING SECTION BOUNDARY LAYER CHARACTERISTICS — FULL MODEL	FIG 5.29
CHECK					
APR					
APR				BOEING	PAGE 5.54

D1 4100 3260 ORIG 3/71

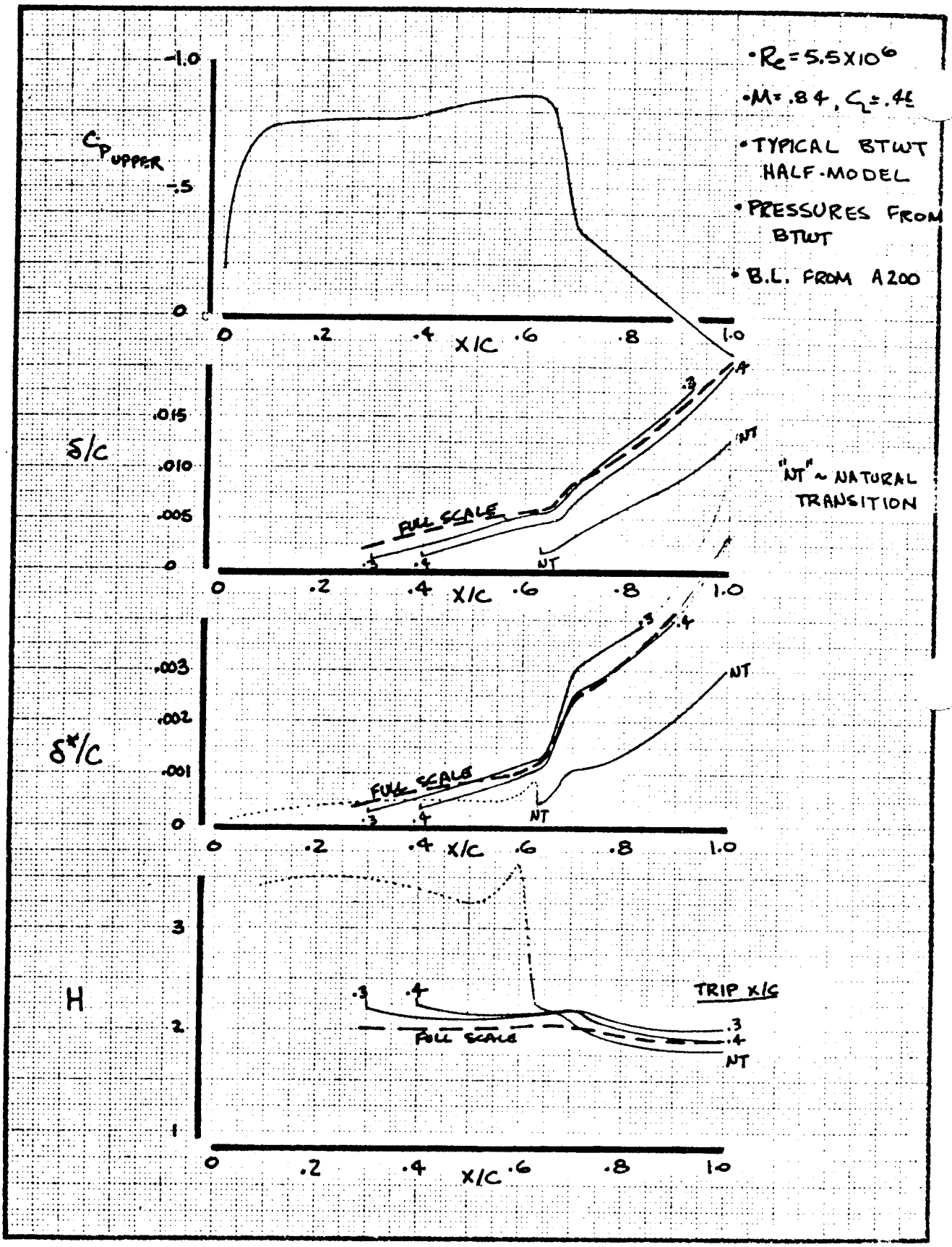

CALC	GILLETTE	2-29-72	REVISED	DATE	UPPER WING SECTION BOUNDARY LAYER CHARACTERISTICS — HALF-MODEL
CHECK					
APR					
APR					

BOEING

FIG 5.30

5.55

D1 4100 3260 ORIG 3/71

342

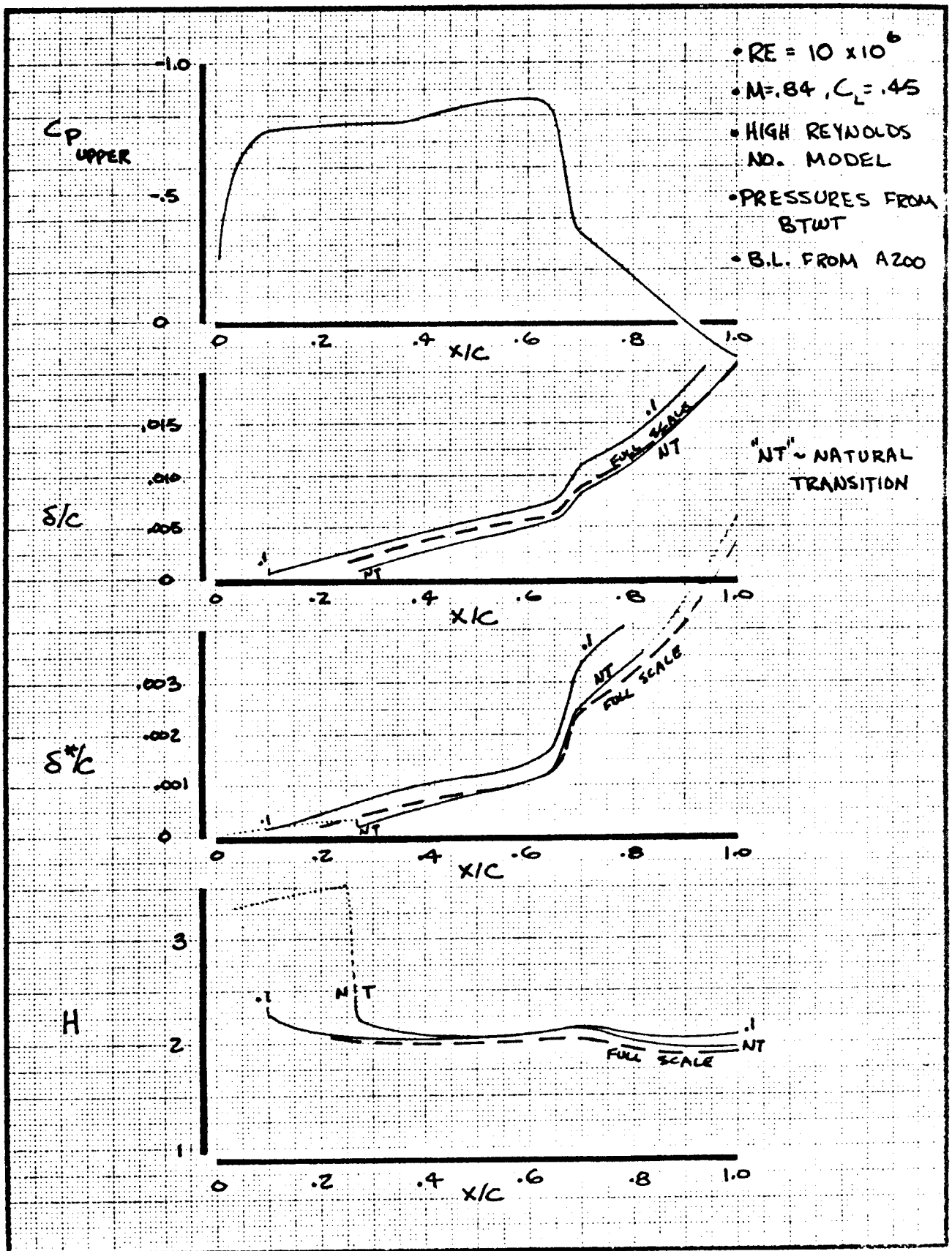

CALC	GILLETTE	12-29-77	REVISED	DATE
CHECK				
APP				
APP				

UPPER WING SECTION BOUNDARY LAYER CHARACTERISTICS ~ HIGH-RE MODEL FIG 5.31

BOEING

PAGE 5.56

D1-4100-3240 ORIG 3/71

343

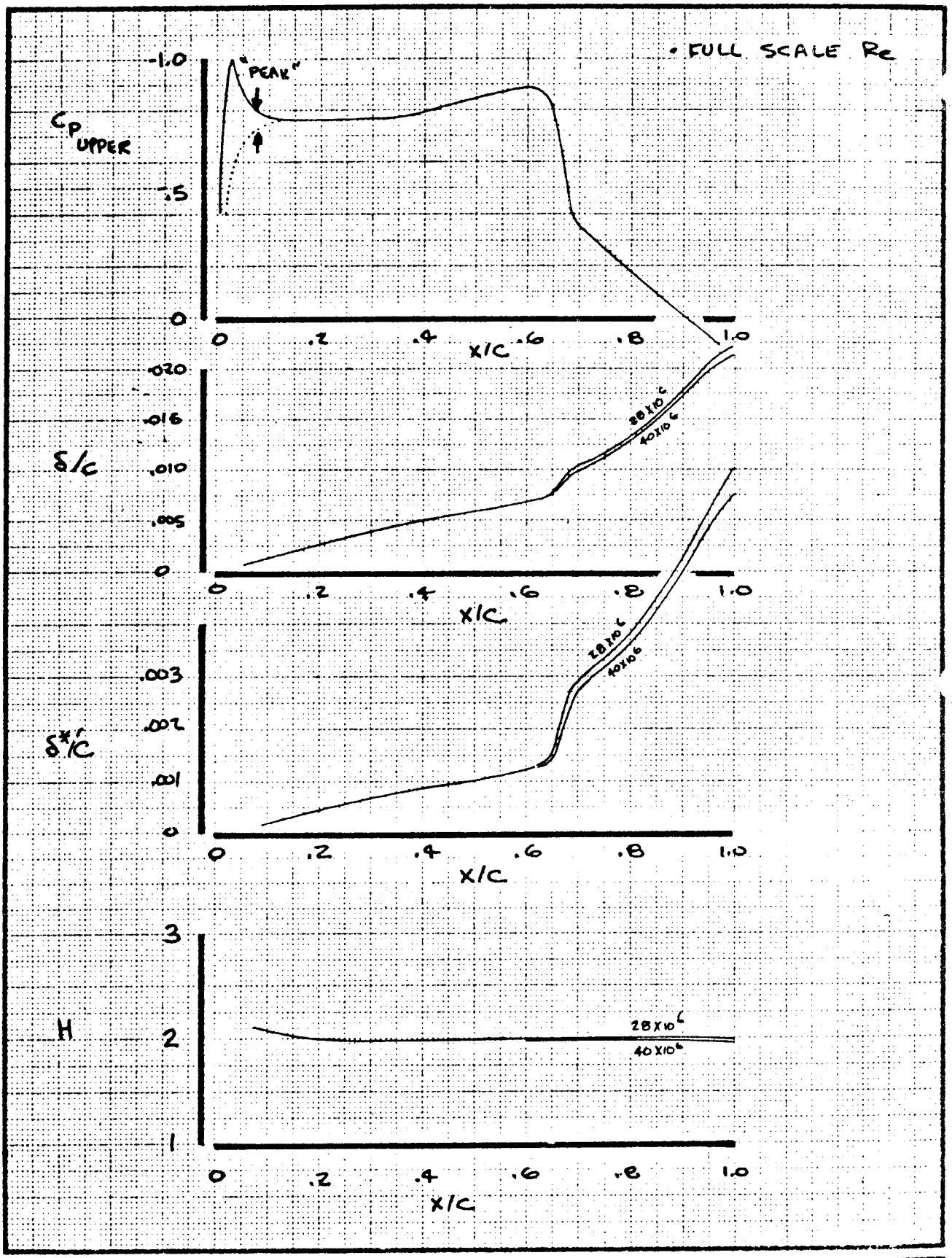

CALC	GILLETTE	1-28-78	REVISED	DATE	UPPER WING SECTION BOUNDARY LAYER CHARACTERISTICS ~ FULL SCALE FIG 5.32
CHECK					
APR					
APR					BOEING 5.57

D1 4100 3260 ORIG. 3/71

3444

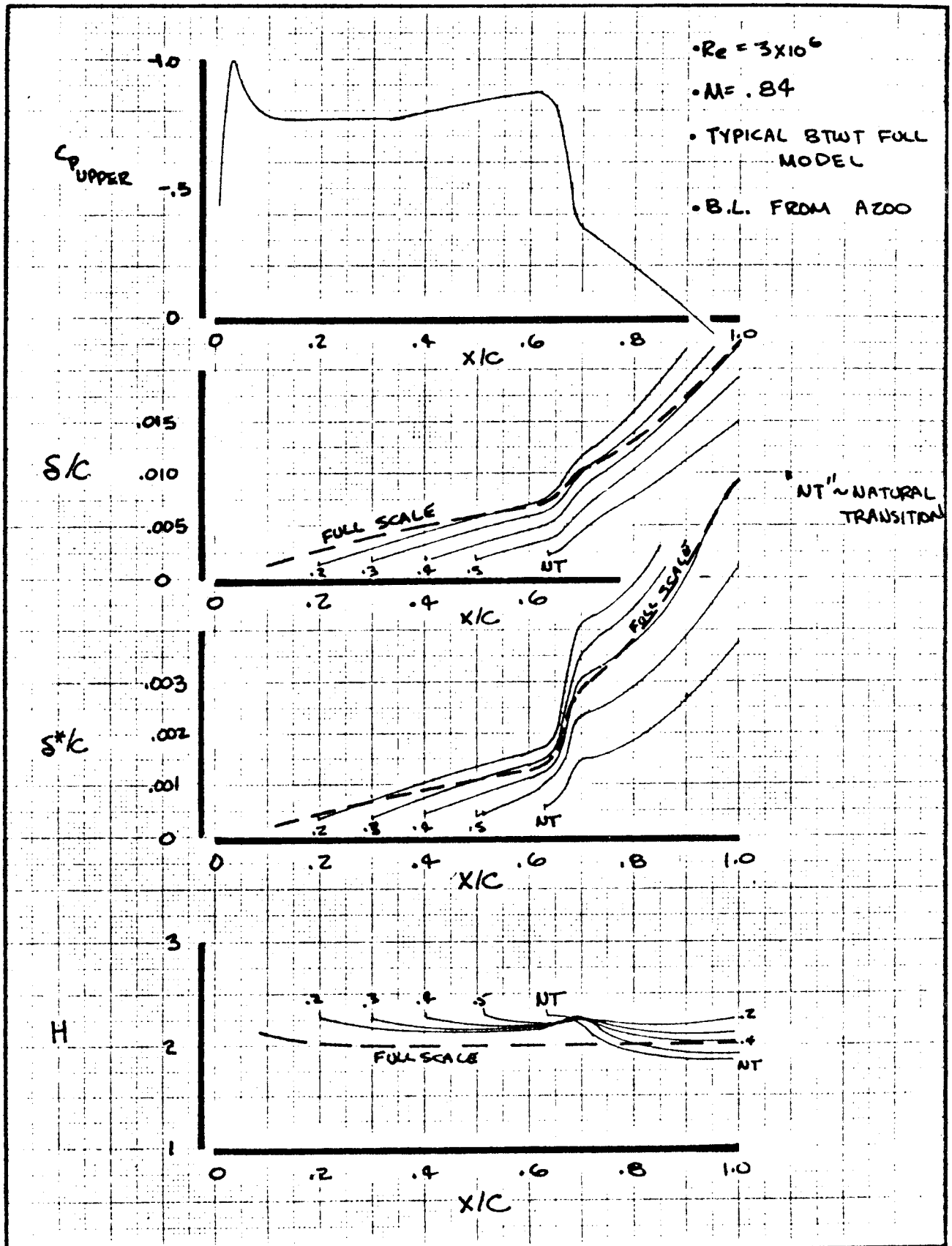

CALC	GILLETTE	1.28.78	REVISED	DATE	UPPER WING SECTION BOUNDARY LAYER CHARACTERISTICS ~ FULL MODEL	
CHECK						FIG 5.33
APR						
APR					THE BOEING COMPANY	PAGE 5.58

W.E ALBANESE 1981

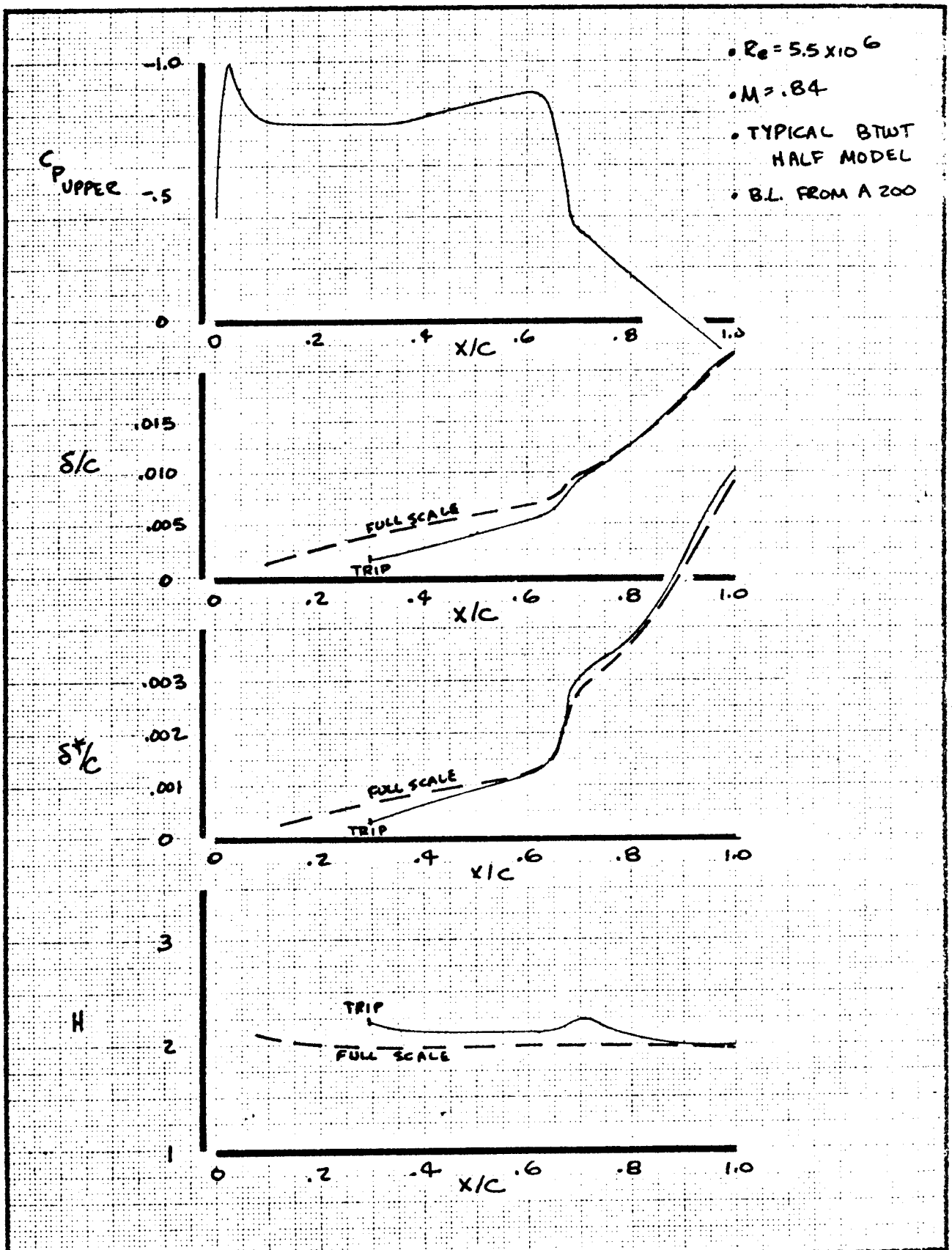

CALC	GILLETTE 1-28-72	REVISED	DATE	UPPER WING SECTION BOUNDARY LAYER CHARACTERISTICS ~ BTWT HALF MODEL
CHECK				
APR				
APR				

FIG. 5.34

BOEING

5.59

D1 4100 3200 ORIG. 3/71

346

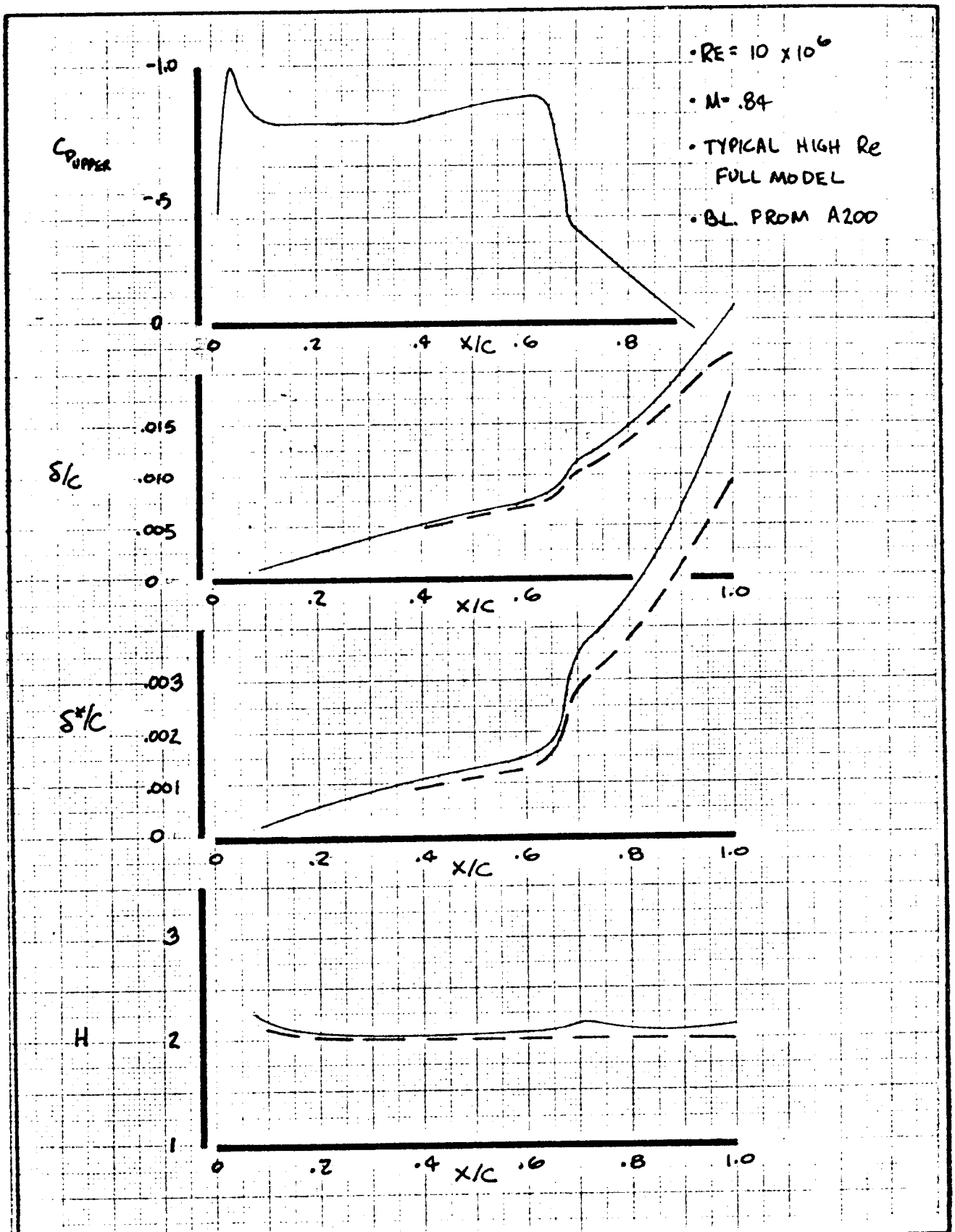

CALC	GILLETTE	1-28-78	REVISED	DATE	UPPER WING SECTION BOUNDARY LAYER CHARACTERISTICS ~ HIGH RE. TEST
CHECK					FIG 5.35
APR					
APR					THE BOEING COMPANY
					PAGE 5.60

DI 4100 3240

K-E ALBANENE 1661 TRACING PAPER

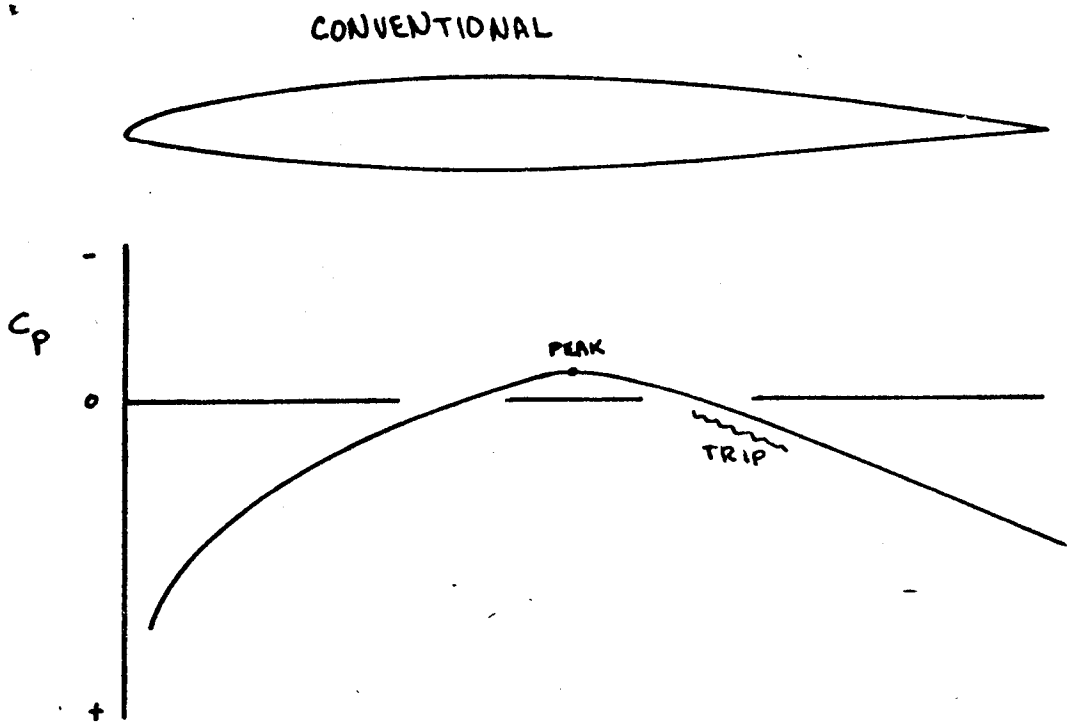

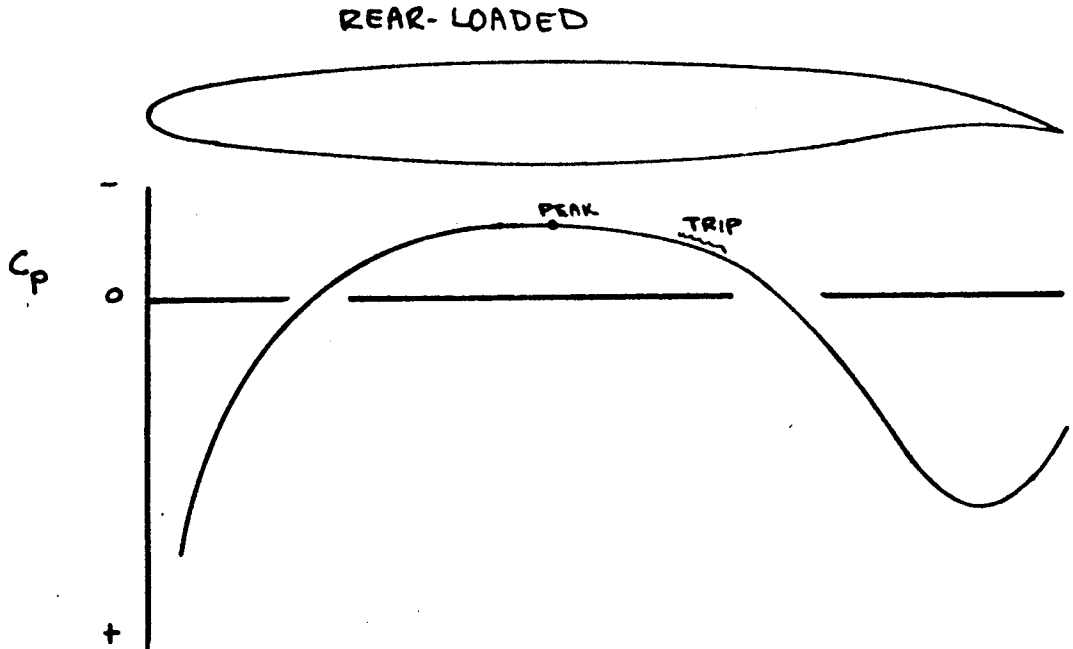

FIGURE 5.36 LOWER SURFACE AFT TRIP STRIP

348 1.28.78 GRLETTE

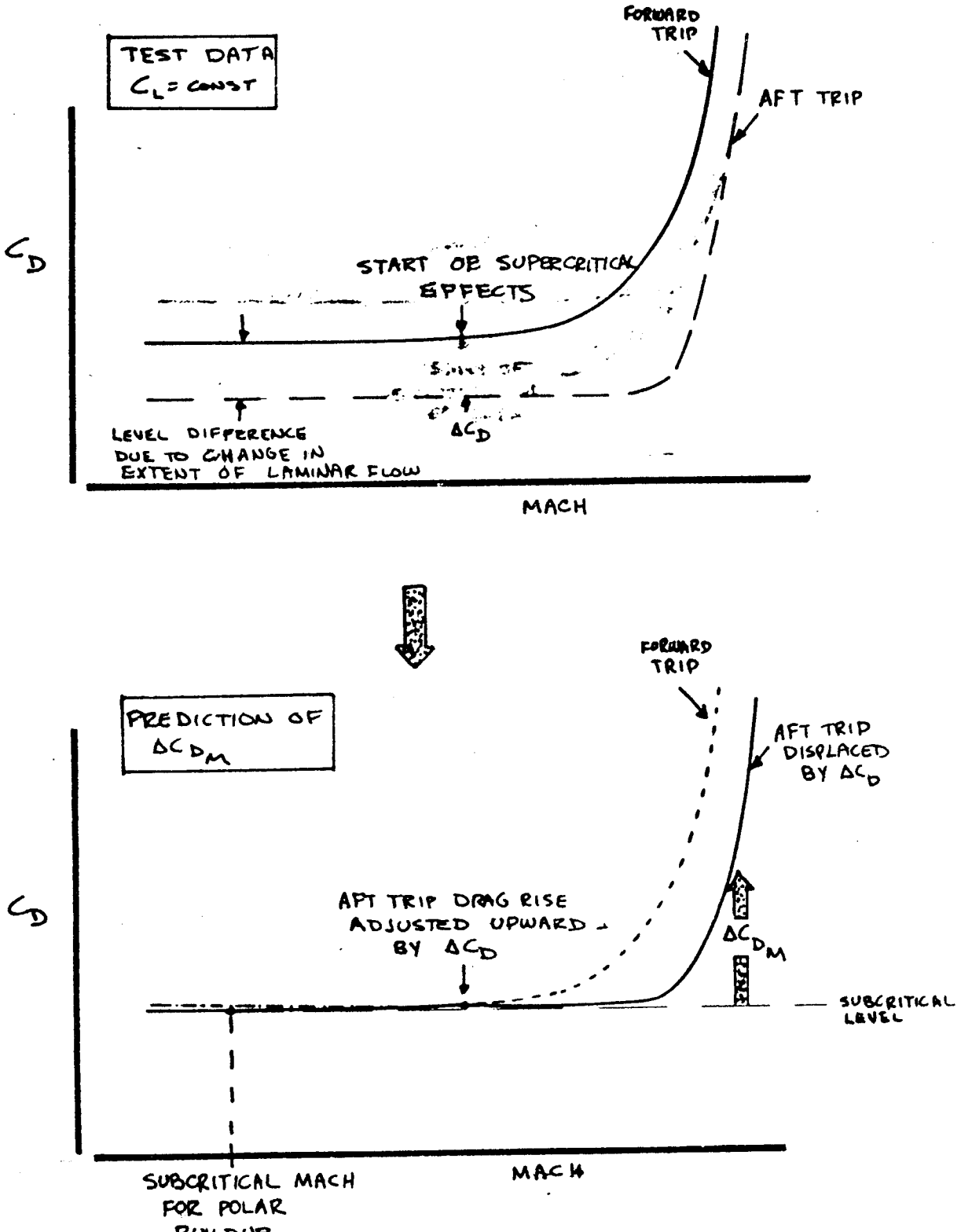

FIGURE 5.37 DETERMINATION OF FULL SCALE ΔC_{D_M}

1-28-78 LETTE

D.5.62

(a) 707-TYPE WING SECTIONS AT CRUISE MACH

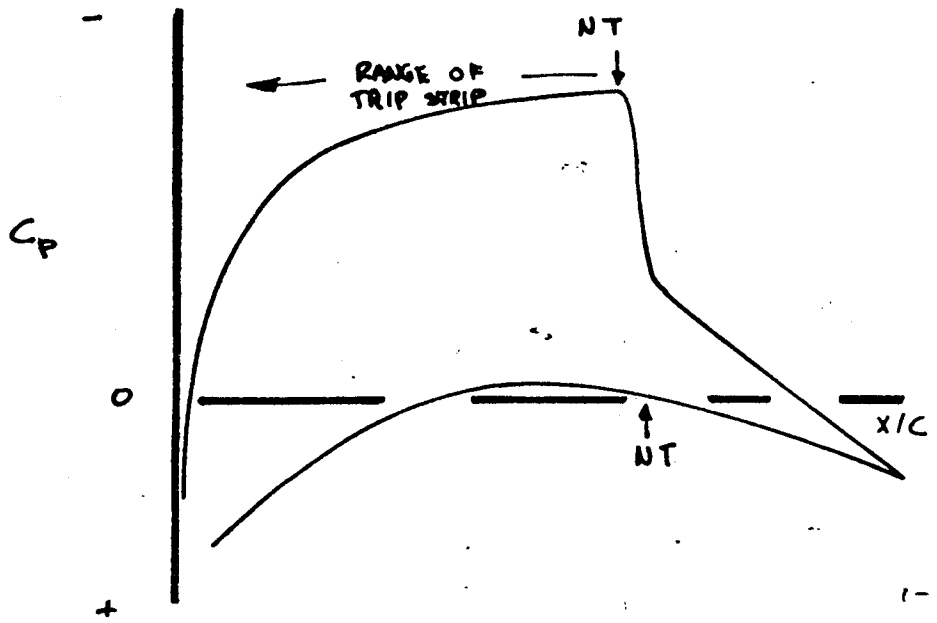

NT ~ NATURAL TRANSITION POINT IN TRANSONIC TUNNEL

(b) ALTERNATE WING SECTION

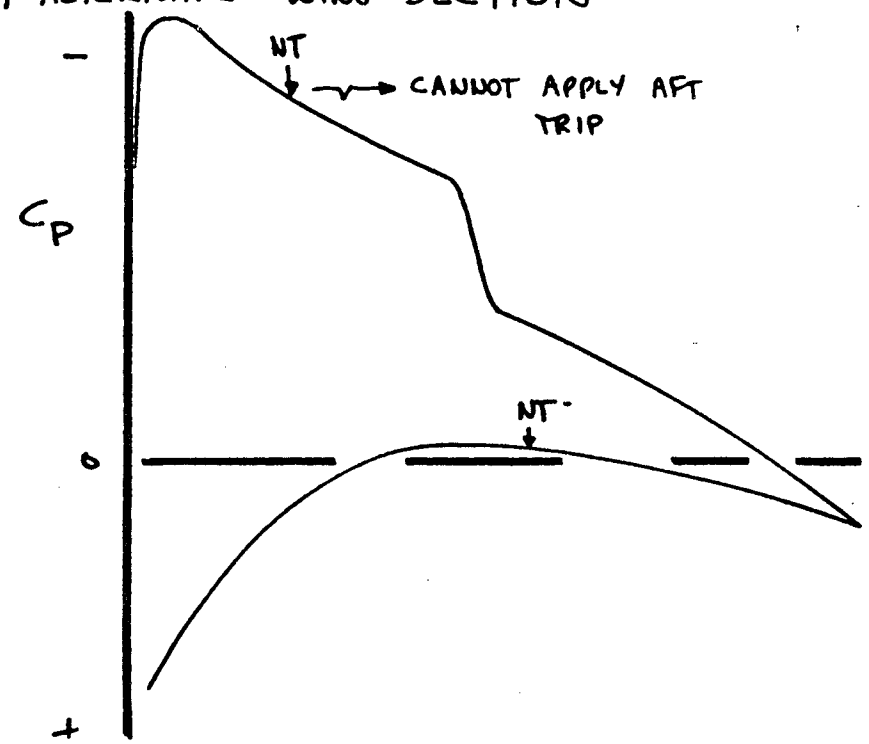

FIGURE 5.38 LIMITATION TO AFT TRIP STRIP APPLICATION

1.28.78
GILLETTE

350

(a) FLOW OVER A FLAT PLATE

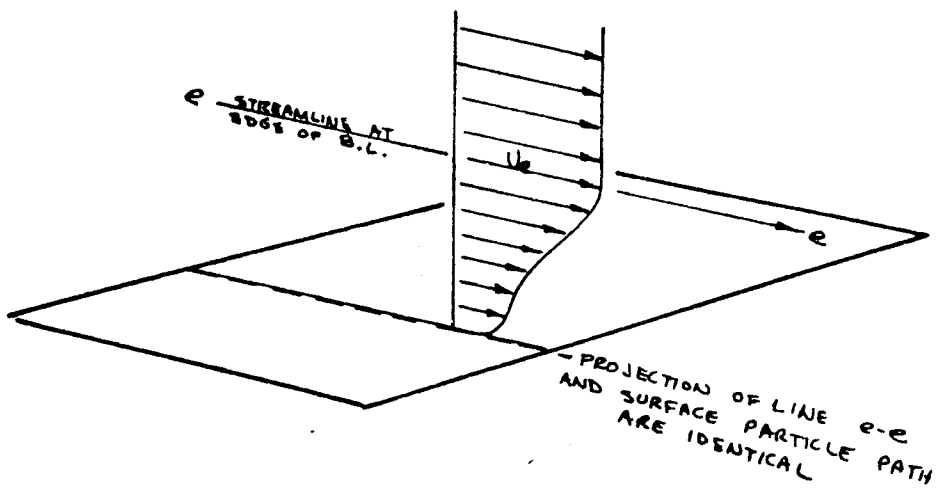

(b) FLOW OVER A SWEPT WING

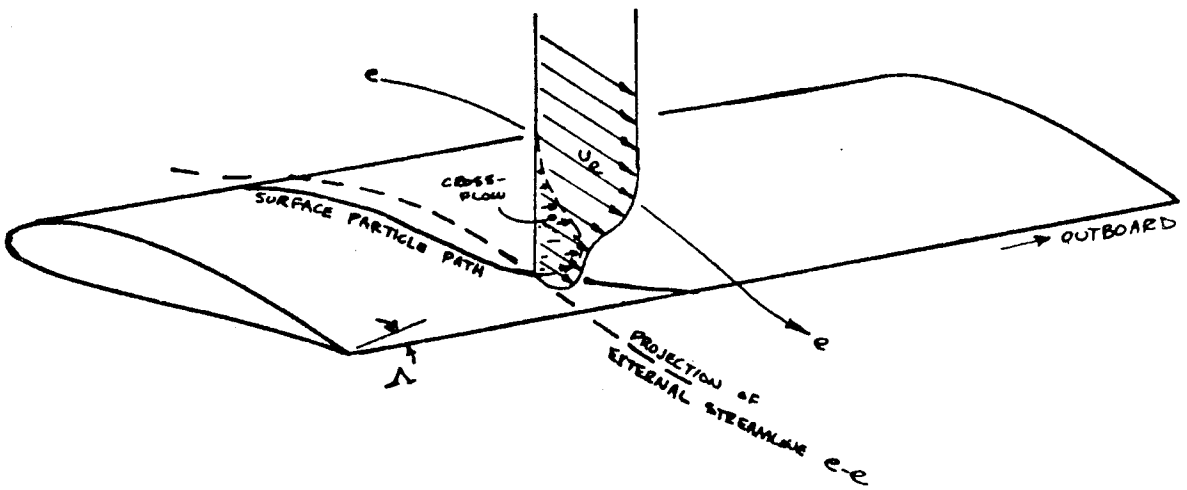

FIGURE 5.39 EFFECT OF BOUNDARY LAYER CROSSFLOW

1.28.78
GILLETTE

351

(a) BOUNDARY LAYER SURFACE FLOW IS INFLUENCED BY DIRECTION OF PRESSURE GRADIENT

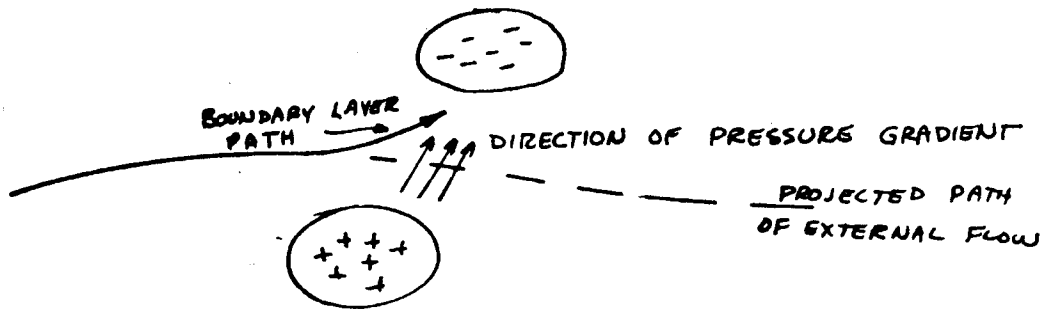

(b) CONDITIONS ON SWEPT WING UPPER SURFACE

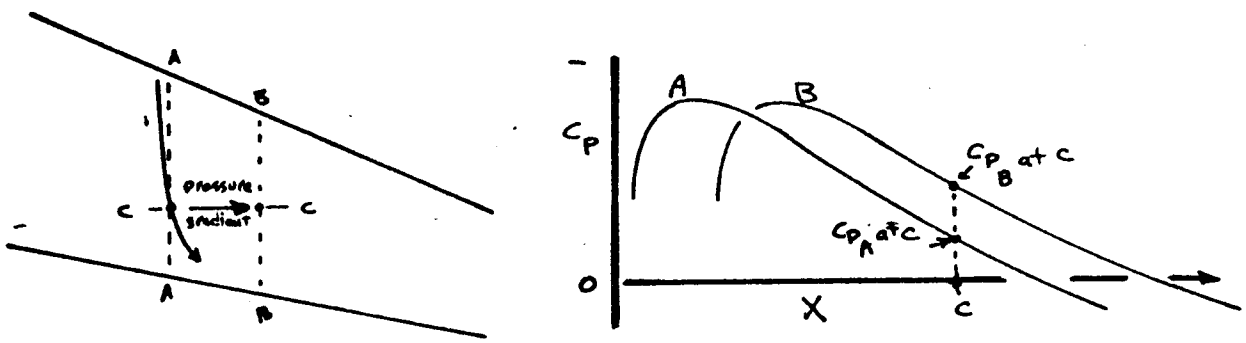

(c) DIRECTION AT SURFACE EXISTS ONLY AT SURFACE

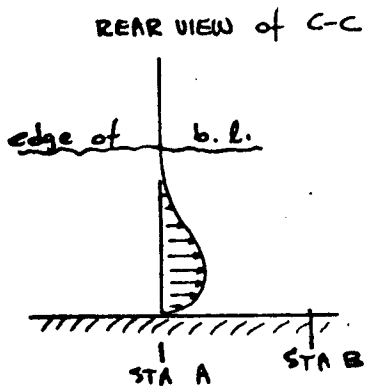

FIGURE 5.40 CAUSE OF BOUNDARY LAYER CROSSFLOW

(a) SURFACE PATTERN ON A SEPARATED WING

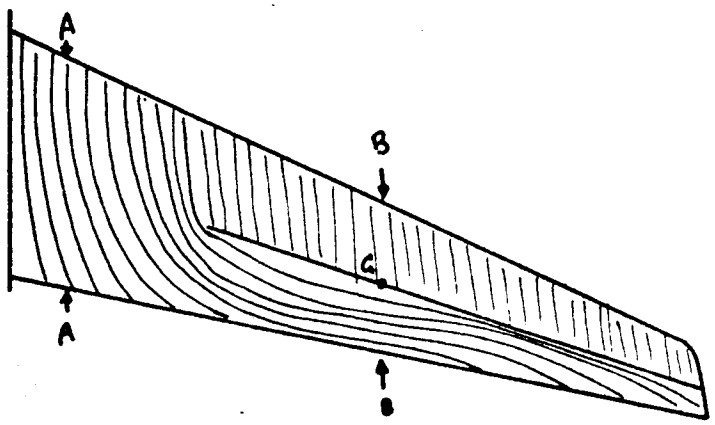

(b) AT SECTION A-A

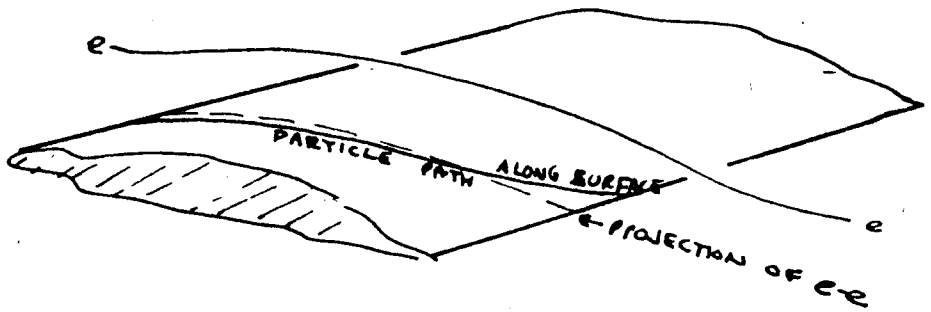

(c) AT SECTION B-B

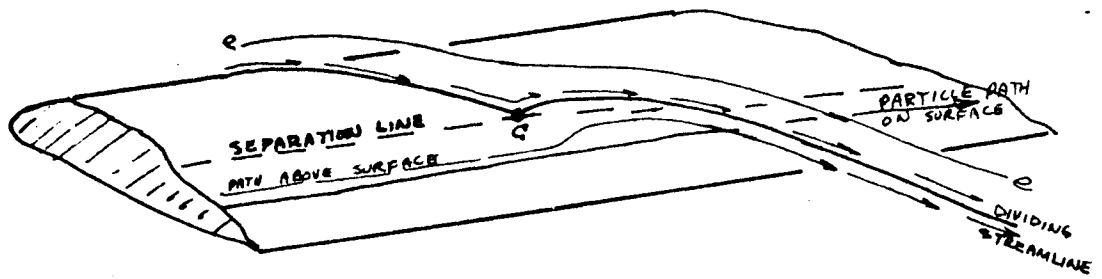

FIGURE 5.41 THREE-DIMENSIONAL SEPARATION

1.28.78
LAVELETTE

(a) Nor Vortex Flow

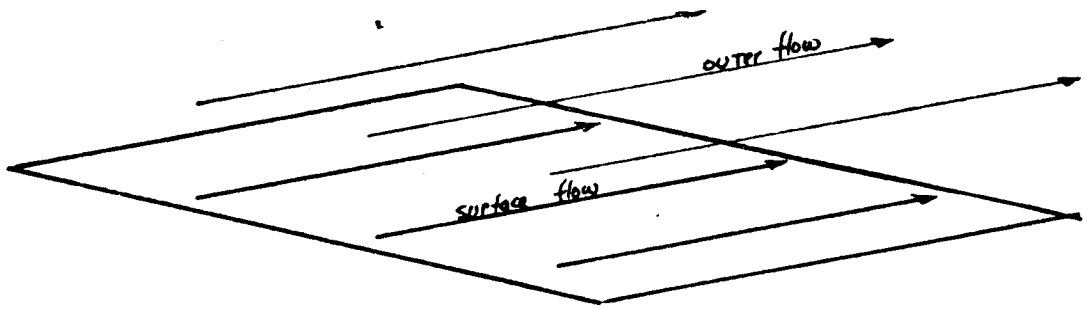

(b) Vortex above the surface

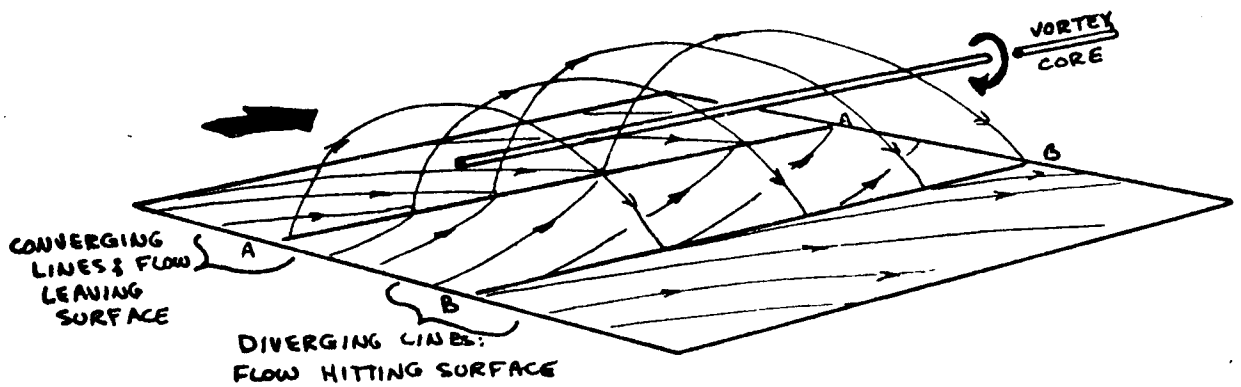

FRONT VIEW
(LOOKING DOWNSTREAM)

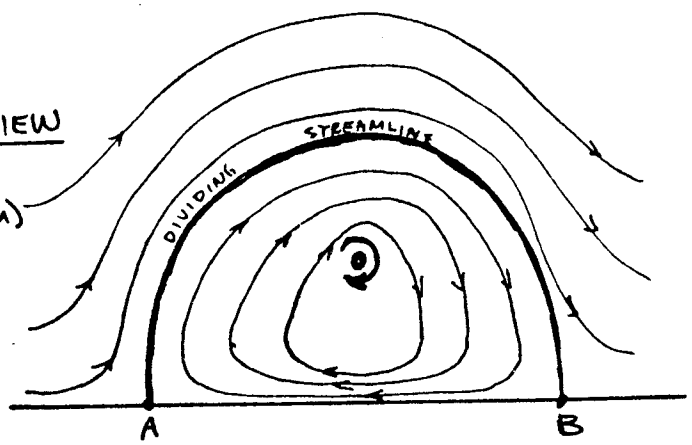

LINES AA AND BB ARE CALLED LIMITING STREAMLINES

FIGURE 5.42 EFFECT OF VORTEX ON SURFACE FLOW

(a) OBLIQUE SHOCK

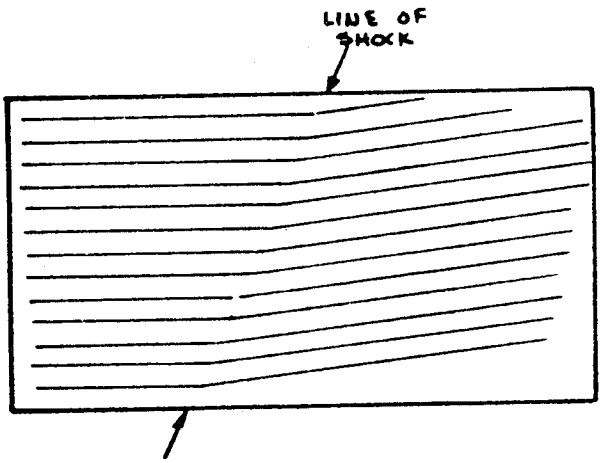

(b) NORMAL SHOCK WAVE LEAVES NO SIGN UNLESS:

① CAUSES CHANGE IN BOUNDARY LAYER CONDITION

② IS FINITE IN LENGTH

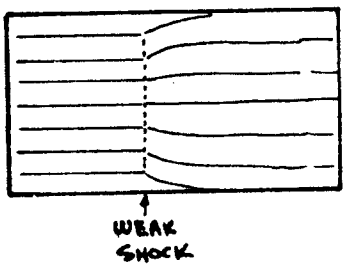

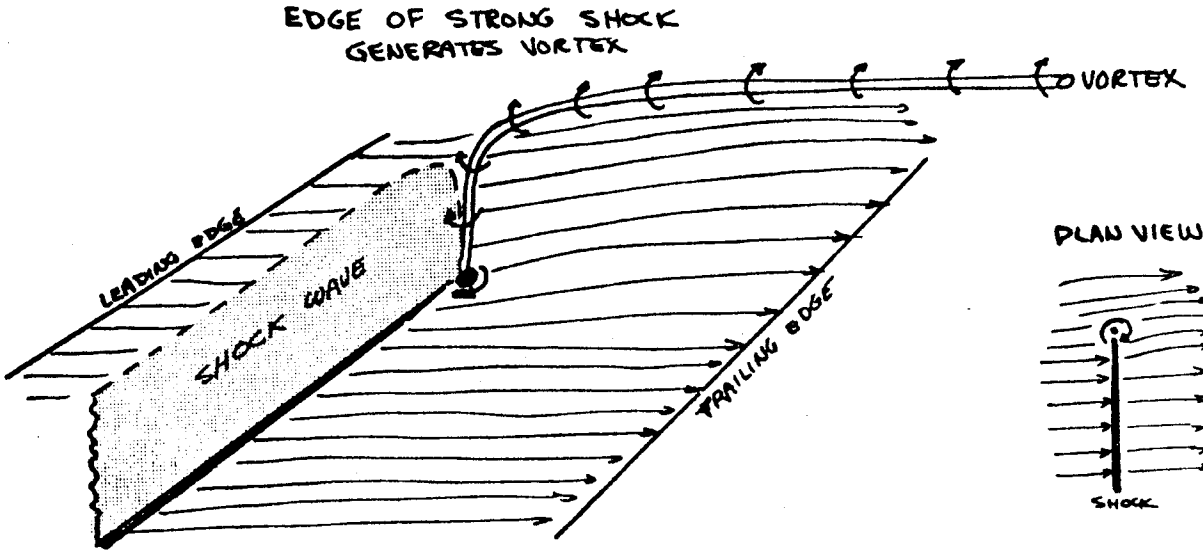

FIGURE 5.43 SURFACE STREAMLINES BENEATH SHOCK WAVES

1.28.78
KLETTE

P.5.68

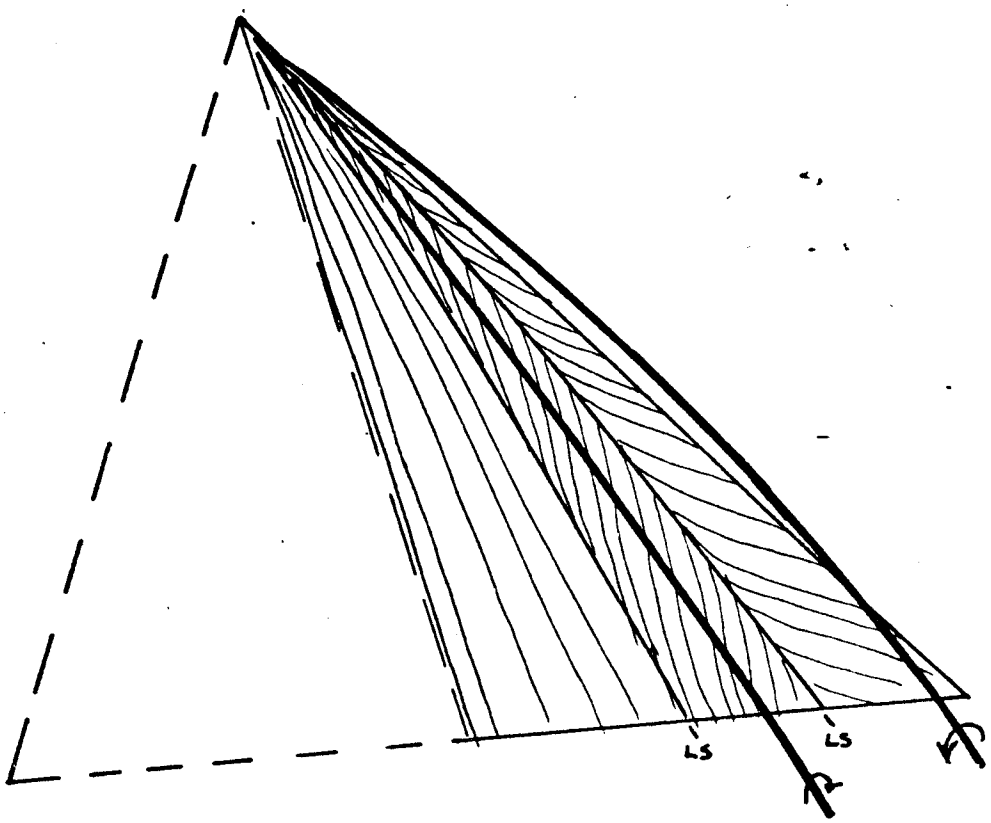

LS - LIMITING STREAMLINE

DS - DIVIDING STREAMLINE

REAR VIEW

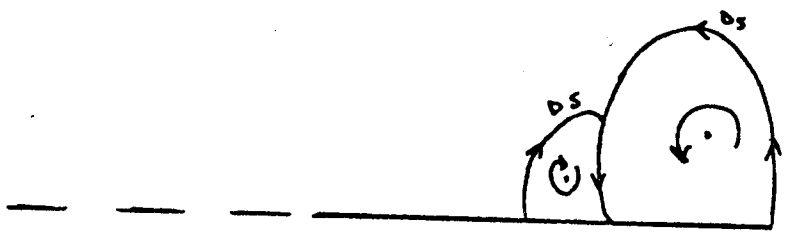

FIGURE 5.46 DELTA-WING SURFACE FLOW AT HIGH ANGLE OF ATTACK

1.28.78
Gilotte

P.S.71

CHAPTER 7. TRANSONIC AND SUPERSONIC DESIGN

CHAPTER 6 LOW SPEED WING DESIGN AND TESTING

CHAPTER 6 LOW SPEED WING DESIGN AND TESTING

6.1 INTRODUCTION

To attempt to cover the entire world of low speed wing design and testing in one three hour lecture is a tall order. We can in this time only scratch the surface and explore some of the processes that are involved.

6.1.1 High Lift Design and Testing Process

As an illustration of the effort involved in low speed design and testing, Figure 1 shows the wind tunnel hours and manpower expended in the 727, 737 and 747 programs up to first flight. This Figure does not include the Aerodynamics manpower involved in the design and testing. The effort is large and growing, and Figure 2 illustrates that it is not a unique problem to Boeing. Indeed, if the present trends continue, it could pace the development program for the airplane. The hope for the future is to put more reliance on the analytical tools and eliminate part of the iterative trial and error wind tunnel testing. Figure 3 attempts to illustrate this process wherein the use of the analytical tools can reduce the testing load to only that required for verification. This is of course an idealized presentation, but the approach should reduce the rapid acceleration in testing.

6.1.2 Definitions of Major Parameters

The parameters involved in high lift design and their influence on the airplane sizing is a critical issue we should address early. Figure 4 shows a thumbprint plot of wing loading and

6.1.2 Continued

thrust loading for a parametric family of airplanes designed to a fixed payload and range without considering low speed performance. There appears to be an optimum airplane at 401,000 lb. Now if we look at the takeoff profile shown on Figure 5, we see that the low speed takeoff performance contains the same parameters (W/S and T/W) plus $C_{L_{max}}$, L/D in climbout and ground roll drag. The landing profile shown on Figure 6 basically contains similar parameters. It is possible then to superimpose the low speed performance goals in terms of takeoff and landing field lengths or approach speed on the thumbprint plot. Figure 7 shows the thumbprint with the low speed performance added. Since the configuration was designed for a range of 5700 miles, an 11,000 field typical of the large hub airports was chosen as the maximum. This requirement forced a change in the wing and thrust loading and increased the design take off weight by 13,000 lb. The low speed parameters that affected this change were again $C_{L_{max}}$, L/D and drag level. The standard method for displaying high lift data is shown on Figure 8 and not surprisingly is a plot of CL vs L/D. The envelopes for flaps up, $5^{o}/15^{o}$ and $30^{o}/60^{o}$ are shown with a total envelope line that is tangent to each flap angles. If the configuration drag polars were represented by some minimum flaps up drag level and elliptical induced drag, the heavy black line would be obtained. The various shadings between this line and the flap envelope line are a crude attempt to show why the real airplane cannot achieve the ideal performance levels. The consequences of being able to recover some of the decrement from the ideal polar is shown on Figure 9. If even half of the increment could be recovered, significant benefits in takeoff performance and noise could be achieved. This is one of the basic challenges of the high lift aerodynamicist, to push the L/D, CL curve up and to the right.

6.1.3 Current Airplane Levels and Trends.

The demonstrated $C_{L_{max}}$ levels of previous Boeing designs is shown on Figure 10. The progress from the early designs which had no leading protection to the current product line is quite apparent, however, there is some technology buried in this Figure which will be discussed a little later. The demonstrated L/D, CL performance levels for takeoff and landing are shown on Figure 11 and 12. The data points shown on Figure 11 are the points on the flap polars that correspond to the takeoff lift coefficient C_{LV_2} with each point representing a specific flap angle. Similar data for landing, shown on Figure 12 with the approach lift coefficient ($1.3V_S$) levels shown. All of the data shown with the exception of the 751 data is certified data indicating that the 737-200 Advanced is our best low speed performer. Figures 13 thru 16 show the geometry of the current product line. Figure 13 shows the 707-320B flap system which features part span flat slotted kruger flaps and double slotted fixed geometry (does not change with flap angle) trailing edge flaps with normal extension (not streamwise). The 727 system shown on Figure 14 shows the slotted slats on the outboard leading edge and flat kruger flaps inboard. The less powerful devices inboard were incorporated in order to obtain good flaps down stall characteristics. The 727 was our first triple slotted variable geometry trailing edge flap. The flaps have streamwise motion on a track and rollers and the segments move relative to each other giving a large fowler motion. The streamwise motion resulted in a flap that has very little buffeting relative to the 707 normal extending flaps. The 737 geometry shown on Figure 15 is very similar to the 727 in concept except that the slats have two extended positions, one sealed for takeoff and one slotted for landing. The 737 by virtue of it being a twin, requires high L/D levels for adequate

6.1.3 Continued

takeoff performance, and the sealed low angle slat was incorporated to meet this requirement. The slat moves to higher deflections and slots for the higher flap angles where $C_{L_{max}}$ becomes the dominant requirement. The 747 system shown on Figure 16, uses a triple slotted flap similar to the 727 and 737, but incorporated a new type of leading edge device, the variable camber kruger flap outboard of the inboard nacelle. The flap is basically a flexible fiberglass panel that forms the lower surface of the leading edge retracted, but with extension the panel is warped by a linkage and a curved bullnose segment deployed at the leading edge. This results in a very powerful curved slotted aerodynamic leading edge flap. The 747 incorporates a flat sealed kruger inboard, again to tailor the flaps down stall characteristics. A variant of the variable camber kruger developed on the 7X7 program is shown on Figure 17. This flap employes the flexible panel only over part of its chord with a resulting simplified linkage. This flap called the flex kruger is a candidate for our next airplane. The 747 SP incorporates a single slotted linkage supported flap with normal extension. The use of a single slotted flap was made possible by the reduction in takeoff weight for the 747 SP and the flap itself was a significant weight saver. A double slotted linkage supported flap with normal extension is shown on Figure 18. This flap was developed in the 7X7 program and the comparisons on Figure 18 with the triple slotted track and roller system indicate why this type of flap is being considered for our next airplane. Figure 19 shows a summary of the high lift device development at Boeing and Figure 20 shows the chord fractions of the wing devoted to the high lift system. The trend is obvious, with the high lift system being forced down in size to get more inspar box structure. The larger inspar box structure if it can be attained with adequate low speed performance should allow a higher aspect ratio wing and will provide fuel volume.

This points out that the high lift technology developed has been partly taken out as a structural benefit. Figure 21 shows high lift technology ($C_{L_{max}}$) as a function of flap area to wing area. This figure puts a little different light on the data of Figure 10. The major advance in the 727 appears to have been the increase in wing area available for the high lift system. The 737 and 747 however appear to be higher and higher technology levels with further potential on the shelf waiting to be applied. This technology can be used as an aerodynamic benefit (constant flap to wing area ratio) or as a structural benefit reducing flap area while maintaining $C_{L_{max}}$. Figure 22 shows the impact of these two approaches.

6.2 WING SIZING AND ANALYTICAL STUDIES.

Now that we have an appreciation for the parameters involved, technology and history, we can look at examples of how the high lift system affects the airplane design process. There is no preliminary design type high lift prediction method available at Boeing at present. So that the primary tool used for prediction is a program called LOWLAM which was developed to make adjustments to wind tunnel data for small geometry variations. During a development program, the wind tunnel model definition is usually out of date relative to the baseline definition. Consequently, adjustments must be made to the data to account for the differences. The tool developed for this purpose LOWLAM is the only tool available to predict low speed performance and it is therefore used. LOWLAM builds up the low speed characteristics using the procedure outlined in Figure 23 using tables of values extracted from wind tunnel or flight data on similar configurations. LOWLAM then is the method used in the initial sizing. The analytical studies and wing sizing is part of a total process that is illustrated on Figure 24, and these studies

are the prelude to the wind tunnel testing, analysis and design cycle that leads to a configuration committed to flight test.

6.2.1 Wing Sizing Studies

The principal elements in the wing design cycle are shown on Figure 25. During the early phases of wing selection the structural efficiency, detail design, growth considerations and some of the structural arrangement issues do not get into the cycle, and it is only after some appreciable work that the details of the wing structural design can be considered. As an example of the complexity of the wing selection process, some of the analytical studies performed on the 7X7 are shown on Figure 26. The studies include planform (sweep and aspect ratio), cruise speed, airfoil, growth and wing area. The typical assumptions about the high lift system are shown on Figure 27, where a high lift geometry is assumed and is stretched to fit as aspect ratio, sweep and wing area are varied. The LOWLAM program mentioned earlier is used to develop the low speed performance of the geometries. A typical thumbprint for a one stop transcontinental airplane is shown on Figure 28. The assumptions buried in this thumbprint in addition to a fixed payload range are aspect ratio, sweep and high lift geometry. Figure 28 indicates that the wing loading is picked by the approach speed requirement and the thrust loading by the initial cruise altitude requirement. Figure 29 shows a similar thumbprint for a nonstop transcontinental airplane and again the approach speed criterion determines the takeoff wing loading, and initial cruise altitude the thrust loading. Both of the thumbprint charts presented are for three engine airplanes and the limiting conditions are typical, however two engine airplanes usually place more stringent requirements on the high lift system, particularly takeoff

requirements.

6.2.2 Flap System Study

Another typical study performed during the wing sizing cycle is the trade involved in flap type. Figure 30 shows an example of the types of flaps studied in a 7X7 flap trade study. The LOWLAM program was used to develop the low speed performance data, and high speed and weight considerations were included in the evaluation. Since the airplane was approach speed limited the primary low speed parameters of interest were approach L/D and CL. The low speed parameters used in the study are shown on Figure 31, with the symbols representing the approach CL and L/D for each system. The weight performance trades are shown on Figure 32. There is no clear optimum, the flap with the lowest approach speed has the highest weight. Based on some judgment, the main/aft double slotted flap was chosen as the recommended system based on its moderate weight penalty and reasonable approach speed benefit. This choice was also augmented by the inability of the single slotted flap to meet approach altitude requirements even with overspeed as shown in Figure 33.

6.2.3 Flap Parametric Study

The assumption to this point in the analytical studies is that the flap span, chord, fowler motion, leading edge type are all fixed. How then do we know they are reasonable for the type of configuration we are looking at, and assure ourselves that some other geometry would not be superior? The LOWLAM program and data base can be used to evaluate geometry variations from the base configuration. Figure 34 shows for a fixed trailing edge flap the effect of leading edge device type on the performance envelope. The sealed slat is superior at low lift levels and

6.2.3 Continued

the variable camber flap is best at the higher takeoff lift levels and landing. For a twin engine airplane that needs L/D at lower lift levels the sealed slat looks promising (a la 737), and for a trijet the variable camber kruger appears most promising for approach speed. Figure 35 shows the trade on trailing edge flap type with a fixed leading edge type. The single and double slot appear even at the low lift levels but the double slot has the performance edge at the higher lift levels. Therefore if you need the lift levels of the double slot as in an approach speed designed airplane you would probably choose it. Note that the abscissa of Figures 34 and 35 is not a simple CL value but the product of CL and wing area. This is done so that we can overlay the performance requirement for a particular airport on the curves with generality and interpret the results in terms of takeoff weight and approach speed for the landing case. Figure 36 shows an example of this technique overlaid (red) on a study performed to evaluate the merits of trailing edge flap fowler motion. The overlay could go on any of the flap trade study plots plots presented in this section and used to evaluate the merits of a particular change. The basic data of Figure 36 shows that fowler motion obtained by moving the cove location from .8C to the trailing edge with a fixed flap chord has relatively small effects on the performance envelope. The explanation for this effect is shown on the green overlay which shows that the lift gain due to the fowler motion is negated by the increased down trim lift required and the drag increases due to the larger flap. Another method of obtaining fowler motion by increasing flap chord holding a fixed cove location indicates very similar results but with larger changes in L/D and attitude at a fixed flap angle. Figures 38 and 39 show the effects of flapping over the inboard and outboard ailerons and the effect of simply drooping the ailerons. At the higher lift levels the full span flap appears quite promis-

ing with 7 knot lower approach speed. Figure 40 shows the effect of a span change on the wing with a corresponding flap span change. Span appears to be a benefit at all lift levels with the major benefit at the lower lift levels. The data shown in this section, while the best we have, should be used carefully because it used the LOWLAM approach and data base which is not very close to the configurations being evaluated. The data is valuable in giving guidance as to what direction to explore in the wind tunnel however.

6.3 ANALYSIS TOOLS

In the introduction, we talked about the so called rational design method for high lift design and the importance of the analytical tools in this process. Figure 41 shows the process again and lists the tools required. The two dimensional tools appear to be in reasonable shape as discussed in Chapter 3. The two to three dimensional correlation methods is currently pretty crude as are the wind tunnel to flight methods. Probably the most useful tool coming along for the high lift wing design task is the three dimensional potential flow methods. Methods like the panel method program A230 have been available for some time however the application of this tool to the high lift problem has been rather spotty. Figure 42 shows the paneling model of an early 7X7 model (QSH). This model took longer to construct than a wind tunnel model, and the results shown in Figure 43 were quite disappointing. The lift levels are low, which is the wrong direction to be explained by viscous effects. The configuration was rather complicated and was at a high flap angle, so the next attempt to use A230 was on a simple flap system for the 727-300 at a low flap angle. Figure 44 shows the theoretical model and Figure 45 the results. Again quite disappointing. The flaps in the previous two attempts were faired over and the slots were

not modeled. The next attempt with A230 then included a slotted leading edge configuration as shown in Figure 57. A slotted trailing edge was not attempted due to the complexity of the model. The results shown on Figure 48 were again poor, however some of the details of the pressure distributions were quite useful to the designers. At this point an effort was undertaken to establish why A230 was doing such a poor job. It was found that the modeling of the trailing vorticity in the vicinity of the flap ends had a large effect on the program answers. A combination theoretical experimental program was undertaken to establish better modeling techniques for flapped configurations. Figure 48, 49 and 50 show a comparison of the experimental results with the program predictions using the new modeling techniques evolved in the wind tunnel. The results are much improved, and the differences can be explained in terms of the viscous effects. Figure 51 a and b shows the old versus new modeling scheme. The differences are in what is done with the trailing vorticity in the vicinity of the flap ends. Figure 52 shows the modeling comparison of a full span flap with a cutout. Figure 53 shows the effect of the revised modeling techniques on the span load prediction. The improvement in the test/theory correlation is obvious. Figure 54 shows the test/theory correlation for a new three dimensional program emerging at Boeing. Again the correlation is quite good and the differences can be explained by viscous effects.

6.4 TESTING PROGRAM

There are some items in every test program that if tested three dimensionally could not be evaluated within reasonable resource constraints. One approach to problems like this is to evaluate them two dimensionally and imply the answers in the three dimensional environment. This is not a risk free approach as Figure 55 indicates. There really is very little of a three

dimensional wing that could be treated as an infinite swept surface. However experience such as that shown on Figure 56 indicates that the two dimensional to three dimensional correlation is quite good if somewhat qualitative.

6.4.1 Two Dimensional Testing

Based on the above thinking many airplane programs have two dimensional tests included in their wind tunnel plans to investigate special problems such as the effect of airfoil choice or high lift performance. To investigate this on a three dimensional wing would be risky, expensive and time consuming, yet it can be done quite reasonably in a two dimensional environment. Figures 57, 58 and 59 show the results of such a study for the 7X7 program. Figure 59 illustrates the airfoil sensitivity without a high lift system. With leading and trailing edge device deployed the data on Figures 58 and 59 indicate less difference between the airfoils and that some leading edge position changes must be expected in a three dimensional test. This is only an illustration of one way in which two dimensional testing can be used in a development program.

6.4.2 Three Dimensional Testing

Three dimensional testing is the key element in the high lift development of a new airplane. Figure 61 shows a typical low speed model in the University of Washington's Aeronautical Laboratories 8' by 12' wind tunnel (UWAL). The low speed configuration is usually developed in UWAL at the Reynold's numbers available, checked in a high Reynolds number facility (usually NASA 12' pressure tunnel) and scaled to full scale without modification. The three dimensional test program is extremely complex and time consuming. An appreciation for this

6.4.2 Continued

complexity can be obtained by looking at a run summary for a single test entry in the UWAL tunnel, see Figure 62 a and b. The test includes combinations of leading edge chord and angle with multiple trailing edge angles, tail on and tail off, differing types of leading edge device, etc., etc., etc. The three dimensional effects can quite often give unusual and unpredictable results and in general must be tested or you can get some nasty surprises. Sample leading edge flap shapes from this test are shown on Figure 63, which at model scale are difficult to tell apart, but the performance shown on Figure 64 indicated a substantial performance benefit for the NP6A shape. This device apparently does not sacrifice $C_{L_{max}}$ for takeoff L/D. Figures 65 thru 70 show a typical trailing edge flap optimization from a low speed test and the sensitivities to flap position so that proper trades can be negotiated with the project. Figure 70 shows the matrix of main/aft flap angles tested and the performance effects of various sequencing alternatives, while Figure 71 shows the effects of gap and overlap. There is no one optimum position or sequencing and choices must be made based on the critical performance requirements. An example of the type of compromise that might be imposed is shown on Figure 72. The project groups would like to use common actuators and linkages for the leading edge devices across the span which usually results in constant gap and height in inches instead of the constant percent chord gap that gives the best performance. The flap mechanisation scheme can have an influence as shown on Figure 73. This shows the effects of three trailing edge flap linkage systems on the performance envelope. Sometimes even the desired shapes cannot be achieved and Figure 74 shows an interesting result from the 7N7 program where the project achievable shape was actually slightly better than the aero baseline configuration. Please note however, this doesn't happen very often. The trades are more likely to look like

370

those shown on Figures 75 and 76 where significant performance penalties are imposed by the projects constraints. If the penalties are large enough the whole system must be recycled to achieve an adequate total system.

6.4.3 Detail Design Testing

In every test program there are usually some design details that must be evaluated in the wind tunnel. An excellent example is the effects of the flap support system on the flow over the flap. It is difficult to simulate the flap support system details on the three dimensional high lift model because of scale. Figure 77 shows a flow visualization picture from a 747 SP low speed test showing a significant separation on the flap due to the flap support system. To attempt to solve this problem on a small scale three dimensional model would be impossible. Instead a flap segment was built for the two dimensional tunnel with a scale large enough to allow the details to be worked. Figure 78 shows the model in the BRWT that was used to develop the aerodynamic treatment around the flap supports. The merit of the configuration changes was measured in terms of drag and buffet intensity. Figures 79 and 80 show the effects of the tailoring performed around the flap supports. At flaps 30^{o} the effects are quite dramatic and the 30^{o} flap would probably not have been used without the fixes. Figures 81 and 82 show the geometries of the tailoring around the flap supports. Such changes could not have been evaluated at the three dimensional high lift model scale.

6.4.4 High Reynold Number Testing

Almost all of the high lift development testing is done in the University of Washington low speed wind tunnel (UWAL) at low

6.4.4 Continued

Reynolds numbers. Previous two dimensional testing (see Chapter 3) has indicated that different Reynolds number sensitivities can be expected with changes in flap system. One significant question then in every airplane program then becomes, what are the Reynolds number effects on the performance of the high lift system? This can only be answered by testing at higher Reynolds number. The 737 and 747 have both been tested in the NASA's pressure tunnel at the Ames Research Center in California. Figure 83 shows the effect of Reynolds number on $C_{L_{max}}$ for the 747. Note that the maximum Reynolds number tested was only 6.5 X 10^6 while full scale is 40 to 50 x 10^6. The effects shown on Figure 83 indicated a rather mild effect of Reynolds number. Figures 84 and 85 show two sets of drag polars obtained with varying Reynolds number and show an interesting trend. Both polars show an increasing drag level with increasing Reynolds number, huh! How can that be, everybody knows drag goes down with increasing Reynolds number. The reason that this occurs is that the model was not tripped and had significant laminar boundary layer runs at the lower Reynolds numbers. The extent of laminar run decreases with increasing Reynolds number causing the drag to increase. The question then is, is this the correct way to test, and are the results meaningful? Figure 86 shows the Reynolds number effects on $C_{L_{max}}$ from the 737 testing at Ames. The Reynolds number sensitivity on this airplane is much larger than on the 747 and appears to be configuration dependent. Figures 87 and 88 show the sensitivity of the pitching moments to Reynold number. The configurations are much different in terms of pitchup, but the Reynold number effects are really quite mild except at low CL's and Reynolds numbers where the laminar boundary layer is causing some very non-linear behavior. The bottom line for the high Reynolds number testing is shown on Figure 89 and indicates that a linear extrapolation of the high Reynolds number wind tunnel data on a log of Reynolds

372

number scale gives a very good estimate of the full scale maximum lift values. These tests are very expensive since they require special models to withstand the high total pressures that go with the high Reynolds numbers; and the outside facilities are also costly. Consequently such tests are usually done after the configuration has been frozen, and consequently they are usually too late in the program to have a major effect unless a problem is uncovered.

6.5 FACILITIES AND TESTING METHODS

Almost all of the high lift testing performed at Boeing is done in the University of Washington's 8' x 12' low speed wind tunnel. A picture of a model installed in UWAL is shown on Figure 90. The test Reynolds number at this facility is about 1×10^6 based on the typical model mean aerodynamic chord. An alternate facility shown in Figure 91 is the Convair low speed wind tunnel in San Diego. The UWAL system uses a single strut with a pitch arm, while a separate pitch strut is used in the Convair tunnel. The third major tunnel used in high lift development is the 20' x 20' low speed tunnel at the Boeing Vertol facility in Pennsylvania shown on Figure 92. This tunnel requires a sting mounted model with an internal balance while both Convair and UWAL have main balances external to the tunnel. We have shown several examples of how the Boeing Research Wind Tunnel has been used for high lift development and Figure 93 shows another example of its use for three dimensional testing. A unique requirement for high lift testing is the requirement for testing in the presence of the ground. Figure 94 shows one approach to this type of testing, the fixed ground board. The installation shown in the UWAL facility is unique in that it has a trough to allow the tail to go below the ground level. This allows the determination of $C_{L_{max}}$ in ground effect. Figure 95 shows another approach in the Vertol facility which has a moving ground belt

on the tunnel floor that matches the tunnel speed and eliminates the boundary layer build up on the ground. The fixed ground board has a boundary layer associated with it that does not represent the flight environment and the boundary layer can effect the data. The flow visualization methods employed three dimensionally are similar to those used two dimensionally and were discussed in Chapter 3. An appreciation of the complexity of the flow field about a high lift model can be obtained from Figures 96 and 97 which show total pressure survey obtained behind a 747 model in UWAL. The flow is complex, however such surveys can identify problem areas on the wing and can be used to understand the physics of potential fixes.

CHAPTER 6 REFERENCES

1. Gratzer, L. B., "Analysis of Transport Applications for High Lift Schemes," AGARD-LS-43-71, Lecture Series 43 on Assessment of Lift Devices, Feb. 1971.

2. D6E 10512-1, "Wing Selection for the Model 7X7 Family Airplanes," 7X7 Technical Staff, April 1975.

3. D6-26011TN, "Low Speed Aerodynamic Prediction Method," M. Grainger, June 1970.

4. AE-727-235, "Differences Between TEA-230 and Experimental Force Data on High Lift Configurations," N. R. VanDevender, May 1975.

5. D6-45114TN, "Experiment Development of a Technique for Modeling High-Lift Configurations in Three-Dimensional Potential Flow Programs", C. Verna, Dec. 1977.

6. B-8291-AERO-820, "Aerodynamic Wind Tunnel Test Summary, BRWT 098", P. E. Robertson, March 1977.

7. B-8291-AERO-996, "Aerodynamic Wind Tunnel Test Summary, UWAL 1208", Mel Rogers, November 1977.

8. B-8291-AERO-997, "Aerodynamic Wind Tunnel Test Summary, UWAL 1210", S. E. Tolzmann, Jan. 1978.

9. D6-34119TN, "Low Speed Aerodynamic Refinement of 747 SP Inboard Flap Center Support", T. Kriha and M. Grainger, April 1975.

10. D6-30470TN, "Results of High Reynolds Number Testing of a Low Speed Model of the 747", E. G. Dickson, Jan. 1969.

375

11. D6-32166TN, "737-100 Variable Reynolds Number Wind Tunnel Test Analysis with Flight Test Comparisons", D. E. Wear, August 1968.

WIND TUNNEL PROGRAMS
THRU FIRST FLIGHT

WIND TUNNEL OCCUPANCY HOURS	727	737	747
HIGH SPEED	1803	3818	7070
LOW SPEED	2500 (2.2)	2563 (3.2)	7279 (7.2)
W.T. ENGINEERING MAN HOURS	90,363 (49)	91,090 (49)	229,639 (124)
W.T. SHOP MAN HOURS	240,968 (130)	197,885 (107)	529,039 (286)

FIGURE 1
PG. 19

Total Wind Tunnel Test Hours for Development of Various Aircraft

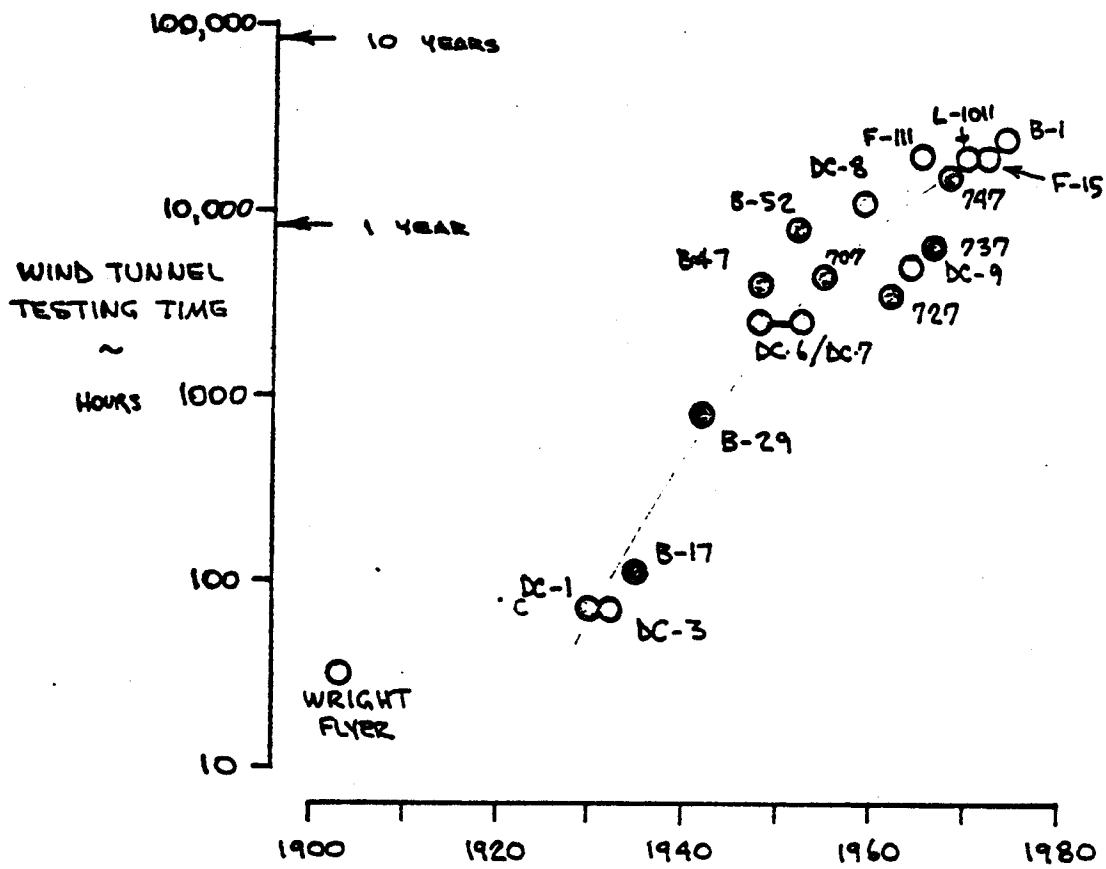

FIGURE 2

ENGR.			REVISED	.DATE		P 6.20
CHECK						
APR						
APR						
					BOEING	

D1 4100 5320 REV. 8/71

J19-047

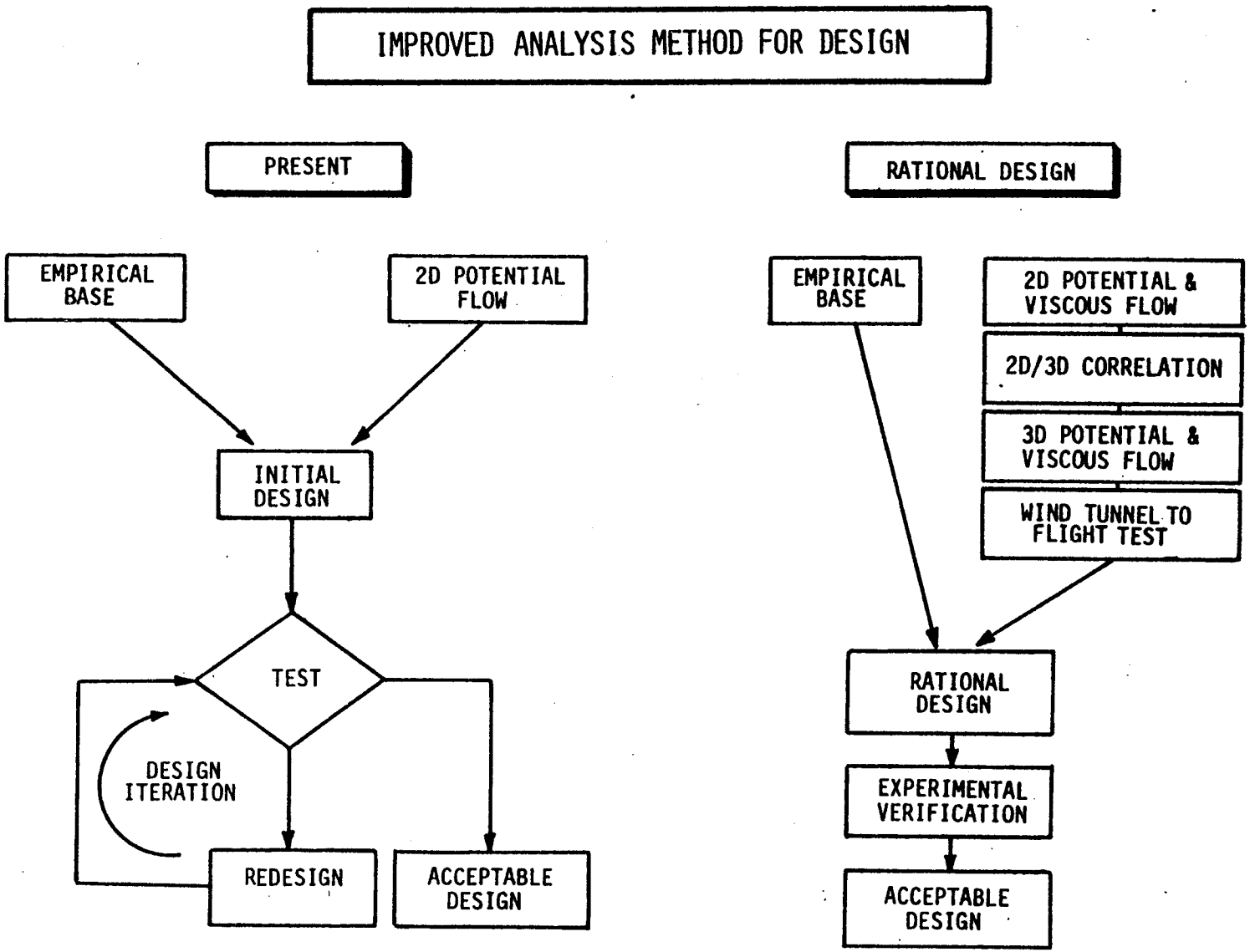

FIGURE 3
P6.21

C

CRUISE PERFORMANCE

PAYLOAD = 42,000 LB
RANGE = 5700 NM
MACH NO. = 0.815 (LRC)

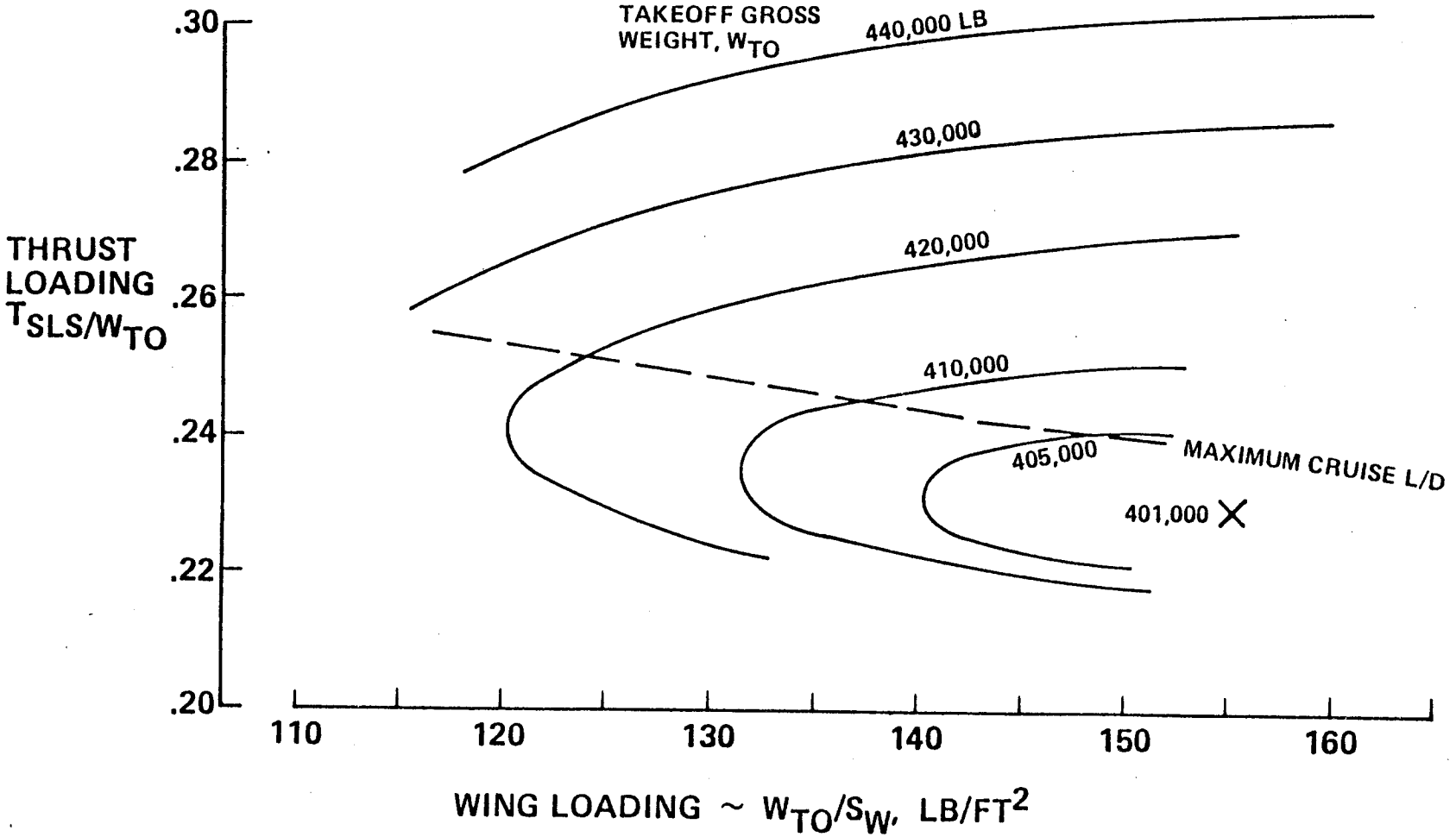

II SUB 4
P 6.22

TAKEOFF PROFILE

GROUND RUN	CLIMBOUT
$f\left(\frac{T}{W}, \frac{W}{S}, C_{L_{MAX}} \right.$ & $\left. C_D, \mu\right)$	$f\left(\frac{T}{W}, \frac{L}{D}\right)$

SECOND SEGMENT CLIMB
TAN $\gamma \geq .03$
(1-ENGINE OUT)

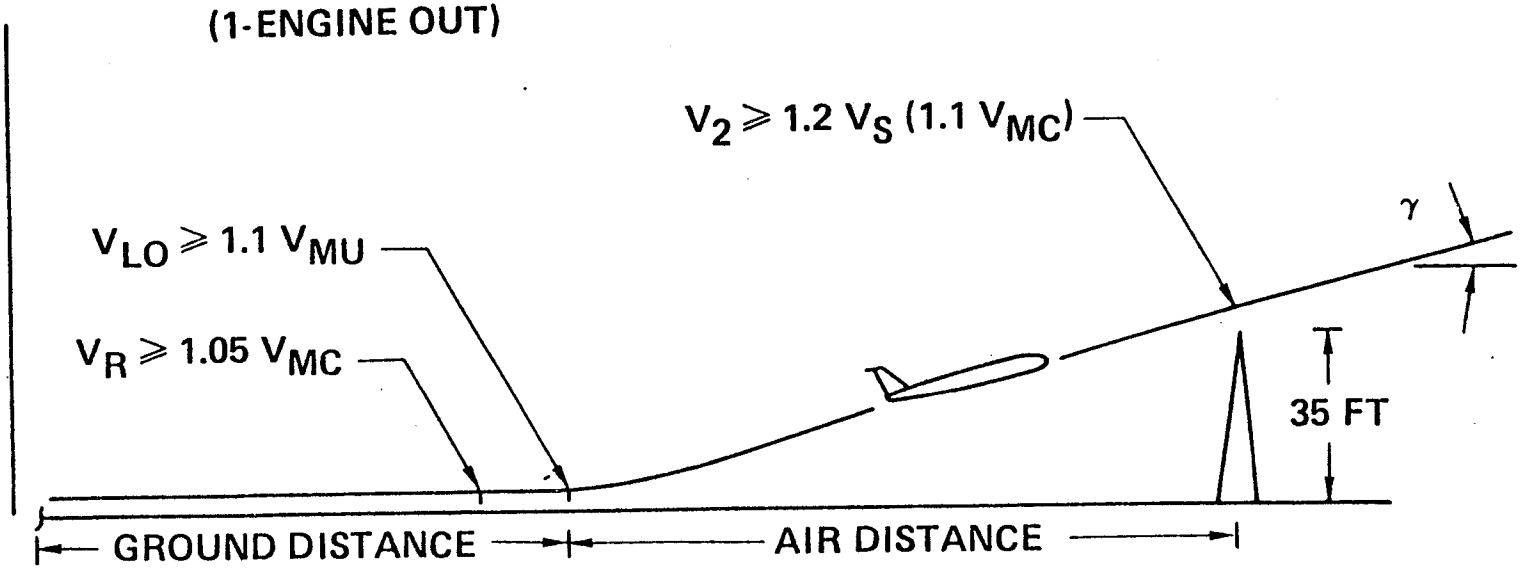

FIGURE 5
D6-23

LANDING PROFILE

APPROACH	GROUND RUN	GO-AROUND
f ($C_{L_{MAX}}$, $\frac{W}{S}$ & L/D)	f ($C_{L_{MAX}}$, W/S & C_D, μ, T_{REV})	$f\left(\frac{T}{W}, \frac{L}{D}\right)$

APPROACH

$V_{APP} = 1.3\ V_S$

TAN $\gamma_1 \geqslant .027$

(1-ENGINE OUT APPROACH FLAPS)

GO-AROUND

TAN $\gamma_2 \geqslant .032$

(ALL ENGINE LANDING FLAPS)

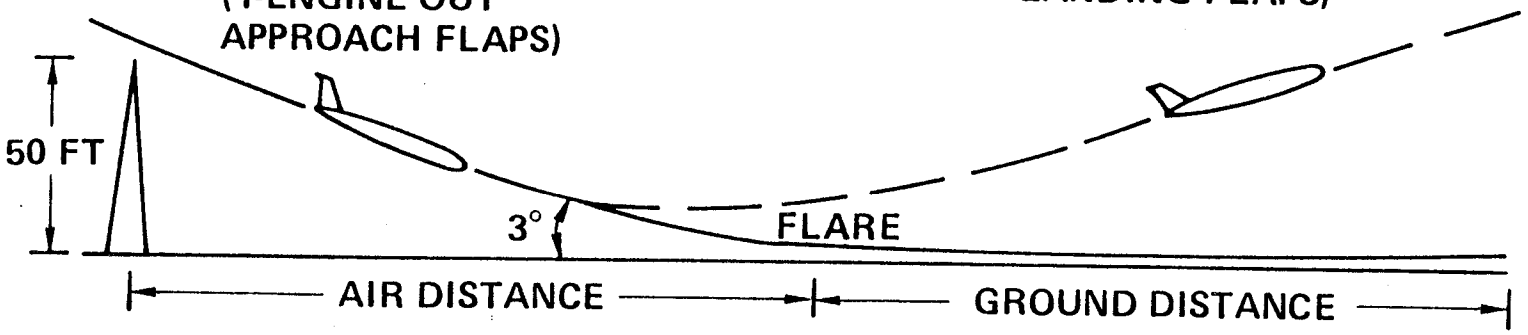

FIGURE 6
P 6.24

LOW-SPEED PERFORMANCE

PAYLOAD = 42,000 LB
RANGE = 5700 NM
MACH NO. = 0.815 (LRC)

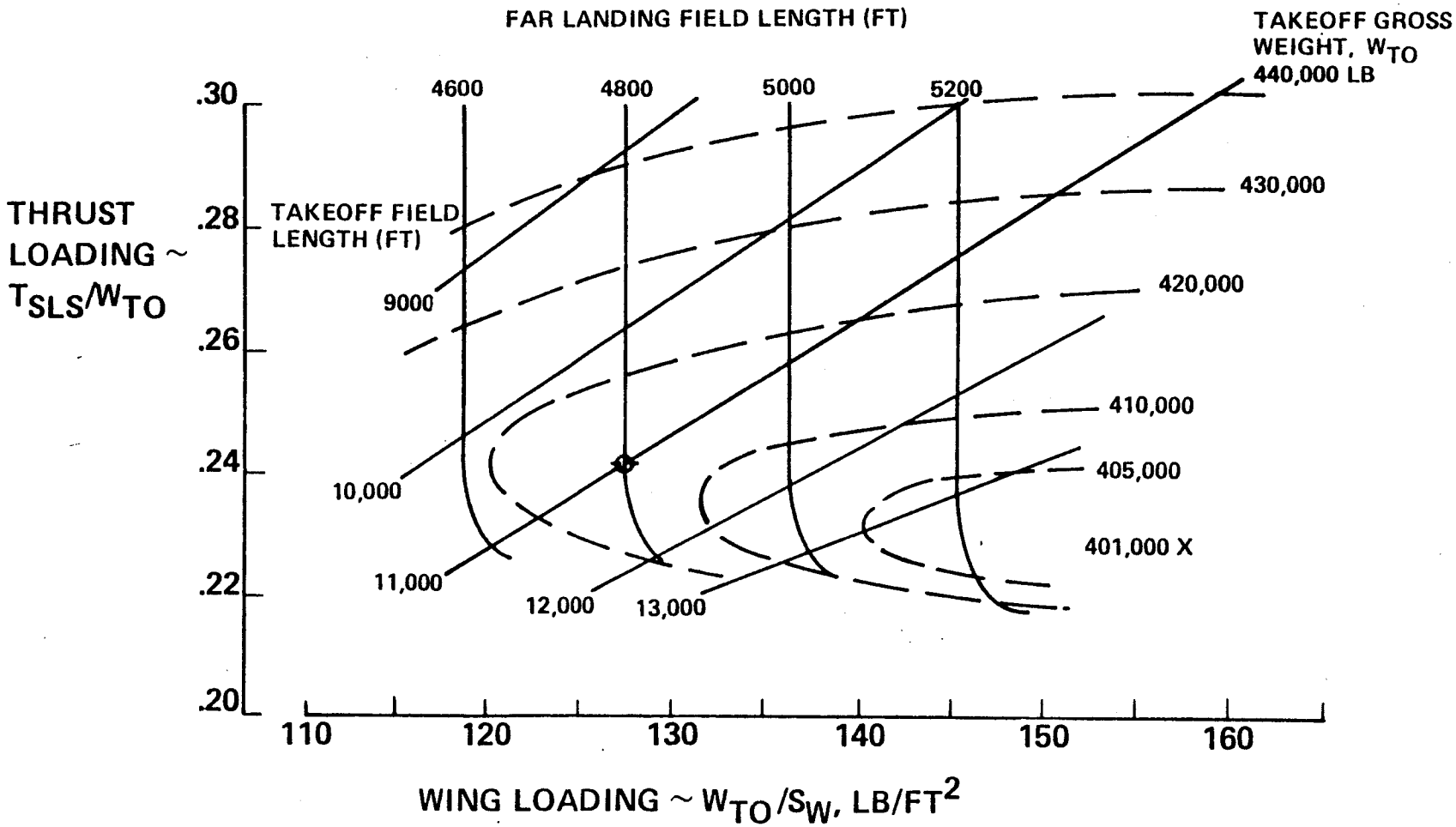

Figure 7
D6.2.5

ASPECT-RATIO = 8.0
WING SWEEP = 35°

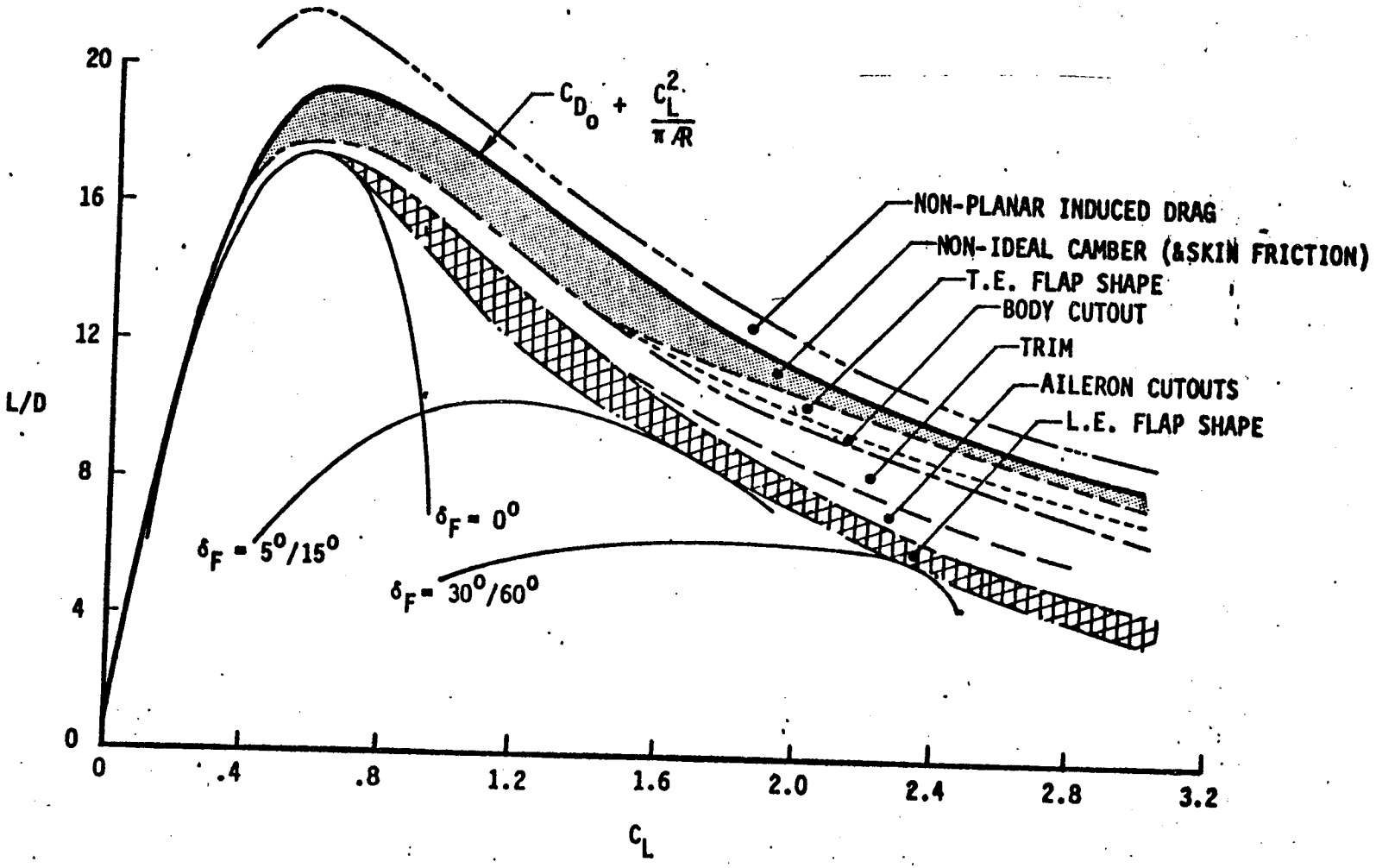

LIFT-DRAG CHARACTERISTICS

FIGURE 8
PG. 269

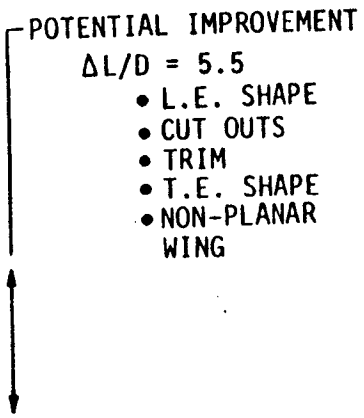

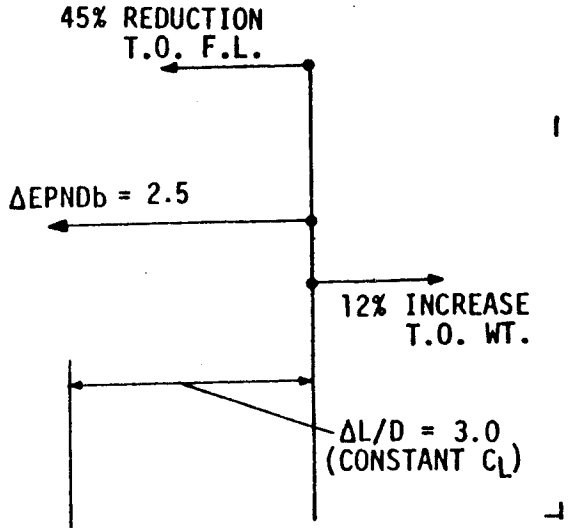

D6.26b

FIG 9 O/L
R&D

HIGH LIFT POTENTIAL PERFORMANCE IMPROVEMENTS

ASPECT-RATIO = 8.0
WING SWEEP = 35°

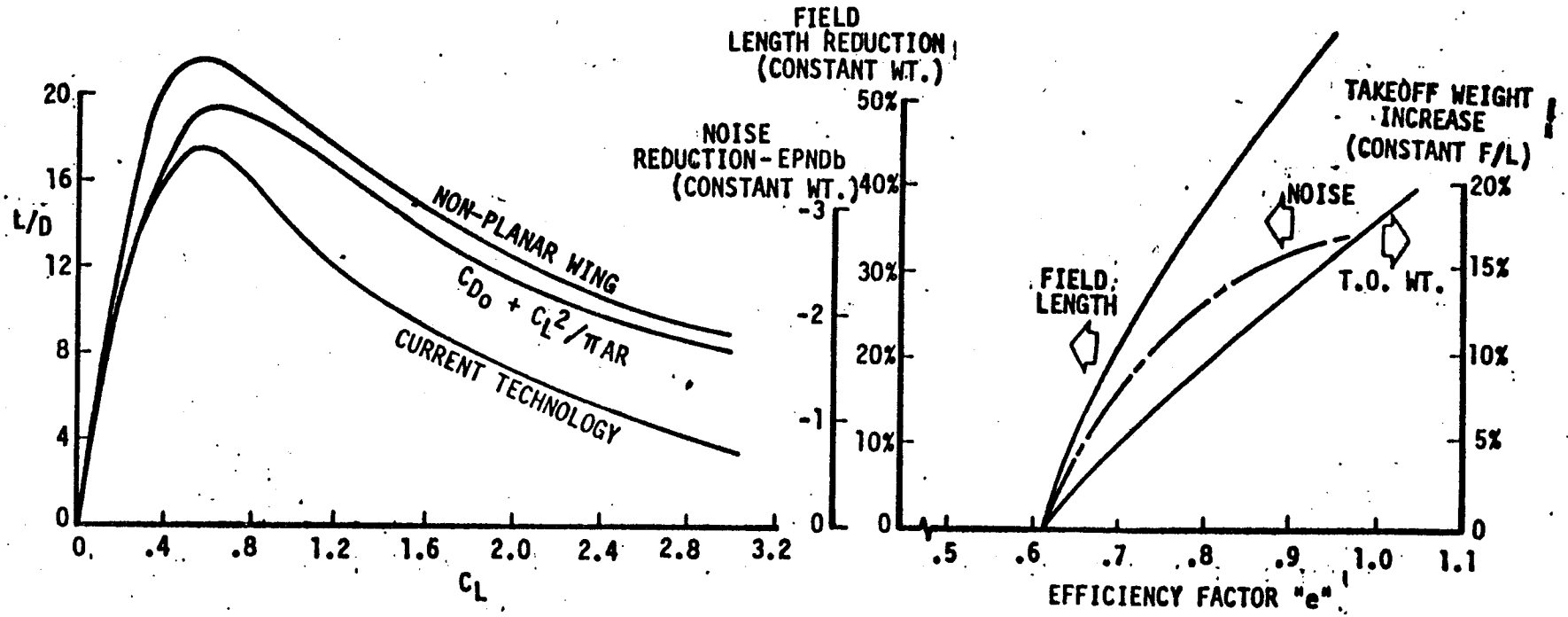

FIGURE 9
PG. 27

DEMONSTRATED $C_{L_{MAX}}$ LEVELS

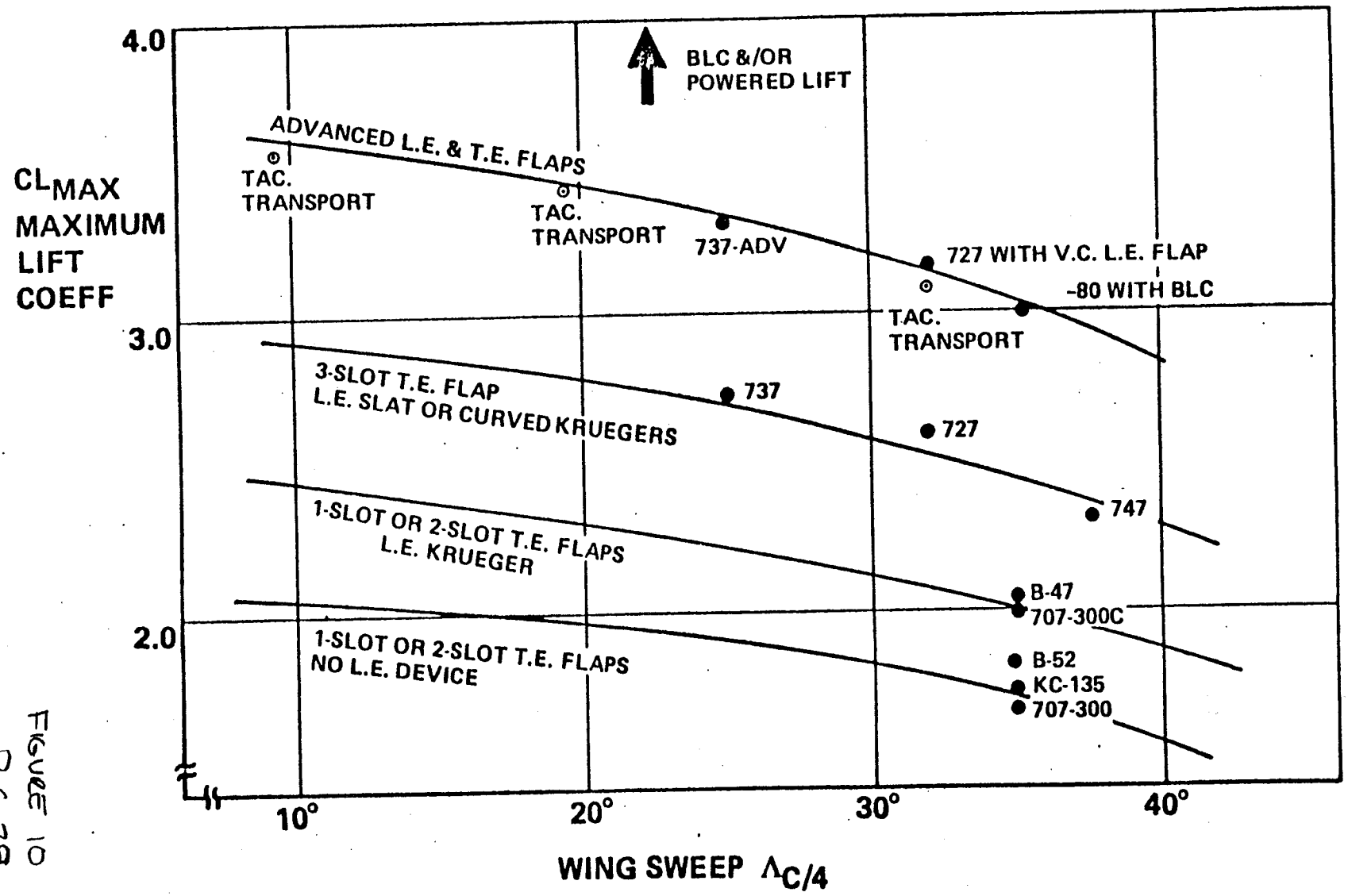

FIGURE 10
D6.28

TAKEOFF PERFORMANCE COMPARISON

● CERTIFIED DATA EXCEPT 751

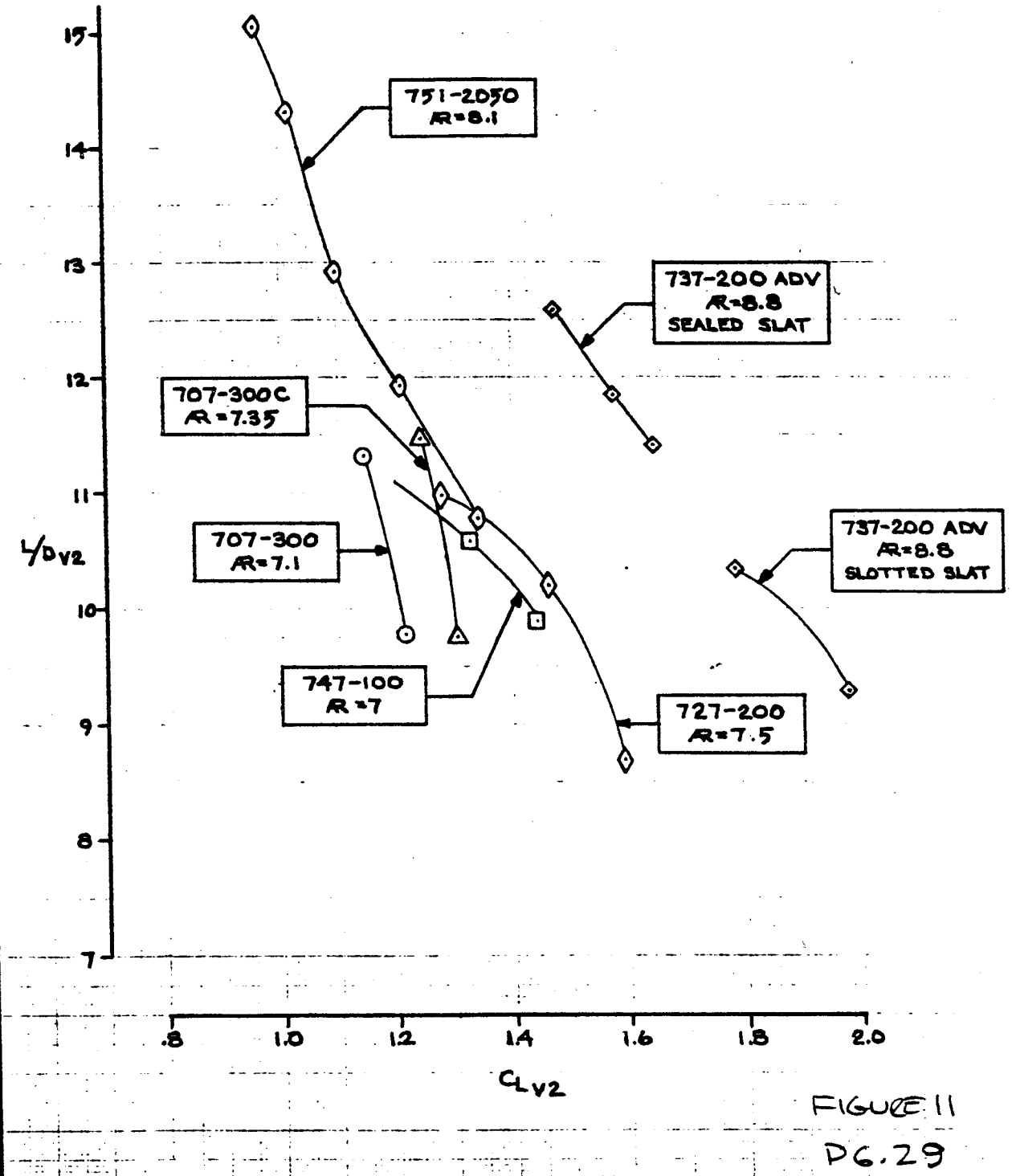

FIGURE 11

PG. 29

CALC	R.O.	7/17/74	REVISED	DATE		
CHECK			R.O.	8/20/74		
APR						
APR						
COPY	B. Matthias	11/29/71			THE BOEING COMPANY	PAGE

D1 4100 3240 ORIG 3/71

J15-047

LANDING PERFORMANCE COMPARISON

● CERTIFIED DATA EXCEPT 751

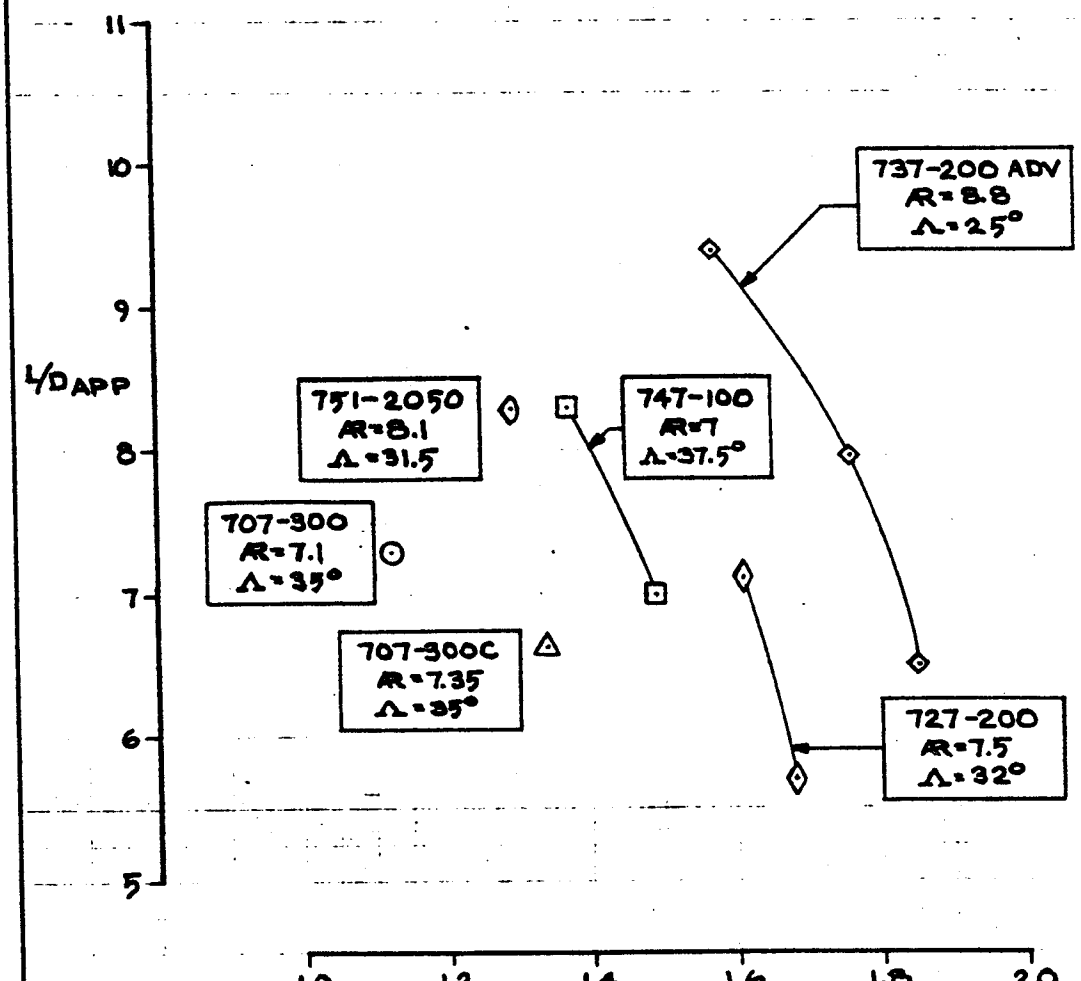

FIGURE 12
P6.30

CALC	R.O.	5/17/74	REVISED	DATE	
CHECK			R.O.	8/27/76	
APR					
APR					
	B. Mathias	11/22/77			

THE BOEING COMPANY

PAGE

D1 4100 3240 ORIG 3/71

J15-047

389

390

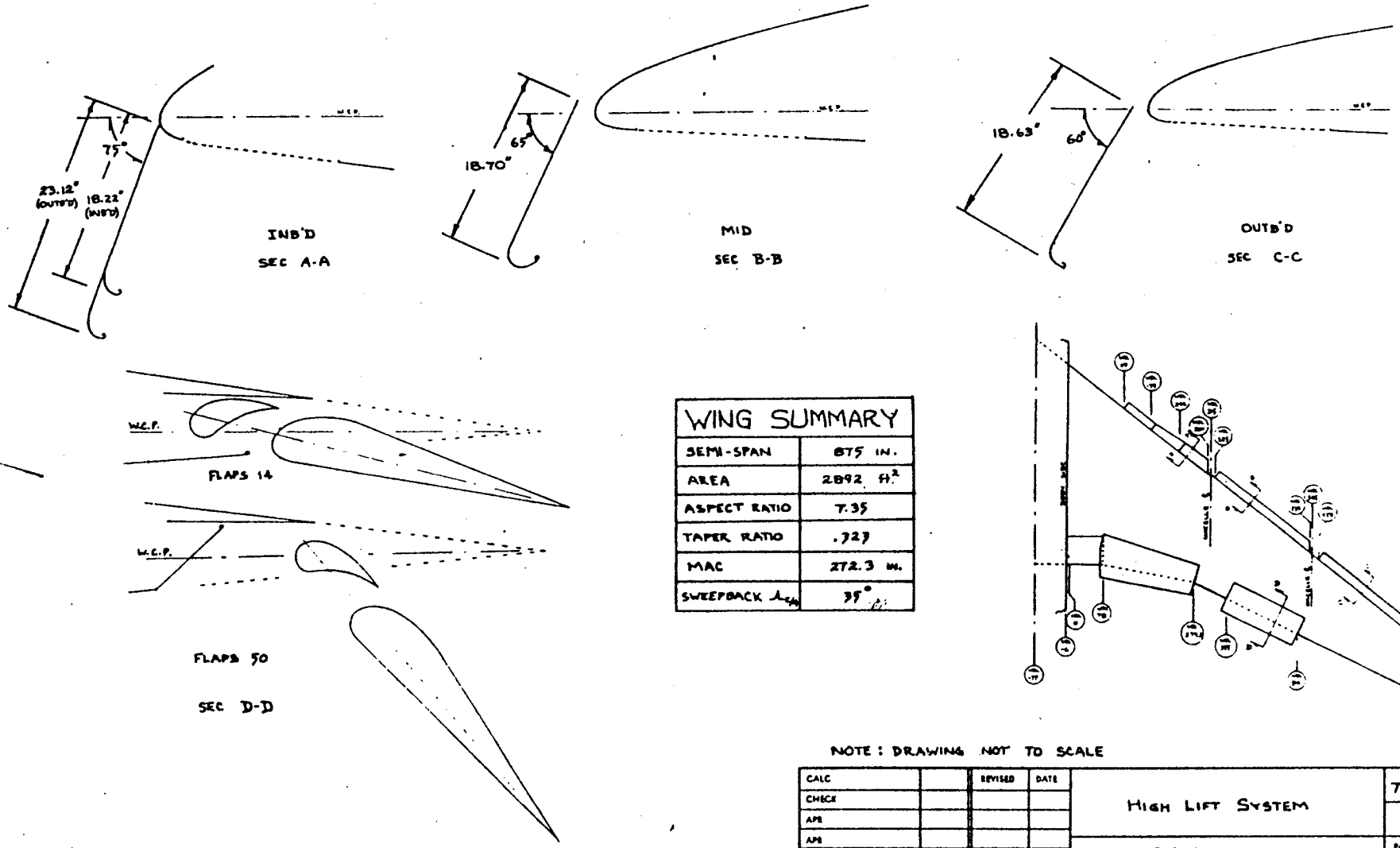

WING SUMMARY	
SEMI-SPAN	875 IN.
AREA	2892 FT.^{2}
ASPECT RATIO	7.35
TAPER RATIO	.227
MAC	272.3 IN.
SWEEPBACK $\Lambda_{c/4}$	35°

NOTE : DRAWING NOT TO SCALE

CALC		REVISED	DATE	HIGH LIFT SYSTEM	707-320B
CHECK					
APR					
APR				THE BOEING COMPANY	PAGE
J.L. LEE	9-17-70				

AD 1017 B

8-7900

FIGURE 3
D 6.31

391

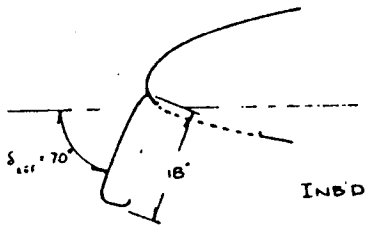

INB'D

SEC A-A

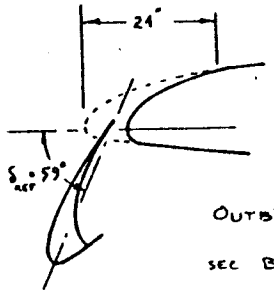

OUTB'D

SEC B-B

WING SUMMARY	
SEMI-SPAN	648 IN.
AREA	1560 ft^2
ASPECT RATIO	7.48
TAPER RATIO	.372
MAC	180 IN.
SWEEPBACK $\Lambda_{c/4}$	32°

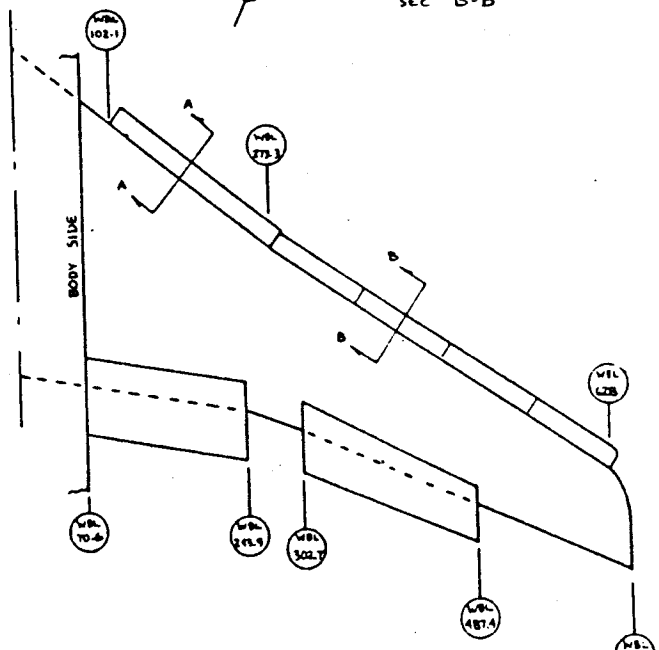

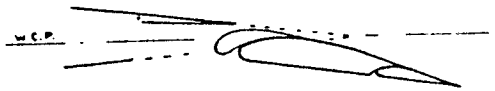

FLAPS 10

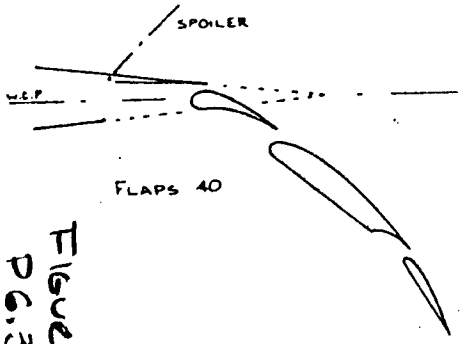

FLAPS 40

NOTE: DRAWING NOT TO SCALE

		REVISED	DATE		
CALC				HIGH LIFT SYSTEM	727
CHECK					
APR					
APR				THE BOEING COMPANY	PAGE
J.L. LEE	9-16-70				

D 1817 B

8-7900

FIGURE 14
P6.32

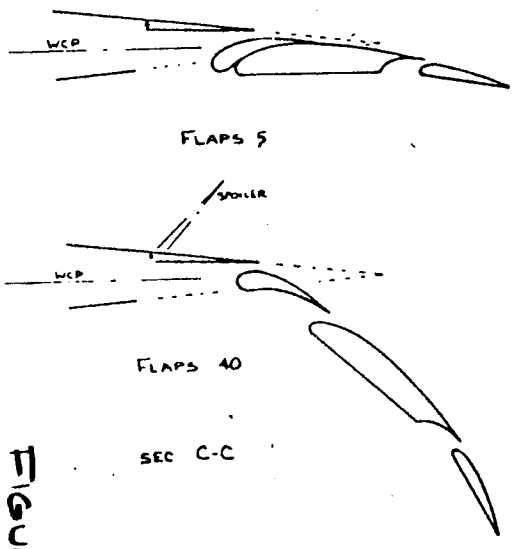

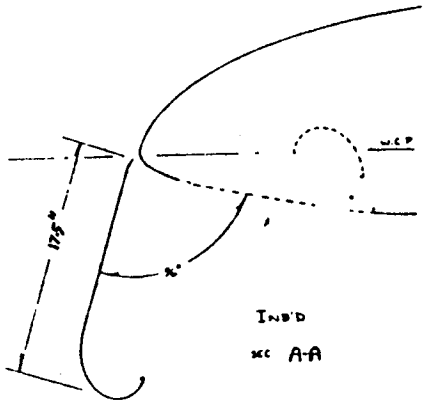

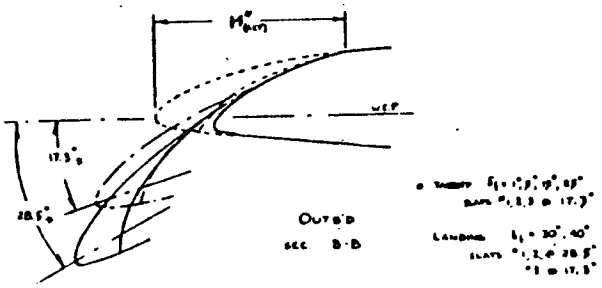

WING SUMMARY	
SEMI-SPAN	557.5 INCHES
AREA	980 FT²
ASPECT RATIO	8.83
TAPER RATIO	.341
MAC	134.5 IN.
SWEEPBACK $\Lambda_{c/4}$	25°

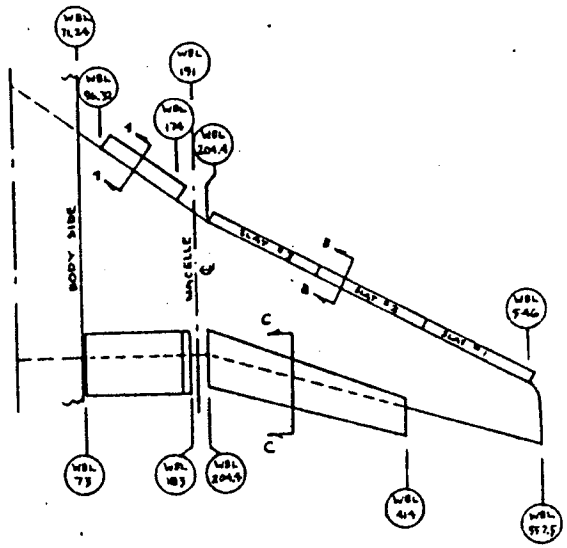

NOTE : DRAWING NOT TO SCALE

CALC		REVISED	DATE	HIGH LIFT SYSTEM	737-100
CHECK					
APR					
APR				THE BOEING COMPANY	PAGE
J.L LEE	9-16-70				

6-7900

FIGURE 15
D6-33

AD 1017 B

393

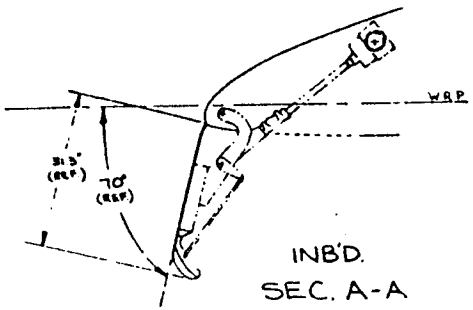

INB'D.
SEC. A-A

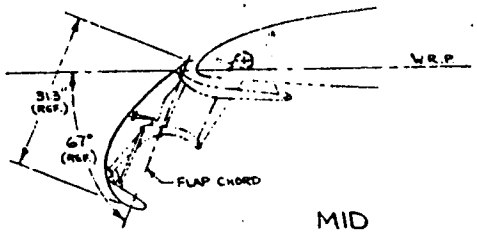

MID
SEC. B-B

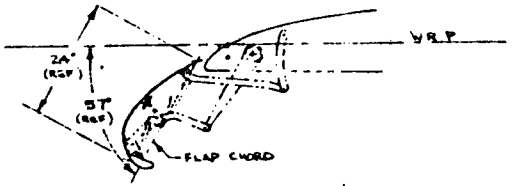

OUTB'D.
SEC. C-C

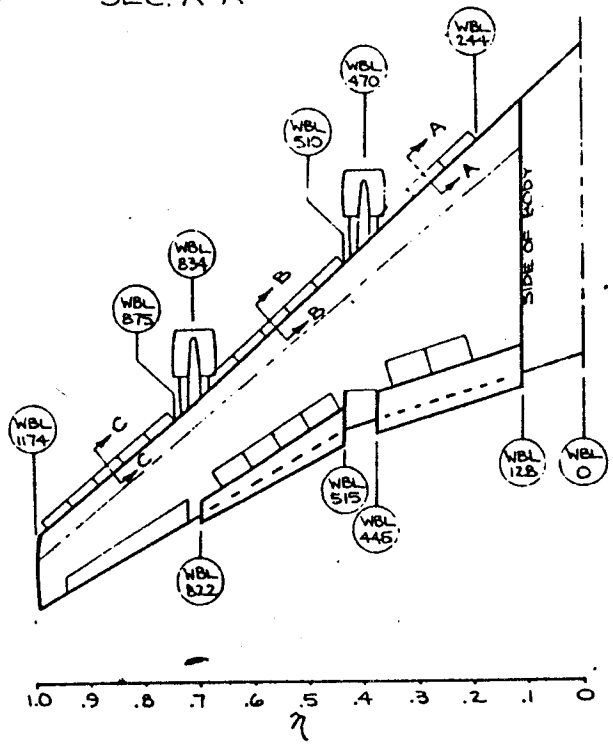

WING SUMMARY	
SEMI-SPAN	91 FEET-10 INCHES
AREA	5500 SQ. FEET
ASPECT RATIO	6.96
TAPER RATIO: TIP CHORD / BASIC CHORD	.356
TIP CHORD / ROOT CHORD	.245
MAC (BASIC ONLY)	321.1795 INCHES
SWEEPBACK, C/4	37½°
DIHEDRAL	7°
INCIDENCE	2°

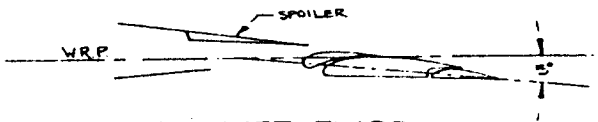

TAKEOFF FLAPS

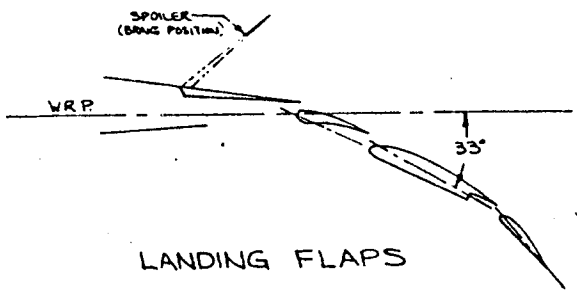

LANDING FLAPS

NOTE: DRAWING NOT TO SCALE.

CALC	M. LANG	7/30/68	REVISED	DATE	HIGH LIFT SYSTEM	747
CHECK	JWB MARTIN	9/17/68				
APP						
APP					THE BOEING COMPANY	PAGE
					RENTON WASHINGTON	

FIGURE
PG. 34

LEADING EDGE FLAP

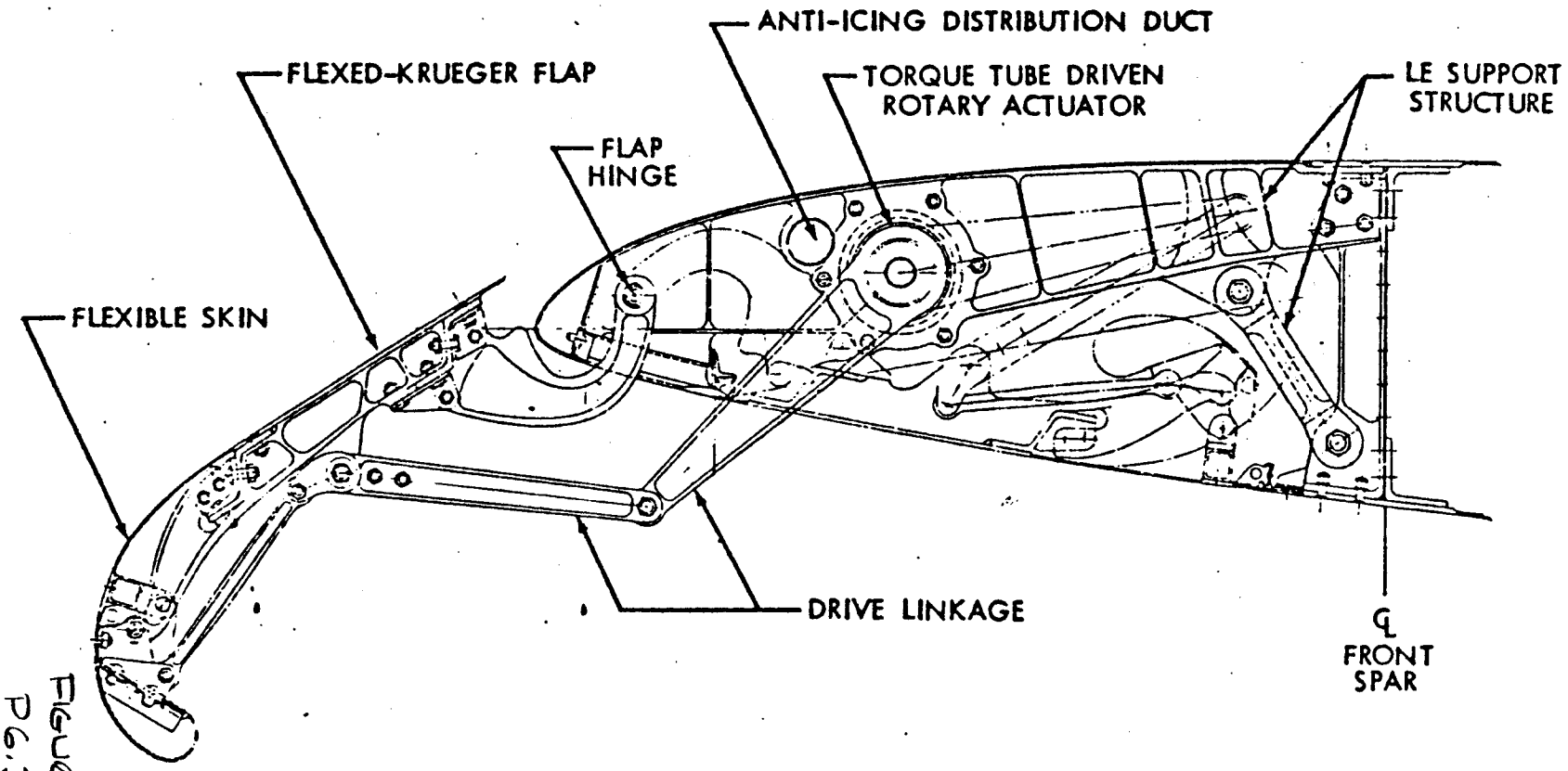

FIGURE 7
P6.35

DOUBLE-SLOTTED LINKAGE SUPPORTED FLAP

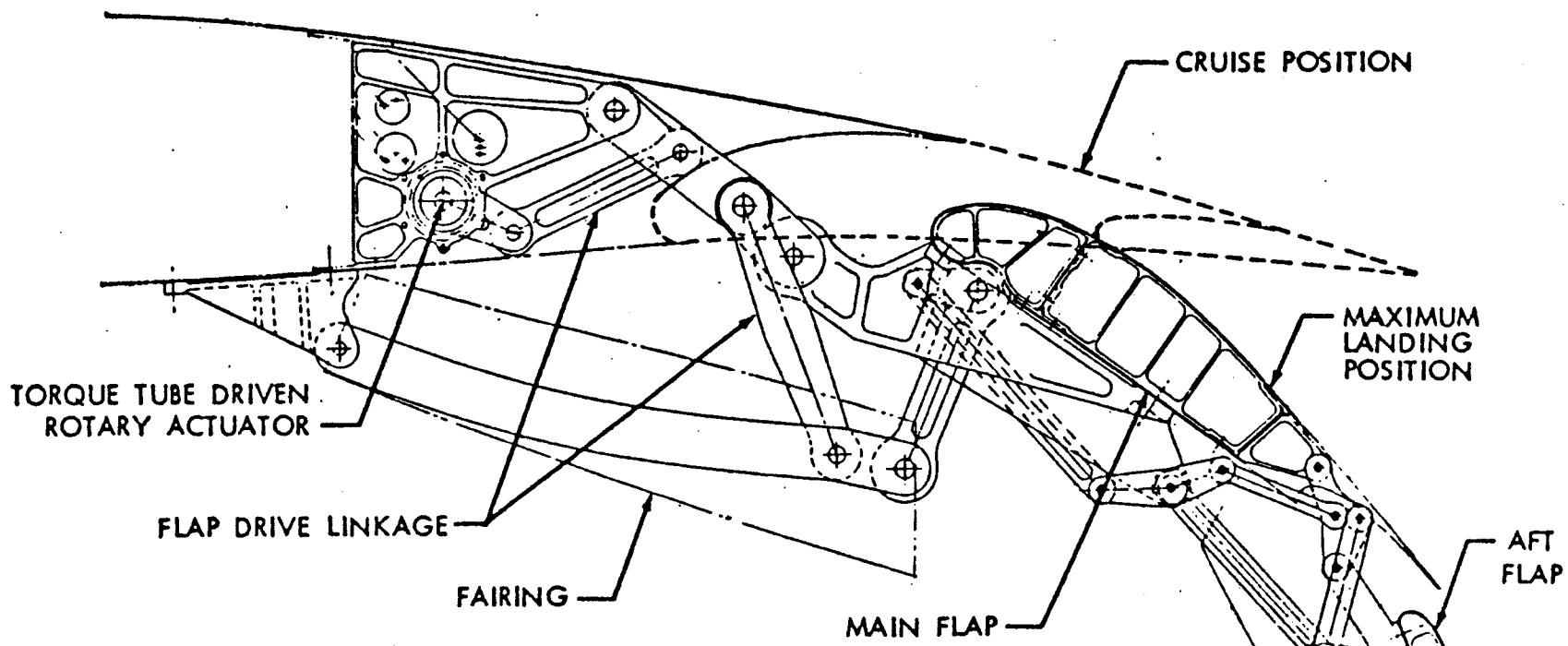

• WEIGHT	26% LIGHTER
• CRUISE DRAG	33% LESS
• COMPLEXITY	40% LESS
• MAINTAINABILITY COST	18% LESS
• OWNERSHIP COST (MAINT+DELAYS & CANCELLATIONS)	28% LESS

AS COMPARED TO:

TRIPLE-SLOTTED, EXTERNAL TRACK SUPPORTED FLAP (727/737/747 TYPE)

Figure D6.36-3

Aerodynamic Technology	HIGH LIFT TECHNOLOGY	BOEING

- KRUEGER + CIRCULAR ARC TRACK SUPPORTED DOUBLE SLOT

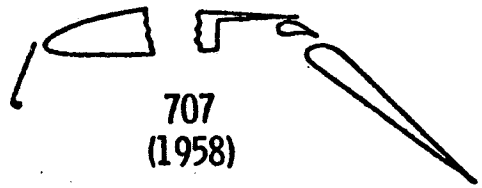

707
(1958)

- SLAT + TRACK SUPPORTED - TRIPLE SLOTTED

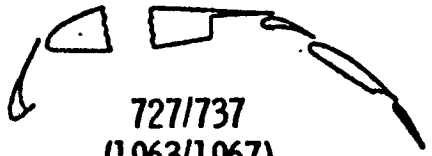

727/737
(1963/1967)

- VARIABLE CAMBER + TRACK SUPPORTED - TRIPLE SLOTTED

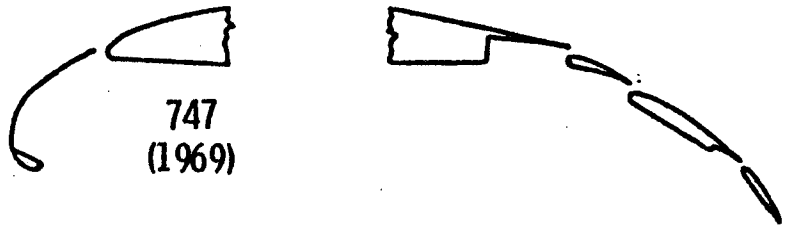

747
(1969)

- SIMPLIFIED VARIABLE CAMBER + LINKAGE SUPPORTED SINGLE OR DOUBLE SLOTTED

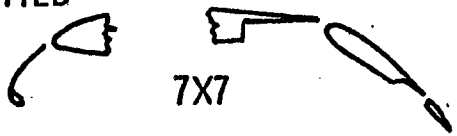

7X7

Figure 6.3.7

Aerodynamic Technology	HIGH LIFT TECHNOLOGY	BOEING

COMPARISON OF RETRACTED HIGH LIFT SYSTEM SIZE

- Streamwise Section
- 60% Semi-Span

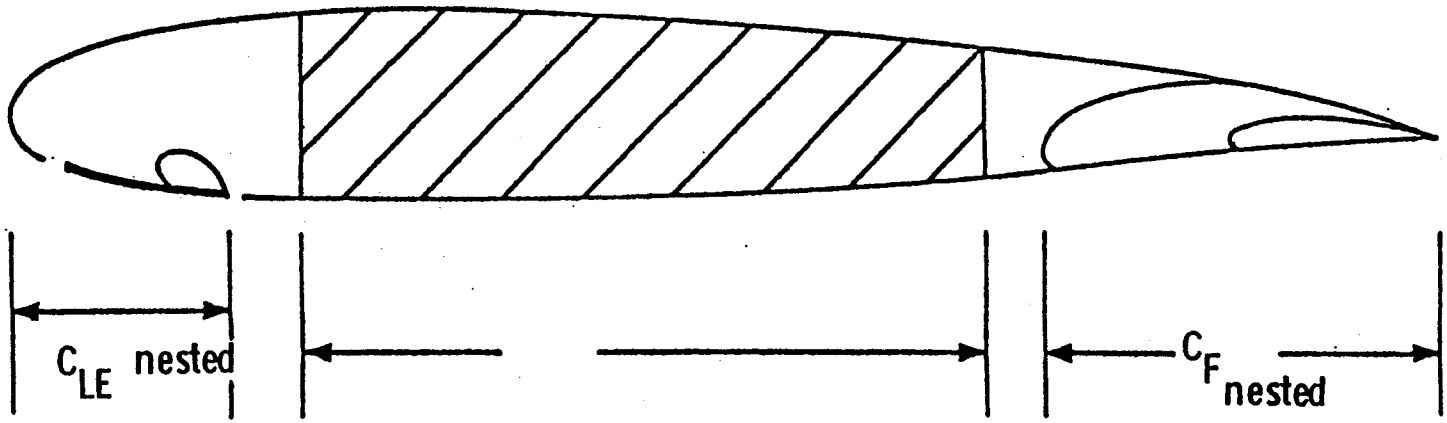

	$\frac{\text{nested } C_{LE}}{C}$	$\frac{C_{box}}{C}$	$\frac{\text{nested } C_F}{C}$
727	.19	.41	.32
737	.12	.45	.29
747	.15	.48	.27
7X7	.18	.53	.22

FIGURE 20
P6.38

Aerodynamic Technology	HIGH LIFT TECHNOLOGY	BOEING

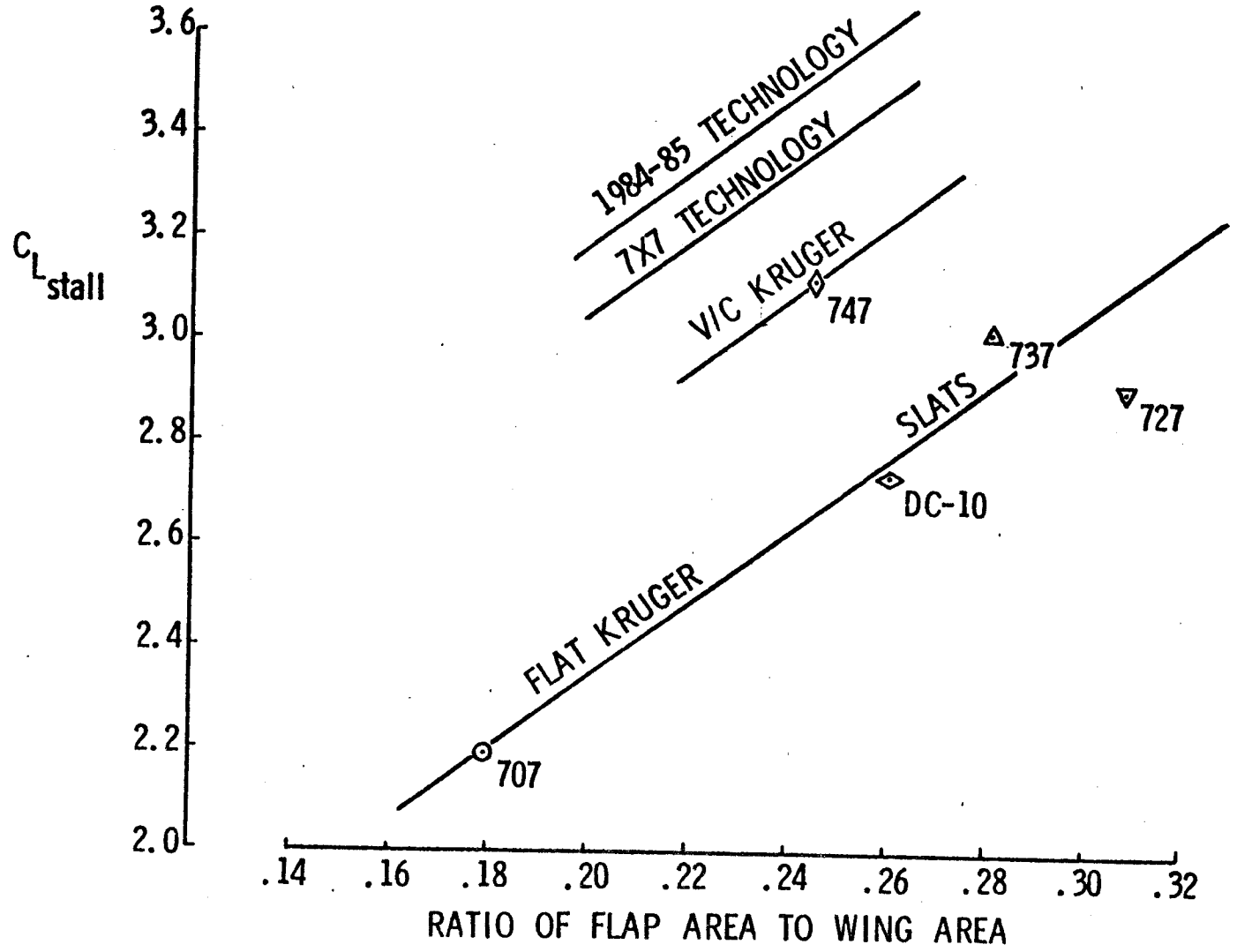

FIGURE 21
PG. 39

Aerodynamic Technology	HIGH LIFT TECHNOLOGY	BOEING

	777 ERA	747 ERA	7X7/7N7 ERA	1984-5 ERA
$C_{L_{stall}}$ WITH CONSTANT $\frac{S_{flap}}{S_{wing}}$	2.7	3.1	3.4	3.5
V_{app} WITH CONSTANT $\frac{S_{flap}}{S_{wing}}$	136	127	121	119
$\frac{S_{flap}}{S_{wing}}$ WITH CONSTANT $C_{L_{stall}}$	.305	.245	.210	.195

Figure 22
P6.40

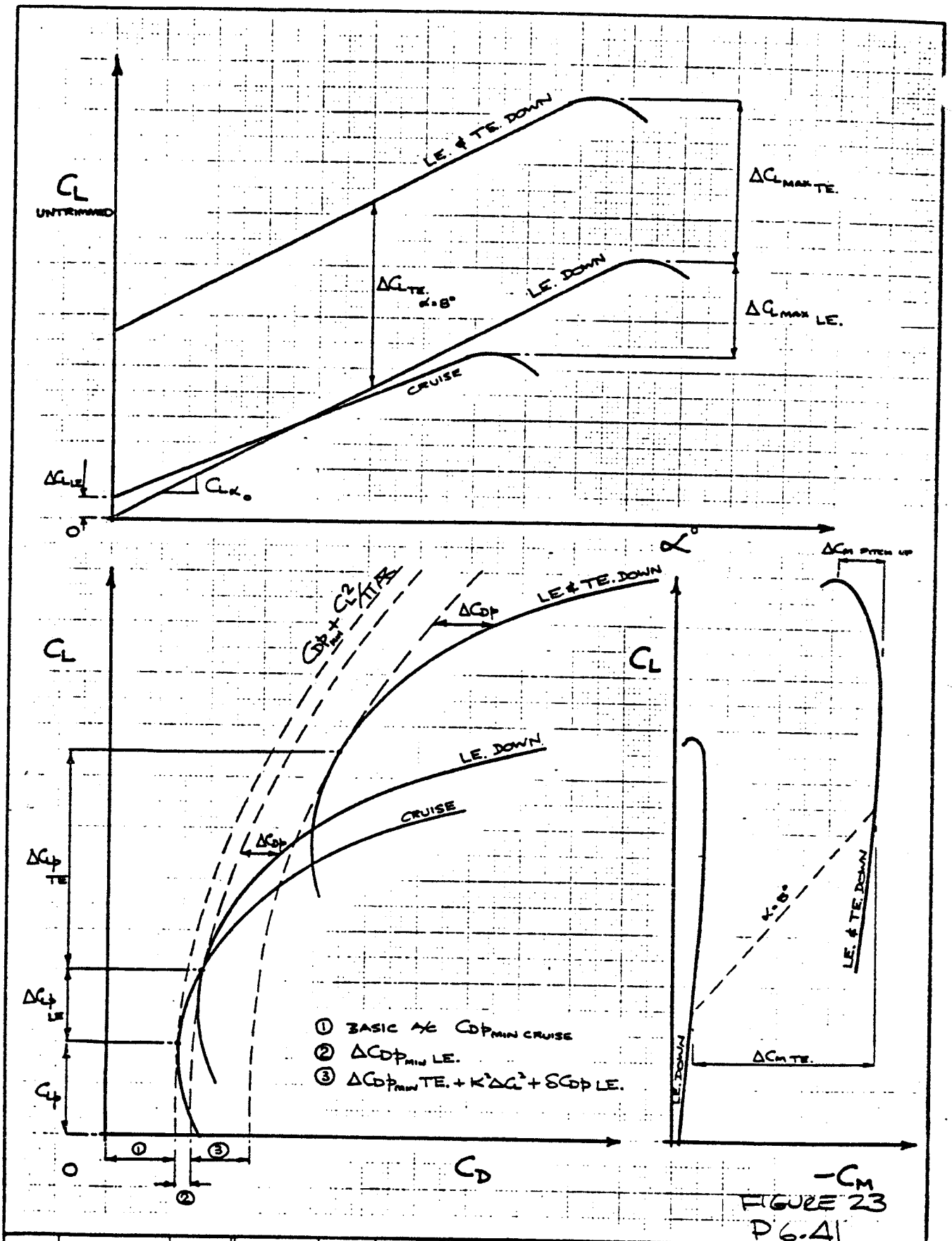

FIGURE 23
P6-41

CALC	M. GRANGER	FEB 7	REVISED	DATE	DEFINITION OF LE. & TE. FLAP INCREMENTS
CHECK					
APR					FIG.
APR					
					THE BOEING COMPANY PAGE

AD 481 C-R4

K-E ALBANENE 186L

P. 401

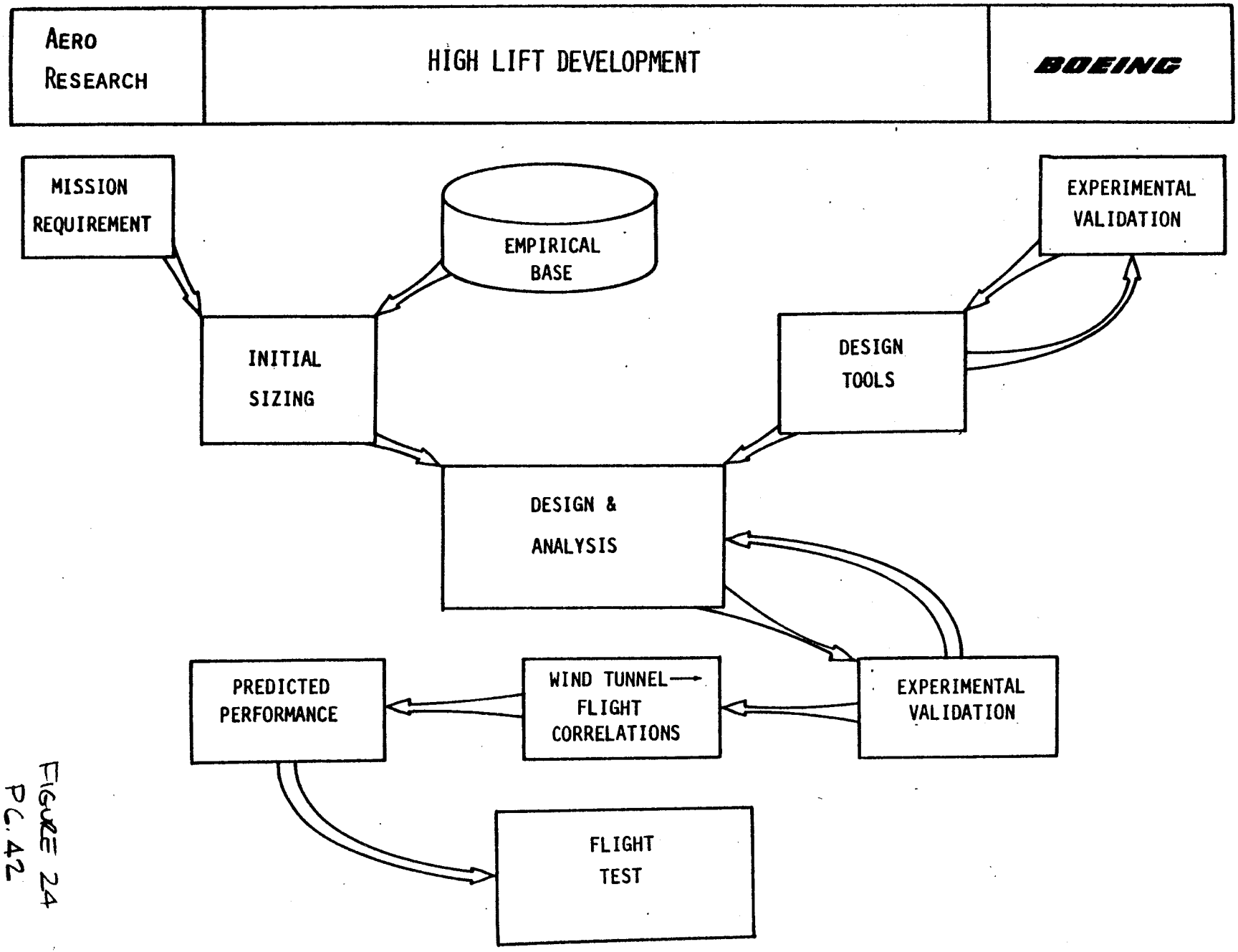

FIGURE 24
PG. 42

PRINCIPAL ELEMENTS IN WING DESIGN CYCLE

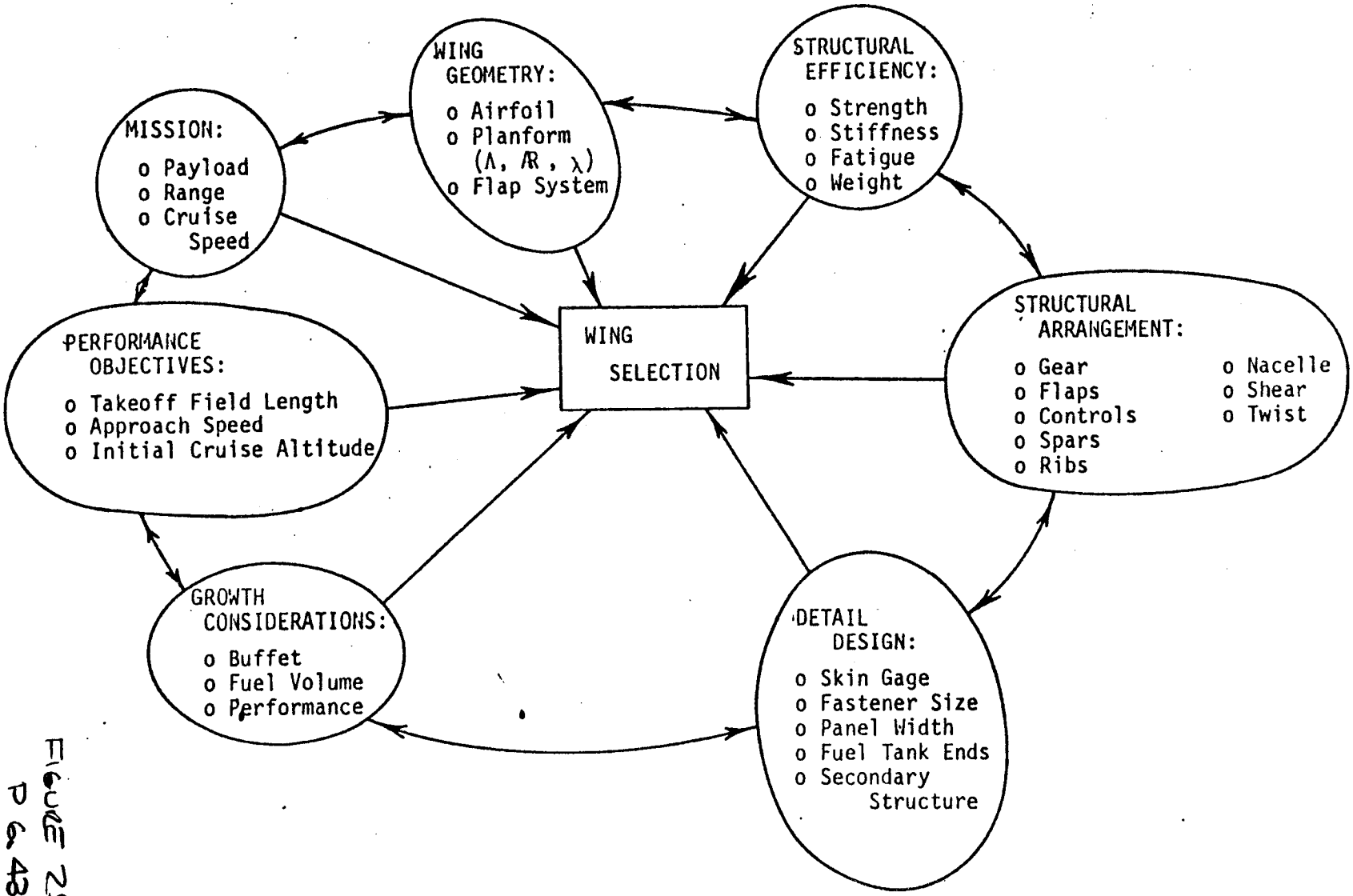

FIGURE 25
P 6 43

403

7X7
WING EVOLUTION

ANALYTICAL STUDIES	DOCUMENT SECTION	REF.	RESULTS
• PRELIMINARY DESIGN SPEED STUDY .70 ≤ M_{crv} ≤ .83	III.3	1	• M_{crv} = .78 • Ac/4 = 22°
• PRELIMINARY PLANFORM STUDY M_{crv} = .78, Λ = 22°, 8 ≤ AR ≤ 12		2	• ASPECT RATIO = 10
• TWIST STUDY	III.3c	17	• NEGLIGIBLE PENALTY FOR CONSTANT WING
• CRUISE SPEED/WING AREA TRADES		9	• WING LOADING, W/S ≈ 120 PSF • CRUISE ALTITUDE ≈ 33,000/37,000 FT.
• TRAILING EDGE FLAP TRADES M_{crv} = .78, R = 10, Λ = 22°	III.5	3, 4 & 10	• DOUBLE SLOTTED FLAP • REDUCED CHORDS AND TAPER MOTION
• CLASS II PLANFORM RESULTS M_{crv} = .78 and .82, Λ = 22° and 27° 8 ≤ R ≤ 11	III.4	4, 6 & 7	• CONFIRM ASPECT RATIO = 10
• GROWTH EVALUATION M_{crv} = .78, R = 10, Λ = 22°		5	• 3600 N.MI. RANGE CAPABILITY • FUEL VOLUME & CRUISE BUFFET MARGIN LIMIT GROWTH
• CRUISE SPEED REFINEMENTS R = 10 M_{crv}/M_{crit} = 22°/.787, 25°/.807, 27°/.827	III.6	11 & 12	• Ac/4 = 22°, R = 10 • M_{crit} = .827, M_{crv} = .80
• WING SWEEP EVALUATION M_{crit} = .827, Λ(c/c) = 25°/0.6, 27°/93, 30°/10.5	III.7	16	• Ac/4 = 30°
• WING AERODYNAMICAL SPACES WITH FIXED ENGINE/VARIABLE ENGINE Λ = 30°, R = 10, M_{crv} = .75, .78, .80		13	• PAYLOAD CAPABILITY INSENSITIVE TO ± 10% AREA FROM BASELINE
• STRUCTURAL ARRANGEMENT REFINEMENTS Λ = 32°, b_o = 150 FT.	III.8	14	• ALTERNATE PLANFORM FOR STRUCTURAL EFFICIENCY • Λ = 30°, AR = 9.4
• AIRFOIL AFT CAMBER ANALYSIS Λ = 32°, R = 10, M_{crv} = .80			• AFT CAMBER WEIGHT PENALTY SMALL (STUDY NOT RELEASED)
• WING AREA SENSITIVITY - MEDIUM RANGE MISSION Λ = 30°, R = 10, M_{crv} = .80, FIXED ENGINE	III.9A	15	• APPROACH SPEED LIMITS MINIMUM AREA • +5% WING AREA (FOR GROWTH) HAS MINIMAL PENALTY
• ULTIMATE FINAL GROWTH CAPABILITY Λ = 30°, R = 10, M_{crv} = .80 (Wing area and engine growth variable)	III.9B	18	• $R_{4300/4700}$ N.MI. RANGE CAPABILITY WITH BASELINE WING, 5000 NMI WITH +5% AREA • BUFFET MARGIN AFTER TAKEOFF CRITICAL

NOTE:
• Boeing studies discussed in technical note.

• 4300 N.MI. range with standard body
4700 N.MI. range with short body.

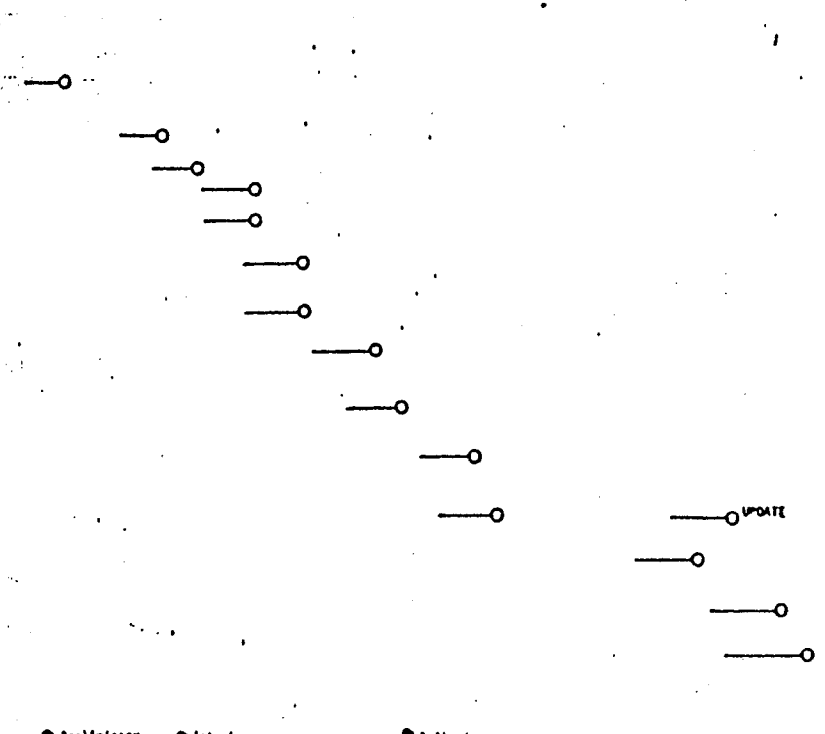

FIGURE 26
PG. 44

404

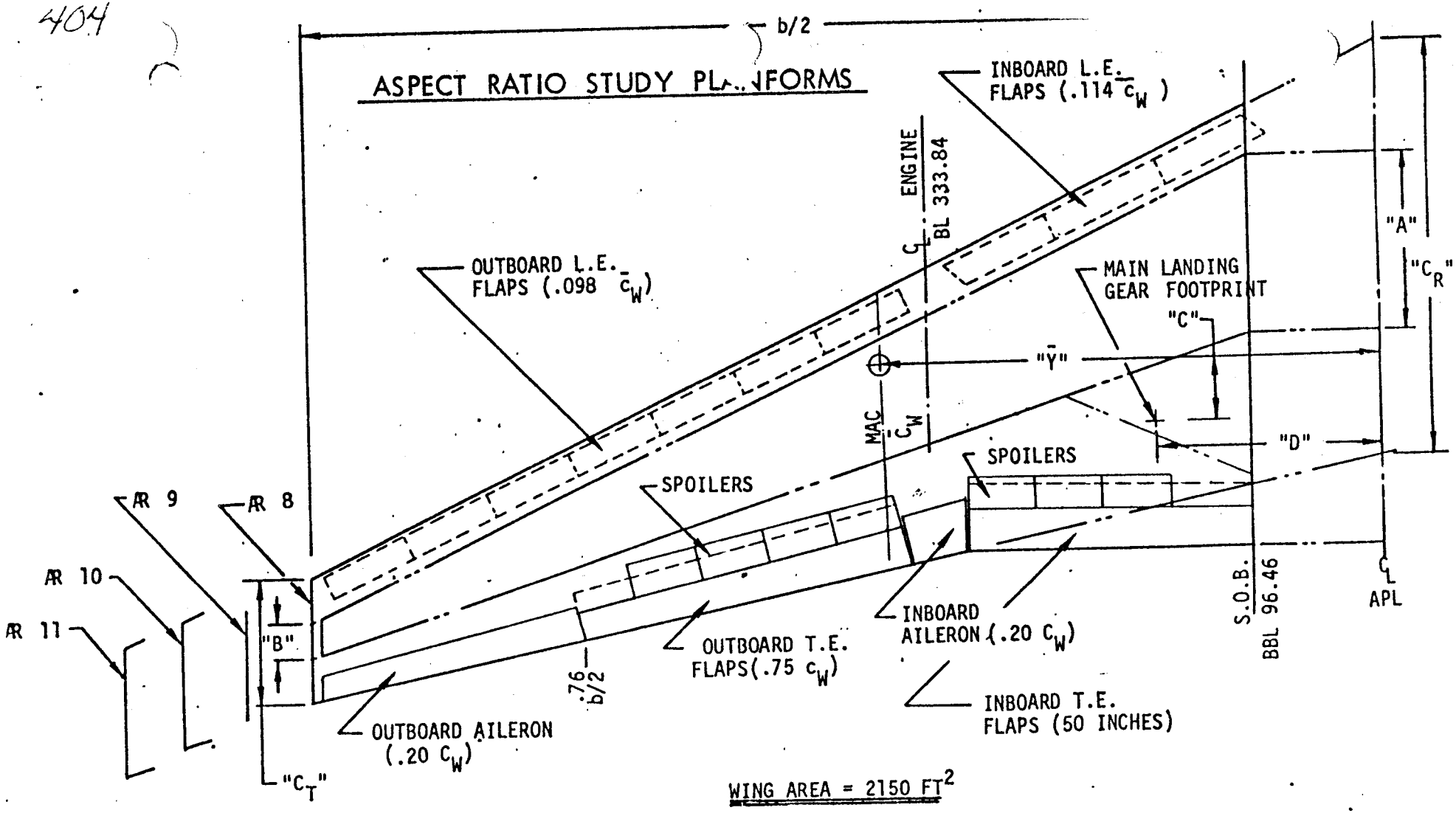

WING AREA = 2150 FT^2

ASPECT RATIO	TAPER RATIO	ROOT CHORD	MEAN AERODYNAMIC CHORD		WING BOX ROOT CHORD	WING BOX TIP CHORD	MAIN LANDING GEAR LOCATION		SPAN
AR	λ	"C_R"	"$\bar{c}_w$"	"$\bar{Y}$"	"A"	"B"	"C"	"D"	b/2
8	.300	302.5	215.7	323.0	130.0	26.0	44	168.0	787.0
9	.3345	278.0	200.86	348.5	130.0	26.0	52	168.0	834.5
10	.353	259.43	188.87	369.5	130.0	26.0	53	168.0	880.0
11	.367	245.03	179.78	390.0	130.0	26.0	56	168.0	922.7

Figure 27
P.C.45

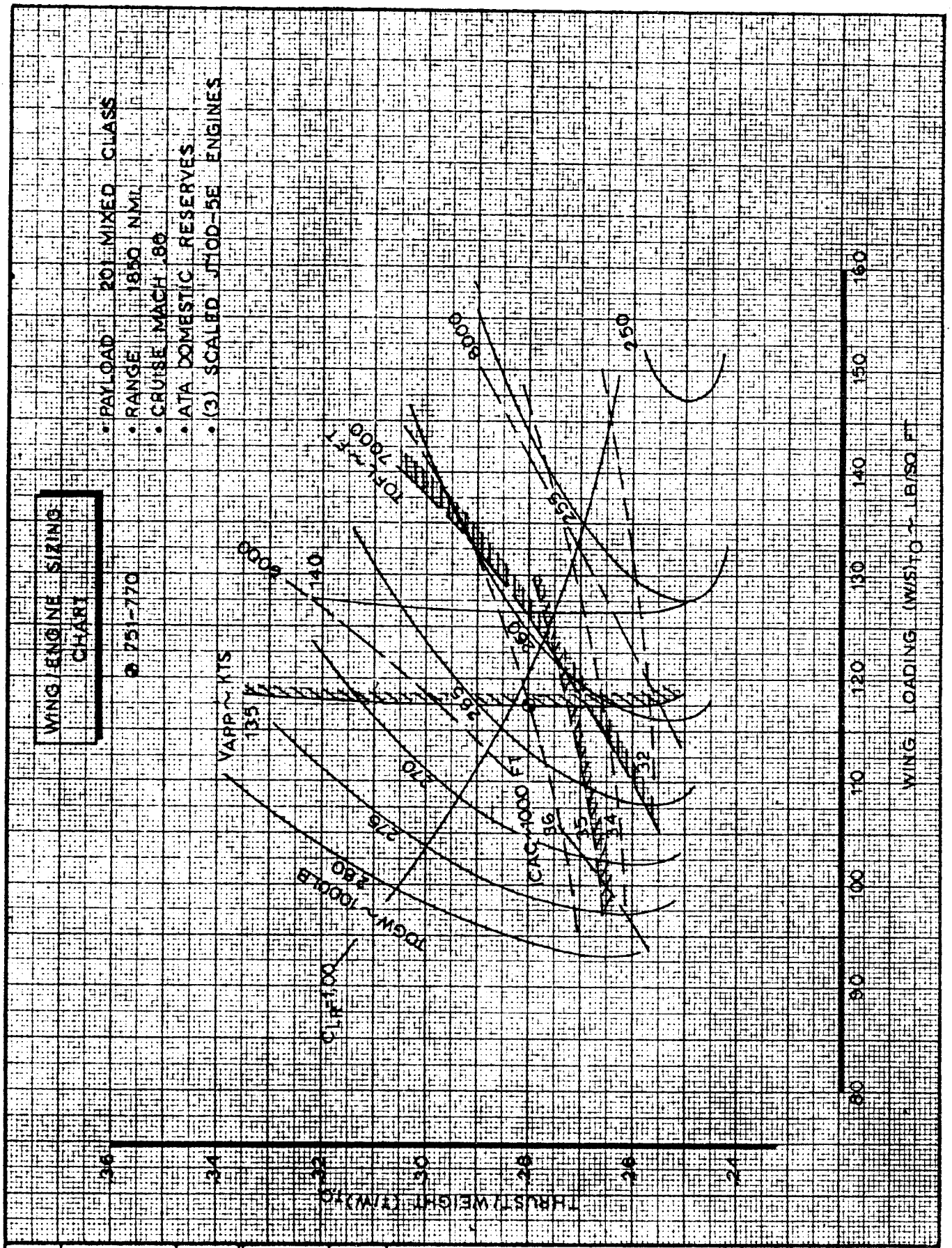

CALC			REVISED	DATE	FIG 28 P6.46
CHECK					
APR					
APR					THE BOEING COMPANY
					PAGE

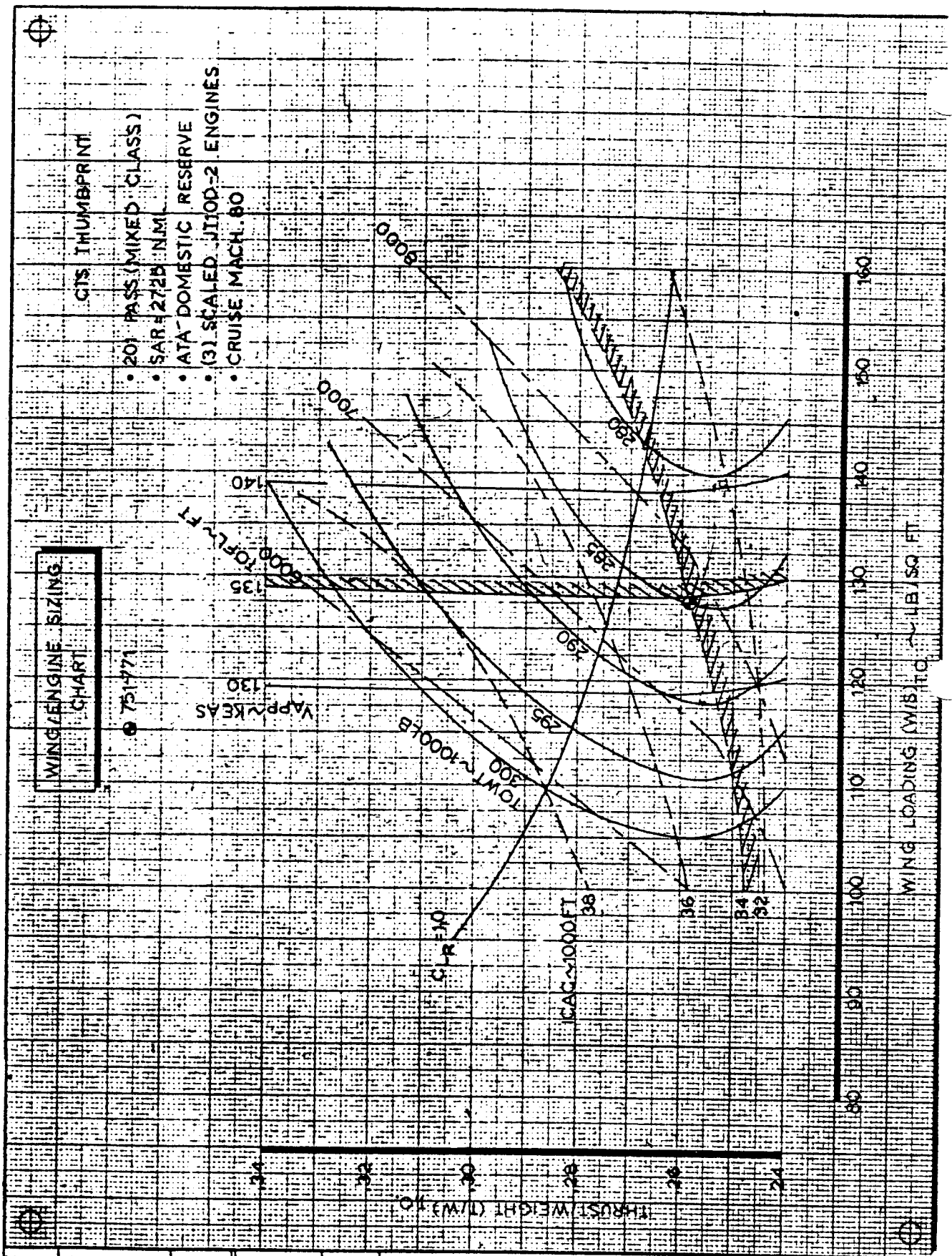

			REVISED	DATE
CALC	S Kimmo	3/13/75		
CHECK	[signature]	3/14/75		
APR				
APR				

FIGURE 29
PG. 47

THE BOEING COMPANY

D1 4100 3240

K&E ALBANENE 1961

FLAP SYSTEMS STUDIED

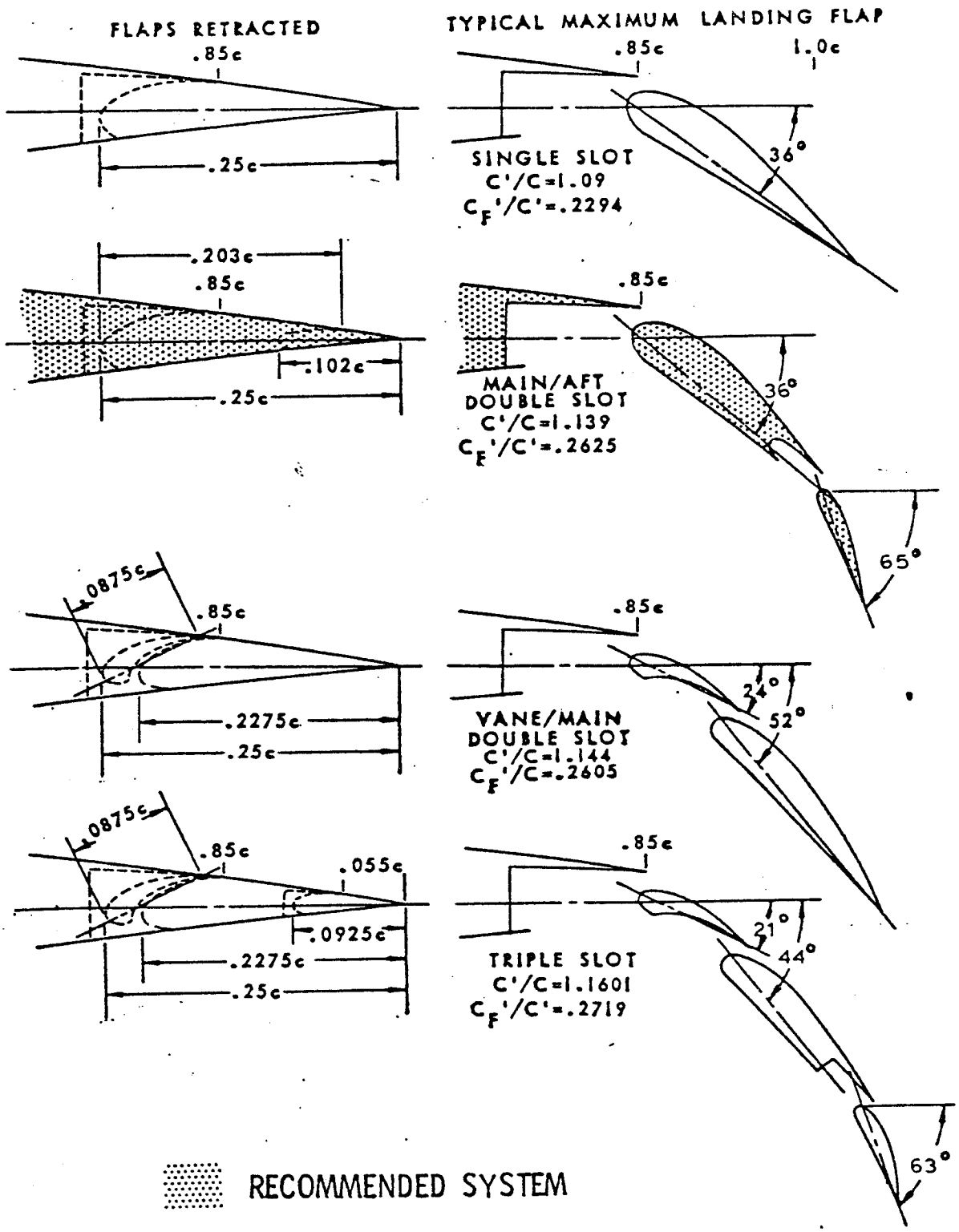

FIGURE 30
PG. 48

407

LANDING PERFORMANCE
FLAP ENVELOPES

751-701-10

- $\Lambda_{C/4} = 22°$, AR = 10
- C.G. @ .06 c
- CURVED LE FLAPS; .105 c INBD; .095 c OUTBD
- UNDERWING NACELLES
- 36% b/2 TE FLAPS WITH 5.4% b/2 AILERON CUTOUTS
- NESTED FLAP CHORD = .25 c
- COVE @ .82 c

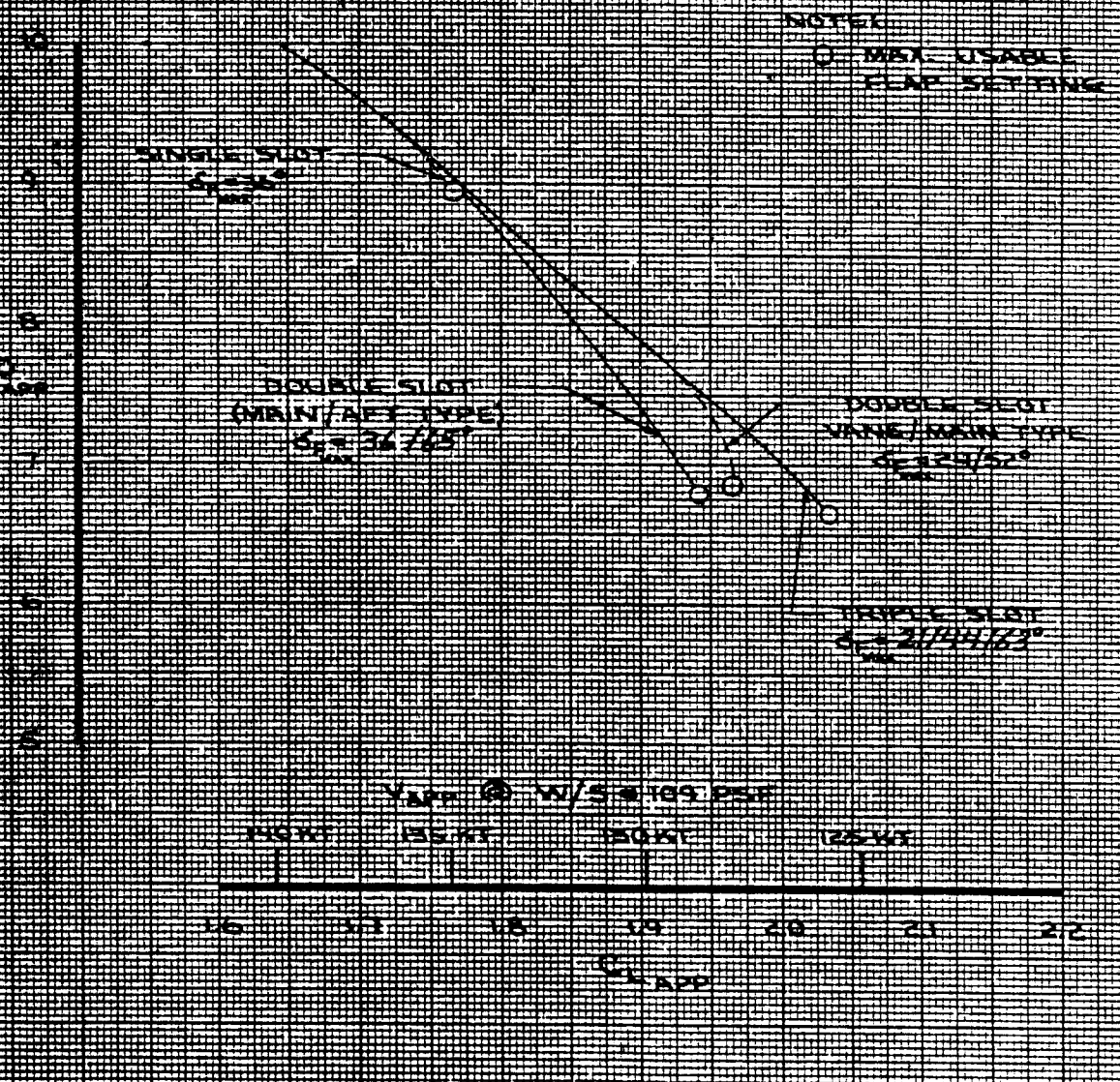

CALC	R. OWEN	3/12/74	REVISED	DATE
CHECK				
APR				
APR				
cruce	SD	5/27/74		

FIGURE 31
P6.49

.THE BOEING COMPANY

PAGE

408

TRAILING EDGE FLAP TRADES

Model 751-721/-722
S_W = 2,250 Ft.^{2}
$\Lambda c/4 = 22^o$
AR = 10

WEIGHT/DRAG COMPARISON

TABLE 7A

FLAP TYPE	INSTALLATION WEIGHT ΔOEW LBS.	CRUISE DRAG ΔC_D~%
Single Slot	Base	Base
Double Slot		
Main/Aft	630	1%
Vane/Main	1080	1%
Triple Slot	1680	1%

@ MAX. LDG. FLAP

APPROACH SPEED/NOISE/ATTITUDE COMPARISON

TABLE 7B

FLAP TYPE	δ_F ~DEG	APPROACH SPEED ~KTS.	APPROACH NOISE (ΔFAR~EPNdB)	[1] BODY ATTITUDE θ_B~DEG
Single Slot	36	135	-8.2	4.4
Double Slot				
Main/Aft	36/65	129	-5.2 [2]	1.0 [2]
Vane/Main	24/52	128	-5.0 [2]	2.1 [2]
Triple Slot	21/44/63	124	-5.0 [2]	1.6 [2]

[1] Maximum allowable body attitude $\theta_B = 4.5^o$, for adequate pilot vision and flare margin.

[2] At constant approach speed of 135 knots (minimum for single slot), noise/attitude is -8.2 ΔEPNdB/4.4^o.

TABLE 7

FIGURE 32
P 6.50

GLIDE SLOPE CAPABILITY

$V_{REF} = 1.3\ V_S$
MAX. FLAP ANGLE

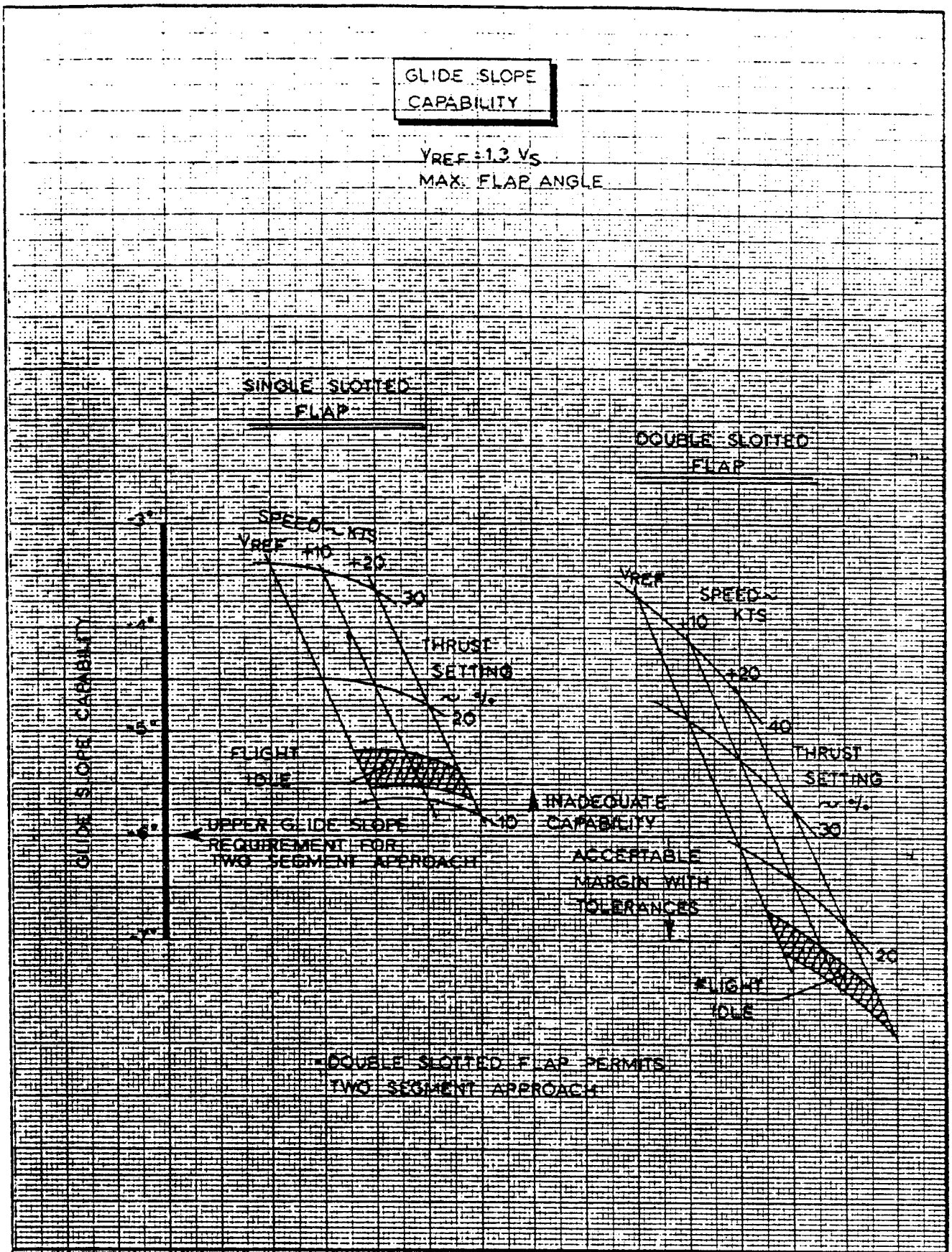

			REVISED	DATE
CALC				
CHECK				
APR				
APR				

FIGURE 33
P6-51a

THE BOEING COMPANY

PAGE

D1 4100 3240

K-E ALBANENE 1964 TRACING PAPER

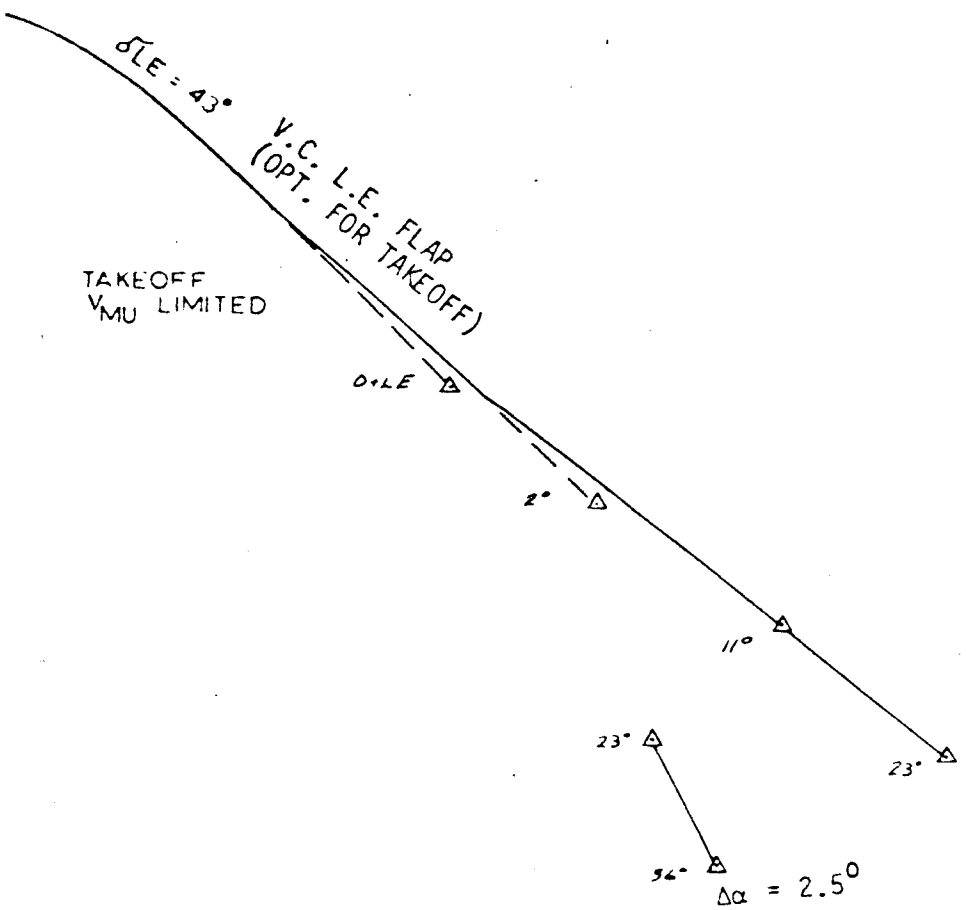

FIG 34 O/L
RED

PG. 516

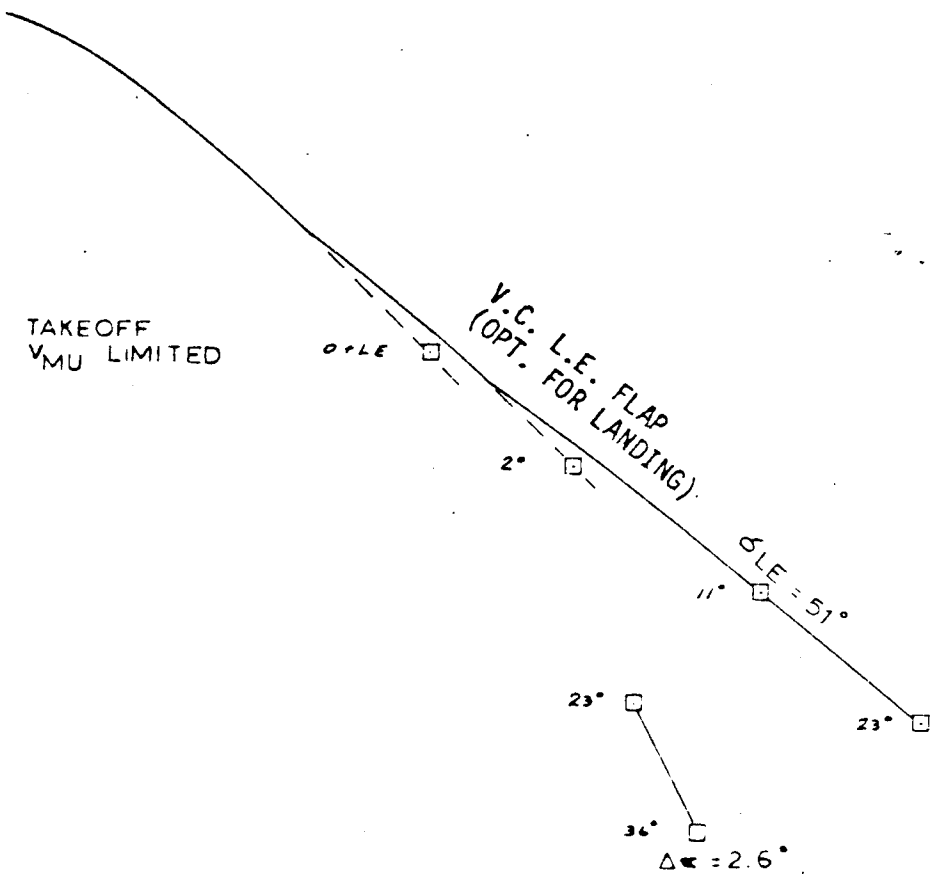

FIG 34 O/L
GREEN

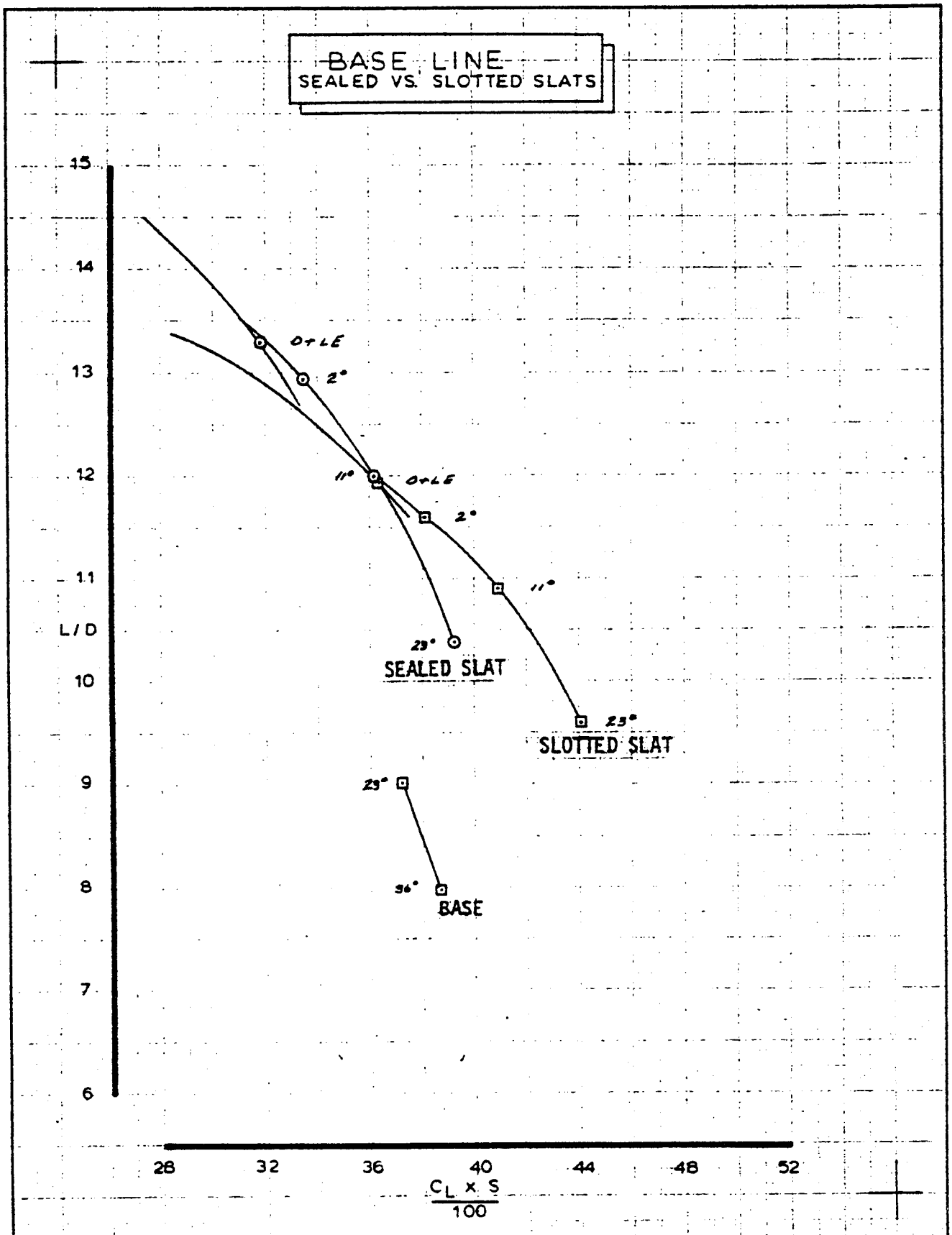

CALC			REVISED	DATE	FIGURE 34 PG. 52
CHECK					
APR					
APR					THE BOEING COMPANY
					PAGE

D1 4100 3240 ORIG 3/71

J15-047

SINGLE-VS DOUBLE-SLOT T.E.

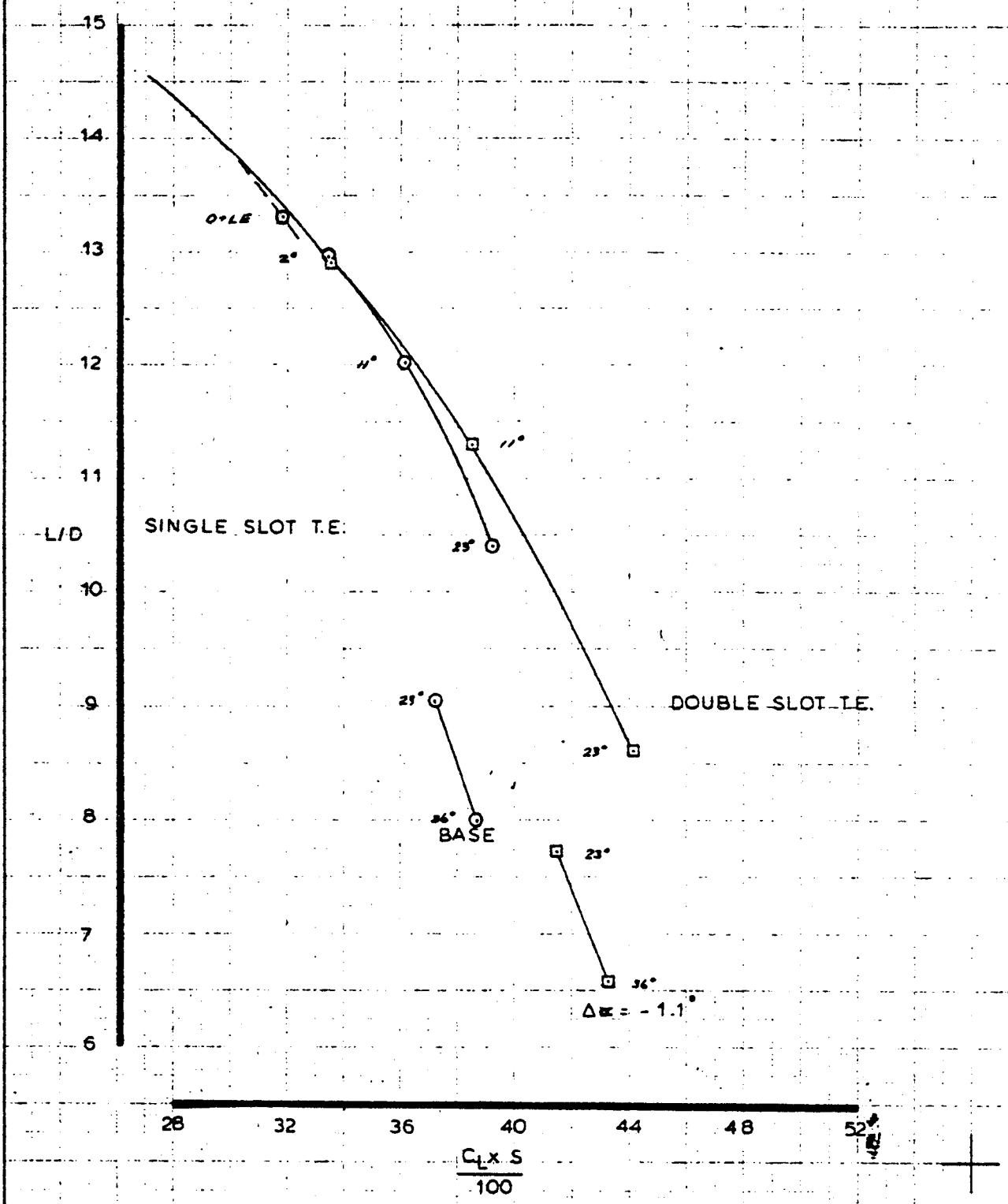

CALC			REVISED	DATE	FIGURE 35 P 6.53 a	
CHECK						
APR						
APR						
					THE BOEING COMPANY	PAGE

D1 4100 3240 ORIG 3/71

J15-047

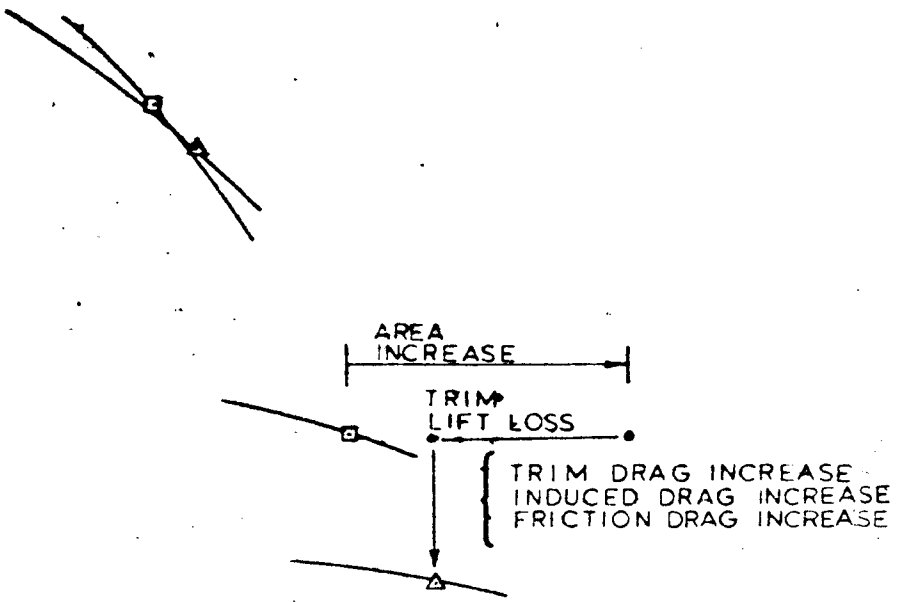

FIG 36 O/L
GREEN

P6.536

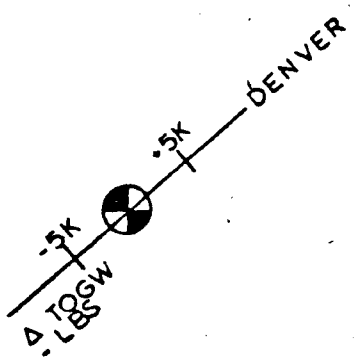
DENVER
+5K
-5K
Δ TOGW - LBS

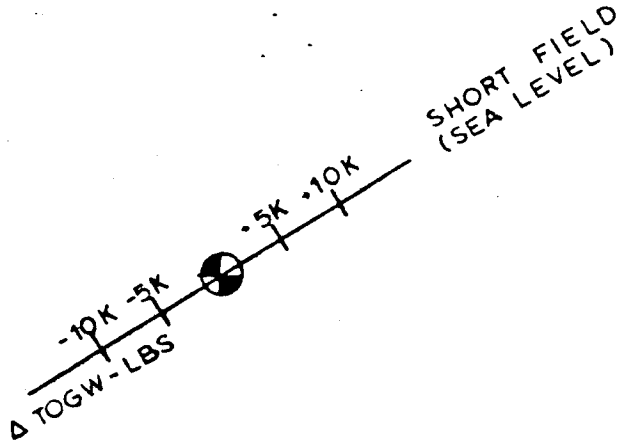
SHORT FIELD (SEA LEVEL)
+5K +10K
-10K -5K
Δ TOGW - LBS

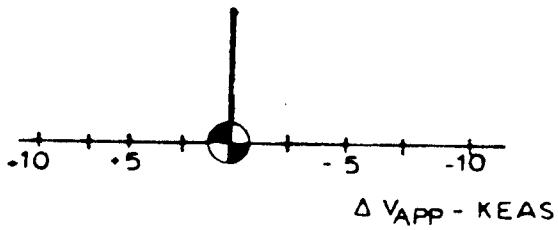
-10
+5
-5
-10
Δ VAPP - KEAS

FIG 36 C/L
RED

FOWLER MOTION-TRADE
CONSTANT CHORD FLAP

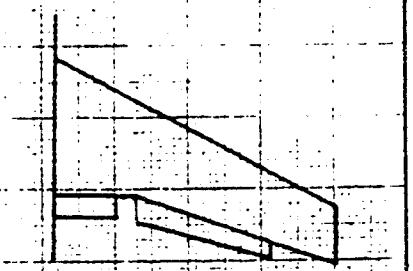

COVE T.E.

.8C .9C 1.0C

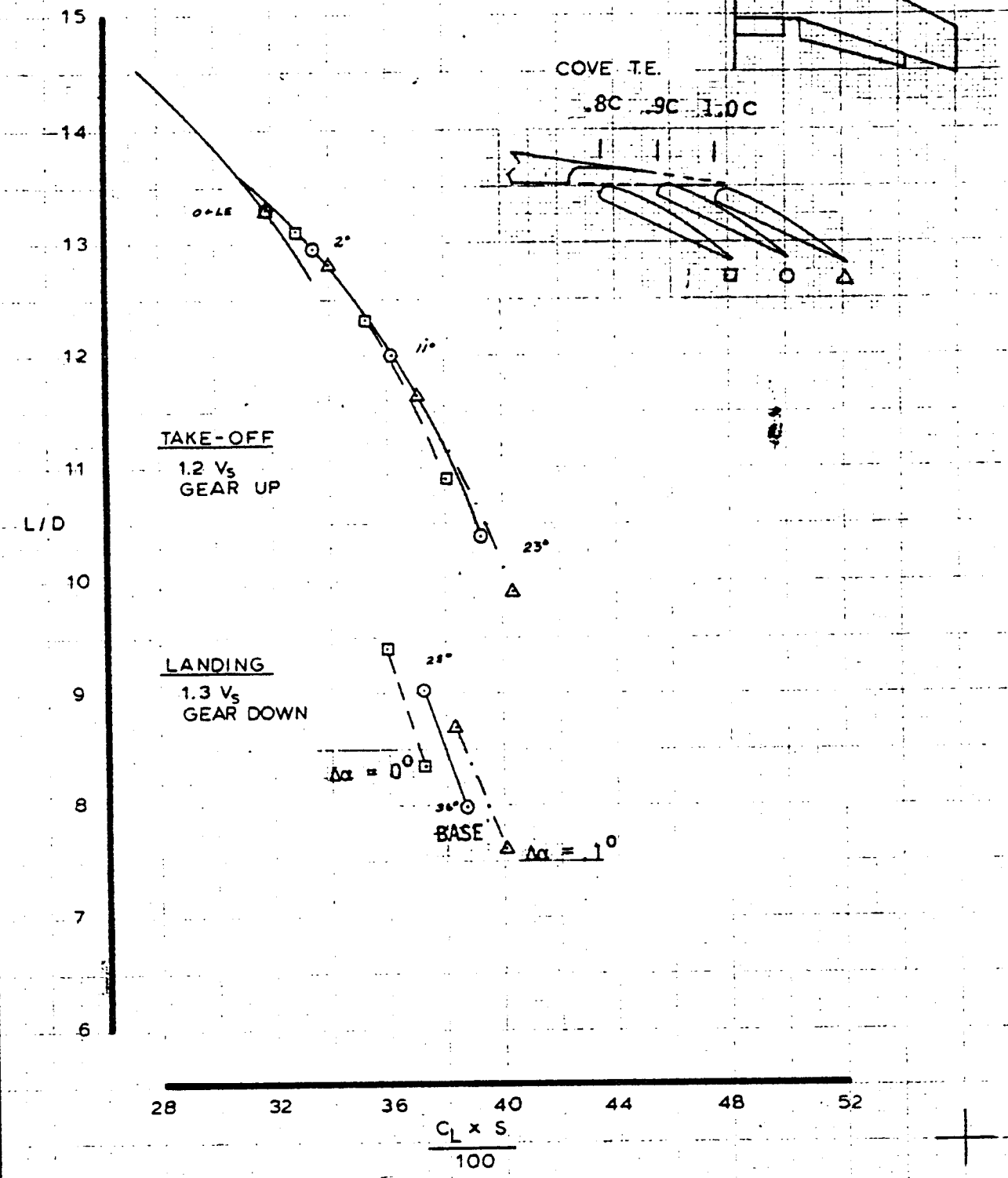

CALC			REVISED	DATE	FIGURE 36 P6.54
CHECK					
APR					
APR					THE BOEING COMPANY
					PAGE

D1 4100 3240 ORIG 3/71

J15-047

FLAP CHORD STUDY
CONSTANT COVE

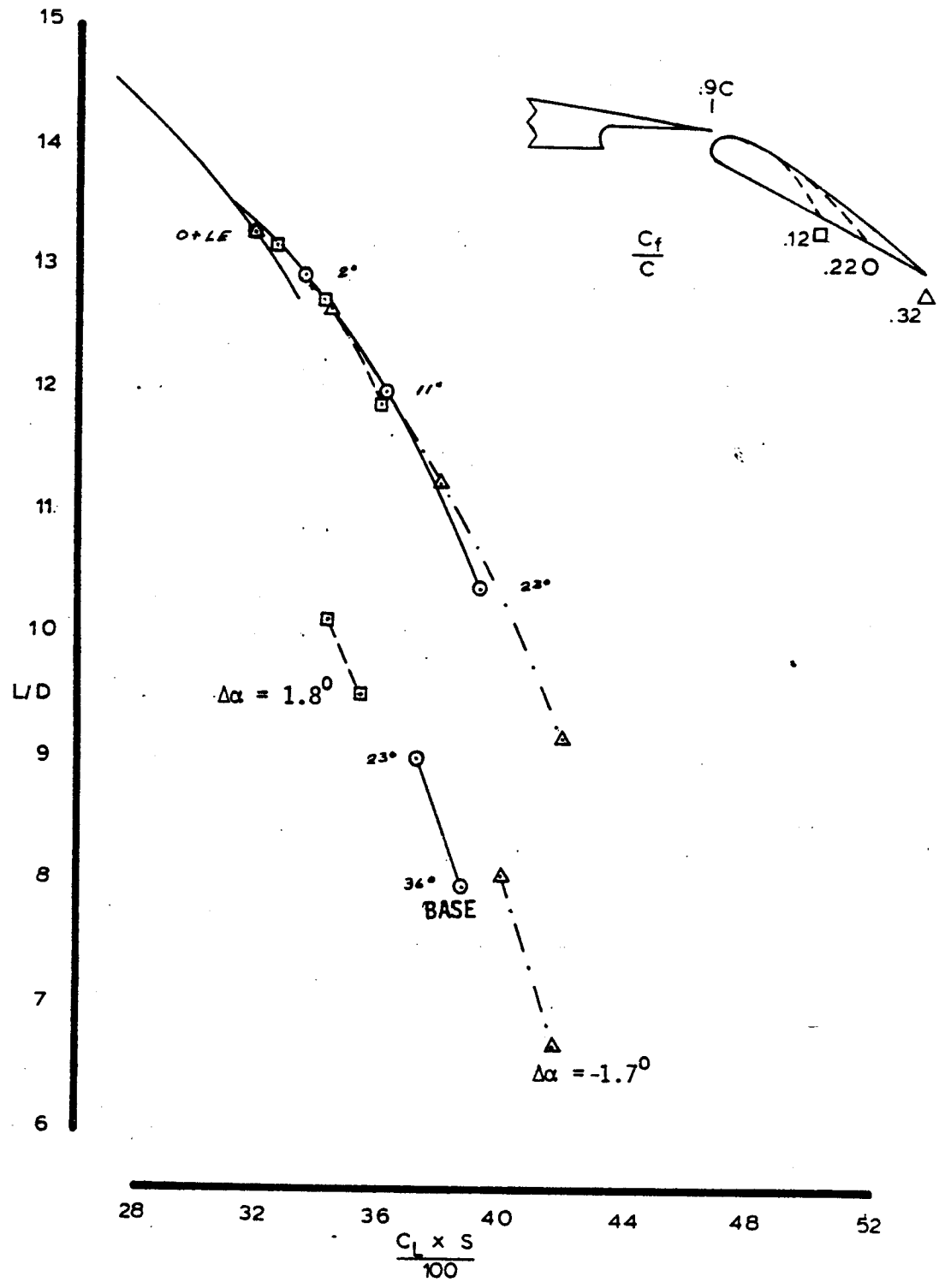

CALC			REVISED	DATE	FIGURE 37 PG.55
CHECK					
APR					
APR					
					THE BOEING COMPANY

PAGE

D1 4100 3240 ORIG 3/71

J15-047

H.S. AILERON CUT-OUT OPTION

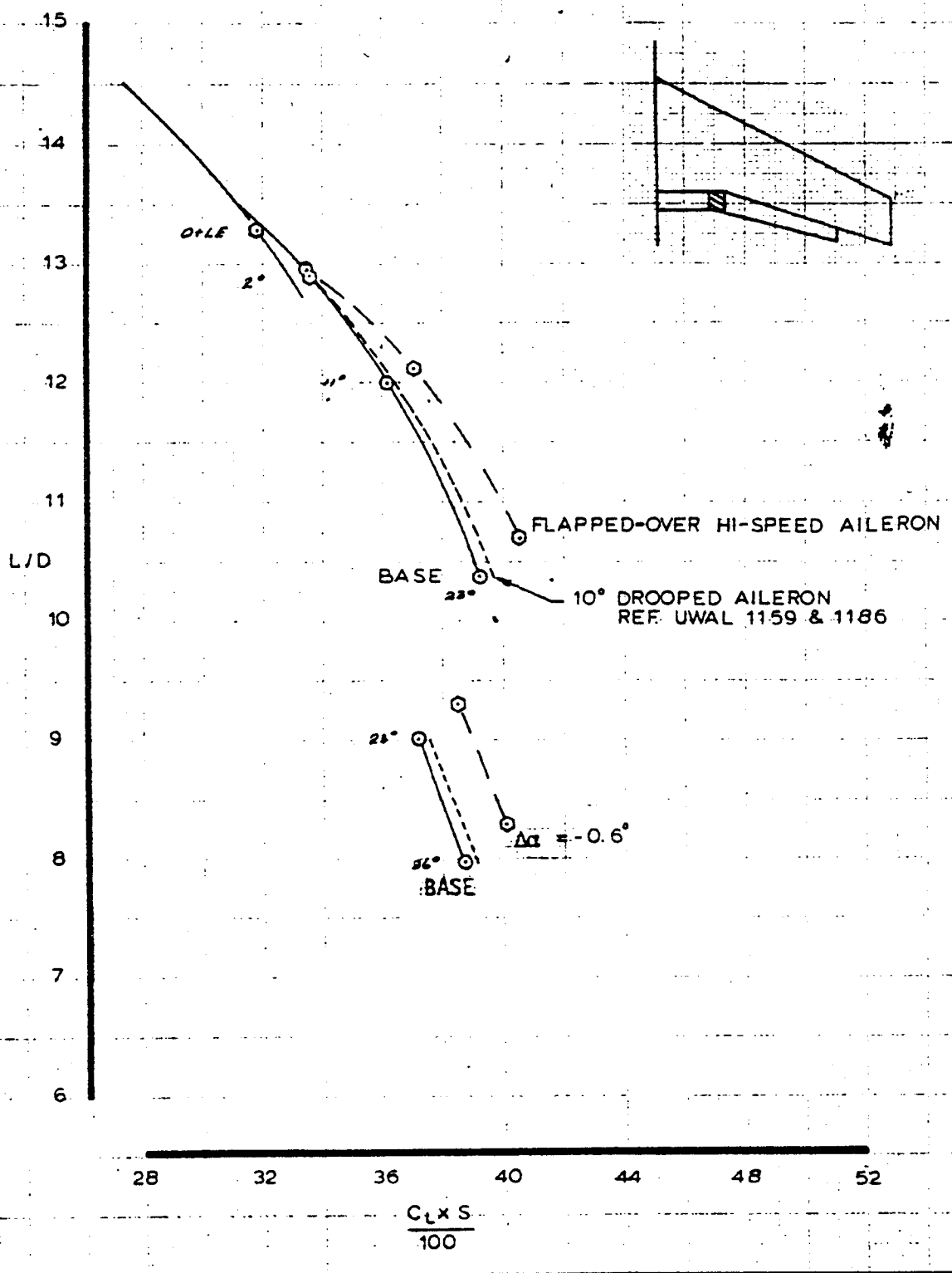

CALC			REVISED	DATE	FIGURE 38 PG. 56	
CHECK						
APR						
APR					THE BOEING COMPANY	PAGE

D1 4100 3240 ORIG 3/71

J15-047

414

H.S. & L.S. AILERON DROOP OR FLAP

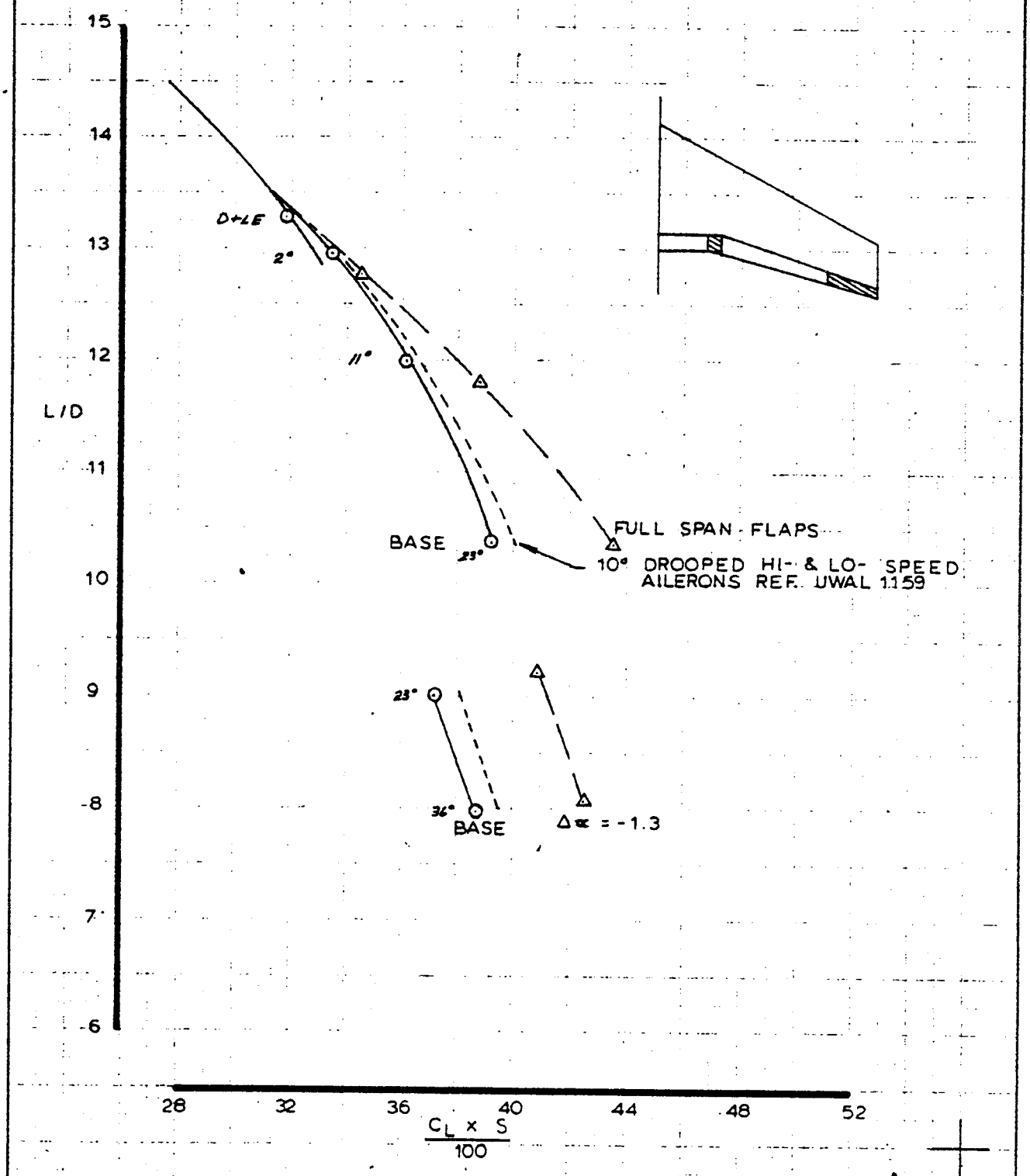

CALC			REVISED	DATE	FIGURE 39 P6.57
CHECK					
APR					
APR					
					THE BOEING COMPANY

PAGE

420

WING SPAN TRADE

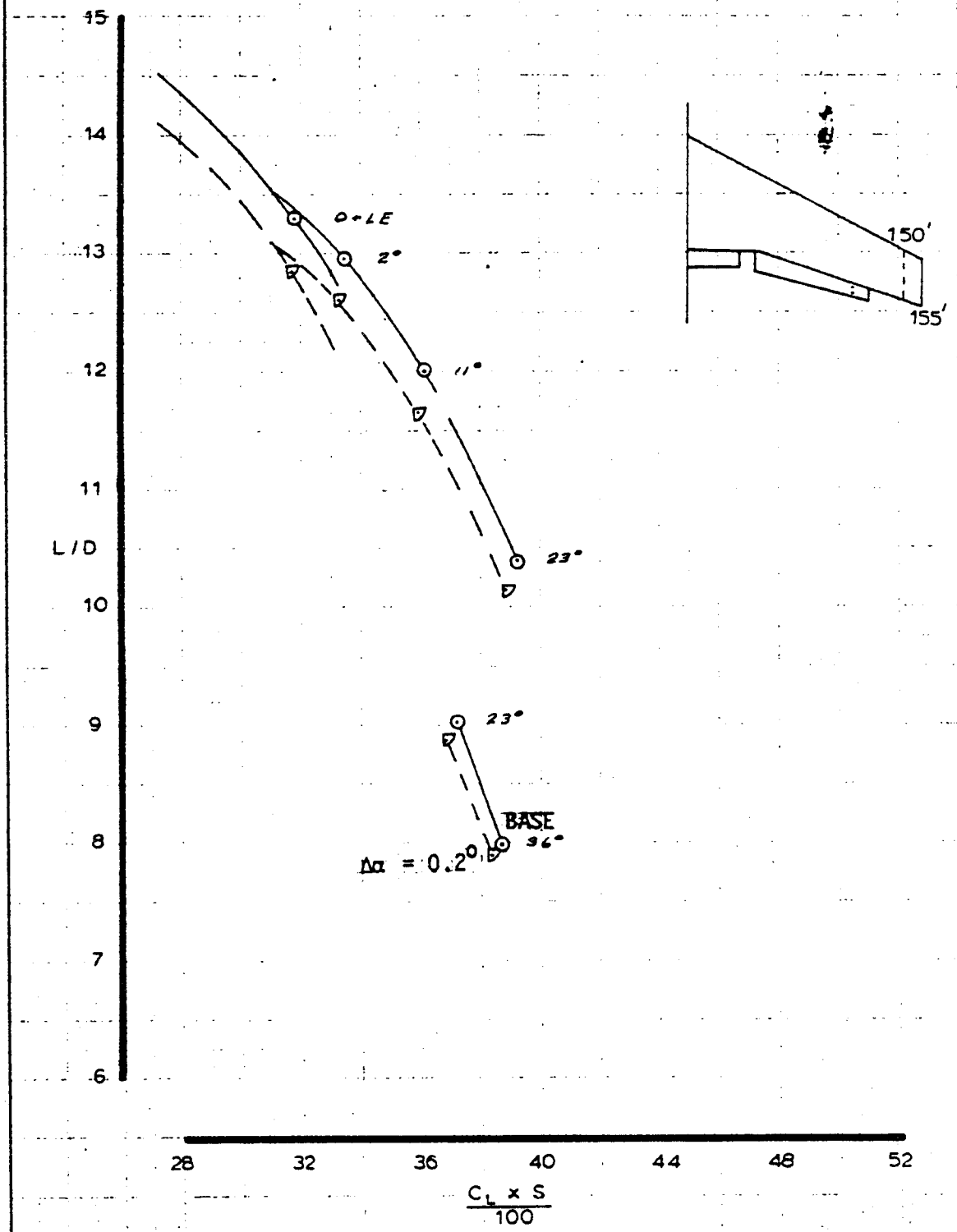

CALC			REVISED	DATE	FIGURE 40 P6.58
CHECK					
APR					
APR					THE BOEING COMPANY
					PAGE

D1 4100 3240 ORIG 3/71

J15-047

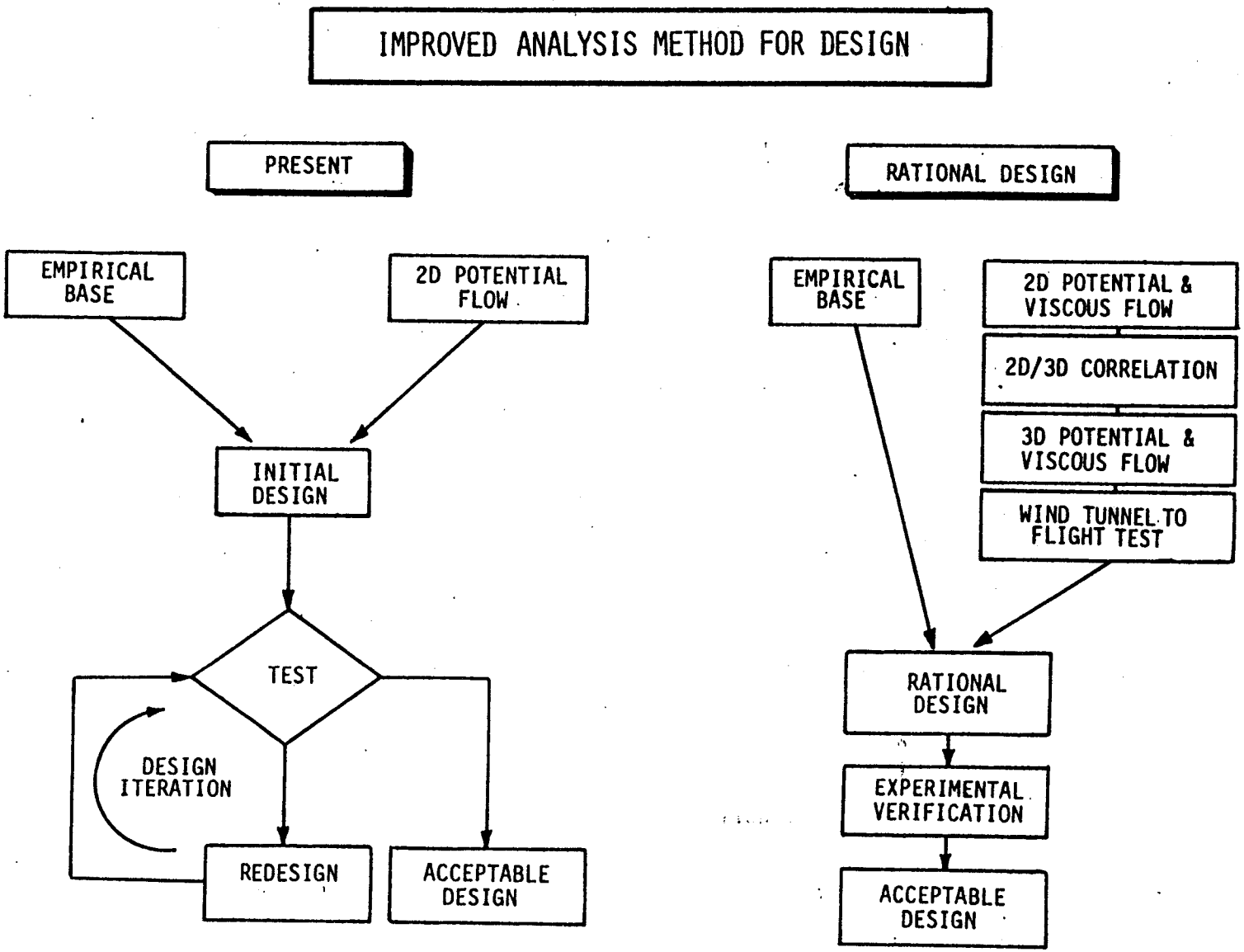

FIGURE 41
P6.59

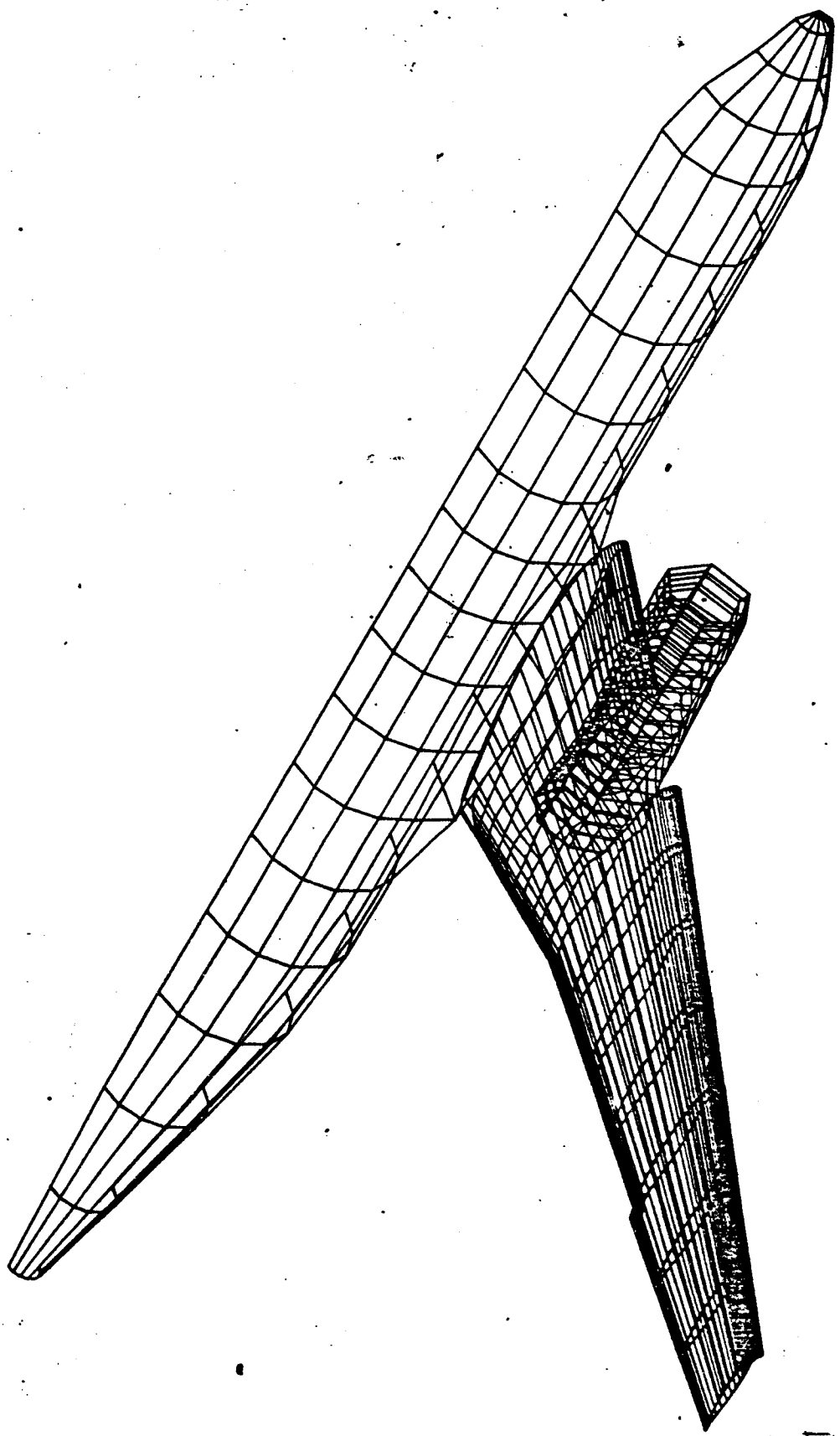

SOURCE PANEL SINGULARITIES

FIGURE 42
PG. 60

4/23

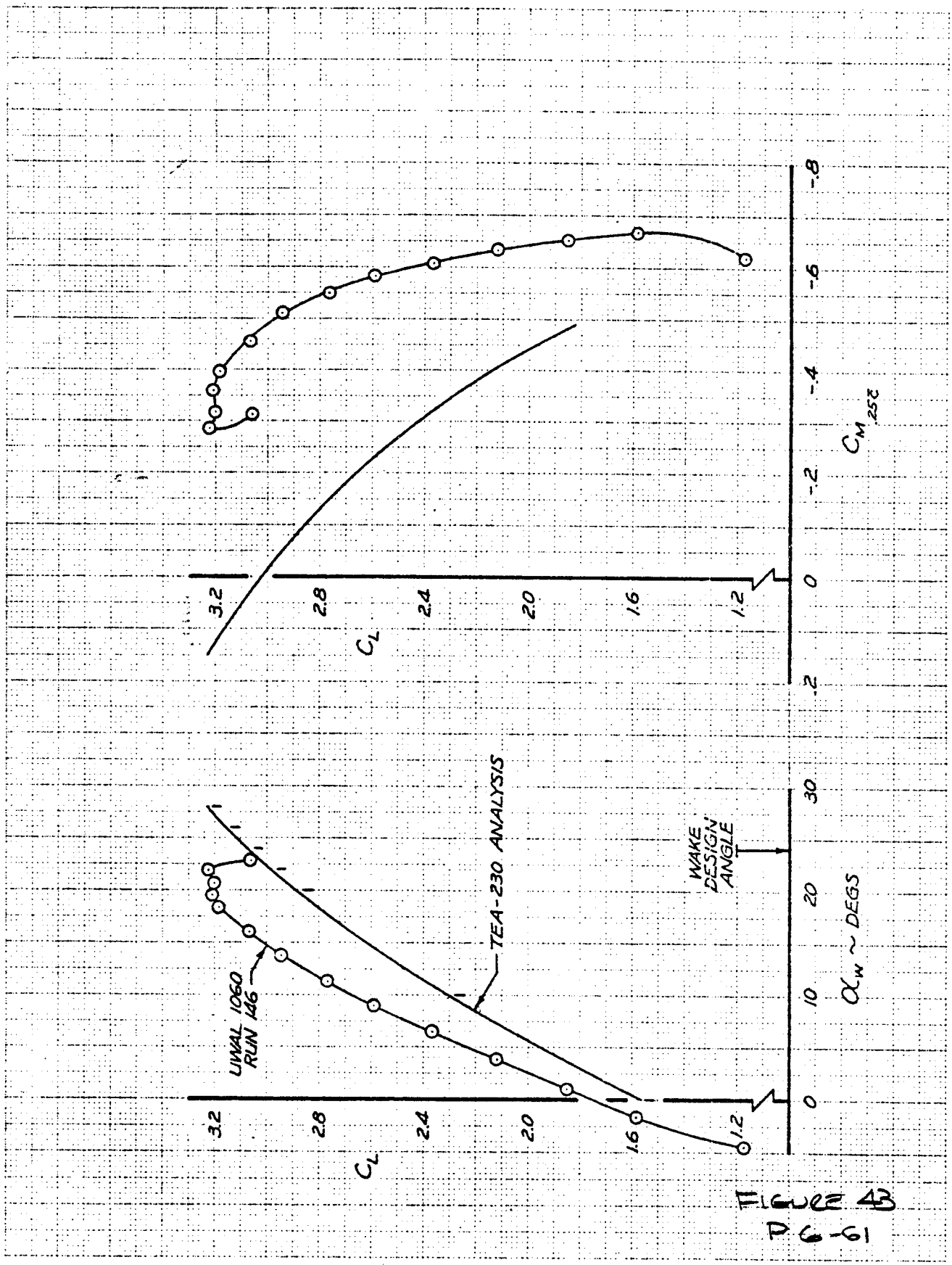

FIGURE 43
P 6-61

CALC	VAN DEVENDER 4-30-75	REVISED		DATE	QSH LANDING CONFIGURATION ~ COMPARISON OF THEORETICAL AND EXPERIMENTAL LIFT AND PITCHING MOMENT
CHECK					
APR					
APR					THE BOEING COMPANY
					PAGE

424

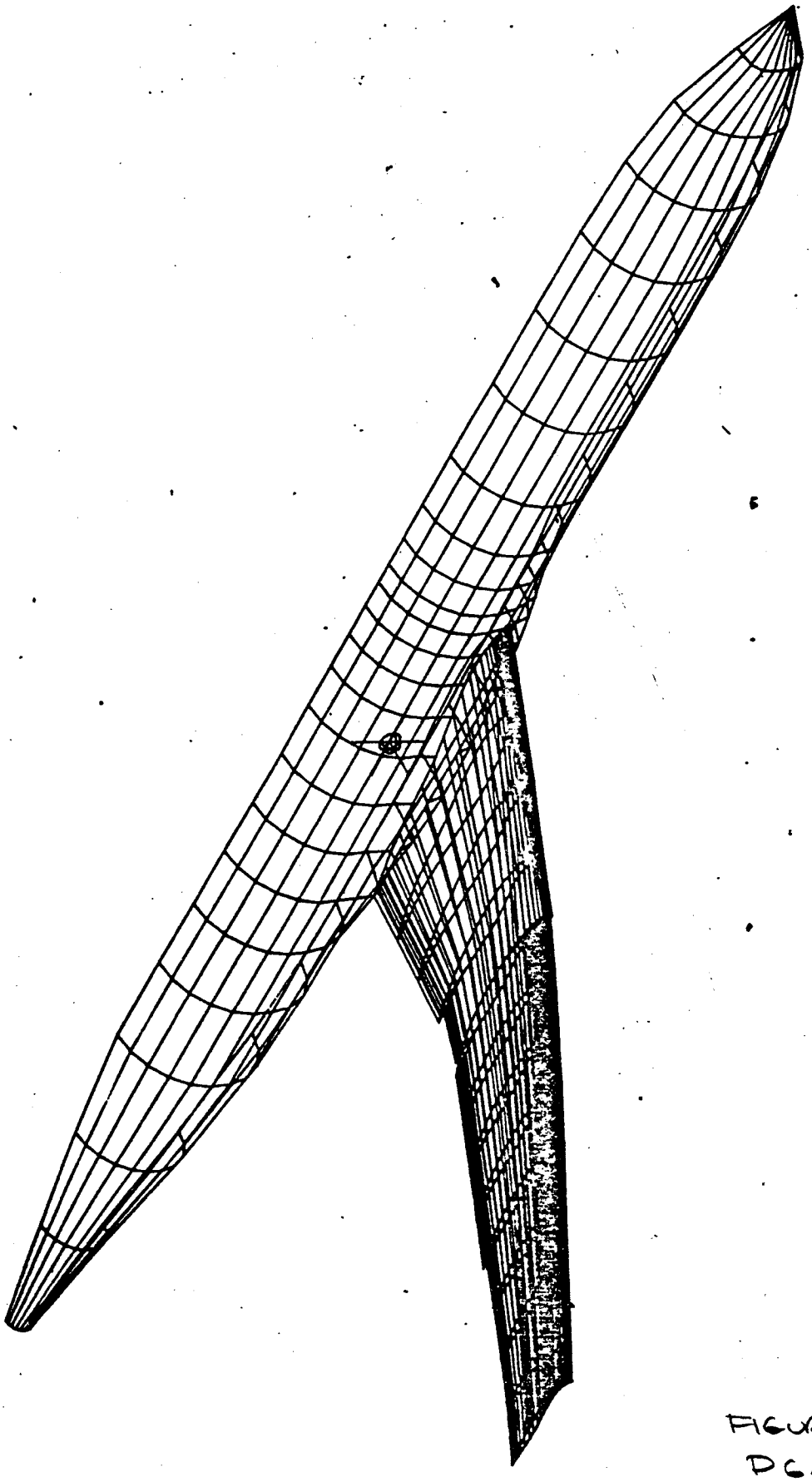

SOURCE PANEL SINGULARITIES

FIGURE 44
DC.62

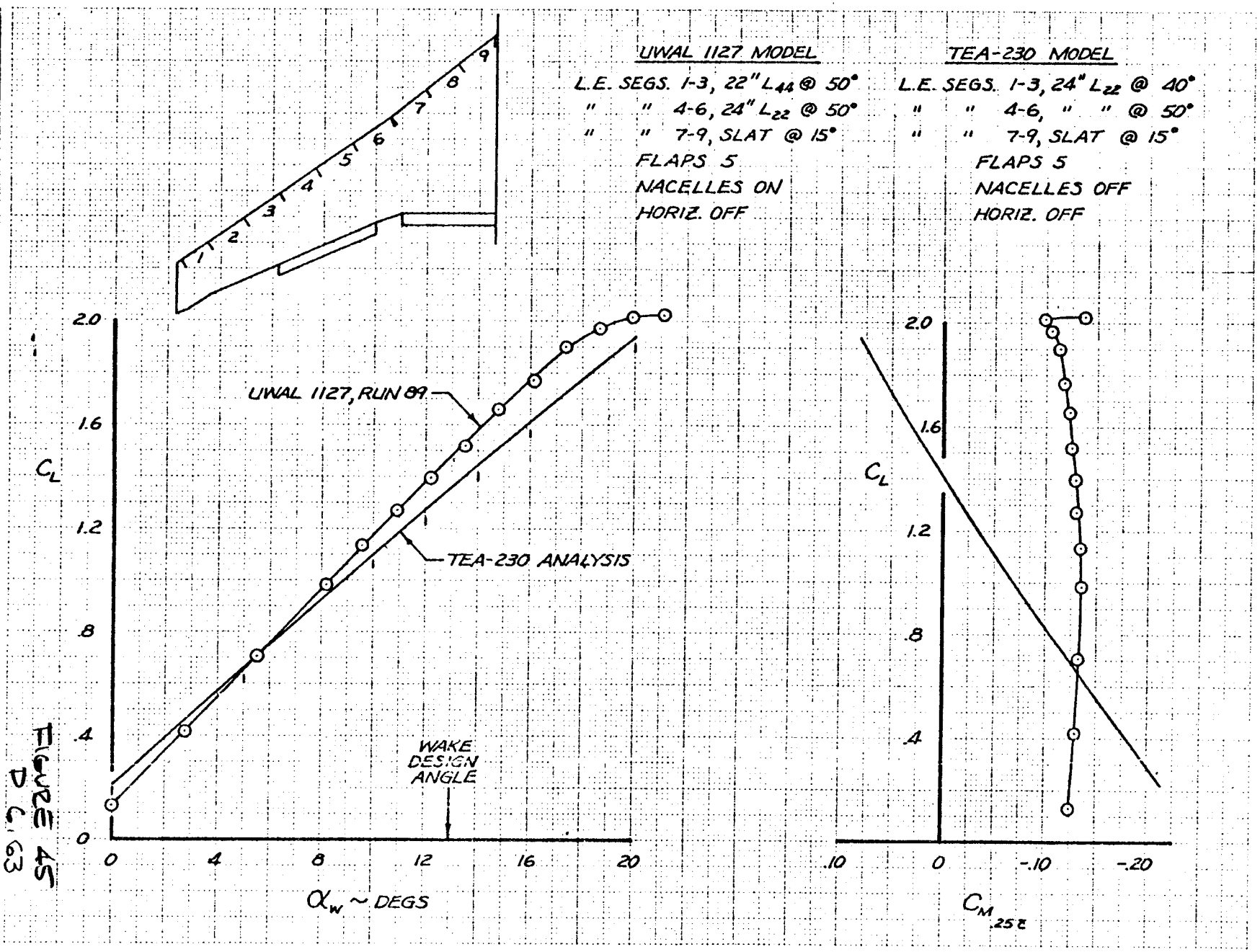

CALC	VANDENBERGE 4-30-75	REVISED	DATE
CHECK			
APR			
APR			

THE BOEING COMPANY

727-3004 TAKEOFF CONFIGURATION ~ COMPARISON OF THEORETICAL AND EXPERIMENTAL LIFT AND PITCHING MOMENT

PAGE

Figure 45
D6-63

SINGULARITY MODEL OF 7X7 LANDING CONFIGURATION

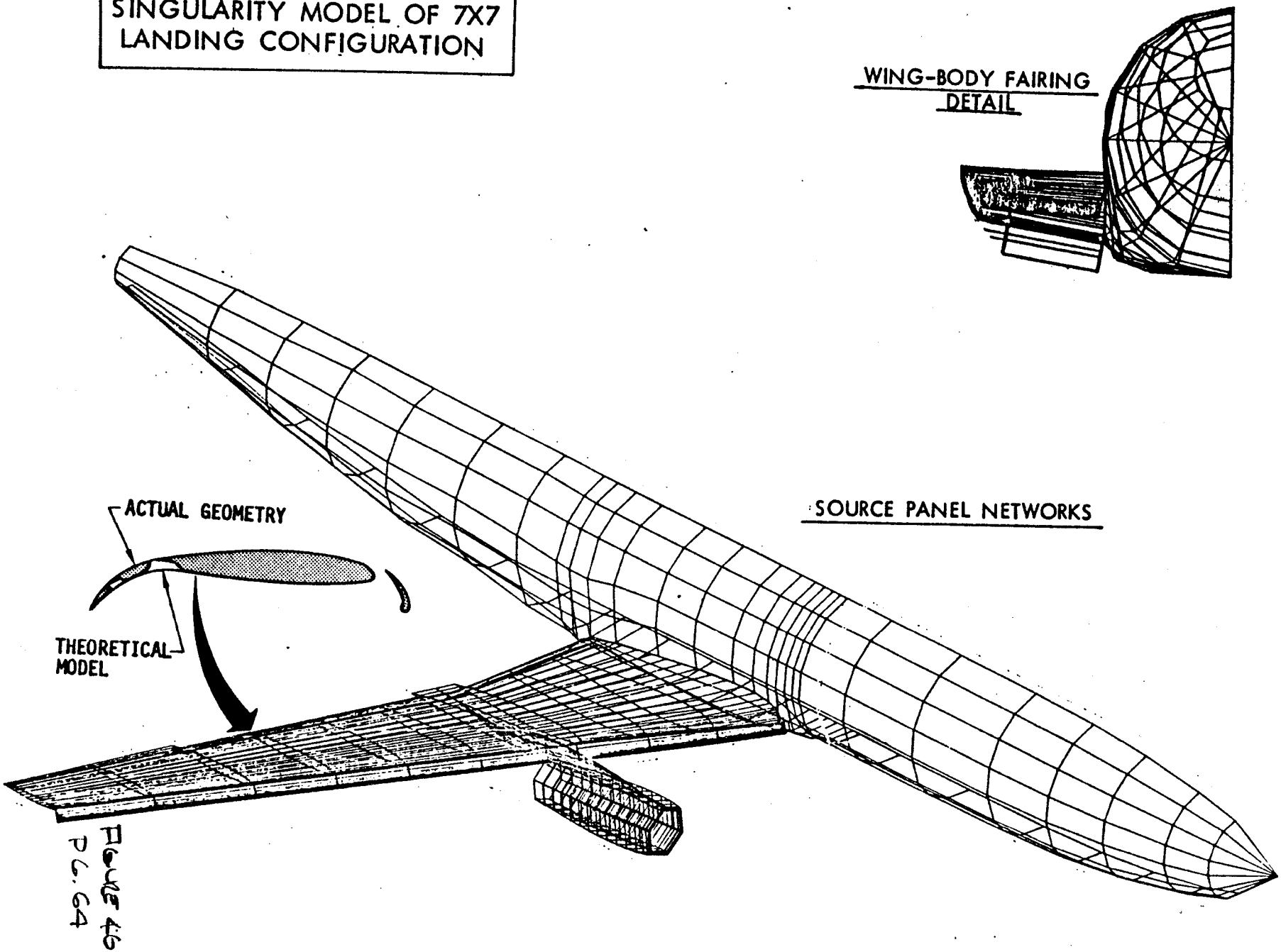

Figure 46
P.G. 64

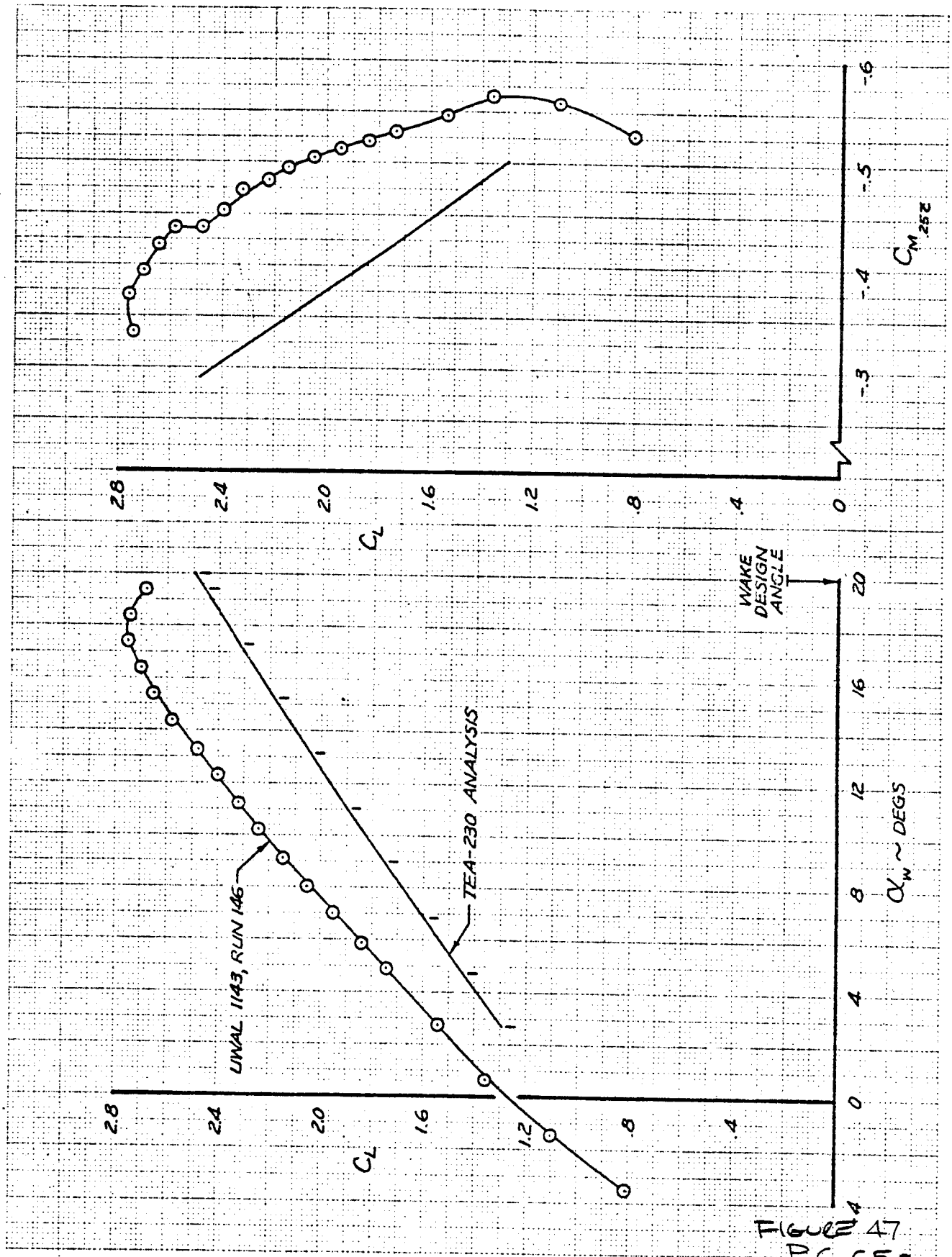

FIGURE 47
P-6.650

CALC	VANDEVENDER 4-30-75	REVISED	DATE	7X7 LANDING CONFIGURATION ~ COMPARISON OF THEORETICAL AND EXPERIMENTAL LIFT AND PITCHING MOMENT	
CHECK					
APR					
APR				THE BOEING COMPANY	PAGE

D1 4100 1260 ORIG 3-71

K+E ALBANENE TOOL & TRACING PAPER

428

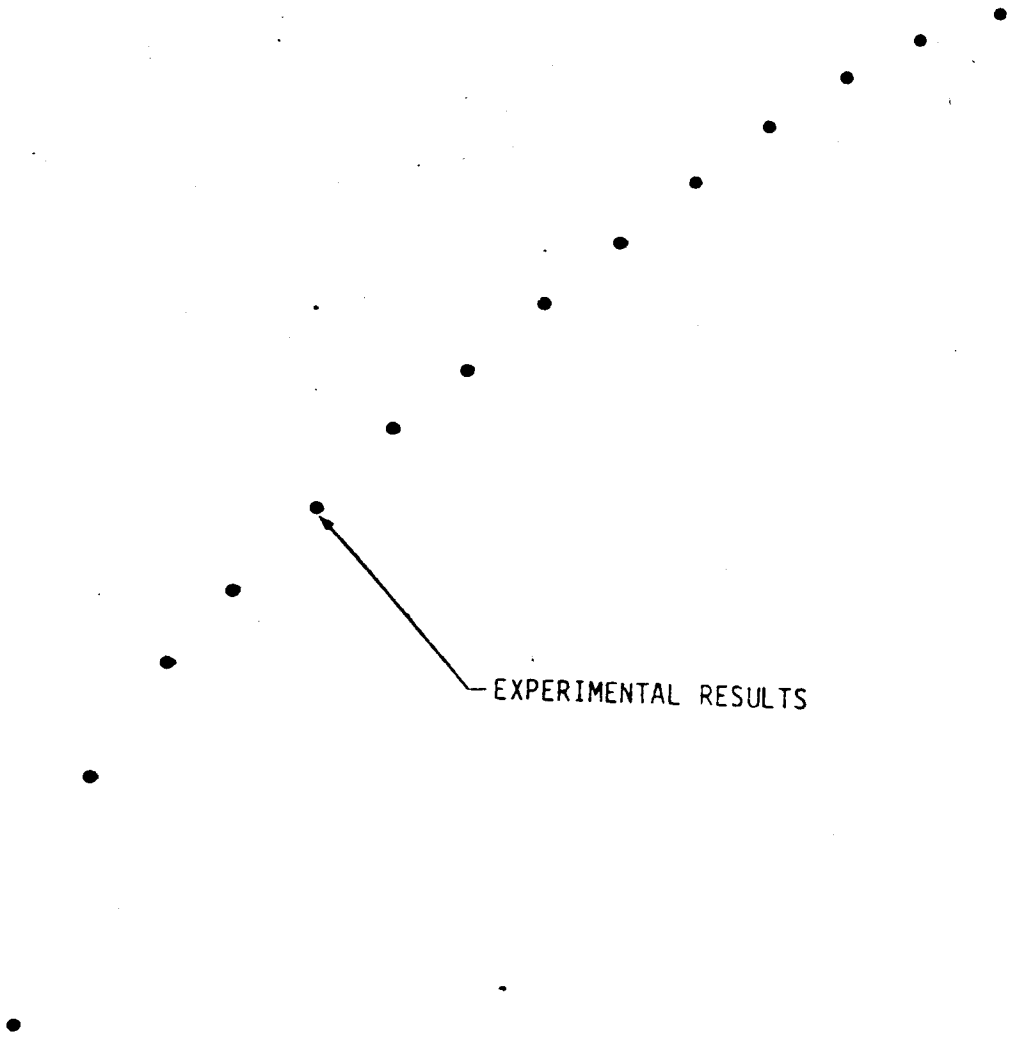

P C.656

FIG 49 O/L
RED

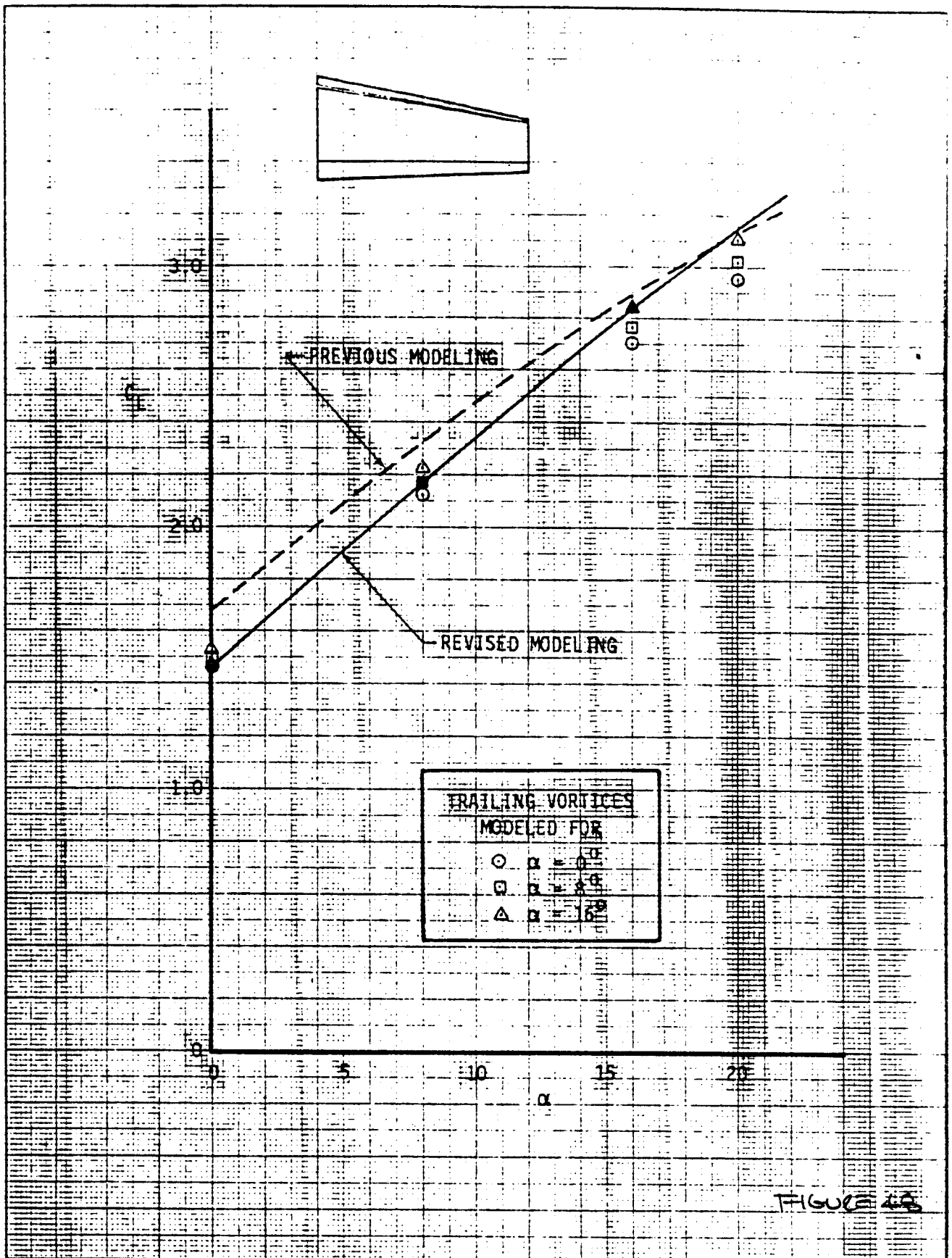

FIGURE 46

CALC			REVISED	DATE	A372 LIFT CURVE FOR WING WITH FULL SPAN TRAILING EDGE FLAP
CHECK					
APR					
APR					THE BOEING COMPANY

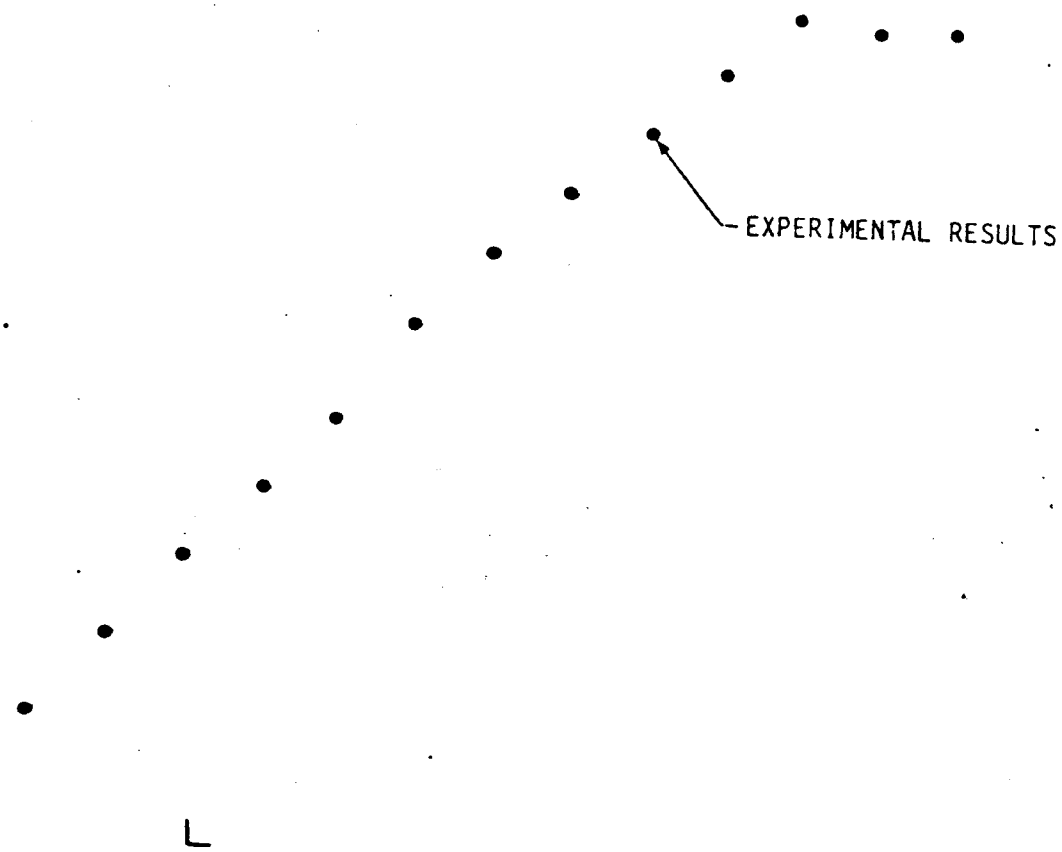

FIG 49 O/L
REV.

PG. 666

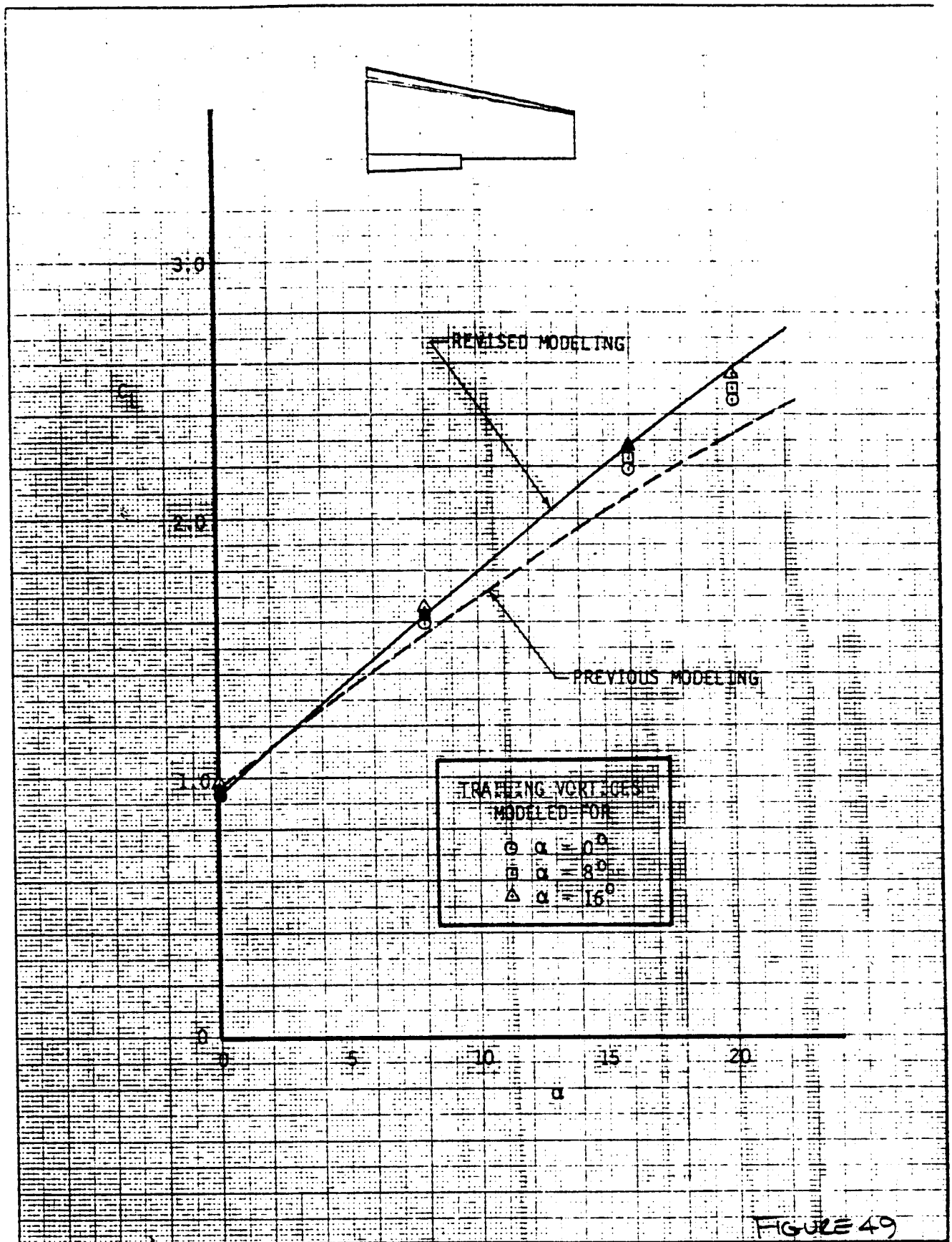

FIGURE 49

CALC	Verma	8/22/77	REVISED	DATE
CHECK				
APR				
APR				

A372 LIFT CURVE FOR WING WITH PART-SPAN TRAILING EDGE FLAP

THE BOEING COMPANY

PAGE D6.679

4132

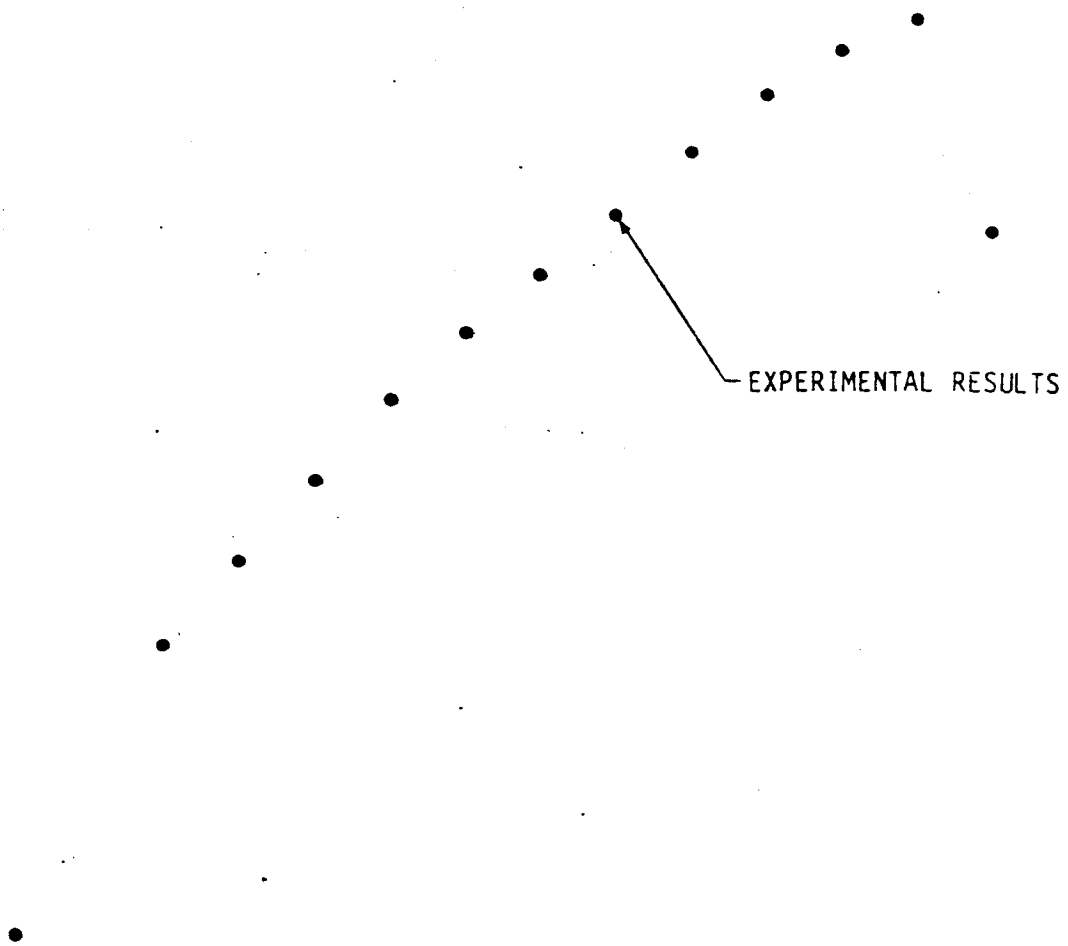

FIG 50 O/L
RED

PG. 676

413

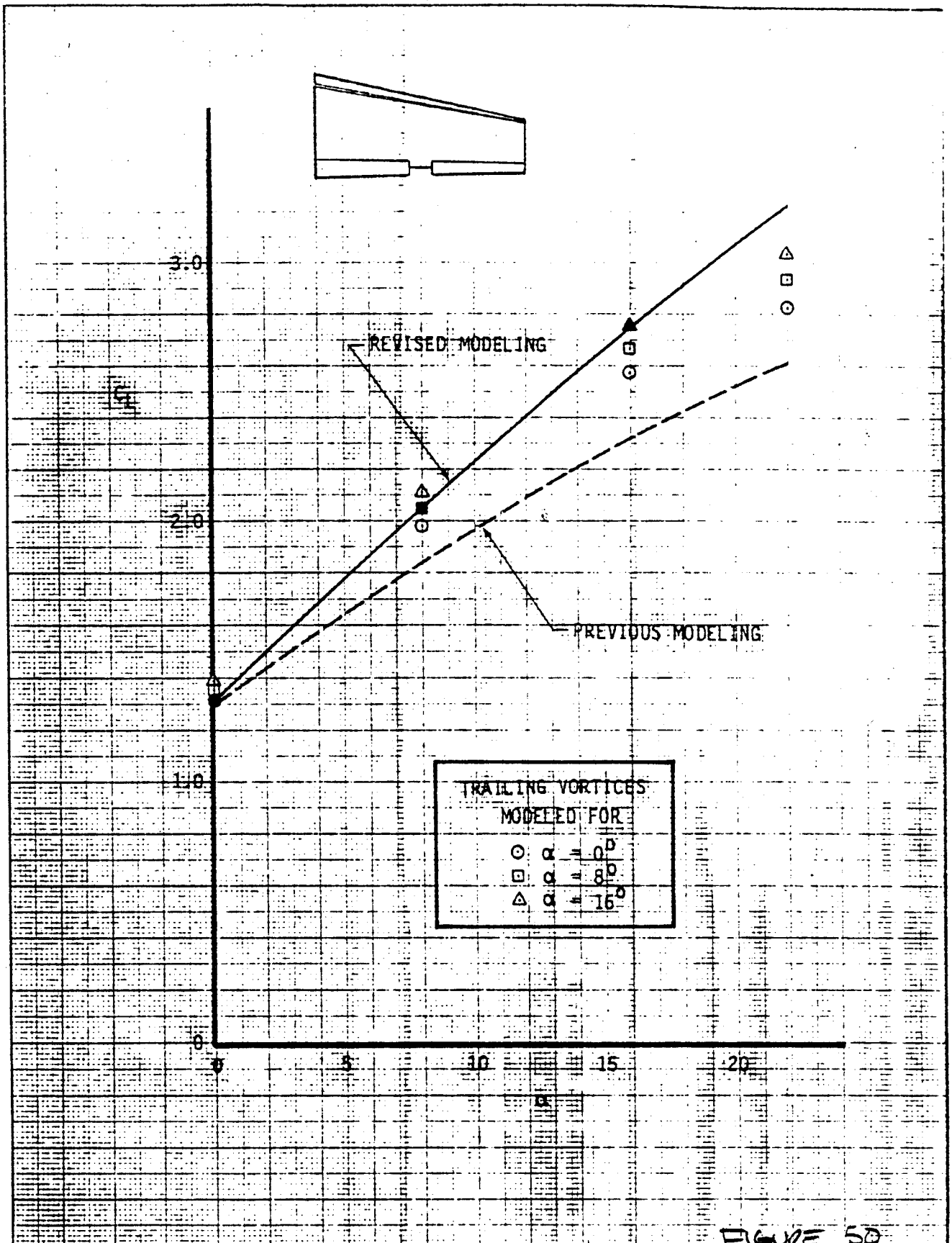

FIGURE 50

CALC	eVerma	5/22/77	REVISED	DATE
CHECK				
APR				
APR				

A372 LIFT CURVE FOR WING WITH PART-SPAN TRAILING EDGE FLAP AND CUT-OUT

THE BOEING COMPANY

PAGE P6 68

D1 4100 324

K-E ALBANENE 1881

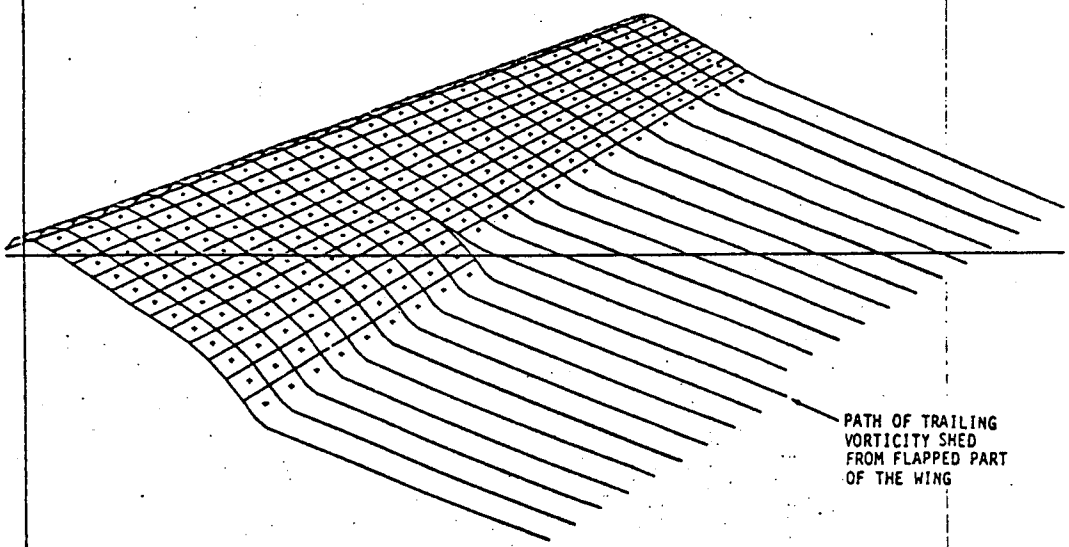

FIGURE 51a

PREVIOUS MODELING OF A WING WITH SLOTTED FULL-SPAN LEADING EDGE FLAP AND SLOTTED PART-SPAN TRAILING EDGE FLAP.

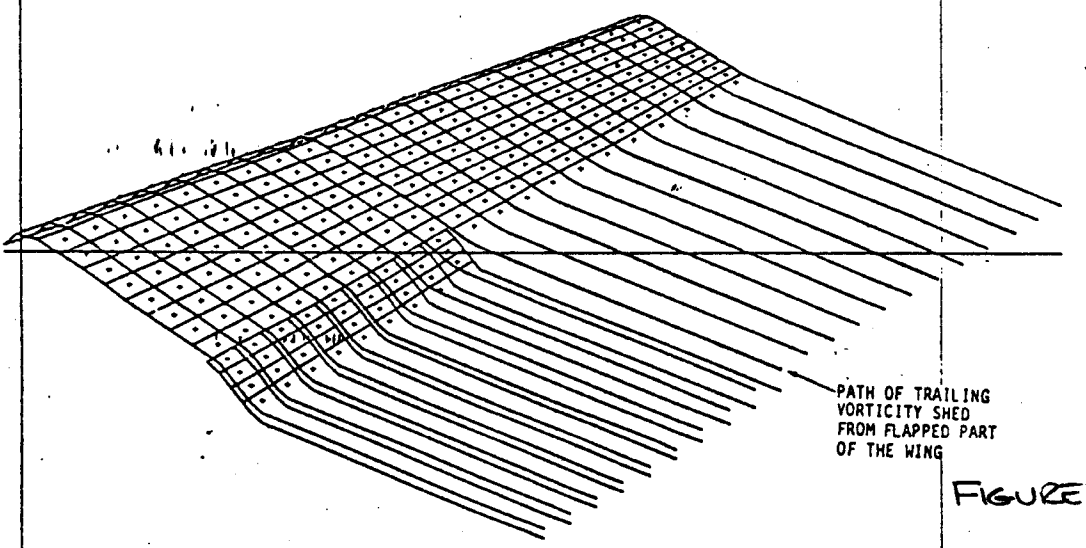

FIGURE 51b

REVISED MODELING OF WING WITH SLOTTED FULL-SPAN LEADING EDGE FLAP AND SLOTTED PART-SPAN TRAILING EDGE FLAP.

P6.69

135

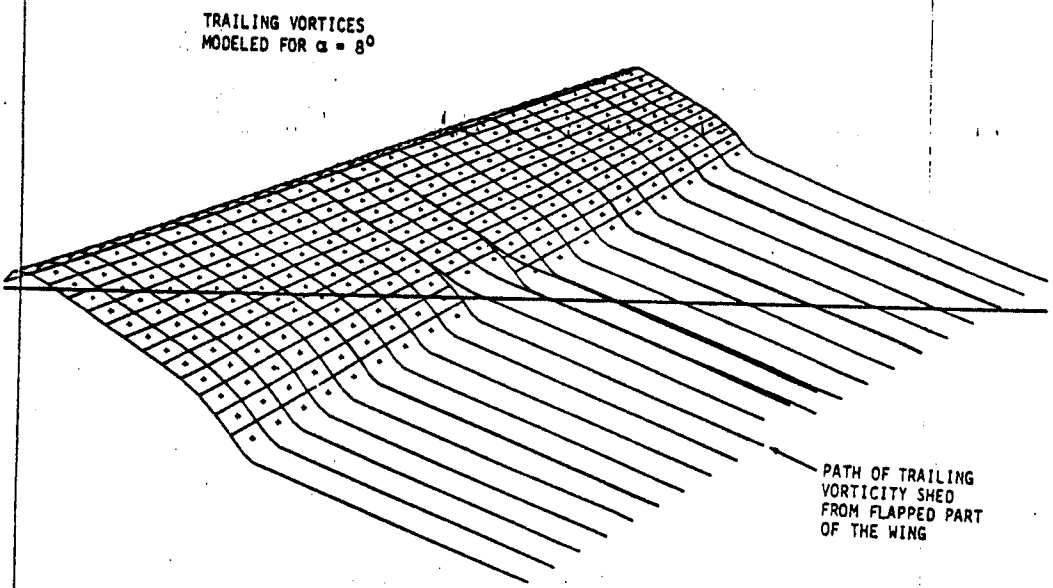

FIGURE 52a

PREVIOUS MODELING OF A WING WITH SLOTTED FULL-SPAN LEADING EDGE FLAP AND SLOTTED PART-SPAN FLAPS WITH CUT-OUT.

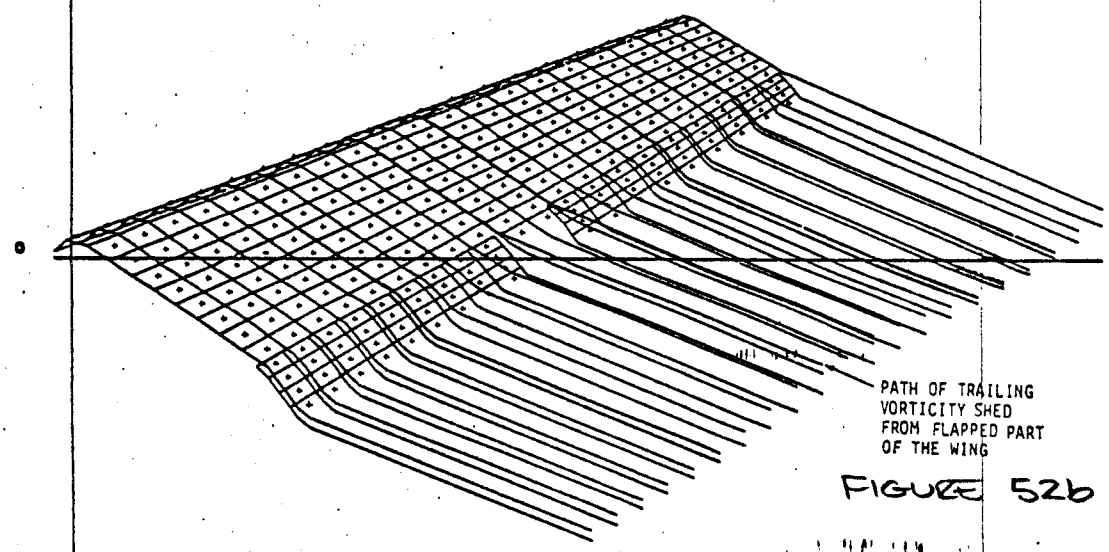

FIGURE 52b

REVISED MODELING OF A WING WITH SLOTTED FULL-SPAN LEADING EDGE FLAP AND SLOTTED PART-SPAN FLAPS WITH CUT-OUT.

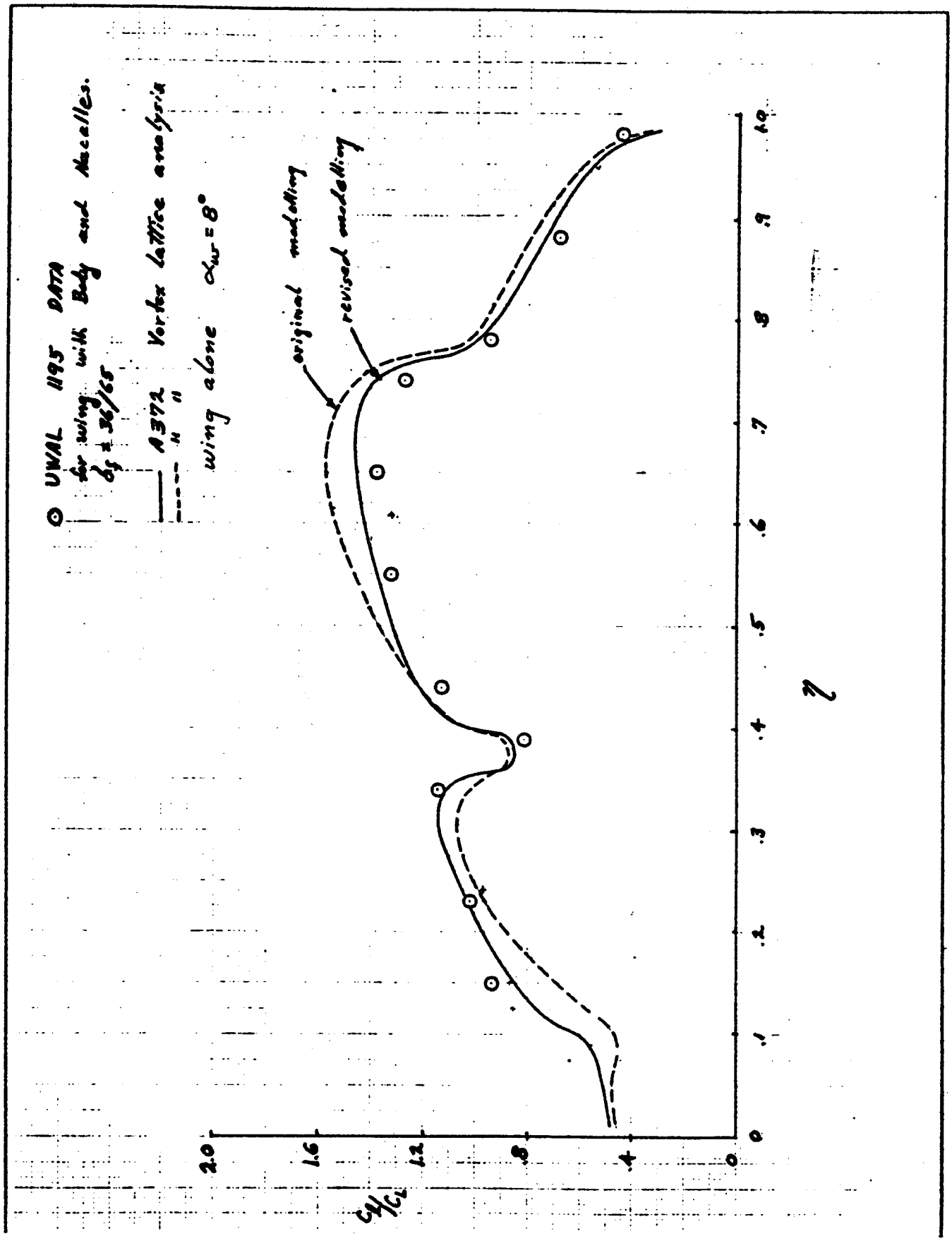

FIGURE 53
P6.71

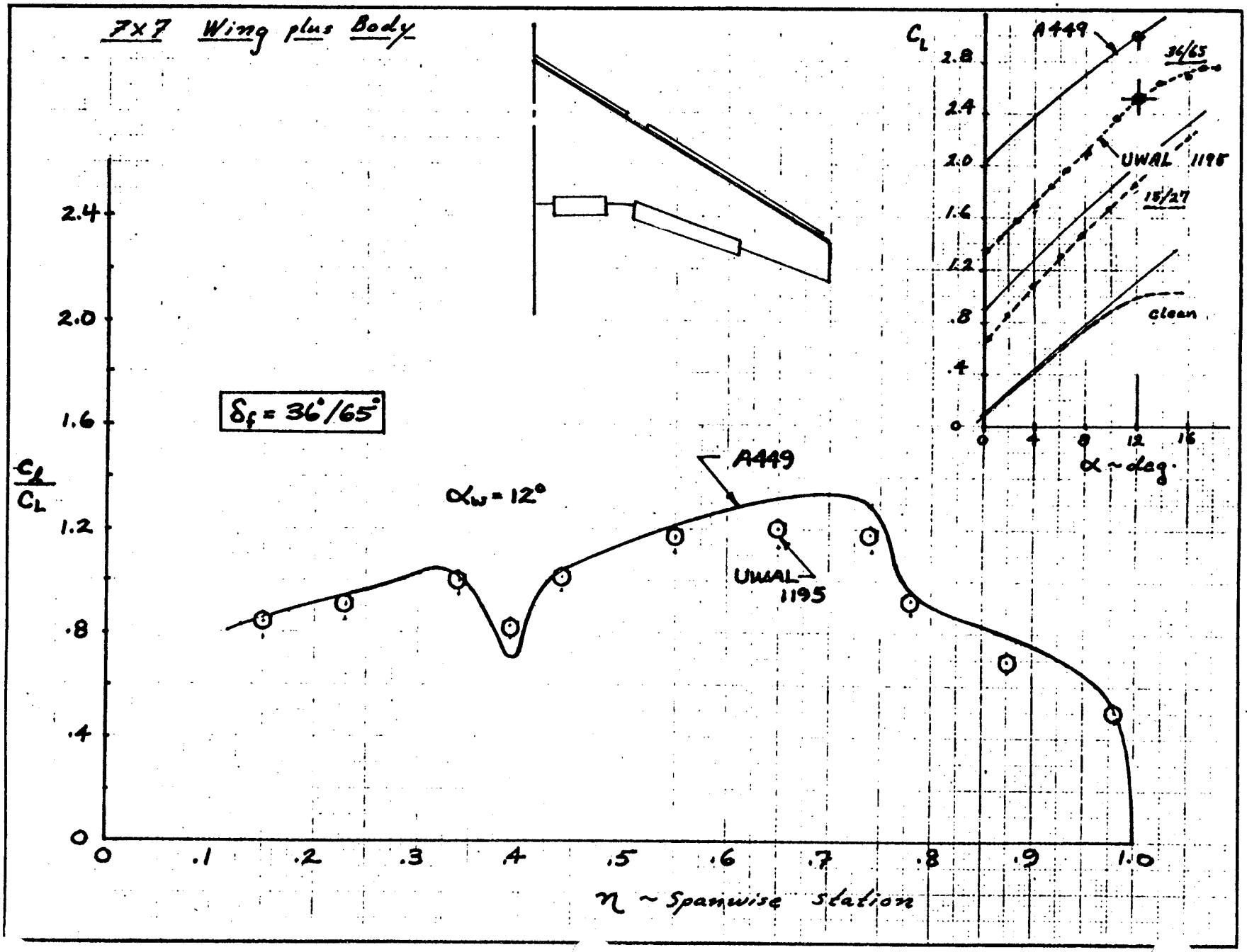

FIGURE 54
P6.72

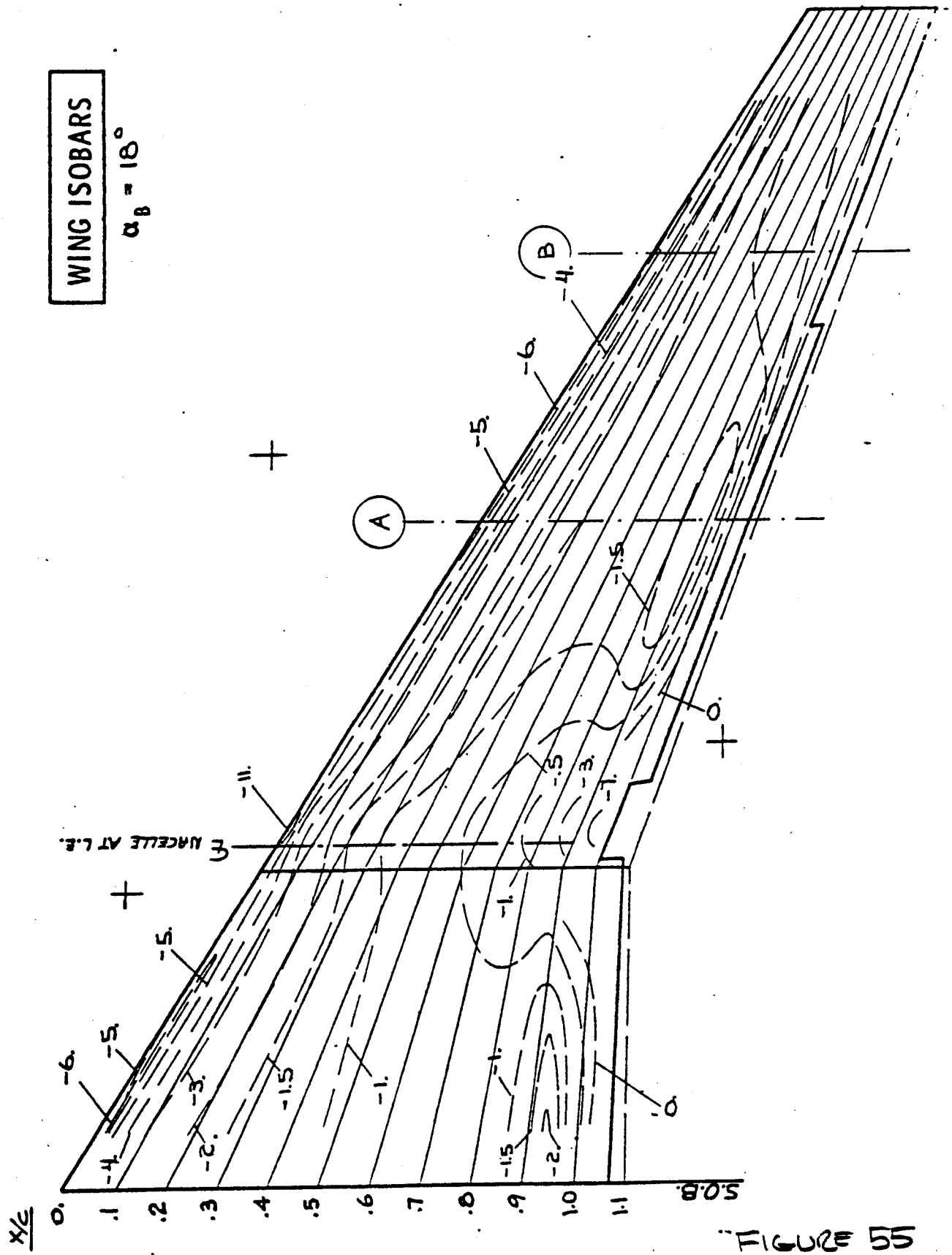

FIGURE 55
P6. 73

AERODYNAMIC TECHNOLOGY	TWO TO THREE DIMENSIONAL CORRELATION	BOEING

EXPERIMENTAL DATA 7X7 AIRFOIL

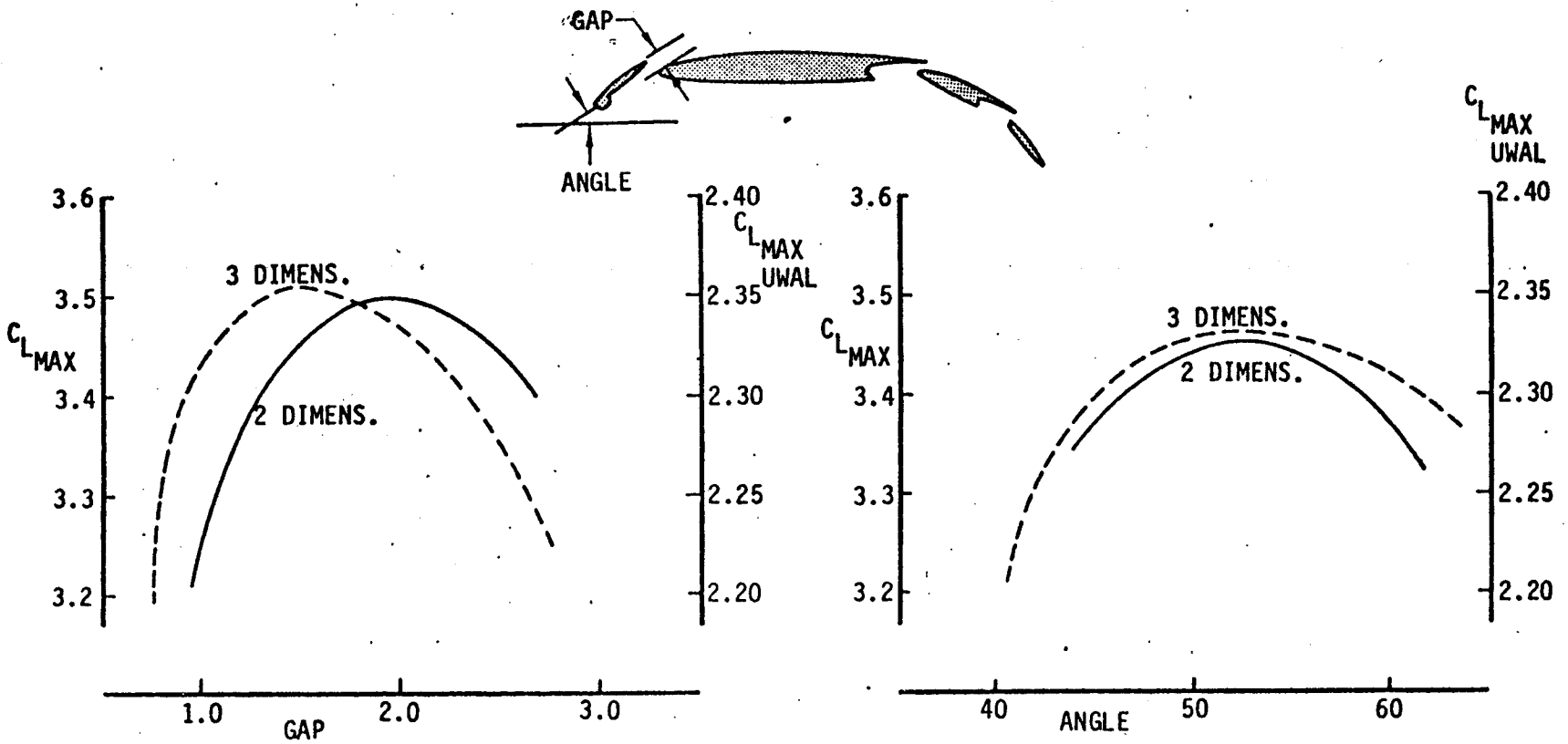

FIGURE 56
P6.74

ANALYSIS IN 1976

+ PRESSURE DISTRIBUTION CORRELATIONS

+ INDUCED THREE DIMENSIONAL EFFECTS
(CAMBER, THICKNESS)

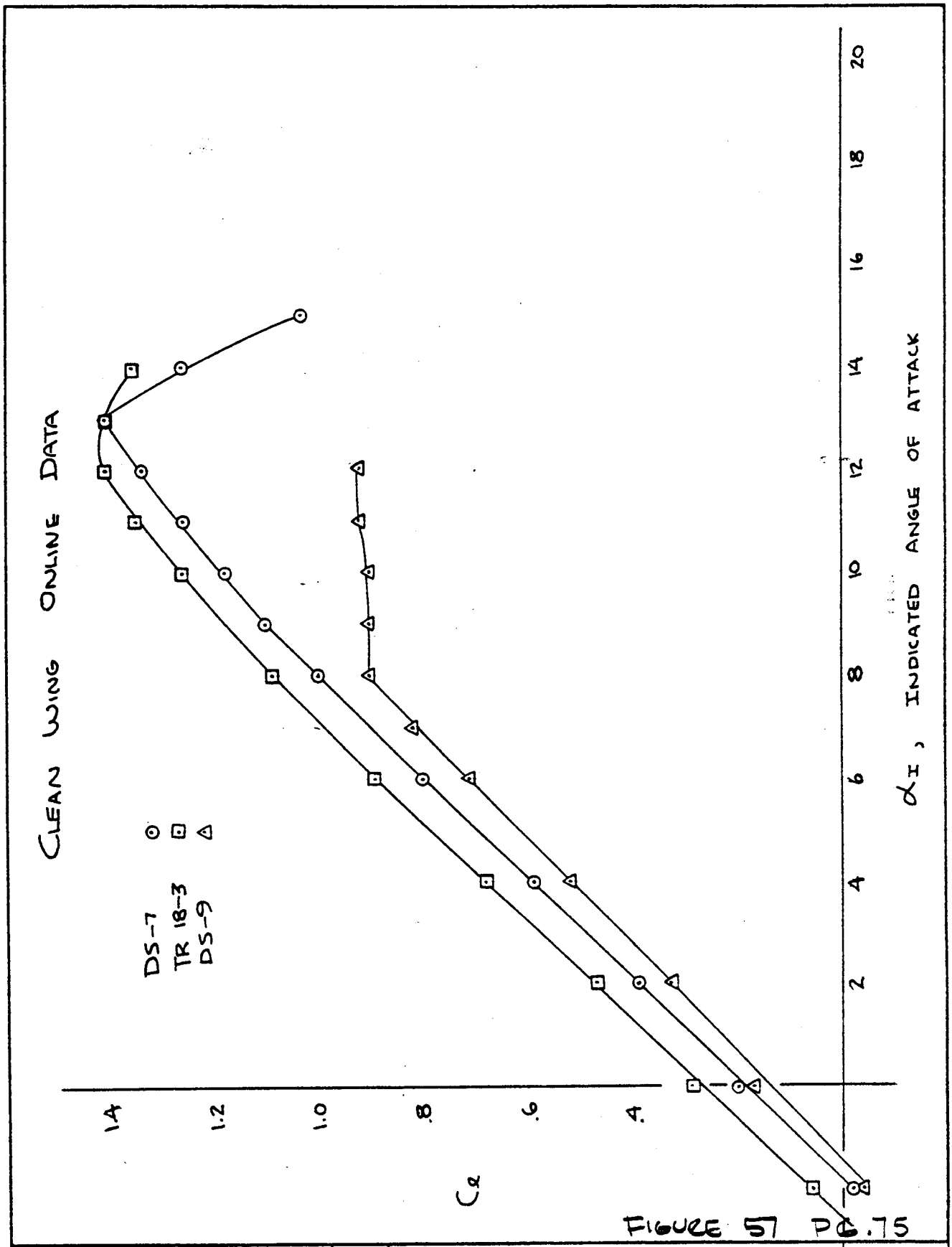

FIGURE 57 PG. 75

CALC	PR	2/21/77	REVISED	DATE	Cemax Comparison Basic Wing Sections
CHECK					
APR					
APR					THE BOEING COMPANY
					PAGE

AD 461 C-R6

K·E ALBANENE 1961 8.5 G-8000 TRACING PAPER

442

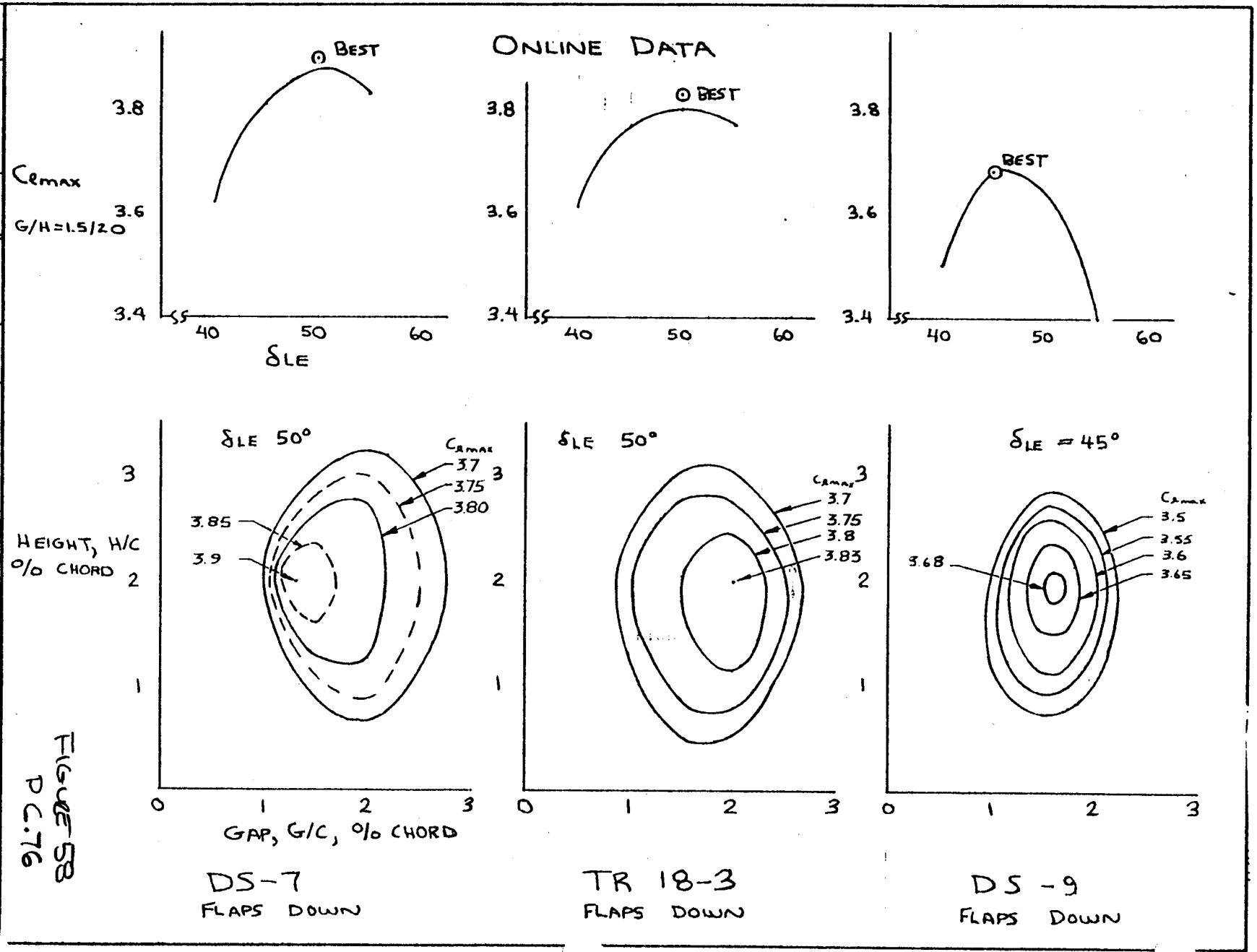

FIGURE 58
PC.76

SECTION COMPARISON FLAPS DOWN
Cℓmax VS LEADING EDGE POSITION

THE BOEING COMPANY

PAGE

	CALC	PR	2/19/77	REVISED	DATE
	CHECK				
APR	APR				

D1 4100 3240

K+E ALBANENE 1881 TRACING PAPER

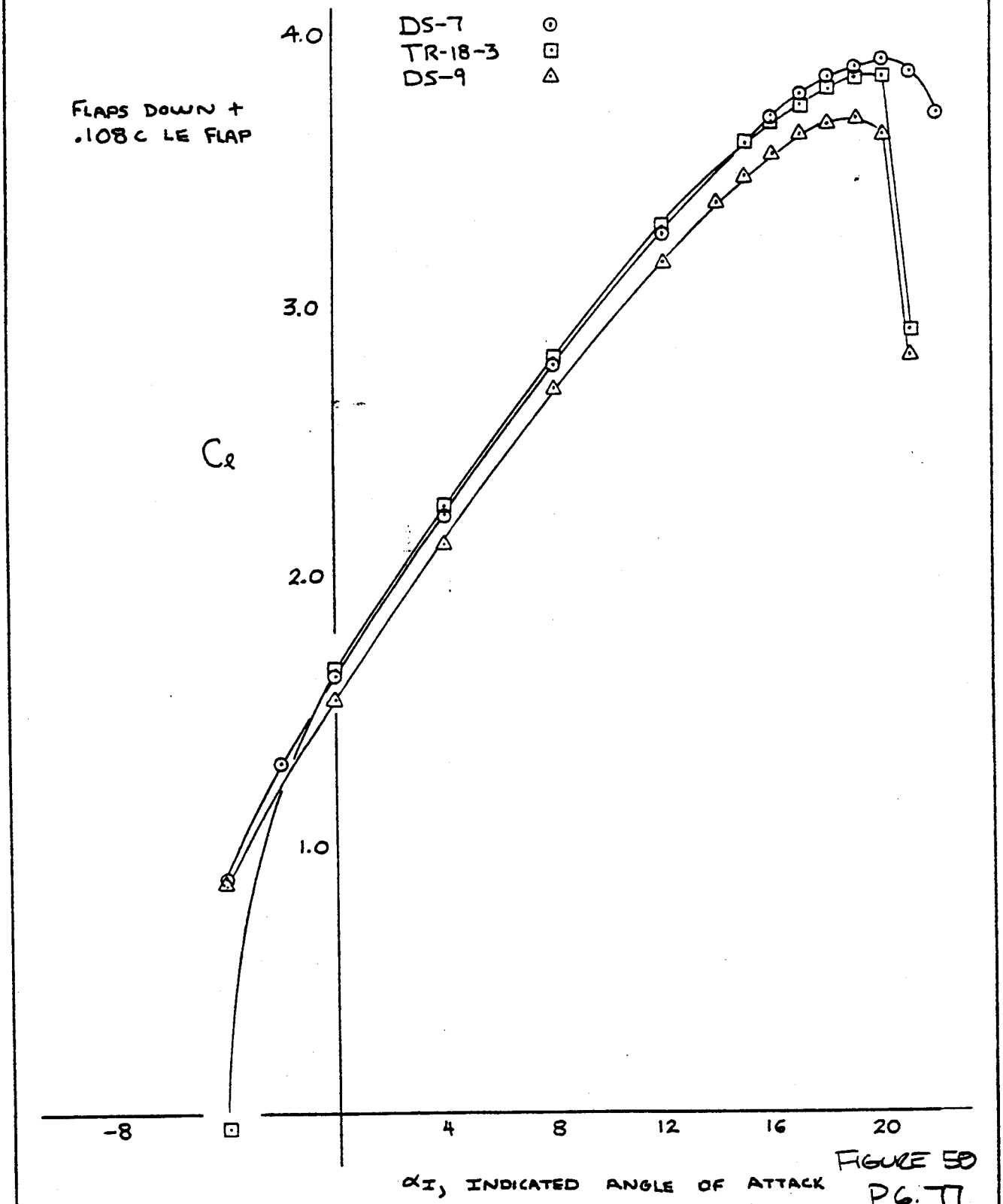

FIGURE 50
PG. 77

CALC	PR	2/21/77	REVISED	DATE
CHECK				
APR				
APR				

SECTION COMPARISON FLAPS DOWN
BEST LEADING EDGE POSITION

THE BOEING COMPANY

PAGE

AD 461 C-R6

K+E ALBANENE 1984 8.5 G-8000 TRACING PAPER

274

FIGURE [illegible] MODEL [illegible]

Figure 61
P 6.73

445

UWAL 1210 RUN SUMMARY

TE FLAPS ~ RUN NUMBER

CONFIGURATION "TRI-JET WITH T-TAIL"	LE FLAPS $C_{LE}/C_{W_{REF}}$ INB'D	LE FLAPS $C_{LE}/C_{W_{REF}}$ OUTB'D	LE FLAPS δ_{LE} INB'D	LE FLAPS δ_{LE} OUTB'D	OUTB'D LE FLAP TWIST	HORIZ TAIL OFF 0+LE	HORIZ TAIL OFF 2° SINGLE SLOT	HORIZ TAIL OFF 20/43° TAPERED AFT FLAP	HORIZ TAIL OFF 36/65° CONSTANT AFT FLAP	HIGH-α 36°/65° TAIL OFF	HIGH-α 36°/65° δ_H=+2°
CLEAN WING w/ TE FLAP BRKTS	—	—	—	—	—	1	—	—	—	—	—
UPDATED BASELINE LE FLAP BUILDUP											
• OLD BASELINE LE	.1039	.1247	52.3°	$50.6°_{AVE}$	PROJECT	2	3	4	5	6	7
• UPDATED NAC SEAL SEAL	✓	✓	✓	✓	✓	19	18	9	17	15	16
• SMALLER OUTB'D LE FLAP	✓	.1116	✓	✓	✓	20	21	22	23	24	25
• SMALLER INB'D LE FLAP	.0940	✓	✓	✓	✓	31	30	29	28	27	26
OUTB'D LE FLAP TWIST, δ_{LE} AND STEPPED CHORD STUDIES											
• OVERSIZE INB'D LE w/NOISE BRKT	.1039	.1116	52.3°	$50.6°_{AVE}$	PROJECT	45, 111, 136, 209	34	40	46	—	—
• UNTWISTED OUTB'D LE FLAP	✓	✓	✓	51°	0°	—	47	48	—	—	—
• REDUCED δ_{LE} OUTB'D ~ L/D	✓	✓	✓	43°	✓	—	66, 87	67	88	—	—
• REDUCED CHORD INB'D LE	.0940	✓	✓	✓	✓	110	89, 109	90, 105	106	107	108
• ADJUSTABLE LE BRKTS INB'D	✓	✓	✓	✓	✓	—	93	91	—	—	—
• STEPPED CHORD OUTB'D LE	.1039	.1200 .1070	✓	43/35	8° PANEL 3	—	119, 126	118	127	—	—
• REDUCED CHORD INB'D LE	.0940	✓	✓	✓	✓	133	132	131	128	129	130
• ALTERNATE STEPPED CHORD LE	✓	✓	✓	✓	8° PANEL 5	—	134	135	—	—	—
NP6A - L48 LE SECTIONS											
• NP6A INB'D ~ L48 OUTB'D @ L/D	.1039	.1116	52.3°	35.1°	0°	—	162, 166	161, 165	—	—	—
• NP6A INB'D ~ L48 OUTB'D @ $C_{L_{MAX}}$	✓	✓	✓	49.2°	✓	—	147	148	—	—	—
• L48 INB'D & OUTB'D @ L/D	.0940	✓	53.7°	35.1°	✓	189	180, 188	181	190	191	192
• L48 INB'D & OUTB'D @ $C_{L_{MAX}}$	✓	✓	58.8°	49.2°	✓	205	199, 204	198	206	207	208
• FLIGHT CONTROLS BASE WITH REDUCED INBD CHORD	.0803	.1116	52.3°	43°	0°	—	275	276	274	273	272

Figure 62a
P.G. 79

UWAL 1210 LE TRADE STUDY RUN SUMMARY

CONFIGURATION "TRI JET WITH T-TAIL"	LE FLAP VARIATIONS								TE FLAP / RUN NUMBERS
	δ_{SLAT} SEAL	$C_{LE}/C_{W_{REF}}$ INB'D	$C_{LE}/C_{W_{REF}}$ OUTB'D	δ_{LE} INB'D	δ_{LE} OUTB'D	G/C_W IN/OUT	X/C_W IN/OUT	OUTB'D LE FLAP TWIST	VARIATIONS ABOUT TAKEOFF FLAPS 2 LDG FLAPS 20/45
• UPDATED SLAT SEAL	VARY	.1039	.1247	$52.3°_{AVE}$	$50.6°_{AVE}$	PROJ/PROJ	PROJ/PROJ	PROJECT	RUNS 9 → 16
OUTB'D LE FLAP TWIST δ_{LE} AND STEPPED CHORD STUDIES									
• UNTWISTED OUTB'D LE FLAP	25°	.1039	.1116	$52.3°_{AVE}$	VARY	PROJ VARY	PROJ PROJ	0°	RUNS 47 → 56
• STEPPED CHORD LE OUTB'D	✓	✓	.1200 .1070	✓	✓	PROS PROS	✓	✓	RUNS 112 → 127
NP6A - L48 LE SECTIONS									
• NP6A INB'D - L48 OUTB'D @ C_{LMAX}	✓	✓	.1116	✓	VARY	PROJ/1.5	PROJ/1.5	0°	RUNS 137-152, 194-197
• NP6A-INB'D ~ L48 OUTB'D @ L/D	✓	✓	✓	✓	35.1°	PROS/VARY	PROJ/VARY	✓	RUNS 149 → 166
• L48 INB'D & OUTBD @ L/D	✓	.0940	✓	VARY	✓	VARY/1.5	VARY/2.0	✓	RUNS 167 - 188
• L48 INB'D & OUTBD @ C_{LMAX}	✓	✓	✓	✓	49.2°	1.0/2.0	1.0/1.5	✓	RUNS 198 - 204
LE FLAP CHORD TRADES									
• LARGE CHORD ANGLE TRADES	✓	.1162	.1378	VARY	VARY	PROS PROS	PROS PROS	PROJECT	RUNS 210 - 221
• MEDIUM CHORD ANGLE TRADES	✓	.0940	.1116	✓	✓	✓	✓	✓	RUNS 94-104, 234-239
• SMALL CHORD MINIMUM TRAVEL	✓	.0803	.0853	✓	✓	✓	✓	✓	RUNS 222 - 233
LE FLAP INB'D/OUTB'D SPLIT									C_{LMAX} & PITCHUP - δ_F 36/65, 2°
• INB'D/OUTB'D LE SPLIT	✓	.0940	VARY	$52.3°_{AVE}$	REDUCED	✓	✓	✓	RUNS 240 - 253
✓	✓	VARY	.1116	✓	✓	✓	✓	✓	RUNS 254 - 259
✓		✓	VARY	✓	✓	✓	✓	✓	RUNS 260 - 265
• INB'D LE FLAP GAP, SEAL AND δ_{LE} TRADES	✓	.0940	.1116	VARY	43°	VARY/PROS	✓	0°	RUNS 266 - 271

FIGURE 6.2b
P 6.80

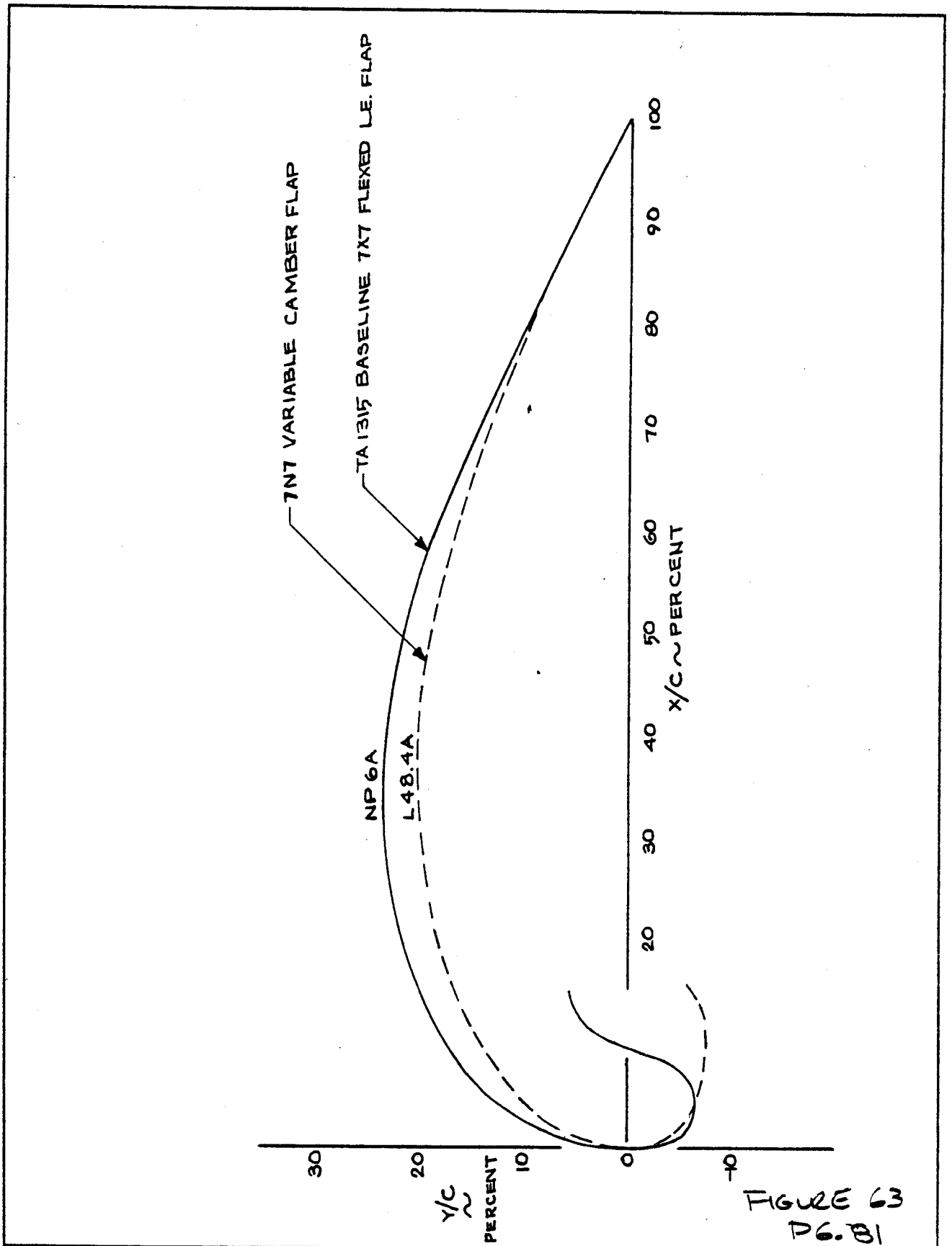

FIGURE 63
P6.81

CALC			REVISED	DATE	COMPARISON OF LEADING EDGE FLAP SHAPES	UWAL1210 TA1315E-10
CHECK	R.D.	12/15/77				
APR						
APR						
TRACE	B.MATTHIAS	12/15/77			THE BOEING COMPANY	PAGE

D1 4100 3240 ORIG 3/71

J15-047

4417

NP6A LE FLAP SECTION INBOARD

- TRI-JET "T-TAIL
- $C_{D_{P_{MIN}}}$ = .0184
- ADJUSTED FOR LE BRKT DRAG
- NO TRIM DRAG
- FWD CG = .04 MAC
- UPDATED SLAT SEAL

- NO OUTB'D LE FLAP TWIST
- $C_{LE}/C_{W_{REF}}$ .1039 INB'D
  .1116 OUTB'D

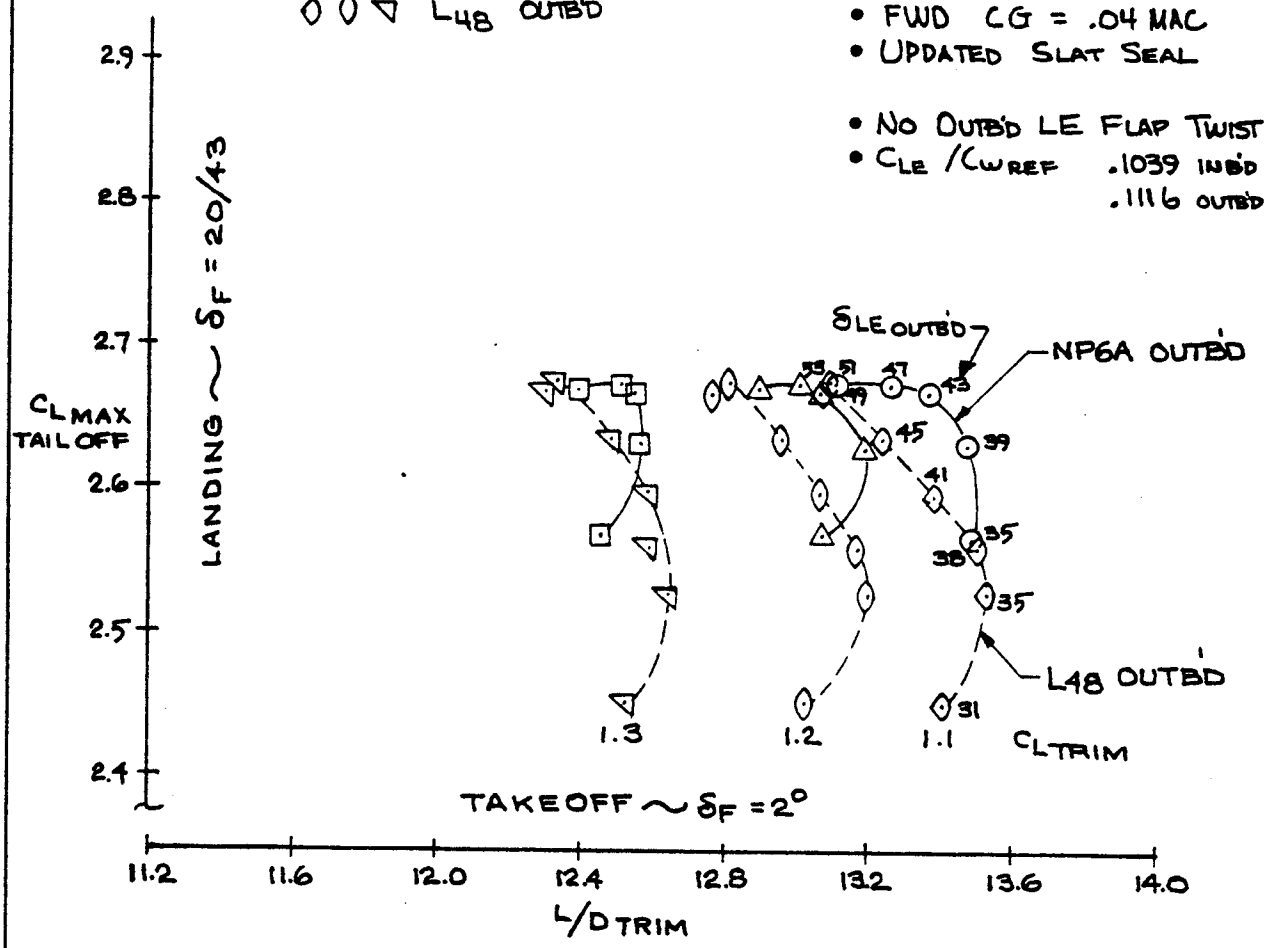

$C_{W_{REF}}$ = Cw @ ⅔ = .35 INBOARD
Cw @ ⅔ = .65 OUTBOARD

FIGURE 64
P6 82

CALC	BEK	10/24/77	REVISED	DATE	COMPARISON OF THE EFFECT OF OUTB'D LE FLAP SECTION GEOMETRY ON $C_{L_{MAX}}$ AN L/D TRIM
CHECK					
APR					
APR					
TRACE	B. Matthias	12/11/77			THE BOEING COMPANY

UWAL 1210
TA1315E-10
PAGE

J15-047

DOUBLE-SLOT FLAP

NOTE: 1.) SEE FIGURE 1 FOR GAP & OVERLAP DEFINITION
2.) 7X7 LE. VC FLAP $C_{LE}/C = .11/.095$

——— RECOMMENDED SCHEDULES

⊗ BEST GAP AND OVERLAP POSITIONS (FIGURE 12)

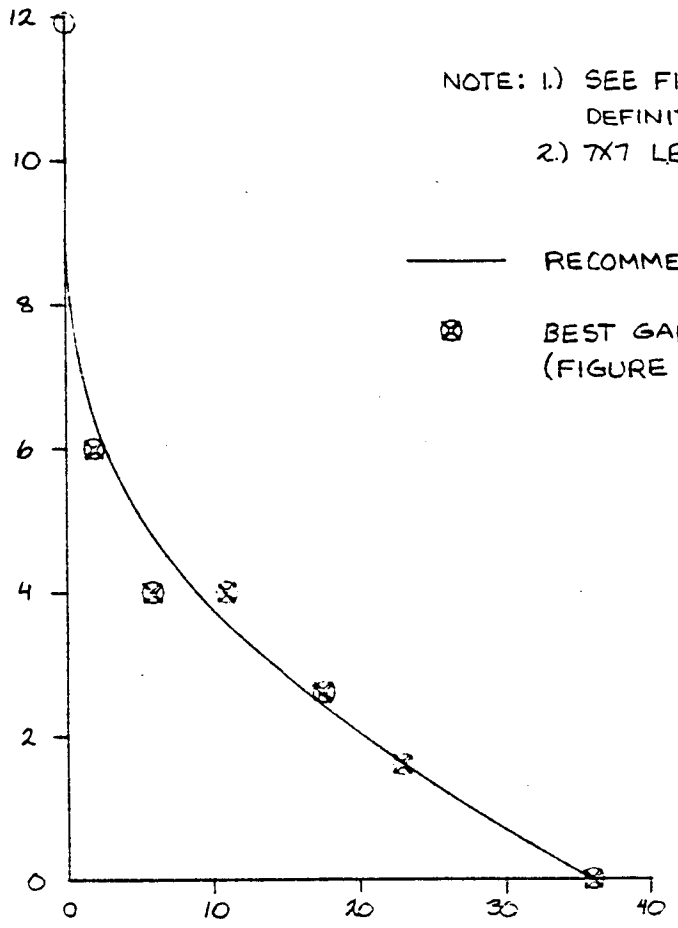

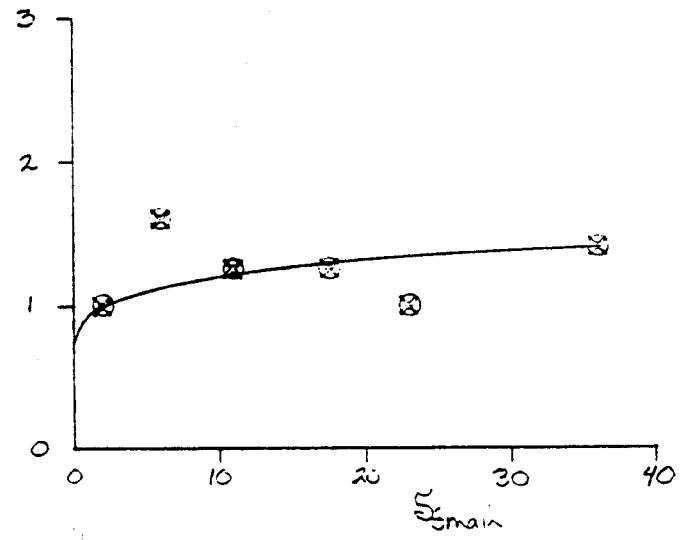

FIGURE 65
D6.83

CALC	MR	11/7/77	REVISED	DATE	TWO-SLOT FLAP MAIN FLAP GAP & OVERLAP SCHEDULE	UWAL 1208
CHECK						TA1315 E 9
APR						
APR					THE BOEING COMPANY	PAGE

D1 4100 3240

K+E ALBANENE 1951

NOTES: 1.) ΔL/D INCREMENTS AT $C_{L_{V_2}}$ (α BODY LIMITS) ARE DERIVED FROM BEST L/D ENVELOPE OF GAP & OVERLAP POSITIONS (FIG. 6).
2.) SEE FIGURE 1 FOR GAP & OVERLAP DEFINITIONS

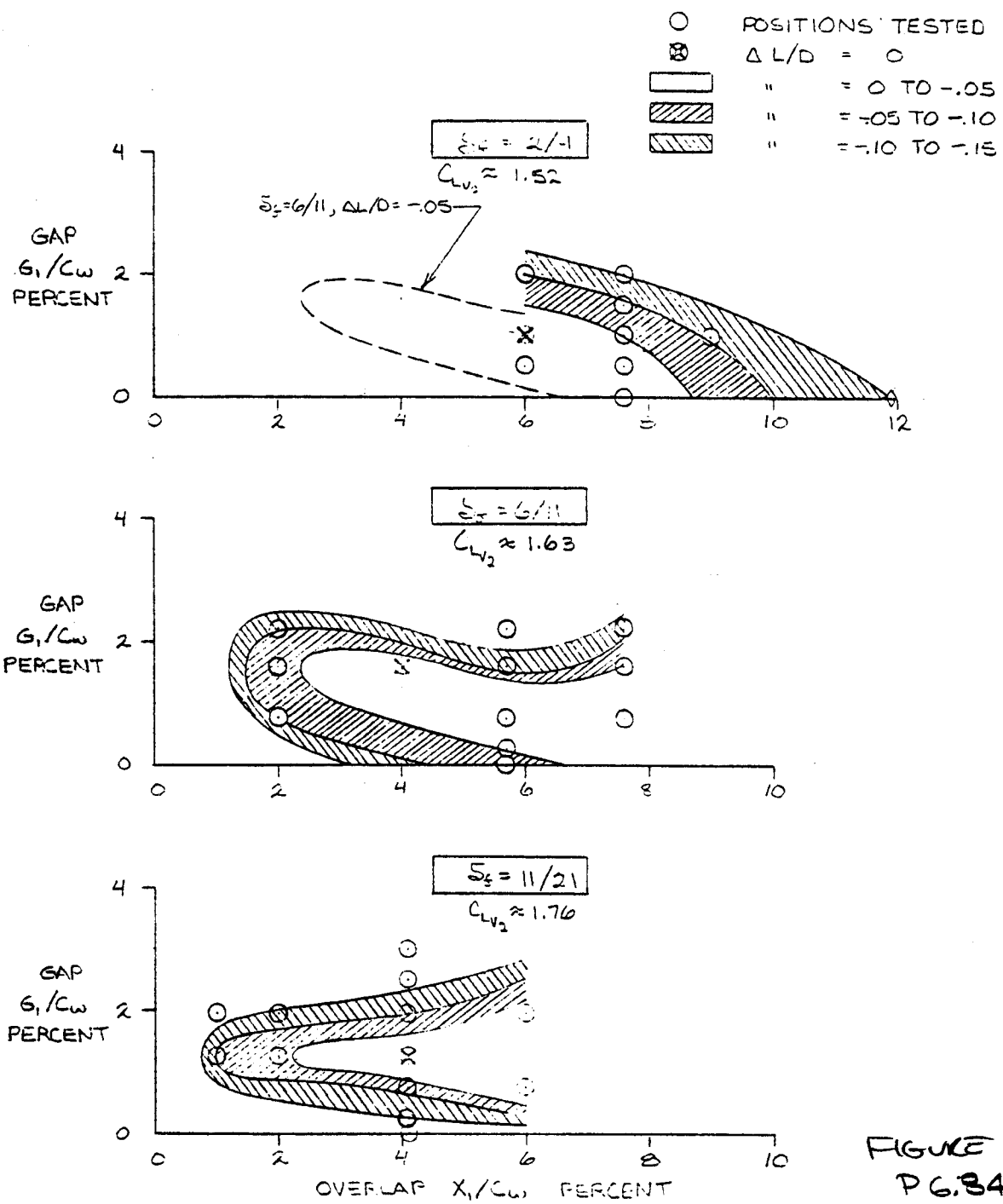

FIGURE C.6
P 6.84

CALC	ROGERS	9/6/77	REVISED	DATE	T.E. FLAP GAP & OVERLAP POSITIONS TWO-SLOT FLAP 7X7 L.E. VC FLAP C_{LE}/C = .11/.095
CHECK					
APR					
APR					
					THE BOEING COMPANY

D1 4100 3240

KOF ALBANENE 1961

NOTES: 1.) ΔL/D INCREMENTS AT $C_{L_{V_2}}$ (α BODY LIMITS) ARE DERIVED FROM BEST L/D ENVELOPE OF GAP & OVERLAP POSITIONS
2.) SEE FIGURE 1 FOR GAP & OVERLAP DEFINITIONS

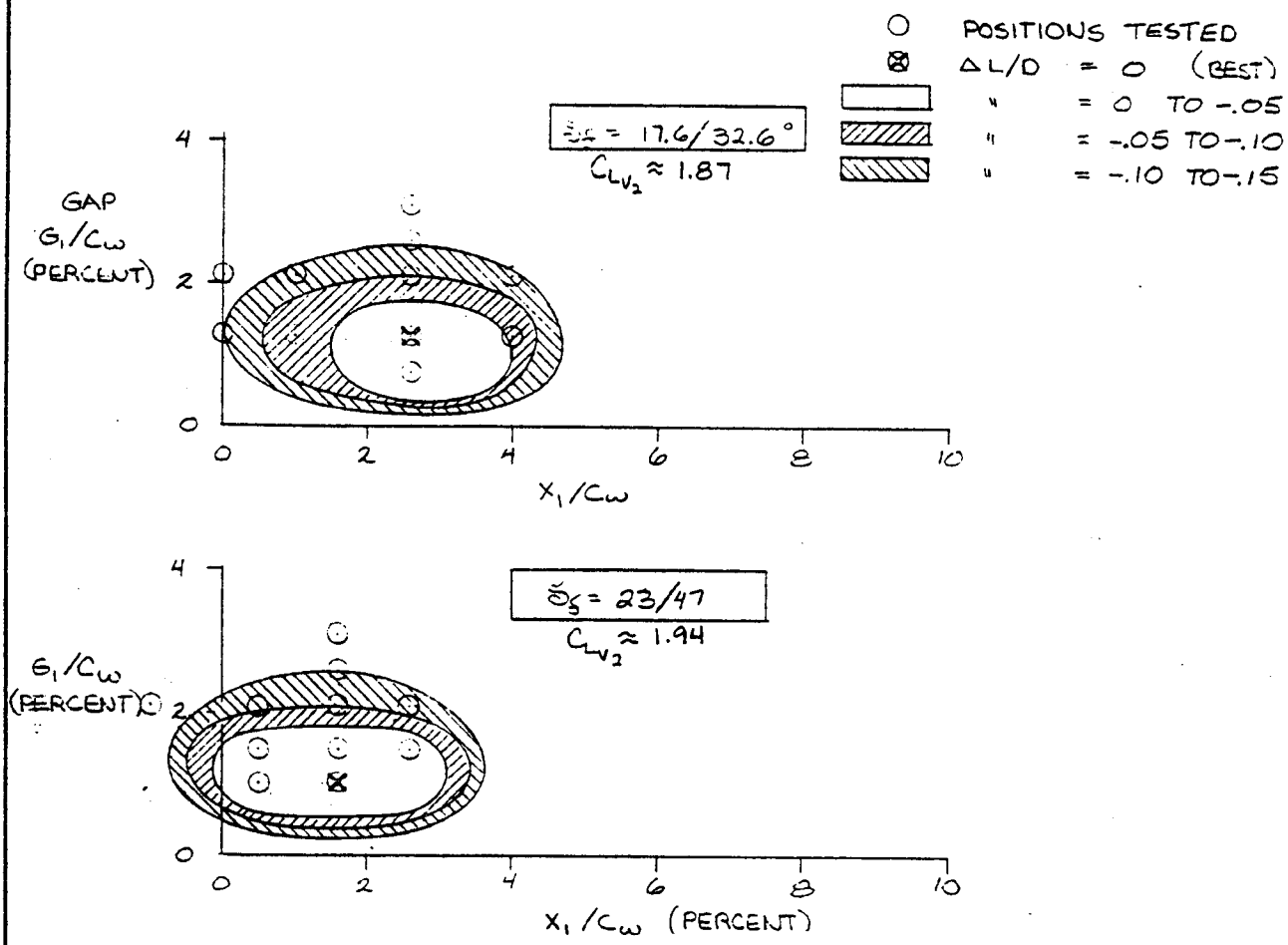

FIGURE 67
P6.85

CALC	MR	10/17/7-	REVISED	DATE	TWO-SLOT FLAP GAP & OVERLAP SUMMARY 7X7 L.E. VC FLAP $C_{LE}/C = .11/.015$	DWG 120?
CHECK						TA 131E ES
APR					THE BOEING COMPANY	PAGE
APR						

D1 4100 3240

KoE ALBANENE 1961

TRAILING EDGE AFT FLAP GAP & OVERLAP GRID

NOTES
1.) SEE FIGURE 1 FOR GAP & OVERLAP DEFINITIONS

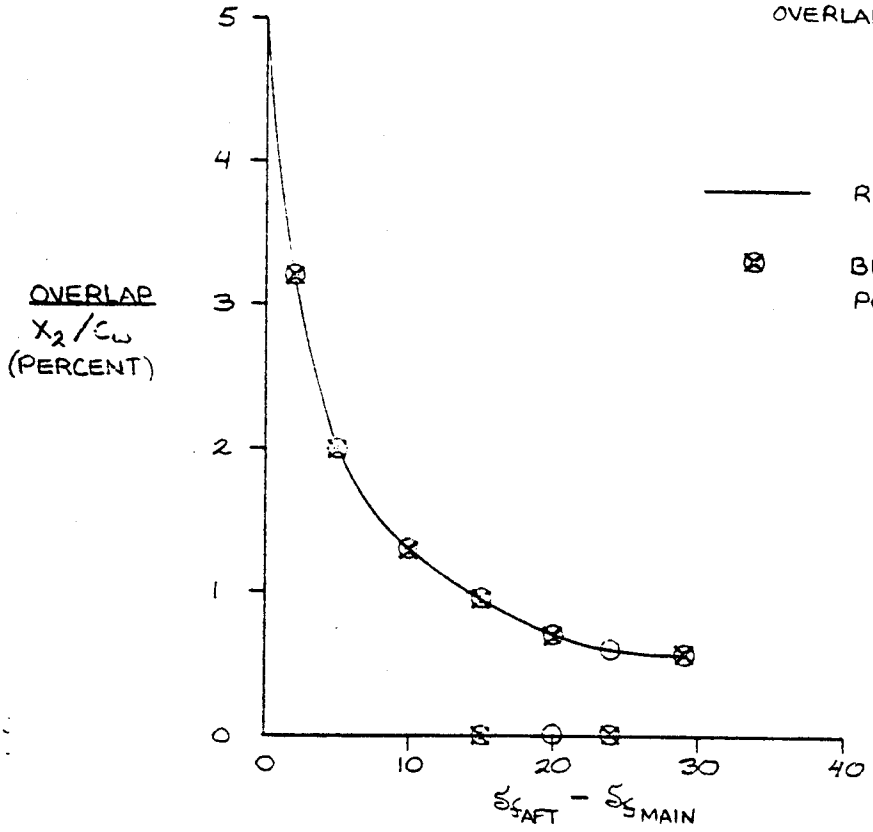

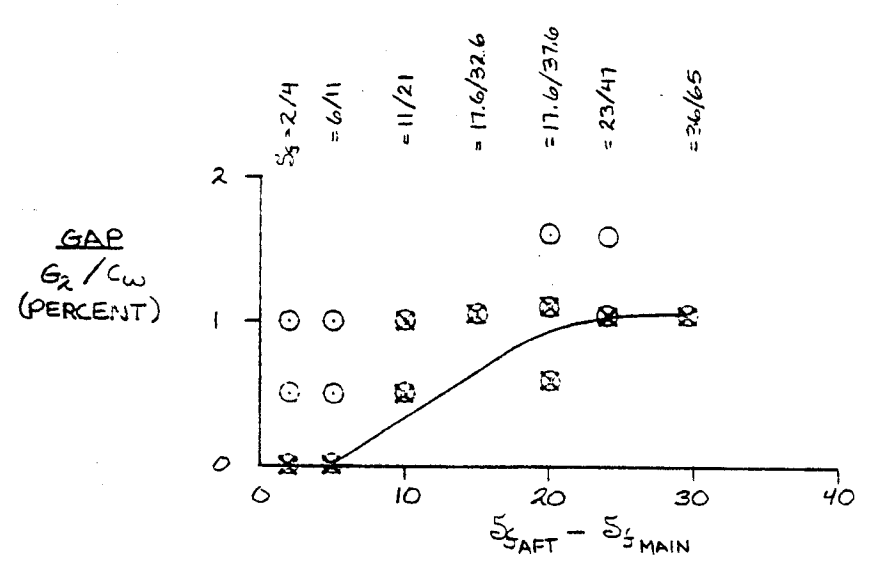

FIGURE 68
P6.86

CALC	ROGERS	10/6/71	REVISED	DATE	TWO-SLOT FLAP AFT FLAP GAP & OVERLAP SCHEDULE	UWAL 1208
CHECK						TA 1315 E9
APR						
APR					THE BOEING COMPANY	PAGE

D1 4100 3240

K+E ALBANENE 196L

1452

NOTES: 1.) GAPS AND OVERLAPS ARE CONSTANT & REFERENCED TO STREAMWISE CHORD AT MID-SPAN OF OUTBOARD FLAP (C_w = 170.685), SEE FIGURE 1

2.) ⊠ "BEST L/D" POSITIONS

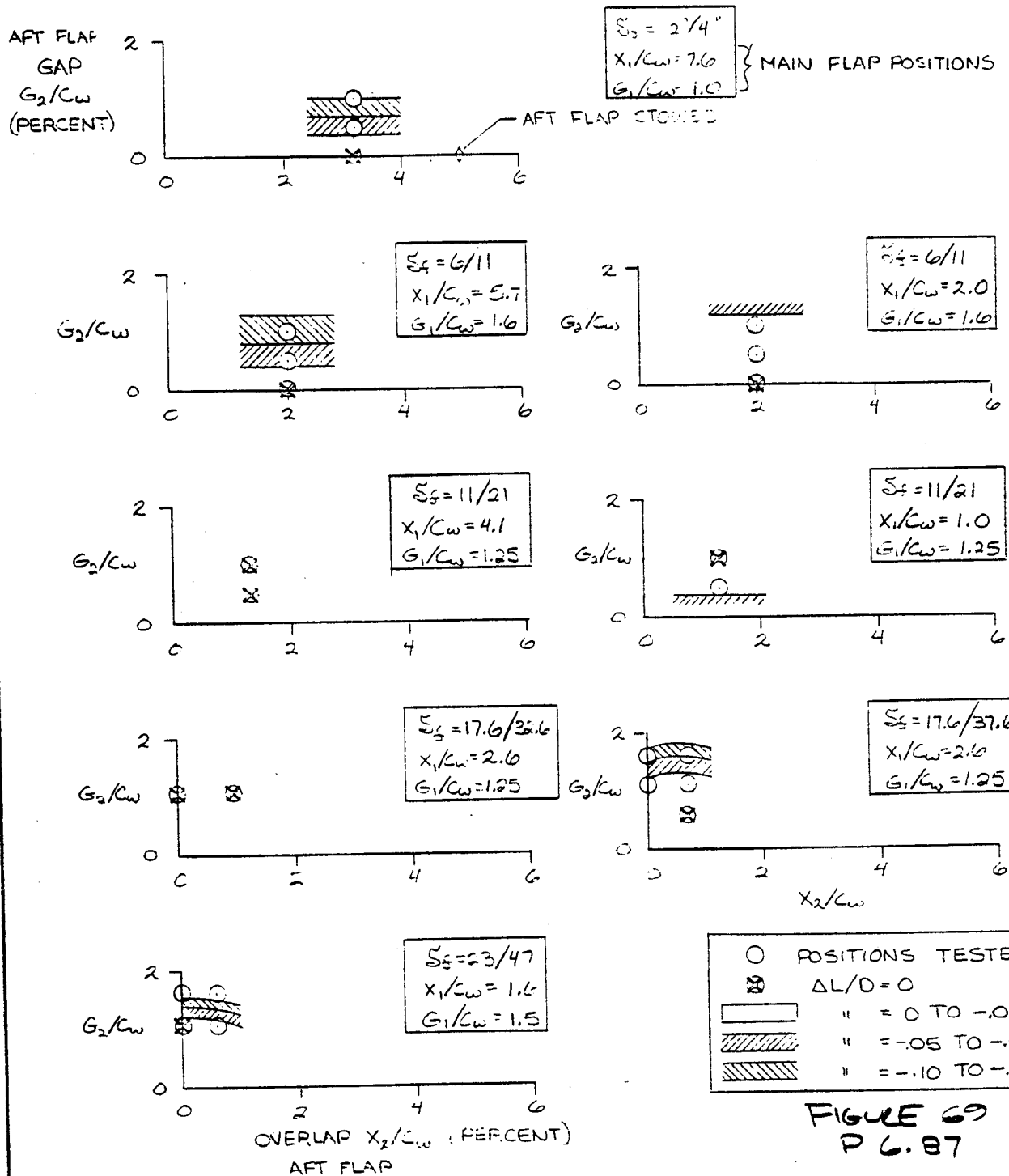

FIGURE 69
P 6.87

CALC	MR	10/27/77	REVISED	DATE	TRAILING EDGE AFT FLAP GAP & OVERLAP GRID	UWAL 1208
CHECK						TA 1315 E9
APR						
APR					THE BOEING COMPANY	PAGE

K+E ALBANENE 1965

1653

454

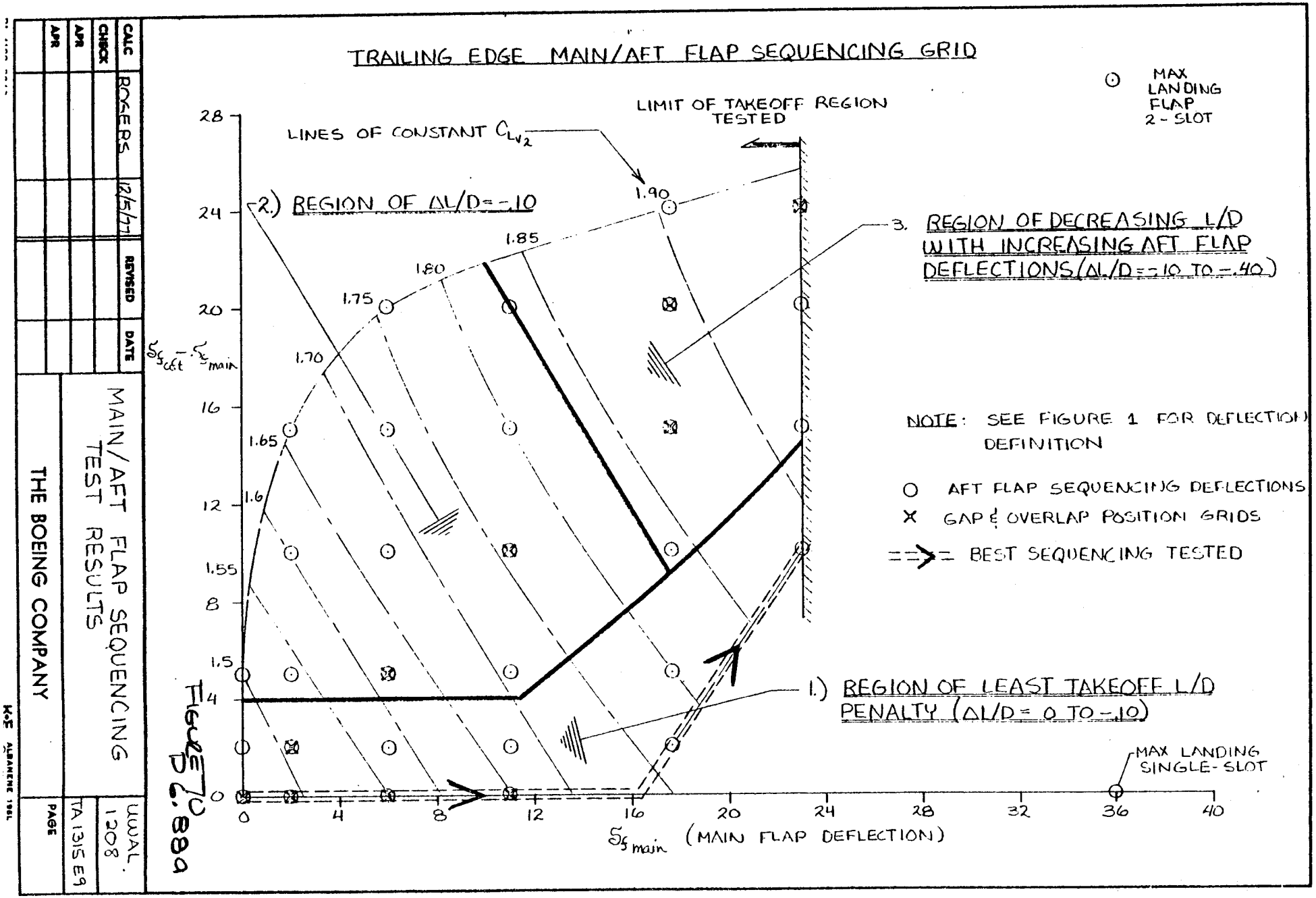

CALC	ROGERS	12/5/77		
CHECK			REVISED	
APR			DATE	
APR				

THE BOEING COMPANY

MAIN/AFT FLAP SEQUENCING TEST RESULTS

UWAL 1208

PAGE TA 1315 E9

K+E ALBANENE 1981

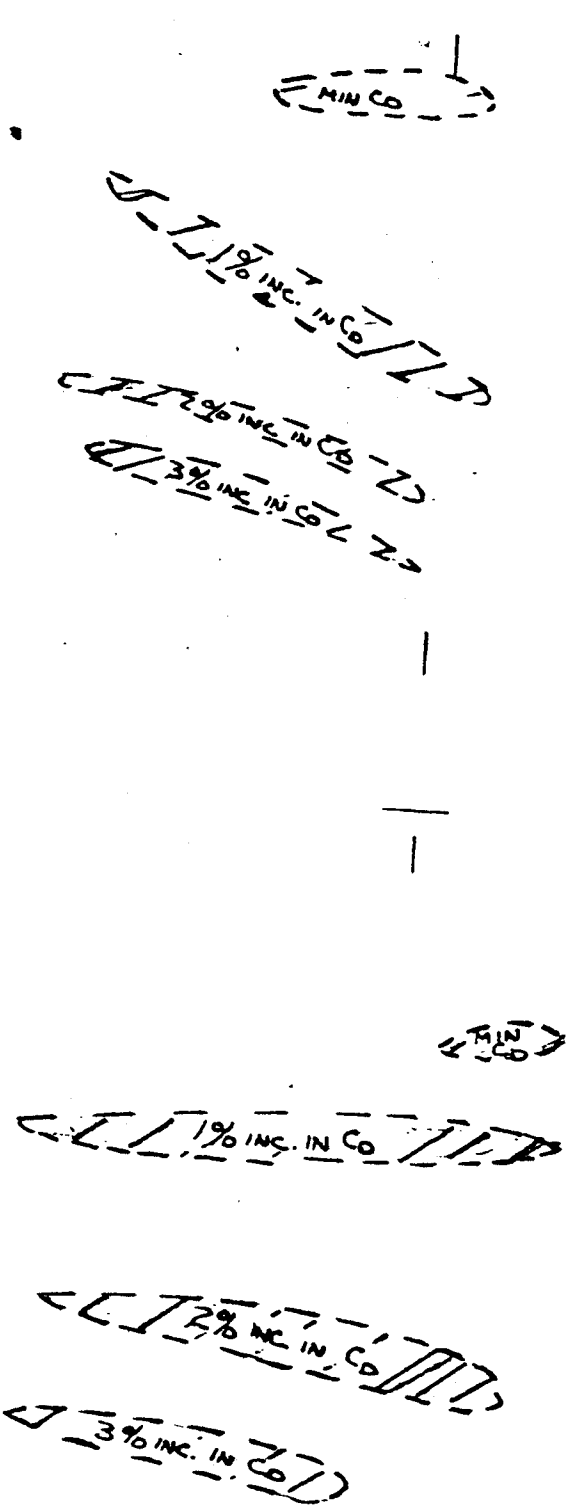

LANDING FLAP GAP/OVERLAP
SENSITIVITY TO MINIMUM DRAG

P6.886

FIG 71 O/L
BLUE

455

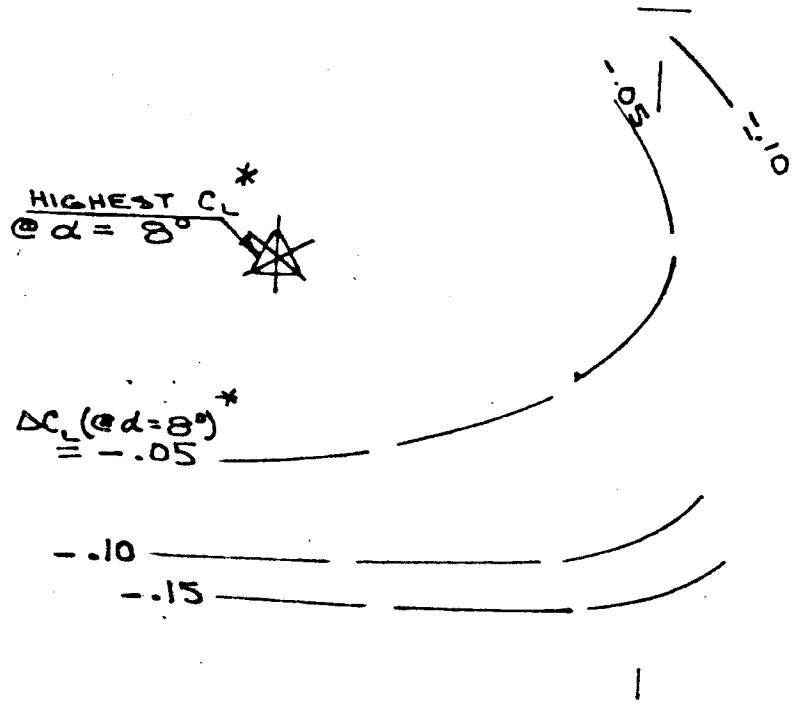

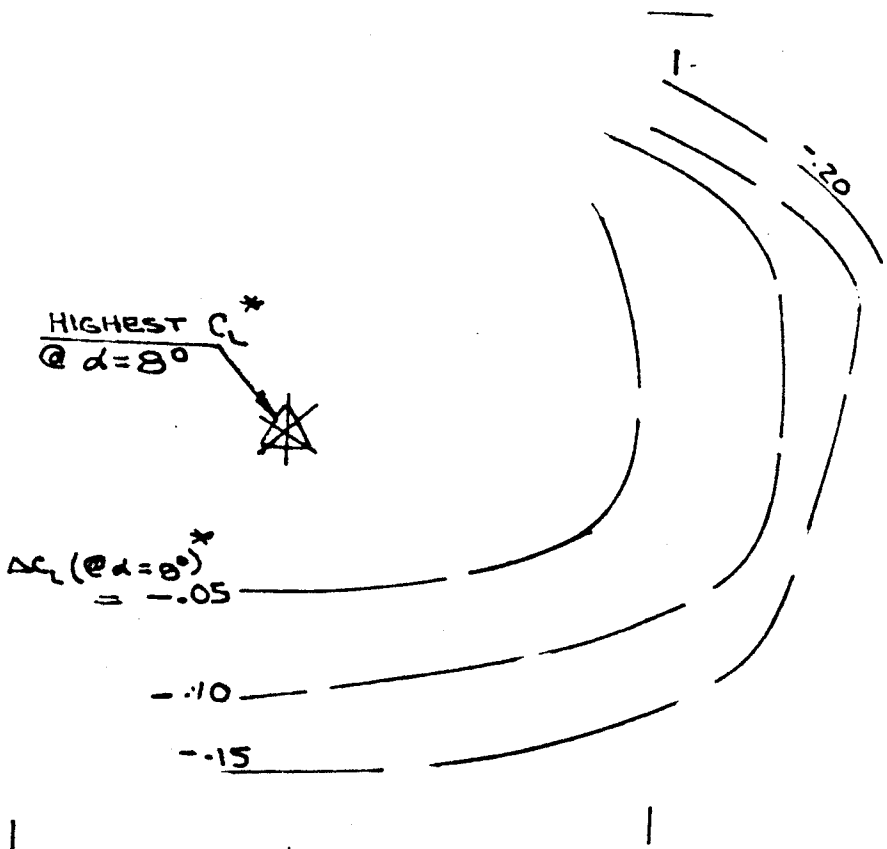

*. ΔC_L (@ $\alpha = 8°$) OF −.05 EQ. TO $\Delta \alpha_{APP} \approx +.5°$.

LANDING FLAP GAP/OVERLAP SENSITIVITY AT $\alpha = 8°$

FIG 71 O/L RED

PG 88C

456

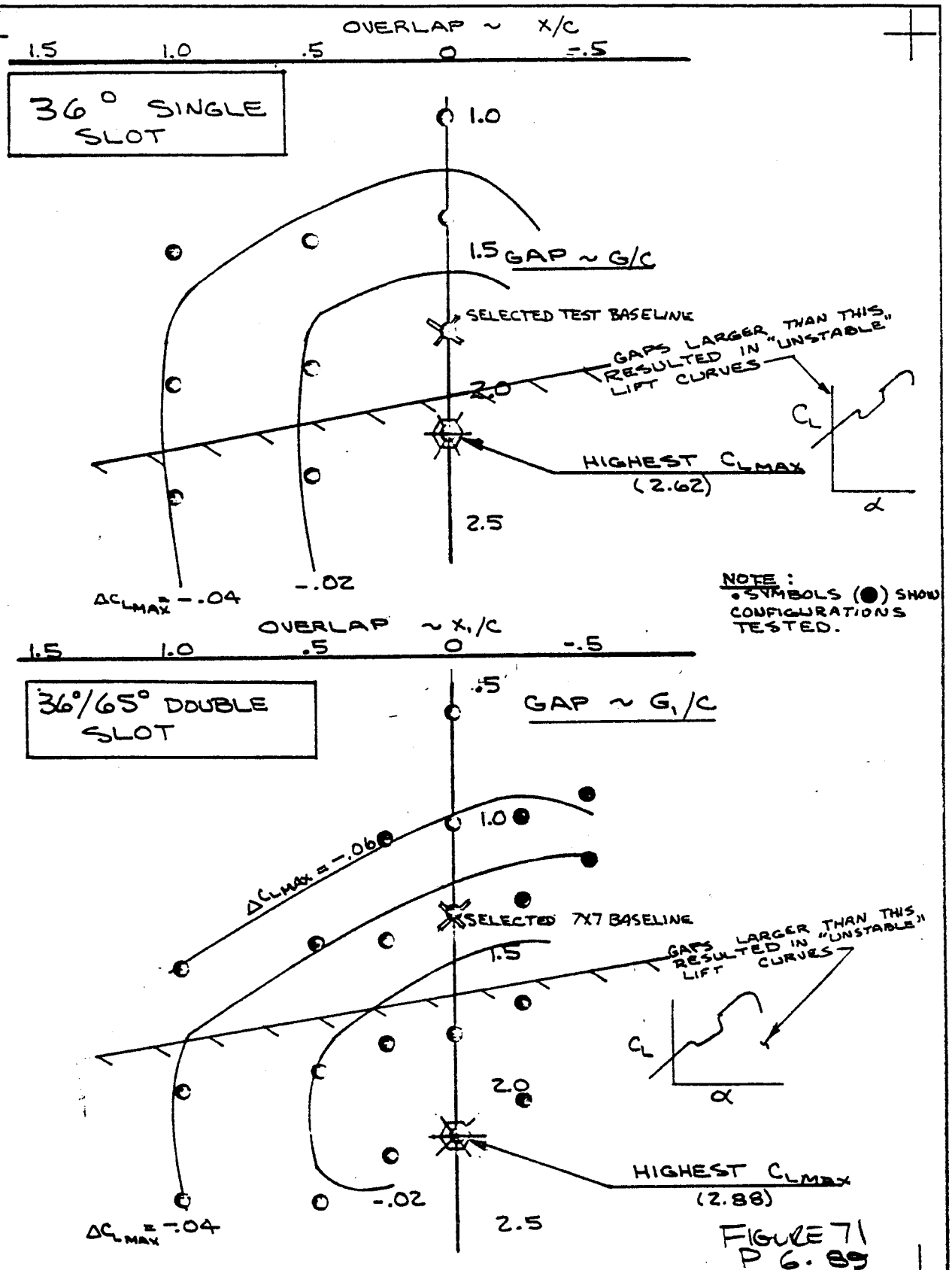

FIGURE 71
P 6.89

CALC	R.O.	10/28/77	REVISED	DATE	LANDING FLAP GAP/OVERLAP SENSITIVITY TO MAXIMUM LIFT	
CHECK						
APR						
APR					THE BOEING COMPANY	PAGE

457

CALC	R.E. Buchholz	1/12/77	REVISED	DATE
CHECK				
APR				
APR				

FIGURE 72
D 6.90

THE BOEING COMPANY

PAGE

4588

FLAP LINKAGE TYPE COMPARISON

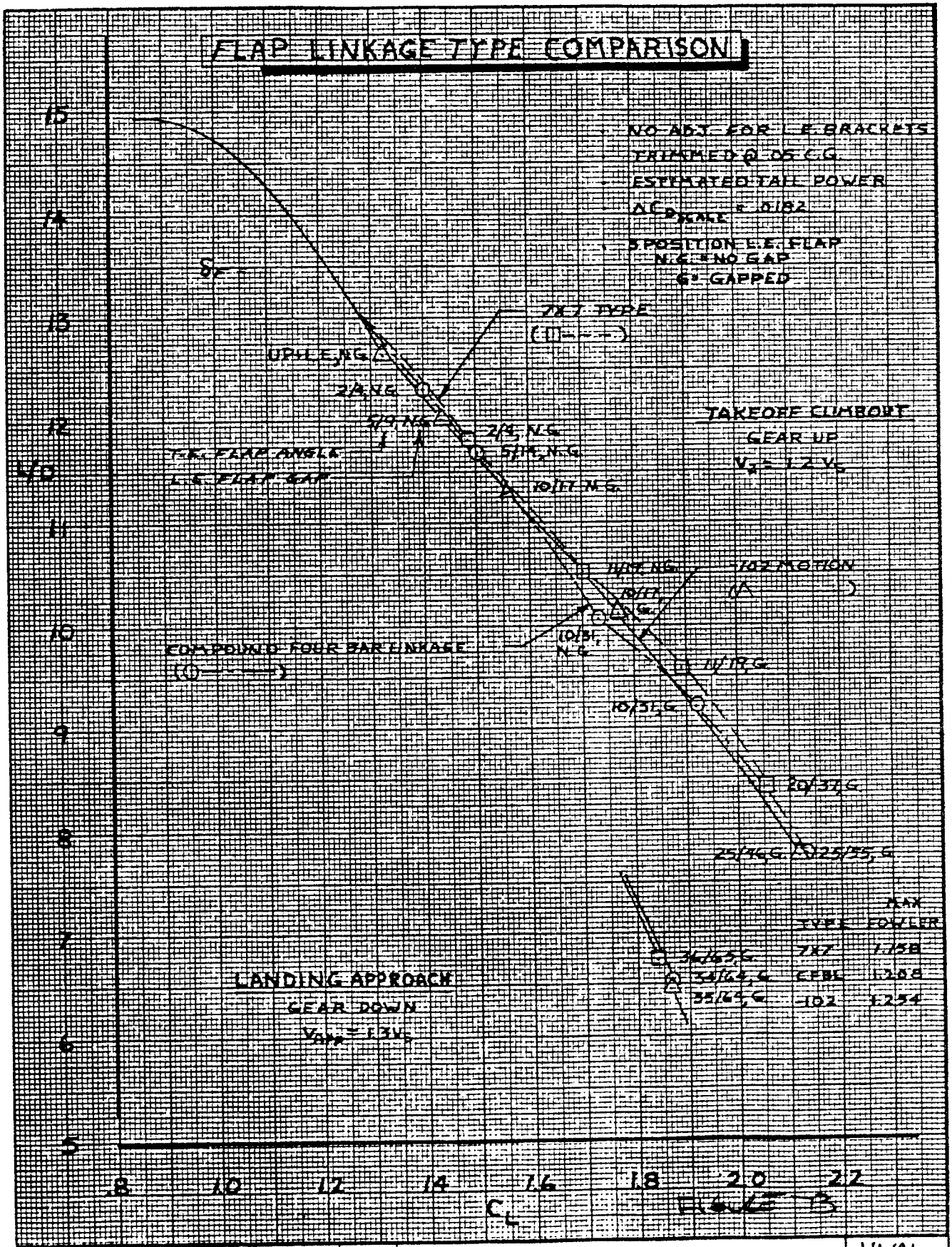

CALC	R.E. Buchholz 1/6/77	REVISED	DATE	FLAP LINKAGE TYPE COMPARISON	UWAL 1193
CHECK					
APR					
APR				THE BOEING COMPANY	PAGE P6.91
	N WELEVER 1-21-77				

K-E ALBUQUERQUE

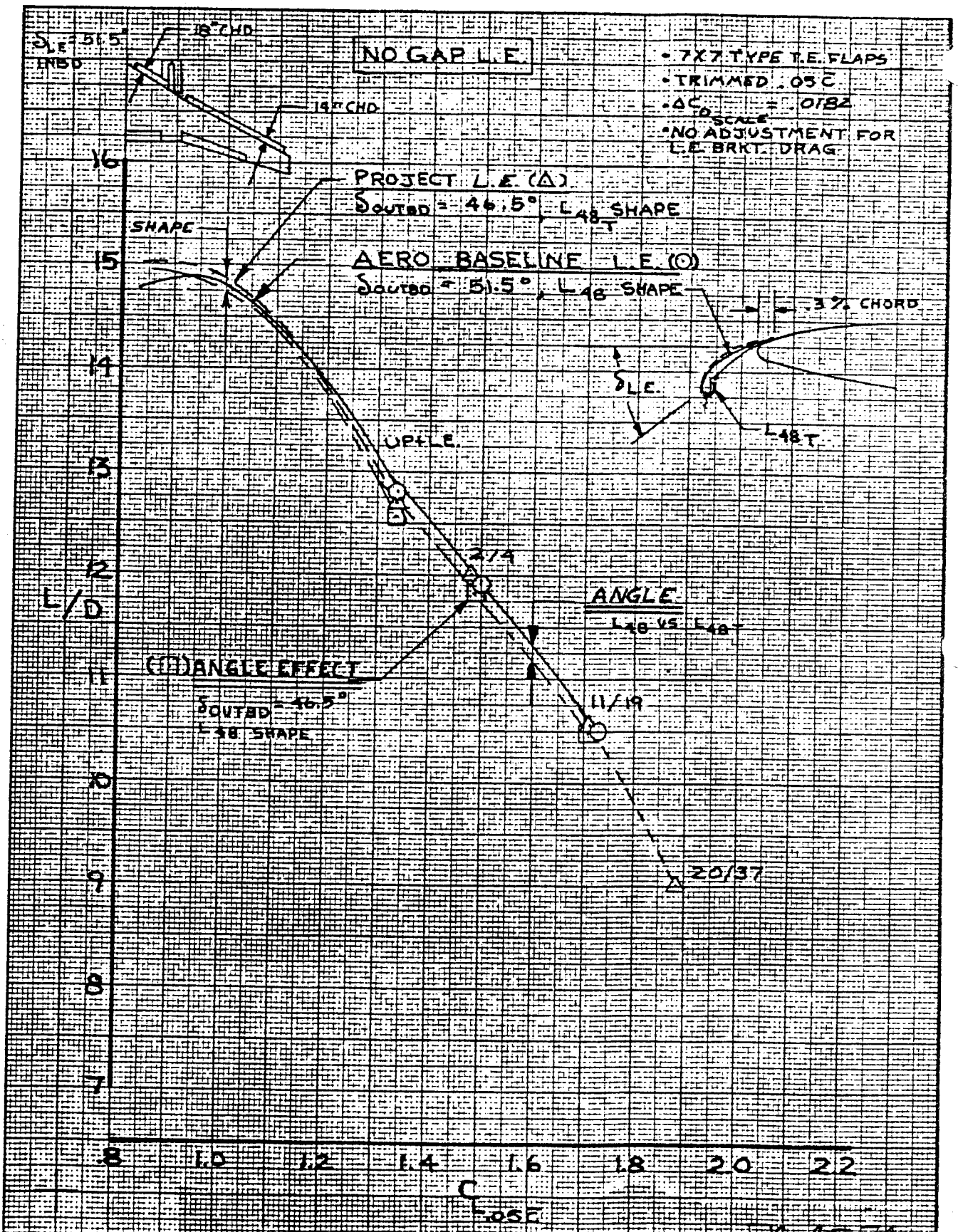

CALC	W. ROBERTS	1-12-77	REVISED	DATE
CHECK				
APR				
APR				
	N. WELEUER	1-12-77		

EFFECT OF SHAPE & ANGLE
NO GAP L.E.

UWAL 1193

THE BOEING COMPANY

PAGE P6.92

460

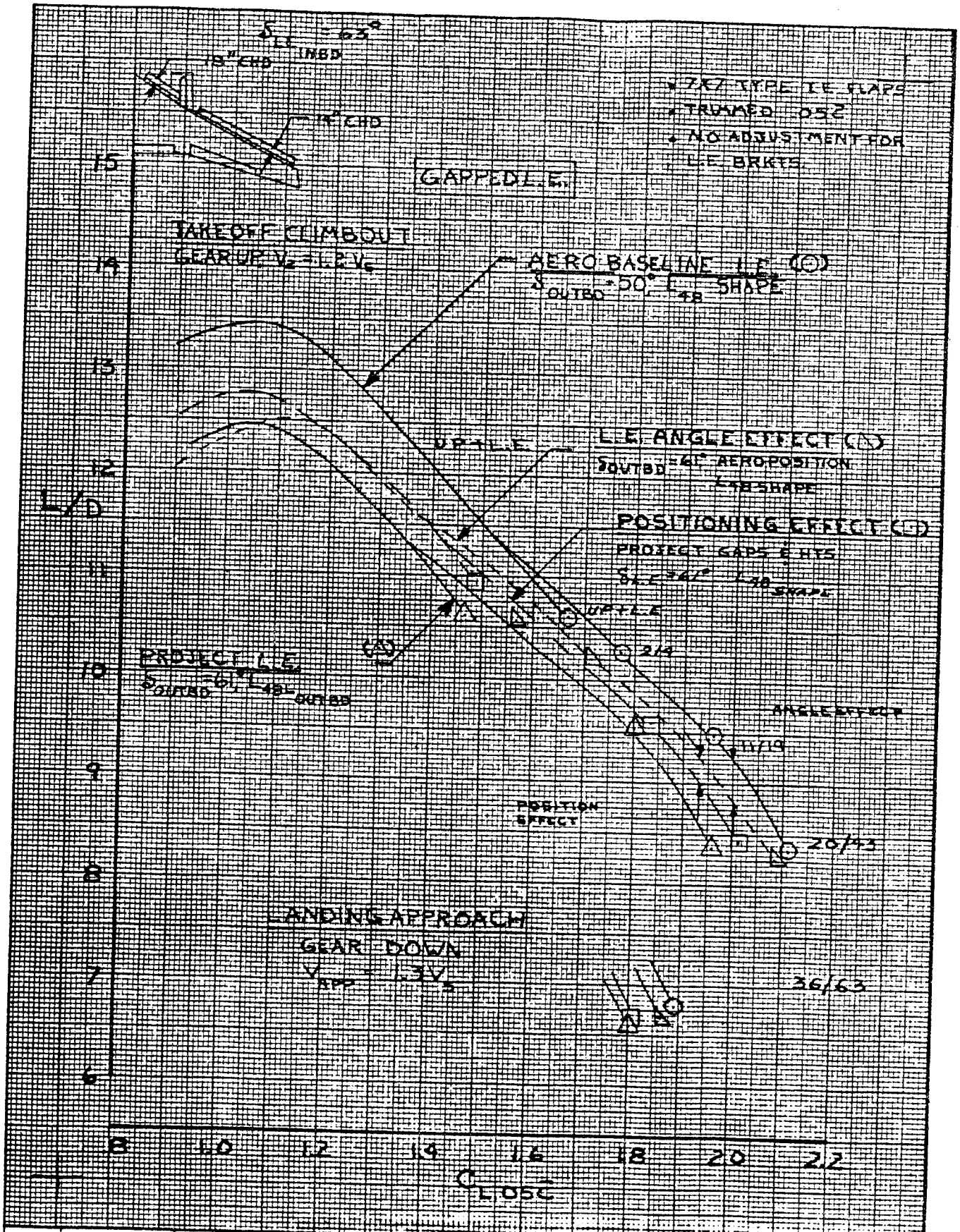

CALC	W. ROBERTS	1-11-77	REVISED	DATE	RULE 75 — EFFECT OF L.E. SHAPE, POSITION, & ANGLE: GAPPED L.E.
CHECK					THE BOEING COMPANY
APR					UWAL 1193
APR					PAGE D6-93
	M. WELIVER	1/11/77			

461

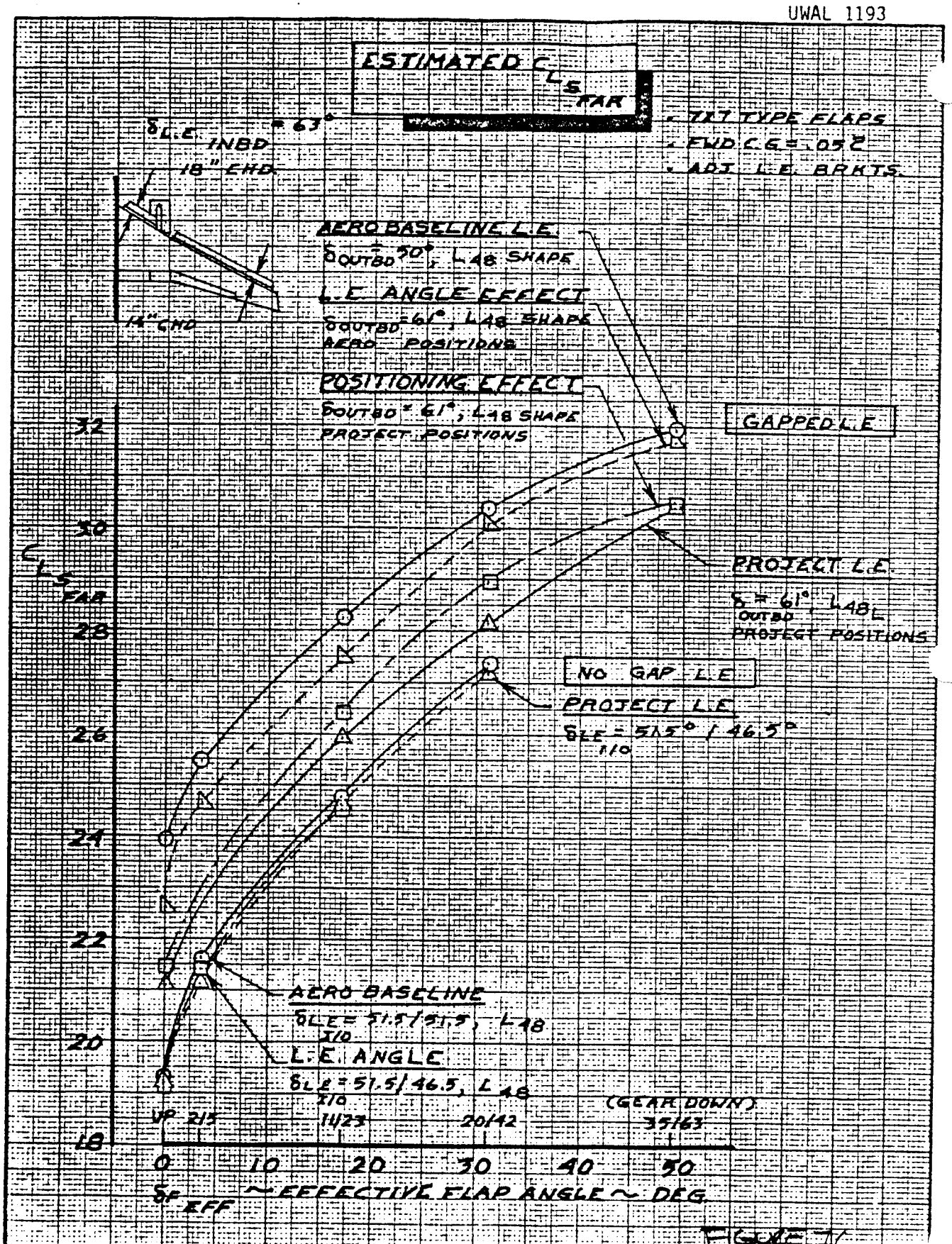

FIGURE 7C

CALC	W. ROBERTS	1-4-77	REVISED	DATE	EFFECT OF OUTBD LEADING EDGE SHAPE, POSITION & ANGLE ON STALL C_{L_S}	7NT
CHECK						
APR						
APR					THE BOEING COMPANY	PAGE P6.94
	N. WHITEVER	3-2-77				

4602

FIGURE 77
PG. 95

UWAL 110.

REV SYM

747SP INBD FLAP FLOW WITHOUT FIXED
25 SCALE [illegible] WALL FINNE

BOEING

463

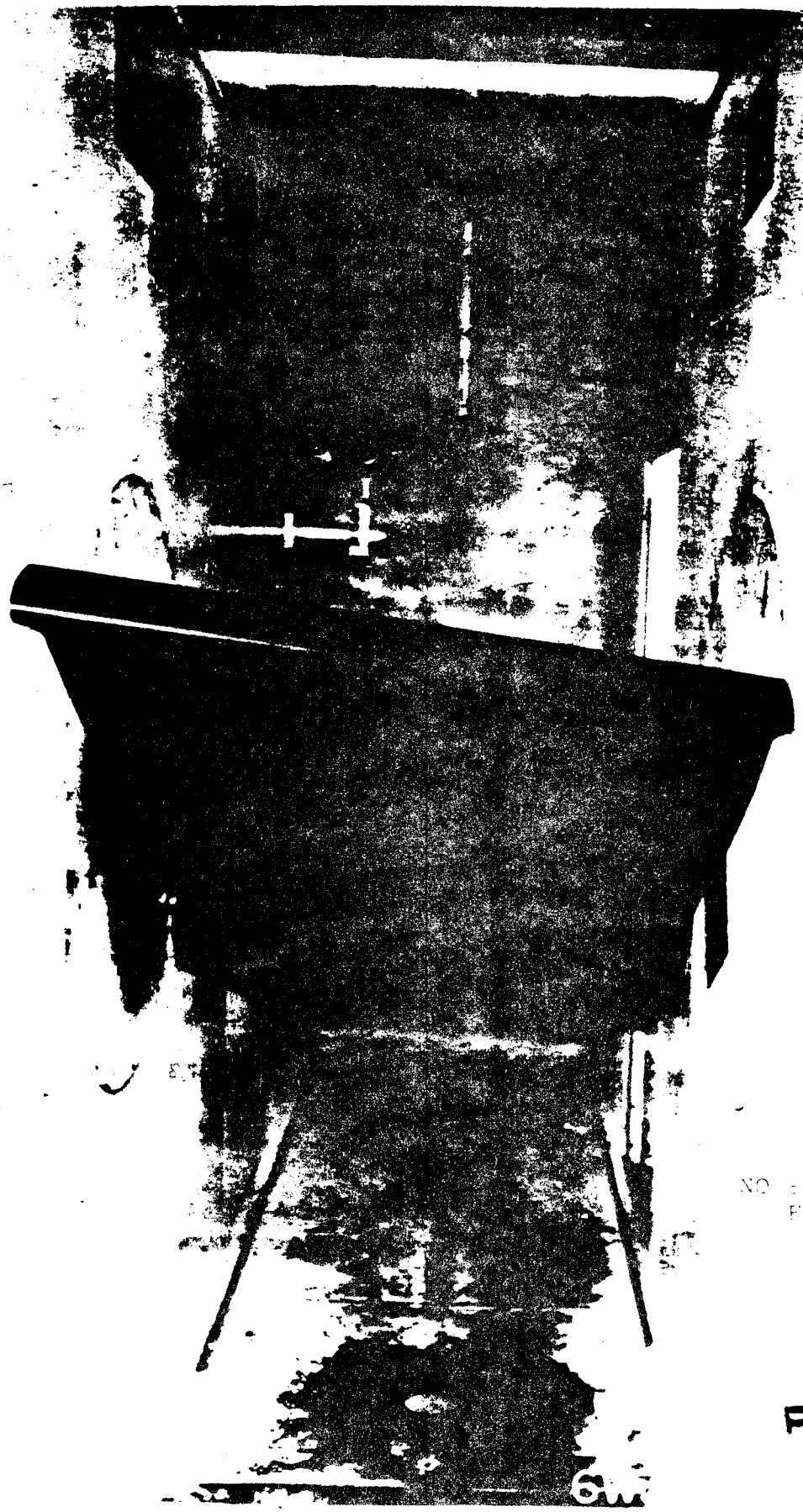

FIGURE 78
PG. 96

BRWT 074

TE 1303 E-1

REV SYM

747 SP, INBOARD FLAP MODEL INSTALLATION IN 3'x8' BRWT

BOEING

PAGE

	APR	APR	CHECK	CALC
				M. Iwanaga
				18 MAR 75
				REVISED
				DATE

THE BOEING COMPANY

DRAG LEVEL ~ FLAPS 30 & 20
INBOARD FLAP CENTER SUPPORT

PAGE

TE 1303 E-1
747SP

Figure 79
P6.97

FLAP EFFICIENCY

FLAPS 30

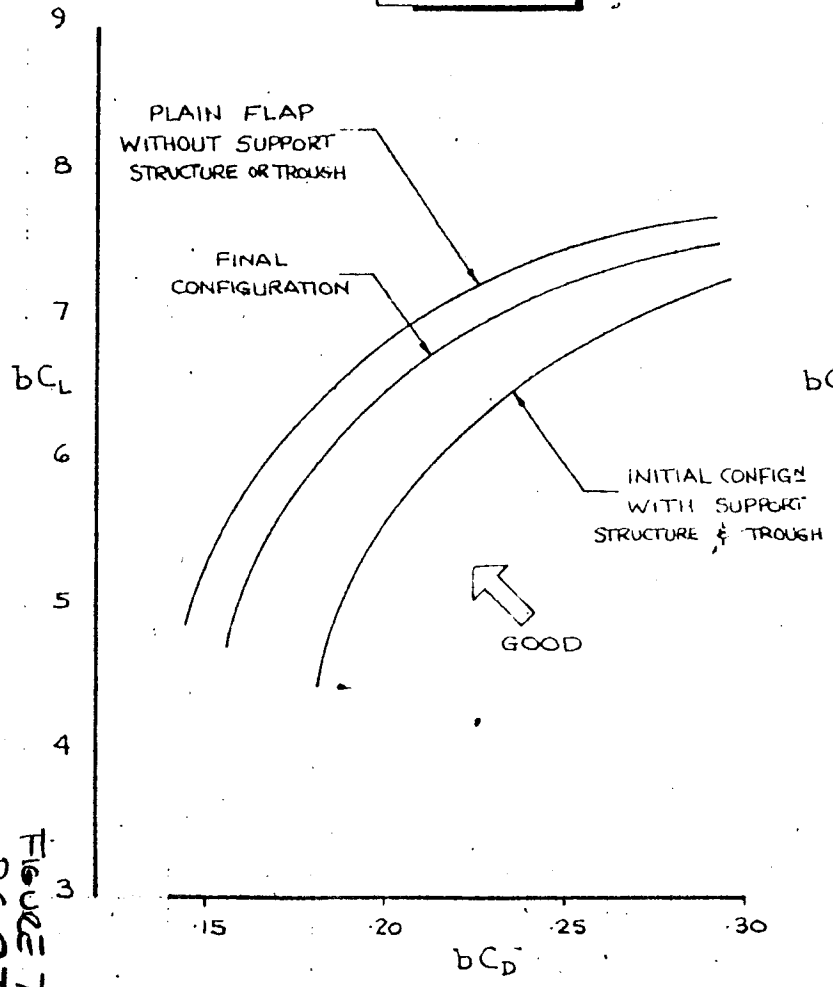

FLAPS 20

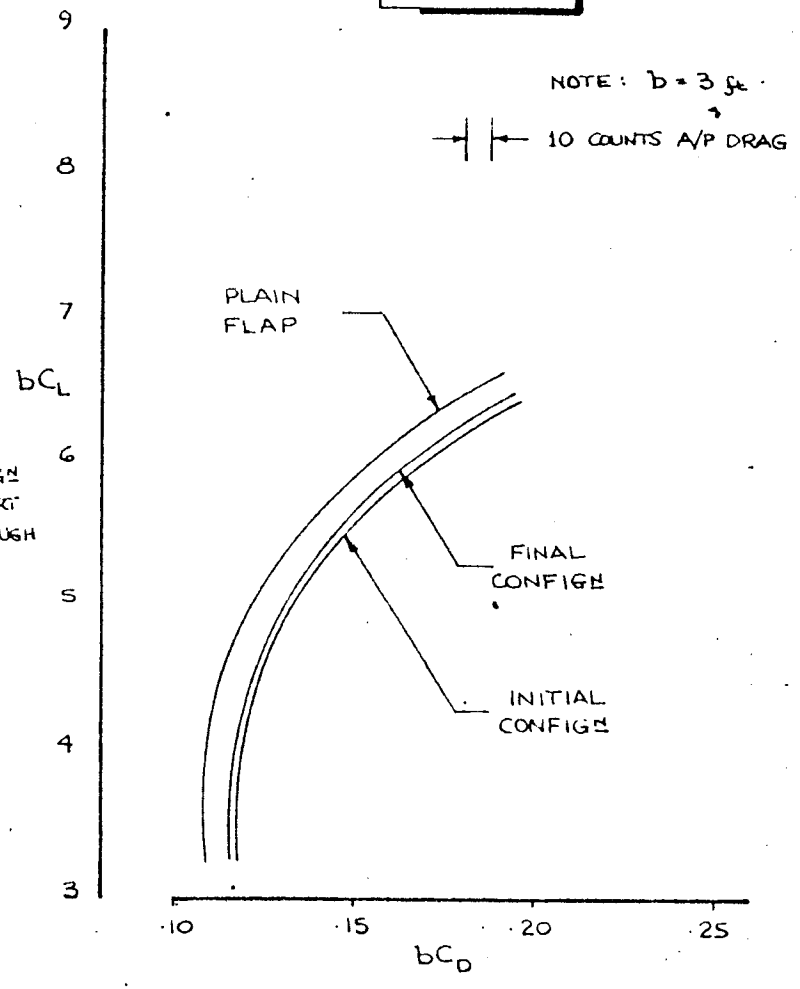

BRWT 074

FIGURE 80
P 6.98

CALC	M. Grainger	18 MAR 75	REVISED	DATE	BUFFET INTENSITY ~ FLAPS 30 & 20 INBOARD FLAP CENTER SUPPORT
CHECK					
APR					
APR					

TE 1303 E-1
747SP

THE BOEING COMPANY

PAGE

K+E ALBANENE 1961

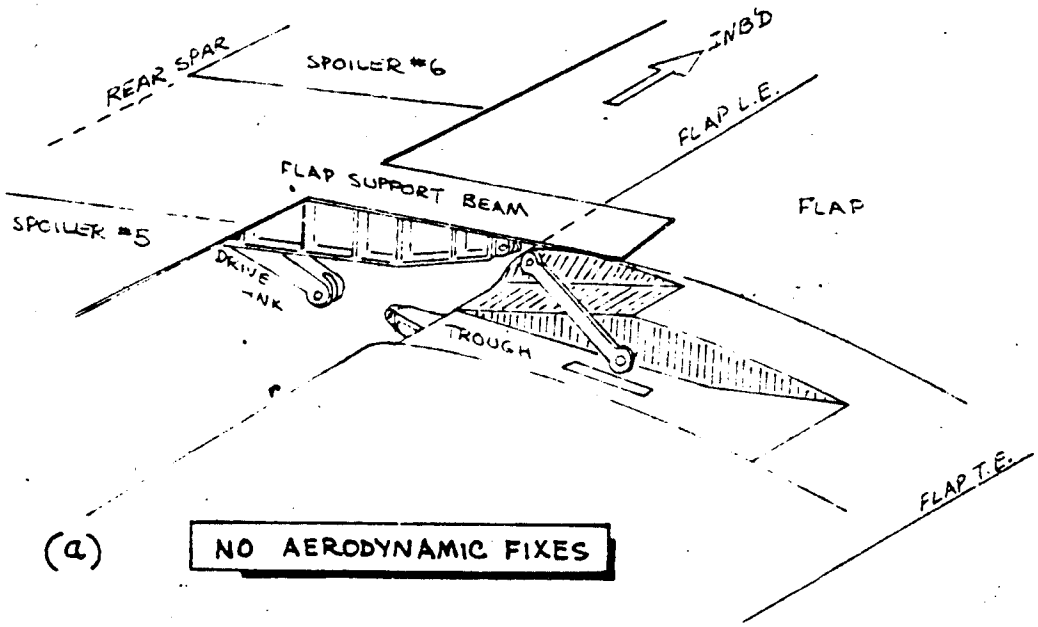

(a) NO AERODYNAMIC FIXES

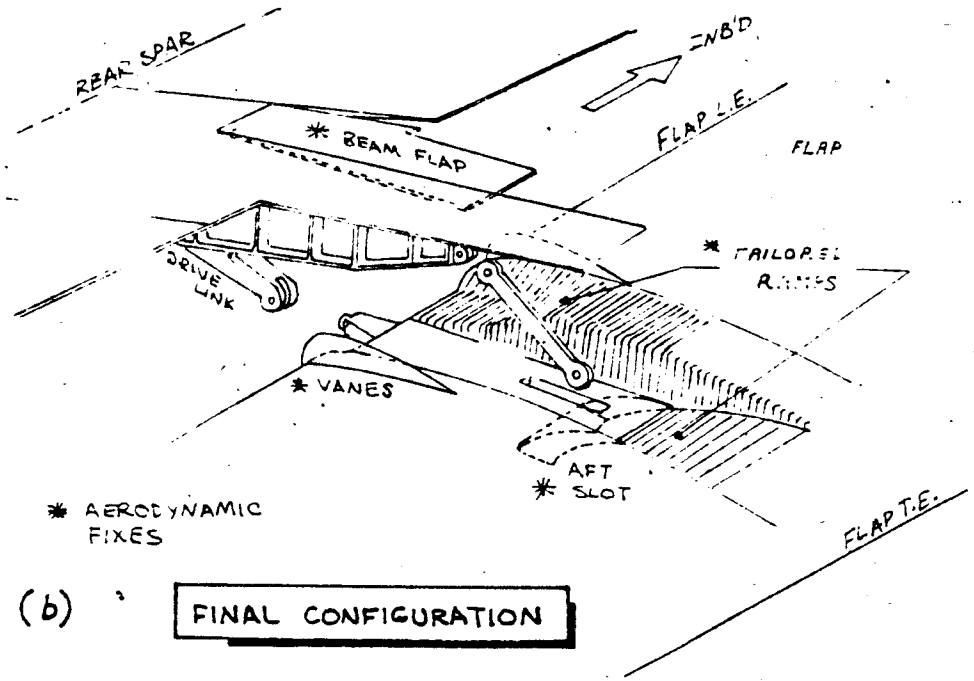

(b) FINAL CONFIGURATION

FIGURE 81
P 6.99

BRWT 074

C. Kilen 10/31/74 M. Grange	COMPARISON OF SUPPORT GEOMETRIES, INBOARD FLAP BOEING	TE 1303 E-1 747SP

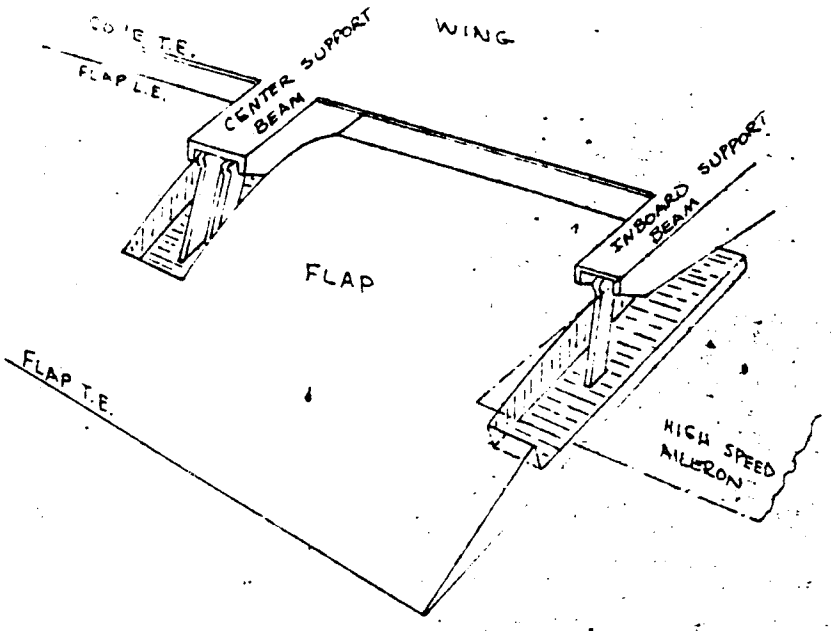

NO AERODYNAMIC FIXES (a)

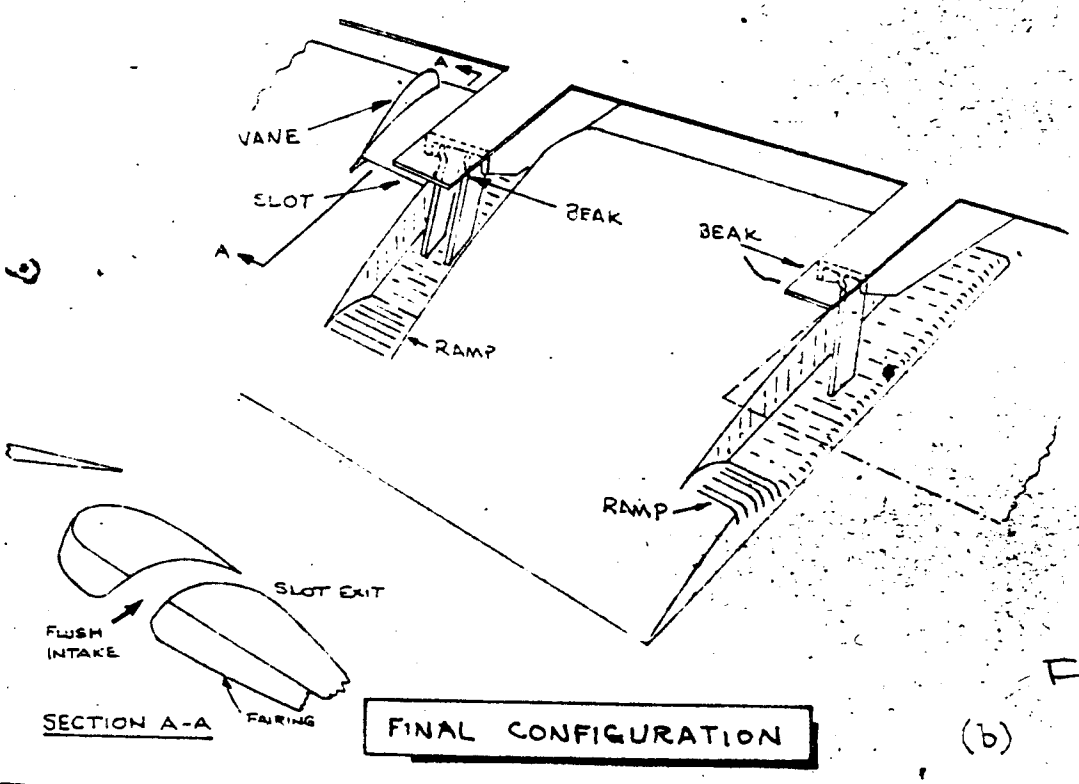

FINAL CONFIGURATION (b)

FIGURE 32
PG. 100

T. Kisha 11/1/74
Drawing — 26 Mar 75

COMPARISON OF SUPPORT GEOMETRIES, OUTBOARD FLAP

TE1303E-2
747SP

BOEING

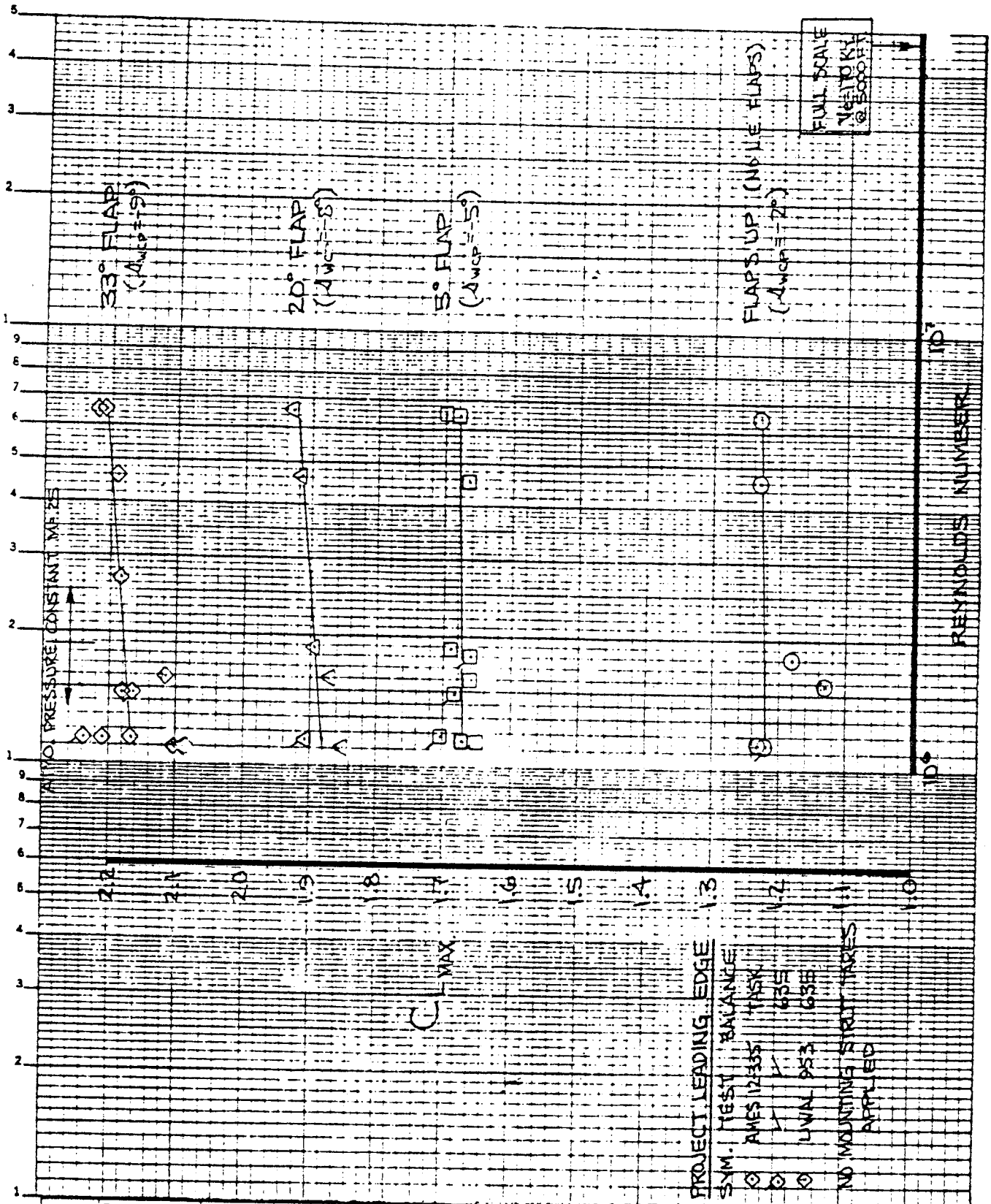

CALC	DICKSON	6-22-68	REVISED	DATE
CHECK	[signature]	1/22/69	DICKSON	D-1568
APR				
APR				
INK	M. LANG			

EFFECT OF REYNOLDS NUMBER ON $C_{L\,MAX}$

THE BOEING COMPANY

CONTRACT NO.

FIGURE 83

TE-1065I-1

PAGE P6.101

TD 462-R2

6-7000

470

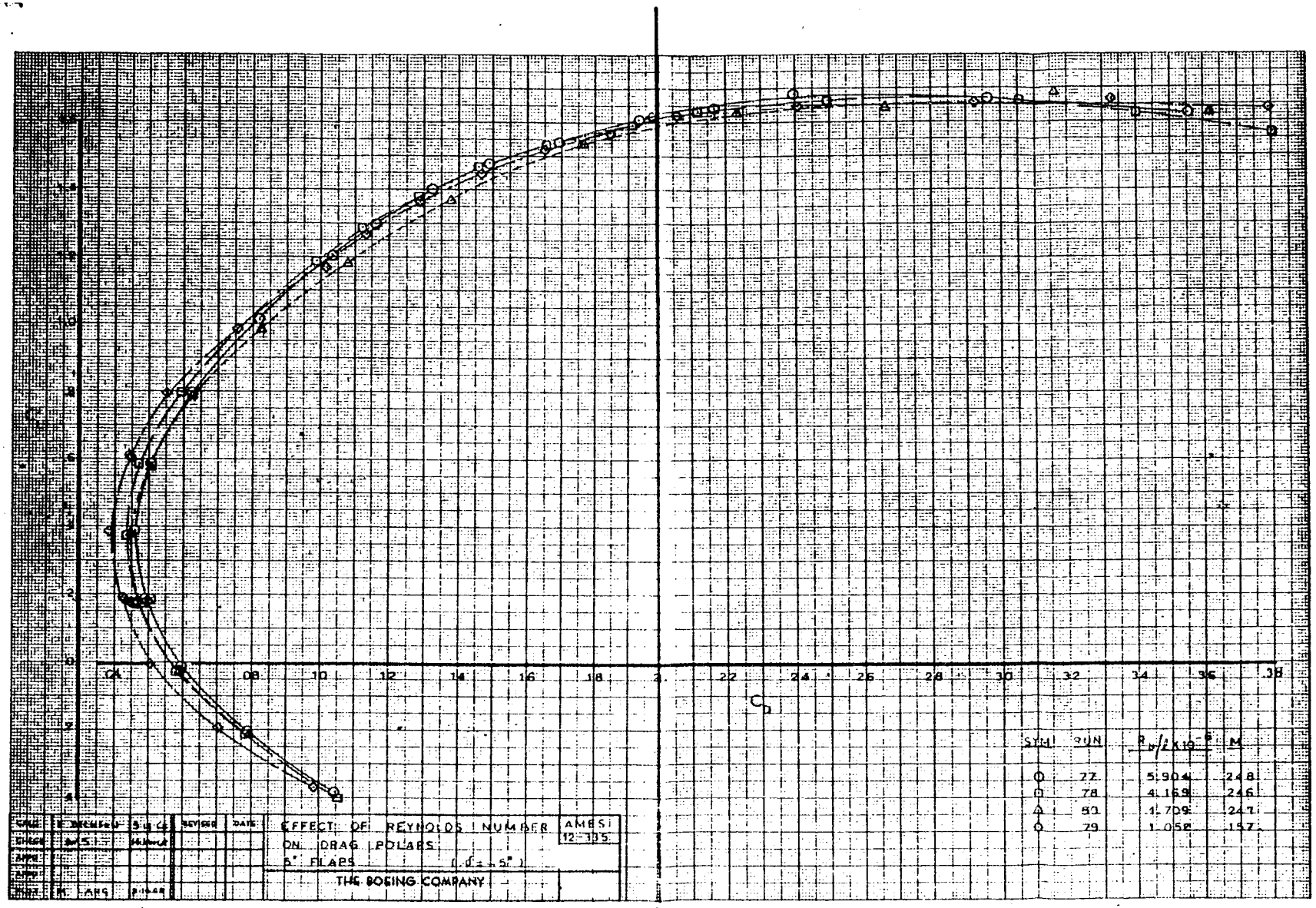

53

Fig 84
Pg. 102

471

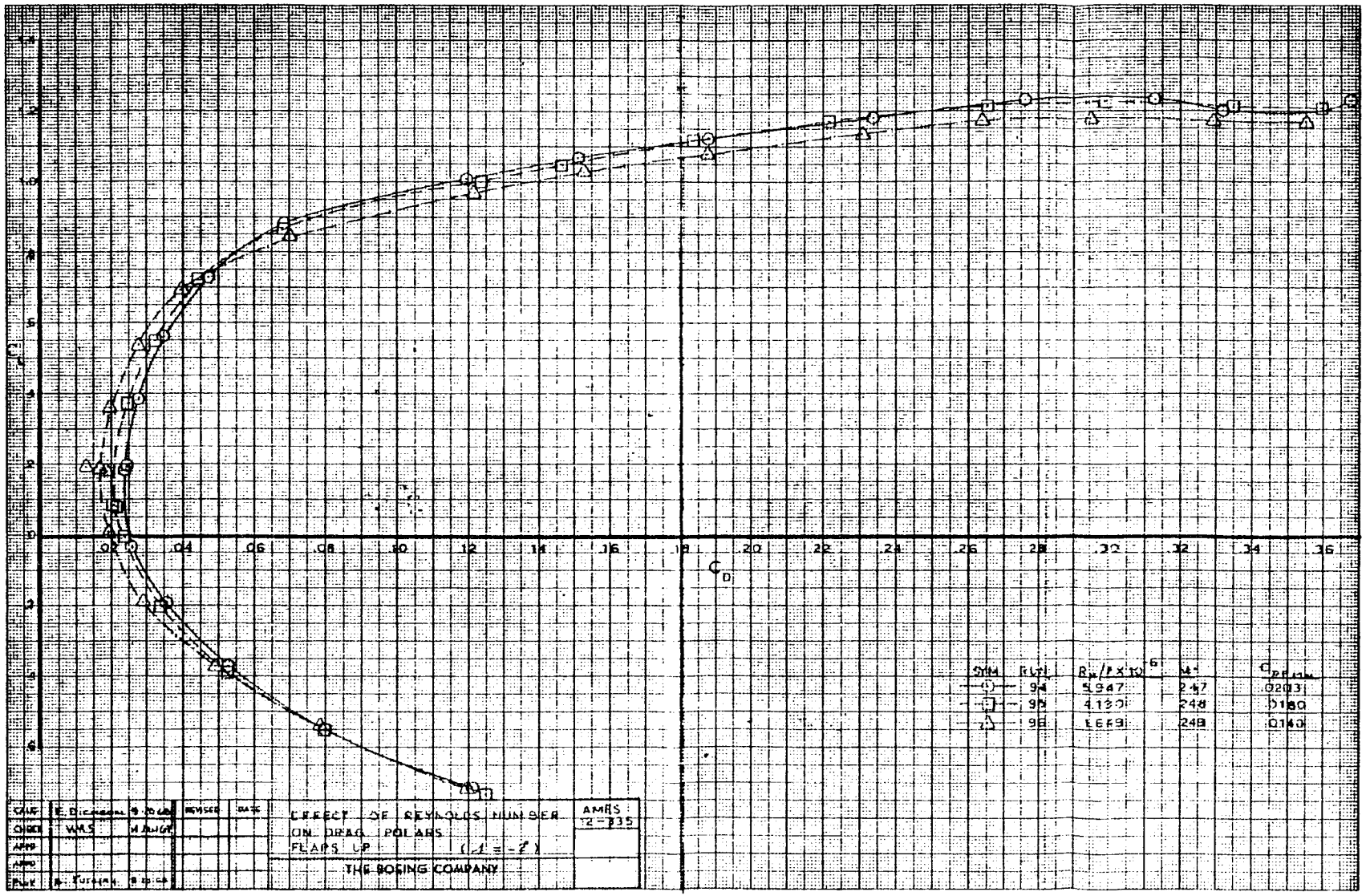

D6-10383

TR 85

472

46 4973

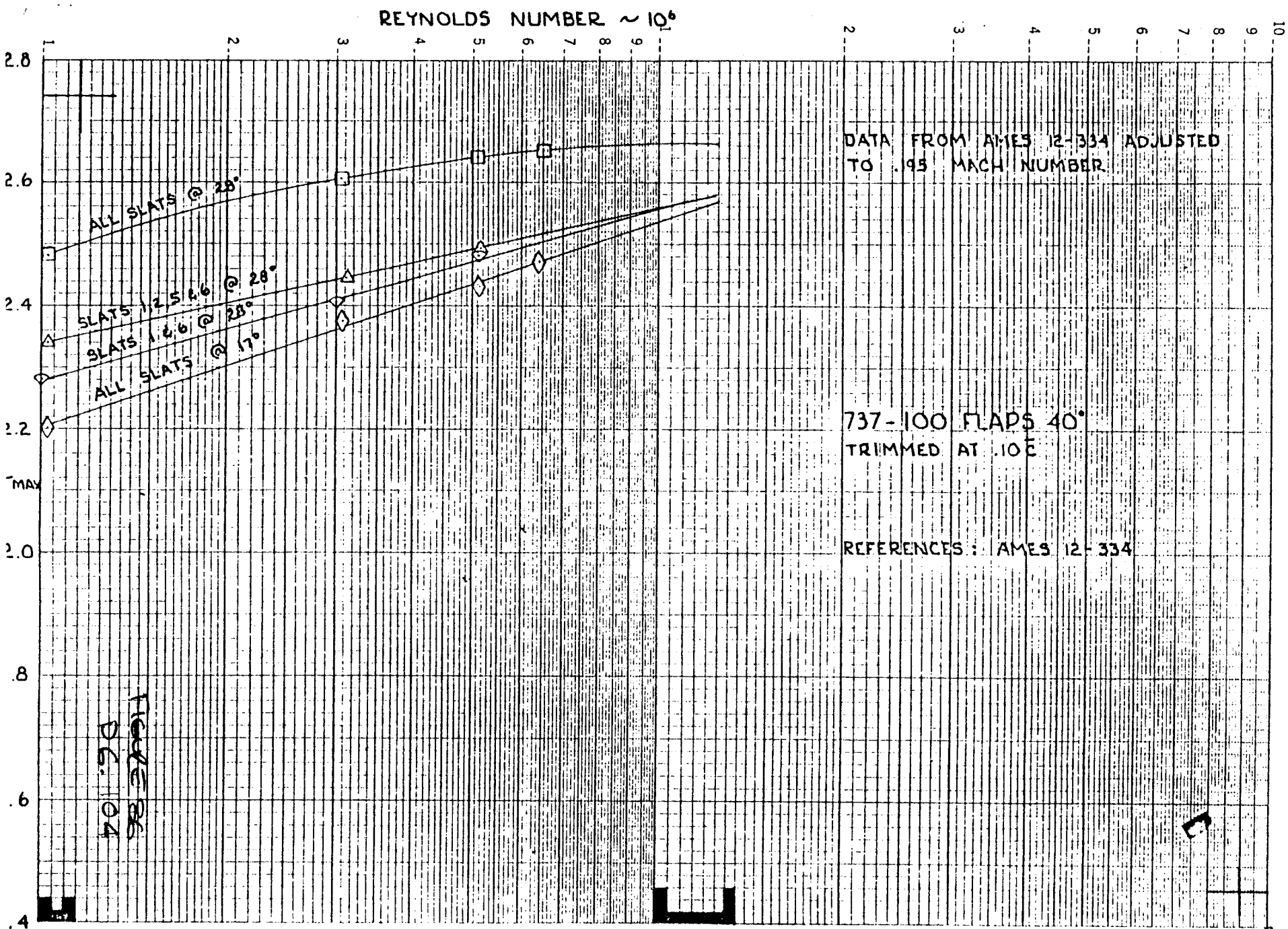

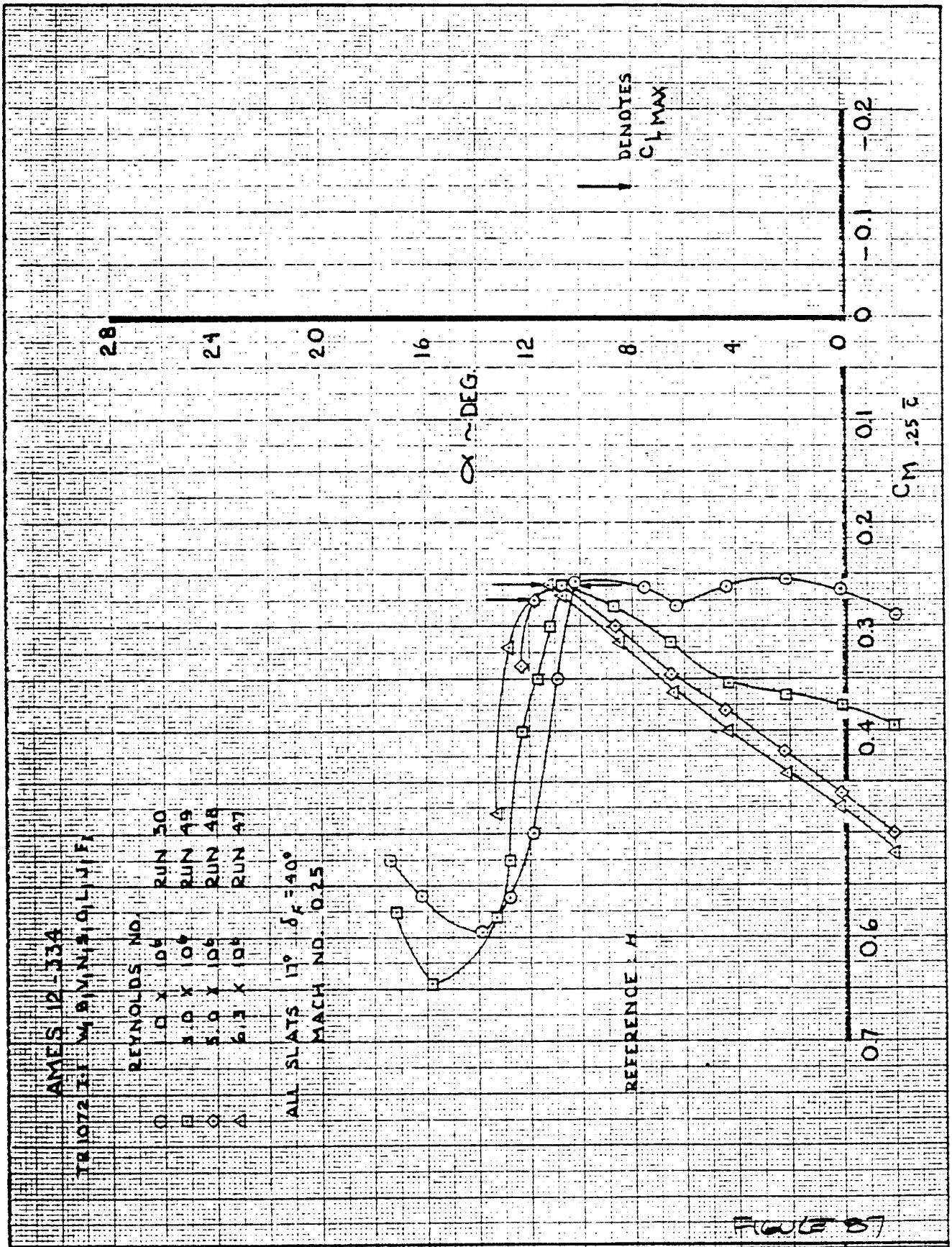

FIGURE 87

CALC	BUCHHOLZ	4-9-75	REVISED	DATE
CHECK				
APR				
APR				
INK	HALL	4-10-75		

EFFECT OF REYNOLDS NUMBER ON PITCHING MOMENT

THE BOEING COMPANY

PAGE D6.105

K-E ALBANENE 1954

473

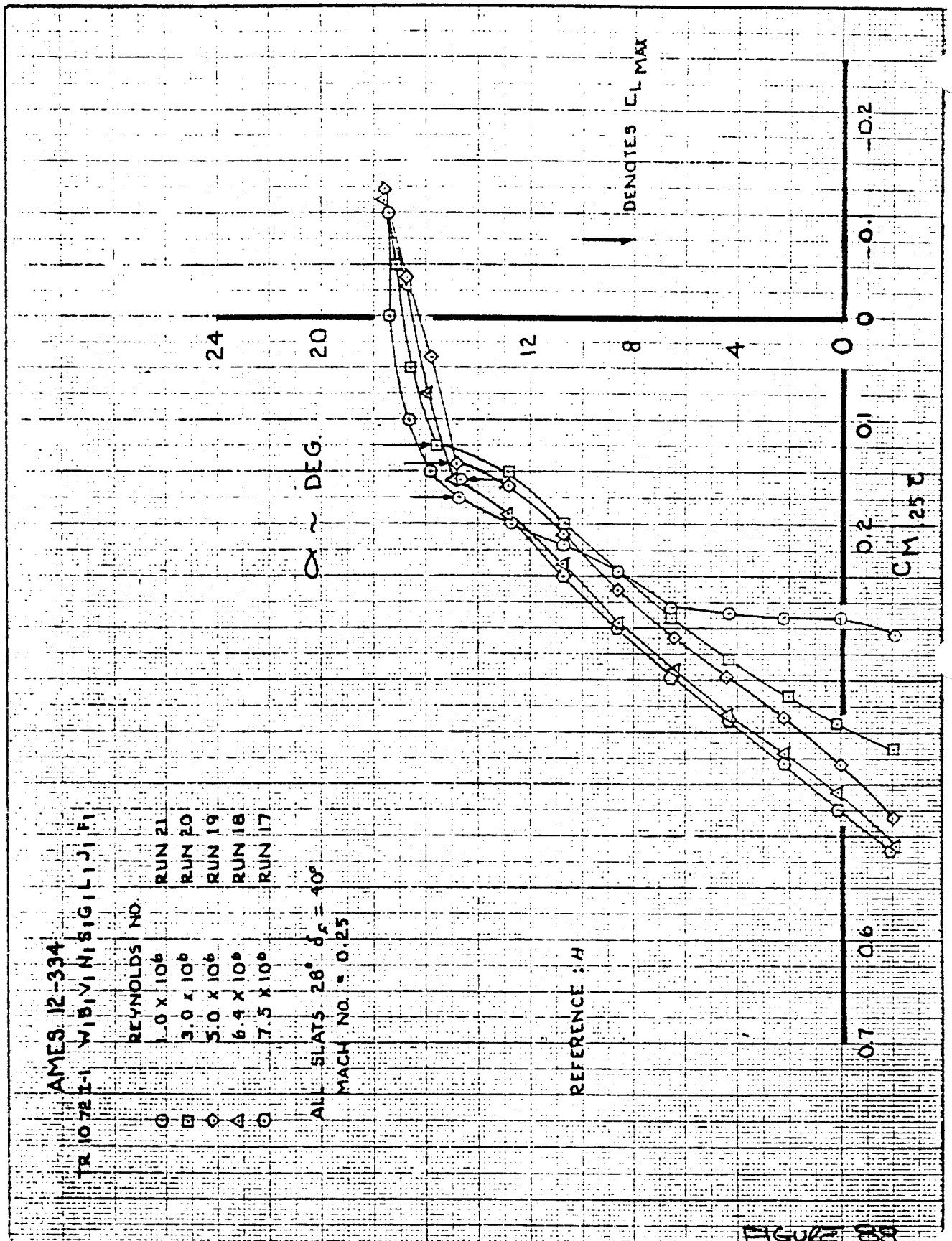

FIGURE 88

CALC	BUCHHOLZ	4.9.15	REVISED	DATE
CHECK				
APR				
APR				
INK	HALL	4-10-15		

EFFECT OF REYNOLDS NUMBER ON PITCHING MOMENT

THE BOEING COMPANY .

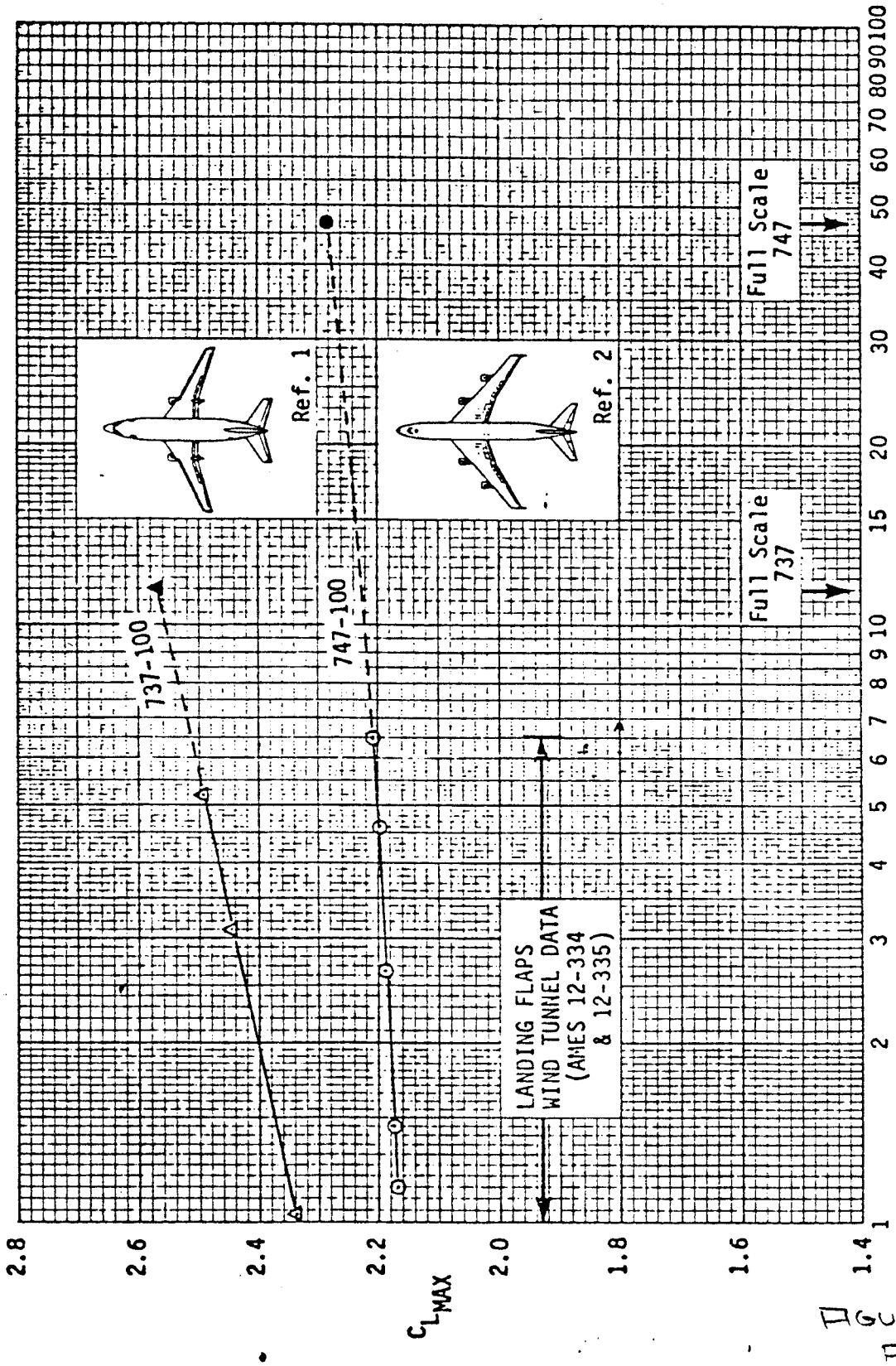

FIGURE 89
P 6.107-

ENGR.			REVISED	DATE	REYNOLDS NUMBER EFFECT ON 737 & 747 MAXIMUM LIFT	
CHECK						
APR						
APR					BOEING	

D1 4100 5320 REV. 8/71

J19-047

475

FIGURE

Figure 30
Pg. 108

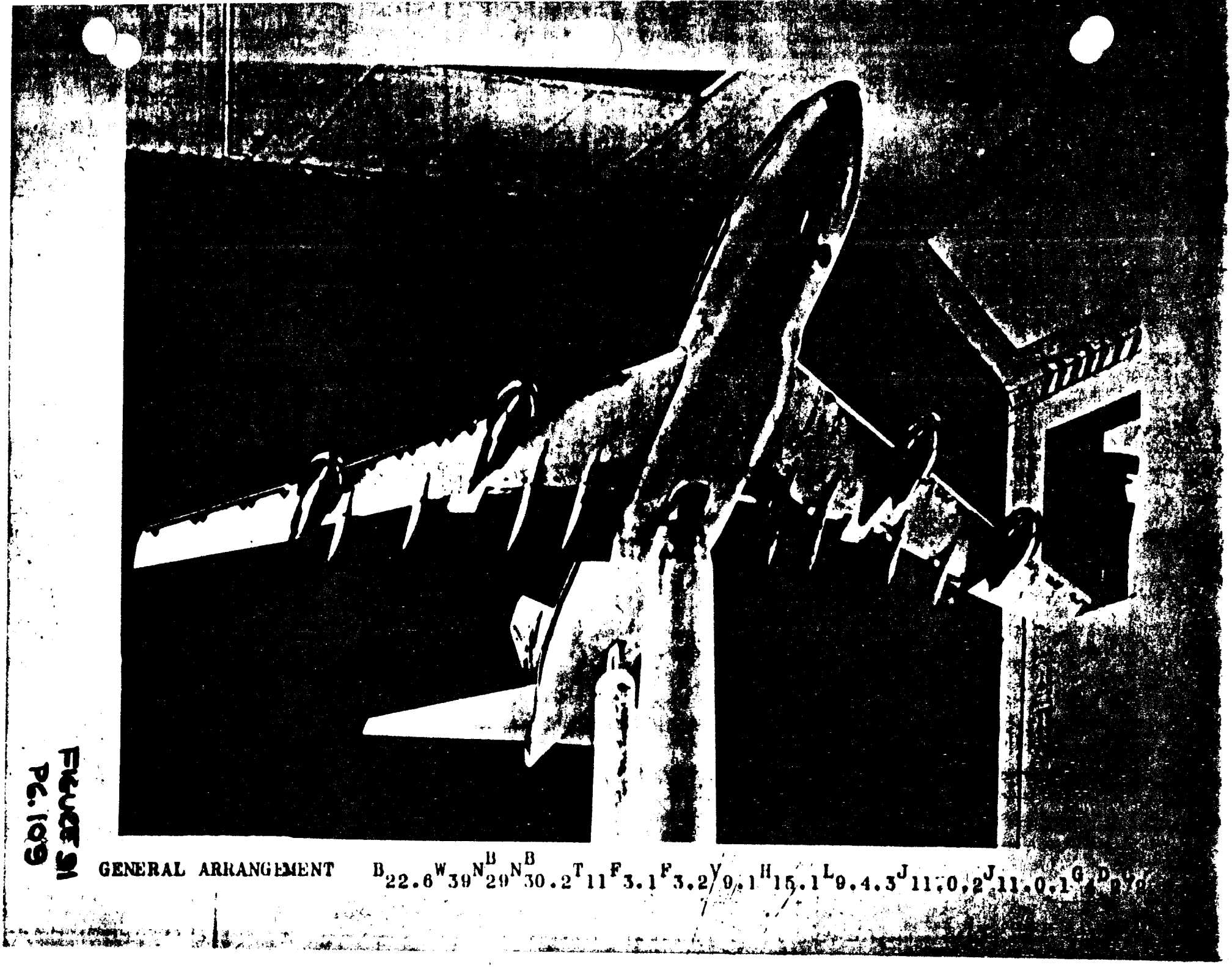

FIGURE 91
PG. 109

GENERAL ARRANGEMENT $B_{22.6}{}^{W}{}_{39}{}^{N}{}^{B}_{29}{}^{N}{}^{B}_{30.2}{}^{T}{}_{11}{}^{F}{}_{3.1}{}^{F}{}_{3.2}{}^{V}{}_{9.1}{}^{H}{}_{15.1}{}^{L}{}_{9.4.3}{}^{J}{}_{11.0.2}{}^{J}{}_{11.0.1}{}^{G}{}_{4}{}^{D}{}_{9.6}$

USB R&D FULL MODEL AT 20' X 20' BVWT

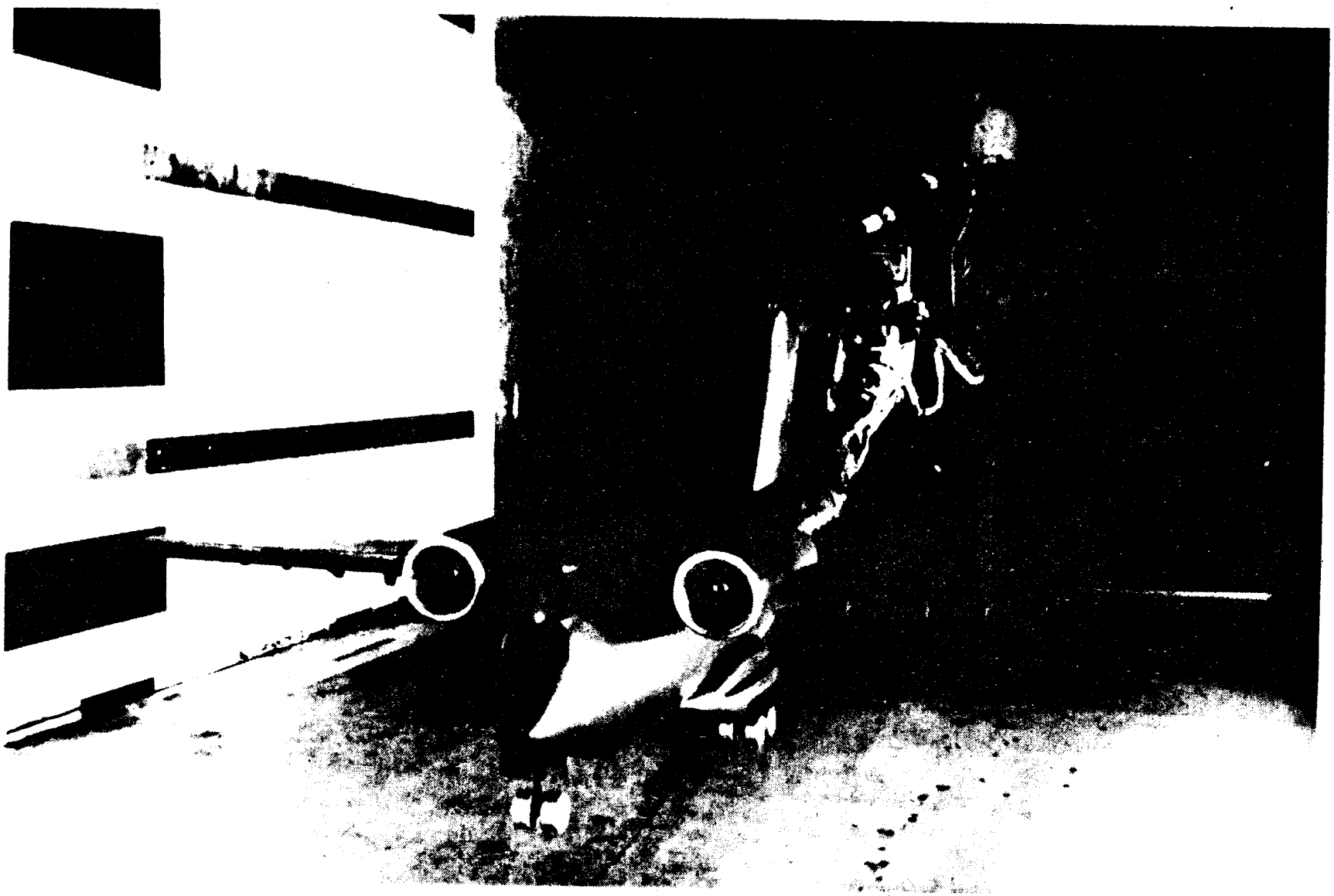

FIGURE 92
PG.110

USB R&D PART SPAN MODEL AT 3' X 8' BRWT

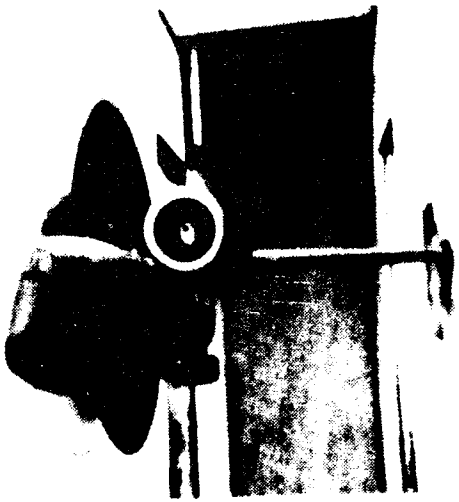

FRONT VIEW

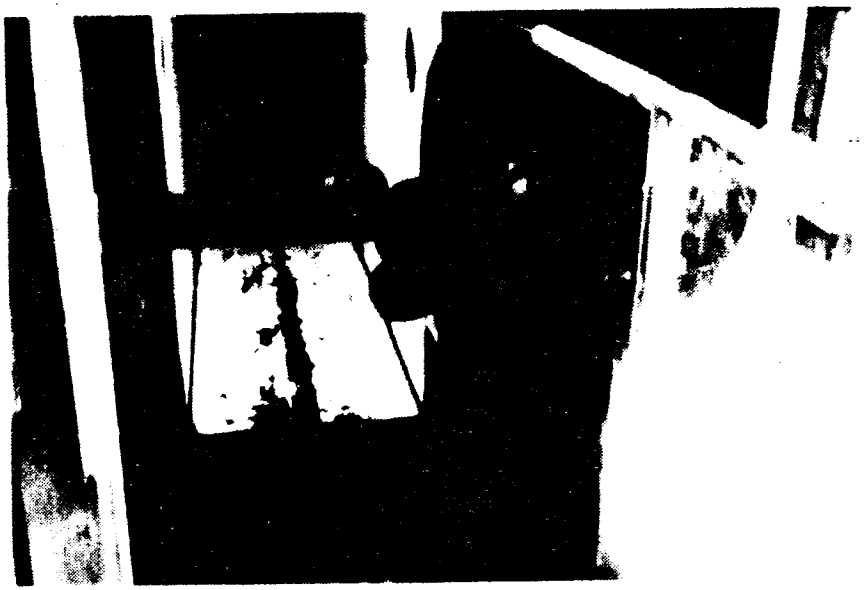

REAR VIEW

Figure 93
Pg. 111

FIGURE 94
PG. 112

YC-14 WIND TUNNEL MODEL
LOW SPEED AT BVWT

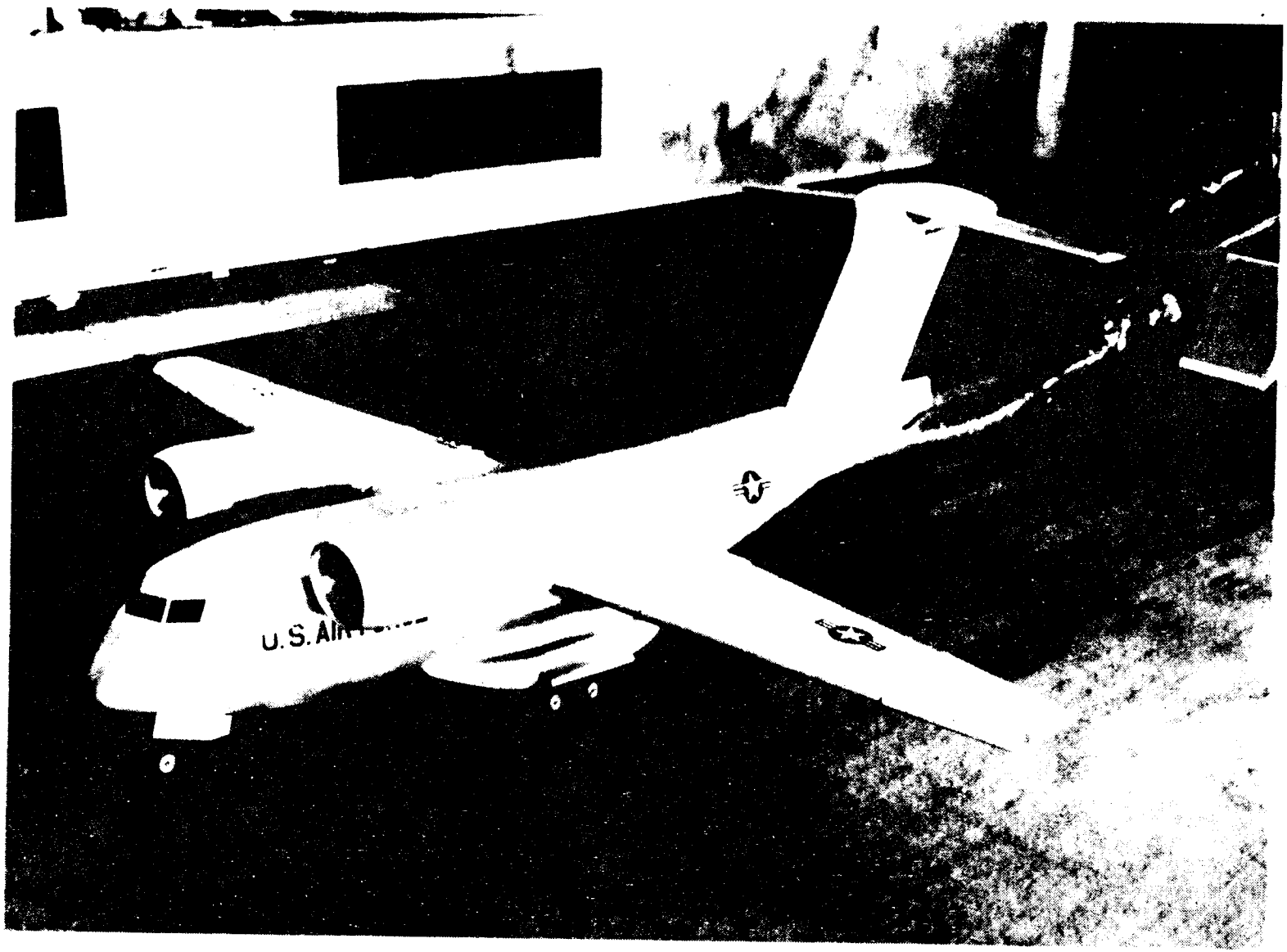

Figure 95
p. 113

α = 8°

NO LEADING EDGE DEVICES

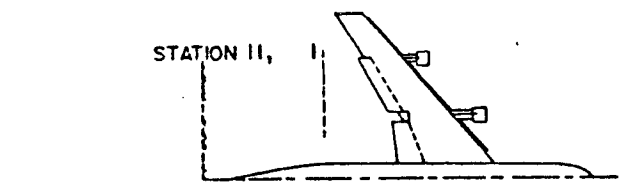

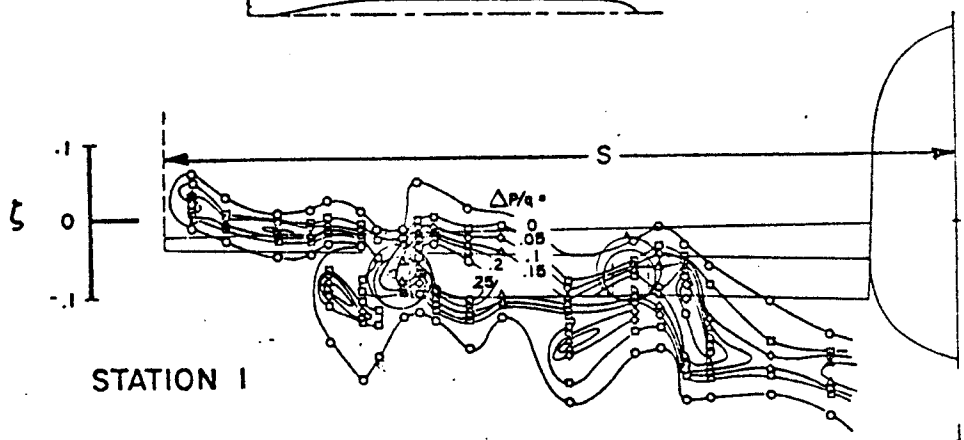

STATION I

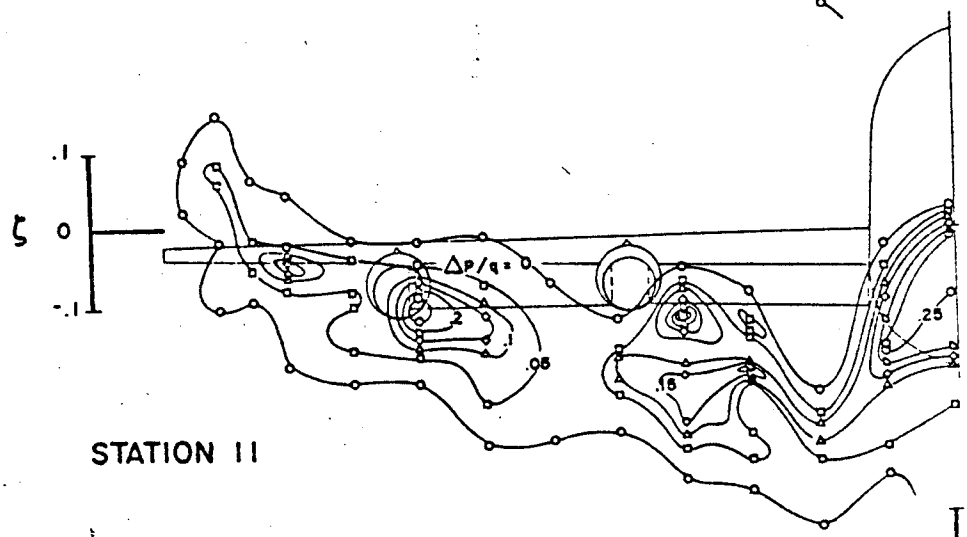

STATION II

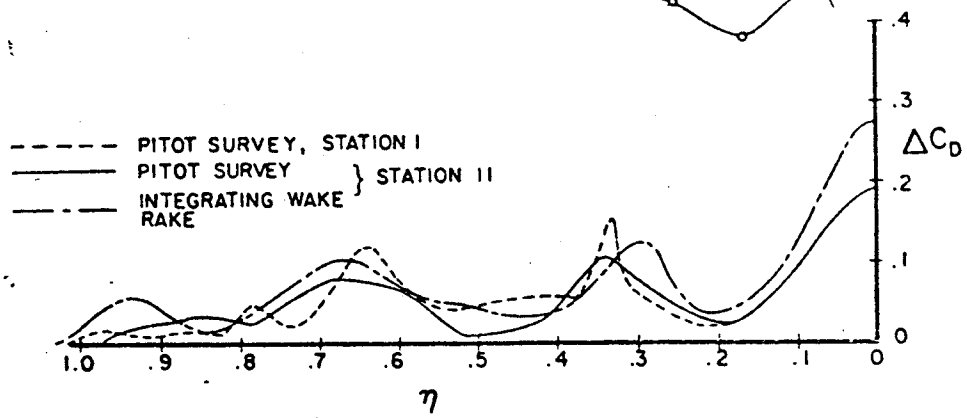

WAKE SURVEY BEHIND TAKE-OFF CONFIGURATION

AD 1346 D

FEIFEL 3-73

REV SYM

BOEING NO. FIG 96

PAGE P6.114

6-7000

32

CHAPTER 7. TRANSONIC AND SUPERSONIC DESIGN

CHAPTER 7. TRANSONIC AND SUPERSONIC DESIGN

7.1 INTRODUCTION

Most transport aircraft cruise at a speed range of 0.75 to 0.85 Mach. This band of operation is achieved with wings of moderate thickness and aspect ratio and at sweep angles (25^{o} to 37.5^{o}) which to not incur unacceptable stability and control effects. Then there are two current transport aircraft which operate at about Mach 2, although at considerably reduced fuel efficiency. Thus there is a large speed range where no transports are in operation, or where substantial improvements in efficiency are required. The first range is from 0.92 to 0.98 Mach for so-called Near-Sonic Transports (NST). These aircraft would cruise up against the limit where sonic booms are first formed. The second category is in the range from Mach 1 to about 1.2, where sonic booms are formed but are diminished by atmospheric effects before they strike the ground. These aircraft are called transonic transporst (TST). Then there is the conventional supersonic transport (SST), operating from about Mach 1.8 to 2.8, and finally the hypersonic transport (HST) which operates at Mach 6 and above.

Figure 7.2 compares the flight regimes, speed, and aerodynamic efficiency of the various transports. Note that as cruise Mach increases, the cruise altitude also increases. Of course, the cruise speed goes up with Mach number; at M=6 it is more than 4100 mph. The effect on time to go 5,000 miles is impressive; at M=0.8, more than nine hours are required, at M= 2.5, little over three hours, and at M=6, slightly more than one hour. But the Concorde is known for its poor fuel efficiency at M=2. The aerodynamic efficiency, L/D, is shown to drop abruptly at M=1, thenslowly decrease thereafter. The L/D of the Concorde is about 6; current design methods would produce a value nearer to 10. However,the Brueget range equation (eq. 1.28) contains the term $M\,L/D$. Inclusion of speed into aerodynamic efficiency changes the story; at M=4, ($M\,L/D$) is around 30, whereas at M=0.80, it is only 15. That means that the engine for a Mach 4 aircraft could have twice the specific fuel consumption before the range factor of the M=4 transport would be less than for the subsonic transport.

Because of this consideration, transports that operate above sonic speeds cannot be precluded from future consideration. This chapter will outline the main aerodynamic considerations of the various aircraft.

7.2 Near Sonic Transport (NST)

Boeing extensively studied a near-sonic transport from 1969 to 1971. It was even given a description - the 767. But Figure 7.1 shows why it did not reach production. Relative to a conventional M=.80 transport, the NST cruising at M=.98 would reduce time for a 5,000 mile trip by only 1.5 hours (15%) for a loss in $M(L/D)$ of 15%. For a transcontinental trip, the time saving would be even smaller --- less than one hour. When coupled with higher weight required by the higher speed and a poorer engine cycle, the economics of the NST clearly did not work out favorably for the small increase in speed. And that conclusion was prior to the fuel crunch! Nonetheless, the NST is truly the aerodynamicist's airplane, because the slighest deviation from the rigid requirements of transonic aerodynamics can cost 5% to 10% in performance. And, aerodynamic tailoring lessons

7.2 (Cont.)

are best learned near M=1, due to the extreme sensitivity of the flow field to slight errors in design. Because of the 767 program, Boeing learned more about near-sonic aerodynamics than anyone else, including NASA. The material in Section 7.2 is taken from Coord. Sheets which summarized the 767 high-speed testing. Only three copies of these are known to exist; the originals have disappeared. Thus no references will be given for this section.

7.2.1 Wing Body design

The wing design follows rules and procedures established in Chapter 4, in that the wing can be successfully designed at a subcritical Mach number, typically 0.80. But before the wing is designed, the sonic area rule must be considered. It must be obeyed explicity or the design will fail.

Sonic area rule The sphere is a body of revolution whose length, l to diameter, d is one. The critical Mach number of the sphere has been measured by various experimenters to lie between 0.55 Mach and 0.65 Mach, depending on Reynolds number. That is to say, the longitudinal area distribution, obtained by cutting the sphere with a series of planes normal to the flow, has a limiting speed of around 0.6 Mach. As l/d is increased, the critical Mach number will increase. When l/d is around 9, the body of revolution will have a critical Mach number of better then 0.95 Mach.

Sonic area rule says that near or at M=1, the disturbance caused by an object spreads almost perfectly perpendicular to the object (see Figure 7.2). Thus, the shape of the object would not matter, only its longitudinal distribution of normal area. If two bodies have the same normal area distribution, then they will have the same limiting Mach number. Furthermore, the Mach performance of the two bodies will be the same as that of a body of revolution having the same area distribution. When the wing is added, the wing's normal area distribution is to be removed from the body, so that the total normal area is unchanged (Figure 7.3). Conversely, a wing-body geometry can be converted into an "equivalent" body in the same manner. The characteristics of the equivalent body will be denoted the "configuration" characteristics; the shock wave on the equivalent body will be the configuration shock, etc. These configuration characteristics will exist in addition to those caused by the wing itself. The area rule concept suggests that the drag rise of the wing-body geometry would be no better than that of the body of revolution.

Thus the first step is to study bodies of revolution and discover an area distribution which (a) will allow the desired Mach number, and (b) produce a pressure distribution which is favorable to the wing. Boeing tests indicated that a fineness ratio of about 9 would provide a critical Mach number of 0.98 or higher. More than one distribution for the area would produce the same capability. Figure 7.4 shows two such options. Figure 7.4a shows the flow about a body which used the TR 38 airfoil's upper surface ordinate as a radius. At M=0.99, the flow is well behaved, with a single configuration shock at 67% body length. In the region

7.2.1 (Cont.)

where the wing would be mounted, the local Mach number created by the area distribution will be around M=1.06, meaning that the wing would have to be designed for this kind of flow field.

Figure 7.4b shows a second body, based on a Whitcomb airfoil instead Both bodies have a fineness ratio of 9, both have their maximum area at 38% body length, and both have critical Mach numbers in excess of 0.99. But because their shape is slightly different, the local Mach distribution on the two is different. The second body, having a more blunt nose, develops two configuration shocks, and the wing location tends to be in a region of slower flow than on Figure 7.4a. Consequently, the body of Figure 7.4b would be chosen for wing-body design work.

Before considering the wing design further, the importance of the configuration area distribution, its flow field and its shock wave must be accepted. The components of the configuration will always sum to a normal area, whose characteristics cannot be ignored. Suppose a fighter aircraft were flying at about M=.90 near the ground, on a 95^{0} day. The area distribution of the fighter would generate a slightly supersonic flow field around the comp ete configuration, in addition to any local shock waves that might appear on the wings or other part of the aircraft. Within that supersonic area would be Mach characteritic lines, inclined at an angle given by their local Mach number. Suppose one of the lines were inclined by about 21^{0}, for a characteristic angle of 69^{0}. The local Mach of this line would be 1.07(= 1/sin 69^{0}) and the local temperature ratio would be 0.8137 (from Table 1.4). This would produce a local static temperature of -8^{0}F along that line. If the air were moist, then along some characteristic line where the local static temperature dropped below the dew point, the air would condense out and form a fog. At the shock wave, the static temperature would return to near ambient and the fog would disappear. Furthermore, since this flow field is conical, the circular plane where the fog disappeared would appear to be slightly curved to an observer slightly ahead of the aircraft. Figure 7.5 and its overlay show exactly this phenomenon, for an F-14 fighter making a low-level pass at M=0.90. The appearance of the moisture marks a portion of the characistic network, not a shock as described in AW&ST. The moisture disappears where the configuration flow has gone subsonic. What is shown is not the wing flow field; it is the result of the area distribution of the F-14 flying through humid air at high subsonic speeds. Note that the extent of the supersonic flow caused by the area distribution extends to a region larger than the wing span.

Trapezoidal wing The sequence to design the wing contour is the same as for subsonic wings, except that the body will not be cylindrical, but contoured according to the total area rule. The simplest wing would be a

7.2.1 (Cont.)

trapezoid. Performance of a wing of 42.5 sweep with a taper of 0.25 and TR 38 as it's outboard section is shown on Figure 7.6. Also shown for comparison is the drag rise of the basic area distribution. Obviously, the wing's performance is less than expected. Yet, the same procedures had been followed as had been done for subsonic wings, a procedure which led to the outboard wing pressure distribution being identical to TR 38 corrected by sweep theory. But for the transonic case, at M=0.98, the outboard airfoil pressures are not at all like those of TR 38, as seen on Figure 7.7.

The trapezoidal wing is then altered in such a way as to change the observed pressures on W_2 to become like TR 38. Also, the raked tip of W_2 is raked somewhat less, since tunnel data indicate that more rake has been included than is necessary. The pressures on the modified wing, W_2, are indeed like those of TR 38 (Figure 7.8) but the performance in terms of drag rise, is no better (Figure 7.9). The polar shape is dramatically improved, however, demonstrating the degree of care that must be used during the design of the tip.

Perhaps the problem is that the area rule has not been totally satisfied. In the preceeding designs, care has been taken to see that the normal geometric area was correct. But there are also changes in the flow area about the wing, due to streamtube expansion. Consider a "tube" of flow approaching the wing, as drawn on Figure 7.10. It's area decreases as it approaches the sonic line of the supersonic flow above the wing. Based on the area of the streamtube as it crosses the sonic line, it is 0.03% larger ahead of the wing where the flow is M=0.98. Once inside the supersonic flow over the wing, however, the streamtube expands rapidly. If the flow over the wing reached 1.25 Mach, the streamtube would have grown by 4.5%. Imagine all the stream tubes undergoing this change all along the wngs's upper surface, and it can be seen that area is being added to the geometric area because of stream tube expansion resulting from lift effects on the wing's upper surface. If those could be summed for the whole wing, then an additional area would have to be removed from the body to compensate for the extra area due to lift.

In the time period when the 767 was being done, "lift compensation" area could not be directly calculated. More specifically, the shape of the curve could be calculated, but the magnitude could not. There was also some question as to the proper chordwise position for the removal of this area. Whitcomb of NASA had experimentally derived a shape and magnitude for the shape. So a test was run with the trapezoidal wing, placing the lift compensation area removal in three locations:

(a) near the wing leading edge, so as to feed its influence along wing characteristic lines,
(b) at about mid root-chord, also to feed along characteristic lines,
(c) near the root trailing edge, in the idea that the influence would feed laterally.

487

7.2.1 (Cont.)

The lift compensation area was removed axisymmetrically from the body for (a) and (b). For (c), however, the lift compensation area was removed only from the upper body, since the streamtube expansion would occur only above the wing and not below it. Furthermore, the body was done in such a way that

(1) The desired total area rule, made of body, wing and lift compensation normal areas, was satisfied.
(2) The normal area distribution above the dividing stream sheet (the curved plane of the wing's forward and rearward stagnation lines) was smooth and included all the lift compensation area,
(3) The normal area distribution below the dividing stream sheet was also smooth.

The results of testing these three bodies with the trapezoidal W_2 were quite dramatic. The airfoil pressures at 75% semispan are shown on Figure 7.11. Part (a) shows the pressures with the uncompensated body; the indication is that the wing flow separates at the shock. Part (b) gives the effect of the forward hole. The supersonic expansion of the entire forward wing has been suppressed. Obviously, the strong secondary expansion and shock wave caused separation. The mid-position of part (c) shows the flow beginning to appear normally. Then, part (d) reveals the long-sought result; an outboard pressure distribution that is not separated and looks like TR 38. But the expected drag rise improvement has not been achieved (Figure 7.12) The reason: the abrupt body contours required to provide the lift compensation area produced a local contour shock on the body.

Obviously, the same total area must be provided, but in a way to reduce the abrupt local body contours. This could be achieved by transferring some normal area from the body to the wing by means of a large wing strake as illustrated on Figure 7.13. The drag rise with the strake is now almost the same as that of the equivalent body. By this series of tests, two fundamental rules of transonic design were discovered:

1. The total area rule, comprized of both geometric areas and flow areas, must be satisfied.

2. Contouring must not be allowed to result in local curvature shocks, or the benefits of contouring will be lost.

Use of a traversing ceiling shadowgraph provided a final refinement to the wing-body design. It was noted that where the wing shock wave intersected the configuration shock would be the point of most severe separation (Figure 7.14). A change in total area distribution which would move the configuration shock wave aft past the wing tips might result in a further improvement in the wing-body drag rise. Recalling the area distributions of Figure 7.4a and 7.4b this would mean changing from something like that of 7.4b to one like 7.4a, which would move the shock aft, at the expense of a higher local wing flow field Mach number; this is just the reverse of the design decision made earlier. The experimental result of this alteration to the total area is shown on Figure 7.14. The drag rise of the wing-body at C_L=0.4 is now completely dominated by the configuration drag rise, and no

7.2.1 (Cont.)

further improvements could be expected in the wing-body design.

Unless, of course, the wing section were to be changed. A direct substitution of TR 38 by TR 38-1 was tried, and illustrates the design dilemma often encountered. Firgure 7.15 provides the drag rise of the two wings. The drag level of the TR 38-1 wing is less than that of the TR 38 wing everywhere, and often by as much as 20-30 drag counts (about 8-10% airplane drag), although the critical Mach number is less.

7.2.2 Engine Integration

The integration of the propulsion system with the airframe must be done carefully on typical subsonic aircraft to avoid inefficiencies on the order of one to two percent airplane drag. On the near-sonic transport that integration becomes much more difficult, because losses of five percent or more could be realized by an improper design. Later chapters will deal in detail with nacelle design and integration for subsonic aircraft. The special features of NST engine integration will be dealt with here.

Fan cowl design The fineness ratio of the fan cowl is an important design criteria for the near-sonic nacelle. Figure 7.16 shows how the fineness ratio is defined and what part of the area distribution is important. Since the capture streamtube approaches from far upstream, the normal area of the nacelle that affects the transonic flow development is the total enclosed area minus the capture streamtube area. This small area distribution will also have a configuration shock and a limiting Mach number capability. Figure 7.16 shows the drag level and drag rise of two nacelles having different fineness rations; the higher ratio is necessary for the NST despite its higher drag level.

Effects of contraction ratio, inlet shape and position of maximum thickness were all evaluated. The most dominant characteristic seemed to be fineness ratio. Based on test data, the following fan cowl design characteristics were selected:

Fan cowl fineness ratio	= 2.71
Inlet contraction ratio	= 9%
$D_{hilight}/D_{max}$	= 0.855
Position of max diameter	= 0.51
Cruise capture ratio	= 0.80

Incidentally, because of their small size, and because they were sting-mounted, the full extent of the configuration shock about the nacelles could be seen. At about M=0.99, the diameter of the configuration shock was about ten times the diameter of the nacelle.

7.2.2 (Cont.)

Wing-mounted nacelles Early tests of inboard and outboard wing-mounted nacelles indicated penalties of 10% airplane drag and a loss in Mach number of 0.02 to 0.04. Clearly, this kind of installation effect could not be tolerated. The solution for the inboard and outboard nacelle were found to be completely different.

The first cure attempted was how the area ruling for the nacelle should be done. Initial attempts removed the area of the nacelle shown on Figure 7.16 from the body by making a uniform reduction in body radius. This was found to be completely ineffective. The proper procedure is shown on Figure 7.17, where the area of the inboard nacelle and pylon are removed from the lower body, entirely below the wing dividing streamsheet. This caused an awful-looking hole in the lower body contour, but the data on Figure 7.17 show that this procedure was quite successful.

Nacelle area ruling for the outboard nacelle, whether removed from the complete body or from only the lower streamsheet area, proved to be completely ineffective. Test data showed however that the outboard wing was distorting the wing span load and shock pattern to a larger degree than on subsonic aircraft. The key to the outboard nacelle installation was found to be a retwisting of the wing to allow for the additional loading effects of the outboard nacelle. Figure 7.18 indicates the degree of retwisting required, as well as the resulting performance. Note that the retwisted wing is tested only with the nacelle on. The shock position of the retwisted wing with nacelle was identical to that of the original untwisted wing.

Body-mounted nacelles Successful integration of aft body-mounted was found simply to require that the body be area-ruled for the nacelle area and that the nacelles and pylons be properly aligned. The design of the S-duct proved to be more interesting, as detailed on Figure 7.19. The original S-duct had a concavity as shown, just ahead of the position of the main configuration shock. A noticable gain in performance was achieved by altering the contour to prevent rearward facing area from being subjected to the reduced pressures ahead of the configuration shock.

7.2.3 Other Details

Cab Ordinarily, the cab design does not have a large impact on the performance of the airplane. Thus, some slight liberties were taken with the total area rule in the design of the first project cab. The result (Figure 7.20) was a la penalty in speed of about 0.035 Mach. The second design, done in such a way as to completely satisfy the total area rule, was a complete success (also on Figure 7.20).

Gear Pods Because of the high transonic speed, it was felt that gear pods, rather than a yehudi with body-stowed gear, might prove an advantage because of the increased speed allowed by using the gear pods as "speed pods", a Whitcomb. However, a suitable gear pod design was not found, probably because they were much larger than desired for just a speed pod. The results were very poor, and further work was abandoned (Figure 7.21).

7.2.3 (Cont.)

Empennage At the beginning of the NST program, Whitcomb of NASA had decreed that only a T-tailed airplane would be successful, since it allowed a good area ruling between the aft body, the fin and the horizontal tail. The speed performance of the T-tail was certainly acceptable (Figure 7.22), although Boeing improved the T-tail design by adding an area fairing based on the local area rule of the upper fin the horizontal tail.

However, the strake required for 0.98 Mach cruise caused extreme pitchup, and the T-tail design suffered from lock-in stall. The low tail was then examined for the NST. The performance (Figure 7.23) was as good or better than the T-tail. The reason for this was simple; the aft body closure causes the low tail to fly in a speed regime below free stream, whereas the T-tail operates at essentially free stream conditions. And, the low tail was able to avoid lockin stall.

The design of both low and T-tails was done analytically, to optimize their performance. Boeing to date has always built horizontal tails without twist. But for the low tail, the body creates a local change in upwash. And for the T-tail, the pod at the tip of the fin also changes the downwash. These effects cause the flat tail to have a poor span load. For the NST, the tails were given twist, as shown on Figure 7.24.

At the conclusion of the wind tunnel test program, Boeing was able to put together three different configurations, all having an indicated critical Mach number of 0.97 or higher. These are shown on Figure 7.25. During the wind tunnel exploration leading to the configurations, it became clear that there is a "sonic triangle," three rules which must rigorously be followed at near-transonic speeds. Figure 7.26 shows the transonic aerodynamiast at his drawing board, perched on a very rickety three-legged stool. Each leg represents one of the rules; if any one breaks, his design will be a failure. The rules:

1. Total area rule must be satisfied.
2. Local area rule within the total must be satisfied.
3. While satisfying (1) and (2), local surface curvatures must not be generated which cause local shocks.

7.3 TRANSONIC TRANSPORT

Figure 7.1 shows that a transport flying at M=1.25 would reduce the time to travel 5000 miles by 1/3, as compared to a conventional transport. A transport flying at this low supersonic Mach number would also be able to operate overland, because of the way the sonic boom is attenuated by the atmosphere. Figure 7.27 (Reference 7.1) shows that, with no headwind or tail wind, an aircraft travelling at M=1.12 (at 55,000 feet altitude;not shown on the chart) would have its sonic boom dissipated before it reached the ground. A typical headwind would further attenuate the boom and the aircraft could fly at 1.25 Mach. The same wind velocity as a tailwind, however, would diminish the cruise condition for boomless flight to 1.05 Mach. In comparison, a Mach 2 aircraft would always cause a sonic boom to be felt on the ground. The figure also shows the variation in maximum boomless cruise Mach number for typical winter and summer operation; the design condition is from 1.05 Mach to 1.25 Mach. This is in sharp contrast to the typical subsonic aircraft, which will have only a single design Mach number.

Designing a configuration to operate efficiently over this range of Mach numbers will turn out to be difficult, and a configuration study described later concluded that a very unusual configuration would yield the best performance in this flight regime. But first, it is necessary to understand the drag buildup for wing-bodies at supersonic conditions. The drag can be defined to be made of:

$$C_{D_{WB}} = C_f \frac{A_{wet}}{S_W}$$ (skin friction x wetted area, C_{D_F})

$$+ \frac{K_o}{\pi} \frac{V^2}{S_W^3} P^2 \left(\frac{S}{\ell}\right)^2$$ (wave drag due to volume $\sqrt{}$ spread over length ℓ, C_{D_W})

$$+ \frac{1}{2\pi} K_v \frac{P}{(S/\ell)} C_L^2$$ (vortex drag due to lift spread over span $\approx S$, C_{D_V})

$$+ \frac{\beta^2}{\pi} K_w P \left(\frac{S}{\ell_w}\right)^2 C_L^2$$ (wave drag due to lift spread over length ℓ_w, $C_{D_{WL}}$)

where $P = \frac{S_W}{2S\ell}$ = planform shape factor

S= planform semispan

ℓ= total configuration length

ℓ_W= length from wing apex to wing trailing edge at tip

V= peak volume

S_W= wing planform area

$\beta^2 = M^2 - 1$

K_o, K_v, K_w = drag constants that depend on the geometry of the aircraft

The relative magnitudes of these components for a delta-wing are shown on Figure 7.28. The wave drag due to volume, C_{D_W}, arises from the supersonic version of the sonic area rule, and is the drag caused by the equivalent area distribution of the configuration. At Mach =1, for the sonic area rule, the configuration is cut with planes normal to the flight direction to get the equivalent area. For supersonic Mach numbers, however, the procedure is more complex. The configuration must be cut by planes inclined at the angle given by the freestream Mach number, where $\mu = \sin^{-1} 1/M_\infty$. But the cutting plane can be inclined at angle μ in the vertical direction, or at 90^0, etc:

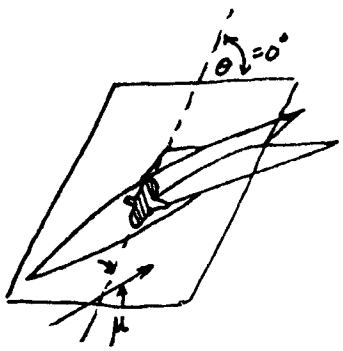

CUT AT $\theta = 0^\circ$

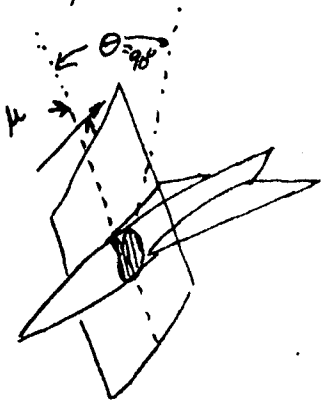

CUT AT $\theta = 90^\circ$

As the configuration is rolled through various angle θ's, different equivalent areas will arise.

For any one of the θ-dependent equivalent bodies, the volume-dependent wave drag is determined by:

$$\frac{D_W(\theta)}{q} = -\frac{1}{2\pi} \int_0^\ell \int_0^\ell A''(x_1)\, A''(x_2)\, \log_2 |x_1 - x_2|\, dx_1 dx_2$$

where X_1 and X_2 are lengthwise variables of integration and A" is the second derivative of the body area distribution. Finally, the wave drag due to volume of the aircraft at a given Mach number is calculated from the integrated average of all the equivalent-body wave drags:

$$\frac{D_W}{q} = \frac{1}{2\pi} \int_0^{2\pi} \frac{D_W(\theta)}{q}\, d\theta$$

For a given wing-body geometry, the valve of D_W/q depends on the Mach number. Conversely the optimum supersonic area distribution is dependent on the design Mach number, with the trend being very steep near Mach =1. Figure 7.29 compares the volume wave drag for a series of bodies optimized to different Mach numbers. Note that the drag of the wing-body optimized for 1.05 Mach increases by 11% when operated at 1.25 Mach; conversely, the drag of the wing-body optimized for 1.25 Mach increases by about 40% when operated at 1.05 Mach. So, designing an aircraft to operate efficiently over a range from 1.05 to 1.25 Mach would require compromises.

Another disadvantage to conventional aircraft arises in the equivalent wing-body area distribution, as shown on Figure 7.30. This is that the equivalent areas of both wing panels are additive. Suppose the wing were made such that one panel swept forward and one swept aft. Two benefits would be realized: (1) the wing areas would add such that their total would be less, and (2) the total area would be less for the same body volume, resulting in less wave drag. Then, suppose the wing were placed on top of the body, on a pivot. Then two additional improvements would be realized (1) the area ruling could be adjusted for the particular Mach number (1.05 to 1.25) by changing sweep, and,(2) superior low speed characteristics would be realized by setting the wing to zero sweep for landing and takeoff. This unusual configuration, proposed by R.T. Jones of NASA, was included in a TST study done by Boeing under NASA contract (Reference 7.2). The remarks below concerning configuration options for a TST are taken from that reference. Wing design rules for supersonic flight will be discussed in Section 7.4.

Five configurations were chosen for the TST study, as shown on Figure 7:

(1) Model 1-2 -- a "conventional" design, having a fixed swept wing

(2) Model 2-2 -- the same configuration as Model 1-2, except having a pivoted "swing wing" like the F-111 and B-1

(3) Model 3-2 -- a fixed tailed-delta configuration derived from the 2707-300 SST

(4) Model 4-2 -- a twin-fuselage yawed wing design, and

(5) Model 5-3 -- a single-fuselage yawed wing design

The design mission was 3000 nautical miles at Mach 1.05 to 1.25 and 190 passengers. Figure 7.31 shows the initial versus the final, sized OEW to do the missions. The weight comparison between Model 2-2, the swing wing and Model 3-2, the delta, parallel the results of the SST program; the swing-wing is 74% heavier than the delta. The Model 3-2 delta-wing had the lightest OEW at 229,000 lbs, but the Model 5-3 yawed wing was not much heavier at 251,000 lbs. (This light weights are because the study assumed that by 1985, all aircraft will be made of advanced composites).

But the yawed wing concept (and the swing wing as well) offer aerdynamic advantages because they can alter their geometry for better performance at cruise and for takeoff and landing. Figure 7.32 compares cruise drag at M=1.2, C_L=0.26 for the five configurations. Here the advantage of the yawed wing Model 5-3 clearly stands out; it has a cruise L/D of 12.7, due largely to a very small wave drag allowed by its higher equivalent fineness ratio was about 18.5, which is twice the fineness ratio required by the NST to cruise at 0.98 Mach. Finally, Figure 7.33 shows the take-off gross weight of the five configurations to perform the design mission. The Model 5-3 yawed wing uses the least fuel and has the smallest TOGW, but it is only slightly better than the fixed-delta Model 3-2. The swing-wing is again notable for being extremely poor.

In summary, the yawed-wing approach to designing a TST appears to be the best, especially when community noise is considered (its L/D at low speeds is far superior to the delta wing). And should the design actually enter production some day, the acrobatics of the airplane will be very entertaining. Consider the case where the wing is stuck in the yawed position and the pilot is making an approach to SEA-TAC about 30^{o} off the approach path. Figure 7.34 shows that by merely doing an elevator loop at the right time, he will change his flight path by 30^{o}. Obviously the yawed-wing concept would require a complex flight control system.

7.4 SUPERSONIC TRANSPORT (SST)

Wing-body design for the supersonic speed regime is governed by a set of empirically observed design rules which establish limits for separation-free operation. Within these limits, the aerodynamics of the wing-body geometry are well predicted by analysis. Before considering these limits, which arise due to viscosity, the inviscid design of the wing-body must be discussed.

The wing-body is dominated by three guidelines, (1) the total supersonic area rule must be obeyed, (2) the leading edge should be subsonic, and (3) the proper camber and twist must be achieved. The total supersonic area rule was discussed in Section 7.3 above. The subsonic leading edge is simply to place the leading edge behind the Mach cone emanating from the wing apex; to do so means that the velocity normal to the leading edge will be subsonic. Figure 7.35(a) shows the case of a wing having less sweep than the shock angle. In this case, the leading edge will have flow normal to it which is supersonic. A shock wave will originate all along the leading edge and the leading edge will have to be sharp. This will cause difficulties at subsonic Mach numbers. Then, the shock from the wing apex will lie across the wing and finally, the shock near the trailing edge will raise the pressures to near static values again. The wing section with the supersonic leading edge will have three shock waves on it. But if the leading edge is swept more than that of the oblique shock from the apex, then the flow normal to the leading edge will be subsonic (since the flow across (normal) to the swept shock will drop to less than M=1; see Chapter I) and the pressures will be much different on the airfoil. There will be no shock at the leading edge nor on the airfoil, until the shock near the trailing edge. Furthermore, the wing leading edge can be made round.

The third requirement is that the proper twist and camber be applied. For the 2-D supersonic airfoil discussed in Chapter 2, it is recalled that camber in supersonic flow causes wave drag. Thus, proper distribution of the airfoil camber, so that the airfoil is uncambered relative to the distorted flow field caused by the wing's vorticity, can make significant improvements to the supersonic performance. Figure 7.36 shows the theoretical improvement in drag due to applying the proper twist and camber to an arrow wing; also shown is an idea of the wing shape (Reference 7.3).

Also, placement of the wing relative to the body has an important effect on drag-due-to-lift, by affecting the degree of improvement achieved by camber and twist. Figure 7.37 compares the (L/D) max of twisted, cambered arrow wings to that of a flat wing for high-, mid- and low-wing configurations. Clearly the mid-wing position is preferred.

A simplifying assumption of linearized theory is that airfoil thickness distribution has no influence on drag-due-to-lift. Indeed, in Chapter 2, it was shown that thickness affected only the wave drag due to thickness. Generally this assumption is valid for flat lifting surfaces at small angles of attack. It is less likely that thickness effects would cancel on warped surfaces such as those involved in optimum camber and twist. Figure 7.38 shows how the selection of thickness form affects the gain in L/D when going from flat to cambered wings. The thin circular arc is closest to the optimum. Increasing thickness or blunting the leading edge substantially reduces the benefit due to camber.

The data on Figure 7.38 is from wind tunnel testing and thus has viscous flow effects. It is likely that the cambered wing potential has been lost due to these effects. Boeing has developed four design rules for prevent undue loss because of viscous effects (Reference 7.4). These are to avoid (1) high suction pressures at the leading edge, (2) strong spanwise flow, (3) a strong inboard shock caused by the body, and (4) trailing edge operation.

In theoretical flow, the leading edge pressures can reach very low values. But in real flows, these pressures will cause boundary layer separation and a leading edge vortex, as described on Figure 7.39. Experience has shown that this will happen if the leading edge peak pressure is more negative than 80% of the theoretical vacuum value given by:

$$C_{p_{vacuum}} = \frac{-1}{\frac{\gamma}{2} M_\infty^2}$$

Above this, leading edge vortex flow is likely.

The second criteria comes from the tendency in supersonic flow for a wing with constant section to have lower pressures outboard, thus causing spanwise flow. This is depicted on Figure 7.40. Also, making the root thicker will tend to reduce the spanwise flow. The criteria, then, is that the upper surface C_p values be similar along the whole span.

Inboard shock separation arises from the effect of the body, which is usually curved in the region of the wing because of area rule requirements. Figure 7.41 shows how the forward shock is associated with flow conditions near the inboard portion of the wing. The local flow on the upper wing surface is swept inward, then must turn and run parallel to the body. This turning occurs through a series of compression waves which coalesce into the inboard shock. If the required turning is large enough, the shock strength may become sufficiently strong to separate the boundary layer. Empirical separation data for flow across a glancing shock wave indicate that a pressure rise of 50% across the shock will cause separation. Using simple sweep theory, the local flow turning angle (δ_M) can be related to the freestream Mach number, M_∞, wing leading-edge sweep, Λ, and local Mach number, M_L. If it is then assumed that the flow turns abruptly to flow parallel to the body surface, the oblique shock equations can be used to calculate the pressure rise.

A way to avoid the glancing shock caused by the body contouring would be to blend the body with the wing as shown on Figure 7.42. This in fact is one of the main advances above the 2707-300 SST of early 1970-vintage. The effect is clearly seen on Figure 7.1; the cruise L/D is increased from about 7.5 to 8.5 by this technique.

The remaining criterion is to avoid too strong a shock wave at the airfoil trailing edge. Wing planforms with a supersonic trailing edge (swept less than $\sin^{-1} 1/M_L$) develop this trailing edge shock to raise the pressure to free stream conditions. The strength of the trailing-edge shock is directly associated with the upper surface pressure at the trailing edge. Correlations show that a pressure rise exceeding $1+0.3M_T$ can result in separation. Additional experimental studies of flow across swept compression corners suggest that the effect of trailing edge sweep can be accounted for by the use of the local normal Mach number ($M_{n_e} = M_e \cos\Lambda_{TE}$) in determining the allowable pressure rise. These two limits are shown on Figure 7.43.

Using all these criteria together against measured oil flow patterns is done on Figure 7.44. The pressures are analytical; the criteria have predicted the kind and extent of separation very well. Using all these criteria allow a wing to be designed which can come close to achieving the improvement allowed by camber and twist relative to the flat wing.

Most of the discussion above has dealt with the arrow wing. From purely the point of view of cruise L/D for the wing-body geometry, the arrow wing is an improvement over the delta wing because (1) the part of the delta wing which has been removed to make the arrow wing was producing very little lift, thus adding skin friction for not much lift, and (2) has a subsonic leading edge. Yet the final version of the 2707-300 was a delta wing. The main reasons are that the nacelle favorable interference is utilized better on the delta wing (discussed in Chapter 9), the delta is structurally better (less flexibility), there is more fuel volume, plus other reasons outside the scope of this course. Finally, the upper surface isobar pattern for the LES at 1.8 Mach is shown on Figure 7.45 for comparison to subsonic isobars shown in Chapter 4.

7.5 HYPER SONIC TRANSPORT (HST)

The hypersonic transport offers dramatic reductions in trip time, is boom-free because of its attitude, and has a M(L/D) almost twice that of subsonic aircraft. If the propulsion system integration and structural problems were not so large, the HST might receive more interest. Design of the HST wing-body will undoubtedly be towards a delta wing-blended body concept. The design procedures for this kind of configuration at hypersonic speeds follows the same general considerations as for the SST and will not be discussed further.

REFERENCES

7.1 "A Preliminary Climatology of the Threshold Mach Number," G.T. Haglund, paper presented at the Fourth Conference on Aerospace Meterology, Am. Meterol. Soc. and AIAA (Las Vegas, Nevada), May 1970, p.p. 399-413.

7.2 "High Transonic Speed Transport Aircraft Study, Final Report," R. M. Kulfan and nine other authors, NASA CR-114658(D6-60232), September, 1973.

7.3 "Supersonic Aerodynamic Characteristics of Some Simplified and Complex Aircraft Configurations which Employ Highly Swept Twisted- and-Cambered Arrow-Wing Planforms," F. Edward Mclean and D.E. Fuller, presented at the AIAA/ASD Symposium, WPAFB, November, 1963.

7.4 "Real Flow limitations in Supersonic Airplane Design," R.M. Kulfan and A. Segalla, AIAA Paper 78-147, Jan.1978.

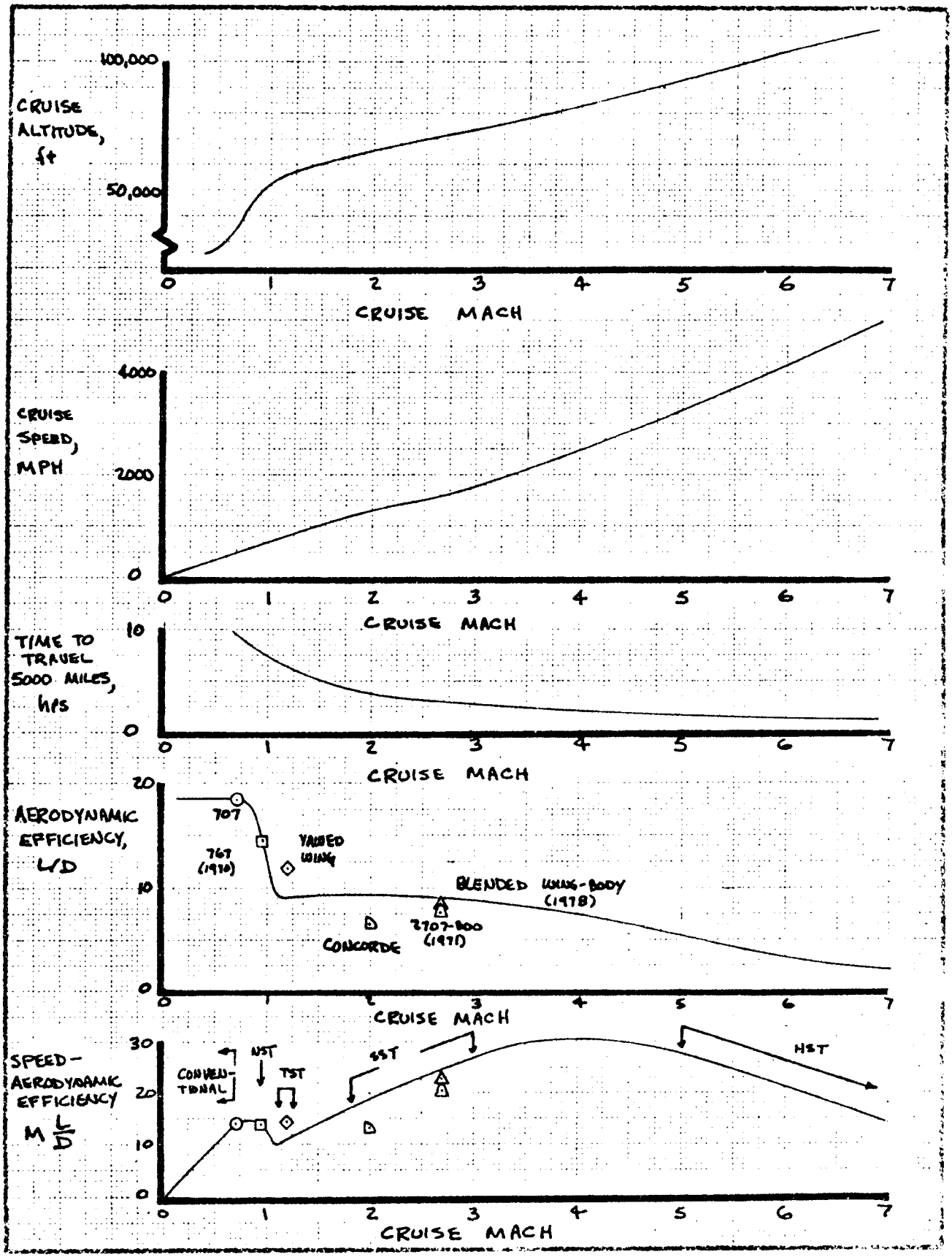

CALC GILLETTE 2-12-78	REVISED	DATE	EFFECT OF CRUISE MACH ON TIME AND AERODYNAMIC EFFICIENCY
CHECK			FIG 7.1
APP			
APP			7.16

(a) AT THE SONIC SPEED, THE AERODYNAMIC EFFECT OF AN OBJECT SPREADS NEARLY PERPENDICULARLY TO THE FLOW

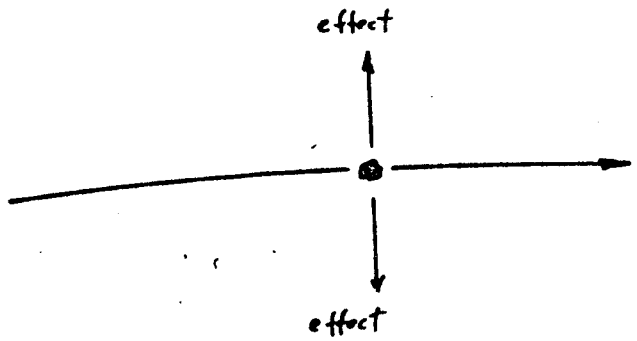

(b) THIS EFFECT LEADS TO THE SONIC AREA RULE:

BODY 1 ~ BODY OF REVOLUTION

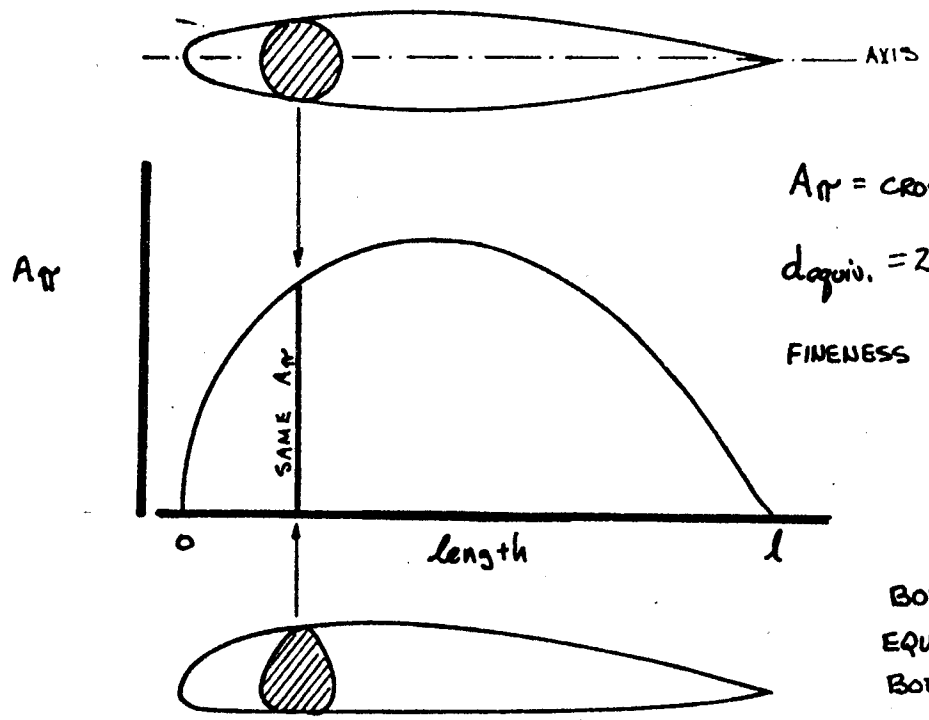

A_{π} = CROSS SECTION AREA

$$d_{equiv.} = 2\sqrt{\frac{A_{\pi_{max}}}{\pi}}$$

$$\text{FINENESS RATIO} = \frac{l}{d_{equiv.}}$$

BODY 1 IS EQUIVALENT TO BODY 2 AT M=1

BODY 2 ~ NONSYMMETRIC

FIGURE 7.2 SUBSONIC AREA RULE ~ EQUIVALENT BODY

500 2·4·78 GILLETTE

(a) EQUIVALENT BODY OF REVOLUTION

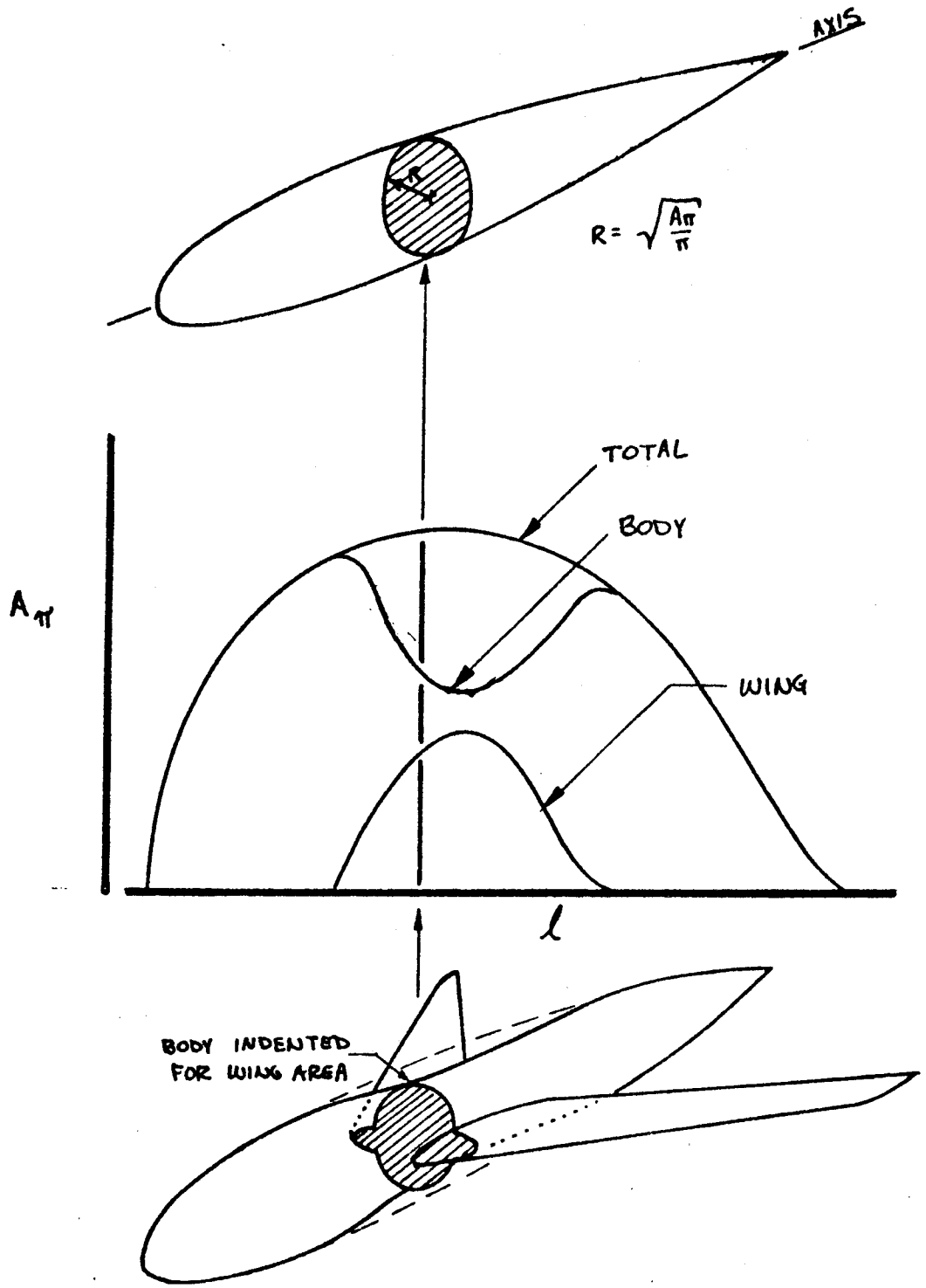

(b) WING-BODY

FIGURE 7.3 BODY INDENTATION FOR WING AREA

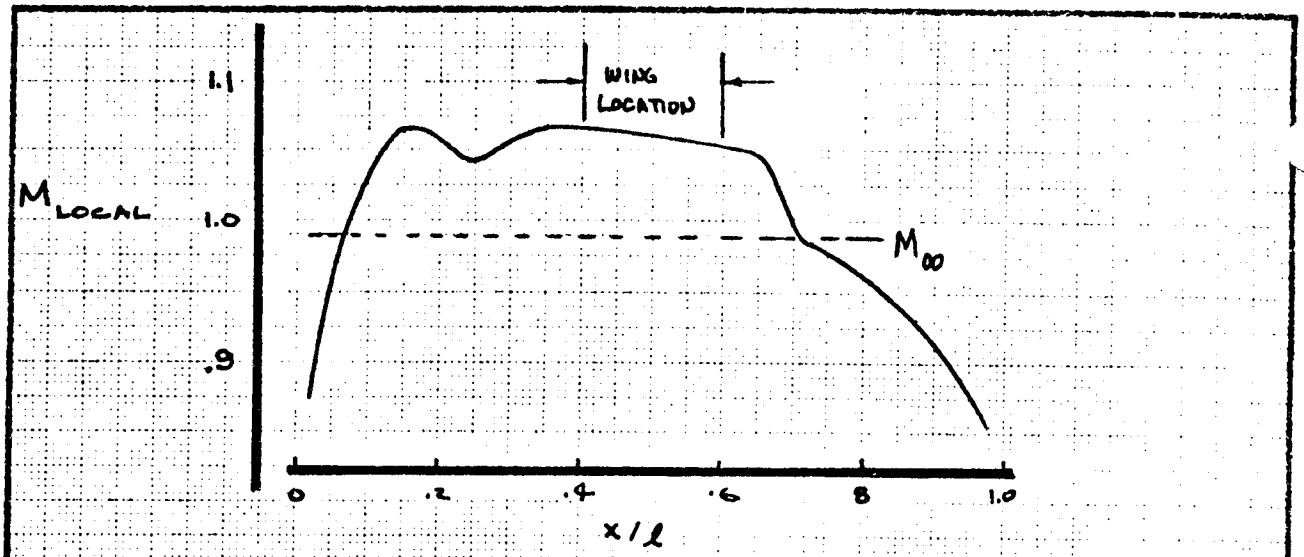

NOTE: PATTERN IS AXISYMMETRIC

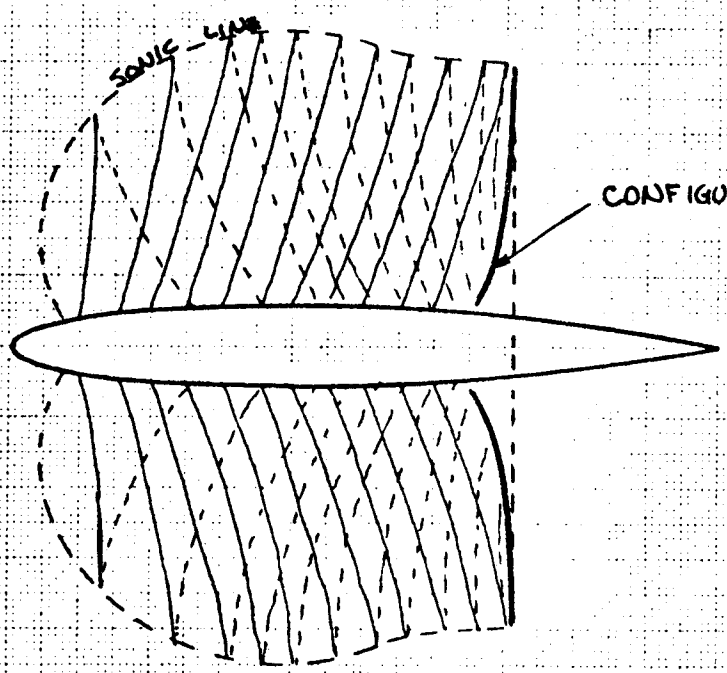

CALC	GILLETTE	2-4-78	REVISED	DATE	FLOW ABOUT BODY OF REVOLUTION DERIVED FROM TR 38
CHECK					
APP					
APP					

D1 4100 3260 ORIG. 3/71

BOEING

FIG 7.4a

502

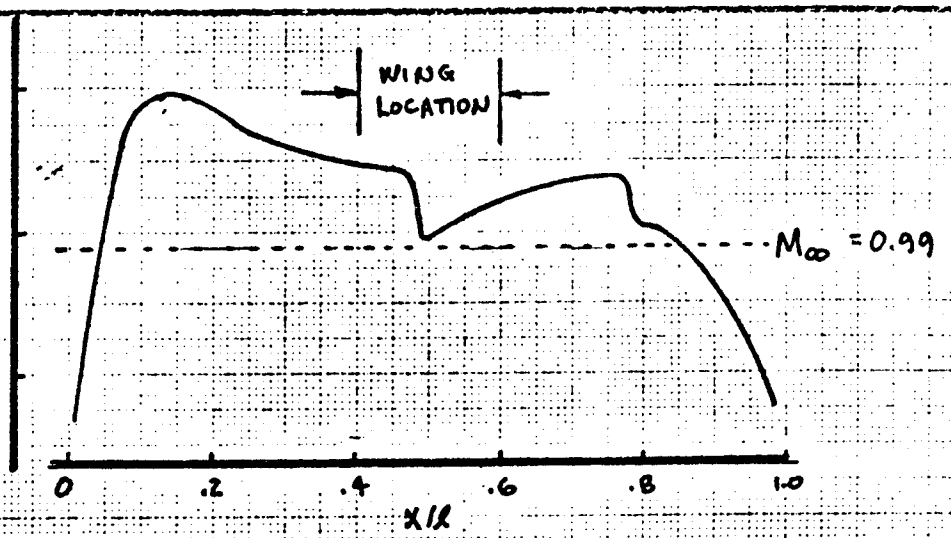

NOTE: PATTERN IS AXISYMMETRIC

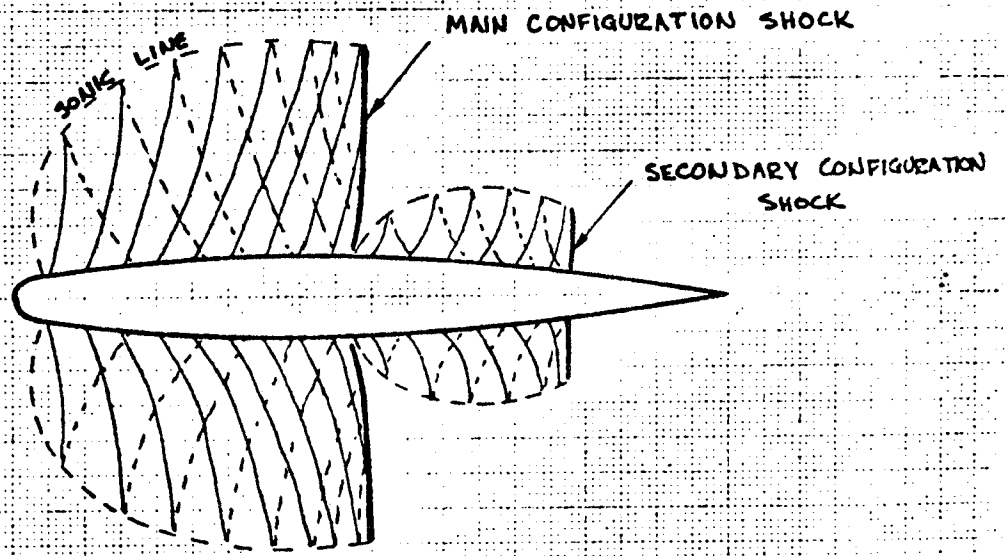

CALC	GILLETTE	2-9-78	REVISED	DATE
CHECK				
APP				
APP				

FLOW ABOUT BODY OF REVOLUTION DERIVED FROM WHITCOMB AIRFOIL

FIG 7.4-b

GRUMMAN

PAGE 7.20

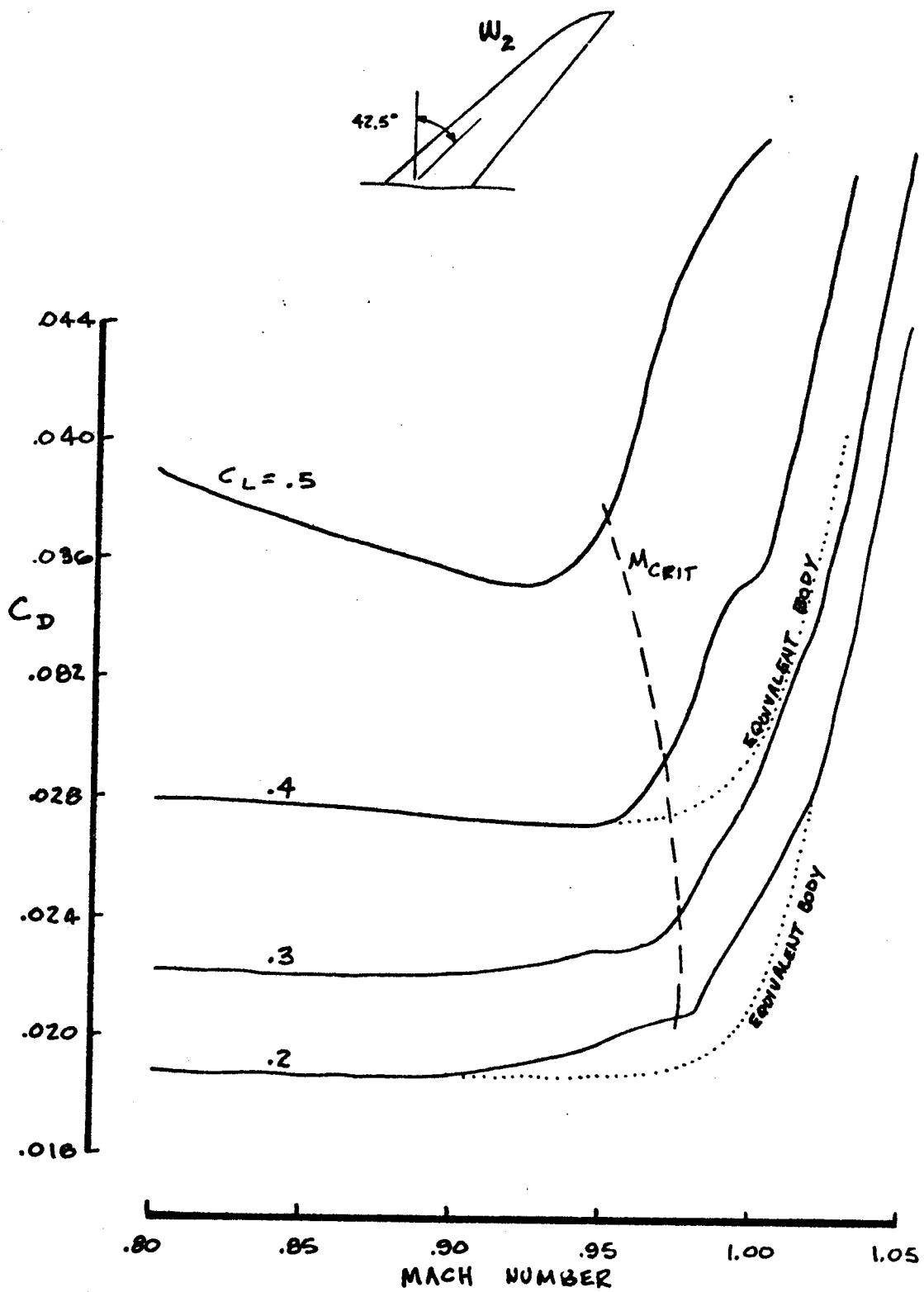

FIGURE 7.6 DRAG RISE OF TRAPEZOIDAL WING

4.78
LOTTE

504

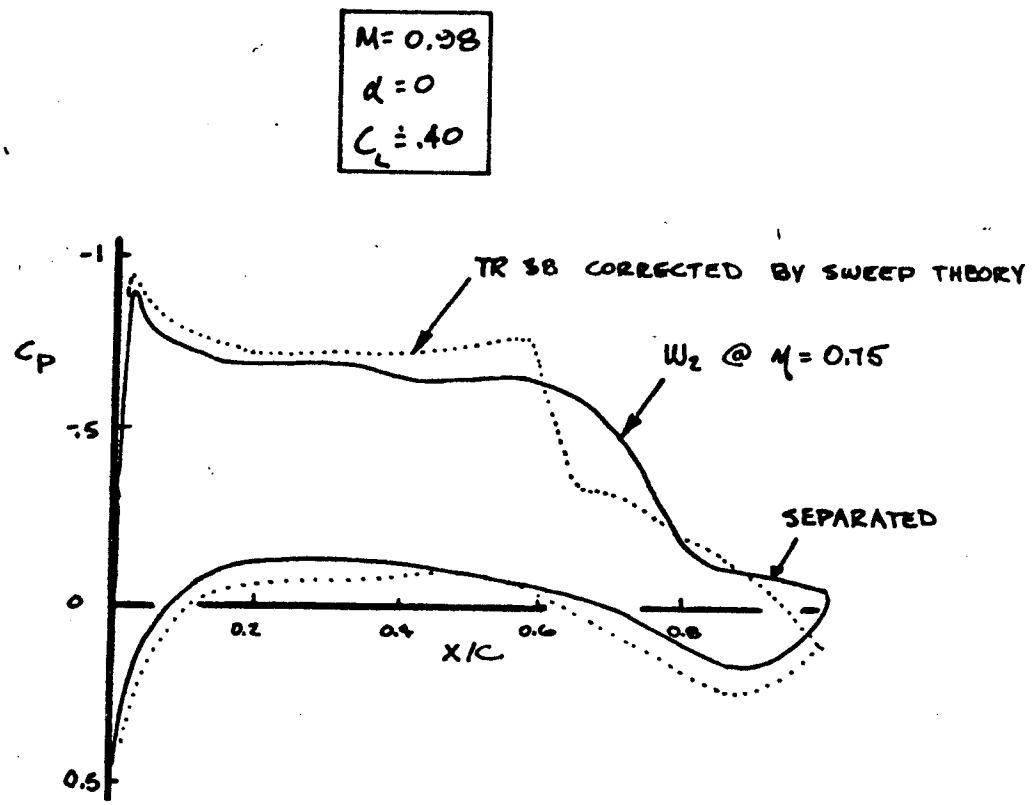

FIGURE 7.7 OUTBOARD PRESSURES ~ WING COMPARED TO TR 38

.78
GILLETTE

505

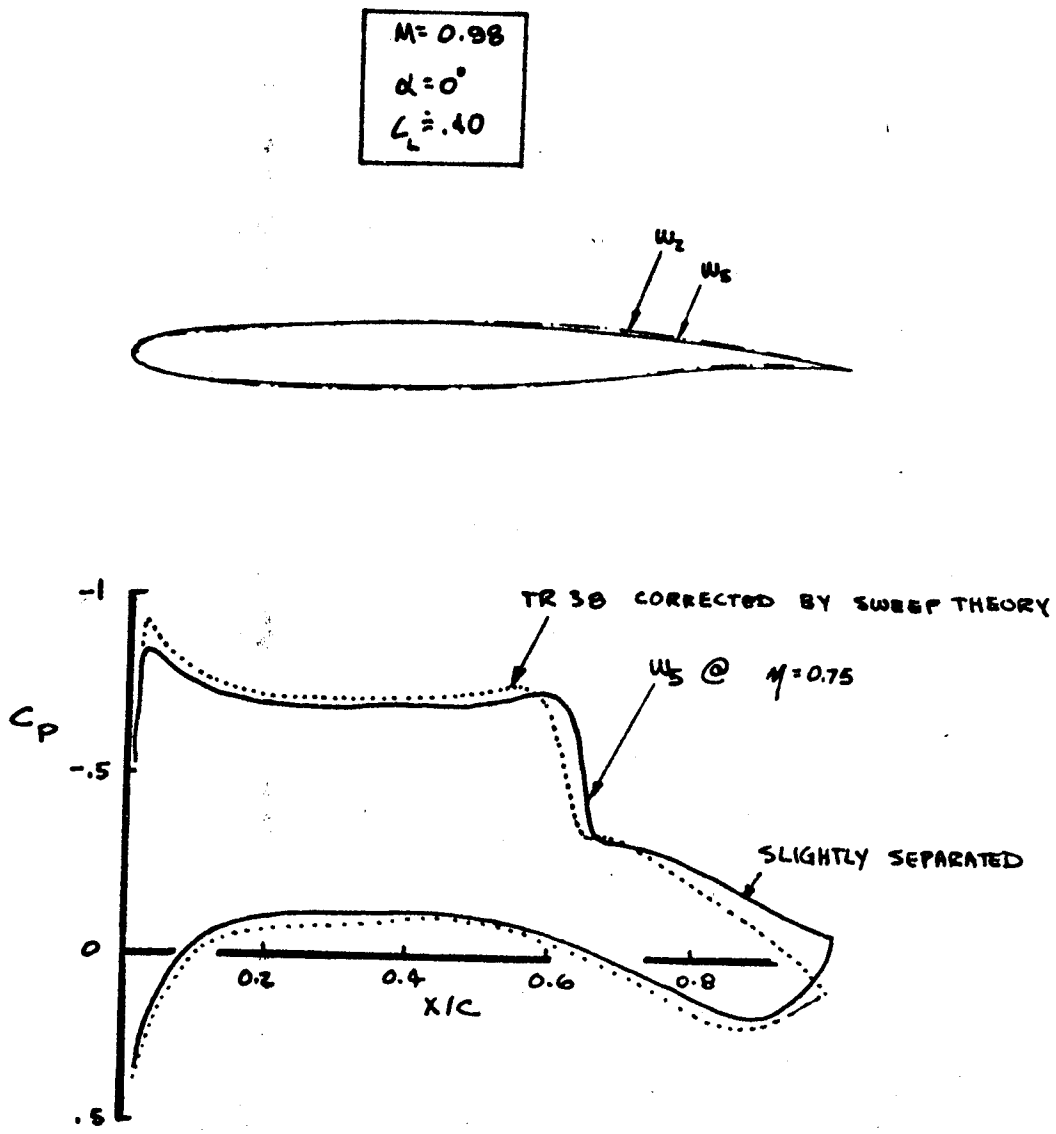

FIGURE 7.8 OUTBOARD PRESSURES — REVISED WING COMPARED TO TR 38

2.4.78
ILLETTE

506

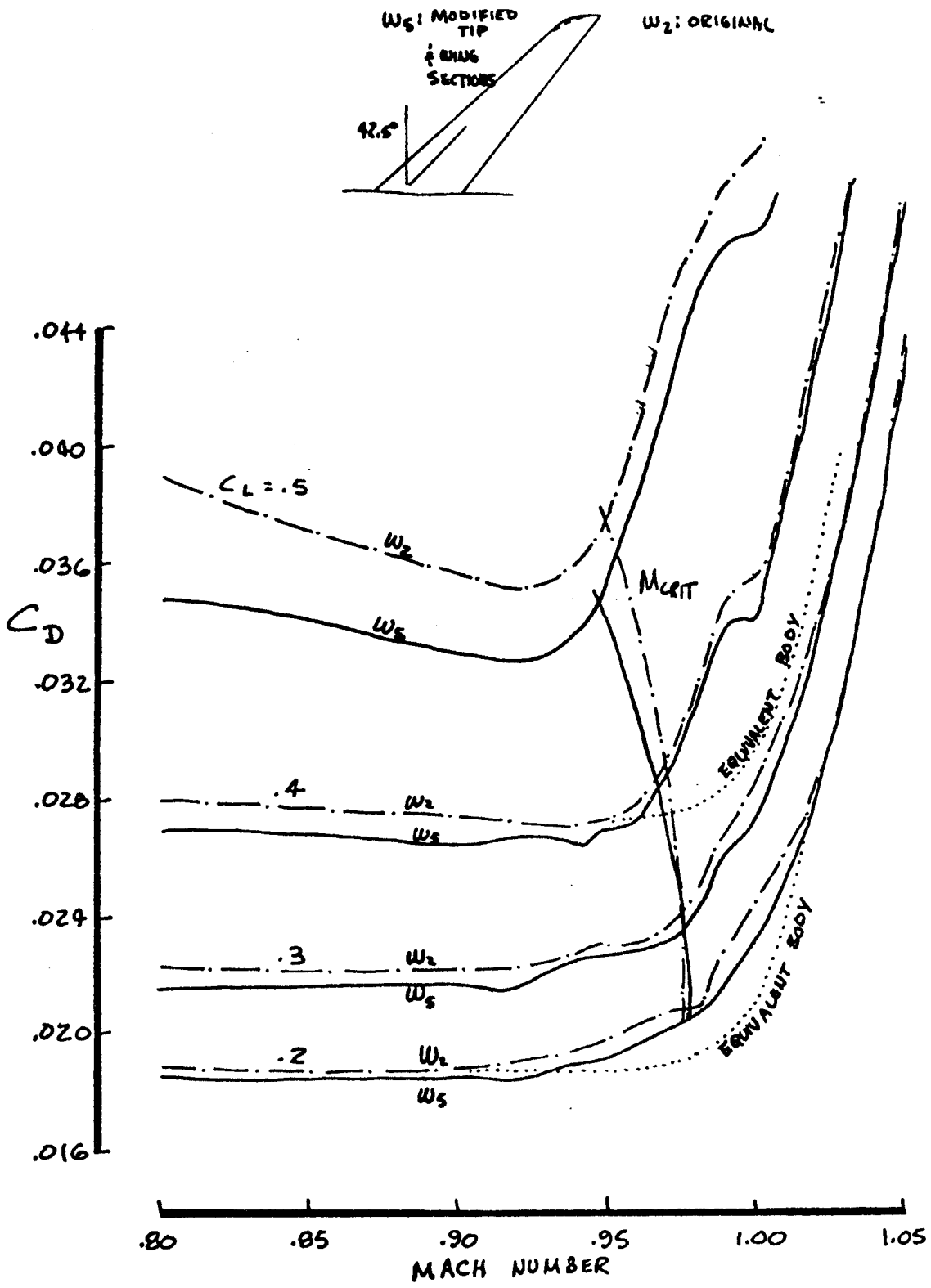

FIGURE 7.9 DRAG RISE OF MODIFIED TRAPEZOIDAL WING

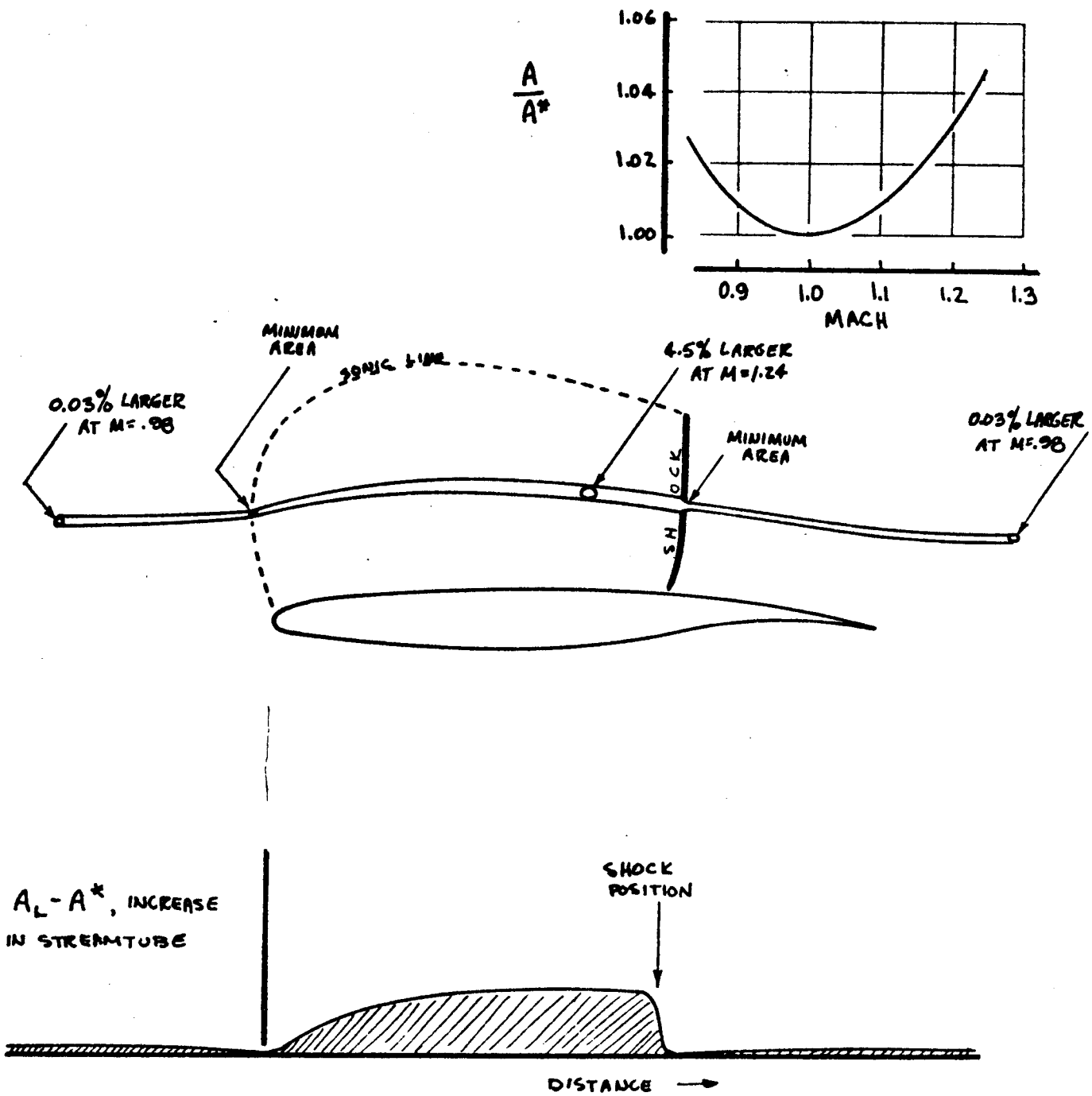

FIGURE 7.10 STREAMTUBE EXPANSION DUE TO UPPER SURFACE LIFT

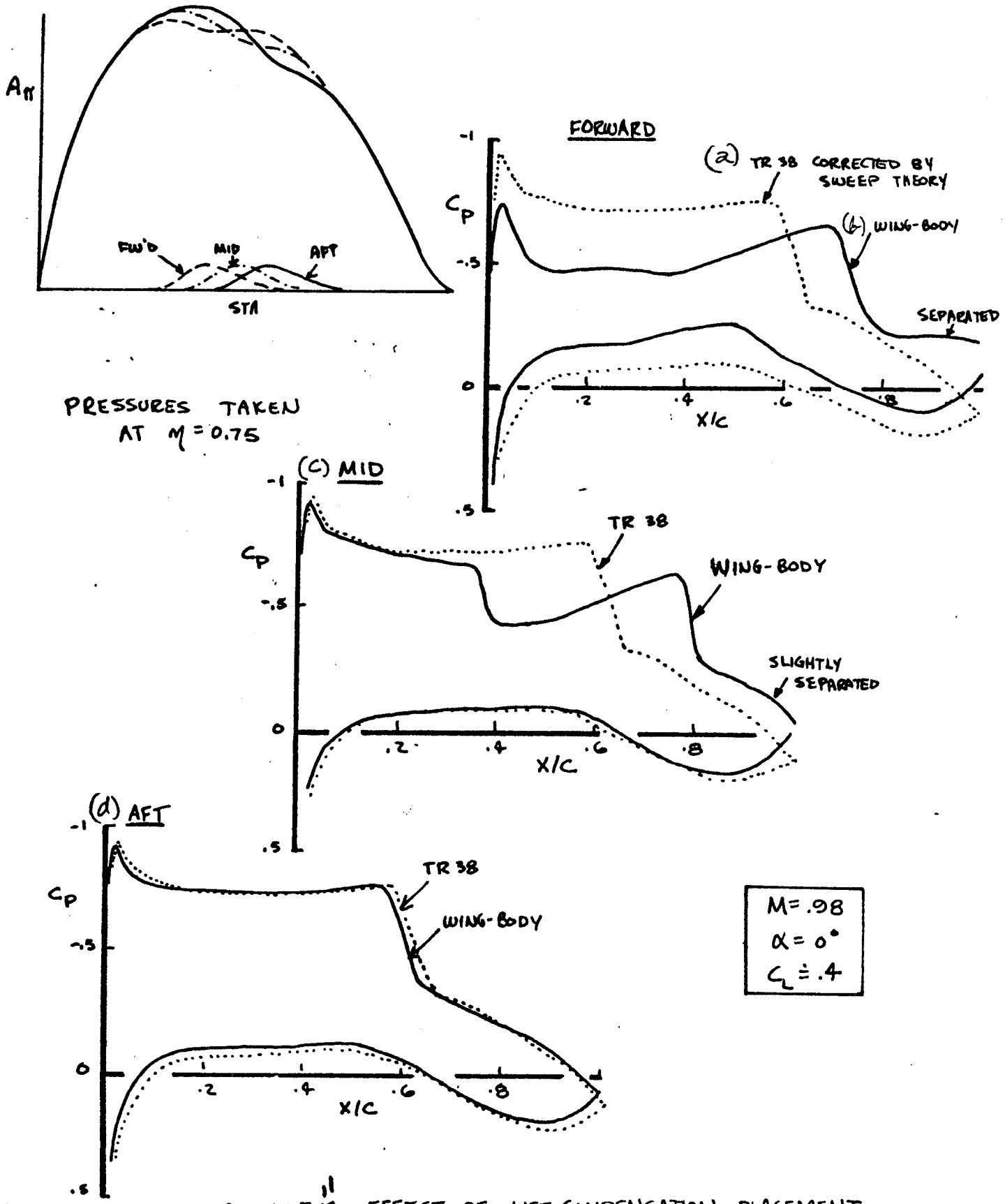

FIGURE 7.11 EFFECT OF LIFT COMPENSATION PLACEMENT ON OUTBOARD WING PRESSURES

D.7.27

2.4.78
GILLETTE

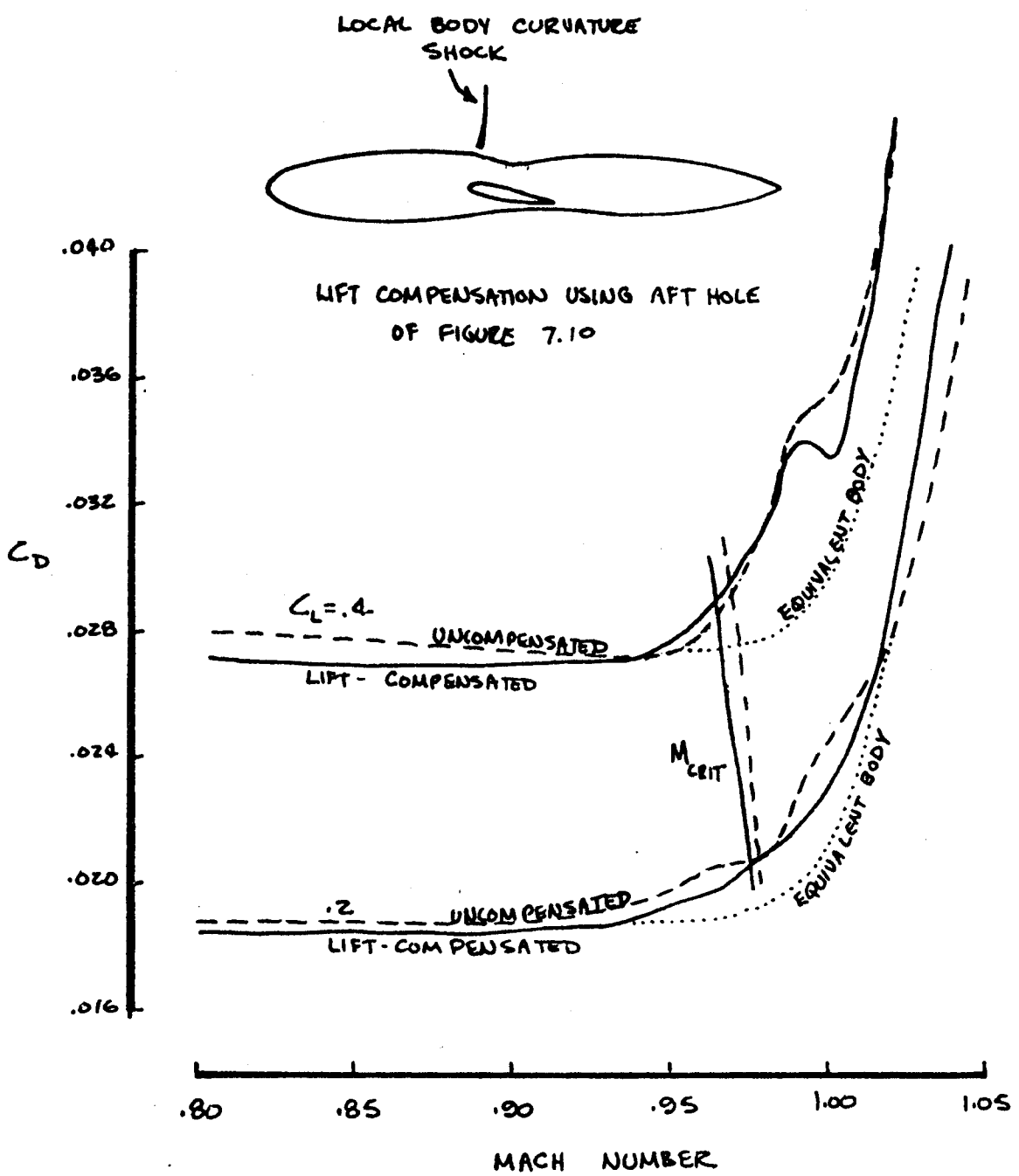

FIGURE 7.12 DRAG RISE OF LIFT-COMPENSATED TRAPEZOIDAL WING

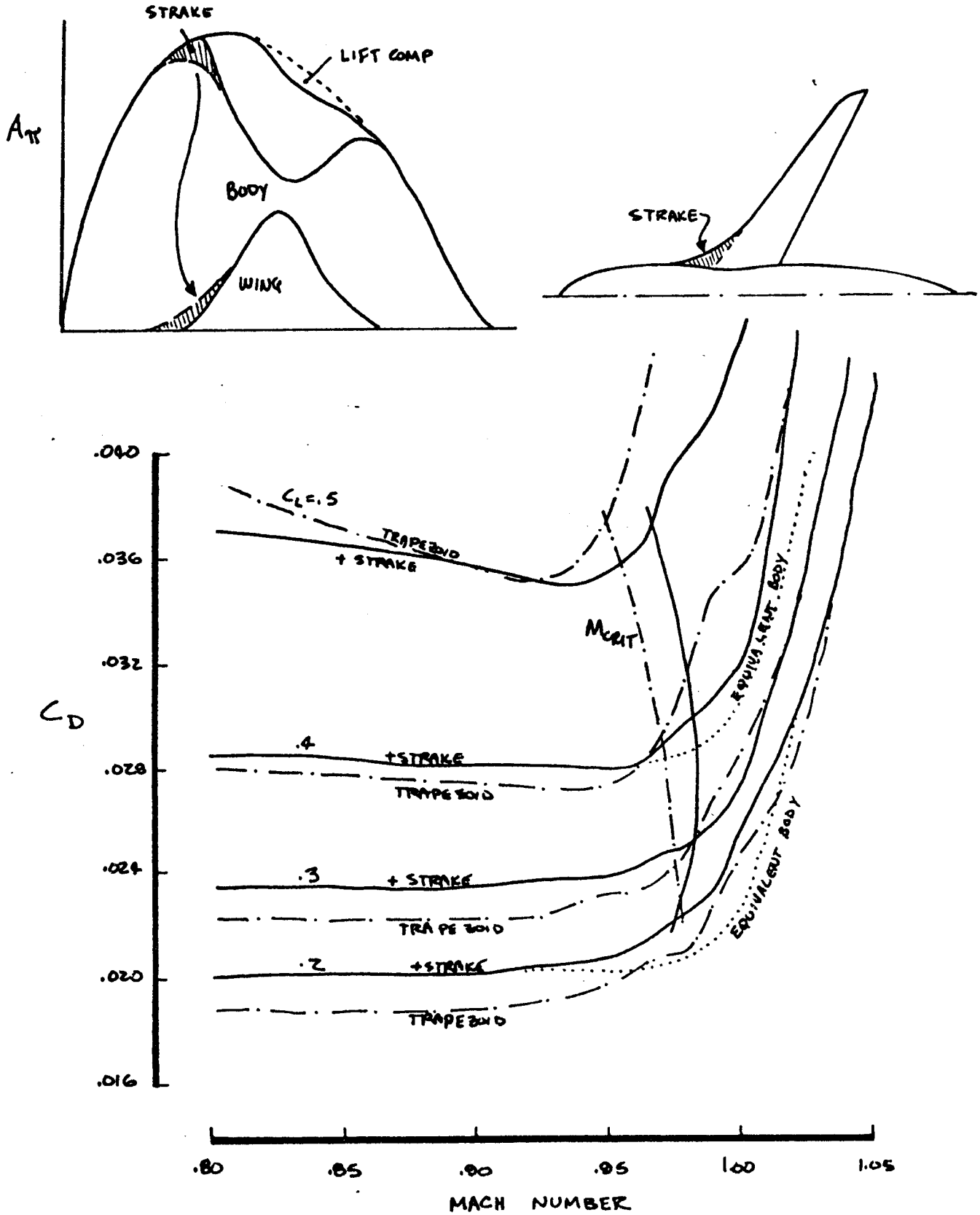

FIGURE 7.13 EFFECT OF WING STRAKE ON LIFT-COMPENSATED DRAG RISE

5/1 2.4.78 GILLETTE

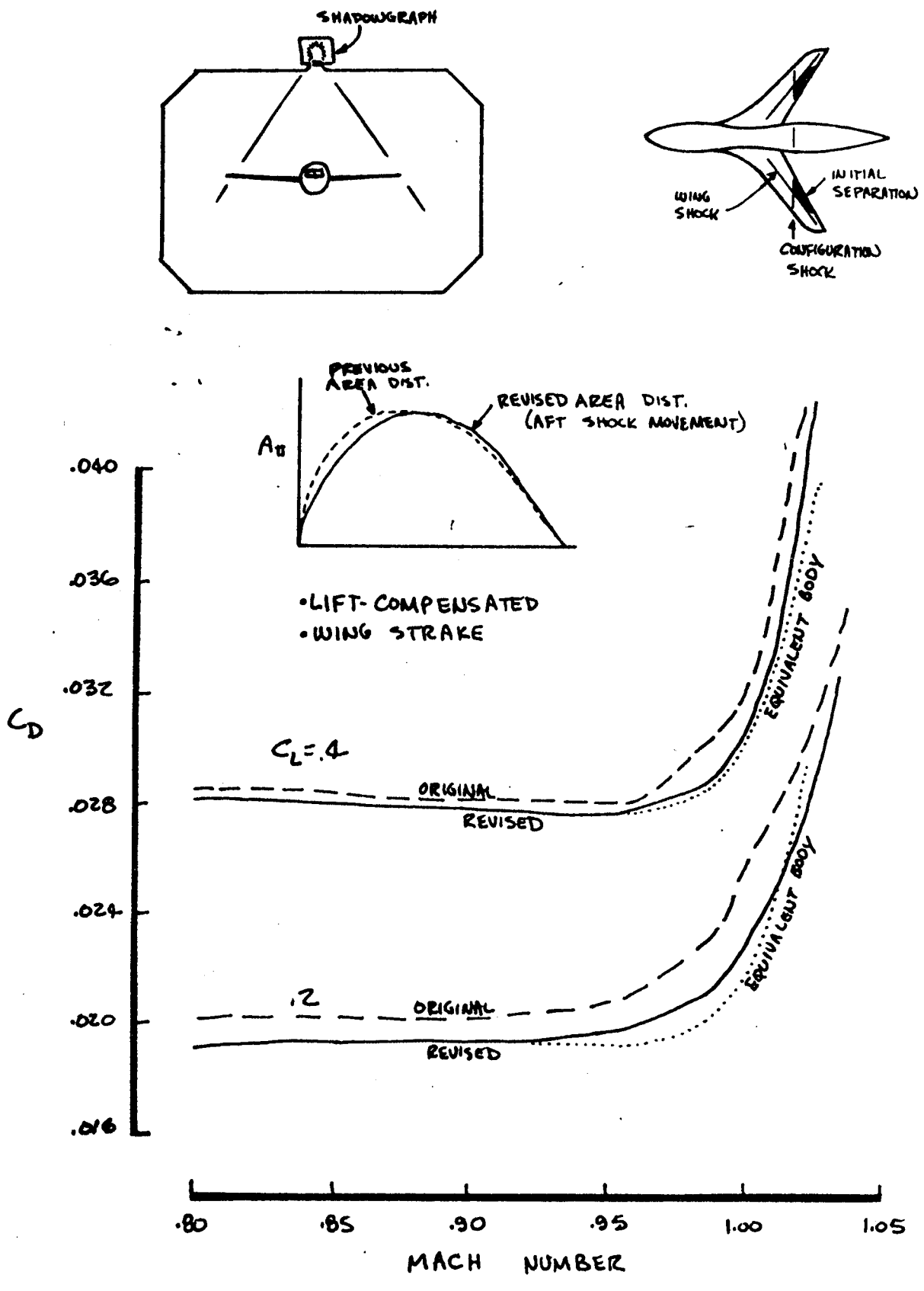

FIGURE 7.14 EFFECT OF CONFIGURATION SHOCK PLACEMENT

2.4.78
GILLOTTE

P.7.30

5/2

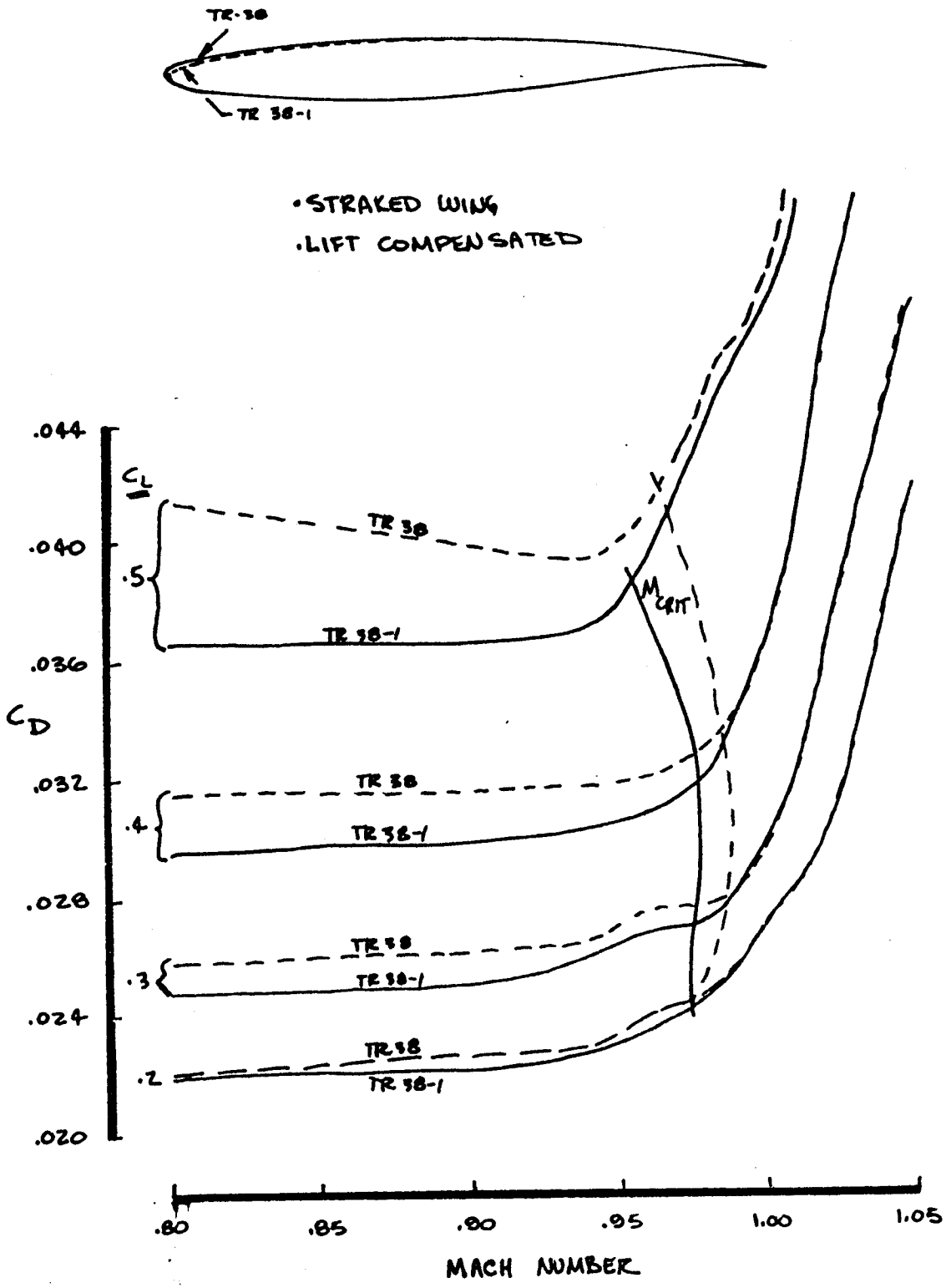

FIGURE 7.15 EFFECT OF SECTION CHANGE

5/3 2.4.78 GILLETTE

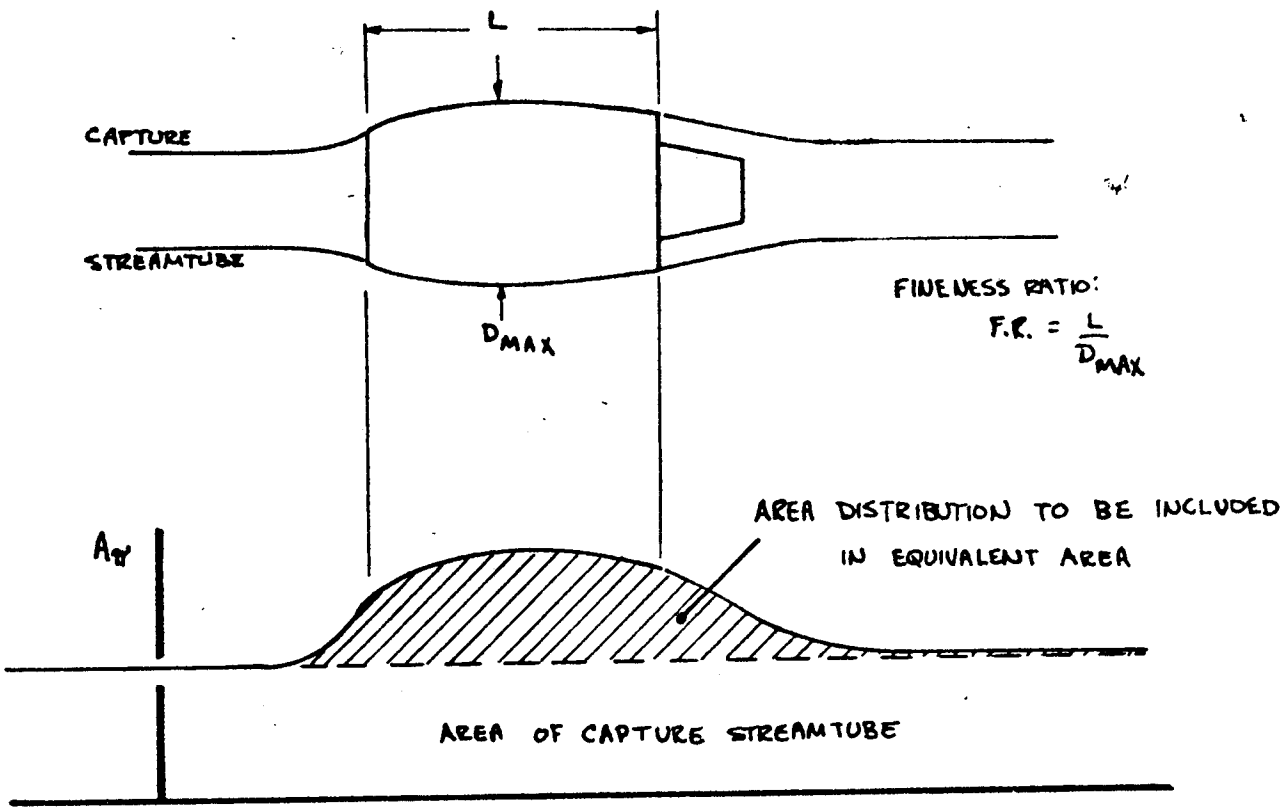

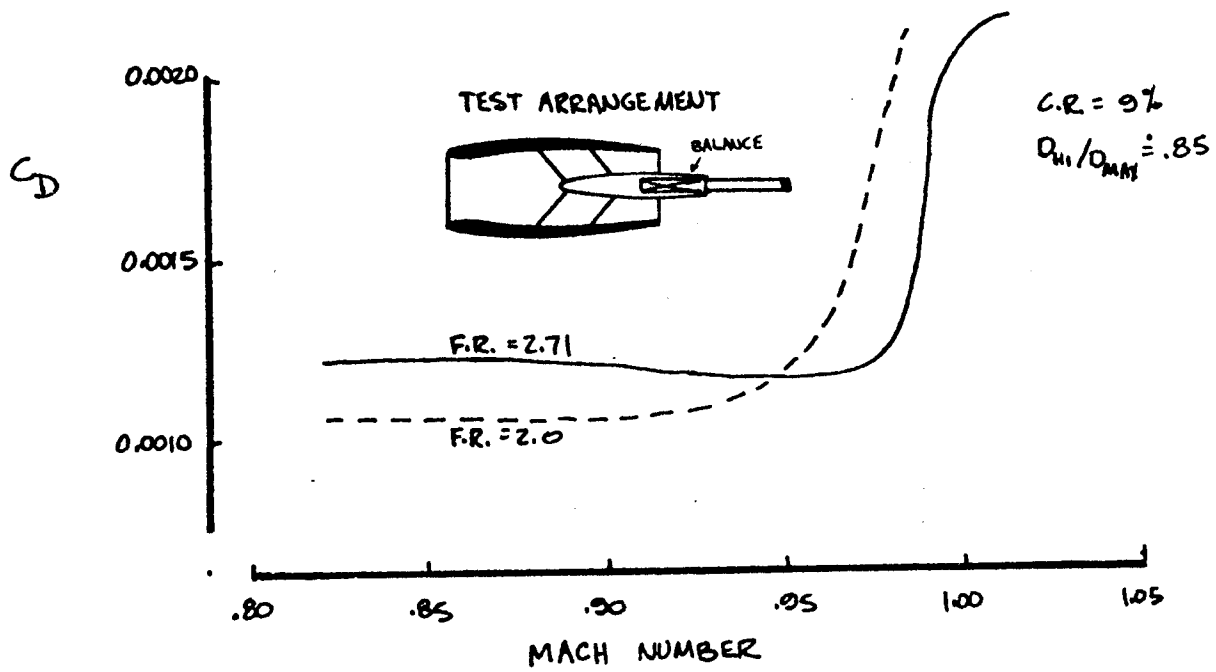

FIGURE 7.16 NST NACELLE DESIGN

2.5.78
GILLETTE

P 7.32

514

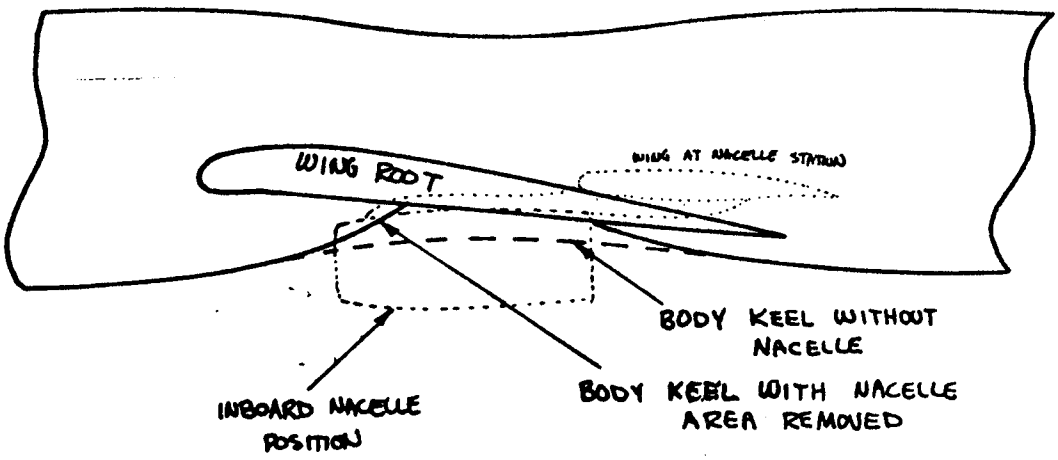

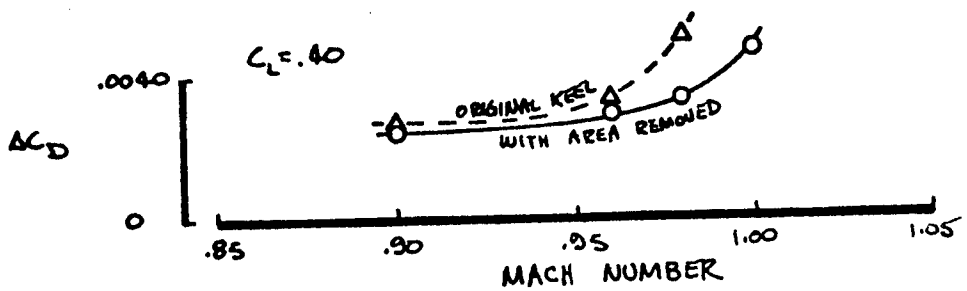

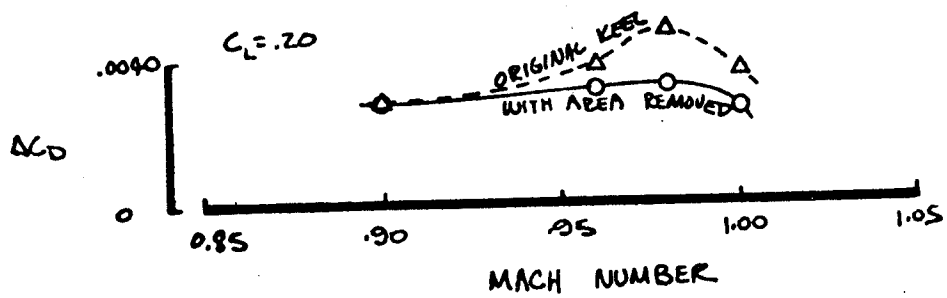

FIGURE 7.17 INBOARD WING-MOUNTED NACELLE AREA COMPENSATION

5/5 2.5.78 GILLETTE

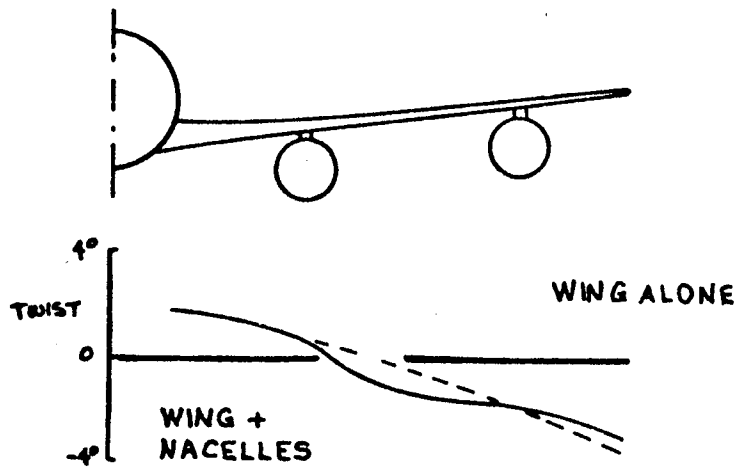

NOTE: NACELLE AREA NOT INCLUDED IN TOTAL AREA RULE

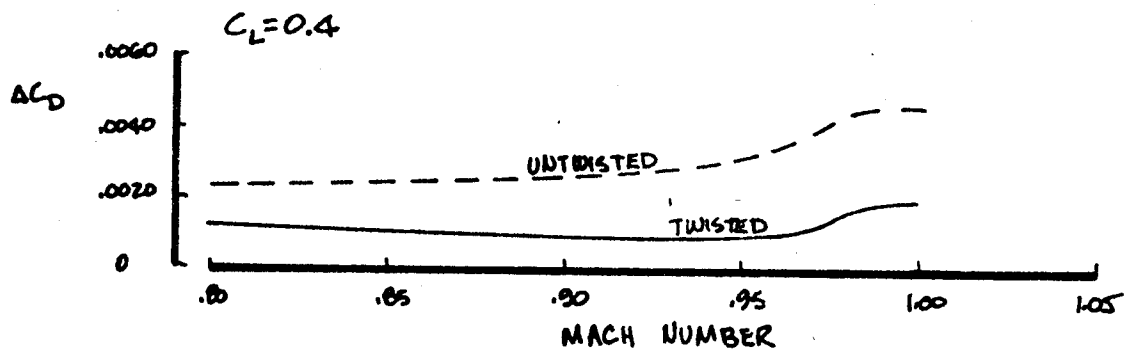

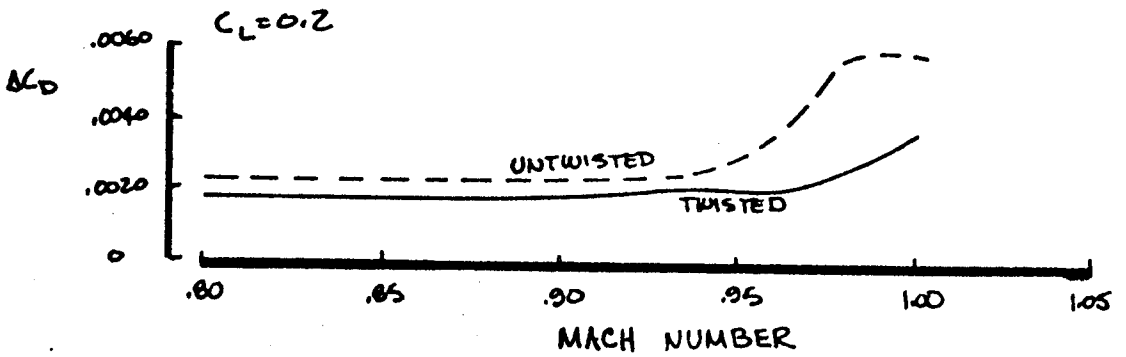

FIGURE 7.18 WING RE-TWIST FOR OUTBOARD WING-MOUNTED NACELLE

2.5.78 GALLETTE

5/6

NACELLE INTEGRATION

S-DUCT

- LOCAL CONTOURING CRITICAL —
  REVISION REDUCED AFT-FACING AREA
  AHEAD OF SHOCK WAVE

$$\Delta C_D = C_{D_{ORIGINAL}} - C_{D_{REVISED}}$$

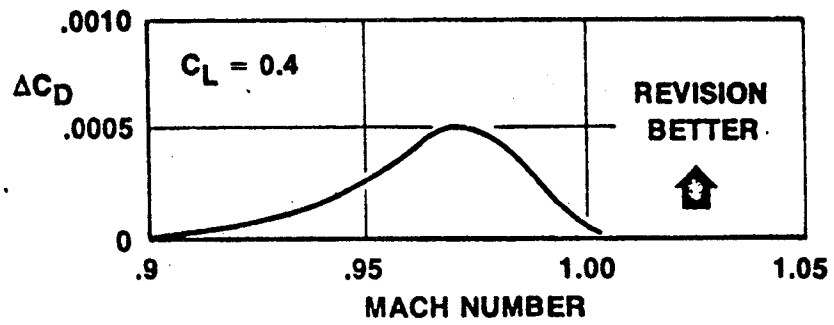

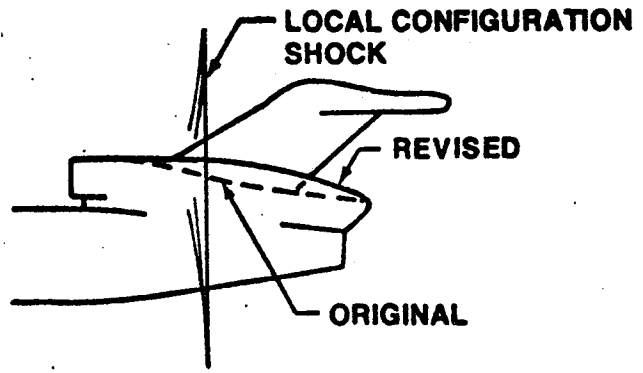

- INLET SHAPE SIMILAR TO WING-MOUNTED NACELLE

D735-10053-1

BOEING

FIGURE 7.19 NST S-DUCT DESIGN

SONIC TRANSPORT

CAB

- MUST SATISFY TOTAL AREA RULE
- MUST NOT HAVE LARGE LOCAL CURVATURES

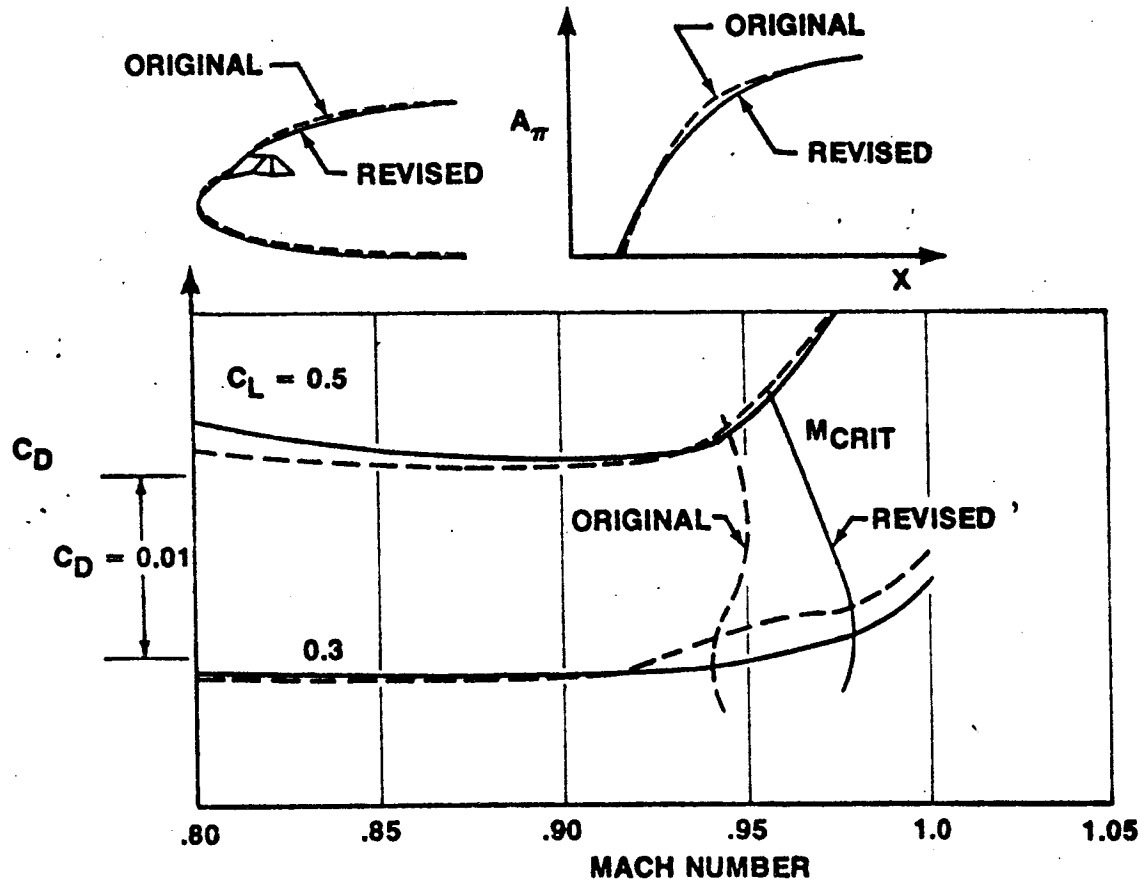

BOEING

FIGURE 7.20 CAB DESIGN

7.36

GILLETTE 2.12.78

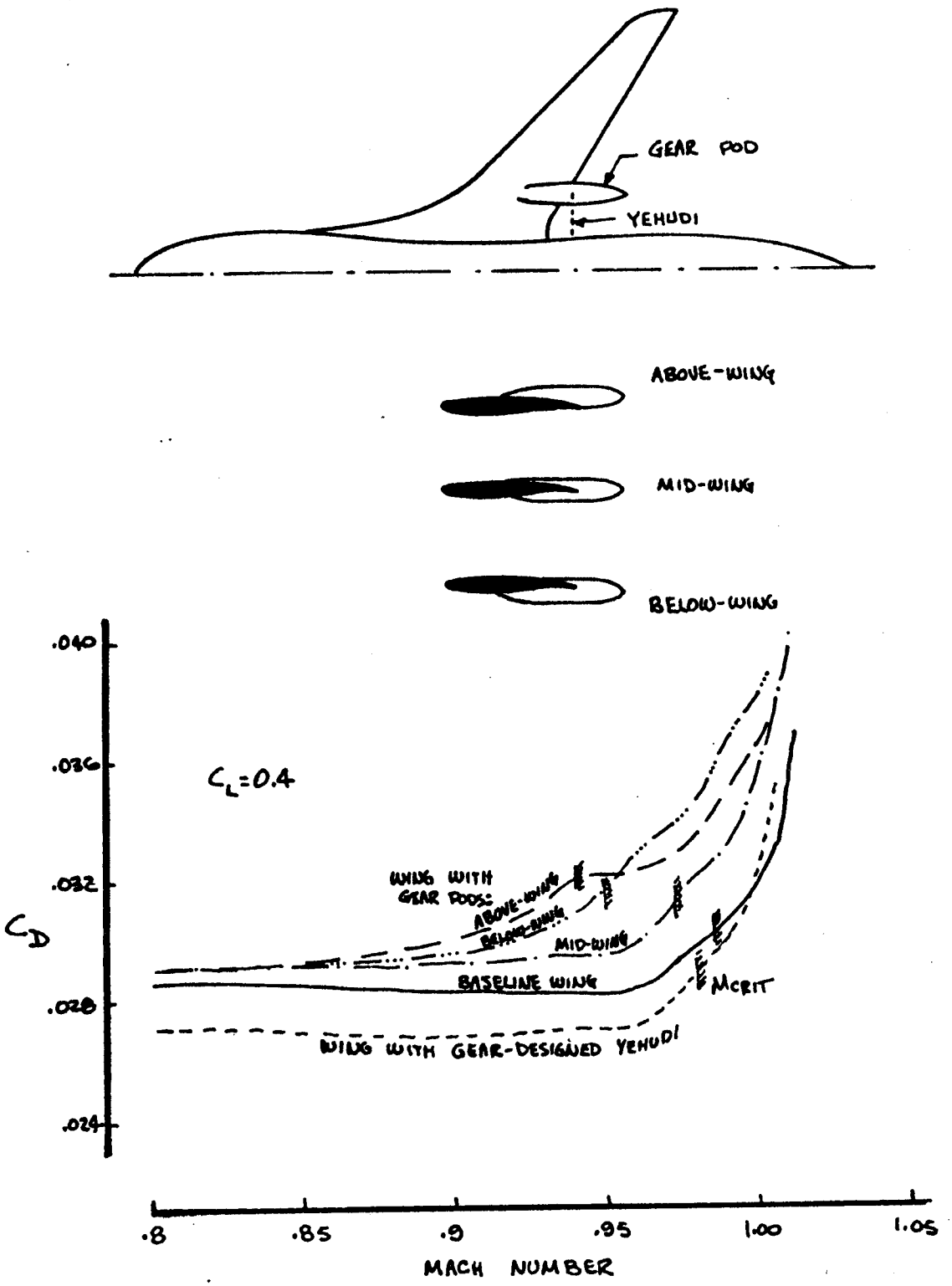

FIGURE 7.21 GEAR PODS VERSUS YEHUDI FOR GEAR STOWAGE

519 2.5.78 GILLETTE

EMPENNAGE DESIGN

T-TAIL REQUIRES LOCAL AREA RULE

- HORIZONTAL TAIL IS IN FREESTREAM FLOW
- LOCAL AREA MUST BE SMOOTH

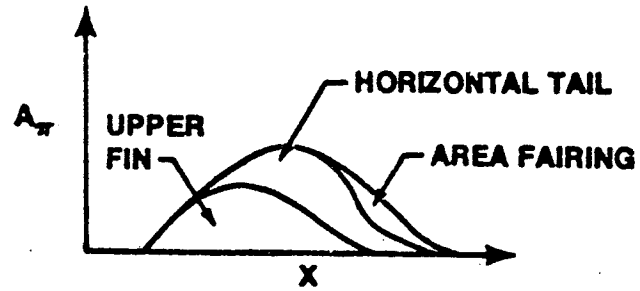

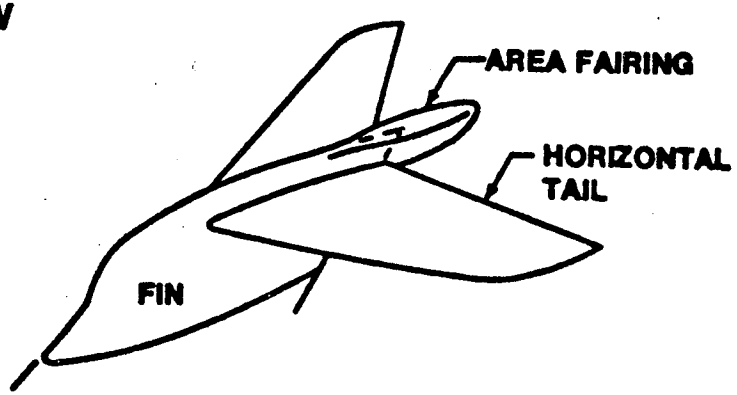

- FAIRING IMPROVES SPEED AND STABILITY

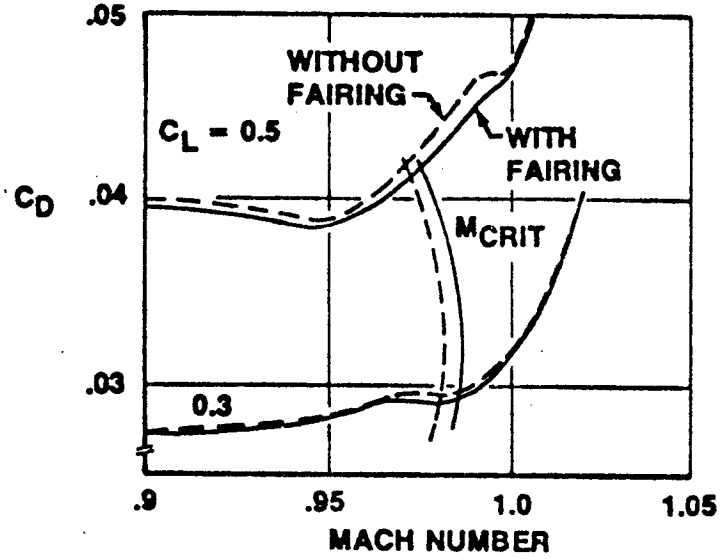

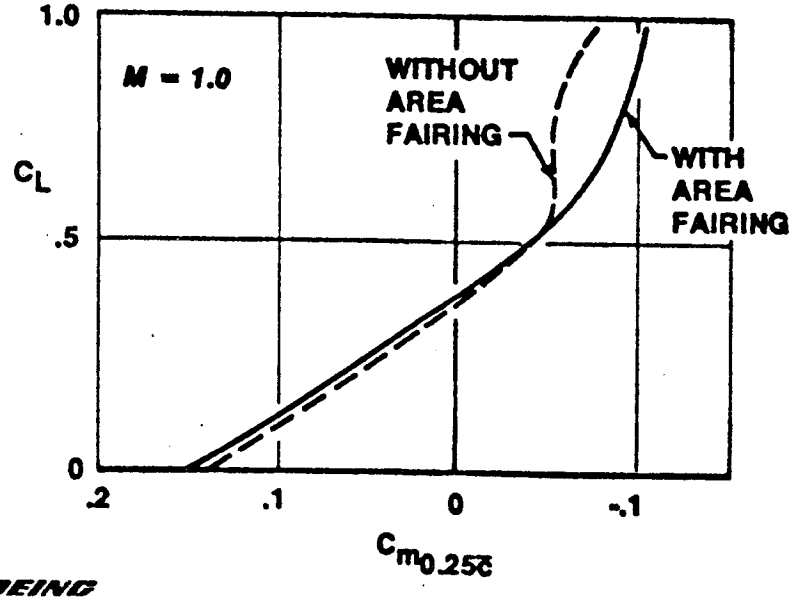

BOEING

FIGURE 7.22 NST T-TAIL DESIGN

EMPENNAGE DESIGN

LOW TAIL

- LOW TAIL IS IN REDUCED MACH FIELD CAUSED BY BODY CLOSURE
- FIN AND HORIZONTAL TAIL DISPLACED FOR GOOD LOCAL AREA RULE
- PERFORMANCE SUPERIOR T-TAIL

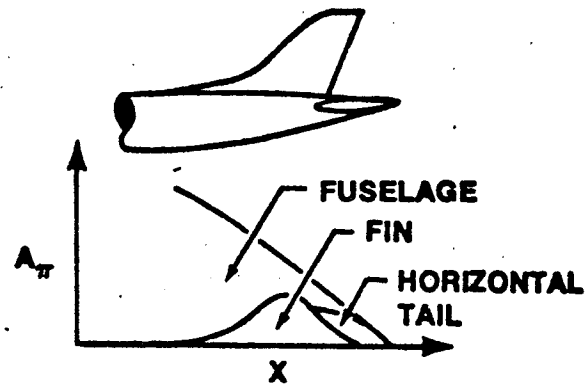

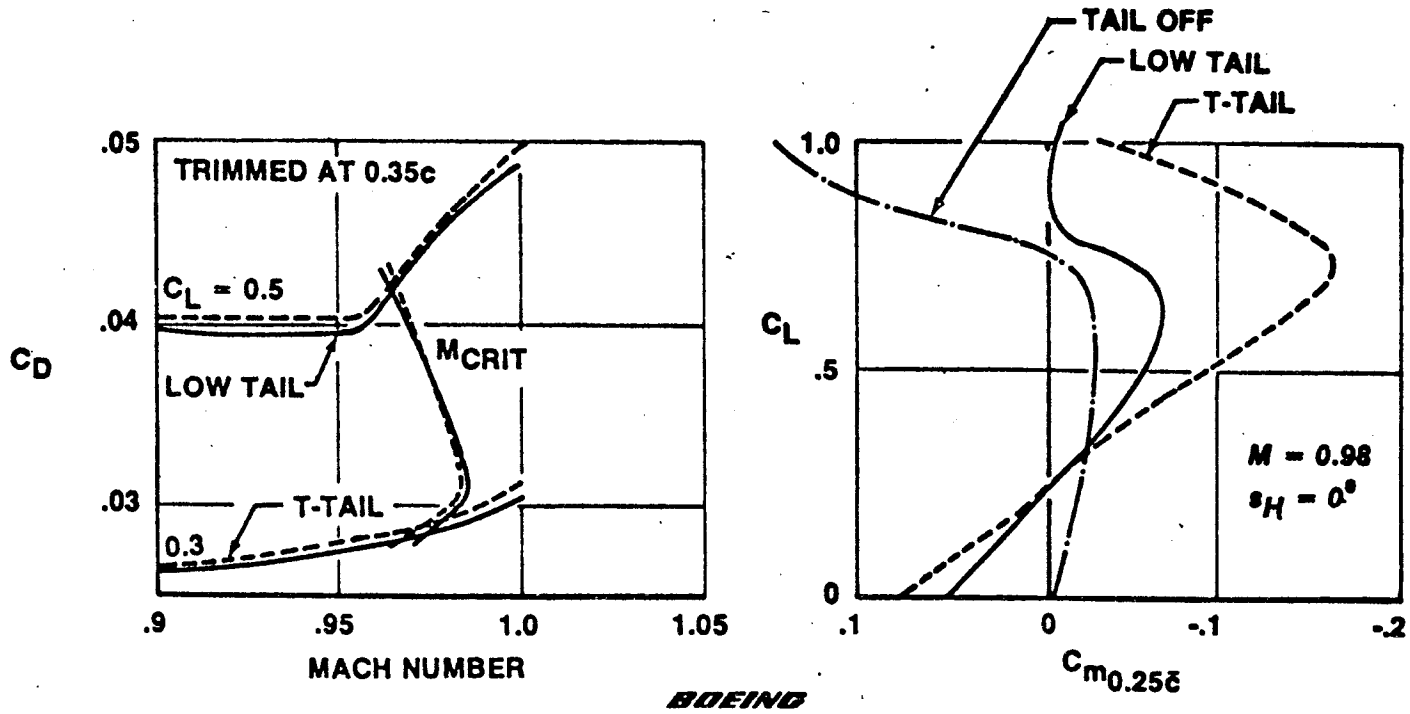

GILLETTE 2.12.78

FIGURE 7.23 NST LOW TAIL DESIGN

EMPENNAGE DESIGN

HORIZONTAL TAIL TWIST

- FLAT (UNTWISTED) TAIL WILL HAVE POOR ISOBAR AND SHOCK PATTERN
- LOW TAIL AND T-TAIL DESIGNED BY ANALYSES IN FLOW FIELD EFFECTS — BODY AND FIN UPWASH EFFECTS LARGE

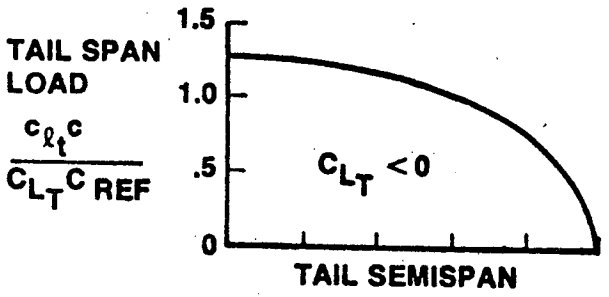

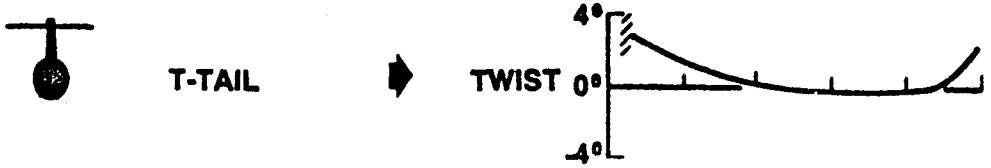

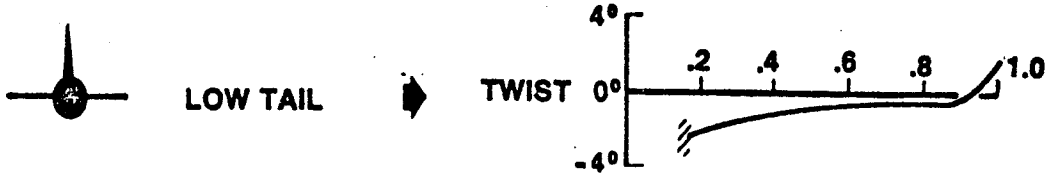

BOEING

FIGURE 7.24 NST TAIL TWIST

04.7.0

GILLETTE
2.12.78

522

THE SONIC TRIANGLE

MORAL:

IF EITHER —

(1) TOTAL AREA RULE

OR

(2) LOCAL AREA RULE

OR

(3) SURFACE CURVATURE

IS IGNORED,

THEN —

AERODYNAMICIST FALLS ON HIS _____.

2.4.2.1

BOEING

FIGURE 7.26 THE SONIC DESIGN TRIANGLE

GILLETTE 2.12.78

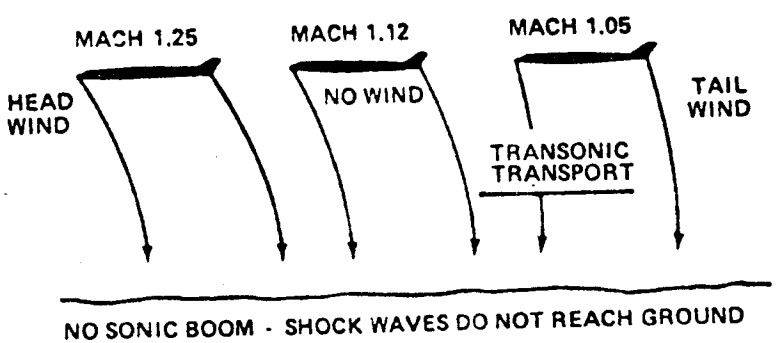

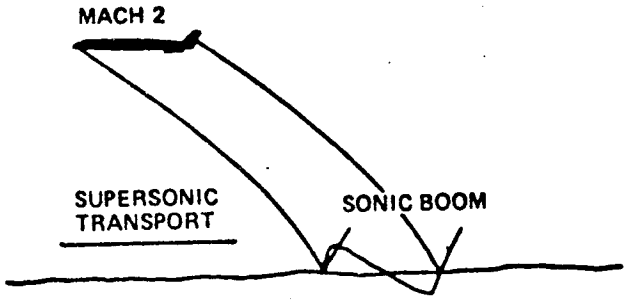

REFERENCE 2.0

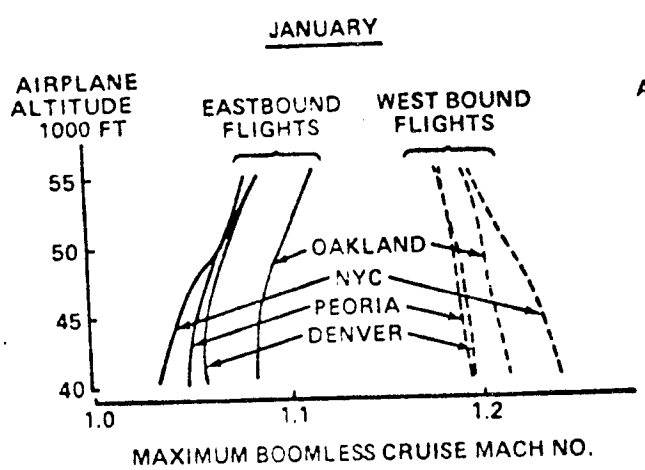

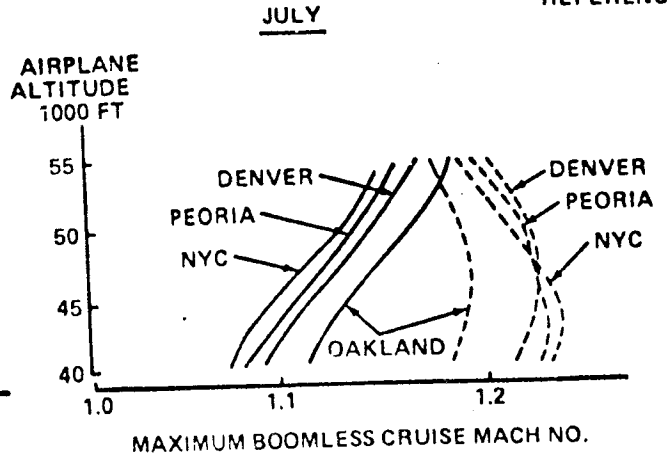

7.27

FIGURE 7.7.–AVOIDING SONIC BOOM

TRACE GILLETTE 2.12.78

CONTRIBUTIONS TO SUPERSONIC CRUISE DRAG

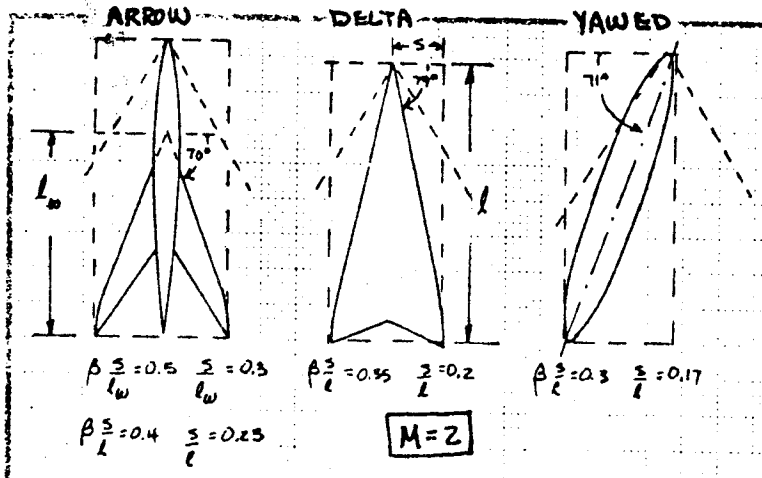

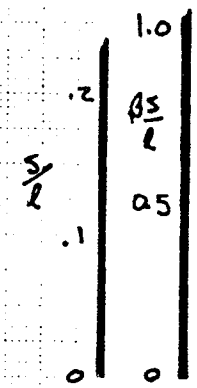

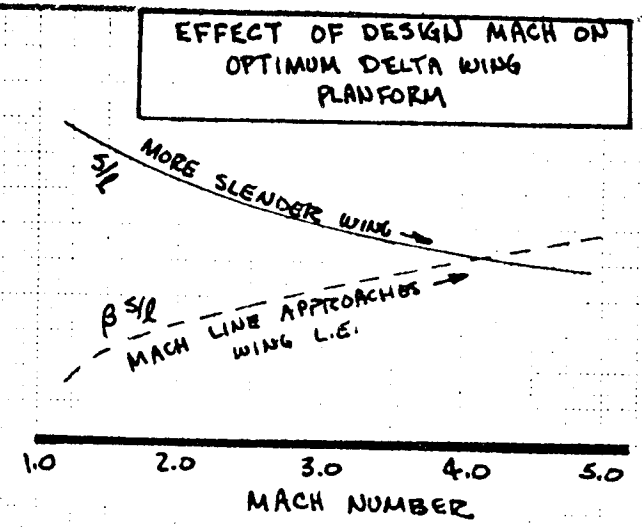

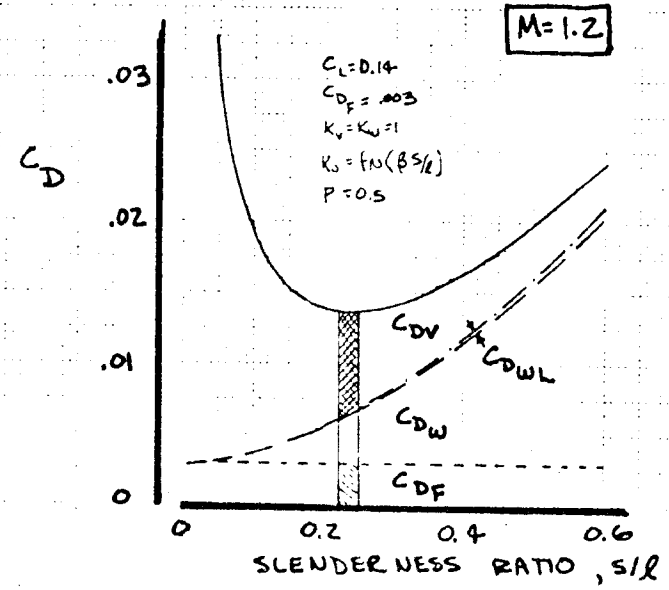

DELTA WING DRAG CONTRIBUTIONS

C_{D_F} - friction drag

C_{D_W} - WAVE DRAG DUE TO VOLUME

$C_{D_{WL}}$ - WAVE DRAG DUE TO LIFT/LENGTH

C_{D_V} - WAVE DRAG DUE TO LIFT/SPAN

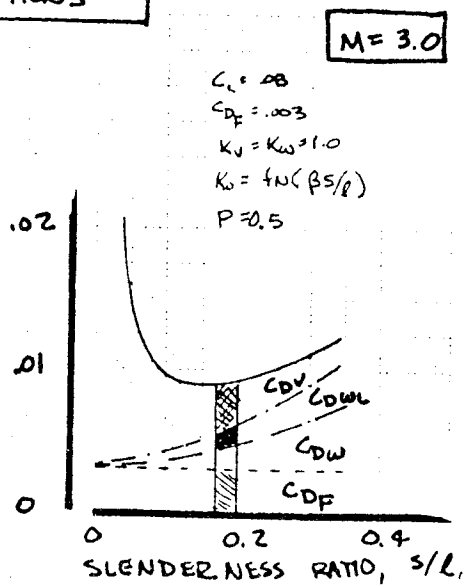

FIG 7.28

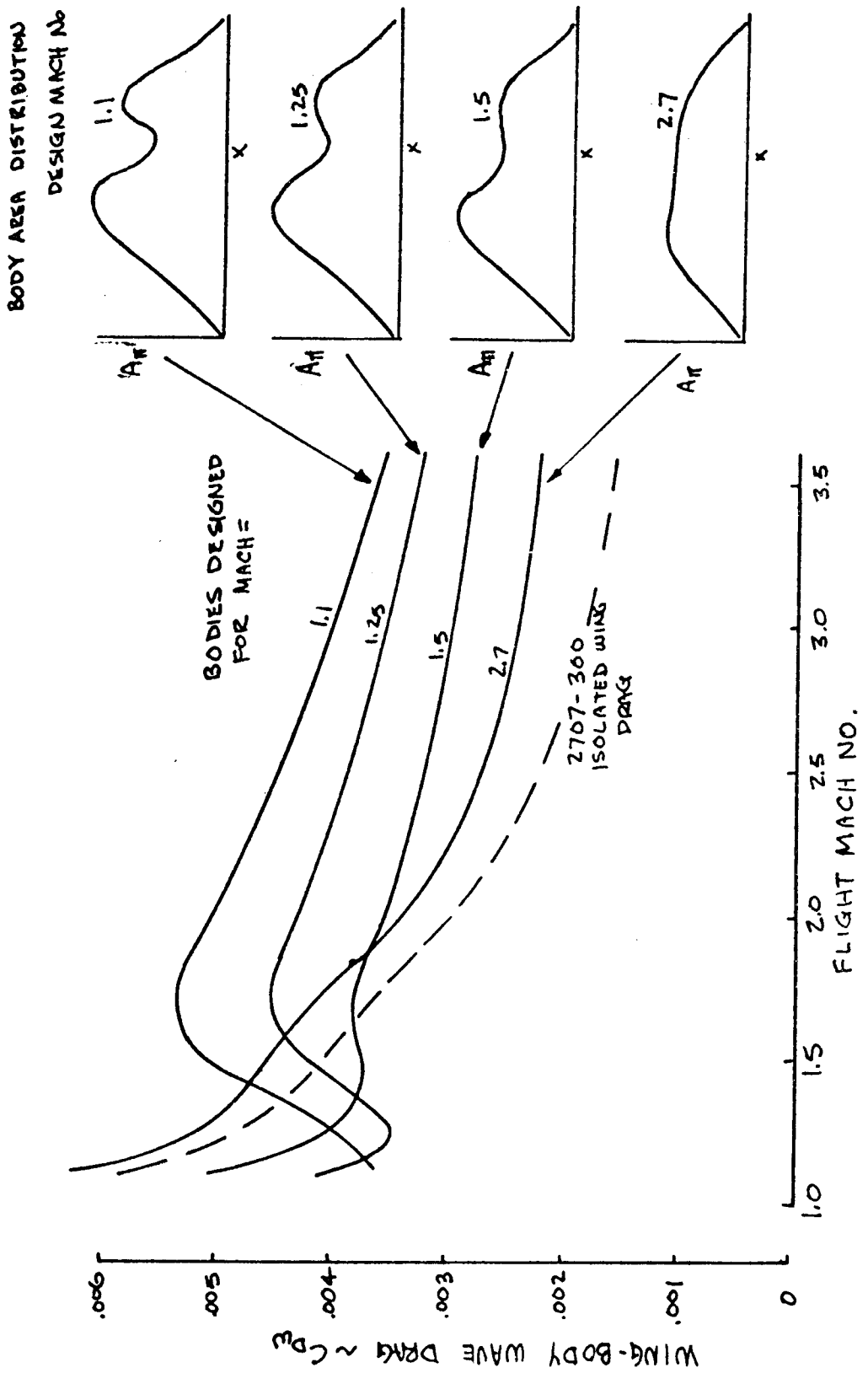

FIGURE 7.29 WAVE DRAG OF AREA-RULED CONFIGURATIONS

GILLETTE
2-12-78

(a) CONVENTIONAL

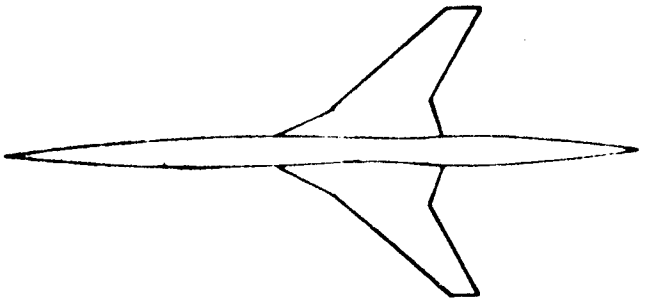

- LEFT HAND & RIGHT HAND WINGS ADD AREA AT THE SAME STATION
- BODY CONTOUR CHANGE IS LARGE

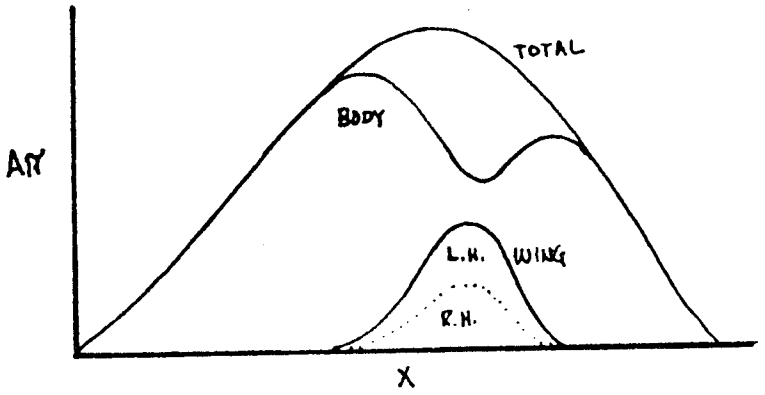

(b) YAWED WING

- LEFT HAND & RIGHT HAND WINGS ARE DISPLACED; DO NOT ADD AREA AT THE SAME STATION
- BODY CONTOURING IS MINIMAL
- TOTAL AREA IS REDUCED FOR GIVEN PAYLOAD ~ HIGHER FINENESS RATIO ACHIEVED

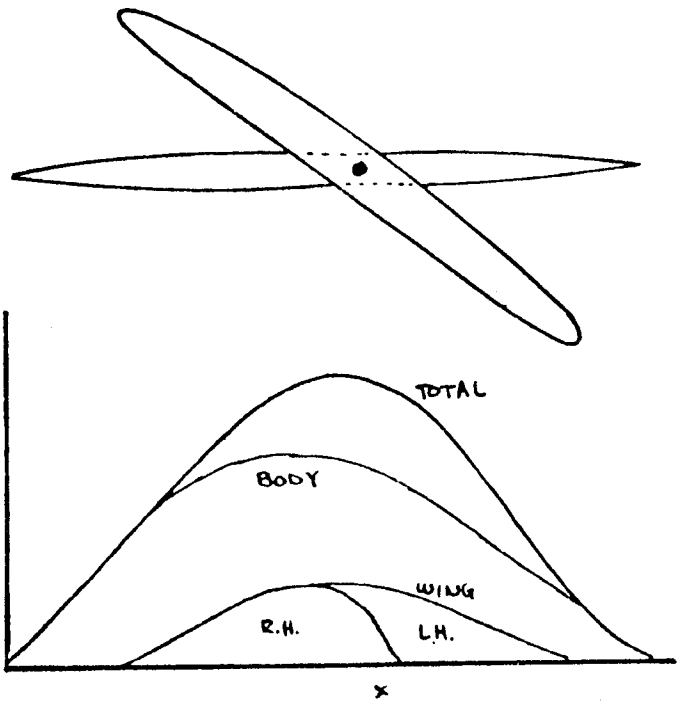

FIGURE 7.30 SUPERSONIC AREA DISTRIBUTION ~ CONVENTIONAL VS YAWED WING

GILLETTE 2.12.78

P.7.46

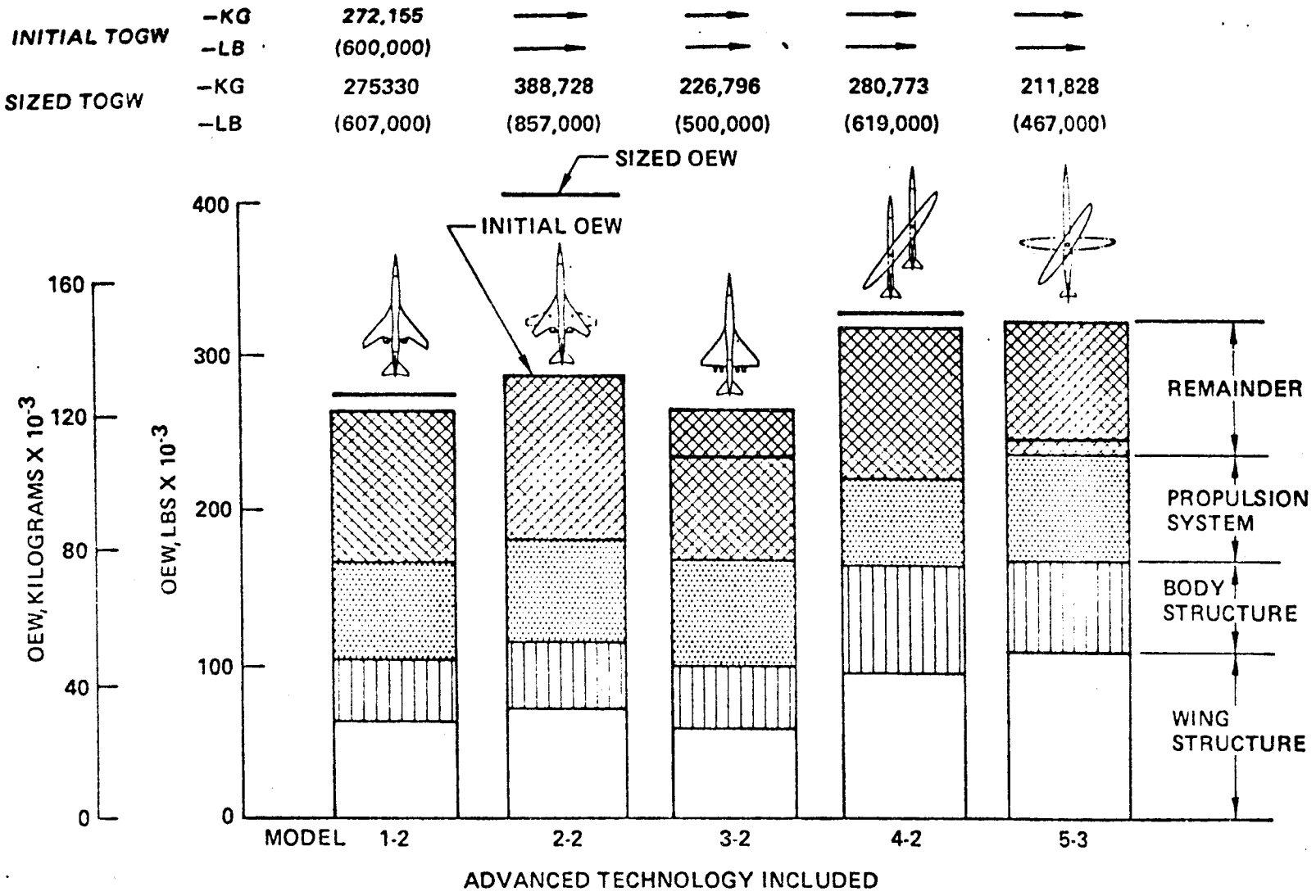

FIGURE 18.–BASE CONFIGURATION WEIGHTS COMPARISON

7.3/

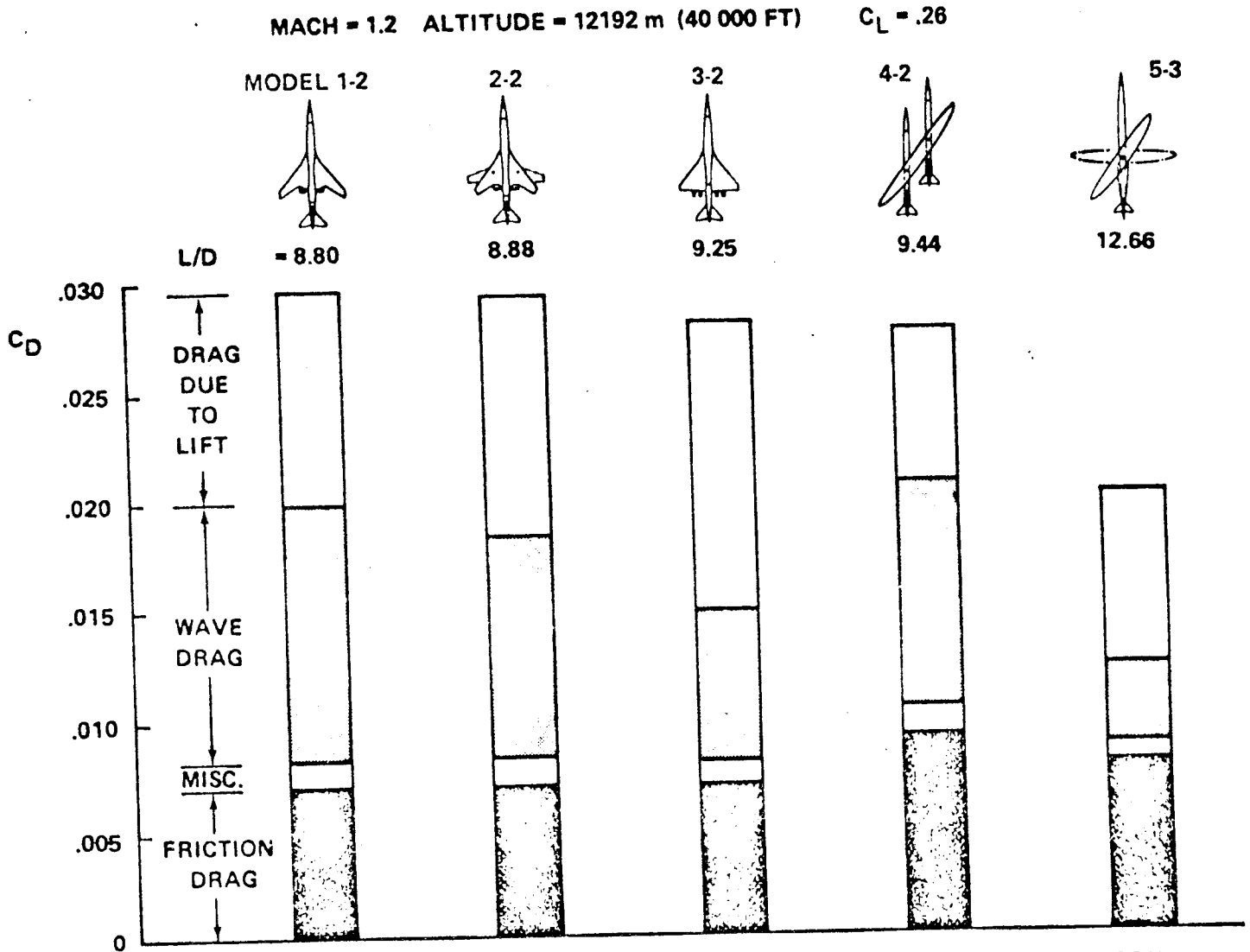

FIGURE 69.–UNCYCLED BASELINE CONFIGURATION CRUISE DRAG COMPARISON

7.32

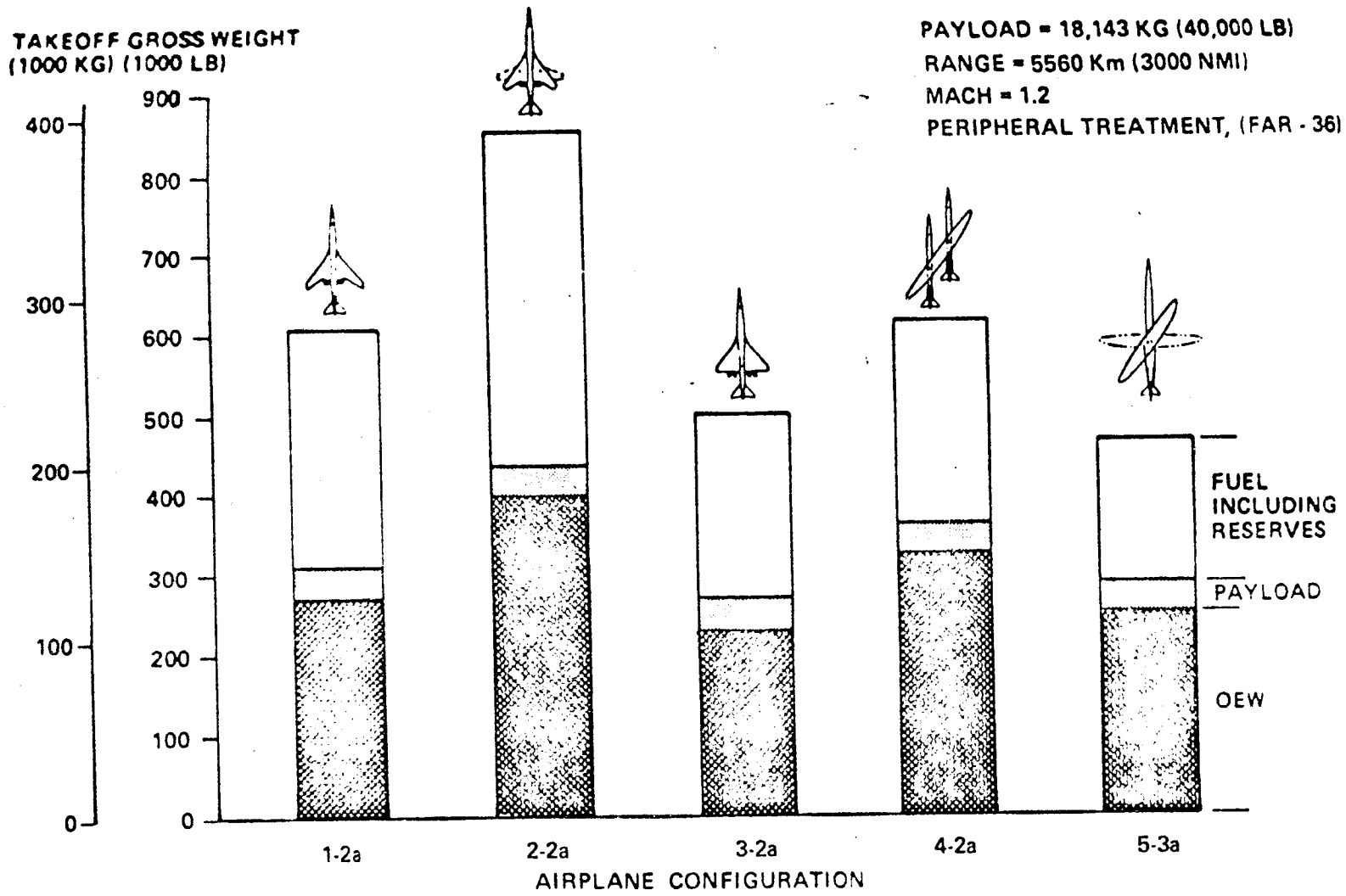

FIGURE 27.–SIZED AIRPLANES GROSS WEIGHT SUMMARY

7.33

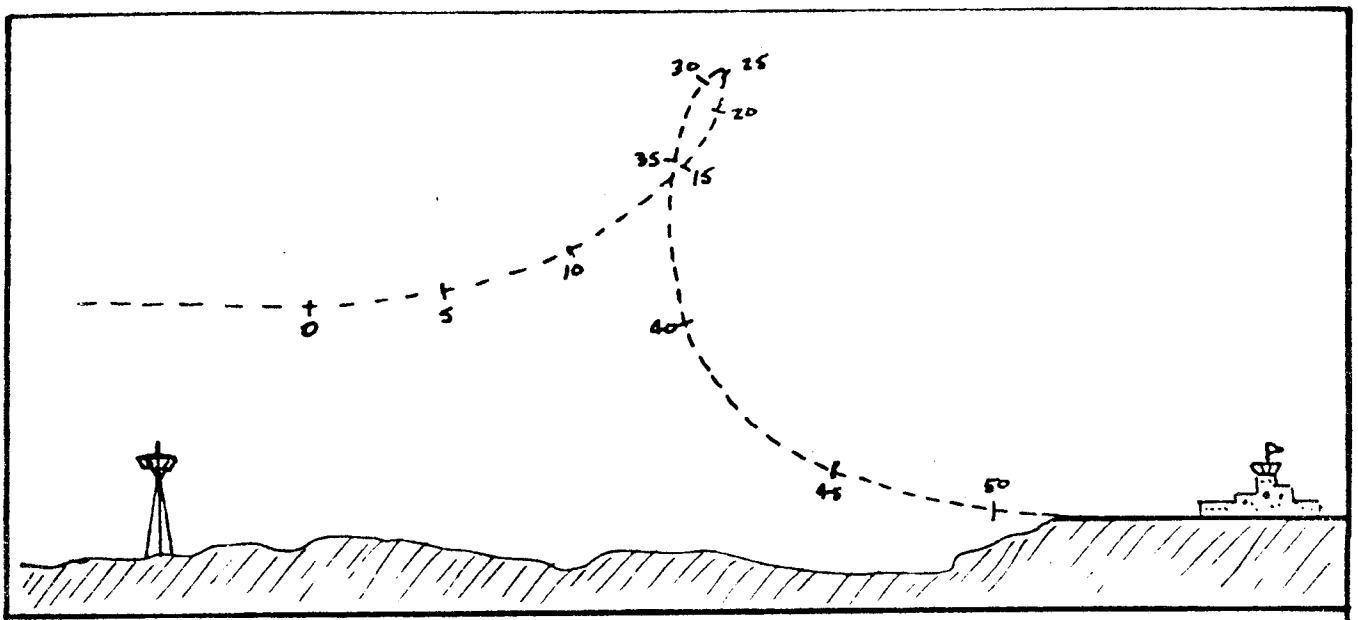

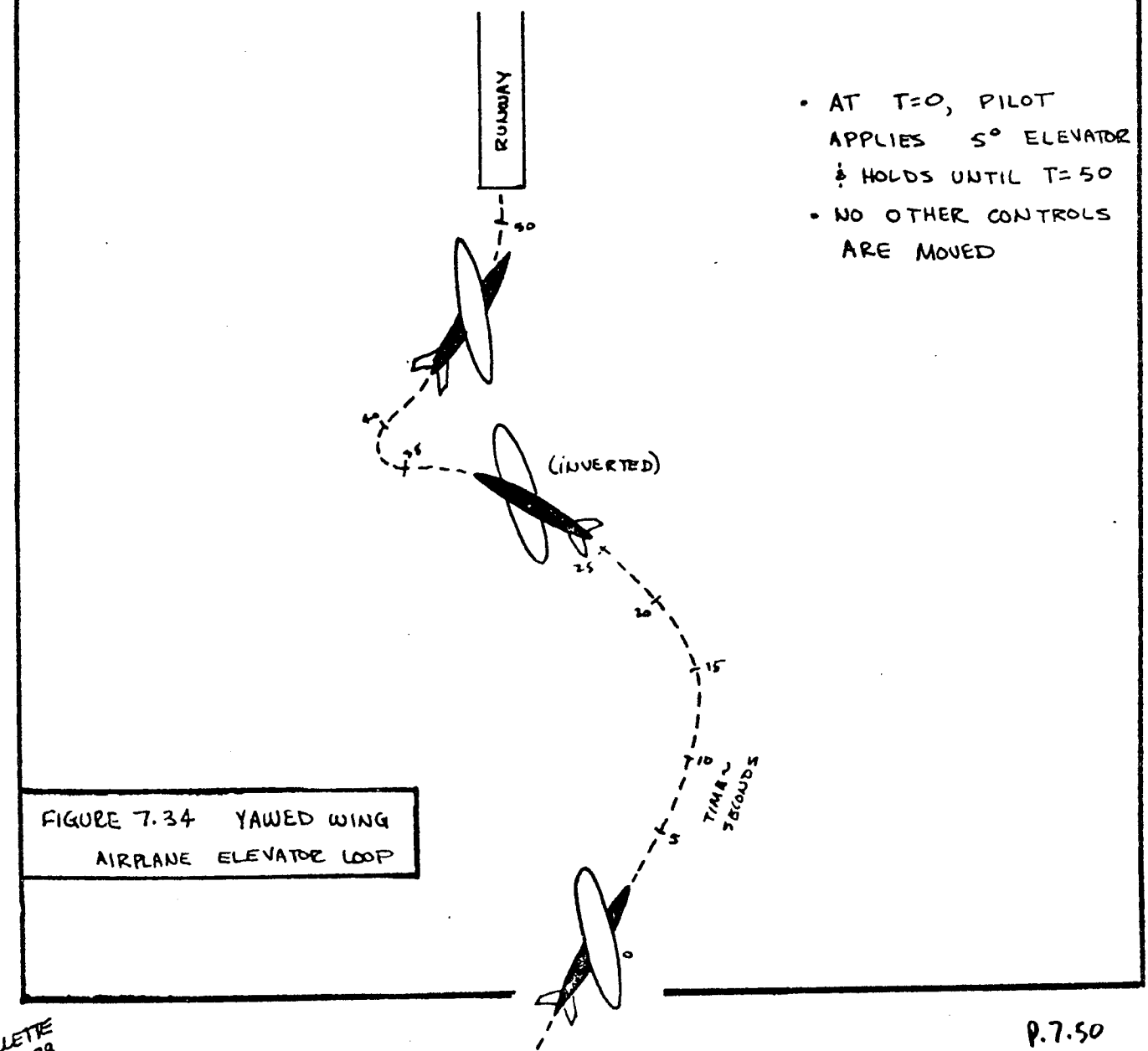

- AT T=0, PILOT APPLIES 5° ELEVATOR & HOLDS UNTIL T=50
- NO OTHER CONTROLS ARE MOVED

FIGURE 7.34 YAWED WING AIRPLANE ELEVATOR LOOP

GILLETTE 2-12-79

(b) SUBSONIC LEADING EDGE

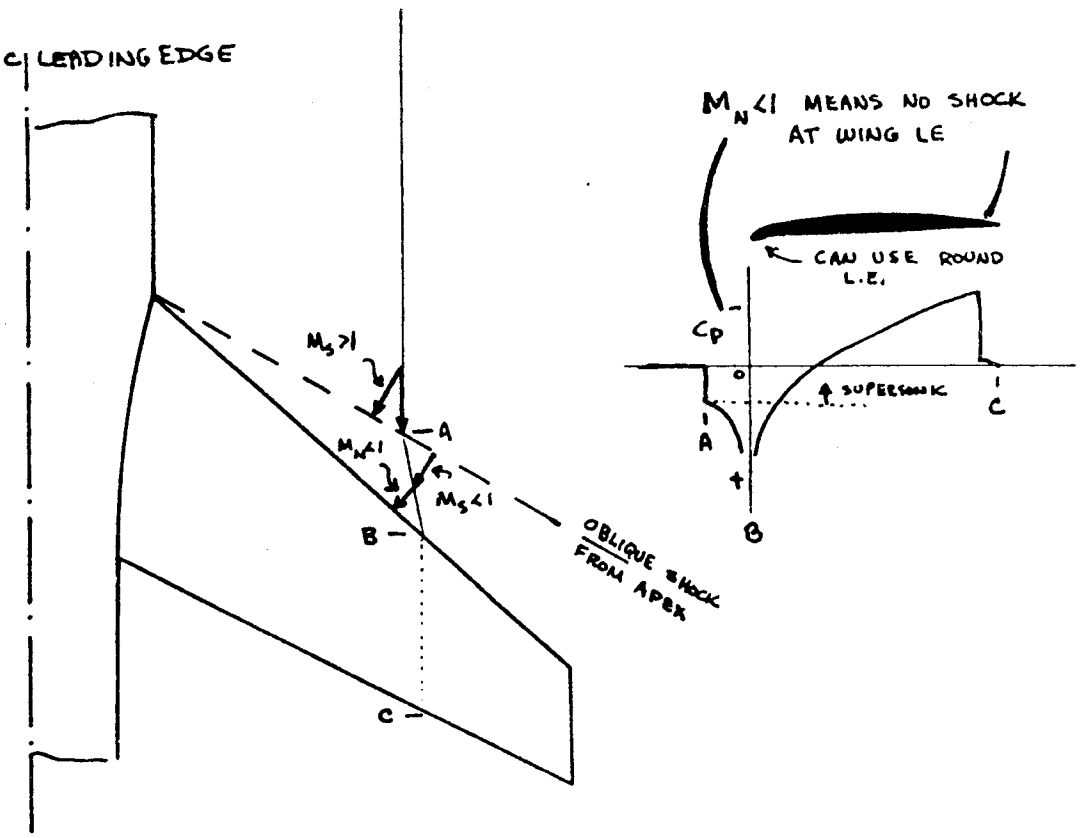

(a) SUPERSONIC LEADING EDGE

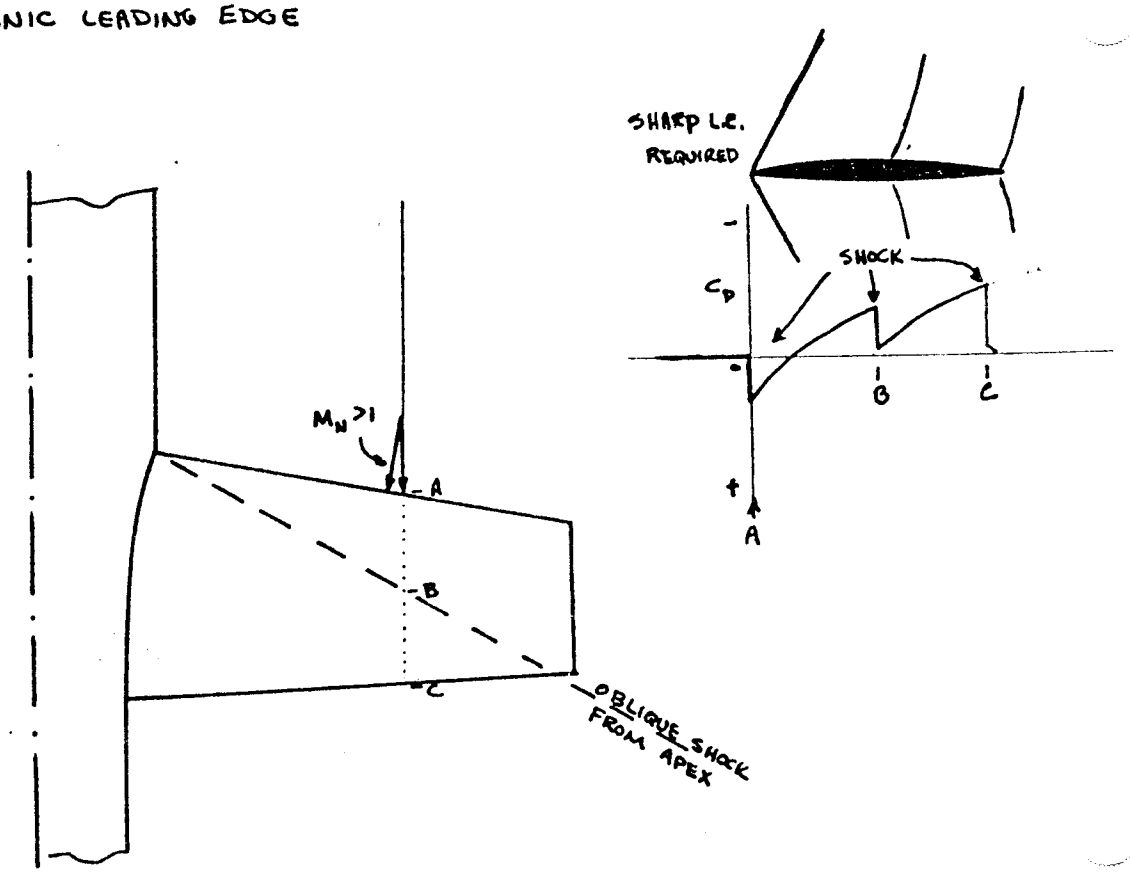

FIGURE 7.35 SUBSONIC VS SUPERSONIC LEADING EDGE

538 GWLOTTE 2.12.70

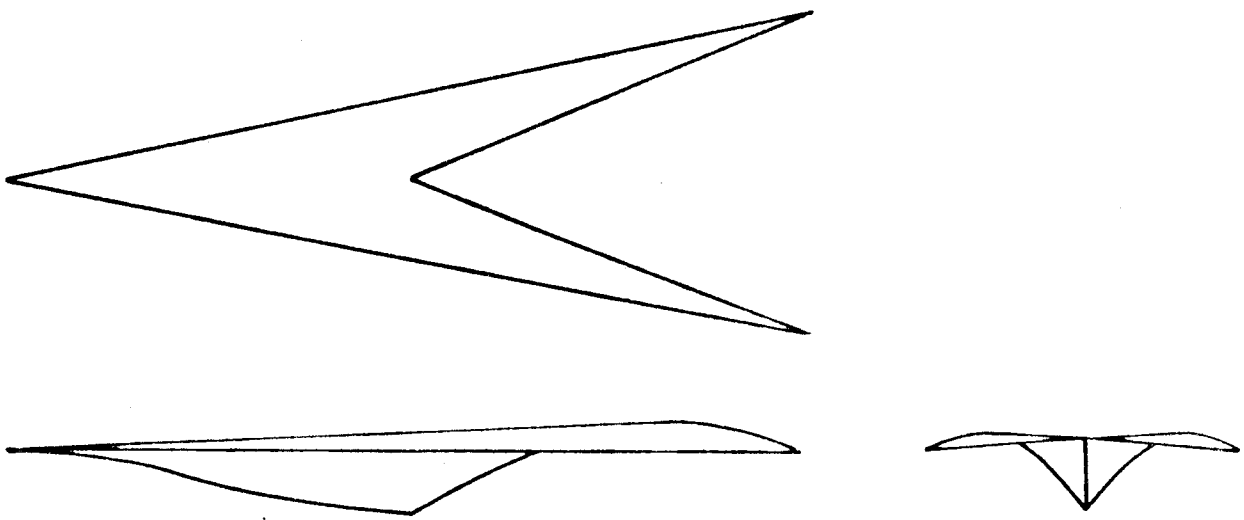

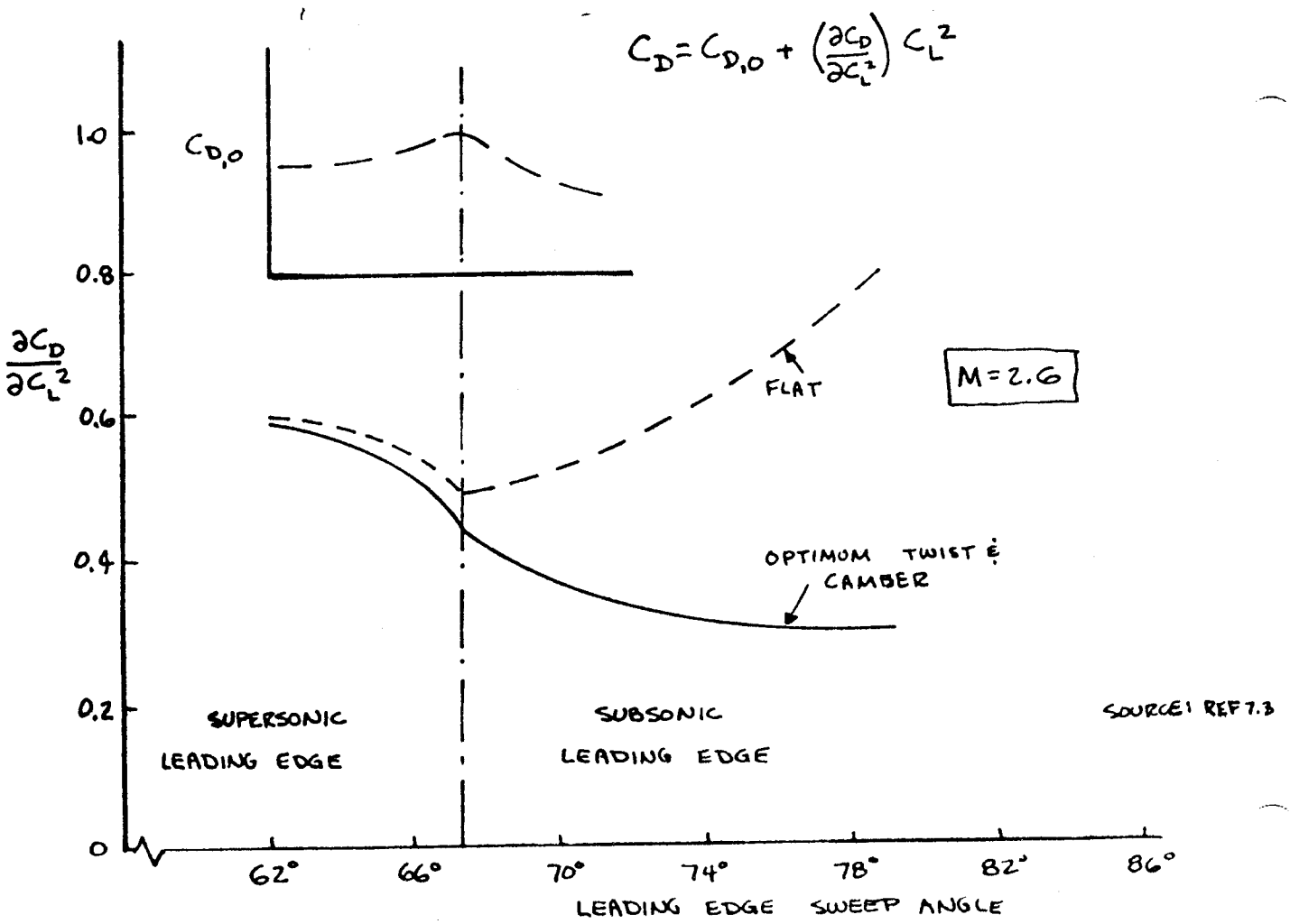

FIGURE 7.36 SUPERSONIC CAMBER AND TWIST

GILLETTE 2.12.78

P.7.52

$M = 2.0 \qquad C_L \doteq 0.08 \qquad R_e = 4.4 \times 10^6$

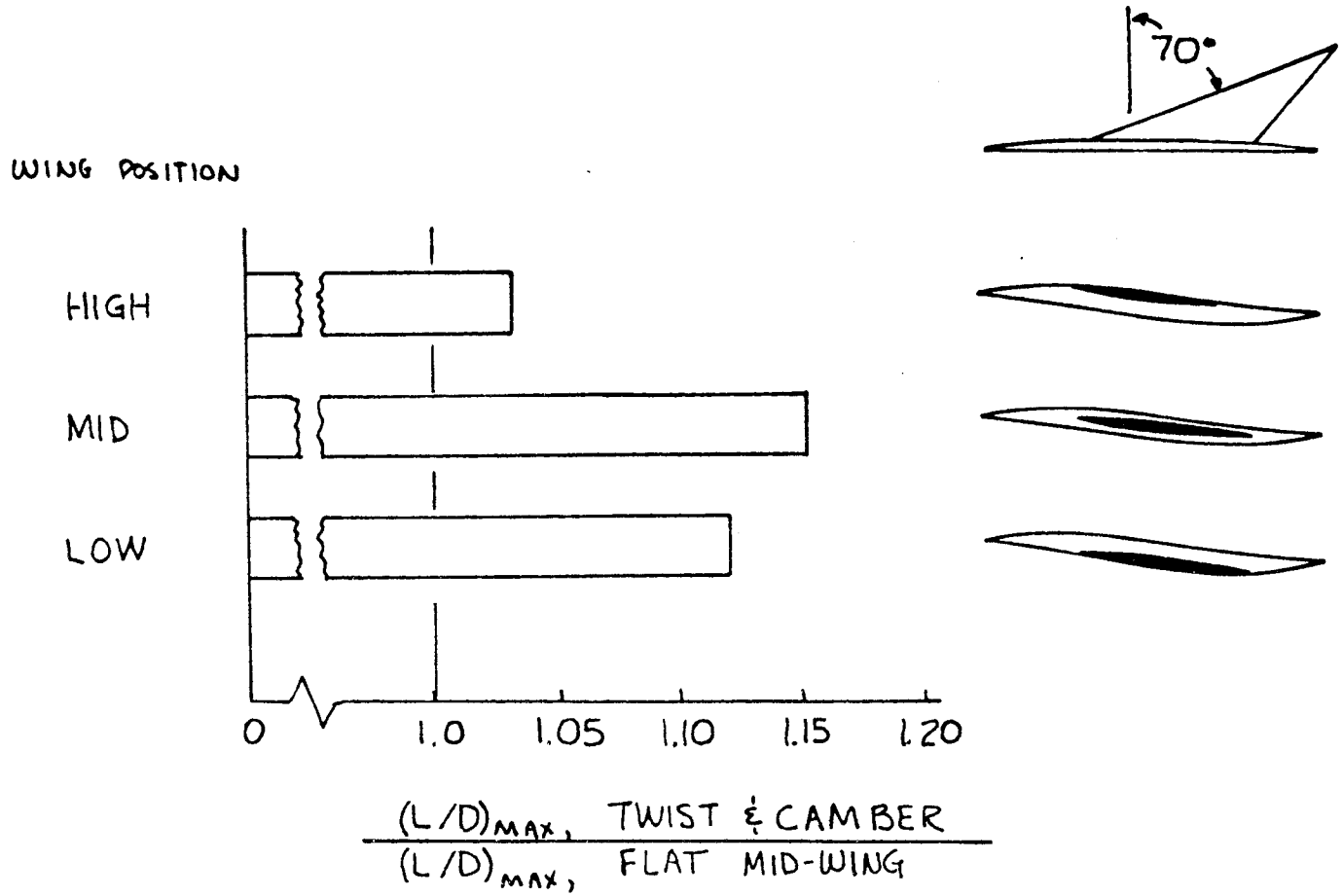

SOURCE: REF. 7.3

FIGURE 7.37 EFFECT OF WING POSITION ON SUPERSONIC $(L/D)_{MAX}$

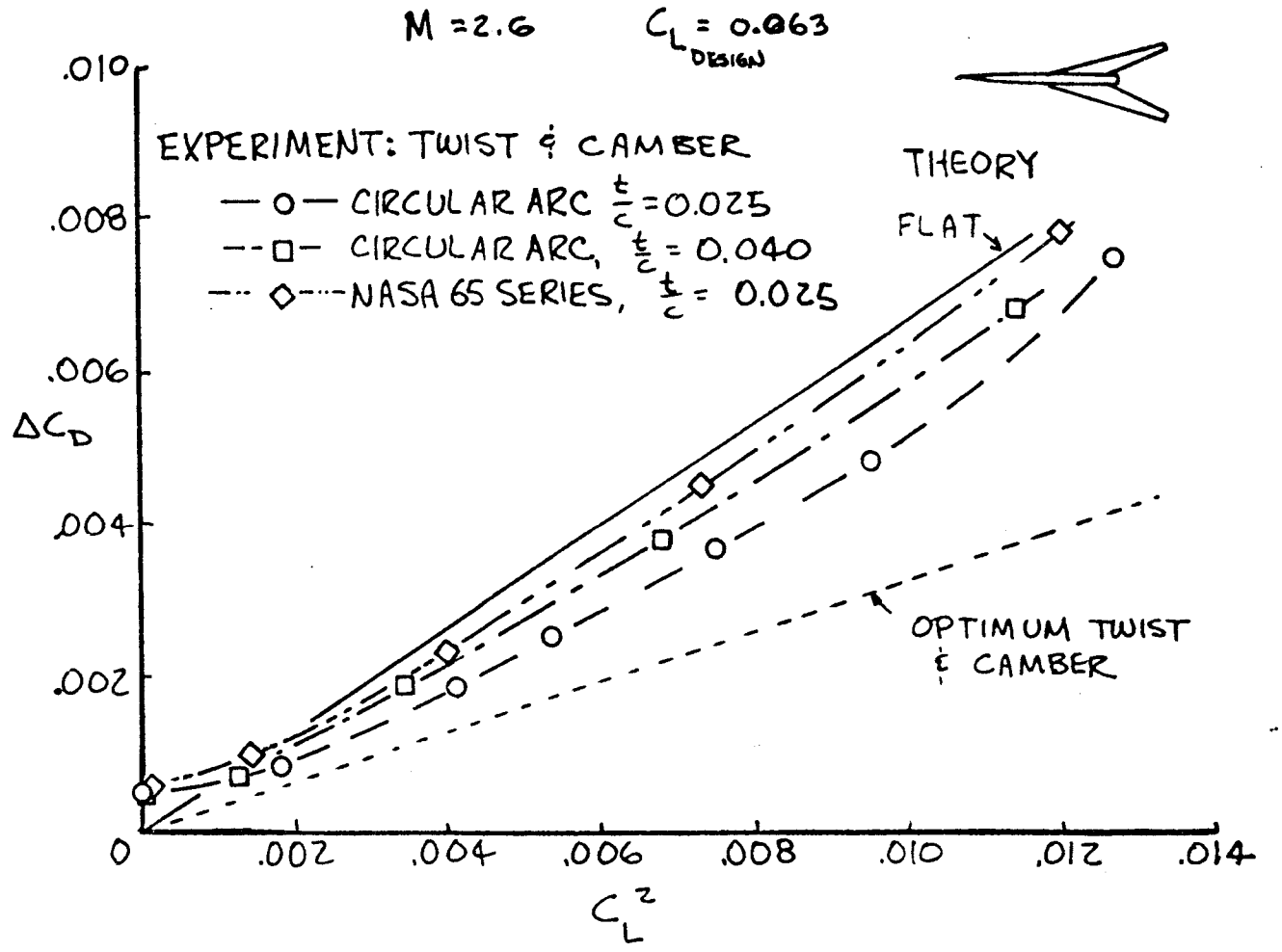

FIGURE 7.38 EFFECT OF SECTION SHAPE ON DRAG

0.7.54

GILLETTE
2.12.78

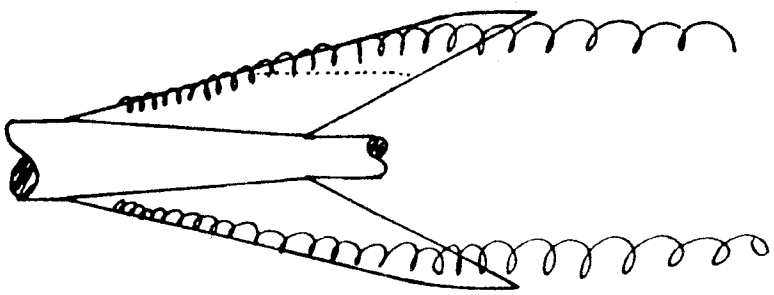

LE VORTEX WILL FORM

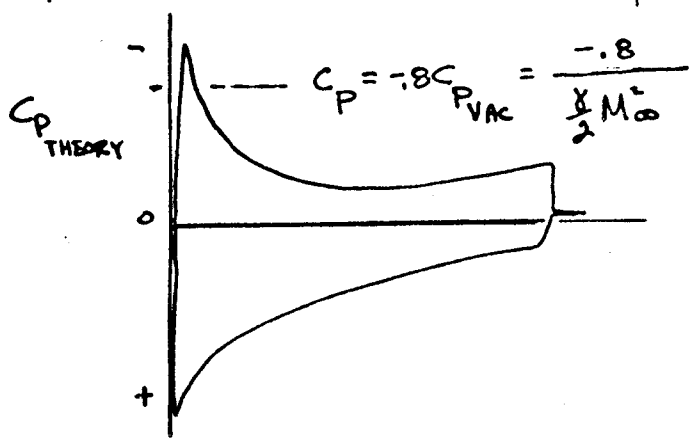

NO LE VORTEX

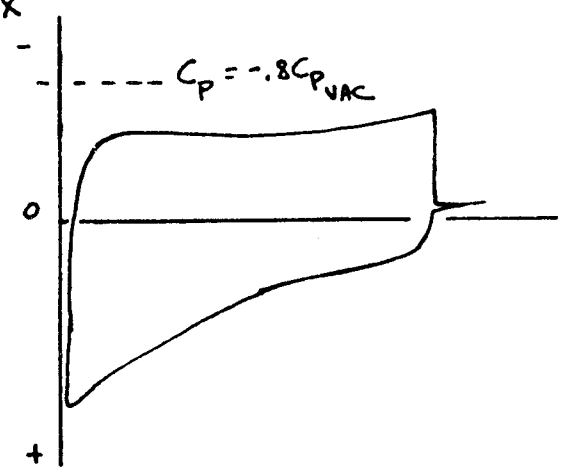

SOURCE: REF 7.4

FIGURE 7.39 LEADING EDGE VORTEX FORMATION CRITERION

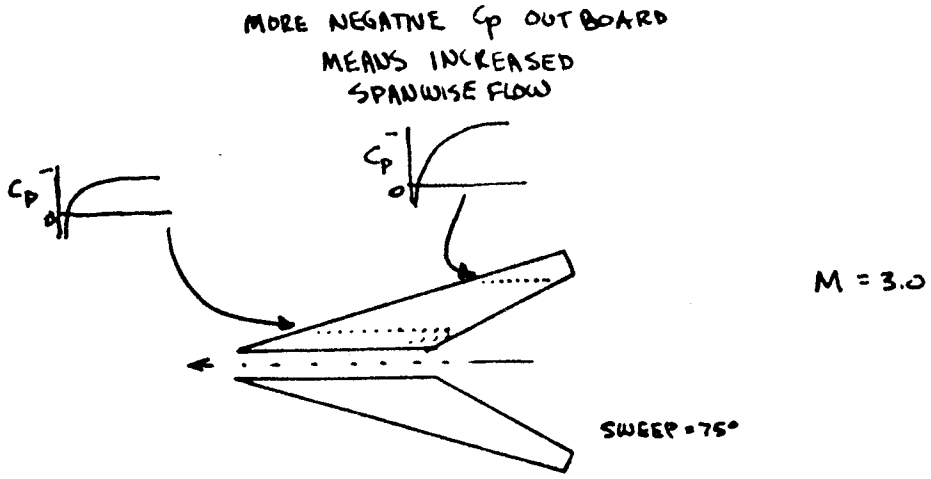

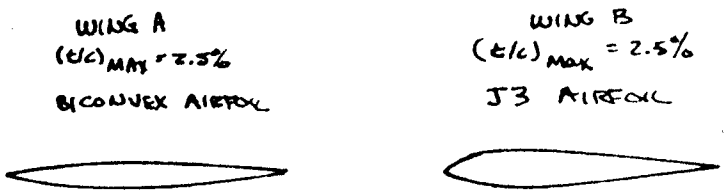

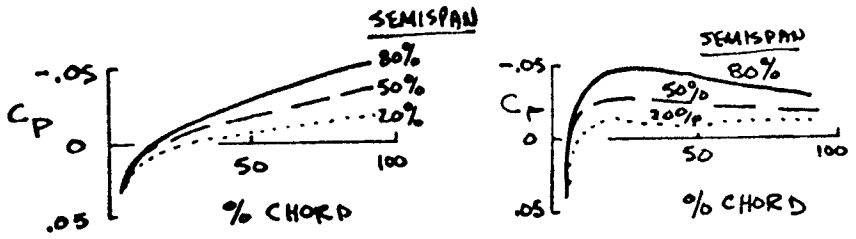

WING C

SOURCE: REF 7.4

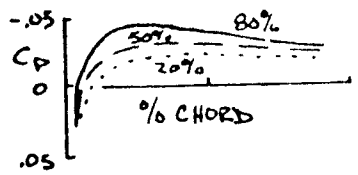

- $(t/c)_{max}$ at side of body = 4%
- t/c outboard = 2.5%
- SECTION CHANGE FROM BICONVEX AT ROOT TO J3 AT TIP

WING C HAS LESS SPANWISE FLOW

FIGURE 7.40 SPANWISE FLOW LIMITATION CRITERIA

GILLETTE
2.19.78

P.7.56

537

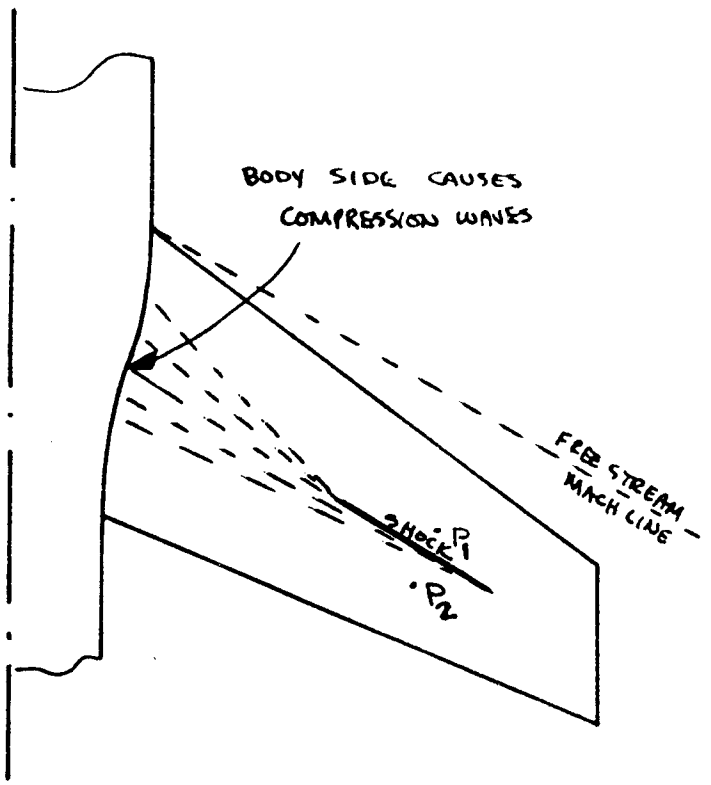

SEPARATION WILL OCCUR WHEN

$$\frac{P_2}{P_1} > 1.5$$

SOURCE: REF 7.4

FIGURE 7.41 PRESSURE RISE THROUGH BODY-CAUSED SHOCK ~ CRITERION TO AVOID SEPARATION

GILLETTE
2.12.78

538

(a) CONVENTIONAL SST ~ 2707-300 (1971)

- $(L/D)_{CRUISE} \doteq 7.5$
- SEPARATE BODY

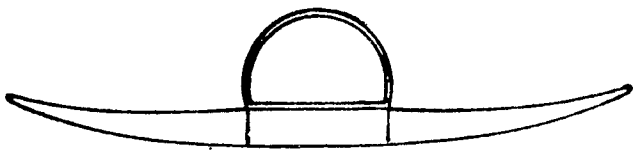

(b) BLENDED WING-BODY SST ~ 1978

- $(L/D)_{CRUISE} \doteq 8.5 \rightarrow 10$

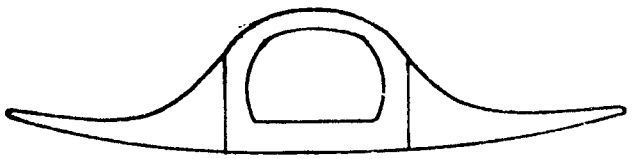

- SERIOUS PROBLEM – WHERE TO PUT WINDOWS

FIGURE 7.42 BLENDED VS. CONVENTIONAL SST

GILLETTE
2.12.78

P 7.58

539

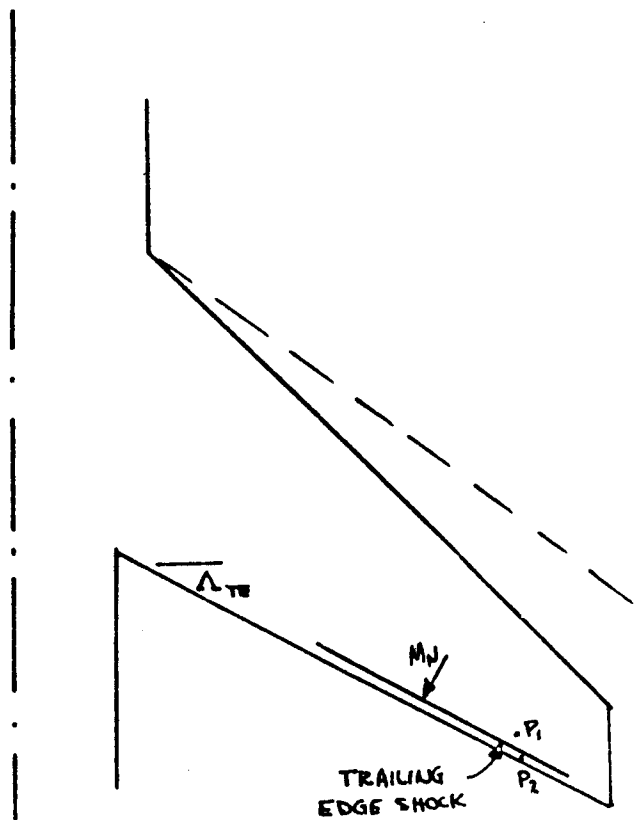

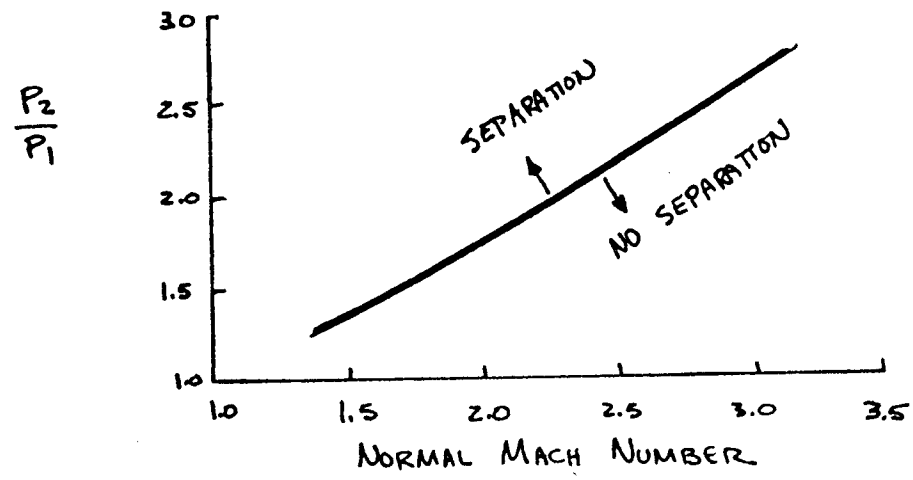

SOURCE: REF. 7.4

FIGURE 7.43 PREVENTION OF TRAILING EDGE SHOCK-INDUCED SEPARATION

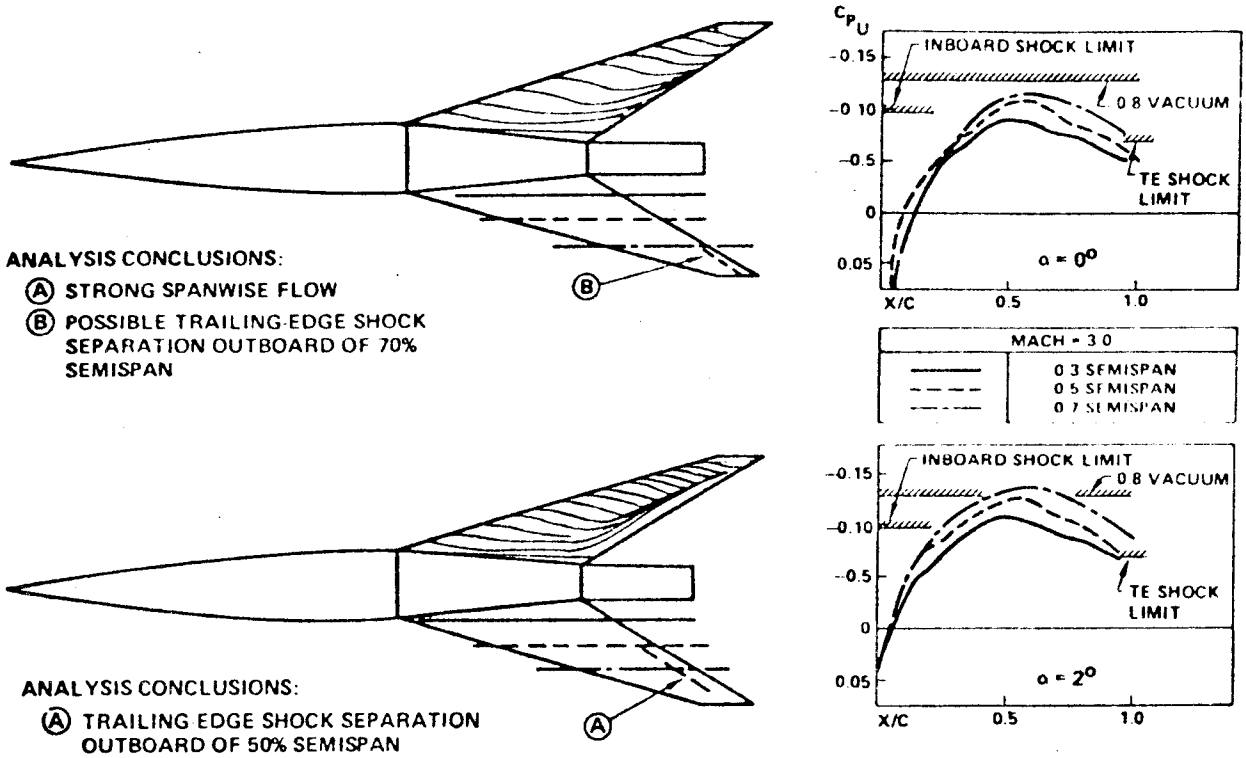

Figure 7.44A Comparison of Experimental and Predicted Shock Separation

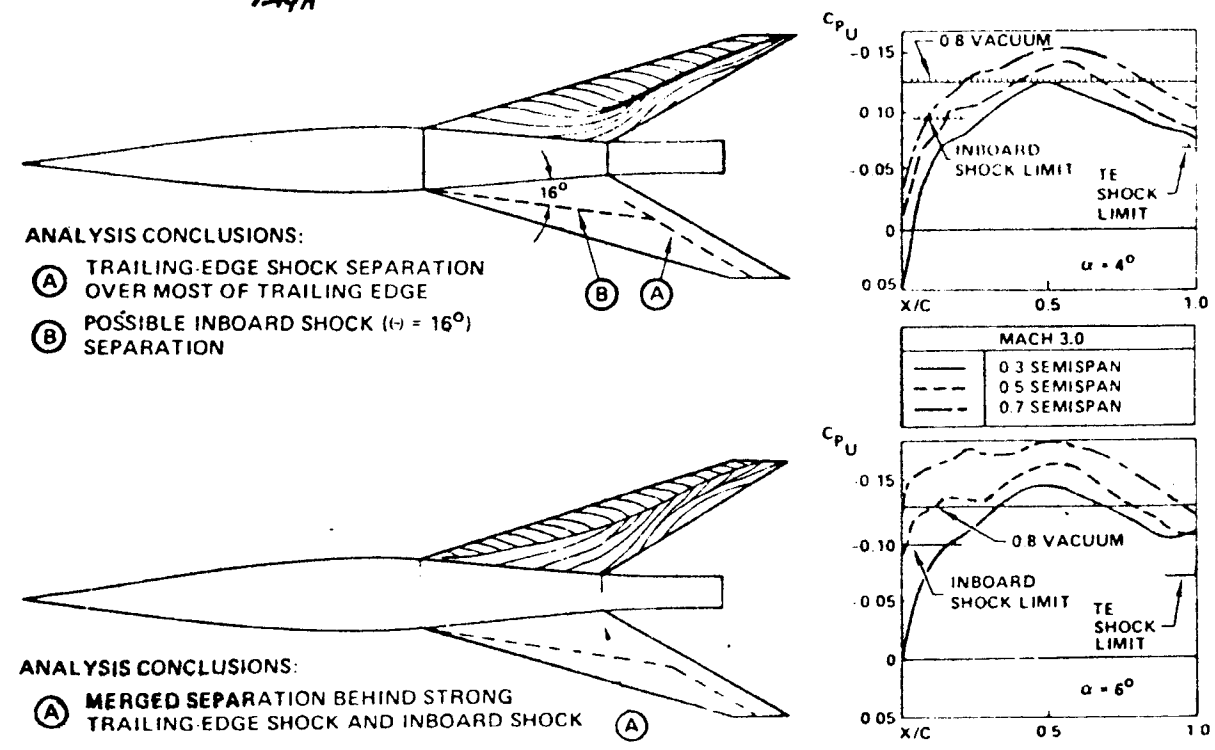

Figure 7.44B Comparison of Experimental and Predicted Shock Separation (Concluded)

P.7.60

M=1.8 C_L= 0.10

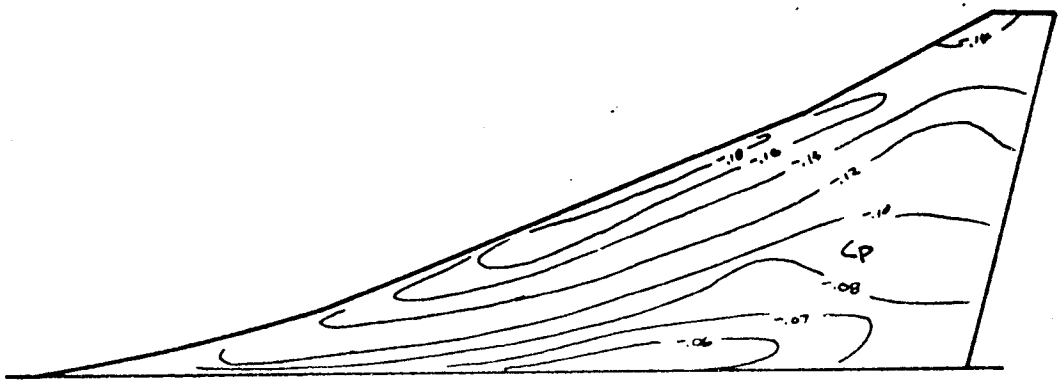

FIGURE 7.45 UPPER SURFACE ISOBARS ON LES-21G

CHAPTER 8 STABILITY AND CONTROL CONSIDERATIONS

CHAPTER 8 STABILITY AND CONTROL CONSIDERATIONS

8.1 INTRODUCTION

The objective of this chapter is not to make you a stability and control expert, but to give you enough insight into the problems and criteria that affect the basic shape of the airplane and therefore, affect the configuration aerodynamicist.

8.1.1 Stability Versus Control

Stability is defined as the tendency for a system to return to its original unperturbed state of equilibrium after it has been disturbed. For example, if an airplane is subjected to an increase in angle of attack, a resulting nose down pitching moment (tending to reduce the angle of attack) would represent a stable system. Control is then the ability to trim the system for various levels of equilibrium and of changing that equilibrium state (e.g., angle of attack). Figure 1 shows four possible combinations of stability and trim showing that for a stable and trimmable system, a negative $dC_m/d\alpha$ is required and that a positive C_m at $\alpha = 0^\circ$ is required. The control aspect pertains to the ability to change the equilibrium state, for example; to change the trimmed angle of attack by changing the C_m at $\alpha=0^\circ$ by using the stabilizer or elevator. Stability and control are basically always opposing each other, since a very stable system requires large control inputs while a slightly stable system requires relatively less control input.

8.1.2 Axes Systems and Definitions

The basic axes system used in stability and control work is shown on Figure 2. Usually the problem is broken down into two major areas, longitudinal and lateral/directional stability and control. Longitudinal stability and control involves translation in the X and Z directions and pitching about the Y axis. The lateral/directional stability and control involves rotation about the Z and X axis and translation in the Y direction. Usually, the longitudinal and lateral/directional motions are not heavily coupled and can be treated to a large extent separately and will be treated as such here. Figure 3 shows the various types of stability that will be encountered from the stable dynamically damped case (a) to the dynamically unstable case (c). Every airplane has at least two or probably three of these possibilities in its equations of motion. The definitions of the sign conventions used in stability and control work are shown on Figure 4. We will now look at static longitudinal stability and control and then look at the lateral/directional aspects before discussing the dynamic aspects.

8.2 LONGITUDINAL STABILTY AND CONTROL

The approach taken in this course has been to avoid equations and mathmatics, however, some playing with the equations can be of great benefit in understanding longitudinal stability and control and how the data is manipulated into a useful form.

8.2.1 Basic Longitudinal Equations

The basic forces acting on the airplane in steady unaccelerated flight as are shown:

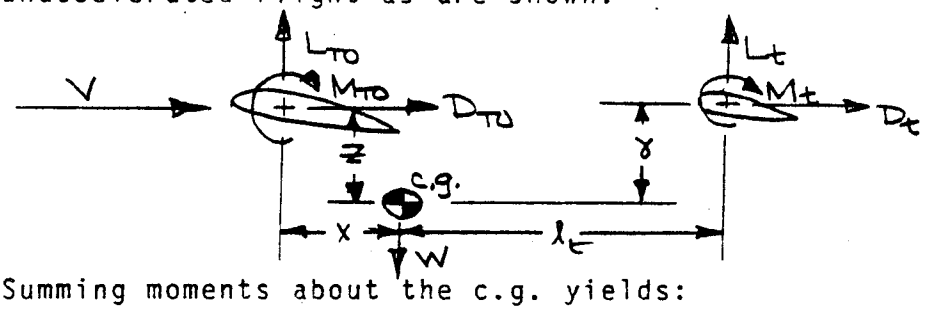

Summing moments about the c.g. yields:

$$M_{cg} = M_{TO} + xL_{TO} + zD_{TO} + M_t + \gamma D_t - l_t L_t \qquad (1)$$

Some assumptions are usually made that the terms zD_{TO}, M_t and γD_t are small. These assumptions are usually quite good for conventional configurations but should be questioned and evaluated if there is any doubt. Using the definitions of pitching moment and lift coefficients, the equation (1) may be rewritten as follows:

$$M_{cg} = C_{m_{TO}} q S \bar{c} + x C_{L_{TO}} q S - l_t C_{L_t} q_t S_t \qquad (2)$$

Dividing through (2) by qsc yeilds:

$$C_{m_{cg}} = C_{m_{TO}} + \frac{x}{\bar{c}} C_{L_{TO}} - \frac{l_t S_t}{S \bar{c}} \frac{q_t}{q} C_{L_t} \qquad (3)$$

where: $\bar{V}_H = \dfrac{l_t S_t}{S \bar{c}}$ = tail volume coefficient

$\eta_t = q_t/q$ = dynamic pressure ratio

then equation (3) becomes:

$$C_{m_{cg}} = C_{m_{TO}} + \frac{x}{\bar{c}} C_{L_{TO}} - C_{L_t} \eta_t \bar{V}_H \qquad (4)$$

Differentiating (4) with respect to C_L yields:

$$\left(\frac{dC_m}{dC_L}\right)_{cg} = \left(\frac{dC_m}{dC_L}\right)_{TO} + \frac{x}{\bar{c}} - \frac{dC_{L_t}}{dC_L} \bar{V}_H \eta_t \qquad (5)$$

The derivative of C_{L_t} with respect to C_L can be rewritten as follows:

$$\frac{dC_{L_t}}{dC_L} = \frac{dC_{L_t}/d\alpha_t}{dC_L/d\alpha_w} \frac{d\alpha_t}{d\alpha_w} = \frac{C_{L_{\alpha_t}}}{C_{L_{\alpha_w}}} \frac{d\alpha_t}{d\alpha_w} \qquad (6)$$

5/15

Now let us look at the relationship between wing and tail angle of attack using the following diagram:

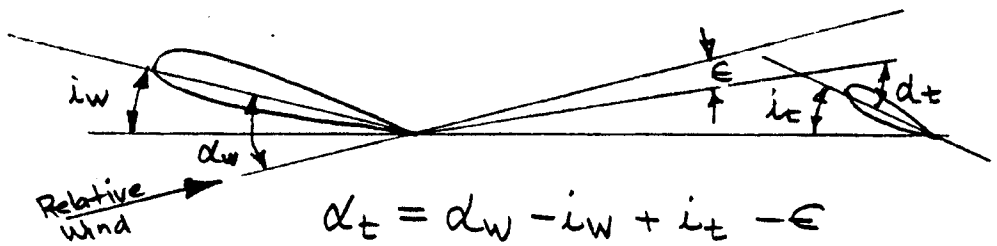

$$\alpha_t = \alpha_w - i_w + i_t - \epsilon \qquad (7)$$

Where ϵ is the downwash angle at the tail due to the wing. Differentiating with respect to α_w yields:

$$\frac{d\alpha_t}{d\alpha_w} = 1 - \frac{d\epsilon}{d\alpha} = 1 - \epsilon_\alpha \qquad (8)$$

Substituting (8) into equation (6), we obtain:

$$\frac{dC_{Lt}}{dC_L} = \frac{C_{L\alpha t}}{C_{L\alpha w}}(1-\epsilon_\alpha) \qquad (9)$$

Substituting (9) into equation (5), we get:

$$\left(\frac{dC_m}{dC_L}\right)_{cg} = \left(\frac{dC_m}{dC_L}\right)_{TO} + \frac{X}{\bar{c}} - \frac{C_{L\alpha t}}{C_{L\alpha w}}\eta_t \bar{V}_H (1-\epsilon_\alpha) \qquad (10)$$

We can rewrite the X/C term using the following diagram as follows:

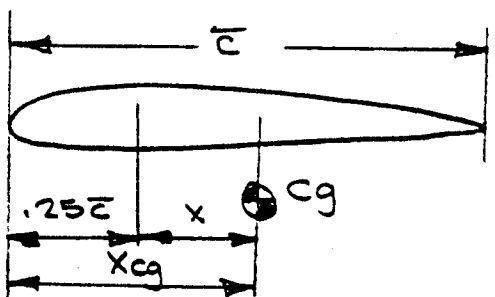

$$\frac{X}{\bar{c}} = \frac{X_{cg} - .25\bar{c}}{\bar{c}} = X_{cg}/\bar{c} - .25 \qquad (11)$$

Substituting (11) into equation (10) gives the equation:

$$\left(\frac{dC_m}{dC_L}\right)_{cg} = \left(\frac{X_{cg}}{\bar{c}} - .25\right) + \left(\frac{dC_m}{dC_L}\right)_{TO} - \frac{C_{L\alpha t}}{C_{L\alpha w}}\eta_t \bar{V}_H (1-\epsilon_\alpha) \qquad (12)$$

546

Equation (12) now shows us that the stability is affected by the c.g. position, the tail off stability level and by a tail term. The tail term is in turn sensitive to tail and wing lift curve slopes, , downwash due to the wing and tail volume coefficient. One aspect of particular interest is that a c.g. shift is equivalent to a change in dC_m/dC_L. Figure 5 shows how using this term, we can look at the pitching moments about other c.g.'s simply by skewing the axis by the Xcg/c ratio. The scheme also indicates the c.g. at which the configuration is neutrally stable (neutral point). Going back to our force balance diagram, we can sum the forces in the vertical direction as follows:

$$W = L = L_{TO} + L_t \tag{13}$$

or (13) can be expressed as:

$$C_L q S = C_{L_{TO}} q S + C_{L_t} q_t S_t \tag{14}$$

This may be rewritten:

$$C_L = C_{L_{TO}} + C_{L_t} \eta_t \frac{S_t}{S} \tag{15}$$

From equation (15) the tail lift increment is:

$$\Delta C_{L_{TAIL}} = C_{L_t} \eta_t \frac{S_t}{S} \tag{16}$$

From equation (3), the pitching moment tail increment is:

$$\Delta C_{m_{TAIL}} = - C_{L_t} \eta_t \frac{S_t}{S} \frac{l_t}{\bar{c}} \tag{17}$$

Equations (16) and (17) yields:

$$\Delta C_{m_{TAIL}} = - \Delta C_{L_{TAIL}} \frac{l_t}{\bar{c}} \tag{18}$$

or (18) becomes

$$\left(\frac{\Delta C_m}{\Delta C_L}\right)_{TAIL} = - \frac{l_t}{\bar{c}} \tag{19}$$

This expression is also very useful when looking at wind tunnel pitching moment data for the slope of the tail effect at a constant angle of attack as shown below:

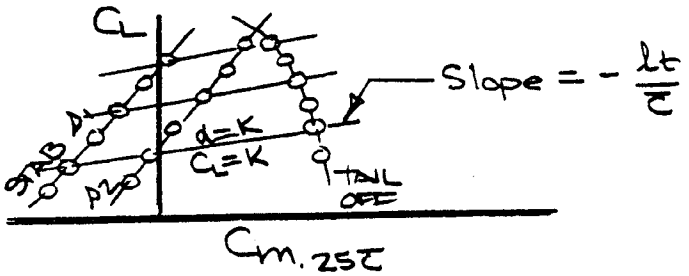

This will allow us to find the tail increment at constant wing C_L or α and will be used later when we discuss tail sizing. Now, armed with equations (12) and (19), we are ready to look at how the horizontal stabilizer is sized and how the wind tunnel data is used.

8.2.2 Stabilizer Sizing and Design Criteria

The horizontal stabilizer must be sized to handle the full c.g. range of the airplane. This implies some set of design criteria for the extremes of the c.g. range. The design criterion is the most critical of the set, and this criterion can change from configuration to configuration. A typical set of criteria are as follows:

Forward c.g. limit
- landing trim
- mistrim takeoff
- landing flare
- stall characteristics

Aft c.g. limit
- maneuvering stability
- speed stability
- ground tip up
- deep stall

For the forward c.g., the ability to trim the pitching moments for the landing flaps is usually the most critical case, but the ability to handle the mistrim takeoff, landing flare and stall characteristics must be checked. These last three criteria are legitimately related more to elevator power that stabilizer effectiveness, but since elevator and stabilizer power are related, we lump them into the stabilizer design criteria. The aft c.g. is usually limited by either maneuvering stability (elevator per g) or speed stability (stick force gradient with speed), but tip up on the ground on takeoff and high angle of attack stall characteristics can impact the aft limit. Since the forward c.g. trim and aft c.g. stability are usually the most critical, lets examine how we can design a stabilizer using these criteria. Figure 6 shows how the flaps introduce a large nose down pitching moment that must be trimmed to 1.3 times the stall speed by a down load on the stabilizer. Figure 7 shows how this appears on a pitching moment curve and using the techniques we found in the longitudinal equations, we can see that the more forward the C.G., the larger the tail load required for trim. The tail load is simply obtained as follows:

$$\Delta C_{m_{\text{Due to tail}}} = -C_{L_t}\bar{V}_H \qquad (20)$$

5/8

or

$$C_{L_t} = - \frac{\Delta C_{m\ \text{Due to tail}}}{\overline{V}_H} \qquad (21)$$

We can also see that for a given tail off pitching moment that the achievable forward limit is set by the tail lift capability and tail volume coefficient. Note that there is a c.g. at which the airplane will trim without a tail. Using this point and the lift capability of the tail, we can construct Figure 8. The slope in Figure 8 is primarily set by the tail lift available, but Figure 9 shows that the tail off pitching moments are a strong function of the maximum lift that the flaps are producing. Therefore, the slope in Figure 8 is also sensitive to the lifting power or stall speed of the wing flap system. Figure 10 shows a comparison of the pitching moments of several Boeing airplanes at landing flaps, and the 737 stands out as having the most severe requirements. The tail lift coefficients are shown based on total area and on the exposed area outside the body. Again, the 737 has the most severe requirements. The lift levels available on the 707 and 727 would not have been adequate for the 737 and during the development cycle of the airplane, several methods were evaluated to improve the lift capability of the tail. We should also note that not all of the tail lift capability can be utilized since any separation on the tail would cause buffet that would shake the whole airplane. We are interested in the usable or buffet free lift capability of the stabilizer. Some of the methods and the corresponding lift levels found during the 737 development are shown below:

CONFIGURATION	$C_{L_{t_{MAX}}}$	$C_{L_{t_{USABLE}}}$
NO AUXILIARY LIFT DEVICES	.79	.65
4 GEARED ELEVATOR	.84	.72
8 GEARED ELEVATOR	.89	.77
FULL SPAN L.E. DROOP	.93	.88
FULL SPAN L.E. KRUGER FLAP	1.03	.98
FULL SPAN DROOP + 4 ELEVATOR	.98	.92
FULL SPAN KRUGER + 4 ELEVATOR	1.08	1.02
CAMBERED TAIL	.89	8.15

The original configuration with no auxiliary devices used airfoil sections similar to the 707/727 sections which have only a slight amount of camber. High lift devices on the stabilizer proved quite effective as did the geared elevator, but the combination of increase camber and geared elevator was chosen for the airplane as being the lightest and least complicated solution, but high lift devices on the stabilizer were given serious consideration. The final airfoil shown on Figure 11 compared to the 707/727 section is quite highly cambered.

From the previous section, we saw that the stability is a functon of the center of gravity position and the stability decreases as the c.g. moves aft. The aft c.g. limit is therefore usually set by stability considerations which can be viewed as static or dynamic stability as shown on Figure 12. Both the static (C_{m_α} or stick force vs velocity) and dynamic (elevator per g) stability are functions of the basic tail on and tail off pitching moments. The pitching moments are functions of Mach number and are usually critical flaps up at Mach numbers close to the cruise conditions. Figure 13 shows typical tail on and tail off pitching moments at some condition close to cruise. Using our knowledge of the longitudinal equations, we can determine the c.g.'s at which the configuration is neutrally stable tail on and tail off. This information can be plotted as shown on Figure 14 and from the earlier discussion of the longitudinal equations, we know that the slope of Figure 14 is proportional to the parameter:

$$\frac{\Delta C.g.}{\Delta \nabla_H} \propto \frac{C_{L_{\alpha_t}}}{C_{L_{\alpha_W}}} (1-\epsilon_\alpha) \qquad (22)$$

For increased stability, we can increase $\overline{V}_H$, increase tail aspect ratio (increase $C_{L_{\alpha_t}}$), decrease wing aspect ratio (decrease $C_{L_{\alpha_W}}$) or increase $(1-\epsilon_\alpha)$ which implies reducing the downwash term . The downwash term is sensitive to tail position above the wing, with low tails having $\epsilon_\alpha \approx .6$ and tee tails having values of .4. We therefore see that for a fixed $\overline{V}_H$ tee tails are about 50% more efficient. We can now combine the forward and aft c.g. lines on one plot as shown with the overlay on Figure 14. If we apply some margin of stability to the aft limit, we can now choose a tail size for fixed c.g. limits, or for a fixed c.g. range choose a minimum tail size and the correpsonding c.g. limits. To meet these limits, the wing may have to move on the body until the airplane balances. The process has been fairly orderly and simple to this point; however, nonlinearities can get you into trouble quite quickly. Figure 15 shows the tail off stability levels of several bodies tested during the 737 development.

The bodies all have similar stability levels. Figure 15 shows some tail on data using some of these same bodies. The tail was identical in each case and since the bodies had varying length the $\overline{V_H}$ varied. At low Mach numbers, the anticipated $\overline{V_H}$ effect is apparent, however, at higher Mach numbers, the tail with the lowest $\overline{V_H}$ has the highest stabiity. Another example of nonlinear behavior is shown on Figures 17 a, b and c which shows the effect of cambering the stabilizer on the pitching moments. The cambered and symmetric tails had identical planforms and $\overline{V_H}$, yet, the cambered tail shows much better characteristics. The reasons for these nonlinear characteristics is not well understood and this type of data is one reason that the Flight Controls group usually insists on testing every change no matter how trivial it appears. Some appreciation of how these nonlinearities can occur can be obtained by looking at the data on Figure 18, which shows some pressure data taken on the 737 stabilizer. Note that the root of the tail is lifting up while the outboard is lifting down. This is caused by the tail being essentially flat and untwisted. The design computational tools are only now evolving; that could result in a stabilizer design that accounts for the body effects and wing downwash effects.

8.2.3 Elevator Requirements

As discussed in the previous section, the elevator and stabilizer requirements are closely related. The primary functions of the elevators are to maneuver the airplane, to trim other maneuvers such as stalls and go-arounds where the stabilizer trim is too slow, and to provide longitudinal trim redundancy for the stabilizer by providing an alternate trim source. The primary function (maneuvering) can be viewed as shown on Figure 19. At a constant velocity the elevator per g is a function of center of gravity position. As c.g. moves aft, stability is reduced and the control deflection required for maneuvering is reduced. The point where the elevator per g becomes zero is refered to as the maneuver point. Flying at this c.g. is not safe because it is too easy to over load the airplane and cause structural damage. All unaugmented airplanes have their aft c.g. limits forward of the maneuver point by some margin (typically 10% c). Figure 19 also shows that the maneuver point is effected by elastic deflections of the airframe and controls. Calculation of the aeroelastic effects is one of the biggest challenges during an airplane design and is consequently one of the least accurate steps in the design. The elevator per g is also a function of velocity and in general the higher the velocity the more important the aeroelastic effects become (See Figure 20). During the design of a new airplane, criteria regarding minimum levels of elevator per g and ratios of minimum (aft c.g.) to maximum (forward c.g.) are usually established. Typical values are 2 degrees/g and a ratio of 16 to 18 in maximum to minimum. The minimum level is set by the maneuver margin and if a margin, is chosen this picks the minimum elevator per g. Figure 19 can be used to understand this. The ratio of maximum to minimum is determined by the capability of the elevator feel system.

Since most of our products have hydraulically powered elevators and stick force systems the range at elevator per g is limited by the maximum hydraulic pressure available.

8.2.4 Complicating Factors

Some complicating factors in longitudinal stability and control have been partically discussed or alluded to such as aeroelastics and Mach number effects. A little more detailed discussion at this time would aid in understanding the mechanism of these effects. One of the primary aeroelastic effects is the influence of wing deflection due to load. Figure 21 shows the effect of deflection due to load on a swept wing. As the wing bends the wing sweep introduces an effective change in the spanwise twist. This twist change effects the span load and consequently produces changes in pitching moment. The higher the load the more the deflection and the bigger the changes in the aerodynamic forces. Similar type changes occur due to deflection of the aft body and tails. Calculation of these effects assumes a good definition of the structure and the aerodynamics forces, and the procedure in general assumes linear characteristics. These assumptions are in general not true and some errors in the design may be introduced. Mach number effects can take many forms, two of which are shown on Figure 22.

Figure 22a shows perhaps the most common and most trouble-some Mach number effect, loss in stability and high speed pitchup. These characteristics are rendered more difficult to fix because they involve both the wing and the tail. Tee tail airplanes tend to have some what better characteristics but almost all configurations tend to exhibit these characteristics to some extent. Figure 22b shows another much less serious Mach number effect known as "Mach tuck". The pitching moments are for a constant stabilizer angle and the W/ line represents changing speed at a fixed weight and altitude. The small section of unstable slope between .8 and .9 Mach number makes the airplane difficult to trim, but can usually be compensated for by having a trimmer that applies an elevator function versus Mach number that effectively straightens out the nonlinearity. The last complicating factor is the reason the designers tend to stay away from tee tail configurations if they can "deep stall". Figure 23 illustrates the characteristic. As the angle of attack is increased the tail enters the wing wake and down wash field reducing the tails effectiveness. If the stabilizer remains in the wake for a significant angle of attack range the airplane can arrive at the top point of the $\delta e = 0^{\circ}$ line where the airplane is trimmed and stable but in a very steep descent due to the high drag of the separated wing. The wing wake also reduces the elevator effectiveness and thus can reduce the capability of the stabilizer to produce the nose down recovery moments. Figure 23 shows an unacceptable case where the elevator is not powerful enough to effect recovery. The solution to this problem may be additional tail area, more elevator power or a more forward aft c.g. limit.

.2.5 Typical Geometry and Longitudinal Data

With all the background we now have let us look at some typical geometry and longitudinal data and see if it makes sense. Figure 24a shows the planform of the 737 stabilizer. This figure shows the size of the buried area in the body, the 25% chord elevator, the elevator mass balance horn at the tip and the stabilizer hinge line relative to the mean aerodynamic chord. Figure 24b shows the elevator aerodynamic balance configuration. As the elevator deflects the hinge line pressures are vented across the internal balance panels reducing the hinge moment or force required to deflect the elevator. This aerodynamic balance was used to reduce the forces to the level that manual reversion could be used in the unlikely event of a double hydraulic failure. The 737 was the last Boeing airplane to include this philosophy. Figure 25 shows typical flap up low speed pitching moment data. The t/c slope can be seen quite easily and down wash can be obtained from this data quite easily by taking advantage of the knowledge that where tail on and off curves cross the tail load is zero and consequently:

$$\alpha_t = 0 = \alpha_w - i_w + i_t - \epsilon \qquad (23)$$

Everything is known except ϵ which can therefore be solved for. Figure 16 shows some typical landing flaps longitudinal data. The t/c slope again can be observed as can the tail stall at the high stabilizer angle low angle of attack case. This data could be used directly to determine the forward c.g. that the airplane could handle. Figure 27 shows similar data but with elevator deflection, and again we can see evidence of tail stall. Taking advantage of the relationship that:

$$\Delta C_m = - C_{L_t} \eta_t \bar{V}_H \qquad (24)$$

55M

we can develop the tail lift capability as shown on Figure 28. Here we can see the effect of elevator angle on the maximum lift capability of the tail. Figure 29 shows the effect of the proximity of the ground on the longitudinal characteristics. Note the significant loss in maximum lift on the wing, however the stabilizer maximum lift appears to be adequate. The stabilizer contribution to longitudinal stability is given by:

$$\Delta\left(\frac{dC_m}{dC_L}\right)_T = \frac{C_{L_{\alpha t}}}{C_{L_{\alpha w}}} \eta_t \overline{V}_H (1-\epsilon_\alpha) \qquad (25)$$

Figure 30 a and b show typical values and indicates the degree to which they are influenced by Mach number. Figure 31 shows the flaps up low Mach number downwash data and illustrates that the assumption of linear downwash characteristics may not be quite right. Figure 32 shows the elevator and stabilizer capability to handle trim and stall requirements. Figure 33 shows the elevator program required to componsate for the "Mach tuck" characteristic of the 737. The elevator requirement is quite small to straighten out the trim curve.

8.3 Lateral Directional Stability and Control

8.3.1 Basic Lateral Directional Equations.

The basic forces acting on the airplane in the lateral directional planes are as follows:

$$N_{SIDESLIP} + N_{RUDDER} + N_{LAT.\,CONTROL} + N_{THRUST} = 0 \quad (\text{YAWING MOMENT})$$
$$Y_{SIDESLIP} + Y_{RUDDER} + Y_{LAT.\,CONTROL} + W\sin\phi = 0 \quad (\text{SIDE FORCE})$$
$$L_{SIDESLIP} + L_{RUDDER} + L_{LAT.\,CONTROL} = 0 \quad (\text{ROLLING MOMENT})$$

Using the definitions of yawing moment, side force and rolling moment coefficients and the derivative form of the coefficients with respect to sideslip, rudder and wheel angle, these equations may be rewritten:

$$\begin{aligned} C_{n_\beta}\beta + C_{n_{\delta r}}\delta_r + C_{n_{\delta w}}\delta_w + C_{n_{eo}} &= 0 \\ C_{y_\beta}\beta + C_{y_{\delta r}}\delta_r + C_{y_{\delta w}}\delta_w + C_L\sin\phi &= 0 \\ C_{l_\beta}\beta + C_{l_{\delta r}}\delta_r + C_{l_{\delta w}}\delta_w &= 0 \end{aligned} \qquad (27)$$

These equations are coupled because sideslip angle produces large forces in each quation which requires control deflections to balance it out. Some of the derivatives are quite weak and can be used to partially uncouple the equations. If $C_{n_{\delta w}}$, $C_{y_{\delta r}}$ and $C_{l_{\delta r}}$ are assumed small then the rolling moment equation uncouples. Visualizing the coupling of the static lateral directional equation can be aided by studying Figure 34. This Figure shows the complete lateral directional balance for a particular flight condition. On this curve you can examine for example the rudder-sideslip trade, engine out characteristics with varying amounts of rudder. Many of the design conditions we will be discussing can be seen quite clearly using this approach.

554

8.3.2 Fin Sizing and Design Criteria

Design criteria for sizing the vertical tail are as follows:

Adequate directional stability
Dutch roll stability
Engine out tameness

Adequate directional stability is usually expressed in terms of the derivative or yawing moment coefficient per unit sideslip angle. A minimum value of .002/degree seems reasonable. In order to understand this derivative lets look at its components.

$$N_{SIDESLIP} = N_{\substack{SIDESLIP \\ TAILOFF}} + L_V l_V \qquad (28)$$

Where L_V is the tail lift, and l_V is the fin moment arm about the c.g. Using the definition of yawing moment coefficient this equation can be rewritten.

$$C_{n_{SIDESLIP}} = C_{n_{\substack{SIDESLIP \\ TAILOFF}}} + C_{L_V} \eta_V \bar{V}_V \qquad (29)$$

η_V and $\bar{V}_V$ are similar parameters to those found in the longitudinal equation with $\bar{V}_V$ being the vertical tail volume coefficient and η_V the dynamic pressure ratio at the tail. Differentiating with respect to sideslip angle β we get:

$$C_{n_\beta} = C_{n_{\beta_{TAILOFF}}} + C_{L_{\beta_V}} \eta_V \bar{V}_V \qquad (30)$$

We can rewrite the $C_{L_{\beta_V}}$ term as:

$$C_{L_{\beta_V}} = C_{L_{\alpha_V}} \frac{d\alpha_V}{d\beta} = C_{L_{\alpha_V}} \left(\frac{\beta - \sigma}{\beta}\right) \qquad (31)$$

where α_V is the total angle of attack of the fin which include the sideslip and a sidewash parameter similar to downwash in the longitudinal equation. The sidewash comes about from cross flow on the body due to the body itself and the asymmetric downwash due to sideslip. The directional equation now becomes.

$$C_{n_\beta} = C_{n_{\beta_{TAILOFF}}} + C_{L_{\alpha_V}} \left(1 - \frac{d\sigma}{d\beta}\right) \eta_V \bar{V}_V \qquad (32)$$

Since the tail off directional stability is always negative, the vertical tail must overcome this instability and provide the desired C_{n_β} level. Figure 35 shows very simply how the vertical provides the directional stability. The Dutch roll stability criterion is much more difficult to describe and quantify since the Dutch roll maneuver is a dynamic maneuver. Figure 36 shows a view of the airplane from above and behind during a Dutch roll. The maneuver is more prominent on swept wing airplanes because the wing sweep causes the airplane to roll when hit by a side gust. A dynamic simulation of the airplane is required in order to establish adequate stability

and tail size has an influence in every stability derivative that effects the answer. A damping ratio $\zeta \geq .05$ is usually specified which in more simple language means that the Dutch roll oscillation damps to half its original value in two cycles. The Dutch roll period is in the order of 4 to 8 seconds, so we are talking about 8 to 16 seconds to half amplitude. Engine out tameness is a criterion that has not been applied to all of Boeing's product line. The 737 was the first airplane designed to this criterion because it was competing with the DC-9 and had to have very docile engine out characteristics. The criterion requires that the pilot must be able to control an engine failure at 1.3 times the stall speed without using the rudder. The pilot simply lets the airplane sideslip into the live engine and lets the fin balance the engine moment. The mechanics of the static maneuver is shown on Figure 37. A dynamic simulation time history is shown on Figure 38 and it can be seen that the engine can be handled without rudder by allowing the airplane to sideslip.

8.3.3 Rudder Requirements

The rudder and fin requirements are related in a similar way that the elevator and stabilizer requirements are, so that for a given set of assumptions on rudder chord and deflection the fin size may be required to increase for satisfactory characteristics. The primary requirements for the rudder are that it must provide adequate crosswind capability and engine out control at low speeds. A simplified picture of how the rudder provides crosswind capability is shown on Figure 39. The rudder introduces sideslip by balancing the lift on the fin due to sideslip and allowing the airplane to fly a flight path that is not aligned with the relative wind. The pilot has been found willing to accept some crab angle during approach that allows even higher crosswind to be achieved. This is illustrated as follows:

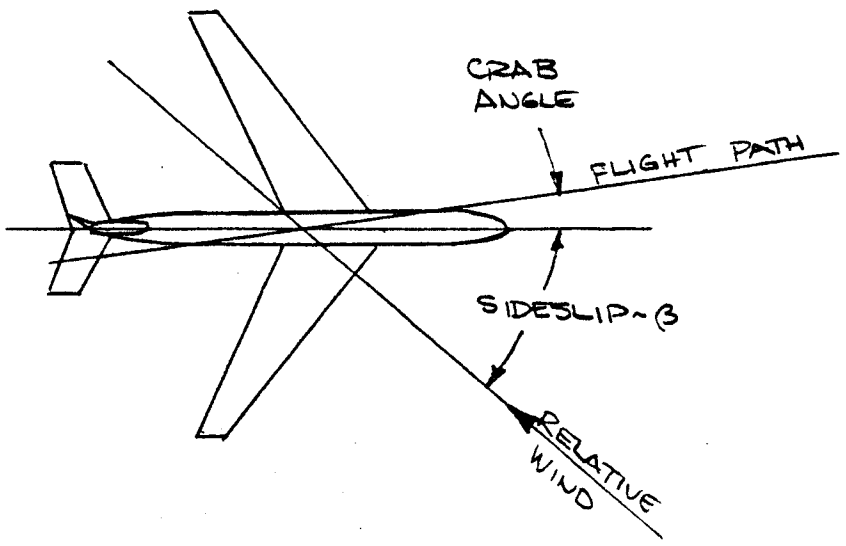

55

The maximum sideslip and the other control requirements can be seen very nicely on Figure 34. Probably the most severe requirement for the rudder to meet is engine out control. The mechanism of how the rudder controls is also very easy to see as shown on Figure 40, where the yawing moment due to asymmetric thrust is balanced by the yawing moment due to the rudder. Figure 34 can again be used to see how the controls are used to balance asymmetric thrust. For the air minimum control speed demonstration a 5 bank angle is allowed, and Figure 34 shows how this helps in engine out control. Figure 41 shows how the minimum control speed can be determined using this approach.

8.3.4 Typical Geometry and Lateral Directional Data

Again, with some background behind us let us look at some typical geometry and lateral directional data and see if it makes sense. Figure 42 shows the planform of the 737 fin. The 737 fin has a relatively high aspect ratio of 1.8 and a 25% chord rudder that incorporates the tip horn for mass balance. Figure 43 shows the rudder configuration which has some unique features. The 737 rudder does not require aerodynamic balance like the elevator and the rudder has no manual reversion capability. The rudder mass balance was included in flat slabs that extend forward of the rudder and protrude as the rudder is deflected. The slabs act as vortex generators and actually improve rudder effectiveness. Figure 44 shows some typical directional stability at landing flaps as determined in the wind tunnel.

Note that the airplane is directionally unstable tail off and that the tail lift increment between tail on and tail off shows evidence of tail stall that is a function of rudder angle. Figure 45 shows how the directional stability derivative varies with lift and flap angle. Note that the directional stability far exceeds the .002 per degree level discussed under fin sizing. Figure 46 shows the extraction of fin lift versus sideslip angle from data similar to Figure 44. The effect of rudder angle on maximum lift is similar to the elevator effectiveness discussed previously. Figure 47 shows the Mach number effect on the vertical tail contribution to directional stability and again it bears a strong resemblance to the compressibility effects on the wing and horizontal stabilizer.

8.3.5 Lateral Control Design Requirements

The lateral control design requirements are among the most important in the design process because the lateral control system is basically a rate control. Lateral control inputs produce basically a roll rate, and as a consequence of this it should be capable of overpowering the other controls which are basically displacement controls, e.g. a rudder angle can produce a sideslip displacement. Because of this requirement

that the lateral control be able to handle full directional control two of the lateral control requirement read like directional criteria. The lateral control design requirements are that the system must provide for:

Adequate roll rate capability
Engine out tameness
Crosswind capability

Figure 48 shows how that as the lateral control system provides a rolling moment, the roll rate of the wing provides a roll damping in the opposite direction that balances the aileron effect and results in a steady roll rate. The lateral control system is usually not designed by roll rate requirements, but the system must be adequate for control and manuevering the airplane. The lateral control system has a phenomenun associated with it that is unique, aileron reversal. As the aileron is deflected it causes moments on the wing that tend to unload the aileron effect. At high speeds the moments due to the aileron can twist the wing to the extent that the opposite sign of rolling moment is obtained. This aileron reversal is the key reason that most high speed jet aircraft do not use their outboard ailerons at high speed and must rely on spoilers and inboard airlerons for lateral control. Figure 49 illustrates how the aileron reversal can occur. The tameness criterion discussed earlier under fin sizing must also be considered in the lateral control design. Figure 50 shows that the directional balance is obtained by allowing the airplane to sideslip.

The sideslip produces large rolling moments that must be balanced by the lateral control system. This can be seen by looking at Figure 34 again. The crosswind capability requirement is a similar type of balance only the full rudder deflection is producing the sideslip angle. The rolling moment due to sideslip is large on swept wing airplanes and causes them to have much more powerful lateral control systems. The lateral control must be able to overpower the directional system and should have some additional margin for control of heading even with full yawing moment applied. An additional criterion for the lateral control system is that it should not cause the airplane to buffet. Low tail airplanes can suffer from buffet if the spoiler wake impinges on the tail surfaces. Designing around this criterion usually results in stabilizer dihedral, delayed inboard spoiler deployment or any of a long list of fixes that con compromise the configuration.

8.3.6 Typical Geometry and Lateral Data

The lateral control system of the 737 is shown on Figure 51. The components are, an outboard all speed aileron, three flight spoiler panels per side and an inboard ground speed brake

panel per side. Because of its low wing sweep, the 737 outboard aileron does not suffer from aileron reversal and is used at all speeds. This eliminated the need for an inboard all speed aileron. The rolling moment due to sideslip characteristics of the 737 are shown on Figure 52a tail off and 52b tail on. Note that the tail off configuration is a significant fraction of the total airplane rolling moment due to sideslip. Figure 53 shows the roll control power of the 737 in landing flap configuration and a sensitivity to angle of attack is apparent. Knowing the roll damping, this data could be used to calculate the roll rate capability of the airplane. Figure 54 shows the yawing moments induced by the lateral control system. Comparing this data to the directional stability data, it can be seen that in this landing flap configuration, the yawing moments due to lateral control are significant. Most of the yawing moment comes from the spoilers which are not deflected symmetrically and consequently produce a drag that causes the yawing moments. The 737 chose not to use the inboard spoiler panels for lateral control to avoid tail buffet. However, the outboard panels did cause a significant pitching moment when deployed. Figure 55a shows the spoiler programming that was developed to minimize the pitchup effect at the lower wheel angles. Figure 55 b shows how this programming minimized the pitchup at the lower wheel angles used most of the time with a small sacrifice in control power.

8.4 DYNAMIC MODES

The airplane has some controls fixed dynamic modes that are of some interest. We will not attempt to develop the modes from the equations of motion, but will instead briefly describe the modes and how they affect the airplane.

8.4.1 Longitudinal Dynamic Modes

There are two basic longitudinal dynamic modes. Both modes are periodic, one with a short period called the "short period" mode and the other a long period mode call the "phugoid" model The short period mode is basically a constant speed mode where angle of attack is varied. This mode is usually heavily damped and has periods in the order of 2 to 6 seconds. This is the mode that is excited by an elevator pulse, and damps out rapidly. The phugoid mode is a constant angle of attack mode and has extremely long periods of the order minutes. This mode is troublesome on low drag jet aircraft and is a mode in which potential and kinetic energy are exchanged at constant angle of attack over periods of several minutes. This mode can cause difficulties in setting up cruise conditions, but it is usually not a significant design condition.

559

8.4.2 Lateral Directional Dynamic Modes

The lateral directional dynamic equations of motion have two basic modes, one periodic, one aperiodic. The periodic mode we have already discussed is called the "Dutch roll" mode. Despite many attempts to design for Dutch roll characteristics, the mode is difficult to predict and success has been quite poor. All swept wing transport airplanes have a lightly damped Dutch roll modes and artifical damping in the form of a yaw damper is commonly added. The aperiodic mode is called the spiral mode and this mode can be either divergent or convergent. It is not uncommon to have both cases on a configuration due to configuration or speed changes. The divergence, if it is present, is very mild, but if left unattended for several minutes, the airplane would go into a steep spiral turn. The spiral mode is usually not considered in design and has not been troublesome on any of Boeing's products.

560

STATIC STABILITY

REQUIREMENTS:

1. STABILITY
2. TRIM
3. CONTROL

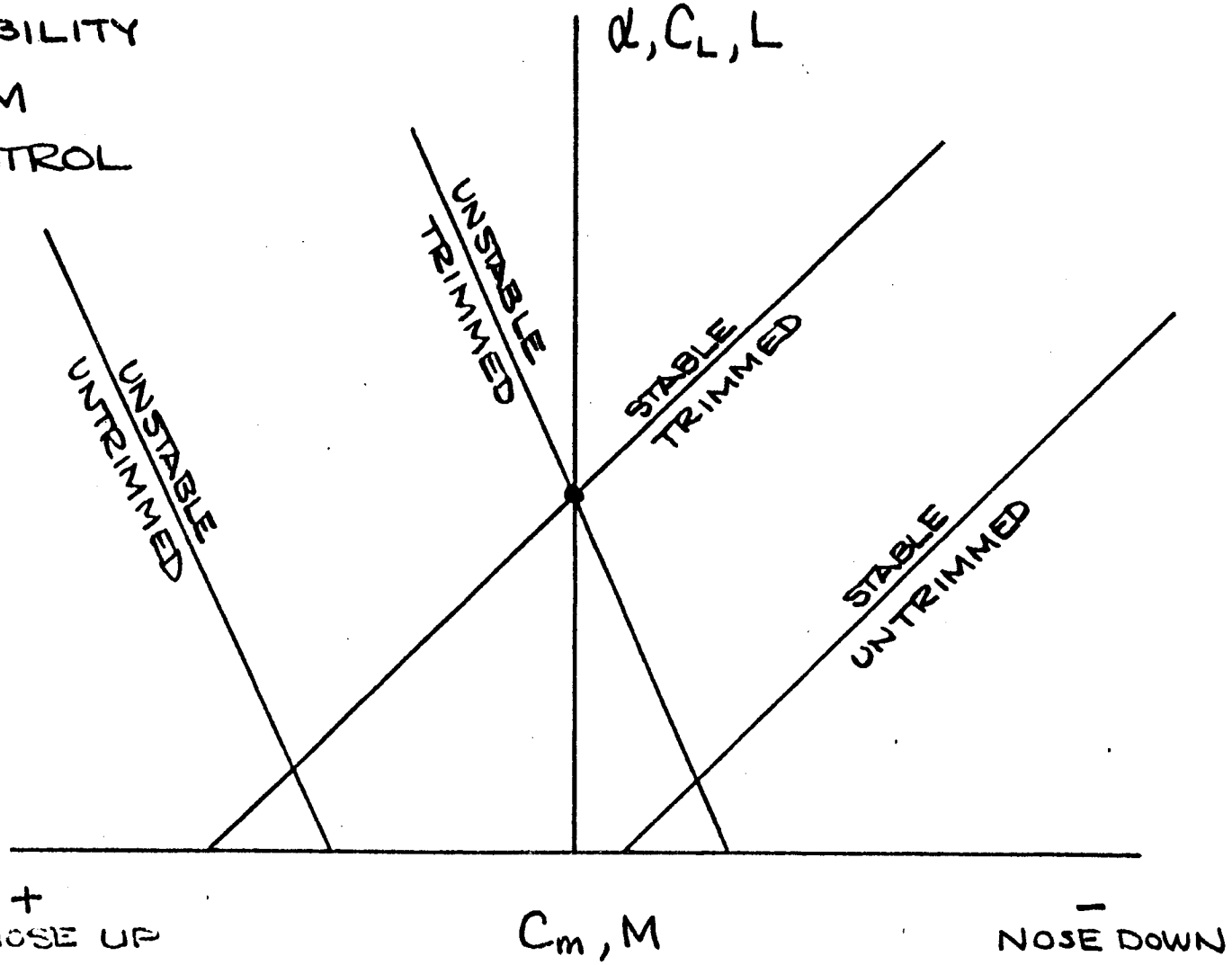

FIGURE 1.
P8.18

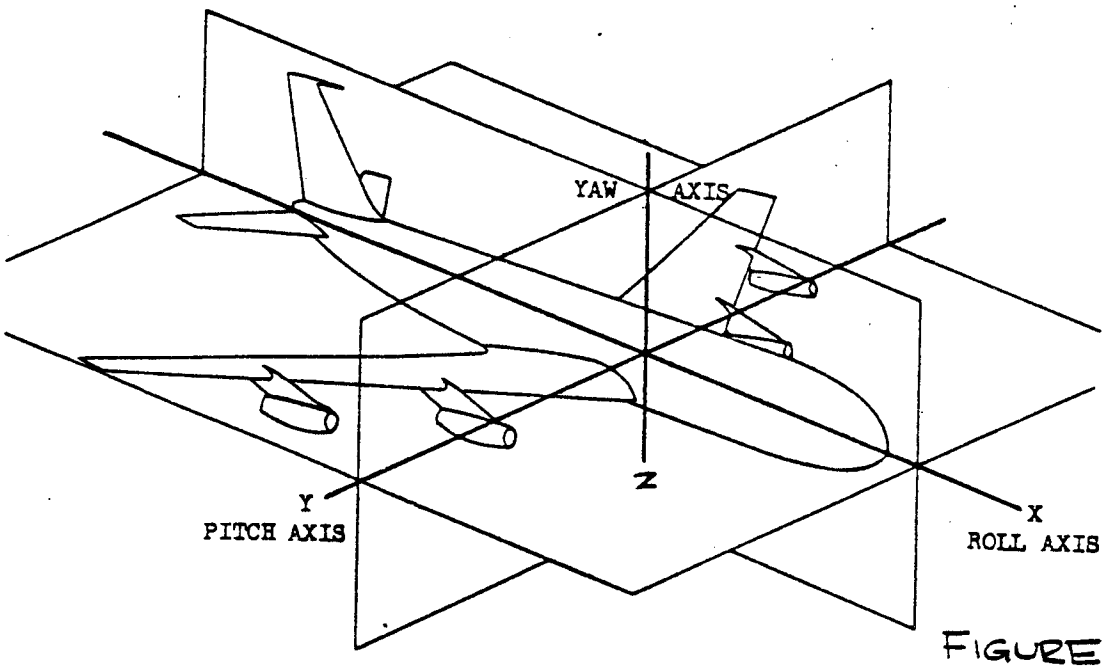

FIGURE 2.

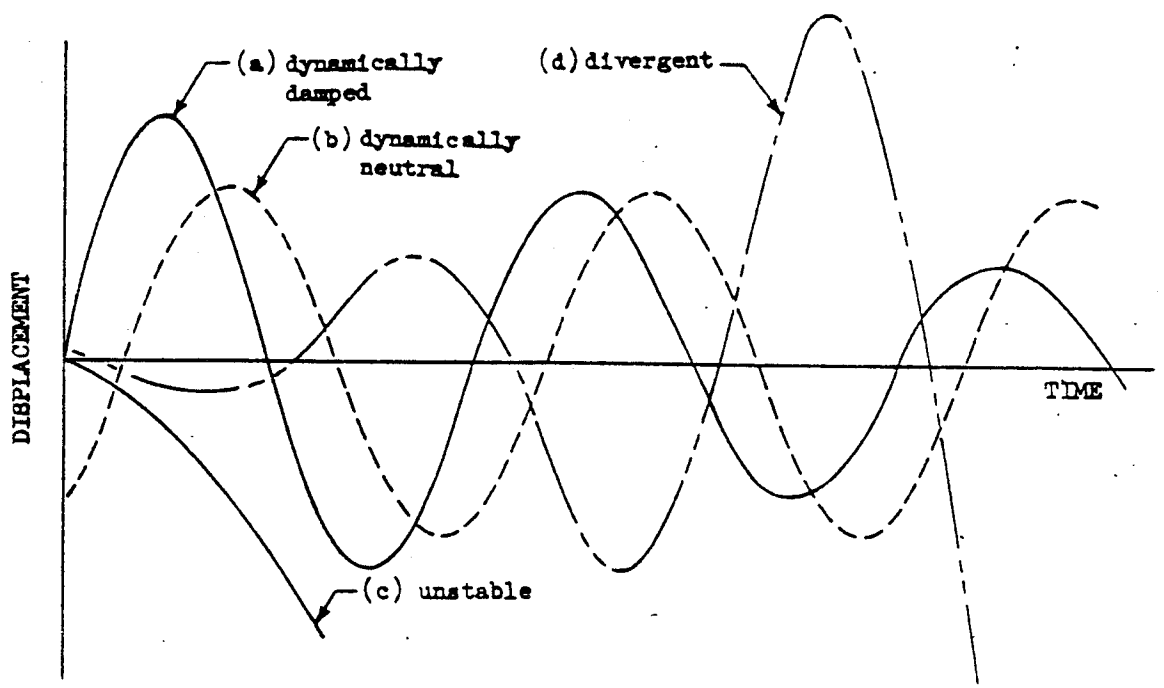

FIGURE 3

562

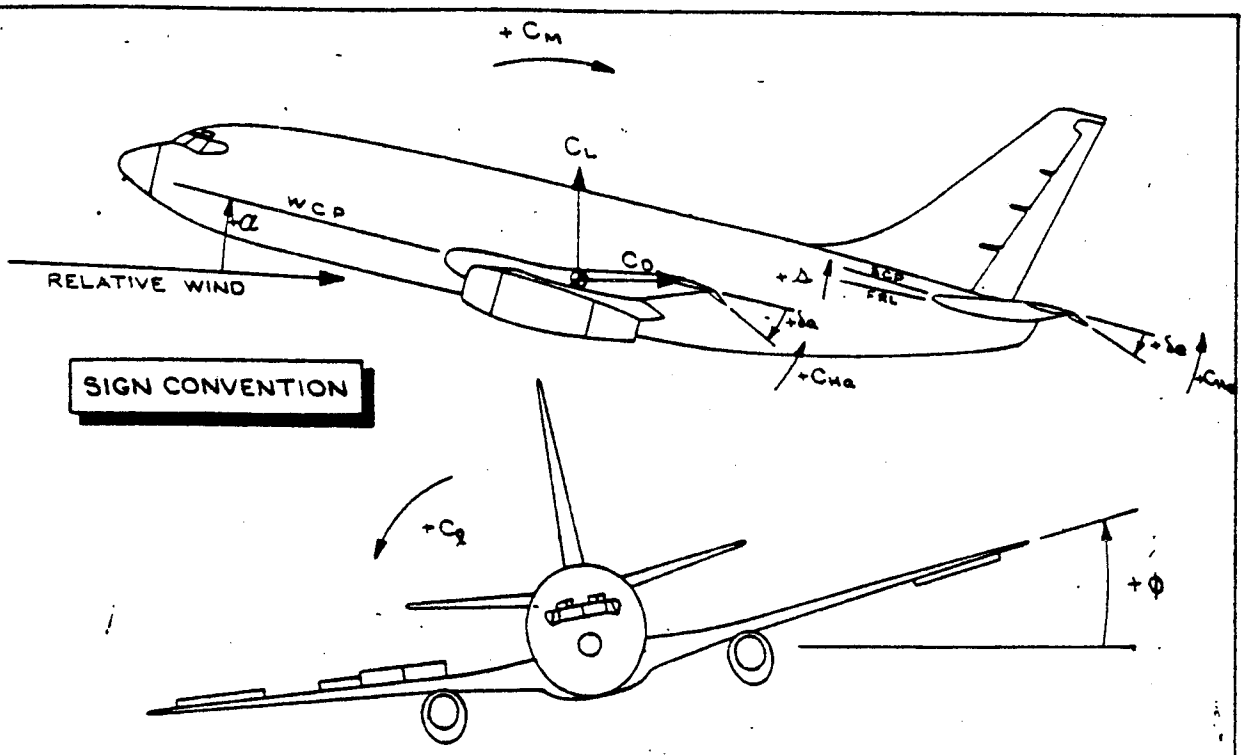

POSITIVE δ_a (AILERON TRAILING EDGE DOWN ON LEFT WING) GIVES POSITIVE C_ℓ
POSITIVE δ_{sp} (SPOILER TRAILING EDGE UP ON RIGHT WING) GIVES POSITIVE C_ℓ

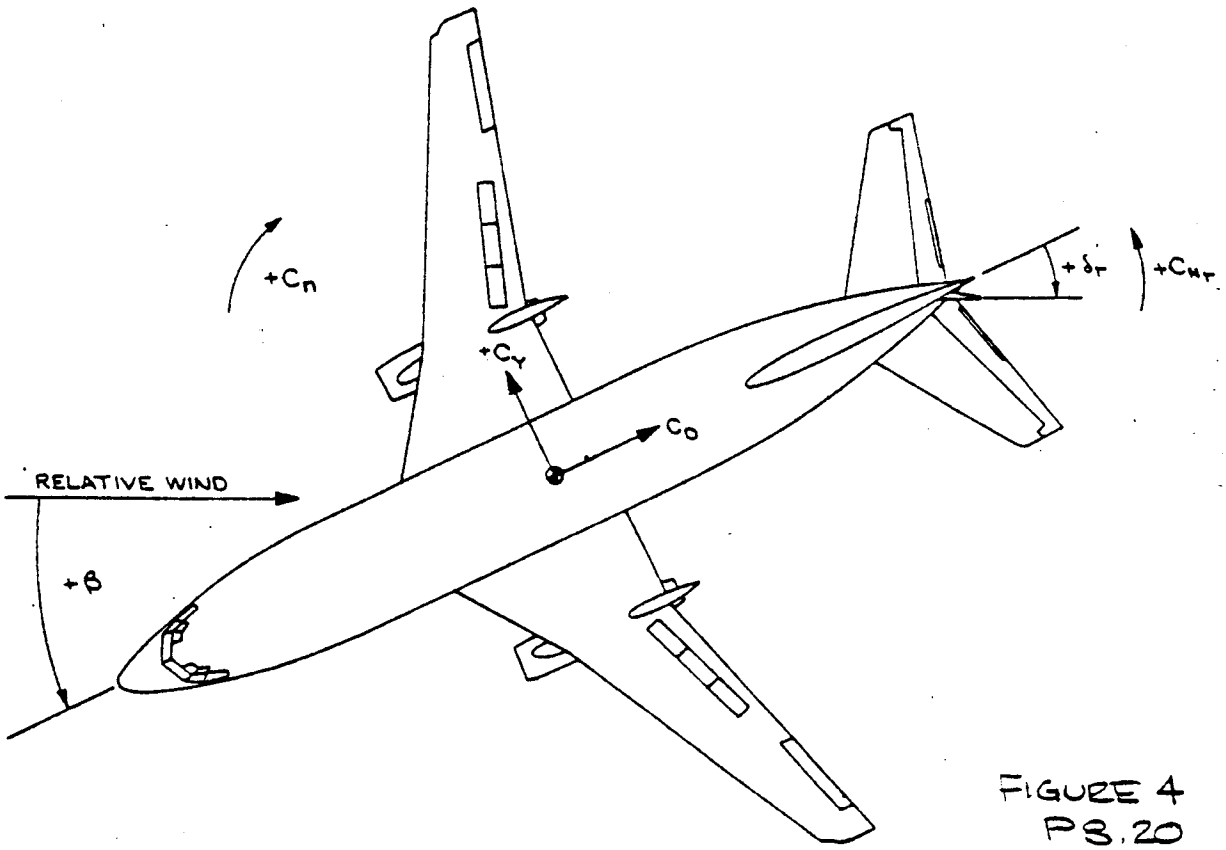

FIGURE 4
PS.20

737-100

EM. 3-25-66

P8.21

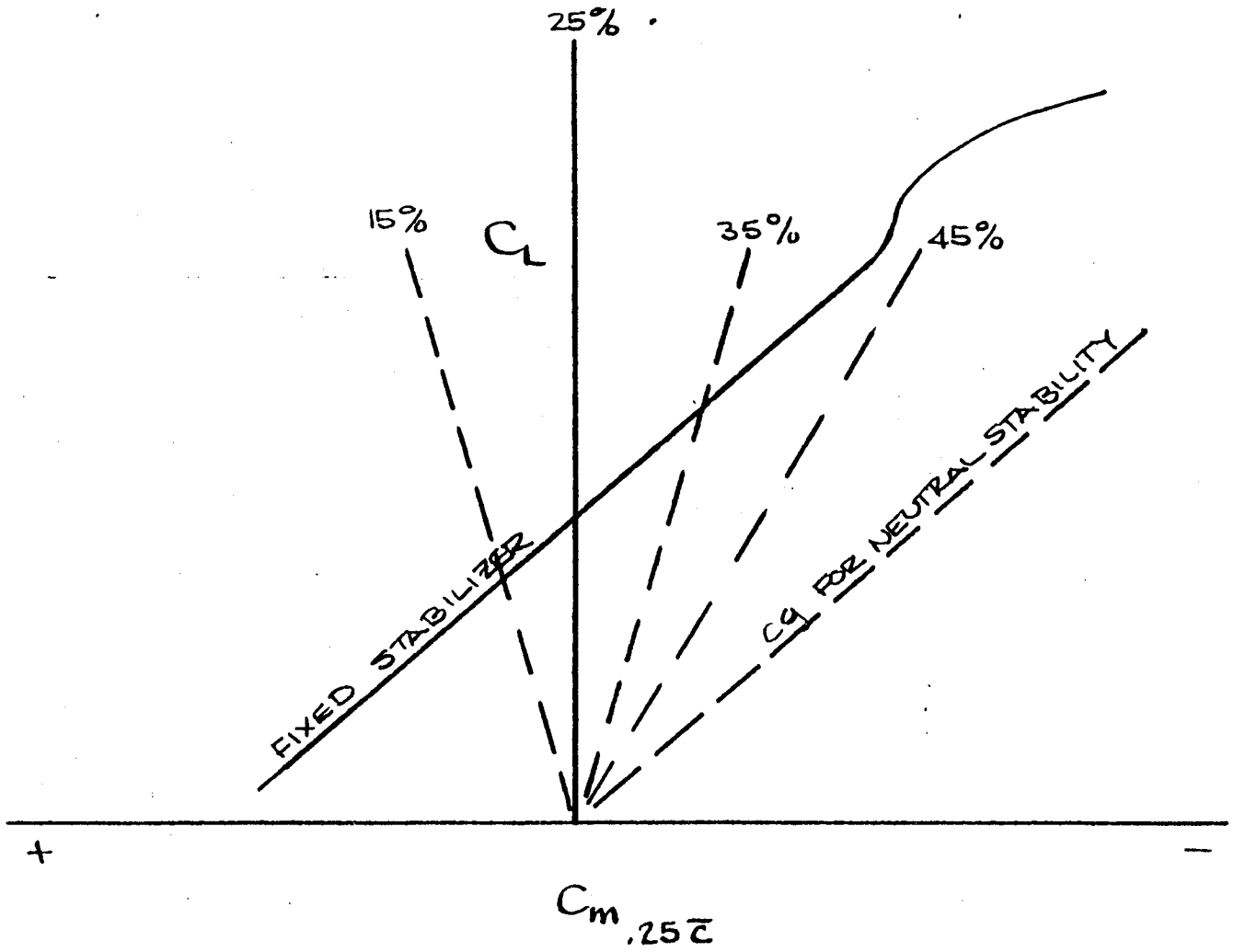

FIGURE 5

TRIM CAPABILITY

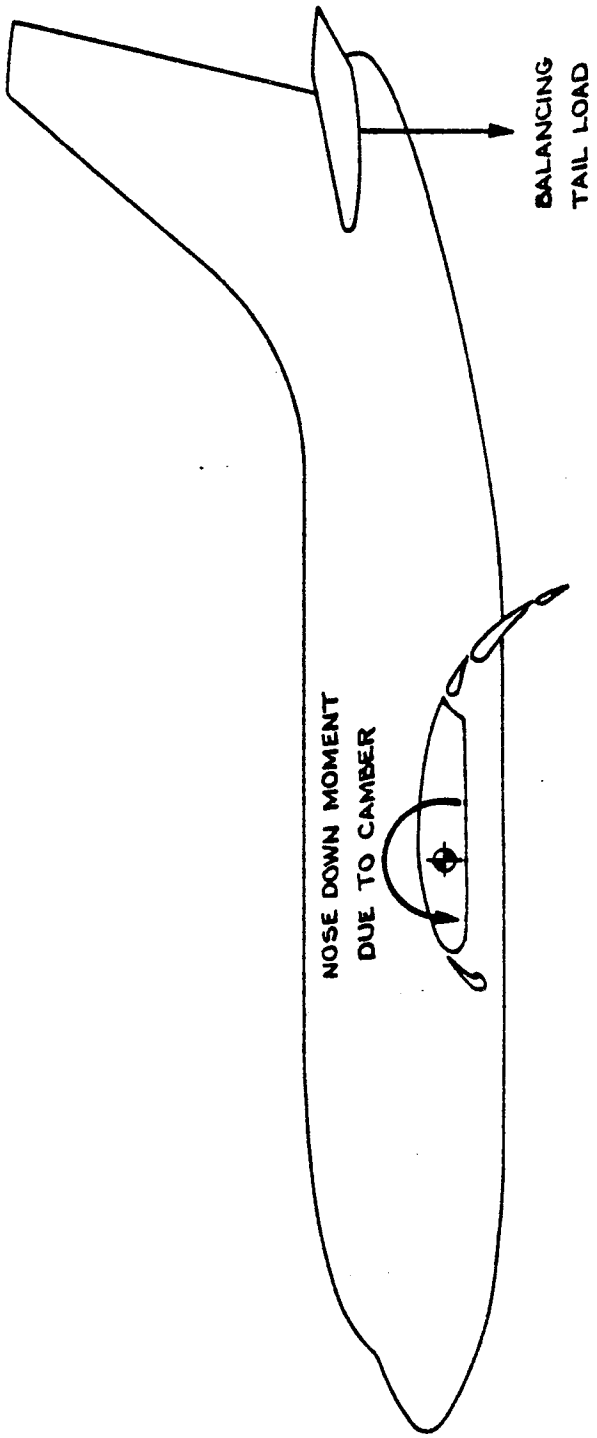

ENGR.			REVISED	DATE		FIGURE 6
CHECK						P8.22
APR						
APR					THE BOEING COMPANY RENTON, WASHINGTON	

AD 1017-R6

6-7000

565

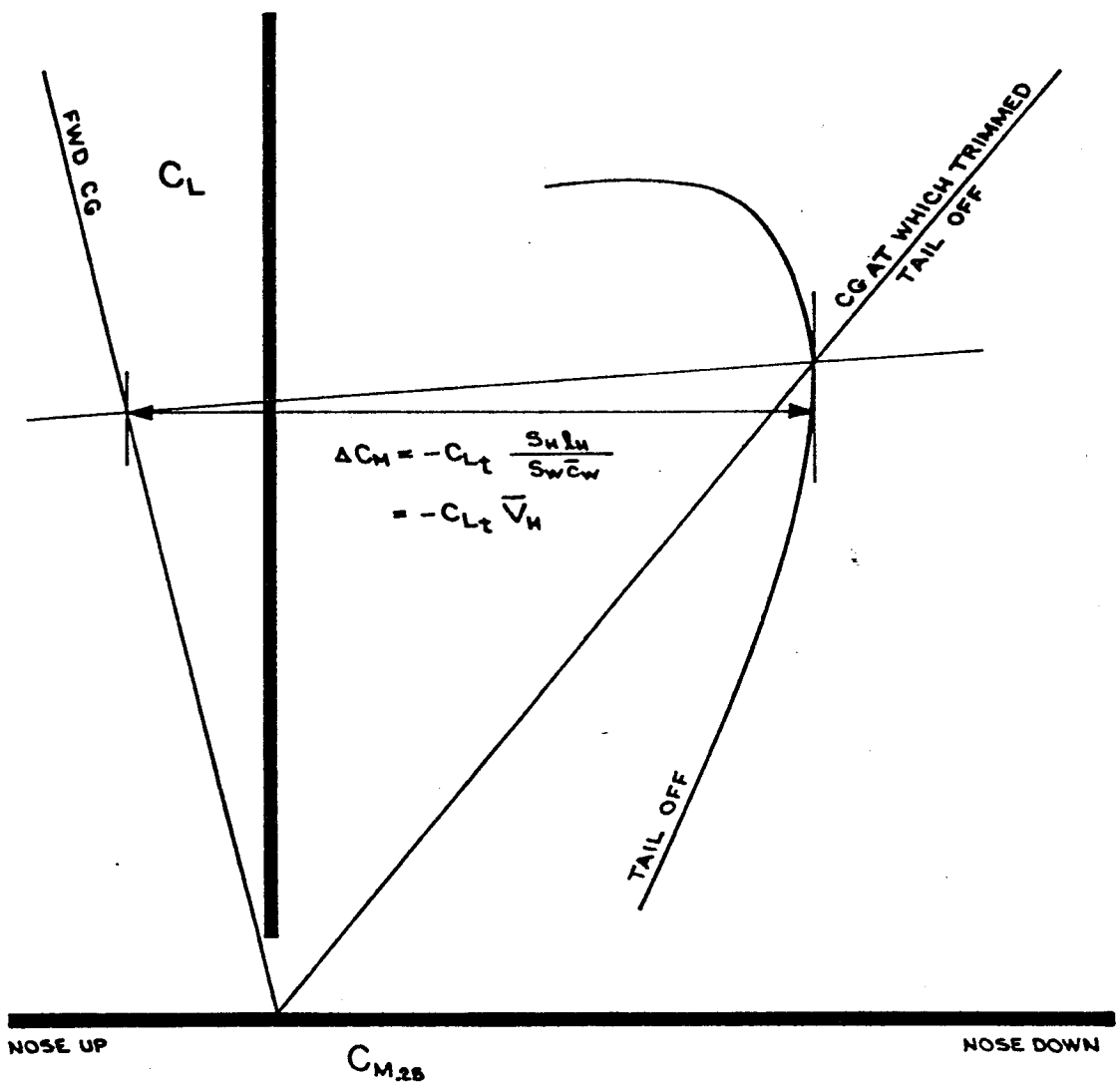

P8.23

ENGR.			REVISED	DATE		FIGURE 7
CHECK						
APR						
APR					THE BOEING COMPANY RENTON, WASHINGTON	

AD 1017-R8

8-7000

566

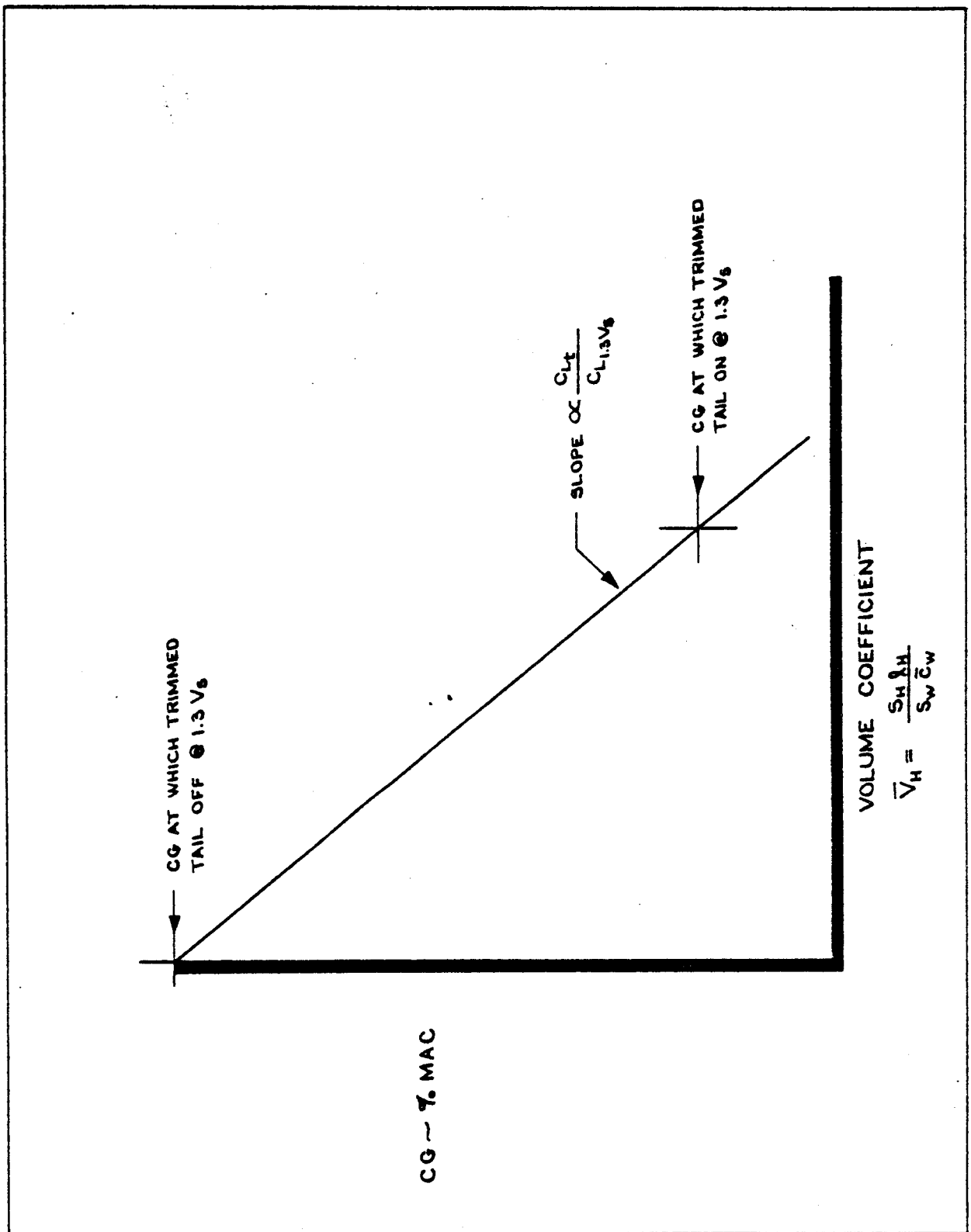

ENGR.			REVISED	DATE		FIGURE 8
CHECK						P 8.24
APR						
APR					THE BOEING COMPANY RENTON, WASHINGTON	

AD 1017-R8

6-7000

567

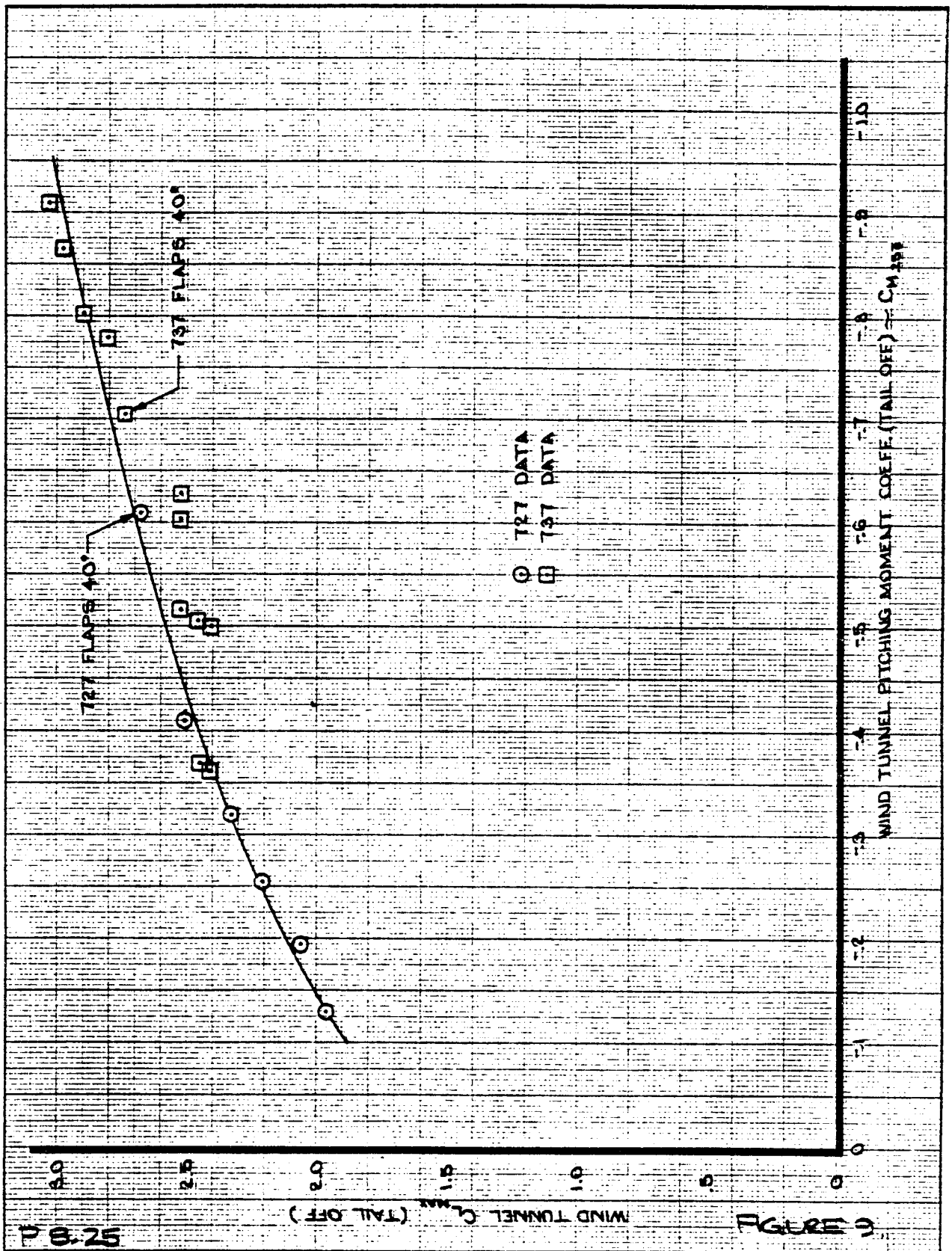

FIGURE 3

P 8.25

CALC	M°INTOSH	12-16-64	REVISED	DATE	EFFECT OF $C_{L_{MAX}}$ ON TAIL OFF PITCHING MOMENTS	727 737
CHECK						
APR						
APR					THE BOEING COMPANY	PAGE
INK	MARSHALL	1-25-65				

TD 461 C-R4

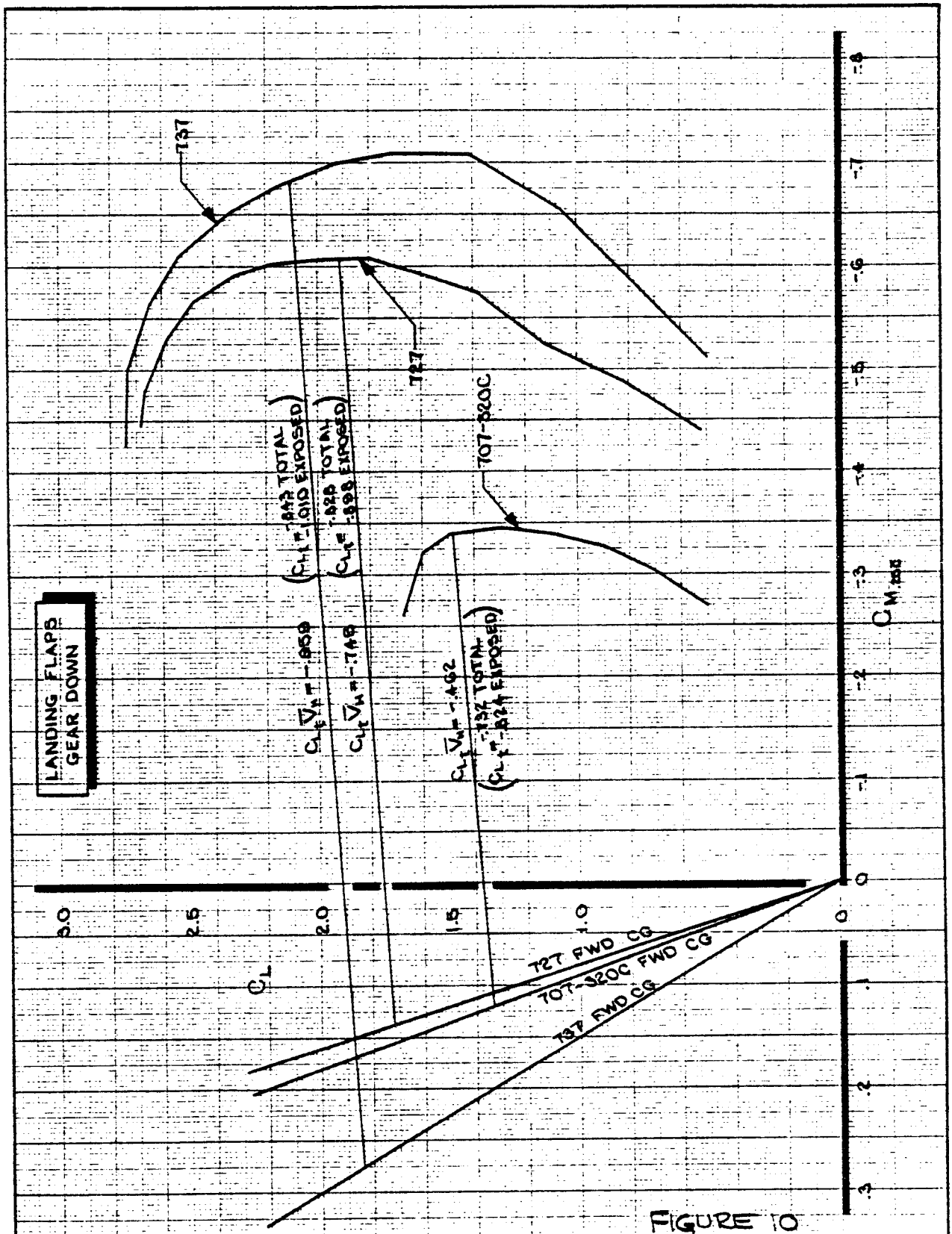

FIGURE 10

CALC	McINTOSH	6-16-66	REVISED	DATE	COMPARISON OF 727, 707, AND 737 MAXIMUM TAIL LOADS	727, 707, 737-100
CHECK						P8.26
APR						
APR					THE BOEING COMPANY	PAGE
mm	MARSHALL	6-16-66				

TD 461 C-R4

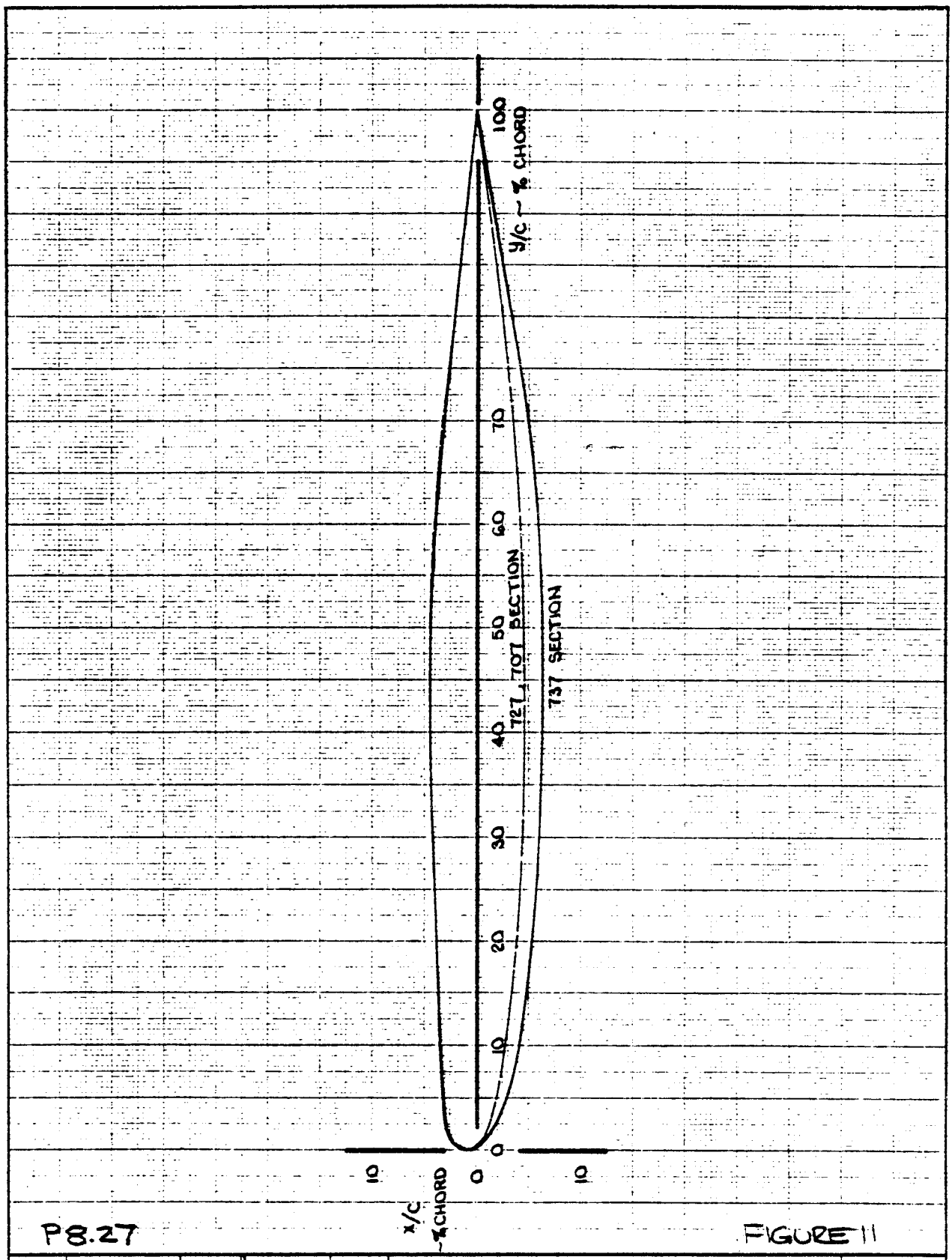

P8.27

FIGURE 11

CALC	McINTOSH	6-18-66	REVISED	DATE	COMPARISON OF 727, 707, AND 737 STABILIZER AIRFOIL SECTIONS	727, 707 737
CHECK						
APR						
APR					THE BOEING COMPANY	PAGE
INK	MARSHALL	6-18-66				

TD 461 C-R4

570

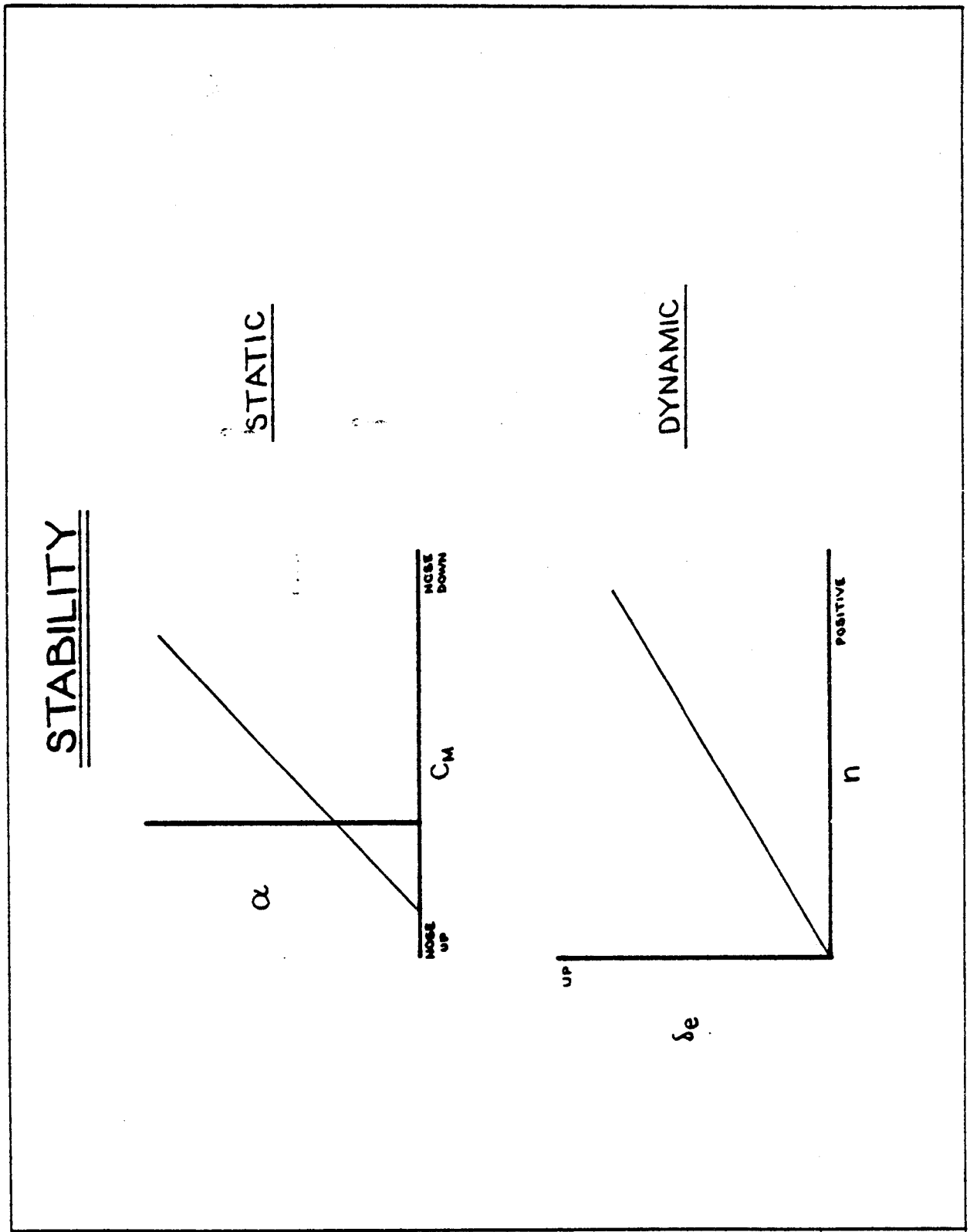

ENGR.			REVISED	DATE	FIGURE 12
CHECK					P8.28
APR					
APR					THE BOEING COMPANY RENTON, WASHINGTON

AD 1017-R6

6-7000

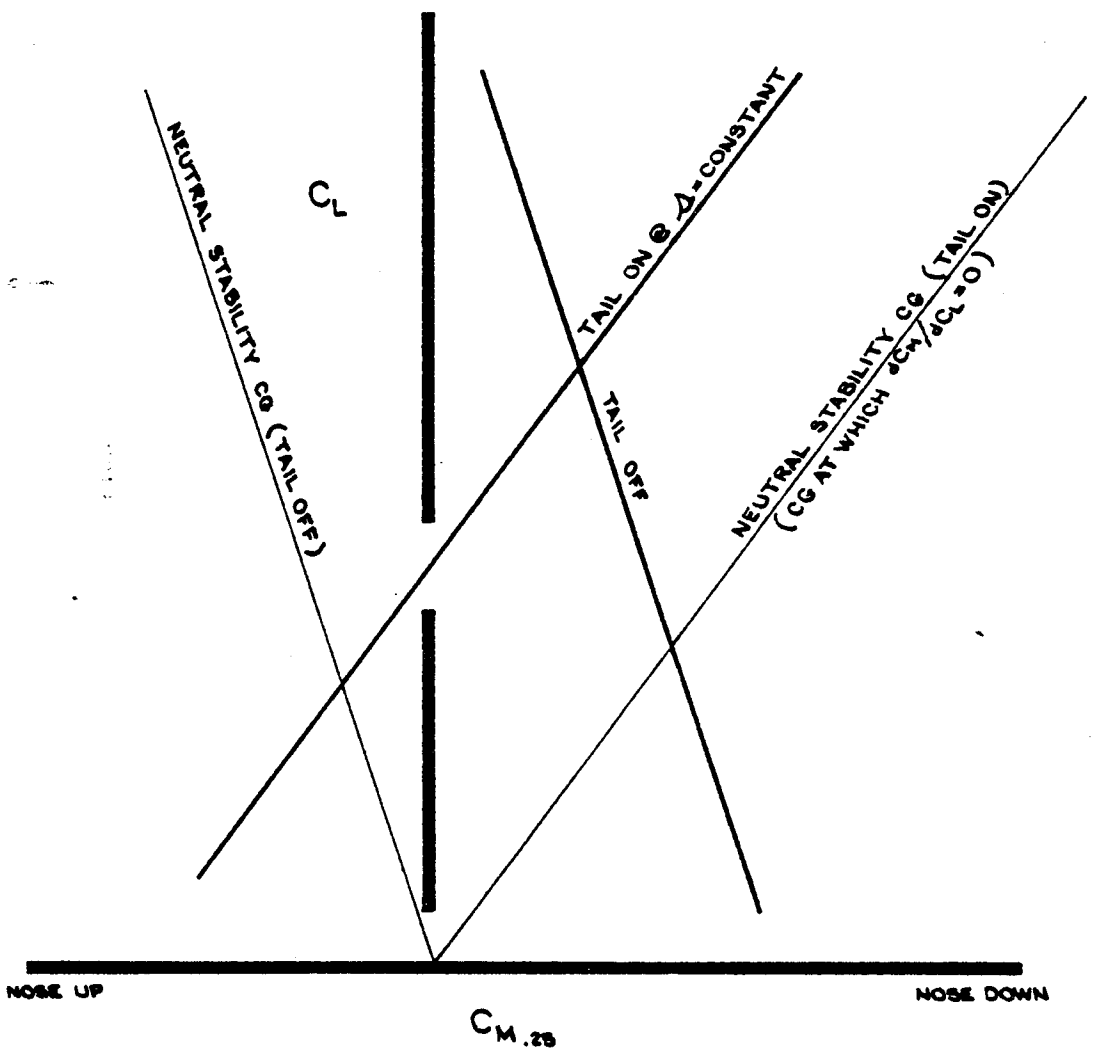

P8.29a

ENGR.			REVISED	DATE		FIGURE 13
CHECK						
APR						
APR					THE BOEING COMPANY RENTON, WASHINGTON	

AD 1017-R6

8-7000

572

AD 1017-R6

ENGR.			
CHECK			
APR			
APR			
	REVISED	DATE	

THE BOEING COMPANY
RENTON, WASHINGTON

CG ~ % MAC

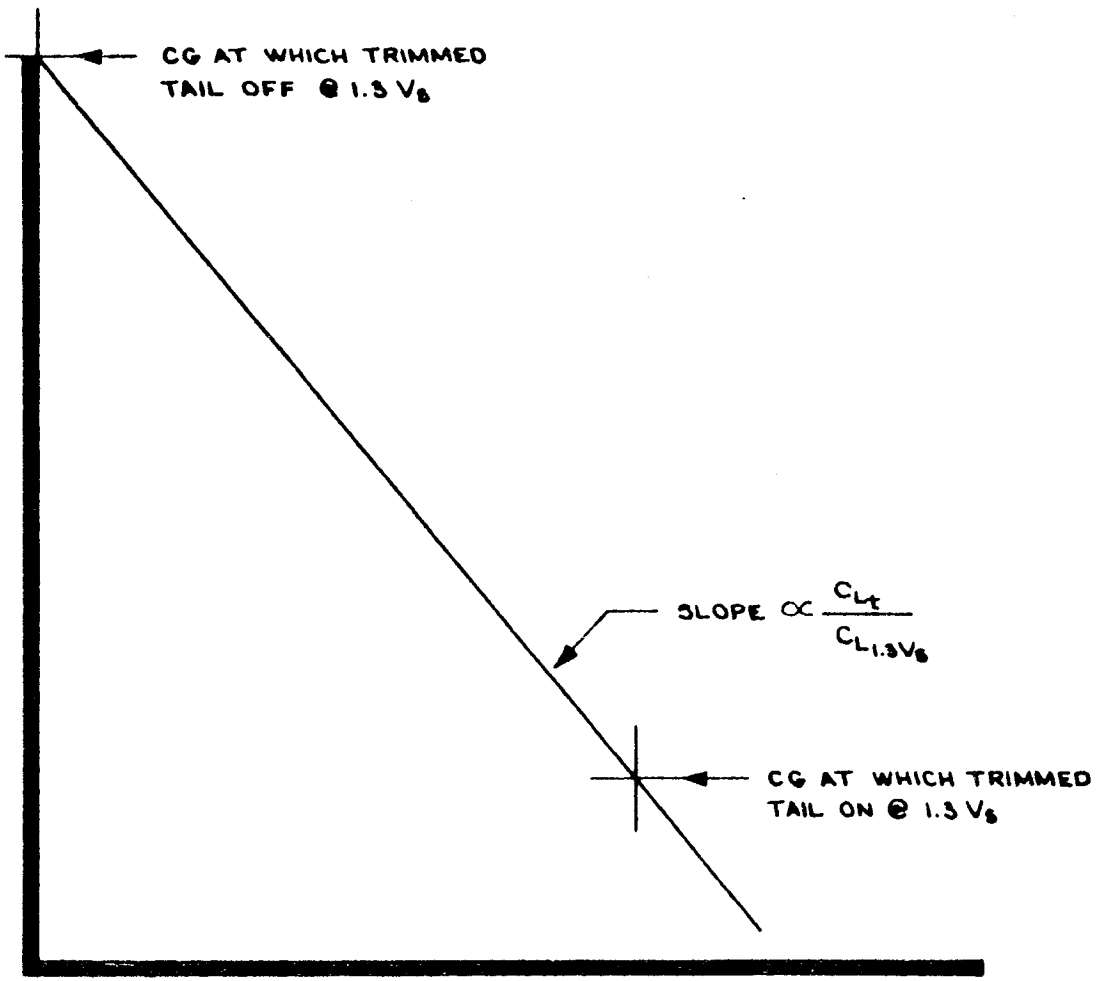

VOLUME COEFFICIENT

$$\bar{V}_H = \frac{S_H \ell_H}{S_W \bar{c}_W}$$

P 8.296

O/L FIG 14 - REV

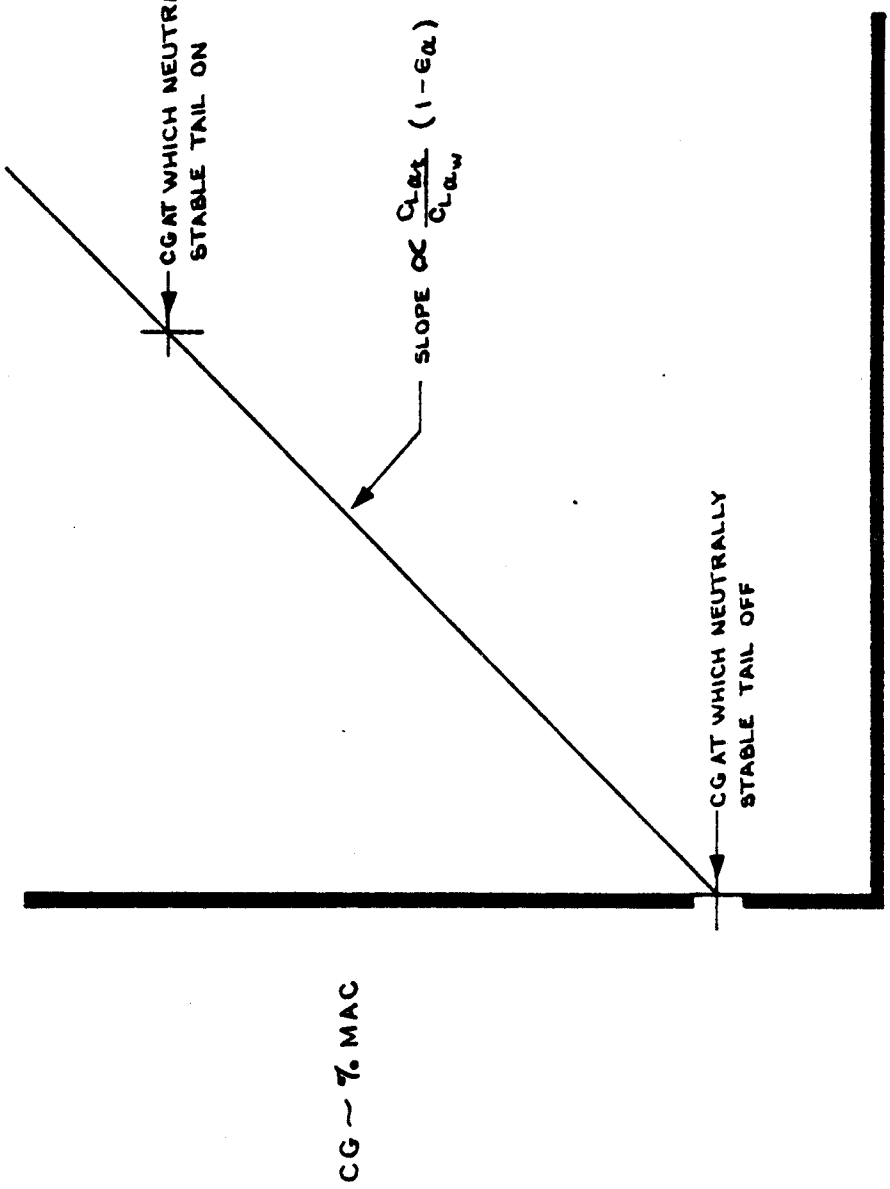

ENGR.			REVISED	DATE	FIGURE 4
CHECK					P8.30
APR					
APR					THE BOEING COMPANY RENTON, WASHINGTON

AD 1017-R6

8-7000

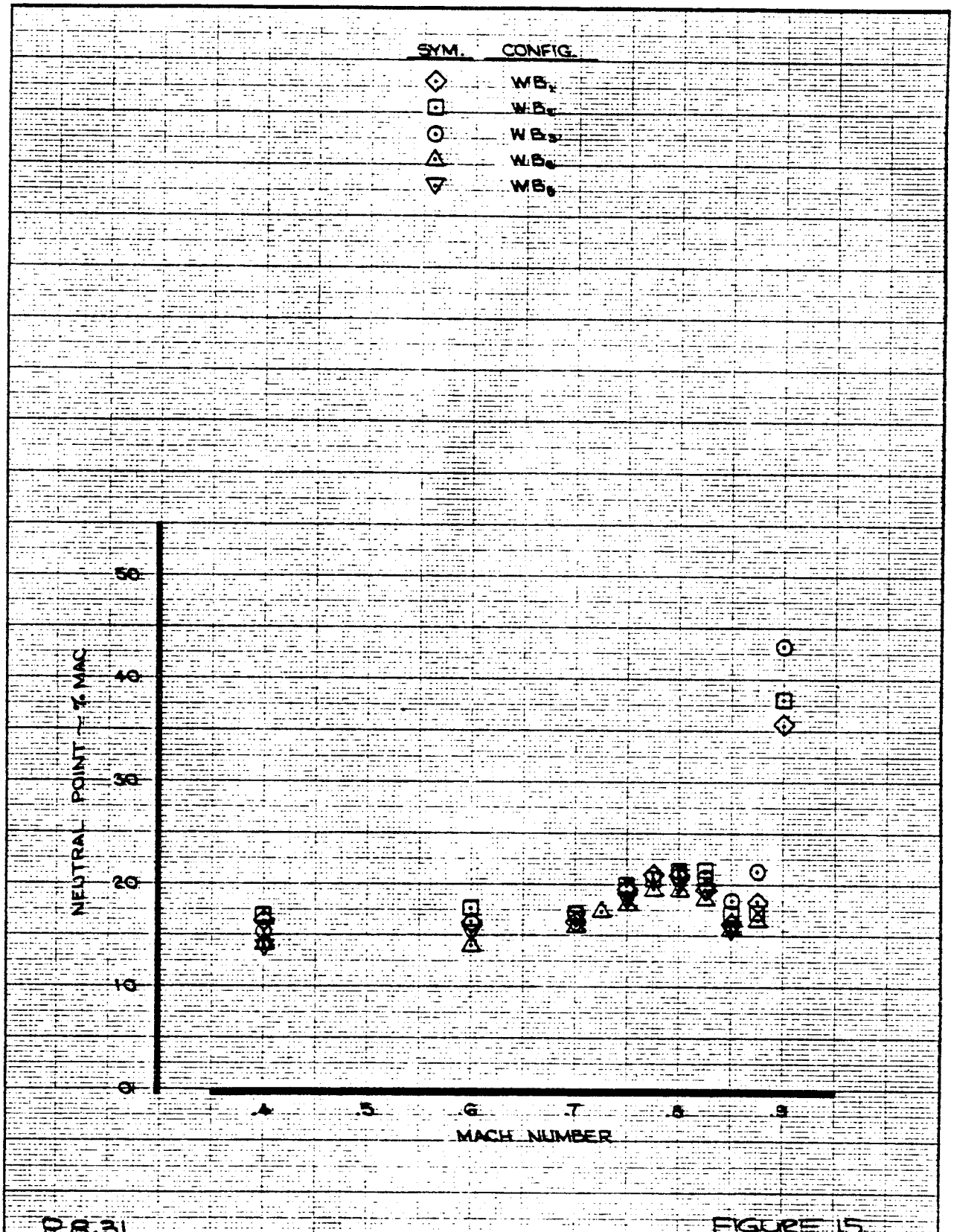

P 8.31

FIGURE 15

CALC	McINTOSH	1-23-63	REVISED	DATE	EFFECT OF VARIOUS BODY SHAPES ON TAIL OFF NEUTRAL POINT	737
CHECK						
APR						
APR					THE BOEING COMPANY	PAGE
INK	MARSHALL	1-25-63				

TD 461 C-R4

575

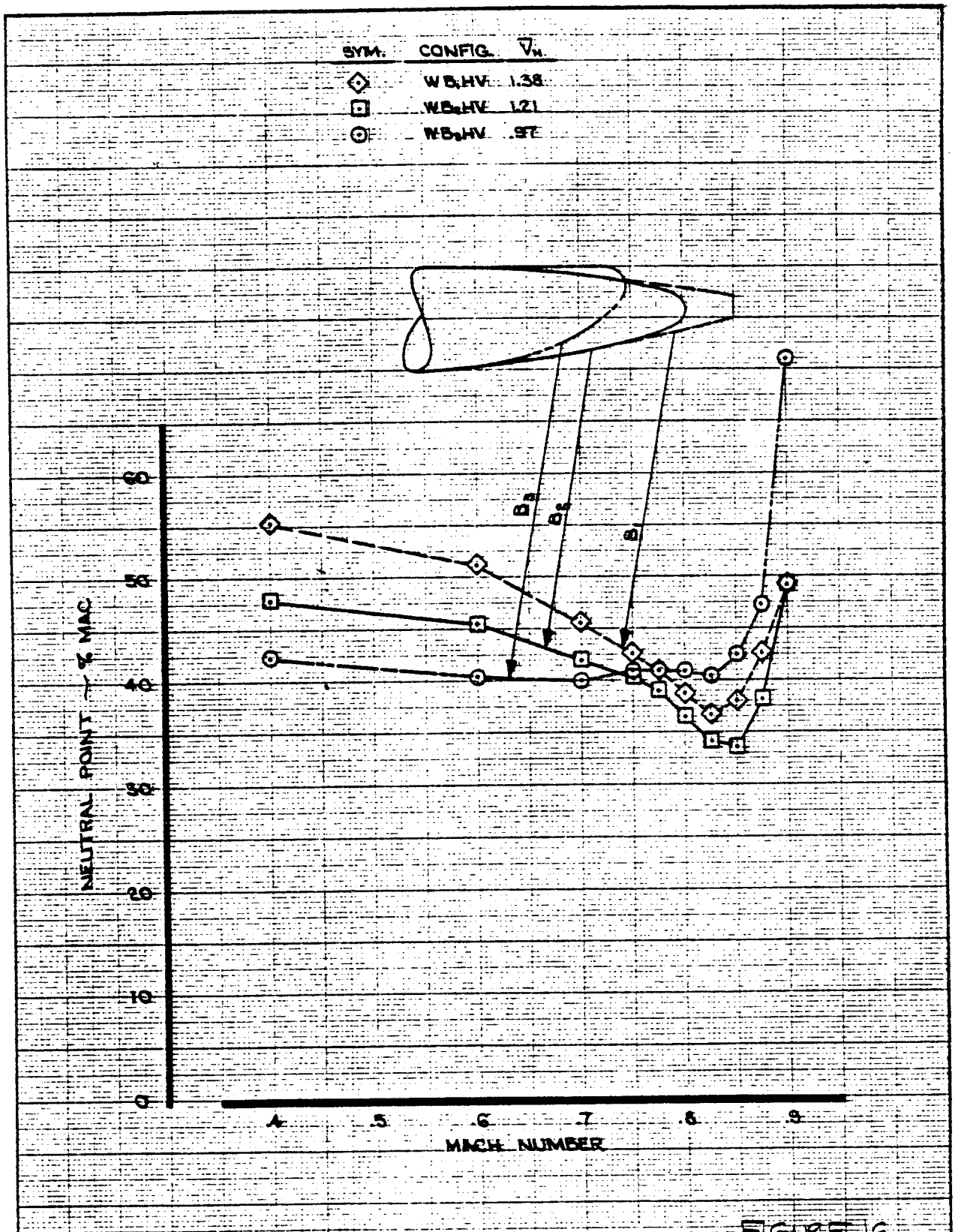

FIGURE 16

CALC	McINTOSH	11-16-64	REVISED	DATE	EFFECT OF AFT BODY SHAPE ON TAIL ON NEUTRAL POINT	737
CHECK						P3.32
APR						
APR					THE BOEING COMPANY	PAGE
IWK	MARSHALL	1-28-65				

TD 461 C-R4

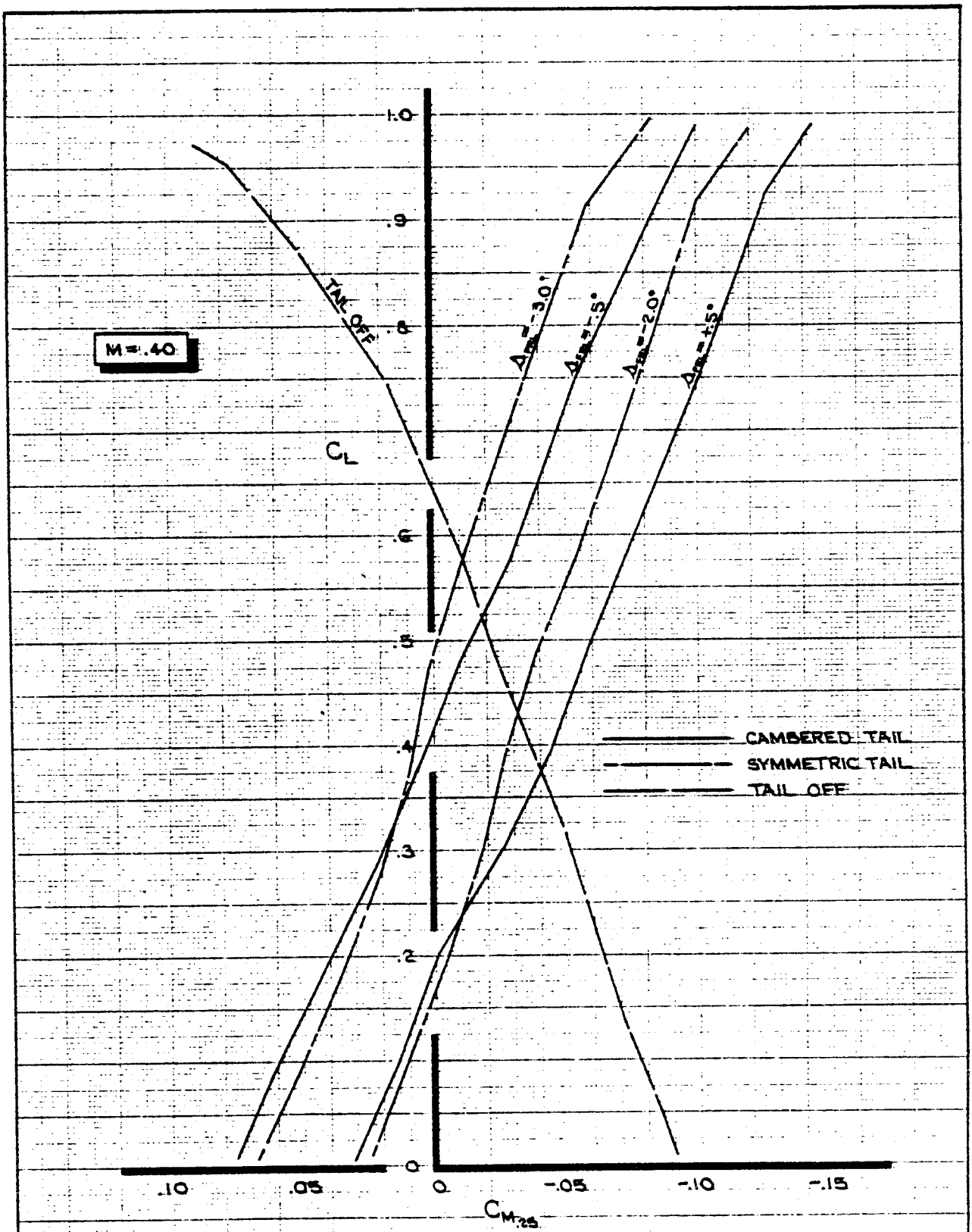

P 8.32

FIGURE 17a

CALC	M°INTOSH	2-27-65	REVISED	DATE	EFFECT OF STABILIZER CAMBER ON STABILITY ~ M=.40 ~	737-100
CHECK						
APR						
APR					THE BOEING COMPANY	PAGE
[illegible]	MARSHALL	6-18-66				

TD 461 C-R4

577

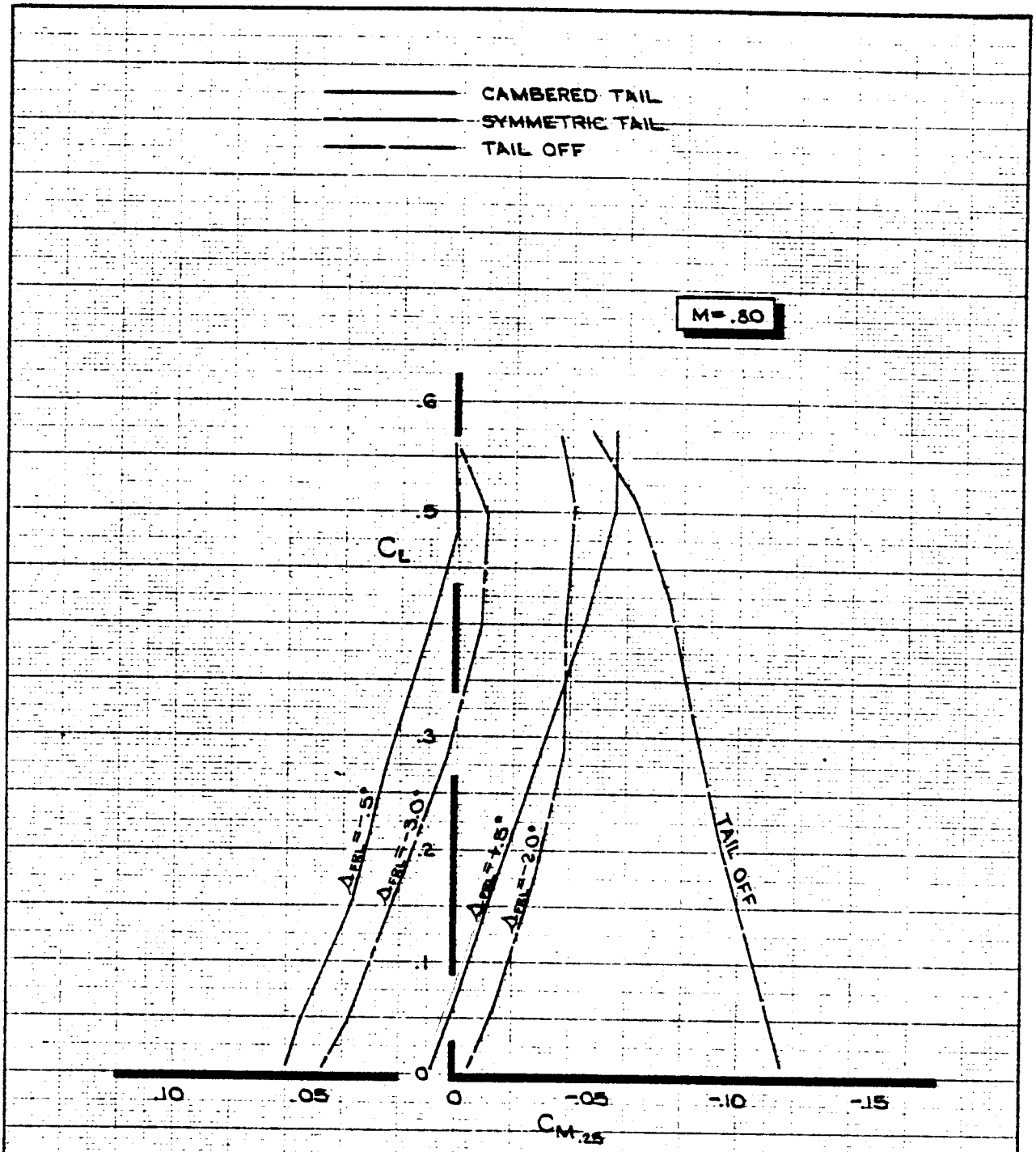

FIGURE 17b

CALC	McINTOSH	2-27-68	REVISED	DATE	EFFECT OF STABILIZER CAMBER ON STABILITY ~ M = .80 ~	737-100
CHECK						P 8-34
APR						
APR					THE BOEING COMPANY	PAGE
INK	MARSHALL	6-18-68				

TD 461 C-84

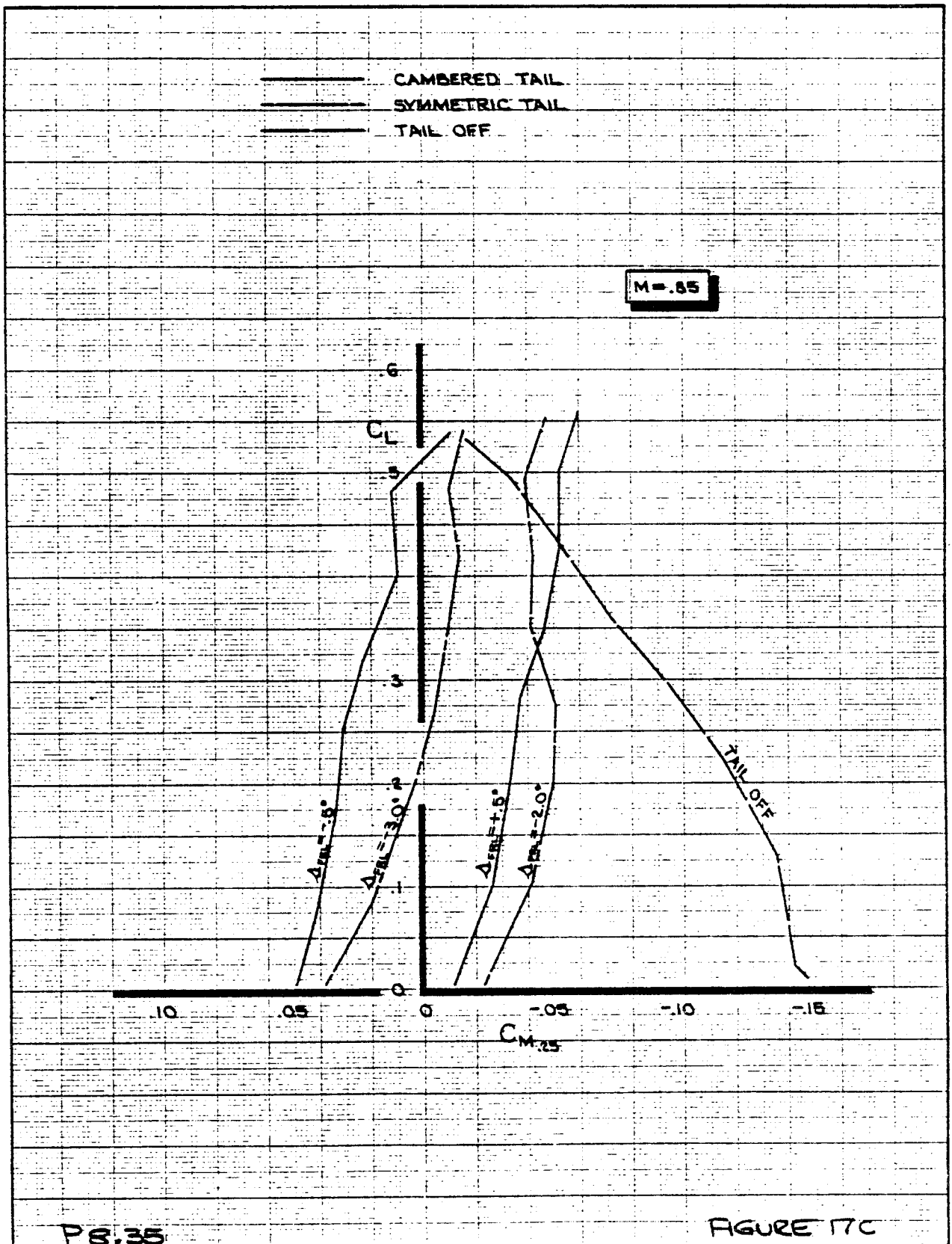

P8,35

FIGURE 17C

CALC	McINTOSH	2-27-68	REVISED	DATE	EFFECT OF STABILIZER CAMBER ON STABILITY ~M=.85~	737-100
CHECK						
APR						
APR					THE BOEING COMPANY	PAGE
INIT	MARSHALL	6-18-68				

TD 461 C-R4

579

580

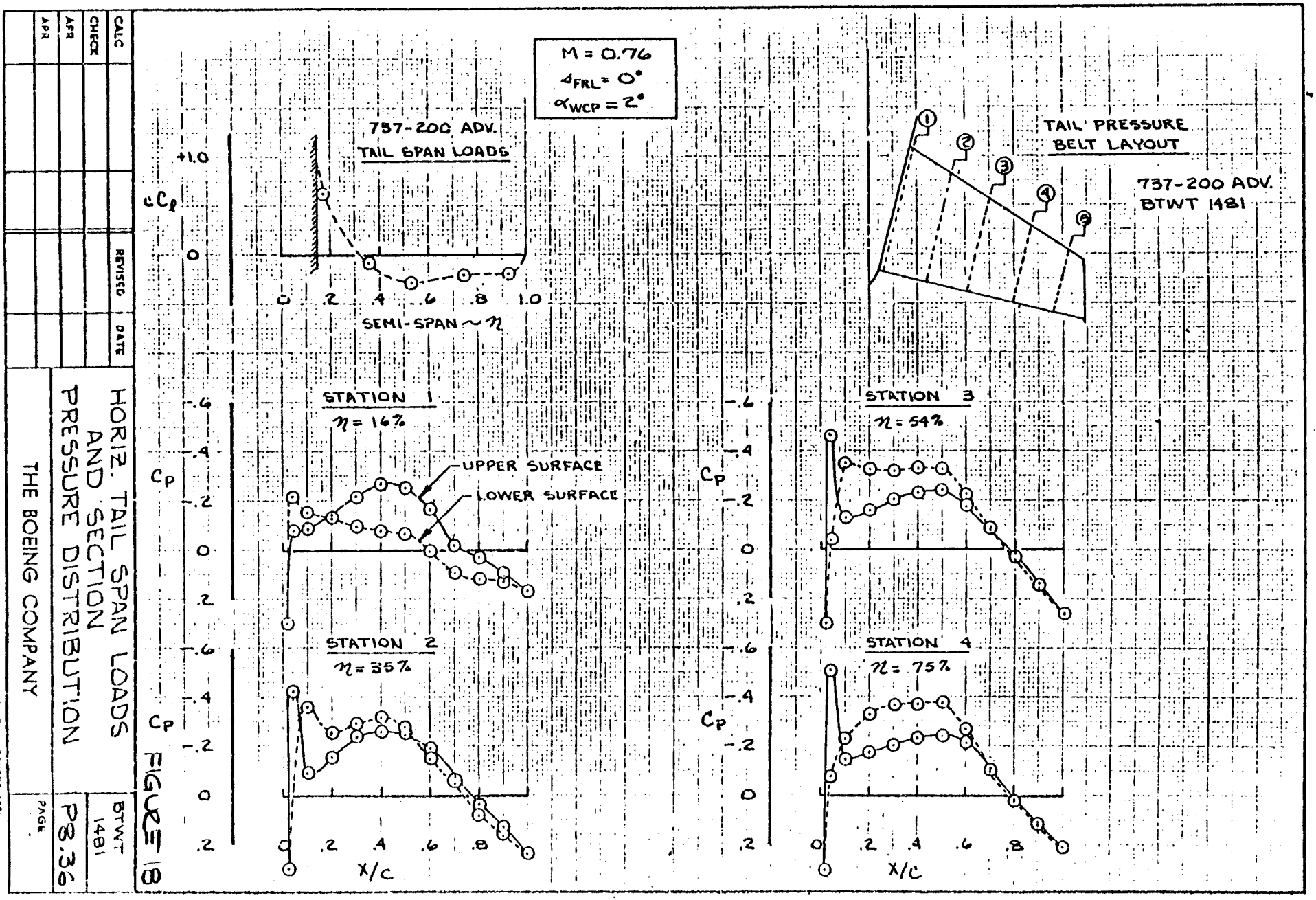

FIGURE 18

HORIZ. TAIL SPAN LOADS AND SECTION PRESSURE DISTRIBUTION

THE BOEING COMPANY

BTWT 1481

PAGE P8.36

	CALC	CHECK	APR	APR
	REVISED	DATE		

D1 4100 3240

K-E

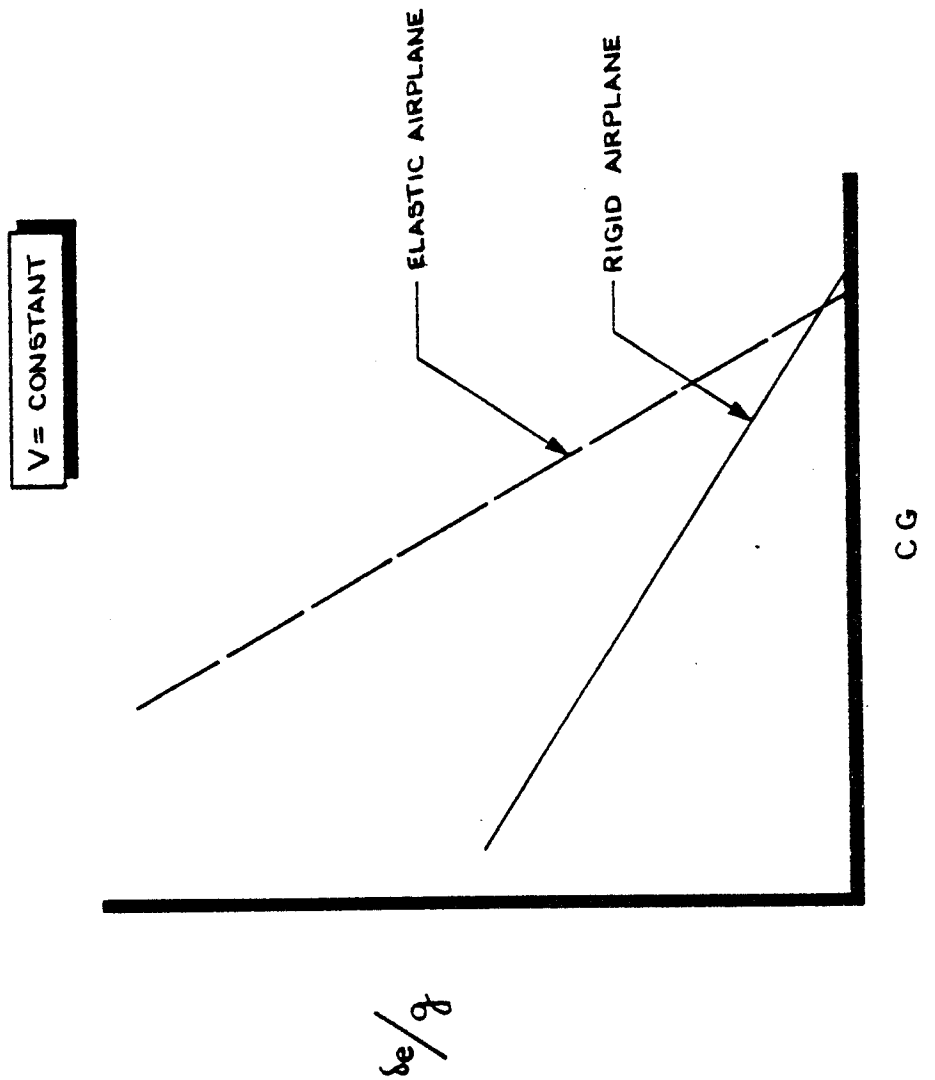

P8.37

ENGR.			REVISED	DATE		FIGURE 19
CHECK						
APR						
APR					THE BOEING COMPANY RENTON, WASHINGTON	

AD 1017-R6

6-7000

581 11

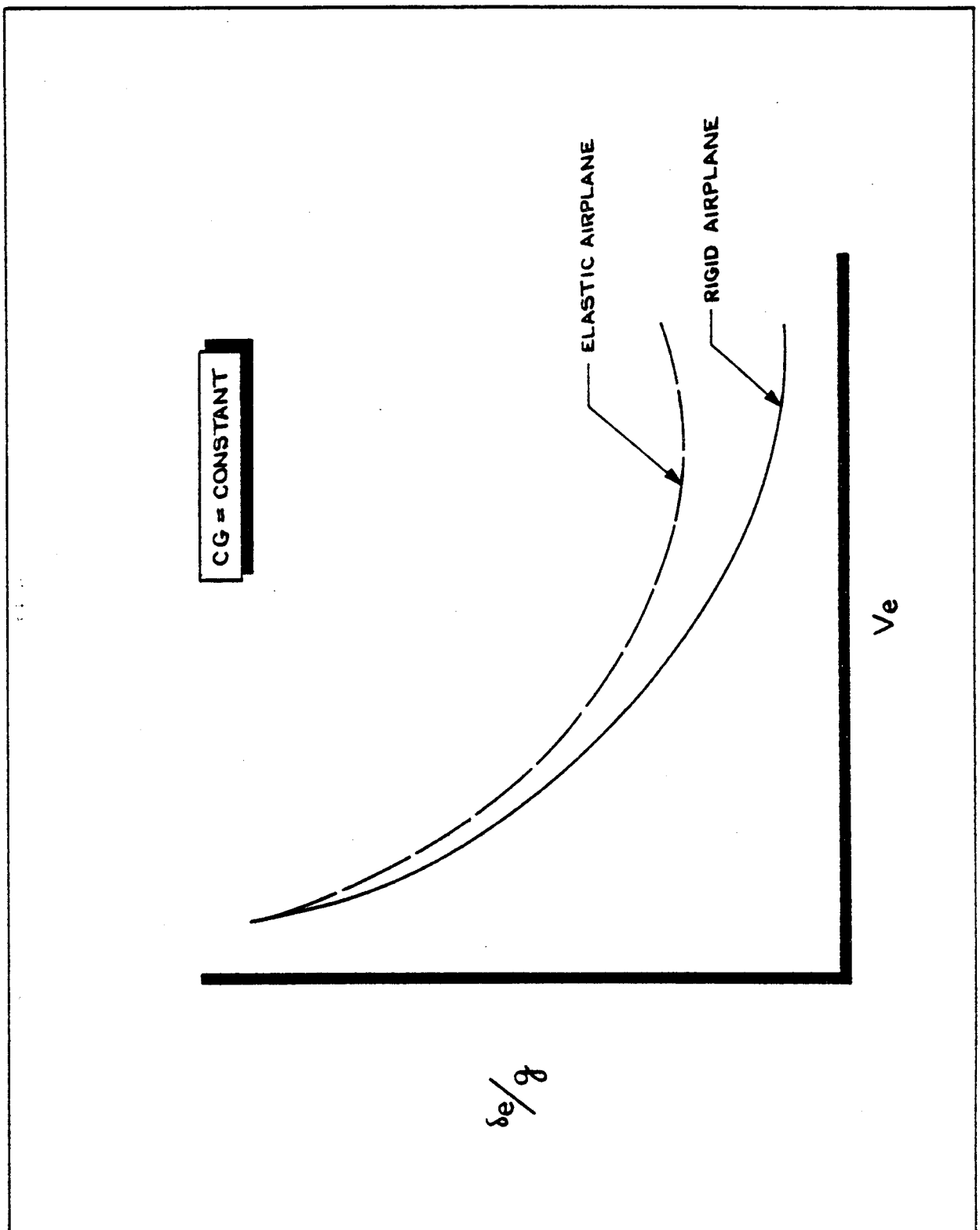

ENGR.			REVISED	DATE
CHECK				
APR				
APR				

THE BOEING COMPANY
RENTON, WASHINGTON

FIGURE 20
P8.38

AD 1017-R6

8-7000

582 10

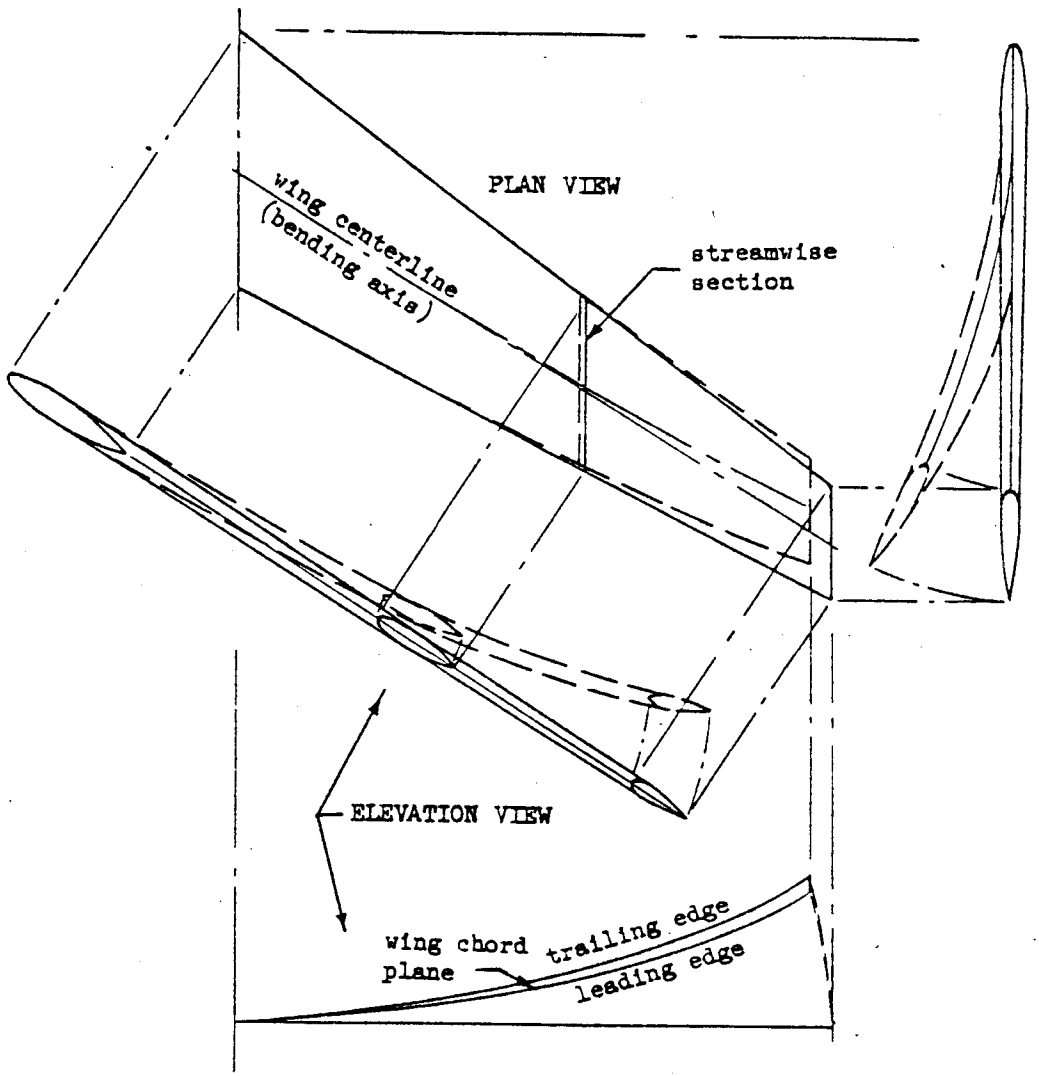

FIGURE 21

583

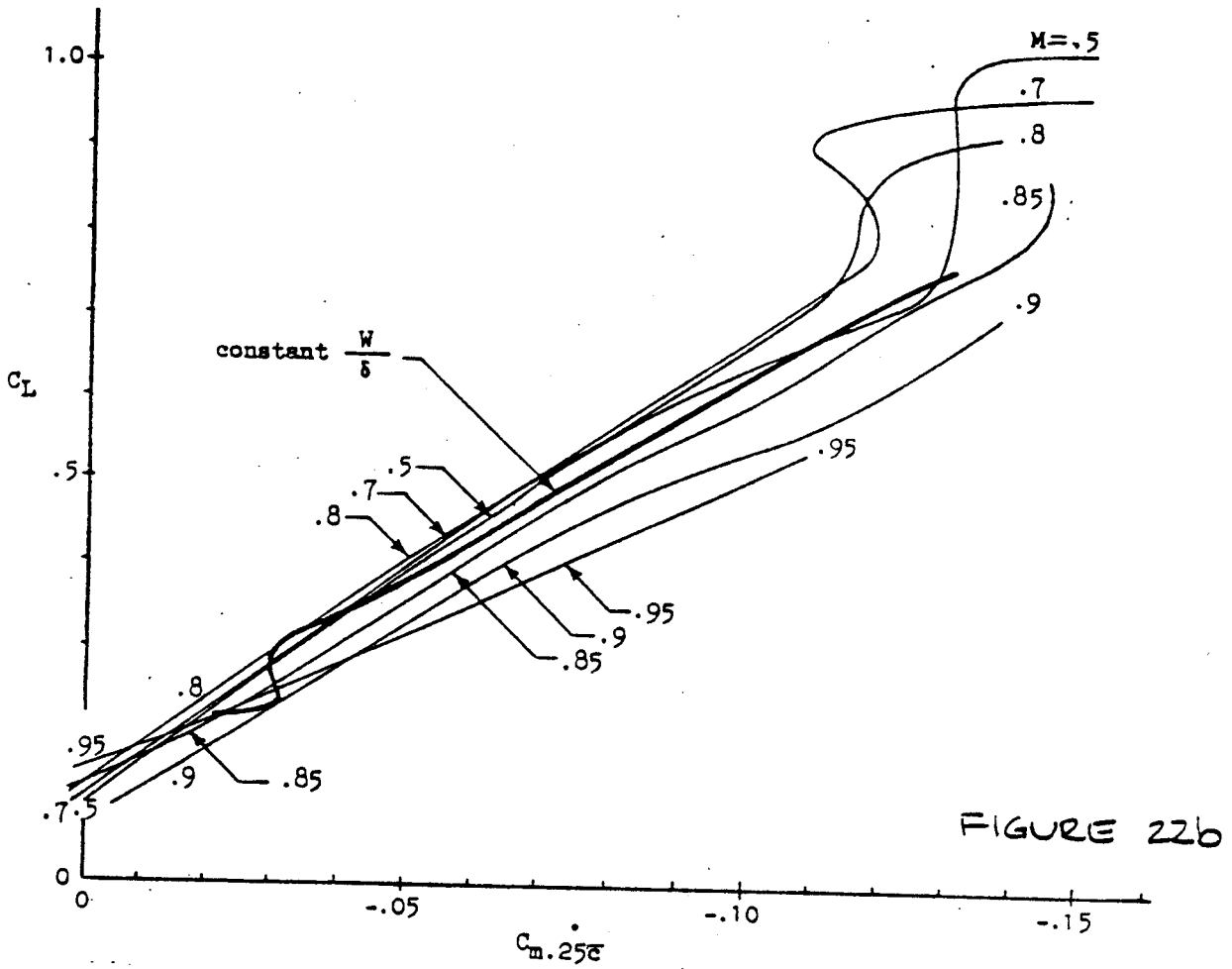

FIGURE 22b

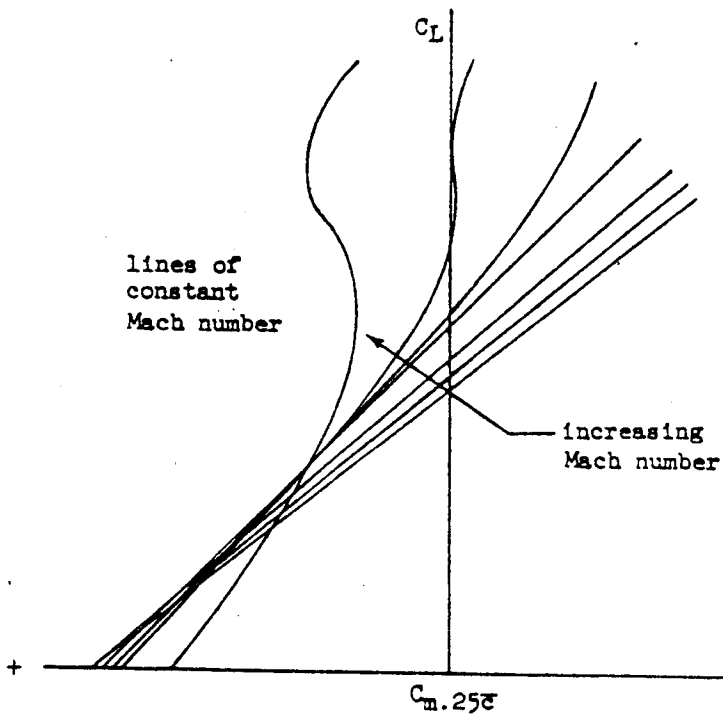

FIGURE 22a

– P 8.40

DEEP STALL

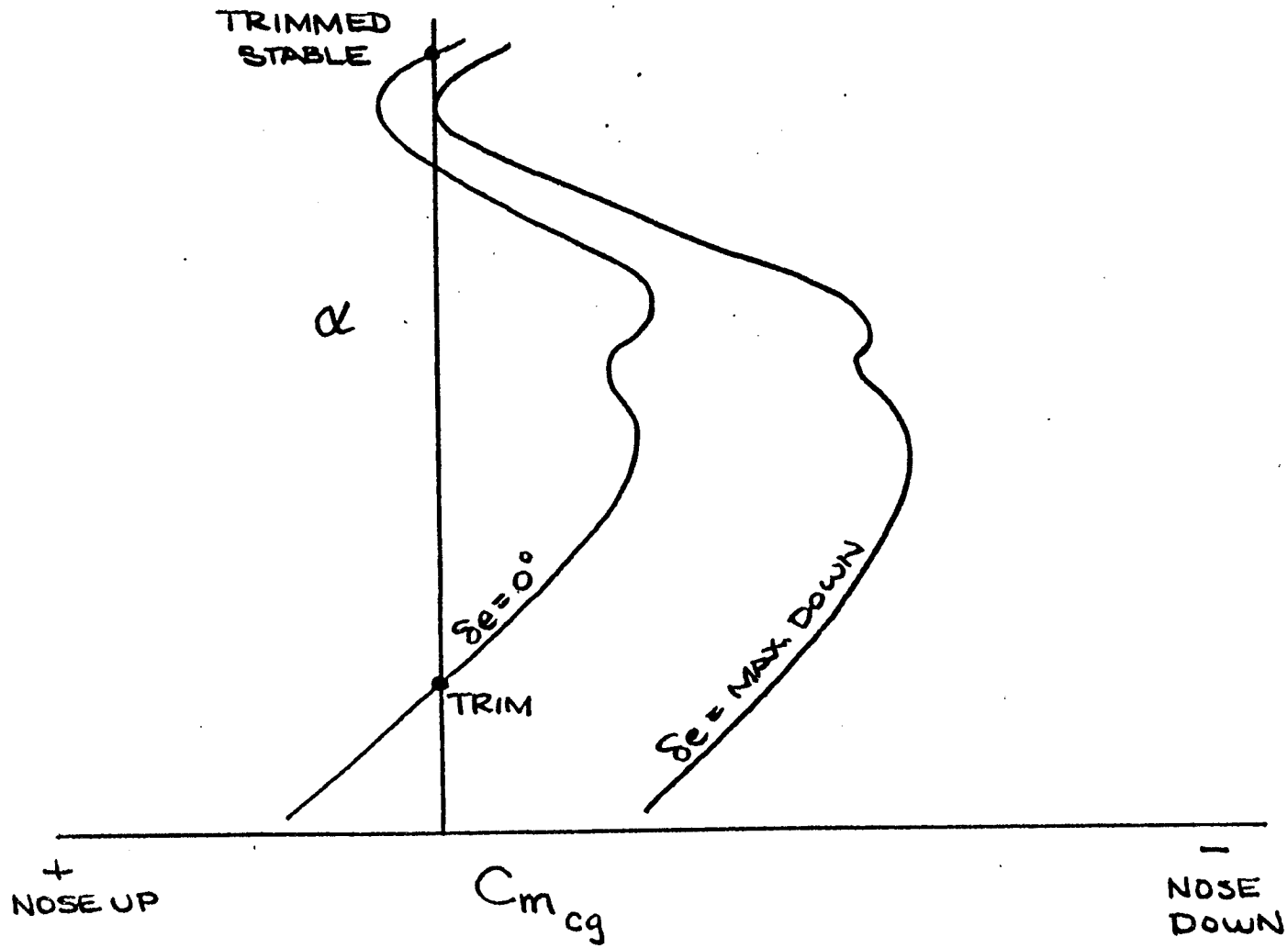

FIGURE 23

586

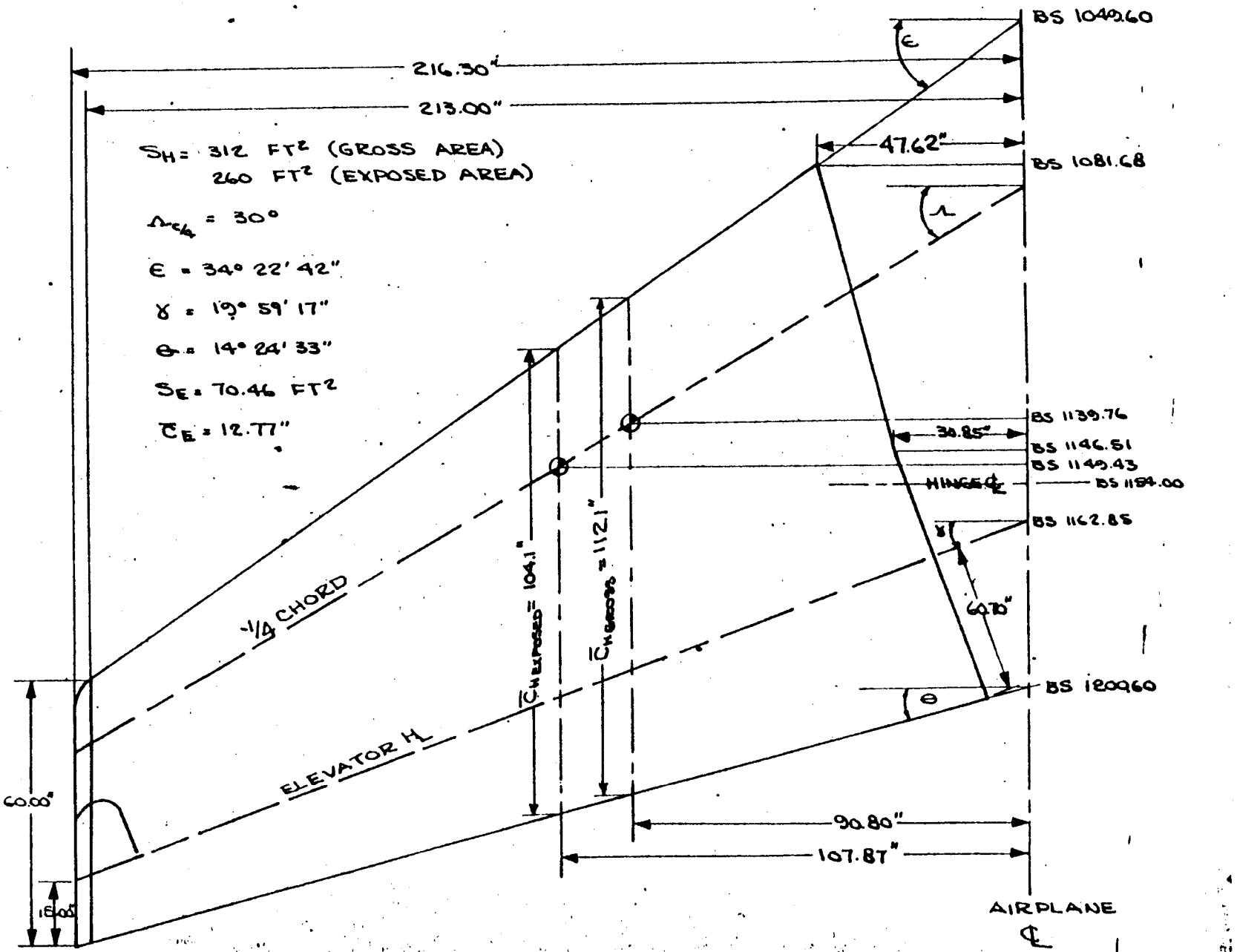

FIGURE 249 REF. DWG 65-73721

ENGR.	STEINHAUER	8-8-66	REVISED	DATE
CHECK				
APR				
APR				
INK	Burbon	8-10-66		

THE BOEING COMPANY
RENTON, WASHINGTON

HORIZONTAL STABILIZER
GEOMETRY

737-100

PAGE P8.42

AD 1017-66

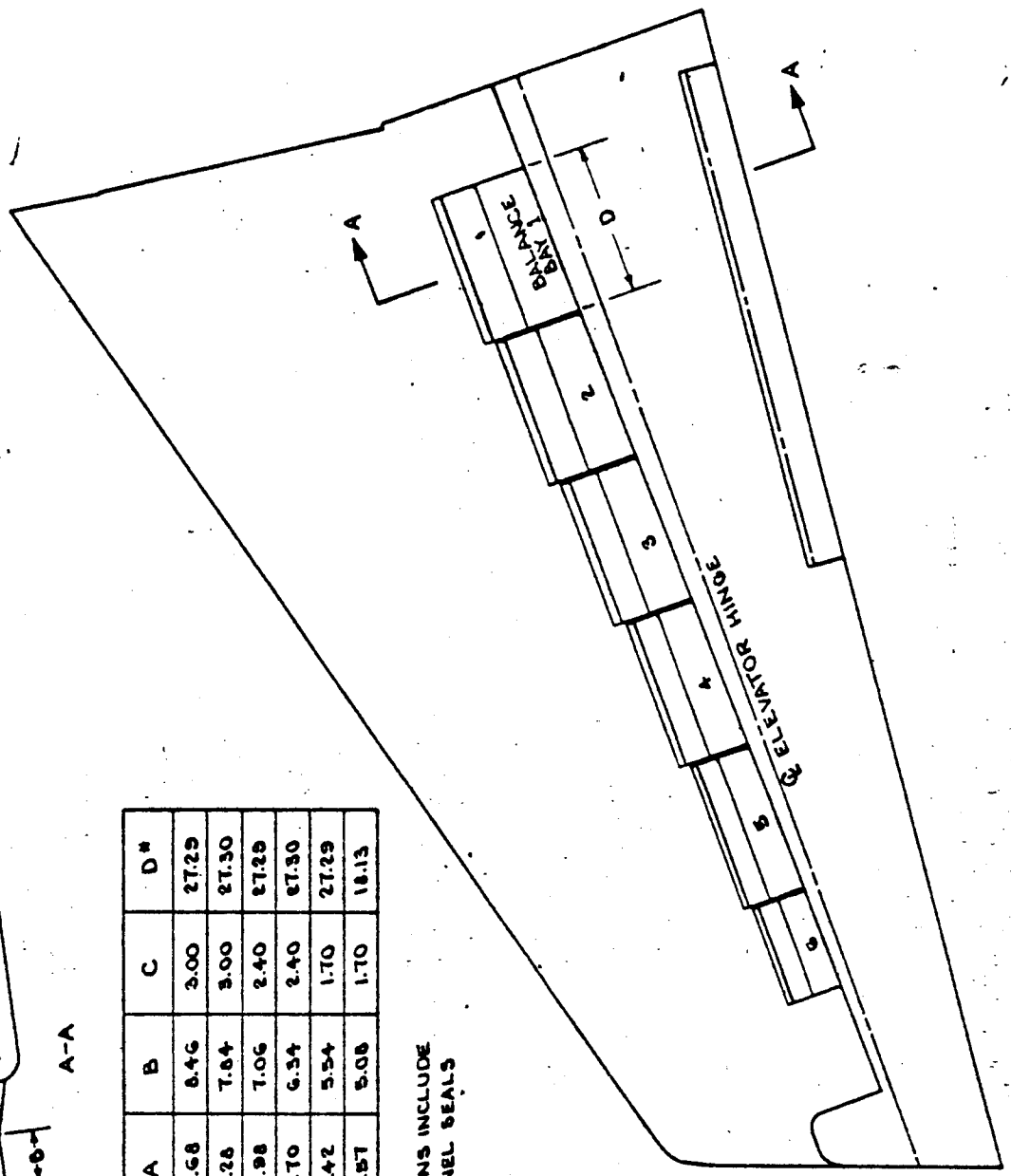

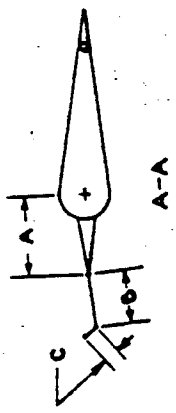

BAY NO.	A	B	C	D*
1	13.68	8.46	3.00	27.29
2	12.26	7.84	3.00	27.30
3	10.98	7.06	2.40	27.29
4	9.70	6.34	2.40	27.30
5	8.42	5.54	1.70	27.29
6	7.57	5.08	1.70	18.13

* "D" DIMENSIONS INCLUDE BALANCE PANEL SEALS

FIGURE 26

P8.43

ENGR.	MARSHALL	12-2-66	REVISED	DATE	ELEVATOR BALANCE PANEL GEOMETRY
CHECK	JACOBSON	12-12-66			
APR					
APR					

737-100

THE BOEING COMPANY
RENTON, WASHINGTON

PAGE

AD 1017-R6

6-7000

587 p3

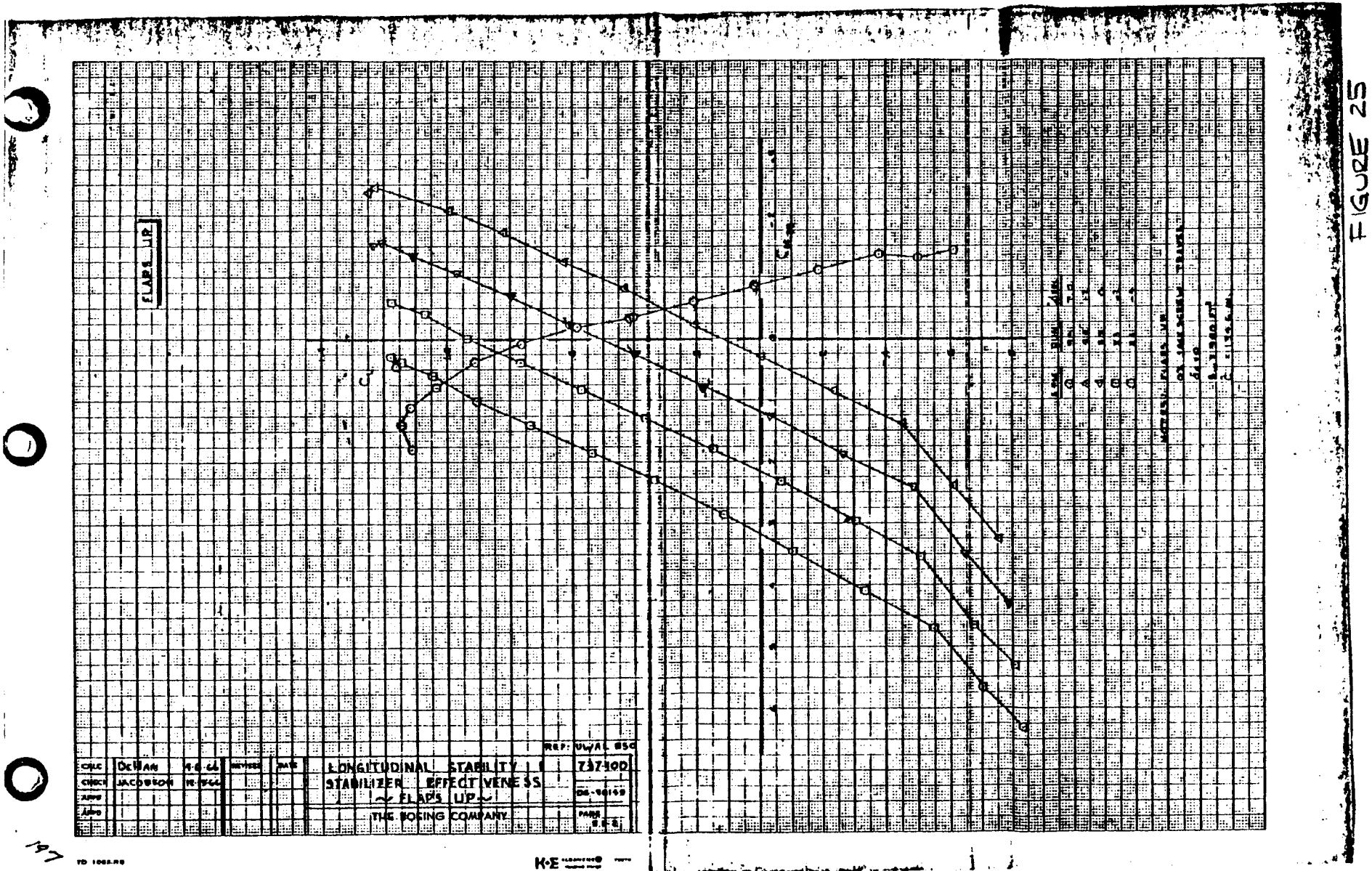

FIGURE 25
P8.44

589

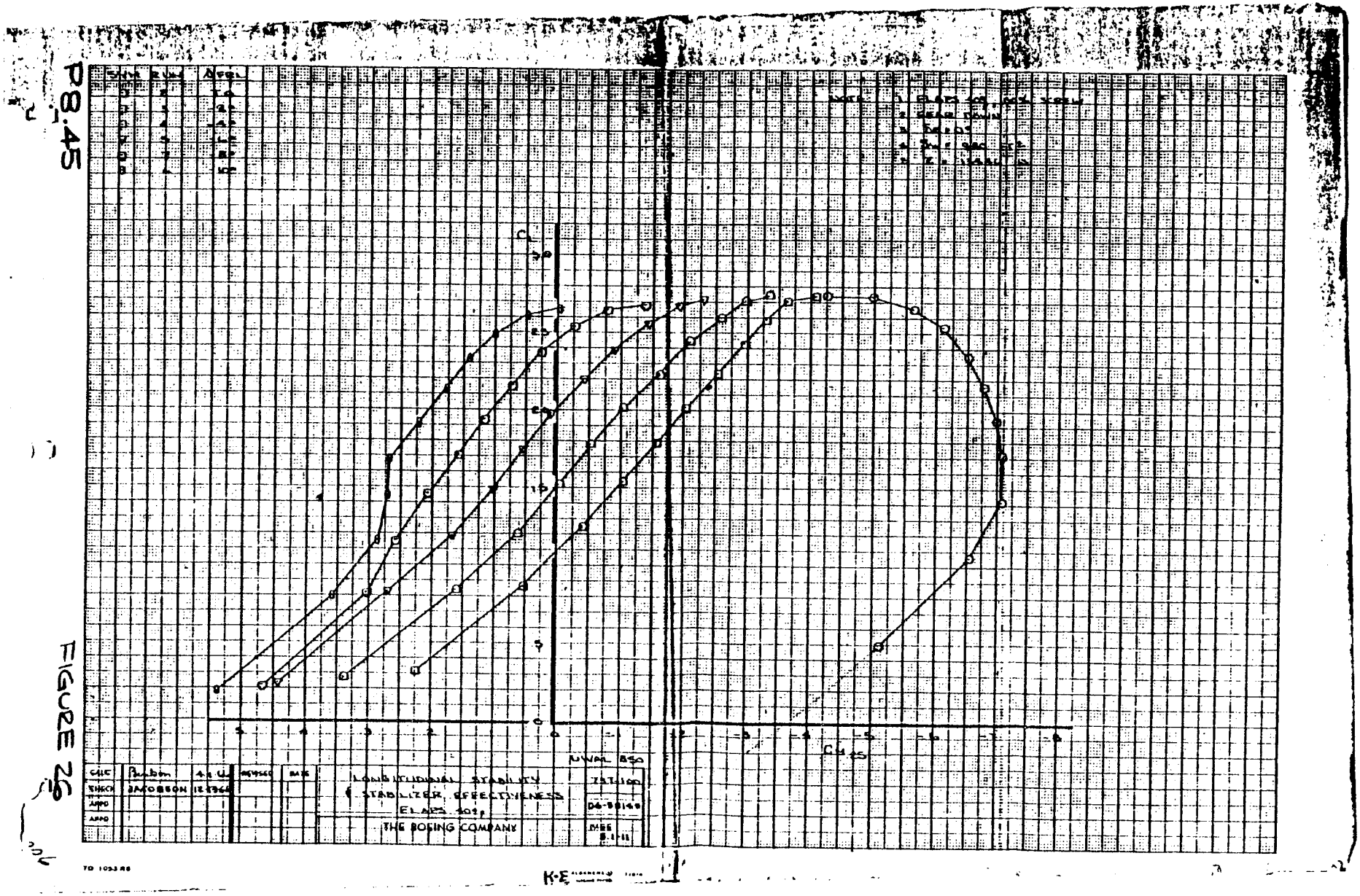

P8.45

FIGURE 26

590

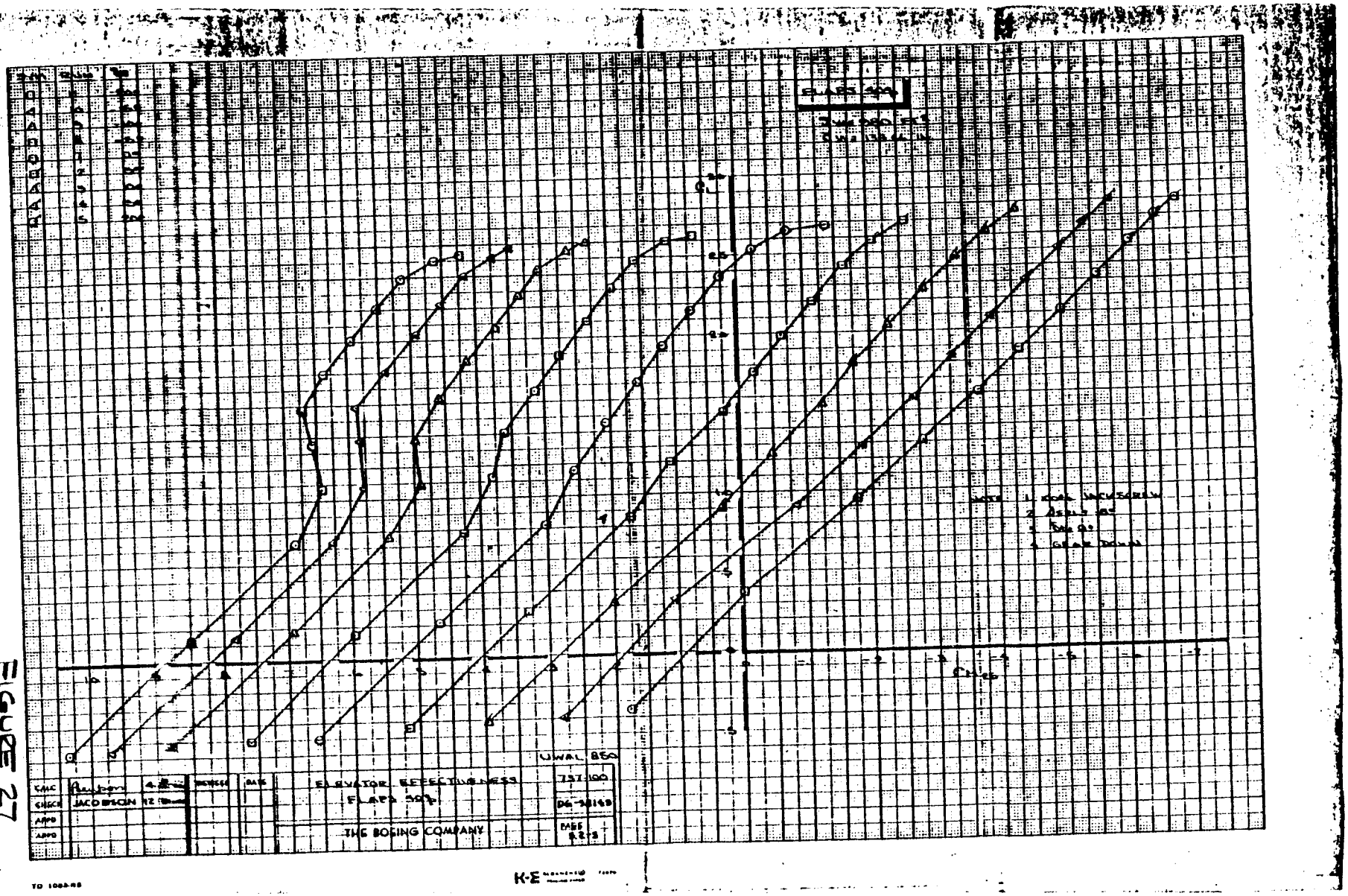

FIGURE 27
P8.46

591

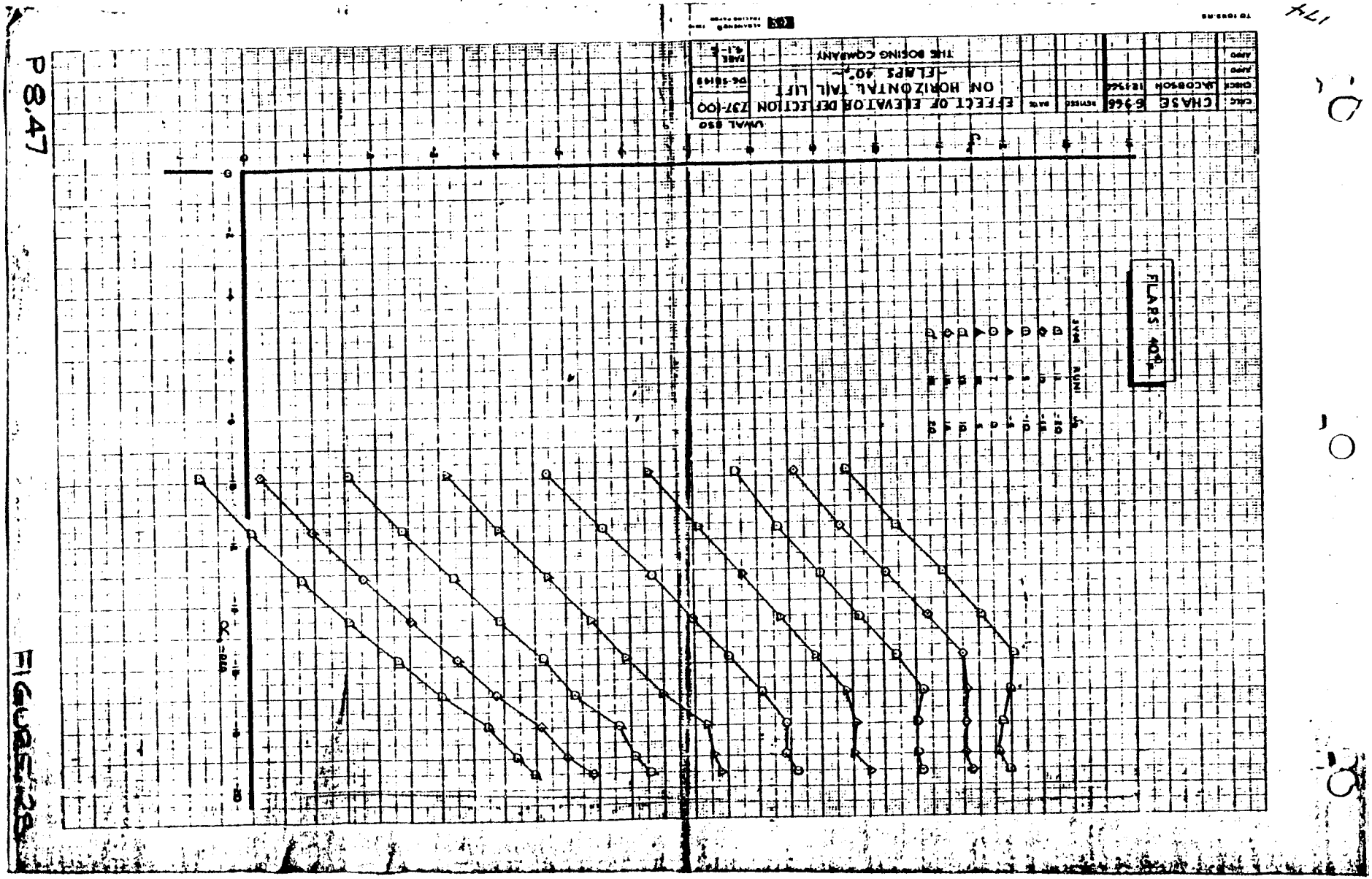

FIGURE 28

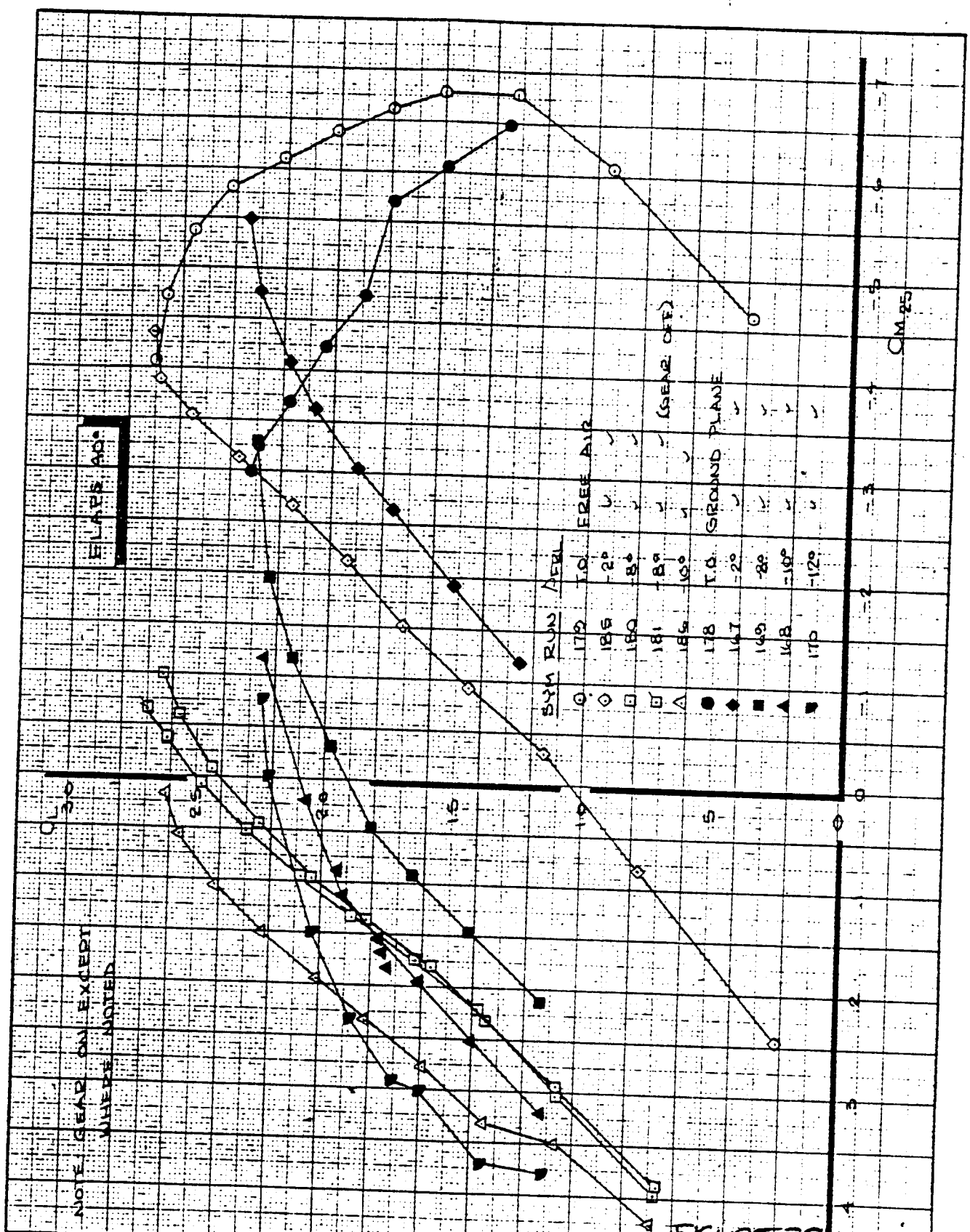

FIGURE 29

CALC	Benson	8-13-66	REVISED	DATE	LONGITUDINAL STABILITY AND STABILIZER EFFECTIVENESS FLAPS 40°	737-100
CHECK	JACOBSON	12-15-66				PB.48
APR					THE BOEING COMPANY	PAGE -
APR						

TD 461 C24

UWAL 8E6

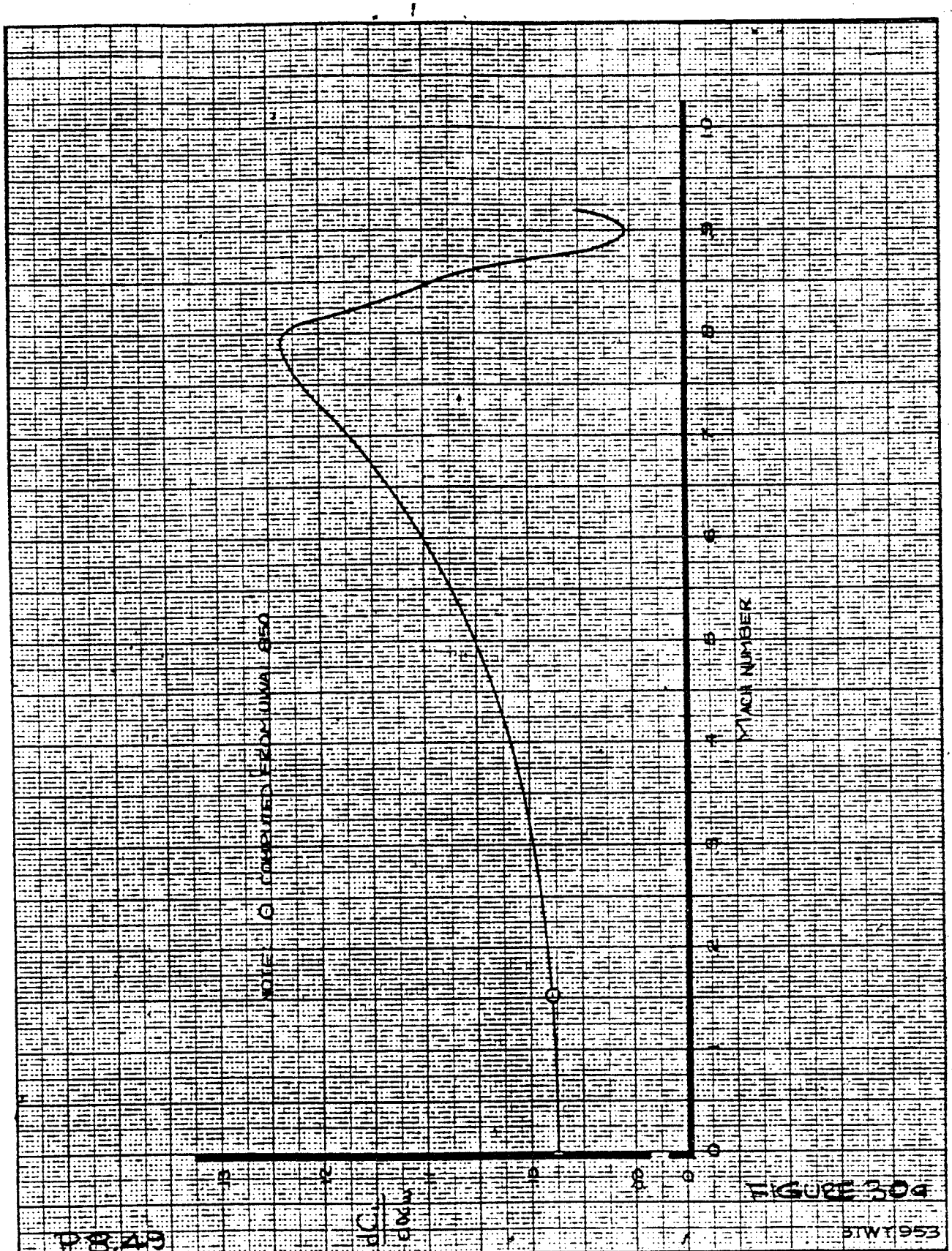

FIGURE 304

3IWT 953

P8.43

CALC	STEINHAUER	8-10-66	REVISED	DATE	EFFECT OF MACH NUMBER ON LIFT CURVE SLOPE TAIL ON
CHECK					
APR					THE BOEING COMPANY
APR					

737-100

PAGE

TD 461 C-R4

101

593

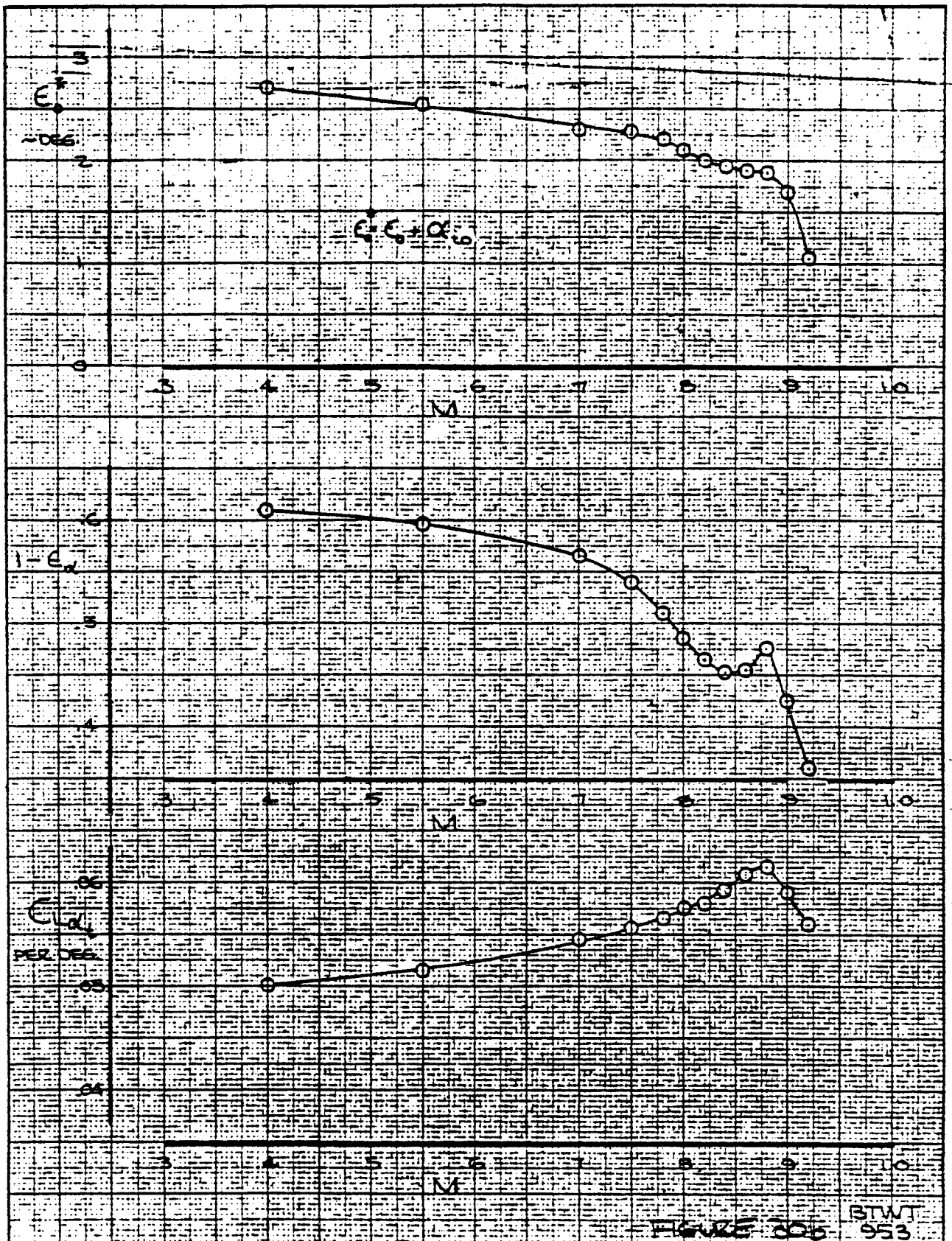

FIGURE 305

BTWT 953

CALC	JACOBSON	3/12/6	REVISED	DATE	DOWNWASH CHARACTERISTICS AND HORIZONTAL TAIL LIFT CURVE SLOPE	T37-100
CHECK						P8.50
APR						
APR					THE BOEING COMPANY	PAGE
INK	CHASE	3/12/66				

TD 461 C-R4

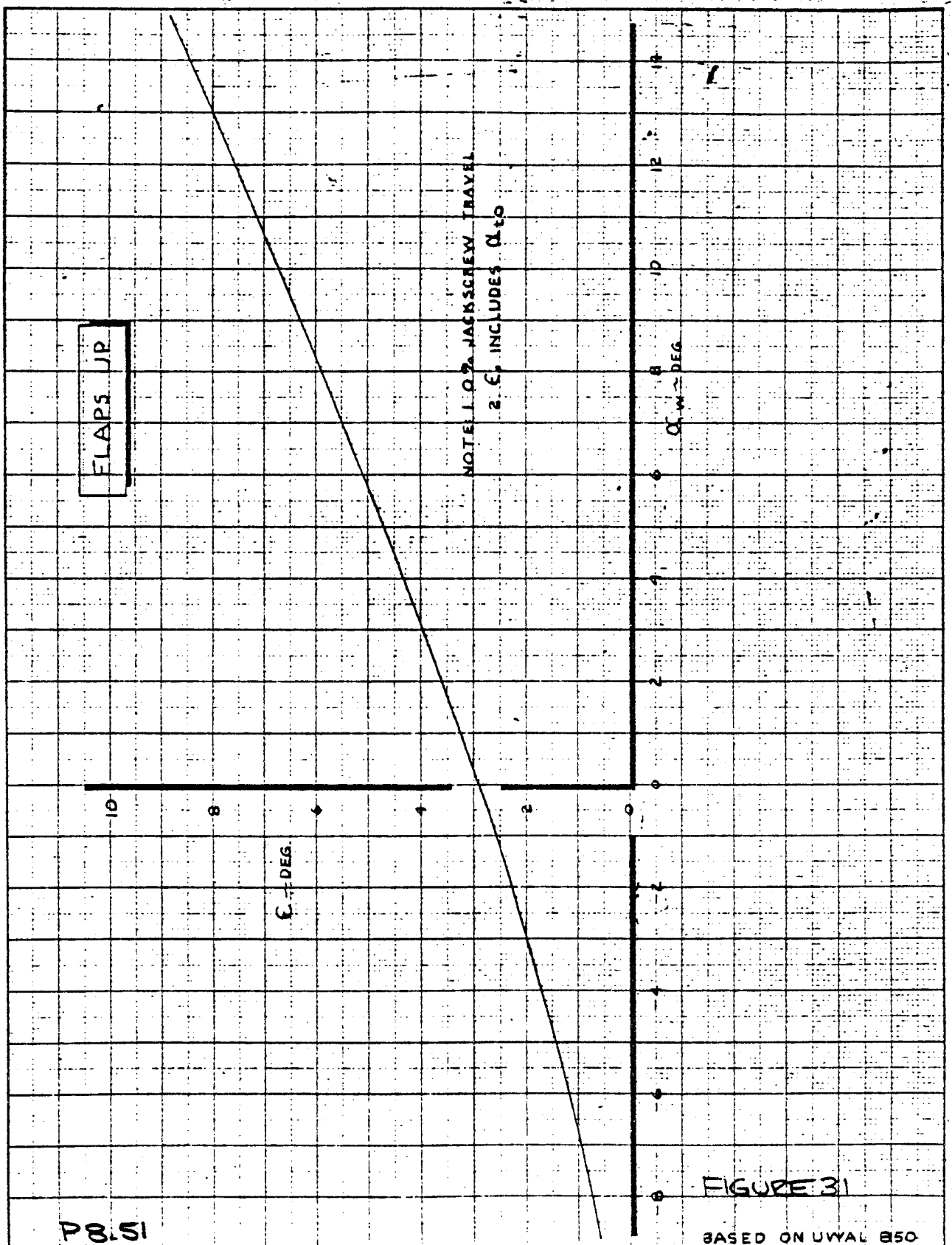

FIGURE 31

P8151

BASED ON UWAL 850

CALC	CHASE MARSHALL	7-27-66	REVISED	DATE	DOWNWASH AT HORIZONTAL TAIL ~FLAPS UP~ 737-100
CHECK	JACOBSON	12-13-66			
APR					
APR					THE BOEING COMPANY PAGE
INK	CHASE	7-27-66			

TD 461 C-84

595 178

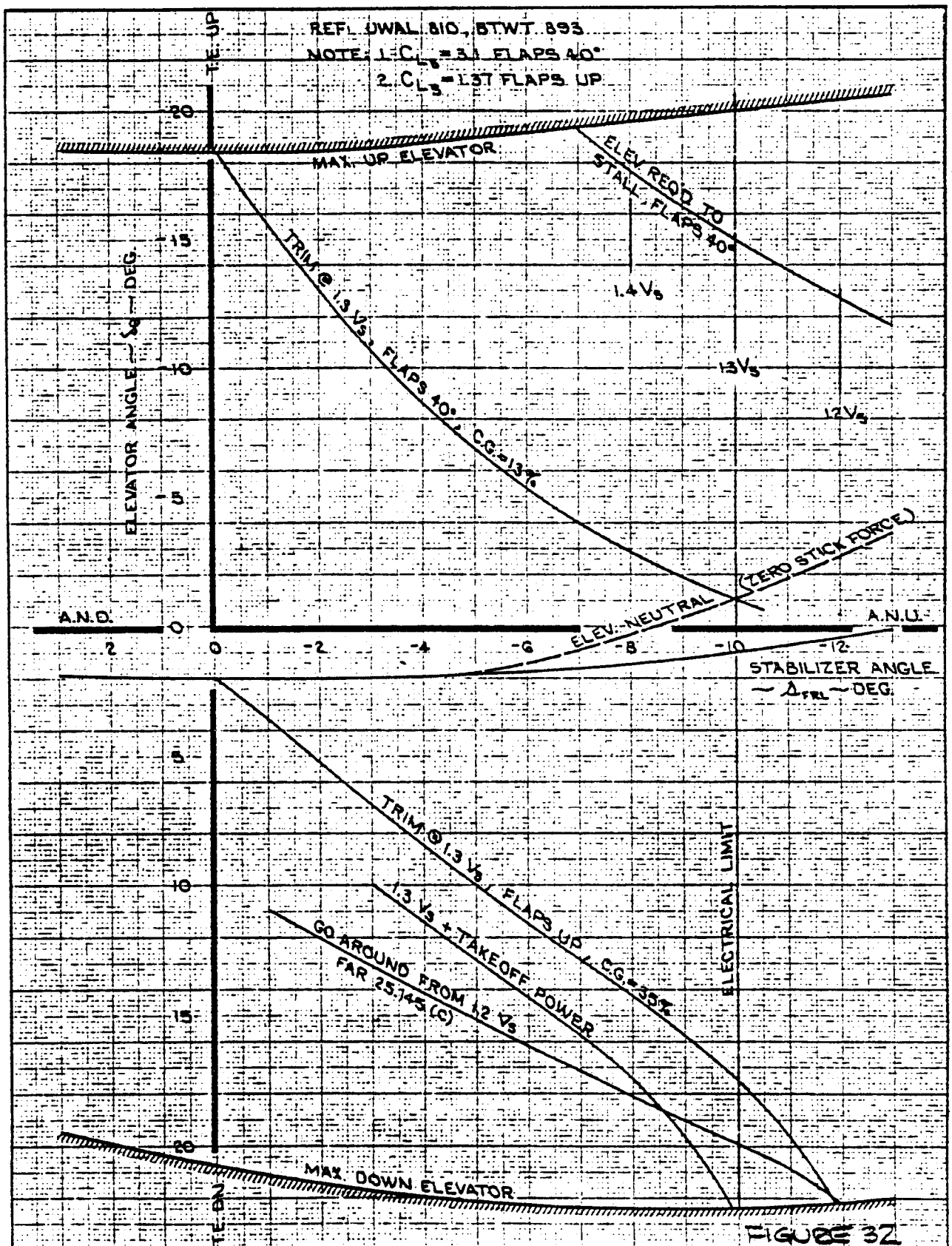

FIGURE 32

CALC	McINTOSH	6-7-65	REVISED	DATE	STABILIZER AND ELEVATOR TRIM AND STALL REQUIREMENTS	737
CHECK						P8.52
APR						
APR					THE BOEING COMPANY	PAGE
INK	MARSHALL	6-10-65				

596

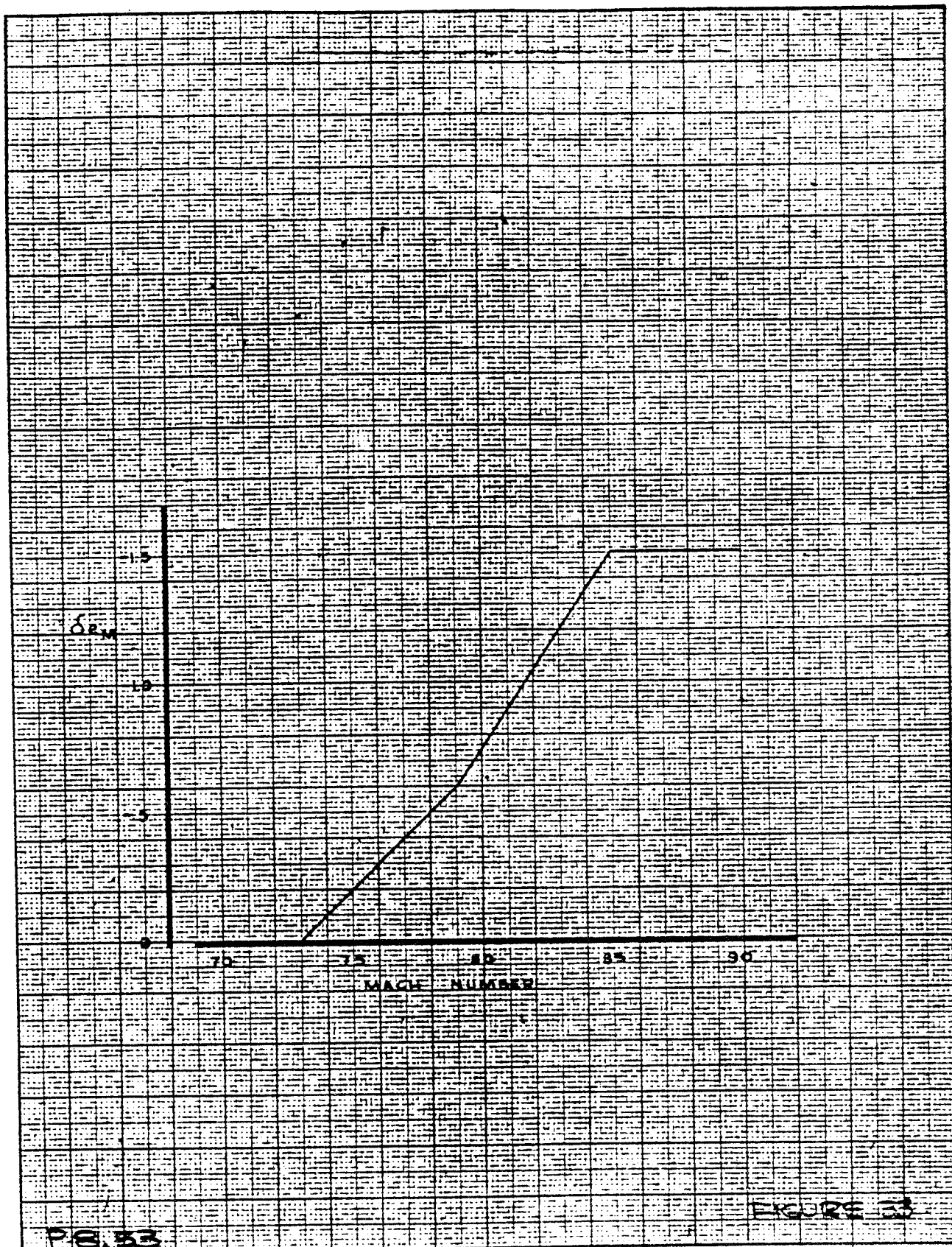

FIGURE 3.

P8.53

CALC	RUMSEY	3-4-66	REVISED	DATE	LONGITUDINAL CONTROL MACH TRIM PROGRAM — 737-100
CHECK					
APR					
APR					THE BOEING COMPANY — PAGE
INK	DEHAN	4-1-66			

TD 461 C-64

50

597

STATIC LATERAL DIRECTIONAL BALANCE

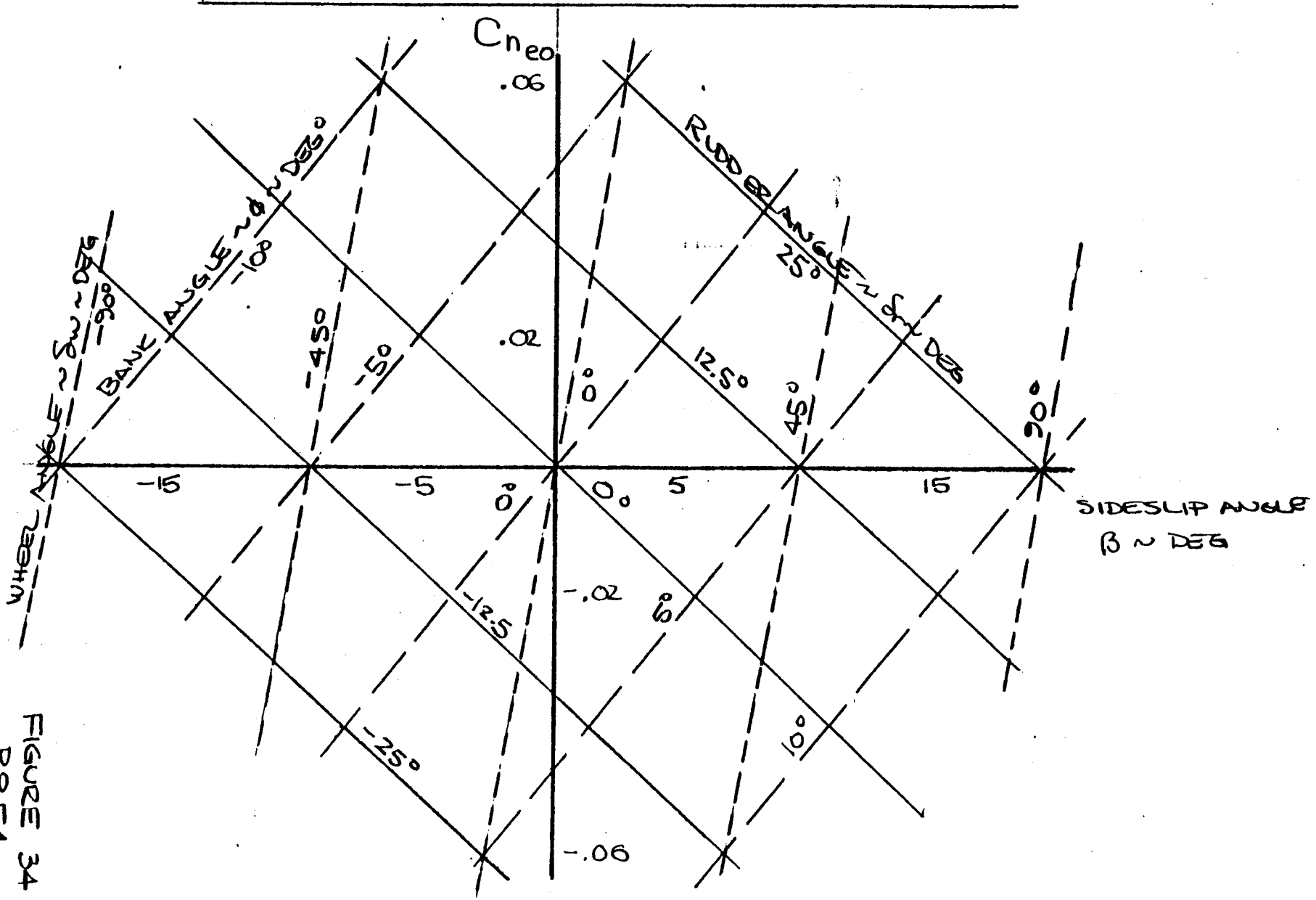

FIGURE 34
P8.54

DIRECTIONAL STABILITY

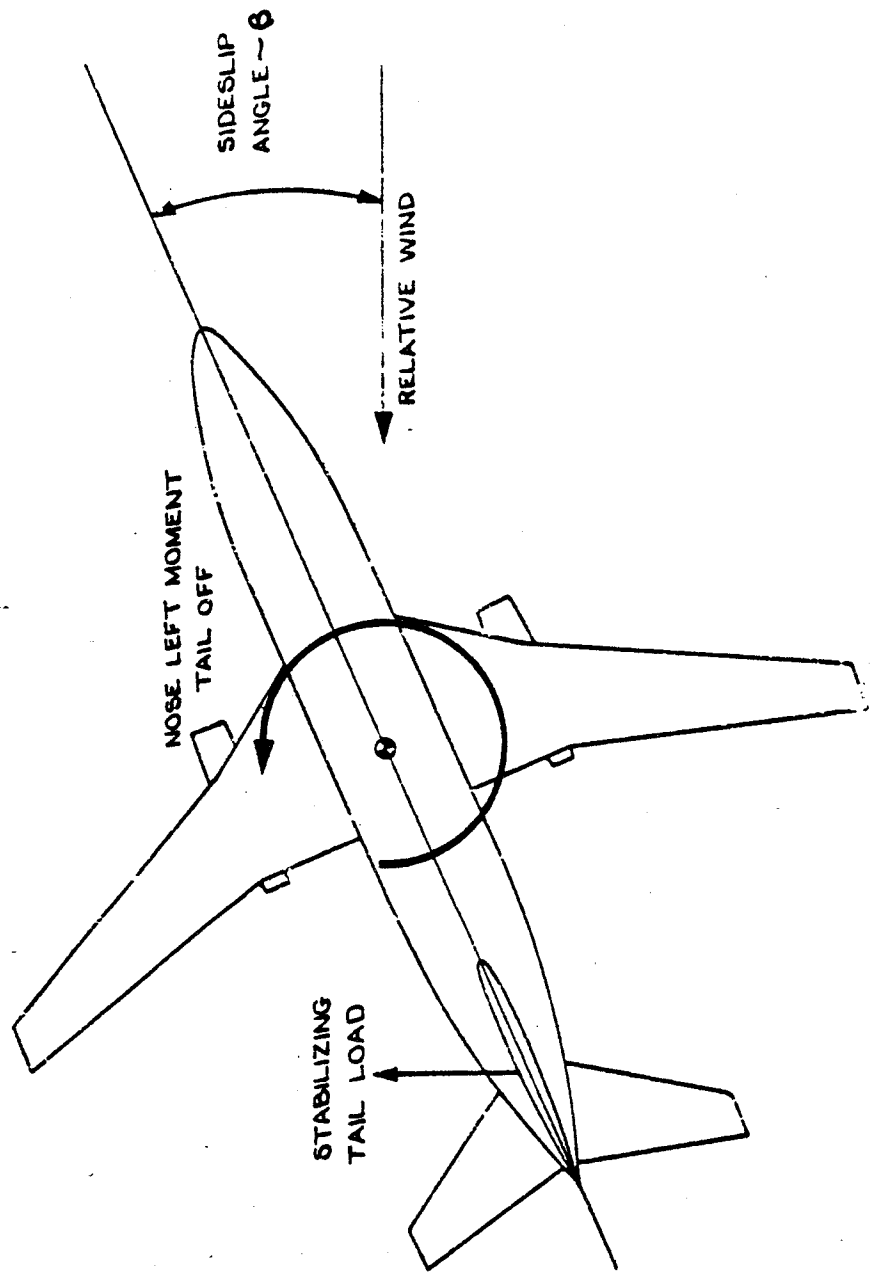

P 8.55

			REVISED	DATE	
ENGR.					FIGURE 35
CHECK					
APR					
APR					

THE BOEING COMPANY
RENTON, WASHINGTON

AD 1017-R8

8-7000

599

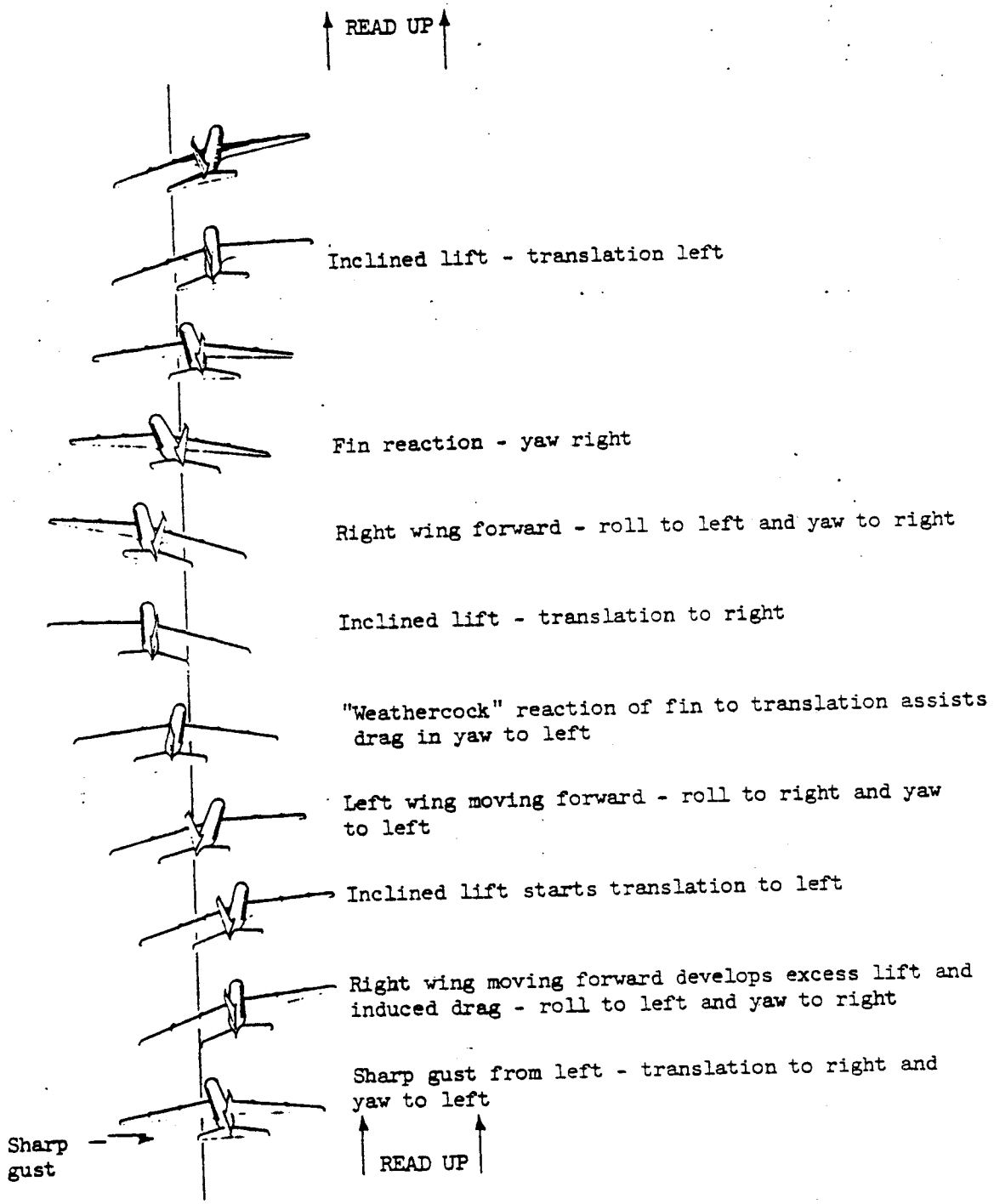

First cycle of a typical Dutch Roll development as viewed from aft and above the airplane.

FIGURE 36
P8.56

ENGINE OUT TAMENESS

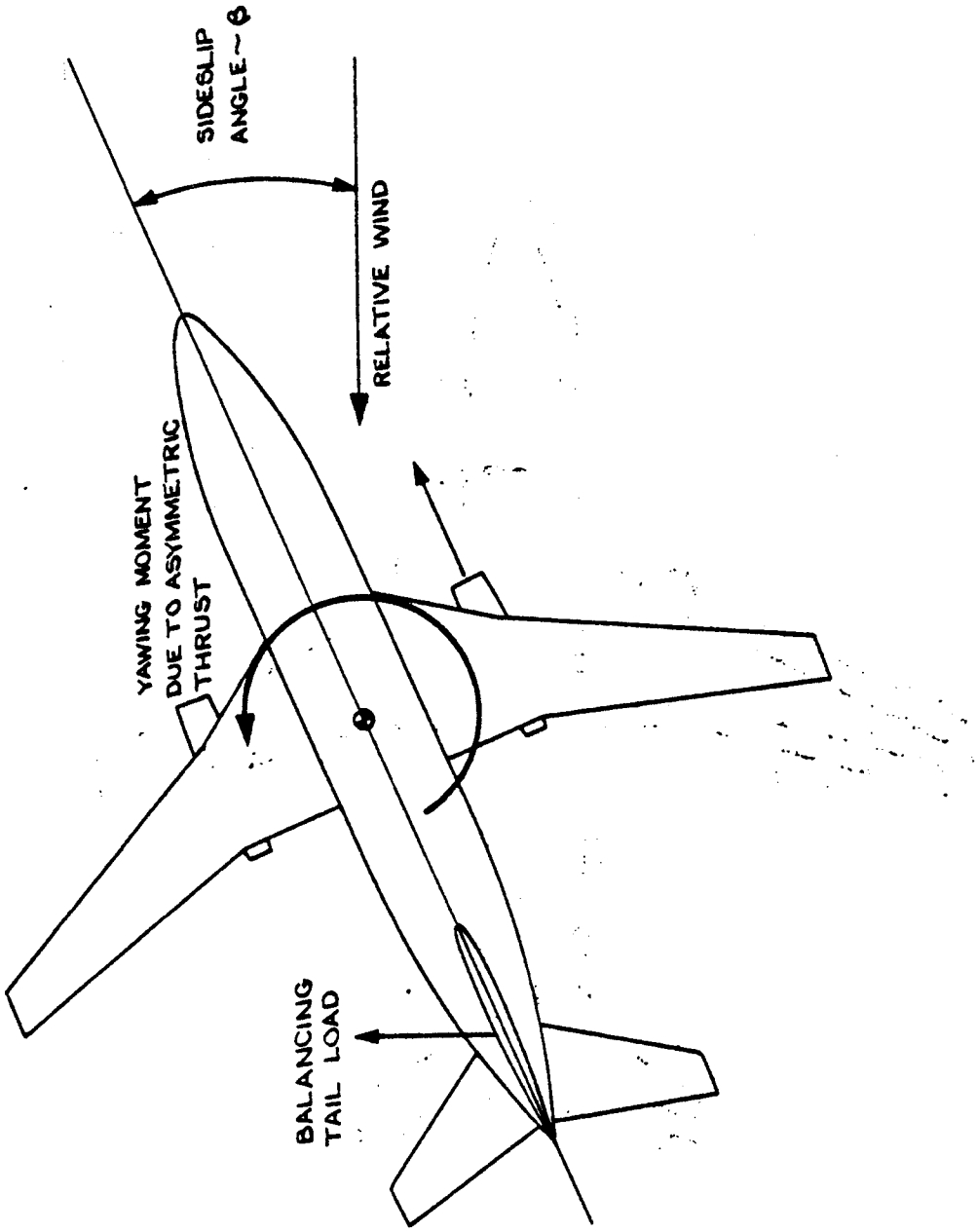

P 8.57

ENGR.			REVISED:	DATE		FIGURE 37
CHECK						
APR						
APR					THE BOEING COMPANY RENTON, WASHINGTON	

AD 1017-R6

6-7000

601 3

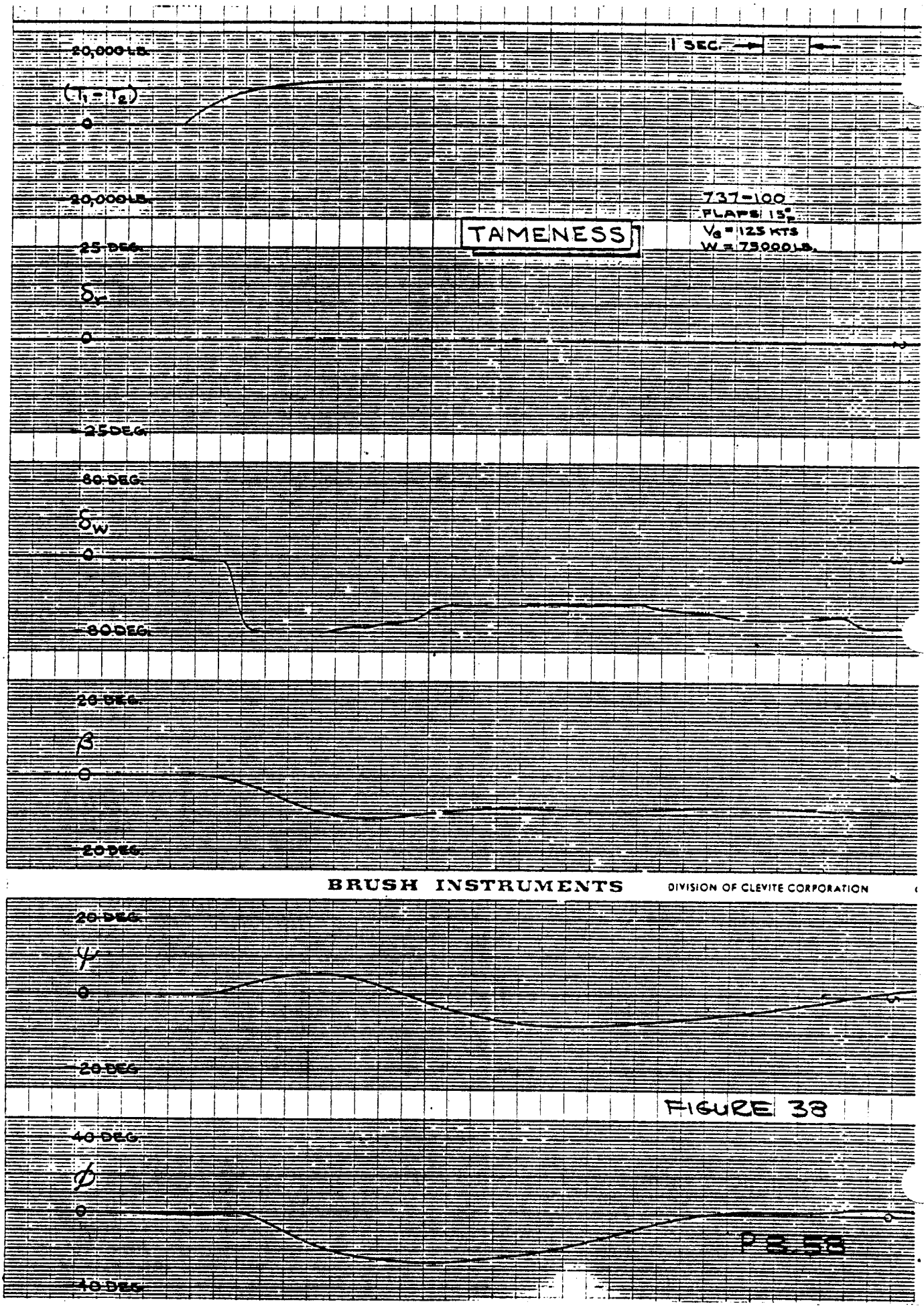

FIGURE 38

P8.58

602

CROSSWIND CAPABILITY

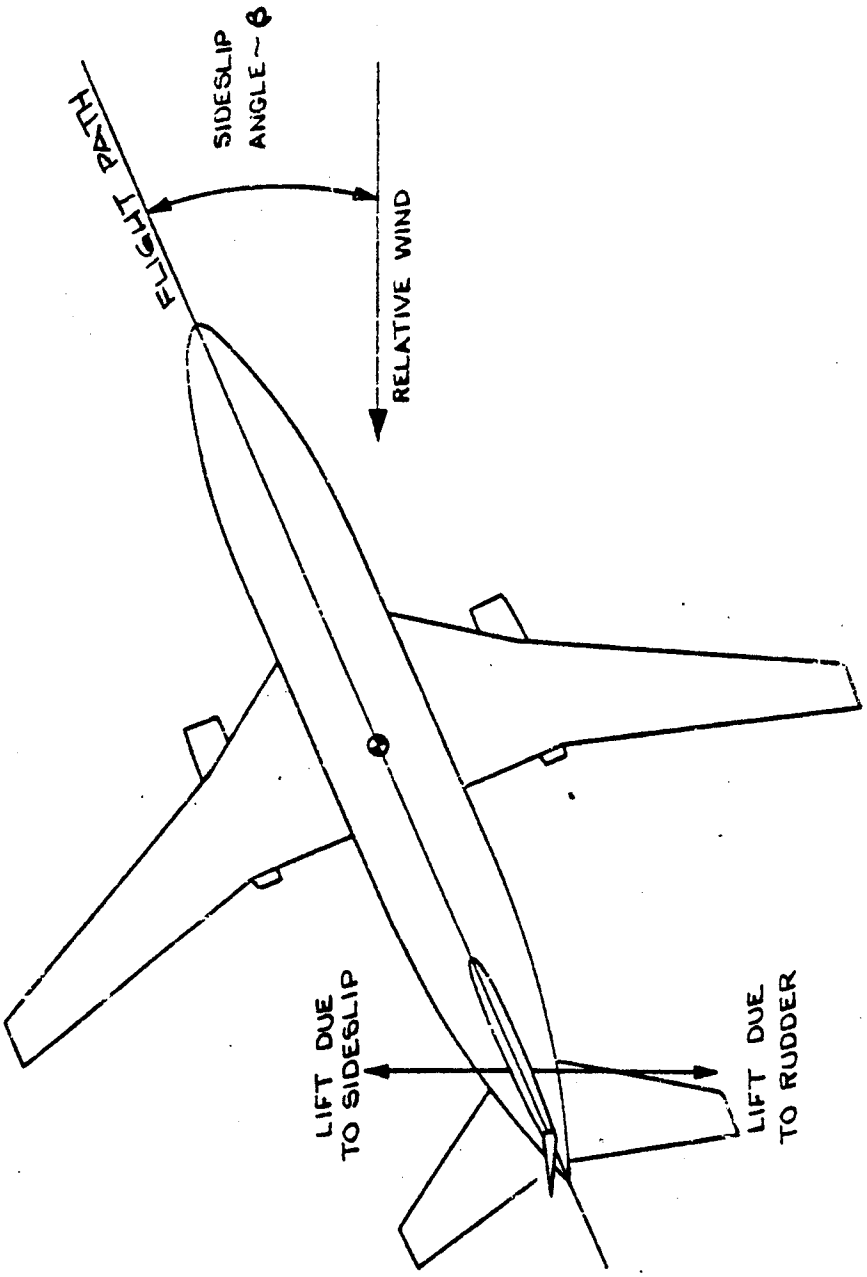

P 8.59

ENGR.			REVISED	DATE
CHECK				
APR				
APR				

THE BOEING COMPANY
RENTON, WASHINGTON

FIGURE 39

AD 1017-R6

6-7000

603 6

604

ENGINE OUT CONTROL

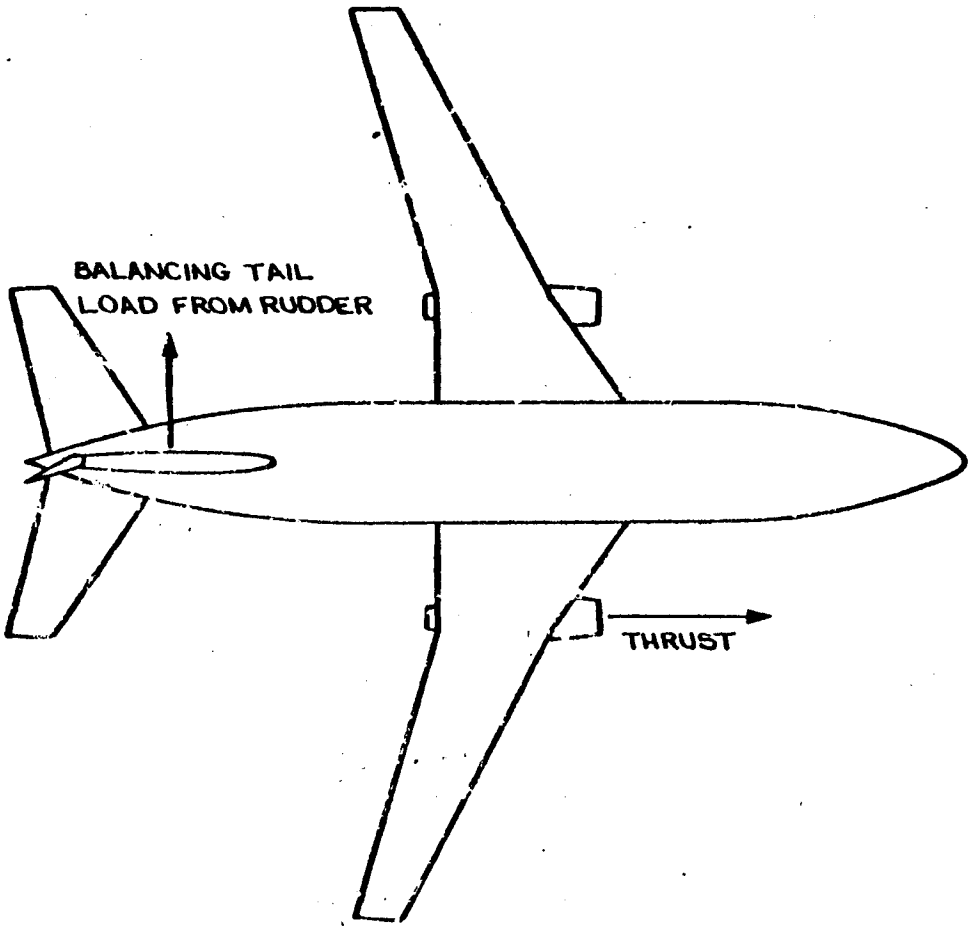

FIGURE 40

	CALC	CHECK	APPD	APPD
REVISED				
DATE				

THE BOEING COMPANY
RENTON, WASHINGTON

PAGE P8.60

TO 573 D-83

6-7000

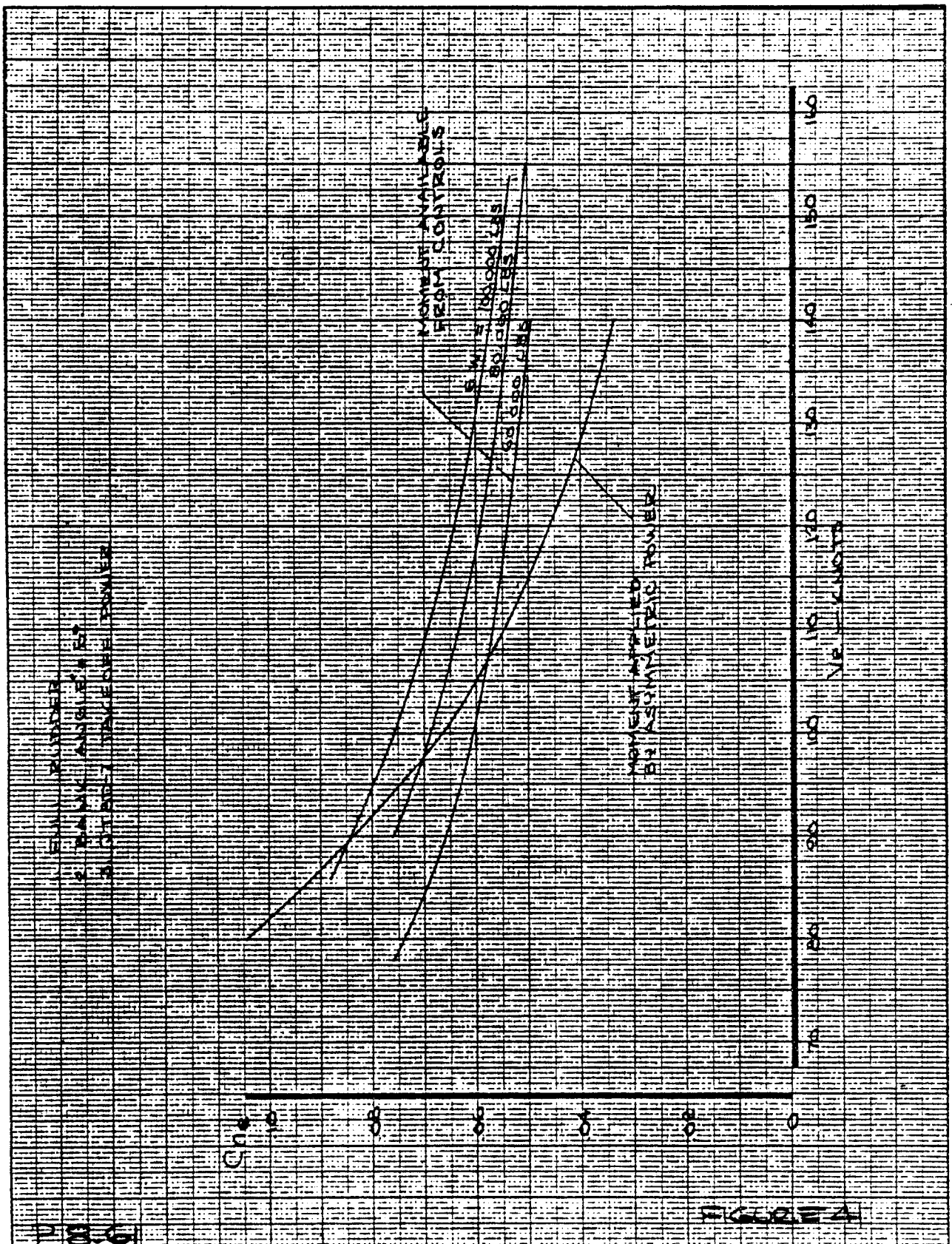

P 8-6

CALC	CUSHING	8.12.66	REVISED	DATE	FREE AIR ENGINE OUT CONTROL	737-100
CHECK						
APR						
APR					THE BOEING COMPANY	PAGE
INC	Benton	8.12.66				

TD 441 C-R4

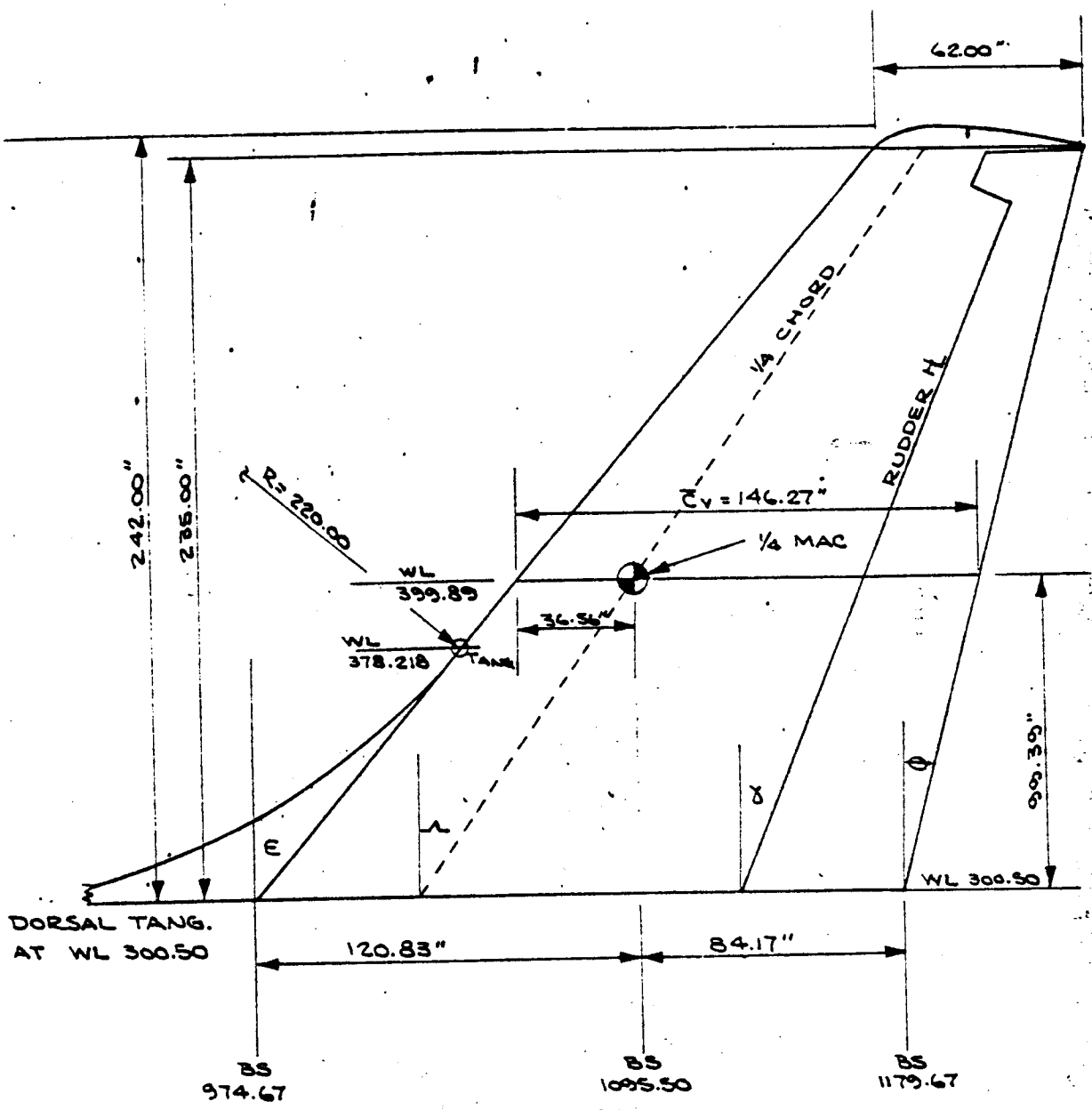

Λ = 35°
ϵ = 40° 17' 44"
θ = 14° 24' 52"
γ = 22° 2' 8"

S_V = 224.35 FT^2
AREA DOES NOT INCLUDE THE DORSAL FIN

FIGURE 42

REF: DWG. 65-73713

ENGR.	CUSHING	8-2-66	REVISED	DATE	VERTICAL STABILIZER GEOMETRY	737-100
CHECK						P3.62
APR						
APR					THE BOEING COMPANY RENTON, WASHINGTON	PAGE
INK	BENTSON	8-3-66				

AD 1017-66

6-7000

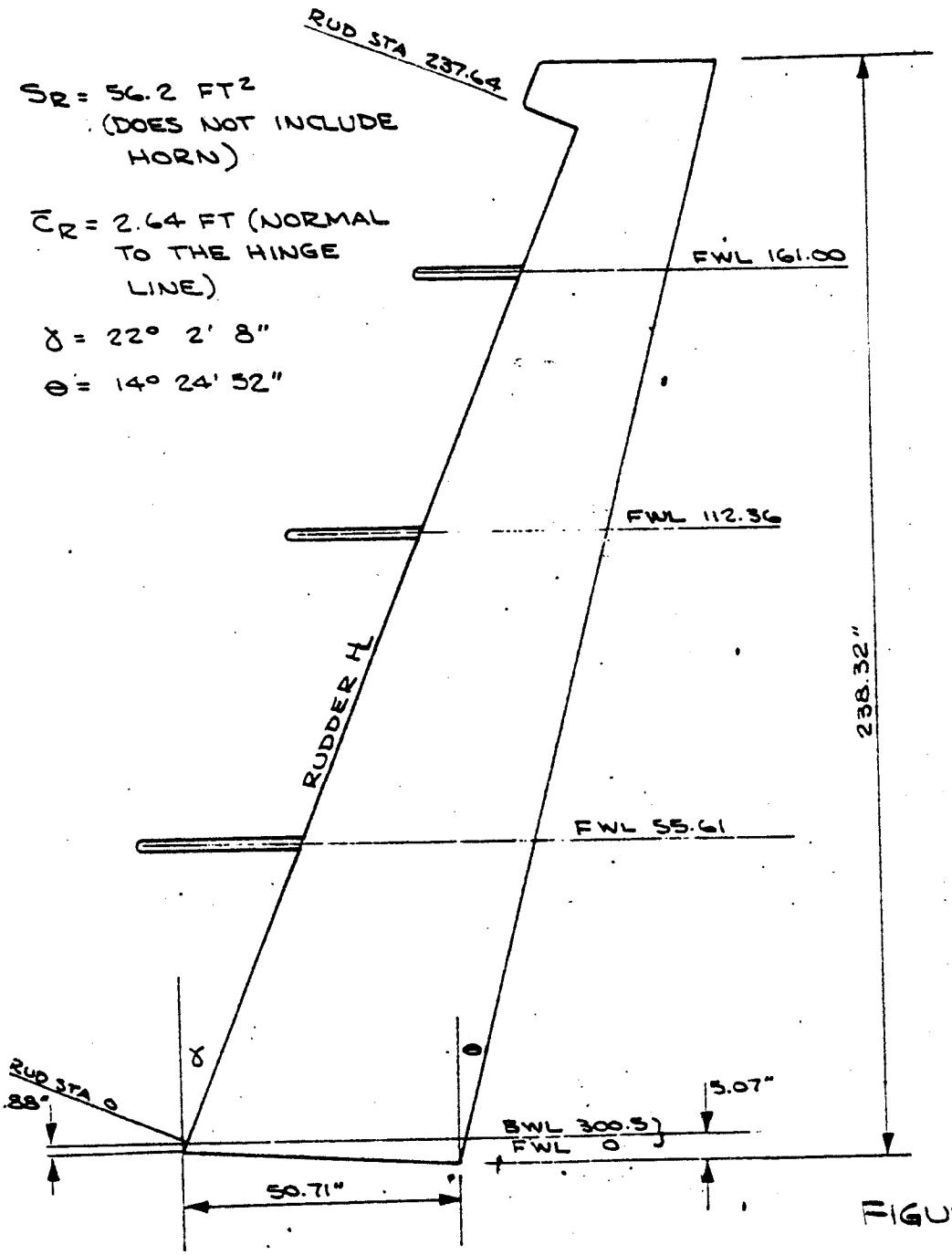

FIGURE 43

REF: DWG. 65-73713

P8.63

ENGR.	CUSHING	8.2.66	REVISED	DATE	RUDDER GEOMETRY	737-100
CHECK						
APR						
APR					THE BOEING COMPANY RENTON, WASHINGTON	PAGE
INK	BENTSON	8.3.66				

AD 1017-R6

607

FLAPS 40°

$C_{L_{\beta=0}} = 1.938$

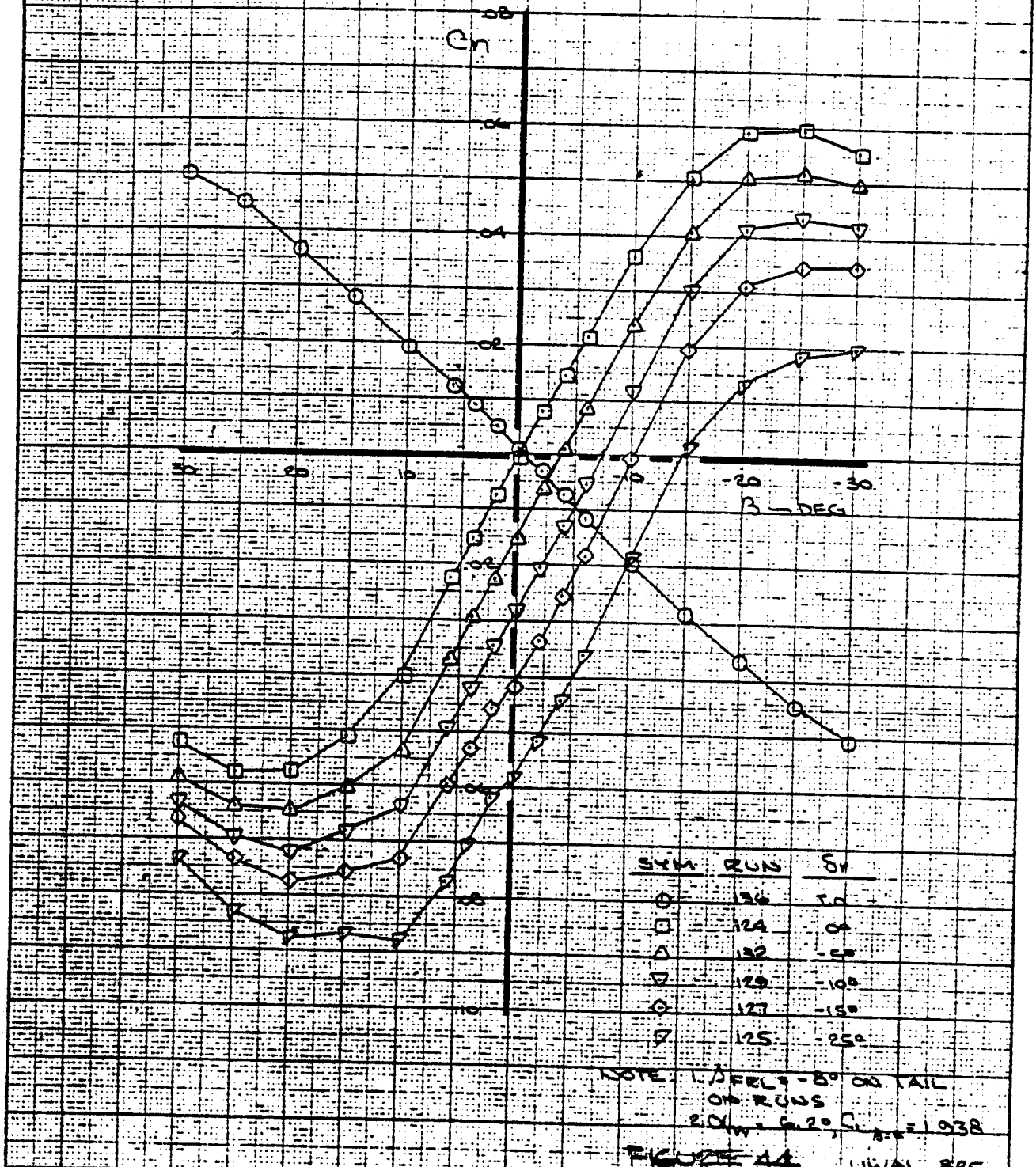

SYM	RUN	δ_W
○	126	T.O.
□	124	0°
△	132	-5°
▽	129	-10°
◇	127	-15°
▽	125	-25°

NOTE: 1. $\beta_{FEL} = -8°$ ON TAIL ON RUNS

2. $\alpha_W = 6.2°$, $C_{L_{\beta=0}} = 1.938$

FIGURE 44 UWAL 825

CALC	Benton	10.17.5	REVISED	DATE	YAWING MOMENT DUE TO RUDDER IN SIDESLIP FLAPS 40° $\alpha_W = 6.2°$	737-100
CHECK	Cushing	12/14/66				P8.64
APR					THE BOEING COMPANY	PAGE
APR						

TD 461 C-64

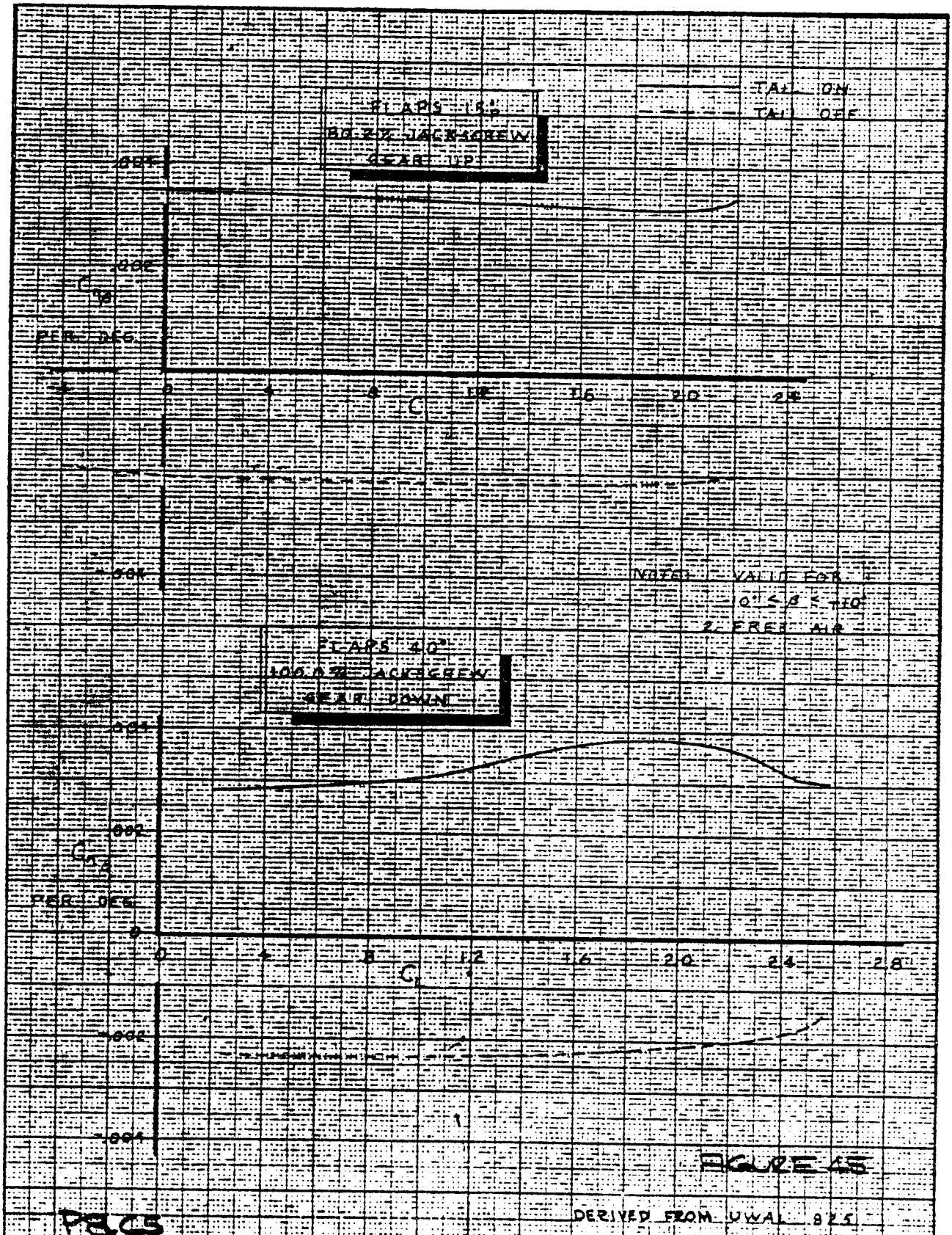

FIGURE 45

DERIVED FROM UWAL 825

CALC	KRAFT	8/10/66	REVISED	DATE	YAWING MOMENT DUE TO SIDESLIP	737-100
CHECK						
APR						
APR					THE BOEING COMPANY	PAGE

TD 461 C-88

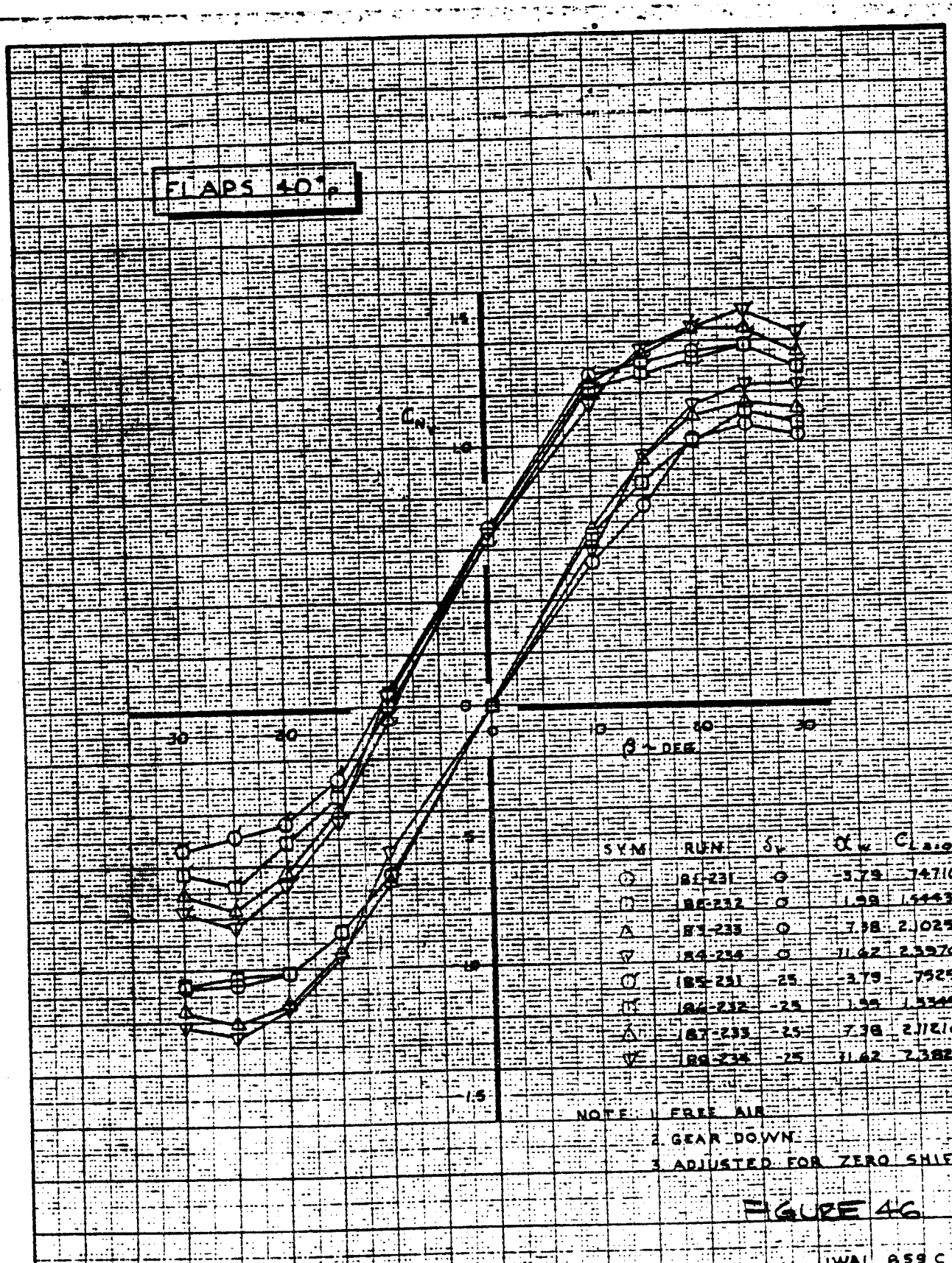

SYM	RUN	δ_w	α_w	$C_{L_{\alpha_w}}$
○	181-231	0	-3.79	.74716
□	182-232	0	1.99	1.54431
△	183-233	0	7.38	2.10253
▽	184-234	0	11.62	2.39705
◐	185-231	-25	-3.79	.75251
◧	186-232	-25	1.99	1.53492
◭	187-233	-25	7.38	2.11214
▼	188-234	-25	11.62	2.38267

NOTE: 1. FREE AIR
2. GEAR DOWN
3. ADJUSTED FOR ZERO SHIFT

FIGURE 46

JWAL 859 C

CALC	KRAFT	8-7-66	REVISED	DATE	EFFECT OF ALPHA ON VERTICAL FIN NORMAL FORCE AND RUDDER POWER ~FLAPS 40°F~	737-100
CHECK						P&66
APR						
APR					THE BOEING COMPANY	PAGE
INK	CHASE	8-10-66				

TD 441 C-24

$$\Delta C_{n_V} = \left[C_{L_{\alpha_V}} (1 - d\sigma/d\beta)\, \beta \right] \bar{V}_V$$

$\bar{V}_V = .0891$

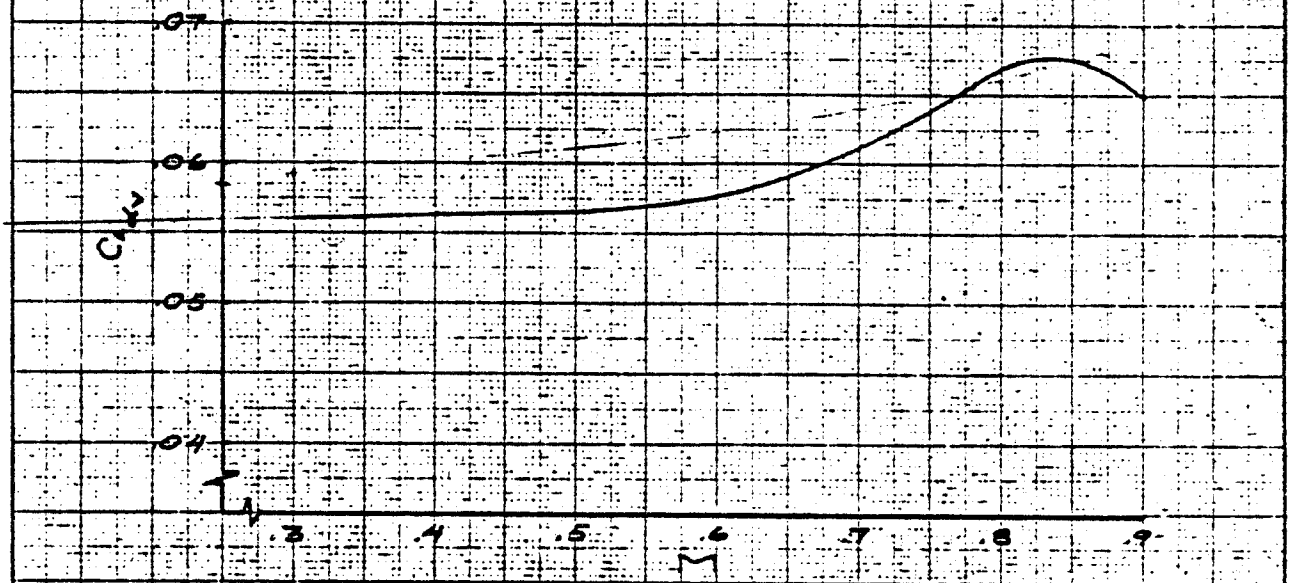

NOTE: THE ABOVE $C_{L_{\alpha_V}}$ TO BE USED WITH THE APPROPRIATE $(1 - d\sigma/d\beta)$ COMPUTED FROM BTWT 926

DERIVED FROM BTWT 926

P8.67

FIGURE 47

CALC	Cushing	12/17/65	REVISED	DATE	VERTICAL STABILIZER LIFT CURVE SLOPE	737-100
CHECK						
APR						
APR					THE BOEING COMPANY	PAGE

TD 461 C-86

6/11 192

LATERAL CONTROL - RATE CONTROL

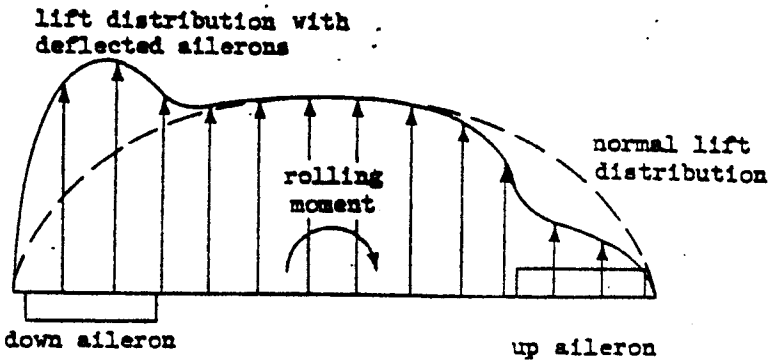

a

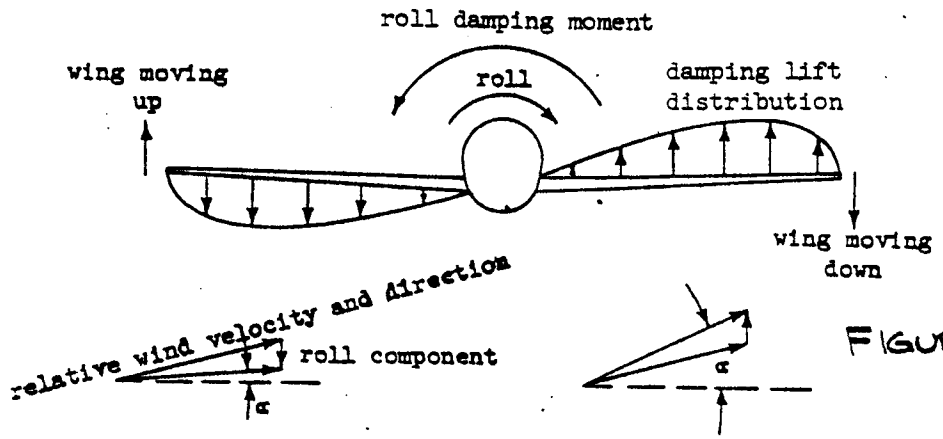

FIGURE 48

b

AILERON REVERSAL

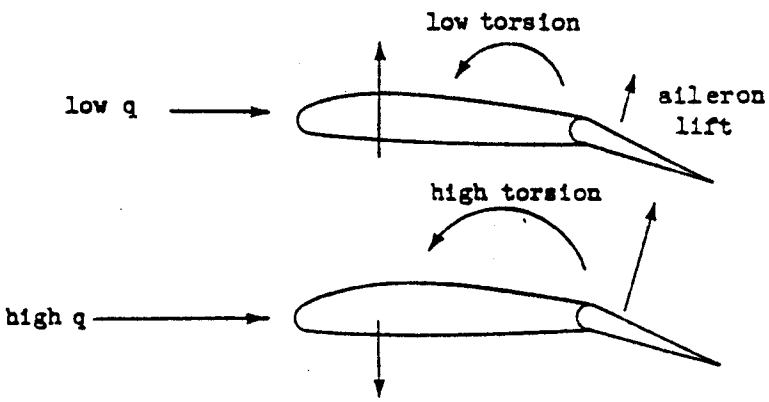

FIGURE 49
P8.68

6/8

ENGINE OUT TAMENESS

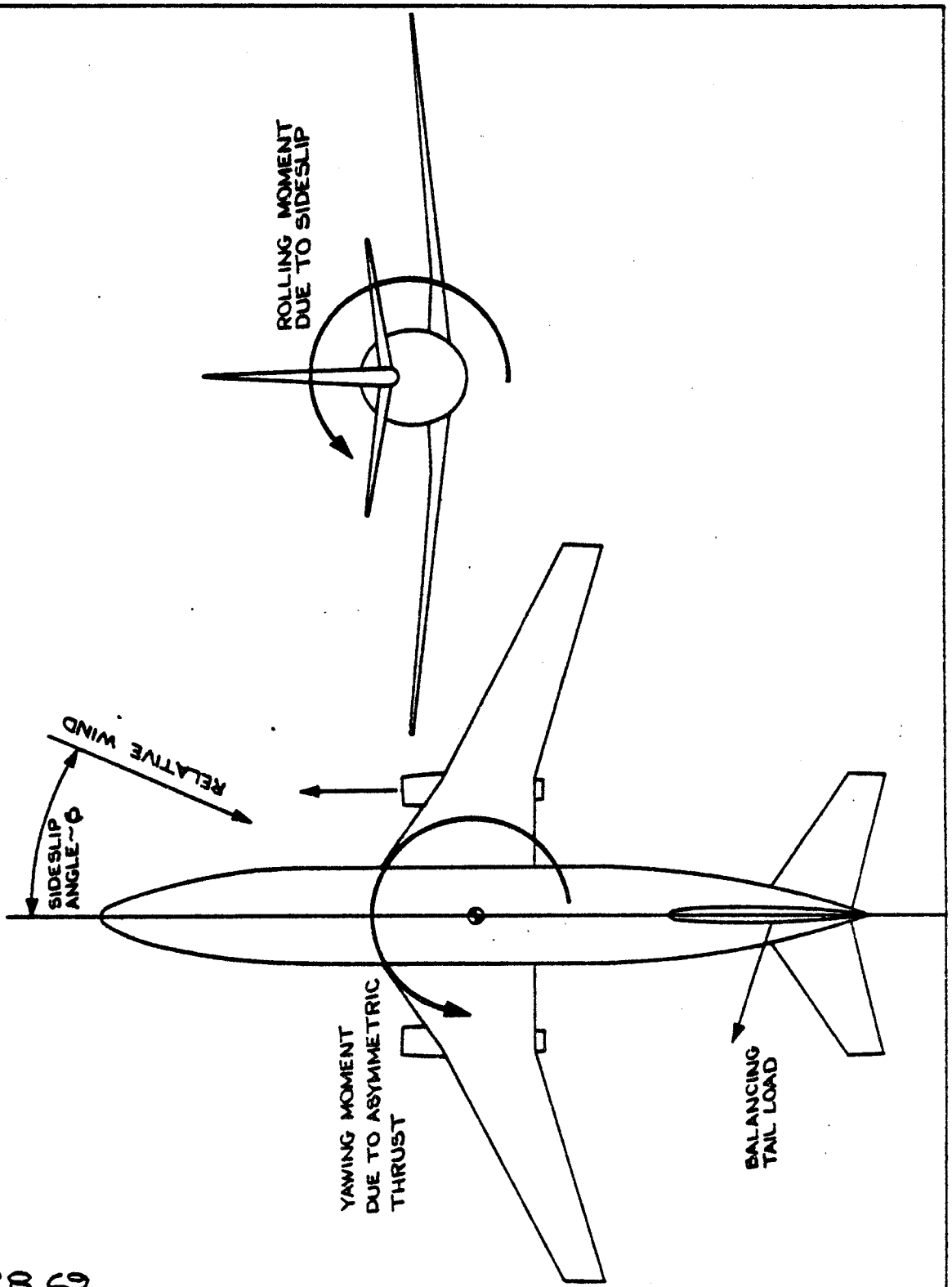

P8.69

ENGR.			REVISED	DATE	FIGURE 50
CHECK					
APR					
APR					

THE BOEING COMPANY
RENTON, WASHINGTON

AD 1017-R8

6-7000

613
9

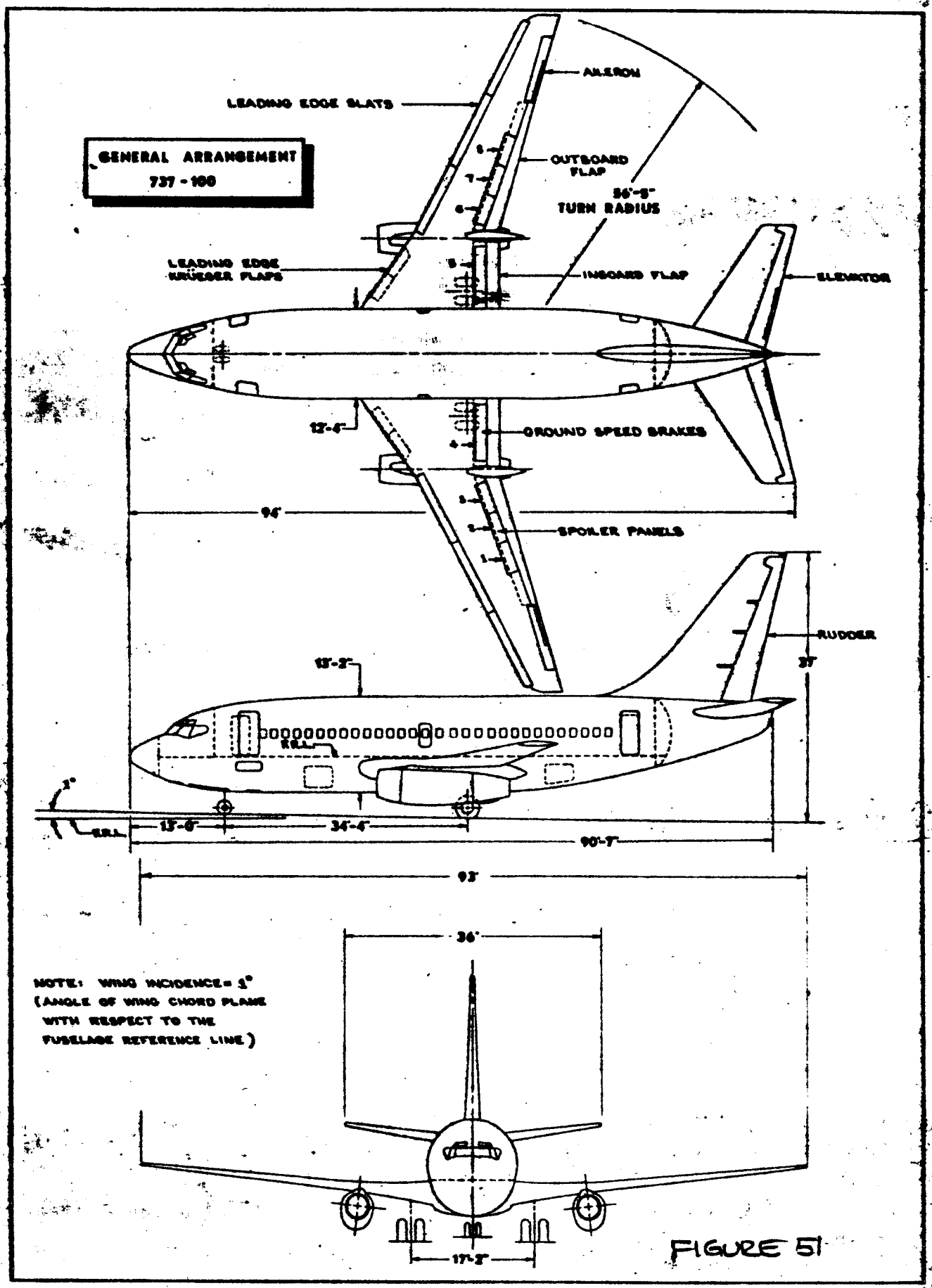
GENERAL ARRANGEMENT
737 - 100
LEADING EDGE SLATS
AILERON
OUTBOARD FLAP
36'-8"
TURN RADIUS
LEADING EDGE KRUEGER FLAPS
INBOARD FLAP
ELEVATOR
12'-6"
GROUND SPEED BRAKES
94'
SPOILER PANELS
RUDDER
37'
15'-2"
3°
13'-6"
34'-4"
90'-7"
93'
36'
NOTE: WING INCIDENCE = 1°
(ANGLE OF WING CHORD PLANE
WITH RESPECT TO THE
FUSELAGE REFERENCE LINE)
17'-2"

FIGURE 51

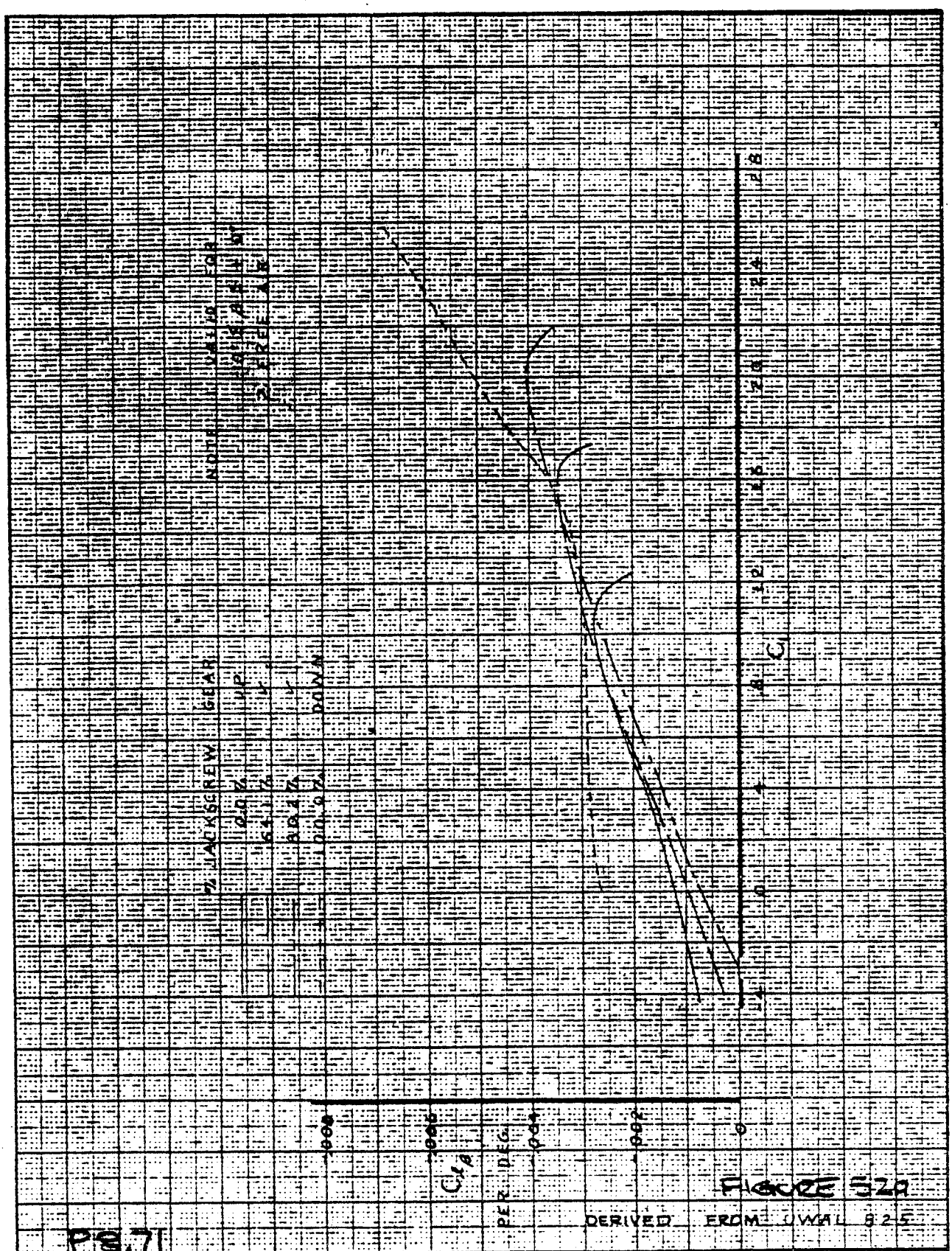

FIGURE 329

DERIVED FROM UWAL 8-2-5

P871

CALC	KRAFT	8/10/64	REVISED	DATE	ROLLING MOMENT DUE TO SIDESLIP ~ TAIL OFF ~	737-100
CHECK						
APR						
APR					THE BOEING COMPANY	PAGE

TD 441 C-64

H13

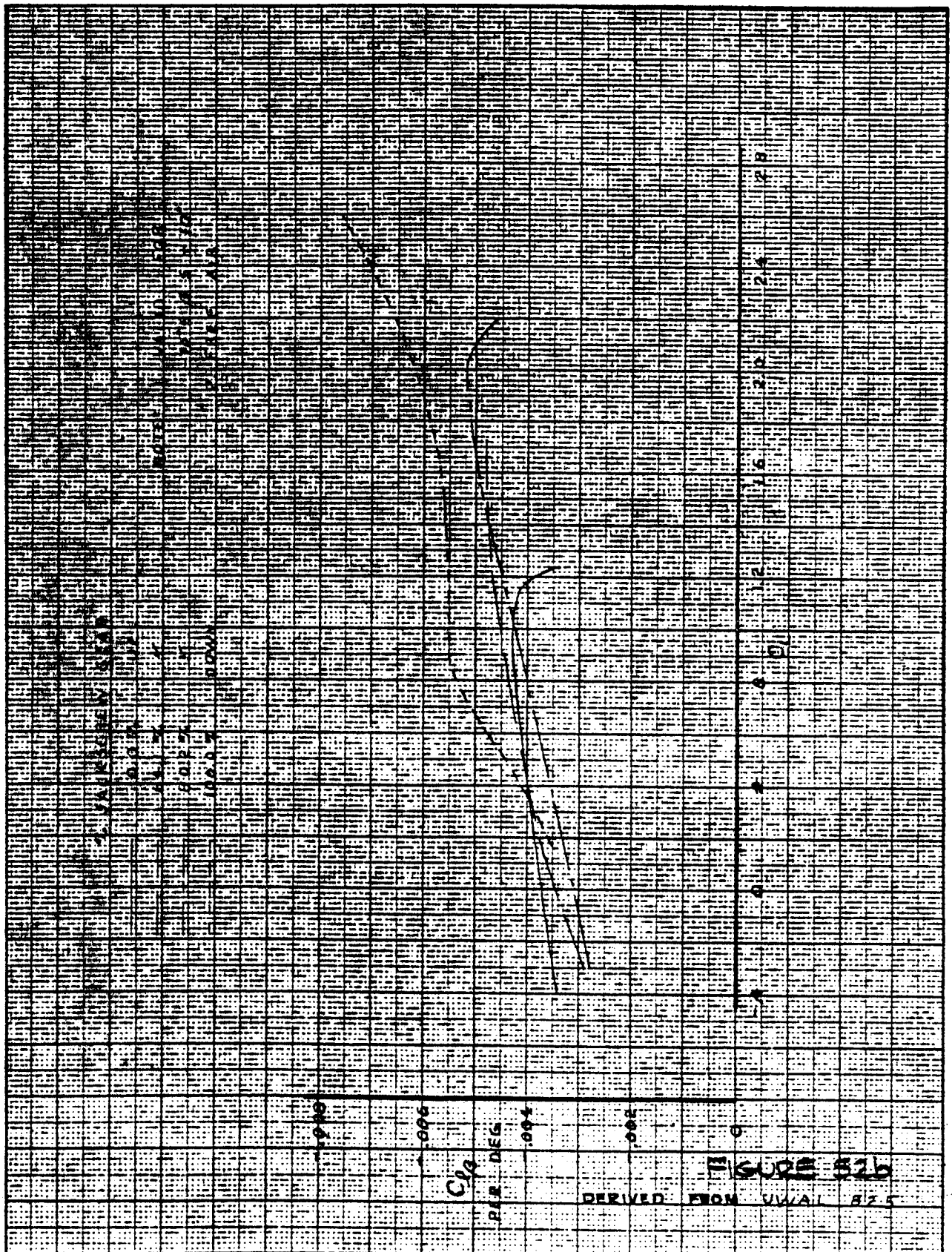

FIGURE 32b

DERIVED FROM USAF DATCOM

CALC	KRAFT	8/8/66	REVISED	DATE	ROLLING MOMENT DUE TO SIDESLIP ~ TAIL ON ~	737-100
CHECK						P 8.72
APR					THE BOEING COMPANY	PAGE
APR						

TD 461 C-64

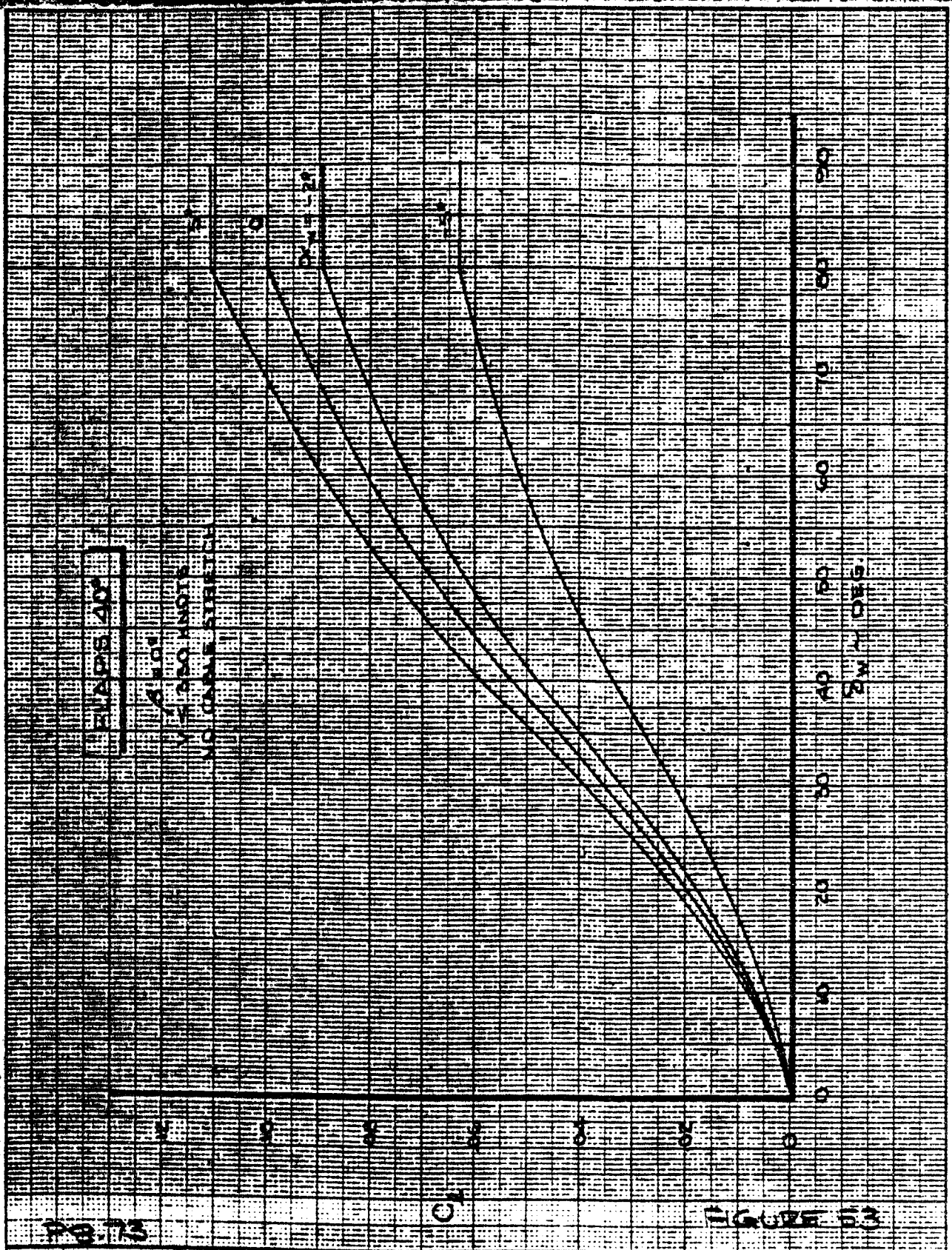
FLAPS 40°
V = 250 KNOTS
NO DRAG STRUT
δA = 0°
δA = 20°
δA = 40°
δA = 60°
δA = 80°
δA = 100°
δA = 120°
δA = 140°
δA = 160°
δA = 180°
δA = 200°
δA = 220°
δA = 240°
δA =

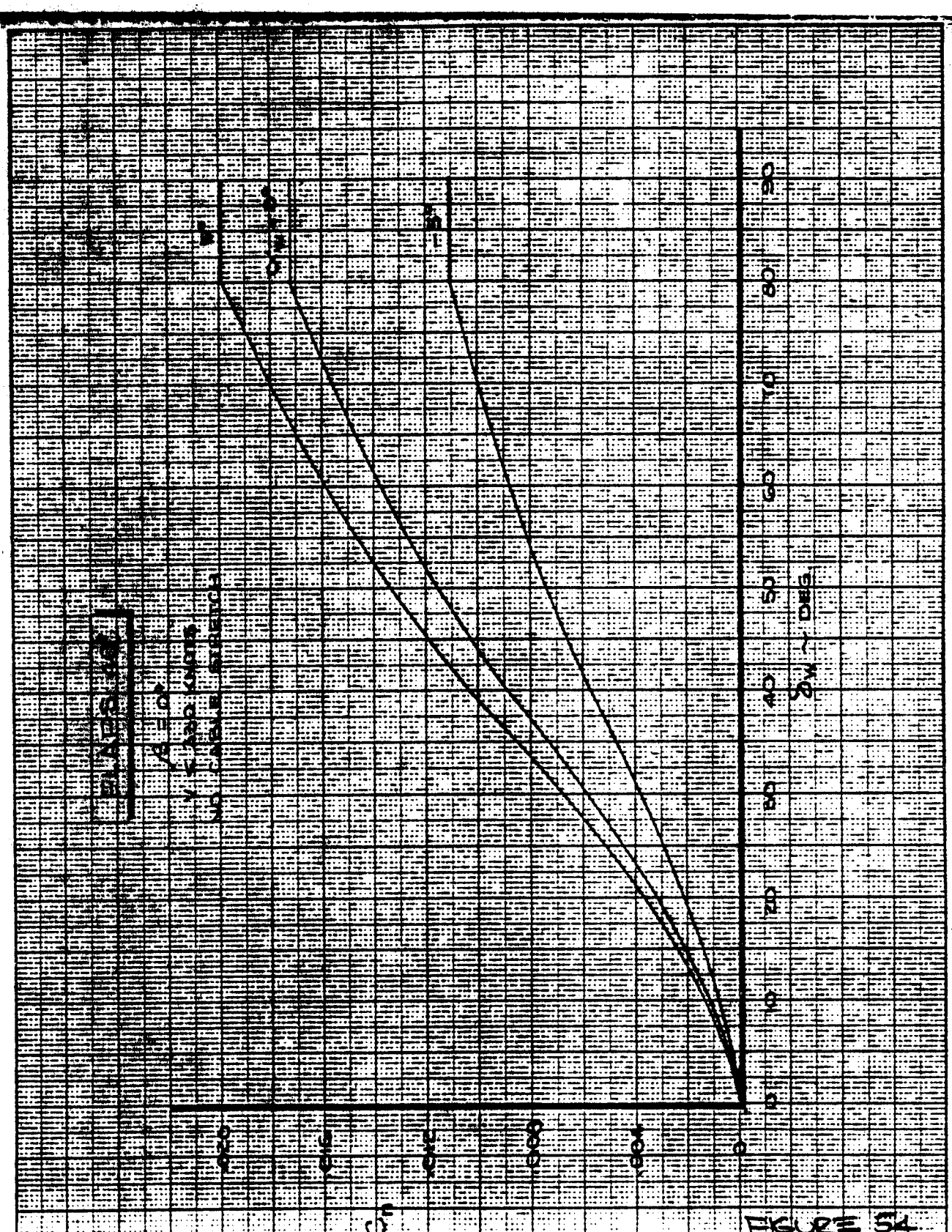

FIGURE 54

CALC	CUSHING	3-3-66	REVISED	DATE	YAWING MOMENT DUE TO LATERAL CONTROL	T37-100
CHECK						PG. 74
APR					THE BOEING COMPANY	PAGE
APR						
INK	M. THOMAS	8-11-66				

TD 41 C-R4

316

810

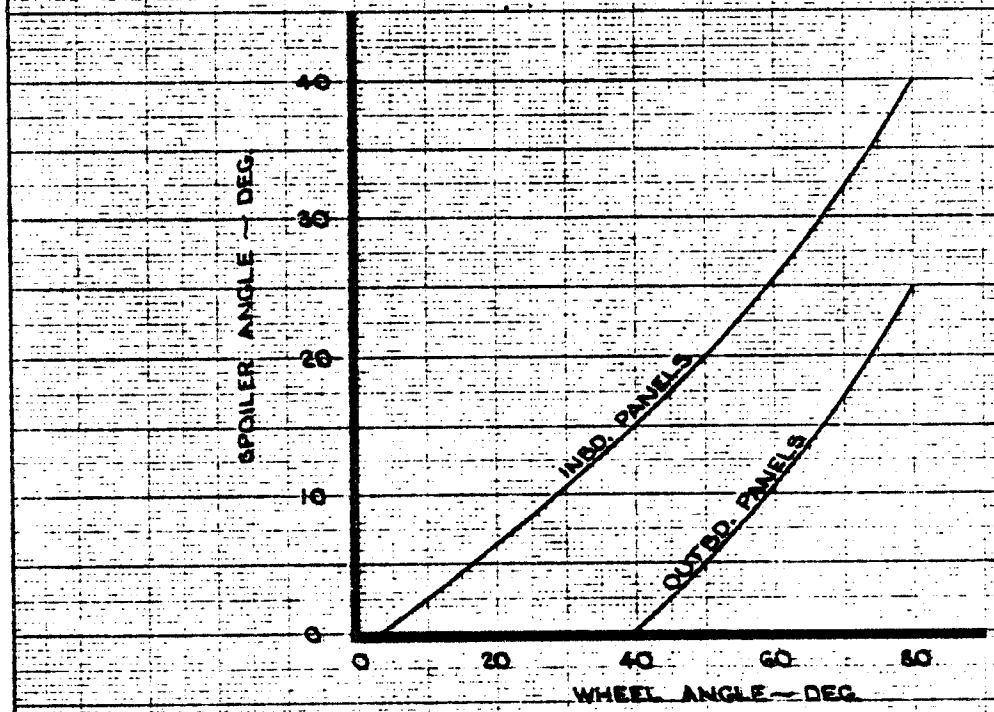

FIGURE 559

P8.75

CALC	McINTOSH	6-20-66	REVISED	DATE	SPOILER PROGRAM	737
CHECK						
APR						
APR					THE BOEING COMPANY	PAGE
INIT.	MARSHALL	6-20-66				

TD 461 C-R4

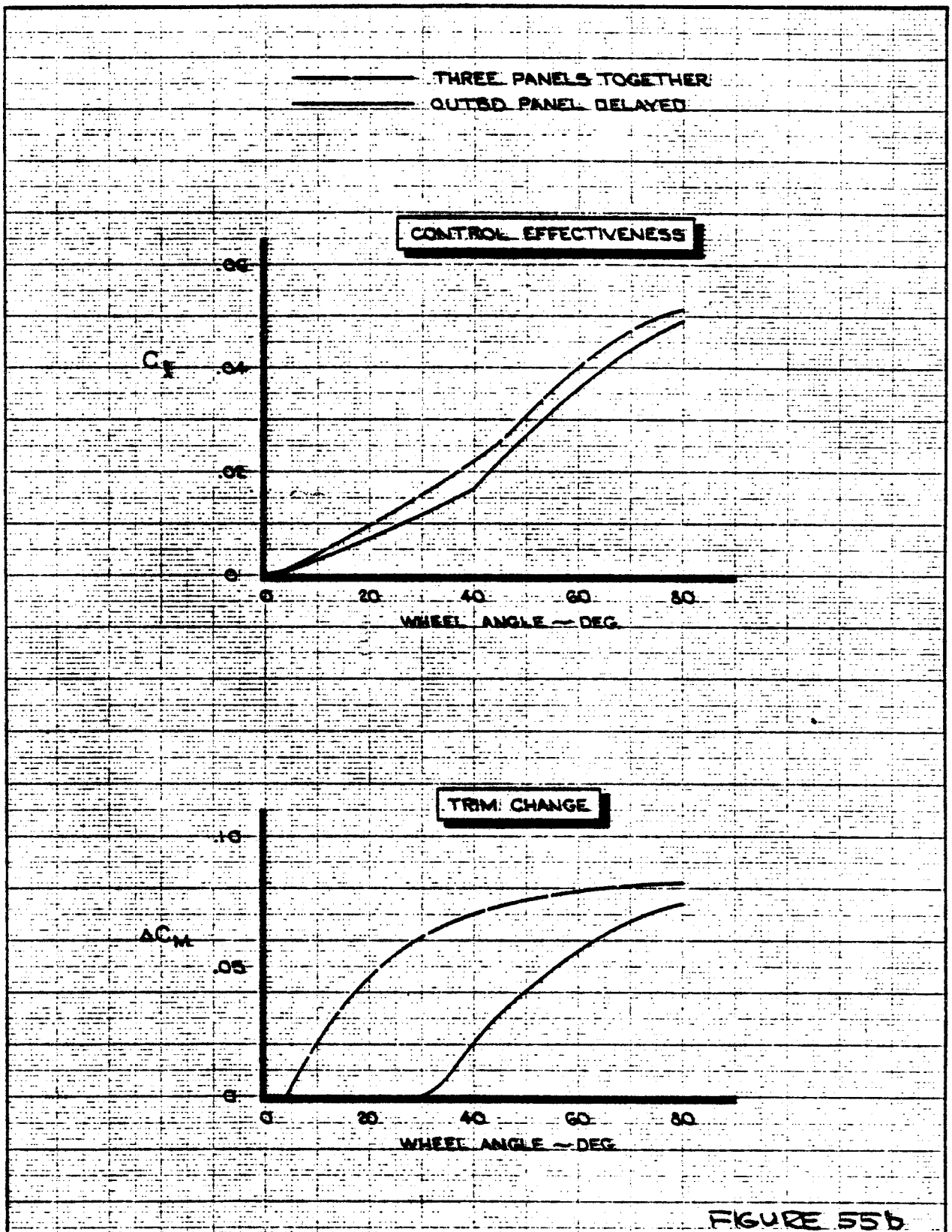

FIGURE 55b

CALC	McINTOSH	6-20-66	REVISED	DATE	EFFECT OF SPOILER PROGRAM ON TRIM CHANGE AND CONTROL EFFECTIVENESS	737
CHECK						P3.76
APR						
APR					THE BOEING COMPANY	PAGE
INIT.	MARSHALL	6-20-66				

TD 461 C-24

CHAPTER 9. ENGINE INSTALLATION DESIGN

CHAPTER 9. ENGINE INSTALLATION DESIGN

Preceding chapters have outlined the design and testing procedures for the wing and body parts of the configuration. This is where the aerodynamicist would like to stop; further details, such as the empennage and the engine installation, while providing necessary additions in the form of control and thrust, at the same time reduce the aerodynamic efficiency. In the case of the engine installation, the aerodynamicist seeks to find an installation which would incorporate the power plant with the least additional drag. But the aerodynamicist does not get the only vote; Figure 9.1 gives the concept of the preferred nacelle as viewed by other staffs. Obviously, accomodating all these various requirements into a very small package makes the nacelle design and engine packaging one of the major challenges of the entire airplane design.

At Boeing, design responsibility for the nacelle is divided along the boundary of the flow that enters the nacelle; that going outside belongs to Aerodynamics and that going inside is the responsibility of Propulsion. This artificial division often causes sharp debate during the nacelle design, especially in the case of the inlet.

Nacelle design is often hampered by a number of misconceptions which reduce the design freedom. These will be dealt with individually in various parts of this Chapter, but one of the more serious ones is that nozzles produce thrust. In fact, the inlet produces thrust and the nozzle incurs a net drag force. Figure 9.2, taken from Reference 9.1, shows the distribution of forces throughout a typical jet engine. Note that the "forward gas load," 57,836 lbs. is all distributed forward of the turbine, and the "aft gas load" on the turbines and exhaust nozzle reduce this thrust by 46,678 lbs to a net of 11,158 lbs. For this and other reasons, the inlet is a far greater design challenge than is the nozzle.

This Chapter will discuss aerodynamic design considerations of the exterior of subsonic and supersonic inlets and then exhaust nozzles as they impact aerodynamic design. Then, installation problems for wing and body-mounted engines will be addressed.

9.1 NACELLE INLET DESIGN

9.1.1 General Considerations

The nacelle inlet has several key functions to perform, as detailed in Figure 9.3. The foremost one, and the basic reason for the inlet, is to provide a very uniform flow to the engine fan face over a wide range of conditions. This can be achieved in a relatively short distance. Consider, for example, an axisymmetric inlet derived from the CF6 installation on the 747 on Figure 9.4 from Reference 9.2. The shape of the inlet flow profile is given at various stations inside the inlet at 0^0, 4^0 and 10^0 angle of attack as calculated by A230 potential flow theory. Note that, at 10^0 angle of attack, the flow has straightened to a completely uniform flow at the station labelled "diffuser", which is an ℓ/d value of only 0.53. The total ℓ/d of the inlet is 0.85; the larger value is required to achieve the necessary acoustic lining for noise reduction.

627

A further example of the ability of the inlet to straighten the flow is given on Figure 9.5 from Ref. 9.3. Shown is an inlet operating at max power in a 35-knot crosswind, that is, at 90° angle of attack. Although the local Mach number on the windward inside of the inlet exceeds sonic velocity, at the fan face the velocity is the same on windward and leeward sides. Figure 9.5 also shows that the dominant characteristic in achieving good crosswind capability is the "inlet contraction ratio."

The inside of the inlet is designed by the Propulsion Staff, and the only impact it has on the aerodynamic design is as follows:

(1) Engine airflow demands will size the throat area,
(2) The aircraft operational envelope will specify the required inlet contraction ratio,
(3) The combination of throat area and C.R. size the hilite radius, which in turn sets the size of the nacelle exterior.

The most important aerodynamic reason for the inlet is to provide thrust recovery. Before describing the nature of this function, some terms must be defined (Figure 9.6). Of interest to the current discussion is the inlet velocity ratio, V_{wi}/V_∞ (which may be expressed also as inlet area ratio, Potential flow considerations show that the forward thrust due to lip suction on the inner and outer surfaces of the inlet will be given by (Ref. 9.4):

$$F_{inlet} = q_\infty A_{ff}\left(1 - \frac{V_{wi}}{V_\infty}\right)^2 , \quad A_{ff} = \text{forward facing area} \qquad (9.1)$$

This ideal thrust is independent of the geometry of the inlet, but can be severely limited by viscous considerations. This will be dealt with in Section 9.1.2 below.

Further nacelle design considerations concern initial internal flow compression, noise reduction by use of acoustic lining, and shielding against foreign object damage. These do not concern the aerodynamic design directly, except that in today's era of environmental concern, the length of the inlet for subsonic aircraft will invariably be chosen by acoustic criteria.

9.1.2 Subsonic Inlet Design

NACA 1-series inlets As in the case of airfoil design, early nacelle inlet design was dominated by NACA information. During WWII, NACA studied several cowl shapes to find one which gave a low drag (ie, good thrust recovery), resulting in one labelled "Cowl B" which gave a critical Mach number of about 0.84, although with a great degree of drag creep. In 1945, a series of tests were run on systematic variations of Cowl B, now denoted NACA 1-series cowl shapes, in order to improve the performance. The nomenclature for the NACA 1-series is:

NACA 1- XX-YYY

where XX = d/D RATIO
YYY = x/D RATIO
} see Fig 9.7

623

These cowl shapes led to modest increases in performance and became the standard for inlet shapes at that time. These were used, for example, on the B-47, early B-52, and J-57 - powered KC-135 and 707-120 aircraft. The general design selection for a NACA 1-series cowl is shown on Figure 9.8. As an example, to design the inlet for 0.84 Mach and a cruise V_{HL}/V_∞ of 0.70 would require the inlet to have an X/D of 0.85 and a d/D of 0.85; in other words, NACA 1-85-75. The fundamental source of data on NACA 1-series inlets is Reference 9.5.

The continuing interest in NACA 1-series cowls is demonstrated by Reference 9.6, in which is reported a series of NASA tests of NACA 1-series inlets at speeds up to 1.29 Mach, done in 1974. In fact, the NACA 1-85-75 inlet is contained in that report, and Figure 9.9 gives the drag performance of that inlet as a function of Mach and inlet mass flow ratio. Note that in general, at the lower subsonic Mach numbers, the drag shape is characterized by a drag level, independent of capture ratio, until a point where the exterior flow begins to fail, and "spillage drag" is incurred. This occurs as shown on Figure 9.10 because of the appearance of shock waves on the outer cowl. Note at higher capture ratios how the pressure distribution is quite favorable. In spite of this, however, is the general tendency for drag creep to occur. This points out the first of two limitations to NACA 1-series inlets, that of drag creep.

The second, and more serious, limitation is described on Figure 9.11. The NACA 1-series inlets are all of low contraction ratio; typically less than 4.5%, for acceptable drag performance. When the contraction ratio of the NACA 1-series cowl goes over about 5%, the drag level and Mach number deteriorate dramatically. They do so because the design inlet velocity ratio gets lower, from around 0.7 to 0.6 as the inlet hilite is increased at the same threat diameter.

Boeing 65-series inlets In 1959, Boeing ran a series of tests on inlet cowls designed to operate at higher contraction ratios and thereby at lower inlet velocity ratios. Since lowering the inlet velocity ratio is similar to increasing angle of attack on an airfoil, the new cowls were designed by combining NACA 65-series airfoils with NACA airfoil camber. The result (Reference 9.7) is shown in Figure 9.12. This new technology cowl, first applied to the fan-engined 720B and 707-320B, provided a good high-speed cowl design.

But the fan engine change in mass flow from cruise to low speed was such that auxiliary blow-in doors were required for low speed operation, as on the 707 and 720B with JT3D and 737 with JT8D. This was acceptable from a performance viewpoint, and was applied to the early JT9D installation on the 747. Then came more stringent noise rules, and the blow-in door inlet had to be abandoned.

Current inlets In order to provide good crosswind capability at low speeds and high power settings without blow-in doors, a further increase in inlet contraction ratio was required. The revised 747 inlet (as well as subsequent designs) have contraction ratios of 25% or larger, requiring inlet velocity ratios of around 0.5 at cruise. Recalling the analogy between cowl inlet velocity ratio and airfoil angle of attack, inlet designers now were forced to turn to transonic airfoils (peaky) to achieve acceptable performance at 0.85 Mach, V_{M}/V_{∞} =0.5 with fixed-lip cowls. The first design attempt, the fixed-lip inlet for the JT9D-7, was not a large success. Far better performance was achieved on the design of the CF6 inlet for the 747. Further refinement was done for the JT9D-70 installation on the 747, although Boeing eventually bought an aerodynamically inferior nacelle for the JT9D-70 from Rohr. Figure 9.13 compares the performance levels of the three cowls described above.

The 747 Aerodynamics Staff conducted extensive design activity during the period from 1969 through 1975. From that work has come several design rules for transonic inlets. The design art is based on the shape of the suction loop, just as in the case of transonic airfoils. Figure 9.14 shows the drag characteristics and suction loops of a family of inlets designed to the same mission; note as in the case of transonic airfoils that the triangular suction loop design must be avoided. The design rules obtained from the 747 test program are contained on Figure 9.15 as stated in Ref. 9.8. Design of transonic inlets utilizes first the incompressible A280 computer program, then the nonlinear transonic TEM 318C program. A comparison of theory to test is given on Figure 9.16.

Design variations The circular inlet resulting from current design activities will seldom be axisymmetric. There will always be a design trade between increasing the capture ratio or inlet velocity ratio for aerodynamic reasons and going the other direction to increase the inlet contraction ratio for crosswind capability. The trades are so important that often the inlet contraction ratio is tailored, that is 25% at the top, going to 28% at the sides for crosswind, then to 30% on the keel for low-speed-high-angle-of-attack reasons.

A further variation is in the plane of the inlet. Most production inlets are planar, being titled for best alignment with the approaching airstream at cruise. The swept inlet, Figure 9.17, has been investigated analytically at Boeing. This inlet, having a sharp upper lip but a generous lower lip would produce a greater range in off design airflow capability without compromising the high-speed design.

A totally different swept inlet is shown on Figure 9.18, which features an inlet with an "acoustic deflector" which would face downward. The performance data (acquired on a DC-9 model) are somewhat surprising in that the acoustic deflector inlet had a higher operating angle of attack capability at low speed than did the standard inlet, due to the appearance of two vortices on the deflector.

The point of discussing these two inlets is that the aerodynamicist has the capability today to design unorthodox inlets by means of analysis. This capability should always be remembered when a new project is approached.

9.1.3 Supersonic Inlets

The technology of subsonic inlets is concentrated on the external design, where highly refined contours are required to achieve acceptable aerodynamic performance. For supersonic flight, the situation is reversed. Blunt inlets lips cannot be tolerated because of supersonic wave drag, so the external aerodynamic drag becomes quite simple, and highly acceptable to analysis by computer. It should be pointed out before proceeding that there are two shapes for inlets, either axisymmetric or two dimensional, as detailed on Figure 9.19. Then, there are two choices to where the compression is done, either externally or internally. Supersonic inlets are very complex mechanically, having a number of bypass, spillage, dump, buzz, bleed and trap doors. For low supersonic flight, below about Mach 2, the two-dimensional inlet seems to be favored, whereas above about Mach 2.5, the axisymmetric version is preferred. At least that was the conclusion of the Boeing SST program of the 1970's.

9.2 NACELLE COWL AND NOZZLE DESIGN

9.2.1 General Considerations

The nacelle cowl and nozzle are considered to be all those parts aft of the inlet. This is a rather nebulous definition, but the "inlet" is considered to be that part to approximately the engine's fan face. Then begins the cowl, leading to the nozzle. Figure 9.20 lists the functions of the cowl and nozzle. The cowl simply connects the inlet to the nozzle, while providing a streamlined covering around the engine's systems and accessories.

Four main functions are listed for the nozzle. Note that producing thrust is not one of them. This is a serious misconception which must be dispelled. Besides reviewing Figure 9.2, consider the convergent nozzle shown on Figure 9.21. Shown are the external and internal surface pressures. The external changes from a value below ambient to a value at the exit plane which is slightly above ambient. The pressure inside the nozzle starts at a high pressure, then decreases as the flow accelerates to the exit, where the internal and external pressures are equal. Examination of Figure 9.21 will reveal that the pressure force felt by the nozzle is in downstream direction, which is the drag direction. Figure 9.2 points out that the forward propulsive force felt by the physical parts of the engine, nacelle and airframe arises in the inlet, the compressor and diffuser ahead of the combustor. This argument applies always to the convergent nozzle, which is most often used for subsonic installations. For the convergent-divergent nozzle, found on supersonic aircraft, the nozzle may actually have a net forward load. The main point, however, is that the nozzle should not be thought of as the propulsive device.

What then are the main functions of the nozzle? They are (1) to get rid of the "used-up" exhaust gas as efficiently as possible, with the least losses, and (2) produce a back pressure to both the fan and core that will cause them to remain on the desired point of their operating cycle throughout the aircraft's flight regime. These two functions will allow greater freedom in

626

Current inlets In order to provide good crosswind capability at low speeds and high power settings without blow-in doors, a further increase in inlet contraction ratio was required. The revised 747 inlet (as well as subsequent designs) have contraction ratios of 25% or larger, requiring inlet velocity ratios of around 0.5 at cruise. Recalling the analogy between cowl inlet velocity ratio and airfoil angle of attack, inlet designers now were forced to turn to transonic airfoils (peaky) to achieve acceptable performance at 0.85 Mach, V_{M_1}/V_∞ =0.5 with fixed-lip cowls. The first design attempt, the fixed-lip inlet for the JT9D-7, was not a large success. Far better performance was achieved on the design of the CF6 inlet for the 747. Further refinement was done for the JT9D-70 installation on the 747, although Boeing eventually bought an aerodynamically inferior nacelle for the JT9D-70 from Rohr. Figure 9.13 compares the performance levels of the three cowls described above.

The 747 Aerodynamics Staff conducted extensive design activity during the period from 1969 through 1975. From that work has come several design rules for transonic inlets. The design art is based on the shape of the suction loop, just as in the case of transonic airfoils. Figure 9.14 shows the drag characteristics and suction loops of a family of inlets designed to the same mission; note as in the case of transonic airfoils that the triangular suction loop design must be avoided. The design rules obtained from the 747 test program are contained on Figure 9.15 as stated in Ref. 9.8. Design of transonic inlets utilizes first the incompressible A280 computer program, then the nonlinear transonic TEM 318C program. A comparison of theory to test is given on Figure 9.16.

Design variations The circular inlet resulting from current design activities will seldom be axisymmetric. There will always be a design trade between increasing the capture ratio or inlet velocity ratio for aerodynamic reasons and going the other direction to increase the inlet contraction ratio for crosswind capability. The trades are so important that often the inlet contraction ratio is tailored, that is 25% at the top, going to 28% at the sides for crosswind, then to 30% on the keel for low-speed-high-angle-of-attack reasons.

A further variation is in the plane of the inlet. Most production inlets are planar, being titled for best alignment with the approaching airstream at cruise. The swept inlet, Figure 9.17, has been investigated analytically at Boeing. This inlet, having a sharp upper lip but a generous lower lip would produce a greater range in off design airflow capability without compromising the high-speed design.

A totally different swept inlet is shown on Figure 9.18, which features an inlet with an "acoustic deflector" which would face downward. The performance data (acquired on a DC-9 model) are somewhat surprising in that the acoustic deflector inlet had a higher operating angle of attack capability at low speed than did the standard inlet, due to the appearance of two vortices on the deflector.

The point of discussing these two inlets is that the aerodynamicist has the capability today to design unorthodox inlets by means of analysis. This capability should always be remembered when a new project is approached.

9.1.3 Supersonic Inlets

The technology of subsonic inlets is concentrated on the external design, where highly refined contours are required to achieve acceptable aerodynamic performance. For supersonic flight, the situation is reversed. Blunt inlets lips cannot be tolerated because of supersonic wave drag, so the external aerodynamic drag becomes quite simple, and highly acceptable to analysis by computer. It should be pointed out before proceeding that there are two shapes for inlets, either axisymmetric or two dimensional, as detailed on Figure 9.19. Then, there are two choices to where the compression is done, either externally or internally. Supersonic inlets are very complex mechanically, having a number of bypass, spillage, dump, buzz, bleed and trap doors. For low supersonic flight, below about Mach 2, the two-dimensional inlet seems to be favored, whereas above about Mach 2.5, the axisymmetric version is preferred. At least that was the conclusion of the Boeing SST program of the 1970's.

9.2 NACELLE COWL AND NOZZLE DESIGN

9.2.1 General Considerations

The nacelle cowl and nozzle are considered to be all those parts aft of the inlet. This is a rather nebulous definition, but the "inlet" is considered to be that part to approximately the engine's fan face. Then begins the cowl, leading to the nozzle. Figure 9.20 lists the functions of the cowl and nozzle. The cowl simply connects the inlet to the nozzle, while providing a streamlined covering around the engine's systems and accessories.

Four main functions are listed for the nozzle. Note that producing thrust is not one of them. This is a serious misconception which must be dispelled. Besides reviewing Figure 9.2, consider the convergent nozzle shown on Figure 9.21. Shown are the external and internal surface pressures. The external changes from a value below ambient to a value at the exit plane which is slightly above ambient. The pressure inside the nozzle starts at a high pressure, then decreases as the flow accelerates to the exit, where the internal and external pressures are equal. Examination of Figure 9.21 will reveal that the pressure force felt by the nozzle is in downstream direction, which is the drag direction. Figure 9.2 points out that the forward propulsive force felt by the physical parts of the engine, nacelle and airframe arises in the inlet, the compressor and diffuser ahead of the combustor. This argument applies always to the convergent nozzle, which is most often used for subsonic installations. For the convergent-divergent nozzle, found on supersonic aircraft, the nozzle may actually have a net forward load. The main point, however, is that the nozzle should not be thought of as the propulsive device.

What then are the main functions of the nozzle? They are (1) to get rid of the "used-up" exhaust gas as efficiently as possible, with the least losses, and (2) produce a back pressure to both the fan and core that will cause them to remain on the desired point of their operating cycle throughout the aircraft's flight regime. These two functions will allow greater freedom in

Current inlets In order to provide good crosswind capability at low speeds and high power settings without blow-in doors, a further increase in inlet contraction ratio was required. The revised 747 inlet (as well as subsequent designs) have contraction ratios of 25% or larger, requiring inlet velocity ratios of around 0.5 at cruise. Recalling the analogy between cowl inlet velocity ratio and airfoil angle of attack, inlet designers now were forced to turn to transonic airfoils (peaky) to achieve acceptable performance at 0.85 Mach, V_{HL}/V_{∞} =0.5 with fixed-lip cowls. The first design attempt, the fixed-lip inlet for the JT9D-7, was not a large success. Far better performance was achieved on the design of the CF6 inlet for the 747. Further refinement was done for the JT9D-70 installation on the 747, although Boeing eventually bought an aerodynamically inferior nacelle for the JT9D-70 from Rohr. Figure 9.13 compares the performance levels of the three cowls described above.

The 747 Aerodynamics Staff conducted extensive design activity during the period from 1969 through 1975. From that work has come several design rules for transonic inlets. The design art is based on the shape of the suction loop, just as in the case of transonic airfoils. Figure 9.14 shows the drag characteristics and suction loops of a family of inlets designed to the same mission; note as in the case of transonic airfoils that the triangular suction loop design must be avoided. The design rules obtained from the 747 test program are contained on Figure 9.15 as stated in Ref. 9.8. Design of transonic inlets utilizes first the incompressible A280 computer program, then the nonlinear transonic TEM 318C program. A comparison of theory to test is given on Figure 9.16.

Design variations The circular inlet resulting from current design activities will seldom be axisymmetric. There will always be a design trade between increasing the capture ratio or inlet velocity ratio for aerodynamic reasons and going the other direction to increase the inlet contraction ratio for crosswind capability. The trades are so important that often the inlet contraction ratio is tailored, that is 25% at the top, going to 28% at the sides for crosswind, then to 30% on the keel for low-speed-high-angle-of-attack reasons.

A further variation is in the plane of the inlet. Most production inlets are planar, being tilted for best alignment with the approaching airstream at cruise. The swept inlet, Figure 9.17, has been investigated analytically at Boeing. This inlet, having a sharp upper lip but a generous lower lip would produce a greater range in off design airflow capability without compromising the high-speed design.

A totally different swept inlet is shown on Figure 9.18, which features an inlet with an "acoustic deflector" which would face downward. The performance data (acquired on a DC-9 model) are somewhat surprising in that the acoustic deflector inlet had a higher operating angle of attack capability at low speed than did the standard inlet, due to the appearance of two vortices on the deflector.

The point of discussing these two inlets is that the aerodynamicist has the capability today to design unorthodox inlets by means of analysis. This capability should always be remembered when a new project is approached.

9.1.3 Supersonic Inlets

The technology of subsonic inlets is concentrated on the external design, where highly refined contours are required to achieve acceptable aerodynamic performance. For supersonic flight, the situation is reversed. Blunt inlets lips cannot be tolerated because of supersonic wave drag, so the external aerodynamic drag becomes quite simple, and highly acceptable to analysis by computer. It should be pointed out before proceeding that there are two shapes for inlets, either axisymmetric or two dimensional, as detailed on Figure 9.19. Then, there are two choices to where the compression is done, either externally or internally. Supersonic inlets are very complex mechanically, having a number of bypass, spillage, dump, buzz, bleed and trap doors. For low supersonic flight, below about Mach 2, the two-dimensional inlet seems to be favored, whereas above about Mach 2.5, the axisymmetric version is preferred. At least that was the conclusion of the Boeing SST program of the 1970's.

9.2 NACELLE COWL AND NOZZLE DESIGN

9.2.1 General Considerations

The nacelle cowl and nozzle are considered to be all those parts aft of the inlet. This is a rather nebulous definition, but the "inlet" is considered to be that part to approximately the engine's fan face. Then begins the cowl, leading to the nozzle. Figure 9.20 lists the functions of the cowl and nozzle. The cowl simply connects the inlet to the nozzle, while providing a streamlined covering around the engine's systems and accessories.

Four main functions are listed for the nozzle. Note that producing thrust is not one of them. This is a serious misconception which must be dispelled. Besides reviewing Figure 9.2, consider the convergent nozzle shown on Figure 9.21. Shown are the external and internal surface pressures. The external changes from a value below ambient to a value at the exit plane which is slightly above ambient. The pressure inside the nozzle starts at a high pressure, then decreases as the flow accelerates to the exit, where the internal and external pressures are equal. Examination of Figure 9.21 will reveal that the pressure force felt by the nozzle is in downstream direction, which is the drag direction. Figure 9.2 points out that the forward propulsive force felt by the physical parts of the engine, nacelle and airframe arises in the inlet, the compressor and diffuser ahead of the combustor. This argument applies always to the convergent nozzle, which is most often used for subsonic installations. For the convergent-divergent nozzle, found on supersonic aircraft, the nozzle may actually have a net forward load. The main point, however, is that the nozzle should not be thought of as the propulsive device.

What then are the main functions of the nozzle? They are (1) to get rid of the "used-up" exhaust gas as efficiently as possible, with the least losses, and (2) produce a back-pressure to both the fan and core that will cause them to remain on the desired point of their operating cycle throughout the aircraft's flight regime. These two functions will allow greater freedom in

630

doing the nozzle design, as will be demonstrated later. Note that neither requires the nozzle to be very long, as in the case of the JT3D and early JT9D-7 installations.

This leads to the third purpose for the nozzle, which is to provide engine noise reduction by providing surface area to apply acoustic treatment. The 3/4-duct nacelles currently in use are of that length only because of noise reasons. Otherwise they would be short like the JT3D and JT9D-7.

The fourth function of the exhaust nozzle is to use the exhaust jet as an active aerodynamic device for reducing the interference between the engine installation and the airframe. This will be discussed in further detail in Section 9.3.

Nozzles come in two general shapes, round and rectangular. There are special merits for each.

9.2.2 Axisymmetric Nozzles

Over 95% of the worlds jet engine nozzles are axisymmetric, or at least elliptic, which also falls within the general category of being round. Exceptions are the USB nozzle and 2-D nozzle (discussed in Section 9.2.3) and the DC-8 JT3D fan exhaust (which is not discussed at Boeing). Recalling the main functions of the nozzle, there are a number of nozzle concepts available, as detailed on Figure 9.2.2. The first case, the no external boattail geometry of 9.22a, offers the aerodynamic advantage for the isolated nacelle of having probably only skin friction drag and no additional pressure drag due to the boundary layer thickening. In addition there would be very little suppression of the fan exhaust stream due to free stream velocity. But the core nozzle and plug would be very long, and this heavy with high propulsive losses due to scrubbing.

The second case, on Figure 9.22b, has a slight fan cowl boattail angle, from 6^{o} to 10^{o} or so. There will now be some additional drag on the fan cowl due to closure, but the propulsive losses may be less and the weight considerably less. Most production 3/4-duct nacelles are like 9.22b. Then, Figure 9.22c shows a new concept pioneered by the British on the RB.211 and also being used on the CFM-56 for the 707. That approach is to carry a high fan cowl boattail angle, as large as possible without separation occurring, which will be in the range of 14^{o} to 18^{o}. The core nozzle is also very short, with all turning being done internally. This design has the least weight, and test data show that the propulsive efficiency (getting rid of the exhaust) is as high or higher than a design of the type shown on 9.22b. The high boattail angle design may also offer advantages in installation drag, as will be discussed in Section 9.3.

Having chosen the type of nozzle philosophy, there is a choice of how much boattail angle can be carried relative to the fan jet, as detailed on Figure 9.23. The ideal case would be to have no boattail relative to the jet, as shown on part (a). But for structural reasons, it may be necessary to have some boattailing. Part (b) shows that, on the basis of airfoil data, the half-angle should not exceed 6 or 7 degrees. A lower limit may in fact be stated by the Propulsion Staff because of flow suppression.

631

The remaining task is to join the inlet and the exit. This is influenced by the location of the nacelle, and will be discussed further below. For the isolated nacelle, the inlet and exit may be joined in a variety of ways which fall into two categories as described on Figure 9.24. The first is the traditional nacelle having continuous curvature. This applies a continually adverse pressure gradient to the boundary layer. An alternative concept would be to have a "tight-wrapped" cowl having the same inlet and exit radii, but with a thinner cylindrical portion. The pressure distribution would be such that the boundary layer would be relaxed over the mid-portion before undergoing a more harsh trailing edge closure. By careful design, the total drag of the two would be the same. The tight-wrapped cowl would have less weight and perhaps less interference drag, but might suffer poorer off-design performance than the continuously curved cowl.

9.2.3 Two-dimensional nozzles

The two principal types of 2-D nozzles are drawn on Figure 9.25. Both have the same design constraints in terms of external boattail angles as for axisymmetric nozzles. In particular, high boattail angles, either relative to the local freestream or to the jet are to be avoided. Except for USB cases such as the YC-14, two-dimensional nozzles have not see wide use to date.

9.3 WING-MOUNTED INSTALLATIONS

9.3.1 General Considerations

The most frequent location for the engine installation is on the wing, rather than on the body. Reasons favoring the wing placement include:

(1) the wing bending moment is relieved by the weight of the nacelle and pylon,
(2) aircraft loadability (c.g. range) is more flexible than with an aft-body mount,
(3) in many cases, inspection during airport turnaround is easier,
(4) often the wing mount will provide favorable inteference, especially for supersonic vehicles,
(5) there is less danger to the aircraft from an engine fire(in the case of pylon-mounted nacelles).

The last point was emphasized by George Schairer at an AIAA meeting where he described the design of the B-47. At that time, there was a debate between aircraft designers on the merits of engines in the wing root (ie, the Comet) versus engines on the wing in pods. The British preferred the "buried"designs, on the basis that the form drag would be less. But Boeing decided for the B-47, that the engines should be in pods mounted on pylons for the simple reson that an engine fire would result in the nacelle and pod falling off the airframe. Recall that the B-47 was being done in the late 1940's, just after WWII during which many B-17's and B-29's were lost due to an engine fire burning the wing off.

The principle disadvantages of the wing mount are:

(1) foreign object ingestion into the engine is high, unless the engines are mounted over the wing,
(2) cutouts are required in the flap system, therby reducing high lift efficiency,
(3) the aerodynamic design is difficult, to avoid undue drag at cruise,
(4) engine-out yawing moments may be difficult to control at low speeds
(5) the engine installation may cause flutter of the wing-pylon-nacelle system,
(6) engine damage due to ground strike is likely.

The aerodynamicist cannot make the choice of engine position regarding wing or body mount. This choice will arise from many factors, of which the aerodynamic performance is only one. The single most dominant factor is likely to be loadability.

9.3.2 Subsonic Nacelle Integration

Subsonic wing-mounted nacelle integration is dominated by the goal of reducing the effect of the nacelle and pylon on the wing's lift capability. In the absence of separation, the dominant effect of the nacelle installation is on span load, and thereby, induced drag. Figure 9.25 shows the analytically calculated effect of a typical installation on the wing span load. Note the local loss in lift at the nacelle and the general reduction in overall lift at constant angle of attack. Correlation between the analytically predicted increase in induced drag and the measured interference drag is extremely good. Figure 9.27 shows the effect of the 737 nacelle and pylon on the wing span load; obviously in this kind of installation, where the pylon is really a "bifurcator" or fairing, it is much more difficult to achieve the proper tailoring. The design which will tend to reduce interference, then polish the installation with the design of the pylon.

Underwing nacelles The first choice involves the position of the nacelle relative to the wing. General guidelines are poor, but Figure 9.28 shows the geometrical relation of designs which have entered production. Note that a boundary can apparently be drawn relating fore and aft position to vertical separation. A notable exception is the CFM56 installation on the 707; this design will be examined in further detail later.

The reason for drawing a chart like Figure 9.28 is that there is no single best location for the nacelle, for the reasons portrayed on Figure 9.29. Reverse thrust considerations completely exclude a range of positions as shown because the reversed efflux cannot clear the wing. Aerodynamics in general would prefer to move the nacelle down and ahead from the wing, although the point is soon reached where the increasing pylon wetted area more than offsets the reduced interference drag. Flutter considerations would force the nacelle rearward and aft as would weight reasons. Ground clearance also forces the nacelle upward. Obviously, its the classical case of aerodynamics against the rest of the world.

633

The next step following choice of the position of the nacelle is to align the nacelle (which is still axisymmetric at this stage of the design sequence) for best performance. Using the nozzle axis as an indicator of the vector direction of the gross thrust, the quantity $\frac{1}{TSFC}\left(\frac{L}{D}\right)$ in the range equation can be altered by proper orientation of the thrust vector. Suppose the chosen (C_L, C_D) design point for the airplane was below the C_L for $(L/D)_{max}$. Then the thrust vector would want to point downward (ie, reducing the overall lift) so as to drive the wing C_L towards (L/D) max. If the design point were above the C_L for (L/D) max, then the thrust would want to be pointed upwards (nacelle tilted nose up) to allow C_L to decrease towards C_L for (L/D) max. Countering the improvement in L/D is an apparent increase in $\frac{1}{TSFC}$ because of the increase in gross thrust required due to misalignment of the nozzle. These concepts are illustrated on Figure 9.30. For a value of δ_T, and $C_{L_{airplane,\ \delta T}} = 0$, the equations are:

$$K = \frac{\beta_T \sin \delta_T}{1 + \beta_T (\cos \delta_T - 1)} \qquad \text{(a factor)}$$

where $\beta_T = \dfrac{\text{engine gross thrust}}{\text{engine net thrust}}$

δ_T = nozzle axis angle relative to free stream (positive is nose up)

Then $C_{D_{airplane,\ \delta_T}} = \dfrac{C_{D\,airplane,\ \delta T=0}}{1 + \dfrac{K}{\partial C_L / \partial C_D}}$

where $\partial C_L / \partial C_D$ is the slope of the local drag polar at $C_{L_{airplane,\ \delta T=0}}$, $C_{D_{airplane,\ \delta T=0}}$

and $C_{L_{airplane,\ \delta T}} = C_{L_{airplane,\ \delta T=0}} - K\, C_{D_{AIRPLANE,\ \delta T}}$

$$\left(\frac{1}{TSFC}\right)_{\delta_T} = \frac{1}{\cos \delta_T}\left(\frac{1}{TSFC}\right)_{\delta T=0}$$

so the change in the range equation due to δ_T is given by:

$$\frac{\left(\frac{1}{TSFC}\right)\left(\frac{L}{D}\right)_{\delta_T}}{\left(\frac{1}{TSFC}\right)\left(\frac{L}{D}\right)_{\delta T=0}} = \frac{\cos \delta_T \left(\frac{C_{L\,airplane,\ \delta_T}}{C_{D\,airplane,\ \delta_T}}\right)}{\left(\frac{C_{L_{airplane,\ \delta T=0}}}{C_{D_{airplane,\ \delta_T=0}}}\right)}$$

or,

$$\frac{\Delta RF}{RF} = \cos \delta_T \left[1 + \frac{K}{\partial C_L / \partial C_D} - \frac{C_D}{C_L} K \right] \qquad (9.1a)$$

where C_L and C_D are the points on the trimmed airplane's polar at $\delta_T = 0$ where the design mission will be flown. This procedure assumes that (1) C_L will change very little over the range of δ_T, so that the linear approximation of $\partial C_L / \partial C_D$ for the polar will be acceptable, and (2) TSFC is invariant with thrust over the small change in thrust required.

An example is given on Figure 9.31 for a case where the design point is below the point for $(L/D)_{max}$ (case A) and above the point for $(L/D)_{max}$ (case B). Note that for case A, the thrust angle is negative (jet towards the wing) and for case B, the jet is pointed away from the wing. Obviously, it is not desirable to point the jet towards the wing surface, because of possible impingement. So, for cases like A, where the design point is below the point for $(L/D)_{max}$, the nozzle axis should be made at least parallel to the wing.

Equation 9.1 poses a difficulty for new designs where the final polar is not known. The best guess to the trimmed polar will have to be used, along with a best guess as to the design point. Once the airplane polar is know, then equation 9.1 can be used to assess the penalty in range factor for the final configuration. Incidentally, equation 9.1 does show that the C_L for $(L/D)_{max}$, the ratio $\partial C_L / \partial C_D$ and C_L / C_D are equal, so the last two terms disappear and $\Delta R/R = \cos \delta_T$. To find δ_T for maximum $\Delta R/R$ equation 9.1 is solved using β_T, $\partial C_L / \partial C_D$, C_L, C_D and a range of δ_T values. Figure 9.31 shows how the δ_T for best performance will be found.

The final δ_T will be the angle of the nozzle axis relative to the free stream direction. This is quite different from the angle of the nozzle relative to the wing in the manufacturing jig.

In particular,

$$\delta_T = \alpha_{Body} + \alpha_{wing\ incidence} + \delta_{Twist} + \delta_{engine} \qquad (9.2)$$

where: α_{Body} = body angle relative to the free stream at the C_L design point

$\alpha_{wing\ incidence}$ = angle of wing defining plane relative to body axis

δ_{twist} = Angle of local wing defining plane at the nacelle station at cruise relative to jig position (wing leading edge up is positive)

δ_{engine} = angle between engine thrust axis and local wing defining plane (nacelle nose up is positive,

635

It is usually assumed for axisymmetric nozzles that the thrust axis will be along the nozzle axis. Usually, equation 9.2 is solved for engine. For example, assume:

α_{Body} = 1.9^0 for the design C_L

α_{Wing} = 2.0^0 incidence relative to body

δ_{Twist} = -1.9^0 due to aeroelastics

δ_T = 2.6^0 from use of equation 9.1

Then $\delta_e = \delta_T - \alpha_{Body} - \alpha_{wing} - \delta_{Twist}$

$= 2.6 - 1.9 - 2.0 + 1.9$

$= 0.6^0$ (nacelle nose up)

In this example, the angle between the nozzle centerline and the local wing defining plane will be 0.6^0 to achieve the desired δ_T at cruise. As mentioned before, if δ_T is less than zero, the nacelle will be aligned parallel to the local wing chord plane ($\delta_T = 0$) to prevent scrubbing of the jet on the wing lower surface.

The next step, having now chosen the pitch orientation of the axisymmetric nacelle, is to align the inlet. Figure 9.32 shows how the procedure is done. The nacelle is placed at its angle relative to free stream for the cruise condition. Drooping the inlet face to be perpendicular to free stream would improve its alignment. But further droop is required to align the inlet with the incoming flow field, which will have upwash. The degree of upwash may be guessed, but any serious program will use an A230 clean-wing solution to calculate the upwash. Then, the inlet droop can be chosen to perfectly align the inlet with the flow. Typical values have been between 3^0 and 4^0. But in some cases, the inlet has been drooped 1^0 to 2^0 more than required for alignment, with no noticeable increase in nacelle drag. Since this aids the low speed operation of the inlet, the additional droop would be preferred.

Part of the reason that over-drooping the inlet can be done without penalty is demonstrated on Figure 9.33. So far, the nacelle has remained axisymmetric. But engine and airplane accessories are usually contained in the nacelle also, and the keel of the nacelle by experience has been found to be a good place for these accessories. Adding the accessory bump to the bottom of the nacelle causes quite a bump which may penalize the nacelle in drag rise. The more the inlet is drooped, the lower the curvatures will be on the keel line, and thus the better the performance of the nacelle when installed. The limit is reached when the curvature on the crown of the fan cowl becomes such that it will develop additional supersonic flow. Analysis in A230 will show when the production nacelle is in trouble in this regard.

The next step is to align the nacelle in the plan view. Figure 9.34 shows that this is simply a balancing between alignment of the nacelle in toe-in to prevent nacelle misalignment drag (from the nacelle's yaw polar) and the loss in TSFC due to pointing the vector off-direction. Typically, the optimum toe-in will be

936

about one-half degree less than that for perfect alignment of the inlet with the wing-body induced crossflow, the reduction being due to the TSFC effect. An example on Figure 9.39 shows that the improvement in range factor due to toe in is on the order of 0.1%. When included with the best pitch alignment, the optimum alignment of the nacelle results is only 0.2% improvement in range factor relative to the nacelle being pointed straight ahead, but, in the early design stages, the proper toein and tilt are easily applied.

So far, the orientation of the nacelle, its droop and keel line have been discussed. The next natural step is the addition of the pylon to the design sequence. At this point, a number of variables come into play, including the fan nozzle design. The pylon and fan nozzle the two important design items to be used in reducing the interference drag. Consider the nacelle, pylon and wing shown on Figure 9.35a. This is representative of the"typical" installation. The primary is fairly long, with a gradual initial plume angle and the pylon has an airfoil contour. The wing lower surface, the pylon and the fan plume (which appears as a boundary to the aerodynamic flow field) all have curvature at the same place which would cause flow acceleration. The result is usually a strong flow acceleration on the pylon, especially the inboard side, which of course is felt by the wing as a large loss in lift near the nacelle.

The design concepts to alleviate this flow problem are shown on Figure 9.35b. First, the closure rate on the fan plume is increased. This moves the curvature concentration of the fan plume forward, and at the same time creates an aerodynamic "hole" which tends to suppress the flow velocities. Second, the pylon is made slab-sided in the region of danger. This tends to further suppress the flow velocities. Combination of these two concepts on the 707/CFM56 installation resulted in nearly interference-free performance.

Pylon camber can be used to further reduce the installation effects and in fact, gain a net drag reduction for the installation. The way this is done is illustrated on Figure 9.36, by causing a favorable discontinuity in span load. For the underwing nacelle, the load is to be directed outward which fortunately is also in the direction to suppress the tendency to develop supersonic flow on the lower surface. Also, because the favorable effect arises from a change to span load, it is likely that the improvement for cambering the nacelle would be higher at an outboard position than at an inboard one..

An additional design choice involces whether the pylon goes over the wing leading edge or not. The preferred way is to keep the pylon below the wing leading edge stagnation stream line. Not only does this improve the high speed performance but the low speed as well. If the pylon must go over the wing, then two considerations arise. First, the contour should follow a streamline on the clean wing. Second, the area change of the pylon over the wing should be gradual, since it is in a supersonic flow field. These are illustrated on Figure 9.37.

All these effects can be explored analytically with program A230, which has been demonstrated to produce extremely good agreement for the wing-nacelle-pylon case. But the modelling time is long (2 months) and not many aerodynamicists are trained to do this task, which represents perhaps the most difficult use to which A230 is exercised.

The previous discussion pertained to the case where the nacelle and pylon are clearly separate. The 737 belongs to a class where the nacelle completely dominates the flow field. Attempts can be made with the pylon to achieve a suitable area ruled shape, but in all likelyhood the wing would have to be designed in the presence of the nacelle. Again, program A230 can be used in this cycle.

Design of overwing installations must rigorously follow certain rules. Figure 5.38 illustrates the penalty in performance when an axisymmetric nacelle and symmetric pylon are placed on top of the wing in a supersonic flow field. Also shown is the performance of a contoured one. Figure 9.38 gives the general design procedure which relies on A230.

(1) Compute streamline forward from the nacelle exit in the wing-body flow field (no nacelle).

(2) Make the inboard-to-lower quadrant of the nacelle fit the streamlines exactly to about 10% chord ahead of the wing. Design the rest of the nacelle (top and outboard sides) to contain the engine and accessories. Design the inlet droop as before.

(3) Add the nacelle to the A230 model. Trace streamlines between the nacelle and wing; these become the inboard side of the pylon. Of course, the D-duct nacelle does not follow this step.

(4) Analyze the full model in A230 for serious contour problems.

The reason for the streamline contouring is that the nacelle is in the wing's supersonic flow field, and the inboard side of the nacelle must look like part of the natural wing flow or a normal shock is likely to appear. Overcontouring the outboard side simply causes the shock to have increased sweep, which is favorable.

9.3.3 Supersonic Nacelle Integration

There is probably no reason to install the nacelles on top of a supersonic wing, because sizable gains in performance are realized by the underwing installation. Figure 9.39 shows two cases of underwing nacelles for a four-engine SST. One case utilizes two engines per pod with 2-D inlets. The other has four separate axisymmetric nacelles. In each case, the nacelles create a pressure increase due to their shock wave pattern which benefits the wing. According to Reference 9.9, the separate axisymmetric pods are clearly superior because (1) the total nacelle cross sectional area is less and the nacelle area can be better distributed in each area rule roll angle (recall how the supersonic area distribution is generated) and (2) the nacelles can be distributed so that their effect is better spread along the wing. Once the nacelles are spread out, then the wing is reflexed (see Figure 9.39) to use the pressure rise behind the nacelle shock waves to reduce trim drag. The result at M=2.2 was a gain of about 2% in L/D in the case studied, by using the nacelle pressure field to reduce trim drag.

9.4 BODY-MOUNTED INSTALLATIONS

9.4.1 General Considerations

Reasons favoring the placement of nacelles on the aft body include:

(1) the nacelle is in an environment of reduced upflow and crossflow, relative to the wing-mounted nacelle, thus making the inlet design easier,

(2) interference drag is less likely than with a wing-mounted nacelle,

(3) engine object ingestion is reduced,

(4) engine-out yawing moments are small.

The principal disadvantages are:

(1) Aircraft loadability and c.g. travel are reduced,

(2) cabin noise may be difficult to control,

(3) local area ruling may be required,

(4) flow blockage by the nacelles may cause lock-in stall.

9.4.2 Side-body nacelles.

The design of the side-mounted nacelle installation is very simple. First, the wing-body configuration is modelled in A230, to find the upflow at the inlet face, Second, the nozzle axis alignment is found by use of Equation 9.1. The relation of engine tilt to the body axis will then by given by:

$$\delta_{engine} = \delta_T - \alpha_{body} \qquad (9.3)$$

where δ_{engine} = the angle between engine axis and airplane axis (nacelle nose up is positive)

δ_T = optimum thrust alignment angle relative to free stream

α_{body} = body angle of attack at the design point where δ_T is calculated

Then, the inlet droop is calculated:

$$\alpha_{droop} = -(\delta_T + \alpha_{upwash}) = -\alpha_{inlet}$$

similar to that shown on Figure 9.32 for the underwing nacelle. In planview, the nacelle is made parallel to the body side. The pylon

is also aligned with the average flow field.

The principle problem with aft-body mounted nacelles occurs when the local area of the aft body plus nacelles is sufficient to cause a local configuration shock wave. Data from the 727 program and other sources suggest that when the ratio

$$\frac{A_{\pi\ nacelles,\ pylons} + A_{\pi\ center\ engine\ inlet} + A_{\pi\ aft\ body}}{A_{\pi\ uncontoured\ body}} > 1.5 \qquad (9.5)$$

then a local configuration shock is likely and the aft body must be area-ruled. Figure 9.41 illustrates this with the Fan Jet Falcon 30 which had to use a contoured body when the third engine was added; with two nacelles and the original body, the ratio from equation 9.5 was about 1.36. With the S-duct, the ratio increased to about 1.59. But with the contoured body, the ratio was reduced to about 1.1. The contouring and its success can be verified in program A230 by modelling the geometry and solving for the surface pressures at the cruise Mach number. If no supersonic pressures are present, then the contouring is likely to be successful.

9.4.3 Center Engine

Two styles of center engine installation have been used in the past; the S-duct and the DC-10 straight-through nacelle. The design in either case for the exterior lines is straight forward, in that δ_T, then ℓ_e are calculated as before, and then the nozzle alignment is calculated. Again, program A230 is used to determine initial alignment then verify the pressure gradients of the final design.

CHAPTER 9 REFERENCES

9.1 "The Jet Engine", Rolls-Royce Limited T.S.D. 1302, July 1969.

9.2 D6-43834TN, "An Aerodynamic Study of the Outboard CF6-45 Installation on the 747SP", N.R. Van Devender, Oct. 1976.

9.3 "Nacelle Installation Analysis for Subsonic Transport Aircraft", W. B. Gillette, AIAA Paper 77-102.

9.4 "Two-dimensional Symmetrical Inlets with External Compression", P. Ruden, NACA TM 1279.

9.5 "The Development and Application of High-Critical-Speed Nose Inlets", NACA Report 920, 1948.

9.6 "An Investigation of Several NACA 1-Series Axisymmetric Inlets at Mach Numbers from 0.4 to 1.29", R.J. Re, NASA TM X-2917, March, 1974

9.7 "Development of High Critical Speed Nose Inlet - Thin Cowls", R. J. Loken, D6-3990, November, 1959.

9.8 "Cowl Design Methodology", K.A. Schippers, D6-41800 TN (unreleased).

9.9 "Nacelle Integration Study on a Mach 2.2 Supersonic Cruise Aircraft", H. R. Welge, et al, J. Aircraft, Vol. 14, No. 11, November, 1977.

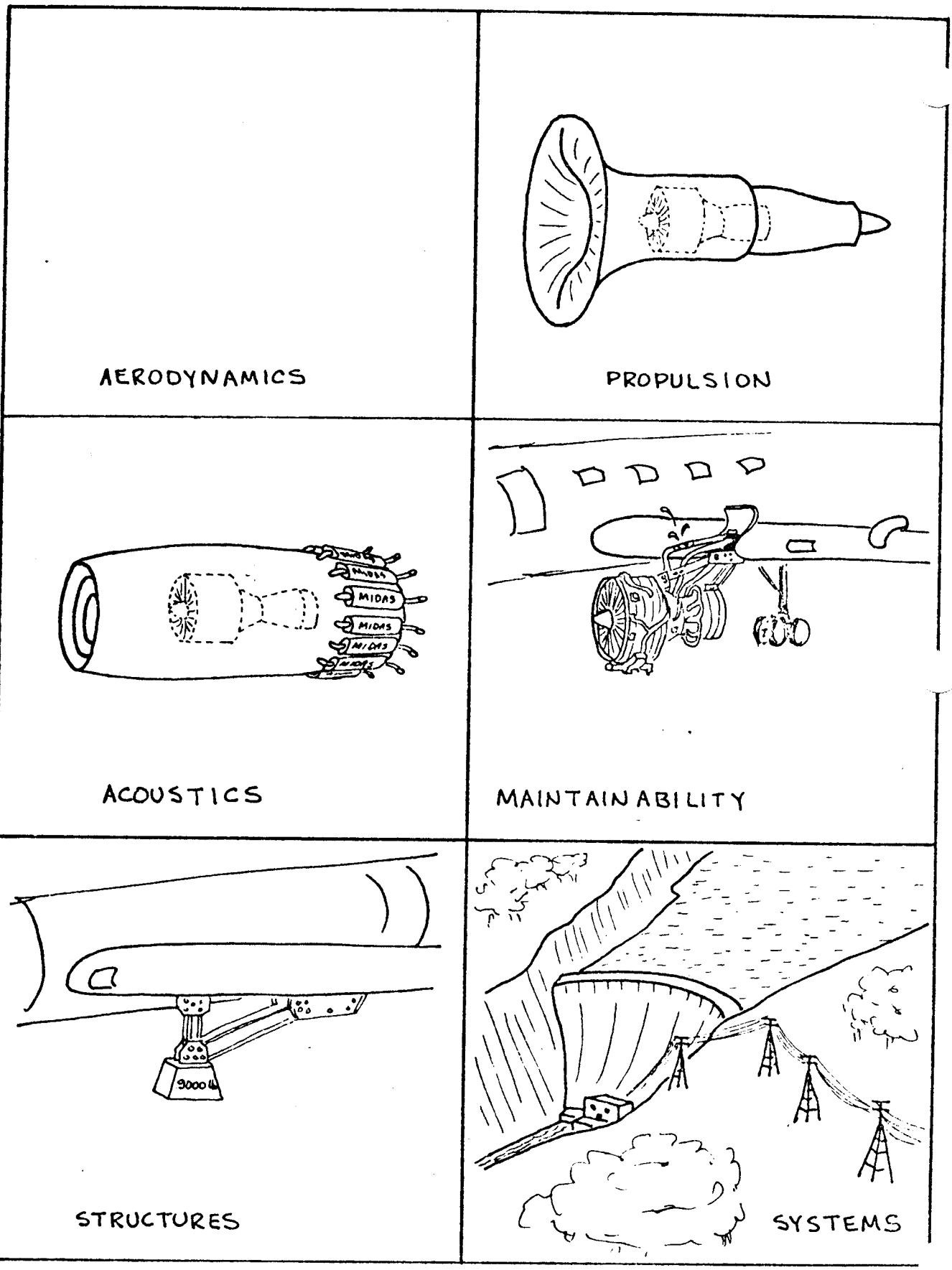

FIGURE 9.1 SELECTED VIEWPOINTS OF THE PREFERRED NACELLE

GILLETTE 2·18·78

GILLETTE
2·18·78

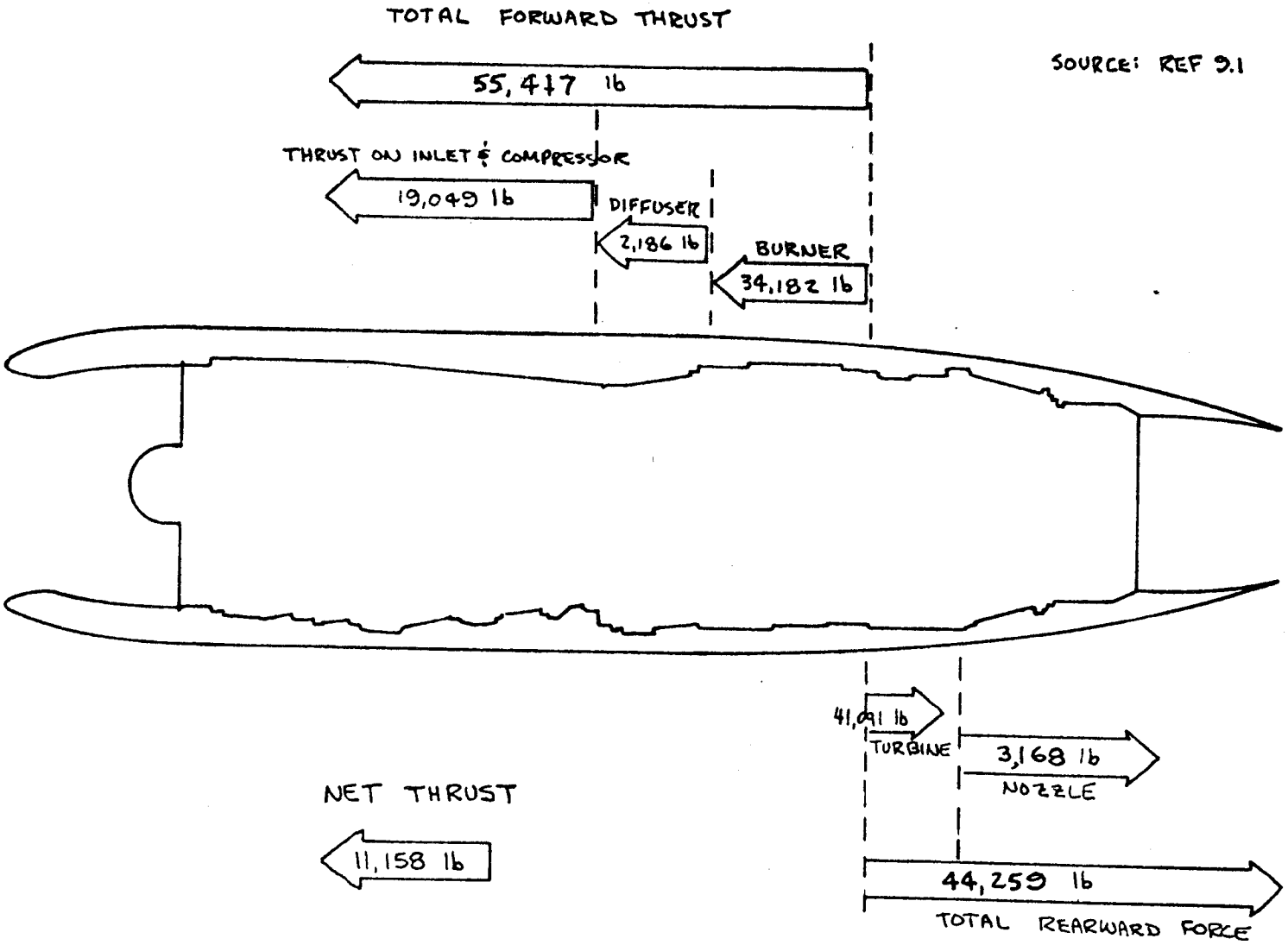

FIGURE 9.2 SOURCES OF THRUST IN A JET ENGINE

P.9.18

NACELLE INLET DESIGN CONSIDERATIONS

INLET FUNCTION	DESIGN GOAL	DOMINANCE IN:		
		Propulsion Contour design	Aero Contour Design	Length Selection
1. FLOW STRAIGHTENING	Present the engine with a low-distortion, even flow field at the fan face over a wide range of airplane conditions.	Most	Little	Little
2. THRUST RECOVERY	Achieve the theoretical inlet thrust over a wide range of conditions.	Little	Most	Some
3. NOISE REDUCTION	Provide engine noise reduction for field and flight operation.	None	None	Most
4. INITIAL FLOW COMPRESSION	Produce some of the flow pressure rise required by the engine cycle.	Most	None	Some
5. SHIELD AGAINST F.O.D.	Reduce the amount of foreign objects ingested by the engine.	None	None	Some

Figure 9.3 Nacelle Inlet Design Considerations.

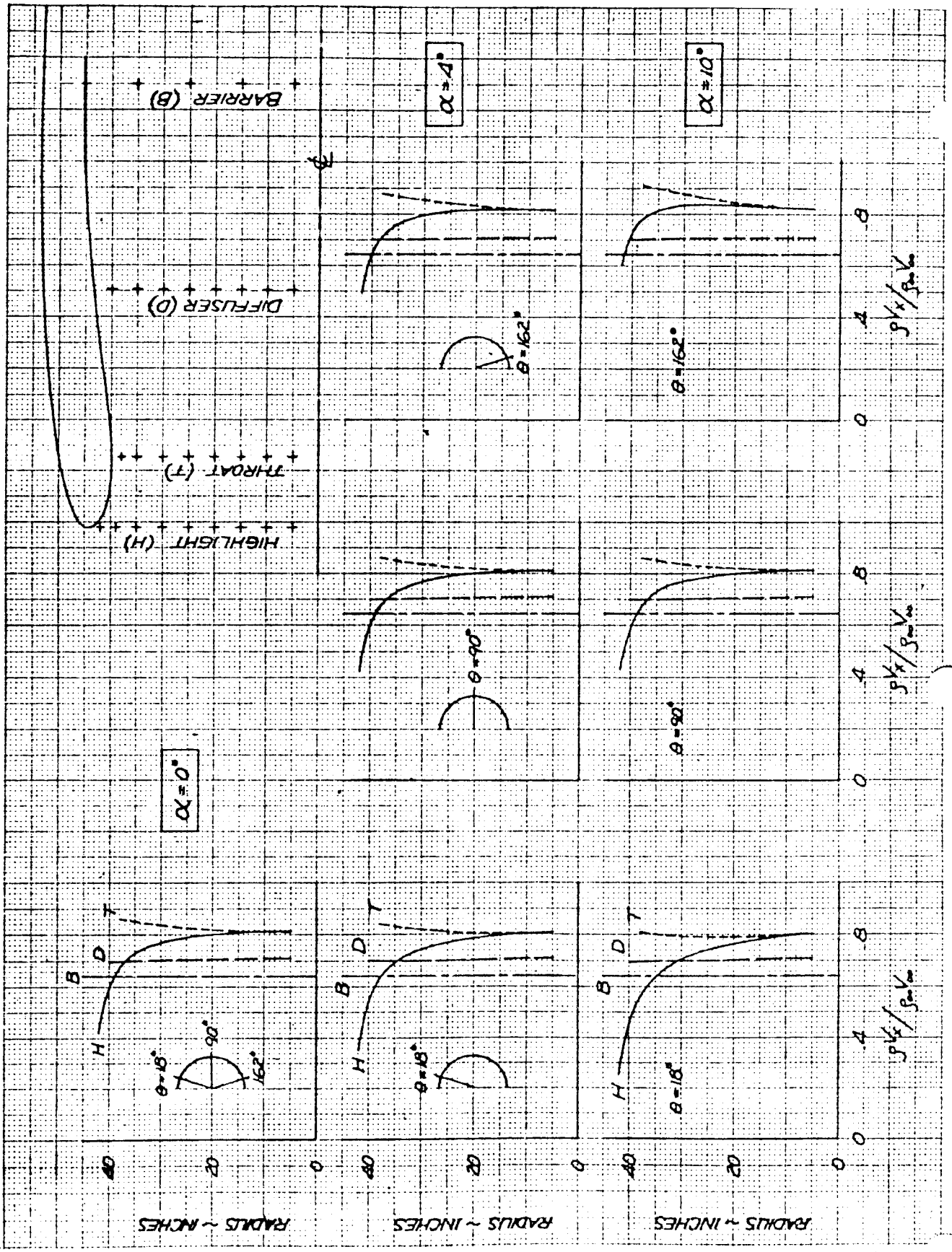

CALC	VANDEVENDER	1-6-76	REVISED	DATE	MASS FLUX DISTRIBUTIONS ~ CF6-45 AXISYMMETRIC COWL ~ A230 ANALYSIS, M=.80	D6-43834TN
CHECK						FIG. 9
APR					THE BOEING COMPANY	PAGE 89
APR						

DI 4100 3260 ORIG 3/71

K·E ALBANENE 1951

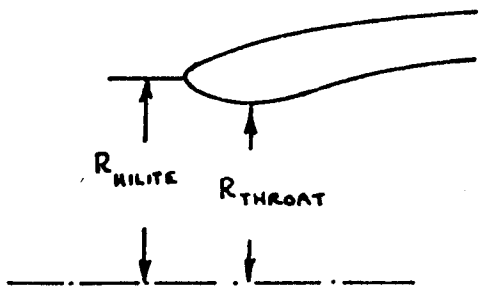

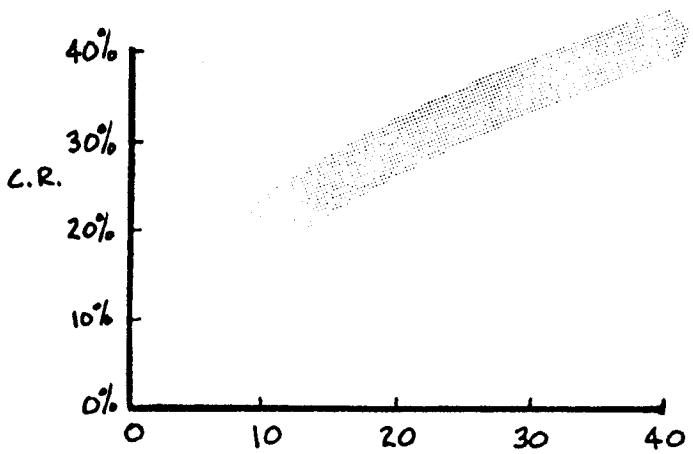

CONTRACTION RATIO ≡ C.R.

$$= \frac{A_{HILITE}}{A_{THROAT}}$$

$$= \frac{R^2_{HILITE}}{R^2_{THROAT}}$$

USUALLY EXPRESSED IN PERCENT; CR = 1.28 WOULD BE DENOTED "28% CONTRACTION RATIO"

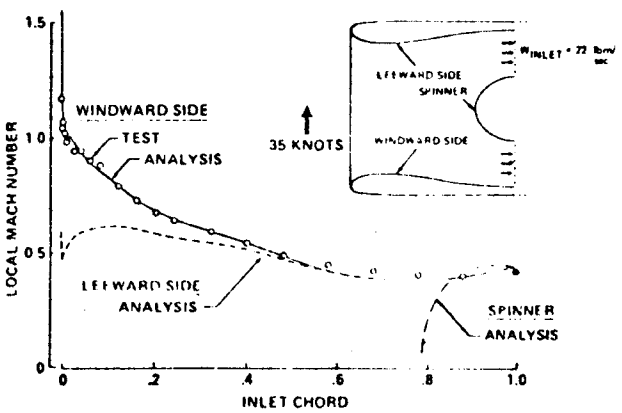

Comparison of Analysis and Test for Cowl at 90° Angle of Attack.

SILLETE 2-19-78

FIGURE 9.5 INLET CROSSWIND CAPABILITY

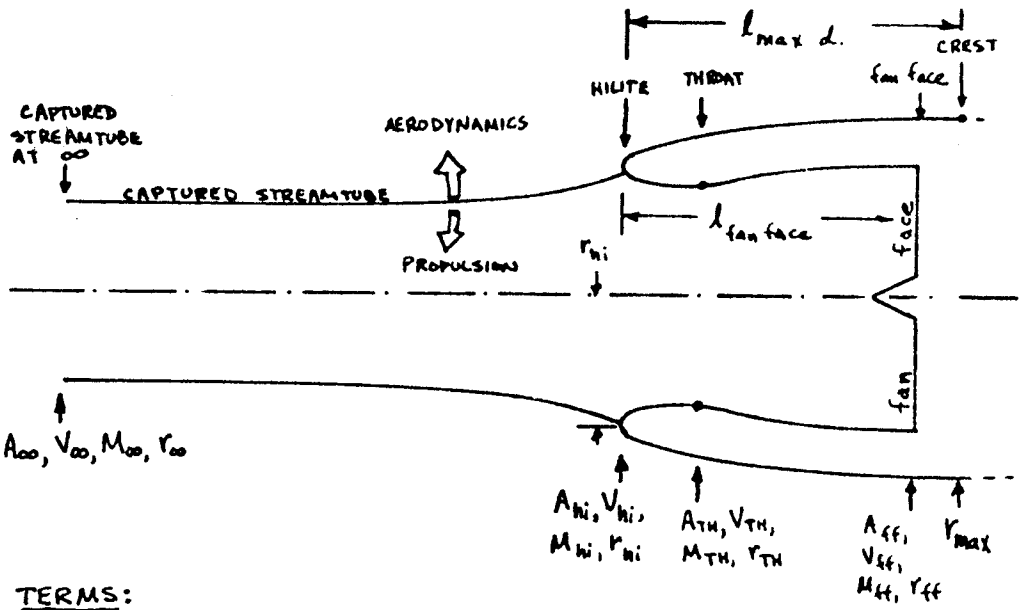

TERMS:

INLET VELOCITY RATIO = $\frac{V_{hi}}{V_\infty}$

INLET OFFSET RATIO = $\frac{r_{hi}}{r_{max}}$

INLET AREA RATIO = A_∞ / A_{hi}

INLET CONTRACTION RATIO = r_{hi}^2 / r_{th}^2

RELATION BETWEEN AREA RATIO & VELOCITY RATIO:

$$\frac{A_\infty}{A_{hi}} = \frac{V_{hi}}{V_\infty}\left[\frac{\gamma-1}{2}M_\infty^2 - \frac{\gamma-1}{2}M_\infty^2\left(\frac{V_{hi}}{V_\infty}\right)^2 + 1\right]^{\frac{1}{\gamma-1}}$$

INLET WEIGHT FLOW = $g\rho_\infty V_\infty A_\infty = g\rho_{hi} V_{hi} A_{hi} = g\rho_{ff} V_{ff} A_{ff} \equiv \dot{w}_A$ (lbm/sec)

INLET WEIGHT FLOW RATIO = $\frac{\rho_{hi} V_{hi} A_{hi}}{\rho_\infty V_\infty A_{hi}}$

INLET CORRECTED WEIGHT FLOW = $\frac{\dot{w}_A\sqrt{\theta_T}}{\delta_T}$

$\theta_T = \frac{T_{TOTAL,\,°R}}{518\,°R}$ $\qquad \delta_T = \frac{P_{T,\,psia}}{14.7}$

CONDITION	SHAPE OF CAPTURE STREAMTUBE	V_{HI}/V_∞	A_∞/A_{HI}
LOW SPEED, HIGH POWER	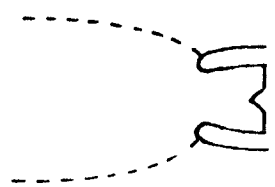	>1	>1
NO SPILLAGE	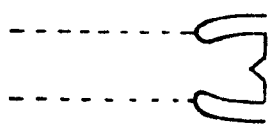	=1	=1
CRUISE	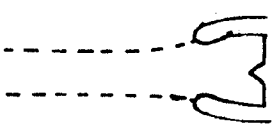	<1	<1

FIGURE 9.6 DEFINITION OF INLET TERMS

GILLETTE 2.19.78

649

NACA 1—SERIES ORDINATES

[Ordinates in percent]

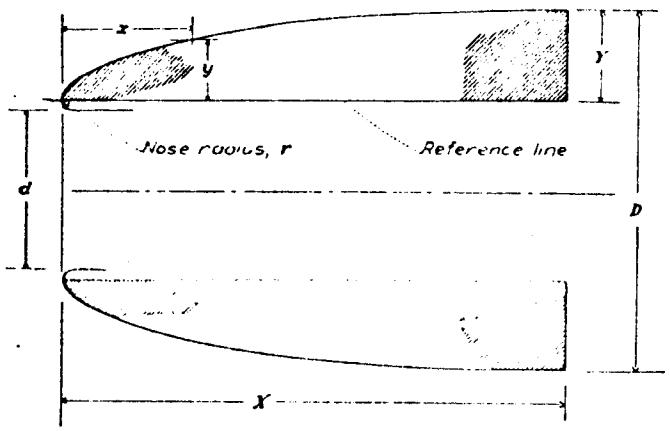

$$X=\left(\frac{X}{D}\right)D$$

$$Y=\frac{D-d}{2}-r$$

For $r = 0.025Y$: $Y = \frac{D-d}{2.05} = \frac{D\left(1-\frac{d}{D}\right)}{2.05}$

x/X	y/Y	x/X	y/Y	x/X	y/Y	x/X	y/Y
0	0	13.0	41.94	34.0	69.06	60.0	89.11
.2	4.80	14.0	43.66	35.0	70.09	62.0	90.20
.4	6.63	15.0	45.30	36.0	71.05	64.0	91.23
.6	8.12	16.0	46.88	37.0	72.00	66.0	92.20
.8	9.33	17.0	48.40	38.0	72.94	68.0	93.11
1.0	10.38	18.0	49.88	39.0	73.85	70.0	93.95
1.5	12.72	19.0	51.31	40.0	74.75	72.0	94.75
2.0	14.72	20.0	52.70	41.0	75.63	74.0	95.49
2.5	16.57	21.0	54.05	42.0	76.48	76.0	96.16
3.0	18.31	22.0	55.37	43.0	77.32	78.0	96.79
3.5	19.94	23.0	56.66	44.0	78.15	80.0	97.35
4.0	21.48	24.0	57.92	45.0	78.95	82.0	97.87
4.5	22.96	25.0	59.15	46.0	79.74	84.0	98.33
5.0	24.36	26.0	60.35	47.0	80.50	86.0	98.74
6.0	27.01	27.0	61.52	48.0	81.25	88.0	99.09
7.0	29.47	28.0	62.67	49.0	81.99	90.0	99.40
8.0	31.81	29.0	63.79	50.0	82.69	92.0	99.65
9.0	34.03	30.0	64.89	52.0	84.10	94.0	99.85
10.0	36.13	31.0	65.97	54.0	85.45	96.0	99.95
11.0	38.15	32.0	67.03	56.0	86.73	98.0	99.99
12.0	40.09	33.0	68.07	58.0	87.95	100.0	100.00

Nose radius 0.025Y

EXAMPLE : NACA 1-85-75

$\frac{d}{D} = .85$ $\quad$ $\frac{X}{D} = .75$

SOURCE: NACA R.N. 920

FIGURE 9.7 GEOMETRIC DESCRIPTION OF NACA 1-SERIES INLET COWLS

GILLETTE 2.26.78

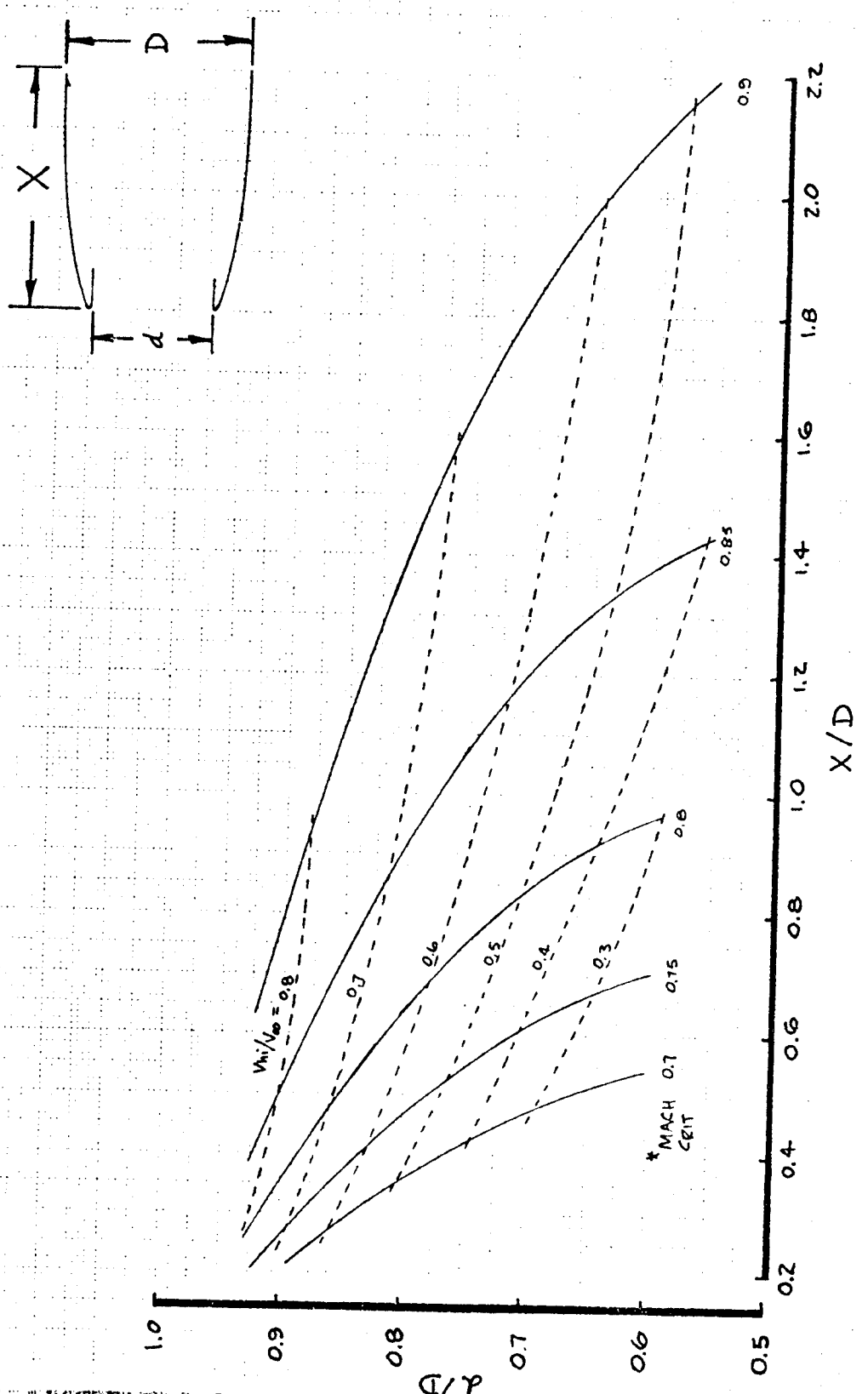

SOURCE: D6-3990

* MACH CRIT IS WHERE LOCALLY SUPERSONIC FLOW FIRST APPEARS

R. LOKEN 7.5.59	NACA 1 SERIES DESIGN CHART	FIGURE 9.8
TRACE GILLETTE 2.19.78		9.24

649

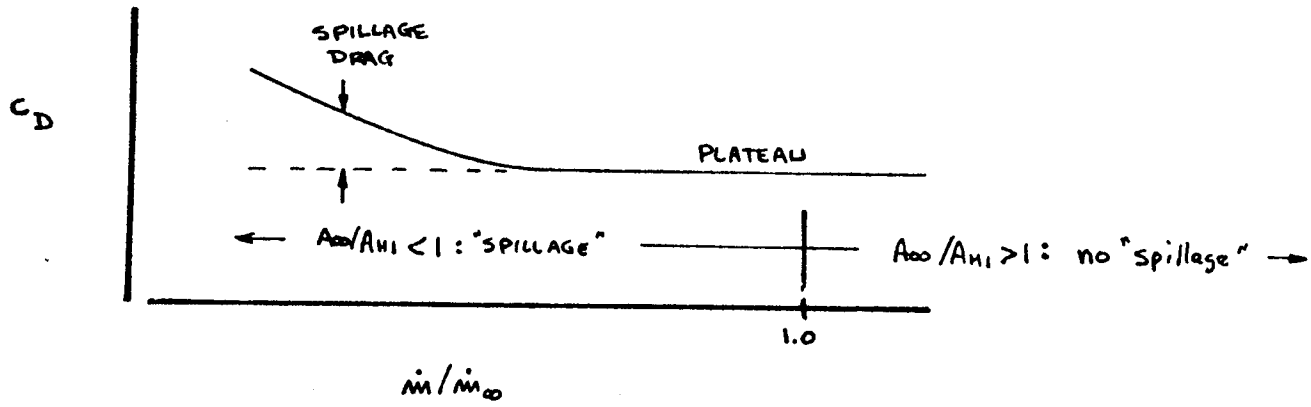

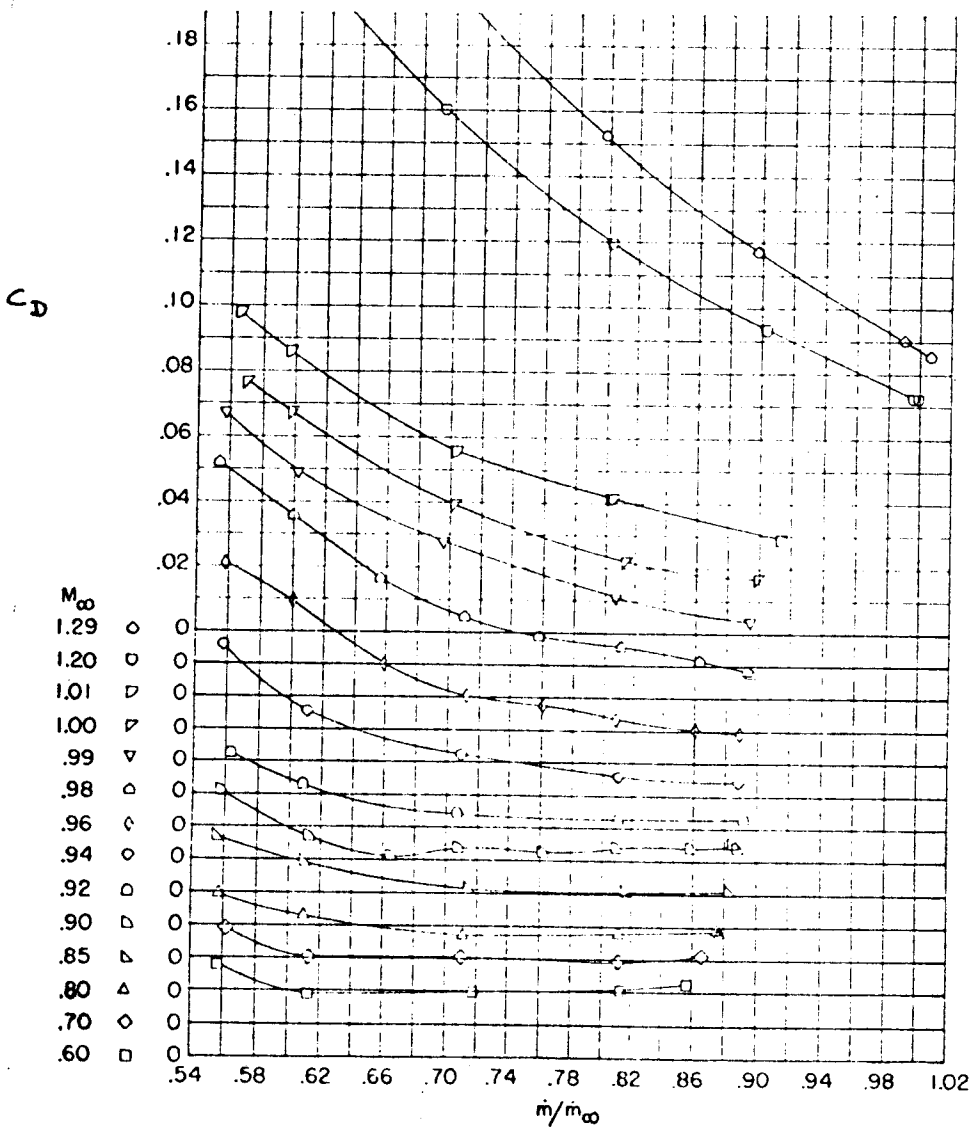

FIGURE 9.9 SPILLAGE DRAG CHARACTERISTICS OF NACA 1-85-75 INLET

GILLETTE 2.26.78

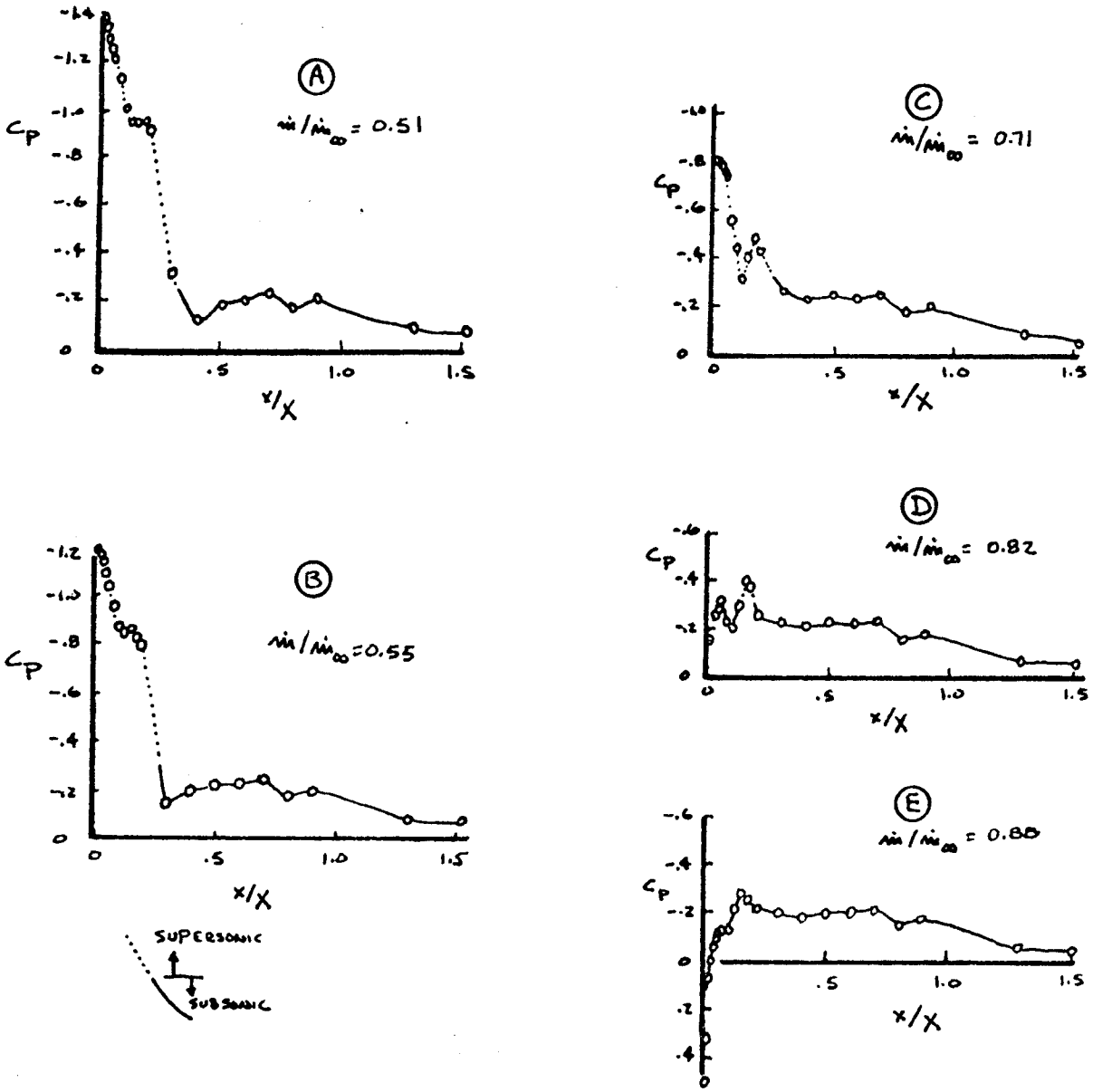

SOURCE: NASA TM X-2917

FIGURE 9.10 NACA 1-85-75 CHARACTERISTICS AT 0.85 MACH

NACA 1-SERIES COWL

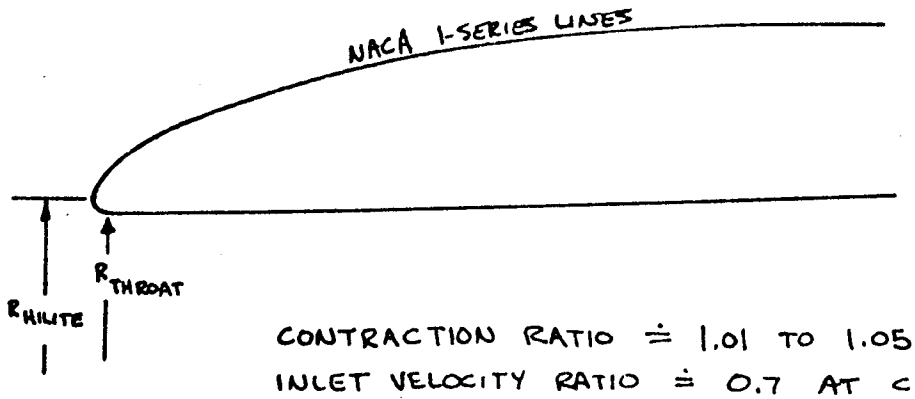

CONTRACTION RATIO ≐ 1.01 TO 1.05
INLET VELOCITY RATIO ≐ 0.7 AT CRUISE

BUT

CROSSWIND CAPABILITY FOR INLET REQUIRES HIGHER CONTRACTION RATIO

BOEING 65-SERIES INLET

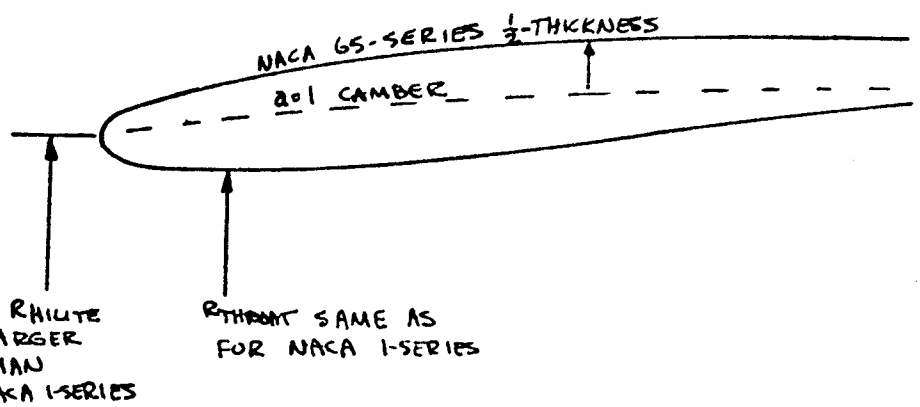

CONTRACTION RATIO ≐ 1.10 TO 1.15
INLET VELOCITY RATIO ≐ 0.6 AT CRUISE; DECREASES RELATIVE TO NACA 1-SERIES BECAUSE R_{HILITE} IS LARGER

FIGURE 9.11 BOEING 65-SERIES INLET

GILLETTE 2.26.78

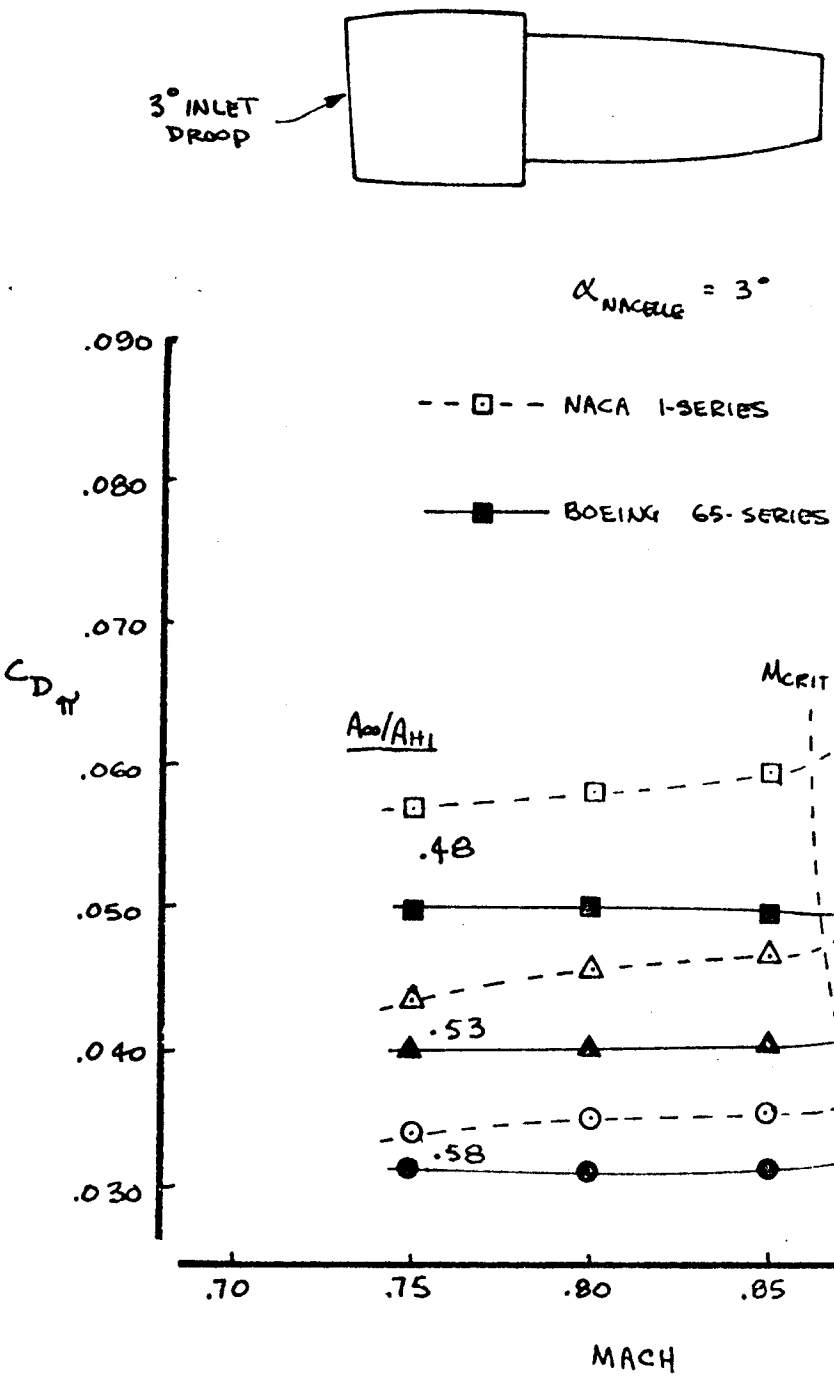

FIGURE 9.12 COMPARISON OF NACA 1-SERIES AND BOEING 65-SERIES INLET DRAG

GILLETTE 2.26.78

P. 9.28

M 5 6

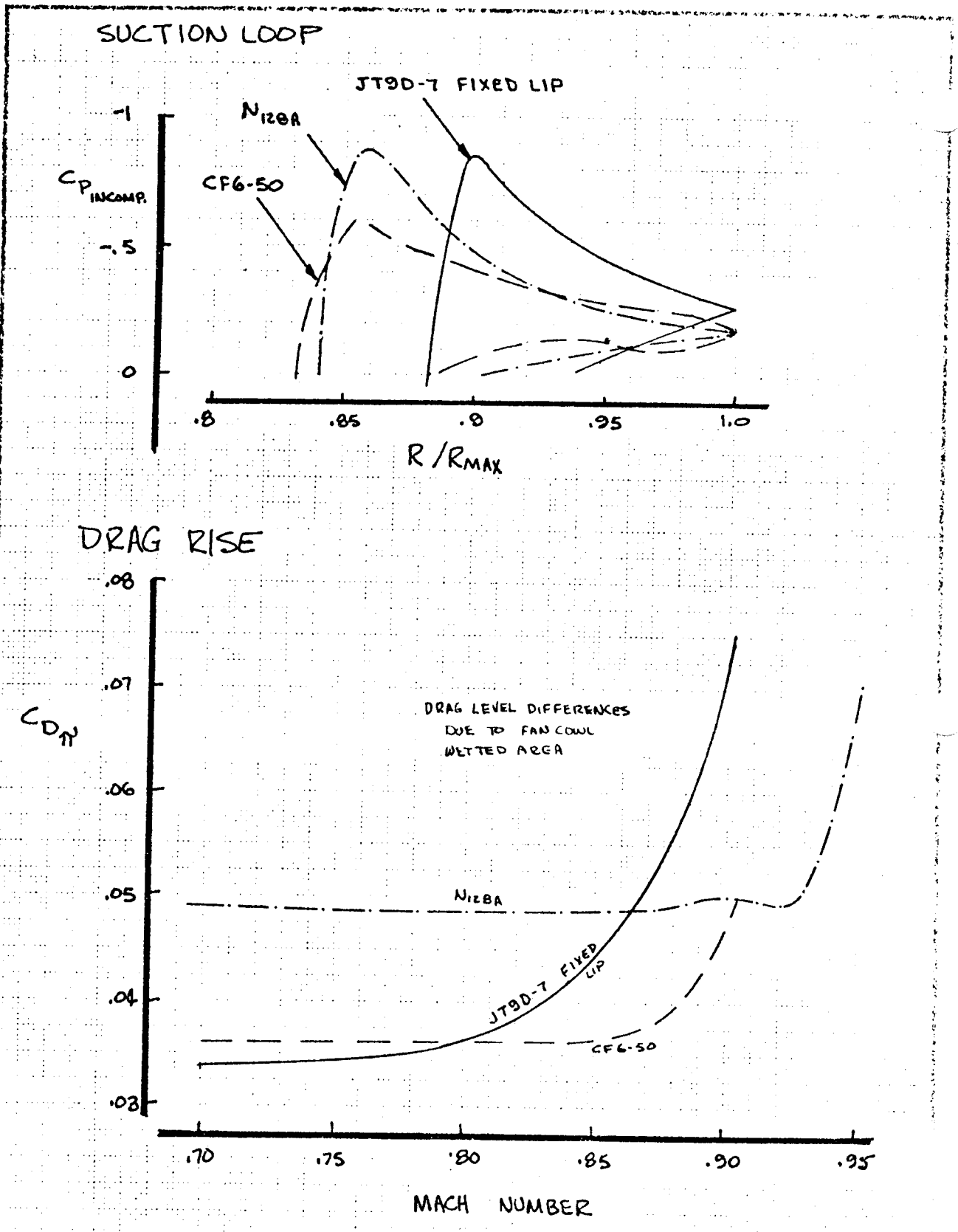

GILLETTE 2.26.78

FIXED LIP TRANSONIC COWLS
DESIGNED FOR THE 747

FIG 9.13

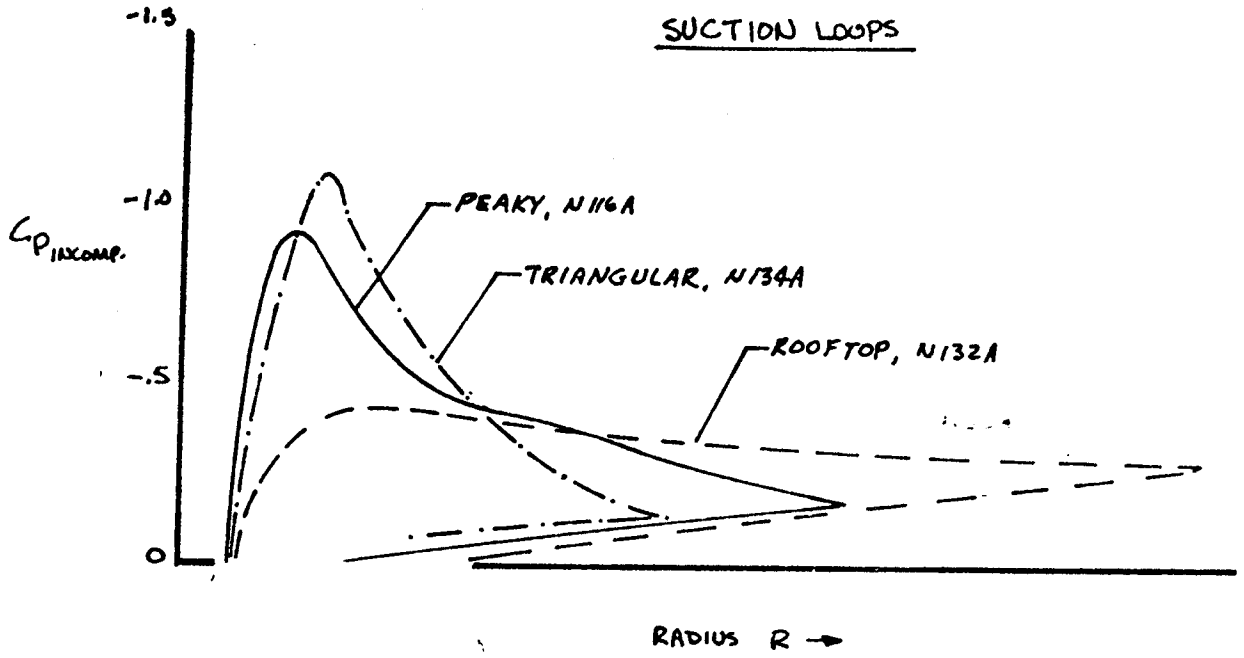

SOURCE: D6-41800TN
K.A. SCHIPPERS

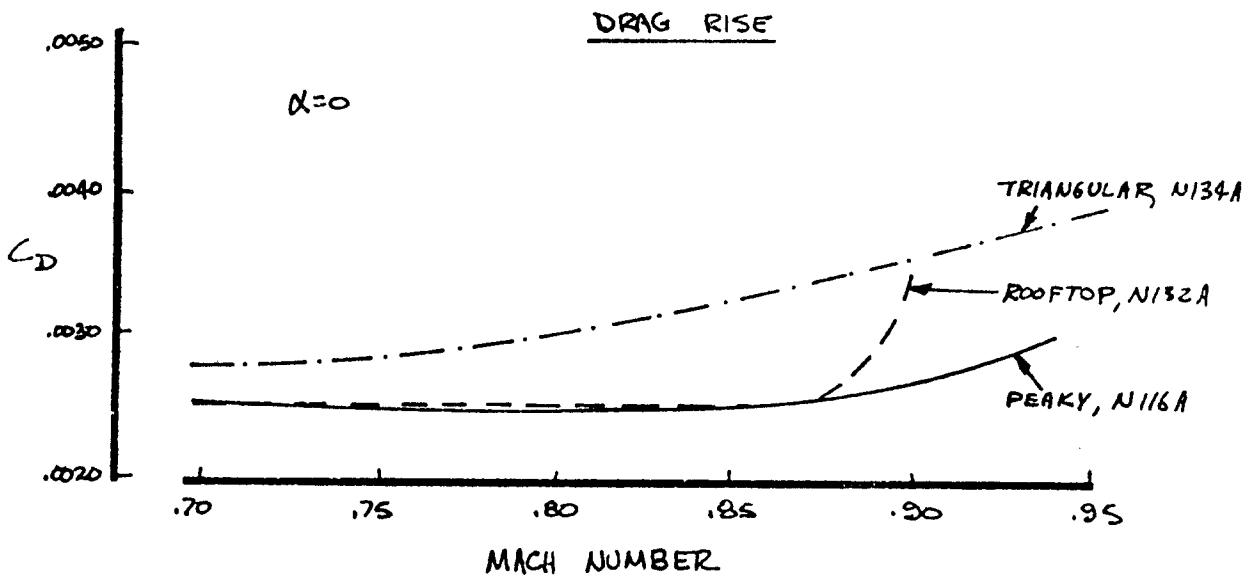

FIGURE 9.14 747 INLET FAMILY STUDY

GILLETTE
2.26.78

959

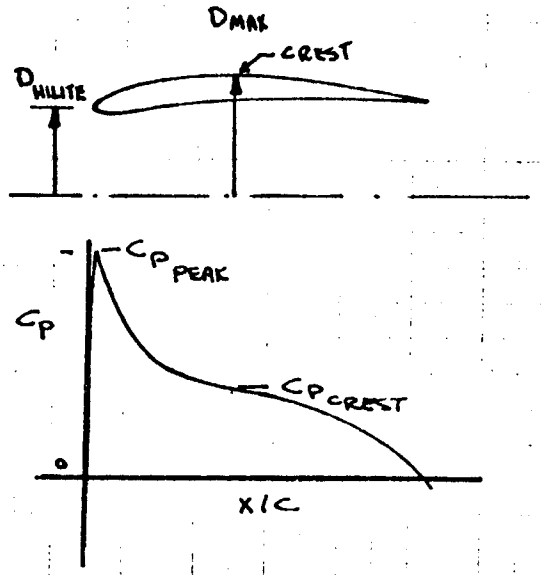

NOTE: $\frac{A_\infty}{A_{HI}} \doteq 0.64$

$M_\infty = 0$

SOURCE: D6-33790TN
R. ROBINSON

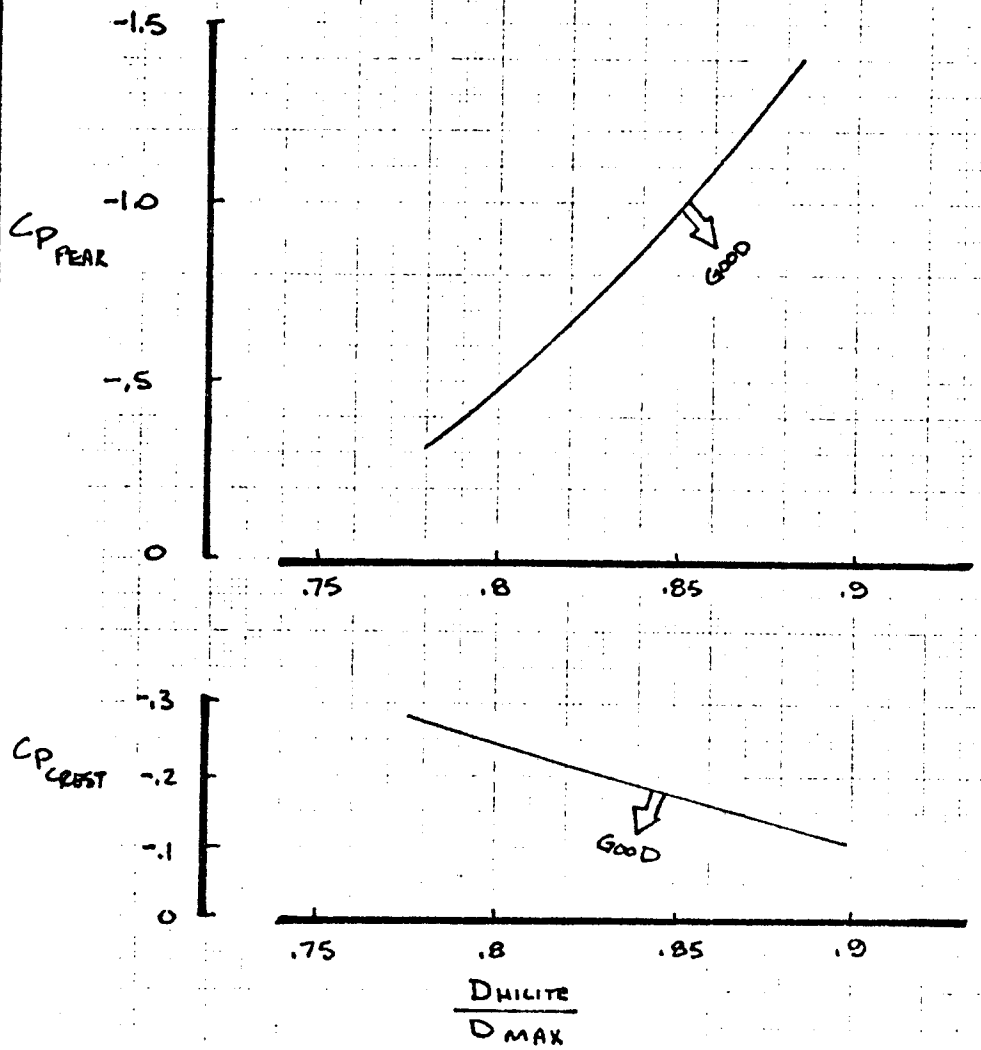

CALC	GILLETTE	2-26-78	REVISED	DATE	747-DERIVED TRANSONIC COWL DESIGN RULES	
CHECK						FIG. 9.15
APR						
APR					THE BOEING COMPANY	PAGE 9.31

DI 4100 3240

K-E ALBANENE 105L TRACING PAPER

656

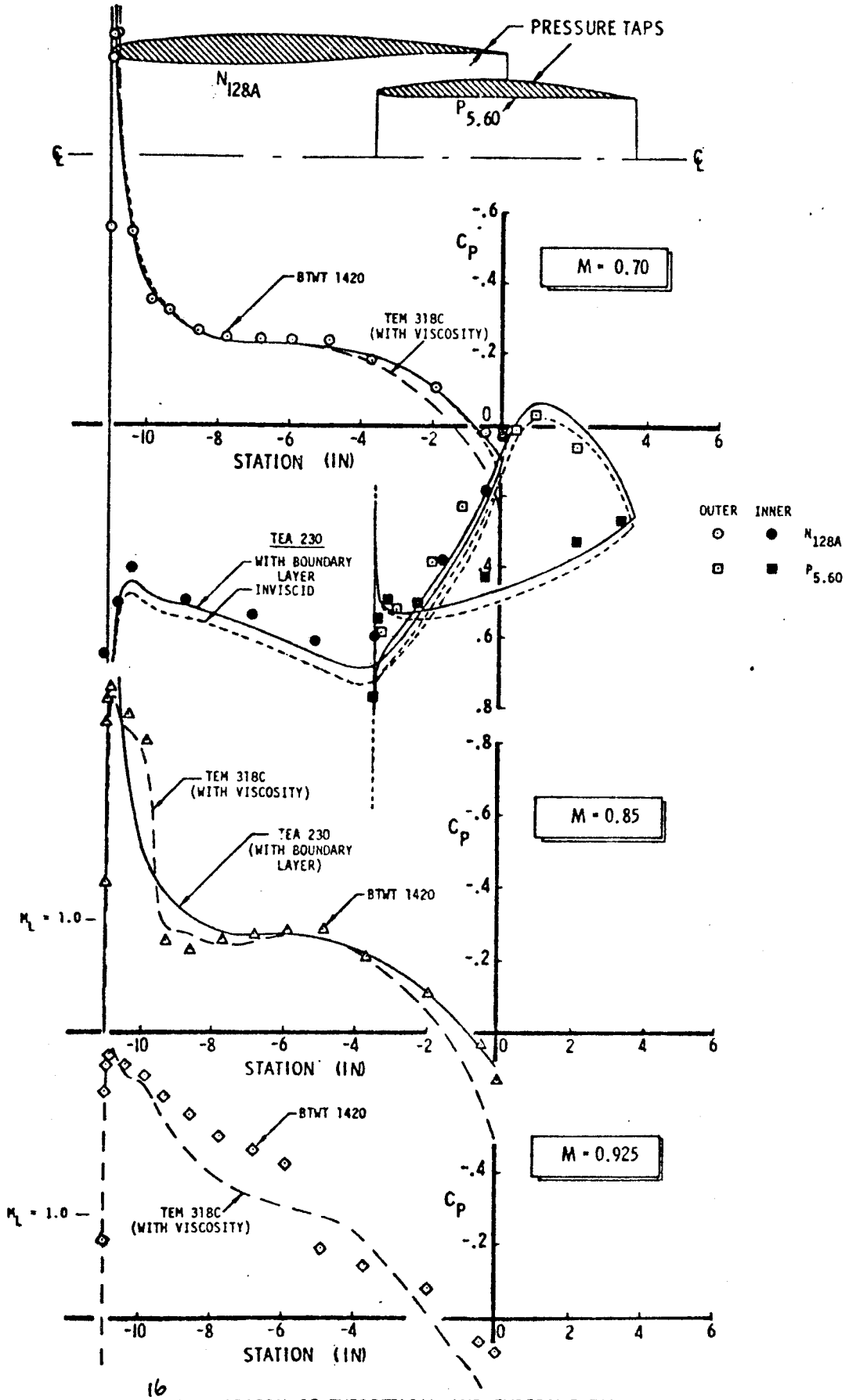

FIGURE 9.16 COMPARISON OF THEORETICAL AND EXPERIMENTAL PRESSURES ON N_{128A} $P_{5.60}$ FLOW NACELLE

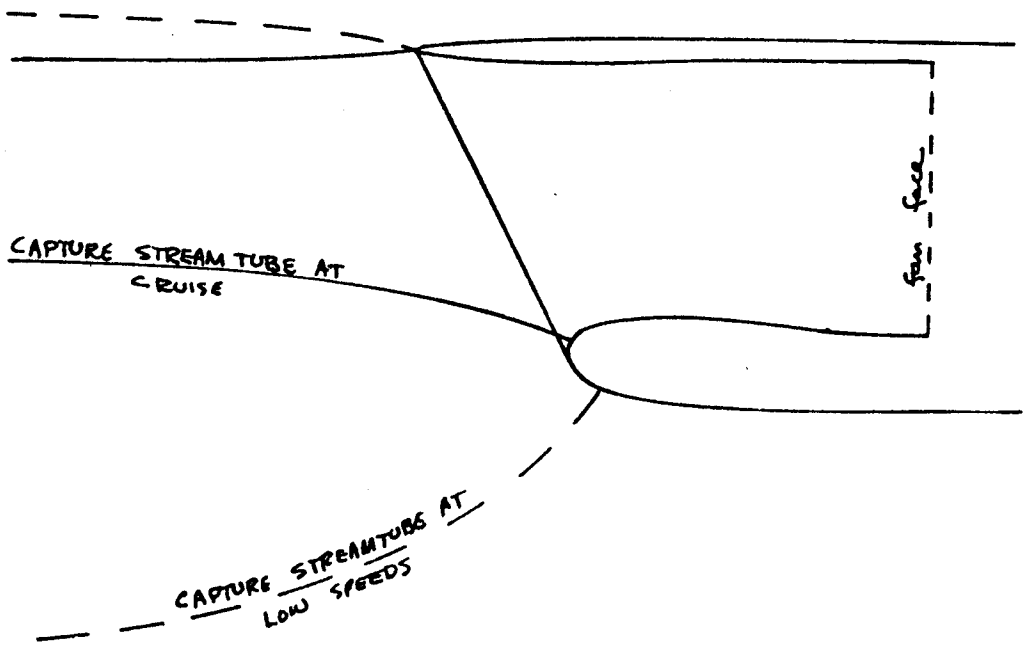

FIGURE 9.17 SWEPT INLET FOR HIGH TRANSONIC SPEEDS

GILLETTE
2.26.78

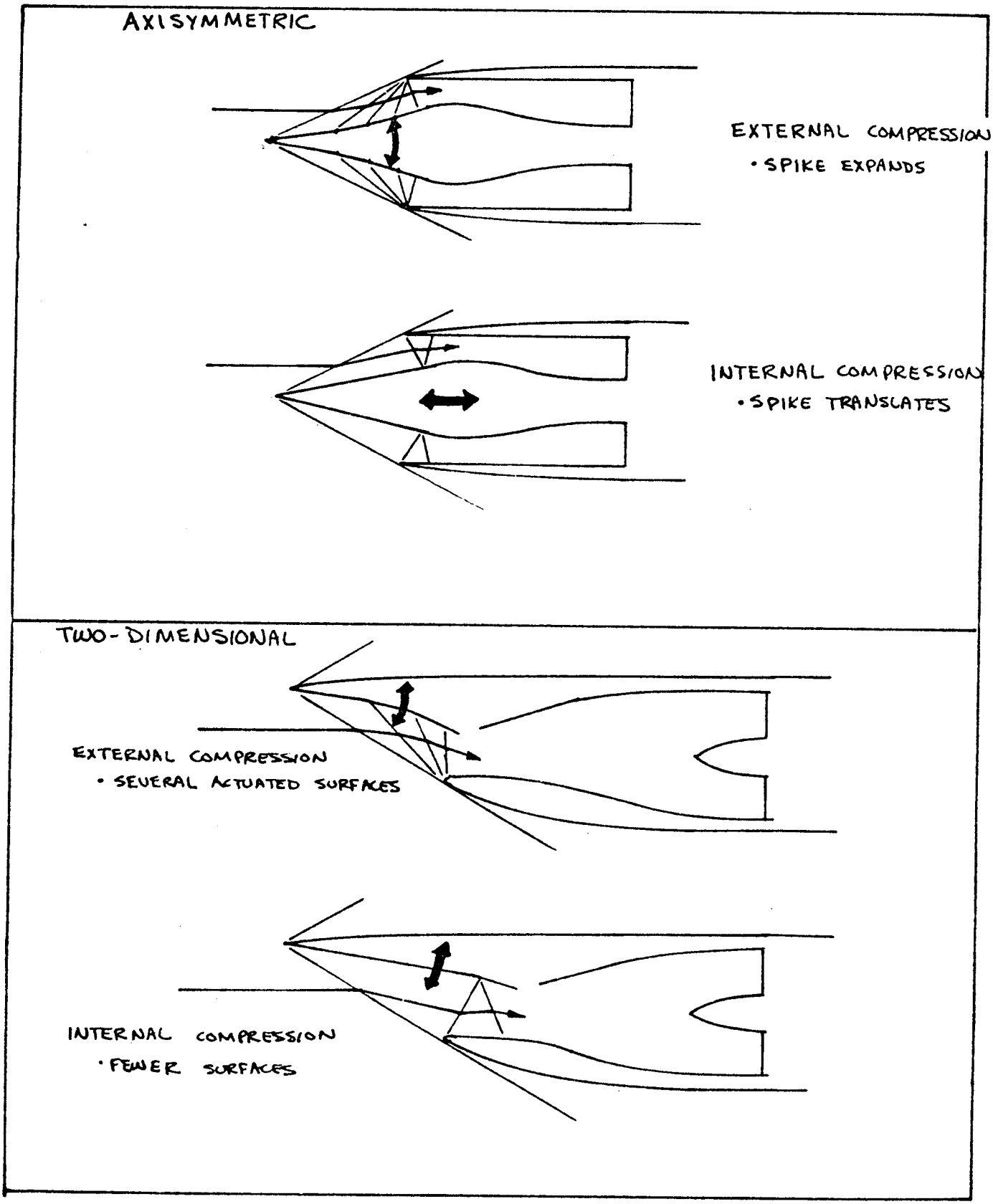

FIGURE 9.19 SUPERSONIC INLETS

GILLETTE
2.26.79

P.9.35

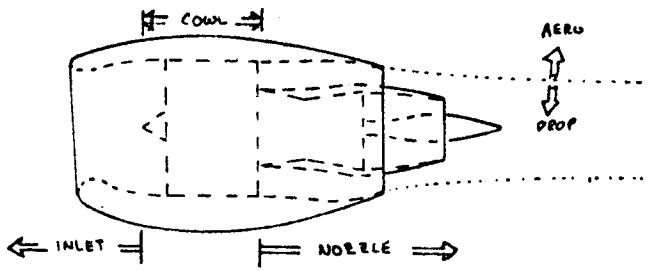

	FUNCTION	DESIGN GOAL	DOMINANCE IN:		
			Propulsion Contour Design	Aero Contour Design	Length Selection
COWL	1. CONNECT INLET TO EXIT	Connect the inlet contours to exit contours to produce the desired aero performance while containing the engine systems and accessories.	Little	Most	Little
NOZZLE	1. GET RID OF EXHAUST GAS	Exhaust the fan and primary gases in the most efficient manner; ie, with the least loss.	Most	Little	None
	2. CONTROL ENGINE CYCLE MATCH	Cause the engine to operate at the desired fan-core match throughout the flight regime.	Most	None	None
	3. NOISE REDUCTION	Provide engine noise reduction through acoustic treatment	None	None	Most
	4. REDUCE INTERFERENCE WITH AIRFRAME	Have an exhaust jet shape that will minimize aero interference	Some	Some	Little

FIGURE 9.20 Nacelle Cowl and Nozzle Design Considerations

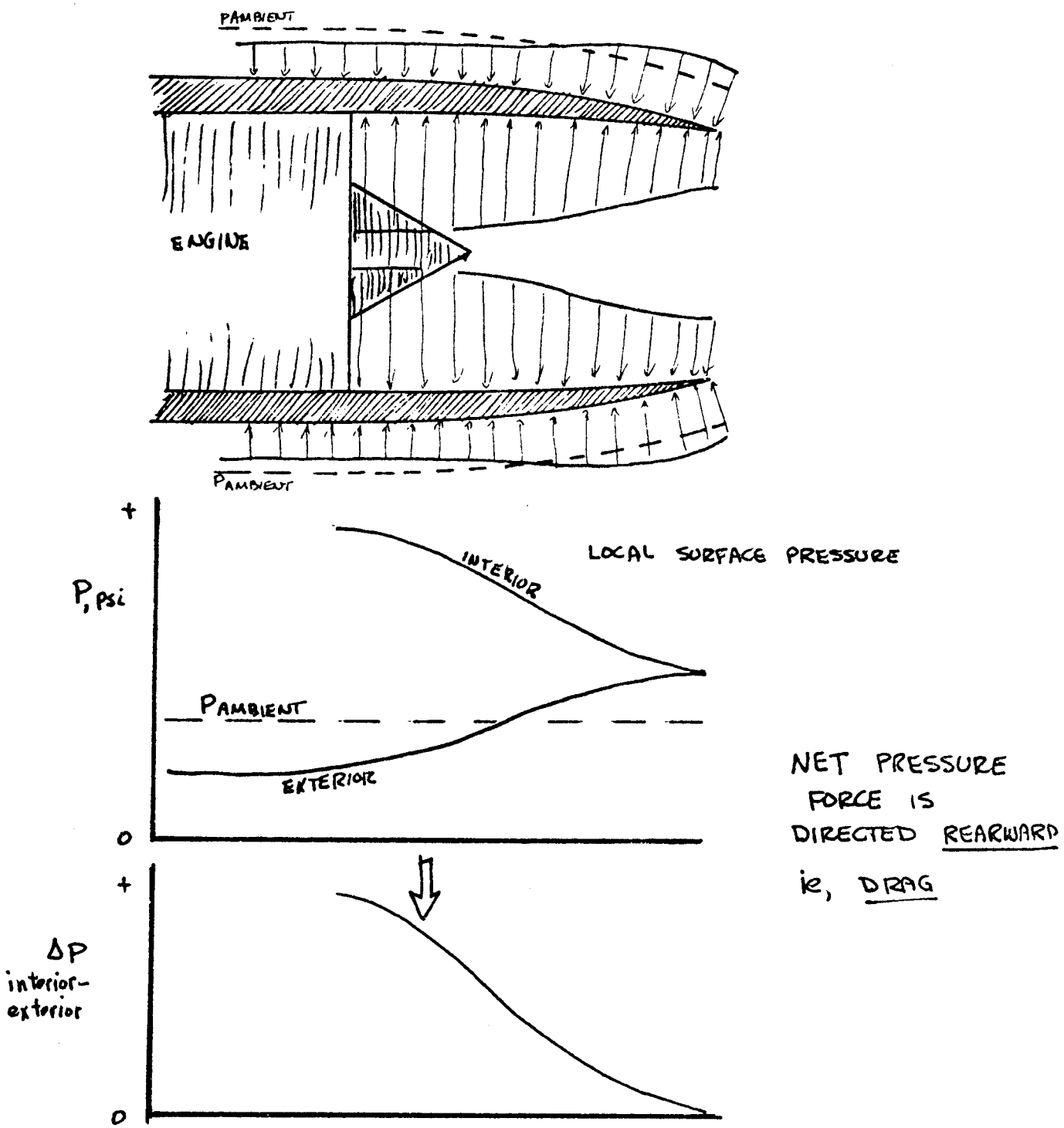

FIGURE 9.21 DIRECTION OF PRESSURE FORCE ON NOZZLE

GILLETTE 2.26.78

9.39

(a) NO EXTERNAL BOATTAIL

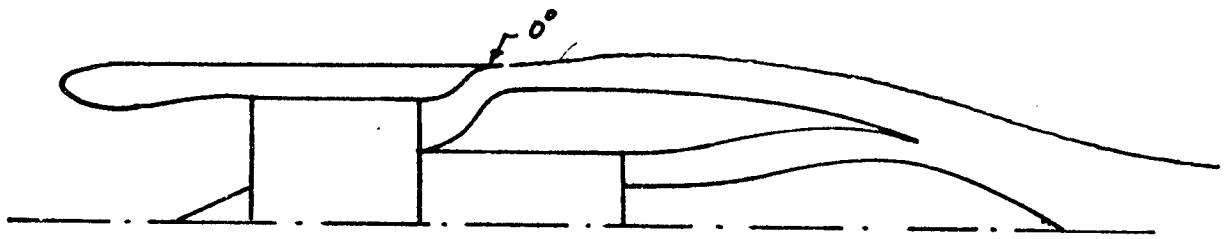

(b) SLIGHT EXTERNAL BOATTAIL

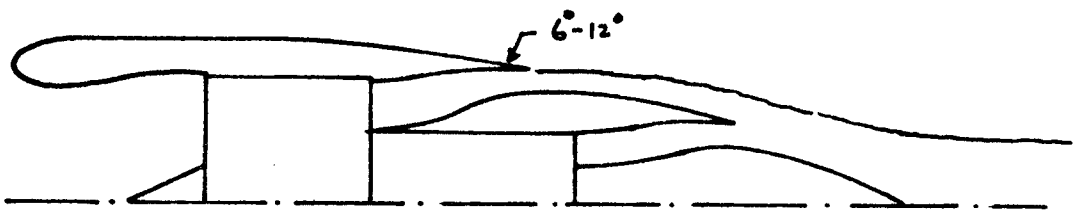

(c) LARGE EXTERNAL BOATTAIL

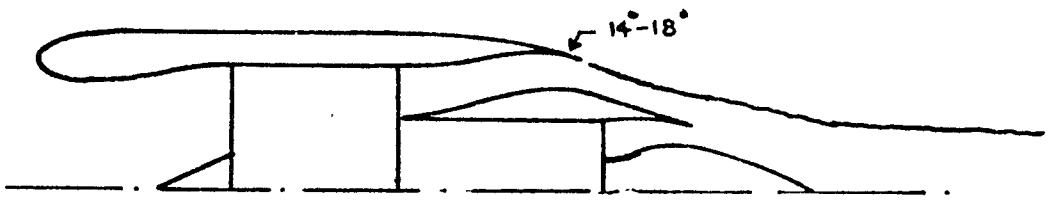

FIGURE 9.22 FAN NOZZLE BOATTAIL CHOICES

GILLETTE
2.26.78

6062

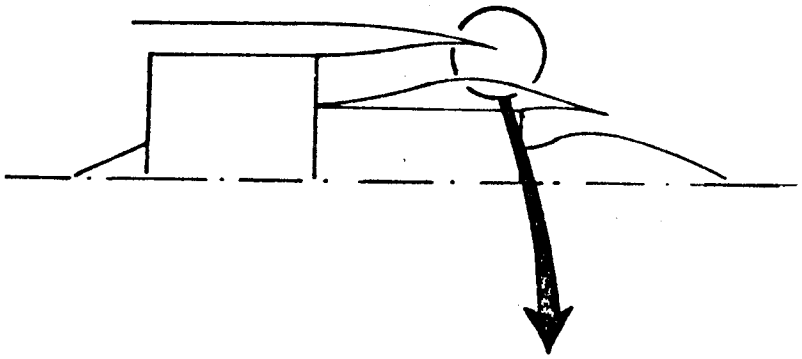

(a) NO RELATIVE BOATTAIL

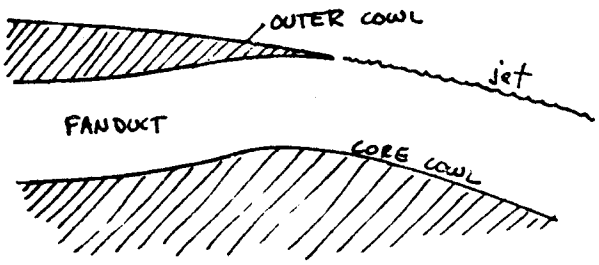

(b)

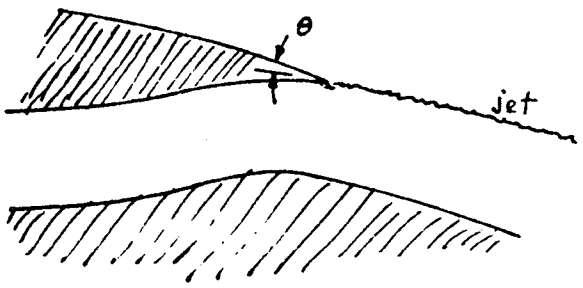

LIMITS ON θ:

(1) SHOULD NOT EXCEED 6°→7°, BASED ON AIRFOIL DATA

(2) SHOULD NOT BE SO LARGE AS TO CAUSE EXCESSIVE SUPPRESSION (PROP STAFF CRITERIA)

FIGURE 9.23 FAN COWL RELATNE BOATTAIL

GILLETTE 2.26.78

663

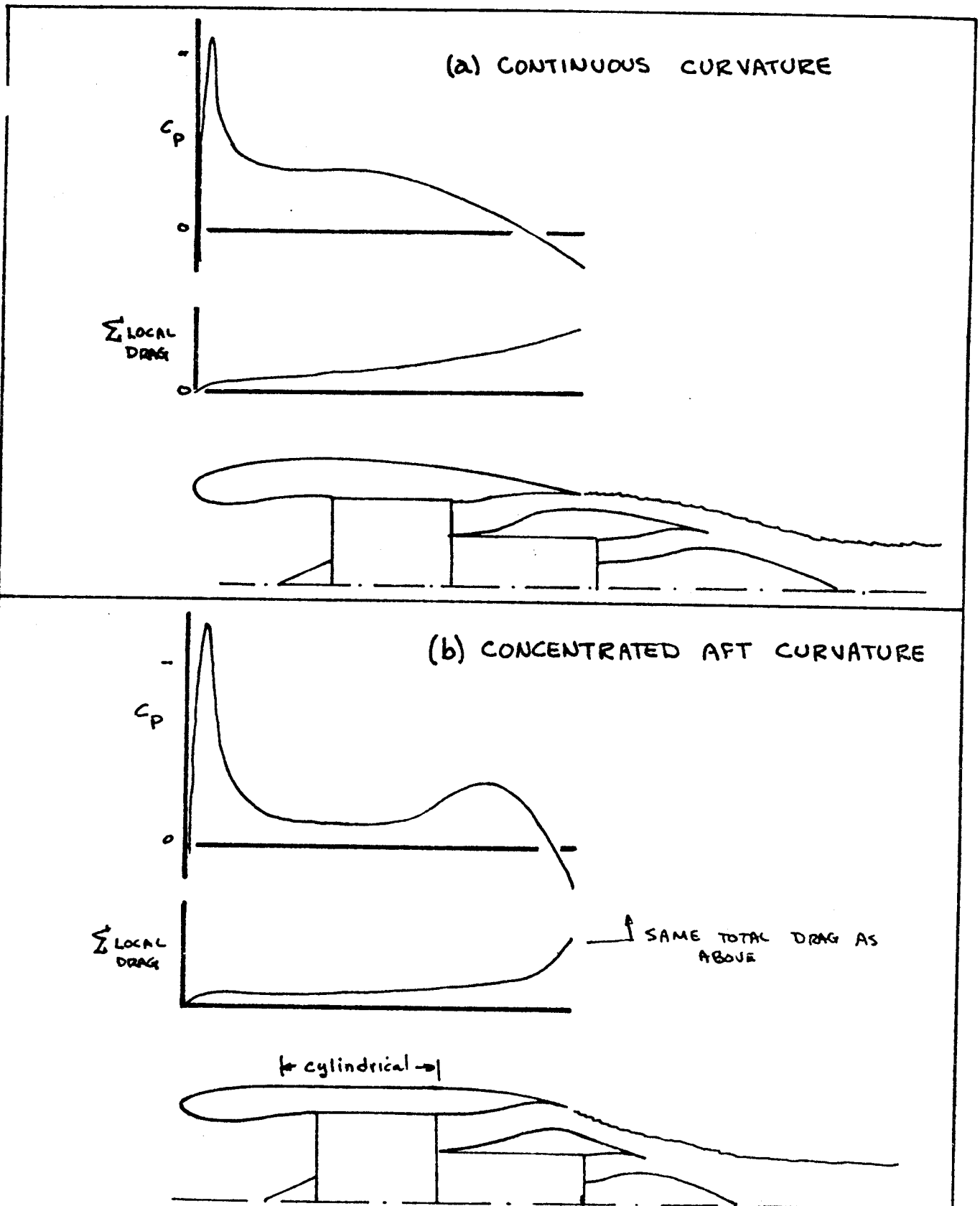

FIGURE 9.24 FAN COWL CURVATURE CONSIDERATIONS

GILLETTE
2.26.79

P.9.40

0604

(a) UPPER SURFACE BLOWING NOZZLE

(b) 2-D FIGHTER NOZZLE

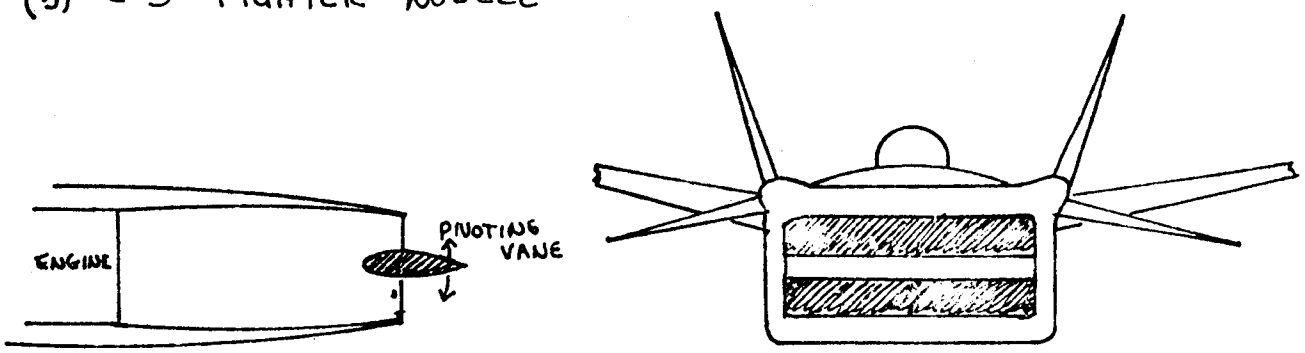

FIGURE 9.25 TWO-DIMENSIONAL NOZZLES

GILLETTE
2.26.78

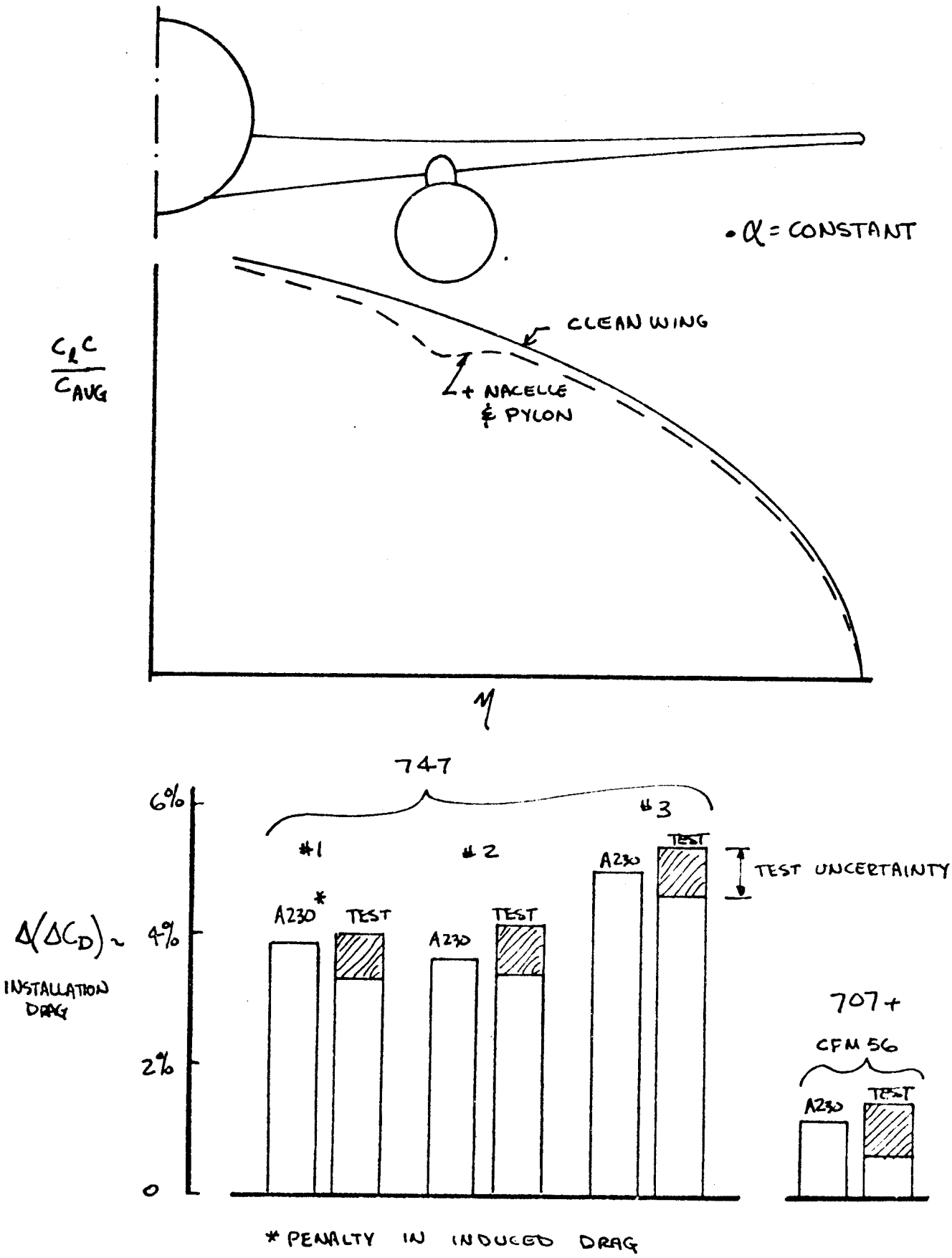

FIGURE 9.26 CORRELATION BETWEEN SPAN LOAD PENALTY & MEASURED NACELLE INSTALLATION DRAG PENALTY

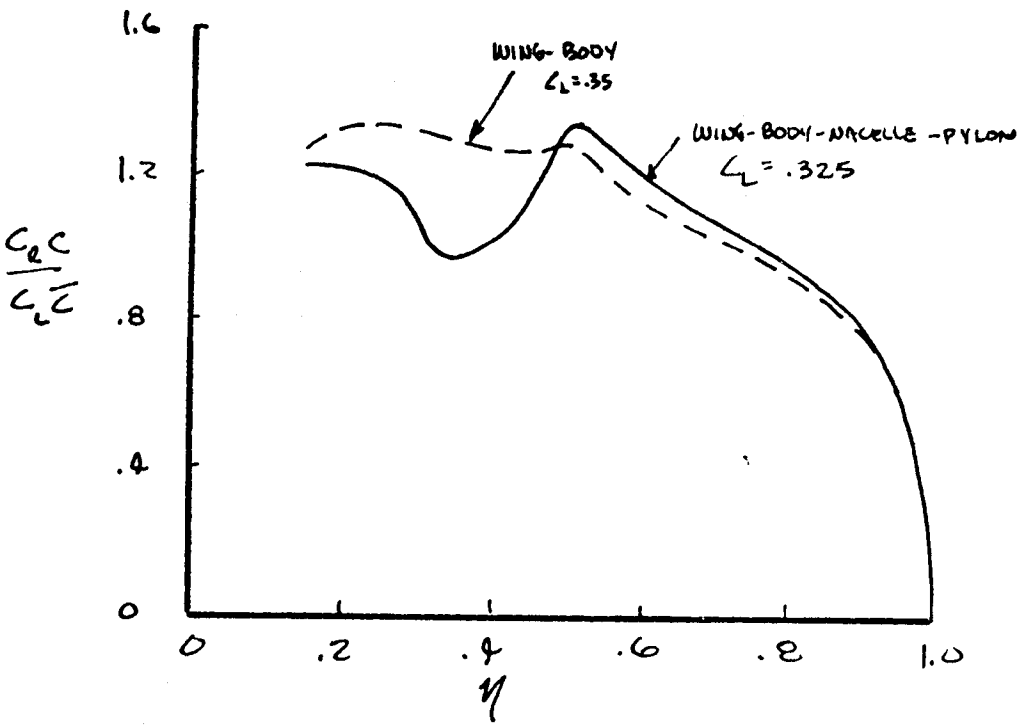

SOURCE: D6-43836TN
R.J. MARHEFKA

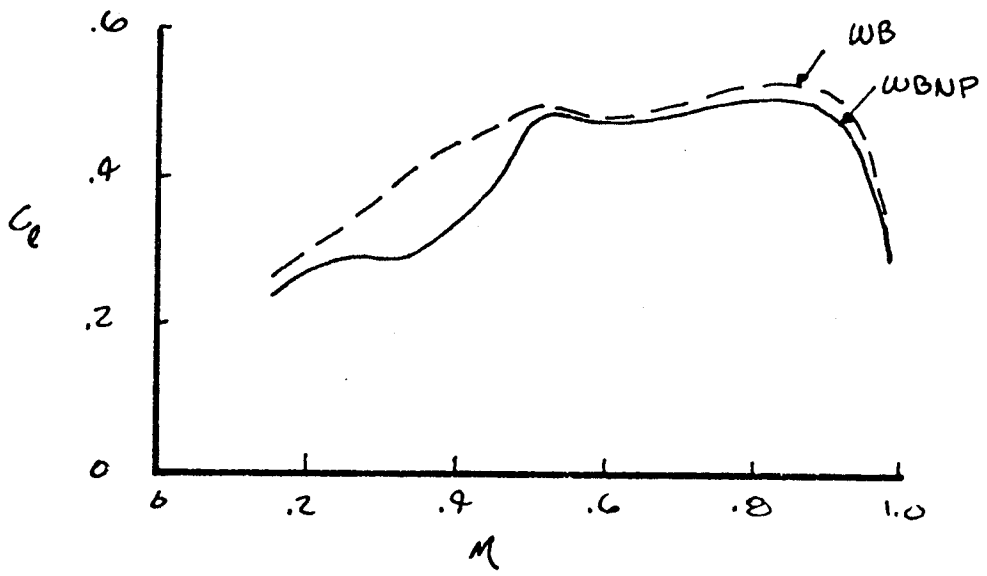

FIGURE 9.27 SPAN LOAD EFFECT OF NACELLE INSTALLATION ON THE 737

GILLETTE 2.26.78

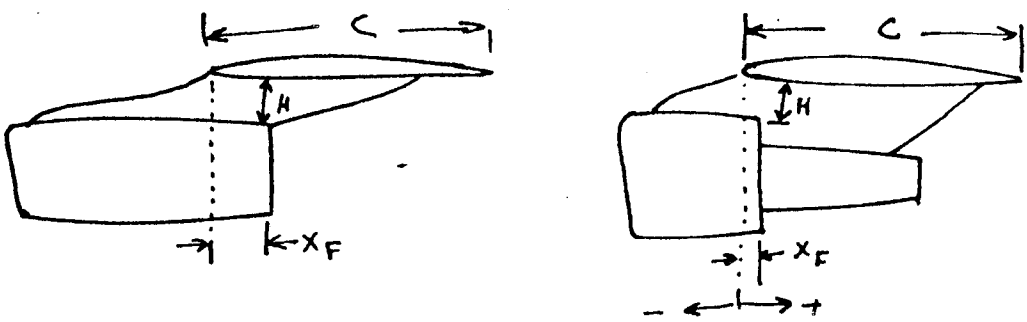

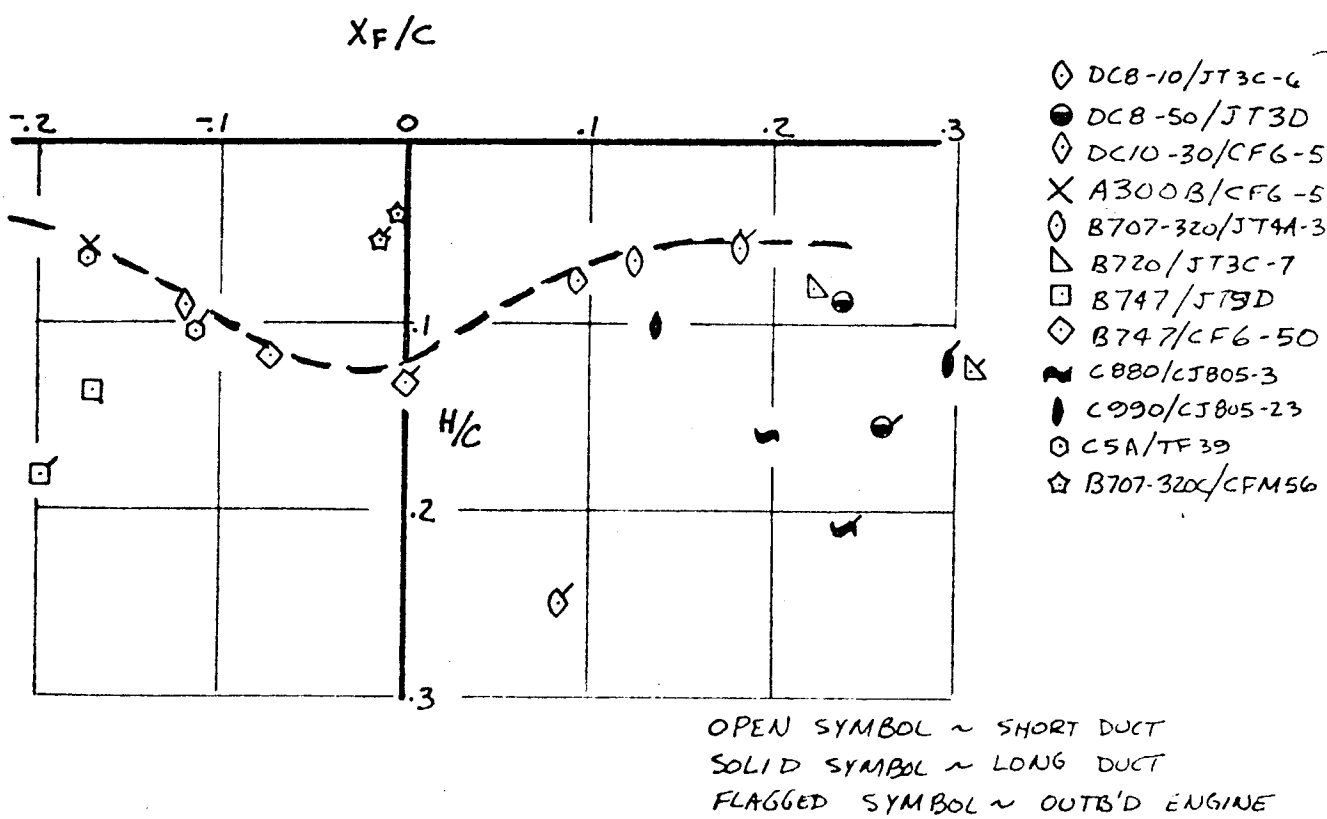

FIGURE 9.28 GENERALIZED UNDERWING NACELLE LOCATION CHART

GILLETTE
2.26.78

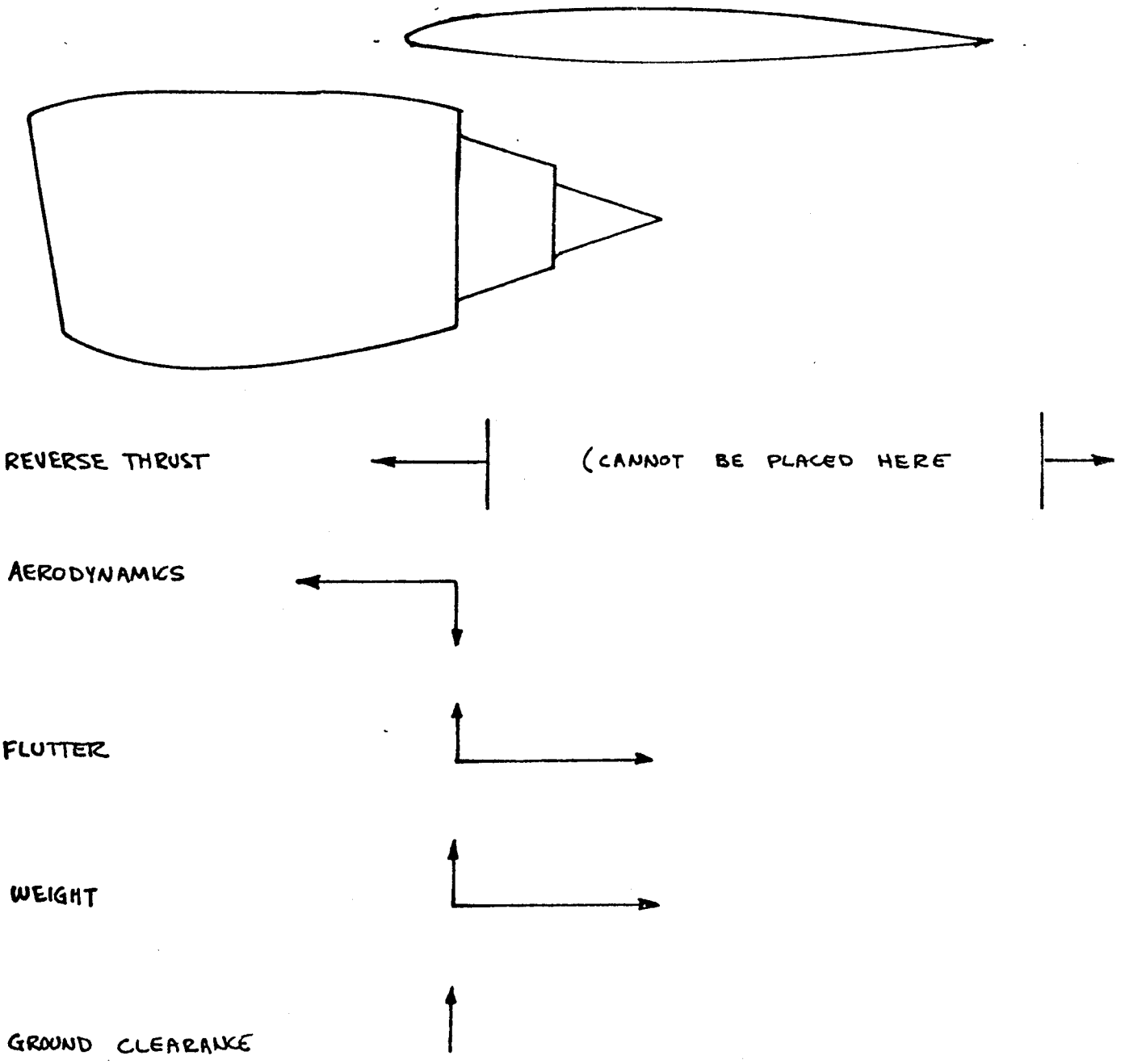

FIGURE 9.29 FAN COWL EXIT PLANE POSITIONING TRENDS

GILLETTE 2.26.78

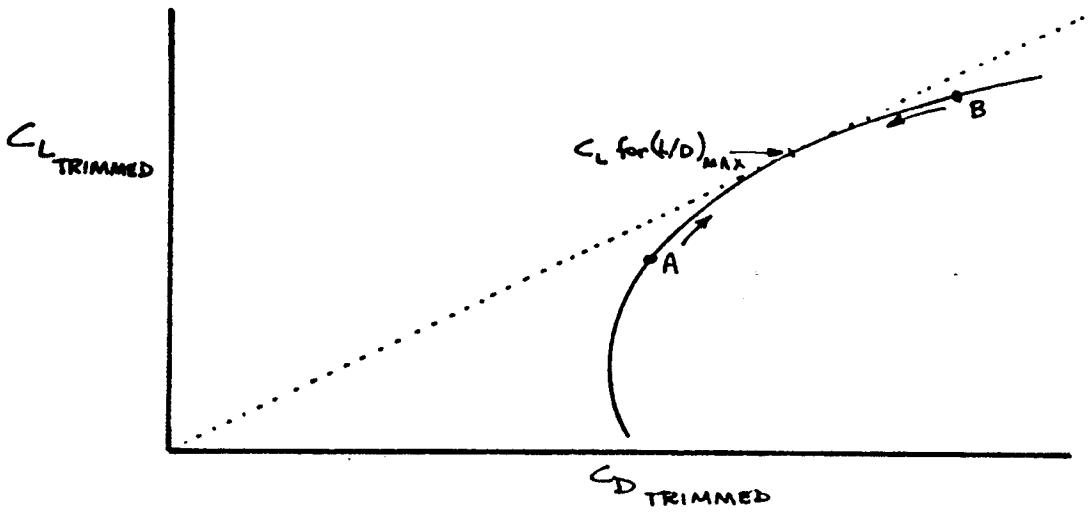

CASE A: nozzle TILT TO CAUSE C_L TO INCREASE:

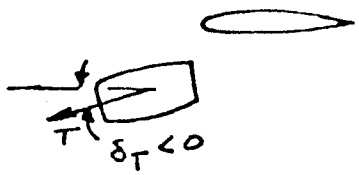

CASE B: NOZZLE TILT TO CAUSE C_L TO DECREASE:

BUT MISALIGNMENT OF NOZZLE REQUIRES MORE THRUST, WHICH PENALIZES $\frac{1}{TSFC}$

GOAL: OPTIMIZE $\Delta\left(\frac{1}{TSFC}\,\frac{L}{D}\right)$ WITH δ_T

FIGURE 9.30 ORIENTATION OF THRUST AXIS IN PITCH

GILLETTE
2.26.78

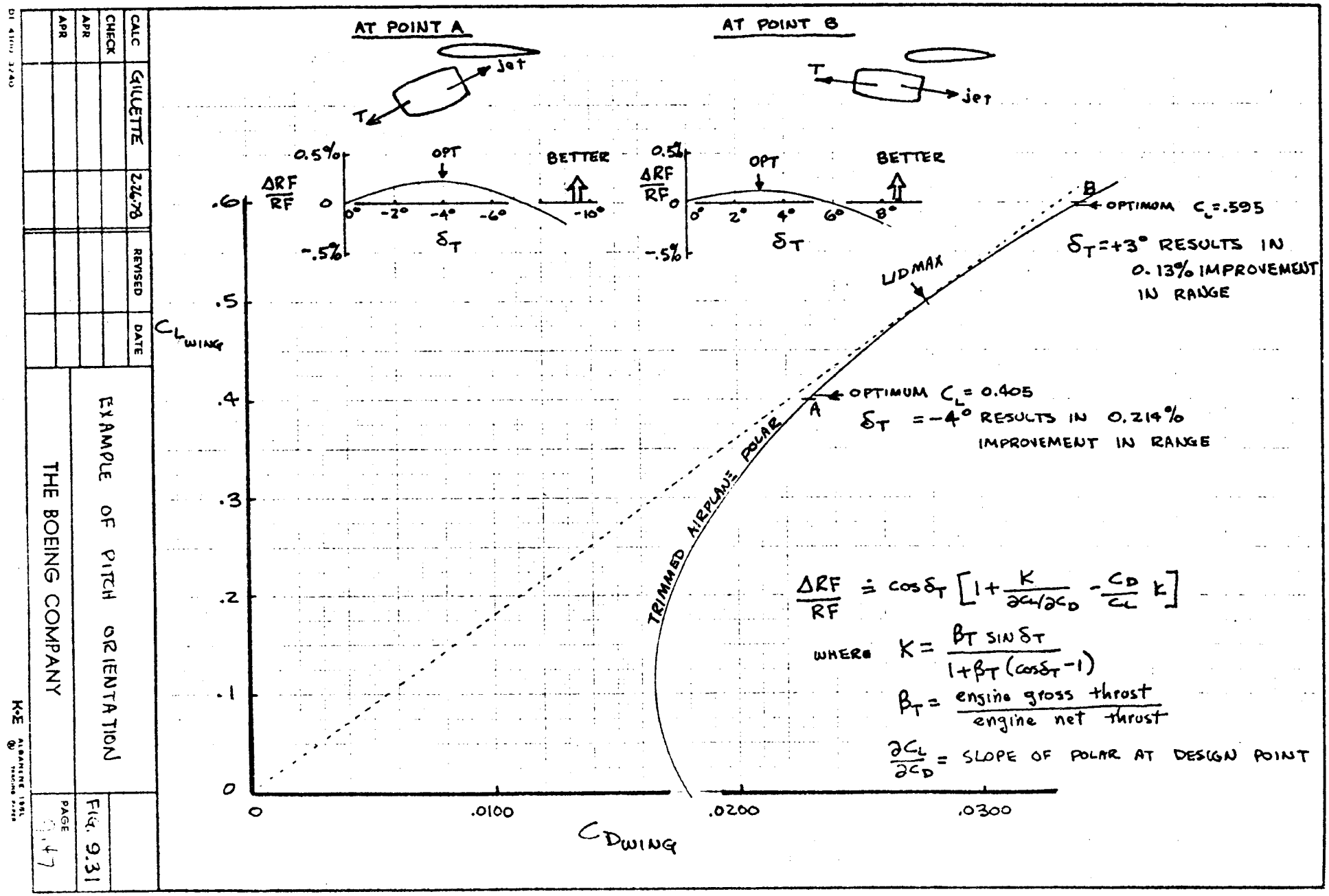

CALC	GILLETTE	2-24-78	REVISED	DATE
CHECK				
APR				
APR				

THE BOEING COMPANY

EXAMPLE OF PITCH ORIENTATION

Fig. 9.31

PAGE 647

K-E ALBUQUERQUE 1981

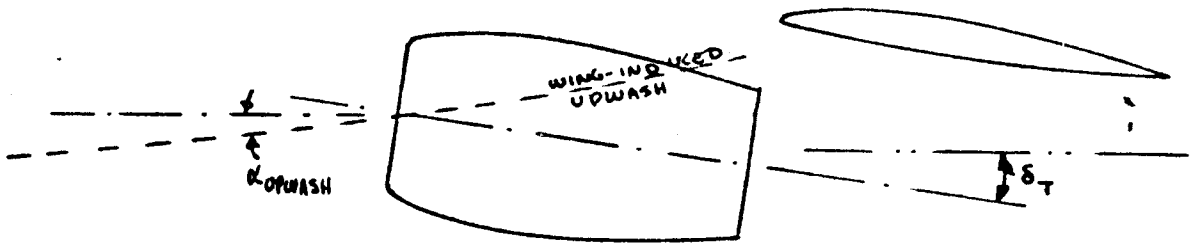

FOR THE AXISYMMETRIC NACELLE

$$\alpha_{INLET} = \delta_T + \alpha_{UPWASH}$$

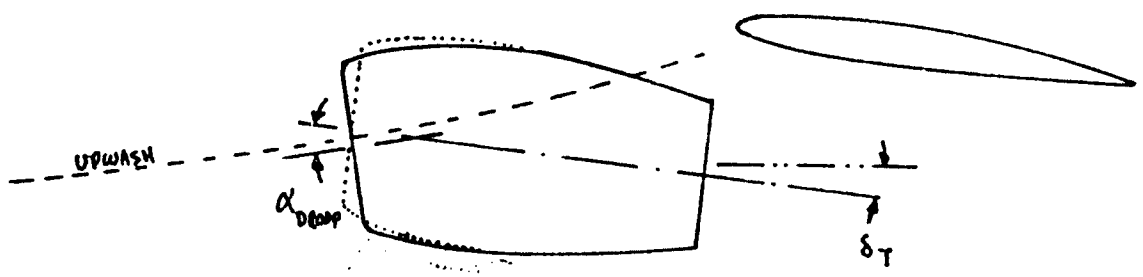

FOR THE DROOPED INLET:

$$\alpha_{DROOP} = -(\delta_T + \alpha_{UPWASH}) = -\alpha_{INLET}$$

FIGURE 9.32 INLET PITCH ALIGNMENT

① AXISYMMETRIC NACELLE

- DESIGNED TO ACHIEVE M_{CRIT} AT DESIGN A_∞/A_{HI}
- REPRESENTS COWL TECHNOLOGY

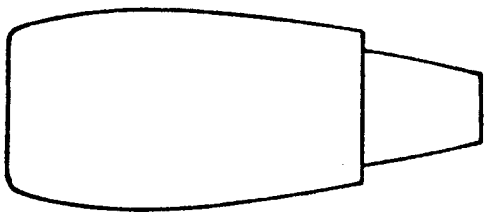

② NACELLE δ_T IS SELECTED AND INLET IS DROOPED

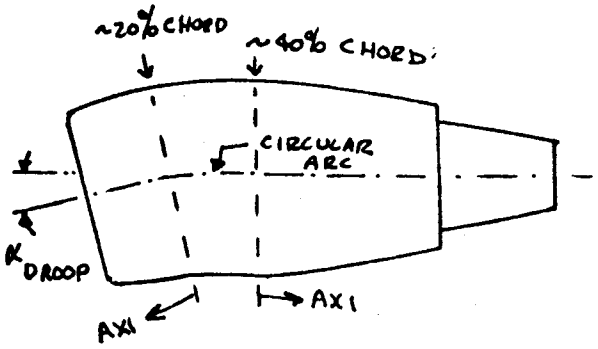

③ ACCESSORY BUMP IS ADDED TO KEEL

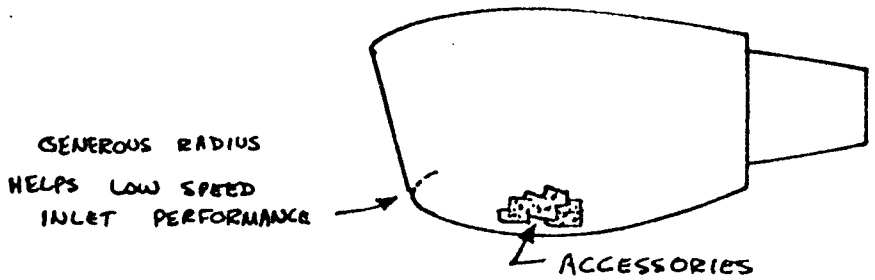

FIGURE 9.33 STEPS FROM THE AXI COWL TO THE AIRPLANE COWL

GILLETTE 2.2678

673

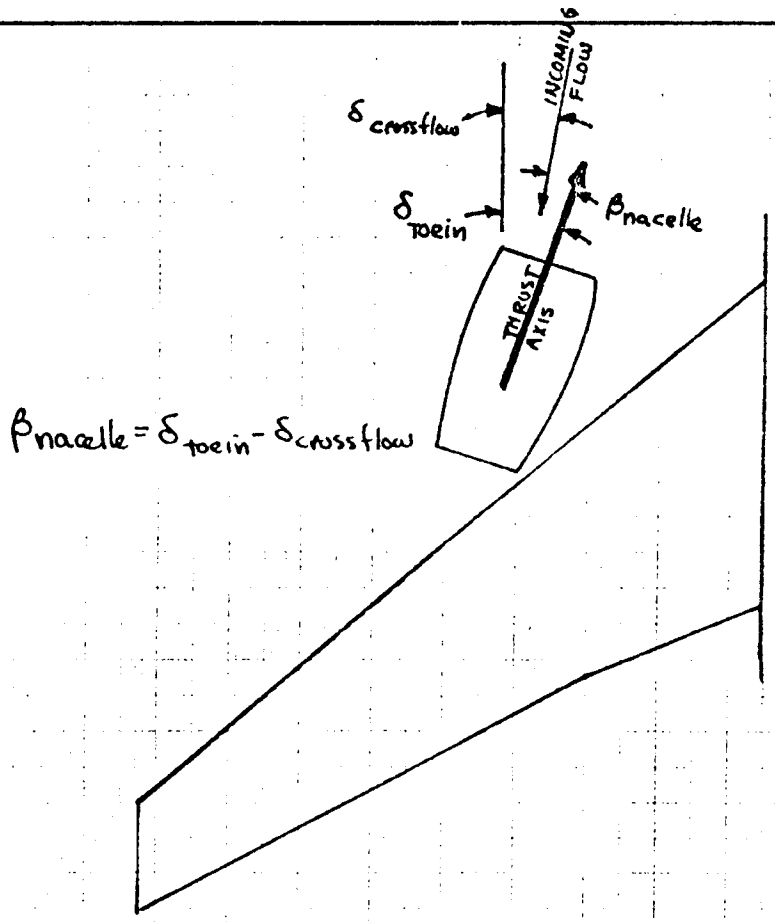

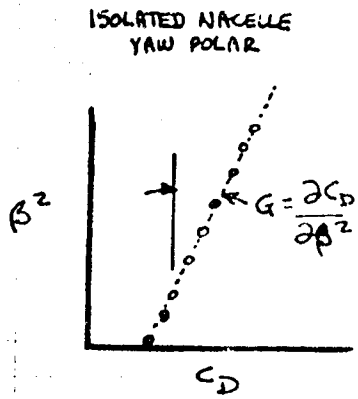

$$\frac{\Delta RF}{RF} = \cos\delta_{toein}\,\frac{C_D}{\left\{C_D + G\left(\underbrace{\delta_{toein} - \delta_{crossflow}}_{\beta_{nacelle}}\right)^2\right\}}$$

EXAMPLE: $C_{D_{AIRPLANE}} = 0.0250$ $\quad G = 1.2\times10^{-5}$ $\quad \delta_{crossflow} = 1.5°$

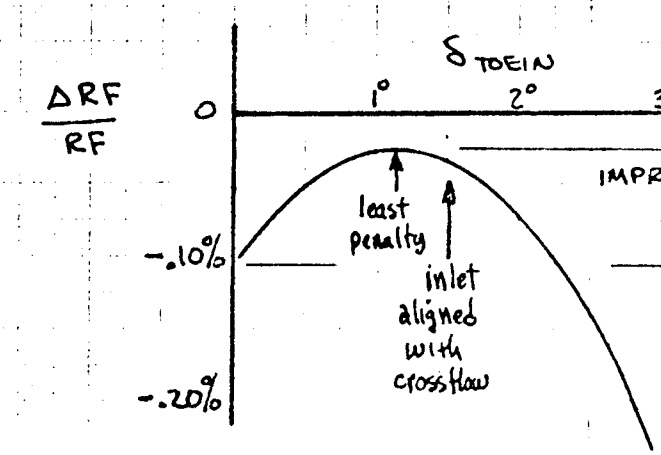

CALC	GILLETTE	2.26.78	REVISED	DATE	RANGE FACTOR IMPROVEMENT DUE TO NACELLE TOE-IN	
CHECK						FIG 9.34
APR						
APR					THE BOEING COMPANY	PAGE 150

D1 4100 3240

K-E ALBANENE LINEN TRACING PAPER

(a) CONVENTIONAL NACELLE

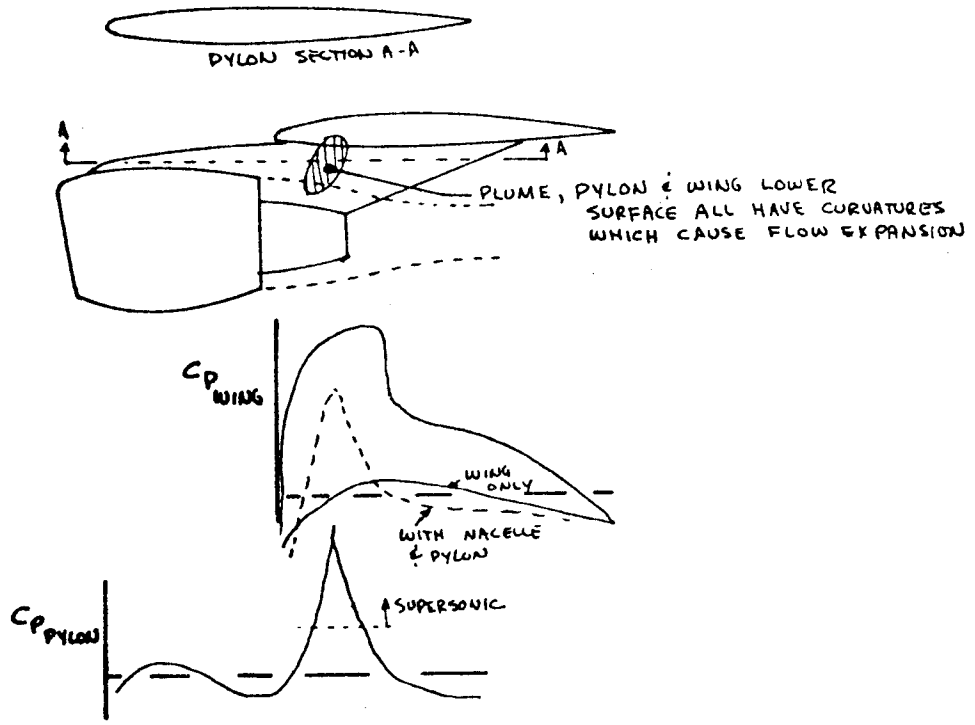

(b) MODIFIED TO REDUCE INTERFERENCE DRAG

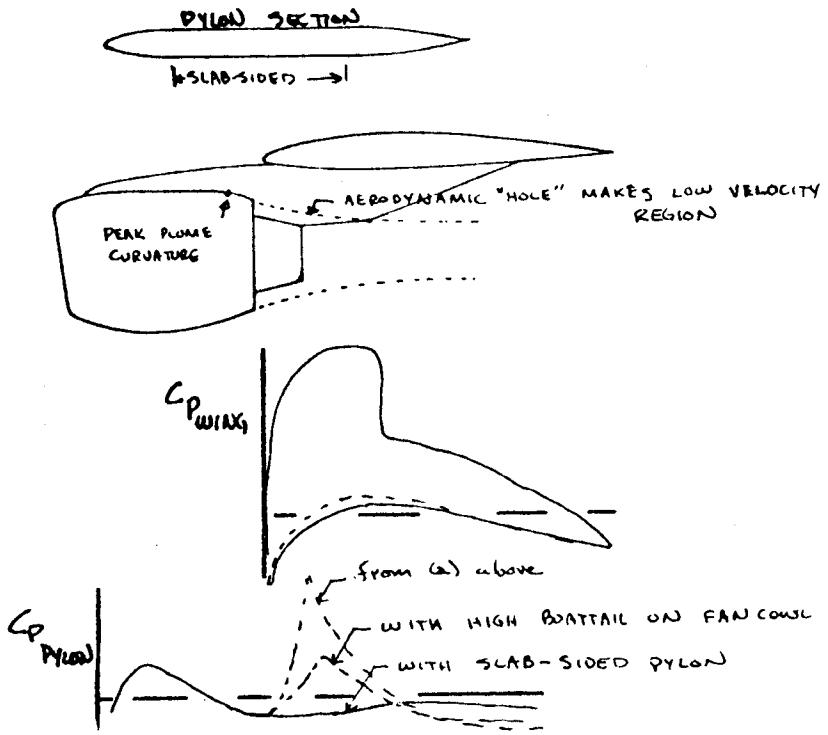

FIGURE 9.35 NACELLE-PYLON DESIGN CONCEPTS TO REDUCE INSTALLATION DRAG

GILLETTE 2.2678

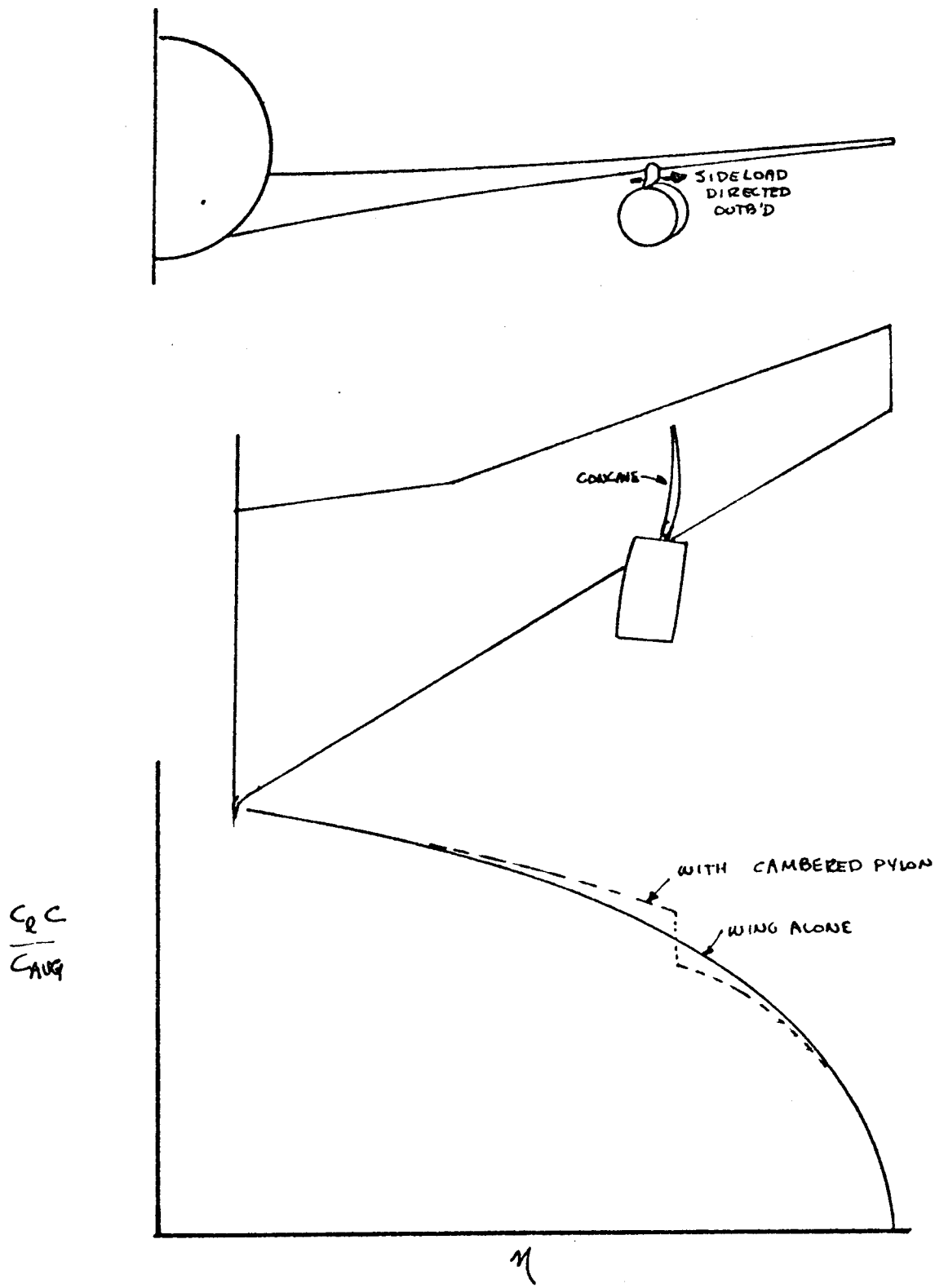

FIGURE 9.36 EFFECT OF CAMBERED PYLON ON SPAN LOADING

GILLETTE
2-26-73

P.9.52

9.0

PREFERRED

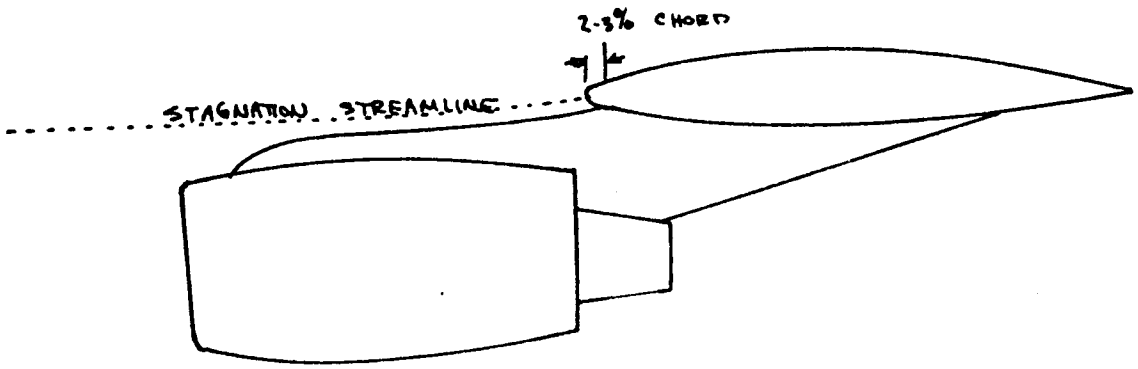

IF MUST GO OVERWING

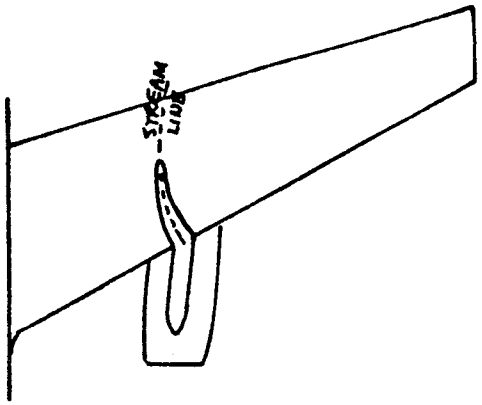

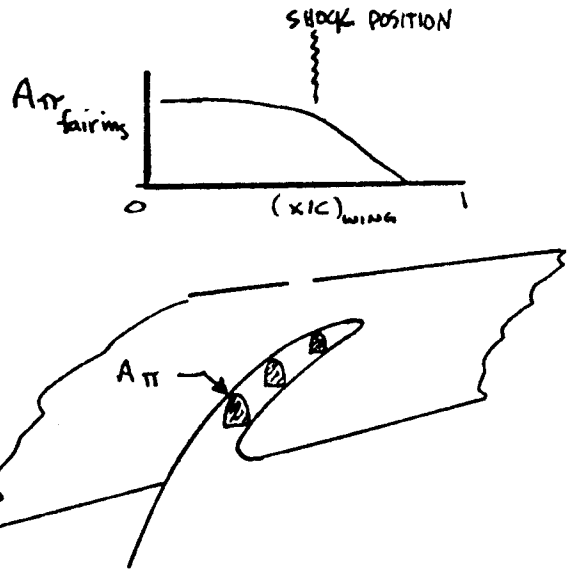

FIGURE 9.37 CONCEPTS FOR OVERWING PORTION OF UNDERWING PYLON

GILLETTE 2.26.78

677

OVER WING GEOMETRY MUST BE CONTOURED ⟹

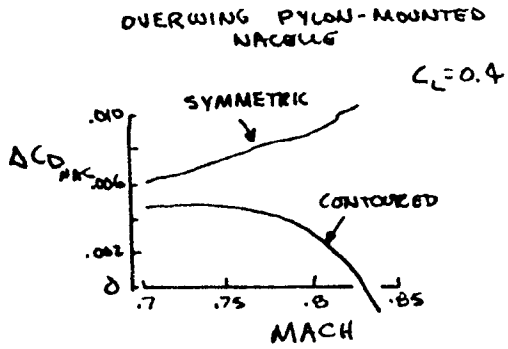

DESIGN SEQUENCE

① GET A230 SOLUTION FOR WING-BODY GEOMETRY. TRACE STREAMLINES FORWARD FROM CRITICAL PART OF NACELLE EXIT

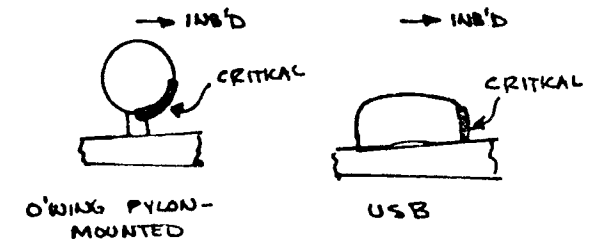

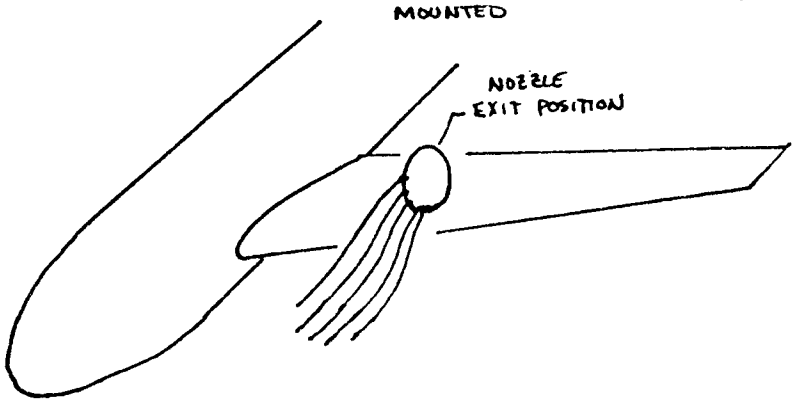

② INSTALL NACELLE, OBEYING THE CRITICAL STREAMLINES TO ABOUT 10% CHORD AHEAD OF THE WING

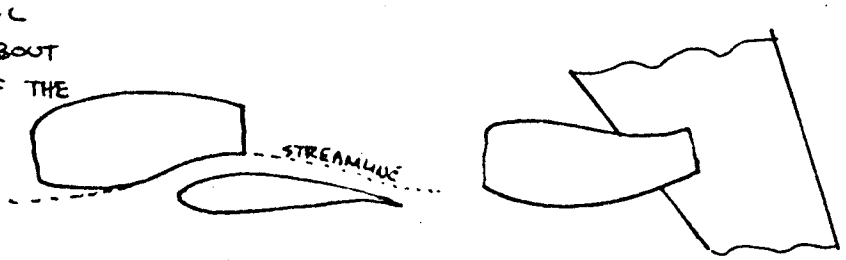

③ ANALYZE W-B-N IN A230. FOR PYLON-MOUNTED NACELLE, TRACE STREAMLINES BETWEEN NACELLE & WING. THESE BECOME INBOARD SIDE OF THE PYLON

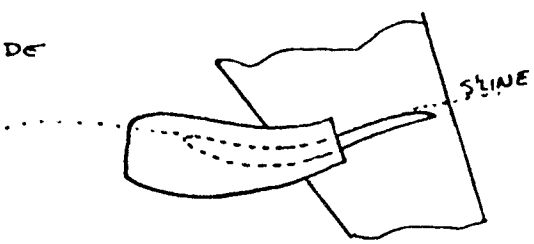

FIGURE 9.38 OVERWING NACELLE CONTOURING

(a) 2-D NACELLES

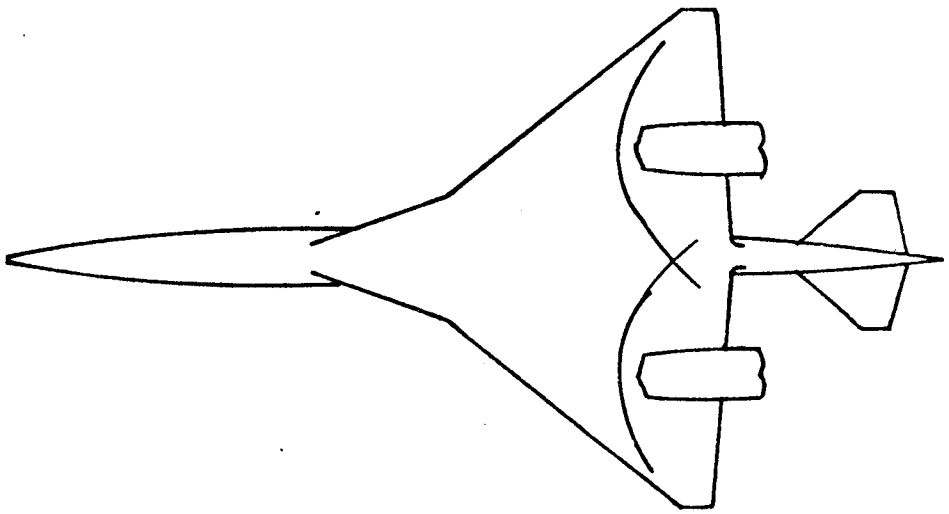

(b) AXISYMMETRIC

- ALLOW BETTER DISTRIBUTION OF OVERPRESSURES DUE TO NACELLE

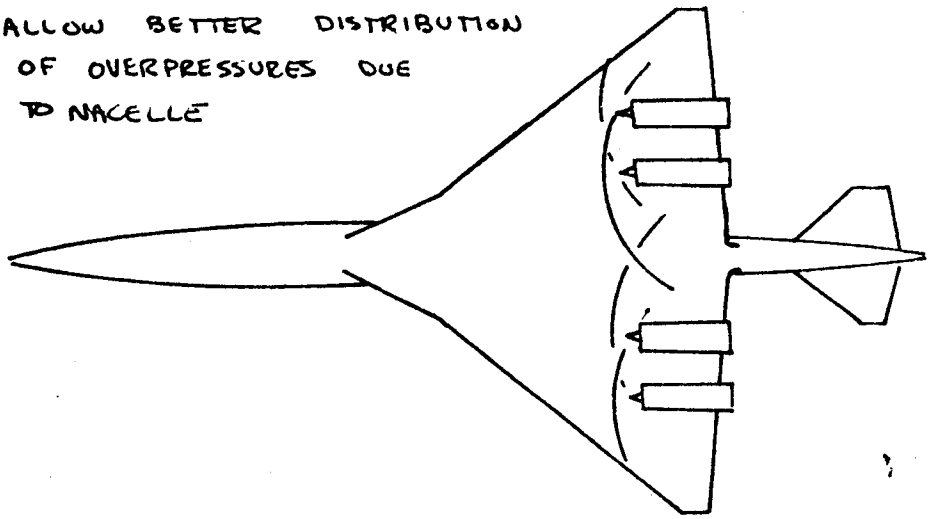

(c) REFLEXED WING

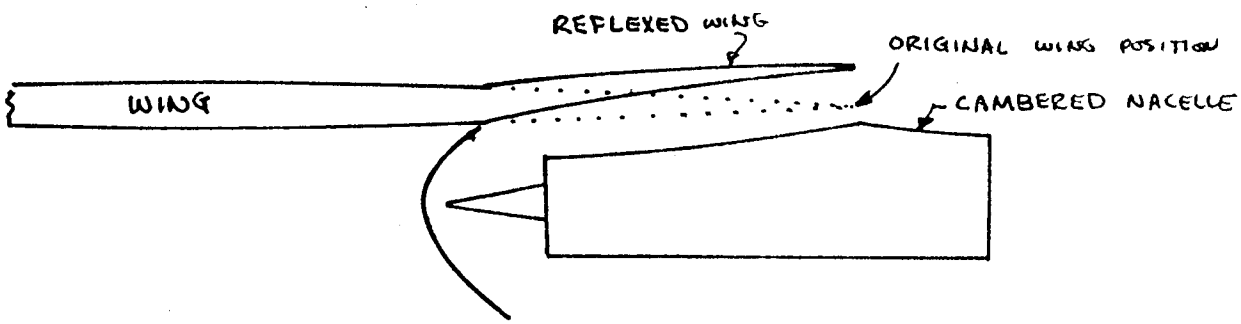

FIGURE 9.39 SUPERSONIC ENGINE INSTALLATION CONSIDERATIONS

GILLETTE 2.26.78

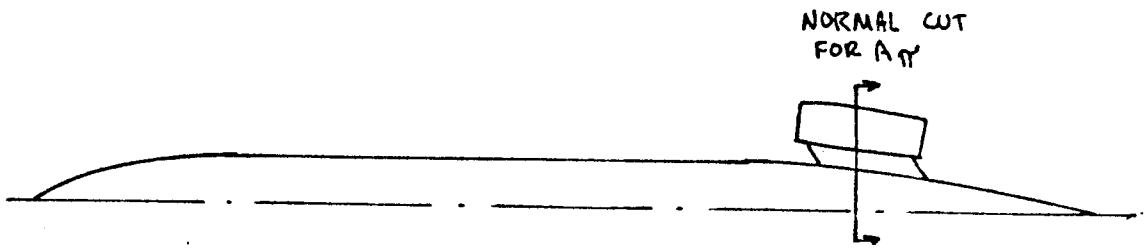

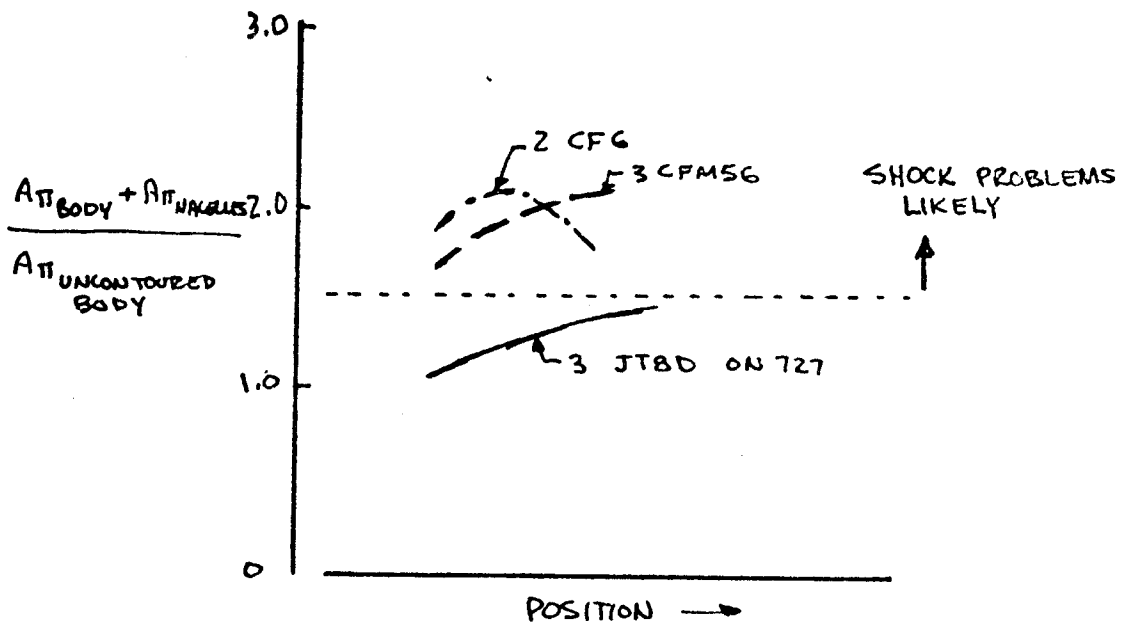

FIGURE 9.40 ANTICIPATION OF SHOCK PROBLEMS ON AFT BODY-MOUNTED NACELLES

GILLETTE
2.26.78

CHAPTER 10. ENGINE INSTALLATION MODEL TESTING

CHAPTER 10. ENGINE INSTALLATION MODEL TESTING

10.1 MODELLING CONSIDERATIONS

Discussion of the propulsion system test requirements would encompass a separate course, unless limited considerably in scope. Consequently, the discussion here will concern only tests of interest to the configuration aerodynamicist These will be the tests required to determine the drag of the aircraft configuration with its powerplant installed and operating. Also, the discussion will be further limited to jet engines, since that is the kind most likely to be encountered at Boeing.

10.1.1 The Real Engine

The basic characteristics of the real engine which are of consequence to the external aerodynamic flow field are outlined on Figure 10.1. Shown is the full scale engine installed in its nacelle. The general case has a pitot-style inlet (so named because it takes free-stream air just like a pitot-static tube) and a mixed-flow exhaust. The inlet condition is characterized by the mass flow into the inlet, and expression of ratio, such as capture ratio, A_∞/A_{HI}, or inlet velocity ratio, V_{HI}/V_∞, will be sufficient to describe the operating characteristics of the inlet.

The nozzle description is more complex due to the changes in the flow caused by the engine cycle. The fan jet will have been given an increase in total pressure, P_T jet $/P_{T_\infty}$, a ratio called fan pressure ratio, or "FPR". There will also have been a slight rise in total temperature due to the work done on the fluid. But the gas characteristics as represented by the ratio of specific heats, γ, remains unchanged.

The primary nozzle flow undergoes larger changes because of combustion. The specific heat ratio, γ, is reduced to a value somewhere around 1.2. There will be a total pressure rise, called EPR (engine pressure ratio) roughly equivalent to the fan total pressure rise. There will be a large rise in total temperature and the weight flow going out the primary will not only be the primary's share of the inlet weight flow ($= W_{inlet}/(1+BPR)$) but will include the fuel weight flow.

For a given flight condition, the net thrust of the engine will be approximately equal to the drag. This the nominal description of the inlet operating condition will be A_∞/A_{HI} for thrust equal to drag, and the exit conditions will be found at the proper FPR (or EPR) which matches the thrust equal to drag situation.

But specification of these top-level parameters does not fully reveal how the real engine would be modeled in the wind tunnel. This is revealed on Figure 10.2, where the requirements for inlet and jet simulation are detailed. Modelling the aerodynamic characteristics of the inlet require, of course, that the inlet geometry be scaled;

$$(\text{Ordinate})_{\text{Model}} = (\text{Ordinate})_{\text{Airplane}} \times \text{Scale Factor}$$

Then, the aerodynamic flow field scaling will occur when the specific weight flow, or the weight flow per unit area is scaled:

$$\left(\frac{\dot{w}_{corrected}}{A_{Hilite}}\right)_{Model} = \left(\frac{\dot{w}_{corrected}}{A_{Hilite}}\right)_{Airplane}$$

where $A_{Hilite,model} = (A_{Hilite,airplane}) \times (\text{Scale Factor})^2$

$\dot{w}_{corrected} = \dfrac{W_{actual}\sqrt{\theta}}{\delta}$,

$\theta = T_T / T_{STANDARD}$

$\delta = P_T / P_{STANDARD}$

Matching these and the externally impressed flow field (angle of attack, nearby geometry such as wing, pylon, etc.) will result in exact simulation of the flow field into the inlet and consequently, the flow characterisitics outside the capture streamtube and onto the exterior of the nacelle.

Simulation of the flow field exterior to the aft end of the nacelle begins with geometry scaling, just as in the case of the inlet:

$$(\text{Ordinate})_{Model} = (\text{Ordinate})_{Airplane} \times \text{Scale Factor}$$

However, scaling the characteristics of the jet are not as simple. There are two general aerodynamic effects of the exhaust jet, (1) The inviscid shape of the jet and (2) the entrainment of outer flow into the jet. Much study has gone into simulation of these two characteristics and to the parameters responsible for their simulation. Regarding the inviscid shape of the jet, the parameters necessary are that:

$$\left[P_{T_{jet}} / P_{T_\infty}\right]_{model} = \left[P_{T_{jet}} / P_{T_\infty}\right]_{AIRPLANE}$$

and to a much lesser degree,

$$\left[T_{T_{jet}} / T_\infty\right]_{MODEL} = \left[T_{T_{jet}} / T_{T_\infty}\right]_{AIRPLANE}$$

In practice, it will turn out that matching the pressure ratio will be simple, so that matching (or nearly so) the inviscid, non-mixed shape of the jet will be relatively simple.

But the entrainment effect whereby outer flow is mixed with the jet is a different matter. Extensive study has been done by NASA into the characteristics of the flow necessary to simulate the mixing effect. Figure 10.3 shows a sample of various combinations of exhaust parameters studied in Reference 10.1. The nozzle geometry had the following characteristics, compared to the

typical range of subsonic transport-type nozzles:

Nozzle characteristic	NASA Test	Typical subsonic Transport
boattail angle	20^0	$12^0 \rightarrow 16^0$
initial inviscid plume angle (relative to nozzle inner wall)	5^0	$2^0 \rightarrow 4^0$
Jet Mach number	1&2	1.2→1.5

The parameter chosen to indicate the degree of success in simulation of the entrainment effect is boattail drag, defined as the integral of the surface pressures on the aft-facing surfaces. Perfect simulation would be represented by a parameter which would cause the boattail drag to collapse to a single curve. The drag data on Figure 10.3 were acquired at two jet Mach numbers and at a range of jet conditions from "cold air" to one (via hydrogen peroxide) which simulates a real hot jet in temperature, γ, and the gas constant, R. First, matching the jet Mach number essentially matches pressure ratio, so that relationship is satisfied by the various correlations of Figure 10.3. Then in order:

(1) mass flow ratio does not collapse the drag data,

(2) momentum ratio has the poorest correlation of all,

(3) internal engergy per unit mass and

(4) ratio of gas constant times temperature produce reasonable correlations, and

(5) kinetic energy per unit mass does not correlate.

In conclusion, the NASA data show that, for a nacelle boattail more severe than typical for subsonic transport, matching pressure ratio and the ratio, γRT, will properly simulate the effect of the jet on the nozzle boattail. Unfortunately, the simulation is achieved only by a gas whose properties are identical to those of the real exhaust, namely, pressure, temperature and gas constant.

The question then becomes, how serious an error is introduced by use of an exhaust gas other than one like the real exhaust? This will be discussed in detail later, but for most applications, the flow will have a fan exhaust whose properties are almost those of the external air, with the hot jet inside. That is, the fan plume forms a boundary between the external flow and the primary jet, thus providing a buffer to the external flow. For mixed flow exhausts, however, this buffer does not exist.

It should also be pointed out that at the NLR in Holland, tests are done using hydrogen peroxide to produce an exhaust gas very much like the real gas. In fact, this is how the engine installation tests were modelled for the A-300. But nowhere in their published data do they show a nacelle drag difference for having used the hot primary jet compared to a cold one.

Returning to Figure 10.2, it appears that simulation of the entrainment effect requires that possibly all the jet characteristics be duplicated on the model, although duplication of the internal energy per unit mass and the (RT) ratio would yield a very good approximation.

The discussion will now turn to how the inlet and exit simulations of Figure 10.2 are best achieved in the wind tunnel.

10.1.2 The Flow Nacelle

Figure 10.4 shows the simplest way to attempt to model the real nacelle. At top is shown the real nacelle, with the engine doing work on the fan and primary flows. The easiest procedure would be to remove the engine, retain the nozzle and exit plug lines from just inside the nozzles, and then put the cleaned-up geometry in the wind tunnel. This kind of nacelle is called the flow nacelle, since the tunnel air flows through the nacelle without having any work done on it.

Consider the plume simulation first. Obviously, the primary jet will not be modelled by the flow nacelle. But the shape of the fan plume would not be seriously in error. This is demonstrated on Figure 10.5, which shows calculated and experimentally measured plume shapes leaving the nozzle of a typical 3/4-duct dual flow nacelle. Recalling that any flow in the tunnel whose total pressure is that of the wind tunnel is denoted as a "ram" flow, or having ram (ie.tunnel) total pressure, Figure 10.5 compares a calculated ram plume to the real power-on plume. The ram plume is the one which the flow nacelle would have,naturally. Note that near the fan nozzle exit, there is very little difference in plume shape between the ram and engine power-on plume. And, for the 0.70 Mach case, also note that both plumes are little changed from the measured plume or from one calculated by a mixing analysis. The conclusion from Figure 10.5 is that the jet plume shapes for the flow nacelle on Figure 10.4 would be very similar to the shape of the real engine plume.

But Figure 10.4 reveals a problem with the flow nacelle plume. Although the shape may be similar to the real engine's plume shape, the density and velocity are less than the real engine's fan plume. The result is that, with the nozzle exit areas of the real engine, the ram flow of the flow nacelle will carry only about 80% of the same mass flow rate as in the real engine case. Thus, the inlet flow will be seriously in error; the capture streamtube will be smaller than in the case of the real engine, and the flow nacelle cowl will be spilling more flow than the real engine cowl. This is a serious error in modelling, since the fan cowl aerodynamics have a far greater effect on nacelle drag than does the exhaust plume. So, some method must be found to force the capture streamtube to have the same shape on the flow nacelle as for the real engine. Four concepts are outlined on Figure 10.6.

The first would be to place a plug in the inlet, sized to make up for the deficiency in capture streamtube area and shaped to force the capture streamtube into the shape of the real engine's capture streamtube. The plug shape would be point-designed by analysis. This concept is acceptable for situations where the angle-of-attack range of the flow nacelle will be small, as in the case of the 727 body-mounted nacelles. In fact, inlet plugs have been used

for 727 transonic testing. But for most applications,the inlet plug is not recommended.

The next concept shown is to first remove the exit plug, then make up for the remaining deficiency in inlet flow by enlarging the primary exit. The length of the primary is usually kept the same as that of the real engine. This has the advantage that the inlet simulation can now be made exact. But as Figure 10.6 shows, the enlarged primary has pushed the fan plume outward, altering its shape thus altering its effect on the nacelle boattail drag and on any nearby aerodynamic components.

This problem is partially resolved by the third concept, where the exit plug is removed, then the production primary outer lines are truncated until the proper inlet mass flow is achieved. In this case, the initial fan plume shape is still correct, and begins to deviate from the powered fan plume boundary only aft of the flow nacelle primary. This procedure is perhaps the best for simulating the dual flow nacelle with a flow nacelle.

But this technique fails when the complete removal of the flow nacelle primary does not result in sufficient inlet mass flow or where there is no primary to remove, as in the case of the full-length nacelle. Figure 10.6 shows that the only choice in this case is to enlarge the exit. Rather than an axisymmetric enlargement, however, the exit is usually ovalized, with the alteration in geometry being away from the region of interest. For a wing-mounted nacelle, for instance, the keel would be ovalized, so that the nacelle crown line and consequently the interaction of the nacelle and wing would be correctly modelled. Of course, corrections would then have to be made for the drag effects of the ovalized part of the flow nacelle.

Having chosen a method of flow nacelle area ratio matching, the next step is to determine the size of exit area required. This can be calculated in two ways, as pointed out on Figure 10.7. The first procedure utilized a discharge coefficient:

$$C_D \equiv \frac{\dot{w}_{ACTUAL}}{\dot{w}_{IDEAL}}$$

WHERE

$$\dot{w}_{IDEAL} = \rho_\infty V_\infty A_{EXIT}$$

That is, the exit mass flux is defined in the ideal case to have free-stream density and velocity when it passes through the nozzle exits. However, due to losses and suppression, the mass flow will invariably be less for a convergent nozzle, so that C_D will be less than one. Suppression is caused by the trailing edge pressures of the nacelle being more positive than free stream, thus causing a back pressure on the nacelle which reduces the exit flow. Values of C_D typically range from 0.85 to 0.99, and values for a new flow nacelle can properly be guessed only after much experience. The required flow nacelle exit area would be:

$$A_{EXIT} = \frac{(\dot{w}_{INLET})_{AIRPLANE} \times (\text{SCALE FACTOR})^2}{C_D \rho_\infty V_\infty}$$

The second procedure is more general, but when properly applied, requires a computed value of exit pressure. Then, the exit Mach number is calculated, the corresponding exit density and velocity ratios are found from the compressible flow tables, and the required model exit area is calculated according to the procedures of Figure 10.7.

But a choice still remains on which actual engine operating condition to match. Figure 10.8 shows that the real engine operates over a range of capture ratios. At low speeds, the capture ratio may typically range from 0.5 at windmill to 1.0 at approach to 1.5 at takeoff rotation. High speed ranges from 0.3 at windmill to 0.5 at flight idle to 0.8 or 0.9 at cruise. The flow nacelle, on the other hand, operates at a single capture ratio with a fixed primary, and, in most cases, has a capture ratio less than unity with the fan nozzle fully removed. In order to change the inlet conditions, the exit area must be changed. For the enlarged primary, exit plugs are often used, the larger plug causing a lower capture ratio. For the case of the truncated primary, the longer primary will simulate a lower capture ratio. To simulate flight idle or windmill, the mass flow must be reduced even further, and a windmill plate is used. This is actually comprized of a pair of serrated plates, adjustable so as to get an exact match to the real engine condition. Figure 10.8 also shows that, above a capture ratio of about one, the flow nacelle exit must be ovalized to properly match the real engine's mass flow.

In summary, it has been shown that the flow nacelle can be made to exactly math the inlet flow of the real engine, and thus the external aerodynamics over most of the nacelle. It cannot match the flow precisely near the fan exit and further aft near the exhaust plume.

10.1.3 The Blown Nacelle

The previous discussion has pointed out that the flow nacelle can be used to properly simulate the fan cowl external aerodynamics aft to near the exit. But the jet simulation will be poor with the flow nacelle. The earliest method used to represent the jet, the blown nacelle, is shown on Figure 10.9. In this concept, there is no inlet, and all the exhaust air is piped into the the nacelle under very high pressure (upwards of 1000 psi). The intent of the blown nacelle is to use compressed air to simulate the pressure ratio of the jet exhaust, but not its swirl, temperature or real gas effects. Of course, the production nozzle geometry is modelled exactly.

Further examination of Figure 10.9 reveals the internal details of the flow nacelle. First, there is a separate air supply for the fan and primary, so that each can be set independently, so as to duplicate the pressure relationship of the real engine. Second, the high pressure air is forced through choke plates, which cause a throttling effect that reduces the total pressure to the desired value (from 8 to 45 psi, depending on condition). Third, screens are placed downstream of the choke plates to smooth out the turbulence in the flow and reduce the spatial pressure distortion (variation from the mean value). Finally a set of total pressure and temperature probes are placed inside the nozzle, where the flow velocity is low, to measure the flow characteristics so that the nozzle performance can be calibrated and the thrust calculated.

Besides the disadvantages quoted above, the most obvious uncertainty about the blown nacelle is that it has no inflow whatsoever, so all the air that would normally enter the inlet must go around the dome of the blown nacelle. The effect this has on the flow field will be discussed in Section 10.2.2

An advantage to the blown nacelle is that any scale for the model can be chosen, with the limits coming from causes such as quantity of high pressure air, model-to-tunnel size limits, etc. But since the blown nacelle is completely fabricated at Boeing, the size of the blown nacelle model is flexible. This is advantageous when an existing model may be tested with a "new technology" engine of a different size, for example, CFM56 engines on a JT3D-powered 707.

10.1.4 The Turbine Powered Simulator Nacelle (TPS)

Figure 10.10 details a very clever mechanical contrivance whose purpose is to simulate the engine characteristics through the use of turbomachinery. High pressure air is supplied to the TPS and is expanded through a three-stage turbine. The turbine drive air is then used to simulate the primary exhaust. The turbine, which in the 5-inch diameter unit shown develops 87 horsepower at its rated speed of 45,000 RPM, then turns a two-stage fan. The bearings are lubricated with turbine oil, naturally. The TPS units come in a variety of sizes characterized by fan face diameter; 5-inch (Boeing has 5 units), 4-inch, 3.5-inch, and 2.8 inch (Boeing has 5 units). All are manufactured by Tech Development of Dayton, Ohio. The TPS is rapidly becoming the standard means of investigating power effects.

The kind of simulation provided by the TPS is outlined on Figure 10.11. Considering the fan jet, it is simulated in pressure ratio, and to a lesser degree, in temperature rise above the free stream air. But the primary jet simulates neither of these. Its controlling parameter is the power it must provide to operate the fan, and its pressure ratio cannot be independently set. In general, it will be at a pressure higher than ram, but less than for the real engine. Furthermore, since it has had a great deal of work taken out of it (don't forget the 87 horsepower), and as a consequence is very cold, typically in the range of 270^0 R (-190^0F). This is opposite of the intended direction temperaturewise for proper primary plume simulation.

Because the primary air enters the TPS from an outside source, only the fan air is taken into the inlet. Thus, the TPS inlet will be deficient in inlet mass flow by:

$$\left(\dot{w}_{INLET}\right)_{TPS} = \left(\dot{w}_{REAL\ ENGINE}\right) \times \left(SCALE\ FACTOR\right)^2 \left[\frac{BPR}{1+BPR}\right]$$

For example, at BPR=4, the TPS takes in only 80% of the real engine's scaled airflow. This shortfall requires that the inlet be contracted. This is done as indicated on Figure 10.13. The goal is the external pressure distribution on the production fan cowl at a given condition.

The contracted TPS fan cowl at its operating condition is then designed by A280 or TEM 318C analysis to have the same chordwise pressure distribution. An exact duplication cannot be achieved on the TPS fan cowl, but the similarity can be close enough that the near-field effect of the fan cowl is modelled. The consequences of the TPS inlet mass flow deficit will be further discussed in Section 10.2.3.

A disadvantage of the TPS relative to the blown nacelle is that it is available in only a few discrete sizes, as mentioned above. This means that the model size for the powered wind tunnel model must be chosen carefully. It may also mean that two different TPS units will be required to examine the aerodynamic effects of re-engining. This is just the case for the JT3D versus the CFM56 on the 707. Matching the TPS to the model size is more than a matter of scaling the geometry. The fan operating characteristics must also be matched, as shown on Figure 10.13. The process begins with the corrected fan weight flow for the real engine at the condition being matched:

(1) Select the condition being matched (either high or low speed), and calculate thrust required, F_N/δ, where F_N is net thrust and δ is the altitude pressure ratio, Pambient/Psealevel.

(2) From the engine characteristics, obtain $\dot{\omega}_{corrected}$, corrected fan weight flow, and $P_{T_{FAN}}/T_{T_\infty}$, fan pressure rise.

(3) On the TPS fan map of $P_{T_{FAN}}/P_{T_\infty}$ versus TPS corrected weight flow (Figure 10.13), draw a line representing the line of real engine FPR (P_{T_F}/P_{T_∞}). Note that there will be three boundaries. The upper boundary is the "Mechanical RPM Limit". Above this speed, the TPS cannot match the real engine's FPR, then the TPS cannot be used. An example is the JT3D, whose cruise FPR is 1.89, compared to about 1.65 for most TPS units. The second limit is the boundary of fan stall. The third limit is that where flow in the fan duct will reach sonic velocities and proper calibration of the internal rakes cannot be done. At these two latter boundaries, usually a TPS $\dot{\omega}_{corr,min}$ and $\dot{\omega}_{corr,max}$ will be read, which encompass a range where the TPS can safely be used.

(4) The TPS scale factor will then be:

$$\left(\sqrt{\frac{\dot{\omega}_{corr,min,TPS}}{\dot{\omega}_{corr,engine}}}\right)_{fan} \leq (\text{SCALE FACTOR}) \leq \left(\sqrt{\frac{\dot{\omega}_{corr,max,TPS}}{\dot{\omega}_{corr,engine}}}\right)_{fan}$$

(5) Compare this range in model scales to the geometrical scaling of the engine. If there is a common scale factor, then that scale factor becomes the one to be used for the TPS model.

With the scale factor chosen, cowls designed to simulate the nozzle geometries and the contracted TPS inlet are fabricated for the TPS unit. As in the case of the blown nacelle, internal pressure and temperature total rakes are installed inside the fan and primary nozzles to allow calibration for thrust.

In summary, the TPS attempts to exactly model the fan flow. In doing so, it provides a poor simulation of the primary flow, because its primary jet is very cold. It has also added some inflow, with an inlet whose inflow is about 80% of the real engine inflow.

10.1.5 The Ejector Nacelle

A fourth style of nacelle is the ejector nacelle, shown on Figure 10.14. This concept attempts to use entrainment inside the nacelle to have inflow and at the same time, have a jet of proper pressure ratio. But the paradox of the ejector nacelle is that as the jet pressure ratio, P_{T_F}/P_{T_∞}, or P_{T_P}/P_{T_∞} is increased by supplying more high-pressure air to the nacelle ejectors, less air can come in the inlet. Figure 10.14 shows that for the design illustrated, the inlet weight flow ratio drops to 60% of the real engine's condition at $P_{T_F}/P_{T_\infty} = 1.5$, which is less inflow than the TPS provides. Consequently, the TPS has replaced the ejector as a powered nacelle concept which can provide inflow and a pressurized jet at the same time.

10.2 THRUST-DRAG BOOKKEEPING

Separation of thrust and drag on the aircraft might seem like a simple matter, since in cruise,

$$\text{DRAG} = \text{THRUST} \times \cos\beta_T \doteq \text{THRUST}$$

where β_T = total angle of thrust relative to free stream direction, including both pitch and toe-in directions.

But, in actual practice, when the fan jet sweeps across the pylon, and when its presence alters the wing pressures, the distinction between thrust and drag is blurred. Thus, one of the most error-prone inter-staff boundaries is that between the Aerodynamic and Propulsion Staffs; it is a perfect example of the proverbial "crack" through which many a missed mile per pound has fallen.

10.2.1 Consequences of Net Thrust

The simplest definition of the thrust and drag of a nacelle, and consequently the differential force felt by the airframe, is developed on Figure 10.15. This draws a control volume at the planes of the inlet and exit. There is a net "sheet metal" force, that is, a force felt by the material the hardware is made of, on the inside of the nacelle and another on the outside. Forgetting about viscosity for the time being, the inside force, or internal thrust, is given by:

$$T_{INT} = \int_e \underbrace{\left(\rho_{I_e} V_{I_e}^2 \cos^2\phi_{I_e}\right)}_{\text{momentum force}} + \underbrace{\left(P_{I_e} - P_\infty\right)}_{\text{pressure force}} dA_{I_e}$$

$$- \int_i \left(\rho_{I_i} V_{I_i}^2 \cos^2\phi_{I_i} + P_{I_i} - P_\infty\right) dA_{I_i} \qquad (10.1)$$

Similarly, the external, or drag force, is given by:

$$D_{EXT} = \int_i \left[\rho_{E_i} V_{E_i}^2 \cos^2\phi_{E_i} + P_{E_i} - P_\infty\right] dA_{E_i}$$

$$- \int_e \left[\rho_{E_e} V_{E_e}^2 \cos^2\phi_{E_e} + P_{E_e} - P_\infty\right] dA_{E_e} \qquad (10.2)$$

The net force acailable to propel the aircraft is

$$\Delta F_{AIRFRAME} = T_{INT} - D_{EXT} \qquad (10.3)$$

The tasks would then be for the Propulsion Staff to predict T_{INT} and for the Aerodynamic Staff to predict D_{EXT}, and the ΔF for the airplane could be predicted.

But this simple procedure does not remain very long. The Propulsion Staff does not like the use of equation (10.2), since, in effect, it requires a survey of the flow parameters at the inlet and exit planes. So, their first step is to extend the boundary of the control volume upstream to a point where free stream conditions exist. This is shown on Figure 10.16. Furthermore, they are concerned only with the flow that goes through the nacelle. So, they divide the flow along the capture streamtube boundary for force accountability purposes. Since the capture streamtube is curved, pressure forces exist along it. But not that P_{SE} and P_{SI} are equal and opposite. When viewed from the interior, a new force arises:

$$T_{ADDITIVE} = \int_i \left(\rho_{I_i} V_{I_i}^2 \cos^2\phi_{I_i} + P_{I_i} - P_\infty\right) dA_{I_i} - \rho_\infty V_\infty^2 A_{I_\infty} \tag{10.4}$$

Likewise, on the outside of the capture streamtube,

$$D_{ADDITIVE} = \rho_\infty V_\infty^2 A_{E_\infty} - \int_i \left[\rho_{E_i} V_{E_i}^2 \cos^2\phi_{E_i} + P_{E_i} - P_\infty\right] dA_{E_i} \tag{10.5}$$

It is very important to note that

$$D_{ADDITIVE} = T_{ADDITIVE} \tag{10.6}$$

and that they are not real forces felt by the airframe, but are the result of a bookkeeping choice. Also note the term in equation (10.4),

$$\rho_\infty V_\infty^2 A_{I_\infty} = (\rho_\infty V_\infty A_{I_\infty}) V_\infty \tag{10.7}$$
$$= \dot{w}_{engine} V_\infty$$

which is given the name "ram drag".

In a similar fashion the downstream boundary for the control volume is extented to a point where the static pressure in the jet equals that of the surrounding flow field. Figure 10.17 shows that, again, equal and opposite forces arise across the fluid boundary dividing Aerodynamics and Propulsion:

$$T_{POST\,EXIT} = \int_\omega \rho_\omega V_\omega^2 dA_{I_\omega} - \int_e \left(\rho_{I_e} V_{I_e}^2 \cos^2\phi_e + P_{I_e} - P_\infty\right) dA_{I_e} \tag{10.8}$$

and

$$D_{POST\,EXIT} = \int_e \left(\rho_{E_e} V_{E_e}^2 \cos^2\phi_{E_e} + P_{E_e} - P_\infty\right) dA_{E_e} - \rho_\infty V_\infty^2 A_{E_\omega} \tag{10.9}$$

Again,

$$D_{POST\,EXIT} = T_{POST\,EXIT} \tag{10.10}$$

and they are bookkeeping forces, not forces felt by the airframe.

The point of all this illustrated on Figure 10.18. Recalling Figure 10.15, the true propulsive thrust is simply T_{INT}. But the Propulsion Staff, for a number of reasons, have chosen to define a "net propulsive thrust" from upstream infinity to downstream equilibrium:

$$T_{NET} \equiv T_{ADD} + T_{INT} + T_{POST\ EXIT} \tag{10.11}$$

which, upon combining equations (10.1), (10.4), and (10.8), become

$$T_{NET} = \underbrace{\int_{\omega} \rho_{\omega} V_{\omega}^2 dA_{I_{\omega}}}_{\text{"GROSS THRUST"}} - \underbrace{\rho_{\infty} V_{\infty}^2 A_{I_{\infty}}}_{\text{"RAM DRAG"}} \tag{10.12}$$

It can easily be seen from equation (10.12) that net thrust is easier to estimate tha T_{INT}. But when the performance meeting is held, the Aerodynamics Staff must now have a "net drag" to match the net thrust of Propulsion. This is shown on Figure 10.19, where, in its simplest form,

$$\Delta F_{AIRFRAME} = T_{INT} - D_{EXT}.$$

But, $T_{NET} = T_{ADD} + T_{INT} + T_{POST\text{-}EXIT}$

and so Aerodynamics must provide

$$D_{NET} = D_{ADDITIVE} + D_{EXT} + D_{POST\text{-}EXIT} \tag{10.13}$$

for the proper thrust-drag bookkeeping to occur. How is the aerodynamicist going to measure net drag in the wind tunnel? The procedure is outlined on Figure 10.20, which shows a powered nacelle mounted to a balance. From above,

$$T_{ADD} + T_{INT} + T_{POST\text{-}EXIT} = T_{NET}$$

$$\text{or,}\quad T_{INT} = T_{NET} - T_{ADD} - T_{POST\text{-}EXIT} \tag{10.14}$$

The balance measures only the real forces;

$$F_{BAL} = D_{EXT} - T_{INT}$$

$$= D_{EXT} - T_{NET} + T_{ADD} + T_{POST\text{-}EXIT}$$

$$= D_{EXT} + D_{ADD} + D_{POST\ EXIT} - T_{NET}$$

$$= D_{NET} - T_{NET}$$

Or,

$$D_{NET} = F_{BAL} + T_{NET} \qquad (10.15)$$

So, to measure the net aerodynamic drag, including additive and post-exit drags, the aerodynamicist measures the total forces on the balance, and adds in the calculated net thrust. This, of course, is what has always been done in wind tunnel testing.

The previous example considered the powered nacelle in potential flow. Figure 10.21 shows the case of the flow nacelle in real flow, with the final result being that the T_{NET} term of equation (10.15) is the negative of the internal drag. That is, the net thrust of a flow nacelle is zero, minus the loss in thrust due to internal drag.

So, the use of net thrust by Propulsion does not present a serious obstacle to the Aerodynamicist. But it has led to a myth; that additive drag is cancelled by lip suction. Part (a) of Figure 10.22 shows that when $A_\infty/A_{HI}=1$, ie, no spillage, there is a certain pressure force, D_{LIP}, on the outside of the inlet. When the capture ratio is reduced, the additive drag term appears on the outside of the capture streamtube, and the velocities increase on the external lip, with the result that the net pressure integral is reduced. Or,

$$D_{NET,LIP} = D_{LIP,\, A_\infty/A_{HI}=1} - T_{SUCTION} \qquad (10.16)$$

The myth is that

$$D_{ADD} = T_{SUCTION} \qquad (10.17)$$

and that is how additive drag is felt by the airframe. Well, the previous discussion has shown that additive drag is cancelled by additive thrust. But to further dispel the myth, consider the case in potential flow shown on part (d) of Figure 10.22. Here there is additive drag, but no lip force! The truth is that D_{ADD} and T_{LIP} do both arise due to A_∞/A_{HI} being other than unity, but they are not numerically related or equal.

One final matter must be considered before discussing the model tests, and that is how to treat the vectors in the net thrust equation. The ram drag term, $(\dot{w}_{engine})\,(V_\infty)$ always comes from the wind axis. But the gross thrust term, $\int_{A_{I\omega}} \rho_\omega V_\omega^2 \, dA_{I\omega}$, is a vector pointed in some direction. The resulting vector, T_{NET}, can be handled in two ways, as illustrated on Figure 10.23. Part (b) shows the scientific way. Think of the model being mounted on a balance, which reads the true vector result of thrust, lift and drag. To obtain the lift-drag polar, the calculated net thrust vector is removed from the balance reading, thus affecting both lift and drag. This bookkeeping method is denoted as a "true thrust vector accounting". Naturally, the true vector direction of the nozzle gross thrust must be known, relative to the nozzle axis, then further corrections added for nacelle tilt, toe-in, aeroelastic deflection of the wing, and

finally wing angle of attack. These are easy to obtain for a wind tunnel model, but difficult to measure for the airplane. Consequently, the aircraft thrust-drag accounting is usually a wind-axis one, denoted by part (a) of Figure 10.23, where thrust is applied along the wind axis, that is, simply as a correction to drag and not to lift.

As long as the bookkeeping between predicted thrust and predicted drag is consistent, then either wind axis or true thrust axis accounting,will yield a valid final result. But wind axis accounting may hid the true drag and prevent realization of a thrust-related drag problem. For example the wind axis accounting on part (2) of Figure 10.23 makes the drag polar more open, or more favorable,than it really is.

10.2.2 Wind Tunnel Bookkeeping with Flow and Blown Nacelles.

The power-on drag of a configuration can be predicted properly by the use of flow and blown nacelles. Figure 10.24 shows the wind tunnel model parts required. At the top is a flow nacelle, designed as previously described in Section 10.1.2. At the bottom is a blown nacelle having the production nozzle geometry modelled exactly. In the middle is the blown nacelle with nozzles representing the flow nacelle. In principle, the blown nacelle with flow nacelle nozzles would want to have exactly the same nozzle as on the flow nacelle. However, the primary of the flow nacelle is much too large for the flow inside to remain attached, so a plug is required, so that the net primary exit area is the same as for the production nacelle. The shape of the exit plug is to follow streamlines out of the flow nacelle primary to a distance past the adjacent aerodynamic objects, such as pylons.

These three parts, flow nacelle, blown nacelle with flow nozzle and blown nacelle with production nozzle each get tested twice, once isolated and once installed. The procedure is outlined on Figure 10.2.5. At the top is the real nacelle on the airplane, having a capture streamtube operating at A_∞/A_* for thrust equal drag and a fan nozzle pressure ratio, FPR, for thrust equals drag. The nacelle-pylon installed drag will arbitrarily be divided into three pieces; form drag, representing the drag of the wetted external surfaces of the isolated nacelle; interference drag, being the increase in drag of the complete configuration over that of the isolated nacelle, without power effects; and blowing drag, being the change in forces when FPR is increased from ram to max power.

The bottom half of Figure 10.25 details the individual tests and the data acquired from each. First run are the isolated nacelles, then the installed nacelles. The flow nacelle is tested to obtain from drag at a wind tunnel Reynolds number. This drag, $C_{DFLOW_{iso}}$, is corrected to full-scale Reynolds number and becomes C_{Diso}. But this measurement has been made with the

wrong nozzle. So, both blown nacelles are tested isolated, with a ram (FPR=1) jet. A drag correction to the flow nacelle is obtained and corrected to full scale Reynolds number. The total form drag is the sum of $C_{D_{iso}}$ and $C_{D_{iso\ nozzle\ geometry}}$. That is, the two isolated nacelles develop a nozzle geometry correction.

The next step is to test the flow nacelle installed. An interference term,

$$\Delta C_{D_{INTERFERENCE}} = C_{D_{WBNP}} - C_{D_{WB}} - C_{D_{Flow_{iso}}} \qquad (10.17)$$

where W denotes wing, B denotes body, N denotes nacelle and P denotes pylon.

But this is the interference drag with the flow nacelle nozzle. A term, $\Delta(\Delta C_{D_{Nozzle\ Geometry}})$ is developed from the two blown nacelles, at ram FPR, installed on the model.

Finally,

$$\Delta C_{D_{TOTAL\ INTERFERENCE}} = \underbrace{C_{D_{INTERFERENCE}}}_{\text{FROM FLOW NACELLE}} + \underbrace{\Delta(\Delta C_{D_{NOZZLE\ GEOMETRY}})}_{\text{FROM BLOWN NACELLES}} \qquad (10.18)$$

These interference terms are considered to be the result of separations in corners, shock waves, and changes to induced drag, and are consequently not corrected for Reynolds number.

The remaining term, blowing drag, is the change in drag from the FPR=ram to FPR= cruise setting for the blown nacelle with production nozzle. It is not understood what blowing drag actually is caused by. In practice, blowing drag is typically 1% of total airplane drag, interference is another 1% to 3%, and form drag is about 5% for a total powerplant drag of 7% to 9%.

10.2.3 Wind Tunnel Bookkeeping with Flow and TPS Nacelles.

The power-on drag of a configuration when measured using TPS rather than a blown nacelle has a different procedure, because the TPS cannot be run at ram without changes in the flow field other than those caused by the jet. Figure 10.26 details the parts required. The flow nacelle shown as item 1 is the same as that for item 1 for the blown nacelle technique, Figure 10.24. The TPS nacelle has a contracted inlet and the production nozzle geometry. The different part is item 2 is a flow nacelle nozzle from item 1, and an exit plug to achieve the capture ratio of the TPS inlet. The purpose of item 2 is to find the aerodynamic effect of the change in fan cowl geometry from the production geometry of item 1 to the TPS geometry of item 3, without inducing a plume change.

Figure 10.27 details the steps in the drag determination using flow and TPS nacelles. Since the TPS nacelle is used differently than the blown nacelle, the drag components of the real airplane are redefined from the blown nacelle case. For the TPS procedure, the installation drag will be made of two components, powered form drag and powered interference drag. Power effects cannot be measured

separately with the TPS.

The model testing begins with the TPS being tested isolated at the real engine FPR, but at the TPS A_∞/A_{HI} . This provides a drag at wind tunnel Reynolds number which is corrected to flight conditions. But this measurement has been made with the wrong fan cowl, so the two flow nacelles are also tested as shown to measure the drag effect of going from TPS cowl at TPS A_∞/A_{HI} to real engine cowl at real engine A_∞/A_{HI} . This increment also is corrected for Reynolds number, and the sum is the form drag of an isolated, powered full scale nacelle.

Now the TPS is installed onto the wing and a drag increment is obtained:

$$\Delta C_{D_{INTERFERENCE}} = C_{D_{WBNP}} - C_{D_{WB}} - C_{D_{TPS,ISO}} \qquad (10.19)$$

But there is still the fan cowl and capture ratio difference of the TPS nacelle which must be corrected. The two flow nacelles are tested, installed, as shown on Figure 10.27 to develope a term $\Delta(\Delta C_{D_{\text{fan cowl geometry}}})$.

The sum of this term and $\Delta C_{D_{\text{interference}}}$ yields a powered interference drag term. Finally, the complete nacelle increment is the sum of the powered form drag and the powered interference drag. If done properly, the blown nacelle technique and the TPS nacelle technique should yield the same result for airplane drag.

10.3 TEST TECHNIQUES

A several-volume document could be written on the calibration and test techniques to be used with the various kinds of nacelles used for model testing. To stay within the scope of this course, only a brief introduction will be given.

10.3.1 Calibrations

Boeing employs two facilities for nacelle calibration. The objective of these calibrations is to measure the characteristic behavior of the nozzles of the various flow, blown and TPS nacelles so that their installed, wind-on thrust can be calculated and removed from the balance reading to yield drag. Figure 10.28 outlines the two facilities. The first is the airflow calibration facility (ACF), otherwise known as the "vacuum tank". This mounts the flow nacelle on TPS nacelle in front on a balance. An ejector in the rear pulls a vacuum on the tank, thus reducing the pressure the nozzle sees. The air outside the tank is P_T and that inside is P_S. Thus, at a ratio of $P_S/P_T = 0.528$, the tank is simulating the exit condition the flow nacelle would see at M=0.80 (in the compressible flow tables, page 1.21, $P_S/P_T = 0.528$ corresponds to $M_\infty = 0.80$). Venturi downstream of the tank measure the total mass flow. The TPS or flow nacelle require a "bellmouth" to guide the flow into the nacelle without losses.

The blown nacelle can either be mounted on the ACF or mounted in a simpler facility, called the thrust stand. Here, the desired pressure ratio is achieved by increasing the pressure in the supply line. A balance measures the force and a venturi measures the mass flow.

The reason for these measurements will be described in a moment. But first, it is necessary to define some nozzle terminology. Figure 10.29 shows a typical dual flow nozzle. Each attempts to produce an ideal thrust,

$$T_{IDEAL} = \frac{\dot{W}_{IDEAL} \; V_{\infty,IDEAL}}{g} \qquad (10.20)$$

where $\dot{\omega}_{ideal}$ is the ideal weight flow (not corrected weight flow) passing through the nozzle, and $V_{\infty,ideal}$, is the velocity of the flow passsing through the nozzle, expanded isentropically to reference free-stream conditions. This ideal velocity is calculated from pressure and temperature measurements made inside the blow or TPS nozzles, and is the reason why the rakes are installed. For the flow nacelle, V_∞ is assumed to be that of the free-stream flow.

But there are two mechanisms which reduce the true thrust below the ideal thrust. The first is flow suppression. The nozzle shape and viscous losses reduce the flow passing through the nozzle. A discharge or flow coefficient is thereby defined as

$$C_D = \frac{\dot{\omega}_{actual}}{\dot{\omega}_{ideal}} \qquad (10.2$$

where $\dot{W}_{actual}$ is the measured true weight flow and $\dot{W}_{ideal}$ is that calculated from the measured flow properties. The second reduction in thrust are the scrubbing, separation and shock losses experienced by the exhaust flow. A velocity coefficient is defined:

$$C_V = \frac{V_{\infty,actual}}{V_{\infty,IDEAL}} = \frac{T_{ACTUAL}}{\frac{\dot{w}_{actual}}{g} V_{\infty,ideal}} \qquad (10.22)$$

In practice, the second form of (10.22) is used to determine C_V. Finally, the actual thrust is

$$T_{actual} = \frac{\dot{w}_{actual} V_{\infty,actual}}{g} = C_V C_D \frac{\dot{w}_{IDEAL}}{g} V_{\infty,IDEAL} \qquad (10.23)$$

For the flow nacelle, the calibration and use is detailed on Figure 10.30. The flow nacelle instrumentation consists of an internal static tap, P_{SN}, and an internal total pressure tap, P_{TN}. The flow nacelle is mounted in the vacuum tank, the internal pressure is varied, and the true weight flow, balance reading, P_{SN} and P_{TN} are recorded. Then, C_D and C_V are calculated and curves of C_D and C_V versus P_{TN}/P_{SN} are drawn. The nacelle is then mounted in the wind tunnel and at a given M_∞ and C_L, the ratio P_{TN}/P_{SN} is obtained by measurement of the internal pressures. In this way, any change the wing may have on the flow-through the nacelle will be automatically measured. The internal drag can now be calculated by considering the flow nacelle to be a powered nacelle. Thus,

$$T_{NET} = \text{GROSS THRUST} - \text{RAM DRAG}$$

or,

$$D_{INTERNAL} = \text{RAM DRAG} - \text{GROSS THRUST}$$

$$= \frac{\dot{w}_{IDEAL}}{g} C_D V_{\infty,IDEAL} - \frac{\dot{w}_{IDEAL}}{g} C_D V_{\infty,IDEAL} C_V \qquad (10.24)$$

$$= \frac{\dot{w}_{IDEAL}}{g} V_{\infty,IDEAL} C_D (1 - C_V)$$

The capture ratio of the flow nacelle is determined from its geometry and from the actual weight flow as given by $\dot{W}_{ideal} \times C_D$.

A complication to TPS and flow nacelle calibration is shown on Figure 10.31. A bellmouth of some kind is required to guide the flow into the nacelle; without it, the inside of the lip would have separated flow. The problem is that both C_V and C_D depend on the size of bellmouth used (Figure 10.31). Testing

without a bellmouth produces the highest losses and consequently the lowest C_V and C_D. A large bellmouth produces the highest values. An uncertainty arises because the wind-on losses are likely somewhere in between. At present, the large bellmouth is preferred since (1) it should yield the highest C_V and C_D and (2) this tends to under-predict internal drag, meaning that the calculated external drag will be larger that the real value, which is a conservative error.

Calibration and use of the blown nacelle (Figure 10.32) is the simplest of three nacelles, because the mass flow is measured by venturi. All that needs to be determined in the calibration is C_V of the fan and primary, which are determined separately. First, the primary is run alone so that $C_{V_{primary}}$ is measured, then both streams are run and the fan C_V is measured by subtracting the calculated primary thrust. In the tunnel, the pressure ratio, P_T/P_∞ is used to look up the calibrated value of C_V, the actual weight flow is measured, and the ideal velocity is calculated from measured quantities inside the nozzles.

The blown nacelle offers an opportunity to measure the effect of the airframe on nozzle efficiency. Figure 10.33 compares a nozzle C_V calibration for the isolated nacelle, then with the wing present. The loss is small ($\approx$0.3%), but is measurable, when the wing is added to the configuration.

Figure 10.34 describes how the TPS nacelle is calibrated and used. The procedure requires that the primary C_V either be measured separately with a blown nacelle or be calculated analytically. Then, the TPS is operated in the vacuum tank. The fan weight flow is obtained and a curve of C_D versus P_{TF}/P_∞ is established. Then, the fan C_V is measured, using the guessed (or measured separately) value of primary C_V. In the wind tunnel, the primary mass flow is measured directly, but the fan mass flow is obtained as a result of the calibration. Ideal fan and primary velocities are calculated from measured properties inside the nozzle, and the thrust can then be determined.

10.3.2 Wind Tunnel Tests.

The actual wind tunnel test of a powered nacelle model is almost anticlimactic. About 75% of the total test cost will have been spent fabricating and calibrating the nacelle model parts, leaving only 25% and two weeks of work to be done in the tunnel.

Figure 10.35 details the standard isolated nacelle test facility. The nacelle is mounted on a swept strut, which is in turn mounted to the tunnel main balance via a "rocking horse". Flow, blown and TPS nacelles can all be tested in pitch on this facility. The drag of the nacelle is obtained by testing with the nacelle and pylon on, then subtracting the force and moment tares of the mount strut alone. Further details of this facility are contained in Reference 10.2.

700

Figure 10.36 shows the usual way in which the cruise drag effects are measured, on a large half-model. The entire model is metric, but only incremental forces involving the nacelle are of interest. The particular case shown is the 747 with two TPS nacelles. The half model is preferred because (1) geometries can be constructed to a better precision than at smaller scales, and (2) the forces being measured are larger, thus allowing better resolution of increments.

Obviously, three-engine configurations cannot be examined on a half model, and neither can effects of power on control and stability be evaluated. The choice now is to build a blown full model, or in the near future, use the 2.8 inch diameter unit now available at BTWT.

CHAPTER 10 REFERENCES

10.1 NASA TR R-444

10.2 C/S B-8285-AERO-114, "Isolated Nacelle Test Facility for BTWT," C. Sun, December, 1977.

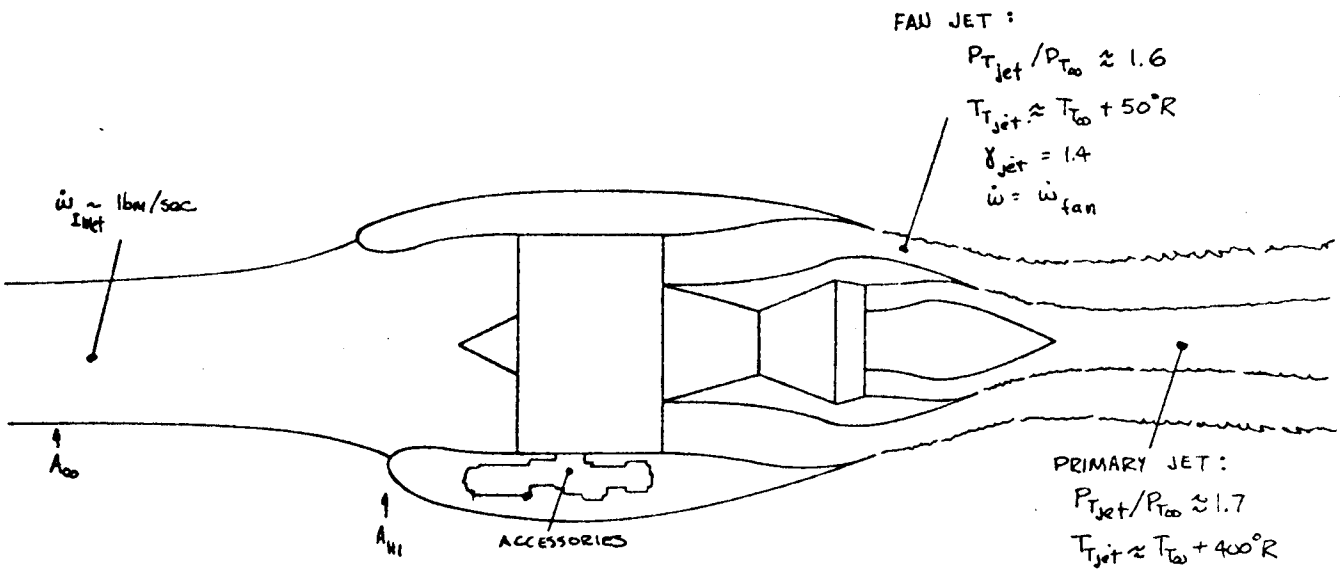

INLET CONDITION

INFLOW = OUTFLOW

$$\dot{w}_{INLET} + \dot{w}_{FUEL} = \dot{w}_{fan} + \dot{w}_{primary} - \dot{w}_{bleed} + \dot{w}_{FUEL}$$

$$BPR = \frac{\dot{w}_{fan}}{\dot{w}_{pri}} \qquad (\underline{B}y\ \underline{P}ass\ \underline{R}atio)$$

INLET OPERATES AT $\frac{A_\infty}{A_{HI}}$ FOR T=D

NOZZLE CONDITION:

(1) $\underline{F}$AN or $\underline{E}$XHAUST $\underline{P}$RESSURE $\underline{R}$ATIO ~ "FPR" or "EPR"

$$= P_{T_{jet}} / P_{T_\infty} \neq f(M)$$

(2) expanded NOZZLE PRESSURE Ratio (FNPR)

$$= \frac{P_{T_{jet}}/P_{T_\infty}}{(P_\infty/P_{T_\infty})_{M_\infty}} = \frac{P_{T_{jet}}}{P_\infty} = f(M_\infty)$$

(3) NOZZLE OPERATES AT FPR FOR T=D

FIGURE 10.1 CHARACTERISTICS OF THE REAL NACELLE

GILLETTE
3.14.78

703

INLET SIMULATION

1. GEOMETRY SCALED EXACTLY ~ $(\text{ORDINATE})_{\text{MODEL}} = (\text{ORDINATE})_{\text{AIRPLANE}} \times \text{S.F.}$

2. INLET WEIGHT FLOW SCALED ~

$$\left[\frac{\dot{\omega}_{corr}}{A_{HILITE}}\right]_{MODEL} = \left[\frac{\dot{\omega}_{corr}}{A_{HILITE}}\right]_{AIRPLANE}$$

where $[A_{HILITE}]_{MODEL} = [A_{HILITE}]_{AIRPLANE} (S.F.)^2$

and $\dot{\omega}_{corr} = \dfrac{\dot{\omega}_{actual} \cdot \sqrt{\theta}}{\delta}$, $\quad \theta = T_T / T_{T,\,\text{STANDARD CONDITIONS}}$, $\quad \delta = P_T / P_{T,\,\text{STANDARD CONDITIONS}}$

JET SIMULATION

1. GEOMETRY SCALED EXACTLY ~ $(\text{ORDINATE})_{\text{MODEL}} = (\text{ORDINATE})_{\text{AIRPLANE}} \times \text{S.F.}$

2. EFFECT OF JET ON AERODYNAMIC FORCES REQUIRES SIMULATION OF

(a) JET SHAPE, WHICH IS MATCHED WHEN $\left[P_{T_{jet}}/P_{T_\infty}\right]_{Model} = \left[P_{T_{jet}}/P_{T_\infty}\right]_{AIRPLANE}$

AND $\left[T_{T_{jet}}/T_{T_\infty}\right]_{MODEL} = \left[T_{T_{jet}}/T_{T_\infty}\right]_{airplane}$

(b) ENTRAINMENT OF OUTER FLOW INTO THE JET, REQUIRES SIMULATION OF UNIT MASS FLOW, UNIT MOMENTUM, INTERNAL ENERGY/UNIT MASS, KINETIC ENERGY/UNIT MASS, and $R_j T_j / R_\infty T_\infty$; ie, all properties of the jet.

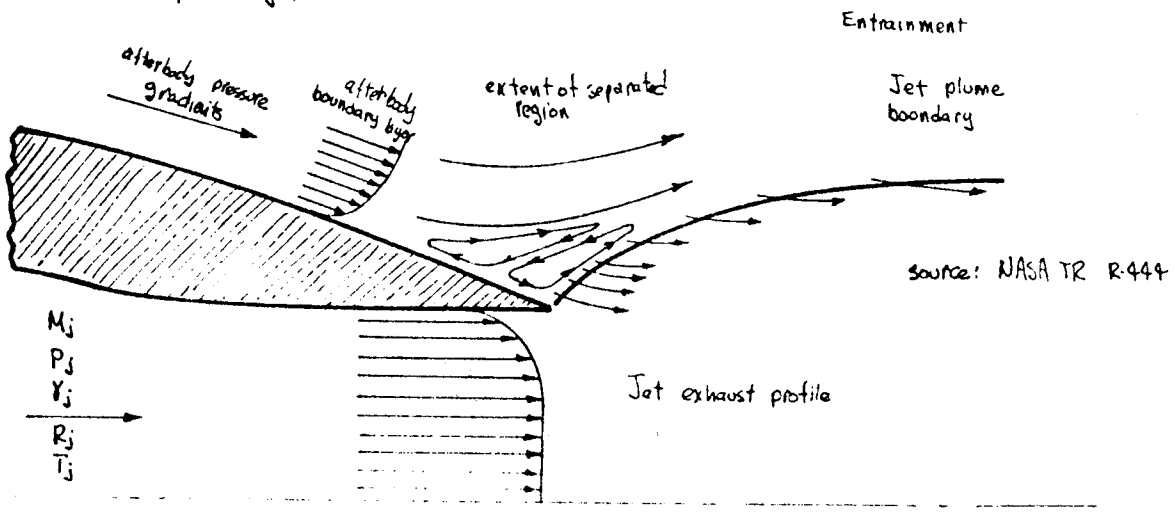

FIGURE 10.2 INLET & JET SIMULATION REQUIREMENTS

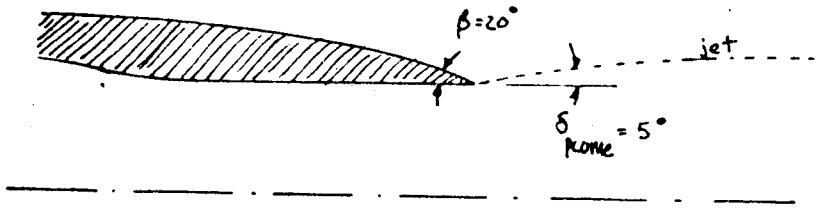

$M_\infty = 0.85$

source: NASA TR R-444

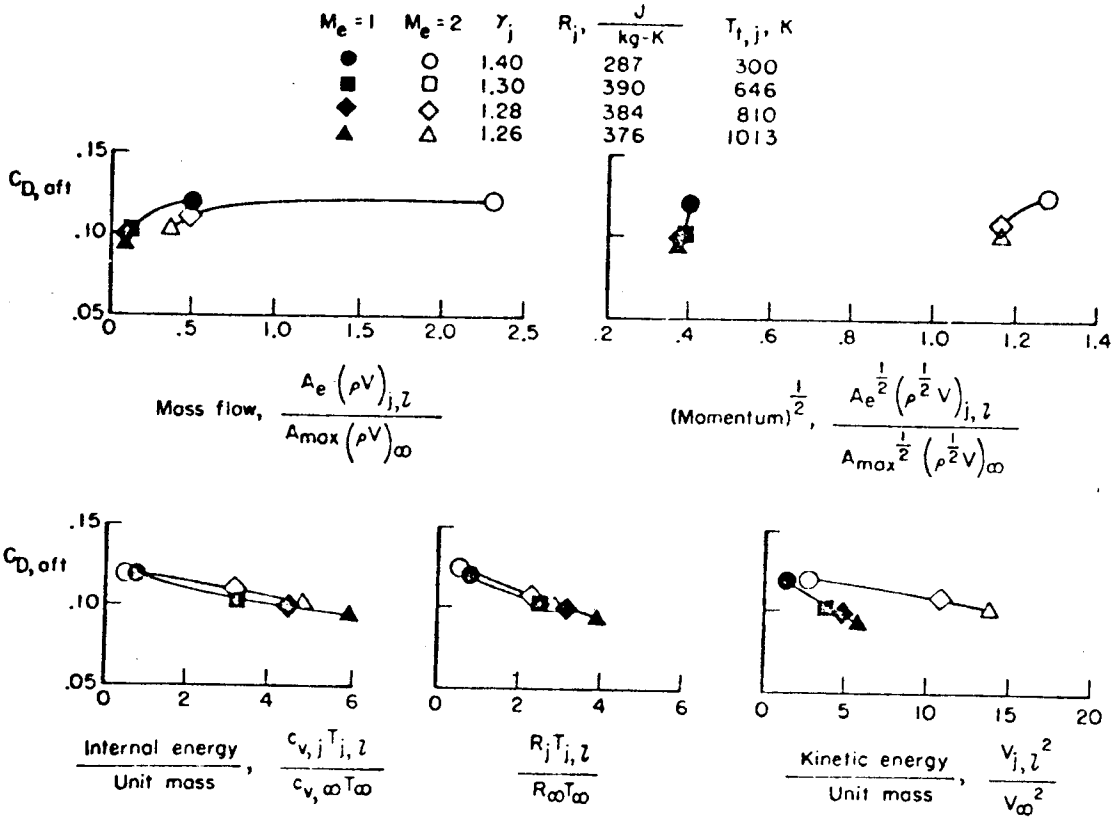

FIGURE 10.3 ATTEMPTS TO MODEL ENTRAINMENT EFFECT

GILLETTE 3.17.78

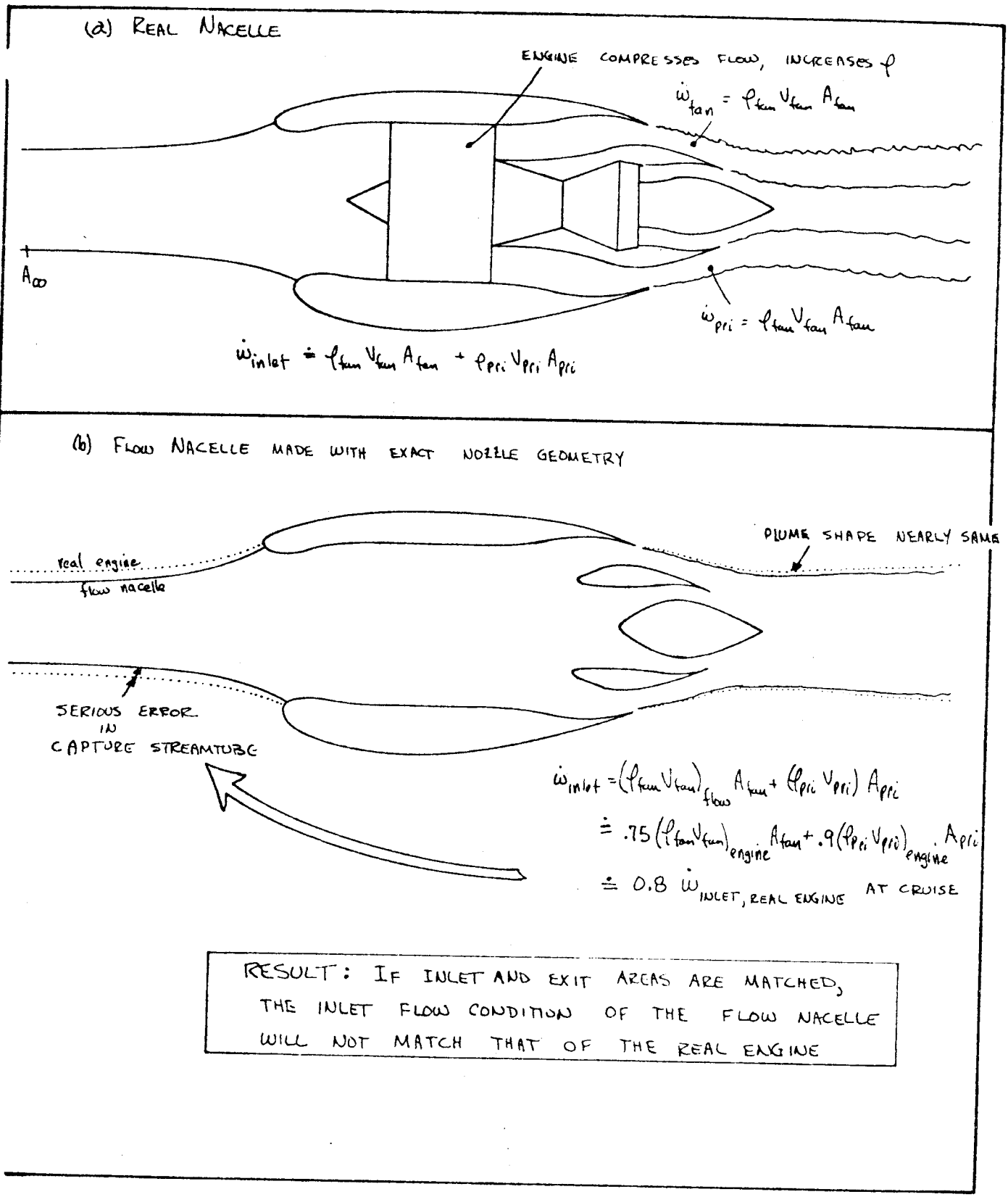

FIGURE 10.4 COMPARISON OF REAL & FLOW NACELLE WITH IDENTICAL INLET & EXIT GEOMETRIES

SILLETTE 3.14.78

706

M=0.70

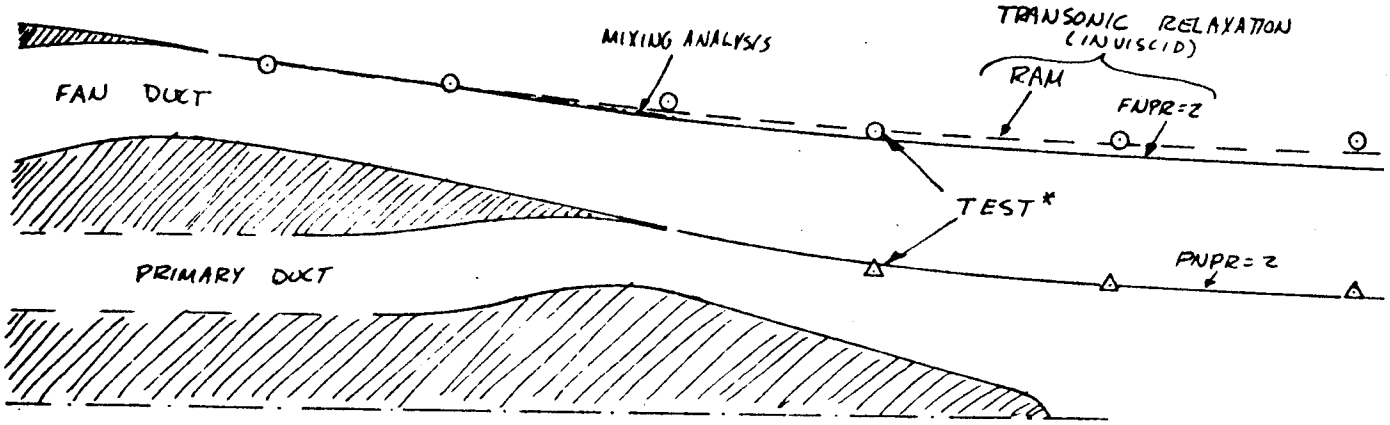

* MINIMUM PRESSURE POINT IN PLUME SURVEY AT NPR = 2.0

M=0.85

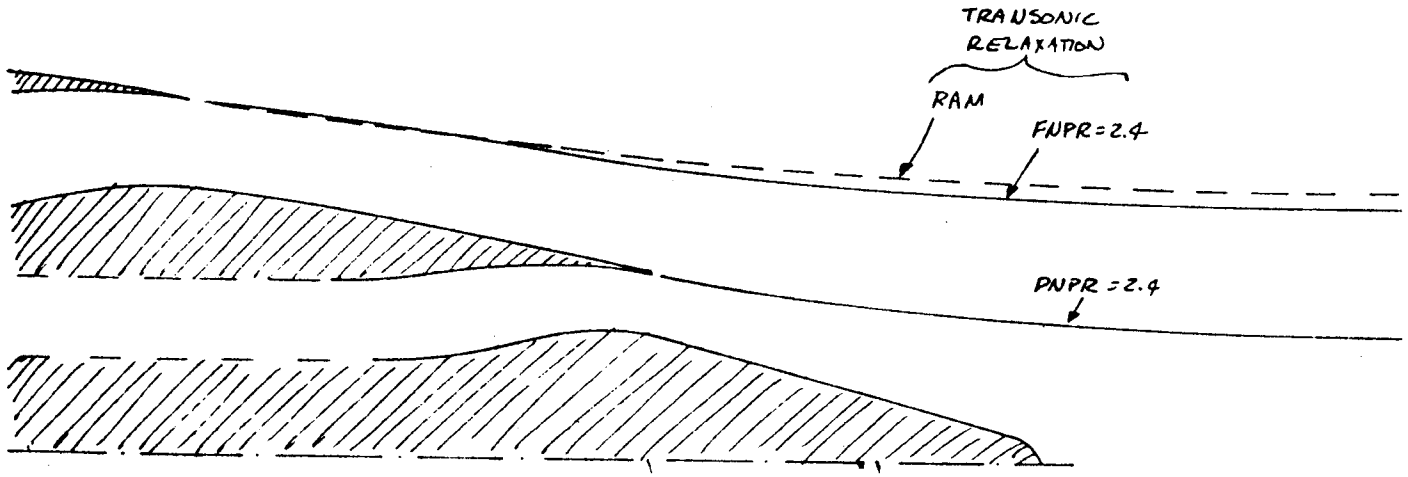

FIGURE 10.5 EFFECT OF PRESSURE RATIO ON JET SHAPE

CONCEPT	NAME	COMMENTS
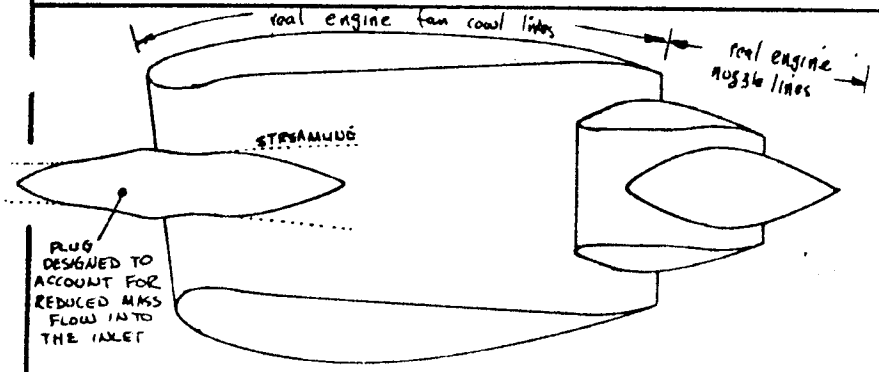	INLET PLUG	• PLUG DESIGNED BY ANALYSIS • POOR FOR HIGH-α TESTING
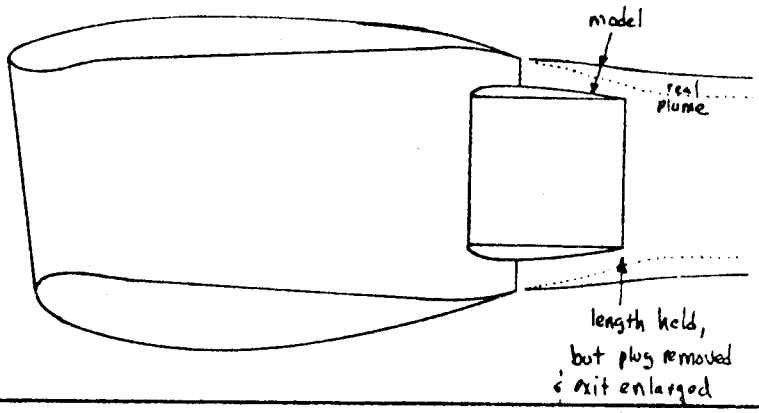	ENLARGED PRIMARY	• LENGTH OF PRIMARY RETAINED • ENLARGED PRIMARY ALTERS PLUME ANGLE AT FAN EXIT • PLUG REMOVED
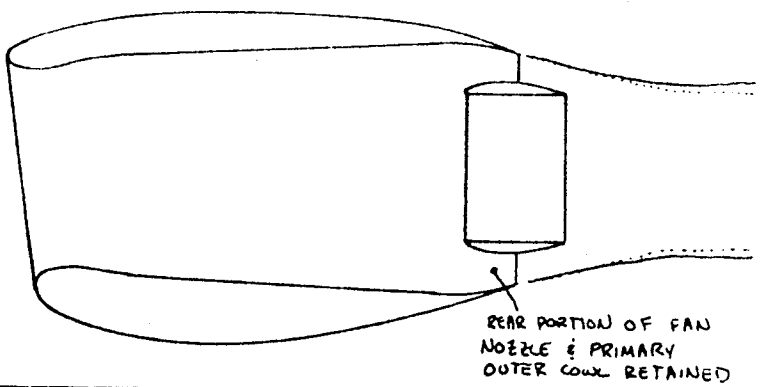	TRUNCATED PRIMARY	• FAN NOZZLE & OUTER PRIMARY LINES RETAINED • NOZZLE TRUNCATED & PLUG REMOVED TO GIVE PROPER MASS FLOW
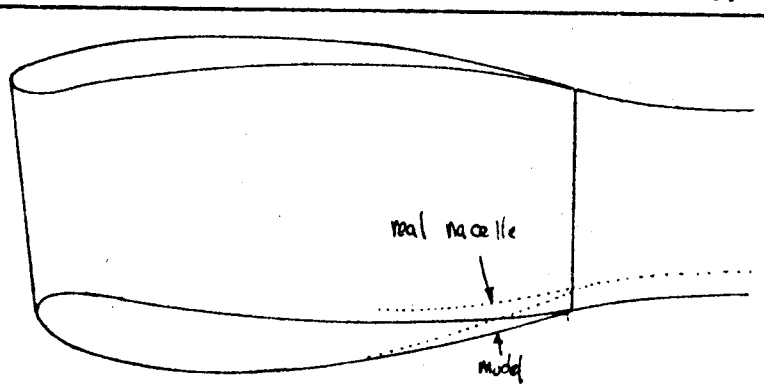	OVALIZED EXIT	• USED FOR FULL-LENGTH NACELLES

FLOW NACELLE PROVIDES: • EXACT SIMULATION OF INLET AT CRUISE
• POOR SIMULATION OF EXHAUST

FIGURE 10.6 TECHNIQUES FOR USING FLOW NACELLE

PROCEDURE 1: ASSUME DISCHARGE COEFFICIENT

(a) GUESS (based on experience)

$$C_D \equiv \frac{\dot{w}_{actual}}{\dot{w}_{ideal}}$$

or, $\dot{w}_{actual} = \dot{w}_{ideal} \times C_D$

where $\dot{w}_{ideal} = \rho_\infty V_\infty A_{EXIT}$ at the M_∞ value where the inlet is to be matched

(b) SINCE $\dot{w}_{INLET} = \dot{w}_{ACTUAL}$,

$$A_{EXIT} = \frac{(\dot{w}_{INLET})_{AIRPLANE}}{C_D \rho_\infty V_\infty} \cdot (\text{SCALE FACTOR})^2$$

where $\dot{w}_{INLET}$ is in terms of corrected weight flow

(c) Range on C_D is from 0.85 to 0.99, TYPICALLY

PROCEDURE 2: ASSUME TRAILING EDGE PRESSURE COEFFICIENT

(a) Guess or calculate $C_{p_{exit}}$

(b) compute M_{exit} from

$$M_{EXIT} = \left\{ \frac{1}{\gamma - 1} \left[\frac{2 + (\gamma-1) M_\infty^2}{\left(1 + \frac{\gamma M_\infty^2 C_p}{2}\right)^{\frac{\gamma-1}{\gamma}}} - 2 \right] \right\}^{1/2}$$

(c) • Find ρ_E/ρ_T & V_E/a^* at M_{EXIT} from compressible flow tables

• find ρ_∞/ρ_T & V_∞/a^* at M_∞ from compressible flow tables

(d) $$A_\infty = \frac{\left[\dot{w}_{corr,\,full\,scale}\right] \cdot (\text{scale factor})^2}{\rho_\infty V_\infty}$$

(e) $$A_{EXIT} = \frac{(\rho_\infty/\rho_T)(V_\infty/a^*) A_\infty}{(\rho_E/\rho_T)(V_E/a^*)}$$

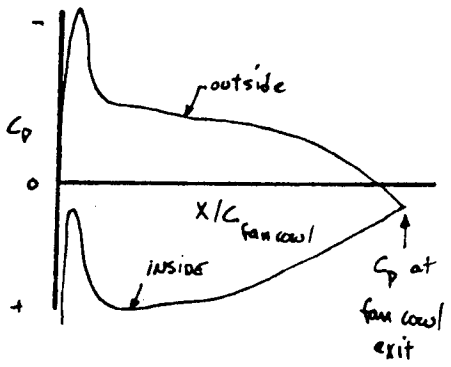

FIGURE 10.7 COMPUTING EXIT AREA REQUIRED FOR FLOW NACELLE

GILLETTE 3.4.78

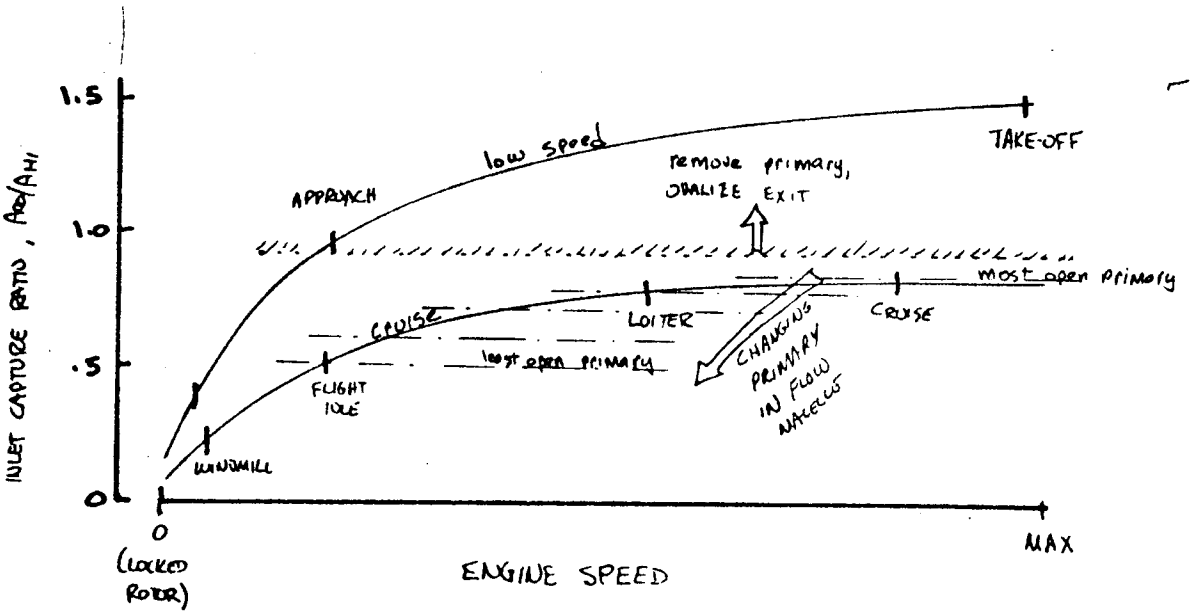

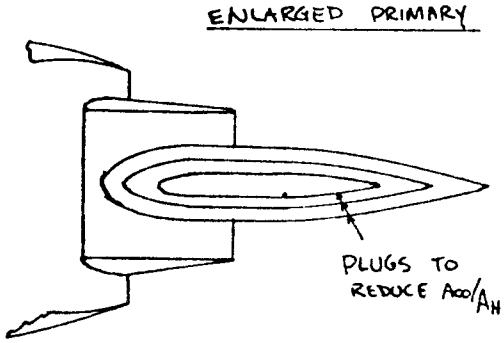

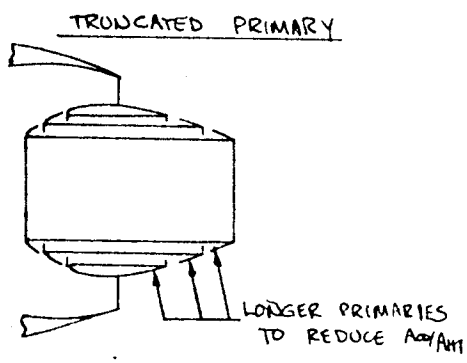

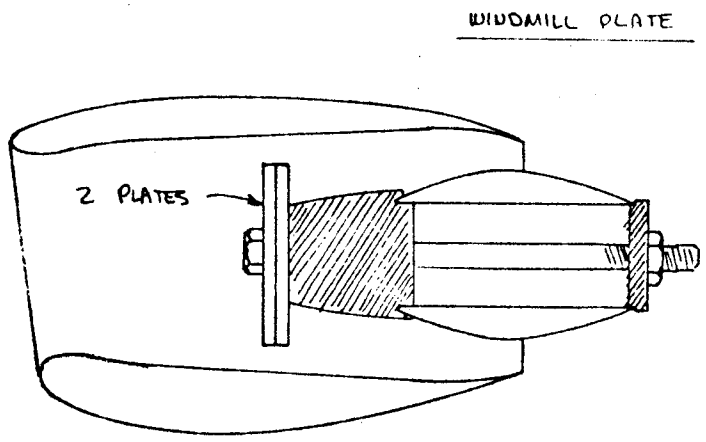

FIGURE 10.8 VARYING INLET CAPTURE RATIO IN FLOW NACELLE

BLOWN NACELLE PROVIDES: (1) NO SIMULATION OF INLET
(2) GOOD SIMULATION OF FAN JET
(3) FAIR SIMULATION OF PRIMARY JET

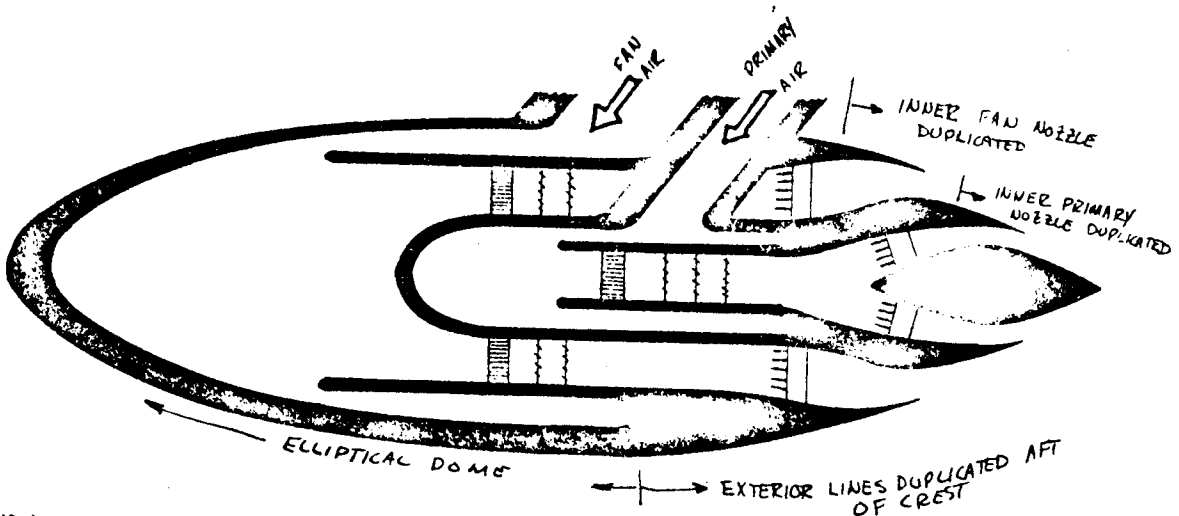

CONTAINS

- CHOKE PLATES TO DROP HIGH-PRESSURE SUPPLY AIR DOWN TO $P_{T_{jet}}/P_T$ TO MATCH REAL ENGINE
- SCREENS TO SMOOTH FLOW & REDUCE DISTORTION
- TOTAL PRESSURE & TEMPERATURE INSTRUMENTATION TO USE IN THRUST CALIBRATION

SIMULATES • JET TOTAL PRESSURE ONLY

DOES NOT SIMULATE •
- SWIRL
- TEMPERATURE
- REAL GAS EFFECTS
- INFLOW INTO NACELLE

FIGURE 10.9 BLOWN NACELLE FOR JET SIMULATION

GILLETTE
3.15.78

TPS PROVIDES: (1) PARTIAL SIMULATION OF INLET FLOW
(2) NEAR-EXACT SIMULATION OF FAN JET
(3) POOR SIMULATION OF PRIMARY JET

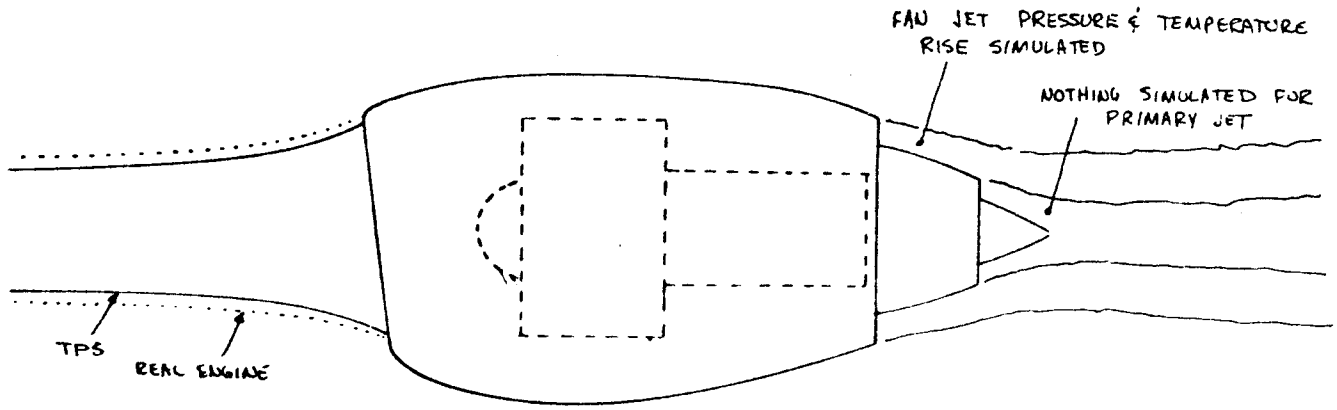

$$\left(\dot{w}_{INLET}\right)_{TPS} \doteq \left(\dot{w}_{REAL\ ENGINE}\right) \times (SCALE\ FACTOR)^2 \times \left[\frac{BPR}{1+BPR}\right]$$

FOR EXAMPLE, AT BPR=4, TPS INLET TAKES IN 80% OF REAL ENGINE INLET FLOW WHEN NOZZLE LINES ARE MATCHED

FIGURE 10.11 SIMULATION PROVIDED BY TPS NACELLE

11/2 GILLETTE 3.15.78

(a) REAL ENGINE AT $\dot{w}$ FOR CRUISE MACH

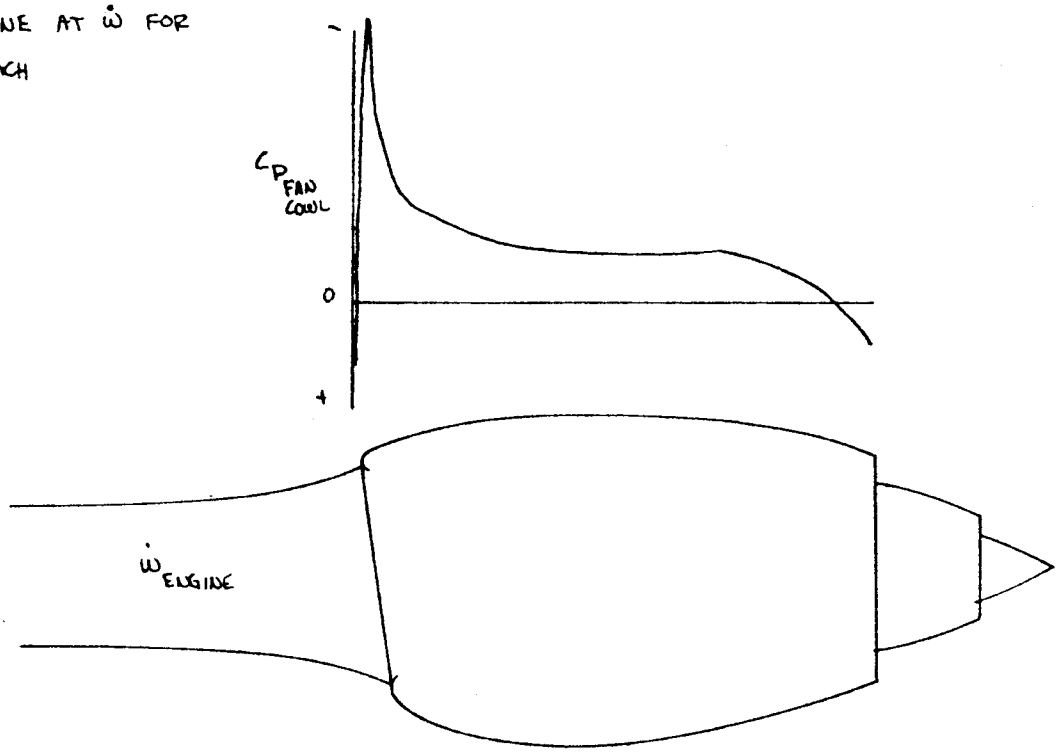

(b) TPS INLET DESIGNED TO APPROXIMATELY THE SAME CHORDWISE C_p AS REAL ENGINE'S FAN COWL

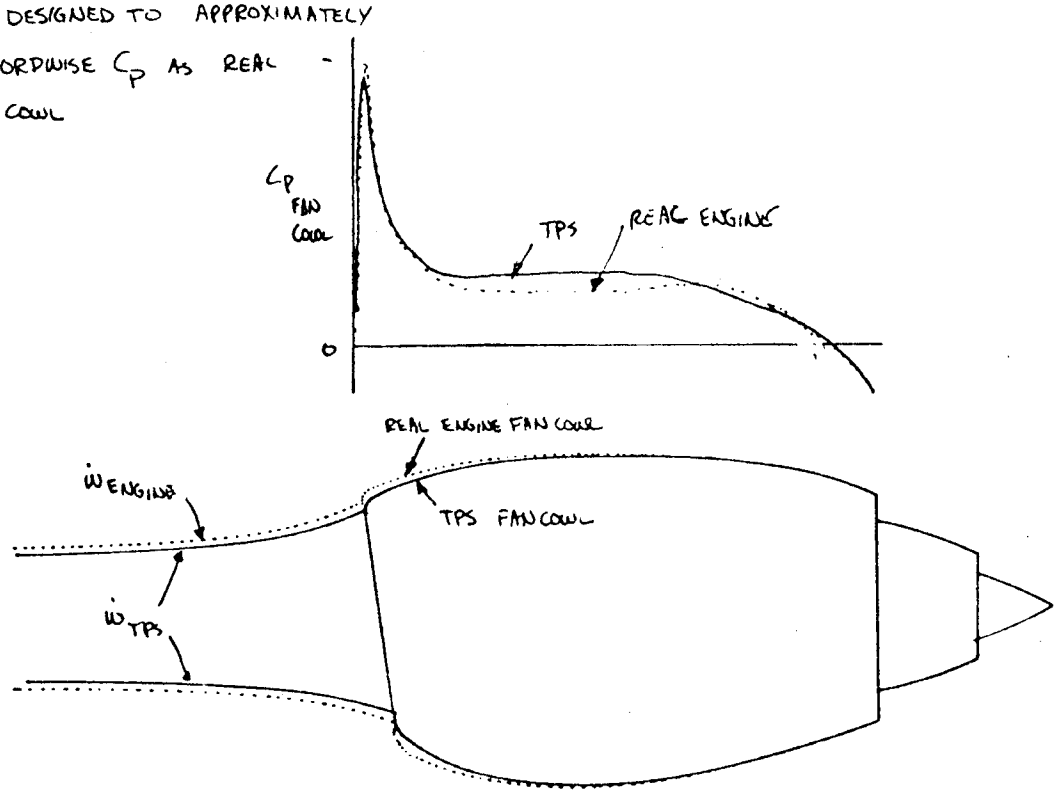

FIGURE 10.12 TPS INLET DESIGN

GILLETTE
3.15.78

7/3

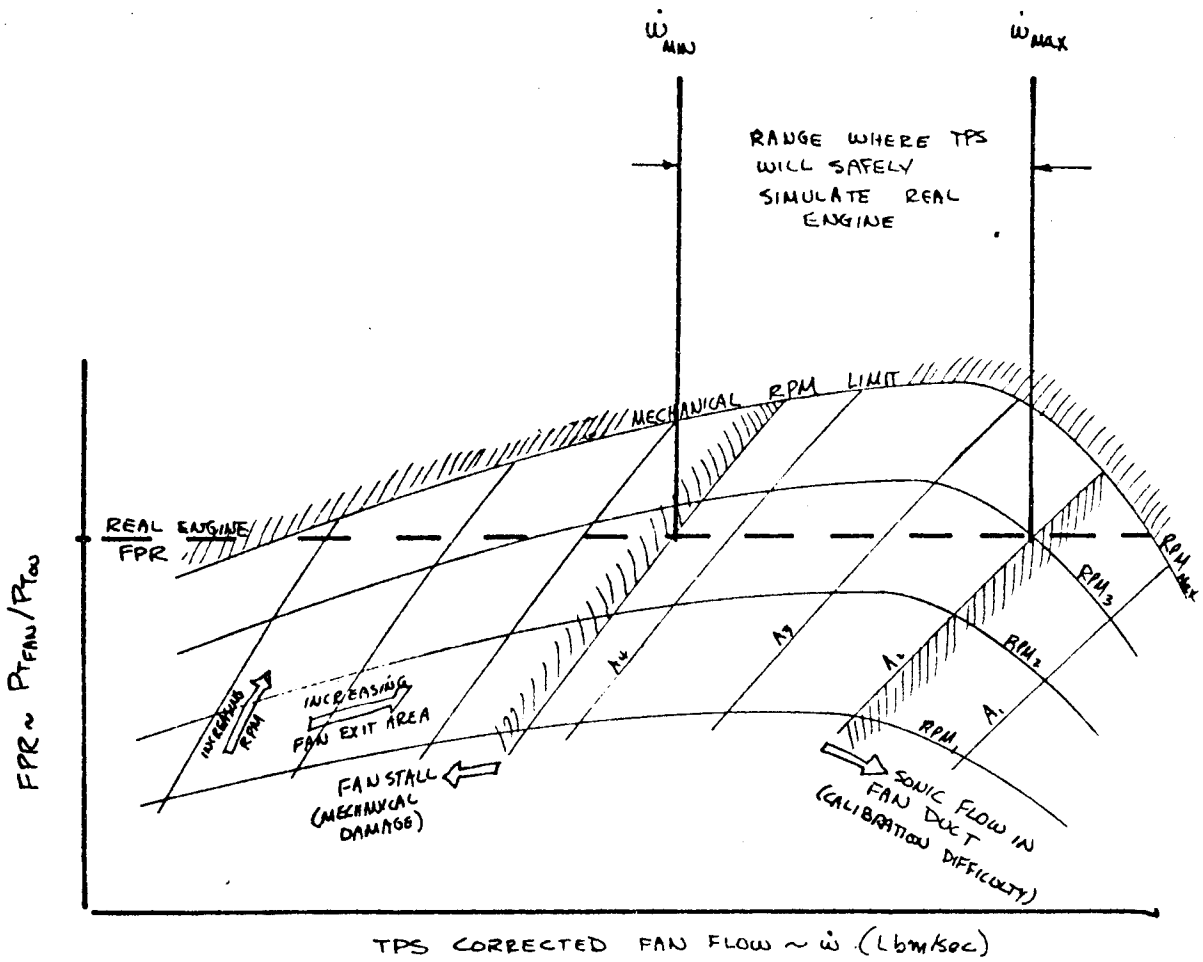

$\dot{w}_{FAN,CORR,ENGINE}$ = CORRECTED CRUISE WEIGHT FLOW FOR REAL ENGINE

$$\text{MINIMUM TPS model scale factor} = \sqrt{\frac{(\dot{w}_{FAN,CORR,MAX})_{TPS}}{\dot{w}_{FAN,CORR,ENGINE}}}$$

$$\text{MAXIMUM TPS model scale factor} = \sqrt{\frac{(\dot{w}_{FAN,CORR,MIN})_{TPS}}{\dot{w}_{FAN,CORR,ENGINE}}}$$

FIGURE 10.13 SELECTING SCALE FACTOR FOR TPS MODEL

GILLETTE
3.15.78

EJECTOR PROVIDES: (1) PARTIAL SIMULATION OF INLET FLOW
(2) POOR SIMULATION OF FAN JET
(3) POOR SIMULATION OF PRIMARY JET

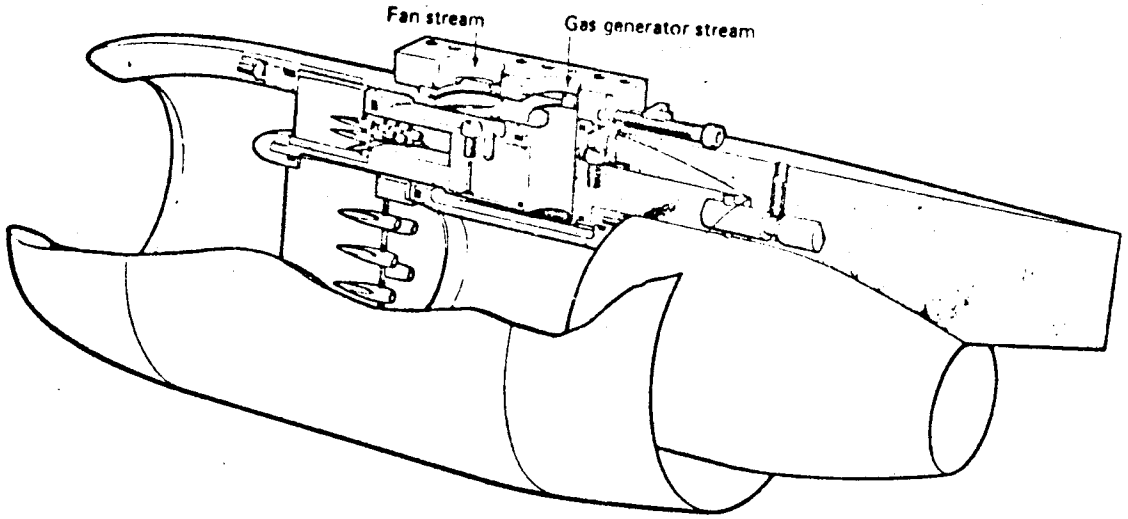

$$\left(\dot{\omega}_{INLET}\right)_{EJECTOR} \doteq 60\% \text{ OF SCALED ENGINE INLET FLOW AT } \left(P_{T_j}/P_{T_\infty}\right)_{EJECTOR} = 1.5$$

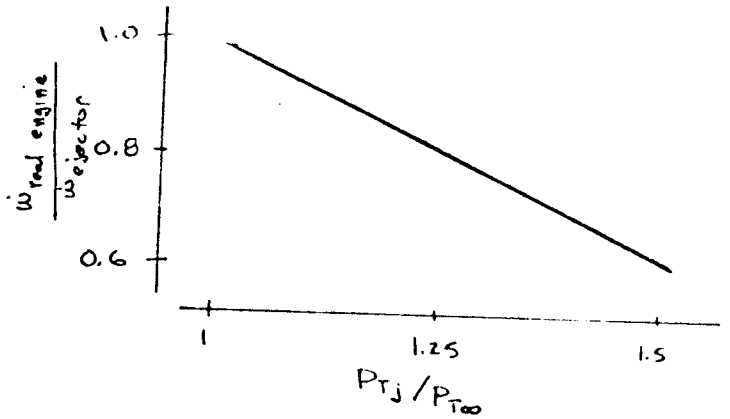

FIGURE 10.14 EJECTOR NACELLE

GILLETTE
3.15.78

7/5

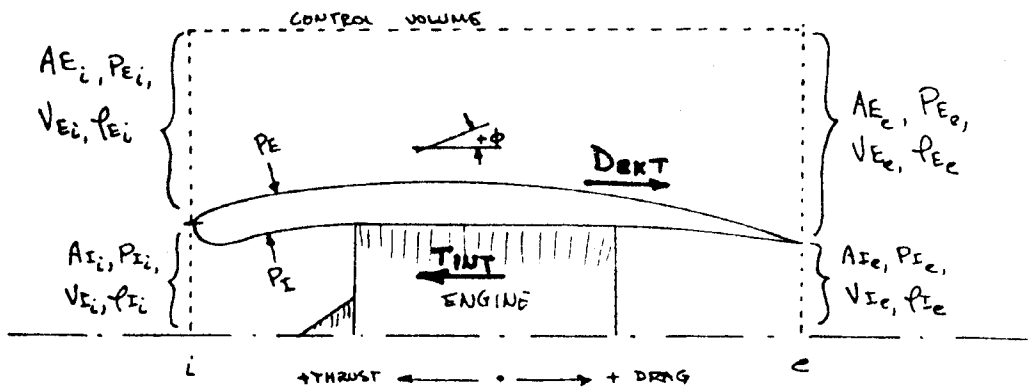

THRUST: $$\int_i P_{I_i}\, dA_{I_i} - \int_e P_{I_e}\, dA_{I_e} + \int_I P_I \sin\phi_I\, dS = \int_e \rho_{I_e} V_{I_e}^2 \cos^2\phi_{I_e}\, dA_{I_e} - \int_i \rho_{I_i} V_{I_i}^2 \cos^2\phi_{I_i}\, dA_i$$

but $$\int_i P_\infty dA_{I_i} - \int_e P_\infty dA_{I_e} + \int_1 P_\infty \sin\phi_I\, dS = 0$$

then $$\int_I \left[(P_I - P_\infty)\sin\phi_I\right] dS = \int_e \left(\rho_{I_e} V_{I_e}^2 \cos^2\phi_{I_e} + P_{I_e} - P_\infty\right) dA_{I_e} - \int_i \left(\rho_{I_i} V_{I_i}^2 \cos^2\phi_{I_i} + P_{I_i} - P_\infty\right) dA_{I_i}$$

$$\boxed{T_{INT} \equiv \int_e \left(\rho_{I_e} V_{I_e}^2 \cos^2\phi_{I_e} + P_{I_e} - P_\infty\right) dA_{I_e} - \int_i \left(\rho_{I_i} V_{I_i}^2 \cos^2\phi_{I_i} + P_{I_i} - P_\infty\right) dA_{I_i}}$$

DRAG: SIMILARLY,

$$\boxed{D_{EXT} \equiv \int_i \left[\rho_{E_i} V_{E_i}^2 \cos^2\phi_{E_i} + P_{E_i} - P_\infty\right] dA_{E_i} - \int_e \left[\rho_{E_e} V_{E_e}^2 \cos^2\phi_{E_e} + P_{E_e} - P_\infty\right] dA_{E_e}}$$

BOOKKEEPING

$$\boxed{\Delta F_{AIRFRAME} = \underbrace{T_{INT}}_{\text{propulsion staff}} - \underbrace{D_{EXT}}_{\text{aerodynamics staff}}}$$

FIGURE 10.15 SEPARATION OF THRUST & DRAG ~ FORCES FELT BY THE AIRFRAME

GILLETTE 3.15.78

7/6

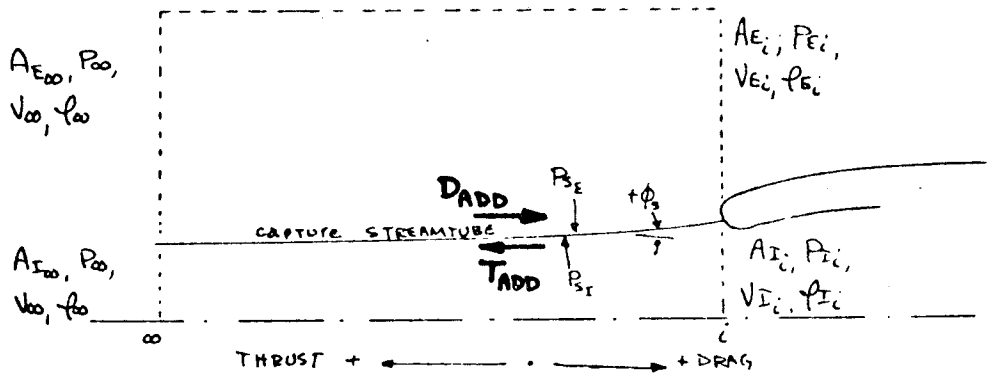

THRUST: $$\int_\infty P_\infty dA_{I_\infty} - \int_i P_{I_i} dA_{I_i} + \int_{\text{STREAMTUBE}} P_{S_I} \sin\phi_s \, dS = \int_i \rho_{I_i} V_{I_i}^2 \cos^2\phi_i \, dA_i - \int_\infty \rho_\infty V_\infty^2 \, dA_{I_\infty}$$

but $$\int_\infty P_\infty dA_{I_\infty} - \int_i P_\infty dA_{I_i} + \int_{\text{STREAMTUBE}} P_\infty \sin\phi_s \, dS = 0$$

so $$\int_{\text{STREAMTUBE}} (P_{S_I} - P_\infty) \sin\phi_s \, dS = \int_i (\rho_{I_i} V_{I_i}^2 \cos^2\phi_{I_i} + P_{I_i} - P_\infty) dA_{I_i} - \rho_\infty V_\infty^2 A_{I_\infty}$$

$$\boxed{T_{ADDITIVE} \equiv \int_i (\rho_{I_i} V_{I_i}^2 \cos^2\phi_{I_i} + P_{I_i} - P_\infty) dA_{I_i} - \rho_\infty V_\infty^2 A_{I_\infty}}$$

DRAG: LIKE WISE,

$$\boxed{D_{ADDITIVE} \equiv \rho_\infty V_\infty^2 A_{E_\infty} - \int_i \left[\rho_{E_i} V_{E_i}^2 \cos^2\phi_{E_i} + P_{E_i} - P_\infty\right] dA_{E_i}}$$

NOTE THAT

$$\boxed{D_{ADDITIVE} = T_{ADDITIVE}}$$

(1) THEY ARE EQUAL & OPPOSITE FORCES ON A STREAMLINE

(2) THEY ARE NOT REAL FORCES, BUT ARE THE RESULT OF A BOOKKEEPING CHOICE

(3) THEY ARE NOT FELT BY THE AIRFRAME

FIGURE 10.16 EXTENDING THE BOUNDARY TO UPSTREAM INFINITY

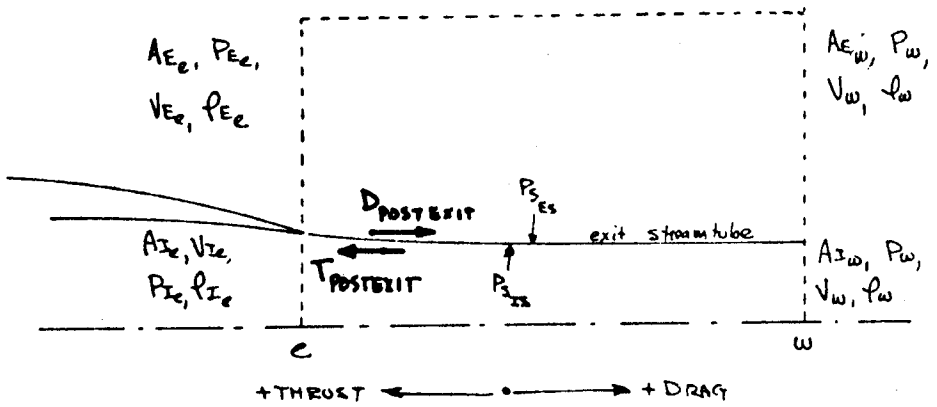

THRUST SIMILARLY TO FIGURE 10-16

$$T_{POST\text{-}EXIT} \equiv \int_{\omega} \rho_\omega V_\omega^2 \, dA_{I_\omega} - \int_{e} \left(\rho_{I_e} V_{I_e}^2 \cos^2\phi_e + P_{I_e} - P_\infty\right) dA_{I_e}$$

DRAG SIMILARLY TO FIGURE 10-16

$$D_{POST\text{-}EXIT} \equiv \int_{e} \left[\left(\rho_{E_e} V_{E_e}^2 \cos^2\phi_{E_e} + P_{E_e} - P_\infty\right] dA_{E_e} - \rho_\infty V_\infty^2 A_{E_\omega}\right.$$

NOTE THAT

$$D_{POST\text{-}EXIT} = T_{POST\text{-}EXIT}$$

(1) THEY ARE EQUAL & OPPOSITE FORCES ON A STREAMLINE

(2) THEY ARE NOT REAL FORCES, BUT ARE THE RESULT OF A BOOKKEEPING CHOICE

(3) THEY ARE NOT FELT BY THE AIRFRAME

FIGURE 10.17 EXPANDING THE BOUNDARY TO DOWNSTREAM INFINITY

GILLETTE 3.16.78

(a) FROM FIGURE 10.15, PROPULSIVE THRUST COULD BE DEFINED AS:

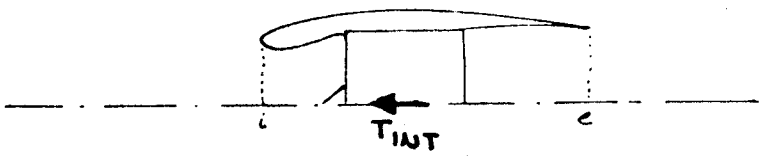

$$T_{INT} = \int_e (\rho_{I_e} V_{I_e}^2 \cos^2\phi_{I_e} + P_{I_e} - P_\infty)\, dA_{I_e} - \int_i (\rho_{I_i} V_{I_i}^2 \cos^2\phi_{I_i} + P_{I_i} - P_\infty)\, dA_{I_i}$$

and represent the change in momentum from the inlet to exit plane. This would be the true thrust felt by the airframe. BUT, THE integrals for T_{INT} ARE difficult to evaluate, and change with airplane q, M, C_L, etc.

(b) PROPULSION STAFF USUALLY DEFINES A DIFFERENT THRUST:

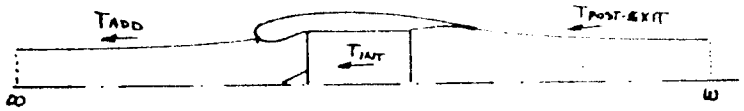

$$T_{NET} \equiv T_{ADD} + T_{INT} + T_{POST-EXIT}$$

$$= \int_i (\rho_{I_i} V_{I_i}^2 \cos^2\phi_{I_i} + P_{I_i} - P_\infty) dA_{I_i} - \rho_\infty V_\infty^2 A_{I_\infty}$$

$$+ \int_e (\rho_{I_e} V_{I_e}^2 \cos^2\phi_{I_e} + P_{I_e} - P_\infty) dA_{I_e} - \int_i (\rho_{I_i} V_{I_i}^2 \cos^2\phi_{I_i} + P_{I_i} - P_\infty) dA_{I_i}$$

$$+ \int_\omega \rho_\omega V_\omega^2 dA_{I_\omega} - \int_e (\rho_{I_e} V_{I_e}^2 \cos^2\phi_{I_e} + P_{I_e} - P_\infty) dA_{I_e}$$

$$= \underbrace{\int_\omega \rho_\omega V_\omega^2 dA_{I_\omega}}_{\text{GROSS THRUST}} - \underbrace{\rho_\infty V_\infty^2 A_{I_\infty}}_{\text{RAM DRAG}}$$

FIGURE 10.18 PROPULSION STAFF NET THRUST

GILLETTE
3.16.78

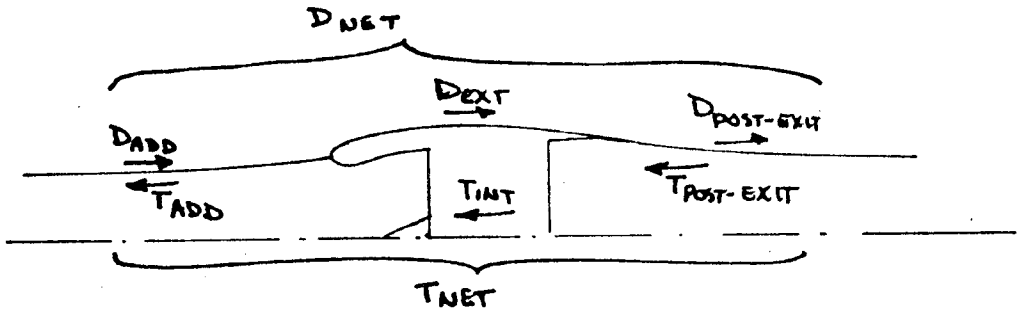

(a) $\Delta F_{AIRFRAME} = T_{INT} - D_{EXT}$

• THESE ARE THE TWO FORCES FELT BY THE AIRFRAME

(b) FOR CONVENIENCE, PROPULSION STAFF DEFINES:

$$T_{NET} = T_{ADD} + T_{INT} + T_{POST-EXIT}$$

(c) AERO STAFF MUST THEN DEFINE

$$D_{NET} = D_{ADD} + D_{EXT} + D_{POST-EXIT}$$

(d) $\Delta F_{AIRFRAME} \stackrel{?}{=} T_{NET} - D_{NET}$

$$= T_{ADD} + T_{INT} + T_{POST-EXIT} - D_{ADD} - D_{EXT} - D_{POST-EXIT}$$

$$= T_{INT} - D_{EXT} + (T_{ADD} - D_{ADD}) + (T_{POST-EXIT} - D_{POST-EXIT})$$

$$= T_{INT} - D_{EXT} \quad \text{Q.E.D.}$$

SO, AERO STAFF MUST DETERMINE D_{NET}, WHICH INCLUDES

$$D_{ADDITIVE} + D_{POST-EXIT}$$

FIGURE 10.19 DRAG TERM REQUIRED FOR THRUST-DRAG BOOKKEEPING

620 GILLETTE 3.16.78

(a) THRUST-DRAG BOOKKEEPING REQUIRES THAT

$$D_{NET} = D_{ADDITIVE} + D_{EXT} + D_{POST\text{-}EXIT}$$

BE DETERMINED.

(b) CONSIDER THE NACELLE IN POTENTIAL FLOW:

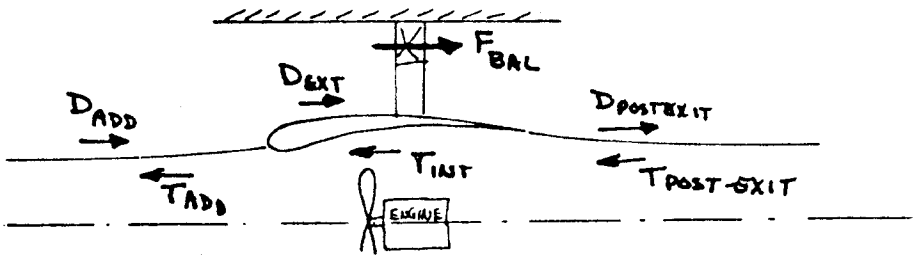

F_{BAL} = FORCE MEASURED BY WIND TUNNEL BALANCE

(c) FOR THE CAPTURED STREAMTUBE, IN POTENTIAL FLOW,

$$T_{ADD} + T_{INT} + T_{POSTEXIT} = T_{NET}$$

OR, $$T_{INT} = -T_{ADD} - T_{POSTEXIT} + T_{NET}$$

(d) THE BALANCE MEASURES ONLY SURFACE FORCES:

$$F_{BAL} = D_{EXT} - T_{INT}$$

$$= D_{EXT} + T_{ADD} + T_{POST\text{-}EXIT} - T_{NET}$$

BUT $T_{ADD} = D_{ADD}$, $T_{POSTEXIT} = D_{POSTEXIT}$

$\therefore$,

$$\boxed{F_{BAL} = D_{EXT} + D_{ADD} + D_{POSTEXIT} - T_{NET} = D_{NET} - T_{NET}}$$

OR, $$D_{NET} = \underbrace{F_{BAL}}_{\text{measured}} + \underbrace{T_{NET}}_{\text{calculated}}$$

FIGURE 10.20 MEASUREMENT OF D_{NET} IN POTENTIAL FLOW

GILLETTE 3/6/78

721

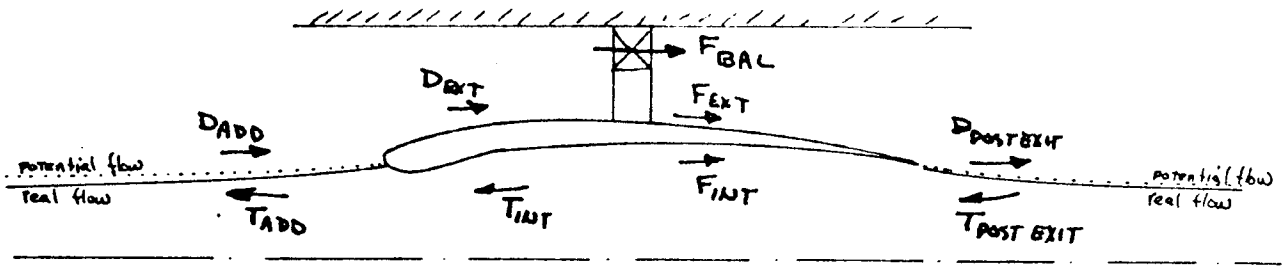

CHANGES FROM FIGURE 10.20:

- F_{EXT}, F_{INT} ARE SKIN FRICTION FORCES
- INLET & EXIT STREAMTUBES ARE SLIGHTLY REDUCED DUE TO INTERNAL FLOW LOSSES IN THE NACELLE

SURFACE PRESSURE FORCES:

$D_{EXT,\,POTENTIAL\,FLOW}$ & $T_{INT,\,POTENTIAL\,FLOW}$ ~ SURFACE INTEGRALS IN POTENTIAL FLOW

$D_{EXT,\,REAL\,FLOW}$ & $T_{EXT,\,REAL\,FLOW}$ ~ SURFACE INTEGRALS IN POTENTIAL FLOW

SIMILARLY TO FIGURE 10.20, IT CAN BE SHOWN THAT

$$F_{BAL} = D_{NET} + F_{INT} + (T_{INT,\,REAL} - T_{INT,\,POTENTIAL\,FLOW})$$

$-\Delta D_{ADD}$ DUE TO CHANGE IN CAPTURE STREAMTUBE

$-\Delta D_{POST\,EXIT\,THRUST}$ DUE TO CHANGE IN EXIT STREAMTUBE

BUT $$\text{FORM DRAG} = \oint c_f \, ds + \oint (P_{real} - P_{potential\,flow})\, ds$$

THUS $$F_{INT} + (T_{INT,\,REAL} - T_{INT,\,POTENTIAL\,FLOW}) = D_{INTERNAL\,FORM\,DRAG}$$

$\therefore$, $$F_{BAL} \doteq D_{NET} + D_{INTERNAL\,FORM\,DRAG}$$

OR, $$\boxed{D_{NET} \doteq F_{BAL} - D_{INTERNAL\,FORM\,DRAG}}$$

"NET INTERNAL THRUST" FOR FLOW NACELLE

FIGURE 10.21 MEASUREMENT OF D_{NET} IN REAL FLOW

122 GILLETTE 5.17.78

(a) When the capture ratio is one, there is no additive drag, but there is a force on the lip:

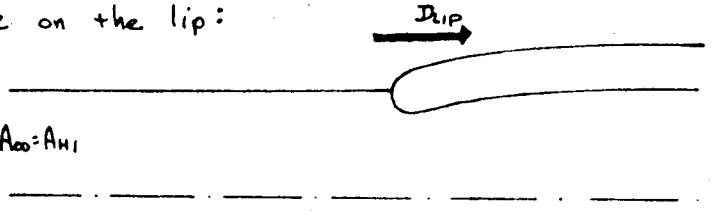

$$D_{LIP} = \int P \sin\phi \, dS$$

(b) When the capture ratio is less than unity, there is additive drag, and a reduction in the force on the lip:

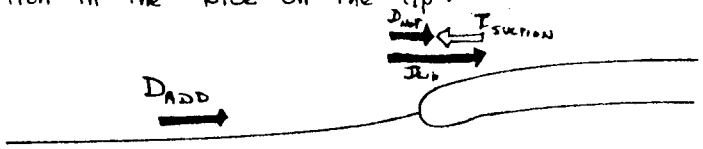

$$D_{Net} = D_{LIP} - T_{SUCTION}$$
$$A_{cowl}/A_{HI} \qquad A_{cowl}/A_{HI} = 0$$

(c) The myth:

$$T_{SUCTION} = D_{ADD}$$

(d) Consider the nacelle with no thickness:

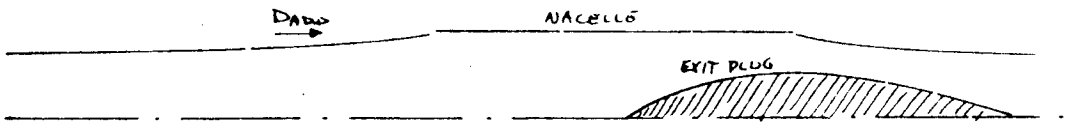

IN THIS case there is no $T_{SUCTION}$, SO

$$T_{Suction} \neq D_{ADD}$$

(e) Figure 10.16 shows that $D_{ADD} = T_{ADD}$, and equilibrium is maintained across the fluid boundary; ie, D_{ADD} is "cancelled" by T_{ADD}

(f) The conclusion:

WHEREAS $T_{SUCTION}$ & D_{ADD} DO ARISE BECAUSE OF THE SAME FLOW MECHANISM, NAMELY, SPILLAGE, THEY ARE NOT NUMERICALLY EQUAL.

FIGURE 10.22 THE LIP SUCTION - ADDITIVE DRAG MYTH

GILLETTE 3.17.78

123

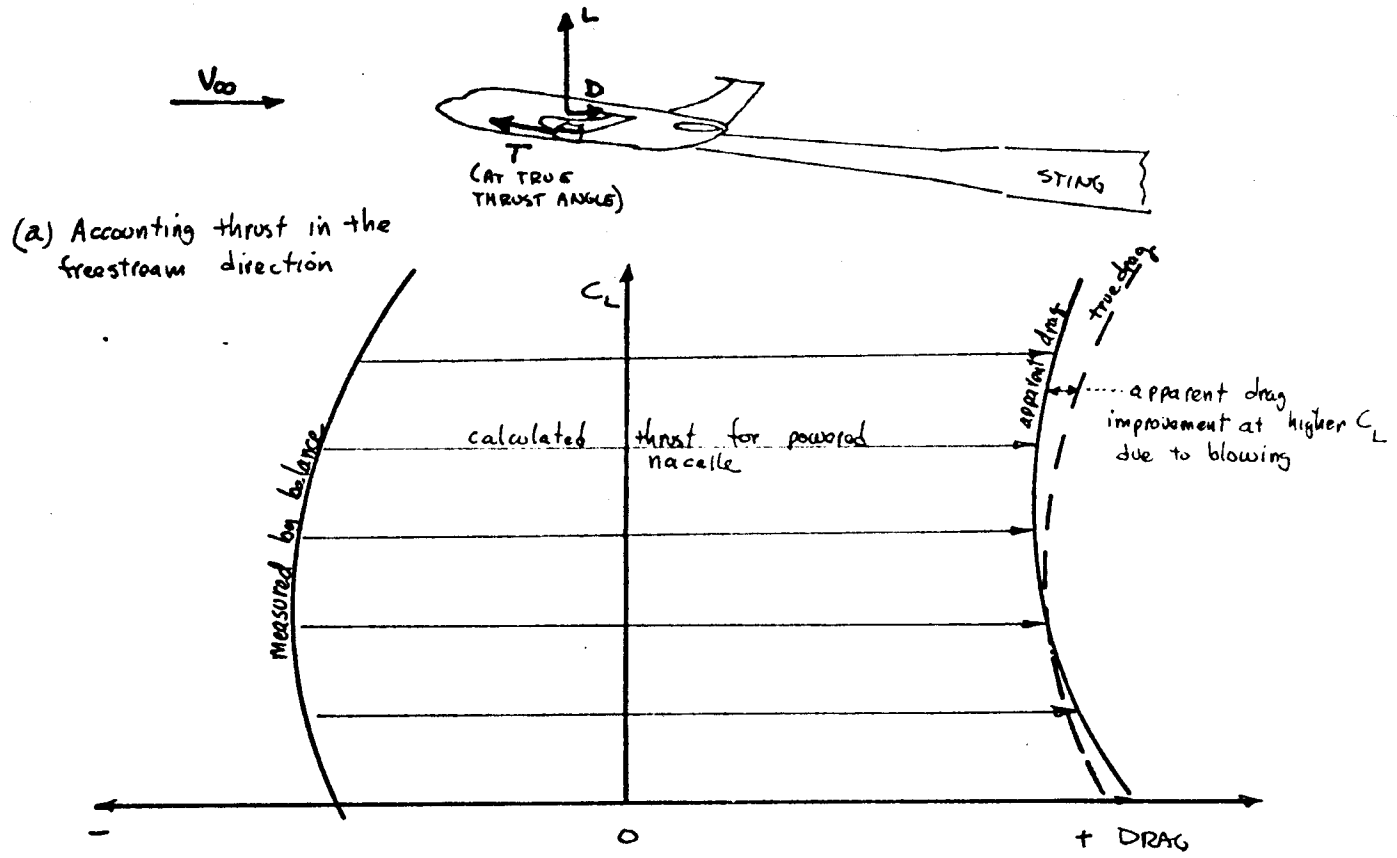

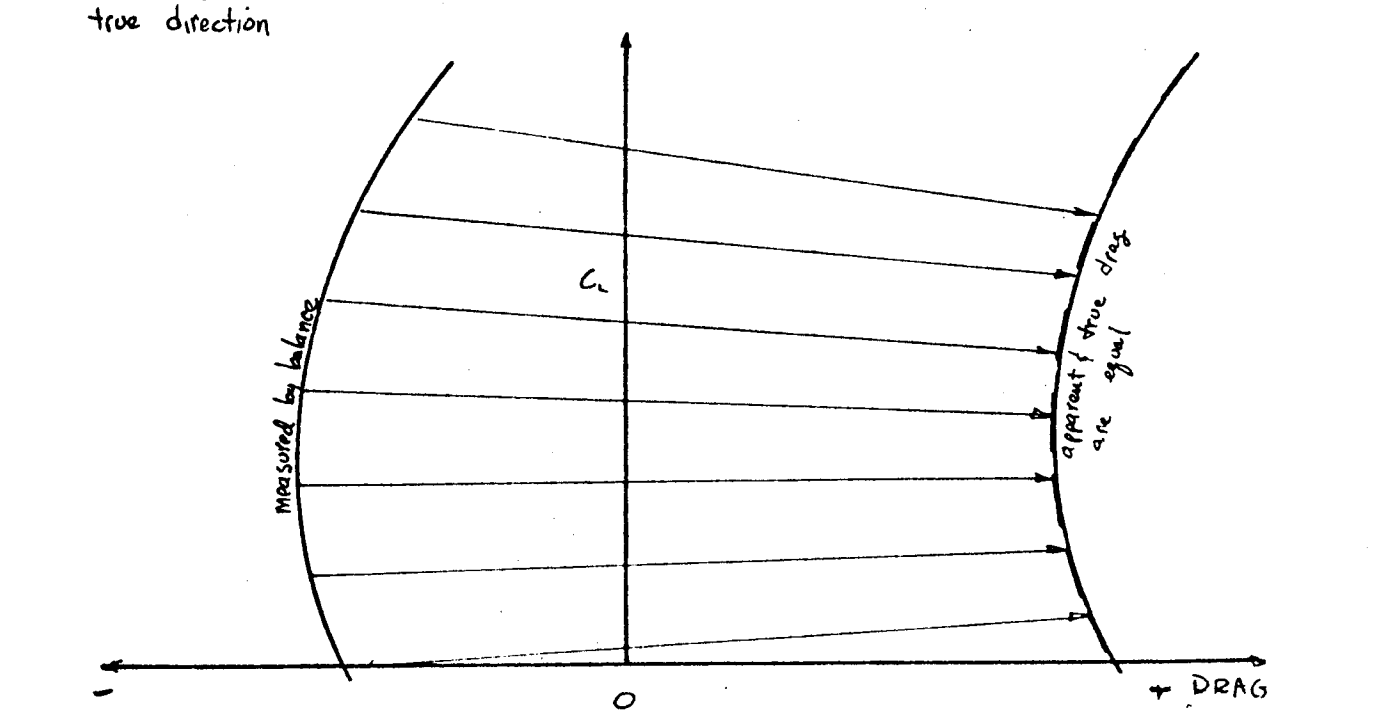

FIGURE 10.23 EFFECT OF THRUST ANGLE ON THRUST-DRAG BOOKKEEPING

GILLETTE 3.17.78

1. FLOW NACELLE

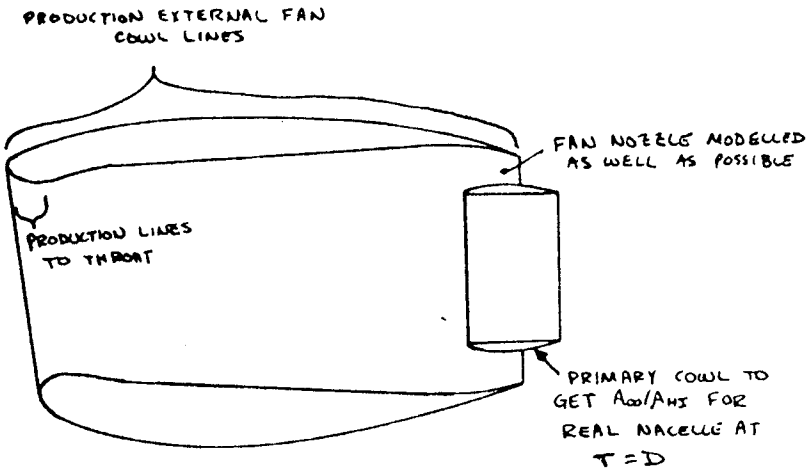

2. BLOWN NACELLE WITH FLOW NACELLE NOZZLE

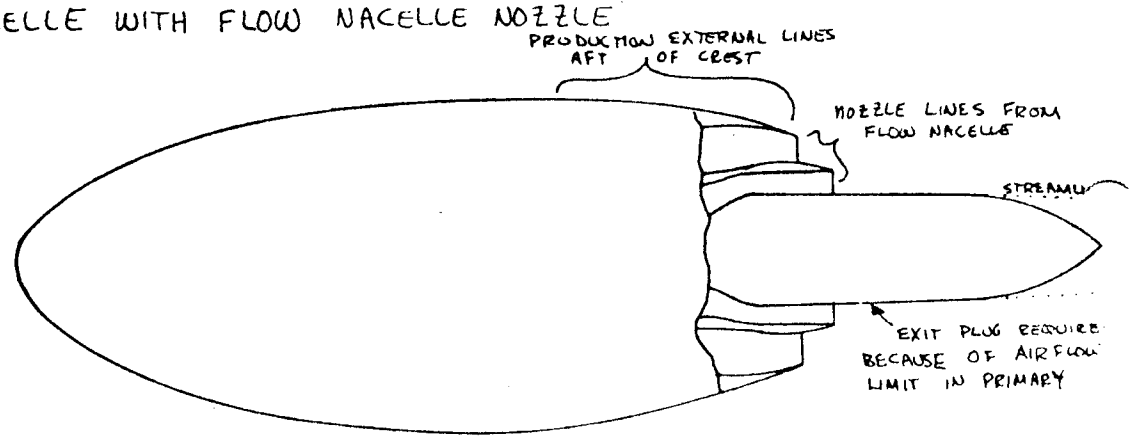

3. BLOWN NACELLE WITH PRODUCTION NACELLE NOZZLE

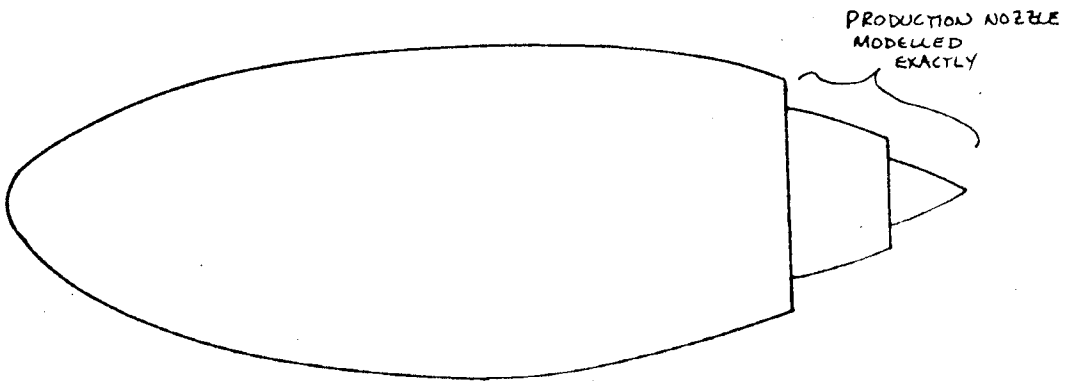

FIGURE 10.24 NACELLE MODELS REQUIRED FOR FLOW-BLOWN TESTING

GILLETTE 3.17.78

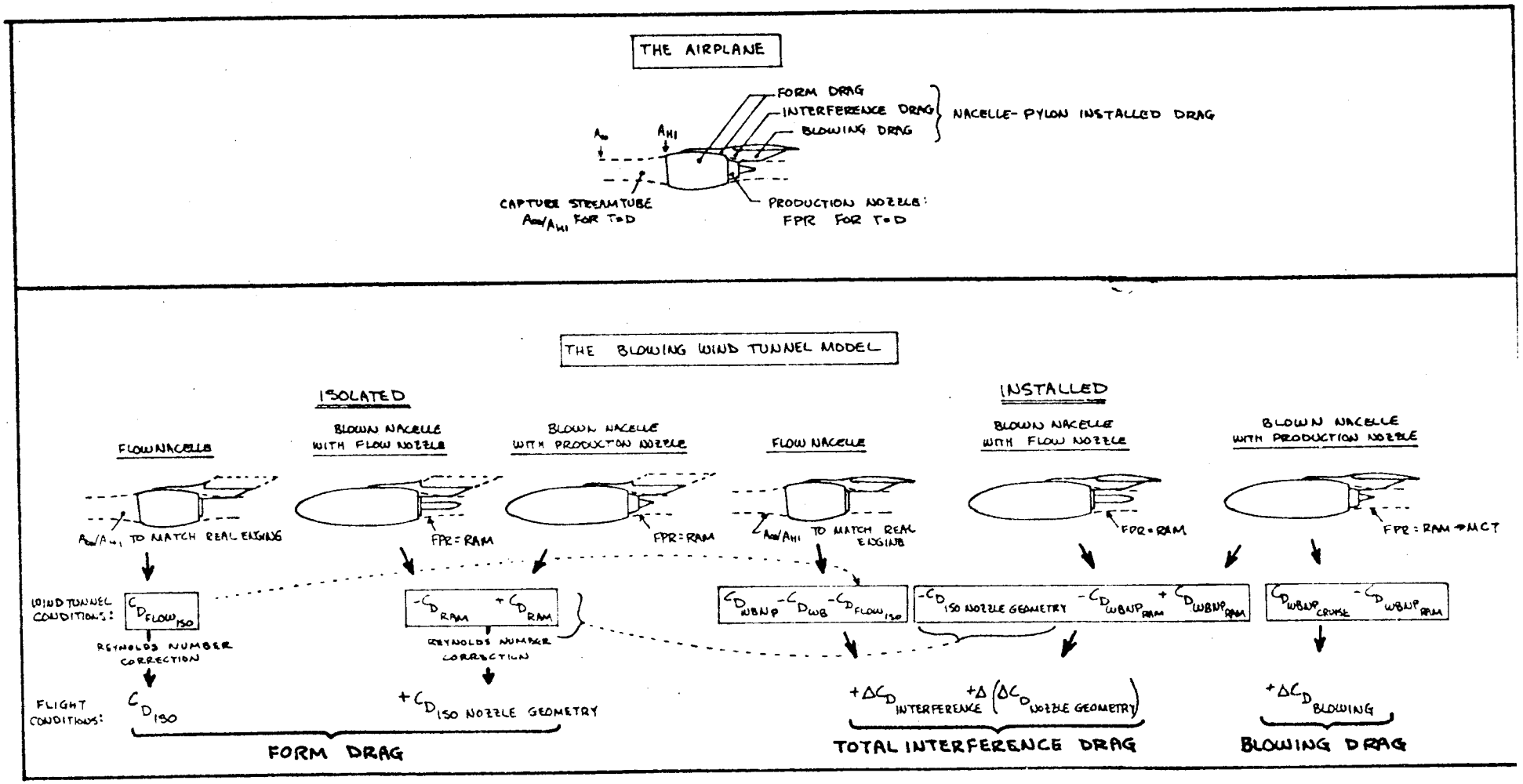

FIGURE 10.25 THRUST-DRAG BOOKKEEPING USING FLOW-BLOWN PROCEDURE

GILLETTE 1.17.98

1. FLOW NACELLE WITH PRODUCTION FAN COWL

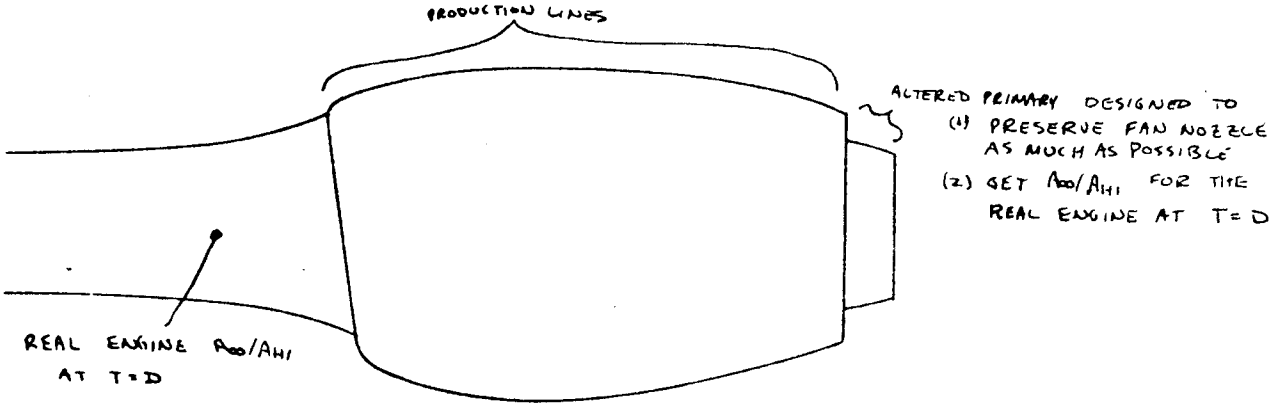

2. FLOW NACELLE WITH TPS FAN COWL

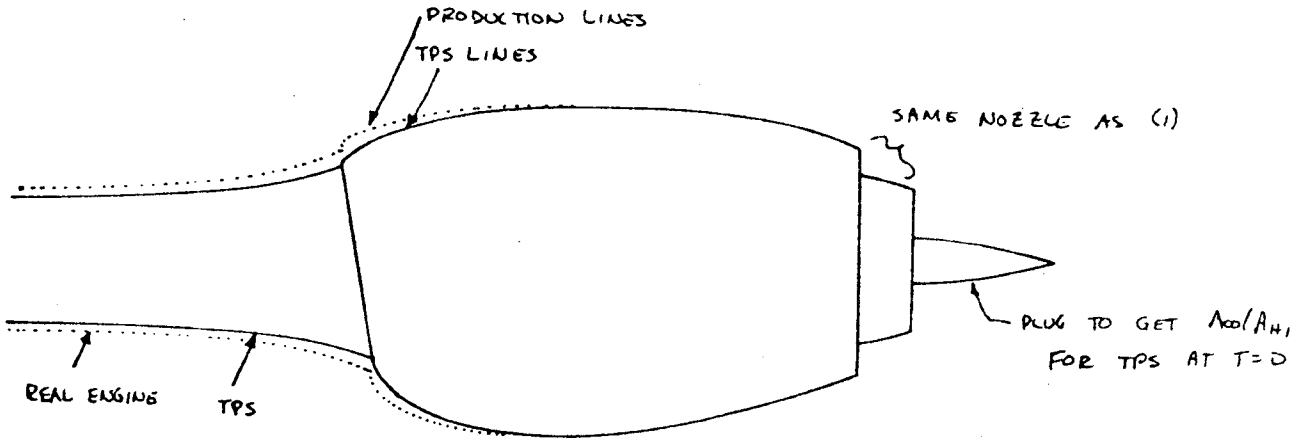

3. TPS NACELLE

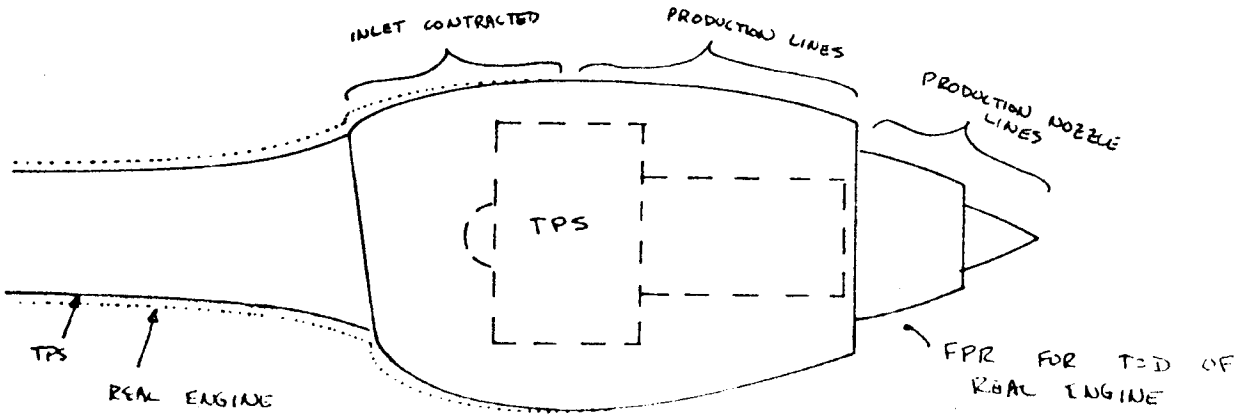

FIGURE 10.26 NACELLE MODELS REQUIRED FOR FLOW-TPS TESTING

GILLETTE 3.17.78

P.10.48

227

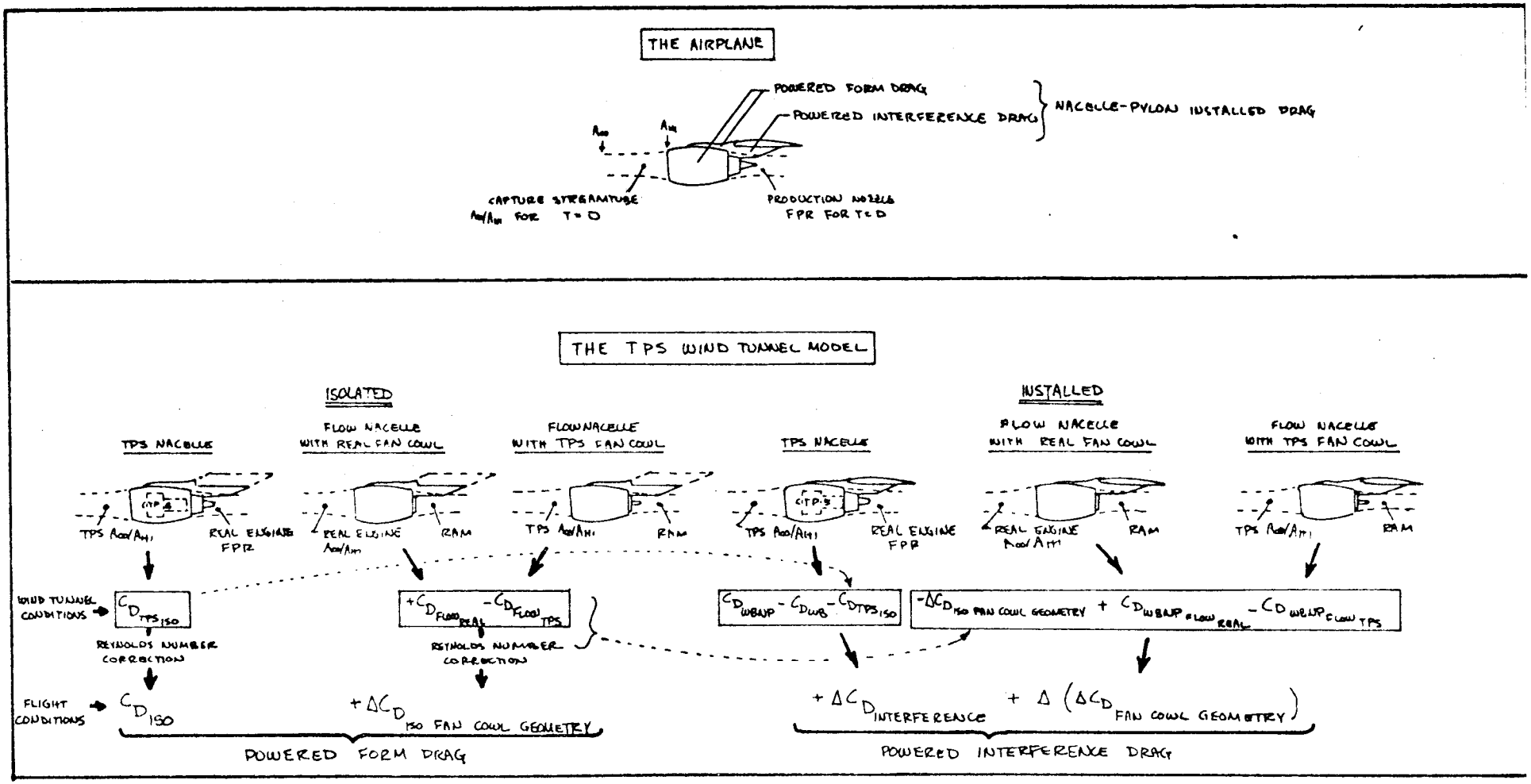

FIGURE 10.27 THRUST-DRAG BOOKKEEPING USING FLOW-TPS PROCEDURE

GILLETTE 5.18.78

(a) ACF ~ AIRFLOW CALIBRATION FACILITY

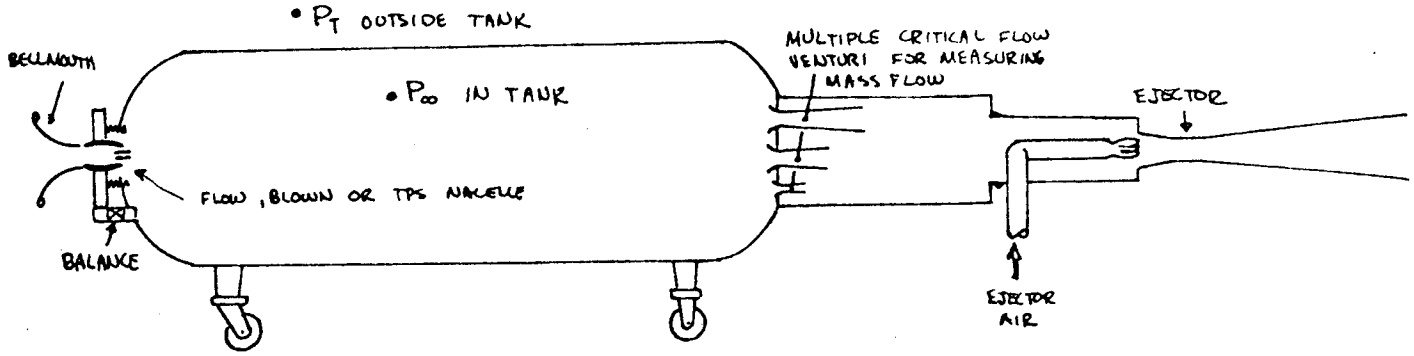

- EJECTOR CREATES VACUUM IN TANK, SO THAT P_T/P_∞ EQUIVALENT TO WIND-ON CONDITIONS CAN BE ACHIEVED ~ NOZZLE FLOW IS INTO PRESSURE FIELD SIMILAR TO WIND-ON TESTING
- BALANCE MEASURES ACTUAL THRUST PRODUCED BY FLOW OR TPS NACELLE
- ACTUAL MASS FLOW IS MEASURED BY VENTURIS

(b) THRUST STAND

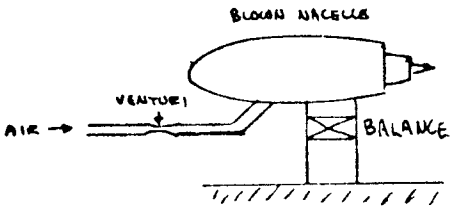

- BALANCE MEASURES ACTUAL THRUST
- VENTURI MEASURES ACTUAL MASS FLOW
- CRUISE PRESSURE RATIO $P_{T_{jet}}/P_\infty$ IS ACHIEVED BY RAISING PRESSURE OF THE SUPPLY AIR

FIGURE 10.28 CALIBRATION FACILITIES

GILLETTE 3.18.78

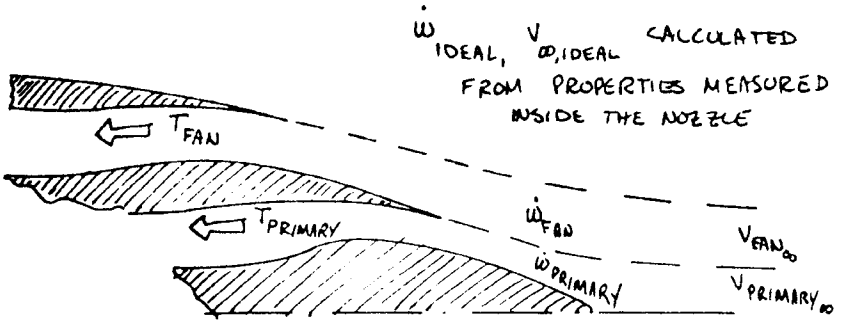

$$\text{FAN IDEAL THRUST} = \frac{\dot{w}_{IDEAL,FAN}\, V_{\infty,IDEAL,FAN}}{g} \quad (lbf)$$

$$\text{PRIMARY IDEAL THRUST} = \frac{\dot{w}_{IDEAL,PRIMARY}\, V_{\infty,IDEAL,FAN}}{g}$$

BUT THERE ARE TWO MECHANISMS THAT REDUCE THRUST

(1) FLOW SUPPRESSION - NOZZLE SHAPE AND VISCOUS EFFECTS REDUCE THE FLOW WHICH CAN COME THRU THE NOZZLE.
"DISCHARGE" OR "FLOW" COEFFICIENT:

$$C_D \equiv \frac{\dot{w}_{ACTUAL}}{\dot{w}_{IDEAL}}$$

(2) LOSSES DUE TO SCRUBBING — THE THRUST IS FURTHER REDUCED BY SKIN FRICTION & PRESSURE DRAG IN THE NOZZLE FLOW.
"VELOCITY" COEFFICIENT

$$C_V \equiv \frac{V_{\infty,ACTUAL}}{V_{\infty,IDEAL}} = \frac{T_{ACTUAL}}{\frac{\dot{w}_{ACTUAL}}{g} V_{\infty,IDEAL}}$$

THUS,

$$\text{THRUST} = \left(\frac{C_D C_V\, \dot{w}_{IDEAL}\, V_{\infty,IDEAL}}{g}\right)_{FAN} + \left(\frac{C_D C_V\, \dot{w}_{IDEAL}\, V_{\infty,IDEAL}}{g}\right)_{PRIMARY}$$

FIGURE 10.29 NOZZLE FLOW TERMINOLOGY

GILLETTE
3-18-78

(a) FLOW NACELLE IS INSTALLED IN ACF WITH BELLMOUTH. P_∞ INSIDE TANK IS VARIED, MASS FLOW, THRUST, P_{S_N} & P_{T_N} ARE MEASURED

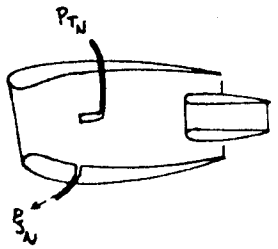

(b) DISCHARGE COEFFICIENT IS DETERMINED

$$C_D = \frac{\dot{w}_{ACTUAL}}{\dot{w}_{IDEAL}}$$

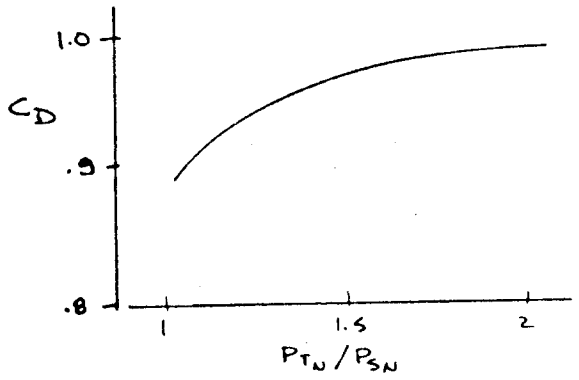

(c) VELOCITY COEFFICIENT IS DETERMINED

$$C_V = \frac{F_{BALANCE}}{\frac{\dot{w}_{ACTUAL}}{g} V_{\infty,IDEAL}}$$

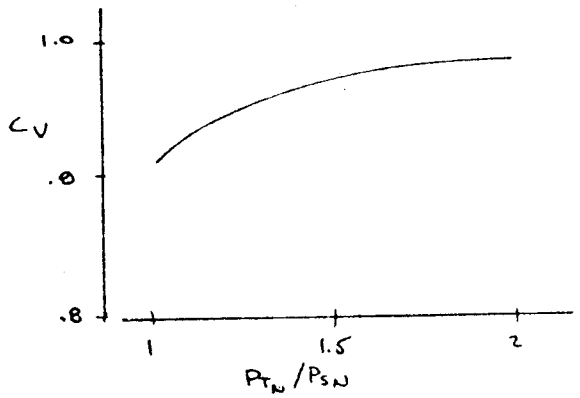

(d) THE NACELLE IS INSTALLED ON THE MODEL IN THE WIND TUNNEL. AT A GIVEN M_∞ & C_{L_1} THE P_{S_N} & P_{T_N} ARE MEASURED, ALLOWING C_D & C_V TO BE READ FROM THE CALIBRATION CURVES. THEN,

(1) $$D_{INTERNAL} = \frac{\dot{w}_{IDEAL}}{g} C_D (1 - C_V) V_{\infty,IDEAL}$$

(2) A_∞/A_{HI} DETERMINED FROM $\dot{w}_2 = \dot{w}_{IDEAL} \cdot C_D$.

FIGURE 10.30 FLOW NACELLE CALIBRATION FOR CAPTURE RATIO & INTERNAL DRAG

GILLETTE 3.18.78

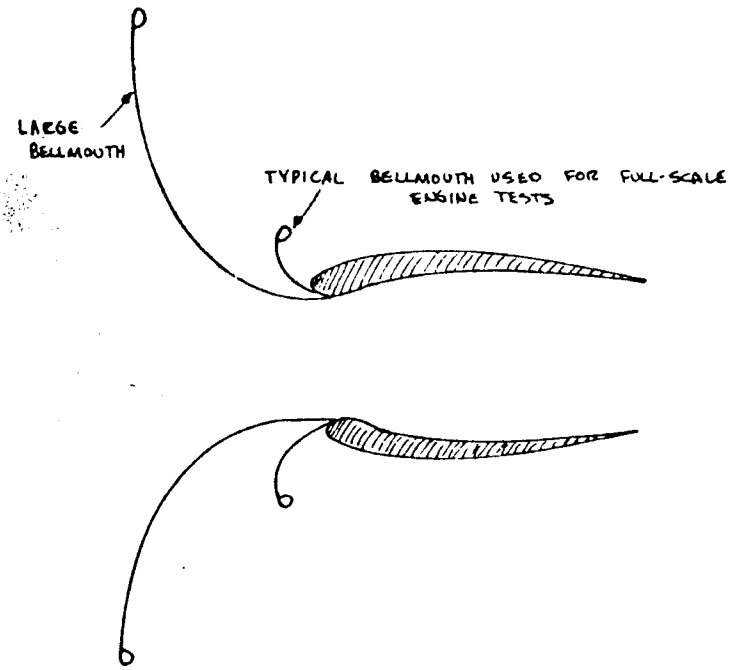

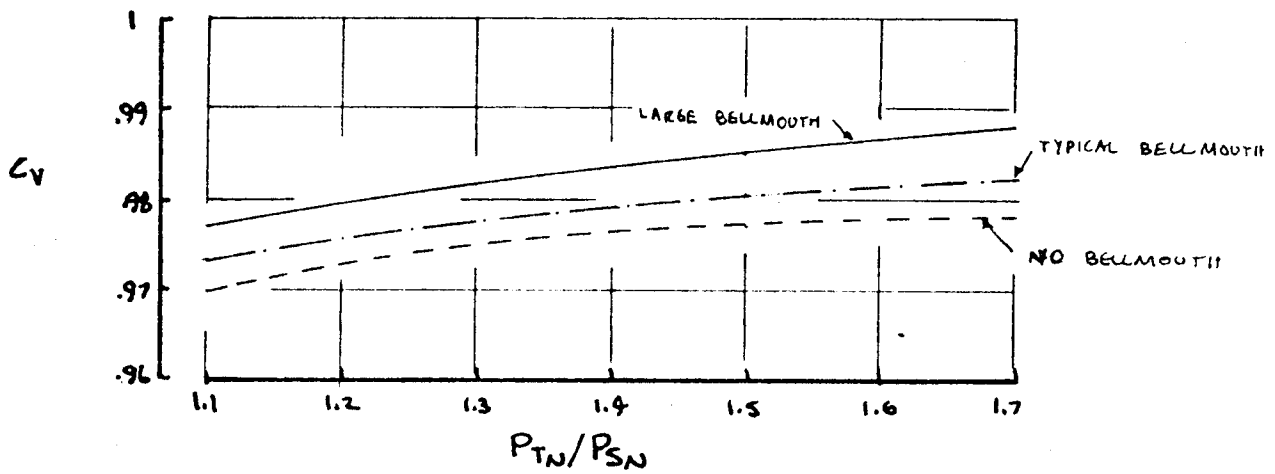

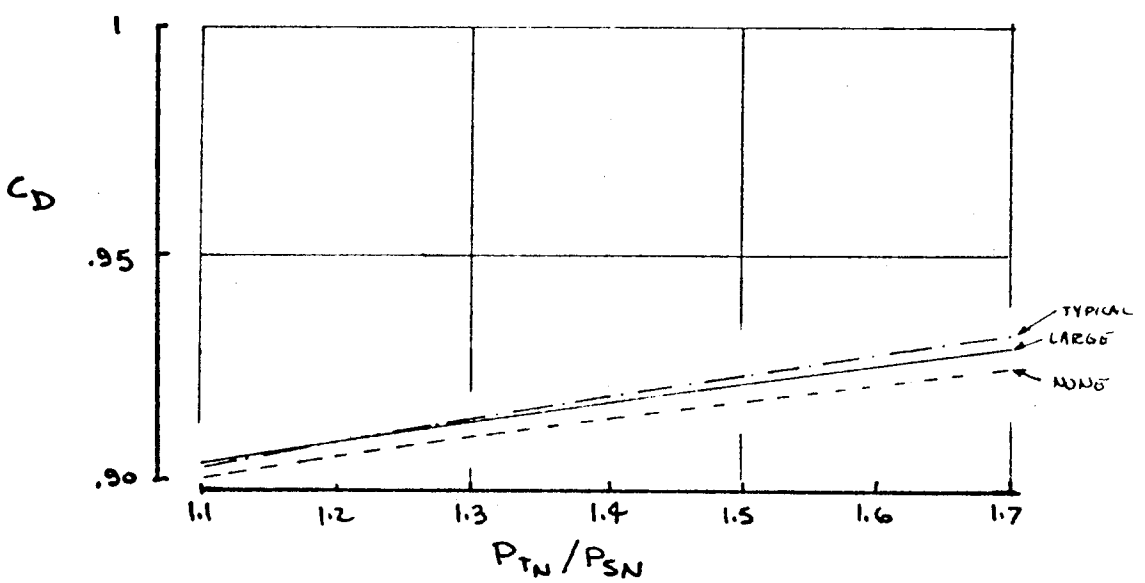

FIGURE 10.31 BELLMOUTH EFFECT

GILLETTE 3.18.78

(a) CALIBRATION CURVES ARE DEVELOPED FOR FAN & PRIMARY VELOCITY COEFFICIENT

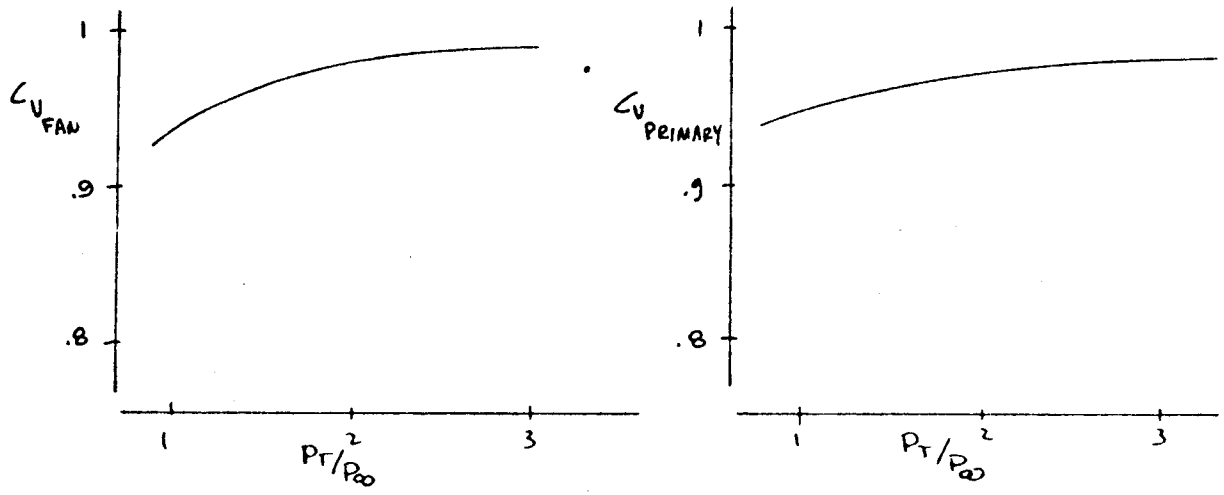

(b) IN THE WIND TUNNEL $\left(\dot{w}_{actual}, P_{T_{jet}}, T_{T_{jet}}\right)_{FAN,\,PRIMARY}$ & P_∞ ARE MEASURED. AT P_T/P_∞, THE APPROPRIATE C_V IS FOUND FROM THE CURVE. $V_{\infty,\,IDEAL,\,FAN}$ & $V_{\infty,\,IDEAL,\,PRIMARY}$ ARE CALCULATED, THEN

$$T_{CALCULATED} = \left(\frac{\dot{w}_{actual}}{g} C_V, V_{\infty,\,IDEAL}\right)_{FAN} + \left(\frac{\dot{w}_{actual}}{g} C_V V_{\infty,\,IDEAL}\right)_{PRIMARY}$$

FIGURE 10.32 BLOWN NACELLE CALIBRATION

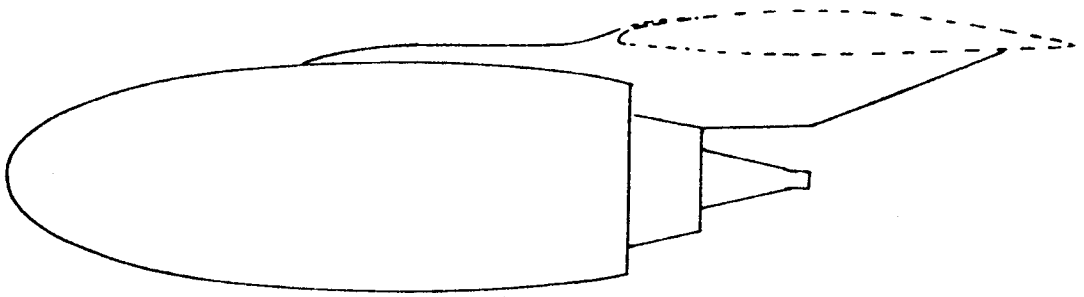

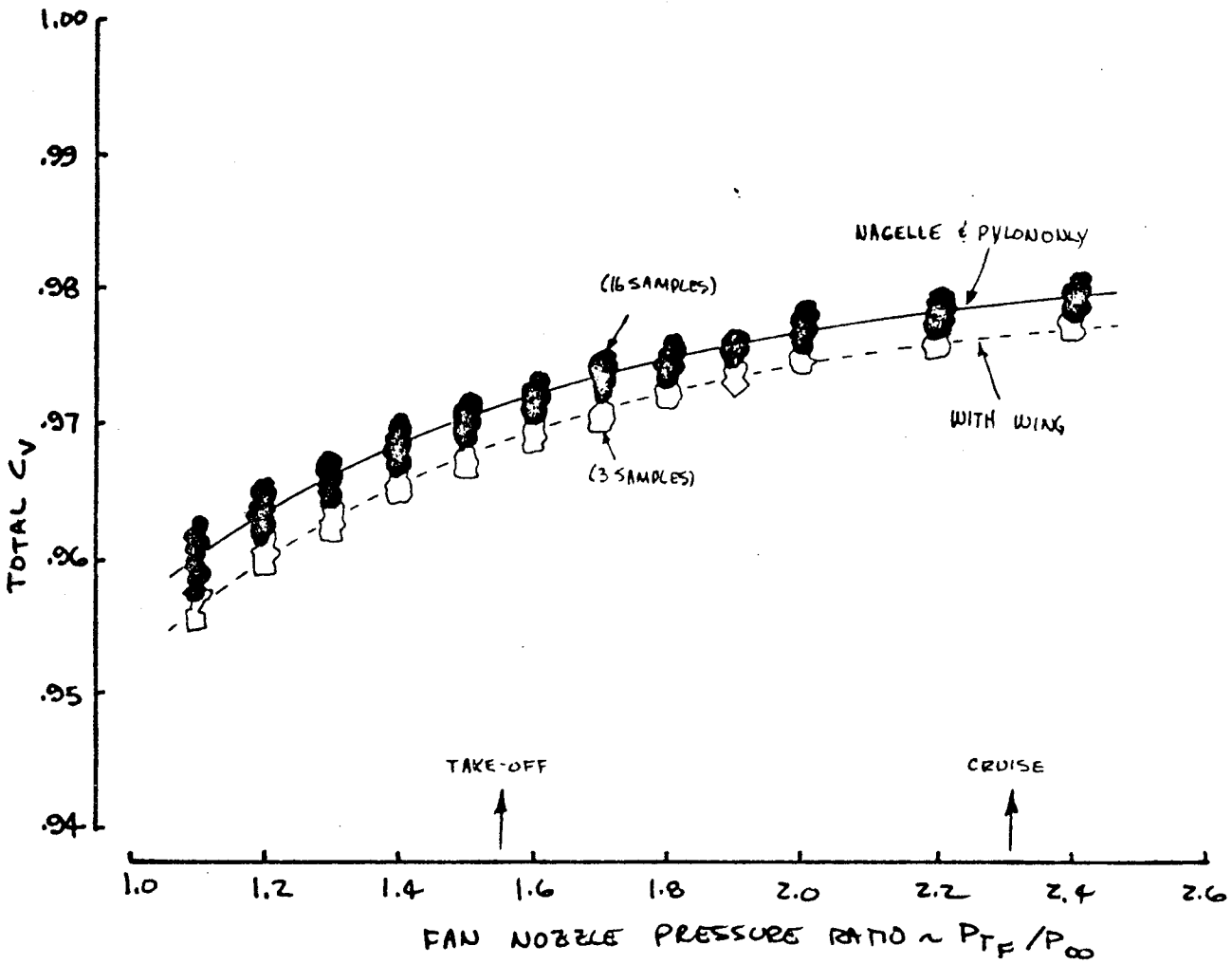

FIGURE 10.33 EFFECT OF NEARBY GEOMETRY ON C_V

GILLETTE
3.18.78

(1) C_V FOR THE PRIMARY NOZZLE MUST BE MEASURED SEPARATELY WITH A BLOWN NACELLE OR CALCULATED ANALYTICALLY

(2) THE TPS IS INSTALLED IN THE ACF AND T_{ACTUAL}, $\dot{w}_{actual,TOTAL}$, $\dot{w}_{actual,PRIMARY}$, $(P_T, T_T)_{FAN}$, $(P_T, T_T)_{PRIMARY}$, P_T & P_∞ ARE MEASURED

(3) $\dot{w}_{IDEAL,FAN}$, $V_{\infty,IDEAL,FAN}$, $V_{\infty,IDEAL,PRIMARY}$ ARE CALCULATED FROM THE MEASUREMENTS OF (2)

(4) $$\dot{w}_{FAN,ACTUAL} = \dot{w}_{ACTUAL,TOTAL} - \dot{w}_{ACTUAL,PRIMARY}$$

$$C_{D_{FAN}} = \frac{\dot{w}_{ACTUAL,FAN}}{\dot{w}_{IDEAL,FAN}} \qquad C_{V_{FAN}} = \frac{T_{ACTUAL} - \frac{\dot{w}_{ACTUAL,PRIMARY}}{g} C_{V_{PRIMARY}} V_{\infty,IDEAL,PRI}}{\frac{\dot{w}_{IDEAL,FAN}}{g} C_{D_{FAN}}}$$

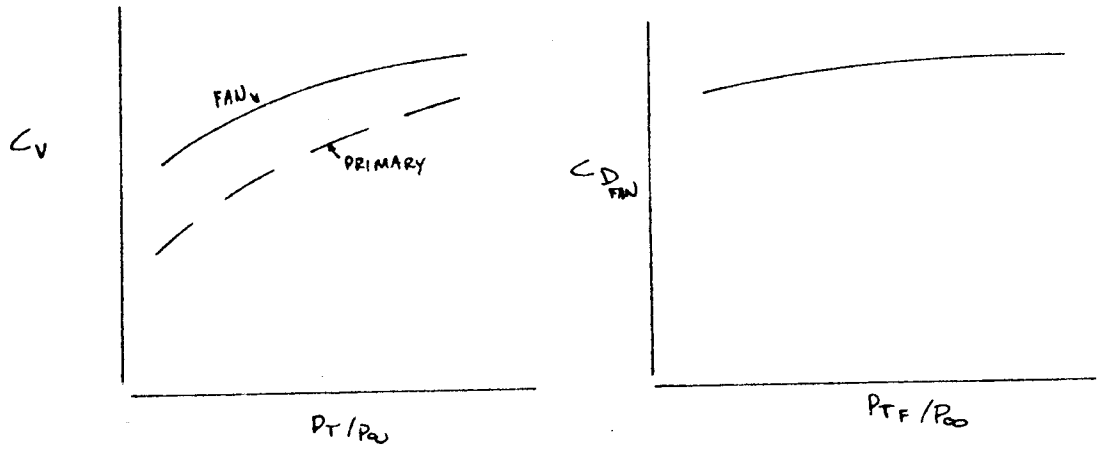

(5) IN THE WIND TUNNEL, $(P_T, T_T)_{FAN}$, $(P_T, T_T)_{PRIMARY}$, $\dot{w}_{ACTUAL,PRI}$, P_∞ ARE MEASURED. THEN $V_{\infty,IDEAL,FAN}$ & $V_{\infty,IDEAL,PRI}$ ARE CALCULATED, $C_{V_{FAN}}$, $C_{V_{PRI}}$ & $C_{D_{FAN}}$ ARE READ FROM THE CURVES.

$$T_{CALCULATED} = \left(\frac{\dot{w}_{IDEAL}}{g} C_V C_D V_{\infty,IDEAL}\right)_{FAN} + \left(\frac{\dot{w}_{actual}}{g} C_V V_{\infty,IDEAL}\right)_{PRIMARY}$$

FIGURE 10.34 TPS NACELLE CALIBRATION

GILLETTE 3.18.78

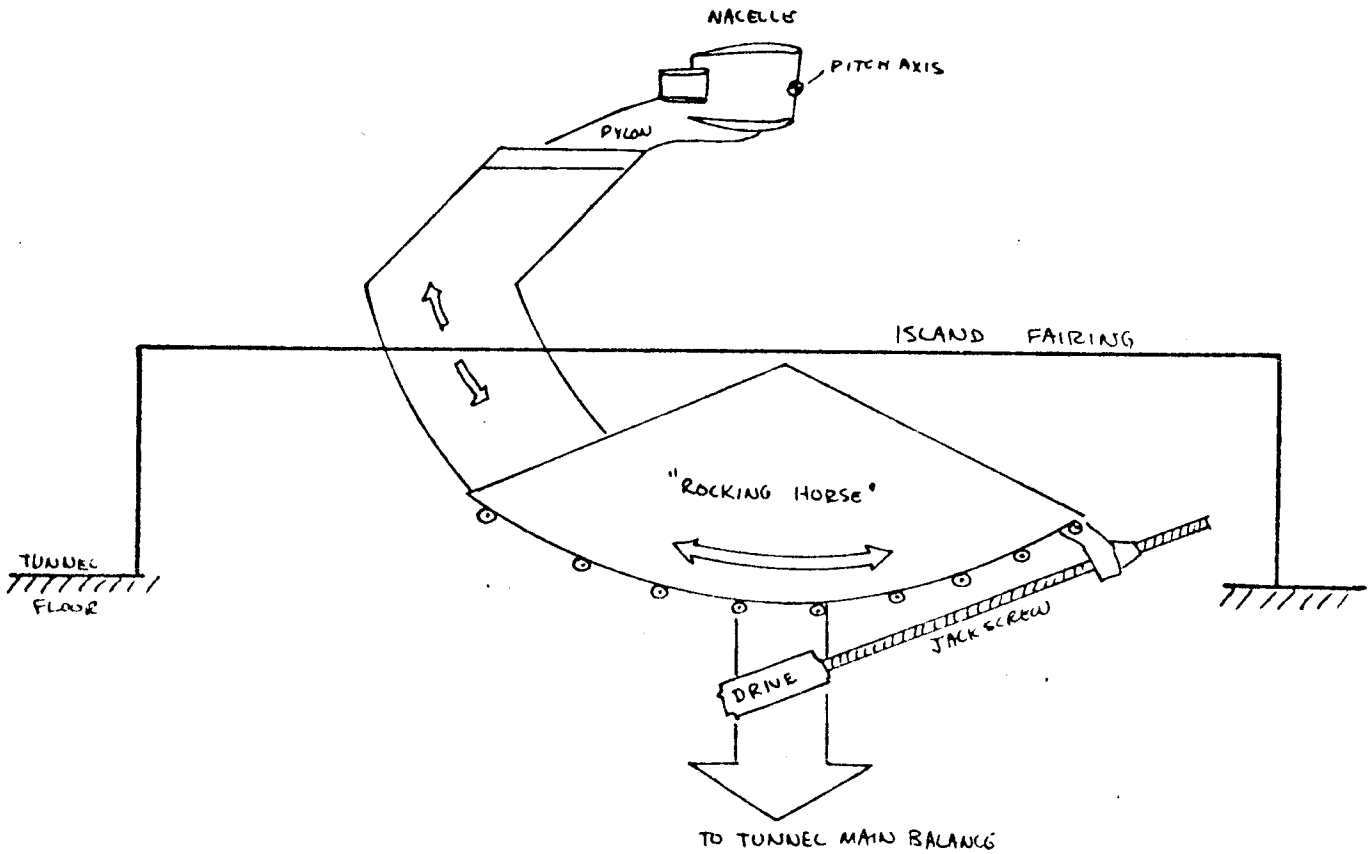

- ALLOWS PITCH TESTING
- UTILIZES TUNNEL MAIN BALANCE
- CAN BE USED FOR FLOW, BLOWN & TPS TESTS

FIGURE 10.35 ISOLATED NACELLE MOUNT SYSTEM

736

GILLETTE 3.4.78

CHAPTER 11. CONFIGURATION DETAILS

737

CHAPTER 11. CONFIGURATION DETAILS

Previous chapters have dealt in detail with the design of airfoil and fan cowl sections, high lift devices, wings, empennages and the nacelle installation. These occupy the majority of the configuration aerodynamicist's time. But there is a small set of configuration details which are important to the overall design and may cause five percent or so of unwanted drag if not designed properly.

11.1 PILOT CAB

The pilot's cab has design requirements other than aerodynamics, such as volume, pilot vision and instrument panel layout, which typically alter the design of the forward fuselage from the aerodynamic ideal. That ideal would have an approximately elliptical shape, as shown on part (a) of Figure 11.1. Assuming that interior volume and pilot vision requirements could be met, then the shape in (a) would be preferred. However, that elliptical shape would require the windshield to be curved in three dimensions, a requirement that is expensive to meet from a manufacturing point of view.

A simpler windshield would be to have panes curved in conical sections; either cylindrical or conical. This is shown in Figure 11.1(b). But the simpler design is not as acceptable to Aerodynamics; a separation will probably occur in the lower windshield corner, and a pair of vortices will be shed, representing an increase in drag and in cabin noise. The drag and noise situation is aggravated by the use of flat panes for the windshield, as indicated on Figure 11.1 (C), where four vortices, caused by sharp corners, are shed by the pilots cab.

Figure 11.2(a) shows boundary layer surveys made in the wind tunnel behind the 737 cab (which is identical to all 7/7/7 cabs) and behind a faired cab having smooth contours. The additional drag represented by the increase in boundary layer momentum thickness due to the 737 cab is clearly demonstrated, as well as the two vortices shed on each side of the front panes. Part (b) details surface isobars measured on the 737 cab; the most notable features are (1) the high positive Cp's at the lower edge of the windshield, and (2) the supersonic flow region on top of the fuselage.

These problem areas can be predicted by analysis and thus design alternates can be examined. The lower half of Figure 11.2 shows an A230 potential flow analysis of a flat pane cabin. The analysis is showing high C_p's in the lower windshield corner ($C_p > +.7$). The boundary layer flowing from the stagnation point on the nose, then along the crown of the nose towards the windshield, will see a sharp adverse gradient and probably separate. A boundary layer analysis along the A230 streamline from the nose towards this area will probably indicate separation. Note also the sharp pressure gradient at the outside corner of the front pane, as indicated by the close spacing of the isobar lines. Separation is likely there as well. Lastly, there is a large region of supersonic flow indicated in top of the cab.

Results of a redesign utilizing a cylindrically curved forward pane, (Figure 11.2, lower right) show an improved surface isobar pattern: (1) the pressure gradient into the lower corner of the windshield has been lessened, (2) the gradient across the edge of the front pane is less severe, and (3) there is much less supersonic flow. It is likely that the curved pane cab will be perhaps 1% better in cruise drag than the flat plane design.

The culprit in causing increased drag and cab noise levels is the vortex (or vortices) that develop as a result of separations. Figure 11.3 shows aerodynamics devices which might alleviate the separations with the 7/7/7 style cabs; inflight testing to date has shown reductions in cabin noise levels, but not in drag. The best way to prevent problems obviously is with the initial design.

11.2 WING-BODY STRAKE

The session on wing-body test techniques (Chapter 5) discussed the classical separation caused by the circular cylinder protruding from a flat plate and related it to the separation typically existing in the wing-body juncture. Figure 11.4 shows schematically how the separation can be predicted. First, a potential flow solution (program A230) is done for the wing-body configuration. Then, a boundary layer solution is done for the flow along the dividing streamline. Typically, the boundary layer will not be able to traverse the adverse (decelerating) gradient and will separate before reaching point B in the corner.

Figure 11.5 reveals the aerodynamic cure; a small strake. The philosophy of the strake is not to "divide" the flow, but to turn the flow in the dividing streamline and get it headed out the wing leading edge without causing separation. In fact, a properly designed strake can turn the flow from the body out onto the wing leading edge without causing the Cp's to be any more positive than those along the wing leading edge. Lastly, the design of the strake can be reviewed analytically, in 3-D potential flow, since an effective design will not have viscous separations. The performance gain achievable with a wing root strake is on the order of 1% to 2%. Figure 11.6 shows the flow on a 747 wind tunnel model without a strake, while Figure 11.7 shows the separation-free flow resulting from a properly-designed strake.

11.3 WINGLETS

Figure 11.8(a) recreates the shed vortex situation for a wing of limited span which causes induced drag. Recall from Chapter 4 that the downwash caused by the shed vorticity is the culprit which rotates the local section lift vector aft, thus leading to an induced drag. And the shed vorticity, related to $\partial\Gamma/\partial y$, is the greatest at the tip, where the tip vortex exists. Part (b) of Figure 11.8 shows how an end plate carries this shed vorticity concentration away from the plane of the wing. There is not a large change in span load resulting from the winglet, but wind tunnel model data show a potential for large drag reduction due to the winglet; reductions on the order of 4% or 5% in cruise drag are possible.

Of course, for the same length of winglet, the tip vortex would be moved further from the wing by laying the wing down flat, that is, as a span extension. The winglet improves induced drag by operating on the efficiency

factor, e, in the equation

$$D_{INDUCED} = \frac{1}{q\pi}\left(\frac{L^2}{b^2}\right)\frac{1}{e}$$

On the other hand, a span extension reduces induced drag through the square of the span. For a new design, the first choice would be for more span rather than a winglet, in the absence of an artifical airport gate restriction on span. But for an existing airplane whose wing structure is fixed, the winglet gets a second chance. The reason is revealed on Figure 11.9, which compares the percentage change in wing bending moment at various g-loadings from cruise to 2.5g's due to either a 10% span extension or a 16% winglet. (The percentages refer to the length of the span extension or of the winglet relative to the original semispan). The upper part of Figure 11.9 shows that the span increase raises the wing bending moment at cruise on the wing, but diminishing to no increase at the root. However, as the load factor is increased to the 2.5g structural design limit, the wing bending moment and especially the root moment, where there is a production break requiring a joint, increase considerably. This is because the 10% span extension has moved the centroid of lift outboard.

The 16% winglet, chosen to yield the same increase in performance, has just the opposite effect. This is because of wing deflection: as the wing is loaded up, it bends, thus tilting the winglet normal load, and eventually pointing it below the wing root, thus reducing the wing root bending moment:

This has important implications for the selection of the winglet instead of a span extension for wings already in production, which may already be at their wing root bending moment limit.

Since the primary aerodynamic mechanism behind the winglet's effect is it's displacement of the tip vortex from the wing plane, the winglet could be placed above or below the wing and get the same movement of the tip vortex. Figure 11.10 shows that other considerations enter. If the winglet is pointed up there is a good possibility of a shock wave forming in the corner between the winglet and the wing, thus offsetting the performance gain of the winglet. Increasing the cant angle of the winglet by beginning to lay it flat will alleviate the corner flow problem, and increase the drag benefit, but the wing bending moment is also increased. The downward pointed winglet is easier to integrate because the corner problems are less due to lower velocities on the wing lower surface, but the downward-pointed winglet can be applied only to the high-body mounted wing (ie, C-141, etc.), and the increase in wing root bending moment is the greatest. When all these trades have been made the optimum cant angle is usually between 6^0 and 15^0 off vertical. Details of winglet design and optimization are contained in Reference 11.1.

In summary, the winglet aerodynamic design consists of analyzing a series of shapes in A230 to see that pressure gradients in the corner between the wing and the winglet are not so severe as to cause separation. Any such effect will rapidly negate the induced drag benefit.

11.4 EXCRESCENCE

Th previous discussions have covered the testing of the aircraft for features that are visible from a distance. That is, the geometry is smooth. But when viewed up close, there are a multitude of small items which contribute to the overall drag, but individually are too small to be effectively tested in the wind tunnel, because of model scale and test Reynolds number limits. These items fall into a general category called "excrescence". Figure 11.11 shows that there are four general categories of excrescence items:

(1) discrete items -- antennas, drain masts, probes, access doors, etc.,

(2) mismatch -- non-flush alignment at skin joints, gaps at joints,

(3) internal airflow -- drag caused by air leakage through the configuration, and

(4) roughness---fastener heads, corogard paint, etc.

Lest it be felt that excrescence is a minor item, Figure 11.12 compares the effect of excrescence drag on the cruise range of Boeing's commercial aircraft, as detailed in Reference 11.2. The range is from 5% for the 737 down to 2% for the 747. Furthermore, Figure 11.12 breaks down the 747 excrescence drag into pieces; discrete items dominate the added drag, being in all cases at least half of the total excrescence drag.

As the design of an aircraft is nearing the final stages, and specific manufacturing and project design details are becoming known, the configuration aerodynamics staff will begin to monitor the excrescence items to look for alternative designs which would have less drag. Since the drag of each item is so small, it is meaningless to express the effect in percent drag. Instead, the drag effect is converted to a weight which would have an equivalent effect on fuel usage. For example, on Figure 11.13, it is stated that one drag count (.0001) has the same effect on trip fuel on the 707 at 5,000 NMI range as 1028 lbs of weight. So, a drag item worth 1/10 of a count (.00001) doesn't sound like much, but its equivalence in weigh, 103 lbs, is important. This also allows an evaluation of the total effectiveness of the drag change; if a design change would save an equivalent weight of 30 lbs, in drag, but cost 40 lbs of actual weight to achieve, then obviously the change would not be made.

Two examples from 747 experience are quoted on Figure 11.13 from the 747 program; both were adopted since the drag equivalent weight due to the change (13 lbs OEW for the rain nozzles and 75 lbs OEW for the radome strips) was far more than the actual weight increase required by the redesign.

The aerodynamicist must also recognize that certain realities of production affect the smoothness requirements (gap size, allowable panel mismatch, fastener head, etc.) that are established by aerodynamics as guides for the designers. Figure 11.14 shows how the aircraft is divided into critical areas, where the boundary layer is thin and the drag sensitivity due to surface features is high, and noncritical areas, where the boundary layer is thick and surface roughness requirements are less stringent. Representative callouts are on Figure 11.14.

The aerodynamicist becomes actively involved in the design of the discrete excrescence items. Figure 11.15 details the logic sequence used to achieve the best shape for the discrete item. The choice is basically between items that are fin-like (antennas, drain masts, etc.), which are designed according to wing design rules. Those items which are "bump-like" are designed to different constraints. In all cases, the local Mach number is an important input to the design, and the best results will be realized when the device is aligned with the local flow.

11.5 VORTEX GENERATORS

In spite of careful design, occasionally the aerodynamicist discovers during flight test that the boundary layer is not behaving as expected, and some part of the aircraft's performance envelope is being adversely affected by separation. The aerodynamicist then reaches into his kit and produces the aspirin of the aerodynamics world -- the vortex generator.

Figure 11.16 illustrates the basic operation of the vortex generator. It is a device which extends into the potential flow outside the boundary layer, and through the generation of a vortex, exchanges low momentum boundary layer air for high momentum external air. As is does so, the vortex core drifts when viewed from ahead or behind as shown on the figure. The vortex generator is simply a flow exchanger.

Figure 11.17 shows several typical vortex generator shapes. In contrast to the wing, which wants to minimize the tip vortex, the vortex generator wants a very powerful vortex. This suggests a low aspect ratio wing at a high angle of attack. Types a, b and c have found use on aircraft. At times, the boundary layer is too thick for a practical sizing of these three types, so the vortex generator is mounted on a stand to move it completely out of the boundary layer. Type d is often used in wind tunnel diffusers; type e is now used on the 737 APU door.

There are two general uses of vortex generators on aircraft. Figure 11.18a illustrates their use to block excessive crossflow, by forming an aerodynamic "brush," whereby the vortex radical velocity opposes the undesired boundary layer crossflow. This kind of application is denoted co-rotating, because the shed vortices all have the same rotation. Figure 11.18b shows the more typical use, that of general mixing, to re-energize a boundary layer that is very near to separation. This kind of application is termed co-rotating. They currently appear on the 707 wing ahead of the high speed aileron and on the horizontal tail ahead of the elevator, on the 727 fin and inside the S-duct, and on the 737 wing and aft body. This kind of vortex generator is almost a Boeing trademark.

Sizing and placement rules are listed on Figure 11.19, as well as chordwise placement. Proper selection of the best vortex generator pattern can be done only in flight, because both the phenomenon being cured and the placement of the vortex generators are dependent on Reynolds number.

Obviously, the vortex generator increases drag, since it generates a vortex. It is possible that the total drag may be reduced, if the vortex generators reduce a separation that occurs at cruise. But if vortex generators are required for that purpose, then the configuration is in deep trouble aerodynamically The most common use of vortex generators is to increase control power at the limits of the flight envelope; the 707 and 737 wing vortex generators and those on the 707 and 727 empennages are for this reason. Those on the 737 aft body are there to reduce a "vertical bounce" felt on some aircraft. But in mose cases, the vortex generator is viewed as an excrescence item by the configuration aerodynamicist.

Figure 11.20 shows several other flow control devices which generate vortices. The DC-9 vortilon (vortex pylon) is an ingenious aerodynamic device which sheds a vortex at high angles of attack only. The purpose of the vortex is to change the downwash at the horizontal tail and thereby prevent lock-in, or "deep" stall. It relies on the change in flow at high angle of attack to (1) cause it to be in a high crossflow field, and (2) shed its vortex over the wing upper surface.

The 727 wing fence, shown on Figure 11.20b, is another approach to the same kind of situation. At cruise, it is aligned with the local flow; note sometime how it is curved. At high angle of attack, however, it sheds a vortex which blocks the crossflow on the aft portion of the wing and alters the flow at the horizontal tail.

Not shown are the large vortex generators seen on the DC-10. These are not for the purpose of changing the nacelle flow pattern, but are to position a strong vortex close to the wing surface where there are no leading edge devices because of the pylon. Appropriately enough, these are called "engine ears". Say it rapidly and you have a good description of the configuration aerodynamicist; an engineer who tries to successfully mix potential flow and boundary layer phenomena, just like a vortex generator.

CHAPTER 11

11.1 D6-41799, "Design and Analysis of Winglets for Military Aircraft," K.K. Ishimitsu, etal, Feb. 1976.

11.2 D6-13784, "747 Excrescence Drag", B. G. Williams, December, 1968.

(a) COMPLETELY SMOOTH
- GLASS CURVED IN 3-D

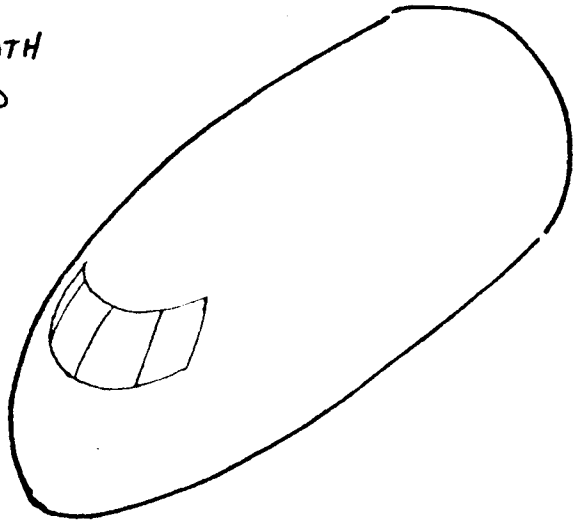

(b) CURVED IN 2 DIMENSIONS
~ CYLINDRICAL OR CONICAL

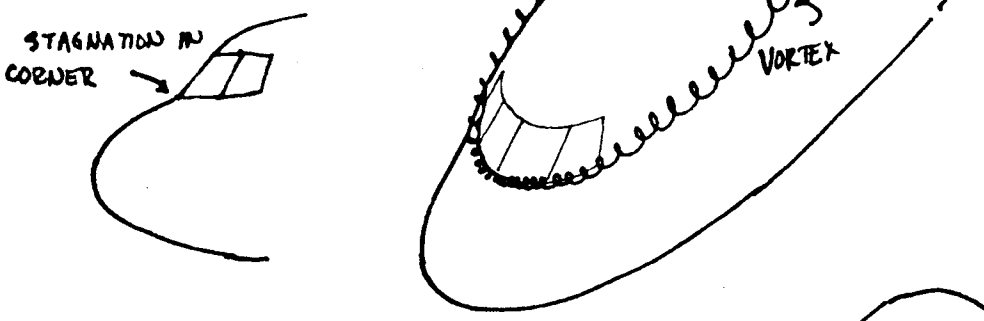

(c) ALL FLAT PANES

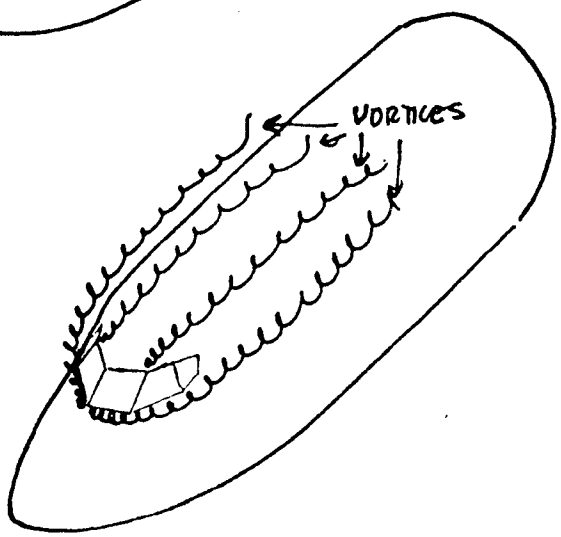

FIGURE 11.1 WINDSHIELD VORTEX FORMATION

GILLETTE
5.23.78

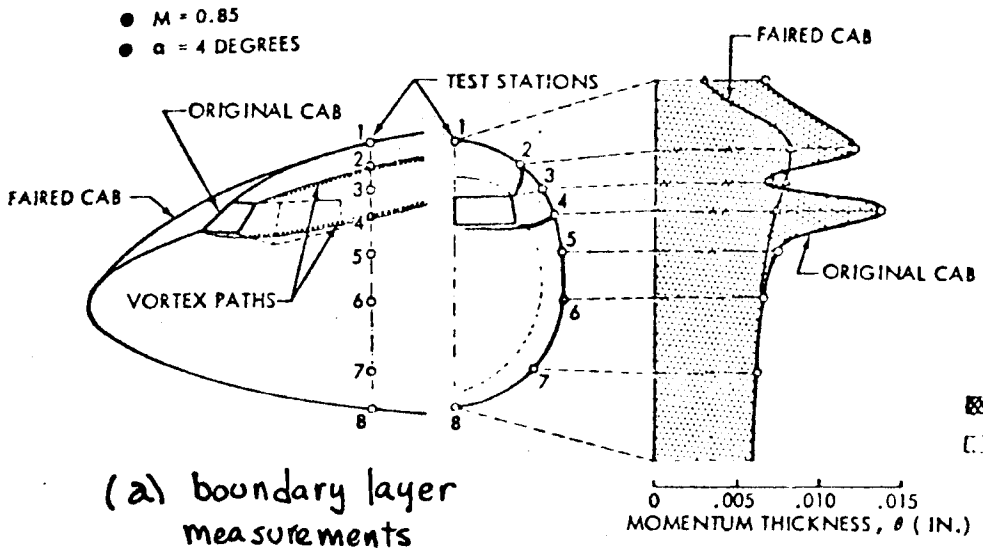

(a) boundary layer measurements

737 CAB

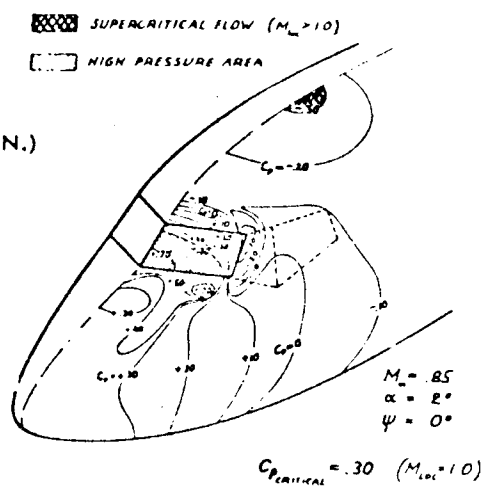

(b) ISOBARS ON THE FOREBODY

NEW CAB

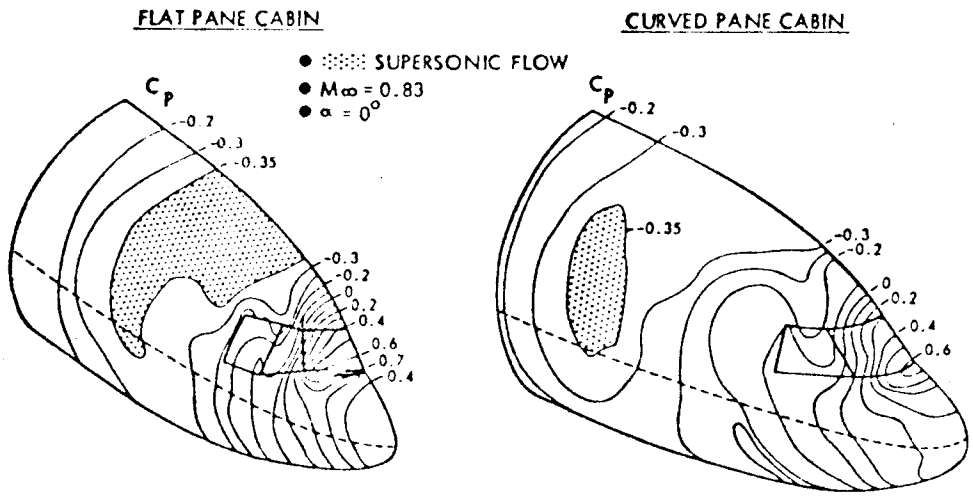

POTENTIAL FLOW EVALUATION OF NEW CAB DESIGNS

FIGURE 11.2 CABIN PRESSURE ANALYSIS

GILLETTE 3.25.78

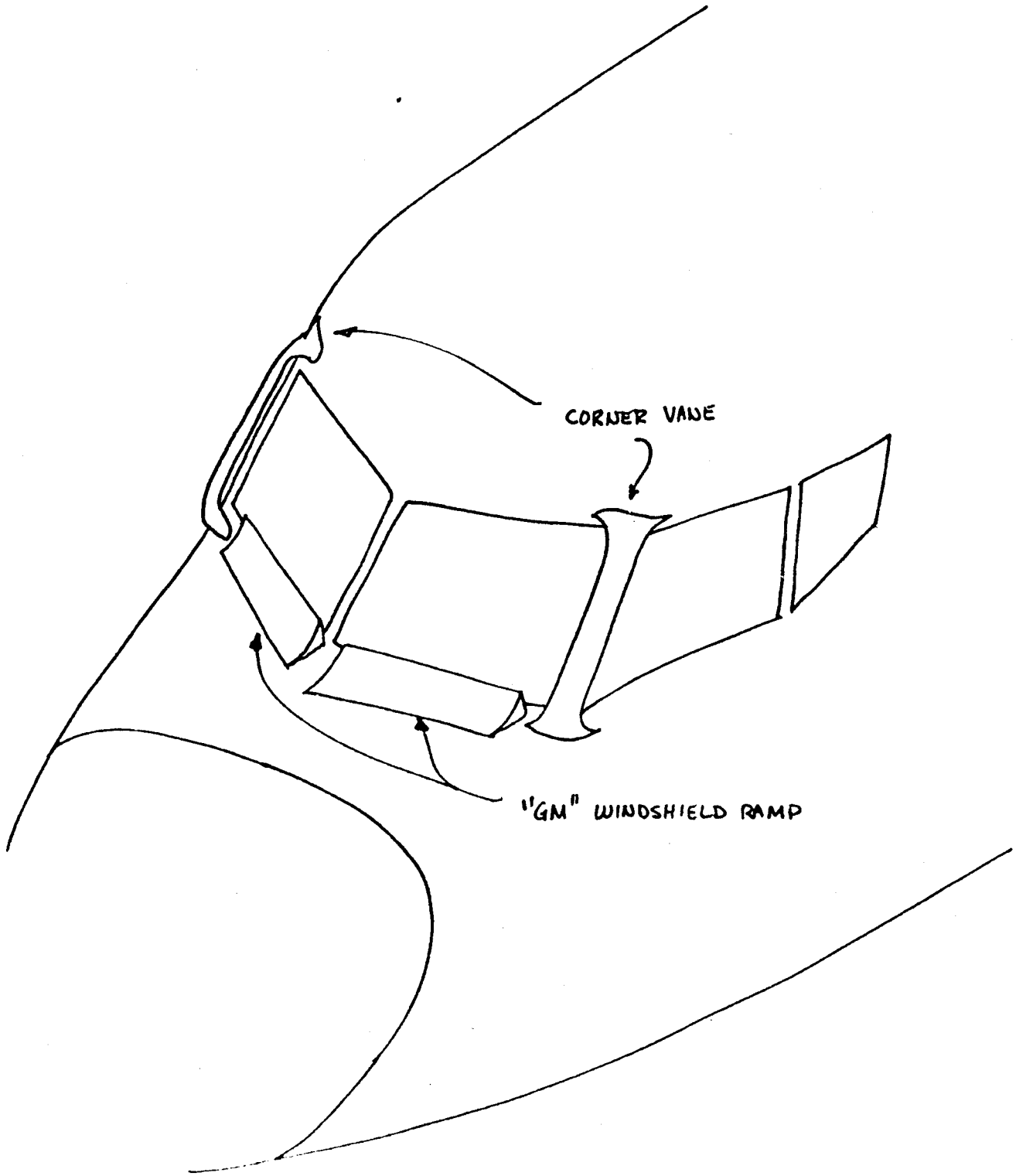

FIGURE 11.3 TYPICAL VORTEX PREVENTERS FOR SHARP-EDGED WINDSHIELDS

GILLETTE 3-23-78

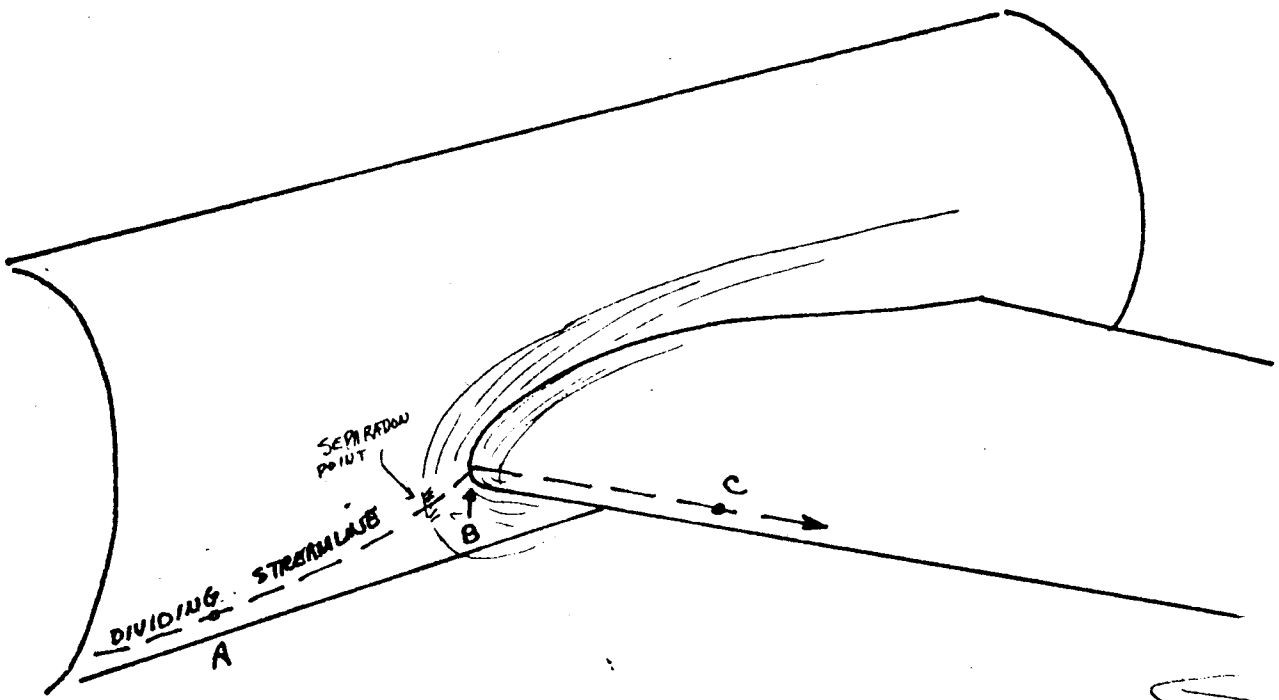

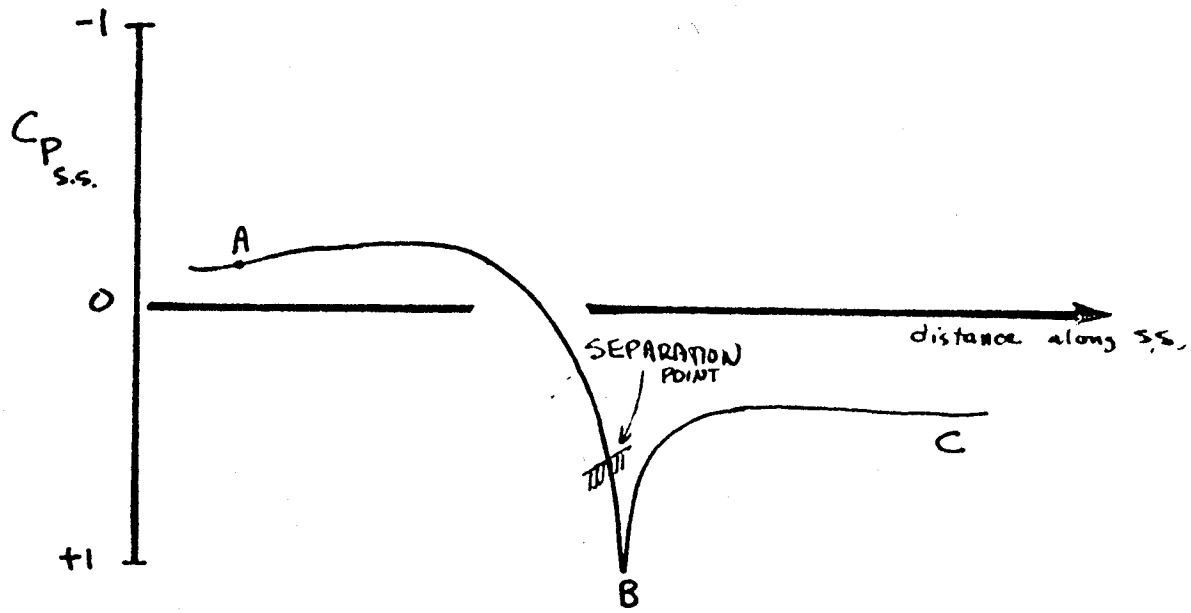

① calculate path of DIVIDING streamline & pressure in potential flow

② COMPUTE boundary layer along streamline, find separation point

FIGURE 11.4 PREDICTION OF WING-BODY JUNCTURE SEPARATION

GILLETTE 3-23-78

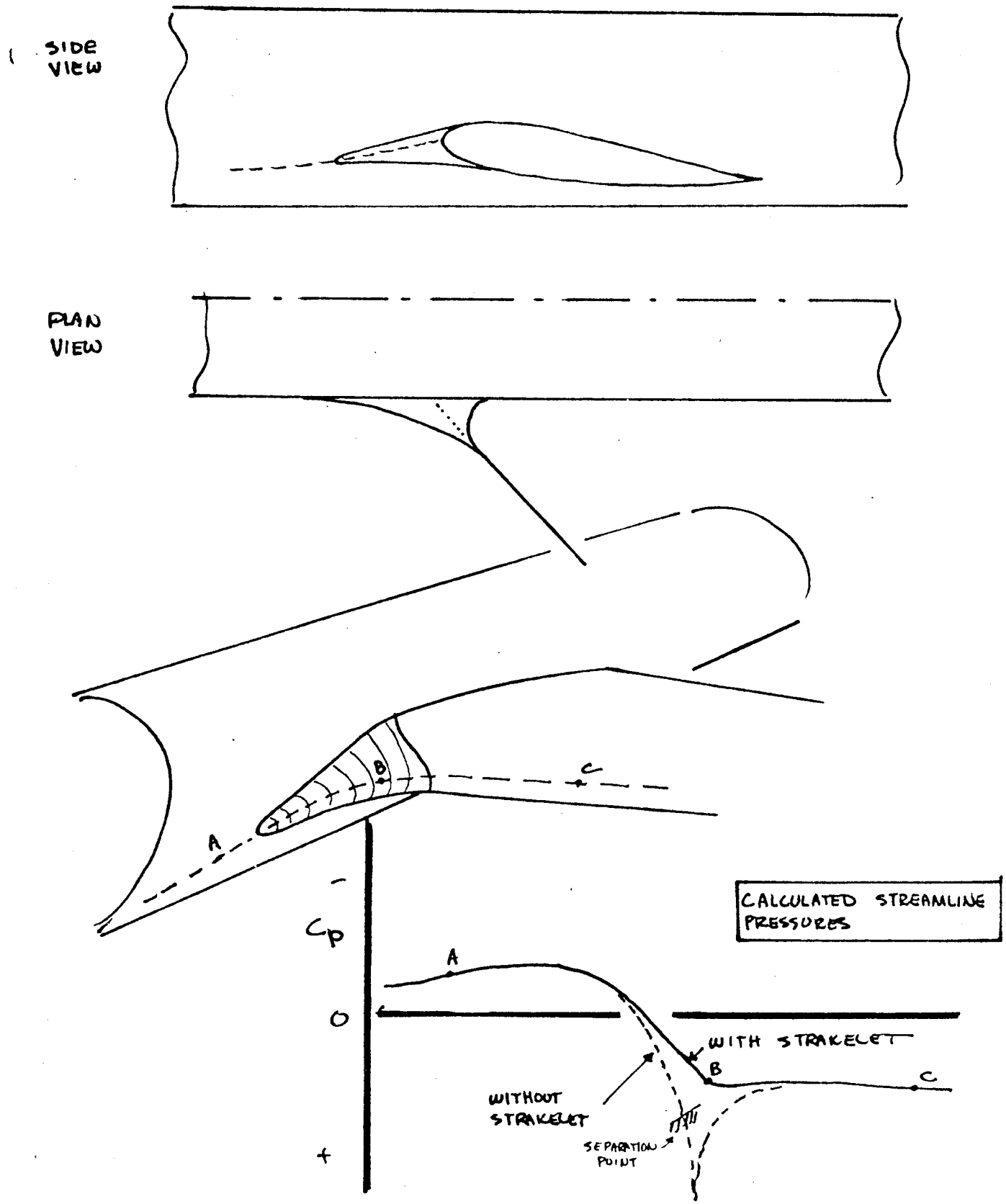

FIGURE 11.5 WING ROOT STRAKE DESIGN

GILLETTE
3.29.78

(a) INDUCED DRAG CAUSED BY SHED VORTICITY

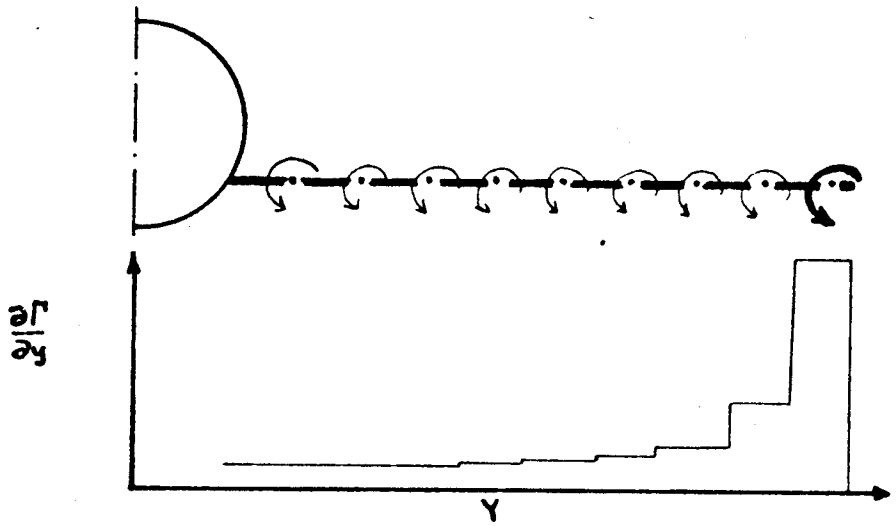

(b) WINGLET MOVES LARGEST SHED VORTICITY AWAY FROM PLANE OF THE WING

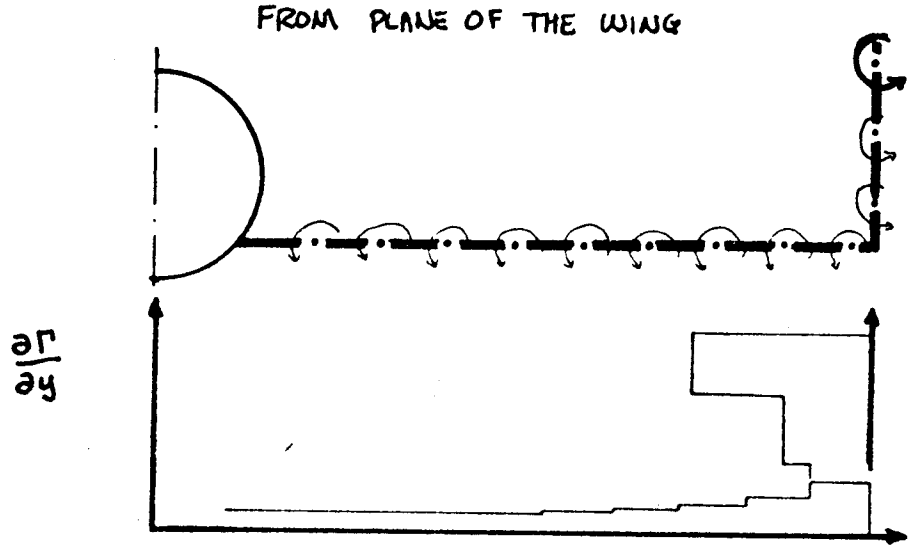

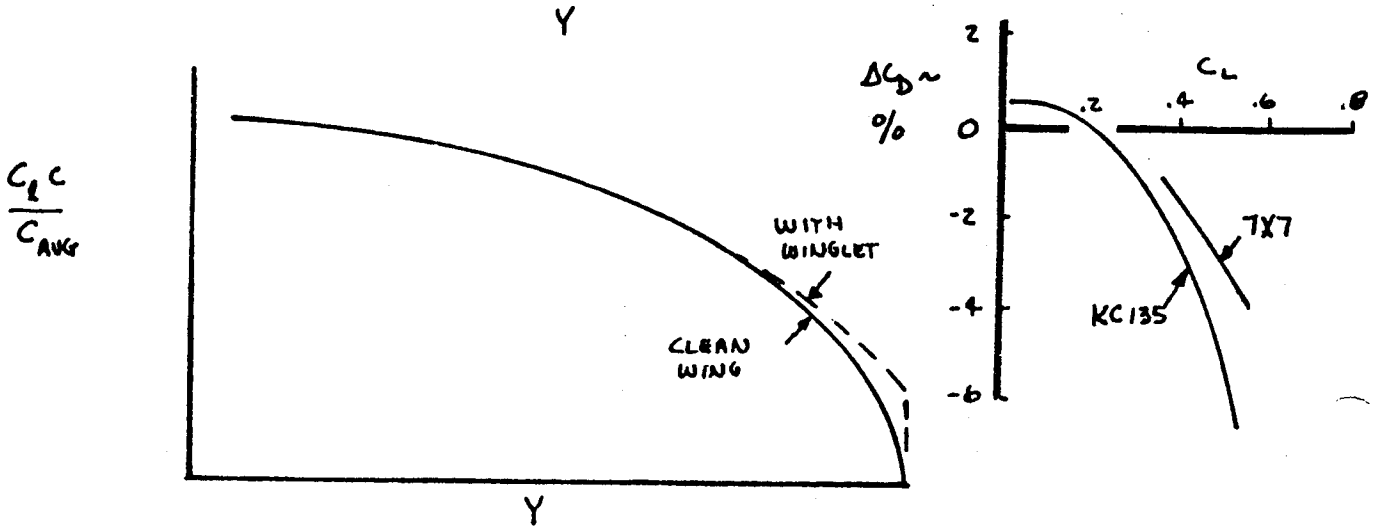

FIGURE 11.8 WINGLET EFFECT

750

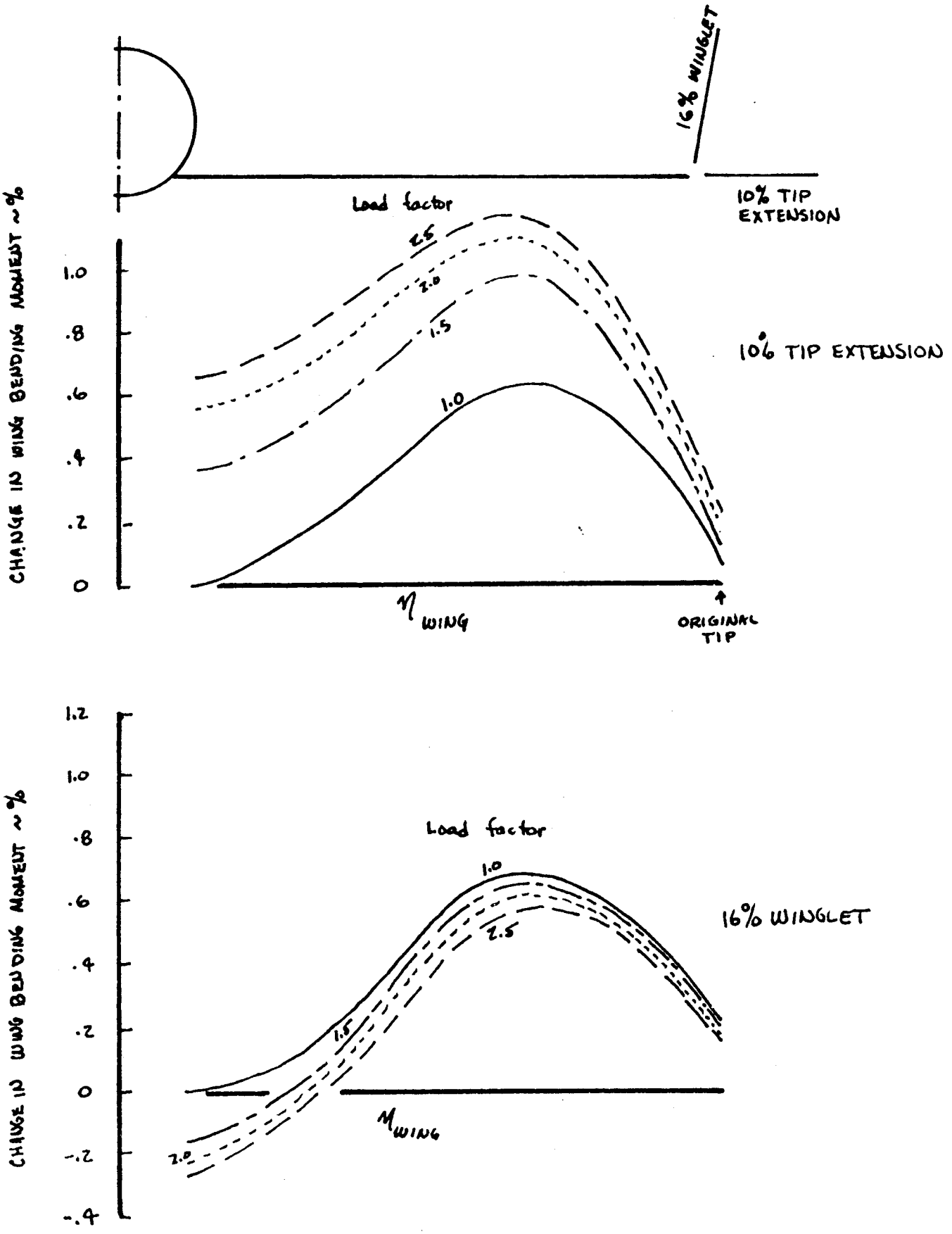

FIGURE 11.9 EFFECTS ON WING BENDING MOMENT

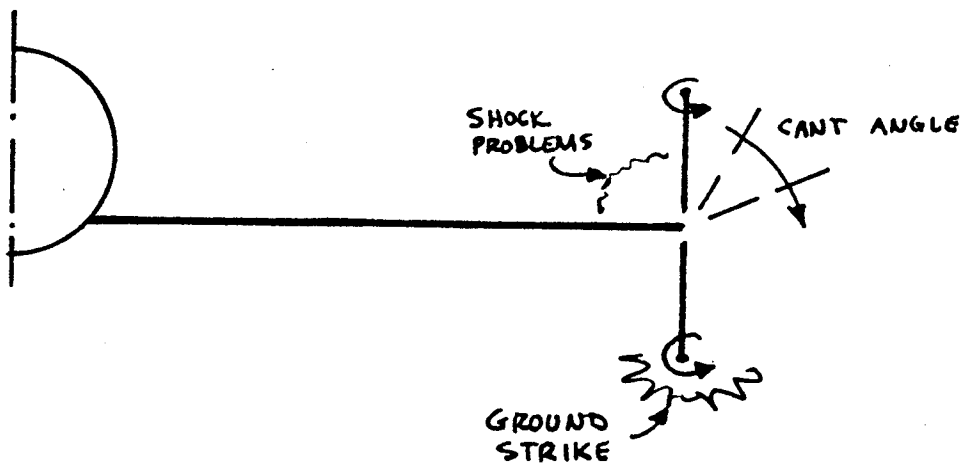

UPPER VS LOWER WINGLET

- UPPER WINGLET HAS DIFFICULT UPPER CORNER PROBLEM DUE TO SHOCKS
- LOWER WINGLET IS EASIER TO INTEGRATE, BUT CAN BE USED ONLY ON HIGH-WING AIRCRAFT

CANT ANGLE

- DRAG BENEFIT INCREASES AS WINGLET IS ROTATED TOWARD WING PLANE

but

- WING WEIGHT INCREASES DUE TO WING BENDING MOMENT AT 2.5 g's AS WINGLET GOES FROM STRAIGHT UP TO STRAIGHT DOWN

FIGURE 11.10 WINGLET POSITION & CANT

752

GILLETTE
3-25-78

FOUR CATEGORIES OF EXCRESCENCE

1. DISCRETE ITEMS

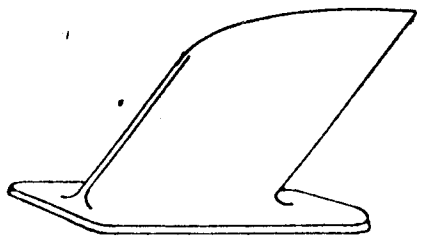

2. MISMATCH

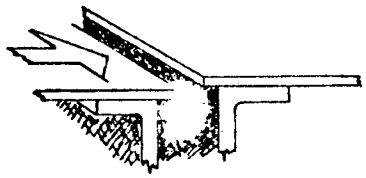

3. INTERNAL AIRFLOW

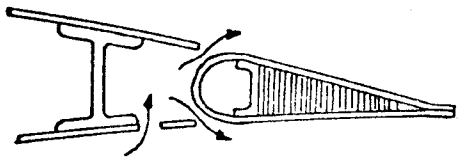

4. ROUGHNESS

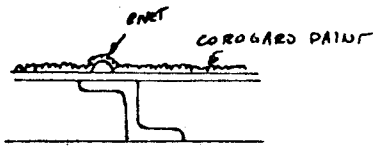

IN GENERAL ~ ANY ITEM WHICH CANNOT BE SIMULATED IN THE WIND TUNNEL

FIGURE 11.11 EXCRESCENCE ITEMS

752 GALETTE 3.26.78

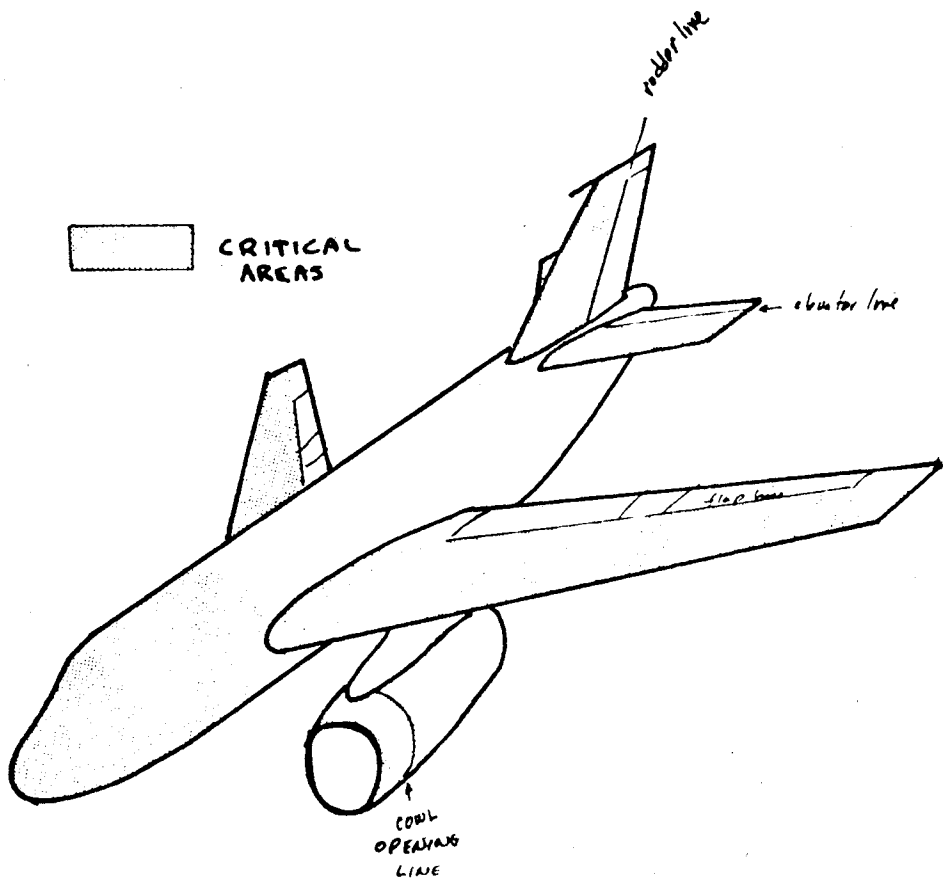

- IN CRITICAL AREAS (THIN BOUNDARY LAYER)

  STEPS, MISMATCHES KEPT SMALL ~ $\pm$.015" NORMAL TO FLOW
  $\pm$.030" TRANSVERSE TO FLOW

  GAPS KEPT SMALL ~ .030", NO SEALANT

- IN NONCRITICAL AREAS

  STEPS, MISMATCHES LARGER ~ $\pm$.030" NORMAL TO FLOW
  ~ $\pm$.050 TRANSVERSE

  GAPS FILLED WITH AERO SMOOTHER

FIGURE 11.14 EXCRESCENCE CALLOUTS FOR SMOOTHNESS

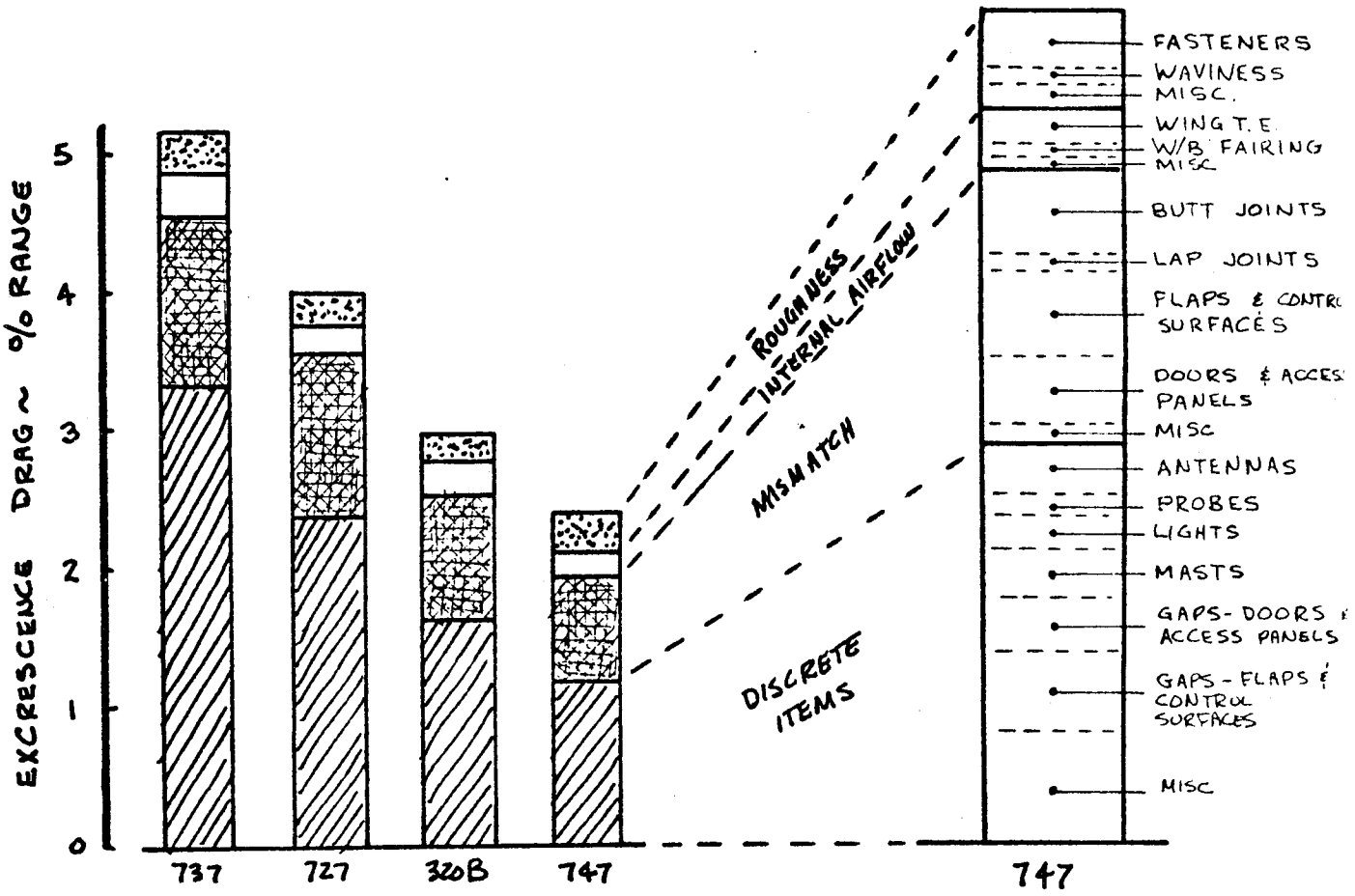

SOURCE: D6-13784

FIGURE 11.12 TYPICAL EXCRESCENCE DRAG

75-

DESIGN DECISIONS ON DISCRETE ITEMS ARE BASED ON "WEIGHT-EQUIVALENT DRAG" BENEFIT

EXAMPLE: AT 5000 NMI RANGE, 1% DRAG ON THE 707 HAS THE SAME PENALTY IN BLOCK FUEL AS 2200 LBS O.E.W. SINCE CRUISE DRAG IS .0214, THEN 1 DRAG COUNT (.0001) HAS THE SAME EFFECT AS 1028 Lbs OEW. I.E, IT COULD REQUIRE 1028 Lbs OEW TO ACHIEVE A CHANGE WORTH 1 DRAG COUNT BEFORE THERE WOULD BE NO GAIN IN PERFORMANCE.

EXAMPLE: WINDSHIELD WASHING & RAIN REPELLANT NOZZLES

707-727-737

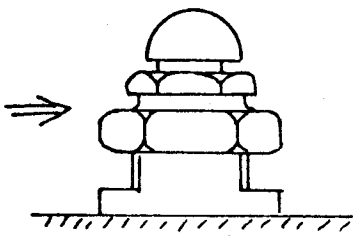

ΔD_{RAG} = 14 lbs OEW

747

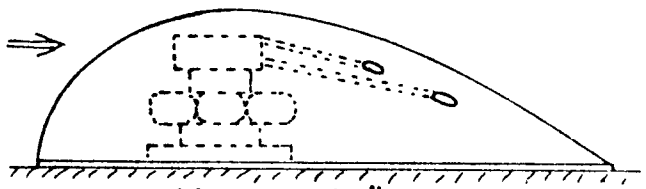

ΔD_{RAG} = 1 lb OEW

EXAMPLE: RADOME LIGHTNING DIVERTER STRIPS

RADIAL

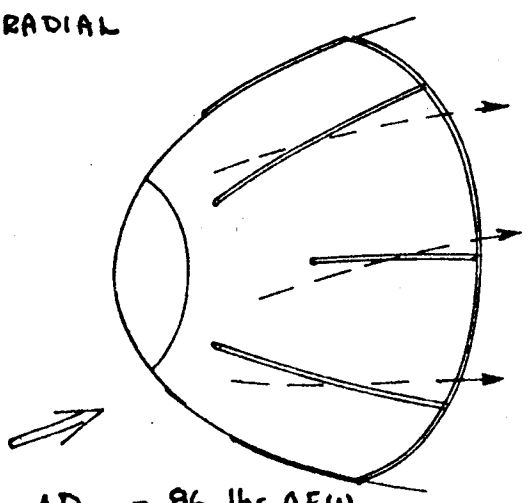

ΔD_{RAG} = 86 lbs OEW

STREAMLINED

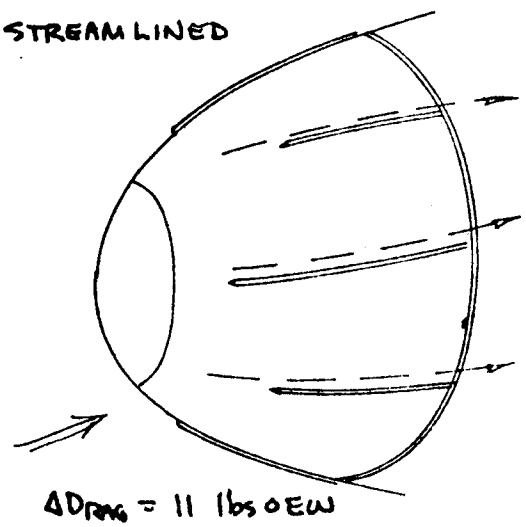

ΔD_{RAG} = 11 lbs OEW

FIGURE 11.13 EVALUATING EXCRESCENCE ITEMS

GARLETTE 3.25.78

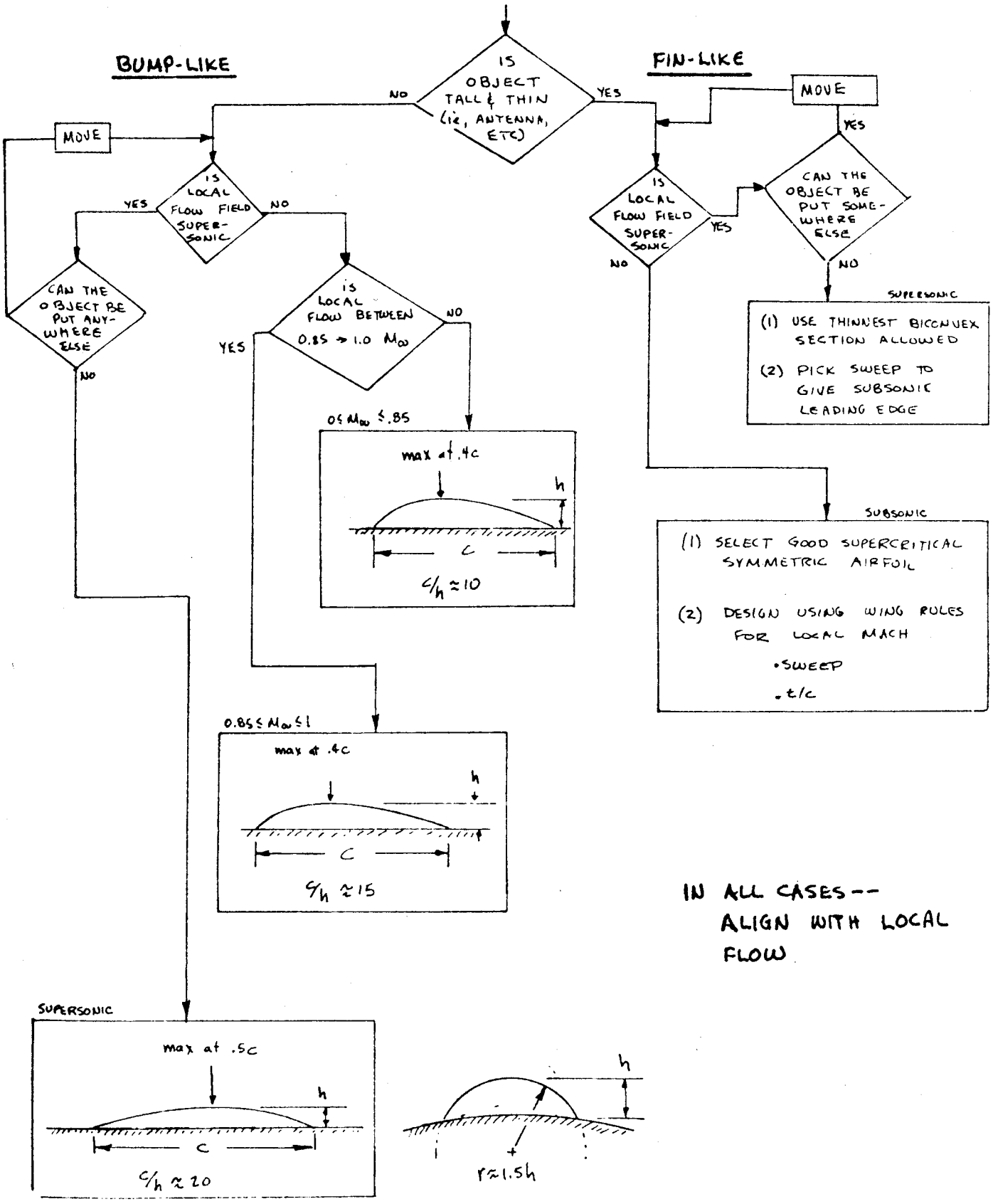

FIGURE 11.15 GENERALIZED DISCRETE ITEM DESIGN SEQUENCE

GILLETTE 3.25.78

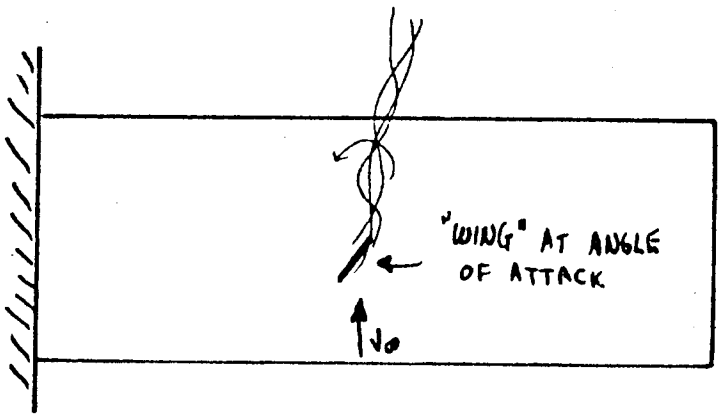

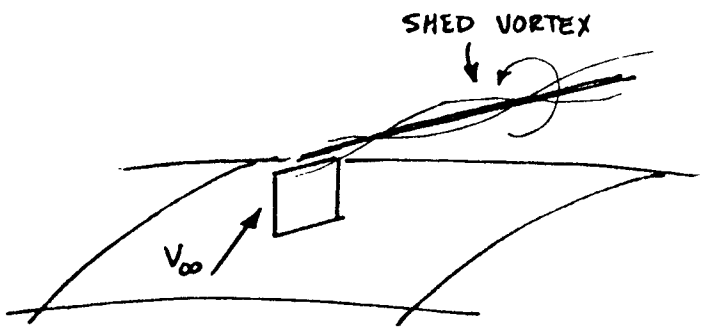

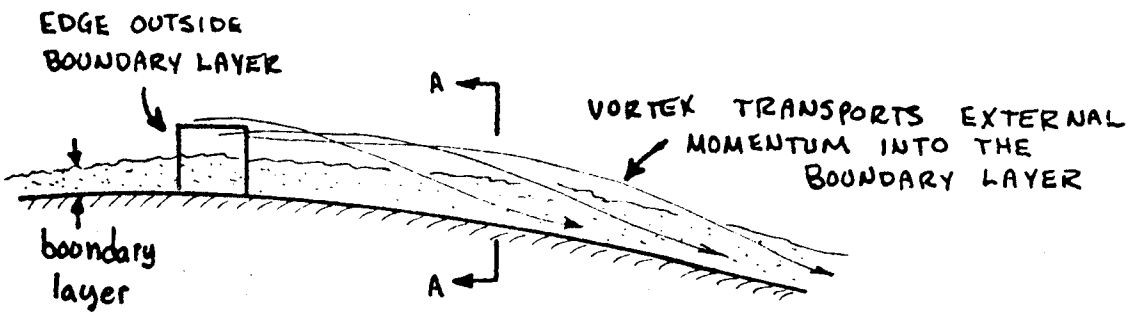

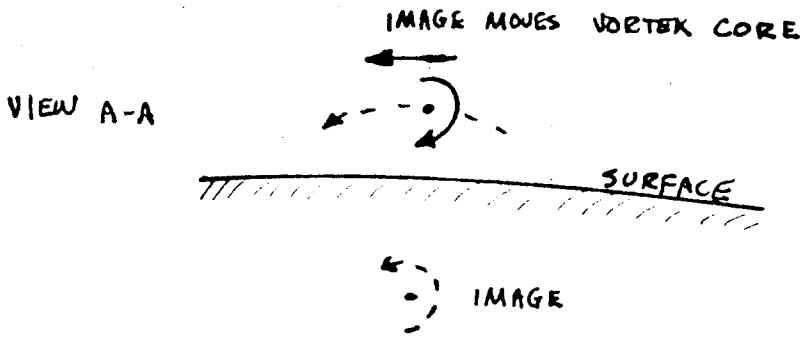

FIGURE 11.16 CHARACTERISTICS OF VORTEX GENERATOR

DESIGN RULES: (1) LOW ASPECT RATIO ⇒ STRONG VORTEX
(2) 12°-15° ANGLE OF ATTACK TO LOCAL FLOW

(a) RECTANGULAR

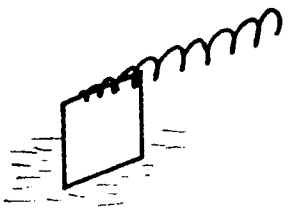

(b) DELTA

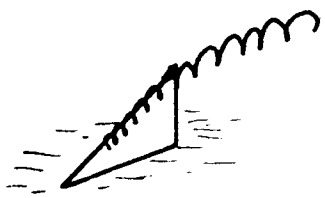

(c) OGIVE

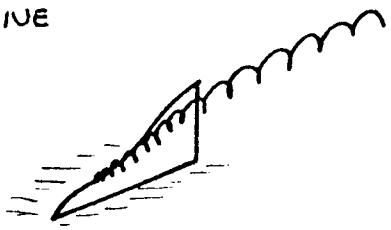

(d) SPADE

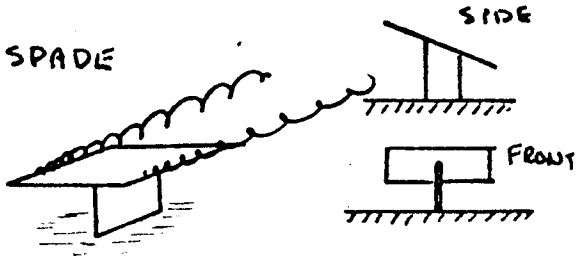

(e) OGIVE ON STAND

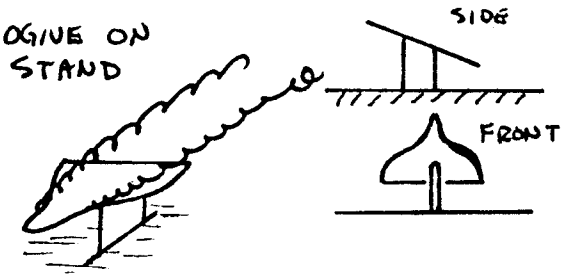

FIGURE 11.17 TYPICAL VORTEX GENERATOR SHAPES

GILLETTE
3.25.78

159

(a) TO BLOCK CROSSFLOW

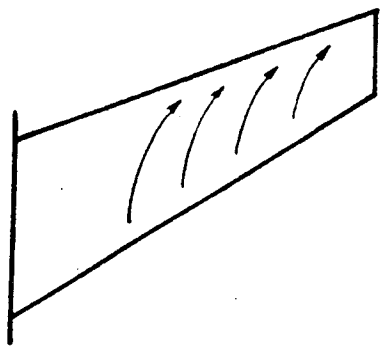

SOLUTION: CO-ROTATING VG's

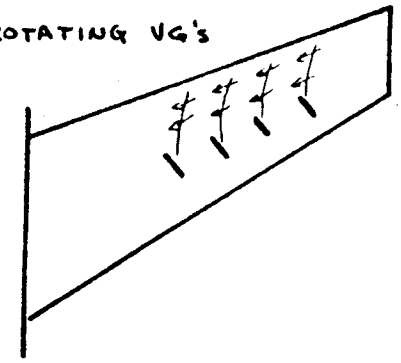

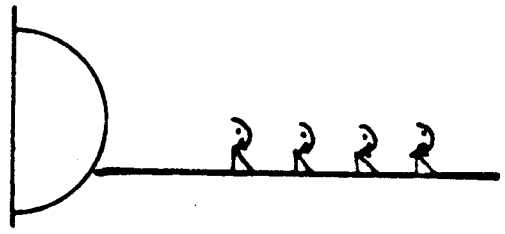

(b) FOR REDUCED SEPARATION & GENERAL MIXING

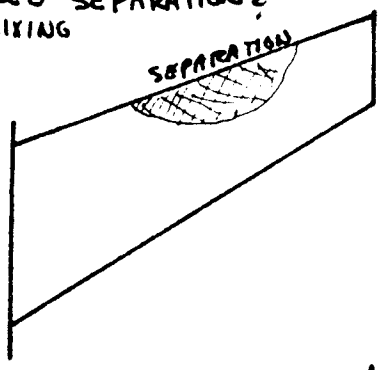

SOLUTION: CONTRA-ROTATING VG's

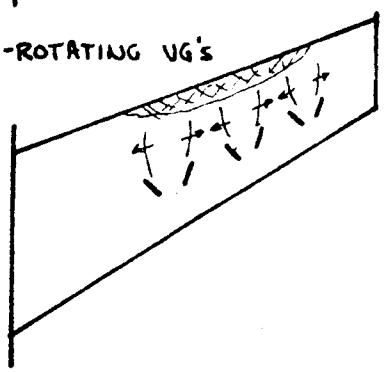

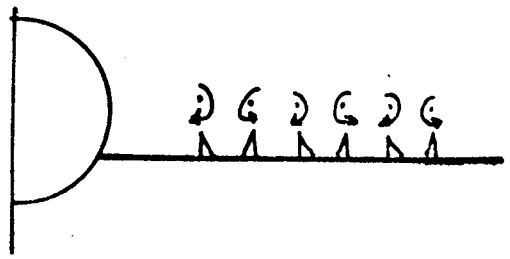

FIGURE 11.18 USES OF VORTEX GENERATORS

GILLETTE
3.25.78

(1) TALL ENOUGH TO GENERATE VORTEX OUTSIDE BOUNDARY LAYER

(2) APPLIED AT 12-15° RELATIVE TO LOCAL FLOW

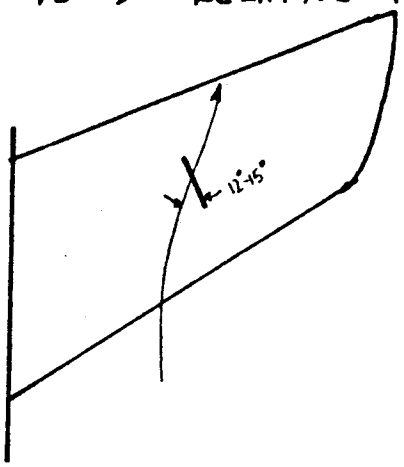

(3) PLACED AHEAD OF POINT WHERE V.G. EFFECT IS REQUIRED

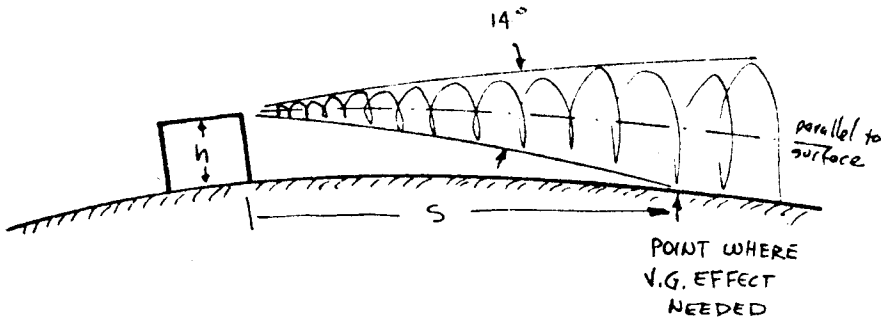

$s \doteq h \tan 7°$

FIGURE 11.19 VORTEX GENERATOR SIZING & PLACEMENT

GRLETTE 3.25.78

DC-9 VORTILON

(a) AT CRUISE

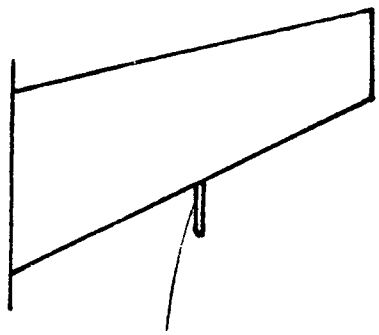

(b) AT HIGH α, LOW SPEED

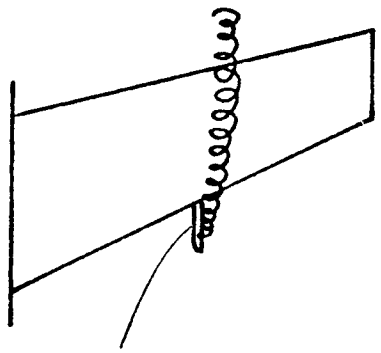

727 WING FENCE

(a) AT CRUISE

(b) AT HIGH α, LOW SPEED

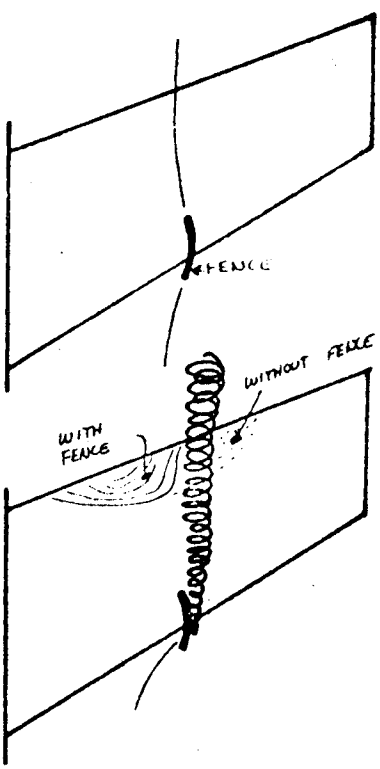

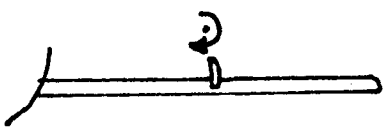

FIGURE 11.20 FLOW CONTROL FENCES

762

GILLETTE
B.25.78

CHAPTER 12 AERODYNAMIC FLIGHT TESTING

CHAPTER 12 AERODYNAMIC FLIGHT TESTING

12.1 INTRODUCTION

The objective in this chapter is to give a broad overview of what is done during an aerodynamic flight test program, the type of data extracted from flight testing and the kinds of instrumentation used to obtain the the data. Flight testing fits into three rather broad areas:

- o Precertification Testing
- o Certification Testing
- o Developmental Testing

Precertification testing is the part of the test program ahead of the FAA involvement during which the performance levels of the airplane are established, the testing techniques are developed and problem areas identified and solved. Every airplane has its own unique handling qualities that can impact the results and the way the testing is performed; a good example would be stall characteristics. If there are minor problems that can be solved without significant modifications, they are incorporated before the FAA certification process begins. In order to know what the problems are, enough testing must be accomplished to establish the performance levels. This precertification testing can account for about half of the total flight test time from first flight through to certification. When the airplane is ready, the certification proccess begins, during which much of the actual flying is performed by FAA pilots. The data generated during the certification testing becomes the basis for certification and must meet the FAA regulations in effect for the airplane. Developmental flight testing is classified as that testing which is performed to develop and validate new concepts, or to solve major performance problems of the airplane. A couple of examples of this type of testing would be, the 727-300 wing testing as an example of the development and validation type, and the 737 aft body testing to solve the "vertical bounce" as an example of the problem solving type. Since the certification and precertification testing involve doing the same type of test, they will be discussed together. It should be emphasized that the testing we will discuss is only the aerodynamic testing, and does not include another large body of testing that is done to support the total development and cetification process.

12.2 CERTIFICATION AND PRECERTIFICATION TESTING

The certification and precertification testing can be broken down into several large blocks that make it easy to understand. These blocks and the amount of testing time involved with the 747 in each block is shown below:

764

TYPE OF TESTING	BOEING	FAA	TOTAL
Pitot Static Calibration	16.3	18.2	34.5
Takeoff Performance	8.1	23.5	31.6
Stall Speeds	19.2	14.1	33.3
Low Speed Performance	16.3	27.6	43.9
Cruise Performance	42.2	--	42.2
Landing Performance	1.1	18.4	19.5
TOTAL TESTING (Hours)	103.2	101.8	205.0

You will note that there is no cruise performance cruise certification testing because there are no certification requirements for cruise drag. Since cruise is where the airplane makes money however, a large block of test time is used to determine the cruise performance of the airplane. The cruise performance is usually guaranteed to the customer, it must therefore be carefully evaluated. Let us now look at each of these blocks of testing in turn.

12.2.1 Airspeed Calibration Testing

Perhaps the place to start is by discussing the FAA certification requirements for the airspeed system. The allowable static pressure error expressed as an altitude error is shown on Figure 1. If the error is within these limits, the system is certificable and the position error is published in the airplane flight manual. If the error is outside the limits, the airspeed system must be modified to get within limits. Measurement of airspeed and altitude is obtained by measuring the free stream static and total pressures. Total pressure is quite easy to obtain since the device for measuring total pressure, the pitot, is quite insensitive to angle of attack and position on the airplane. Normally, the pitot tubes are located near the nose. The free stream static pressure however, is not so easy to obtain and several methods have been used in flight test to obtain a reference static pressure source. The most commonly used method of obtaining a reference static pressure is by use of a trailing cone. Picures of a trailing cone installation on a 727 are shown on Figure 2 and 3. In flight, the cone is extended on a long plastic hose that has static ports in a section of it near the end. Schematically this would look like:

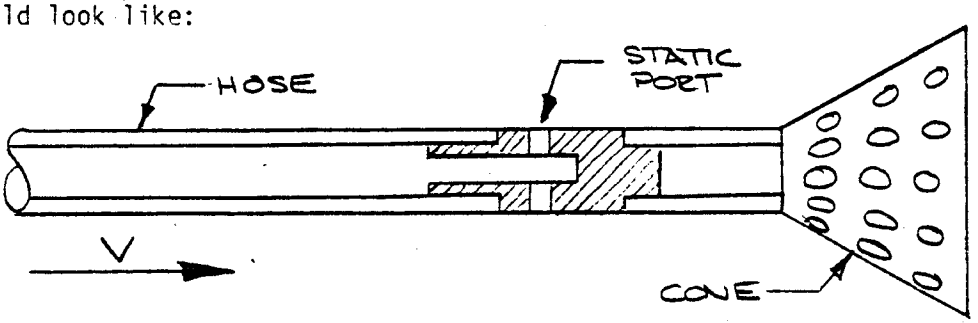

765

The cone trailing behind the airplane enables static pressure to be measured away from the influence of the airplane. This reference static can be used relative to some other static source on the airplane and a calibration of the airplane system obtained. Another method used primarily low speed on airplanes prior to the 747 is the trailing bomb. Schematically, this would appear as:

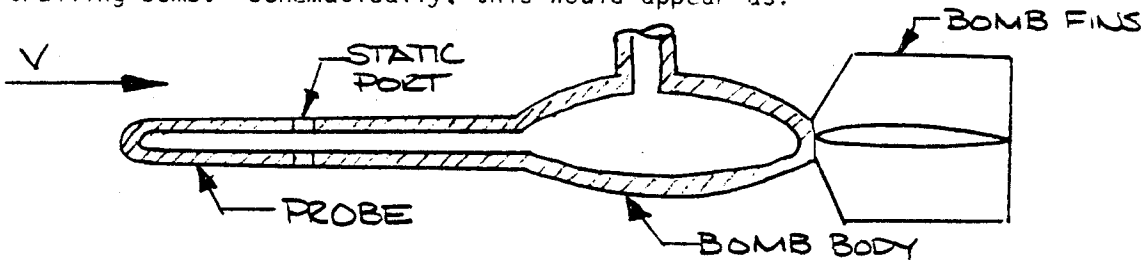

The bomb is lowered from the airplane body and the fins keep the probe aligned with the flight path. Again, the reference static is obtained away from the influence of the airplane. Prior to the advent of the trailing cone, calibrated pacer airplanes were used to fly along side the airplane being calibrated and the flight instruments were read on both aircraft. The differences could be used to obtain a calibration. The pacer airplanes were usually fighters that had been tested with long static probes or on a calibration range with camera and stopwatch. The early 727's and 707's were calibrated using this method. The differences between the reference static source and the ships system can be used to obtain the airspeed or altitude error of the ships system. A typical calibration for the 727-100 is shown on Figure 4. The ships static pressure sources come in several types. The older airplanes (pre 747) relied on static pressure ports in the side of the body which had been selected from wind tunnel tests as having good static pressure and minimum angle of attack and Mach number sensitivity. The wind tunnel selected positions were usually quite adequate, however they alway seem to end up on or near a cargo door. On the 747 a compensated pitot static probe was developed that got around this problem, although static ports are used as a backup system. The compensated probe was built with a bump that causes a pressure that cancels the static pressure error at the probe location. The probe is designed based on wind tunnel static pressures and schematically looks like:

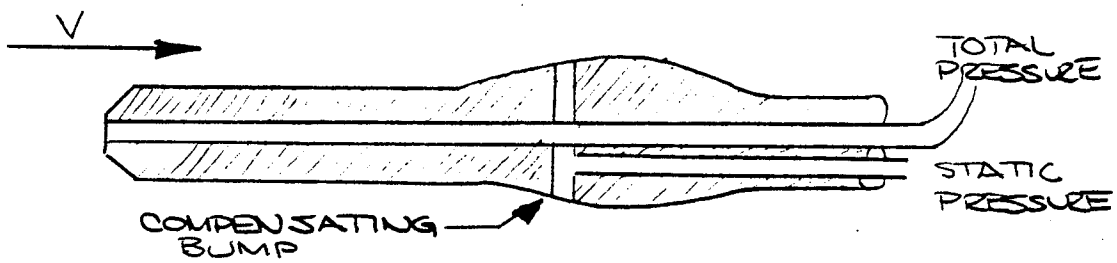

The end result of the airspeed calibration is a page in the airplane flight manual and the calibration is used to correct all flight test data.

12.2.2 Takeoff Performance Testing

Takeoff performance is perhaps the most complicated part of a certification program because the takeoff certification regulations are complex. Takeoff field length requirements are illustrated in figure 5 which shows that the field length is the longest of the all engine takeoff distance +15% or an engine failure at V_1 and continue the takeoff to 35 ft height or engine failure at V_1 and stop. The example shown is for the 727 which is all engine go limited. A detailed look at all of the speeds and their relationships is shown on Figure 6 for the 727-200. Note the delay time following engine fialure and the 3.6 second transition time applied to allow for spoiler deployment and brake application. Also note that for the 727-200 V_1 is equal to V_R. The relationship between the speeds is as follows:

V_{MC} -minimum control speed with one engine suddenly made inoperative, demonstrated on ground V_{MCG} and in free air V_{MCA}

V_1 -critical engine failure, speed below which the takeoff cannot be safely demonstrated. $V_1 \geq V_{MCG}$

V_R -takeoff rotation speed at which the airplane can attain V_2 at the 35 foot height. $V_R \geq 1.05 V_{MCG}$

V_{MU} -minimum unstick speed, the minimum speed at which the airplane can lift off. Must be demonstrated all engine and engine out

V_{LOF} -lift off speed, V_{LOF} dictated by V_R, but all engine $V_{LOF} \geq$ 110% all engine V_{MU} and engine out $V_{LOF} \geq 105\%$ engine out V_{MU}

V_2 -takeoff climb speed is actual speed at 35 feet and $V_2 \geq 1.2 V_S$ also $V_2 \geq 1.1 V_{MCA}$

Since the speeds are related and none of them are directly calculable, flight test becomes the only basis, and since each speed is a function of T/W (or acceleration capability) many takeoffs are required to establish a good base. In addition to the normal speed schedule, abuse testing is also performed to demonstrate the margins available. Examples of two types of abuse are shown on Figures 7 and 8 for the 727-200 which show the effect of late rotation and improper thrust setting. Other parameters that are extracted from the flight test include times from rotation to lift off and V_2. This part of the takeoff does not lend itself to analysis since it is a dynamic maneuver that would need aerodynamic data, gear and the structural data and aeroelastic data. The simple approach is to measure the time during flight test and use the time versus velocity to compute the ground distance covered from rotation to 35 foot height. Figure 9 shows the relationships between the speeds for a V_{MU} limited airplane. Let us now look at how the takeoff data is presented based of flight testing. Figure 10 shows the flight test V_R, V_{LOF} and V_2 data as a function of thrust to weight ratio as ratios of the reference stall speed. Each point represents a takeoff performed with the FAA on board and probably flying the airplane. Figure 11 shows the effect of rapid rotation on the relationship between V_R and V_{LOF}. Again each point is a takeoff. Figure 12 shows the results of the V_{MU} certification. Each point on this curve represents a takeoff performed with the airplane at its geometry limited angle on the ground i.e. dragging its tail on the ground.

767

At this point you can begin to appreciate the scope of the takeoff certification flight testing program. The times from rotation to liftoff and 35 ft height (V_2) are shown on Figure 13. This data is used to calculate the distance from rotation during the dynamic portion of the takeoff run. Figure 14 shows the ground roll parameters extracted from the flight data. These data are difficult to obtain and the split between the pieces is not well understood, however if the numbers are used as shown the correct field lengths can be computed. Figure 15 shows the lift data obtained during the V_{MU} testing of the 747. As the airplane just lifts off, lift is equal to weight and we can compute C_L. The data shows that the preflight concern about stall or buffet near the ground was not justified. If stall or buffet had been encountered a geometry limitation system such as a ventral fin or retractable tail skid would have been required. Note the large scatter in the data.

12.2.3 Stall Speed Testing

During the discussion of takeoff performance the stall speed was used as the reference speed for all of the other speeds. The FAA requires that the stall speeds be determined at:

Forward c.g.
Idle thrust
Trimmed at 1.2 to 1.4 V_S
Entry rate to the stall of 1 knot/second
Acceptable stall characteristics

However the stall characteristics must also be demonstrated at more severe conditions such as:

Aft c.g.
Power on and asymmetric power
During turn and straight stalls

The most interesting of these requirements is the entry rate requirement of 1 knot per second. This entry rate has been defined by the FAA as the average rate between 1.1 V_S and V_S. This does not describe a unique maneuver however as is shown on Figure 16. The fast stall technique or something similar has been found to give lower speeds, but more on that later. The method for defining the stall speed is to perform a series of stalls of various entry rates and plot the minimum speed versus entry rate as shown below:

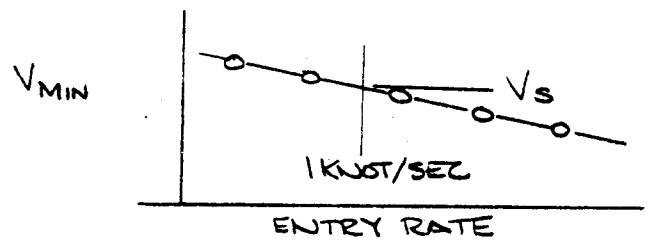

The speed at an entry rate of 1 knot/second is defined as the stall speed. Figure 17 shows the results of the stall speed certification on the 747.

The stall lift coefficient is a function of gross weight and the minimum weight tested sets the maximum lift coefficient value at each flap. This weight effect is not entirely explainable, however it exists on most of our airplanes. The stall lift coefficients maybe converted to stall speeds as shown on Figure 18.

Note that C_L stall is defined as:

$$C_{L_S} = \frac{W}{q_s S}$$

Since the stall maneuver is a dynamic one, the load factor is always less than one and an attempt to sort this out resulted in the definition of another parameter, the so called "1g" stall speed. The "1g" stall speed is found from the same tests as the FAA stall speed by looking at the speed where the normal force or "g" breaks just before the stall. Figure 19 shows this data and comparison with Figure 17 will reveal substantial differences. This approach does not however represent the true maximum lift coefficient achieved during the stall. The "true" maximum lift coefficient is obtained by considering the following equation:

$$C_{L_{MAX}} = \frac{nW}{qS}$$

Where n is normal load factor. This $C_{L_{MAX}}$ is obtained by plotting nW/qS vs time and simply picking the maximum value from the time history. Figure 20 shows the $C_{L_{MAX}}$ data which is again different from the "1g" stall data. Another parameter that is obtained from the FAA stall testing is the initial buffet speeds. If the intial buffet speeds do not provide adequate warning of the stall an artificial device is installed to shake the stick. Figure 21 shows the initial buffet data obtained during certification which results in the speeds shown on Figure 22. Comparison with the stall speed will reveal that the natural stall warning is not very good, and consequently a stick shaker was installed that has the characteristics shown on Figure 23. The buffet speed envelope is determined over the complete flight envelope and the results of the high speed buffet testing is shown on Figure 24. The high speed buffet can limit the airplanes ability to cruise at a given W/S if a load factor margin is chosen for maneuvering. A .3g incremental load factor is usually prescribed as a reasonable margin, but it is not regulatory. For example, at $W/S = 4 \times 10^6$ and M=.85 the buffet C_L is .68. This C_L with a .3g incremental load factor would give a useable C_L of .52 which could limit the flight envelope of the airplane.

The prediction of stall speeds is one of the most important factors in the design of a new airplane. The procedures used in the past have been quite crude and the method was based on the data of Figure 25 and 26. Based on the ratios of flight test to wind tunnel values a nominal value was chosen and the 747 pre-flight estimates are shown. In addition an effect of wing loading was assumed.

The range of values shown on the C_L ratio plots represents the range of wing loadings shown at the bottom of Figure 25, with the symbol representing the highest W/S. You can see from the variation that this prediction method had some serious risks associated with it because everything, all the unknows, were lumped into one parameter. Figure 27a and b show a time history of a 747 stall. The maneuver is dynamic with the minimum speed occuring well beyond the maximum lift point. Note the elevator input just at the normal acceleration or "g" break. Extacting the maximum C_L from a series of stalls on the 747 the data on Figure 28 was obtained. The entry rate does not effect the maximum value, but the weight effect does show up. A simulation program was used to investigate the different stall testing procedures on the 747. The two types of stall procedure shown on Figure 16 were simulated, with the "slow" stall performed with a steadily increasing elevator input until the "g" break after which the elevator was held constant. The "fast" stall was performed with a steadily increasing elevator input until the "g" break when full up elevator was applied. The results of this simulation are shown of Figure 29. The fast stall data correlates quite well with the flight data and gives much higher values than the slow stall. Looking back at Figure 27 we can see that a fast stall procedure was used. A summary of how the stall C_L is built up from wind tunnel data is shown on Figure 30 with comparisons to Flight data. The correlation is excellent and suggests a better procedure for predicting stall speeds from wind tunnel data. An interesting factor that was used in this simulation was the effect of Mach number on the maximum lift capability. Despite the low free stream Mach numbers during a stall, the local velocities on the flaps can reach supersonic values. Increasing the stall demonstration altitude can effect the free stream stall Mach number and compound the effect of the flow super velocities. Figure 31 shows the effect of Mach number on the stall C_L of the 747 SP. The effect is significant and would lead you to try to keep the altitude for stall demonstration to a minimum. Incidentally, Boeing has done most of its stall demonstrations at 10-12,000 feet while MACDAC has used 5-6000 feet.

12.2.4 Low Speed Performance Testing

The FAA requirements for low speed performance can all basically be expressed in terms of the climb gradient available under a variety of conditions. The basic requirement can be expressed as follows:

Flight Condition	FAR Part 25 and SR-422B Rules		
	4-engine airplanes	3-engine airplanes	2-engine airplanes
(1) First takeoff climb segment	0.5%	0.3%	2.4%
(2) Second takeoff climb segment	3.0%	2.7%	1.2%
(3) Final takeoff climb segment (applies from the 400-foot level of second segment to end of takeoff Pattern)	1.7%	1.5%	1.2%
(4) Approach Segment	2.7%	2.4%	2.1%
(5) Landing segment	3.2%	3.2%	3.2%

770

Where the definition of the segments is as follows:

1) Engine out, takeoff thrust, takeoff flaps, gear down at V_{LOF}
2) Engine out, takeoff thrust at 400 feet, takeoff flaps, gear up at V_2
3) This segment, the climbout above 400 feet, is usually divided into two segments:
    a) Third segment during which flaps are retracted and airplane is accelerating in level flight.
    b) Fourth segment in which airplane is in a climb with takeoff thrust.
4) Engine out, takeoff thrust, approach flaps gear up, at landing weight.
5) All engine, takeoff thrust, landing flaps gear down, at landing weight.

The gradient requirements decrease with the number of engines because the fewer the number of engines, the larger the percent thrust loss with an engine failure. In order to meet these requirements the flight testing is performed in such a manner that the gradients can be determined for the complete low speed envelope of the airplane. The basic elements of the low speed testing are:

Drag Polar Determination
Control Drag Determination
Check Climbs

The level flight drag polars are determined with symmetric power over a wide speed range using basically the equation thrust equals drag. Next a series of level flight engine out drag polars are determined and the difference between the all engine and engine out polars is called control or yaw drag. The data is how available to calculate the performance to meet the FAA requirements, but to be certain, a series of check climbs are performed to ensure compliance. Figures 32 and 33 show sample low speed polars for the 747. The points are determined by flying steady conditions and implying the drag from calibrated thrust data. This type of data can be used to develop the low speed envelope which is shown on Figure 34. Here again is the familiar form for presenting the low speed performance data. The engine out drag is determined in a similar manner but of course with an engine out. The difference from the symmetric power polars is usually labeled yaw drag, and is plotted against the engine out yawing moment coefficient. The engine out yaw drag of the 747 is shown on Figure 35. The pilot tries to hold essentially zero bank until he reaches full rudder deflection when he must let the airplane bank and sideslip to balance the engine out moment. With the symmetric polars and yaw drag available, calculations can be carried out to satisfy the low speed performance climb gradient requirements. Final flight check climbs are performed to substantiate that the gradients are indeed achievable.

12.2.5 Cruise Performance Testing

Cruise performance can make or break and airplane. From an economics and operational standpoint, cruise performance certainly has the heaviest influence on the viability of the product, yet there are really no FAA requirements to demonstrate the cruise performance levels. However, since we in general guarantee the cruise performance to each of our customers, a great deal of time is spent in carefully determining and assessing the cruise performance of each new airplane. The procedure used to determine the cruise drag has been to imply the drag based on calibrated thrust values during steady unaccelerated flight. A range of weight and altitude conditions are flown in order to cover the full cruise flight envelope of the airplane. Figures 36 and 37 show typical cruise performance curves extracted from 727-200 flight testing. Figure 36 shows the basic drag data which could be cross plotted into the more familiar C_L versus C_D. Figure 37 shows the fuel mileage data that combines the aerodynamic and propulsion efficiency. These data are however the bottom line since this parameter, miles per pound, determines the range of the airplane. These data are taken over a range of altitude and therefore there is some variaion in Reynolds number. Figure 38 shows the range of Reynolds ndumbers encountered during this testing. At a fixed C_L the Reynolds number variation is quite substantial, and tests conducted to evaluate small configuration changes could be rendered useless by this effect. Tests were performed to demonstrate the Reynolds number effect and the results are shown on Figure 39. The drag variation with Reynolds number is approximately as predicted from boundary layer theory. A similar factor that can effect cruise performance is the airplane center of gravity. Center of gravity is difficult to control accurately in flight and some variation between tests can be expected. Trim drag due to c.g. variations are difficult and time consuming to obtain and trim drag incremnts are not available for every airplane. Trim drag was measured on the 727 and the data substantiated fairly well the values obtained from wind tunnel testing. The official 727-200 trim drag curve is shown on Figure 40. Any testing for small drag changes should track the Reynolds number and c.g. trim drag increments to ensure that the effect being evaluated is not masked. Some recent developments in flight testing may effect the manner in which we obtain cruise drag performance. Figure 41 shows some cruise drag data obrained during accelerating and decelerating conditions on the 727-200. The data was obtained by assuming an equation of the form:

$$T - D = ma$$

instead of the usual form:

$$T - D = 0$$

If accurate acceleration data is available for instance an intertial navigation system then drag data can be obtained during steady accelerated flight. All of the data on Figure 41 does not appear smooth and closer examination revealed that some conditions had experienced heading changes during the test conditions. Eliminating the conditions which exhibited these heading changes the data on Figure 42 was extracted. This data is smooth repeatable and

correlates well with steady state data obtained earlier as shown on Figure 43. This technique could drastically reduce the flight time required to evaluate cruise performance and yield better data because of the larger number of useable points available.

12.2.6 Landing Performance Testing

Landing performance testing is perhaps the most empirical of all of the testing described previously. The FAA rules recognize the inaccuracies in the landing performance by applying large empirical factors to the demonstrated capabilities of the airplane. Figure 44 shows a typical landing profile for the 727. The airplane crosses the end of the runway at 50 foot height and flares to touchdown. The transition region allows for spoiler deflection and brake application followed by a braking segment to a stop. The braking section is the only part of this profile that is calculable, with the flare and transition regions relying on basically statistical data from a series of landings. Note that the FAA defined field length is 1.667 times the demonstrated value. Figure 45 shows the effect of approach speed on the field length from the base of the approach speed equal to 1.3 time the stall speed. The pilots creed of "10 knots for the wife and kids" appears of dubious value. For wet runways the FAA requires smaller factors on the demonstrated values as shown on Figure 46. Note that the thrust reverser has not been assumed in the performance to this point and the capability provides further margin in a normal landing. The air distances to touch down are calculated using the relationship that distance is equal to the average velocity times the time increment where the Δt during the air and transition maneuvers are determined from flight testing. The ground roll part of the landing depends on the stopping capability of the brakes expressed as a braking friction coeffient and the aerodynamic coefficients for the airplane on the ground. The 747 values are shown on Figure 47 and represent a mixture of wind tunnel and flight test data. Determination of ground roll aerodynamic parameters is difficult since you cant sort out the deceleration forces and lift is not equal to drag. Roll out tests with no braking can be used to evaluate the aero parameters, but since they are small relative to the braking forces wind tunnel data is quite often used. The major "stop" portion of the landing is the brakes and their effect is /usually expressed as shown on Figure 48. The parameter WV^2 is the kinetic energy that the brakes must absorb. Similar curves are obtained with various combinations of anti skid and partial brakes as a function of flap angle. The average speeds, times and ratios for the 747 are shown on Figure 49.

12.2.7 Conservativisms in FAA Performance

Lest you get the impression that the FAA rules provide no performance margins lets look at some of the margins built into the rules. For the takeoff portion of the flight envelope we find:

1) Minimum thrust engine assumed for calculation.
2) 50% head wind credit, 150% tailwind credit.
3) Includes climb to 35 feet at runway end.
4) Delay time included for engine failure recognition.
5) Delay time included for aborted takeoff.
6) No thrust reverser credit on stopping.

For the low speed and climb performance the following factors are available.

1) Minimum thrust engine assumed for calculation.
2) Minimum climb gradients are prescribed.
3) Testing conducted at most adverse c.g. condition.

The landing, by virtue of the inaccuracy of the maneuver contains the largest factors as follows:

1) Maximum idle thrust assumed.
2) No credit for reverse thrust.
3) Delay time included for braking.
4) Tires worn to maintenance limits for wet runway tests.
5) Arbitrary field length factors of 1.67 on dry fields and. 1.15 on wet fields.

12.3 DEVELOPMENTAL TESTING

Boeing has done a significant amount of developmental testing in recent history. Any large unknowns have usually been flight validated before a program commitment. An excellent example of this type of testing is the testing performed on the 367-80 "dash eighty" airplane prior to the 727 development. There was concern early in the program about the aft nacelle placement and the engines ability to handle the wing induced flows and wakes. An engine was mounted on the aft body of the "dash eighty" with a stove pipe arrangment to get the exhaust up and away from the stabilizer. This testing proved that the engines could survive quite well on the aft body and in fact this location offered some benefits in terms of flow angularity. A more recent development cycle occured on the 727-300 program where management was concerned about the significant performance benefits claimed for the 727-300 revised cruise and low speed configuration. Fiugre 50 and 51 show sections of the 727 wing undergoing modification in the flight test shops. The cruise wing modification was added to the leading edge ahead of the front spar and flight test were conducted. A baseline test was conducted prior to the installation of the 727-300 leading edge to provide a solid basis for comparison. The results of the testing are shown on Figure 52 and 53 indicating large improvements in cruise drag and fuel mileage particularly in the higher W/δ range. This testing was accomplished before serious guarantee negotiation were started with the prospective customers, and gave us a very credible position for our claims. The change in initial buffet envelope for the modification is shown on Figure 54, again indicating substantial improvements. To be certain that the wing was well understood pressure belts were added and tested as shown on Figure 55., Similar testing was performed with the low speed 727-300 configuration and only poor timing stopped the further development of the airplane.

12.4 INSTRUMENTATION

Instrumentation capabilities have improved dramatically in recent years. The inception of the mini computers and reliable, accurate inertial navigation systems have given us an ability to do not only more accurate testing, but give better on board visibility that enables rapid assessment and adjustment of the testing as it develops. The landing and takeoff instrumentation requirements are shown on Figure 56. Most of the instrumentation is self explanatory with perhaps the exception of the APACS camera. This is basically a camera set up on a fixed station on the ground that takes pictures of some target on the airplane. This is usually a large cross painted near the wing. The camera is calibrated and from pictures the true ground velocity, acceleration and altitudes can be obtained. The stall speed testing requirements are shown on Fiugre 57. The trailing cone was used for the complete envelope of the 747 and will probably become the standard static pressure source for all flight conditions. The pilots seat track accelerometer is used to determine buffet levels. Previous flight testing has relied on the subjective "pilot callout" method for inital buffet determination. Correlation with accelerometer data revealed that the "pilot callout" corresponded to a incremental load factor of .1 g's, so consequently the .1g standard at the pilots seat was adopted as the standard measure for initial buffet. This eliminated scatter in the buffet data and also the "pilots seat" tolerance. The cruise performance instrumentation requirements are shown on Figure 58. The inertial navigation system (INS) and the information it yields has done much to improve the tolerance in cruise drag testing. Using the INS the test engineer on board can detect unsteadly conditions and take data only in stable air. The ability to perform drag testing during accelerating/decelerating conditions also rests on the INS and its capabilities. On board minicomputers are now available with keyboard controls, CRT's and printers that produce real time flight test data. Programs exist for takeoffs, refuse takeoffs, landings, drag and miles per pound and stall speed calculations. This "on line" capability enables rapid assessment of test goals and can reduce testing requirements.

ALLOWABLE STATIC PRESSURE
POSITION ERROR

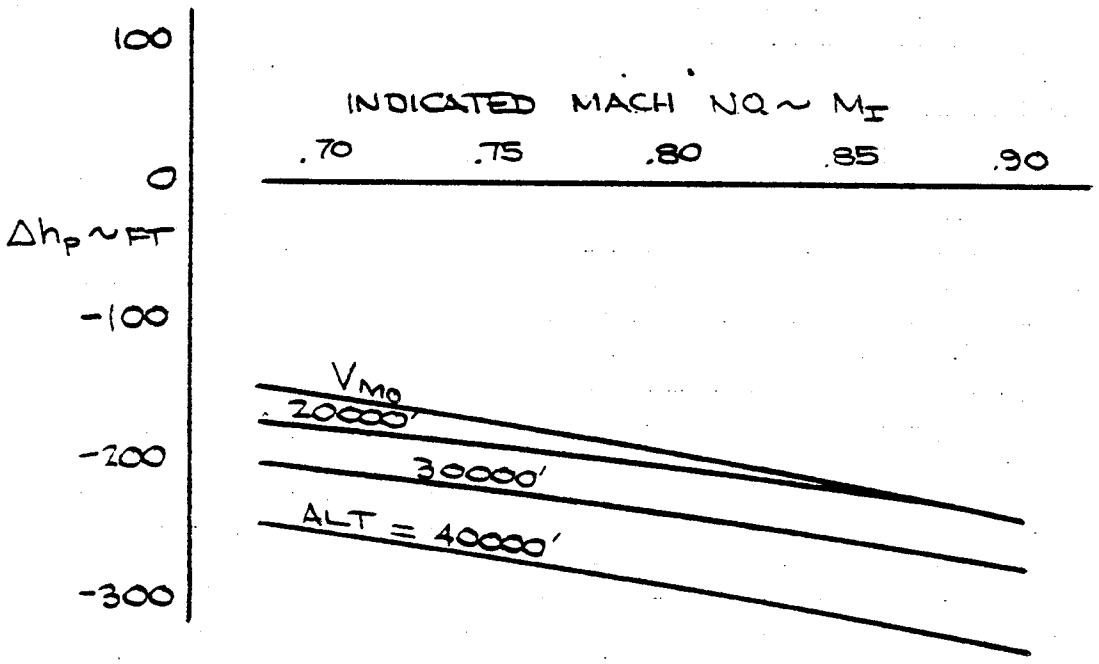

P12.13

FIGURE 1

777

727-200
QB536

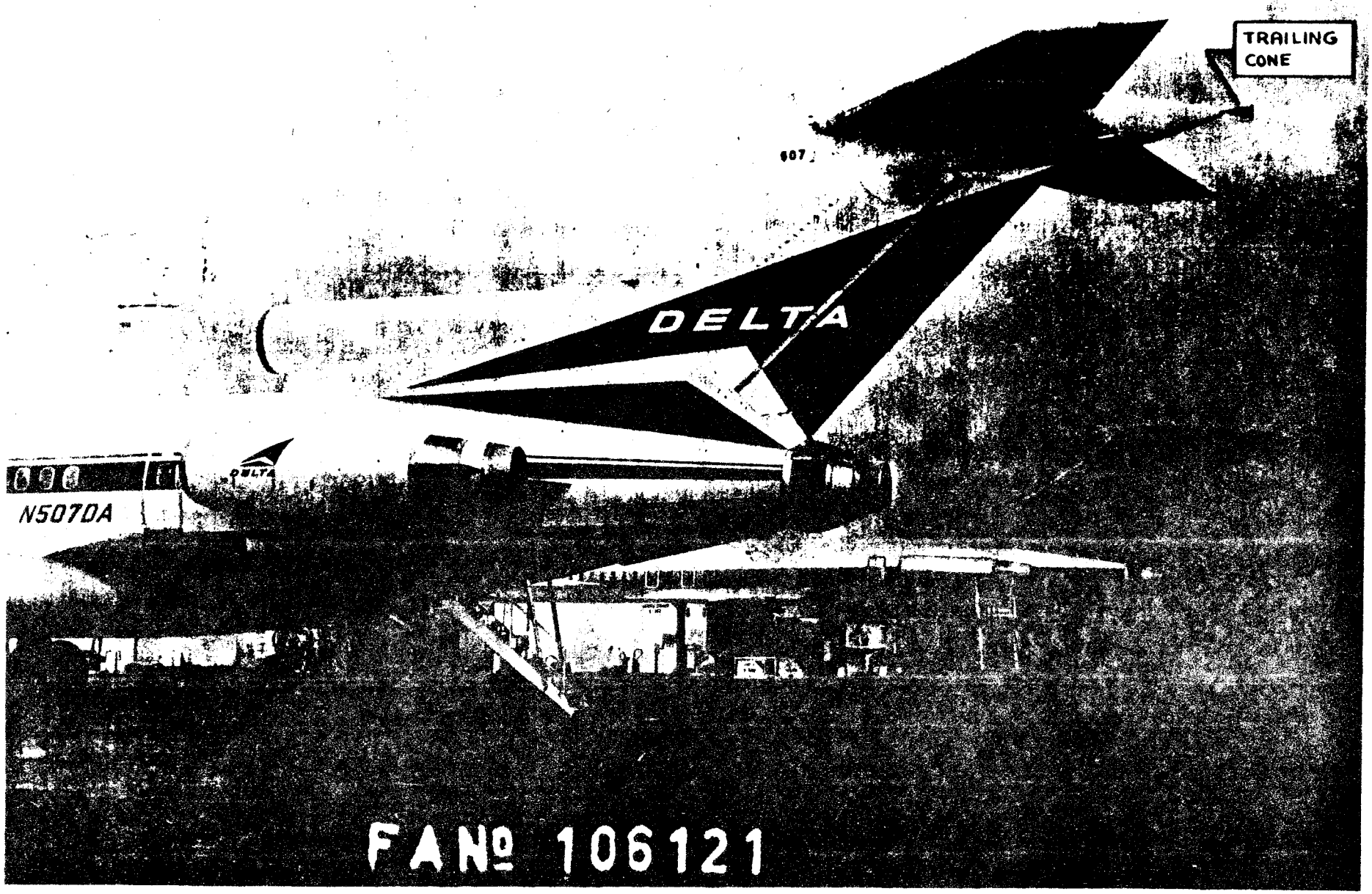

BOEING NO FIGURE 2
PAGE 12.14

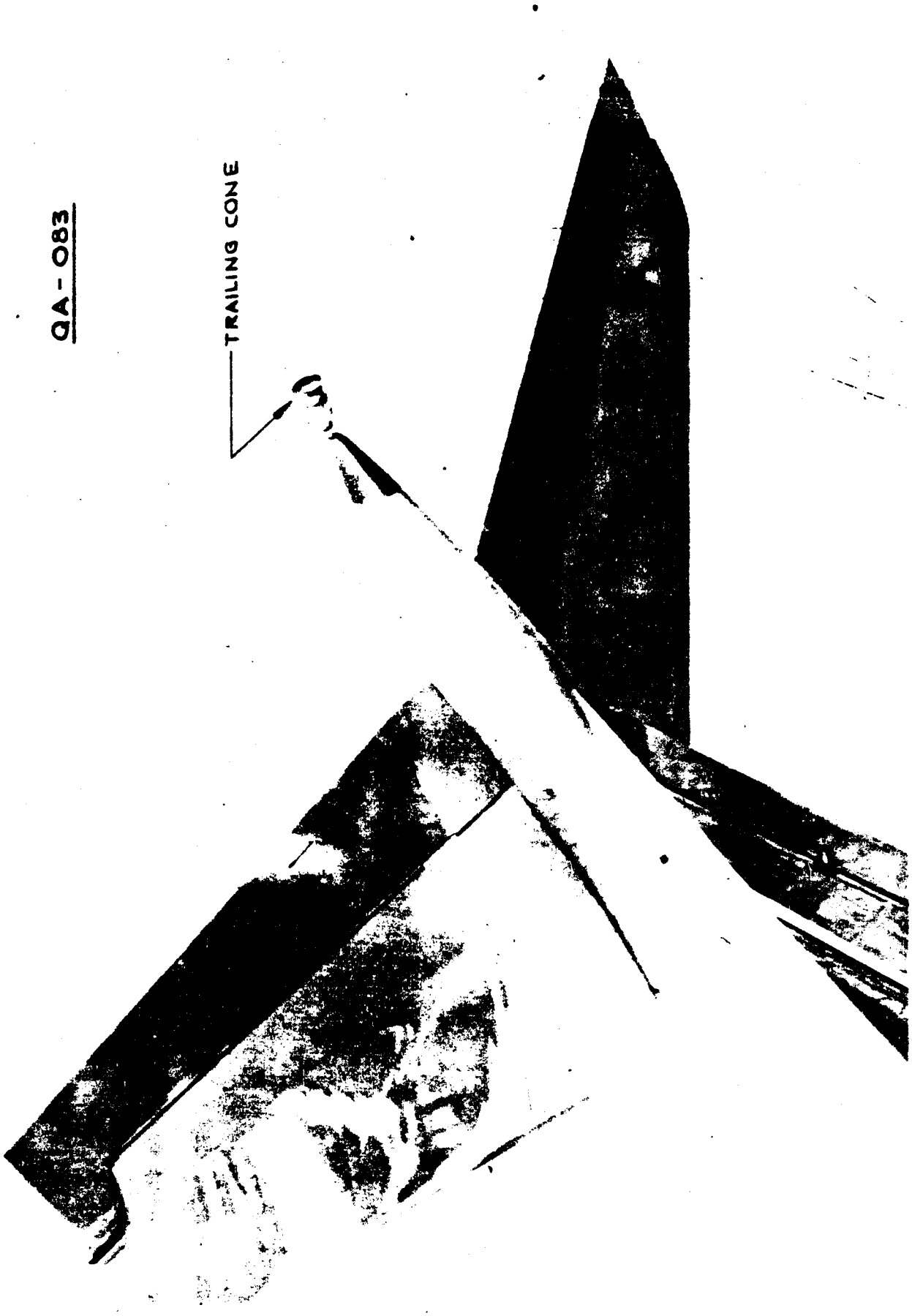
QA-083
TRAILING CONE

SYM	W/S $\times 10^{-6}$ LBS	GW LBS	ALTITUDE FT
○	.450	145,600	28,380
□	.600	149,100	34,000
◇	.700	151,200	36,880
△	.750	160,000	36,850

WING SECTION 56
PARTIALLY SHADED SYM
DENOTE 362-02
SHADED SYM 362-03
FLAGGED SYM 362-04
PART SHADE & FLAG 362-05
SHADED & FLAGGED 362-07

NOTE: UNSHADED SYMBOLS DENOTE BASELINE
TEST 361-06

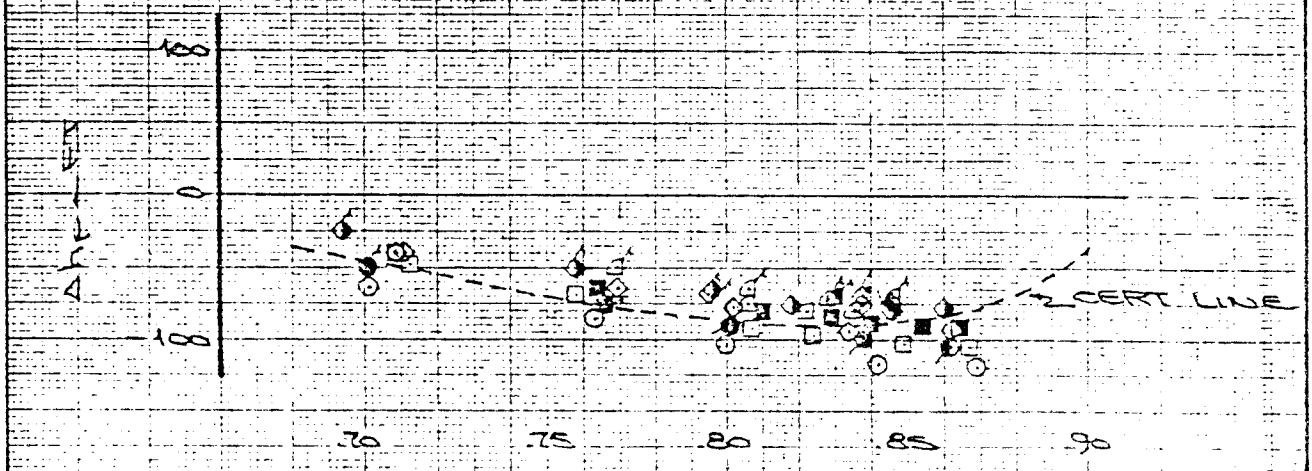

FIGURE 4

CALC	VL	12/17/75	REVISED	DATE	COPILOT'S AIRSPEED SYSTEM CALIBRATION
CHECK	J.A.S.C.	1-24-76			
APR					
APR					THE BOEING COMPANY

727-100 E2

PAGE 12.16

Certified Field Length

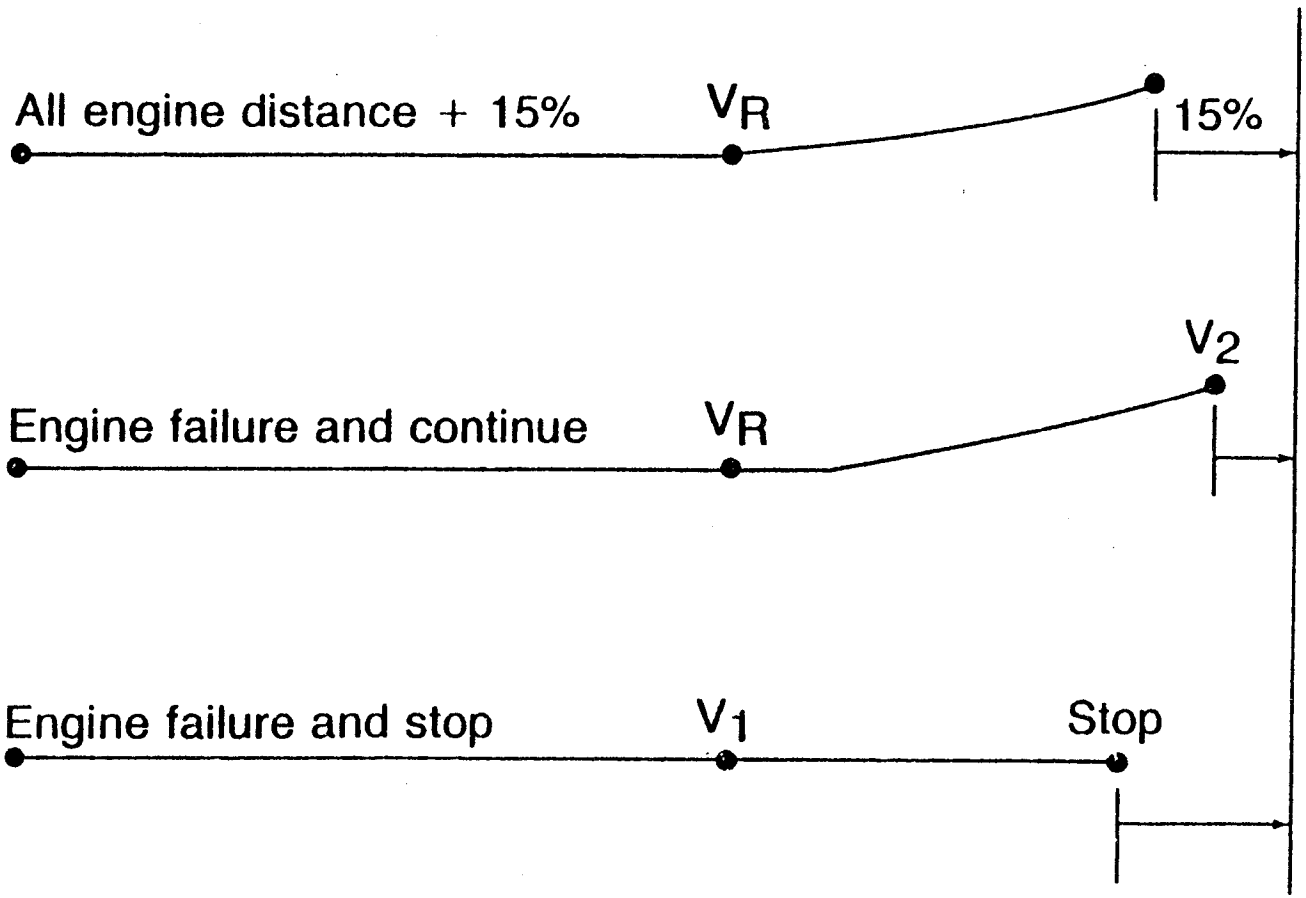

P 12.17

FIGURE 5

781

727-200 C.A.R. Takeoff Field Length

Takeoff at 170 000 lb
15° flaps
84° F sea level
Auto bleed and engine fail light operating

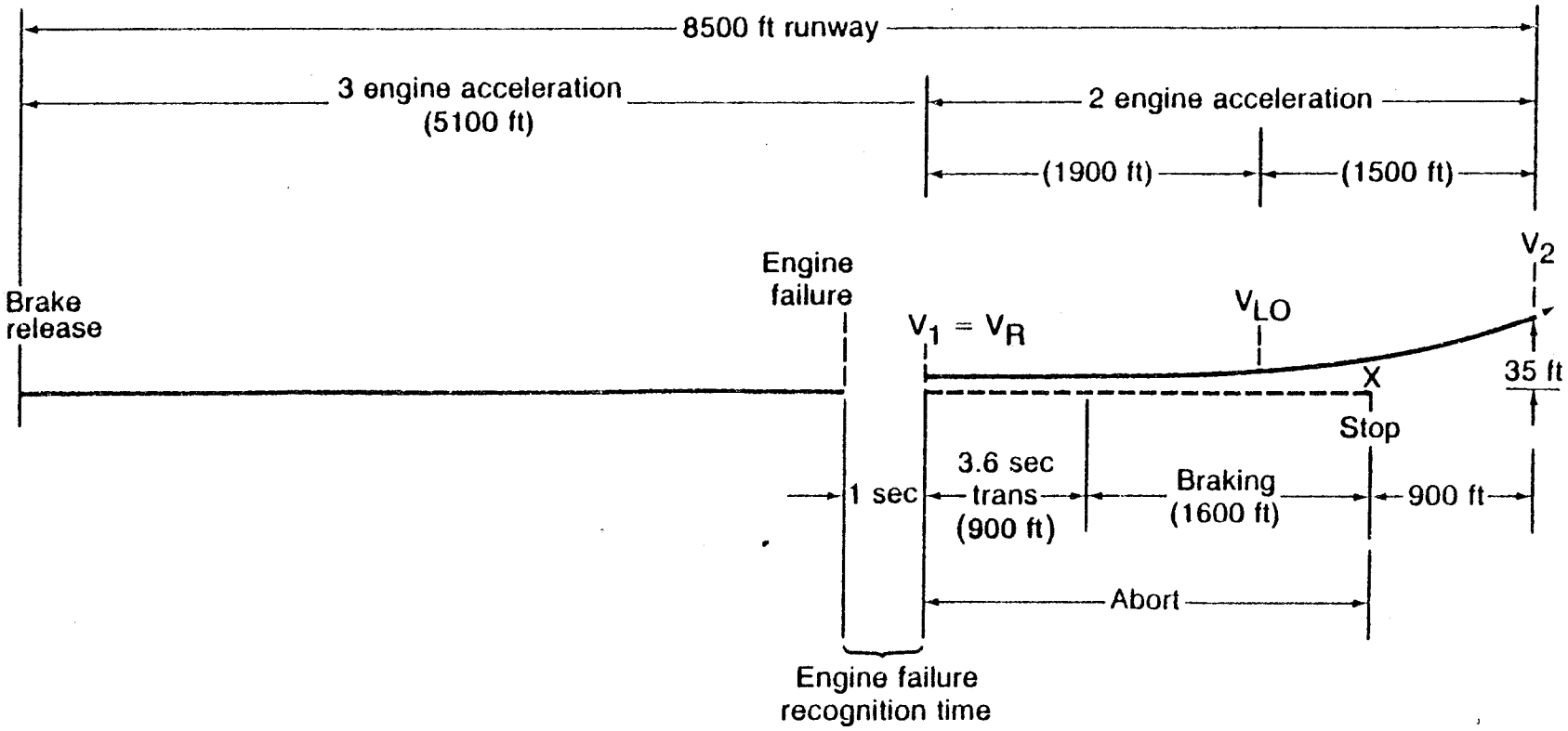

FIGURE 6
P12.18

Late Rotation

Weight, 163 000 lb
Altitude, 1000 ft
Temperature, 60° F

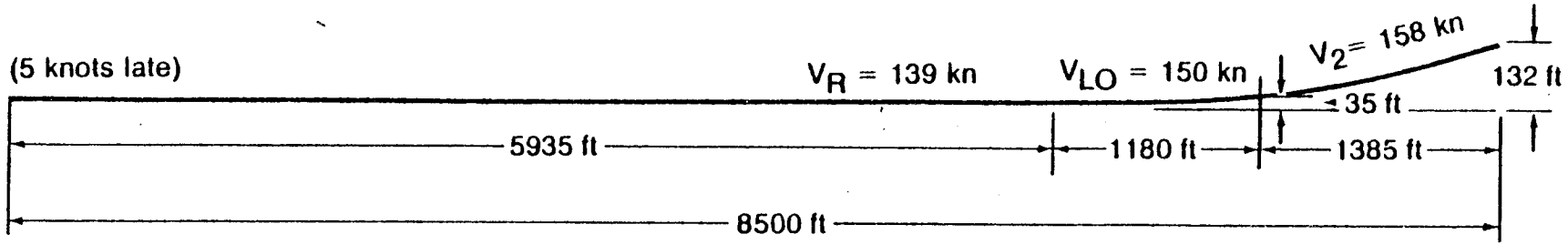

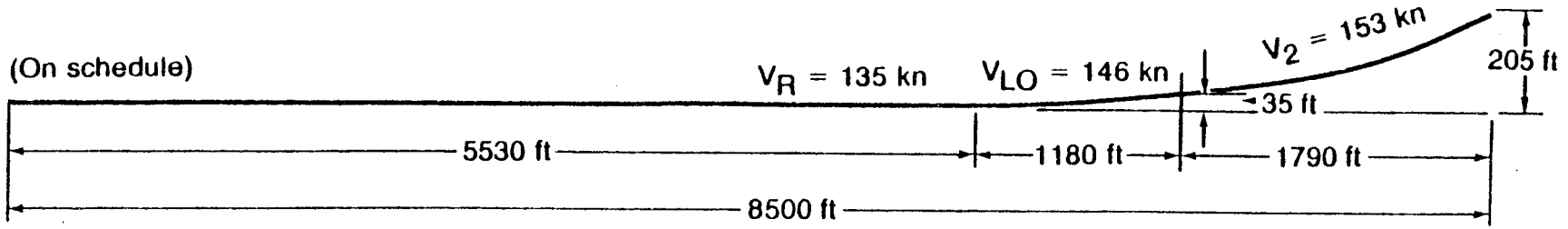

Improper Thrust Setting on Takeoff

170 000 lb
84° F
Sea level
15° flaps

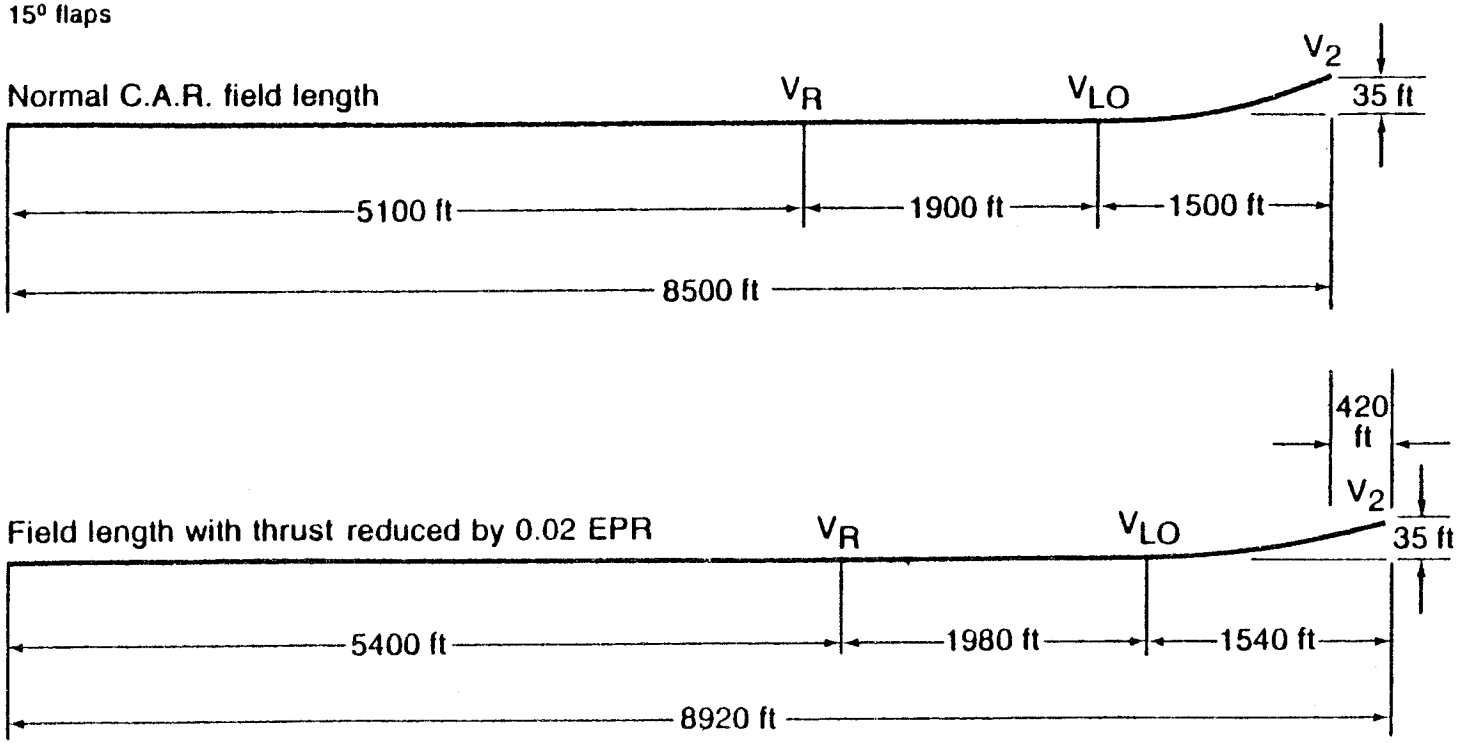

FIGURE 8
P12-20

TAKE-OFF SPEEDS ~ V_{MU} LIMITED

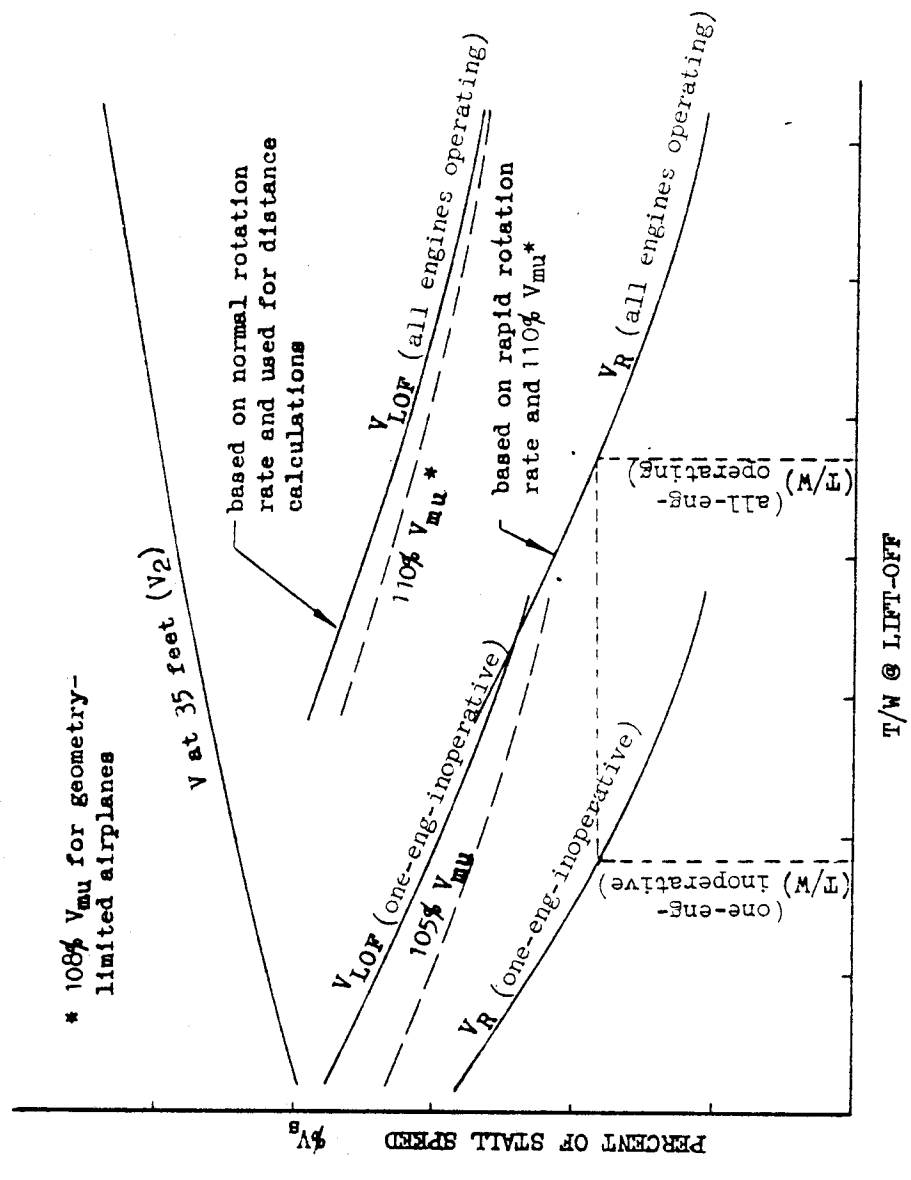

FIGURE 9

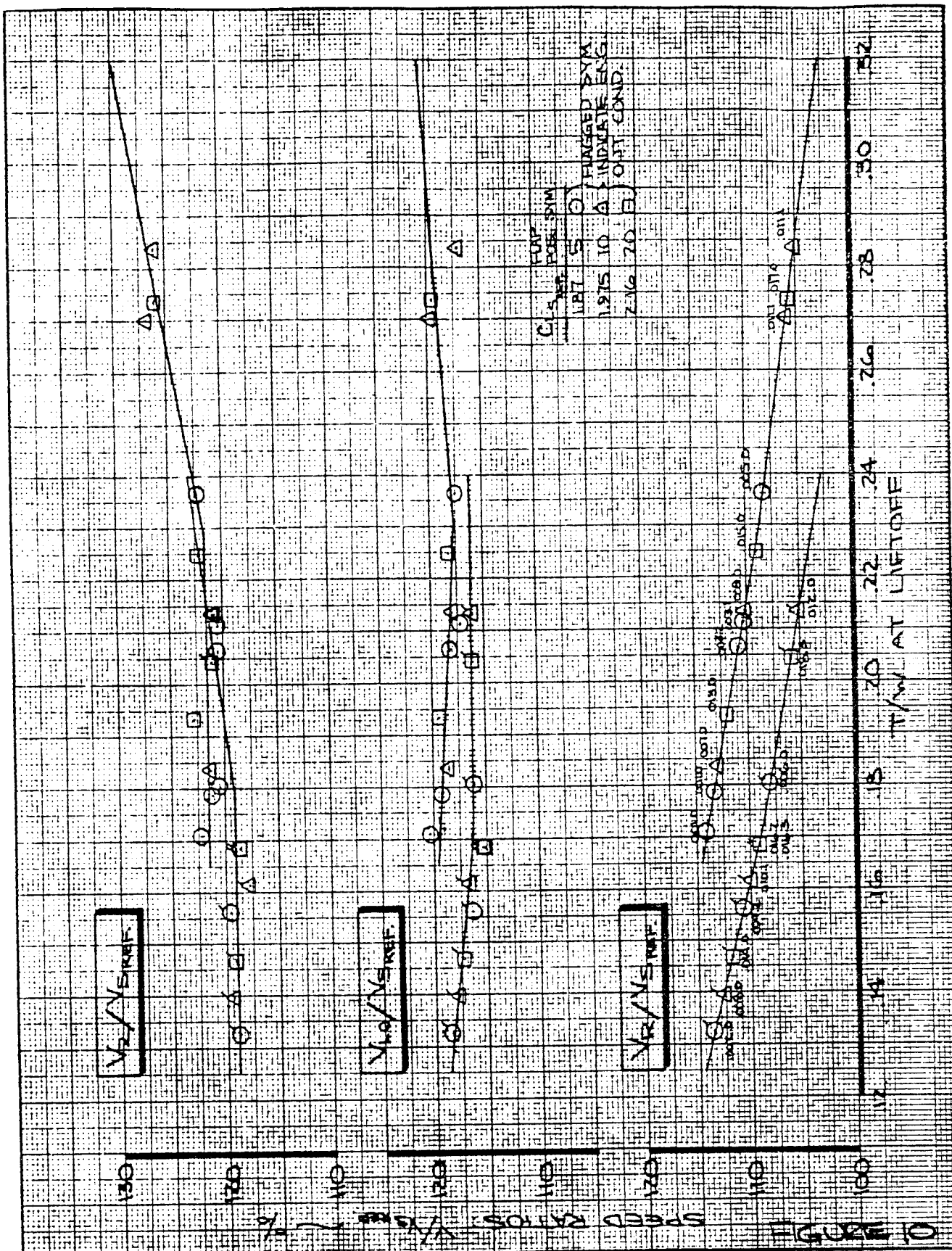

FIGURE 10

CALC	OWEN	11.14.69	REVISED	DATE	NORMAL TAKEOFF SPEEDS ALL FLAP ANGLES ~ ADJUSTED DATA (V_R BASED ON 1.10 V_{MU})
CHECK	Schneider	17Nov69			
APR	[illegible] 69-277	11/17/69			
APR					
	M. LANG	11.14.69			THE BOEING COMPANY

747

PAGE 12.22

AD 461 C-R4

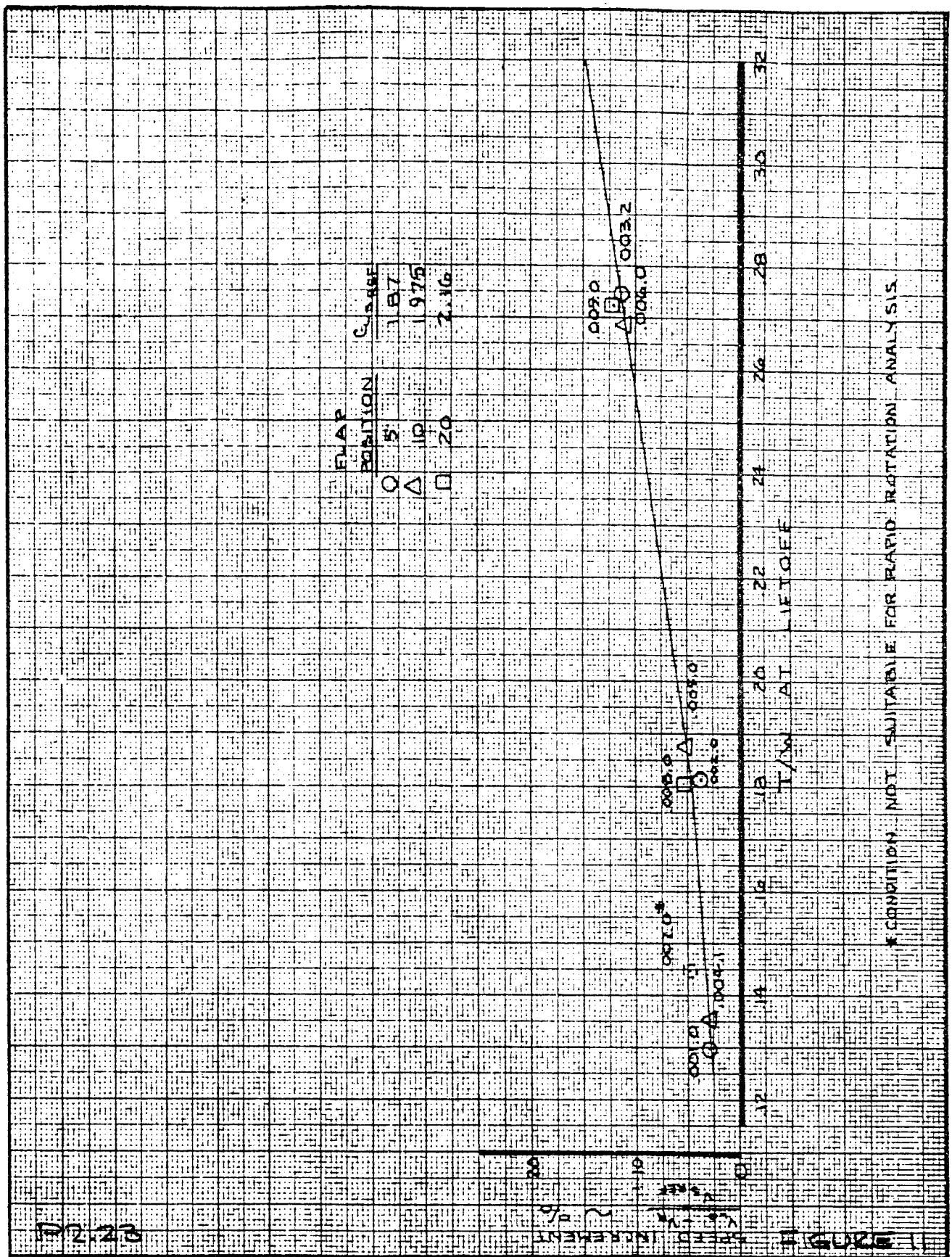

FIGURE 11

D2-23

CALC	OWEN	11/7/69	REVISED	DATE	RAPID ROTATION SPEED INCREMENT ALL FLAP ANGLES	747
CHECK	Schneider	11/11/69				
APR	[illegible]	11/11/69				
APR					THE BOEING COMPANY	PAGE

AD 461 C-R4

186

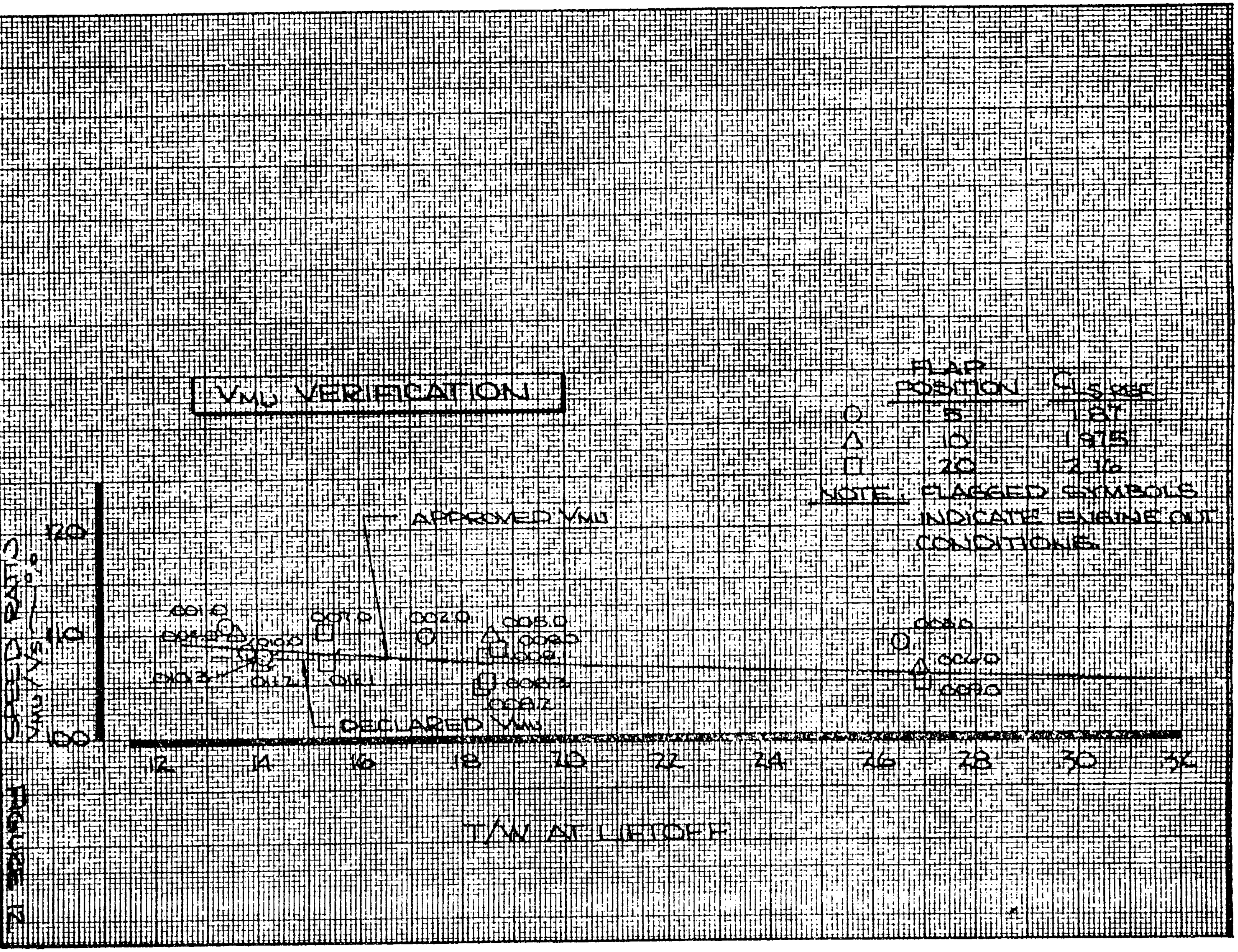

FIGURE 12

CALC	OWEN	11-8-69	REVISED	DATE
CHECK	Schneider	8 Nov 69		
APR	PFS LA-277	11-8-69		
APR				
INK	NELSON	11-8-69		

AD 461 C-R4

MINIMUM UNSTICK SPEEDS

THE BOEING COMPANY

747

PAGE 12.24

787

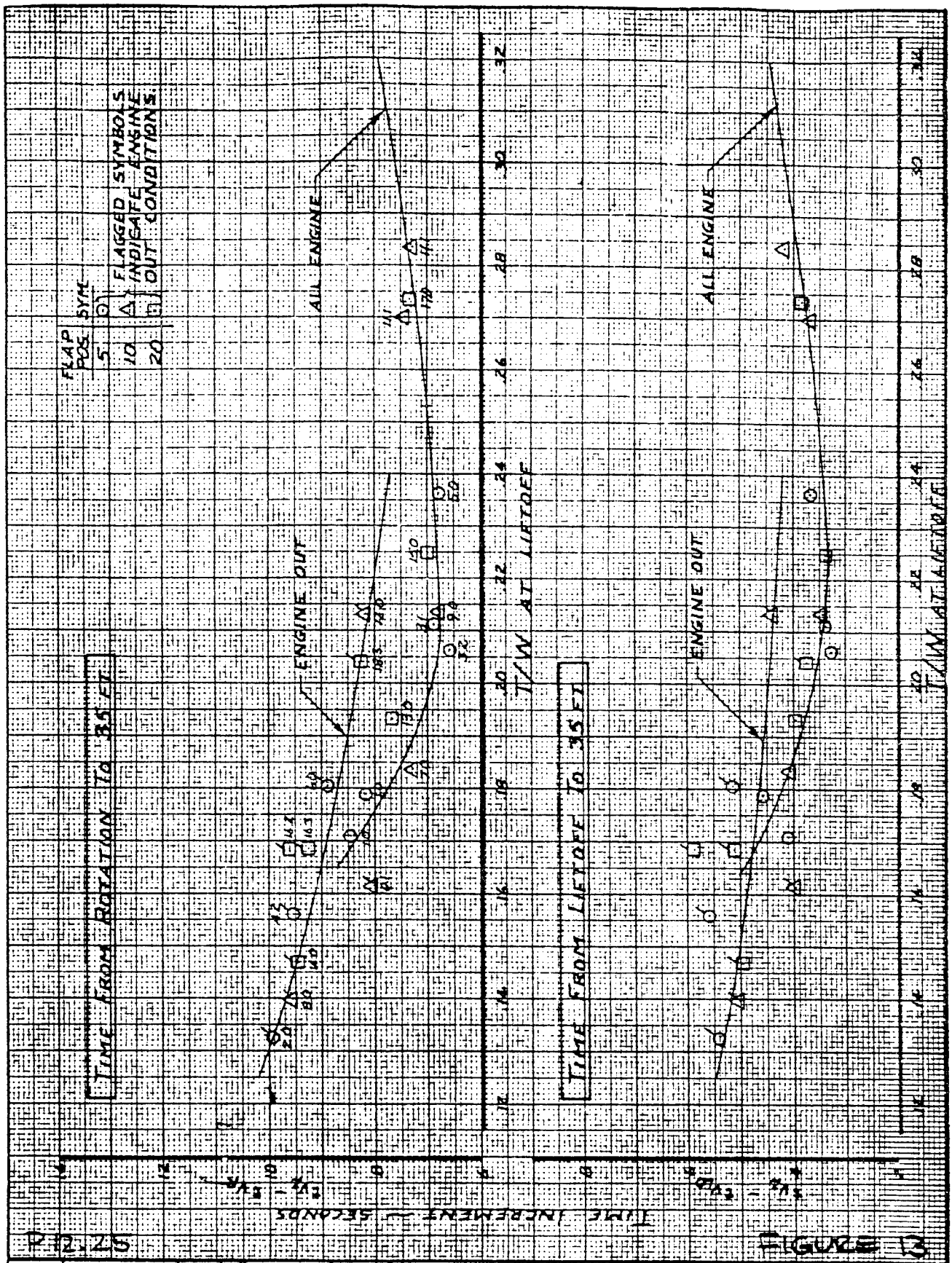

FIGURE 13

P12.20

CALC	OWEN	11/7/69	REVISED	DATE	TAKEOFF TIMES ALL FLAP POSITIONS
CHECK	T JOHNSON	11/11/69	OWEN	11-14-69	747
APR	T.J. Johnson	11/14/69			
APR					
	D. MILES	11/18/69			THE BOEING COMPANY

PAGE

AD 461 C-R4

J18-047

TAKEOFF
GROUND ROLL PARAMETERS
JT9D-3A/-7/-7A ENGINES

Spoilers	Flap	C_L	4 Engine C_D	4 Engine $C_D - \mu C_L$	3 Engine C_D	3 Engine $C_D - \mu C_L$
Spoilers Down	5	.225	.0481	.0450	.0615	.0584
	10	.355	.0460	.0410	.0595	.0545
	20	.615	.0546	.0460	.0657	.0571
Inboard 20° * and Outboard 45°	10	.06			.093	.0922
	20	.235			.1070	.1037
Inboard 45° ** and Outboard 45°	10	-.031			.1100	.1104
	20	.119			.1264	.1247

$\mu_R = .014$

$\alpha_W = 1.5°$

* Original Ground Spoiler System

** Improved Ground Spoiler System

D1 4100 7740 ORIG. 8/71

FIGURE 14

REV SYM B

BOEING NO.

790

P12.27

LIFT CURVE IN GROUND EFFECT

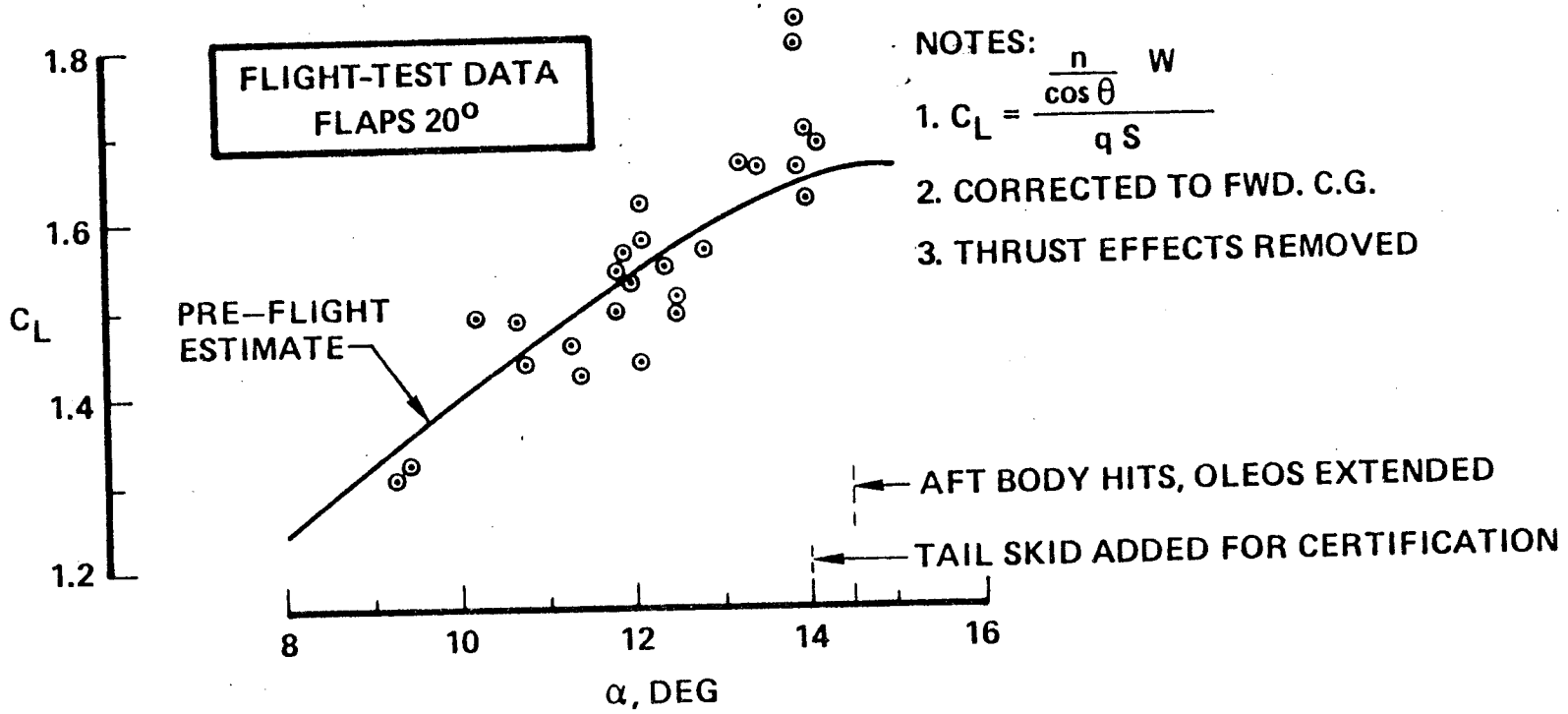

FIGURE 15

791

TWO TYPES OF STALL ENTRY RATE USED FOR STALL DYNAMICS STUDY

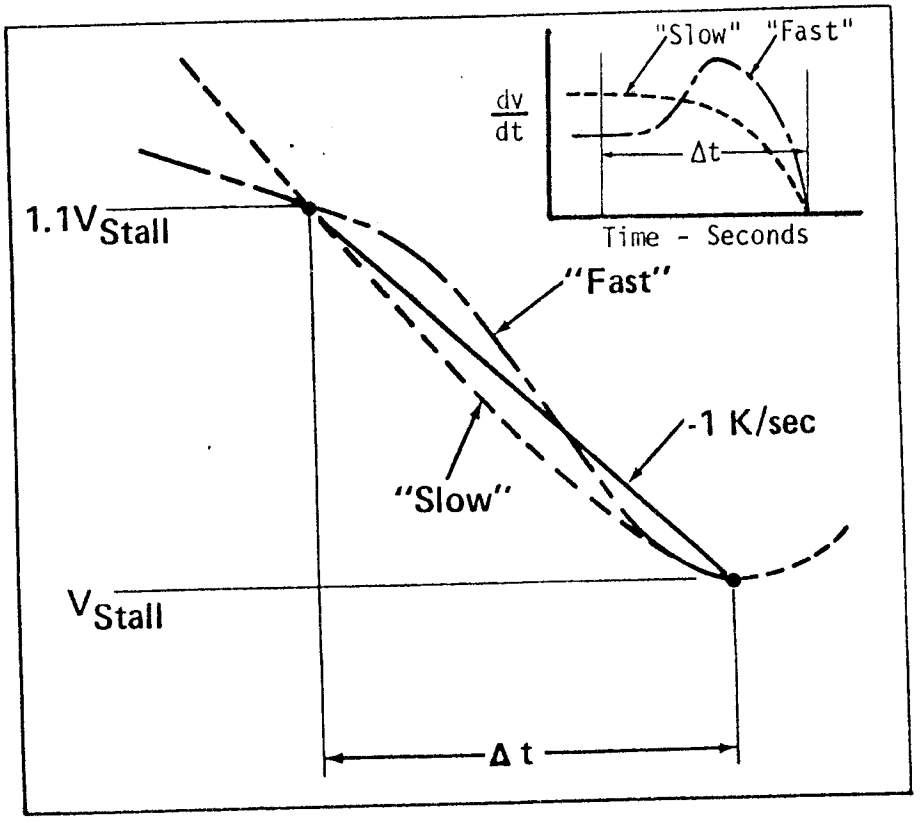

V — knots equivalent airspeed

Time — seconds

FIGURE 16
P12.28

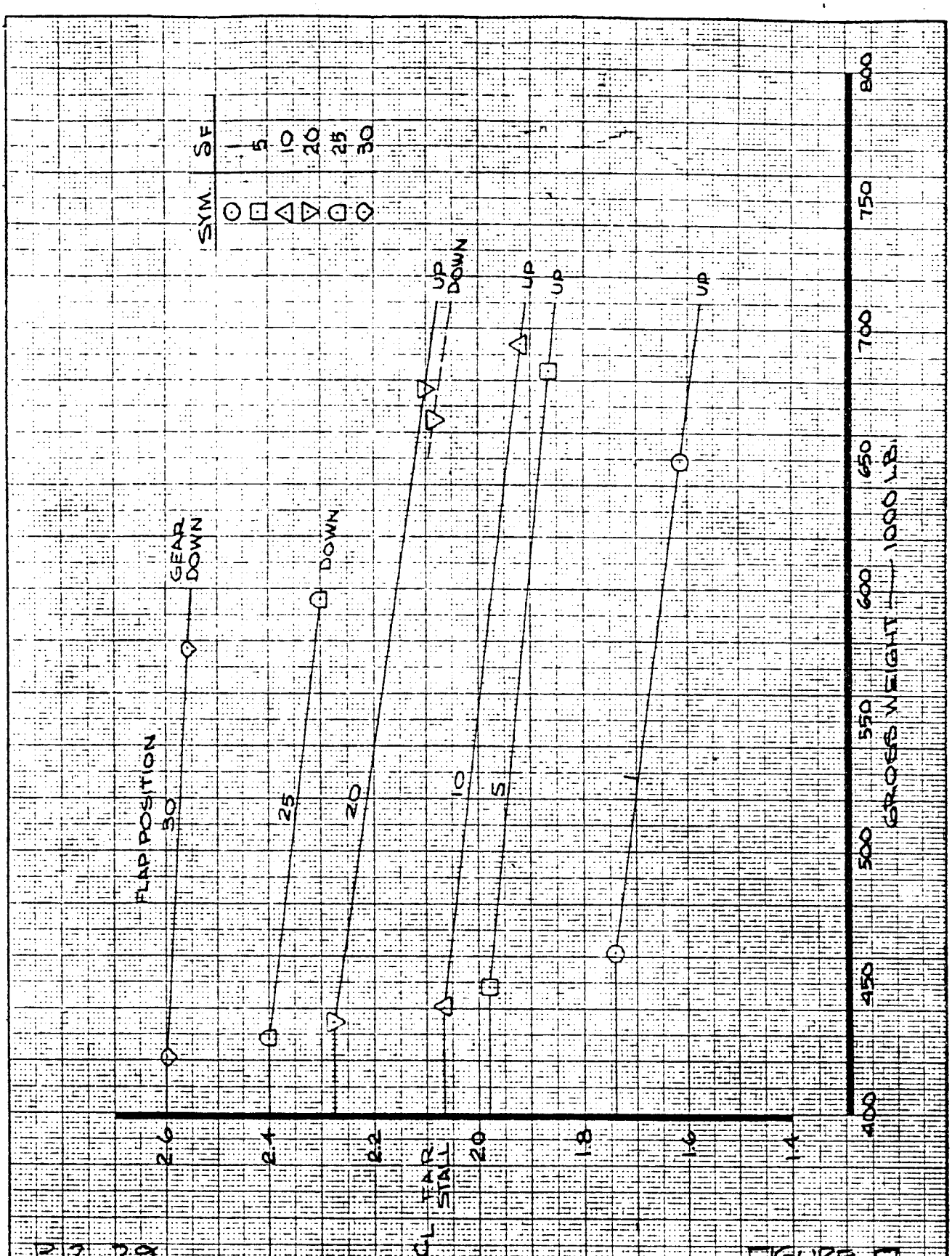

P.2.29

FIGURE F7

CALC	P.E. Hubble	9-22-69	REVISED	DATE	F.A.R. STALL C_L FWD. C.G. LIMIT
CHECK	R. LOKEN	10-1-9	P.E. Hubble	9-30-69	747-100 N93101
APR					
APR					
INK	ESKOLA	9-30-69			THE BOEING COMPANY — PAGE

AD 461 C-R4

K-E ALBANENE 1961

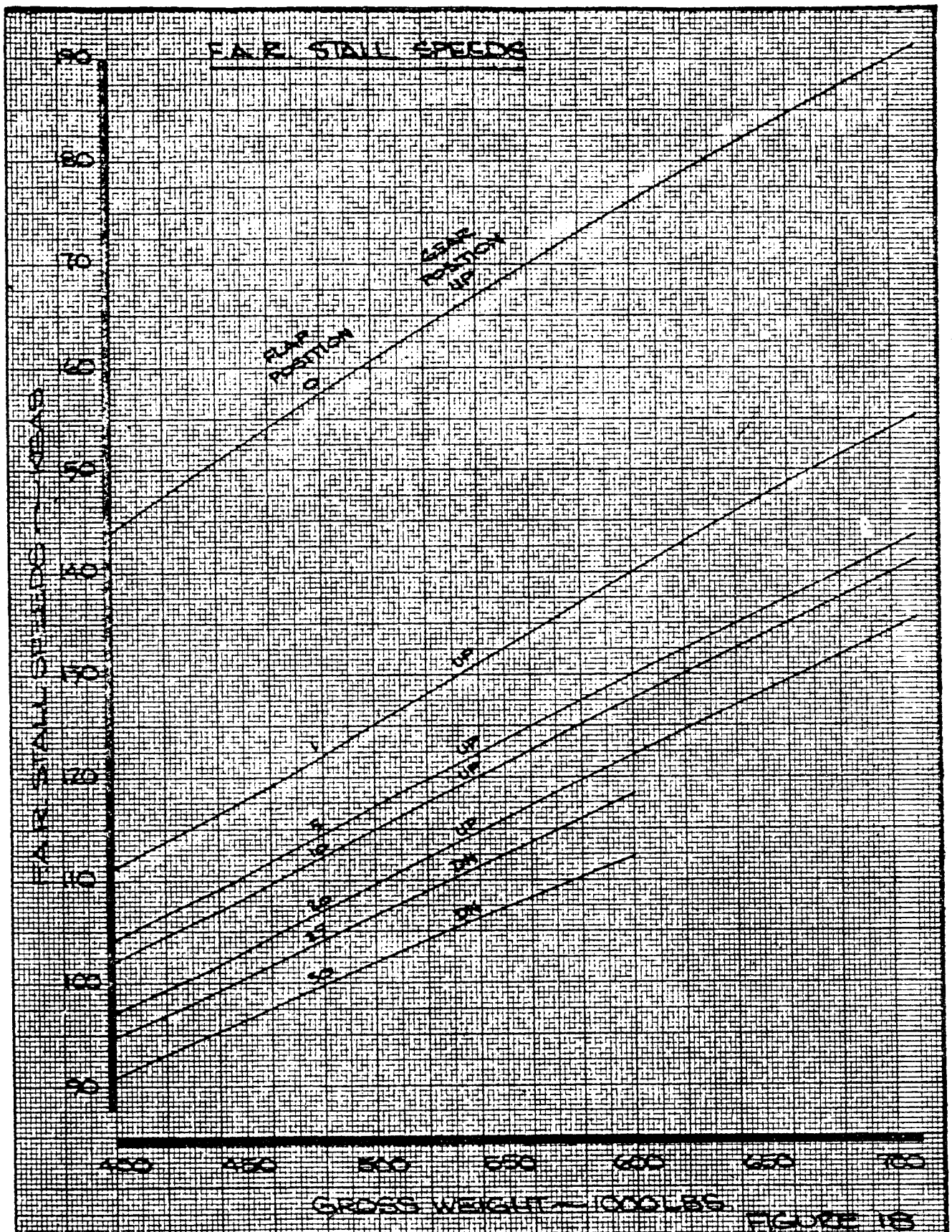

FIGURE 18

CALC	PE Hubble	9-10-69	REVISED	DATE	F.A.R. STALL SPEEDS FORWARD C.G. LIMIT	747-100 N93101
CHECK	Keith	9/19/69				
APR						
APR					THE BOEING COMPANY	PAGE 12.30
INK						

AD 461 C-R4

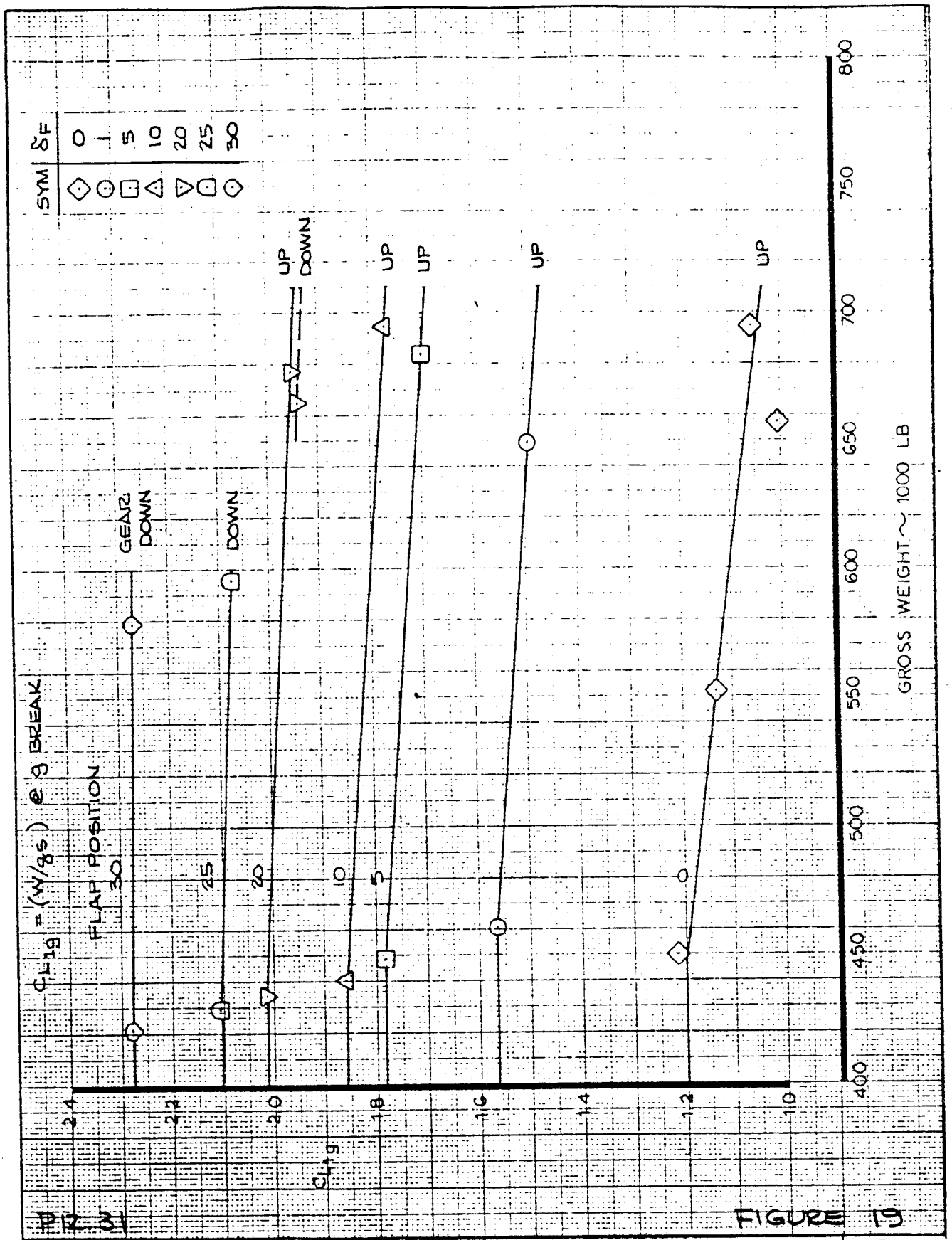

FIGURE 19

CALC	BARTON	10-20-69	REVISED	DATE	STALL CL ("1g") FWD. C.G. LIMIT
CHECK	P.E. HUBBLE	10-23-69			
APR					
APR					
TRACE	ROHNER	28 JULY 5			

747-31
N93101

THE BOEING COMPANY

PAGE

D1 4100 124 REV. 8

K-E ALBANENE 1961 TRACING PAPER

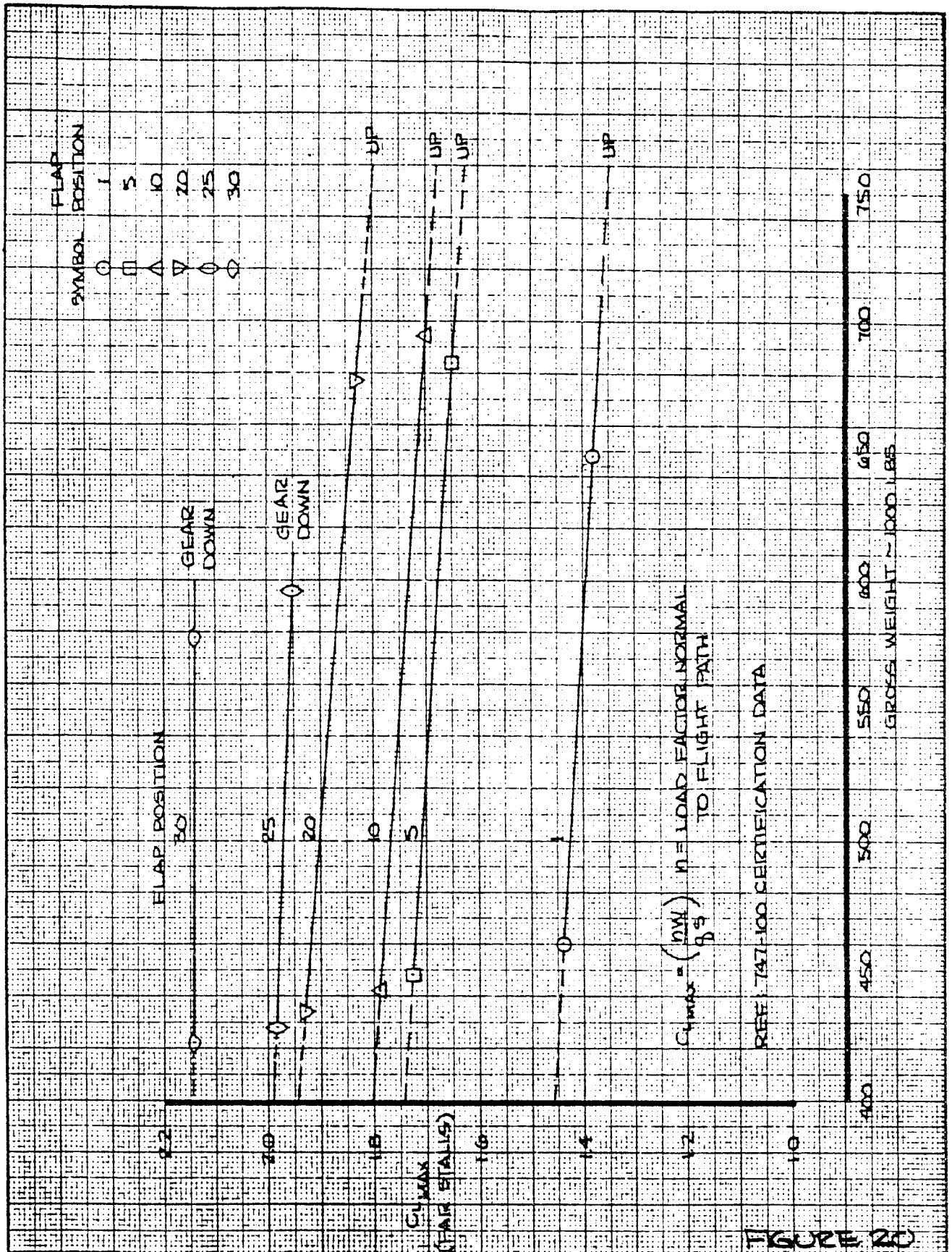

FIGURE 20

CALC	C. BARTON	12.5.69	REVISED	DATE	MAXIMUM FLIGHT LIFT COEFFICIENT CORRECTED TO 1g, FAR. ENTRY RATE, FWD CG LIMIT
CHECK	P.E. HUBBLE	12.17.69	PE HUBBLE	12.17.69	747-100
APR			C BARTON	2.6.70	
APR			REPLOT		
	BONNER	1.6.75	W. PAUL	6.26.75	THE BOEING COMPANY

PAGE 12.32

D1 4100 3241 REV. B

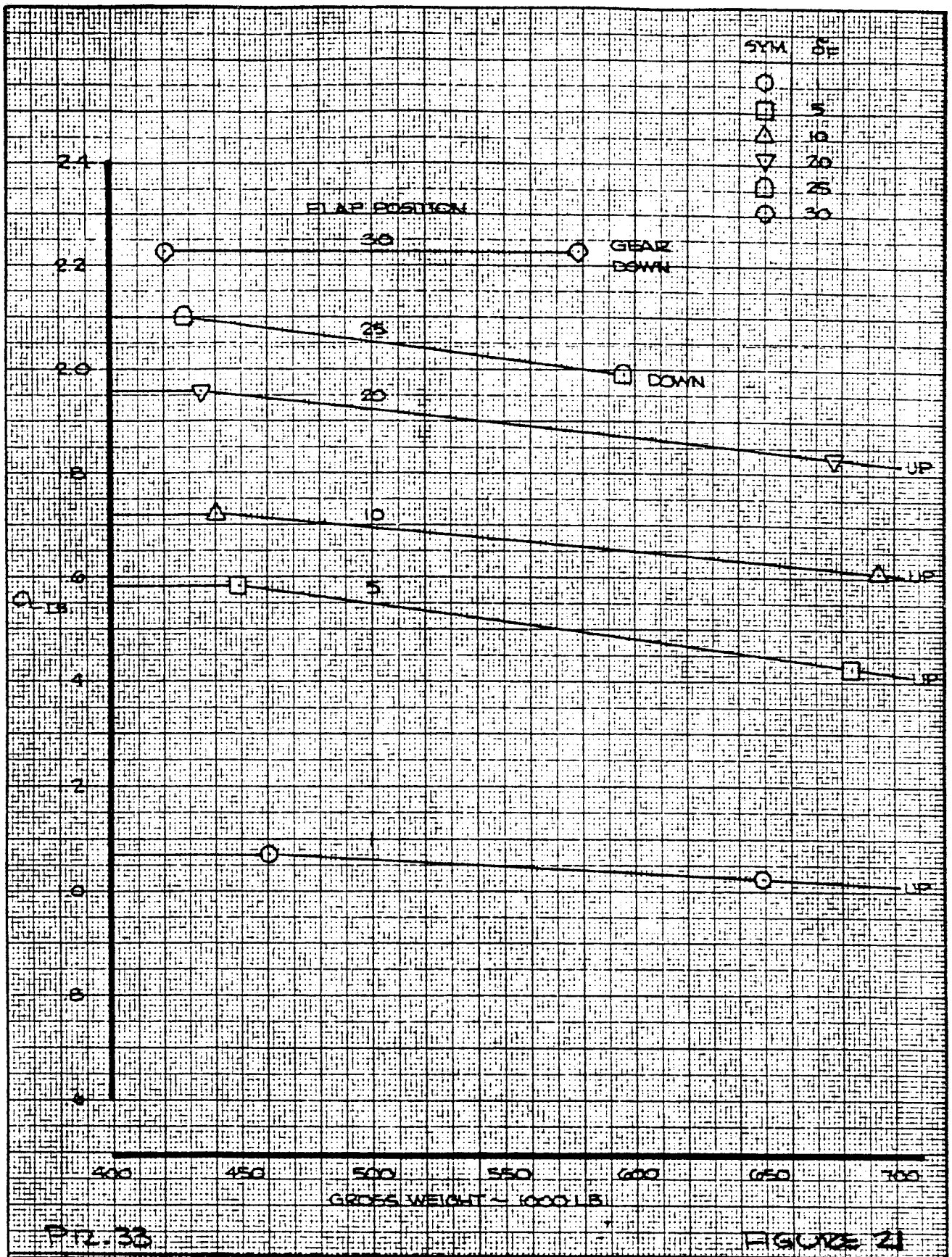

P12-33

FIGURE 21

CALC	P.E. HUBBLE	9-29-69	REVISED	DATE	INITIAL BUFFET, C_{L} I.B. FORWARD C.G. LIMIT	747-31 N93101
CHECK	C.E. BARTON	11-7-69				
APR						
APR						
TRACE	ROHNER	28JN75			THE BOEING COMPANY	PAGE

D1 4100 3240 REV B

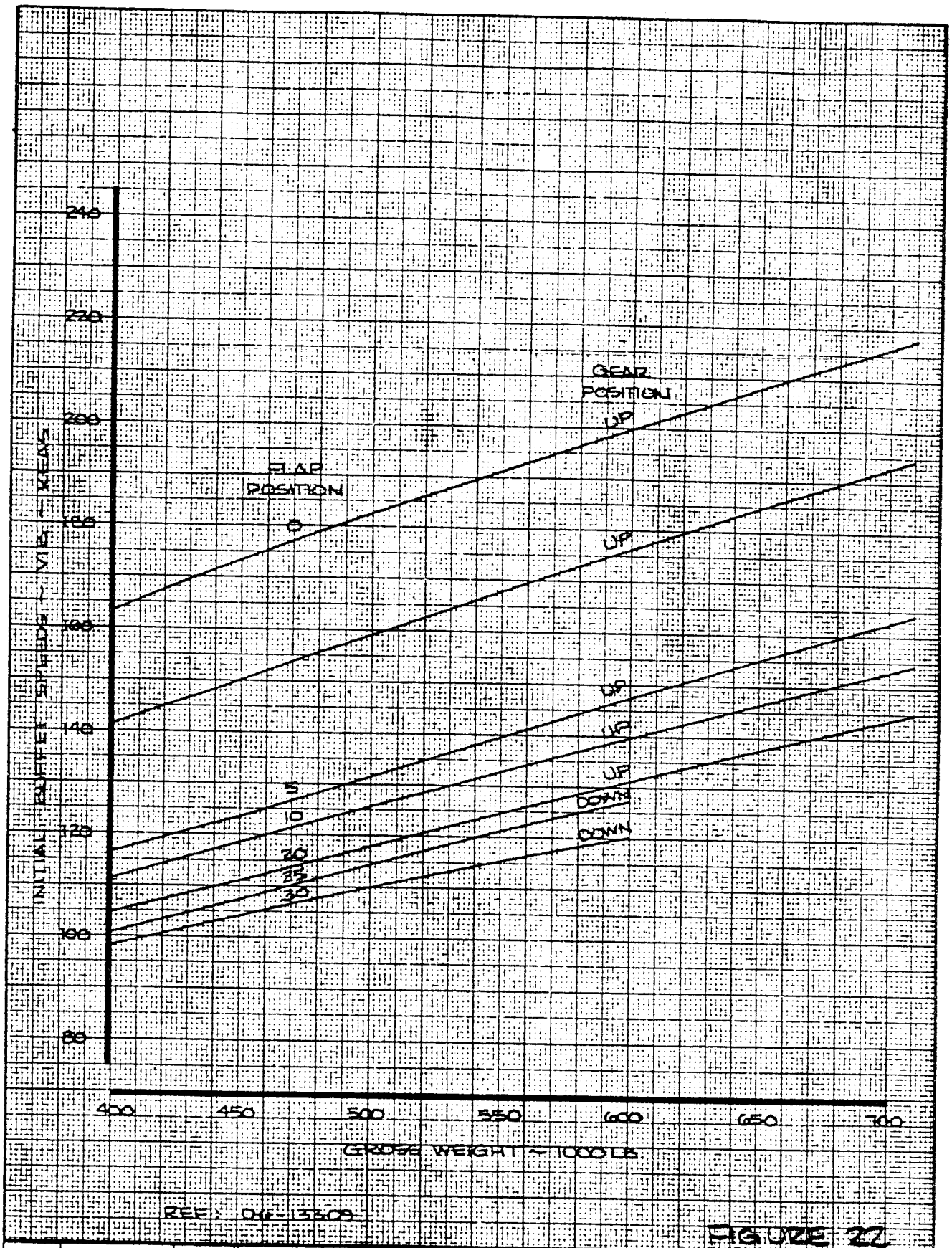

REF: D6-13509-

FIGURE 22

CALC	JWB Martein	12-2-69	REVISED	DATE	INITIAL BUFFET SPEEDS FORWARD C.G. LIMIT	747
CHECK	P.E. HUBBLE	12-3-69				
APR						
APR						
TRACE	ROHNER	28 JAN 70			THE BOEING COMPANY	PAGE 12.34

D1 4100 3240 REV. B

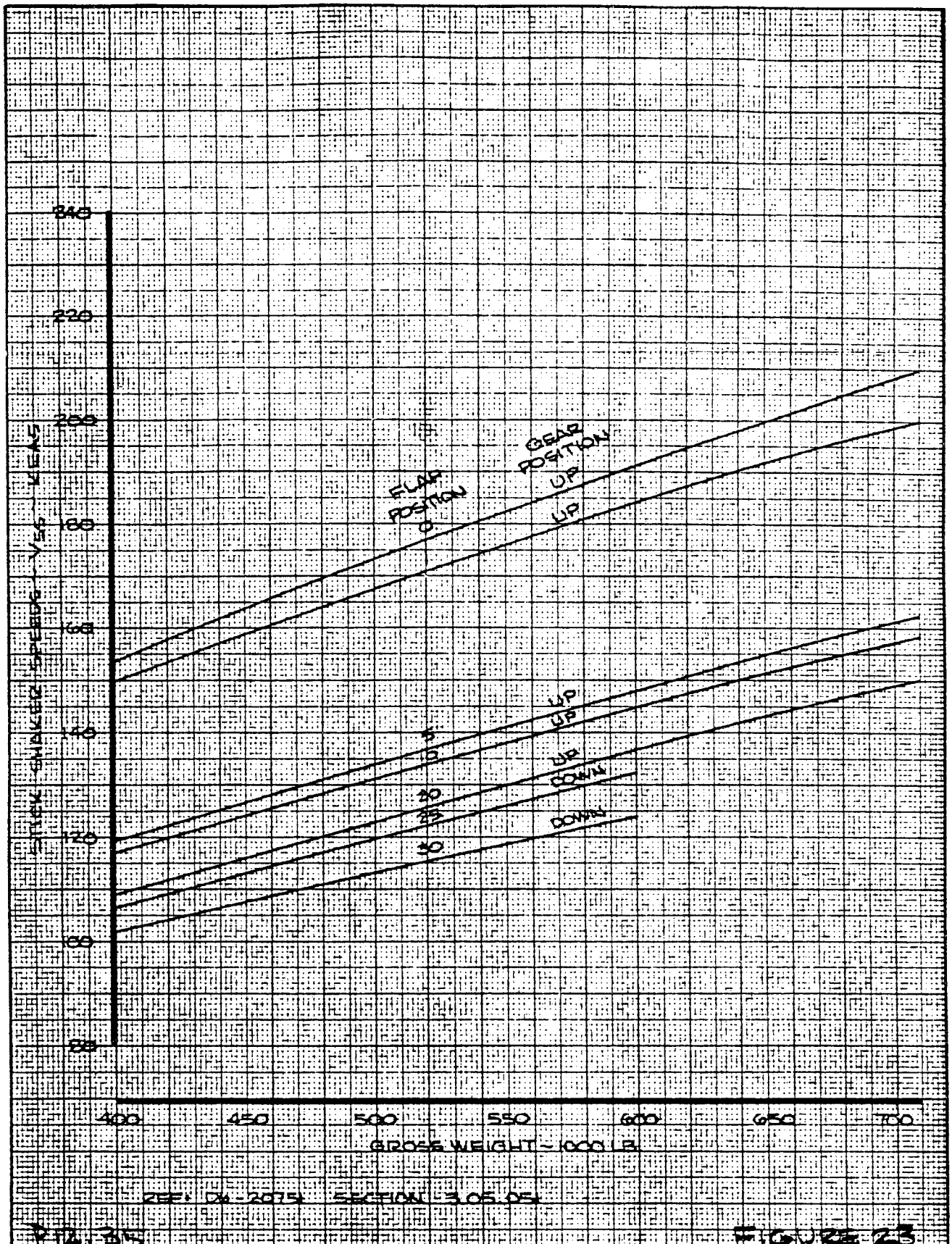

REF: D6-20754 SECTION 3.05.05

PTR-195

FIGURE 23

CALC	JWB MARTIN	9-24-69	REVISED	DATE	STALL WARNING STICK SHAKER SPEEDS (FORWARD C.G. LIMIT) — 747
CHECK	P E HUBBLE	11-24-69	JWB MARTIN	12 9 69	
APR					
APR					THE BOEING COMPANY — PAGE

01 4100 3240 REV. A

198

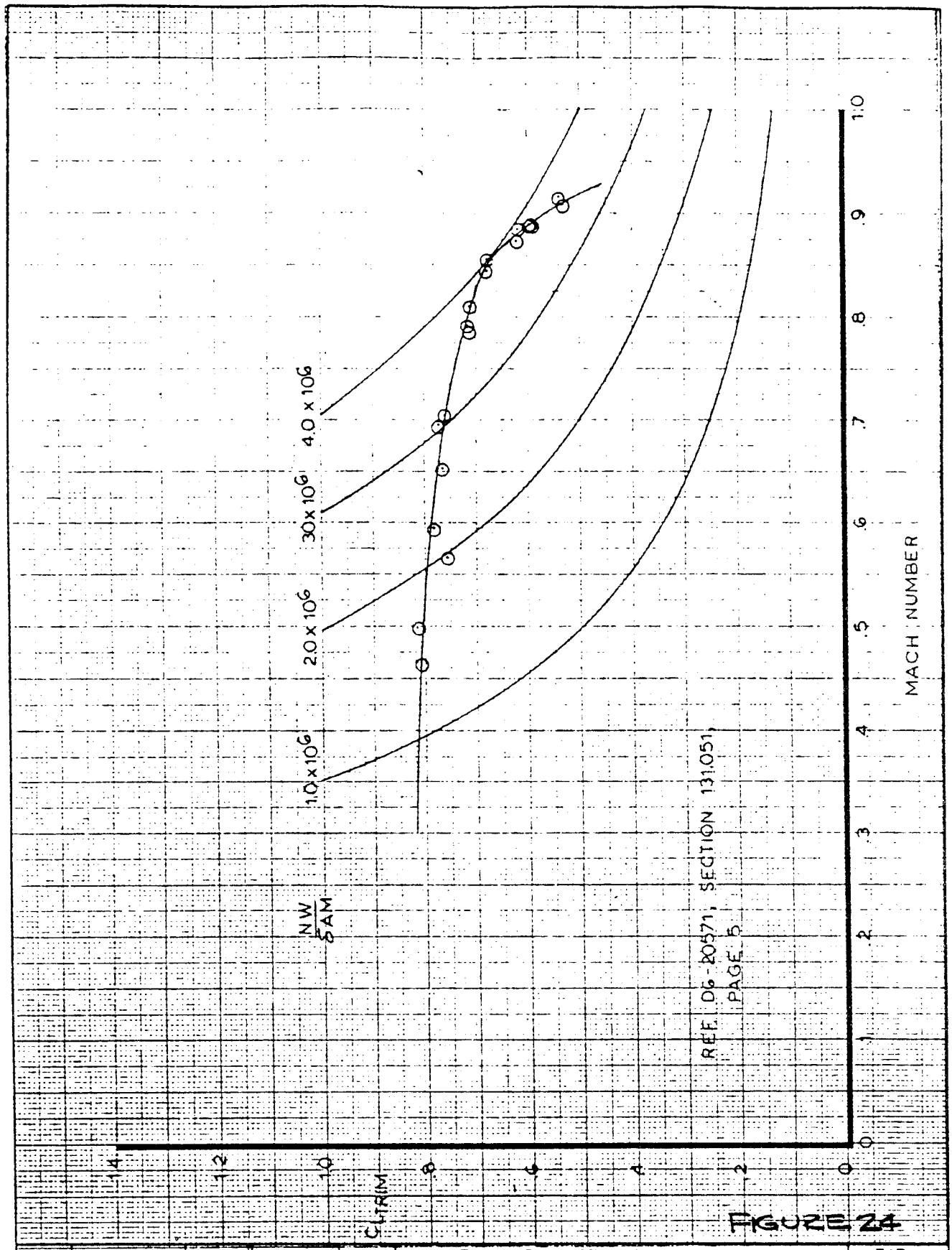

FIGURE 24

CALC	CLEM	10-6-69	REVISED	DATE	INITIAL BUFFET BOUNDARY	747 N93101
CHECK	PARYPA	10-6-69			FLAPS AND GEAR UP	
APR					TEST 5-5	
APR					THE BOEING COMPANY	PAGE 12.36
	J. MORGAN	7/23/75				

REV. B

K-E ALBANENE 1961

800

P12.37

COMPARISON OF FLIGHT F.A.R.$C_{L_{STALL}}$ AND WIND TUNNEL $C_{L_{MAX}}$

NOTES: 1) DATA POINT IS FOR HEAVIEST DEMONSTRATED WEIGHT. BAND SHOWS VARIATION WITH WEIGHT

2) ALL C_L'S ARE FOR AIRPLANE TRIMMED AT FWD C.G. LIMIT

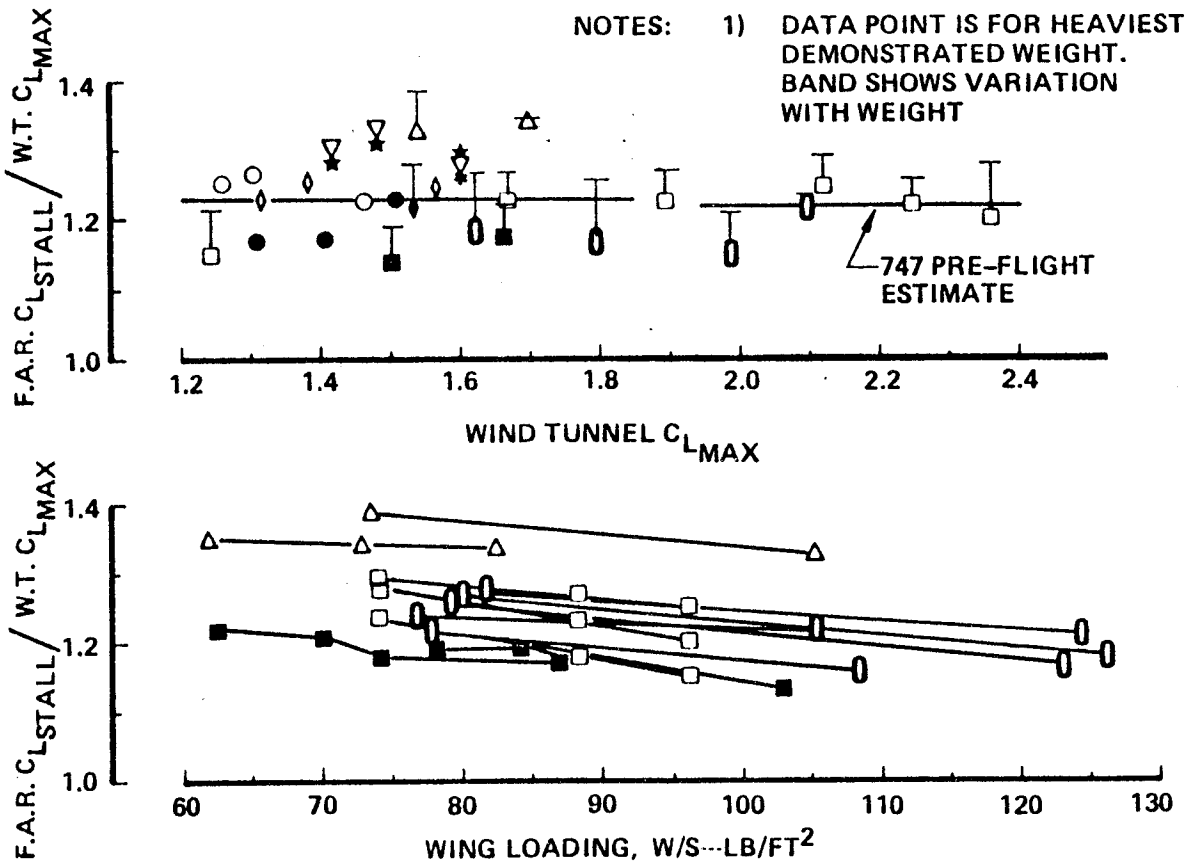

SYM	AIRPLANE
●	707–120
○	707–320
▽	720
★	720B
*	707–120B
◊	707–344
■	707–300B
△	707–300C
□	727–100
0	747

FIGURE 25

801

COMPARISON OF FLIGHT 1 g $C_{L_{STALL}}$ AND WIND TUNNEL $C_{L_{MAX}}$

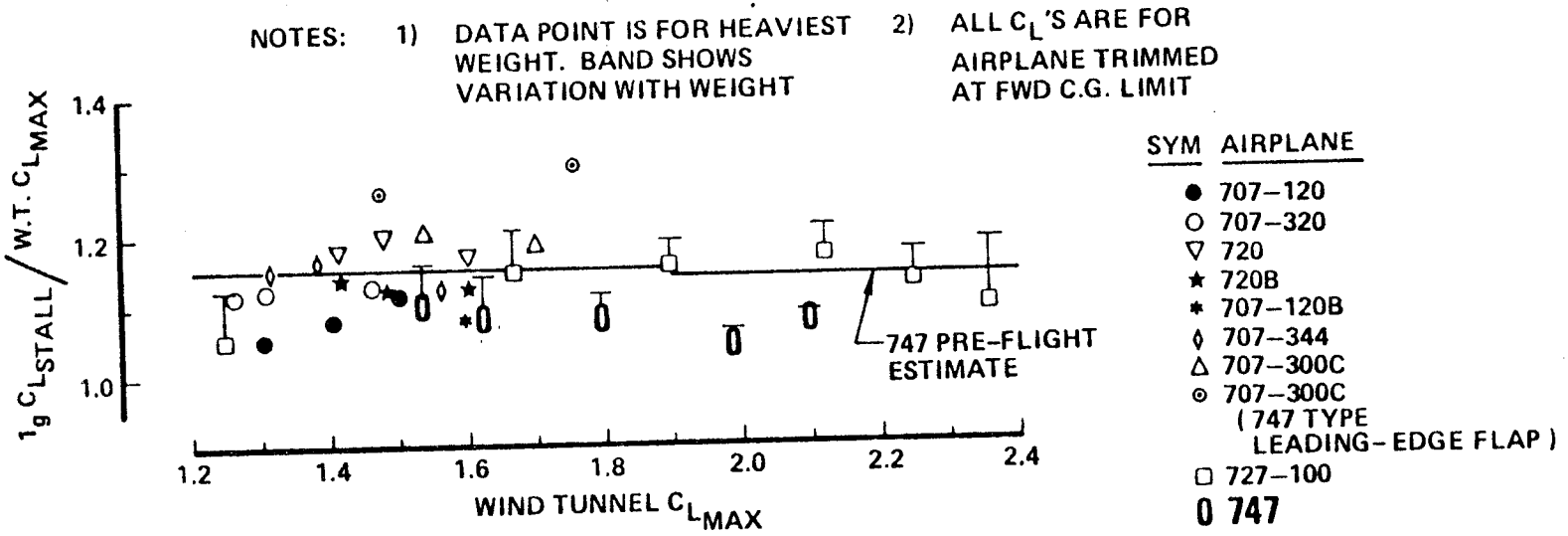

FIGURE 26
P12.38

802

P12.39

FLIGHT RECORD OF A STALL MANEUVER

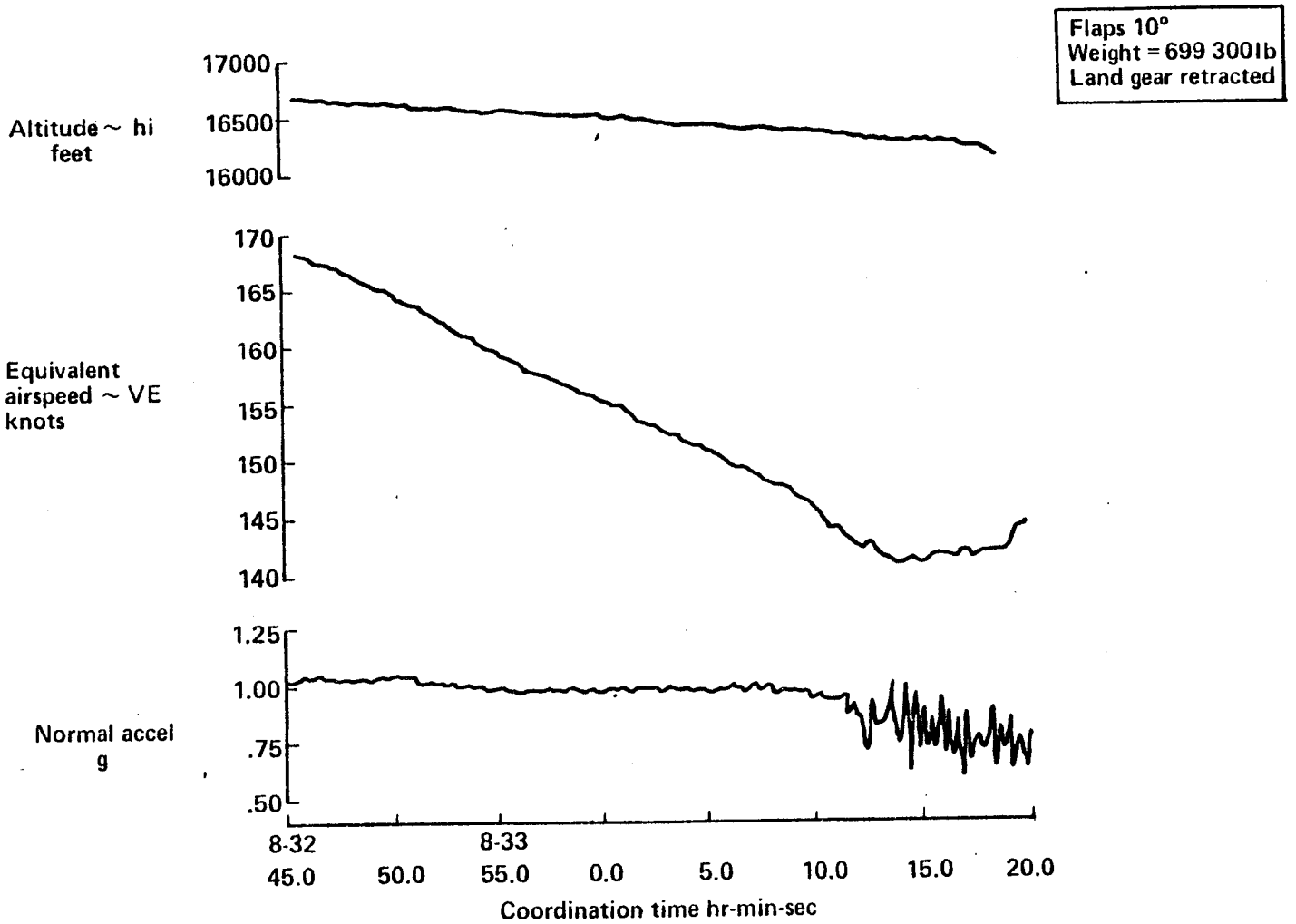

FIGURE 279

FLIGHT RECORD OF A STALL MANEUVER

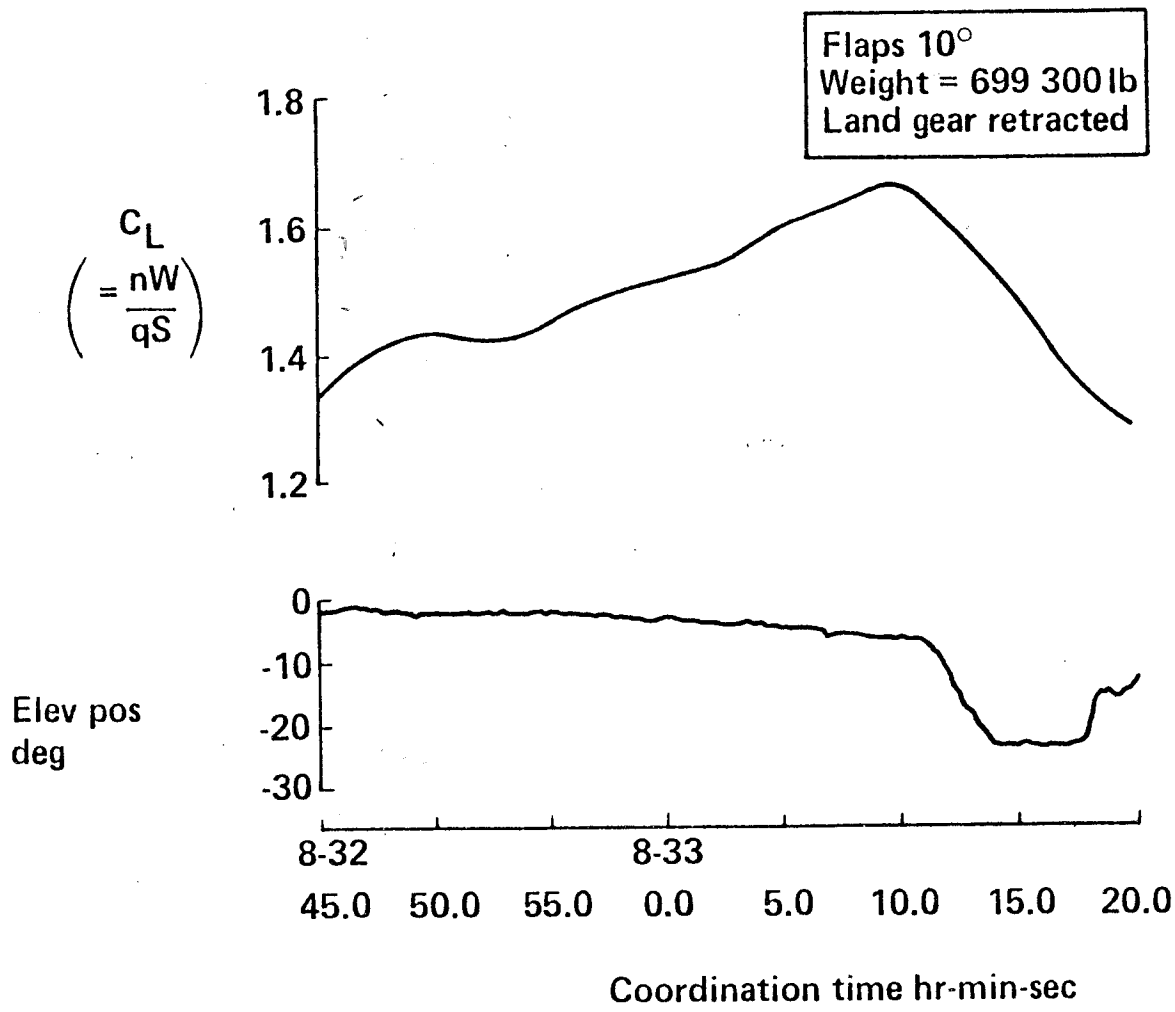

FIGURE 27b
P12.40

804

P12.41

EFFECT OF GROSS WEIGHT AND ENTRY RATE ON $C_{L_{MAX}}$ ACHIEVED IN STALL

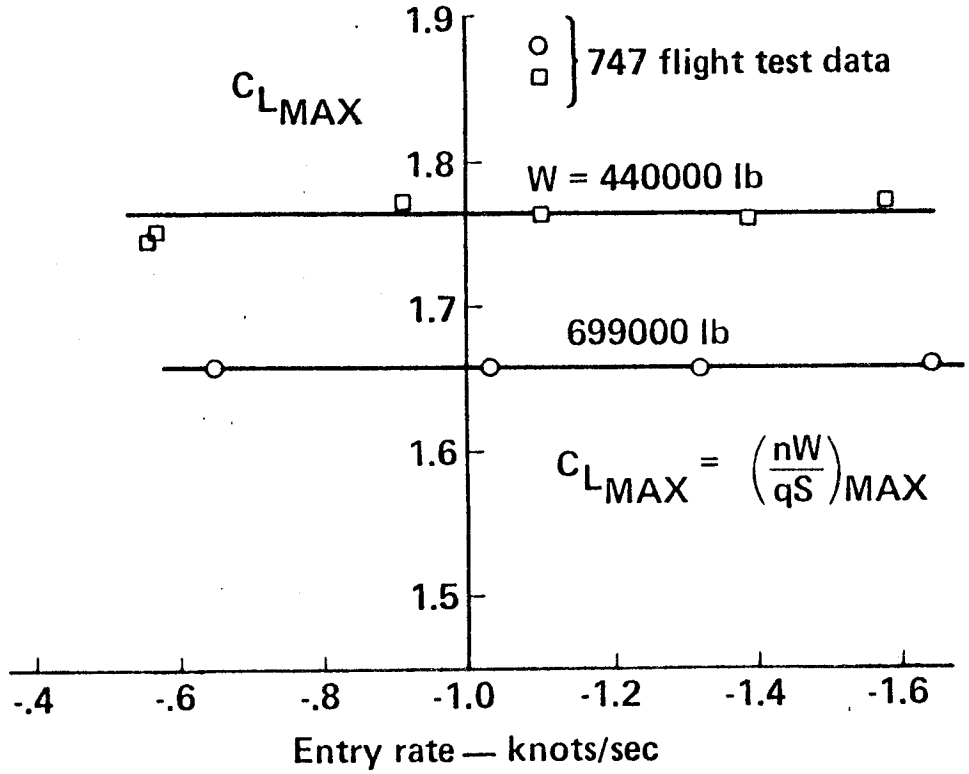

FIGURE 28

EFFECT OF STALL TECHNIQUE AND GROSS WEIGHT ON STALL LIFT COEFFICIENT

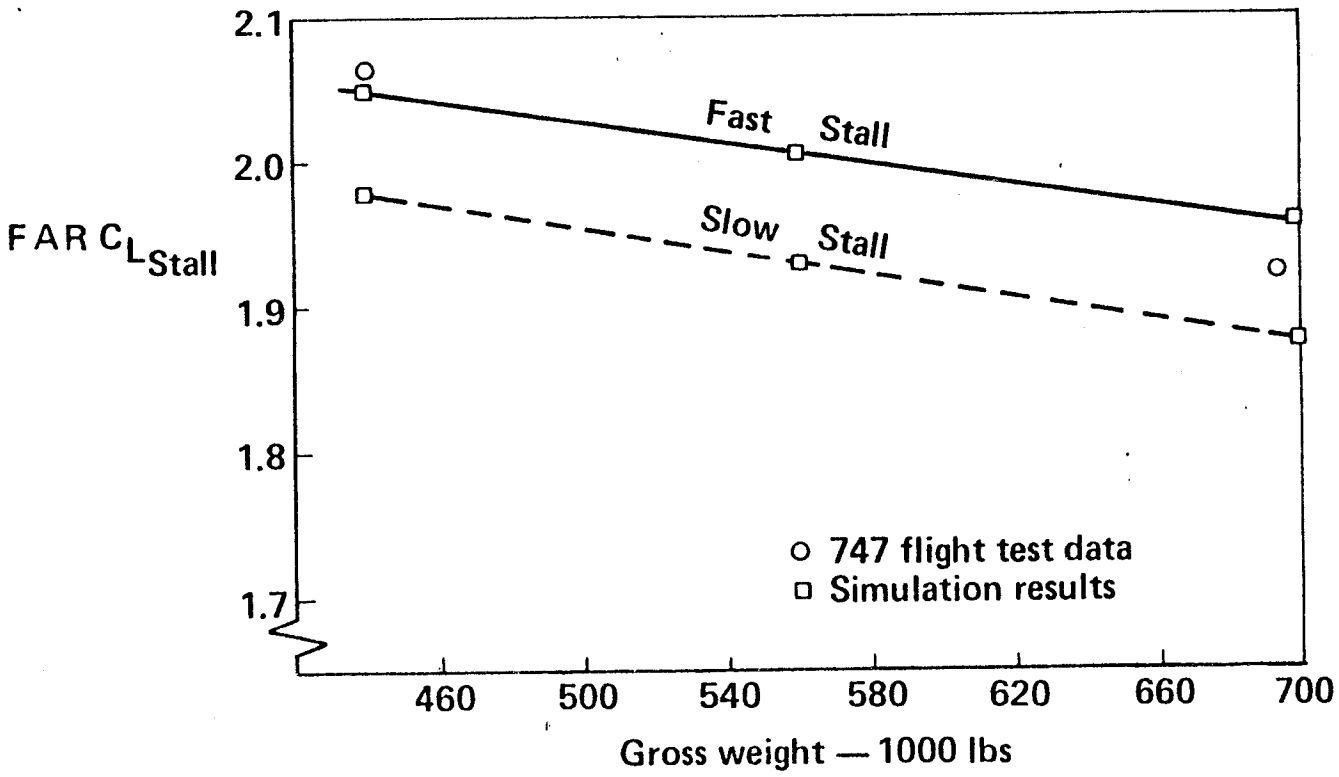

FIGURE 29
P12.42

SUMMARY BUILDUP OF FAR STALL LIFT COEFFICIENT FROM LOW REYNOLDS NUMBER TUNNEL DATA

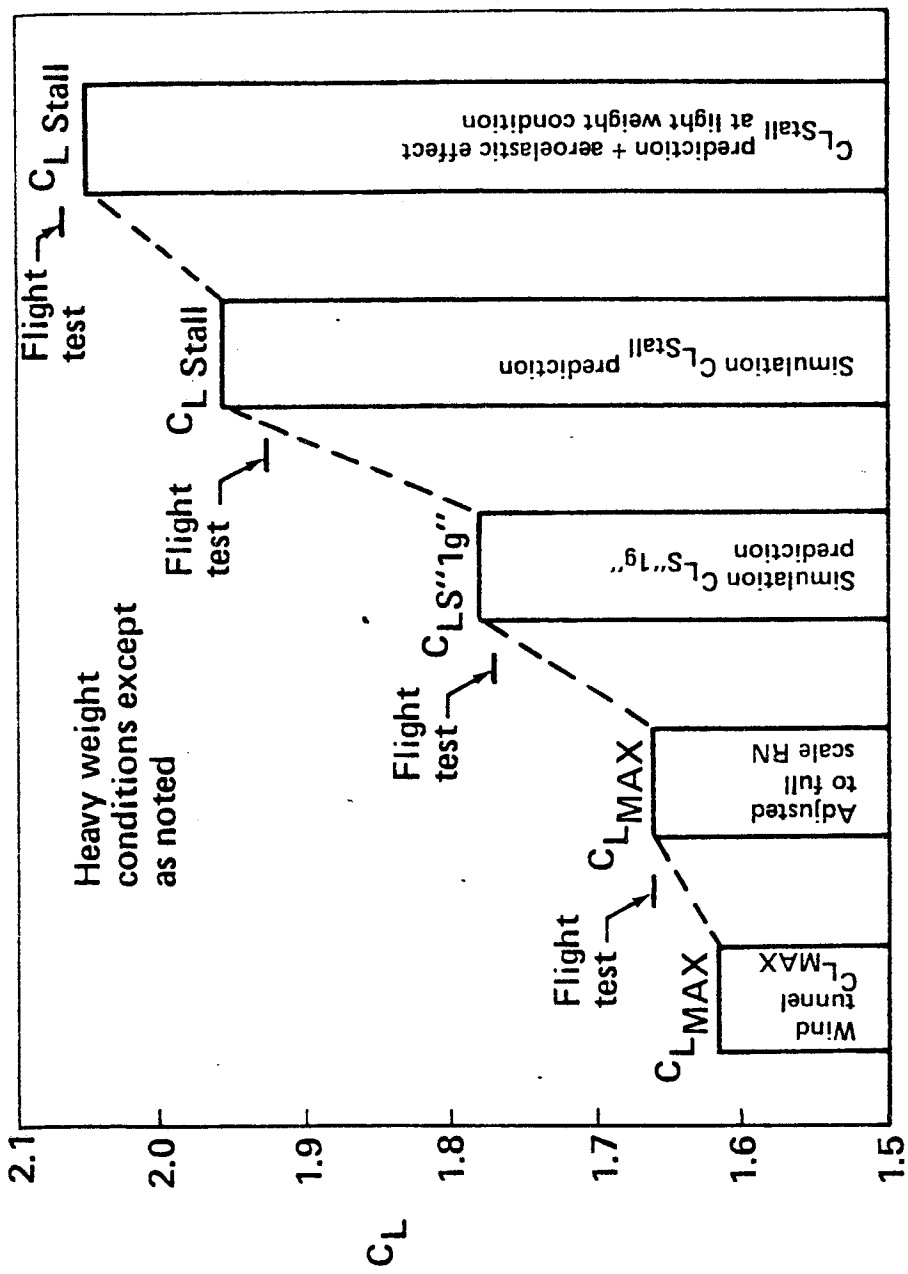

P 12.43

FIGURE 30

806

$$C_{L_{SM}} = C_{L_S} + .033\left[\frac{GW - 550{,}000}{100{,}000}\right]$$

FLAP 30 C.G. = 12% GEAR DOWN

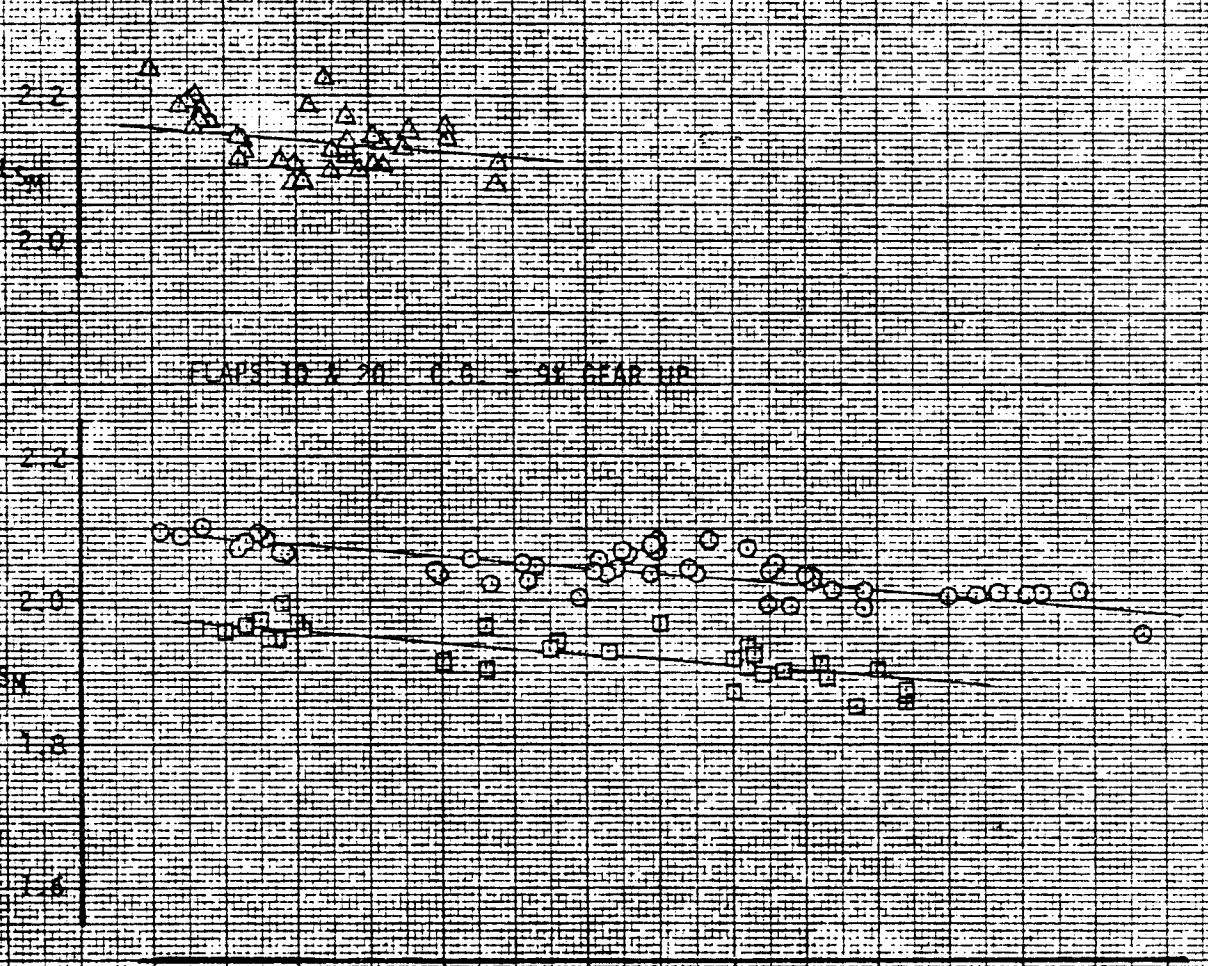

FLAPS 10 & 20 C.G. = 9% GEAR UP

FIGURE 31.

CALC	R.W. Jacquemeyer	10-9-75	REVISED	DATE	747 SP $C_{L_{SM}}$ VARIATION WITH MACH No.	D6-34264
CHECK						
APR						
APR					THE BOEING COMPANY	PAGE 12.44
ENG	J. Hart	2-4-76				

D1 4100 3240

K+E ALBANENE 1966

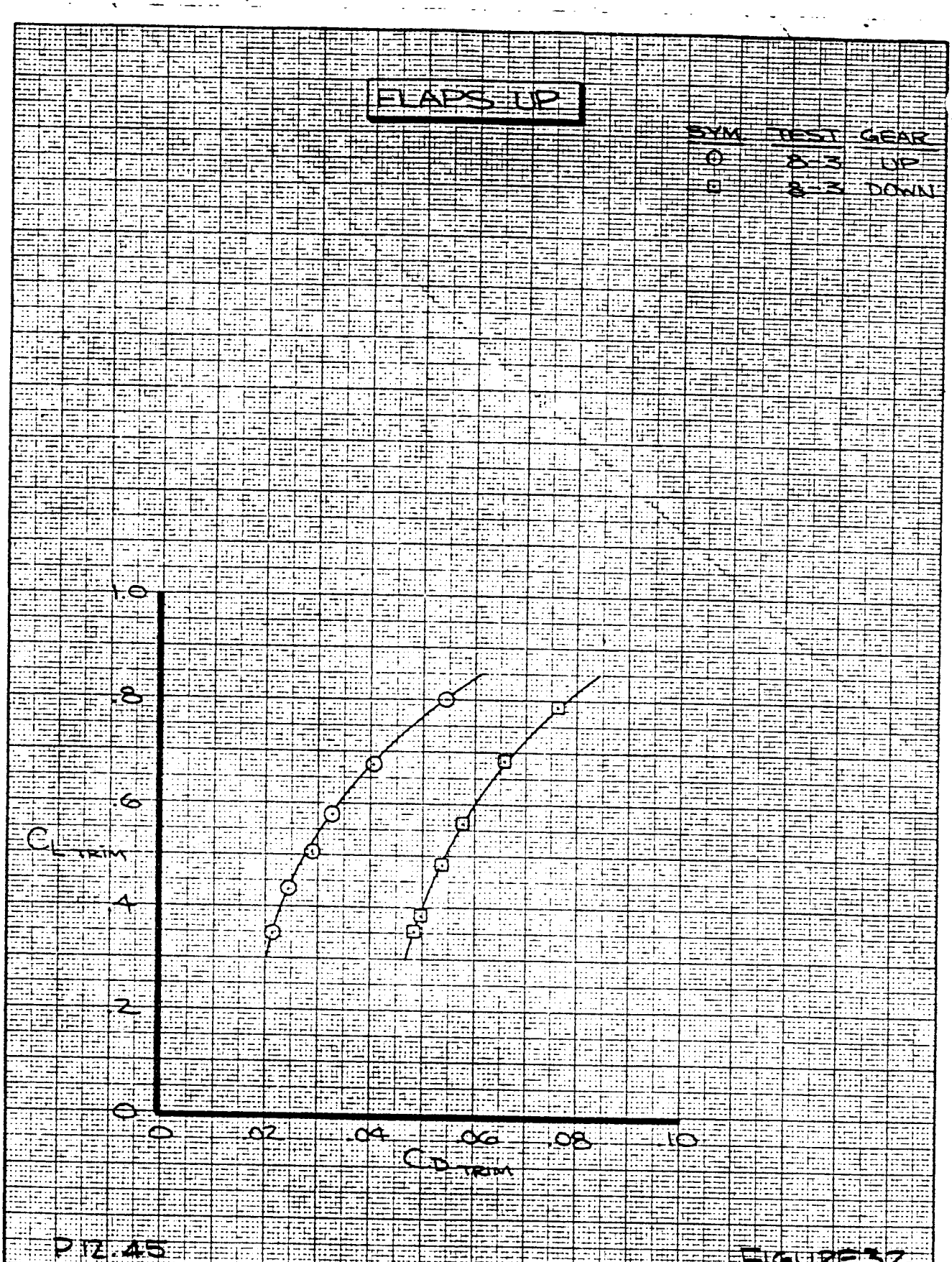

PT2.45

FIGURE 32

CALC	L. KEITH	10/30/69	REVISED	DATE	LOW SPEED DRAG POLAR JT9D-3A/-7/-7A ENGINES
CHECK	PE Hubble	11-11-69			747
APR	M. Z LASZO	11-17-69			
APR					THE BOEING COMPANY
DRAWN	M. LANG	10-30-69			PAGE

AD 461 C R4

REV. B

K-E ALBANENE 1966

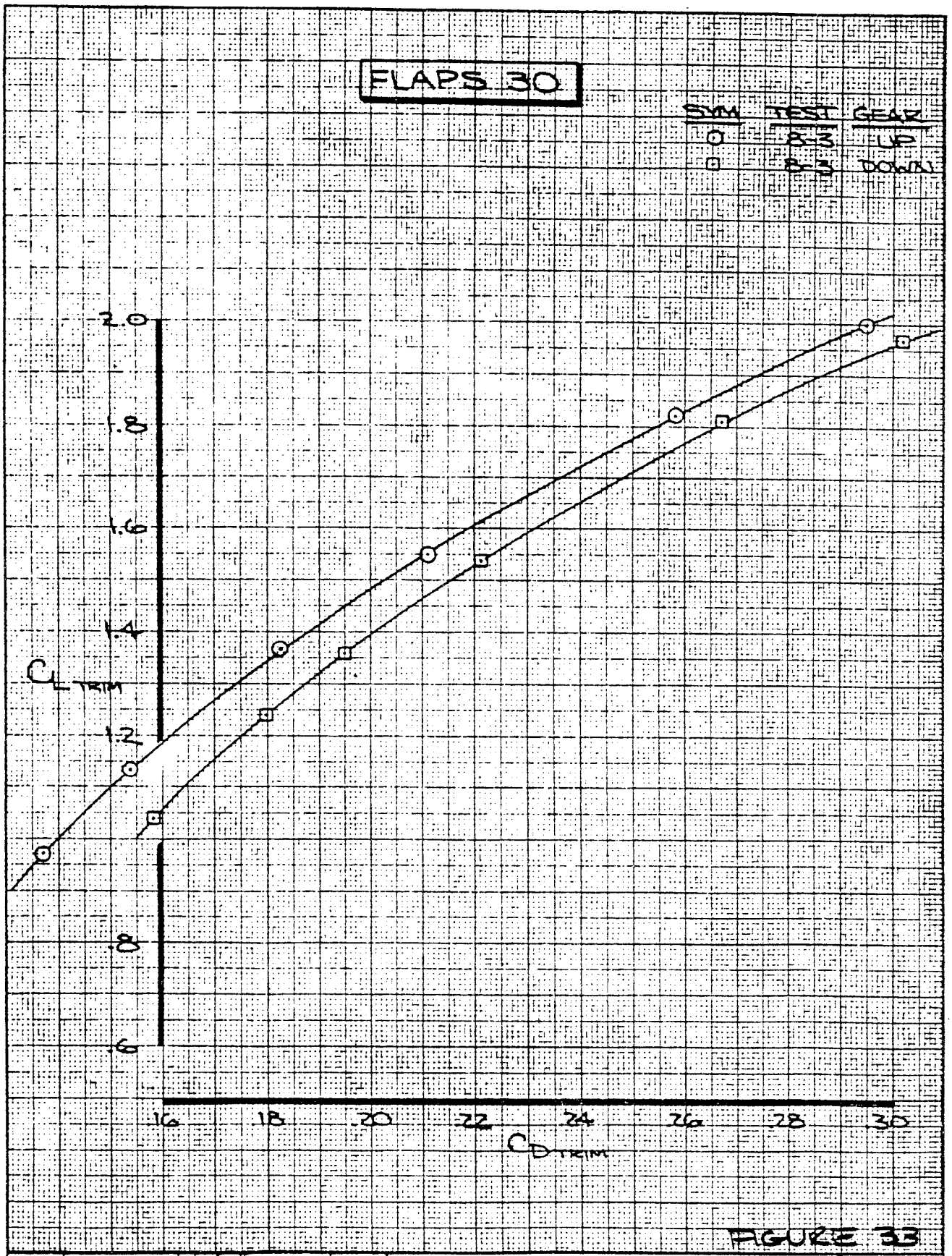

FIGURE 33

CALC	L. KEITH	10/30/69	REVISED	DATE	LOW SPEED DRAG POLAR JT9D-3A/-7/-7A ENGINES THE BOEING COMPANY
CHECK	PE Hubble	11-11-69			
APR	M.E.LA-520	11-17-69			
APR					
DRAWN	M. LANG	10-30-69			

747

PAGE 12.46

AD 461 C-R4 REV. B

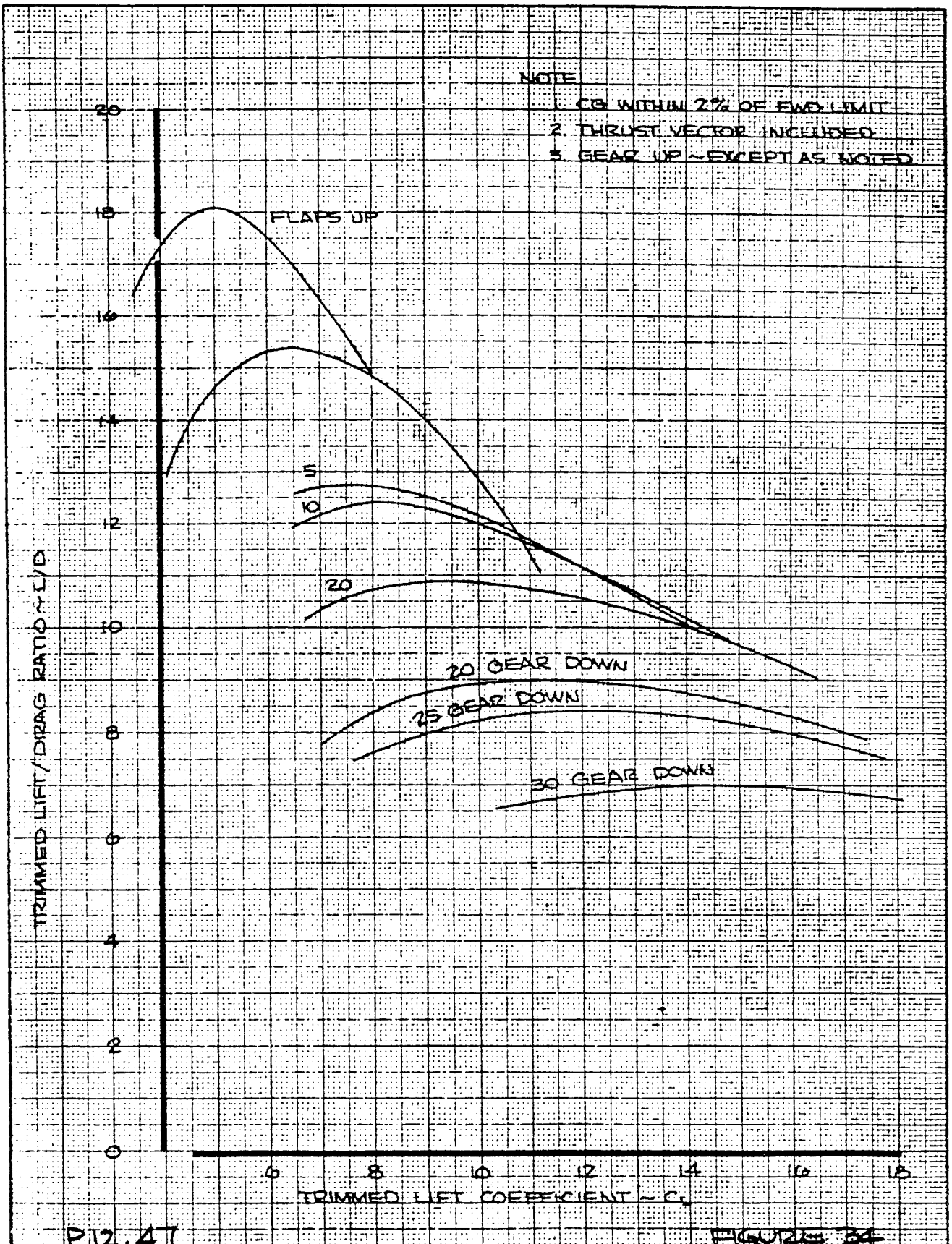

P12.47

FIGURE 34

CAL	WICKLINE	2-2-70	REVISED	DATE	FLAPS DOWN POLARS	747
CHECK			REPLOT		CERTIFICATION RESULTS	
APR			W. PAUL	6-20-75	JT9D-3A / -7 / -7A ENGINES	
APR						
	ROHNER	1 JUL 75			THE BOEING COMPANY	PAGE

FIGURE 35
P12.48

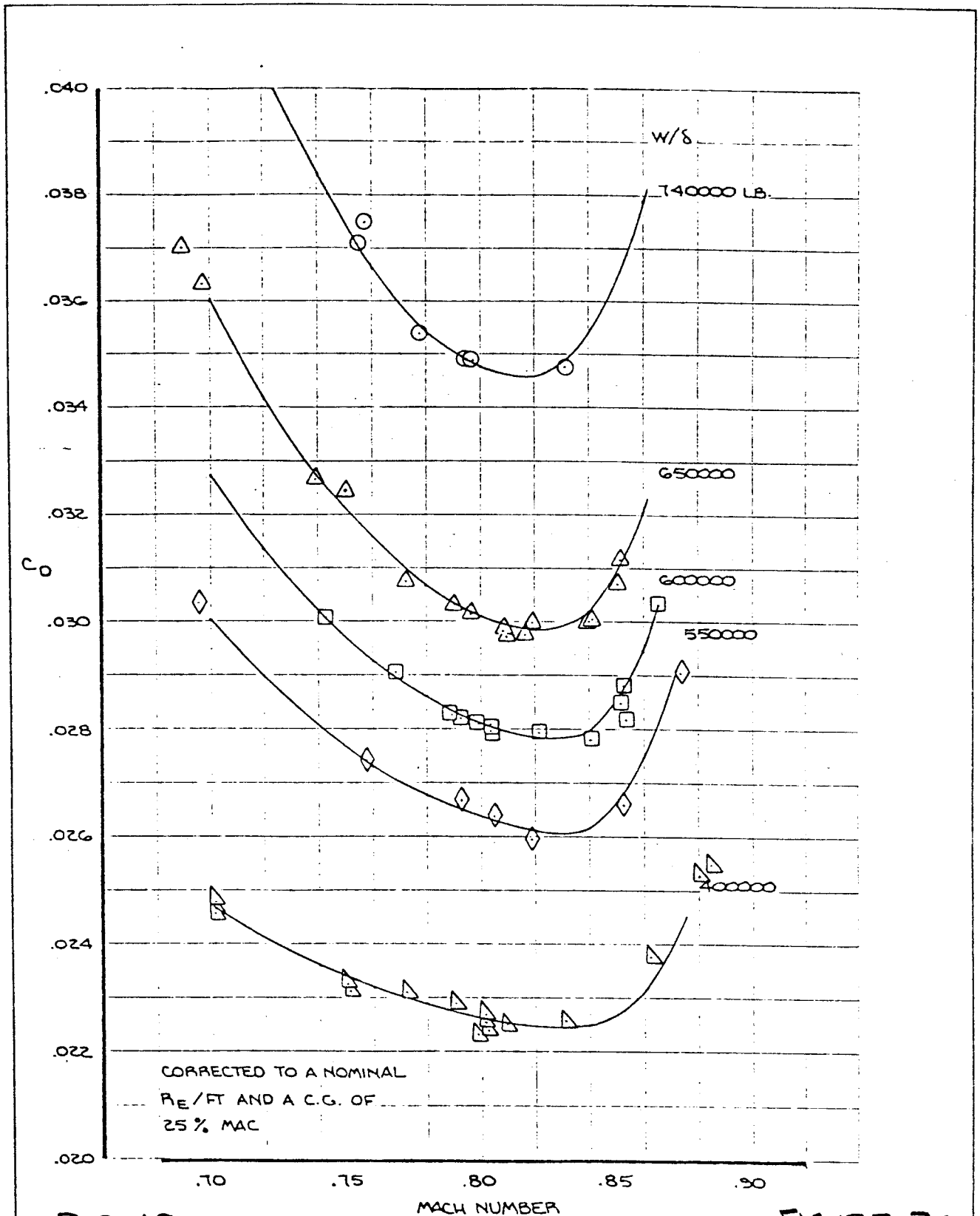

P 12.49

FIGURE 36

CALC	BAESMAN	10-11-77	REVISED	DATE	QB-536 HIGH SPEED DRAG POLAR POLAR # 3
CHECK					
APPD					
APPD					
INK	FELTES				THE BOEING COMPANY

727-200

PAGE

D1 4102 5540 ORIG 3/71

6-5000

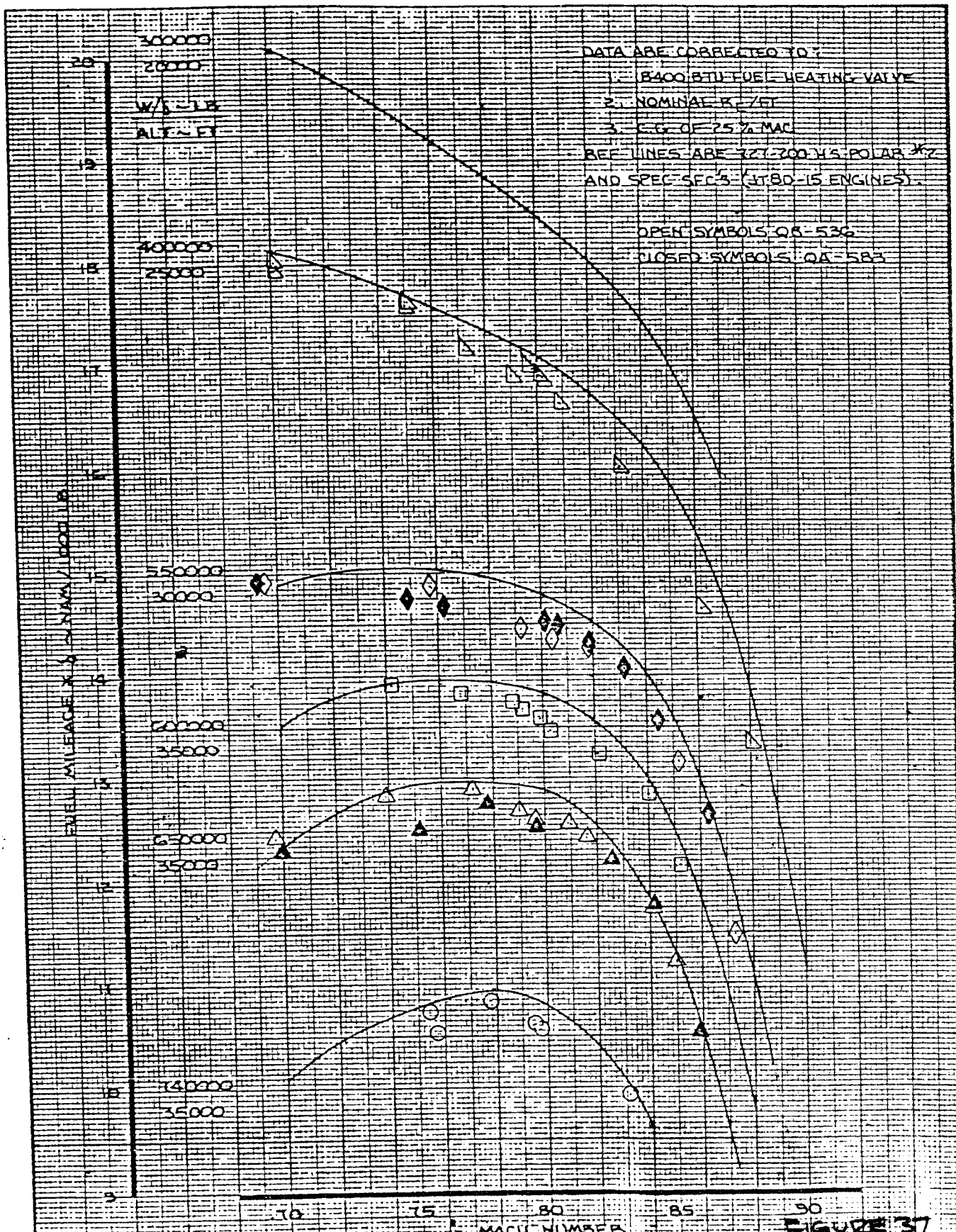

FIGURE 37

CALC	BAESMAN	10-10-77	REVISED	DATE	QA-583 FUEL MILEAGE x δ COMPARED WITH QB-536 FUEL MILEAGE x δ (FLIGHT TESTS 22-08 TO 22-12)	727-200 JT8D-15
CHECK						
APR						
APR					THE BOEING COMPANY	PAGE 12.50
PLOT	FELTES					

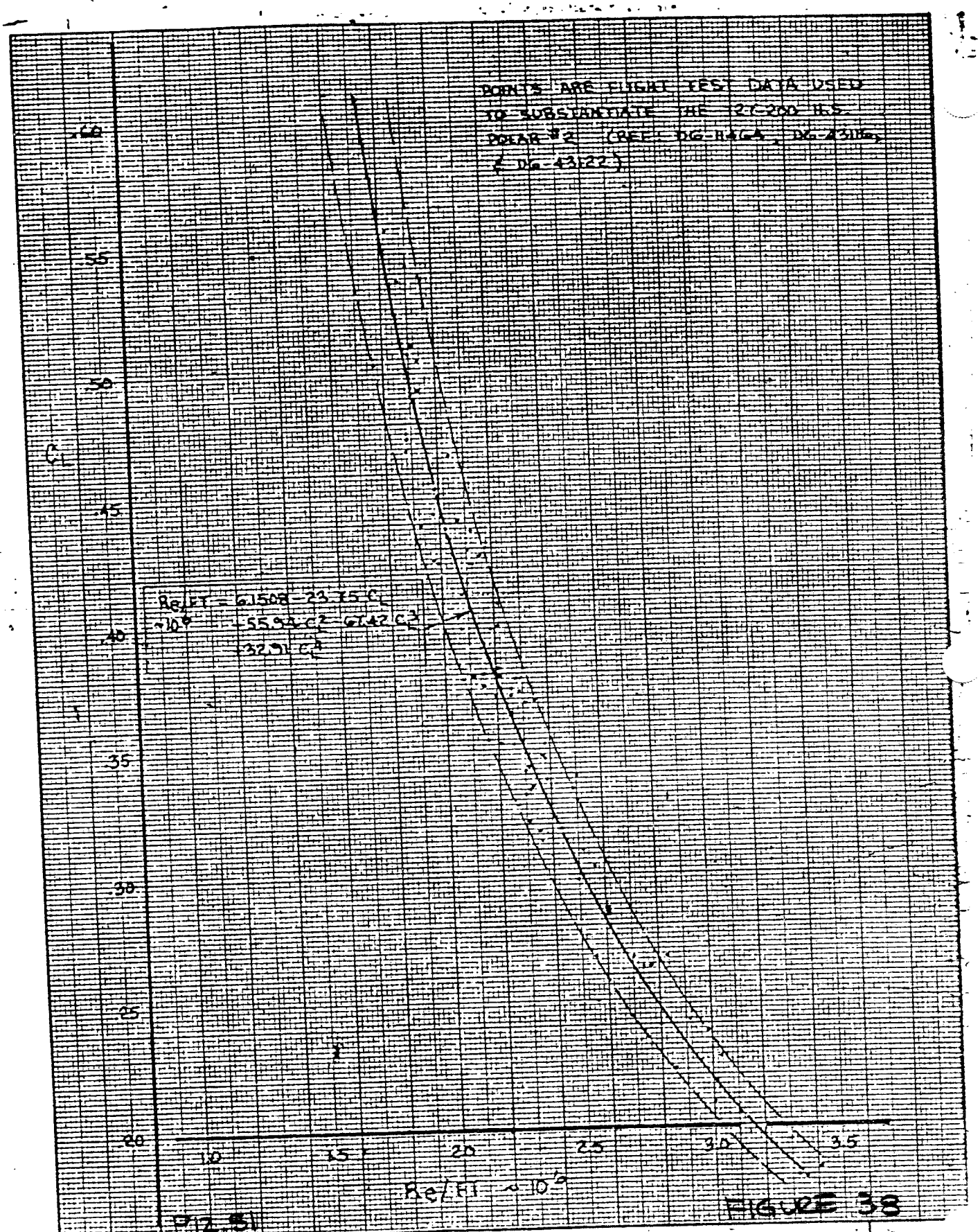

FIGURE 38

CALC	BAESMAN	7-8-76	REVISED	DATE	T2T-200 FLT. TEST Re/FT
CHECK					
APR					
APR					THE BOEING COMPANY
					PAGE

K-E ALBANENE 10 X 10 TRACING PAPER

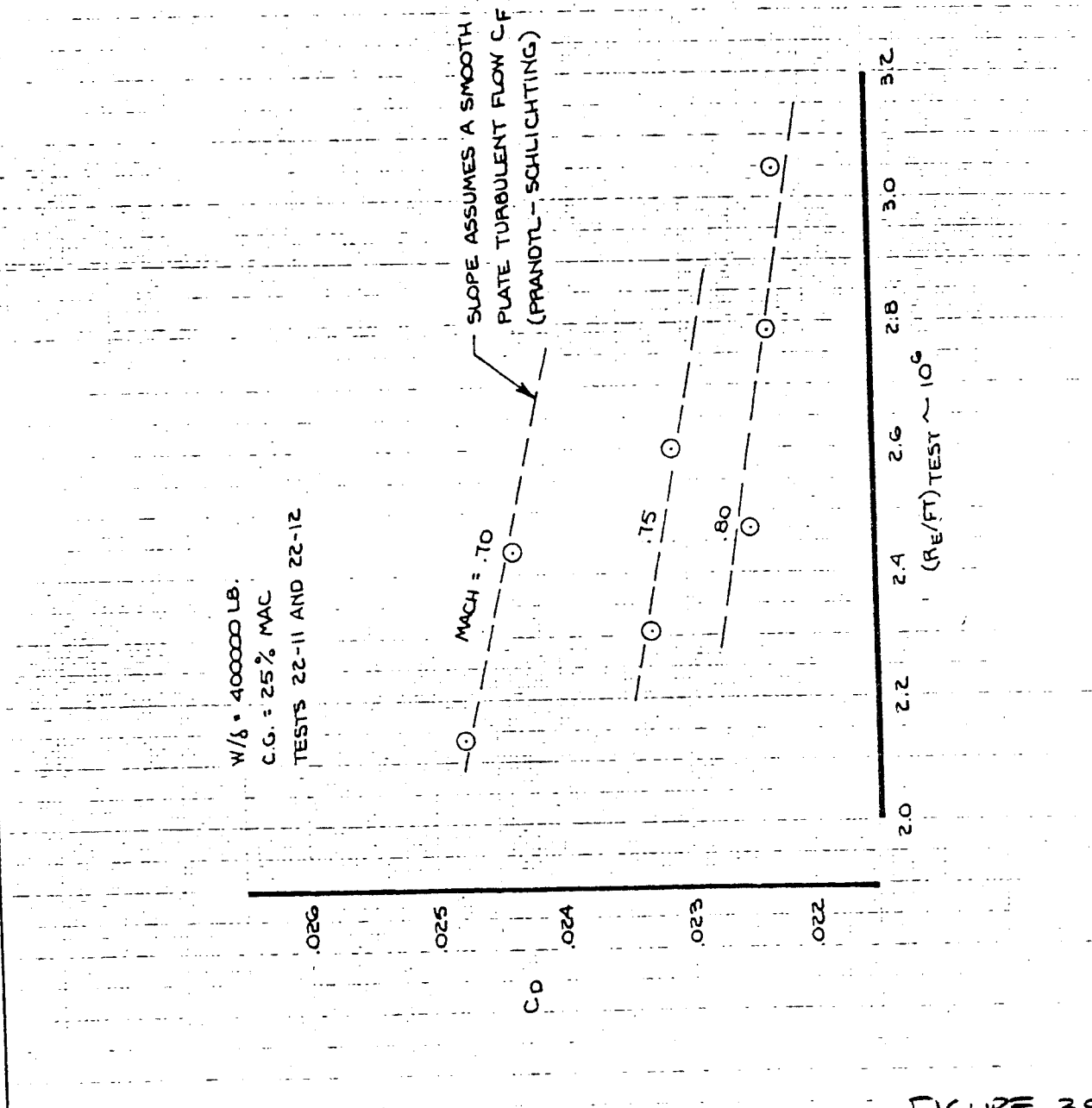

FIGURE 39

CALC	BAESMAN	1-31-78	REVISED	DATE	QB-536 C_D VS R_E/FT AT W/δ = 400000 LB.	727-200
CHECK						
APR						
APR					THE BOEING COMPANY	PAGE 12.52
INK	FELTES					

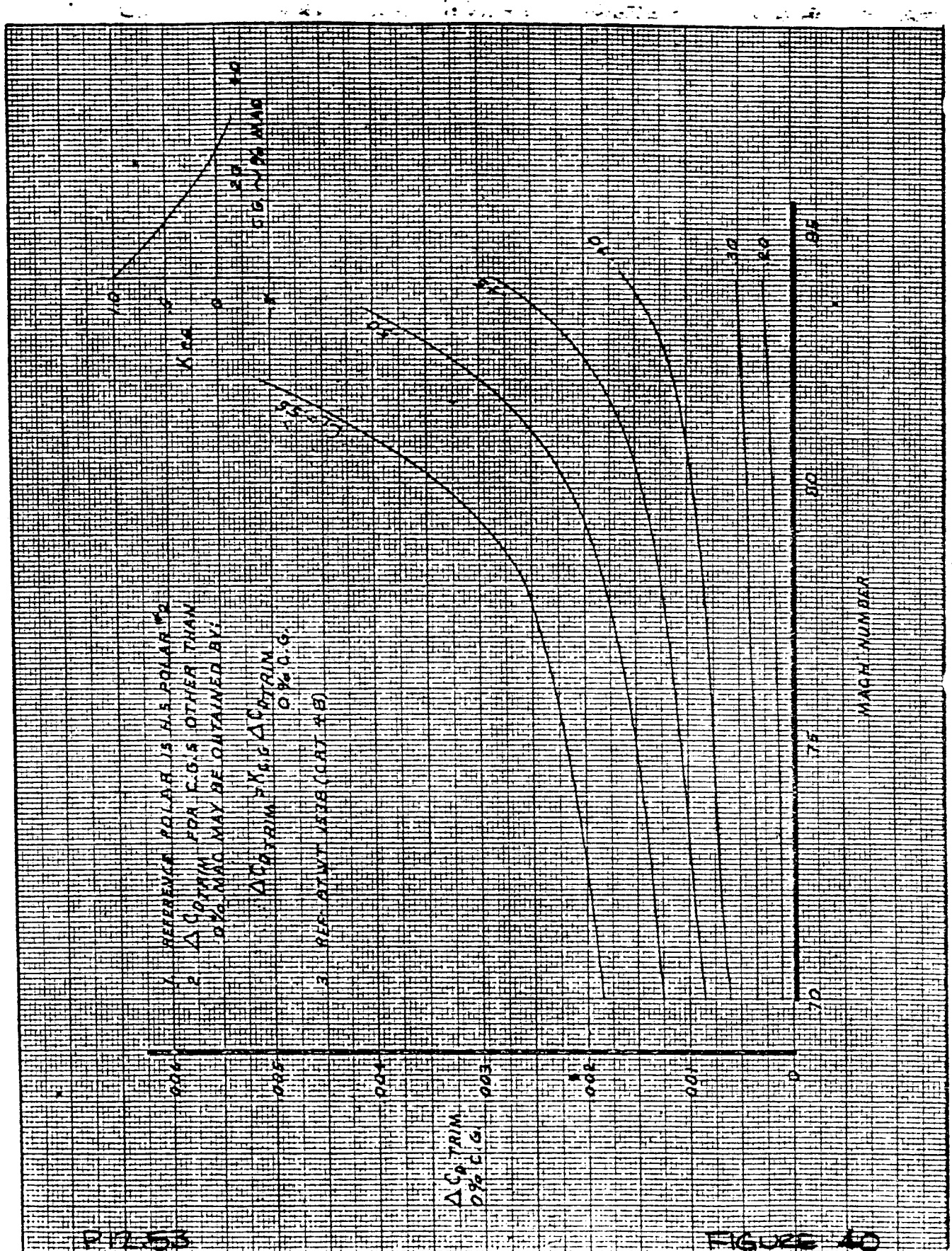

FIGURE 40

CALC	AAESMAN	6-9-77	REVISED	DATE	727-200 $\Delta C_{D_{TRIM}}$ FOR FORWARD C.G. ,
CHECK					
APR					
APR					
	BEECH	6-10-77			THE BOEING COMPANY

PAGE

K-E ALBANENE 1966

817

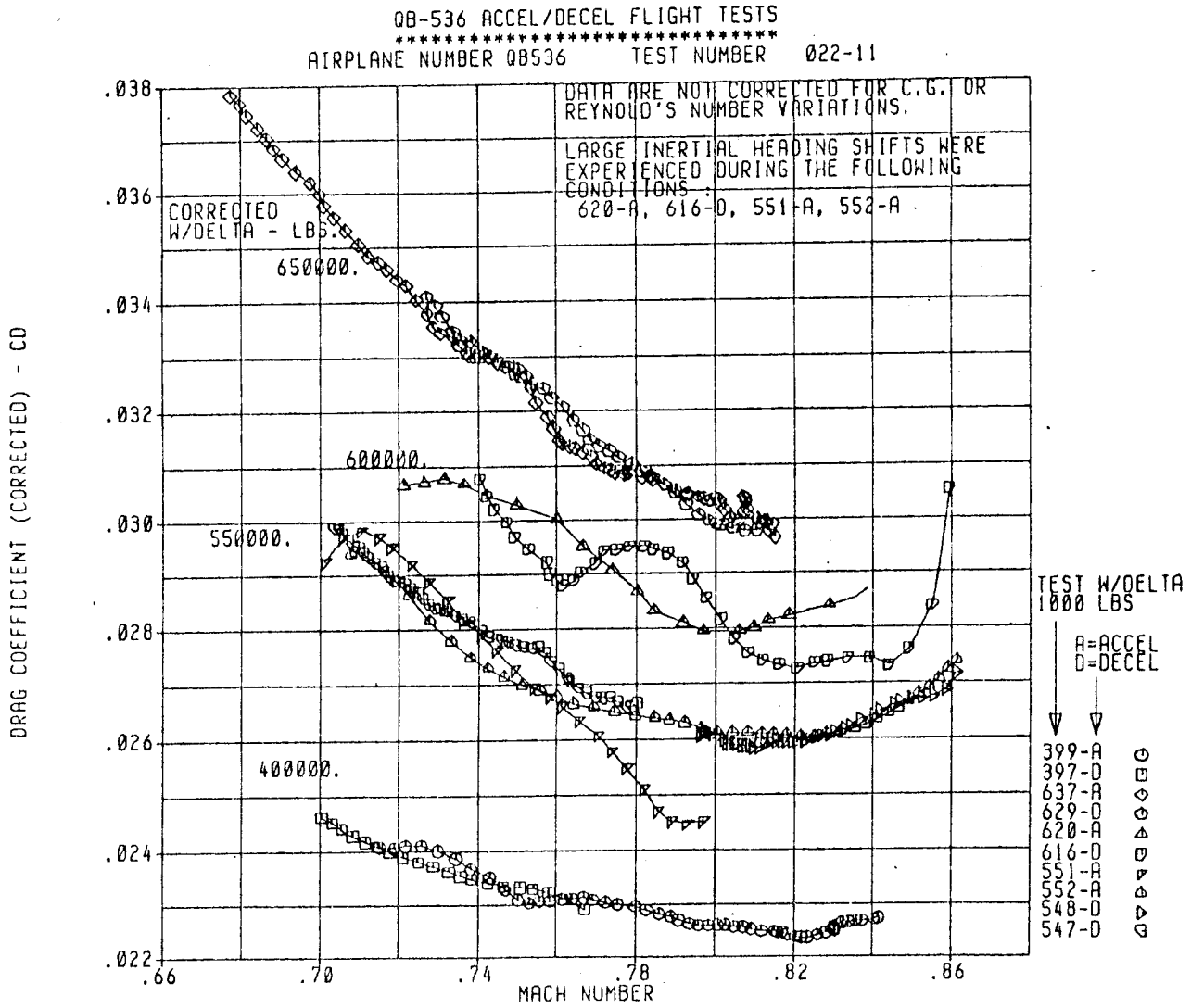

FIGURE 41
P12.54

ACCEL/DECEL C_D VS MACH OBTAINED WITH QB-536

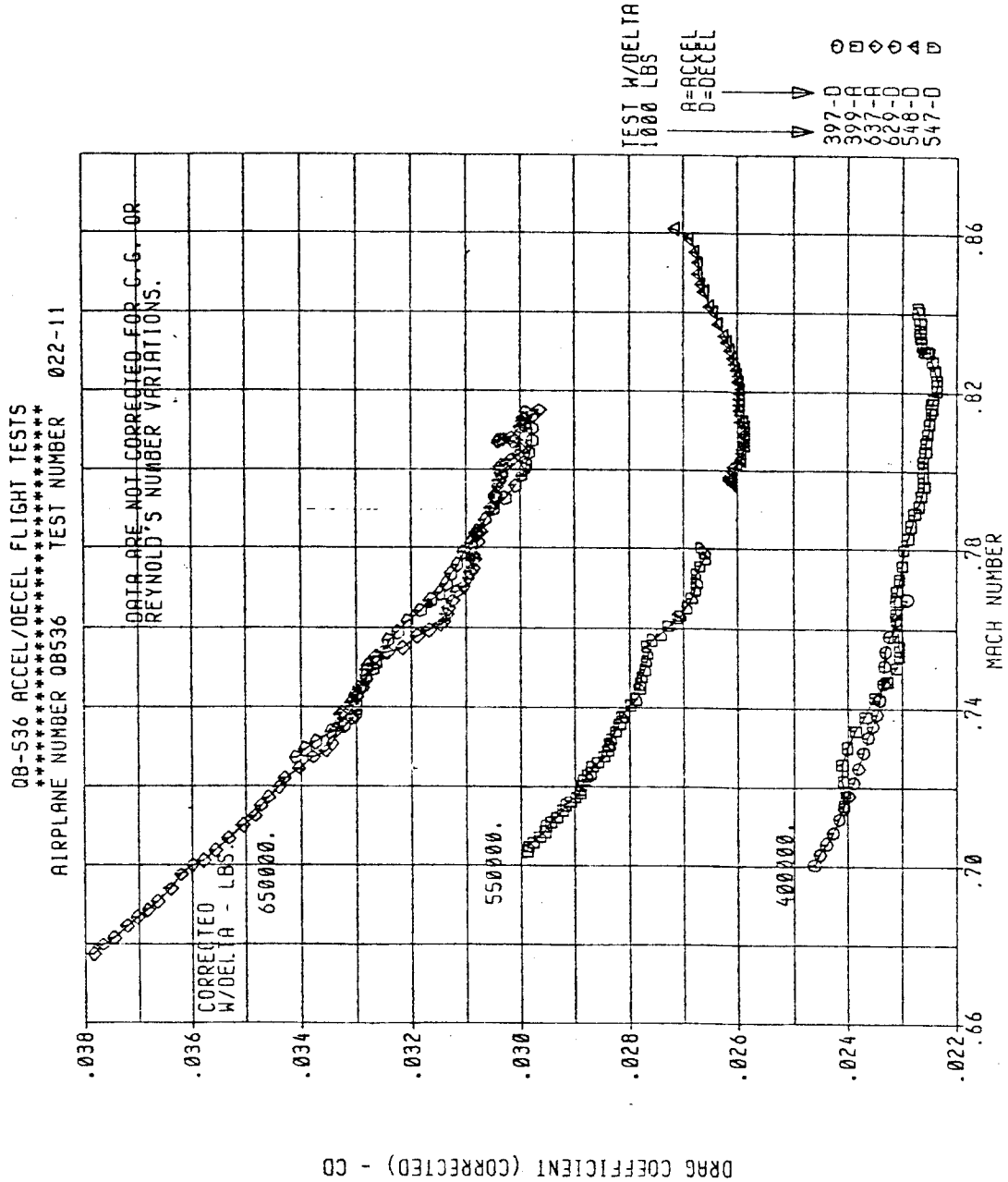

ACCEPTABLE ACCEL/DECEL C_D VS MACH

P12.55

FIGURE 42

818

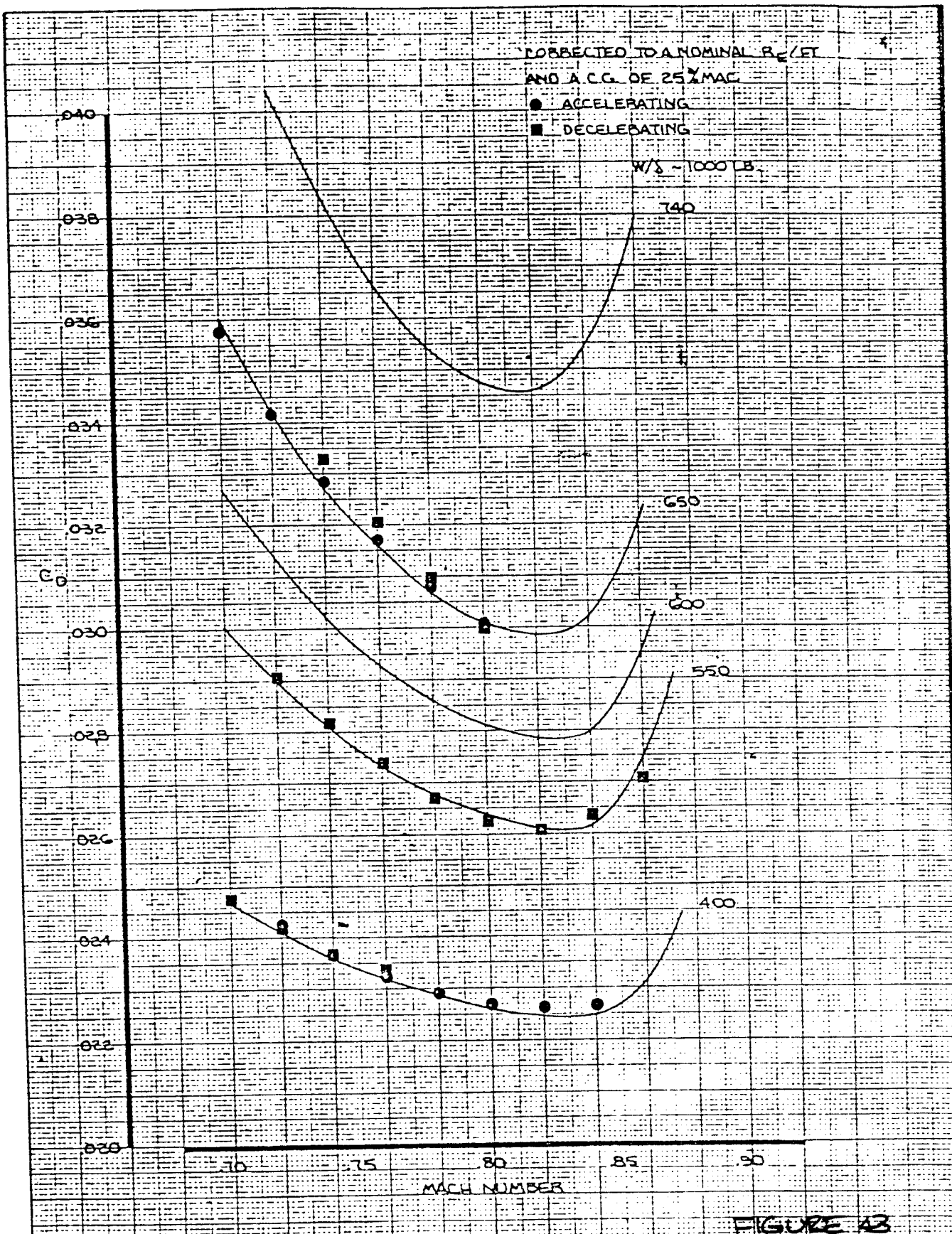

FIGURE 43

CALC	BAESMAN	1-30-78	REVISED	DATE	ACCEL/DECEL DATA COMPARED WITH HIGH SPEED POLAR # 3 QB-536	727-200
CHECK			BAESMAN	2-1-78		
APR						
APR					THE BOEING COMPANY	PAGE 12.56
INK	FELTES					

820

P12.57

C.A.R. Landing Field length

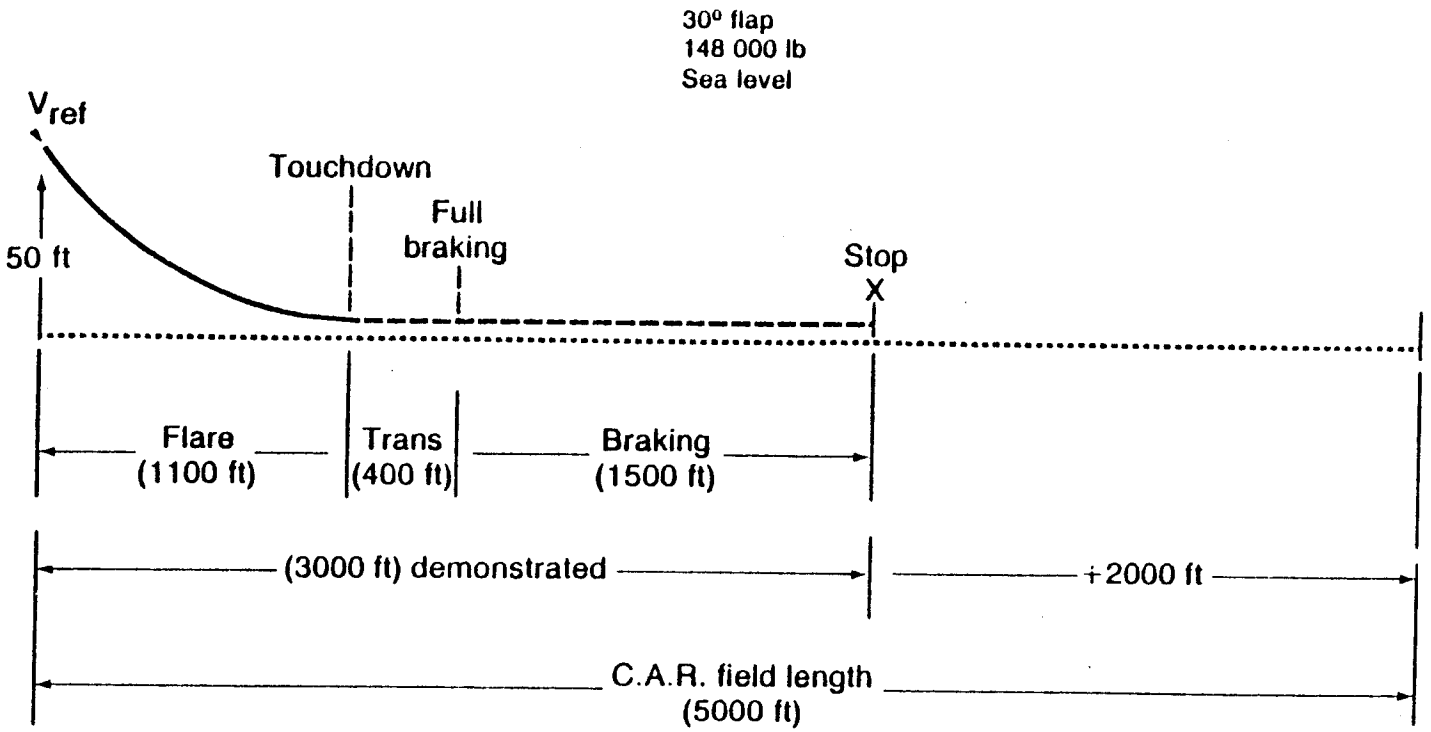

FIGURE A4

Increased Approach Speed

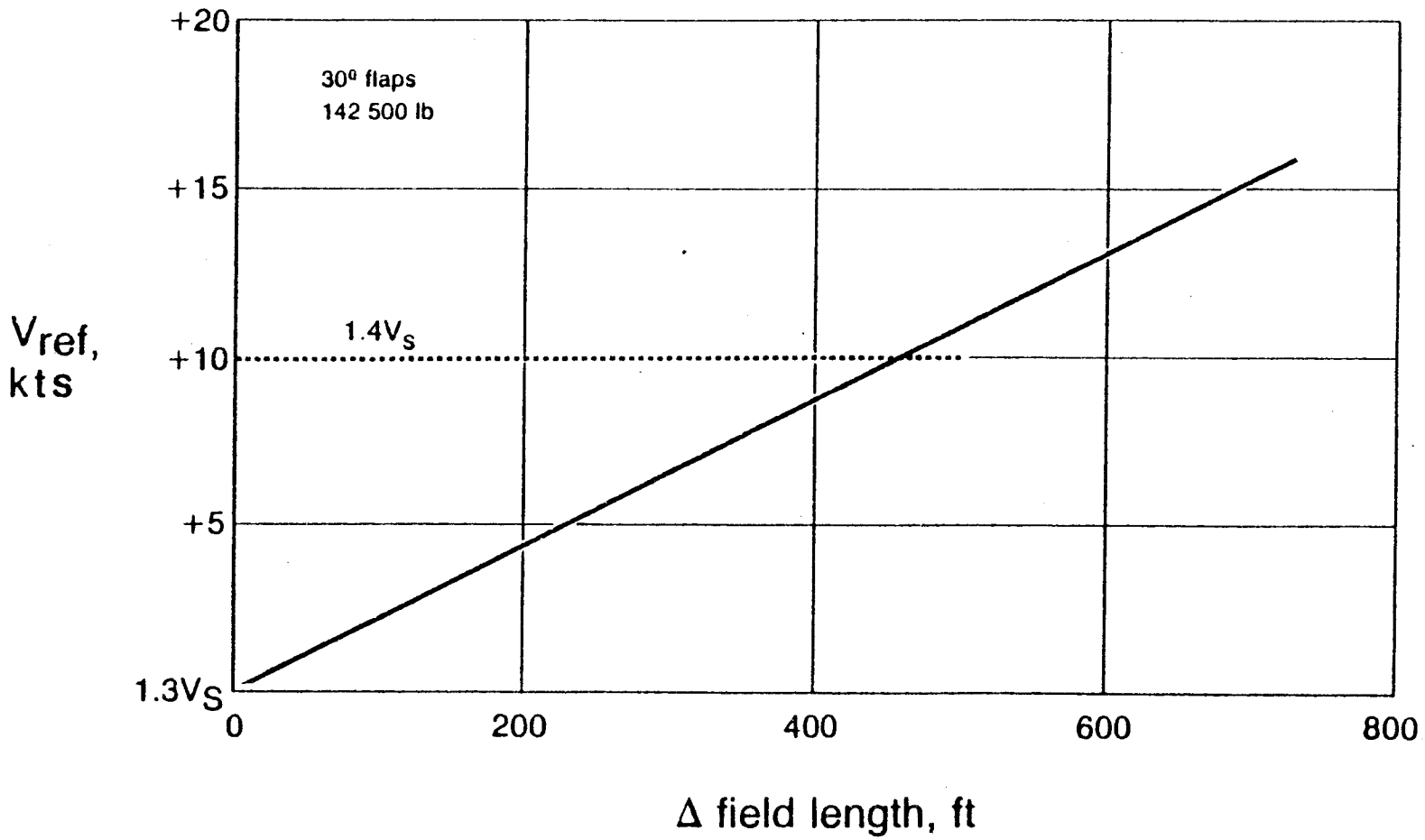

FIGURE 45
PI2.58

P12.59

FIGURE 46

CALC	HALVARSON	7-25-77	REVISED	DATE		
CHECK	NOBLE	7-25-77				
APR						
APR						
INK	FELTES				THE BOEING COMPANY	PAGE

828

LANDING GROUND ROLL PARAMETERS

ALL ENGINES

$\alpha_w = 1.5°$

SPOILERS	FLAP	C_L	C_D
DOWN	25	.93	.0869
	30	1.150	.1317
* INBOARD 20° and OUTBOARD 45°	25	.48	.1370
	30	.67	.1800
** INBOARD 45° AND OUTBOARD 45°	25	.352	.1571
	30	.525	.2009

* original spoiler system

** improved spoiler system

FIGURE 47

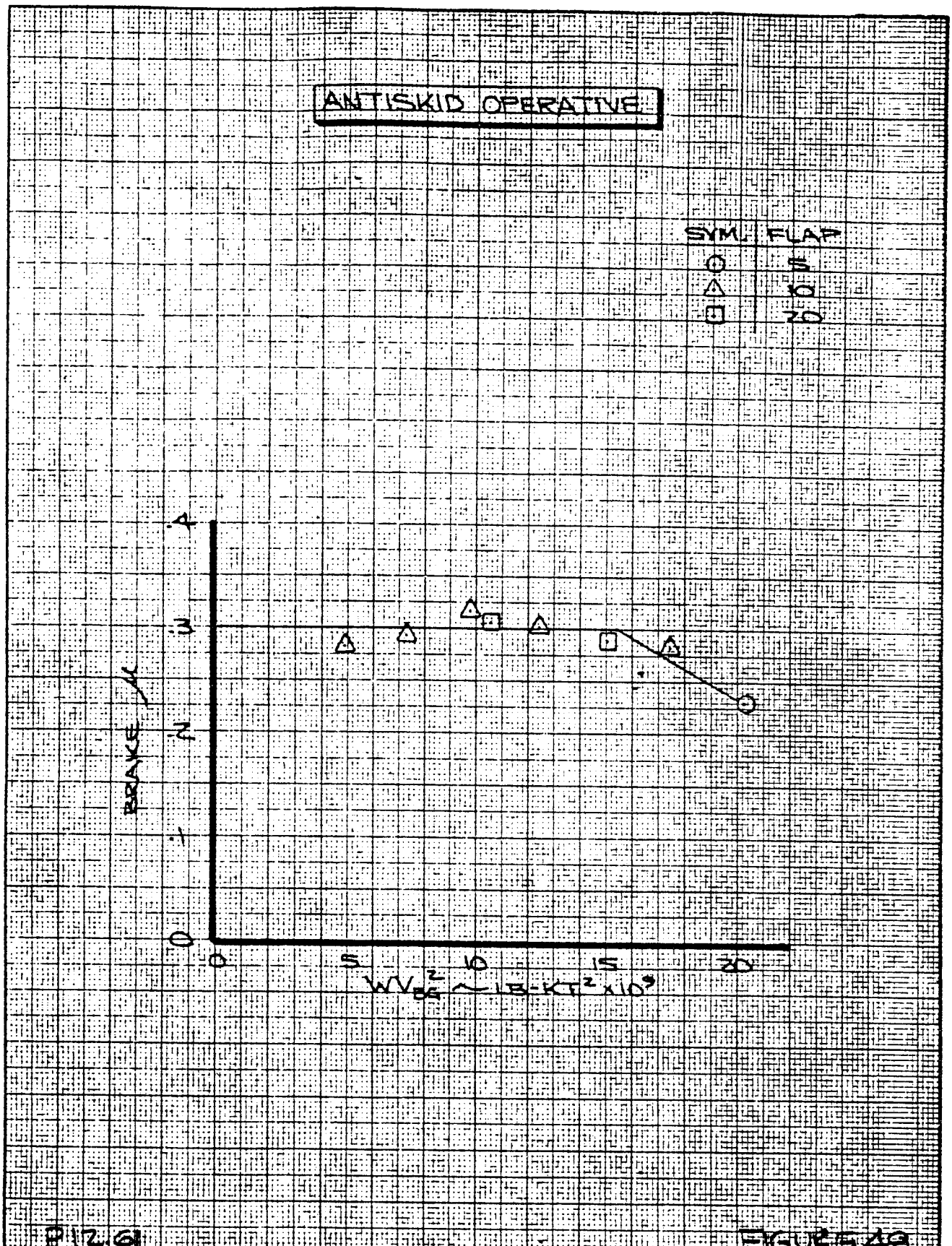

P12.61

FIGURE 49

CALC	BEAN	12-2-69	REVISED	DATE	μ VERSUS WV_{BG}^2 ANTISKID OPERATIVE	747
CHECK	T. JOHNSON	12-4-69				
APR	W.J. LA-520	12-4-69				
APR						
DRAWN	M. LANG	12-3-69			THE BOEING COMPANY	PAGE

AD 461 C-R4

J18-047

The following tabulation presents a summary of data to be used for Flight Manual expansion:

LANDING PARAMETER SUMMARY

ANTI-SKID OPERATIVE

TWO BRAKES INOPERATIVE

* ORIGINAL SPOILER AND ANTI-SKID SYSTEMS

PARAMETER	FLAP POSITION 25	30
Approach Speed Ratio, V_{APP}/V_S	1.3	1.3
Air Time, t_{AIR} 50' to TD	4.716	4.738
V_{TD}/V_{APP}	.9768	.9781
Transition Time	2.0	2.0
Braking Speed, Ratio, J	.9556	.9439
Braking Coefficient, μ_B	.2833	.2833
Ground Roll Lift Coefficient, C_L	.48	.67
Ground Roll Drag Coefficient, C_D	.1370	.1800

*Inboard Spoilers 20°
Outboard Spoilers 45°

NOTE: For performance with improved spoiler and anti-skid systems, see Part 3.0 (747-200F)

D1-4100 7740 ORIG. 3/71

FIGURE 49

825

P12.63

FIGURE 50

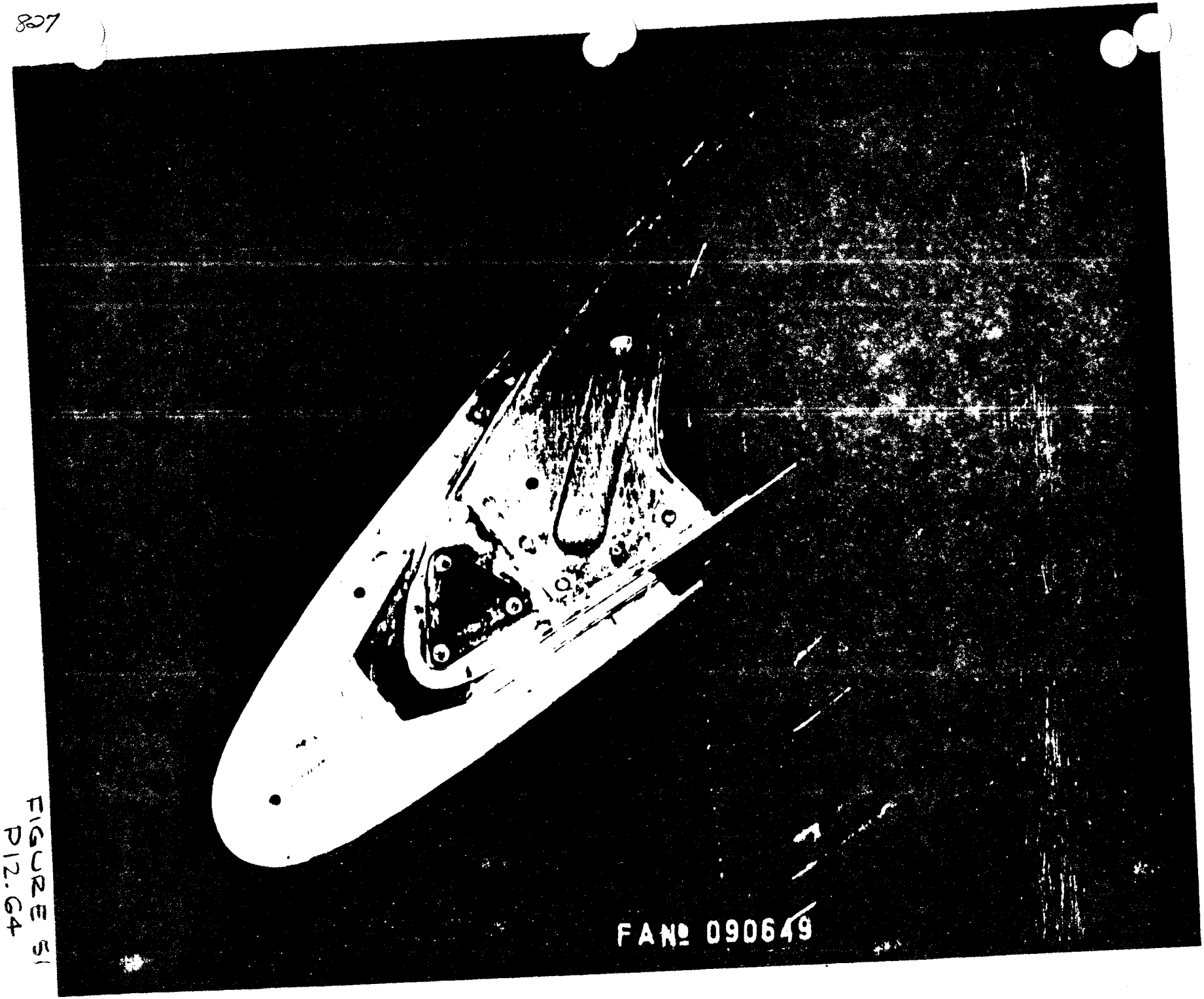

FIGURE 51
P12.64

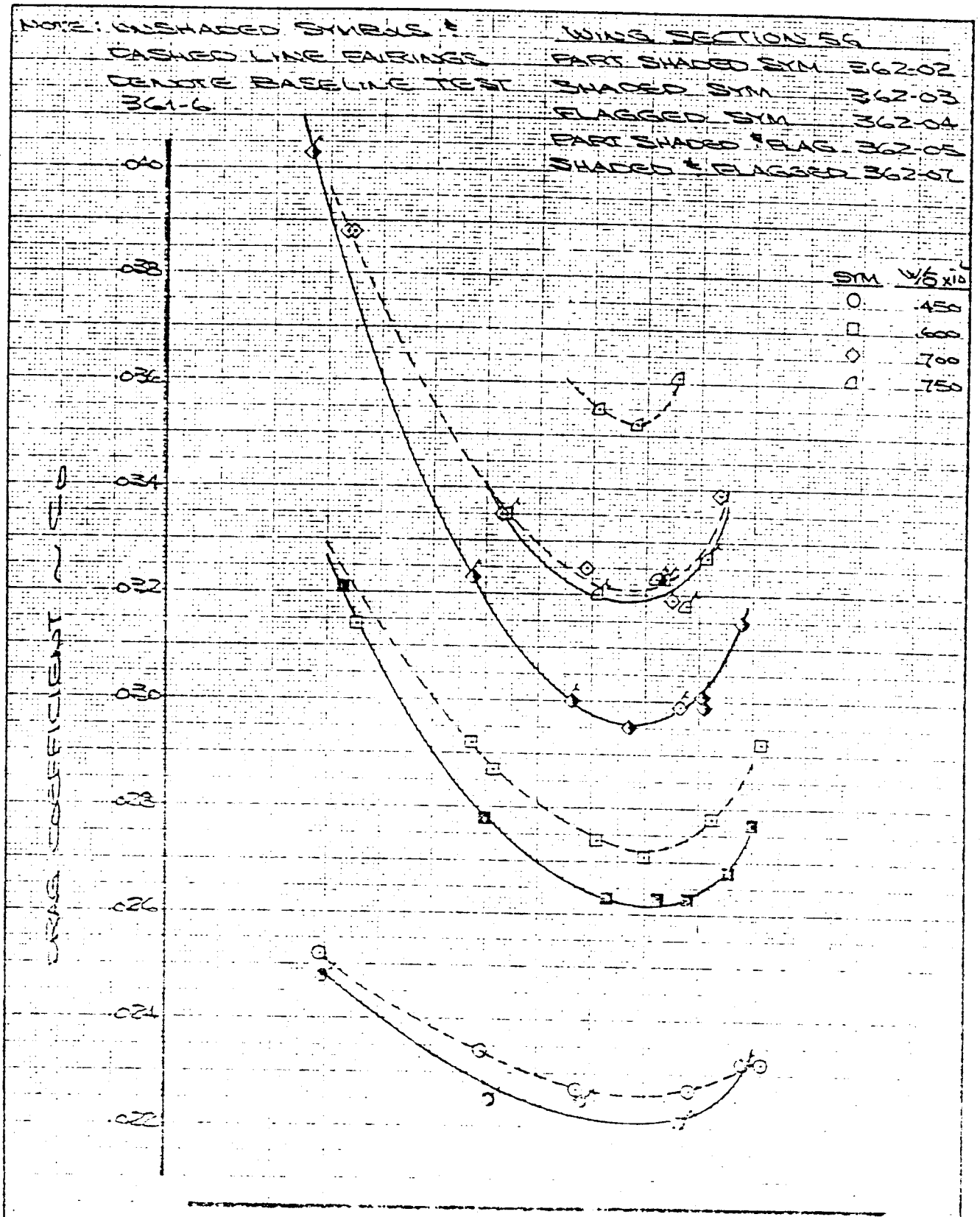

P12.65

FIGURE 52

CALC			REVISED	DATE	CRUISE DRAG FOR MODIFIED LEADING EDGE WING SECTION 56
CHECK	J. A. G.	1-24-74			
APP					
APP					
					THE BOEING COMPANY

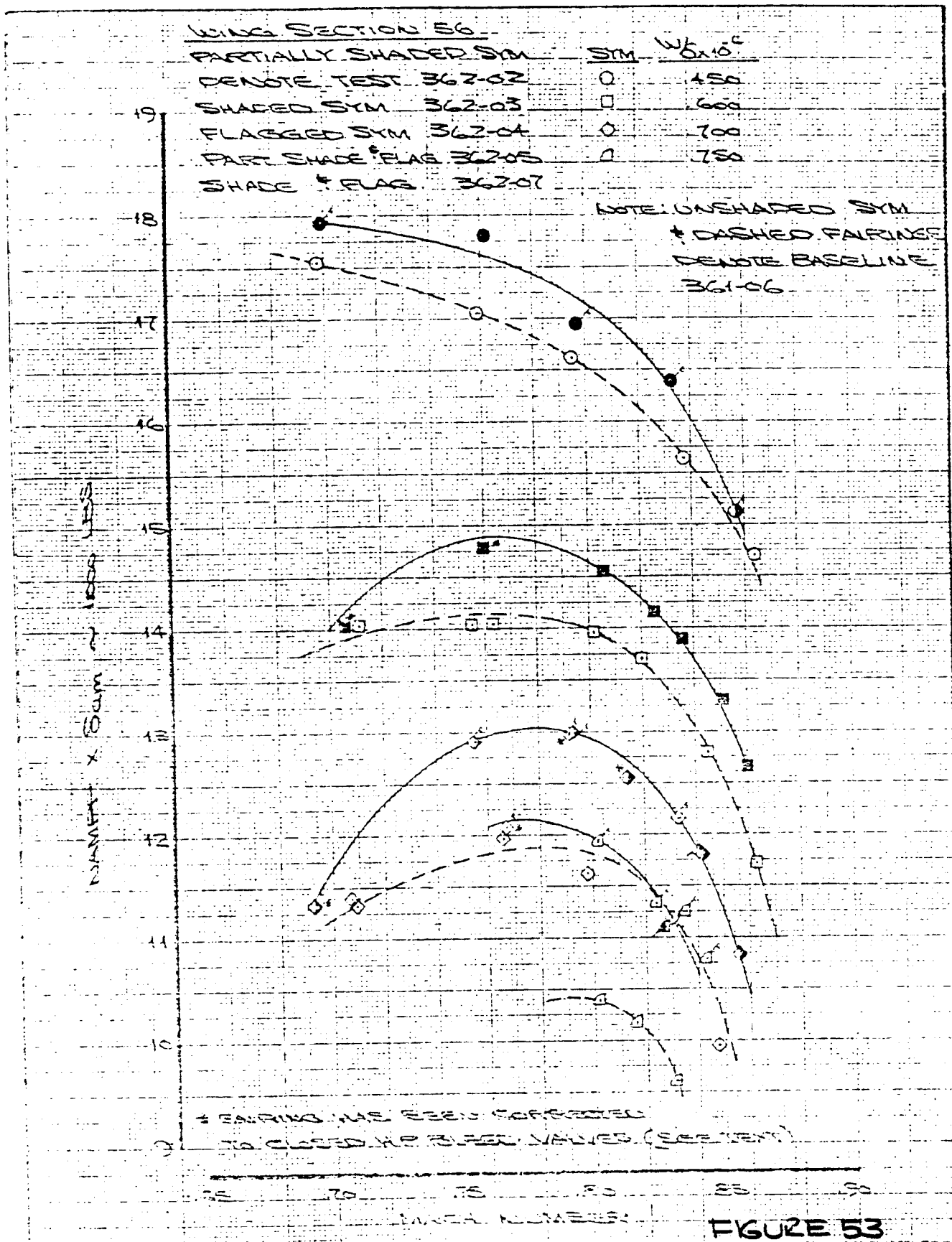

FIGURE 53

	REVISED	DATE	CRUISE DRAG FOR MODIFIED LEADING EDGE WING SECTION 56
T.A.S.C.	1-24-72		727-100 E2
			THE BOEING COMPANY
			PAGE 1266

829

SYM	$W/\theta \times 10^{-6}$	TEST
○	.600	361-06 (BASELINE)
◇	.600	362-07 (WING 56)
◁	.350	362-07 (WING 56)

NOTE: BROKEN LINE FAIRING TEST 362-07 (WING 56)

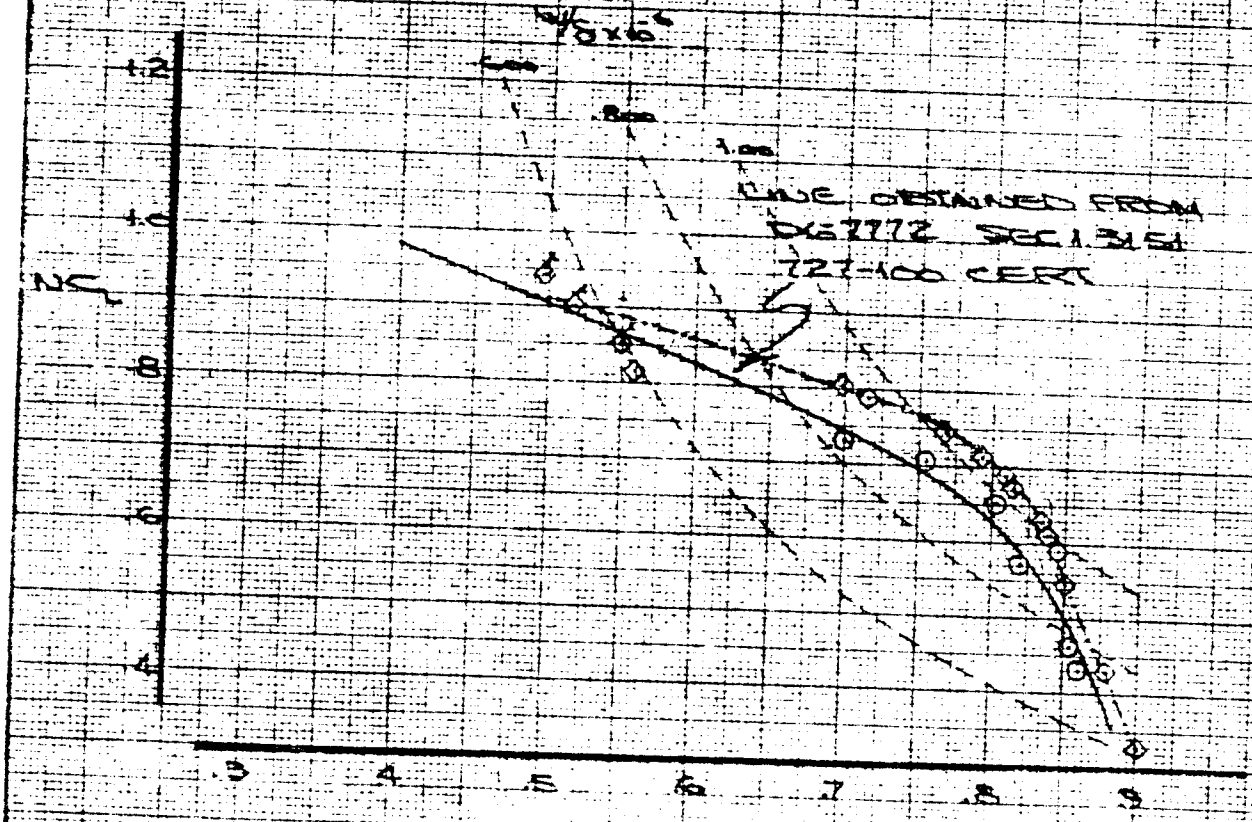

P 12.67

FIGURE 54

CALC	JL	12/18/73	REVISED	DATE	BASELINE BUFFET BOUNDARY FOR MODIFIED LEADING EDGE
CHECK	J.A.G.C.	1-24-74			
APP					
APP					
					THE BOEING COMPANY

727-100 E2

PAGE

127

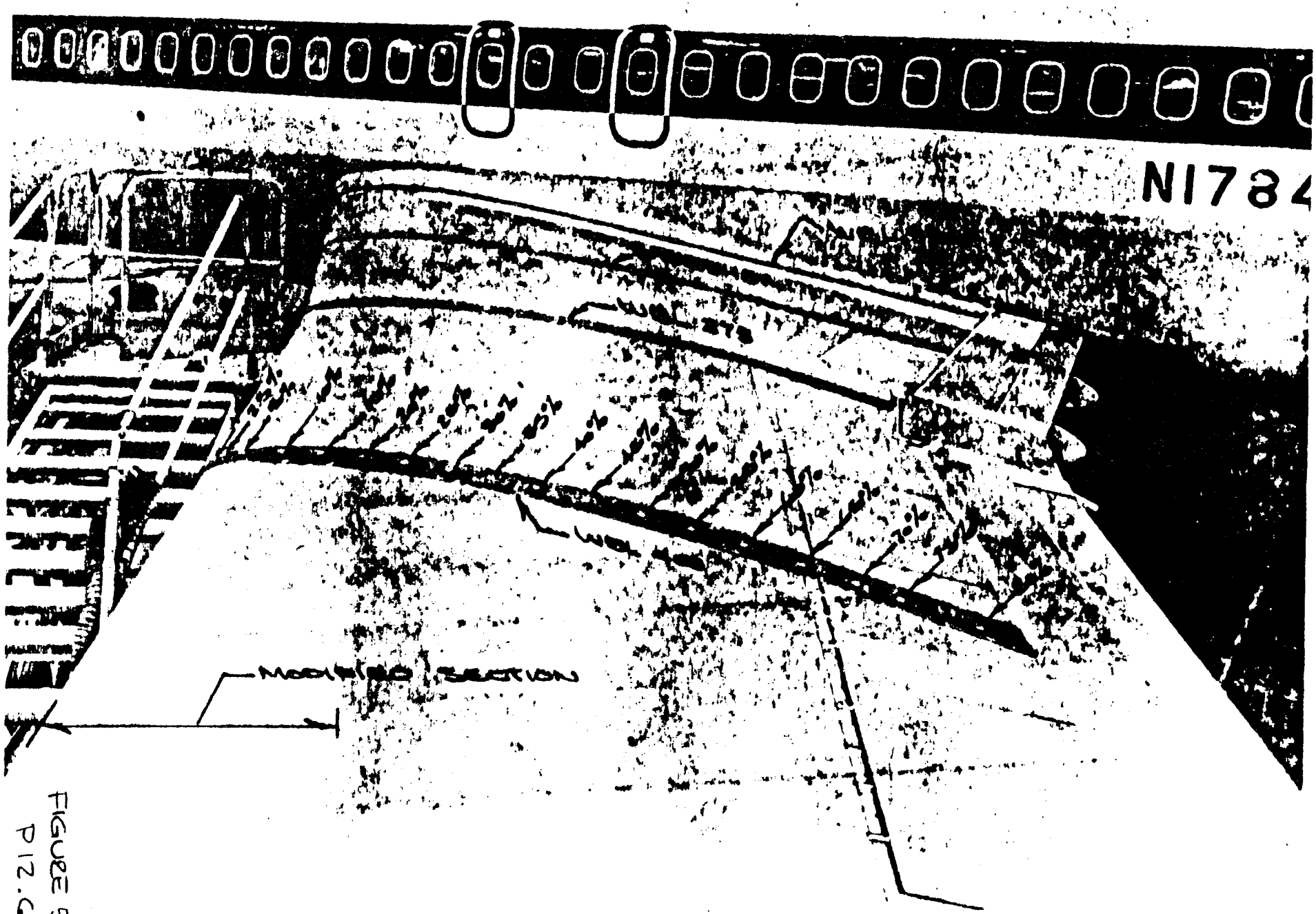

FIGURE 55
P12.68

832

TAKE-OFF & LANDING REQMNTS

ITEM	FUNCTION
• APACS (THEODOLITE CAMERA)	DISTANCE, VELOCITY, HEIGHT
• TRAPPED STATIC • INS	ON BOARD AIRSPEED & DISTANCE
• RADIO ALTITUDE	ON BOARD HEIGHT
• RYAN RATE OF SINK SYSTEM	ON BOARD SINK RATES
• GEAR OLEO POSITION	V_{MU} LIFT-OFF
• AXLE STRAIN GAGES	V_R & V_{LO} PERFORMANCE
• STICK POSITION	ROTATION
• TAIL WAND & TAIL SKID CONTACT	V_{MU} CONDITION MONITORING
• PITCH ANGLE	ON BOARD DATA
• THROTTLE POSITION	ENGINE CUT IDENTIFICATION
• METERED BRAKE PRESSURES	BRAKE APPLICATION
• WHEEL SPEEDS, ANTI SKID VALVE VOLTAGES, BRAKE TEMP'S.	DIAGNOSTIC FOR ANTI SKID PERFORMANCE & BRAKE TEMP. MONITOR.
• ENGINE PERFORMANCE & FUEL FLOW	THRUST AND WEIGHT

P12.69

FIGURE 56

STALL SPEED REQUIRMENTS

ITEM	FUNCTION
• TRAILING CONE (BOMB) AIRSPEED	AIRSPEED, ENTRY RATE, M
• NORMAL & LONGITUDINAL ACCEL.	g-BREAK & CORRECTED C_L
• ANGLE OF ATTACK & STICK SHAKER	α LIMIT & STICK SHAKER EVENT
• PILOTS SEAT TRACK NORMAL g	INITIAL BUFFET
• STICK FORCE, ELEVATOR, STAB TRIM, RUDDER & AILERON POSITION	LONGITUDINAL STABILITY & HANDLING CHARACTERISTICS
• FUEL FLOW	

FIGURE 57
P12.70

DRAG AND NAM / LB REQUIREMENTS

ITEM	FUNCTION
• ENGINE PERFORMANCE AND FUEL FLOW	THRUST, WEIGHT, FUEL FLOW
• TRAILING CONE AIRSPEED,	AIRSPEED, ALTITUDE, M
• GROUND SPEED, HEADING, TRACK ANGLE (INS)	ON BOARD CONDITION MONITOR. AND ENERGY CORRECTIONS
• TOTAL AIR TEMPERATURE	TRUE AIRSPEED & ENGINE PERFORM.
• LONGITUDINAL TRACK ACCEL. (INS)	PILOT AID IN CONDITION MONITOR.
• CONTROL POSITIONS AND SIDESLIP	ESTABLISHES CONTROL REQMNTS DURING YAW DRAG & CHECK CLIMB
• DIFFERENTIAL PRESSURES	CONE VS AIRPLANE SYSTEM

P12.71

FIGURE 58